computation

Special Issue Reprint

10th Anniversary of *Computation*—Computational Heat and Mass Transfer (ICCHMT 2023)

Edited by
Ali Cemal Benim, Rachid Bennacer, Abdulmajeed A. Mohamad, Paweł Ocłoń, Sang-Ho Suh and Jan Taler

mdpi.com/journal/computation

MDPI

10th Anniversary of *Computation*—Computational Heat and Mass Transfer (ICCHMT 2023)

10th Anniversary of *Computation*—Computational Heat and Mass Transfer (ICCHMT 2023)

Guest Editors

Ali Cemal Benim
Rachid Bennacer
Abdulmajeed A. Mohamad
Paweł Ocłoń
Sang-Ho Suh
Jan Taler

MDPI

Basel • Beijing • Wuhan • Barcelona • Belgrade • Novi Sad • Cluj • Manchester

Guest Editors

Ali Cemal Benim
Department of Mechanical and Process Engineering
Düsseldorf University of Applied Sciences
Düsseldorf
Germany

Rachid Bennacer
Recherche: Génie Civil & Envir.
ENS Paris-Saclay
Gif-sur-Yvette
France

Abdulmajeed A. Mohamad
Department of Mechanical and Manufacturing Engineering
University of Calgary
Calgary
Canada

Paweł Ocłoń
Department of Energy
Cracow University of Technology
Cracow
Poland

Sang-Ho Suh
School of Mechanical Engineering
Soongsil University
Seoul
Korea, South

Jan Taler
Department of Energy
Cracow University of Technology
Cracow
Poland

Editorial Office
MDPI AG
Grosspeteranlage 5
4052 Basel, Switzerland

This is a reprint of the Special Issue, published open access by the journal *Computation* (ISSN 2079-3197), freely accessible at: www.mdpi.com/journal/computation/special_issues/029N9ZJN7Y.

For citation purposes, cite each article independently as indicated on the article page online and using the guide below:

Lastname, A.A.; Lastname, B.B. Article Title. *Journal Name* **Year**, *Volume Number*, Page Range.

ISBN 978-3-7258-3464-8 (Hbk)
ISBN 978-3-7258-3463-1 (PDF)
https://doi.org/10.3390/books978-3-7258-3463-1

Contents

Preface . . . . . **ix**

Peter Brearley, Umair Ahmed and Nilanjan Chakraborty
Implications of Using Scalar Forcing to Sustain Reactant Mixture Stratification in Direct Numerical Simulations of Turbulent Combustion
Reprinted from: *Computation* **2024**, *12*, 114, https://doi.org/10.3390/computation12060114 . . . **1**

Juan I. Ramos
Finite Difference Methods Based on the Kirchhoff Transformation and Time Linearization forthe Numerical Solution of Nonlinear Reaction–Diffusion Equations
Reprinted from: *Computation* **2024**, *12*, 218, https://doi.org/10.3390/computation12110218 . . . **18**

Juan I. Ramos
Effects of Anisotropy, Convection, and Relaxation on Nonlinear Reaction-Diffusion Systems
Reprinted from: *Computation* **2024**, *12*, 214, https://doi.org/10.3390/computation12110214 . . . **45**

Pius W. M. Chin
The Theory and Computation of the Semi-Linear Reaction–Diffusion Equation with Dirichlet Boundaries
Reprinted from: *Computation* **2024**, *12*, 142, https://doi.org/10.3390/computation12070142 . . . **66**

Augustín Varga, Ján Kizek, Miroslav Rimár, Marcel Fedák, Ivan Čorný and Ladislav Lukáč
Modeling of Heat Flux in a Heating Furnace
Reprinted from: *Computation* **2023**, *11*, 144, https://doi.org/10.3390/computation11070144 . . . **84**

Natalia Sorokova, Miroslav Variny, Yevhen Pysmennyy and Yuliia Kol'chik
Mathematical Model and Numerical Method of Calculating the Dynamics of High-Temperature Drying of Milled Peat for the Production of Fuel Briquettes
Reprinted from: *Computation* **2023**, *11*, 53, https://doi.org/10.3390/computation11030053 . . . . **100**

Marek Jaszczur, Marek Borowski, Joanna Halibart, Klaudia Zwolińska-Glądys and Patryk Marczak
Optimization of the Small Wind Turbine Design—Performance Analysis
Reprinted from: *Computation* **2024**, *12*, 215, https://doi.org/10.3390/computation12110215 . . . **117**

Hady Aboujaoude, Guillaume Polidori, Fabien Beaumont, Sébastien Murer, Yessine Toumi and Fabien Bogard
Comparative Study of Deflector Configurations under Variable Vertical Angle of Incidence and Wind Speed through Transient 3D CFD Modeling of Savonius Turbine
Reprinted from: *Computation* **2024**, *12*, 204, https://doi.org/10.3390/computation12100204 . . . **135**

Doğan Güneş and Ergin Kükrer
Performance Rating and Flow Analysis of an Experimental Airborne Drag-Type VAWT Employing Rotating Mesh
Reprinted from: *Computation* **2024**, *12*, 77, https://doi.org/10.3390/computation12040077 . . . . **150**

Md Rakibuzzaman, Sang-Ho Suh, Hyung-Woon Roh, Kyung Hee Song, Kwang Chul Song and Ling Zhou
Hydraulic Performance Optimization of a Submersible Drainage Pump
Reprinted from: *Computation* **2024**, *12*, 12, https://doi.org/10.3390/computation12010012 . . . . **171**

Arif Cem Gözükara and Uygar Ateş Ceylan
Numerical Method for Predicting Transient Aerodynamic Heating in Hemispherical Domes
Reprinted from: *Computation* **2024**, *12*, 162, https://doi.org/10.3390/computation12080162 . . . **188**

Ergin Kükrer and Nurdil Eskin
Air–Water Two-Phase Flow Dynamics Analysis in Complex U-Bend Systems through Numerical Modeling
Reprinted from: *Computation* **2024**, *12*, 81, https://doi.org/10.3390/computation12040081 . . . . **201**

W. M. Faizal, C. Y. Khor, Suhaimi Shahrin, M. H. M. Hazwan, M. Ahmad and M. N. Misbah et al.
Computational Fluid Dynamics Analysis of Varied Cross-Sectional Areas in Sleep Apnea Individuals across Diverse Situations
Reprinted from: *Computation* **2024**, *12*, 16, https://doi.org/10.3390/computation12010016 . . . . **215**

Sidhartha Bhowmick, Laxmi Rani Roy, Feng Xu and Suvash C. Saha
Natural Convection Fluid Flow and Heat Transfer in a Valley-Shaped Cavity
Reprinted from: *Computation* **2024**, *12*, 146, https://doi.org/10.3390/computation12070146 . . . **232**

César Augusto Borges da Silva Reis, Daniel Botezelli, Arthur Mendonça de Azevedo, Elisan dos Santos Magalhães and Aristeu da Silveira Neto
Accelerating Conjugate Heat Transfer Simulations in Squared Heated Cavities through Graphics Processing Unit (GPU) Computing
Reprinted from: *Computation* **2024**, *12*, 106, https://doi.org/10.3390/computation12050106 . . . **256**

Ernandes Nascimento, Elisan Magalhães, Arthur Azevedo, Luiz E. S. Paes and Ariel Oliveira
An Implementation of LASER Beam Welding Simulation on Graphics Processing Unit Using CUDA
Reprinted from: *Computation* **2024**, *12*, 83, https://doi.org/10.3390/computation12040083 . . . . **275**

Daniel F. Szambien, Maximilian R. Ziegler, Christoph Ulrich and Roland Scharf
Analysis of a Novel Method for Generating 3D Mesh at Contact Points in Packed Beds
Reprinted from: *Computation* **2024**, *12*, 89, https://doi.org/10.3390/computation12050089 . . . . **293**

Ariel Flores Monteiro de Oliveira, Elisan dos Santos Magalhães, Kahl Dick Zilnyk, Philippe Le Masson and Ernandes José Gonçalves do Nascimento
Numerical Estimation of Nonlinear Thermal Conductivity of SAE 1020 Steel
Reprinted from: *Computation* **2024**, *12*, 92, https://doi.org/10.3390/computation12050092 . . . . **307**

İrem Bağlan and Erman Aslan
Analytical and Numerical Investigation of Two-Dimensional Heat Transfer with Periodic Boundary Conditions
Reprinted from: *Computation* **2024**, *12*, 11, https://doi.org/10.3390/computation12010011 . . . . **326**

Musawenkosi Patson Mkhatshwa
Overlapping Grid-Based Spectral Collocation Technique for Bioconvective Flow of MHD Williamson Nanofluid over a Radiative Circular Cylindrical Body with Activation Energy
Reprinted from: *Computation* **2024**, *12*, 75, https://doi.org/10.3390/computation12040075 . . . . **342**

Rusya Iryanti Yahaya, Norihan Md Arifin, Ioan Pop, Fadzilah Md Ali and Siti Suzilliana Putri Mohamed Isa
Hybrid Nanofluid Flow over a Shrinking Rotating Disk: Response Surface Methodology
Reprinted from: *Computation* **2024**, *12*, 141, https://doi.org/10.3390/computation12070141 . . . **369**

Nazrul Azlan Abdul Samat, Norfifah Bachok and Norihan Md Arifin
Boundary Layer Stagnation Point Flow and Heat Transfer over a Nonlinear Stretching/Shrinking Sheet in Hybrid Carbon Nanotubes: Numerical Analysis and Response Surface Methodology under the Influence of Magnetohydrodynamics
Reprinted from: *Computation* **2024**, *12*, 46, https://doi.org/10.3390/computation12030046 . . . . **383**

Shafquat Rana, Uzair Jamil, Nima Asgari, Koami S. Hayibo, Julia Groza and Joshua M. Pearce
Residential Sizing of Solar Photovoltaic Systems and Heat Pumps for Net Zero Sustainable Thermal Building Energy
Reprinted from: *Computation* **2024**, *12*, 126, https://doi.org/10.3390/computation12060126 . . . **412**

Preface

This Special Issue of Computation presents 23 papers selected from the 14th International Conference on Computational Heat and Mass Transfer (ICCHMT2023). The conference was held in Düsseldorf, Germany, 4-8 September 2023, and was organized by the Düsseldorf University of Applied Sciences. The ICCHMT2023 chairs were Prof. Dr. Ali Cemal Benim from the Düsseldorf University of Applied Sciences, Germany (Local Chair); Prof. Dr. Rachid Bennacer from École Normale Supérieure Paris-Saclay, France (Co-Chair); Prof. Abdulmajeed Mohamad from the University of Calgary, Canada (Founding Chair); Prof. Dr. Paweł Ocłoń from the Cracow University of Technology, Poland (Co-Chair); Prof. Dr. Sang-Ho Suh from Soongsil University, South Korea (Co-Chair); and Prof. Dr. Jan Taler from the Cracow University of Technology, Poland (Co-Chair).

The ICCHMT conference series addresses specifically the research, development, and application of the computational methods in heat and mass transfer, without, however, excluding experimental and theoretical approaches, especially as a means of validation and inspiration. The conferences provide a platform for scientists and engineers to meet regularly to discuss new ideas and developments on computational methods and their applications, as well as a good opportunity for young scientists and engineers to explore the art of computational methods and future perspectives while further broadening their horizons.

The ICCHMT conference series has been successfully organized in various countries including Brazil, Canada, China, Cyprus, France, Italy, South Korea, Poland, and Turkey since 1999 and has established itself as a reference event in the community of engineers and scientists.

The ICCHMT2023 had a great resonance in the technical and scientific communities all over the world. A total of 239 papers from more than 40 countries were presented at the conference. The selected 23 papers for the current Special Issue were then prepared in an extended form and subjected to a separate, regular peer review process steered by the editorial office of Computation.

Ali Cemal Benim, Rachid Bennacer, Abdulmajeed A. Mohamad, Paweł Ocłoń, Sang-Ho Suh, and Jan Taler

Guest Editors

computation

MDPI

Article

Implications of Using Scalar Forcing to Sustain Reactant Mixture Stratification in Direct Numerical Simulations of Turbulent Combustion

Peter Brearley [1,2], Umair Ahmed [2] and Nilanjan Chakraborty [2,*]

[1] Department of Aeronautics, Imperial College London, London SW7 2BX, UK; p.brearley@imperial.ac.uk
[2] School of Engineering, Newcastle University, Newcastle upon Tyne NE1 7RU, UK; umair.ahmed@newcastle.ac.uk
* Correspondence: nilanjan.chakraborty@newcastle.ac.uk

Abstract: A recently proposed scalar forcing scheme that maintains the mixture fraction mean, root-mean-square and probability density function in the unburned gas can lead to a statistically quasi-stationary state in direct numerical simulations of turbulent stratified combustion when combined with velocity forcing. Scalar forcing alongside turbulence forcing leads to greater values of turbulent burning velocity and flame surface area in comparison to unforced simulations for globally fuel-lean mixtures. The sustained unburned gas mixture inhomogeneity changes the percentage shares of back- and front-supported flame elements in comparison to unforced simulations, and this effect is particularly apparent for high turbulence intensities. Scalar forcing does not significantly affect the heat release rates due to different modes of combustion and the micro-mixing rate within the flame characterised by scalar dissipation rate of the reaction progress variable. Thus, scalar forcing has a significant potential for enabling detailed parametric studies as well as providing well-converged time-averaged statistics for stratified-mixture combustion using Direct Numerical Simulations in canonical configurations.

Keywords: scalar forcing; scalar mixing; stratified combustion; mixture fraction; direct numerical simulation

Citation: Brearley, P.; Ahmed, U.; Chakraborty, N. Implications of Using Scalar Forcing to Sustain Reactant Mixture Stratification in Direct Numerical Simulations of Turbulent Combustion. *Computation* **2024**, *12*, 114. https://doi.org/10.3390/computation12060114

Academic Editors: Ali Cemal Benim, Abdulmajeed A. Mohamad, Sang-Ho Suh, Rachid Bennacer, Paweł Oclon and Jan Taler

Received: 23 April 2024
Revised: 20 May 2024
Accepted: 21 May 2024
Published: 3 June 2024

1. Introduction

Forcing the turbulent velocity field enables Direct Numerical Simulations (DNS) of turbulent fluid motion to reach a quasi-stationary state in canonical configurations where no other mechanism is available for turbulence generation. This enables the extraction of converged statistics from DNS data by time averaging, even for a limited domain size. Time-averaged statistics from statistically stationary DNS databases have assisted numerous studies in the field of turbulent non-reacting and reacting flow analyses. Until recently, the benefits of achieving statistical stationarity in DNS of turbulent combustion in canonical configurations with forced turbulence have been limited to premixed combustion simulations, since mixture inhomogeneity in the unburned gas decays under sustained turbulence conditions in the case of partially premixed mixtures. Without any external scalar fluctuation generating mechanism, a statistically quasi-stationary state can only be achieved once the reactants have become perfectly mixed (i.e., premixed combustion). As such, many DNS studies of turbulent stratified-mixture combustion have relied on unsteady decaying turbulence conditions (e.g., [1–13]). However, mixture inhomogeneity in the unburned gas can be sustained with scalar forcing by including an additional term in the species conservation equations, which can be utilised to reach a quasi-steady state for stratified-mixture combustion. An appropriate scalar forcing term offers additional advantages aside from converged statistics, such as enabling precise control over the probability density function (PDF) of the species mass fractions (and the corresponding

mixture fraction) in the unburned gas, enabling comprehensive parametric analyses on the effects of the mixture fraction distribution.

Stratified-mixture combustion offers some benefits compared to premixed combustion, such as allowing for leaner combustion conditions, manipulating the flammability limits, flame propagation rate and pollutant emission rates [14]. Moreover, stratified-mixture combustion can also take place as a result of unintentional inadequate mixing. Lipatnikov [14] and Domingo et al. [15] provided an extensive review of experimental and numerical findings of stratified-mixture combustion. High-performance computing has enabled DNS of stratified-mixture combustion [1–13,16–19], and the vast majority of these studies have been conducted for statistically planar flames in canonical 'flame-in-a-box' configuration [1–13]. Richardson and Chen [16] and Brearley et al. [19] analysed turbulent stratified-mixture combustion using three-dimensional DNS to analyse the effects of the relative alignments of equivalence ratio and reaction progress variable gradients on the global behaviours of burning, flame propagation rate and flame surface area and their modelling implications. Proch et al. [17] and Inanc et al. [18] carried out flame-resolved three-dimensional high-fidelity simulations of turbulent stratified-mixture combustion of a laboratory-scale configuration used in experiments by Barlow et al. [20] and Sweeney et al. [21,22]. The aforementioned DNS analyses on turbulent stratified-mixture combustion offered fundamental physical information on the stratified flame structure [1–3,5,8,13,16,18,19] and flame propagation rate [4,12,16,18]. This information was subsequently utilised to develop closure methodologies for scalar variances and co-variances [3,5,11], turbulent scalar flux [9], flame surface density [10,19], and scalar dissipation and cross-scalar dissipation rates [7,8,13].

The development of a scalar forcing methodology that accurately captures characteristics of turbulent stratified combustion has been the subject of recent research efforts [23,24] where the effectiveness of the methodology was demonstrated mainly for passive scalar mixing. The sensitivity of the method to different turbulence and scalar conditions, including decaying turbulence and different turbulence forcing schemes (Lundgren forcing [25] and Modified Bandwidth forcing [26]) along with different scalar length scales, has been performed in the earlier work by Brearley et al. [24]. It was found that the length scale of the scalar distribution at the end of simulation time is independent of the initial value specified for the scalar length scale and was only dependent on the nature of the velocity forcing scheme. Ideally, the scalar forcing should only influence the root-mean-square (rms) scalar value and the underlying scalar distribution, but should not interfere with other flow properties. Therefore, the evolution of the scalar-to-turbulence integral length scale ratio should be determined by turbulent mixing in the unburned mixture. The mean values of the normalised scalar dissipation rate were shown to change from its initial value for scalar forcing irrespective of the nature of turbulent flow forcing. Furthermore, it has also been shown by Brearley et al. [24] that the PDF shape can be maintained for all turbulence conditions, i.e., decaying turbulence, Lundgren forcing and Modified Bandwidth forcing, without any modifications needed to the scalar forcing method. Brearley et al. [24] also showed that the root-mean-square value of scalar fluctuation is faithfully maintained by the scalar forcing technique for different PDF shapes (i.e., bimodal or Gaussian). However, the influence of sustained mixture stratification on the structure and dynamics of turbulent planar flames is yet to be analysed in detail. Therefore, the main objectives of this paper are (i) to understand the capabilities and limitations of the scalar forcing methodology by simulating a varied DNS database, and (ii) to analyse the statistical behaviours of turbulent burning velocity, flame surface area and reaction zone structure (e.g., the fractional share of front- and back-supported combustion, and the contributions of heat release originating from different modes of combustion) extracted from DNS of turbulent stratified flame simulations where (a) both the scalar field and the turbulence field are forced, (b) only the scalar field is forced and (c) where neither fields are subject to external forcing.

The following section provides the mathematical description of the scalar forcing methodology and Section 3 describes the DNS database. The results and corresponding

discussion are presented in Section 4, which is followed by the conclusions of the work in Section 5.

2. Forcing Methodology

The scalar forcing methodology proposed by Daniel et al. [23] and further developed by Brearley et al. [24] has been adopted for this study as it can maintain a prescribed distribution (i.e., probability density function (PDF)) of a scalar field (e.g., bimodal, uniform, or bell-shaped). Consequently, the mean, root-mean-square (rms) and scalar bounds are also maintained.

A detailed description and derivation of the scalar forcing scheme used here are provided by Daniel et al. [23] for the original scalar forcing scheme and details on the modified scalar forcing scheme to account for the feedback on the scalar dissipation rate to maintain the prescribed rms value of the scalar fluctuations are available in Brearley et al. [24]. It should be recognised here that Daniel et al. [23] originally proposed the scalar forcing methodology based on a reaction analogy to describe mixing. According to this analogy, hypothetical chemical species have reactions which constitute a demixing processes that transform a partially mixed state into the excess pure component. In terms of a scalar field, the reactions transform the regions with below-average scalar values into the lower bound values and regions with above-average scalar values into the upper bound values. Thus, the reactions counteract the effects of diffusion and turbulent mixing. A complete derivation for this is already provided in the work by Daniel et al. [23] and is not presented in the current paper to avoid repetition and to maintain brevity as the main focus of the paper is the application of the scalar forcing methodology to reacting flow simulations of stratified mixtures.

The transport equation of a species mass fraction Y_i under scalar forcing is

$$\frac{\partial(\rho Y_i)}{\partial t} + \frac{\partial(\rho u_k Y_i)}{\partial x_k} = \frac{\partial}{\partial x_k}\left(\rho D \frac{\partial Y_i}{\partial x_k}\right) + \dot{\omega}_i + \rho f_{Y_i} \tag{1}$$

where Y_i represents the reactant species in the unburned gas (i.e., Y_F and Y_O), $\dot{\omega}_i$ is its reaction rate (negligible in the unburned gas where the scalar forcing is applied) and f_{Y_i} is the scalar forcing term (i.e., f_{Y_F} and f_{Y_O}). Daniel et al. [23] developed a forcing scheme capable of satisfying characteristics of fuel-air stratification by considering a hypothetical chemical reaction that converts mixed fluid into its unmixed states, and proposed a forcing term for a generic scalar ψ (the scalar being forced) which is given as [23]:

$$f_\psi = \begin{cases} -(\psi_u - \psi_l) j K \left(\frac{\psi_u + \psi_l - 2\psi}{\psi_u - \psi_l}\right)^g \left(\frac{\psi - \psi_l}{\psi_u - \psi_l}\right)^j & \text{when } \psi \leq \psi_\mathrm{m} \\ +(\psi_u - \psi_l) j K \left(\frac{2\psi - \psi_u - \psi_l}{\psi_u - \psi_l}\right)^g \left(\frac{\psi_u - \psi}{\psi_u - \psi_l}\right)^j & \text{when } \psi > \psi_\mathrm{m} \end{cases} \tag{2}$$

where ψ_l and ψ_u are the chosen lower and upper bounds of ψ respectively with a target mean $\psi_\mathrm{m} = (\psi_u + \psi_l)/2$ assuming a symmetrical scalar distribution. The reaction rate constant of the hypothetical chemical reaction is K, with j and g being the stoichiometric coefficients. The hypothetical chemical reaction is given by:

$$jM + gE_l \rightarrow (2j + g)E_l \quad \text{when } \psi \leq \psi_\mathrm{m} \tag{3a}$$

$$jM + gE_u \rightarrow (2j + g)E_u \quad \text{when } \psi > \psi_\mathrm{m} \tag{3b}$$

where M is a hypothetical chemical species representing the mixed fluid state, E_l and E_u are hypothetical chemical species representing the extra concentrations of unmixed fluid towards the lower or upper bounds of the scalar respectively. Brearley et al. [24] made modifications to Equation (2) to make it more robust for a chemically reacting flow. According to Daniel et al. [23] K value should be chosen such that it corresponds to the desired steady state scalar dissipation rate, which controls the scalar PDF distribution. As in the case of reacting flow simulations the prescribed rms value of scalar fluctuation ψ_0' needs

to be maintained, a rms error signal term $(\psi_0' - \psi')$ to Equation (2) was introduced [24]. Then, K is considered as the constant in the proportional control system to maintain ψ'. The forcing term with these modifications therefore takes the following form:

$$f_\psi = \begin{cases} -(\psi_0' - \psi')(\psi_u - \psi_l) jK \left(\frac{\psi_u + \psi_l - 2\psi}{\psi_u - \psi_l}\right)^g \left(\frac{\psi - \psi_l}{\psi_u - \psi_l}\right)^j & \text{when } \psi \leq \psi_\mathrm{m} \\ +(\psi_0' - \psi')(\psi_u - \psi_l) jK \left(\frac{2\psi - \psi_u - \psi_l}{\psi_u - \psi_l}\right)^g \left(\frac{\psi_u - \psi}{\psi_u - \psi_l}\right)^j & \text{when } \psi > \psi_\mathrm{m} \end{cases} \tag{4}$$

In the case when the scalar field is subject to asymmetries, the above forcing scheme would eventually convert all the fluid into a uniform field of either $\psi = \psi_u$ or $\psi = \psi_l$. Such asymmetries could be introduced in the initial conditions, or due to the flame preferentially propagating through certain mixture compositions. In order to avoid this issue, the expression given by Equation (4) was modified by Brearley et al. [24] to allow for a self-correction mechanism. According to this modification, the instantaneous mean scalar $\langle\psi\rangle$, not to be confused with the target mean ψ_m, is calculated and fed back to the forcing equation which allows for self-regulation of the PDF of ψ. The updated ψ_m when used in the forcing equation yields:

$$\psi_\mathrm{m}^* = K^*(\langle\psi\rangle - \psi_\mathrm{m}) + \psi_\mathrm{m} \tag{5}$$

where K^* is the proportional control constant to maintain ψ_m. In addition, hypothetical lower and upper limits ψ_l^* and ψ_u^* corresponding to ψ_m^* should be evaluated in the following manner:

$$\psi_l^* = \psi_u - 2(\psi_u - \psi_\mathrm{m}^*) \tag{6a}$$

$$\psi_u^* = \psi_l + 2(\psi_\mathrm{m}^* - \psi_l) \tag{6b}$$

Note that these limits do not influence the location of the specified upper and lower bounds ψ_u and ψ_l. In this case ψ_u^* is only used in the calculation of the forcing term for $\psi \leq \psi_\mathrm{m}^*$, and ψ_l^* is only used in the calculation for $\psi > \psi_\mathrm{m}^*$. This yields the modified forcing term as [24]:

$$f_\psi = \begin{cases} -(\psi_0' - \psi')(\psi_u^* - \psi_l) jK \left(\frac{\psi_u^* + \psi_l - 2\psi}{\psi_u^* - \psi_l}\right)^g \left(\frac{\psi - \psi_l}{\psi_u^* - \psi_l}\right)^j & \text{when } \psi \leq \psi_\mathrm{m}^* \\ +(\psi_0' - \psi')(\psi_u - \psi_l^*) jK \left(\frac{2\psi - \psi_u - \psi_l^*}{\psi_u - \psi_l^*}\right)^g \left(\frac{\psi_u - \psi}{\psi_u - \psi_l^*}\right)^j & \text{when } \psi > \psi_\mathrm{m}^* \end{cases} \tag{7}$$

It should be recognised here that when different instantaneous values of global mean $\langle\psi\rangle$ with $\psi_l = 0$ and $\psi_u = 1$ are used, the forcing term naturally reduces to zero at the specified bounds under all conditions. The effects of modifying the stoichiometric coefficients (j and g) change the shape of the forcing term and consequently, the resulting scalar PDF. Following Brearley et al. [24] $j = g = 1$ is considered and a detailed account of the sensitivity to these parameters is provided by Daniel et al. [23]. It has been demonstrated in [24] that the forcing term tends to maintain the required mean values of the scalar, when $\langle\psi\rangle < \psi_\mathrm{m}$ and $\langle\psi\rangle > \psi_\mathrm{m}$, by using the self-correction control system.

For the transport equations of the species mass fractions as shown in Equation (1), the following source terms are used:

$$\begin{aligned} f_{Y_F} &= \begin{cases} -(Y_{F0}' - Y_F')(Y_{Fu}^* - Y_{Fl}) K \left(\frac{Y_{Fu}^* + Y_{Fl} - 2Y_F}{Y_{Fu}^* - Y_{Fl}}\right) \left(\frac{Y_F - Y_{Fl}}{Y_{Fu}^* - Y_{Fl}}\right) & \text{when } Y_F \leq Y_{Fm}^* \\ +(Y_{F0}' - Y_F')(Y_{Fu} - Y_{Fl}^*) K \left(\frac{2Y_F - Y_{Fu} - Y_{Fl}^*}{Y_{Fu} - Y_{Fl}^*}\right) \left(\frac{Y_{Fu} - Y_F}{Y_{Fu} - Y_{Fl}^*}\right) & \text{when } Y_F > Y_{Fm}^* \end{cases} \\ f_{Y_O} &= \begin{cases} +(Y_{O0}' - Y_O')(Y_{Ou}^* - Y_{Ol}) K \left(\frac{Y_{Ou}^* + Y_{Ol} - 2Y_O}{Y_{Ou}^* - Y_{Ol}}\right) \left(\frac{Y_O - Y_{Ol}}{Y_{Ou}^* - Y_{Ol}}\right) & \text{when } Y_O \leq Y_{Om}^* \\ -(Y_{O0}' - Y_O')(Y_{Ou} - Y_{Ol}^*) K \left(\frac{2Y_O - Y_{Ou} - Y_{Ol}^*}{Y_{Ou} - Y_{Ol}^*}\right) \left(\frac{Y_{Ou} - Y_O}{Y_{Ou} - Y_{Ol}^*}\right) & \text{when } Y_O > Y_{Om}^* \end{cases} \end{aligned} \tag{8}$$

where subscripts l and u indicate the chosen lower and upper bounds of the scalar, a subscript m gives the mean value, and a subscript 0 denotes the target value. These quantities

can be derived from the target mixture fraction $\xi = (Y_F - Y_O/s + Y_{O\infty}/s)/(Y_{F\infty} + Y_{O\infty}/s)$ values in the unburned gas, i.e., $Y_F = Y_{F\infty}\xi$ and $Y_O = Y_{O\infty}(1-\xi)$ where $Y_{F\infty} = 1.0$ and $Y_{O\infty} = 0.233$ being the fuel and oxidiser mass fractions in the pure fuel and pure air, respectively, and s is the stoichiometric oxygen-to-fuel mass ratio. Y'_F and Y'_O are the rms values of the respective scalar fields in the unburned gas, and Y'_{F0} and Y'_{O0} are their target values to be maintained. The parameter K is the proportional control constant, that must exceed approximately $K/(1/T_{\text{turb}}) > 10^3$ for the rms value of the scalar fluctuation to be maintained effectively, with greater values being found to have no adverse effects on the results [24]. Quantities marked with a superscript asterisk (*) are altered by the forcing scheme throughout the simulation to maintain the mean mixture fraction $\langle\xi\rangle$ at the target values [23,24] which ensures that the scalar field does not diverge to a fully mixed state at one of the scalar bounds. These quantities in terms of mixture fraction are defined as $\xi^*_m = K^*(\langle\xi\rangle - \xi_m) + \xi_m$, $\xi^*_l = \xi_u - 2(\xi_u - \xi^*_m)$, $\xi^*_u = \xi_l + 2(\xi^*_m - \xi_l)$, where K^* is the proportional control constant in the mean correction control system. A K^* value exceeding 1.0 is required to ensure that the forcing term can effectively prevent the scalar mean from drifting, where values up to 10 have been tested and the target mean value of the scalar is maintained more faithfully for higher values of K^* [24]. The corresponding quantities for the species mass fractions are then evaluated from the mixture fraction using the relations $Y_F = Y_{F\infty}\xi$ and $Y_O = Y_{O\infty}(1-\xi)$.

It should be noted that it is possible to solve an additional transport equation for a passive scalar such as the mixture fraction ξ, and apply scalar forcing to its transport equation only. Then, Y_F and Y_O can be evaluated in the unburned gas only at the end of each timestep from the mixture fraction and reaction progress variable [24]. This is mathematically equivalent to forcing the species mass fractions directly. Interested readers are referred to Brearley et al. [24] for a more thorough discussion on the scalar forcing scheme with its derivation, validation and mathematical properties. The scalar forcing is employed only in the unburned gas where the chemical reaction is negligible, which is characterised by $c < c_\epsilon = 0.001$, where c is the reaction progress variable which monotonically increases from 0 to 1 from the unburned gas to the fully burned gas. The reaction progress variable c is defined as [1]

$$c = \frac{\xi Y_{F\infty} - Y_F}{\xi Y_{F\infty} - \max\left[0, \frac{\xi - \xi_{st}}{1-\xi_{st}}\right] Y_{F\infty}} \tag{9}$$

The forcing scheme [23,24] does not have any impact during the reacting simulations as the forcing term is switched off in the reaction/heat release zone. The value of $c = 0.001$ was chosen as the boundary between the unburned gas and the flame so that the pure mixing relations between the mixture fraction and the species mass fractions can be used without any significant loss in accuracy. In reality, $c = c_\epsilon$ with c_ϵ being a small positive fraction can be a suitable choice. It has been demonstrated elsewhere [24] that reducing c_ϵ from 0.01 by up to two orders of magnitude has a negligible effect on the flame surface area and propagation rate, and will not be repeated in this paper for the sake of conciseness. Interested readers are referred to Brearley et al. [24] for the detailed description of the validation and performance of the aforementioned scalar forcing methodology for passive scalar mixing in non-reacting flows and the performance of this scalar forcing for different values of K and K^*. It was demonstrated that the mean and rms values of the forced scalar are faithfully maintained along with the prescribed PDF for large values of K^* and K (i.e., $K^* \gg 1$ and $K \gg 1/T_{char} \gg 1$ where T_{char} is the characteristic timescale which can be either chemical timescale or eddy turnover time for stratified-mixture combustion). The above information is not repeated here as this paper will principally focus on stratified-mixture combustion simulations in the presence of scalar forcing according to Ref. [24].

3. DNS Database

Table 1 summarises the newly generated DNS database considered for this analysis. The cases (a) and (b) in Table 1 have been simulated under both scalar and velocity forcing, whereas simulations in cases (c) and (d) have been conducted only under scalar

forcing and cases (e) and (f) are allowed to freely mix without the influence of any external forcing and flame-turbulence interaction takes place under decaying turbulence. Only cases (a) and (b) are able to reach a statistically quasi-stationary state as both the scalar and velocity fluctuations are required to be maintained. The remaining cases (c–f) are provided to highlight the influence of the newly developed scalar forcing scheme [24]. Table 1 shows the values of u'/S_b, $\ell/\delta_{L,m}$, $\langle\xi\rangle$, ξ', Damkohler number $Da = \ell S_b/u'\delta_{L,m}$, Karlovitz number $Ka = (u'/S_b)^{3/2}(\ell/\delta_{L,m})^{-1/2}$, ℓ_ϕ/ℓ, domain size and the corresponding grid size, where ℓ and ℓ_ϕ are the integral length scale of turbulence and equivalence ratio $\phi = \xi(1-\xi_{st})/[\xi_{st}(1-\xi)]$ in the unburned gas, respectively, and S_b and $\delta_{L.m}$ are the unstretched laminar burning velocity and thermal flame thickness of the unstretched laminar flame corresponding to $\phi = 0.8$, respectively. The flame thickness $\delta_{L,m}$ is defined as $(T_{ad(\phi=0.8)} - T_0)/\max(\nabla\hat{T}_L)$ where T_0, $T_{ad(\phi=0.8)}$ and $\hat{T}$ are the unburned gas temperature, adiabatic flame temperature for $\phi = 0.8$ and dimensional instantaneous temperature, respectively. The simulations consist of statistically planar methane-air flames propagating into an imperfectly mixed, globally lean fuel-air mixture corresponding to a mean equivalence ratio $\langle\phi\rangle$ of 0.8 and an rms value of equivalence ratio of 0.14.

Table 1. Summary of simulation parameters. For decaying turbulence simulations the values correspond to initial conditions.

Case	Scalar Forcing	Velocity Forcing	u'/S_b	$\ell/\delta_{L,m}$	$\langle\xi\rangle$ ($\langle\phi\rangle$)	ξ' (ϕ')	Da	Ka	ℓ_ϕ/ℓ	Domain	Grid
(a)	yes	yes	4.0	3.0	0.044 (0.80)	0.008 (0.14)	0.75	4.62	1.5	$47.9\delta_{Lm} \times (19.2\delta_{Lm})^2$	1000×400^2
(b)	yes	yes	8.0	3.0	0.044 (0.80)	0.008 (0.14)	0.37	13.1	1.5	$47.9\delta_{Lm} \times (19.2\delta_{Lm})^2$	1000×400^2
(c)	yes	no	4.0	3.0	0.044 (0.80)	0.008 (0.14)	0.75	4.62	1.5	$47.9\delta_{Lm} \times (19.2\delta_{Lm})^2$	1000×400^2
(d)	yes	no	8.0	3.0	0.044 (0.80)	0.008 (0.14)	0.37	13.1	1.5	$47.9\delta_{Lm} \times (19.2\delta_{Lm})^2$	1000×400^2
(e)	no	no	4.0	3.0	0.044 (0.8)	0.008 (0.14)	0.75	4.62	1.5	$47.9\delta_{Lm} \times (19.2\delta_{Lm})^2$	1000×400^2
(f)	no	no	8.0	3.0	0.044 (0.8)	0.008 (0.14)	0.37	13.1	1.5	$47.9\delta_{Lm} \times (19.2\delta_{Lm})^2$	1000×400^2

The cases considered here differ by the rms turbulent velocity fluctuation normalised by the burning velocity of the laminar premixed flame corresponding to the mean equivalence ratio u'/S_b, and whether or not the scalar or velocity forcing schemes are used. All scalar forcing simulations are subject to $K/(1/T_{chem}) = 1.71 \times 10^6$ (where $T_{chem} = \delta_{L,m}/S_b$ is the chemical timescale for $\phi = 0.8$), $K^* = 5.0$ and the target passive scalar bounds are $\xi_l = 0.0337$ and $\xi_r = 0.055$ as these correspond to equivalence ratio values of $\phi_l = 0.6$ and $\phi_u = 1.0$.

The compressible 3D DNS code SENGA+ [27] was used for all simulations. The transport equations are solved in using a 10th-order central difference scheme to calculate spatial derivatives of internal grid points, with the order of accuracy gradually reducing to a one-sided 2nd-order scheme at non-periodic boundaries. Explicit time advancement uses low storage 3rd-order Runge-Kutta scheme [28]. The numerical technique used in this study is standard practice for combustion DNS and has been used in different DNS analyses in the past [1–13]. The four boundaries transverse to the mean direction of the flame propagation are considered periodic, while the two boundaries in the direction of the mean flame propagation are considered to be a partially non-reflecting turbulent inflow and outflow in line with the Navier-Stokes characteristic boundary conditions (NSCBC) [29]. The mean inlet velocity in the forced turbulence cases is gradually adjusted to match the turbulent flame speed to keep the flame within the computational domain. The partially non-reflecting boundaries allow for the acoustic waves to pass through them without any appreciable reflection while arresting the mean pressure drift [29]. The flame is kept

sufficiently away from the non-periodic boundaries at all stages and thus the interaction of the order of accuracy of spatial differentiation with boundary condition implementation does not affect the flame dynamics in the canonical configuration considered for turbulent stratified-mixture combustion.

The chemical mechanism is simplified in this analysis by single-step Arrhenius-type chemistry given by 1 unit mass of fuel + s unit mass of oxidiser $\rightarrow (1+s)$ unit mass of products [30]. Here, s is the stoichiometric oxidiser–fuel mass ratio. The chemical reaction $CH_4 + 2O_2 + 7.52N_2 \rightarrow CO_2 + 2H_2O + 7.52N_2$ yields a value of $s = 4.0$ for methane–air combustion. Both the activation energy and heat release are taken to be functions of equivalence ratio [30]. This chemical mechanism was found to mimic the correct equivalence ratio dependence of the unstretched laminar burning velocity [3,30]. Since the scalar forcing is applied only in the unburned gas, it does not interact with the chemical processes within the flame. The scalar forcing term can be used for any number of species to ensure that the desired mean and standard deviations are maintained. Alternatively, this term can be expressed in terms of mixture fraction and the species mass fractions in the unburned gas in the multi-step chemical system can be tabulated as a function of mixture fraction, as used in the past for detailed chemistry DNS [31] and flame-resolved simulations [32]. Simple thermochemistry is used here as the proof of concept of the application of scalar forcing in DNS of turbulent stratified flames and the simplification of chemistry does not affect the performance of scalar forcing or the conclusions of this analysis.

The initial conditions were prescribed as follows. The isotropic turbulent velocity fluctuations were initialised following the well-known pseudo-spectral method by Rogallo [33], which yields an initially homogeneous, isotropic, divergence-free field for specified values of rms velocity u' and integral length scale ℓ following Batchelor-Townsend spectrum [34]. Mixture inhomogeneity in the unburned gas was initialised with a bimodal distribution according to the pseudo-spectral method by Eswaran & Pope [35] for $\langle\phi\rangle = 0.8$, rms $\phi' = 0.14$ for a normalised integral length scale of equivalence ratio fluctuation $\ell_\phi/\ell = 1.5$.

The turbulence intensity in the cases of turbulent forcing is maintained by including a source term in the momentum equation, given by:

$$\vec{f} = (1-c)\max\left[0, \frac{k_{target}-k}{\Delta t k_{target}}\right]\vec{u}^{HP} \tag{10}$$

where k_{target} is the desired turbulent kinetic energy value, Δt is the timestep size, k is the current level of turbulent kinetic energy, $\tilde{u}_i^{HP} = u_i - \tilde{u}_i$ a high pass filtered velocity fluctuation with $\widetilde{(\ldots)}$ being a conventional low pass filter typically used in the context of LES with a 1D Gaussian filter kernel given by $G(x) = \left(6/\pi\ell_f^2\right)^{1/2}\exp\left(-6x^2/\ell_f^2\right)$ and where $\ell_f = 0.25k^{3/2}/\epsilon$ is a filter length scale where k and ϵ are turbulent kinetic energy and its dissipation rate over the domain to be forced [26]. The factor $(1-c)$ in Equation (10) ensures that the turbulence forcing remains active in the unburned gas but gradually reduces to zero towards the burned gas. The turbulence intensity in flames within the thin reaction zones regime [36] often decays from the unburned gas side to the burned gas side of the flame brush and the integral length scale of turbulence increases due to dilatation and a rise in viscosity with heat release [37,38]. By contrast, in the corrugated flamelets regime, the turbulence intensity may increase from the leading edge to somewhere within the flame brush [37,38]. However, forcing turbulence everywhere in the domain tries to enforce a constant level of turbulence on both sides of the flame brush. In this sense, the flame-turbulence interaction will not be physical if the forcing is applied to the whole computational domain. This is explained in detail by Klein et al. [26]. Whilst, in principle, the turbulent velocity field can be forced throughout the domain, the same conclusions cannot be automatically applied to scalar forcing. The purpose of the scalar forcing scheme is to deliver an inhomogeneous unburned fuel-air mixture with prescribed values of mean and rms values of equivalence ratio to the flame. Scalar forcing within

the flame will artificially alter the fuel and oxidiser concentrations, which, in turn, will affect the burning rate and subsequent mixing of species within the burned gas. Moreover, an active scalar forcing within the flame induces a lot of complexity in the calculation (e.g., scalar fluctuations introduced by forcing cannot be separated from the fluctuations due to chemical reaction), particularly for more detailed chemical mechanisms.

The scalar forcing scheme used was found to be very computationally efficient, adding just 0.7% to the overall computational cost. In contrast, the velocity forcing scheme used adds an additional 86% to the computational cost in comparison to the decaying turbulence simulations.

4. Results & Discussion

Figure 1 shows the distributions of the fuel mass fraction Y_F and the contours of the reaction progress variable c equalling 0.1, 0.5 and 0.9 (left to right) on the central midplane of all simulation cases. The snapshots shown are after 2 chemical timescales (i.e., $t = 2.0\delta_{L,m}/S_b$) have passed, where cases (a) and (b) (first row) have reached a statistically quasi-stationary state. In the remaining cases, achieving statistically stationary conditions is not possible due to the decaying nature of the turbulent velocity or scalar fields. The typical simulation time for stratified-mixture combustion in canonical configurations is limited to a couple of eddy turnover times [1–8,39] and all the cases considered here have shorter turbulent timescale than the chemical timescale. Therefore, the simulation time for the cases considered here ranges from 3.5 to 6.76 eddy turnover times, enabling a quasi-stationary state to be achieved.

Figure 1 shows the flame wrinkling increases with increasing turbulence intensity when the turbulence intensity is sustained with velocity forcing, which is evident by the greater extent of wrinkling of the c contours in $u'/S_b = 8.0$ case (i.e., case (b)) than in $u'/S_b = 4.0$ case (i.e., case (a)). Without turbulence forcing, turbulence intensity in cases (c–f) decays with time, which in turn leads to smaller extents of flame wrinkling in these cases in comparison to cases (a) and (b). Furthermore, when the velocity field is decaying, the extent of wrinkling of the c contours is approximately the same regardless of the initial u'/S_b value due to the higher kinetic energy dissipation rate associated with the initially higher u'/S_b cases, and consequently a faster rate of decay of u'/S_b, which acts to make the turbulence intensities comparable when the statistics are extracted. Figure 1 shows that the mixture inhomogeneity in the unburned gas is sustained in cases (a–d), but the extent of mixture inhomogeneity is relatively smaller in cases (e) and (f) due to the absence of scalar fluctuation generating mechanisms (i.e., scalar forcing).

The extent of the mixing, decay of the turbulent velocity field and effectiveness of the relevant scalar forcing schemes can be seen from Figure 2, which shows the evolution of u'/S_b and ϕ' with time throughout the duration of the simulation. The scalar and velocity forcing schemes are clearly effective at maintaining the respective fields at the desired value. As expected, in the initially higher u'/S_b case (f), both the u'/S_b and ϕ' values decay at a greater rate than in case (e). Moreover, it can be seen from Figure 2 in case (f) the decays mentioned above occur at a faster rate than in case (e) due to greater dissipation rate of kinetic energy ($\sim u'^3/\ell$) for higher values of turbulence intensity for a given value of ℓ.

In order to demonstrate the effects of scalar forcing at maintaining the mixture PDF, the temporal evolution of the equivalence ratio ϕ PDF for all simulations in the unburned gas ($c < 0.05$) and in the flame ($0.05 < c < 0.95$) are shown in Figure 3. The scalar forcing scheme maintains the bimodal nature of mixture inhomogeneity in the unburned gas effectively throughout the simulation. However, the forcing does not directly control the ϕ PDF within the flame as this would unnaturally interfere with the chemical reaction and would produce an unphysical solution. Thus, the mean value of the equivalence ratio $\langle\phi\rangle$ within the flame cannot be directly controlled using the present scalar forcing scheme [24], although it is indirectly controlled by maintaining the PDF in the unburned gas. In its current incarnation, the forcing maintains the PDF sampled over the entire unburned gas volume, so cannot guarantee that the surface immediately upstream of

the flame (e.g., $c = 0.001$) will share the same mean scalar value as the entire unburned gas volume. Therefore, the overall burning rate is expected to fluctuate and the statistics will converge when time averaging over a sufficient duration. The turbulent burning velocity is not expected to reach a plateau in a true sense under a quasi-steady state and it shows oscillations around a mean value as shown in Figure 4. This was demonstrated elsewhere for premixed flames by other authors [40]. Ensuring a consistent $\langle\phi\rangle$ immediately upstream of the flame would require modification to the forcing term to inconsistently modify the length scale and scalar dissipation rate in the unburned gas to redistribute mixture independently from the velocity field, which is possible but raises further questions as to the physicality of the solution.

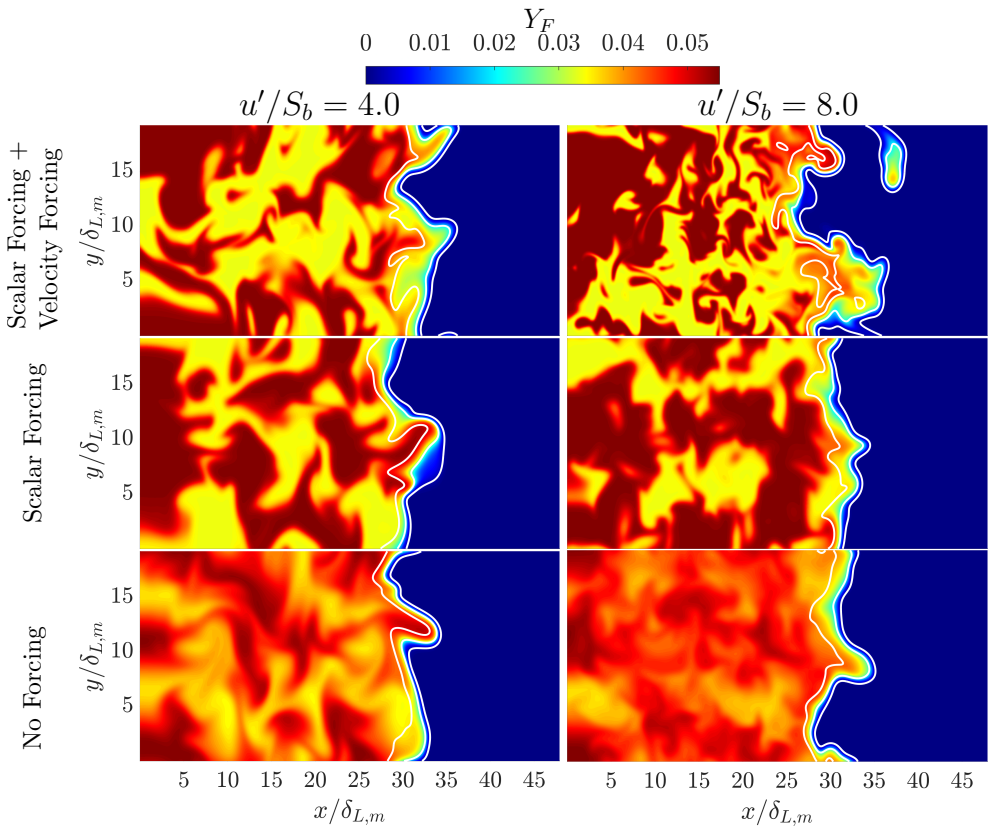

Figure 1. Distributions of the fuel mass fraction Y_F with superimposed reaction progress variable c (Equation (9)) white contours equalling 0.1, 0.5 and 0.9 (left to right) for the central midplane of the simulations. Contours are shown for for $t/T_{chem} = 2.0$.

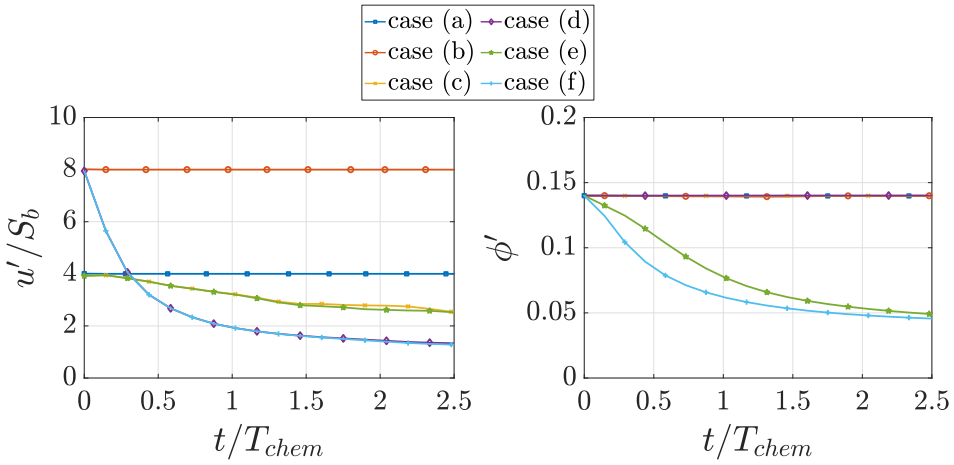

Figure 2. Evolution of the rms turbulent velocity fluctuation normalised by the burning velocity for the laminar premixed $\phi = 0.8$ flame (**left**), and the rms equivalence ratio fluctuation (**right**).

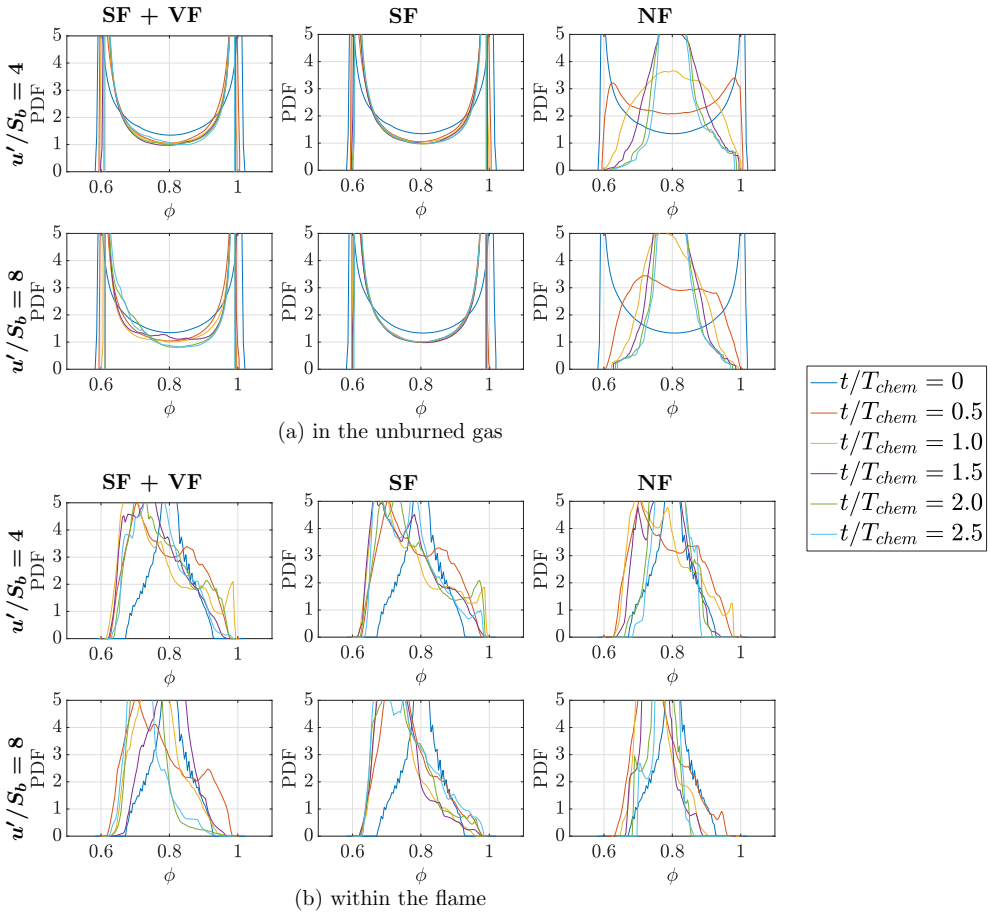

Figure 3. PDFs of ϕ in the (**a**) unburned gas (i.e., $0.1 < c$) and (**b**) within the flame (i.e., $0.1 < c < 0.9$).

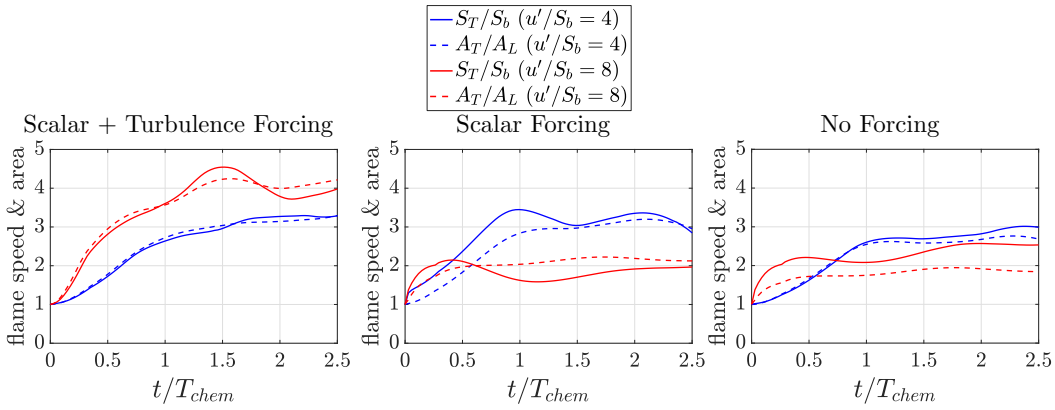

Figure 4. Evolution of the normalised turbulent burning velocity S_T/S_b (solid lines) and flame surface area A_T/A_L (dash lines) for $u'/S_{b(\phi=0.8)} = 4$ and 8 overlaid for the three differing forcing configurations.

The scalar and turbulent forcing schemes in the unburned gas have consequences on the turbulent burning velocity and the flame surface area. Figure 4 shows the temporal evolution of the normalised turbulent burning velocity $S_T = [1/(\rho_0 A_L)] \int_V \dot{\omega}_c \, dV$ (where A_L is the projected flame surface area in the direction of mean flame propagation, ρ_0 is the unburned gas density) and turbulent flame surface area $A_T = \int_V |\nabla c| \, dV$ for the different forcing configurations. Figure 4 shows the cases under the effects of velocity forcing that reach a quasi-stationary state. The sustained turbulence levels result in a higher level of flame wrinkling throughout the duration of the simulations, and thus causes the burning velocity and flame surface area to be higher than the other cases. It is evident from Figure 4

that S_T and A_T continue to oscillate around a constant time averaged value. The turbulent burning velocities S_T for the initially $u'/S_b = 4.0$ cases are found to be counter-intuitively greater than the $u'/S_b = 8.0$ cases for the cases not subjected to velocity forcing. This can attributed to the greater decay in u' already discussed with regards to Figure 2, and also can be explained using the PDF of ϕ within the flame ($0.05 < c < 0.95$) shown in Figure 3. The probability of finding a more reactive $0.8 < \phi < 1.0$ mixture remains consistently higher in the $u'/S_b = 4.0$ case than in the $u'/S_b = 8.0$ case where the greater rate of mixing increases the probability of finding $\phi \approx 0.8$ mixture. It can also be seen from Figure 4 that the combination of scalar and turbulence forcing yields higher values of S_T and A_T than the unforced and only scalar forced simulations. Without scalar forcing, the mixture inhomogeneity reduces with time and the PDF of ϕ converges to a narrow distribution around $\phi = 0.8$ but the forced scalar simulation shows a greater probability of finding more reactive $0.8 < \phi < 1.0$ mixture which acts to increase both S_T and A_T. The turbulent forcing also increases the flame wrinkling due to turbulence in comparison to the unforced turbulence simulations, which in turn increases the flame area generation and the volume-integrated burning rate. It can be seen from Figure 4 that S_T/S_b is similar to A_T/A_L for most cases considered. Without the influence of scalar forcing (i.e., cases (e–f)), S_T/S_b rises above A_T/A_L. With the addition of scalar forcing (i.e., (cases c–d)), the flame speed dips below the flame area for the initial $u'/S_b = 8$ case, but remains above the flame area for the initial $u'/S_b = 4$ case. These effects can be substantiated from the PDF of ϕ within the flame in Figure 3b. The cases not subject to forcing (e–f) have a much higher chance of encountering $\phi = 0.8$ mixture within the flame, while case (d) has a greater probability of encountering the less reactive $0.6 < \phi < 0.8$ mixture than case (c) due to the randomness of mixture inhomogeneity in the unburned gas, despite both cases being subject to scalar forcing.

It is demonstrated in Figure 2 that the desired values for the rms turbulent velocity and equivalence ratio are maintained in the cases where both velocity and scalar forcing are used. Figure 3 shows the PDFs of equivalence ratio in the unburned gas settle to a shape that does not change when the scalar forcing is employed. Finally, in Figure 4, both the turbulent burning velocity and flame surface area oscillate mildly around a mean value, reaching a quasi-steady state. In its current incarnation, the forcing maintains the PDF sampled over the entire unburned gas volume, so cannot guarantee that the surface immediately upstream of the flame (e.g., $c = 0.001$) will share the same mean scalar value as the entire unburned gas volume. Therefore, the overall burning rate is expected to oscillate in an instantaneous sense, so the statistics will converge when time averaging over a sufficient duration. The turbulent burning velocity is not expected to reach a plateau in a true sense under a quasi-steady state and it shows oscillations around a mean value as shown in Figure 4. This was demonstrated elsewhere for premixed flames by other authors [40].

Figure 3 demonstrates that the flame propagates and experiences inhomogeneous mixture throughout its evolution. Thus, it is worthwhile to consider percentage contributions to S_T and A_T of front- and back-supported elements. Such elements can be identified by calculating the flame normal vector alignment with the local mixture fraction gradient, given as

$$\cos\theta_{c\xi} = \frac{\nabla c \cdot \nabla \xi}{|\nabla c||\nabla \xi|} \tag{11}$$

For $\cos\theta_{c\xi} < 0$, the flame is locally propagating into an increasingly rich mixture, and this is referred to as a front-supported flame. Conversely, when $\cos\theta_{c\xi} > 0$, the flame is propagating into an increasingly lean mixture, and this is referred to as a back-supported flame. Figure 5 is a histogram showing the proportion of front- and back-supported contributions to S_T and A_T at different times. These percentage shares for cases continue to fluctuate for all cases as the mixture within the flame changes. It can be seen from Figure 5 that generally, back-supported flame elements with the richer mixture behind the flame contribute mostly to the overall flame speed and area. The qualitative nature of the percentage shares of front- and back-supported flame elements to S_T and

A_T remain unchanged in the presence of scalar forcing but the actual values of these percentage shares are different in cases depending on the presence of turbulence and scalar forcing. It is evident from Figure 5 that the percentage contributions of S_T and A_T to the back-supported and front-supported elements in the quasi-stationary state remain comparable to the only scalar forcing and no-forcing decaying turbulence scenarios for $u'/S_b = 4.0$. However, the percentage shares of back-supported elements increase in the $u'/S_b = 8.0$ cases with scalar forcing and turbulence forcing (i.e., case (b)), but decrease in the other cases (i.e., cases (d) and (f)). The alterations of percentage shares of front- and back-supported contributions to S_T and A_T with turbulence intensity are not the focus of this paper and thus are not discussed further. The findings from Figure 5 essentially demonstrate that the scalar forcing does not artificially alter the front-supported and back-supported contributions to the overall heat release rate in turbulent stratified flame simulations.

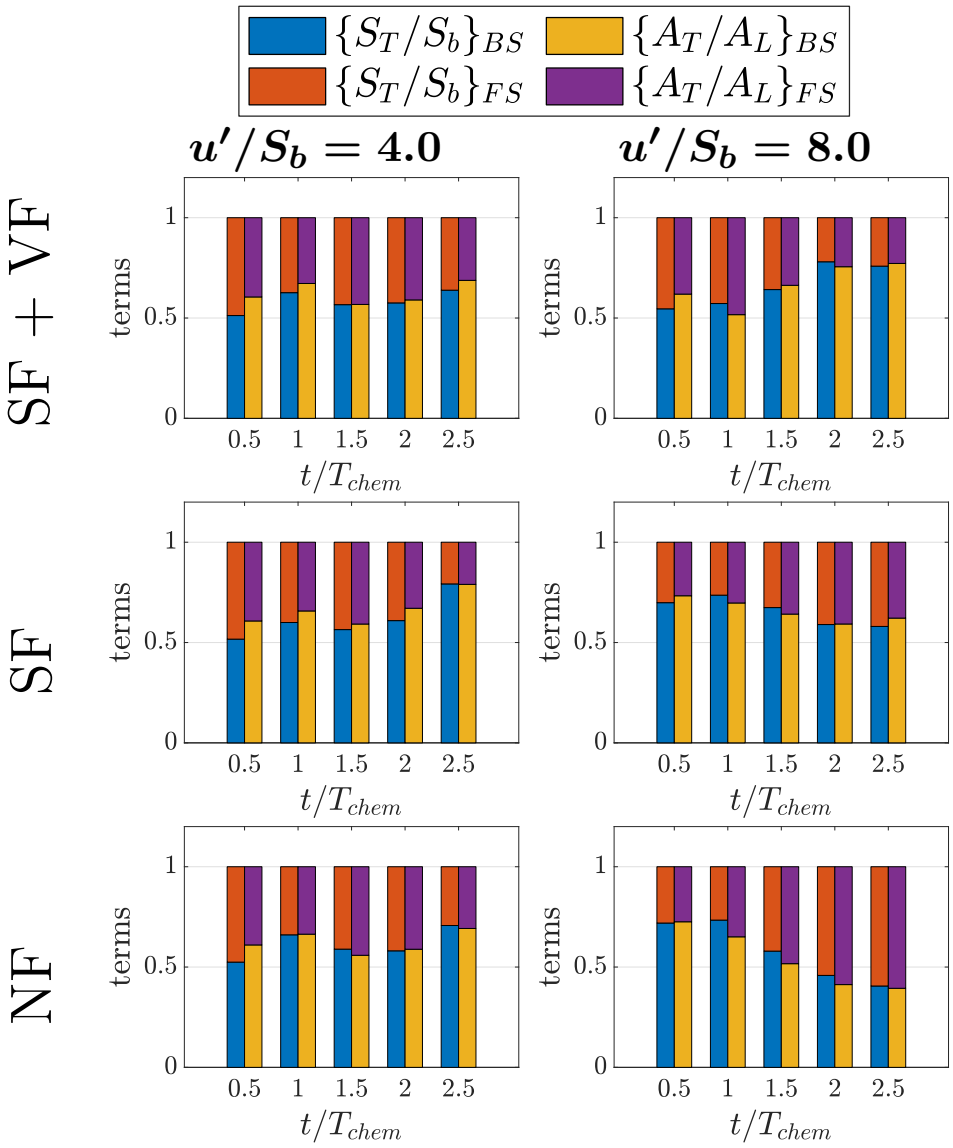

Figure 5. Evolution of the fractional share of front-supported (FS) flame elements and back-supported (BS) flame elements.

As the combustion takes place in inhomogeneous mixtures, it is worthwhile to analyse if the scalar forcing has any impact on the mode of combustion. The mode of combustion

(i.e., premixed and non-premixed) can be quantified in terms of the flame index Ψ, which is defined as [41]:

$$\Psi = \frac{\nabla Y_F \cdot \nabla Y_O}{|\nabla Y_F||\nabla Y_O|} \tag{12}$$

A positive value of Ψ (i.e., $\Psi > 0$) is indicative of premixed combustion, whereas a negative value (i.e., $\Psi < 0$) is indicative of non-premixed combustion [41]. The percentage shares of heat release rate arising from premixed (i.e., $\Psi > 0$) and non-premixed (i.e., $\Psi < 0$) modes of combustion are shown in Figure 6 for the cases considered here, where the total heat release rate is given by

$$\mathrm{HR}_{\mathrm{total}} = \int_V H_\phi |\dot{\omega}_F| \, dV \tag{13}$$

where H_ϕ is the heat release rate per unit mass of fuel, and $\dot{\omega}_F$ is the fuel reaction rate. It can be seen from Figure 6 that more than 99% of the heat release rate occurs due to the premixed mode of combustion irrespective of the nature of scalar forcing. Therefore, scalar forcing does not affect the mode of combustion and thus does not introduce any artificial effects into the flame statistics.

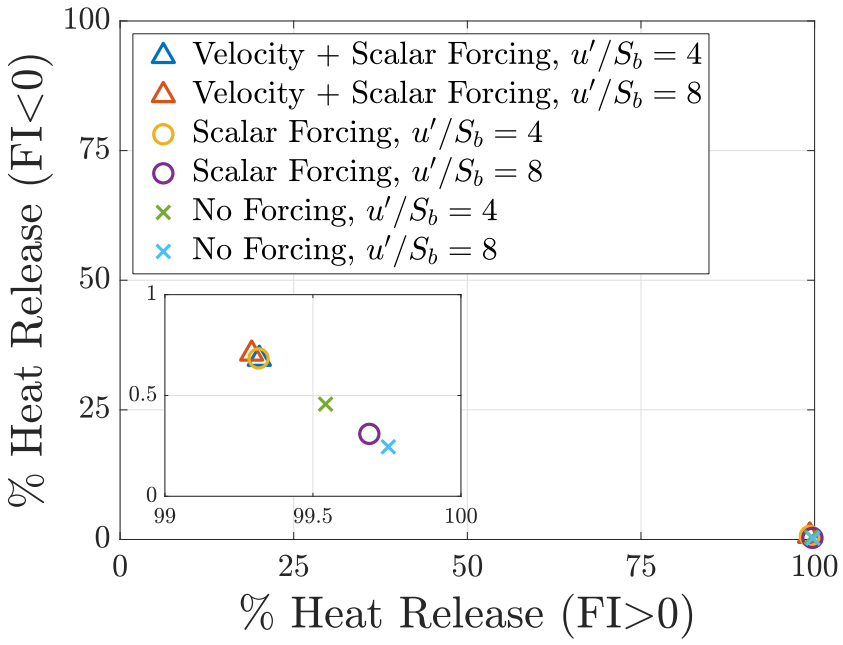

Figure 6. The percentage of heat release coming from premixed vs non-premixed modes of combustion.

The scalar dissipation rate of mixture fraction $N_\xi = D\nabla\xi \cdot \nabla\xi$ and reaction progress variable $N_c = D\nabla c \cdot \nabla c$ and cross-scalar dissipation rate $N_{c\xi} = D\nabla c \cdot \nabla\xi$ (where D is the species diffusivity) affect the reaction rate of reaction progress variable $\dot{\omega}_c \propto [\dot{\omega}_F + N_\xi \partial^2 Y_F/\partial\xi^2 + N_c \partial^2 Y_F/\partial c^2 + 2N_{c\xi}\partial^2 Y_F/\partial\xi\partial c]$ in turbulent stratified flames [11,42,43]. The cross-scalar dissipation rate $N_{c\xi}$ exists within the flame where the scalar forcing does not remain active. Moreover, the magnitude of $N_{c\xi}$ remains negligible in comparison to the magnitude of N_c and thus $\dot{\omega}_c$ is principally determined by N_c as N_ξ remains small within the flame in stratified-mixture combustion [11,42,43]. Figure 7 shows the mean values of scalar dissipation rate for the mixture fraction N_ξ and reaction progress variable N_c averaged upon over bins of their respective scalars. The quantities N_ξ and N_c are evaluated as a postprocessing exercise by evaluating the gradients of $\nabla\xi$ and ∇c using the same spatial differentiation techniques used for DNS simulations. In the case of N_ξ, the mean values are shown for the unburned gas (i.e., $c < 0.1$) only, as this is where the scalar forcing is applied. The mean values of N_ξ within the unburned gas converge towards a steady value for the cases subject to both scalar forcing and velocity forcing (first column), whereas it gradually decays after rising from the initial simulation transients in the cases not subject to any external

forcing (third column) and the cases subject to scalar forcing only (second column), with the effects being most pronounced in the case not subject to any forcing. The mean value of $N_{\tilde{\xi}}$ in the case without scalar forcing will eventually converge to zero as the unburned gas becomes entirely premixed, while in cases with scalar forcing the inhomogeneity is maintained and the mean $N_{\tilde{\xi}}$ converges to some non-zero value. Moreover, both the qualitative variation and peak mean value of N_c remain unaffected by the nature of scalar forcing. Thus, scalar forcing does not introduce any artificiality in terms of micro-mixing within the flame and also in terms of mode of combustion within turbulent stratified flames. Therefore, scalar forcing does not introduce any artificiality in the flame structure in turbulent stratified-mixture combustion. Thus, it can be used to obtain a quasi-stationary state in DNS of stratified-mixture combustion in canonical configurations without any other scalar fluctuation generation mechanism.

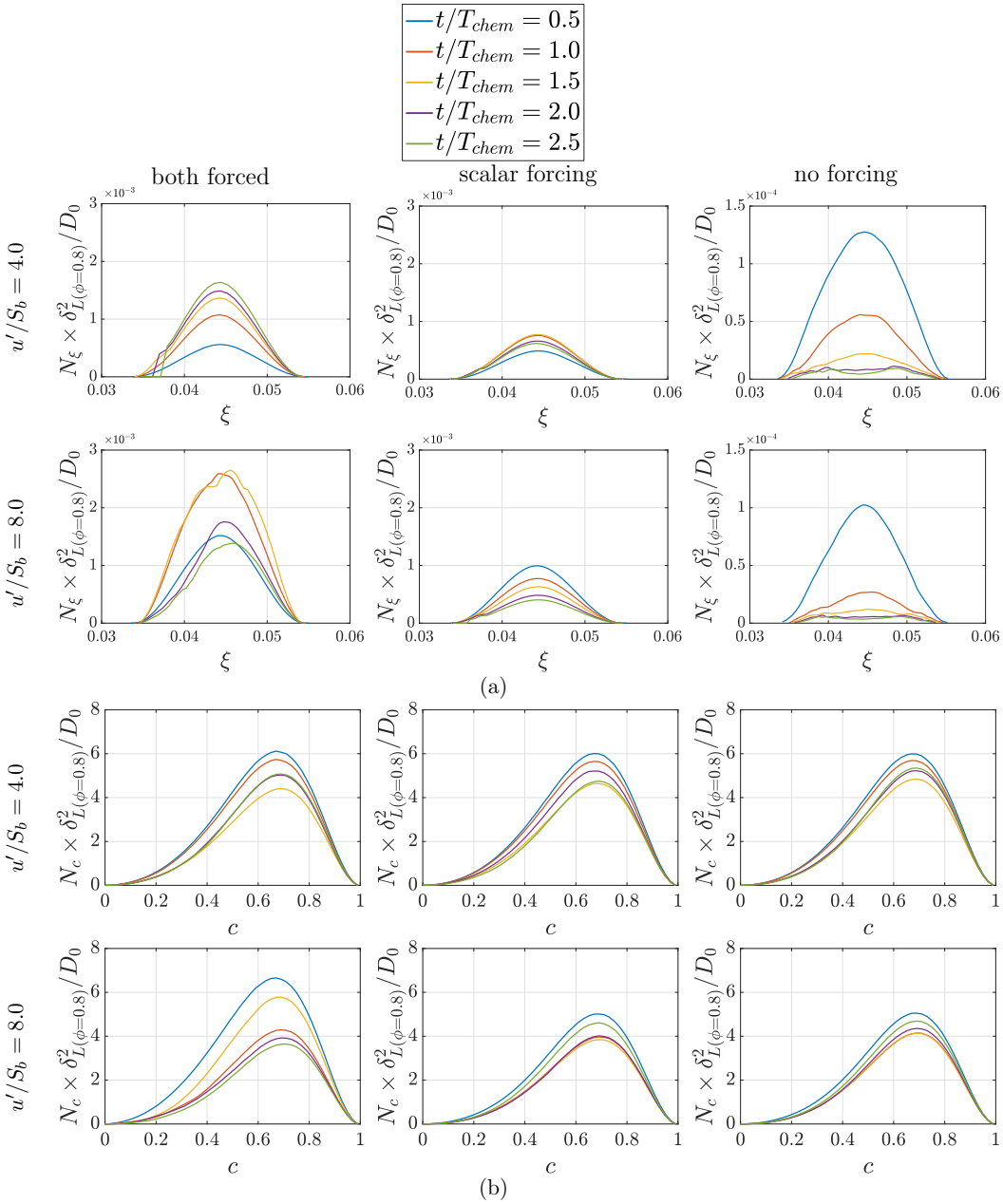

Figure 7. Evolution of the mean values of the normalised scalar dissipation rate $N_{\tilde{\xi}}$ (**a**) and N_c (**b**) conditional upon the range of values of the scalar in question.

5. Conclusions

Maintaining the mixture inhomogeneity in the unburned gas in DNS of turbulent stratified flames in the canonical 'flame-in-a-box' configuration is a challenging task but with the potential to provide great insight into stratified flame physics. The implications of applying a newly developed scalar forcing methodology and its interaction with turbulence forcing in DNS of turbulent stratified flames in the canonical 'flame-in-a-box' configuration have been analysed. The statistical behaviours of turbulent burning velocity, flame surface area and reaction zone structure (e.g., the fractional share of front- and back-supported combustion, and the contributions of heat release originating from different modes of combustion) extracted from DNS of turbulent stratified flame simulations where (a) both the scalar field and the turbulence field are forced, (b) only the scalar field is forced and (c) where neither fields are subject to external forcing have been analysed in detail. The main findings of this analysis are as follows

- The mean mixture composition within the flame may vary during the course of the simulation since the average quantities are maintained in the entire unburned gas volume, leading to fluctuations in the burning rate over time.
- Scalar forcing alongside turbulence forcing may lead to greater values of turbulent burning velocity and flame surface area in comparison to unforced simulations for globally fuel-lean turbulent stratified flames.
- The sustained unburned gas mixture inhomogeneity in the case of scalar forcing alters the percentage shares of back- and front-supported flame elements in comparison to unforced simulations, especially for high turbulence intensities.
- The heat release due to different modes of combustion and the micro-mixing rates characterised by scalar dissipation rates remain unaffected by scalar forcing, suggesting that the scalar forcing does not introduce any artificial influence on the flame structure.

The above findings indicate that the scalar forcing has a high potential for advancing our understanding of stratified-mixture combustion by obtaining well-converged time-averaged statistics using DNS in canonical configurations.

Author Contributions: Conceptualization, P.B., U.A. and N.C.; methodology, P.B. and N.C.; simulation and analysis, P.B.; writing—original draft preparation, P.B. and N.C.; writing—review and editing, P.B., U.A. and N.C.; supervision, U.A. and N.C.; funding acquisition, N.C. All authors have read and agreed to the published version of the manuscript.

Funding: This research was funded by EPSRC grant number EP/R029369/1.

Data Availability Statement: The data supporting the conclusions of this article will be made available by the authors on request.

Acknowledgments: The computational support from CIRRUS, Kelvin II and Rocket-HPC at Newcastle University is gratefully acknowledged.

Conflicts of Interest: The authors declare no conflicts of interest.

References

1. Hélie, J.; Trouvé, A. Turbulent flame propagation in partially premixed combustion. *Proc. Combust. Inst.* **1998**, *27*, 891–898. [CrossRef]
2. Haworth, D.C.; Cuenot, B.; Blint, R.J.; Poinsot, T.J. Numerical simulations of turbulent Propane-Air combustion with non homogeneous reactants. *Combust. Flame* **2000**, *121*, 395–417. [CrossRef]
3. Malkeson, S.P.; Chakraborty, N. A priori direct numerical simulation assessment of algebraic models of variances and dissipation rates in the context of Reynolds-averaged Navier-Stokes simulations of low Damköhler number partially premixed combustion. *Combust. Sci. Technol.* **2010**, *182*, 960–999. [CrossRef]
4. Malkeson, S.P.; Chakraborty, N. Statistical analysis of displacement speed in turbulent stratified flames: A direct numerical simulation study. *Combust. Sci. Technol.* **2010**, *182*, 1841–1883. [CrossRef]
5. Malkeson, S.P.; Chakraborty, N. The modelling of fuel mass fraction variance transport in turbulent stratified flames: A direct numerical simulation study. *Num. Heat Trans. A* **2010**, *58*, 187–206. [CrossRef]
6. Malkeson, S.P.; Chakraborty, N. Statistical analysis of scalar dissipation rate transport in turbulent partially premixed flames: A direct numerical simulation study. *Flow Turbul. Combust.* **2011**, *86*, 1–44. [CrossRef]

7. Malkeson, S.P.; Chakraborty, N. Statistical analysis of cross scalar dissipation rate transport in turbulent partially premixed flames: A direct numerical simulation study. *Flow Turbul. Combust.* **2011**, *87*, 313–349. [CrossRef]
8. Malkeson, S.P.; Chakraborty, N. Alignment statistics of active and passive scalar gradients in turbulent stratified flames. *Phys. Rev. E* **2011**, *83*, 046308. [CrossRef]
9. Malkeson, S.P.; Chakraborty, N. A priori DNS modelling of the turbulent scalar fluxes for low Damköhler number stratified flames. *Combust. Sci. Technol.* **2012**, *184*, 1680–1707. [CrossRef]
10. Malkeson, S.P.; Chakraborty, N. Statistical analysis and a-priori modelling of flame surface density transport in turbulent stratified flames: A direct numerical simulation study. *Flow Turbul. Combust.* **2013**, *90*, 143–187. [CrossRef]
11. Malkeson, S.P.; Chakraborty, N. A-Priori direct numerical simulation modelling of co-variance transport in turbulent stratified flames. *Flow Turbul. Combust.* **2013**, *90*, 243–267. [CrossRef]
12. Brearley, P.; Ahmed, U.; Chakraborty, N. The relation between flame surface area and turbulent burning velocity in statistically planar turbulent stratified flames. *Phys. Fluids* **2020**, *32*, 125111. [CrossRef]
13. Brearley, P.; Ahmed, U.; Chakraborty, N. A Priori Direct Numerical Simulation Analysis of the Closure of Cross-Scalar Dissipation Rate of Reaction Progress Variable and Mixture Fraction in Turbulent Stratified Flames. *Flow Turbul. Combust.* **2022**, *109*, 351–382. [CrossRef]
14. Lipatnikov, A.N. Stratified turbulent flames: Recent advances in understanding the influence of mixture inhomogeneities on premixed combustion and modeling challenges. *Prog. Energy Combust. Sci.* **2017**, *62*, 87–132. [CrossRef]
15. Domingo, P.; Vervisch, L. Recent developments in DNS of turbulent combustion. *Proc. Combust. Inst.* **2023**, *39*, 2055–2076. [CrossRef]
16. Richardson, E.S.; Chen, J.H. Analysis of turbulent flame propagation in equivalence ratio stratified flow. *Proc. Combust. Inst.* **2017**, *36*, 1729–1736. [CrossRef]
17. Proch, F.; Domingo, P.; Vervisch, L.; Kempf, A.M. Flame resolved simulation of a turbulent premixed bluff-body burner experiment. Part I: Analysis of the reaction zone dynamics with tabulated chemistry. *Combust. Flame* **2017**, *180*, 321–339. [CrossRef]
18. Inanc, E.; Kempf, A.M.; Chakraborty, N. Scalar gradient and flame propagation statistics of a flame-resolved laboratory-scale turbulent stratified burner simulation. *Combust. Flame* **2022**, *238*, 111917. [CrossRef]
19. Brearley, P.; Ahmed, U.; Chakraborty, N. Effects of Mixture Distribution on the Structure and Propagation of Turbulent Stratified Slot-Jet Flames. *Flow Turbul. Combust.* **2023**, *111*, 769–797. [CrossRef]
20. Barlow, R.S.; Wang, G.H.; Anselmo-Filho, P.; Sweeney, M.S.; Hochgreb, S. Application of Raman/Rayleigh/LIF diagnostics in turbulent stratified flames. *Proc. Combust. Inst.* **2009**, *32 I*, 945–953. [CrossRef]
21. Sweeney, M.S.; Hochgreb, S.; Dunn, M.J.; Barlow, R.S. The structure of turbulent stratified and premixed methane/air flames I: Non-swirling flows. *Combust. Flame* **2012**, *159*, 2896–2911. [CrossRef]
22. Sweeney, M.S.; Hochgreb, S.; Dunn, M.J.; Barlow, R.S. The structure of turbulent stratified and premixed methane/air flames II: Swirling flows. *Combust. Flame* **2012**, *159*, 2912–2929. [CrossRef]
23. Daniel, D.; Livescu, D.; Ryu, J. Reaction analogy based forcing for incompressible scalar turbulence. *Phys. Rev. Fluids* **2018**, *3*, 094602. [CrossRef]
24. Brearley, P.; Ahmed, U.; Chakraborty, N. Scalar forcing methodology for direct numerical simulations of turbulent stratified mixture combustion. *Flow Turb. Combust.* **2022**, *108*, 1089–1114. [CrossRef]
25. Lundgren, T.S. *Linearly Forced Isotropic Turbulence*; Annual Research Briefs; Center for Turbulence Research: Stanford, CA, USA, 2003.
26. Klein, M.; Chakraborty, N.; Ketterl, S. A comparison of strategies for direct numerical simulation of turbulence chemistry interaction in generic planar turbulent premixed flames. *Flow Turb. Combust.* **2017**, *99*, 955–971. [CrossRef]
27. Jenkins, K.W.; Cant, R.S. DNS of turbulent flame kernels. In *Proceedings of the 2nd AFOSR Conference on DNS and LES, Rutgers University, New Brunswick, NJ, USA, 7–9 June 1999*; Kluwer Academic Publishers: Alphen aan den Rijn, The Netherlands, 1999; pp. 192–202.
28. Wray, A.A. *Minimal Storage Time-Advancement Schemes for Spectral Methods*; Report No. MS 202 A-1; NASA Ames Research Center: Mountain View, CA, USA, 1990.
29. Poinsot, T.J.; Lele, S.K. Boundary conditions for direct simulations of compressible viscous flows. *J. Comput. Phys.* **1992**, *101*, 104–129. [CrossRef]
30. Tarrazo, E.F.; Sánchez, A.L.; Linan, A.; Williams, F.A. A simple one-step chemistry model for partially premixed hydrocarbon combustion. *Combust. Flame* **2006**, *147*, 32–38.
31. Minamoto, Y.; Swaminathan, N.; Cant, R.; Leung, T. Morphological and statistical features of reaction zones in MILD and premixed combustion. *Combust. Flame* **2014**, *161*, 2801–2814. [CrossRef]
32. Sandeep, A.; Proch, F.; Kempf, A.; Chakraborty, N. Statistics of strain rates and surface density function in a flame-resolved high-fidelity simulation of a turbulent premixed bluff body burner. *Phys. Fluids* **2018**, *161*, 2801–2814. [CrossRef]
33. Rogallo, R.S. *Numerical Experiments in Homogeneous Turbulence*; NASA Technical Memorandum; NASA Ames Research Center: Mountain View, CA, USA, 1981; Volume 81315.
34. Batchelor, G.K.; Townsend, A.A. Decay of turbulence in the final period. *Proc. R. Soc. Lond.* **1948**, *A194*, 517–543.
35. Eswaran, V.; Pope, S.B. Direct numerical simulations of the turbulent mixing of a passive scalar. *Phys. Fluids* **1988**, *31*, 506–520. [CrossRef]

36. Peters, N. *Turbulent Combustion*; Cambridge University Press: Cambridge, UK, 2000.
37. Chakraborty, N.; Katragadda, M.; Cant, R. Statistics and modelling of turbulent kinetic energy transport in different regimes of premixed combustion. *Flow Turb. Combust.* **2011**, *87*, 205–235. [CrossRef]
38. Chakraborty, N. Influence of thermal expansion on fluid dynamics of turbulent premixed combustion and its modelling implications. *Flow Turb. Combust.* **2021**, *106*, 753–806. [CrossRef]
39. Jiménez, C.; Cuenot, B.; Poinsot, T.; Haworth, D. Numerical simulation and modeling for lean stratified propane-air flames. *Combust. Flame* **2002**, *128*, 1–21. [CrossRef]
40. Khamedov, R.; Song, W.; Hernandez-Perez, F.E.; Im, H.G. Structure and propagation characteristics of turbulent premixed ammonia-air flames. *Flow Turb. Combust.* **2024**, *112*, 769–791. [CrossRef]
41. Yamashita, H.; Shimada, M.; Takeno, T. A numerical study on flame stability at the transition point of jet diffusion flames. *Proc. Combust. Inst.* **1996**, *26*, 27–34. [CrossRef]
42. Ruan, S.; Swaminathan, N.; Bray, K.; Mizobuchi, Y.; Takeno, T. Scalar and its dissipation in the near field of turbulent lifted jet flame. *Combust. Flame* **2012**, *159*, 591–608. [CrossRef]
43. Bray, K.; Domingo, P.; Vervisch, L. Role of the progress variable in models for partially premixed turbulent combustion. *Combust. Flame* **2005**, *141*, 431–437. [CrossRef]

computation

MDPI

Article

Finite Difference Methods Based on the Kirchhoff Transformation and Time Linearization for the Numerical Solution of Nonlinear Reaction–Diffusion Equations

Juan I. Ramos

Escuela de Ingenier as Industriales, Universidad de Málaga, Doctor Ortiz Ramos, s/n, 29071 Málaga, Spain; jirs@uma.es

Abstract: Four formulations based on the Kirchhoff transformation and time linearization for the numerical study of one-dimensional reaction–diffusion equations, whose heat capacity, thermal inertia and reaction rate are only functions of the temperature, are presented. The formulations result in linear, two-point boundary-value problems for the temperature, energy or heat potential, and may be solved by either discretizing the second-order spatial derivative or piecewise analytical integration. In both cases, linear systems of algebraic equations are obtained. The formulation for the temperature is extended to two-dimensional, nonlinear reaction–diffusion equations where the resulting linear two-dimensional operator is factorized into a sequence of one-dimensional ones that may be solved by means of any of the four formulations developed for one-dimensional problems. The multidimensional formulation is applied to a two-dimensional, two-equation system of nonlinearly coupled advection–reaction–diffusion equations, and the effects of the velocity and the parameters that characterize the nonlinear heat capacities and thermal conductivity are studied. It is shown that clockwise-rotating velocity fields result in wave stretching for small vortex radii, and wave deceleration and thickening for counter-clockwise-rotating velocity fields. It is also shown that large-core, clockwise-rotating velocity fields may result in large transient periods, followed by time intervals of apparent little activity which, in turn, are followed by the propagation of long-period waves.

Keywords: reaction–diffusion equations; Kirchhoff's transformation; heat potential; Rankine vortex fields; piecewise analytically derived finite difference methods

Citation: Ramos, J.I. Finite Difference Methods Based on the Kirchhoff Transformation and Time Linearization for the Numerical Solution of Nonlinear Reaction–Diffusion Equations. *Computation* **2024**, *12*, 218. https://doi.org/10.3390/computation12110218

Academic Editors: Ali Cemal Benim, Rachid Bennacer, Abdulmajeed A. Mohamad, Paweł Oclon, Sang-Ho Suh and Jan Taler

Received: 11 September 2024
Revised: 14 October 2024
Accepted: 15 October 2024
Published: 1 November 2024

1. Introduction

Nonlinear heat and mass transfer problems arising in science and engineering are usually solved nowadays by means of finite difference, finite volume or finite element methods. In nonlinear, steady heat conduction problems, the (spatial) discretization of the energy equation results in a system of nonlinear equations that has to be solved by means of iterative techniques. However, if the thermal conductivity is only a function of the temperature and the boundary conditions are of the Dirichlet or Neumann type, the introduction of the heat potential or Kirchhoff's transformation [1] transforms the nonlinear partial differential equation for the temperature into a linear one for the heat potential [2], and this linear equation may solved analytically in many cases by means of, for example, separation of variables, Fourier transforms, etc. [3–5].

The Kirchhoff transformation has been previously used for determining the nonlinear, steady heat conduction in fuel rod models in nuclear reactors [6], the thermal analysis of semiconductor devices with temperature-dependent and piecewise inhomogeneous thermal conductivity [7], nonlinear mass transfer problems characterized by a concentration-dependent coefficient [8], estimation of the temperature-dependent thermal conductivity [9], the determination of the temperature-dependent thermal conductivity as

an inverse heat conduction problem [10], thermal analysis of microelectronic devices where the thermal conductivity of either the semiconductors or the package depends strongly on temperature [11], etc.

For steady heat conduction problems subject to Robin, i.e., convective, boundary conditions, the use of the Kirchhoff transformation transforms the nonlinear energy equation into a linear one for the heat potential, but the boundary conditions for the latter are rather complex due to the nonlinear dependence of the thermal conductivity or heat potential on temperature. This issue has been addressed in the past by employing apparent temperatures [11], using piecewise polynomial approximations for thermal conductivity, especially near the boundaries where Robin conditions are imposed, etc.

A further problem associated with the Kirchhoff transformation even for the case that the boundary conditions are of the Dirichlet or Neumann types is the determination of the temperature from the heat potential since these variables are nonlinearly related, e.g., [12]. However, since lines of constant temperature correspond to lines of constant heat potential and the latter obeys the Laplace equation, i.e., the maximum and minimum values of the heat potential occur at the domain boundary [13], the maximum and minimum values of the temperature also occur at the boundary.

In addition to the above comments, it must be stated that the Kirchhoff transformation is not useful for problems where the thermal conductivity depends on space.

Other thermal problems where the conductivity is temperature-dependent and generates an asymmetric material response include thermal diodes [14], thermal transistors [15], thermal logic gates [16], thermal memristors [17], hysteresis [18], heat shuttling [19] and pumping [20], and energy harvesting and harnessing [21]. These problems are usually associated with nanoscale phenomena, and may require either phase-change materials or oxides, e.g., vanadium dioxide (VO_2).

In this paper, we consider time-dependent, nonlinear reaction–diffusion problems characterized by thermal and mass inertias (or heat and mass capacities, respectively), and thermal conductivities and diffusion coefficients that depend only on the temperature and density, respectively, make use of the Kirchhoff transformations for temperature and species mass fractions, and present time-linearized finite difference methods for their solution. Dirichlet, Neumann and Robin boundary conditions are considered.

This paper is organized as follows. In Section 2, for the sake of clarity, we consider a one-dimensional, time-dependent, nonlinear reaction–diffusion equation, and present several new approaches based on the Kirchhoff transformation and the heat potential, the energy per unit volume and the temperature. We then employ time linearization for these formulations and describe the implementation of the boundary conditions in detail. In Section 3, one of the formulations presented in Section 2 is used to discretize two-dimensional, nonlinear systems of reaction–diffusion equations characterized by nonlinear heat capacities, thermal inertia, and heat diffusion and reaction. The formulation presented in Section 3 is applied in Section 4 to a two-equation, nonlinear system of advection–reaction–diffusion equations which, for constant mass and thermal capacities and constant mass diffusivity and thermal conductivity, has periodic spiral wave solutions, and the effects of convection, thermal inertia and diffusivity on the wave dynamics are assessed. The final section summarizes the most important findings of the manuscript.

2. One-Dimensional Formulations

As stated above, for the sake of clarity, we shall consider in this section the following one-dimensional, time-dependent, nonlinear reaction–diffusion equation:

$$e(T)_t = (K(T)T_x)_x + S(T), \qquad t < 0, \qquad 0 < x < L, \tag{1}$$

where the subscripts denote partial differentiation, t and x denote the time and spatial coordinates, respectively, e, K, $T(t, x)$ and S denote the energy per unit volume, thermal conductivity, temperature and source/reaction term, respectively, and L denotes the length of the domain.

The energy may be expressed as

$$e(T) = \int_{T_0}^{T} \rho(T)c(T)dt + e(T_0), \tag{2}$$

where ρ and c denote the density and specific heat of the material, respectively, and T_0 is a (constant) reference temperature. Note that ρ, K and c only depend on T, and that the product ρc will be referred to as either thermal inertia or heat capacity. Note also that Equation (1) may also be written as

$$\rho(T)c(T)T_t = (K(T)T_x)_x + S(T). \tag{3}$$

In the next subsections, different formulations for the numerical solution of Equation (1) based on Kirchhoff's transformation are presented. In some of these formulations, the heat potential or Kirchhoff transformation is determined, whereas others are based on either the temperature or the energy per unit volume. However, we shall refer to all the formulations as being of Kirchhoff's type, even if they are not so.

2.1. First Kirchhoff's Formulation

Since K is only a function of T, one may introduce the following heat potential ϕ or Kirchhoff transformation [1,2]

$$\phi(T) = \int_{T_0}^{T} K(T)dt + \phi(T_0), \tag{4}$$

so that Equation (1) becomes

$$e(T)_t = \phi_{xx} + S(T), \tag{5}$$

which, upon time discretization by means of the midpoint rule, results in

$$e^{n+1} - e^n = \frac{1}{2}\Delta t(\phi^n_{xx} + S^n + \phi^{n+1}_{xx} + S^{n+1}), \tag{6}$$

where $t^n = n\Delta t$, $n = 0, 1, 2, \cdots$, and Δt is the time step.

Equation (6) is a two-point, nonlinear boundary-value problem of the integro-differential type on account of the nonlinear dependence of S on T and the nonlinear integral relationships between e and ϕ and T, cf. Equations (2) and (4), respectively. However, upon linearizing ϕ^{n+1} and S^{n+1} as

$$\phi^{n+1} = \phi^n + \phi_T\Delta T + \mathcal{O}(\Delta t^2) = \phi^n + K^n\Delta T + \mathcal{O}(\Delta t^2), \tag{7}$$

and

$$S^{n+1} = S^n + J^n\Delta T + \mathcal{O}(\Delta t^2), \tag{8}$$

respectively, where $J \equiv \frac{dS}{dT}$ is the Jacobian of the source term, and $\Delta T = T^{n+1} - T^n$, Equation (6) becomes

$$e^{n+1} - e^n = \Delta t\left(\phi^n_{xx} + S^n + \frac{1}{2}((K^n\Delta T)_{xx} + J^n\Delta T)\right), \tag{9}$$

whose right-hand side is linear on ΔT, but Equation (9) is still of the integro-differential type owing to the nonlinear integral dependence of e on T, cf. Equation (2). Note that $K^n = K(T^n) = K(T(t^n, x))$ is a function of x.

Upon linearizing e^{n+1} as in Equations (7) and (8), i.e.,

$$e^{n+1} = e^n + \rho^n c^n\Delta T + \mathcal{O}(\Delta t^2), \tag{10}$$

Equation (9) becomes

$$\left(\rho^n c^n \cdot - \frac{\Delta t}{2}((K^n \cdot)_{xx} + J^n \cdot)\right)\Delta T = \Delta t(\phi^n_{xx} + S^n), \tag{11}$$

which is a linear, two-point boundary-value problem for ΔT whose coefficients and right-hand side are functions of x at t^n.

2.2. Second Kirchhoff's Formulation

Since e and ϕ are functions of T, it is easy to derive that $e_t = d(T)\phi_t$, where $d(T) = \frac{\rho c}{K}$ is the inverse of the thermal diffusivity. Use of this expression in Equation (1) yields

$$d(T)\phi_t = d(\phi)\phi_t = \phi_{xx} + s(\phi), \tag{12}$$

where, from Equation (4), $T = \psi(\phi)$, and, therefore, $d(\phi) = d(T) = d(\psi(\phi))$ and $s(\phi) = S(T) = S(\psi(\phi))$.

Equation (12) is too cumbersome on account that it requires the inversion of the potential to determine the temperature, $d(T)$ and $S(T)$, and the nonlinearities of $d(\phi)$ and $s(\phi)$. For this reason, it is more convenient in what follows to consider Equation (12) as

$$d(T)\phi_t = \phi_{xx} + S(T), \tag{13}$$

which could be discretized with second-order temporal accuracy as either

$$d\left(\frac{T^n + T^{n+1}}{2}\right)(\phi^{n+1} - \phi^n) = \frac{1}{2}\Delta t(\phi^n_{xx} + S^n + \phi^{n+1}_{xx} + S^{n+1}), \tag{14}$$

or

$$\frac{1}{2}\left(d^n + d^{n+1}\right)(\phi^{n+1} - \phi^n) = \frac{1}{2}\Delta t(\phi^n_{xx} + S^n + \phi^{n+1}_{xx} + S^{n+1}). \tag{15}$$

However, Equations (14) and (15) are of the integro-differential type due to the dependence of d on T and the nonlinear dependence between T and ϕ (cf. Equation (4)), and may be solved iteratively. But, if we give up second-order accuracy in time, Equations (14) and (15) may be approximated by

$$d^n(\phi^{n+1} - \phi^n) = \frac{1}{2}\Delta t(\phi^n_{xx} + S^n + \phi^{n+1}_{xx} + S^{n+1}), \tag{16}$$

and

$$d^n(\phi^{n+1} - \phi^n) = \Delta t(\phi^{n+1}_{xx} + S^{n+1}), \tag{17}$$

respectively, which are still of the integro-differential type due to the dependence of S on T and the dependence of T on ϕ.

Upon time linearization, Equation (17) may be written as

$$\left(d^n \cdot - \Delta t\left((\cdot)_{xx} + \frac{J^n}{K^n}\cdot\right)\right)\Delta\phi = \Delta t(\phi^n_{xx} + S^n), \tag{18}$$

which is a two-point, linear boundary-value problem for $\Delta\phi$ whose coefficients and right-hand side are functions of x.

If the second-order spatial derivative of Equations (11) and (18) is discretized in an equally spaced grid of spacing Δx by means of the three-point, central, second-order accurate finite difference formula, one obtains a system of linear algebraic equations with a coefficient matrix that is tridiagonal, whose solution may be easily obtained by means of the tridiagonal matrix algorithm, also known as the method of Thomas.

Once $\Delta\phi$ is found from Equation (18), the value of ΔT may be found from Equation (7) as

$$\Delta T = \frac{1}{K^n}\Delta\phi + \mathcal{O}(\Delta t), \tag{19}$$

and $T^{n+1} = T^n + \Delta T$.

It is worth noting that if ΔT from Equation (19) is substituted into Equation (18), one obtains

$$(\rho^n c^n \cdot - \Delta t((K^n \cdot)_{xx} + J^n \cdot))\Delta T = \Delta t(\phi^n_{xx} + S^n), \tag{20}$$

which is the same equation as the one that would have resulted from applying the first Kirchhoff's formulation presented in the previous section to a first-order backward time discretization of Equation (1).

2.3. Third Kirchhoff's Formulation

As stated previously, Equation (20) is a linear, second-order, ordinary differential equation with variable coefficients and right-hand side. However, if the interval $[0, L]$ is discretized into N equally spaced intervals, the grid point locations are $x_i = i\Delta x$, $i = 0, 1, 2, \cdots N$, $\Delta x = \frac{L}{N}$, and, in the interval $I_i \equiv [x_{i-1}, x_{i+1}]$, these coefficients and right-hand side are approximated by their (constant) values at x_i, then Equation (20) becomes

$$A_i(\Delta T)_{xx} - B_i\Delta T = C_i, \tag{21}$$

where

$$A = K^n\Delta t, \qquad B = \rho^n c^n - J^n\Delta t, \qquad C = -\Delta t(\phi^n_{xx} + S^n). \tag{22}$$

The solution of Equation (21) may be written, for $B_i > 0$, as

$$\Delta T(x) = E_i \cosh(\lambda_i(x - x_i)) + F_i \sinh(\lambda_i(x - x_i)) - \frac{C_i}{B_i}, \tag{23}$$

where $\lambda_i = \sqrt{\frac{B_i}{A_i}}$, and E_i and F_i are constants that may be determined from the conditions $\Delta T(x_{i-1}) = \Delta T_{i-1}$, $\Delta T(x_i) = \Delta T_i$ and $\Delta T(x_{i+1}) = \Delta T_{i+1}$. These conditions result in the following three-point finite difference expression

$$(\Delta T)_{i-1} - 2\cosh(\lambda_i\Delta x)(\Delta T)_i + (\Delta T)_{i+1} = 2\frac{C_i}{B_i}(\cosh(\lambda_i\Delta x) - 1), \tag{24}$$

which is a strictly diagonally dominant tridiagonal system whose solution may be obtained by means of the tridiagonal matrix algorithm. The values of E_i and F_i may be easily deduced from the above conditions and are not reported here.

If $B_i = 0$, the solution to Equation (21) is

$$\Delta T(x) = \frac{1}{2}\frac{C_i}{A_i}(x - x_i)^2 + E_i(x - x_i) + F_i, \tag{25}$$

and the node conditions mentioned above result in

$$(\Delta T)_{i-1} - 2(\Delta T)_i + (\Delta T)_{i+1} = 2\frac{C_i}{A_i}\Delta x^2, \tag{26}$$

which could also have been deduced from Equation (24) by taking the limit $B_i \to 0$ and using either the L'Hôpital rule or Taylor's series expansions.

Equation (26) represents a system of linear algebraic equations characterized by a diagonally dominant matrix and whose solution may be obtained by means of the method of Thomas.

The case $B_i < 0$ results in the following tridiagonal system of linear algebraic equations

$$(\Delta T)_{i-1} - 2\cos(\omega_i\Delta x)(\Delta T)_i + (\Delta T)_{i+1} = 2\frac{C_i}{B_i}(\cosh(\omega_i\Delta x) - 1), \tag{27}$$

which is not diagonally dominant and where $\omega_i = \sqrt{-\frac{B_i}{A_i}}$.

At this stage, it is convenient to examine the condition $B_i \geq 0$. To do so, let us consider the term $\lambda_i \Delta x$ that appears in Equation (24). The square of this term may be written as $\frac{\rho c \Delta x^2}{K \Delta t} - \frac{J \Delta x^2}{K} = \frac{1}{Fo} - Da_I$, where Fo denotes the Fourier number based on the grid spacing and the time step or the ratio of the grid diffusion to the real one, and Da_I is the first Damkhöler number, which is the ratio of the reaction rate or source term to heat transport by diffusion. The Fourier number may also be interpreted as the ratio between the heat accumulation rate and the heat transport by conduction. With this interpretation, the positivity of B_i corresponds to an energy accumulation rate larger than the reaction one or a second Damkhöler number smaller than unity [22].

2.4. Fourth Kirchhoff's Formulation

The Kirchhoff formulations presented in the three previous sections were based on either $\Delta\phi$ or ΔT. In this section, a formulation based on Δe is presented.

Using Equations (7), (8) and (10) in Equation (9) results in

$$\left(1 \cdot - \frac{1}{2}\Delta t\left(\left(\frac{K^n}{\rho^n c^n}\cdot\right)_{xx} + \frac{J^n}{\rho^n c^n}\cdot\right)\right)\Delta e = \Delta t(\phi^n_{xx} + S^n), \tag{28}$$

whose solution provides Δe and, using Equation (10), $\Delta T = \frac{\Delta e}{\rho^n c^n}$.

A first-order, backward temporal discretization of Equation (1) yields

$$\left(1 \cdot - \Delta t\left(\left(\frac{K^n}{\rho^n c^n}\cdot\right)_{xx} + \frac{J^n}{\rho^n c^n}\cdot\right)\right)\Delta e = \Delta t(\phi^n_{xx} + S^n). \tag{29}$$

A comparison of Equations (18), (20) and (29) indicates that these three equations are linear and of second-order, and differ in the coefficients of the homogeneous operators for $\Delta\phi$, ΔT and Δe, respectively. Upon a second-order accurate discretization of the second-order derivatives, the discretized form of these equations provides a system of linear algebraic equations characterized by a tridiagonal matrix structure. Furthermore, upon freezing the coefficients of the equations as indicated in the previous section, the resulting linear ordinary differential equations may be solved analytically in a piecewise manner, and one can therefore obtain two new formulations for $\Delta\phi$ and Δe analogous to that of the previous section for ΔT (cf. Section 2.2). These two formulations are not reported here.

2.5. Boundary Conditions

In this section, we discuss the implementation of the boundary conditions in the Kirchhoff formulations presented above.

For Dirichlet conditions, $T(t,0) = f(t)$ and $T(t,L) = g(t)$ are specified. This means that the values of $\phi(t,0)$ and $\phi(t,L)$ and those of $e(t,0)$ and $e(t,L)$ can be determined from Equations (2) and (4), respectively, i.e., Dirichlet boundary conditions for T become the same type of boundary conditions for ϕ and e.

For Neumann boundary conditions, $-K(T(t,0))\frac{\partial T(t,0)}{\partial x} = F(t)$ and $K(T(t,L))\frac{\partial T(t,L)}{\partial x} = G(t)$ which may be written as $-\frac{\partial \phi(t,0)}{\partial x} = F(t)$ and $\frac{\partial \phi(t,L)}{\partial x} = G(t)$, respectively, and imply that $-\frac{\partial \Delta\phi(0)}{\partial x} = F(t^{n+1}) - F(t^n)$ and $\frac{\partial \Delta\phi(L)}{\partial x} = G(t^{n+1}) - G(t^n)$, respectively, can be readily implemented in the second Kirchhoff's formulation for $\Delta\phi$. Furthermore, using the first-order approximation for ΔT from Equation (19), these expressions become $-\frac{\partial (K^n(t^n,0)\Delta T(0))}{\partial x} = F(t^{n+1}) - F(t^n)$ and $\frac{\partial (K^n(t^n,L)\Delta T(L))}{\partial x} = G(t^{n+1}) - G(t^n)$, respectively, and are the boundary conditions to be implemented in the first and third Kirchhoff's formulations presented above.

It is worth noting that the thermal Neumann boundary conditions remain Neumann ones for the heat potential, whereas they remain as such for $K\Delta T$, thus indicating that, for

this type of condition, the second Kirchhoff's formulation, i.e., that based on $\Delta\phi$, may be more convenient than that based on the temperature.

For convection or Robin boundary conditions, i.e., $-K(T(t,0))\frac{\partial T(t,0)}{\partial x} = h_l(T_l - T(t,0))$ and $-K(T(t,L))\frac{\partial T(t,L)}{\partial x} = h_r(T(t,L) - T_r)$, where h_l and h_r are the film heat transfer coefficients on the left and right of the domain $[0, L]$, respectively, and T_l and T_r are the temperatures of the fluids far away from the left and right boundaries of the domain, respectively. These boundary conditions may be written as $-\frac{\partial \phi(t,0)}{\partial x} = h_l(T_l - T(t,0))$ and $-\frac{\partial \phi(t,L)}{\partial x} = h_r(T(t,L) - T_r)$ and involve both T and ϕ at each boundary, i.e., they are boundary conditions of the integro-differential type.

If T_l, T_r, h_l and h_r are assumed to be constant, the Robin boundary conditions may be written as $\frac{\partial \Delta\phi(0)}{\partial x} = h_l\Delta T(0)$ and $-\frac{\partial \Delta\phi(L)}{\partial x} = h_r\Delta T(L)$, which upon making use of Equation (19) may be written as $\frac{\partial \Delta\phi(0)}{\partial x} = \frac{h_l}{K^n(t^n,0)}\Delta\phi(0)$ and $-\frac{\partial \Delta\phi(L)}{\partial x} = \frac{h_r}{K^n(t^n,L)}\Delta\phi(L)$, respectively, which are homogeneous linear Robin boundary conditions for $\Delta\phi$. On the other hand, the use of Equation (19) for $\Delta\phi$ in the above time-linearized boundary conditions results in $\frac{\partial (K^n(t^n,0)\Delta T(0))}{\partial x} = h_l\Delta T(0)$ and $-\frac{\partial (K^n(t^n,L)\Delta T(L))}{\partial x} = h_r\Delta T(L)$ which are also homogeneous and may be written as $\frac{\partial (K^n(t^n,0)\Delta T(0))}{\partial x} = \frac{h_l}{K^n(t^n,0)}K^n(t^n,0)\Delta T(0)$ and $-\frac{\partial (K^n(t^n,L)\Delta T(L))}{\partial x} = \frac{h_r}{K^n(t^n,L)}K^n(t^n,L)\Delta T(L)$, respectively, and are homogeneous for $K\Delta T$.

The boundary conditions for e, i.e., the fourth Kirchhoff's formulation presented in Section 2.4, may be easily obtained from those derived above for $\Delta\phi$ and ΔT upon making use of Equations (7) and (10), but are not reported here.

It is worth noting that the use of time linearization for solving one-dimensional, time-dependent reaction–diffusion equations subject to Robin boundary conditions results in linear, second-order ordinary differential equations subject to homogeneous boundary conditions for the heat potential. As indicated in the Introduction, this is in marked contrast with what occurs when the Kirchhoff transformation is used to solve steady heat conduction problems subject to Robin conditions, which result in nonlinear boundary conditions of the integro-differential type.

2.6. Linearization, Operator-Splitting and Factorization Errors

In the four Kirchhoff's formulations presented previously in this section, two-point boundary-value problems were obtained and the coefficients of the second-order differential equations depended on the thermal inertia, thermal conductivity and Jacobian of the reaction terms. However, one could factorize the two-point boundary-value operator into a sequence of simpler operators. This is what we shall address in this section, where, for the sake of convenience, the thermal inertia will be assumed to be temperature-dependent, whereas the thermal conductivity will be assumed to be constant. Under these conditions, a midpoint temporal discretization of Equation (1) results in

$$e^{n+1} - e^n = \Delta t\left(KT^n_{xx} + S^n + \frac{1}{2}(K(\Delta T)_{xx} + J^n\Delta T)\right), \tag{30}$$

which upon using Equation (10) becomes the following first-order accurate equation

$$\mathcal{L}_{RD}(\Delta T) = \left(1 \cdot - \frac{\Delta t}{2\rho^n c^n}(K(\cdot)_{xx} + J^n\cdot)\right)\Delta T = \frac{\Delta t}{\rho^n c^n}(\phi^n_{xx} + S^n) \equiv RHS^n, \tag{31}$$

which may factorized as either

$$\mathcal{L}_{DR}(\Delta T) = \mathcal{L}_D(\mathcal{L}_R(\Delta T)) = RHS^n + FE_{DR}, \tag{32}$$

or

$$\mathcal{L}_{RD}(\Delta T) = \mathcal{L}_R(\mathcal{L}_D(\Delta T)) = RHS^n + FE_{RD}, \tag{33}$$

where

$$\mathcal{L}_D(\cdot) = \left(1 \cdot - \frac{\Delta t}{2\rho^n c^n} K(\cdot)_{xx}\right), \qquad \mathcal{L}_R(\cdot) = \left(1 \cdot - \frac{\Delta t}{2\rho^n c^n} J^n \cdot)\right) \tag{34}$$

denote the diffusion and reaction operators, respectively, and

$$FE_{DR} = \frac{\Delta t^2}{2\rho^n c^n} K\left(\frac{J^n}{2\rho^n c^n}\Delta T\right)_{xx}, \tag{35}$$

and

$$FE_{RD} = \frac{\Delta t^2}{2\rho^n c^n} \frac{KJ^n}{2\rho^n c^n} (\Delta T)_{xx}, \tag{36}$$

denote the factorization errors. These errors can be accounted for in an iterative manner, which is an easy one for Equation (32) (cf. FE_{RD}), whereas that for FE_{DR} (cf. Equation (33)) requires the second derivative of both the Jacobian and the thermal capacity. Since the factorization errors are of second order, they may be neglected, and Equations (32) and (33) may then be written as

$$\mathcal{L}_D(\Delta T^*) = RHS^n, \qquad \mathcal{L}_R(\Delta T) = \Delta T^*, \tag{37}$$

and

$$\mathcal{L}_R(\Delta T^*) = RHS^n, \qquad \mathcal{L}_D(\Delta T) = \Delta T^*, \tag{38}$$

respectively.

The analytical solution to the second equation of Equation (37) is

$$\Delta T = \frac{\Delta T^*}{1 - J^n/(2\rho^n c^n)}, \tag{39}$$

provided that the denominator is not null, while the first of Equation (37) may be written as

$$K\Delta t(\Delta T^*)_{xx} - 2\rho^n c^n \Delta T^* = -2\Delta t RHS^n, \tag{40}$$

which may be solved by means of finite difference methods or by using the third Kirchhoff's formulation presented previously. A similar procedure may be used for the solution of the reaction and diffusion operators of Equation (38).

As one can easily realize, the solution to Equation (37) may not coincide with that of Equation (38) because of the different order in which the reaction and diffusion operators are solved. The difference between the solutions of these two equations is associated with the factorization and splitting of the operators and may be decreased by diminishing the time step.

3. Multidimensional Formulations

In several dimensions, Equation (1) may be written as

$$e(T)_t = \nabla \cdot (K(T)\nabla T)_x + S(T) = \nabla^2 \phi + S(T), \tag{41}$$

where we have used the heat potential as defined in Equation (4).

Although, as shown in the previous section, Equation (41) may formulated for e, ϕ or T, in this section, we present only the formulation for ΔT; the formulations for $\Delta\phi$ and Δe may be easily obtained from that for ΔT upon making use of the first-order approximations of Equations (7) and (10), respectively.

Upon discretizing Equation (41) by means of the Crank–Nicolson method and linearizing ϕ, S and e as shown in Equations (7), (8) and (10), respectively, Equation (41) may be written as

$$\left(C^n \cdot - \frac{1}{2}\Delta t\left(\nabla^2(K^n \cdot) + J^n \cdot\right)\right)\Delta T = R^n, \tag{42}$$

where $C \equiv \rho(T)c(T)$ and

$$R = \Delta t(\nabla^2 \phi^n + S^n). \tag{43}$$

Equation (42) is first-order accurate in time on account of the linearization of e^{n+1} and valid for systems of nonlinearly coupled reaction–diffusion equations. For such systems, C, K and S are vectors and J is a Jacobian matrix.

Herein, we shall assume that we are dealing with systems of coupled nonlinear reaction–diffusion equations and will use bold symbols to identify both vectors and matrices. With this convection, Equation (42) may be written as

$$\left(\mathbf{C}^n \cdot - \frac{1}{2}\Delta t\left(\nabla^2(\mathbf{K}^n \cdot) + \mathbf{J}^n \cdot\right)\right)\Delta \mathbf{T} = \mathbf{R}^n. \tag{44}$$

In two-dimensional problems, upon multiplication of Equation (44) by $(\mathbf{C}^n)^{-1} \equiv \mathbf{c}$ and factorization of the two-dimensional operator into a sequence of one-dimensional ones, it is easy to obtain

$$\left(\mathbf{I} \cdot - \frac{1}{2}\Delta t\mathbf{c}(((\mathbf{K})^n \cdot)_{xx} + \alpha \mathbf{J}^n \cdot)\right) \cdot \left(\mathbf{I} \cdot - \frac{1}{2}\Delta t\mathbf{c}\left(((\mathbf{K})^n \cdot)_{yy} + \beta \mathbf{J}^n \cdot\right)\right)\Delta \mathbf{T} = \hat{\mathbf{R}}^n, \tag{45}$$

where $\hat{\mathbf{R}}^n = \mathbf{c}\mathbf{R}^n + \mathbf{FE}$, $\mathbf{FE} = \mathcal{O}(\Delta t^2)$ are the factorization errors that occur because of the factorization of the two-dimensional operator into a sequence of two one-dimensional ones, and $\alpha + \beta = 1$. The second-order factorization errors may be neglected because they are of the same or higher order than the ones incurred in the discretization of the system of reaction–diffusion equations, so that Equation (45) may be written as

$$\mathcal{L}_x(\mathcal{L}_y(\Delta \mathbf{T})) = \mathbf{c}\mathbf{R}^n, \tag{46}$$

which can be solved as

$$\left(\mathbf{I} \cdot - \frac{1}{2}\Delta t\mathbf{c}(((\mathbf{K})^n \cdot)_{xx} + \beta \mathbf{J}^n \cdot)\right)\Delta \mathbf{T}^* = \mathbf{c}\mathbf{R}^n, \tag{47}$$

$$\left(\mathbf{I} \cdot - \frac{1}{2}\Delta t\mathbf{c}(((\mathbf{K})^n \cdot)_{yy} + \beta \mathbf{J}^n \cdot)\right)\Delta \mathbf{T} = \Delta \mathbf{T}^*, \tag{48}$$

or, more conveniently,

$$\left(\mathbf{C}^n \cdot - \frac{1}{2}\Delta t(((\mathbf{K})^n \cdot)_{xx} + \beta \mathbf{J}^n \cdot)\right)\Delta \mathbf{T}^* = \mathbf{R}^n, \tag{49}$$

$$\left(\mathbf{C}^n \cdot - \frac{1}{2}\Delta t\left(((\mathbf{K})^n \cdot)_{yy} + \beta \mathbf{J}^n \cdot\right)\right)\Delta \mathbf{T} = \mathbf{C}^n \mathbf{T}^*, \tag{50}$$

because they do not involve multiplication by $\mathbf{c}$. Note that $\mathbf{c} \equiv (\mathbf{C}^n)^{-1}$.

As indicated above, the time linearization method presented in this section is first-order accurate in time due to the use of Equation (10) in determining ΔT from Δe. Since equally spaced grids were used in the x- and y-directions and three-point, second-order-accurate, central finite difference formulae were used to discretize the second-order spatial derivatives, the time step in the calculations was always chosen as $\Delta t \leq \min(\Delta x^2, \Delta y^2)$, so that the temporal and spatial discretization errors were of the same order of magnitude. In addition, Richardson extrapolation in time was used to improve the temporal accuracy of the numerical results.

For linear problems, i.e., constant density, constant specific heat and constant thermal conductivity, and a source term $S(T)$ that depends linearly on T, Equation (2) is linearly proportional to T, J^n is constant, and Equation (30) is a linear one; a similar comment applies to Equation (41). For these conditions, it is well known that the implicit time discretization

and the piecewise analytical approximations of Equations (24) and (26) result in a system of linear algebraic equations and a finite difference method which is linearly stable according to the Fourier–von Neumann linear stability analysis method. Moreover, as stated just after Equation (50), the method presented in this paper is second-order accurate in space and, at least, first-order accurate in time, as one can also easily verify by using Taylor's series expansions of Equations (24) and (26), and, therefore, it is consistent. Therefore, according to the Richtmyer–Lax equivalence theorem, the time linearization method presented here is convergent.

The spatial discretization of the time-linearized Equations (49) and (50) results in the solution of linear one-dimensional/directional problems at each time level (cf. Equations (24) and (26)), while the solution of Equation (42) upon discretization of the second-order spatial derivatives requires the solution of linear multidimensional equations at each time level. By way of contrast, the implicit temporal and spatial discretizations of Equation (41) require the iterative solutions of nonlinear algebraic equations at each time level. However, as stated above, Equation (44) has been obtained from the time linearization of Equation (41) and such a linearization is accurate only if the time step is smaller than the diffusion and reaction times, as stated previously. Furthermore, Equations (49) and (50) have been obtained from the factorization of the multidimensional operators that appear in Equation (44), and such a factorization results in $\mathcal{O}(\Delta t^2)$-factorization errors.

Although not shown here, neither the stability nor the accuracy of the numerical method presented in this paper are affected by the boundary conditions provided that these conditions are discretized by means of implicit finite difference expressions which are stable and consistent and of an order less than or equal to that of the spatial discretization employed at interior points. Nonetheless, it must be stated that a matrix stability analysis of the nonlinear Equation (41) has not been performed.

As stated above, the time-linearized method presented in this paper requires that $S(T)$ and $K(T)$ be differentiable functions. Therefore, provided that this requirement is met, the method may be used to study nonlinear reaction–diffusion problems arising in combustion, chemical engineering, biology, ecology, population dynamics, nanotechnology, etc., where either the thermal inertia or heat conductivity are much stronger nonlinear functions of T than the ones considered in the next section. For example, in combustion, the source term may be expressed as $S(T) = \beta \exp\left(-\frac{E}{\hat{R}T}\right)$ where β is the pre-exponential factor that may depend on T, E is the activation energy, and $\hat{R}$ is the universal gas constant.

4. Results

In this section, some sample results corresponding to the following two-dimensional, two-equation, nonlinear system of advection–reaction–diffusion equations

$$M_u(u_t + Uu_x + Vu_y) = (D_u u_x)_x + (D_u u_y)_y + S_u, \tag{51}$$

$$M_v(v_t + Uv_x + Vv_y) = (D_v v_x)_x + (D_v v_y)_y + S_v, \tag{52}$$

are presented, where

$$M_u = \alpha_u + \beta_u u^{n_u}, \qquad M_v = \alpha_v + \beta_v v^{n_v}, \tag{53}$$

$$D_u = \gamma_u + \theta_u u^{n_u}, \qquad D_v = 0.6(\gamma_v + \theta_v v^{n_v}), \tag{54}$$

$$S_u = \frac{1}{\epsilon}\left(u - u^2 - fv\frac{u-q}{u+q}\right), \qquad S_v = u - v, \tag{55}$$

α_u, α_v, β_u, β_v, γ_u, γ_v, θ_u, θ_v, n_u, n_v, m_u, m_v are constants, $\epsilon = 0.01$, $f = 1.4$, $q = 0.002$, U and V are the velocity components of a Rankine vortex field whose azimuthal velocity is

$$u_\theta = \frac{\Gamma}{2\pi}\frac{r}{R^2} \qquad \text{for} \qquad r \leq R, \qquad u_\theta = \frac{\Gamma}{2\pi r} \qquad \text{for} \qquad r > R, \tag{56}$$

and Γ and R denote the circulation and core radius of the vortex, respectively.

Equations (51) and (52) were solved in a square domain $[-L, L] \times [-L, L]$ where $L = 7.5$, and equally spaced meshes consisting of at least 101×101 grid points and a time step less or equal than 0.0001, using the time linearization method presented in Section 3, homogeneous Neumann conditions and initial conditions identical to those employed in other studies [23]. The convection terms that appear in Equations (51) and (52) were discretized by either second-order-accurate central or first-order-accurate upwind finite differences depending on the magnitude of the local mesh Péclet number.

For $M_u = M_v = 1$, $D_u = 1$ and $D_v = 0.6$, Equations (51) and (52) are known as the two-component Oregonator model, which is somewhat related to the Belousov–Zhabotinsky model and exhibits periodic, counter-rotating spiral wave solutions whose tip rotates around the center of the domain.

The effects of the nonlinear diffusion coefficients D_u and D_v, convection, i.e., Γ and R, and inertia, i.e., M_u and M_v, on the solution of Equations (51) and (52) are described in the next three sections.

4.1. Effects of Nonlinear Diffusion

Figures 1 and 2 show the distributions of u and v, respectively, at different times, for $\Gamma = 0$, $M_u = M_v = 1$, $\theta_u = \theta_v = 0$, and $\gamma_u = 0.7$, $\gamma_v = 0.1$, $\theta_u = 0.5$, $\theta_v = 0.1$, $m_u = 2$ and $m_v = 3$. Both figures clearly indicate the presence of a counter-clockwise spiral wave which is not as smooth as that observed for $M_u = M_v = 1$, $D_u = 1$ and $D_v = 0.6$ (not shown here [23]) due to the spatial variation of D_u and D_v and the fact that the largest value of D_v in Figures 1 and 2 is much smaller than 0.6. As a consequence, v diffuses at a much slower rate than for $D_v = 0.6$ and this is reflected in the distributions of u shown in Figure 1 that also seem to remember the wedge-shape initial conditions used in the numerical experiments reported in this study. Although not shown here, the smoothness of the distributions of both u and v increase as that of the initial conditions is increased.

The distribution of v illustrated in Figure 2 also indicates the presence of a spiral wave which is not as smooth as that corresponding to $M_u = M_v = 1$, $D_u = 1$ and $D_v = 0.6$. Similar trends to those shown in Figures 1 and 2 have been observed in many numerical experiments performed for $\gamma_u = 0.7$, $0 \leq \theta_u \leq 0.5$, $1 \leq n_u \leq 3$, $0.1 \leq \gamma_v \leq 0.6$, $0.1 \leq \theta_v \leq 0.3$ and $1 \leq n_v \leq 3$. The main differences between the results corresponding to different values of the parameters that characterize D_u and D_v can be summarized as follows. The smoothness of the spiral wave solutions increases as γ_u, γ_v, θ_u and θ_v increase; the effects of m_u and m_v are small for $\gamma_u >> \theta_u$ and $\gamma_v >> \theta_v$; the time required for the formation of the periodic spiral wave increases as D_u and D_v decrease; and the thickness of the v distribution decreases as D_u is decreased.

In Figure 3, the time histories of u and v at three selected (monitoring) points are shown for two different sets of parameters that characterize D_u and D_v. The three points at which u and v are illustrated in Figure 3 are located in the main diagonal of the square domain and at the center and midway between the center and the bottom-left and upper-right corners of the domain.

The time traces shown in Figure 3 indicate that u and v at the locations away from the center of the domain exhibit an almost constant amplitude, whereas those corresponding to the center of the domain change with time, thus indicating a time modulation at this location which depends on the parameters that affect the values of D_u and D_v. This modulation is not observed for constant values of D_u and D_v and, therefore, it may be concluded that it is a consequence of the nonlinear dependence of D_u and D_v on u and v, respectively.

Figure 3 also shows that the amplitude modulation of the time traces of both u and v is larger for $(\gamma_v, \theta_v, m_v) = (0.6,\ 0.3,\ 2)$ than for (0.1, 0.1, 3).

In Table 1, the period of the spiral wave is shown as a function of the parameters that characterize the nonlinear diffusion coefficients D_u and D_v in Equations (51) and (52), respectively. For the values of the parameters shown in that table, it is observed that the period is nearly independent of γ_u, decreases as θ_u is increased, and first decreases and reaches a constant value as n_u is increased, in accord with the fact that, since $u(t, x, y) < 1$, $u^{n_u}(t, x, y)$ and therefore D_u decrease as n_u is increased. Similar behavior has been observed for the dependence of the period on γ_v, θ_v and n_v, as reported in Table 1.

Table 1. Period of the spiral wave.

γ_u	θ_u	n_u	γ_v	θ_v	n_v	**Period**
0.90	0.3	2	0.60	0.10	1	2.54
0.60	0.3	2	0.60	0.10	1	2.54
0.70	0.3	2	0.60	0.30	2	1.78
0.70	0.5	2	0.60	0.30	2	1.53
0.70	0.5	0	0.60	0.10	3	4.24
0.70	0.5	1	0.60	0.10	3	1.53
0.70	0.5	2	0.60	0.10	3	1.53
1.00	0.0	1	0.30	0.10	2	4.24
1.00	0.0	1	0.10	0.10	2	4.24
0.70	0.3	1	0.60	0.10	2	1.78
0.70	0.3	1	0.60	0.30	2	1.53
0.70	0.5	3	0.60	0.30	1	2.03
0.70	0.5	3	0.60	0.30	2	1.69
0.70	0.5	3	0.60	0.30	3	1.69

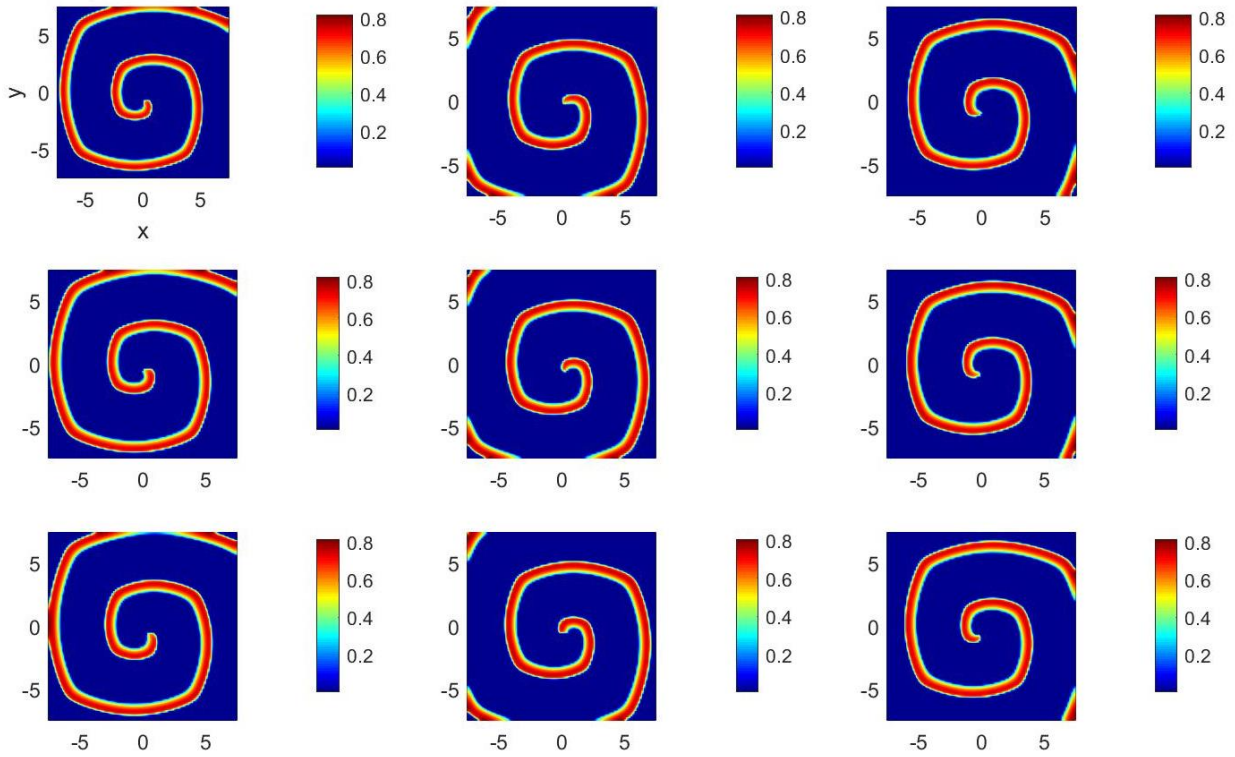

Figure 1. (Color online) $u(t, x, y)$ at (from **left** to **right** and **top** to **bottom**) $t = 50$, 55, 60, 65, 70, 75, 80, 85 and 90 for $\Gamma = 0$, $M_u = M_v = 1$, $\theta_u = \theta_v = 0$, $\gamma_u = 0.7$, $\gamma_v = 0.1$, $\theta_u = 0.5$, $\theta_v = 0.1$, $m_u = 2$ and $m_v = 3$.

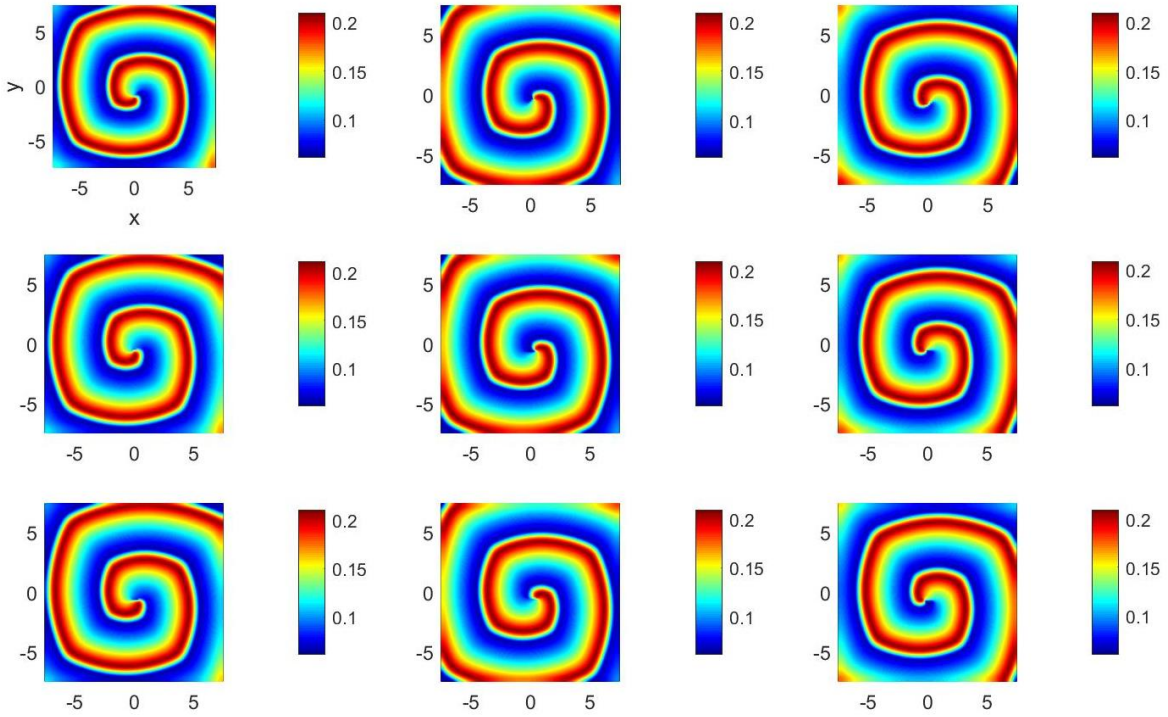

Figure 2. (Color online) $v(t, x, y)$ at (from **left** to **right** and **top** to **bottom**) $t = 50$, 55, 60, 65, 70, 75, 80, 85 and 90 for $\Gamma = 0$, $M_u = M_v = 1$, $\theta_u = \theta_v = 0$, $\gamma_u = 0.7$, $\gamma_v = 0.1$, $\theta_u = 0.5$, $\theta_v = 0.1$, $m_u = 2$ and $m_v = 3$.

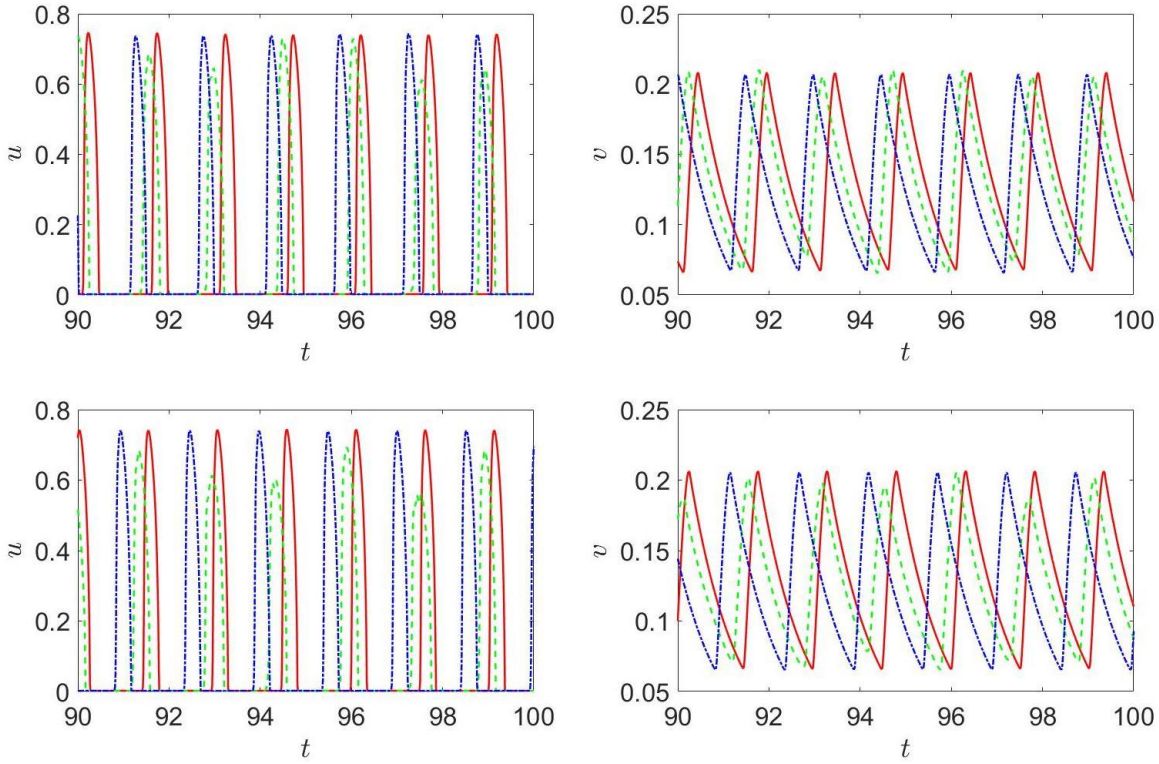

Figure 3. (Color online) $u(t,x,y)$ (**left**) and $v(t,x,y)$ (**right**) at $(x,y) = \left(-\frac{L}{2},-\frac{L}{2}\right)$ (continuous line, red), $(0,\ 0)$ (dashed line, green) and $\left(\frac{L}{2},\frac{L}{2}\right)$ (dashed–dotted line, blue) for $L = 7.5$, $\Gamma = 0$, $M_u = M_v = 1$, $\theta_u = \theta_v = 0$, $\gamma_u = 0.7$, $\gamma_v = 0.1$, $\theta_u = 0.5$, $\theta_v = 0.1$, $m_u = 2$ and $m_v = 3$ (**top**) and $\Gamma = 0$, $M_u = M_v = 1$, $\theta_u = \theta_v = 0$, $\gamma_u = 0.7$, $\gamma_v = 0.6$, $\theta_u = 0.5$, $\theta_v = 0.3$, $m_u = 2$ and $m_v = 2$ (**bottom**).

4.2. Effects of Convection

The effects of convection on the solution to Equations (51) and (52) have been first assessed for $D_u = 1$ and $D_v = 0.6$, $\alpha_u = \alpha_v = 0.75$, $\beta_u = \beta_v = \frac{4}{9}$ and $n_u = n_v = 3$, for different values of $\omega \equiv \frac{\Gamma}{\pi R^2}$ and R. Note that positive values of Γ correspond to a counter-clockwise velocity field and, since, in the absence of convection, the solution to Equations (51) and (52) is characterized by a counter-rotating spiral wave, one is led to think that positive values of Γ will push the wave, whereas negative ones would try to decelerate it.

Figures 4–6 show the u distributions at selected times for $(\omega, R) = (0.5, 2.5)$, $(2.5, 2.5)$ and $(-2.5, 2.5)$, respectively, i.e., Rankine's vortices of the same core but different circulations, and illustrate the effects of the magnitude and direction of the vortex circulation on the spiral wave dynamics. For positive values of ω, the results presented in Figures 4 and 6 indicate that the counter-clockwise-rotating spiral wave is strained and stretched by the counter-clockwise-rotating vortex, and the stretching increases as ω is increased.

The spiral wave shown in Figure 4 is much smoother and thicker than that shown in Figure 1, but that shown in Figure 5 is thicker than that of Figure 4, thus indicating that the wave thickness first decreases as ω is increased from 0, i.e., no vortex field, to about 1, and then thickens as illustrated in Figure 5.

Figure 6 corresponds to a clockwise-rotating vortex field and also exhibits the arm of a counter-rotating spiral wave.

A comparison between Figures 4 and 6 clearly shows that positive values of ω result in spiral wave stretching and thinning, whereas negative ones result in compressed and thicker waves. The distributions of v for the values of the parameters of Figures 4–6 are not shown here for the sake of conciseness.

The effects of ω on the time histories at the three monitoring locations within the domain are illustrated in Figure 7, which indicates that, for $(\omega, R) = (0.5, 2.5)$, the amplitudes of both u and v are not constant, $u(t, -\frac{L}{2}, -\frac{L}{2})$ and $v(t, -\frac{L}{2}, -\frac{L}{2})$ exhibit a higher-amplitude time modulation than $u(t, \frac{L}{2}, \frac{L}{2})$ and $v(t, \frac{L}{2}, \frac{L}{2})$, and the latter is slightly larger than that for $u(t, 0, 0)$ and $v(t, 0, 0)$, respectively. Moreover, the time difference between two subsequent peaks of either u and v is about $\Delta t_{peak} \approx 1.24$ for $(\omega, R) = (0.5, 2.5)$.

By way of contrast, no modulation is observed in Figure 7 for $(\omega, R) = (2.5, 2.5)$ and $(-2.5, 2.5)$, where the time differences between two subsequent peaks of u or v are 3.62 and 1.90, respectively. This indicates that the time difference between subsequent peaks decreases as ω is increased from negative values to zero and then increases as ω is increased. Furthermore, the results presented in Figure 7 indicate that there is no modulation in the time traces of u and v at the three locations considered in that figure for $(\omega, R) = (2.5, 2.5)$ and $(-2.5, 2.5)$, and that there are very tiny differences in the u and v history traces at the three monitoring locations referred to above for $(\omega, R) = (2.5, 2.5)$ in accordance with the u distribution illustrated in Figure 5.

For $(\omega, R) = (2.5, 2.5)$, the v time histories at the off-center monitoring locations are almost identical and exhibit sawtooth shapes of much higher amplitude than the v-time trace at the monitoring point located in the middle of the domain.

Figure 7 also shows that the slope of the time traces of u for $(\omega, R) = (-2.5, 2.5)$ is larger than that for $(\omega, R) = (0.5, 2.5)$ as $t \to t_{peak}$, where t_{peak} denotes the time at which the time histories of u or v reach their maximum values. In addition, the time intervals between two subsequent peaks of either u and v for $(\omega, R) = (2.5, 2.5)$ and $(\omega, R) = (-2.5, 2.5)$ are $\Delta t_{peak} \approx 3.62$ and 1.90, respectively.

The effect of the Rankine's vortex core radius is illustrated in Figure 8 for the same parameters as those of Figure 7 and $\omega = 2.5$, and show similar trends to the ones shown in that figure. For $R = 0.5$, 1 and 2.5, the results of Figure 8 indicate that $\Delta t_{peak} \approx 1.39$, 1.30 and 3.62, respectively, thus indicating that the time interval between two subsequent peaks in the time histories of u and v at selected points within the domain is not a monotonic function of the vortex core radius. Since this time interval is not a monotonic function of ω either, as shown in Figure 7, it may be concluded that both the vortex circulation and core radius play a paramount role in determining the spiral wave dynamics.

Although not shown here, similar results to those illustrated in Figures 4–8 have been found for $\alpha_u = \alpha_v = 1$ and $\beta_u = \beta_v = 0$, i.e., constant values of $D_u = 1$ and $D_v = 0.6$, respectively, and the same vortex velocity fields as in those figures. The reasons for such a similarity are several-fold. First, the values of α_u, α_v, β_u, β_v, n_u and n_v were selected so that the values of $D_u(\max u)$ and $D_v(\max v)$ were equal to 1 and 0.6, respectively, where $\max u$ and $\max v$ are the peak values of u and v corresponding to numerical experiments performed with $D_u = 1$ and $D_v = 0.6$ for $\Gamma = 0$. Second, β_u and β_v are smaller than α_u and α_v, respectively. Third, since $(\max u)$ and $(\max v)$ are less than unity, $(\max u)^{n_u}$ and $(\max v)^{n_v}$ are smaller than $(\max u)$ and $(\max v)$, respectively, so that the values of $D_u(u)$ and $D_v(v)$ depend mainly on the constant values of α_u and α_v, respectively. However, as will be shown in the next subsection, if these conditions are not satisfied, the time required for the formation of a stable propagating wave may be much longer than the times reported in Figures 1–8.

The results presented in Figures 4–8 clearly indicate that there are values of ω and R, e.g., $(2.5, 2.5)$, for which there is a large time interval between subsequent peaks of either u or v.

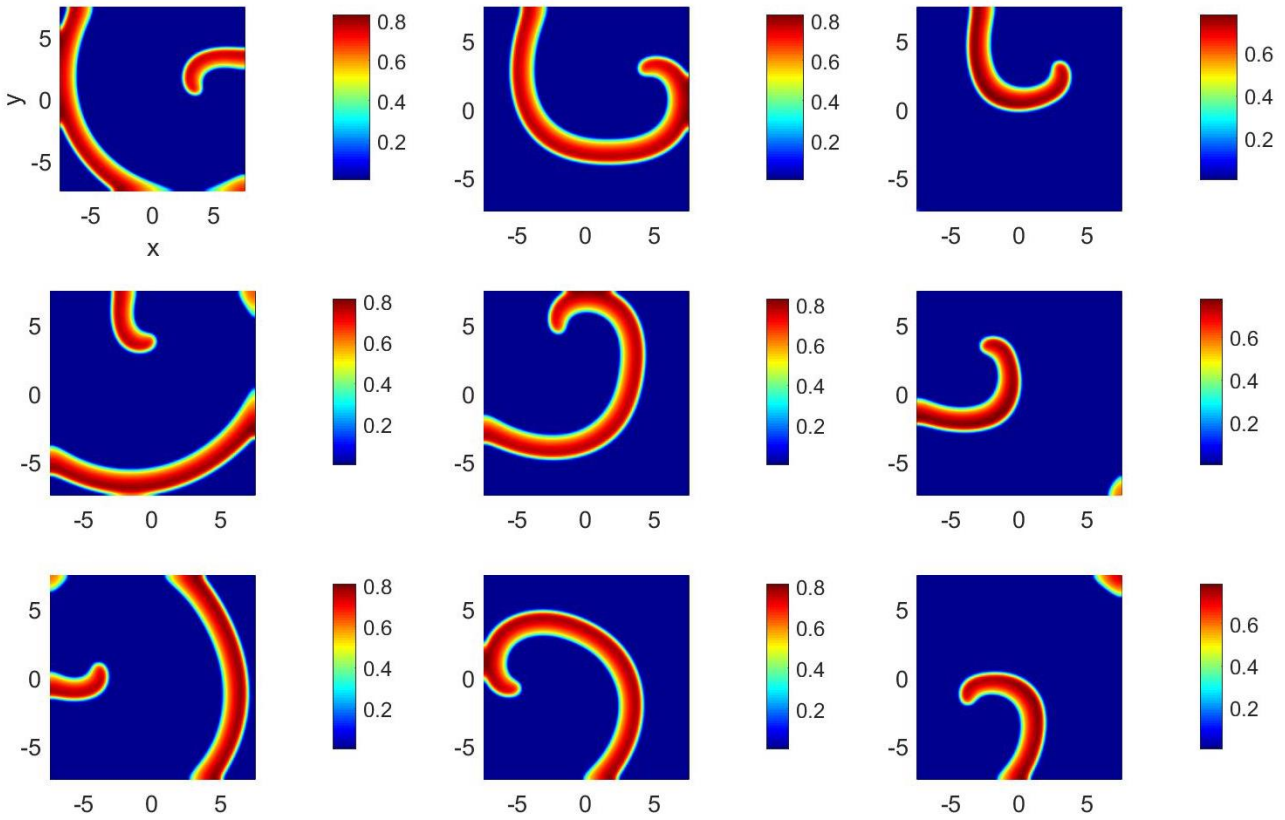

Figure 4. (Color online) $u(t, x, y)$ at (from **left** to **right** and **top** to **bottom**) $t = 50$, 55, 60, 65, 70, 75, 80, 85 and 90 for $D_u = 1$, $D_v = 0.6$, $\alpha_u = \alpha_v = 0.75$, $\beta_u = \beta_v = \frac{4}{9}$, $n_u = n_v = 3$, $\omega = 0.5$ and $R = 2.5$.

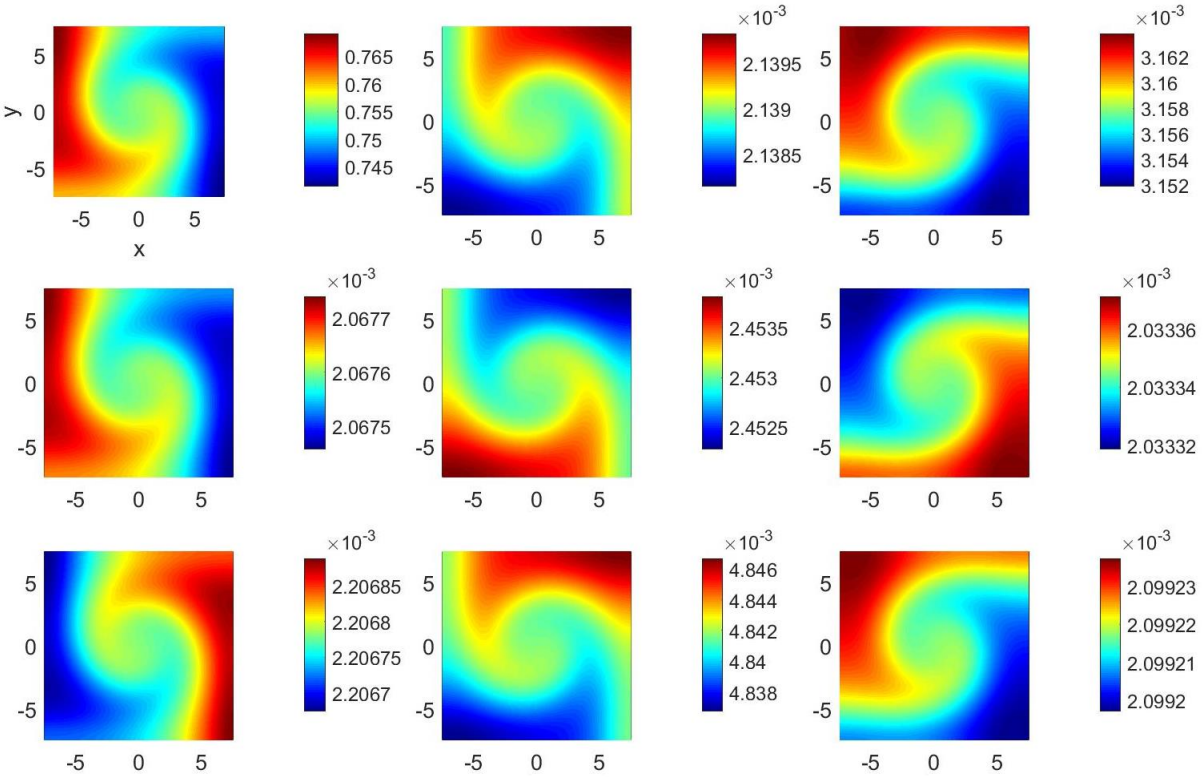

Figure 5. (Color online) $u(t,x,y)$ at (from **left** to **right** and **top** to **bottom**) $t = 50, 55, 60, 65, 70, 75, 80, 85$ and 90 for $D_u = 1$, $D_v = 0.6$, $\alpha_u = \alpha_v = 0.75$, $\beta_u = \beta_v = \frac{4}{9}$, $n_u = n_v = 3$, $\omega = 2.5$ and $R = 2.5$.

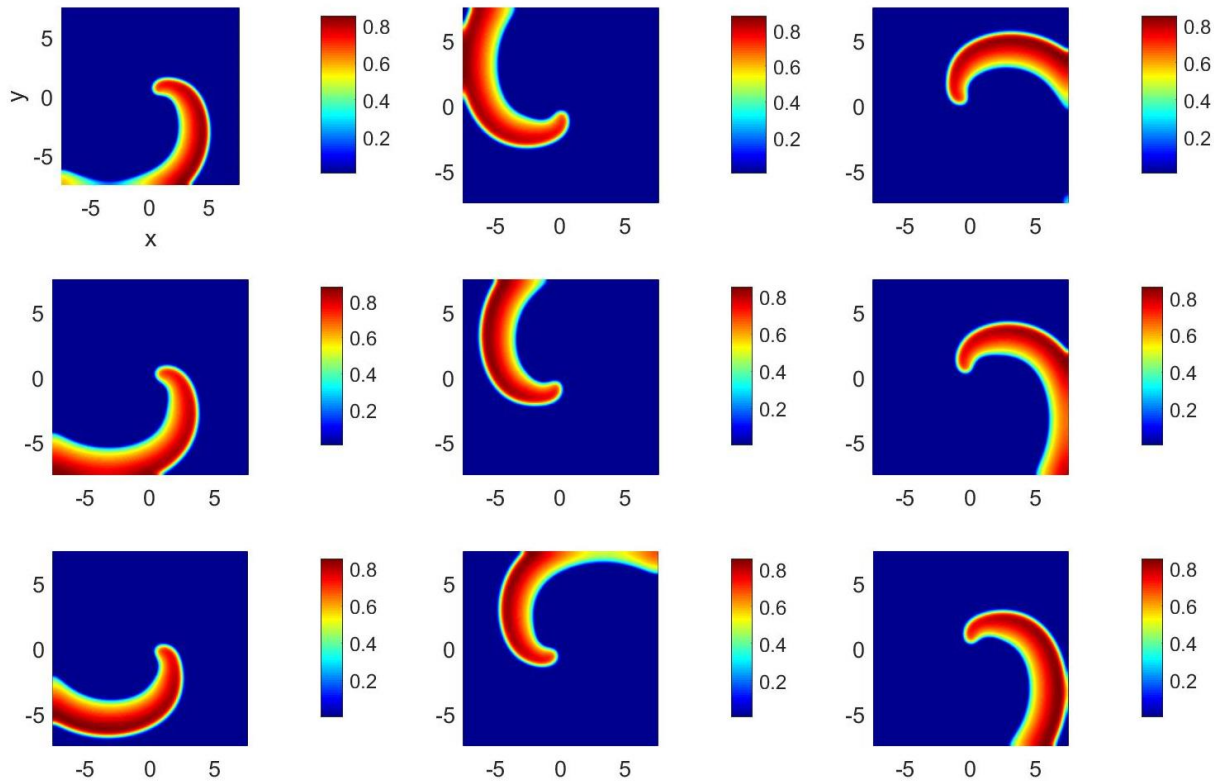

Figure 6. (Color online) $u(t,x,y)$ at (from **left** to **right** and **top** to **bottom**) $t = 50, 55, 60, 65, 70, 75, 80, 85$ and 90 for $D_u = 1$, $D_v = 0.6$, $\alpha_u = \alpha_v = 0.75$, $\beta_u = \beta_v = \frac{4}{9}$, $n_u = n_v = 3$, $\omega = -2.5$ and $R = 2.5$.

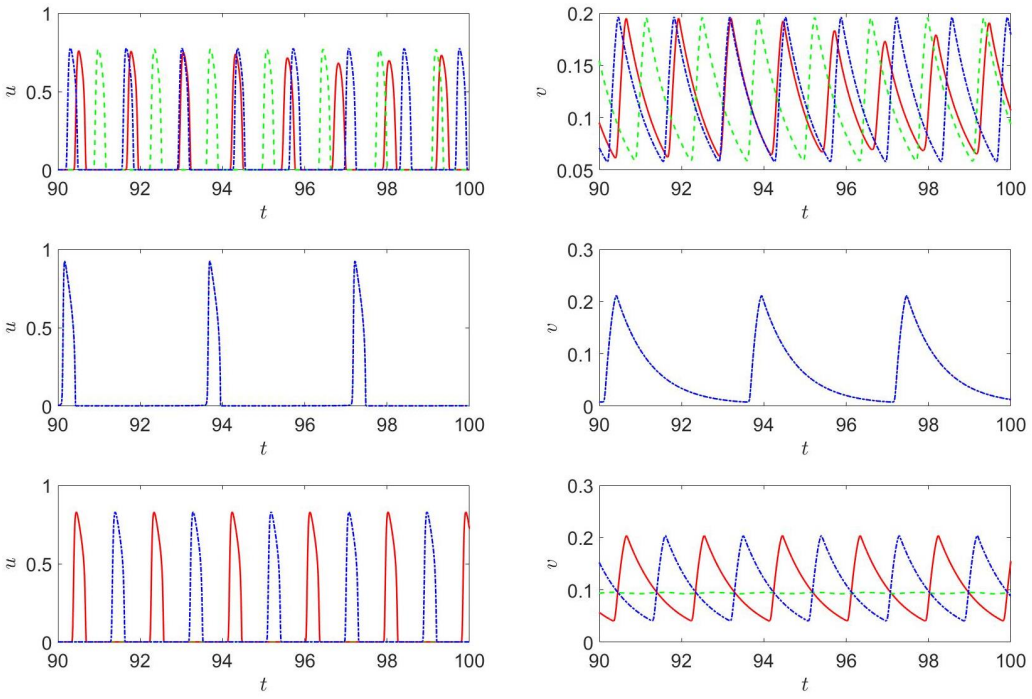

Figure 7. (Color online) $u(t,x,y)$ (**left**) and $v(t,x,y)$ (**right**) at $(x,y) = \left(-\frac{L}{2},-\frac{L}{2}\right)$ (continuous line, red), $(0,0)$ (dashed line, green) and $\left(\frac{L}{2},\frac{L}{2}\right)$ (dashed–dotted line, blue) for $D_u = 1$, $D_v = 0.6$, $\alpha_u = \alpha_v = 0.75$, $\beta_u = \beta_v = \frac{4}{9}$, $n_u = n_v = 3$, and $(\omega, R) = (0.5, 2.5)$ (**top row**), $(2.5, 2.5)$ (**middle row**) and $(-2.5, 2.5)$ (**bottom row**).

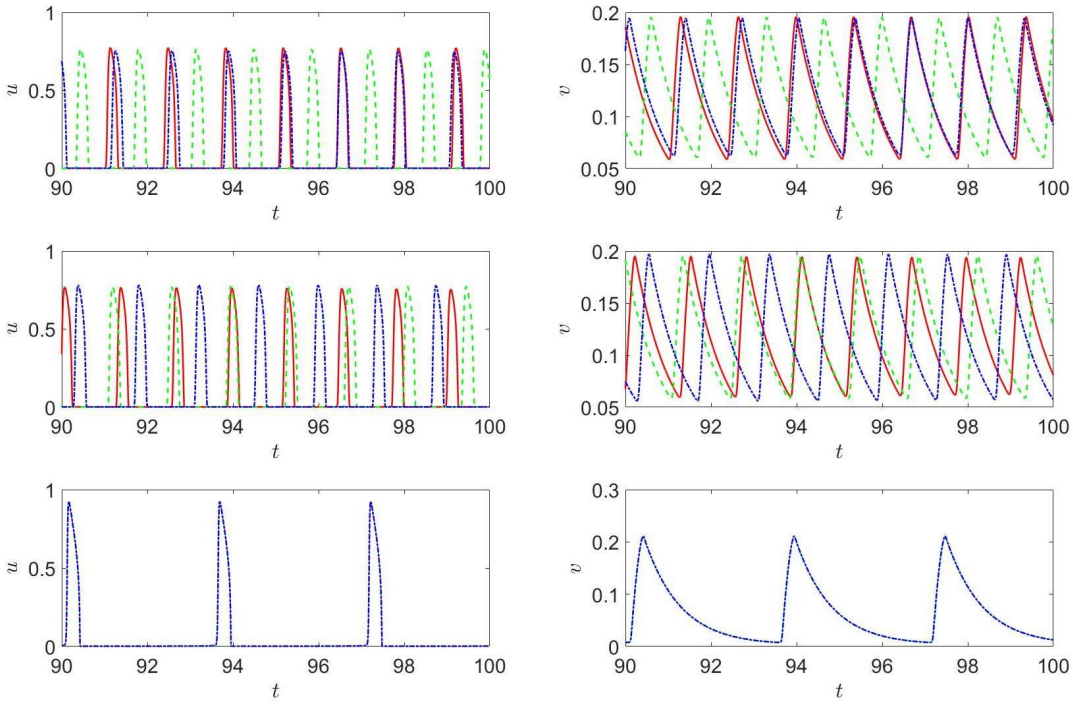

Figure 8. (Color online) $u(t,x,y)$ (**left**) and $v(t,x,y)$ (**right**) at $(x,y) = \left(-\frac{L}{2},-\frac{L}{2}\right)$ (continuous line, red), $(0,0)$ (dashed line, green) and $\left(\frac{L}{2},\frac{L}{2}\right)$ (dashed–dotted line, blue) for $D_u = 1$, $D_v = 0.6$, $\alpha_u = \alpha_v = 0.75$, $\beta_u = \beta_v = \frac{4}{9}$, $n_u = n_v = 3$, and $(\omega, R) = (2.5, 0.5)$ (**top row**), $(2.5, 1)$ (**middle row**) and $(2.5, 2.5)$ (**bottom row**).

4.3. Effects of M_u and M_v

In this subsection, some results corresponding to the effects of M_u and M_v on the numerical solution of Equations (51) and (52) are reported. As indicated in Section 2, we shall refer to these coefficients as the thermal inertia in the case of the energy equation or as density in the case of chemical species, respectively.

For $D_u = 1$, $D_v = 0.6$, $\alpha_u = \alpha_v = 0.75$, $\beta_u = \beta_v = \frac{4}{9}$, and $n_u = n_v = 2$, it has been found that the u and v distributions and the time histories of these variables at the above-referred three locations, shown in Figures 9 and 10, exhibit the same trends as those of Figures 4–6, and that $\Delta t_{peak} \approx 1.48$, 3.95 and 2.14 for $(\omega, R) = (0.5, 2.5)$, $(2.5, 2.5)$ and $(-2.5, 2.5)$, respectively, and approximately 1.54, 1.49 and 3.95 for $(\omega, R) = (2.5, 0.5)$, $(2.5, 1)$ and $(2.5, 2.5)$, respectively, which are larger than those of Figures 7 and 8, respectively, for which $n_u = n_v = 3$. This indicates that, for the same initial conditions and velocity field, the time interval between two subsequent peaks of either u or v decreases as n_u or n_v is increased, i.e., as the nonlinearity of the thermal inertia is increased. Moreover, the amplitude of the modulations of u and v observed for $(\omega, R) = (0.5, 2.5)$ at the three monitoring locations decreases as n_u or n_v is decreased, as illustrated in Figures 7 and 9.

For $D_u = 1$, $D_v = 0.6$, $\alpha_u = 0.75$, $\alpha_v = 0.15$, $\beta_u = \frac{4}{9}$, $\beta_u = \frac{40}{9}$, and $n_u = n_v = 2$ which only differ in D_v from those of Figures 4–6, very interesting and novel phenomena were found, as described next.

For positive values of ω, i.e., counter-clockwise-rotating velocity fields, both u and v exhibit an initially oscillatory behavior followed by a monotonic decrease to small values; this initial decrease is then followed by periodic behavior as shown in Figures 11 and 12. Note that the final truly periodic behavior occurs for much larger times than those observed previously in Figures 1–10.

Figure 11 shows the u and v histories at the three selected monitoring locations within the computational domain for $(\omega, R) = (0.5, 1)$, $(2.5, 1)$ and $(5, 1)$, i.e., vortices that have the same core radius but different circulations, while Figure 12 exhibits the time histories for $(\omega, R) = (2.5, 0.5)$, $(2.5, 1)$ and $(2.5, 2.5)$, i.e., vortices of the same angular speed but different core radii.

Figure 11 indicates that the time intervals of the initial oscillations of both u and v for $\omega = 0.5$, 2.5 and 5 are approximately 53.4, 53.4 and 15.3, respectively. The "silence time interval", defined as the time interval between the end of the initial oscillations and the appearance of the first maximum value of u, and the period of the stable oscillations are approximately equal to 62.7 and 76.3, respectively, and are almost independent of ω. The period observed in Figure 11 is much larger than that shown previously and is a consequence of the small value of D_v.

The time histories exhibited in Figure 12 indicate that the duration of the initial oscillations first increases as R is increased from 0.5 to 1, and then decreases as R is increased from 1 to 2.5. The "silence time interval" and the period of the stable wave are approximately equal to those shown Figure 11, thus indicating that both the time interval and the period do not depend much on the vortex circulation.

For clockwise-rotating vortex fields, the results presented in Figures 13 and 14 are remarkably different from those in Figures 11 and 12, respectively, except for those corresponding to $(\omega, R) = (-2.5, 2.5)$. Figure 13 shows that, after an initial transient period whose duration increases as the vortex circulation is increased, the time histories of u settle to an almost periodic behavior that exhibits amplitude modulation; the amplitude of the modulation increases as the vortex circulation is increased. Figure 13 also shows that the time required to reach almost periodic behavior is much smaller than that of Figure 11, which corresponds to counter-clockwise-rotating velocity fields. Figure 13 also shows that the time traces of v exhibit both a sawtooth pattern that oscillates about $v \approx 0.15$ and amplitude modulation.

The amplitude and frequency of the v-sawtooth patterns illustrated in Figure 13 are smaller and larger, respectively, than those of the v-time histories shown in Figure 11,

thus indicating that the direction of the vortex circulation plays a paramount role on the dynamics of the wave propagation.

Also for clock-rotating vortex fields, the results presented in Figure 14 indicate that vortex core radii smaller than or equal to unity show time histories similar to those illustrated in Figure 13, i.e., the traces of u and v exhibit amplitude modulation whose magnitude increases as R is increased, the traces of v have smaller amplitude and higher frequency than those of Figure 12, and the time required to achieve a stable periodic wave increases as R is increased. However, for $(\omega, R) = (-2.5, 2.5)$, the results presented in Figure 14 show analogous trends to those of Figures 11 and 12, but the durations of both the initial transient and the "silence zone" are approximately equal to 13.4 and 60.5, respectively, and the period of the stable propagation is about 76.3.

The u distributions at selected times corresponding to some of the time histories illustrated in Figures 13 and 14 are presented in Figures 15–17. Figure 15 shows a counter-clockwise-rotating spiral wave which has been substantially distorted by the vortex field and whose tip undergoes large changes in time as compared with the spiral waves observed for $D_u = 1$, $D_v = 0.6$ and $\omega = 0$.

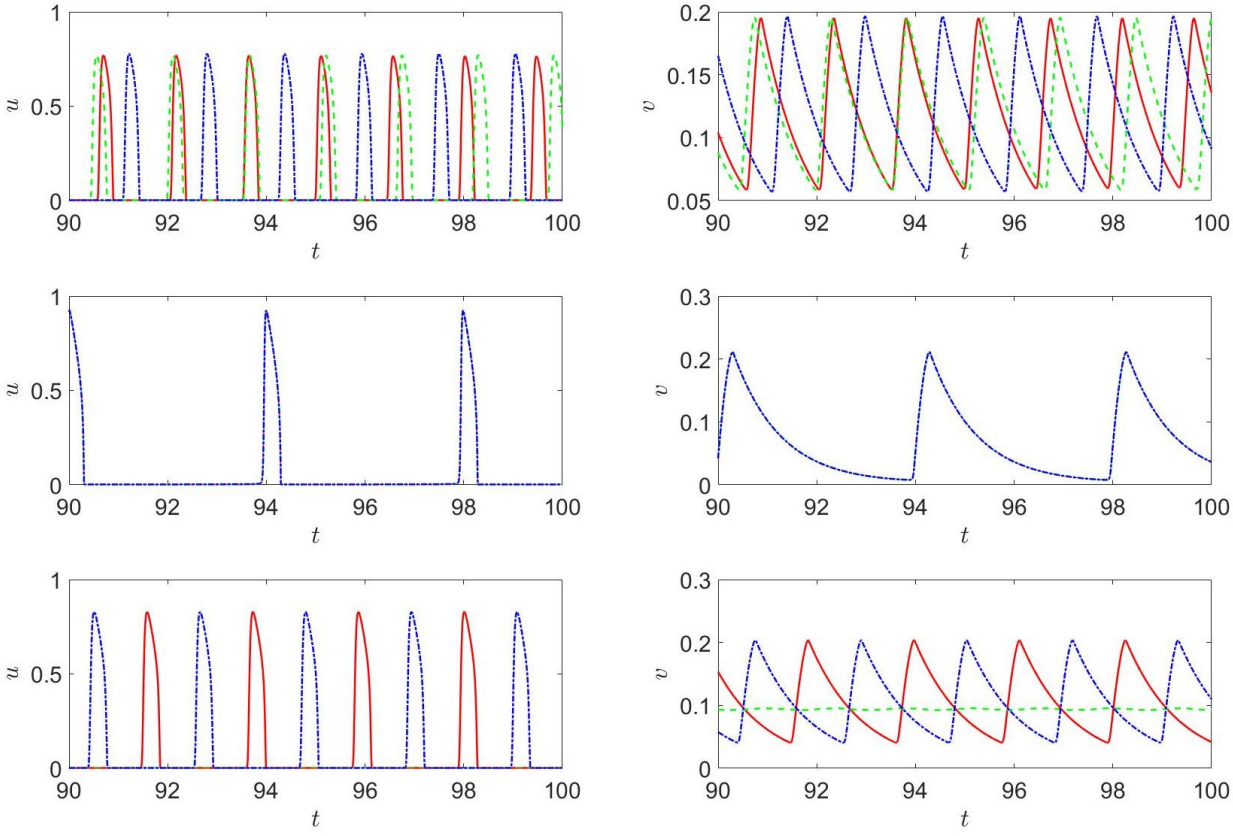

Figure 9. (Color online) $u(t, x, y)$ (**left**) and $v(t, x, y)$ (**right**) at $(x, y) = \left(-\frac{L}{2}, -\frac{L}{2}\right)$ (continuous line, red), $(0, 0)$ (dashed line, green) and $\left(\frac{L}{2}, \frac{L}{2}\right)$ (dashed–dotted line, blue) for $D_u = 1$, $D_v = 0.6$, $\alpha_u = \alpha_v = 0.75$, $\beta_u = \beta_v = \frac{4}{9}$, $n_u = n_v = 2$, and $(\omega, R) = (0.5, 2.5)$ (**top row**), $(2.5, 2.5)$ (**middle row**) and $(-2.5, 2.5)$ (**bottom row**).

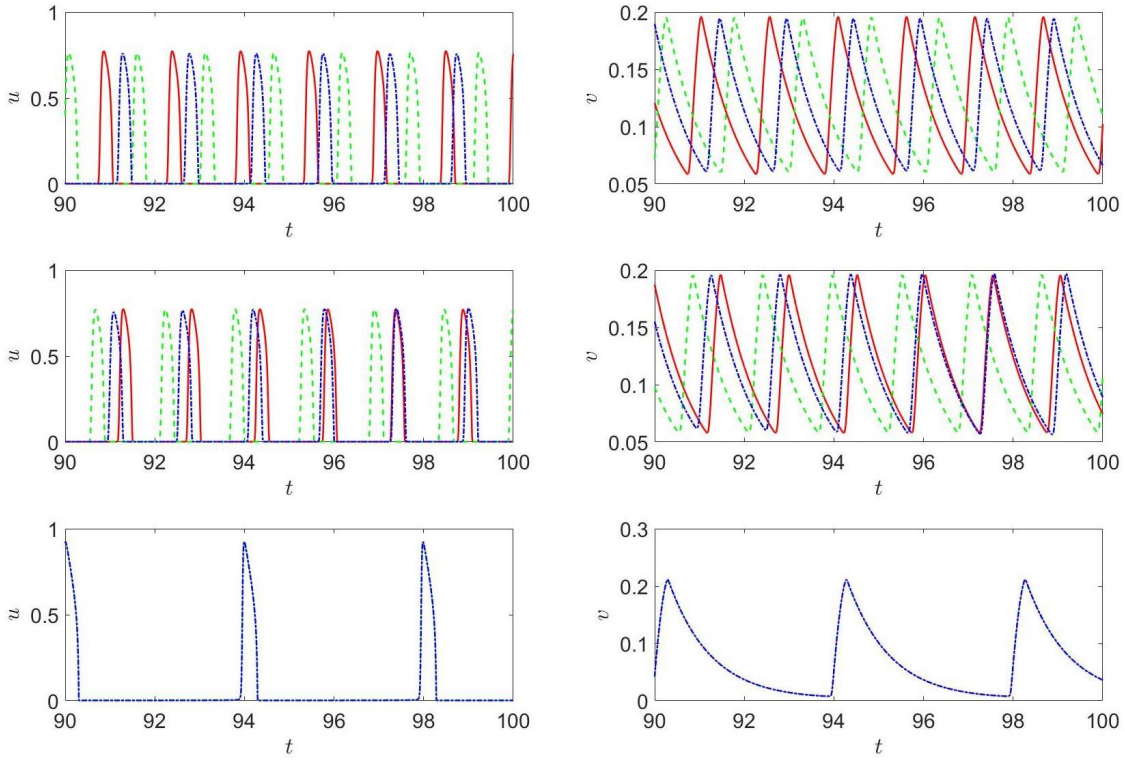

Figure 10. (Color online) $u(t,x,y)$ (**left**) and $v(t,x,y)$ (**right**) at $(x,y) = \left(-\frac{L}{2}, -\frac{L}{2}\right)$ (continuous line, red), $(0,0)$ (dashed line, green) and $\left(\frac{L}{2}, \frac{L}{2}\right)$ (dashed–dotted line, blue) for $D_u = 1$, $D_v = 0.6$, $\alpha_u = \alpha_v = 0.75$, $\beta_u = \beta_v = \frac{4}{9}$, $n_u = n_v = 2$, and $(\omega, R) = (2.5, 0.5)$ (**top row**), $(2.5, 1)$ (**middle row**) and $(2.5, 2.5)$ (**bottom row**).

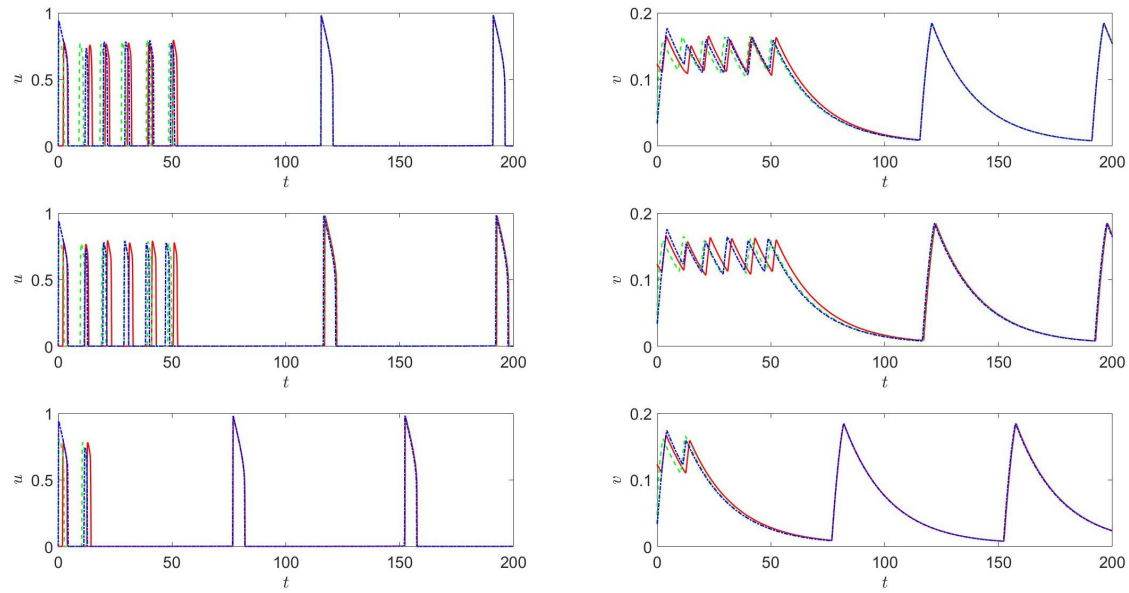

Figure 11. (Color online) $u(t,x,y)$ (**left**) and $v(t,x,y)$ (**right**) at $(x,y) = \left(-\frac{L}{2}, -\frac{L}{2}\right)$ (continuous line, red), $(0,0)$ (dashed line, green) and $\left(\frac{L}{2}, \frac{L}{2}\right)$ (dashed–dotted line, blue) for $D_u = 1$, $D_v = 0.6$, $\alpha_u = 0.75$, $\alpha_v = 0.15$, $\beta_u = \frac{4}{9}$, $\beta_v = \frac{40}{9}$, $n_u = n_v = 2$, and $(\omega, R) = (0.5, 1)$ (**top row**), $(2.5, 1)$ (**middle row**) and $(5, 1)$ (**bottom row**).

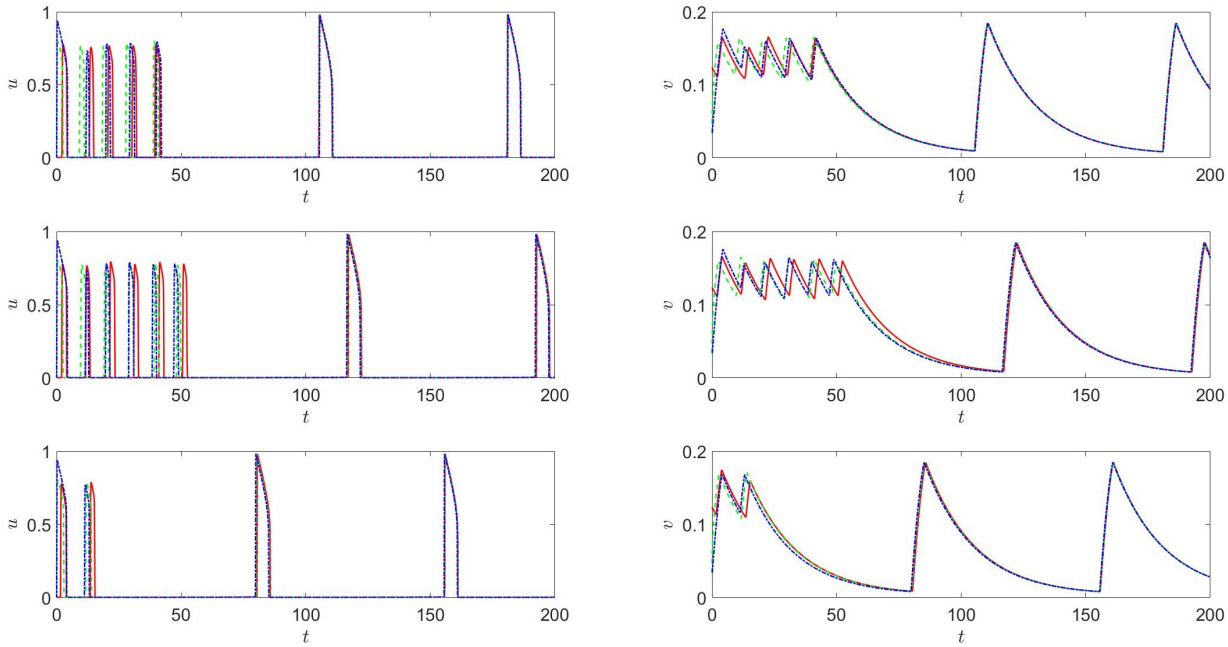

Figure 12. (Color online) $u(t,x,y)$ (**left**) and $v(t,x,y)$ (**right**) at $(x,y) = \left(-\frac{L}{2}, -\frac{L}{2}\right)$ (continuous line, red), $(0,0)$ (dashed line, green) and $\left(\frac{L}{2}, \frac{L}{2}\right)$ (dashed–dotted line, blue) for $D_u = 1$, $D_v = 0.6$, $\alpha_u = 0.75$, $\alpha_v = 0.15$, $\beta_u = \frac{4}{9}$, $\beta_v = \frac{40}{9}$, $n_u = n_v = 2$, and $(\omega, R) = (2.5, 0.5)$ (**top row**), $(2.5, 1)$ (**middle row**) and $(2.5, 2.5)$ (**bottom row**).

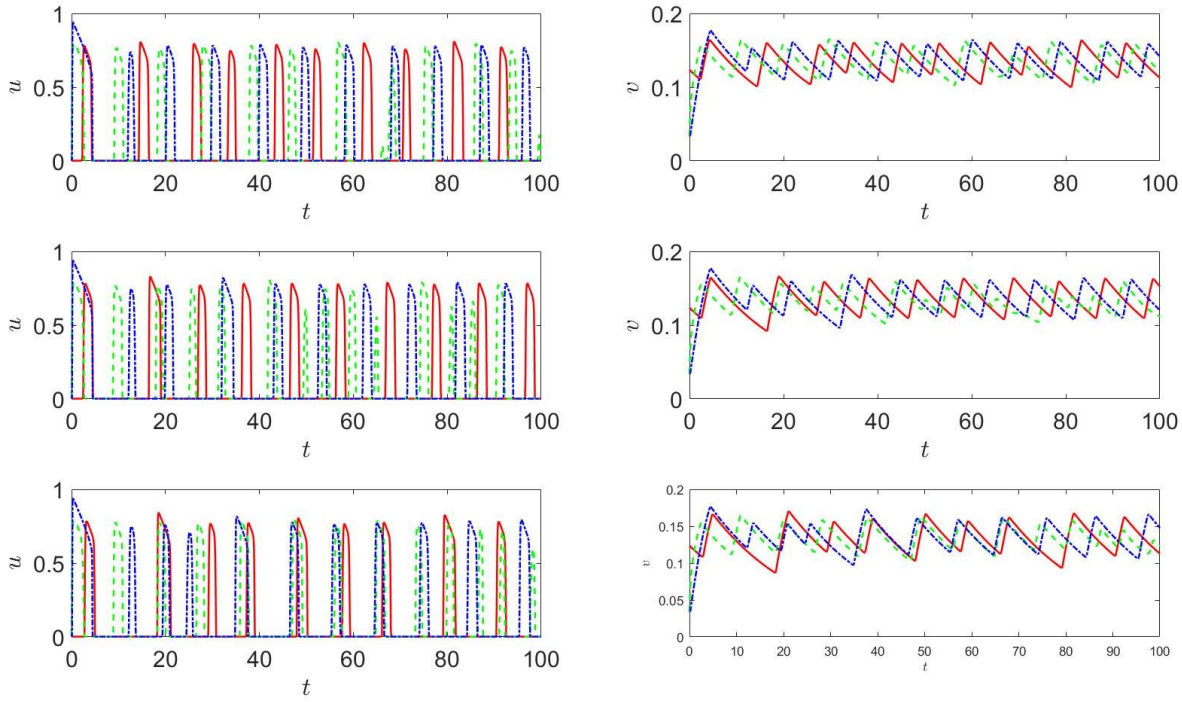

Figure 13. (Color online) $u(t,x,y)$ (**left**) and $v(t,x,y)$ (**right**) at $(x,y) = \left(-\frac{L}{2}, -\frac{L}{2}\right)$ (continuous line, red), $(0,0)$ (dashed line, green) and $\left(\frac{L}{2}, \frac{L}{2}\right)$ (dashed–dotted line, blue) for $D_u = 1$, $D_v = 0.6$, $\alpha_u = 0.75$, $\alpha_v = 0.15$, $\beta_u = \frac{4}{9}$, $\beta_v = \frac{40}{9}$, $n_u = n_v = 2$, and $(\omega, R) = (-0.5, 1)$ (**top row**), $(-2.5, 1)$ (**middle row**) and $(-5, 1)$ (**bottom row**).

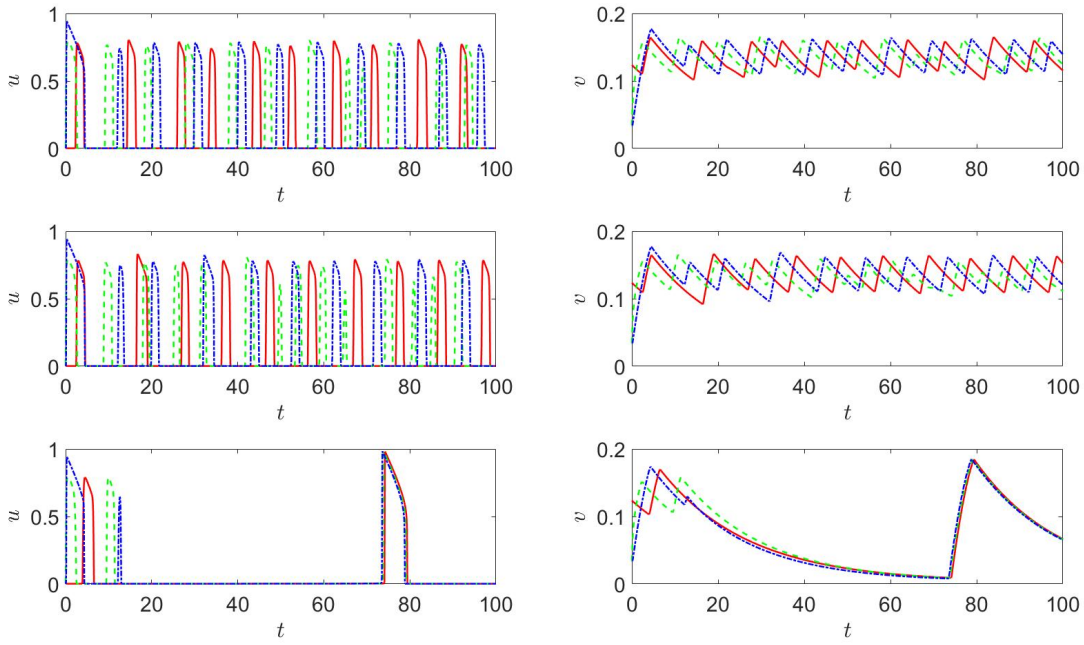

Figure 14. (Color online) $u(t,x,y)$ (**left**) and $v(t,x,y)$ (**right**) at $(x,y) = \left(-\frac{L}{2}, -\frac{L}{2}\right)$ (continuous line, red), $(0,0)$ (dashed line, green) and $\left(\frac{L}{2}, \frac{L}{2}\right)$ (dashed–dotted line, blue) for $D_u = 1$, $D_v = 0.6$, $\alpha_u = 0.75$, $\alpha_v = 0.15$, $\beta_u = \frac{4}{9}$, $\beta_v = \frac{40}{9}$, $n_u = n_v = 2$, and $(\omega, R) = (-2.5, 0.5)$ (**top row**), $(-2.5, 1)$ (**middle row**) and $(-2.5, 2.5)$ (**bottom row**).

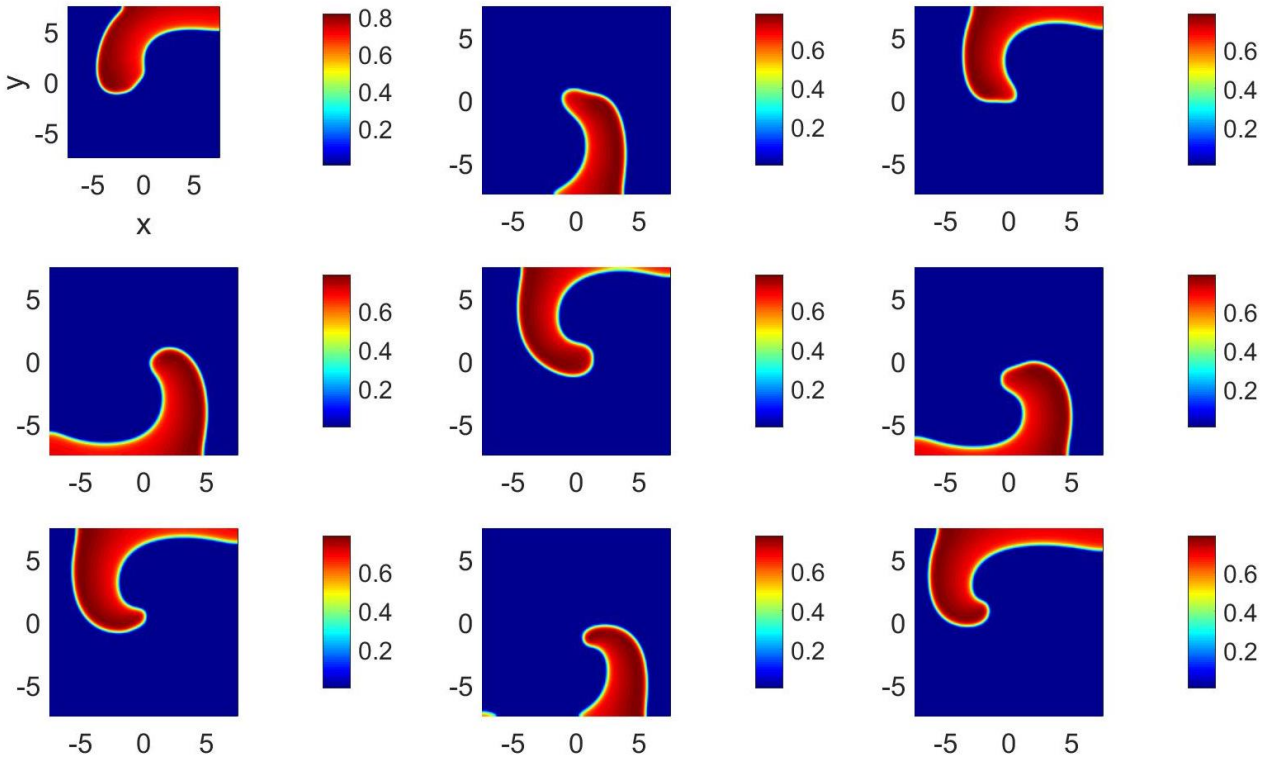

Figure 15. (Color online) $u(t,x,y)$ at (from **left** to **right** and **top** to **bottom**) $t = 50, 55, 60, 65, 70, 75, 80, 85$ and 90 for $D_u = 1$, $D_v = 0.6$, $\alpha_u = 0.75$, $\alpha_v = 0.15$, $\beta_u = \frac{4}{9}$, $\beta_v = \frac{40}{9}$, $n_u = n_v = 2$, $\omega = -2.5$ and $R = 1$.

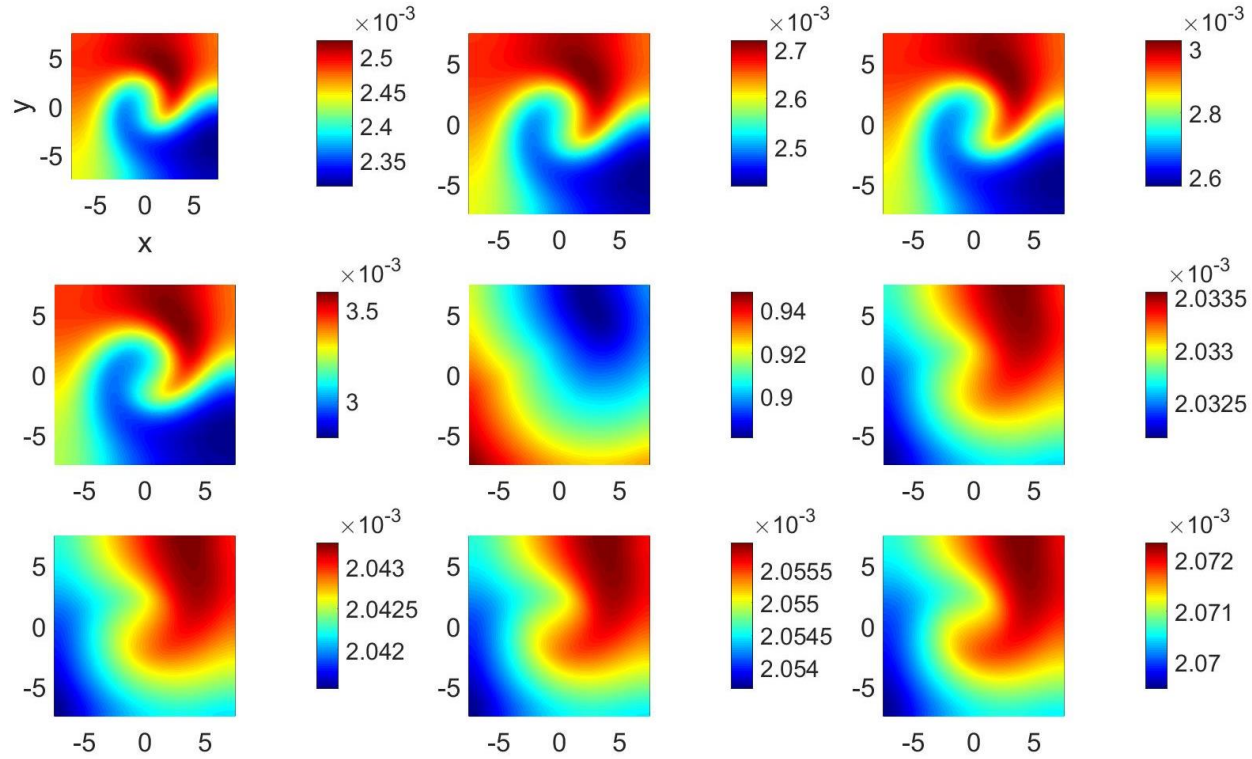

Figure 16. (Color online) $u(t, x, y)$ at (from **left** to **right** and **top** to **bottom**) $t = 50$, 55, 60, 65, 70, 75, 80, 85 and 90 for $D_u = 1$, $D_v = 0.6$, $\alpha_u = 0.75$, $\alpha_v = 0.15$, $\beta_u = \frac{4}{9}$, $\beta_v = \frac{40}{9}$, $n_u = n_v = 2$, $\omega = -2.5$ and $R = 2.5$.

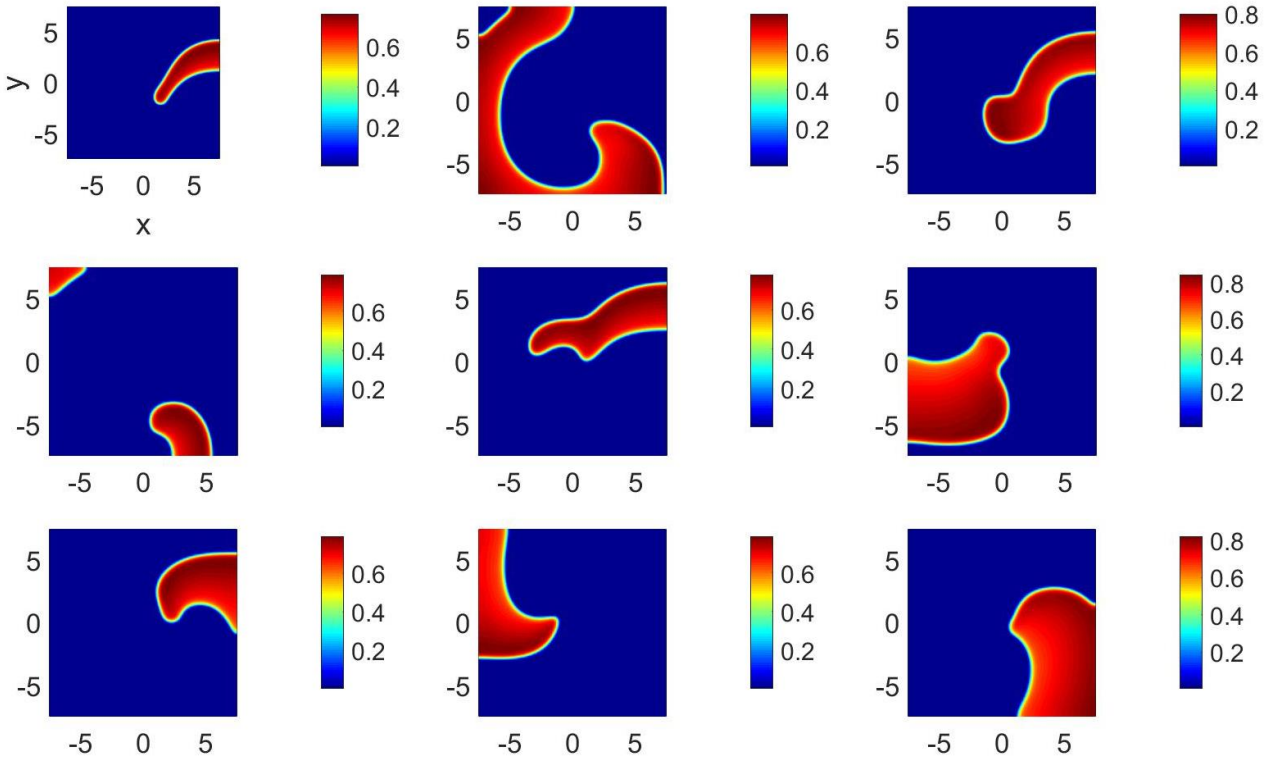

Figure 17. (Color online) $u(t, x, y)$ at (from **left** to **right** and **top** to **bottom**) $t = 50$, 55, 60, 65, 70, 75, 80, 85 and 90 for $D_u = 1$, $D_v = 0.6$, $\alpha_u = 0.75$, $\alpha_v = 0.15$, $\beta_u = \frac{4}{9}$, $\beta_v = \frac{40}{9}$, $n_u = n_v = 2$, $\omega = -5$ and $R = 1$.

For $\omega = -2.5$ and $R = 2.5$, the results shown in Figure 16 are quite different from those of Figure 15, which corresponds to $\omega = -2.5$ and $R = 1$, i.e., a smaller clockwise-rotating vortex of the same angular speed, and indicate that the wave observed in Figure 16 is much thicker than the one shown in Figure 15 due to the larger vortex core radius. Figure 16 also indicates that the period of the wave is larger than that of Figure 15 in accordance with the time histories reported previously in Figures 13 and 14. The middle frame of Figure 16 also shows that the maximum value of u is larger than that shown in Figure 15.

Figure 17 illustrates the u distribution for $\omega = -5$ and $R = 1$, i.e., a clockwise-rotating vortex whose angular speed is twice that of Figure 15, and shows that the wave and especially its tip undergo large changes in shape as functions of time, as indicated, for example, in the second, third, fifth and sixth frames of the figure.

A comparison of Figures 15 and 17 clearly shows that the deformation of the wave shape and tip increases as $|\omega|$ is increased from 2.5 to 5, for $R = 1$. On the other hand, a comparison of Figures 15 and 16 indicates that the width of the spiral wave arms increases as R is increased, i.e., as the vortex core radius is increased.

5. Conclusions

In this paper, four formulations for the study of one-dimensional, time-dependent, nonlinear reaction–diffusion equations whose heat capacity, thermal conductivity and reaction rate are only functions of the temperature have been presented. The formulations are based on the Kirchhoff transformation or heat potential and time linearization, and provide linear, two-point, boundary-value problems at each time level for the temperature, heat potential or energy. Although a formulation based on the piecewise analytical solution of the linear boundary-value problem is also presented for the temperature, similar formulations may be obtained for the energy and heat potential.

The temperature formulation developed for one-dimensional problems has been generalized for two-dimensional, time-dependent systems of nonlinearly coupled reaction–diffusion equations which upon time linearization and factorization of the spatial operators also results in linear, two-point, boundary-value problems at each time level in each space direction; these boundary-value problems may be solved by using any of the two formulations for the temperature developed for one-dimensional, time-dependent reaction–diffusion equations. Although the one- and two-dimensional formulations are presented for reaction–diffusion equations, they are easily generalized to advection–reaction–diffusion equations.

In the absence of a velocity field, it has been found that nonlinear mass diffusion coefficients and heat conductivities result in the formation of counter-clockwise-rotating spiral waves much thinner and less smooth than those observed for constant constant coefficients. The wave's thickness and smoothness increase as the dependence of the thermal conductivity on the the temperature decreases.

For velocity fields corresponding to a Rankine vortex, it has been found that counter-clockwise vortex rotation results in the stretching and thinning of the counter-clockwise spiral wave, for moderate values of the vortex core radius. For large vortex radii, counter-clockwise velocity fields result initially in oscillatory patterns whose duration depends on both the vortex circulation and radius. This initial oscillatory pattern is then followed by a period of very little activity, which is then followed by the formation of almost periodic spiral waves. The durations of both the initial oscillatory behavior and the inactivity period depend on the vortex circulation and radius, but the period of the stable propagating spiral wave is nearly independent of these values.

For clockwise Rankine vortex fields, it has been found that the spiral wave is compressed and undergoes complex thinning and thickening processes and fast changes on its tip, for large vortex core radii. For small vortex radii, the main effect of a Rankine vortex field is the slowing down and the thickening of the spiral wave.

Funding: No funding was received to carry out the research reported in the article.

Data Availability Statement: Data are contained within the article.

Acknowledgments: This paper was supposed to be an enlarged version of the Paper No. 188 entitled "Piecewise–analytical, cell–centered, finite–volume methods for multidimensional advection–reaction–diffusion equations" that was published in the Book of Abstracts of the 14-th International Conference on Computational Heat and Mass Transfer (ICCHMT 2023) held in Düsseldorf on 4–8 September 2023. An extended version of the two-page abstract is scheduled to appear in Springer's Lectures Notes in Mechanical Engineering. In order to avoid unnecessary duplication, the author decided to not enlarge the above-referred paper and instead report the new formulations presented in Section 2 of this paper based on the Kirchhoff transformation and keep the references to time linearization techniques and spiral wave propagation to a bare minimum. The numerical methods that appear in the Book of Abstracts and Lecture Notes in Mechanical Engineering can be easily deduced from the formulation presented in Section 2.3 of this paper. The author is deeply grateful to Ali C. Benim of Düsseldorf University of Applied Sciences (Germany) for his kindness and help before, during and after ICCHMT 2023. The author is also grateful to the referees for their comments on the manuscript.

Conflicts of Interest: The author declares no conflicts of interest.

References

1. Kirchhoff, G. *Vorlesungen über die Theorie der Wärme*; Teubner: Leipzig, Germany, 1894.
2. Vernotte, P. Formes diverses de l'quation de la chaleur. quation intrinsque. *Comptes Rendus Herbomadaires Sances L'Acad. Sci.* **1944**, *218*, 39–41.
3. Carslaw, H.S.; Jaeger, J.C. *Conduction of Heat in Solids*; Oxford University Press: New York, NY, USA, 1959.
4. Arpaci, V.S. *Conduction Heat Transfer: Abridged Edition*; Ginn Press: Needham Heights, MA, USA, 1993.
5. Özişik, M.N. *Boundary Value Problems of Heat Conduction*; International Textbook: Scranton, PA, USA, 1968.
6. Tomatis, D. Heat conduction in nuclear fuel by the Kirchhoff transformation. *Ann. Nucl. Energy* **2013**, 57, 100–105. [CrossRef]
7. Bonani, F.; Ghione, G. On the application of the Kirchhoff transformation to the steady-state thermal analysis of semiconductor devices with temperature-dependent and piecewise inhomogeneous thermal conductivity. *Solid-State Electron.* **1995**, *38*, 1409–1412. [CrossRef]
8. Gama, R.M.S.; Gama, R.P. The Kirchhoff transformation and the Fick's second law with concentration-dependent diffusion coefficient. *WSEAS Trans. Heat Mass Transf.* **2001**, *16*, 59–67. [CrossRef]
9. Kim, S. A simple direct estimation of temperature–dependent thermal conductivity with Kirchhoff transformation. *Int. Commun. Heat Mass Transf.* **2001**, *28*, 537–544. [CrossRef]
10. Mierzwiczak, M.; Kołodziej, J.A. The determination temperature-dependent thermal conductivity as inverse heat conduction problem. *Int. J. Heat Mass Transf.* **2011**, *54*, 790–796. [CrossRef]
11. Bagnall, K.R.; Muzychka, Y.S. Application of the Kirchhoff transform to thermal spreading problems with convection boundary conditions. *IEEE Trans. Compon. Packag. Manuf. Technol.* **2014**, *4*, 408–420. [CrossRef]
12. Givoli, D. Short Communication: Use of the Kirchhoff transformation in finite element analysis. *Int. J. Numer. Methods Heat Fluid Flow* **1993**, *3*, 473–477. [CrossRef]
13. Protter, M.H.; Weinberger, H.F. *Maximum Principles in Differential Equations*; Prentice Hall: Englewood Cliffs, NJ, USA, 1967.
14. Fornieri, A.; Martnez-Prez, M.J.; Giazotto, J. A normal metal tunnel-junction heat diode. *Appl. Phys. Lett.* **2014**, *104*, 183108. [CrossRef]
15. Li, B.; Wang, L.; Casati, G. Negative differential thermal resistance and thermal transistor. *Appl. Phys. Lett.* **2006**, *88*, 143501. [CrossRef]
16. Wang, L.; Li, B. Thermal logic gates: Comparison with phonons. *Phys. Rev. Lett.* **2007**, *99*, 177208. [CrossRef] [PubMed]
17. Yang, F.; Gordon, M.P.; Urban, J.J. Theoretical framework of the thermal memresistor via solid-state phase change material. *J. Appl. Phys.* **2019**, *125*, 025109. [CrossRef]
18. Krapez, J.-C. Influence of thermal hysteresis on the heat shuttling effect: The case of VO_2. *J. Appl. Phys.* **2023**, *133*, 195102. [CrossRef]
19. Latella, I.; Messina, R.; Rubi, J.M.; Benn-Abdallah, P. Radiative heat shuttling. *Phys. Rev. Lett.* **2018**, *121*, 023903. [CrossRef] [PubMed]
20. Li, N.; Hanggi, P.; Li, B. Ratcheting heat flux against a thermal bias. *Europhys. Lett.* **2008**, *84*, 40009. [CrossRef]
21. Ordonez-Miranda, J.; Anufriev, R.; Nomura, M.; Volz, S. Harnessing thermal waves for heat pumping. *Phys. Rev. Appl.* **2024**, *21*, 054037. [CrossRef]

22. Weiland, C. *Mechanics of Flow Similarities*; Springer Nature Switzerland AG: Cham, Switzerland, 2020.
23. Ramos, J.I. Propagation of spiral waves in anisotropic media: From waves to stripes. *Chaos Solitons Fractals* **2001**, *12*, 1057–1064. [CrossRef]

computation

MDPI

Article

Effects of Anisotropy, Convection, and Relaxation on Nonlinear Reaction-Diffusion Systems

Juan I. Ramos

Escuela de Ingenierías Industriales, Universidad de Málaga, Doctor Ortiz Ramos, s/n, 29071 Málaga, Spain; jirs@uma.es

Abstract: The effects of relaxation, convection, and anisotropy on a two-dimensional, two-equation system of nonlinearly coupled, second-order hyperbolic, advection–reaction–diffusion equations are studied numerically by means of a three-time-level linearized finite difference method. The formulation utilizes a frame-indifferent constitutive equation for the heat and mass diffusion fluxes, taking into account the tensorial character of the thermal diffusivity of heat and mass diffusion. This approach results in a large system of linear algebraic equations at each time level. It is shown that the effects of relaxation are small although they may be noticeable initially if the relaxation times are smaller than the characteristic residence, diffusion, and reaction times. It is also shown that the anisotropy associated with one of the dependent variables does not have an important role in the reaction wave dynamics, whereas the anisotropy of the other dependent variable results in transitions from spiral waves to either large or small curvature reaction fronts. Convection is found to play an important role in the reaction front dynamics depending on the vortex circulation and radius and the anisotropy of the two dependent variables. For clockwise-rotating vortices of large diameter, patterns similar to those observed in planar mixing layers have been found for anisotropic diffusion tensors.

Keywords: second-order hyperbolic; advection–reaction–diffusion equations; relaxation; anisotropic diffusion; Rankine vortex fields; time-linearized finite difference method

Citation: Ramos, J.I. Effects of Anisotropy, Convection, and Relaxation on Nonlinear Reaction-Diffusion Systems. *Computation* **2024**, *12*, 214. https://doi.org/10.3390/computation12110214

Academic Editors: Ali Cemal Benim, Abdulmajeed A. Mohamad, Sang-Ho Suh, Rachid Bennacer, Paweł Oclon and Jan Taler

Received: 11 September 2024
Revised: 21 October 2024
Accepted: 22 October 2024
Published: 25 October 2024

1. Introduction

Most of the heat and mass transfer phenomena that arise in science and engineering are usually modeled by means of the well-known Fourier and Fick's second laws, respectively, whereby the heat and mass transfer fluxes are assumed to be linearly proportional to the temperature and concentration gradients, respectively, and the proportionality is, in many cases, assumed to be a scalar rather than a tensor. The application of these laws to problems where the length scales are small, e.g., microfluidics, and/or the heat and mass flux are very large and may not be valid because these laws result in parabolic partial differential equations characterized by an infinite speed of propagation, and delays may occur between, say, the time at which the temperature gradient is imposed and the time at which the heat flux is observed. This delay was usually taken care of in the past by the well-known linear relaxation equation [1]:

$$\frac{dq}{dt} = -\frac{1}{\tau}(q - q_e), \tag{1}$$

where $q(t)$ denotes a variable that depends on time t, q_e is its equilibrium value and τ is the relaxation time, which may also be considered as a delay time.

The solution to the above equation is as follows:

$$q(t) = q_e + (q(0) - q_e)\exp\left(-\frac{t}{\tau}\right), \tag{2}$$

which indicates that the equilibrium value/state is reached in an exponential manner.

Although linear Equation (1) has been frequently used in the past in fluid dynamics, acoustics, heat, and mass transfer [2,3], high-temperature phenomena, biology [4], epidemiology, population dynamics, reaction-diffusion systems [5], thermoelasticity [6], etc., it suffers from several problems. First, its use may result in a violation of the second law of thermodynamics [7]. Second, although its use may be somewhat justified when macroscopic variables only depend on time, there remains the question about the time-derivative that should appear in that equation in moving media [1,8,9]. Third, in moving media, the use of either a partial derivative with respect to time or a material/substantial time derivative does not satisfy the principle of frame-indifference of continuum mechanics [10].

It is interesting to note that the above linear relaxation equation may be written as $q + \tau \frac{dq}{dt} = q_e$ which reminds the reader of the Maxwell–Cattaneo–Vernotte constitutive law [2,11] (cf. Section 2).

As stated above, in many applications of Fourier and Fick laws in heat and mass transfer problems, thermal conductivity, and mass diffusion tensors are assumed to be isotropic and, in many cases are considered to be proportional to the unity or identity tensor. As a consequence, terms associated with the presence of second-order mixed derivatives and cross-diffusion are ignored, even though they are known to play some role in combustion phenomena, e.g., Soret and Dufour, thermodiffusion, barodiffusion, etc. [12]. In particular, cross-diffusion in two-equation, two-dimensional systems of parabolic reaction-diffusion is known to play a paramount role in determining pattern formation and stability, e.g., [13,14]. However, the effects of second-order mixed derivatives on either parabolic or hyperbolic, multi-dimensional advection–reaction–diffusion equations have not received much attention, presumably because these mixed terms couple the two directions of space.

In this paper, we present a numerical study of a two-equation, two-dimensional, nonlinear system of advection–reaction–diffusion equations that accounts for the presence of two relaxation times and the anisotropy of the diffusion tensors in a convective environment.

The formulation and numerical methods presented in this paper apply not only to models of nonlinear heat and mass transfer phenomena where relaxation, advection, anisotropy, and chemistry result in second-order hyperbolic, advection–reaction–diffusion equations, they are also applicable to other models governed by the same type of equations that might be employed in the study and analysis of biological, ecological, epidemiological, etc., processes or systems.

This paper has been arranged as follows. In Section 2, the Maxwell–Cattaneo–Vernotte constitutive law for heat conduction and two constitutive models based on the use of the material or substantial derivative and Christov's frame-indifference model is presented for a single dependent variable in order to emphasize their similarities and differences and point out which constitutive law for heat conduction may be formulated for either only the temperature or both the temperature and the heat flux. In the same section, the one-equation formulation is extended to deal with several dependent variables for the case that the (heat and mass) diffusion fluxes are given by Christov's constitutive model. The numerical method employed in the simulations is presented in Section 4. A summary of a large set of numerical experiments that have been performed for different relaxation times, velocity fields, and coefficients that multiply the second-order mixed-diffusion terms is presented in Section 5. The final section summarizes some of the most common findings on the effects of the anisotropy of diffusion tensors, relaxation time, and velocity field on second-order hyperbolic, advection–reaction–diffusion models of heat and mass transfer and other phenomena described in the manuscript.

2. Formulation

As stated in the introduction, for the sake of clarity, in this section, we first present and compare three constitutive laws for the conduction heat flux that account for relaxation for a single dependent variable. The one-variable formulation is then extended to several variables.

2.1. One-Variable Formulation

In this subsection, we consider the following, time-dependent, multi-dimensional, nonlinear reaction-diffusion equation:

$$\rho c \frac{DT}{Dt} = -\nabla \cdot \mathbf{q} + S, \qquad t > 0, \qquad \mathbf{x} \in \Omega, \tag{3}$$

where ρ and c denote the mass density and specific heat, respectively, which may depend on T, t is time, T denotes the temperature, S is a (nonlinear) source or reaction term, which may depend on t, $\mathbf{x}$, and T; $\mathbf{q}$ is the conduction heat flux vector, $\mathbf{x}$ and Ω denote the spatial coordinates and domain, respectively, $\frac{DT}{Dt} = T_t + \mathbf{v} \cdot \nabla T$ is the material or substantial derivative, the subscripts denote partial differentiation, and $\mathbf{v}$ is the velocity vector.

When Fourier's law is applicable [15], $\mathbf{q}(t, \mathbf{x}) = -\mathbf{K}\nabla T(t, \mathbf{x})$, where $\mathbf{K}$ denotes the positive definite thermal conductivity tensor. Fourier's law assumes that a temperature gradient at $(t, \mathbf{x})$ results in a heat flux at the same location and time; conversely, it also indicates that a heat flux at $(t, \mathbf{x})$ results in a temperature gradient at the same location and time.

The use of Fourier's law in Equation (3) yields the following well-known parabolic equation for T:

$$\rho c \frac{DT}{Dt} = \nabla \cdot (\mathbf{K}\nabla T) + S, \tag{4}$$

which is characterized by an infinite speed of propagation and contains only the temperature.

Equation (4) is subject to the initial condition $T(0, \mathbf{x}) = T_0(\mathbf{x})$ and boundary conditions at the domain boundaries, i.e., on $\partial\Omega$. For Dirichlet's boundary conditions, $T(t, \mathbf{x}_b) = \phi(t)$, where $\mathbf{x}_b$ denotes the spatial coordinates of the boundary and $\phi(t)$ is the boundary temperature. For the Neumann boundary conditions, $\mathbf{q}(t, \mathbf{x}_b) \cdot \mathbf{n} = \theta(t)$, where $\mathbf{n}$ is the unit's outward-pointing vector normal to the boundary $\partial\Omega$ and $\theta(t)$ stands for the heat flux flowing out at the domain boundary. For Robin's boundary conditions, $\mathbf{q}(t, \mathbf{x}_b) \cdot \mathbf{n} = \psi(T(t, \mathbf{x}_b), T_\infty)$, where T_∞ denotes the temperature far away from the domain Ω.

For heat transfer phenomena occurring at the micro- or nanoscale or at very fast rates, it is well known that Fourier's law is not valid. As indicated in the introduction, Maxwell, Cattaneo, and Vernotte assumed that a temperature gradient applied at t results in a heat flux at $t + \tau$, where τ is the relaxation time [2,3], i.e.,

$$\mathbf{q}(t + \tau, \mathbf{x}) = -\mathbf{K}\nabla T, \tag{5}$$

which together with Equation (3) provides a system of delay equations in time for T and $\mathbf{q}$.

A Taylor series expansion of Equation (5) up to $\mathcal{O}(\tau^2)$ may be written as follows:

$$\mathbf{q}(t, \mathbf{x}) + \tau \mathbf{q}_t(t, \mathbf{x}) = -\mathbf{K}\nabla T. \tag{6}$$

By taking the divergence of Equation (6) and using Equation (3), one may easily obtain the following:

$$\rho c \frac{DT}{Dt} + \tau \frac{\partial}{\partial t}\left(\rho c \frac{DT}{Dt}\right) = \nabla \cdot (\mathbf{K}\nabla T) + S + \tau \frac{\partial S}{\partial t}, \tag{7}$$

which is a nonlinear, second-order hyperbolic equation for T whose solutions have a finite speed of propagation. Equation (7) reduces to Equation (4) for $\tau = 0$.

For heat conduction in moving media, it is clear that no information regarding the velocity field is explicitly included in Equation (6). However, if instead of Equation (6), one employs the following:

$$\mathbf{q} + \tau \frac{D\mathbf{q}}{Dt} = -\mathbf{K}\nabla T, \tag{8}$$

and then takes the divergence of this equation and makes use of Equation (3), it is easy to obtain the following:

$$\rho c \frac{DT}{Dt} + \tau \frac{D}{Dt}\left(\rho c \frac{DT}{Dt}\right) = \nabla \cdot (\mathbf{K}\nabla T) + S + \tau \frac{DS}{Dt} + \tau \nabla \mathbf{v} : \nabla \mathbf{q}, \tag{9}$$

which clearly differs from Equation (7) in all the terms containing τ, although it reduces to Equation (7) for $\tau = 0$. Moreover, unless $\tau \nabla \mathbf{v} : \nabla \mathbf{q}$ is nil, Equation (9) contains both T and $\mathbf{q}$ and, therefore, Equations (8) and (9) are coupled and must be solved as a system of (coupled) equations (cf. compare Equations (7) and (9)). This is closely aligned with Christov's frame-indifference formulation of the Maxwell–Cattaneo–Vernotte model of heat conduction [9], i.e.,

$$\mathbf{q} + \tau\left(\frac{D\mathbf{q}}{Dt} - \mathbf{q} \cdot \nabla \mathbf{v} + (\nabla \cdot \mathbf{v})\mathbf{q}\right) = -\mathbf{K}\nabla T, \tag{10}$$

whose divergence may be written as follows:

$$Q + \tau\left(\frac{DQ}{Dt} + Q\nabla \cdot \mathbf{v}\right) = -\nabla \cdot (\mathbf{K}\nabla T), \tag{11}$$

where $Q \equiv \nabla \mathbf{q}$.

For solenoidal velocity fields, i.e., $\nabla \cdot \mathbf{v} = 0$, the use of Q from Equation (3) into Equation (11) yields the following:

$$\rho c \frac{DT}{Dt} + \tau \frac{D}{Dt}\left(\rho c \frac{DT}{Dt}\right) = \nabla \cdot (\mathbf{K}\nabla T) + S + \tau \frac{DS}{Dt}, \tag{12}$$

which differs from Equation (9) in that the latter contains a tensor contraction term, i.e., the last term on the right-hand side of Equation (9).

Equation (11) may also be written as follows:

$$Q + \tau\left(\frac{\partial Q}{\partial t} + \nabla \cdot (\mathbf{v}Q)\right) = -\nabla \cdot (\mathbf{K}\nabla T), \tag{13}$$

which, upon obtaining Q from Equation (3) and substituting it in Equation (11), may be written as follows:

$$\rho c(1 + \tau \nabla \cdot \mathbf{v}) \frac{DT}{Dt} + \tau \frac{D}{Dt}\left(\rho c \frac{DT}{Dt}\right) = \nabla \cdot (\mathbf{K}\nabla T) + S + \tau\left(\frac{DS}{Dt} + S\nabla \cdot \mathbf{v}\right), \tag{14}$$

which is a second-order hyperbolic equation for T, which has a finite speed of propagation and reduces to Equation (4) for $\tau = 0$.

If ρc and $\mathbf{K}$ are constant and the velocity field is solenoidal, Equation (14) is as follows:

$$\rho c \frac{DT}{Dt} + \tau \rho c \frac{D}{Dt}\left(\frac{DT}{Dt}\right) = \nabla \cdot (\mathbf{K}\nabla T) + S + \tau \frac{DS}{Dt}, \tag{15}$$

which may also be written as follows:

$$\rho c \phi + \tau \rho c \frac{D\phi}{Dt} = \nabla \cdot (\mathbf{K}\nabla T) + S + \tau J \phi, \tag{16}$$

for $S = S(T)$, where $J = \frac{dS}{dT}$ denotes the Jacobian of S, and $\phi = \frac{DT}{Dt}$.

The positive definiteness of the thermal conductivity tensor in two dimensions requires that $K_{11} > 0$, $K_{22} > 0$ and $K_{11}K_{22} > K_{12}K_{21}$, where K_{ij}, $i = 1, 2$ and $j = 1, 2$, are the components of $\mathbf{K}$. Moreover, $\nabla \cdot (\mathbf{K}\nabla T) = K_{11}T_{xx} + (K_{12} + K_{21})T_{xy} + K_{22}T_{yy}$ in two dimensions, and exhibits anisotropy if $K_{11} \neq K_{22}$ even for $K_{12} = K_{21} = 0$ or if either K_{12} or K_{21} is not nil.

The eigenvalues of the thermal conductivity tensor may be written as follows:

$$\lambda = \frac{1}{2}(K_{11} + K_{22}) \pm \sqrt{\frac{1}{4}(K_{11} - K_{22})^2 + K_{12}K_{21}}, \tag{17}$$

are both positive on account of the positive definiteness of the thermal conductivity tensor and may be used to estimate the speed of propagation of Equations (7), (9), or (12), as follows.

For a one-dimensional problem with constant heat capacity, i.e., constant ρc, constant velocity v and constant thermal conductivity, these equations may be written as follows:

$$\rho c \tau T_{tt} + \rho c v T_{xt} - K T_{xx} = F(T, T_t, T_x), \tag{18}$$

where its right-hand side only depends on T and its first-order partial derivatives with respect to space and time.

Equation (18) is a linear, second-order, one-dimensional hyperbolic equation whose characteristic lines have slopes given by the following:

$$\frac{dx}{dt} = -v \pm \sqrt{v^2 + 4\frac{K}{\rho c \tau}}, \tag{19}$$

and indicate that there is propagation at finite speed for $\tau \neq 0$ in both directions of the x-axis. For $\tau = 0$, Equation (19) indicates that the propagation speed is infinite, consistent with the fact that Equation (18) is parabolic when relaxation times are zero.

Estimates of the velocity of propagation in several dimensions may be obtained as $v_{th} = \sqrt{\frac{K}{\rho c \tau}}$, which depends on the thermal diffusivity and relaxation time and increases as the relaxation time increases. This velocity estimate is usually larger than $|\mathbf{v}|$ in microfluidics and fast heat transfer phenomena at the microscale and nanoscale; however, v_{th} may be of the same order of magnitude as or even smaller than v in various models, including biological [4], epidemiological [16,17], virus infection [18], forest fire [19], ecological [20], chemistry [21–23], chemical engineering [24], etc.

Using v_{th}, Equation (19) may be written as follows:

$$\frac{dx}{dt} = -v \pm \sqrt{v^2 + 4v_{th}^2},$$

which indicates that $\frac{dx}{dt} \approx \pm 2v_{th}$ for $v_{th} >> |v|$.

2.2. Multi–Variable Formulation

The formulation presented in the previous section has been generalized for coupled heat and mass transfer problems where there is relaxation for both the temperature and the species concentration; in addition, the thermal and mass diffusion coefficients are tensors. This generalization can also be applied to various models, including biological [4], epidemiological [16,17], virus infection [18], ecological [20], chemical [24], etc., which are characterized by second-order hyperbolic, nonlinear advection–reaction–diffusion equations. It reduces to the reaction-diffusion case when the relaxation times or inertia are negligible, and includes both isotropic and anisotropic diffusion tensors, but does not account for cross-diffusion effects.

For several dependent variables, i.e., Y^m, $m = 1, 2, \cdots, NV$, where NV is the number of dependent variables, and constants ρc and $\mathbf{K}$, the nondimensional form of Equation (14) may be written as follows:

$$(1 + \tau^m \nabla \cdot \mathbf{v}) \frac{DY^m}{Dt} + \tau^m \frac{D}{Dt}\left(\frac{DY^m}{Dt}\right) = \nabla \cdot (\mathbf{K}^m \nabla Y^m) + S^m + \tau^m \left(\frac{DS^m}{Dt} + S^m \nabla \cdot \mathbf{v}\right), \tag{20}$$

where Y^m denotes the m-th dependent variable characterized by a relaxation time τ^m, a source term S^m, and a diffusivity tensor $\mathbf{K}^m$.

Equation (20) corresponds to the Christov's frame-indifferent constitutive equations [9] for the diffusion fluxes of all dependent variables, and does not take cross-diffusion effects into account, i.e., the effects of ∇Y^m into the equation for Y^l for $m \neq l$.

Equation (20) is subject to $Y^m(0, \mathbf{x}) = G^m(\mathbf{x})$ and $\frac{\partial Y^m}{\partial t}(0, \mathbf{x}) = H^m(\mathbf{x})$, where G^m and H^m are functions of space. For homogeneous Neumann boundary conditions, i.e., $\mathbf{n} \cdot \nabla Y^m = 0$ at $\partial\Omega$, where $\mathbf{n}$ denotes the unit vector normal to the boundary.

3. Numerical Method

In two dimensions, the domain $[-A, A] \times [-B, B]$, where $2A$ and $2B$ denote the sides of the rectangular domain, was discretized in equally spaced grids consisting of $NX = NI + 1$ and $NY = NJ + 1$ points in the x- and y-directions, respectively, so that the grid spacings in those directions are $\Delta x = \frac{2A}{NI}$ and $\Delta y = \frac{2B}{NJ}$, respectively.

The second-order spatial derivatives that appear in the diffusion term in Equation (20), i.e., $(Y^m)_{xx}$, $(Y^m)_{xy}$, and $(Y^m)_{yy}$, were discretized by means of the well-known, second-order accurate, central difference formulae, whereas the first-order spatial derivatives were discretized by means of either first-order accurate upwind differences or second-order accurate central differences depending on whether the absolute value of the local mesh Péclet number was greater than, less than, or equal to two, respectively.

The spatial discretization discussed in the previous paragraph results in the following systems of second-order, nonlinear ordinary differential equations:

$$\mathbf{M}_{ij} \frac{d^2 \mathbf{U}_{ij}}{dt^2} + \mathbf{D}_{ij} \frac{d \mathbf{U}_{ij}}{dt} = \mathbf{F}_{ij}(x_i, y_j, \mathbf{V}_{ij}), \tag{21}$$

where $\mathbf{U} = (Y^1, Y^2, \cdots, Y^{NV})^T$, the superscript T represents transpose, and the subscript ij indicates the (i, j) grid point. $\mathbf{V}_{ij}$ depends on $\mathbf{U}_{MN}$, where $i - 1 \leq M \leq i + 1$, and $j - 1 \leq N \leq j + 1$. The right-hand side of Equation (21) is a nonlinear function owing to the nonlinear dependence of the source terms of Equation (20) on Y^m.

The components of the mass and damping matrices, i.e., $\mathbf{M}_{ij}$ and $\mathbf{D}_{ij}$, respectively, and $\mathbf{F}_{ij}$ that appear in Equation (21) may be easily deduced from the spatial discretization of Equation (20), but are not reported here.

Assembling Equation (21) for all the grid points—including those at the boundaries where second-order accurate discretizations were used for the first-order spatial derivatives that appeared in the homogeneous boundary conditions—results in the following system:

$$\mathcal{M} \frac{d^2 \mathcal{U}}{dt^2} + \mathcal{D} \frac{d \mathcal{U}}{dt} = \mathcal{F}(\mathcal{U}). \tag{22}$$

Equation (22) was first discretized as follows:

$$\frac{1}{\Delta t^2} \mathcal{M}^n (\mathcal{U}^{n+1} - 2\mathcal{U}^n + \mathcal{U}^{n-1}) + \frac{1}{2\Delta t} (\mathcal{U}^{n+1} - \mathcal{U}^{n-1}) = \frac{1}{4} (\mathcal{F}^{n+1} + 2\mathcal{F}^n + \mathcal{F}^{n-1}), \tag{23}$$

where the superscript n denotes the n-th time level, with $t^n = n\Delta t$, $n = 0, 1, 2, \cdots$, and Δt is the time step.

Equation (23) is second-order accurate in time [25] and represents $NX \times NY$ nonlinear equations, whose solution may be obtained through iterative techniques. However, by linearizing $\mathcal{F}^{n+1}$ about the n-th time level, i.e., $\mathcal{F}^{n+1} = \mathcal{F}^n + \mathcal{J}^n(\mathcal{U}^n - \mathcal{U}^n) + \mathcal{O}(\Delta t^2)$, where $\mathcal{J}^n = \frac{\partial \mathcal{F}^n}{\mathcal{U}^n}$ denotes the Jacobian matrix of $\mathcal{F}$, and neglecting the $\mathcal{O}(\Delta t^2)$, Equation (23) may be written as the following system of linear algebraic equations:

$$\mathcal{P}^n \mathcal{U}^{n+1} = \mathcal{Q}^n, \tag{24}$$

where

$$\mathcal{P}^n = \mathcal{M}^n + \frac{\Delta t}{2}\mathcal{D}^n - \frac{\Delta t^2}{4}\mathcal{J}^n, \tag{25}$$

$$\mathcal{Q}^n = \mathcal{M}^n(2\mathcal{U}^n - \mathcal{U}^{n-1}) + \frac{\Delta t}{2}\mathcal{D}^n\mathcal{U}^n + \frac{\Delta t^2}{4}(3\mathcal{F}^n + \mathcal{F}^{n-1} - \mathcal{J}^n\mathcal{U}^n), \tag{26}$$

are both sparse matrices.

Equation (24) was solved by means of a Krylov space method [26–29] for non-symmetric systems when upwind differences were employed to discretize the first-order spatial derivatives that appear in Equation (20). A Krylov space method for symmetric systems was used when the mesh Péclet number was less than or equal to two and the advection terms were discretized by means of second-order, central differences.

Accuracy Assessment

The accuracy of the time-linearized, three-time-level method described above was first assessed by comparing the numerical results with the exact solution of the following (scalar) equation:

$$\tau u_{tt} + \alpha u_t = Du_{xx} + Eu_{yy} + S(u), \qquad 0 < x < a, \qquad 0 < y < b, \qquad t > 0, \tag{27}$$

subject to homogeneous Dirichlet boundary conditions, as follows:

$$u(t, 0, y) = u(t, a, y) = 0, \qquad u(t, x, 0) = u(t, x, b) = 0, \tag{28}$$

and

$$u(0, x, y) = \sin\Big(\frac{\pi x}{a}\Big)\sin\Big(\frac{\pi y}{b}\Big), \tag{29}$$

where $S(u) = \gamma u$, $\tau \geq 0$, $\alpha \geq 0$, $D \geq 0$, $E \geq 0$ and $\gamma \leq 0$ are constants.

The solution of Equation (27) subject to Equations (28) and (29) may be written as follows:

$$u_{ex}(t, x, y) = \phi(t)\sin\Big(\frac{\pi x}{a}\Big)\sin\Big(\frac{\pi y}{b}\Big), \tag{30}$$

where

$$\phi(t) = \exp\left(-\frac{\alpha t}{2\tau}\right) \qquad \text{for} \qquad \tau = \tau_{cr}, \tag{31}$$

$$\phi(t) = \exp\left(-\frac{\alpha t}{2\tau}\right)\cosh\left(\frac{\alpha t}{2\tau}\Omega\right) \qquad \text{for} \qquad \tau < \tau_{cr}, \tag{32}$$

$$\phi(t) = \exp\left(-\frac{\alpha t}{2\tau}\right)\cos\left(\frac{\alpha t}{2\tau}\omega\right) \qquad \text{for} \qquad \tau > \tau_{cr}, \tag{33}$$

the subscript ex stands for exact solution, $\tau_{cr} = \alpha^2/\left(4\left(D\frac{\pi^2}{a^2} + E\frac{\pi^2}{b^2} - \gamma\right)\right)$ denotes the critical relaxation time, $\Omega = \sqrt{1 - \frac{\tau}{\tau_{cr}}}$ and $\omega = \sqrt{\frac{\tau}{\tau_{cr}} - 1}$.

The critical relaxation time decreases as the diffusion coefficients in the x- and/or y-directions increase, is nil when $\alpha = 0$, i.e., in the absence of temporal damping, and decreases as the absolute value of the reaction increases. (Recall that $\gamma \leq 0$).

The order of convergence of the numerical method presented above for Equation (27) is determined as follows. For a time step equal to k and grid spacings in the x- and y-directions equal to h and H, respectively, the numerical solution may be written as follows:

$$u_{(k,h,h)}(t^n, x_i, y_j) = u_{ex}(t^n, x_i, y_j) + Ck^p + Fh^q + GH^r, \tag{34}$$

where t^n denotes the n-th time level, and x_i and y_j stand for the x- and y-coordinates of the (i, j)-the grid point, and, therefore, the values of p, q, and r may be easily deduced by

obtaining numerical solutions with $k/2$ and $k/4$, $h/2$, and $h/4$, and H and $H/2$, respectively, as follows:

$$p = \frac{1}{\log 2} \log \left| \frac{u_{(k,h,H)}(t^n, x_i, y_j) - u_{(k/2,h,H)}(t^n, x_i, y_j)}{u_{(k/2,h,H)}(t^n, x_i, y_j) - u_{(k/4,h,H)}(t^n, x_i, y_j)} \right|, \tag{35}$$

$$q = \frac{1}{\log 2} \log \left| \frac{u_{(k,h,H)}(t^n, x_i, y_j) - u_{(k,h/2,H)}(t^n, x_i, y_j))}{u_{(k,h/2,H)}(t^n, x_i, y_j) - u_{(k,h/4,H)}(t^n, x_i, y_j)} \right|, \tag{36}$$

and

$$r = \frac{1}{\log 2} \log \left| \frac{u_{(k,h,H)}(t^n, x_i, y_j) - u_{(k,h,H/2)}(t^n, x_i, y_j))}{u_{(k,h,H/2)}(t^n, x_i, y_j) - u_{(k,h,H/4)}(t^n, x_i, y_j)} \right|, \tag{37}$$

respectively, where it is understood that the differences that appear on the right-hand sides of Equations (35)–(37) are taken at the same locations and times.

Once the values of p, q, and r are obtained as indicated above, those of C, F, and G may be easily obtained from the numerical solutions corresponding to k and $k/2$, h and $h/2$, and H and $H/2$, respectively, but are not shown here.

It must be noted that Equation (34) is really an asymptotic approximation whose temporal and spatial errors correspond to the last three terms on the the right-hand side of that equation. This means that, owing to the discretization in both space and time, p, q, C, F, and G might depend on k, h, and H and t^n, x_i, and y_j, if the time step and grid spacings are not small enough. When this occurs, it is convenient to replace the absolute values of the numerators and denominators that appear on the right-hand sides of Equations (35)–(37) with their discrete L_2, L_1, or L_∞ norms. For example, $|u_{(k,h,H)}(t^n, x_i, y_j) - u_{(k/2,h,H)}(t^n, x_i, y_j)|$ is replaced with the following:

$$\sqrt{\frac{1}{NX}\frac{1}{NY}\sum_{i=1}^{NX}\sum_{j=1}^{NY}\Big(u_{(k,h,h)}(t^n, x_i, y_j) - u_{(k/2,h,H)}(t^n, x_i, y_j))\Big)^2}, \tag{38}$$

$$\frac{1}{NX}\frac{1}{NY}\sum_{i=1}^{NX}\sum_{j=1}^{NY}|u_{(k,h,H)}(t^n, x_i, y_j) - u_{(k/2,h,H)}(t^n, x_i, y_j)|, \tag{39}$$

or

$$\max_{1\le i\le NX,\ 1\le j\le NY} |u_{(k,h,H)}(t^n, x_i, y_j) - u_{(k/2,h,H)}(t^n, x_i, y_j)|, \tag{40}$$

respectively.

For $\alpha = D = E = a = b = 1$, $\gamma = 0$ and $\tau = \frac{\tau_{cr}}{10}$, numerical experiments performed with $\Delta t = k = 0.1$, 0.01, and 0.001, and $NX = NY = 41$ and 401, show that at $t = 0.8$, $p = 2.13$ and $q = 1.98$, which are consistent with second-order accuracies in both space and time of the numerical method; $\max_{1\le i\le 401,1\le j\le 401} |u_{(0.001,0.0025,0.0025)}(0.8, x_i, y_j) - u_{ex}(0.8, x_i, y_j)| = 0.7534 \times 10^{-6}$ and it occurs at $i = j = 201$. For the same values of the parameters just mentioned, except for $\gamma = -1$, there is a linear reaction term, and it was found that, at $t = 0.8$, $p = 2.19$, $q = 2.04$, and $\max_{1\le i\le 401,1\le j\le 401} |u_{(0.001,0.0025,0.0025)}(0.8, x_i, y_j) - u_{ex}(0.8, x_i, y_j)| = 0.6389 \times 10^{-6}$, occurring at $i = j = 201$.

Similar results to those described in the previous paragraph have also been found in numerical experiments for $\tau = \tau_{cr}$ and $\tau = 10\tau_{cr}$, $\alpha = D = E = a = b = 1$, and $\gamma = 0$ and -1. For example, for $\gamma = -1$ and $\tau = \tau_{cr}$, $p = 2.02$, $q = 1.94$, and $\max_{1\le i\le 401,1\le j\le 401} |u_{(0.001,0.0025,0.0025)}(0.8, x_i, y_j) - u_{ex}(0.8, x_i, y_j)| = 0.9809 \times 10^{-6}$, while, for $\gamma = -1$ and $\tau = \tau_{cr}$, $p = 1.97$, $q = 1.88$ and $\max_{1\le i\le 401,1\le j\le 401} |u_{(0.001,0.0025,0.0025)}(0.8, x_i, y_j) - u_{ex}(0.8, x_i, y_j)| = 1.1105 \times 10^{-6}$. This indicates that the temporal and spatial orders of convergence decrease slightly whereas the error slightly increases as the relaxation time is increased from subcritical to critical and then supercritical values. This should not come as a surprise since, as stated at the beginning of this subsection, supercritical relaxation times are characterized by a trigonometric dependence on time (cf. Equation (33)), which results in damped oscillatory solutions. On the other hand, a comparison between Equations (31) and (32) indicates that since

the hyperbolic cosine is larger than one, supercritical relaxation times result in monotonically decreasing solutions that are less damped than those corresponding to the critical relaxation time.

Numerical experiments were also performed with nonlinear source terms, e.g., $S(u) = u(1-u)$ in Equation (27), for which no analytical solution is available with and without velocity fields. In such cases, the accuracies of the numerical solutions were assessed by determining both the orders of convergence in time and space, i.e., p, q, and r, respectively, as in Equations (35)–(37), respectively, and $E^t_{k,h,H} \equiv \max_{1\le i\le NI,\ 1\le j\le NJ} |u_{(k,h,H)}(t^n, x_i, y_j) - u_{(k/2,h,H)}(t^n, x_i, y_j)|$, $E^x_{k,h,H} \equiv \max_{1\le i\le NI,\ 1\le j\le NJ} |u_{(k,h/2,H)}(t^n, x_i, y_j) - u_{(k,h,H)}(t^n, x_i, y_j)|$, and $E^y_{k,h,H} \equiv \max_{1\le i\le NI,\ 1\le j\le NJ} |u_{(k,h,H/2)}(t^n, x_i, y_j) - u_{(k,h,H)}(t^n, x_i, y_j)|$, which denote the differences in the numerical solutions obtained with time steps equal to k and $k/2$, grid spacings in the x-directions equal to h and $h/2$, and grid spacings in the y-direction equal to H and $H/2$, respectively. The time step and grid spacings were considered to be adequate and, therefore, the solution was considered to be accurate and acceptable whenever $E^t_{k,h,H} \le 10^{-4}$, $E^x_{k,h,H} \le 10^{-4}$ and $E^y_{k,h,H} \le 10^{-4}$ were satisfied.

For the results presented in the next section, the convergence of the Krylov space method used to solve Equation (24) was set to 10^{-6}, and the time step and grid spacings were determined by trial ande erroor until $E^t_{k,h,H}$, $E^x_{k,h,H}$, and $E^y_{k,h,H}$ were less than or equal to 10^{-4}, 5×10^{-4} and 5×10^{-4}, respectively, for $t \le 100$.

4. Results

The multi-dimensional formulation presented in Section 2.2 has been applied to a two-equation, two-dimensional problem characterized by the following: $u \equiv Y^1$, $v \equiv Y^2$, $\tau_u \equiv \tau^1$, $\tau_v \equiv \tau^2$, $\mathbf{D}^u \equiv \mathbf{K}^1$, $D^u_{11} = D^u_{22} = 1$, $D_{12} \equiv D^u_{12} + D^u_{21}$, $\mathbf{D}^v \equiv \mathbf{K}^2$, $D^v_{11} = D^v_{22} = 0.6$, $d_{12} \equiv D^v_{12} + D^v_{21}$,

$$S_u = \frac{1}{\epsilon}\left(u - u^2 - fv\frac{u-q}{u+q}\right), \qquad S_v = u - v, \tag{41}$$

and a time-independent velocity field corresponding to a Rankine vortex whose azimuthal velocity component is as follows:

$$u_\theta = \frac{\Gamma}{2\pi}\frac{r}{R^2} \quad \text{for} \quad r \le R, \qquad u_\theta = \frac{\Gamma}{2\pi r} \quad \text{for} \quad r > R, \tag{42}$$

$\epsilon = 0.01$, $f = 1.4$, $q = 0.002$, the subscripts u and v refer to the dependent variables $u(t, x, y)$ and $v(t, x, y)$, respectively, and Γ and R denote the circulation and core radius of the vortex, respectively. The velocity field in Cartesian coordinates is given by $\mathbf{v} = (U, V)$, where U and V are the velocity components in the x- and y-directions, respectively, which may be easily obtained from the azimuthal velocity component of Equation (42). Positive values of Γ or ω correspond to counter-clockwise rotating velocity fields.

For $\Gamma = D_{12} = d_{12} = \tau_u = \tau_v = 0$, i.e., in the absence of convection and with isotropic constant diffusion tensors for u and v, it is known that the two-equation system considered in this study has constant-period counter-rotating spiral wave solutions [30]. Therefore, a comparison of these solutions with those obtained with relaxation times $\tau_u \ne 0$ and/or $\tau_v \ne 0$, non-zero velocity fields $\mathbf{v} \ne \mathbf{0}$, and mixed diffusion terms $D_{12} \ne 0$ and/or $d_{12} \ne 0$, will allow us to determine the effects of these parameters on wave propagation.

Equation (20), as well as Equations (41) and (42), were solved in a square domain $[-L, L] \times [-L, L]$ with $L = 7.5$, and the numerical method presented in Section 3, using equally spaced meshes consisting of, at least, 101×101 grid points and a time step less or equal to 0.0001, homogeneous Neumann conditions, and initial conditions identical to those employed in other studies [30]. Since the numerical method presented in Section 3 is second-order accurate in time and second-order accurate in space if the local Péclet number is less than or equal to two, the temporal discretization errors are much smaller than the spatial ones for the numerical experiments reported here. In addition, $\Delta t < \max(\tau_u, \tau_v)$.

Since Equation (23) contains three time levels, the numerical method presented in Section 3 is not self-starting. In order to start the method, the value of $\mathcal{U}^1$, i.e., $\mathcal{U}(\Delta t)$, must be given. This value may be obtained from the following Taylor series expansion:

$$\mathcal{U}(\Delta t) = \mathcal{U}(0) + \mathcal{U}_t(0)\Delta t + \frac{1}{2}\mathcal{U}_{tt}(0)\Delta t^2 + \mathcal{O}(\Delta t^3), \tag{43}$$

where, as stated above, $\mathcal{U}(0)$ and $\mathcal{U}_t(0)$ are provided by the initial conditions, and $\mathcal{U}_{tt}(0)$ may be obtained by making use of Equation (20) at $t = 0$.

Numerical experiments were performed to determine the effects of τ_u and τ_v, $\omega \equiv \frac{\Gamma}{\pi R^2}$ and R, and D_{12} and d_{12}, i.e., the relaxation, velocity field, and anisotropy of the diffusion tensors for u and v, respectively, on the numerical solution, and some of the characteristics of the observed wave dynamics and the wave's period, are reported in Tables 1 and 2, where we have assigned a set number to each numerical experiment. Hereon, the set number will be used instead of specifying the values of all the parameters that correspond to each set.

Table 1. Period and shape of the propagating front. ($\tau_u = \tau_v = 0.01$, D_{12} and d_{12} denote the sums of the off-diagonal elements of the diffusion tensors $\mathbf{D}^u$ and $\mathbf{D}^v$ corresponding to the two dependent variables u and v, sw = spiral wave, scf = small curvature front, lcf = large curvature front.).

Set No.	ω	R	D_{12}	d_{12}	Period	Shape
1000	0.0	0.5	0.0	0.0	1.68	sw
1001	0.0	0.5	0.1	0.0	1.68	sw
1002	0.0	0.5	0.0	0.1	4.21	scf
1003	0.0	0.5	0.1	0.1	4.21	scf
1004	0.5	1.0	0.0	0.0	1.68	sw
1005	0.5	1.0	0.1	0.0	1.68	sw
1006	0.5	1.0	0.0	0.1	4.21	lcf
1007	0.5	1.0	0.1	0.1	4.21	lcf
2004	0.5	1.0	0.05	0.0	1.68	sw
2005	0.5	1.0	0.0	0.05	4.21	scf
2006	0.5	1.0	0.05	0.05	4.21	scf
3004	0.5	2.5	0.05	0.0	1.68	sw
3005	0.5	2.5	0.0	0.05	4.21	scf
3006	0.5	2.5	0.05	0.05	4.21	scf
1016	−0.5	1.0	0.0	0.0	1.68	sw
1017	−0.5	1.0	0.1	0.0	1.68	sw
1018	−0.5	1.0	0.0	0.1	4.21	scf
1019	−0.5	1.0	0.1	0.1	4.21	lcf
4004	−0.5	1.0	0.05	0.0	1.68	sw
4005	−0.5	1.0	0.0	0.05	4.21	scf
4006	−0.5	1.0	0.05	0.05	4.21	scf
5004	−0.5	2.5	0.05	0.0	1.68	sw
5005	−0.5	2.5	0.0	0.05	4.21	scf
5006	−0.5	2.5	0.05	0.05	4.21	scf

Table 2. Period and shape of the propagating front. ($\tau_u = \tau_v = 0.01$, D_{12} and d_{12} denote the sums of the off-diagonal elements of the diffusion tensors $\mathbf{D}^u$ and $\mathbf{D}^v$ corresponding to the two dependent variables u and v, sw = spiral wave, scf = small curvature front, lcf = large curvature front.).

Set No.	ω	R	D_{12}	d_{12}	Period	Shape
1000	0.0	0.5	0.0	0.0	1.68	sw
1001	0.0	0.5	0.1	0.0	1.68	sw
1002	0.0	0.5	0.0	0.1	4.21	scf
1003	0.0	0.5	0.1	0.1	4.21	scf
1011	2.5	1.0	0.0	0.0	1.68	sw
1008	2.5	1.0	0.1	0.0	1.68	sw
1009	2.5	1.0	0.0	0.1	4.21	scf
1010	2.5	1.0	0.1	0.1	4.21	scf
1015	2.5	2.5	0.0	0.0	4.21	lcf
1012	2.5	2.5	0.1	0.0	4.21	lcf
1013	2.5	2.5	0.0	0.1	4.21	lcf
1014	2.5	2.5	0.1	0.1	4.21	lcf
2008	2.5	1.0	0.05	0.0	1.68	sw
2009	2.5	1.0	0.0	0.05	4.21	lcf
2010	2.5	1.0	0.05	0.05	4.21	lcf
20008	2.5	1.0	0.01	0.0	1.66	sw
20009	2.5	1.0	0.0	0.01	4.28	lcf
20010	2.5	1.0	0.01	0.01	4.28	lcf
2012	2.5	2.5	0.01	0.0	4.28	lcf
2013	2.5	2.5	0.0	0.01	4.28	lcf
2014	2.5	2.5	0.01	0.01	4.28	lcf
1023	−2.5	1.0	0.0	0.0	1.82	sw
1020	−2.5	1.0	0.1	0.0	1.82	sw
1021	−2.5	1.0	0.0	0.1	4.19	lcf
1022	−2.5	1.0	0.1	0.1	4.19	lcf
1027	−2.5	2.5	0.0	0.0	2.27	sw
1024	−2.5	2.5	0.1	0.0	2.27	sw
1025	−2.5	2.5	0.0	0.1	4.19	lcf
1026	−2.5	2.5	0.1	0.1	4.19	lcf
2020	−2.5	1.0	0.05	0.0	1.82	sw
2021	−2.5	1.0	0.0	0.05	4.19	scf
2022	−2.5	1.0	0.05	0.05	4.19	scf
2024	−2.5	2.5	0.05	0.0	2.27	sw
2025	−2.5	2.5	0.0	0.05	2.27	lcf
2026	−2.5	2.5	0.05	0.05	2.27	lcf
20020	−2.5	1.0	0.05	0.0	1.88	sw
20021	−2.5	1.0	0.0	0.05	1.88	sw
20022	−2.5	1.0	0.05	0.05	1.88	sw
20024	−2.5	2.5	0.01	0.0	2.28	sw
20025	−2.5	2.5	0.0	0.01	2.28	sw
20026	−2.5	2.5	0.01	0.01	2.28	sw

4.1. The Effects of Anisotropy in the Absence of the Velocity Field

For set 1001 of Tables 1 and 2, i.e., there is no velocity field but there is anisotropy for v, i.e., $d_{12} = 0.1$ and $D_{12} = 0$. The results presented in Figures 1 and 2 clearly indicate the presence of a counter-rotating spiral wave at different times. A similar wave was found for

set 1000 from the same tables, where there is neither a velocity field nor anisotropy for u and v, i.e., $d_{12} = 0$ and $D_{12} = 0$. Figure 2 also indicates that the thickness of the spiral wave arm is thicker for v than for u.

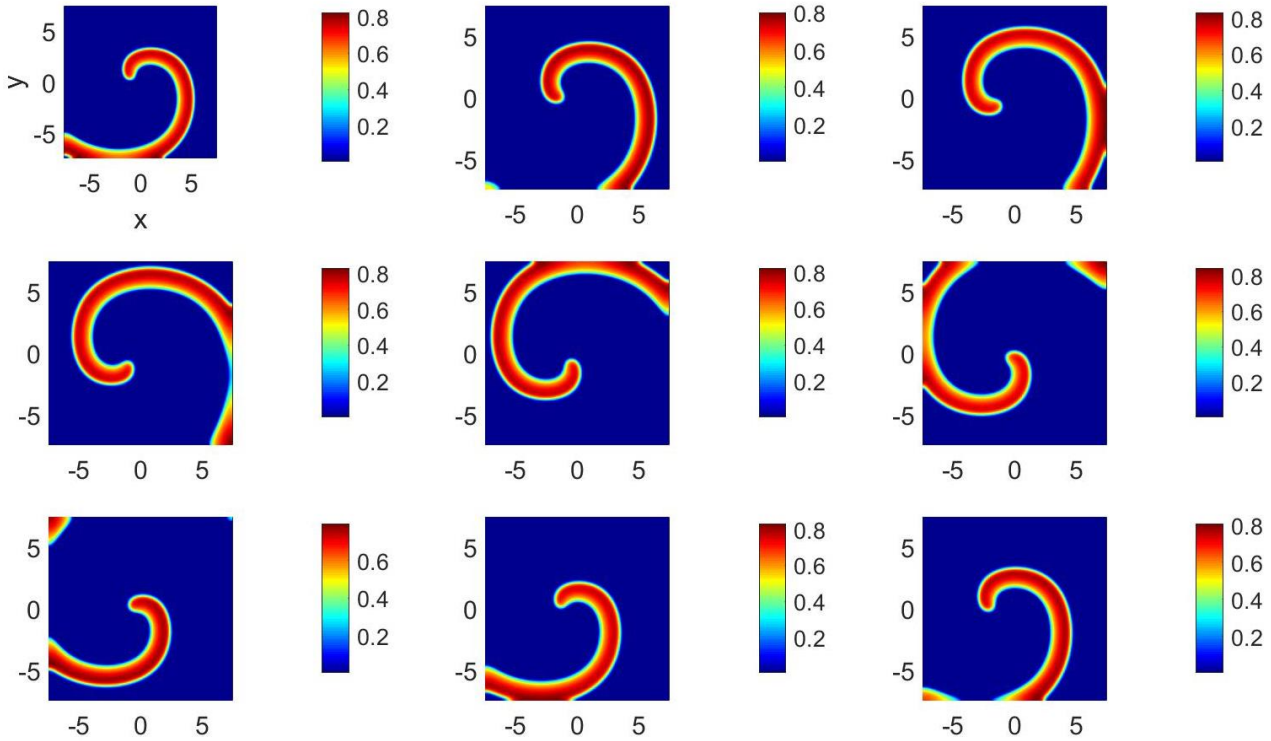

Figure 1. (Color online) $u(t, x, y)$ at (from **left** to **right** and **top** to **bottom**) $t = 50$, 55, 60, 65, 70, 75, 80, 85, and 90 for parameter set 1001.

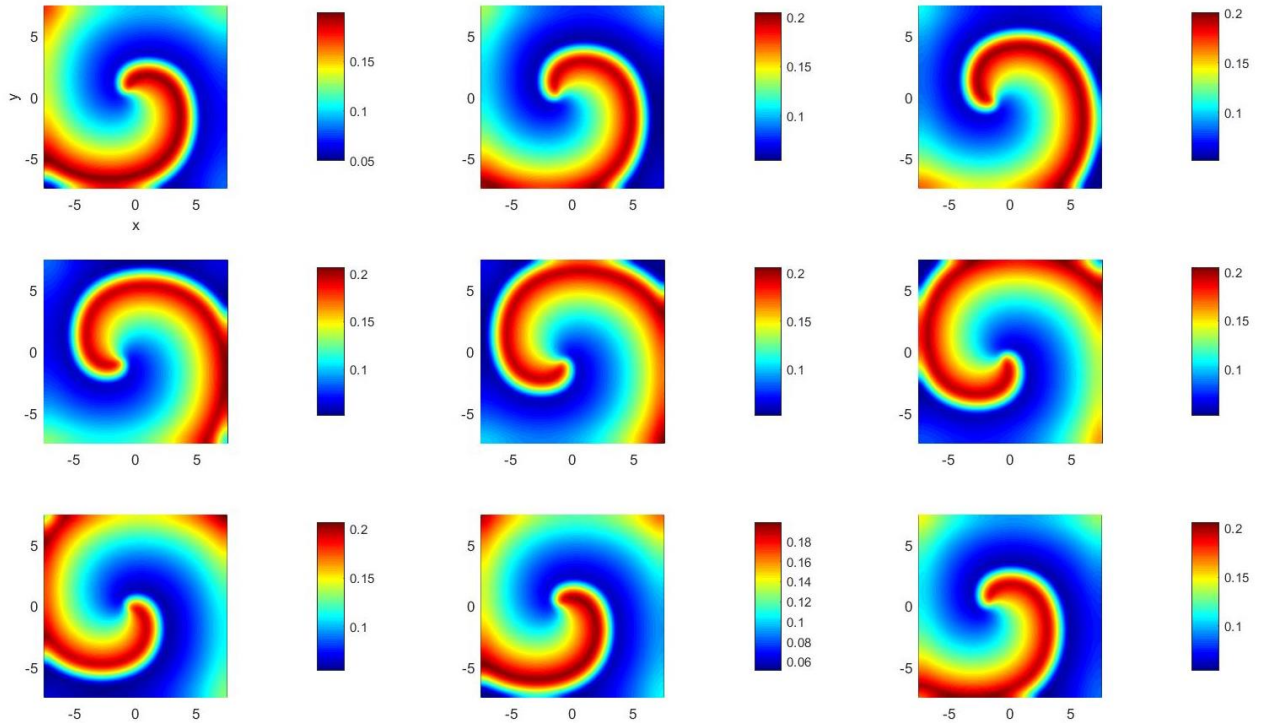

Figure 2. (Color online) $v(t, x, y)$ at (from **left** to **right** and **top** to **bottom**) $t = 50$, 55, 60, 65, 70, 75, 80, 85, and 90 for parameter set 1001.

For set 1002, the results presented in Figures 3 and 4 also correspond to a zero-velocity field, indicating that no spiral wave seems to be present; instead, the spatial distribution of u exhibits very small values for long periods of time, large curvature fronts as illustrated in the third and ninth frames, and very small curvature fronts, as shown in the sixth frame in Figure 3. However, the spatial distribution of v presented in Figure 4 indicates the presence of fronts of larger curvatures than those observed in Figure 3.

Although not shown here, similar results to those in Figures 3 and 4 were obtained for set 1003 of Table 1, indicating that d_{12} has a much larger effect on the spiral wave dynamics than D_{21}. In fact, as indicated in Table 1, the results for sets 1000 and 1001 have the same periods, which are much smaller than those of sets 1002 and 1003.

Figure 4 also indicates that even though v undergoes large changes, they are smaller than those seen in Figure 3. The reason for this behavior will become clear later on after presenting the time histories of u and v at three fixed locations within the computational domain.

In order to understand in greater detail the dynamics of the solution, the values of u and v at three spatial locations were monitored as functions of time. These points are located at $\left(-\frac{L}{2}, -\frac{L}{2}\right)$, $(0,0)$ and $\left(\frac{L}{2}, \frac{L}{2}\right)$, i.e., they are located along the main diagonal of the computational square domain, at the center and halfway between the center of the domain, and at the lower-left and upper-right corners, respectively.

Figure 5 shows the time traces at the three monitoring locations for sets 1000, 1001, 1002, and 1003 of Table 1, clearly indicating that the periods of u and v for sets 1000 and 1001 are nearly identical, indicating that D_{12} does not play an important role in the wave dynamics. By way of contrast, Figure 5 also shows that the results corresponding to sets 1002 and 1003 are nearly identical, but have larger periods than those of the results of sets 1000 and 1001.

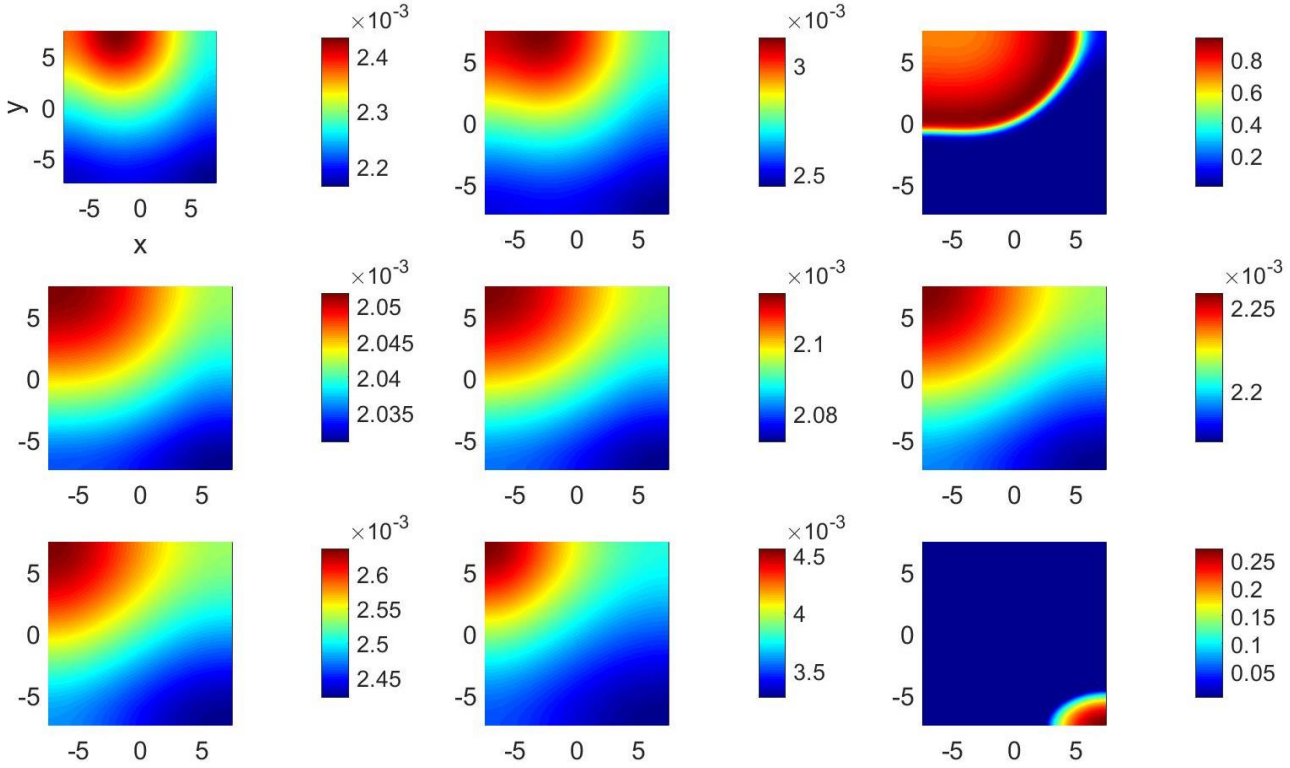

Figure 3. (Color online) $u(t, x, y)$ at (from **left** to **right** and **top** to **bottom**) $t = 50$, 55, 60, 65, 70, 75, 80, 85, and 90 for parameter set 1002.

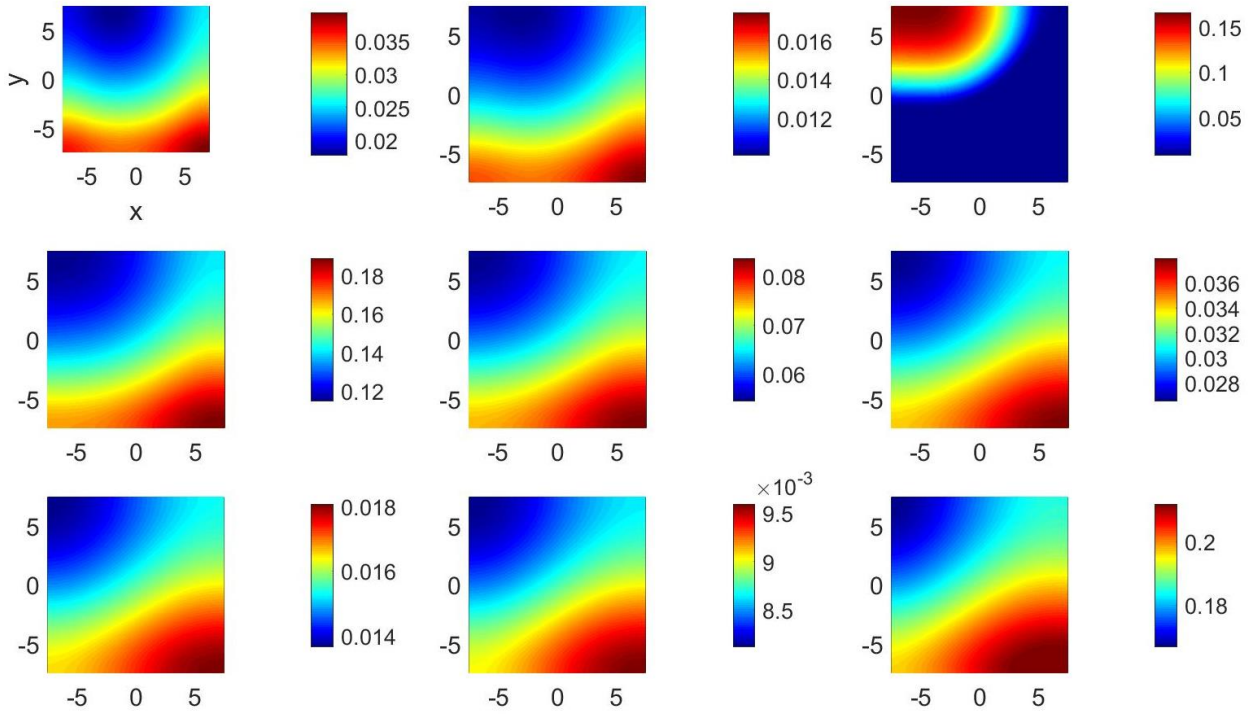

Figure 4. (Color online) $v(t,x,y)$ at (from **left** to **right** and **top** to **bottom**) $t = 50$, 55, 60, 65, 70, 75, 80, 85, and 90 for parameter set 1002.

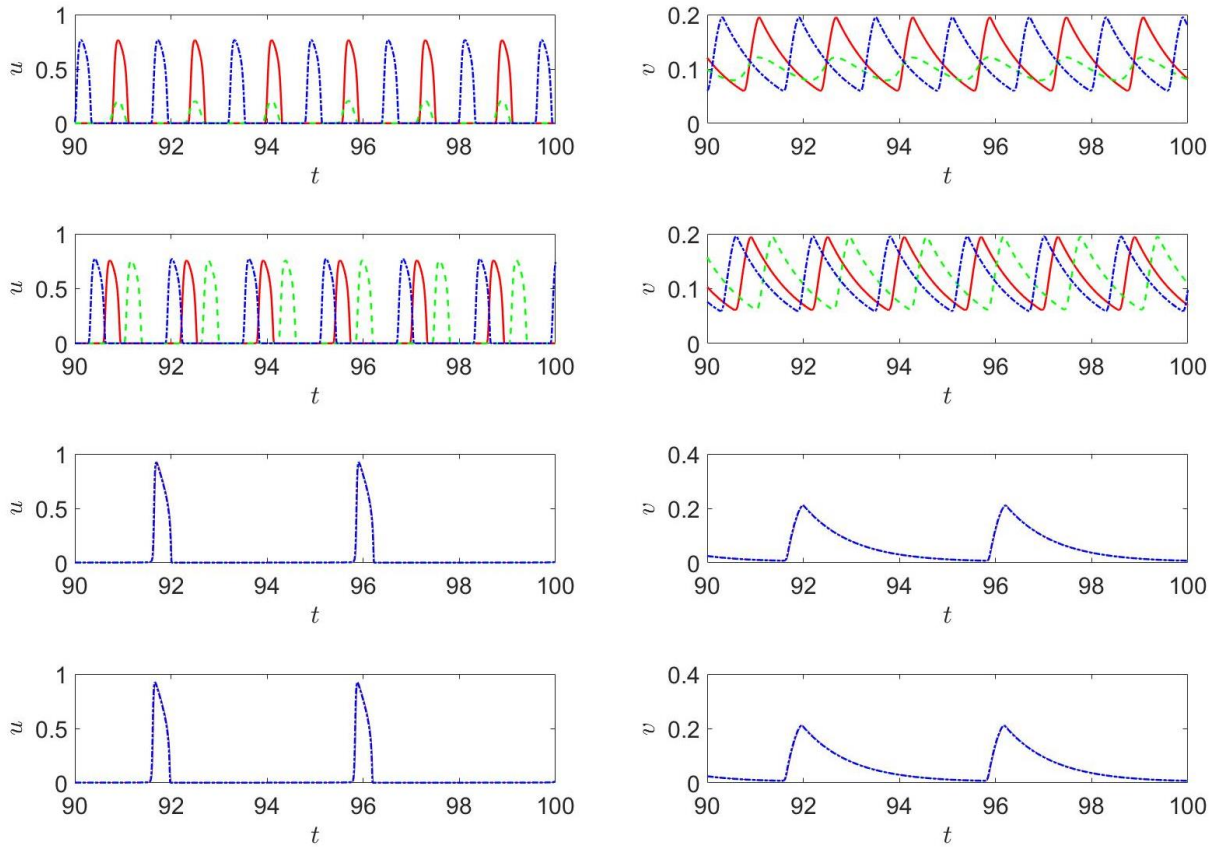

Figure 5. (Color online) $u(t,x,y)$ (**left**) and $v(t,x,y)$ (**right**) at $(x,y) = \left(-\frac{L}{2}, -\frac{L}{2}\right)$ (continuous line, red), $(0,0)$ (dashed line, green) and $\left(\frac{L}{2}, \frac{L}{2}\right)$ (dashed-dotted line, blue) for parameter set 1000 (first row), 1001 (second row), 1002 (third row), and 1003 (third row).

A detailed view of the first two rows in Figure 5 also indicates that the magnitude of v at $\left(\frac{L}{2}, \frac{L}{2}\right)$ is much smaller compared to the other two monitoring locations. Figure 5 also shows that the largest amplitudes of u and v for sets 1000 and 1001 are smaller and larger, respectively, than those for sets 1002 and 1004.

4.2. The Effects of Anisotropy in the Presence of Velocity Field

Figure 6 shows the time histories of both u and v for sets 1011, 2008, 2009, and 2010 in Tables 1 and 2. These sets correspond to a counter-rotating vortex field characterized by $\omega = 2.5$, $R = 1$ and various values of D_{12} and d_{12}. The results obtained for $(D_{12}, d_{12}) = (0.05, 0)$ have been found to differ very little from those corresponding to $(D_{12}, d_{12}) = (0, 0)$, i.e., the isotropic case, and quite a lot from those corresponding to $(D_{12}, d_{12}) = (0, 0.05)$ which, in turn, were found to differ very little from those for $(D_{12}, d_{12}) = (0.05, 0.05)$, once again indicating that D_{12} does not play an important role in the wave dynamics.

Consistent with previously discussed results for $\omega = 0$, the results presented in Figure 6 show that the maximum values of u and v for $(D_{12}, d_{12}) = (0, 0)$ and (0.05, 0) are smaller and larger, respectively, than those for $(D_{12}, d_{12}) = (0, 0.05)$ and (0.05, 0.05), and the period of the latter is larger than that of the former. Figure 6 also shows that the peak values of u and v are nearly of the same magnitudes for $(D_{12}, d_{12}) = (0, 0)$ and (0, 0.05) (cf. compare with Figure 5).

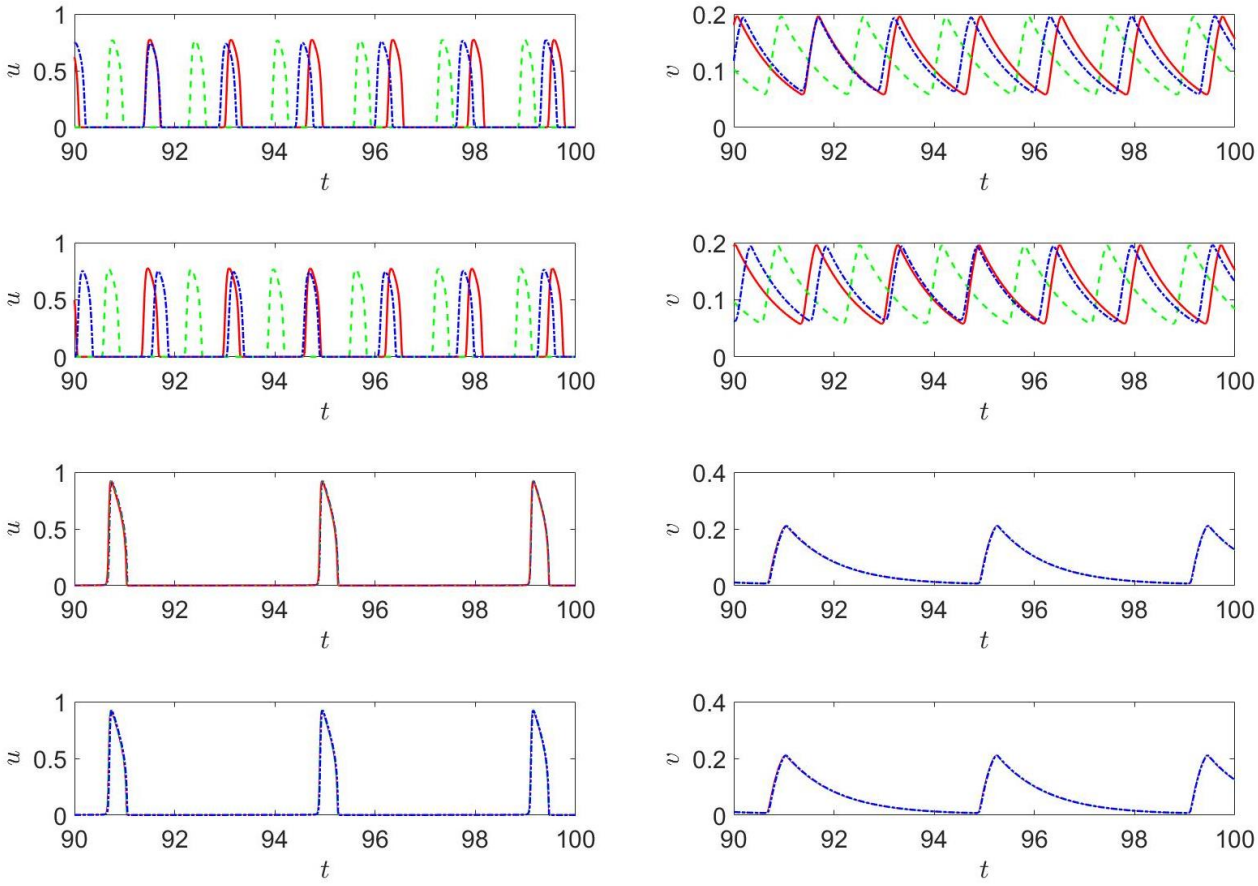

Figure 6. (Color online) $u(t, x, y)$ (**left**) and $v(t, x, y)$ (**right**) at $(x, y) = \left(-\frac{L}{2}, -\frac{L}{2}\right)$ (continuous line, red), $(0, 0)$ (dashed line, green) and $\left(\frac{L}{2}, \frac{L}{2}\right)$ (dashed-dotted line, blue) for parameter set 1011 (first row), 2008 (second row), 2009 (third row) and 2010 (third row).

Similar trends to those corresponding to the two last rows in Figure 6 have also been found in the results corresponding to sets 1002, 1006, 1009; 1003, 1007, 1009; 1002, 5005, 2025; 2009, 2013, 2021, 2025; 1008, 4005, 5005; etc. However, some surprising results were obtained for sets 1023 and 2025 and are illustrated in Figures 7 and 8.

Figure 7 shows similar trends to those observed previously in Figures 5 and 6. However, a major difference is seen for sets 1023 and 2025, i.e., u and v reach very small values at $\left(\frac{L}{2}, \frac{L}{2}\right)$, but their values at the other two monitoring locations differ very little from each other and exhibit a saw tooth pattern. This indicates that no front passes through the location $\left(\frac{L}{2}, \frac{L}{2}\right)$.

The time histories at the three monitoring locations for sets 2009, 2013, and 2021 presented in Figure 8 show similar trends to those exhibited in the last two rows in Figure 7; however, those for set 2025, corresponding to a larger and faster clockwise-rotating velocity field, are nearly identical at the monitoring locations $\left(-\frac{L}{2}, -\frac{L}{2}\right)$ and (0,0). On the other hand, the v history profile at $\left(\frac{L}{2}, \frac{L}{2}\right)$ is of a smaller magnitude and exhibits two relative maxima. The reason for this behavior will become clear when the two-dimensional distributions of u and v at selected times are presented.

In order to further illustrate the effects that anisotropy may have on two-dimensional systems of second-order hyperbolic, nonlinear advection–reaction–diffusion equations, the two-dimensional distributions of v for sets 1024 and 1026 are presented at selected times in Figures 9 and 10, respectively.

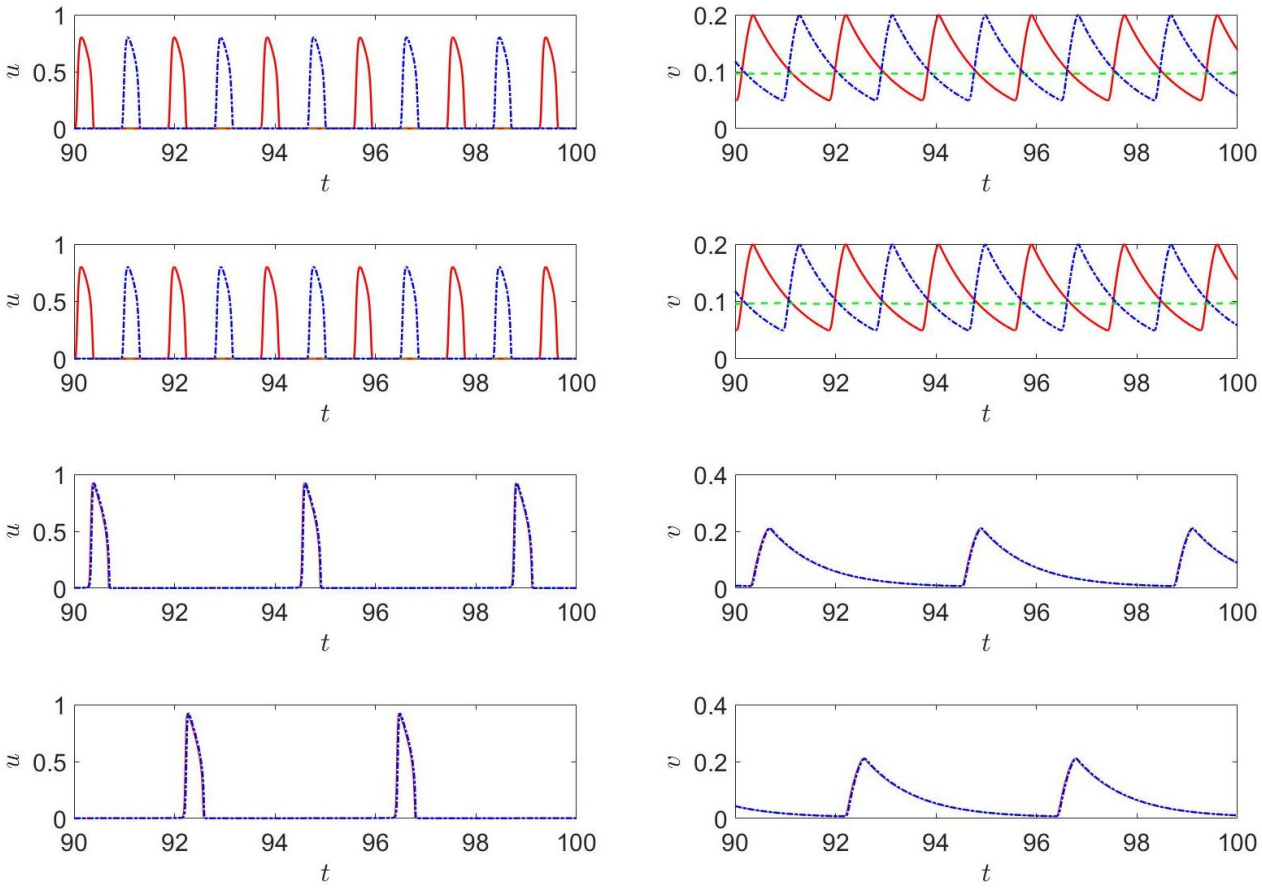

Figure 7. (Color online) $u(t, x, y)$ (**left**) and $v(t, x, y)$ (**right**) at $(x, y) = \left(-\frac{L}{2}, -\frac{L}{2}\right)$ (continuous line, red), $(0, 0)$ (dashed line, green) and $\left(\frac{L}{2}, \frac{L}{2}\right)$ (dashed-dotted line, blue) for parameter set 1023 (first row), 2020 (second row), 2021 (third row) and 2022 (third row).

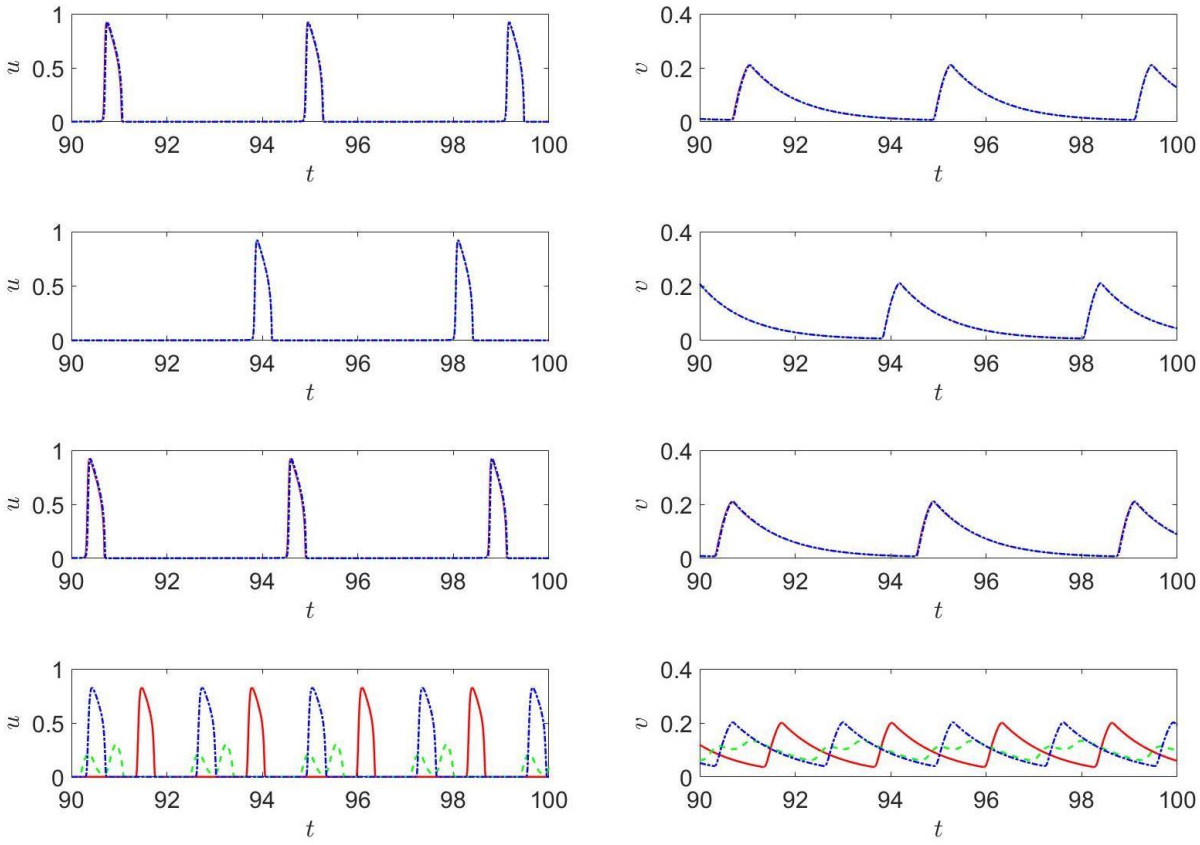

Figure 8. (Color online) $u(t,x,y)$ (**left**) and $v(t,x,y)$ (**right**) at $(x,y) = \left(-\frac{L}{2}, -\frac{L}{2}\right)$ (continuous line, red), $(0,0)$ (dashed line, green) and $\left(\frac{L}{2}, \frac{L}{2}\right)$ (dashed-dotted line, blue) for parameter set 2009 (first row), 2013 (second row), 2021 (third row), and 2025 (third row).

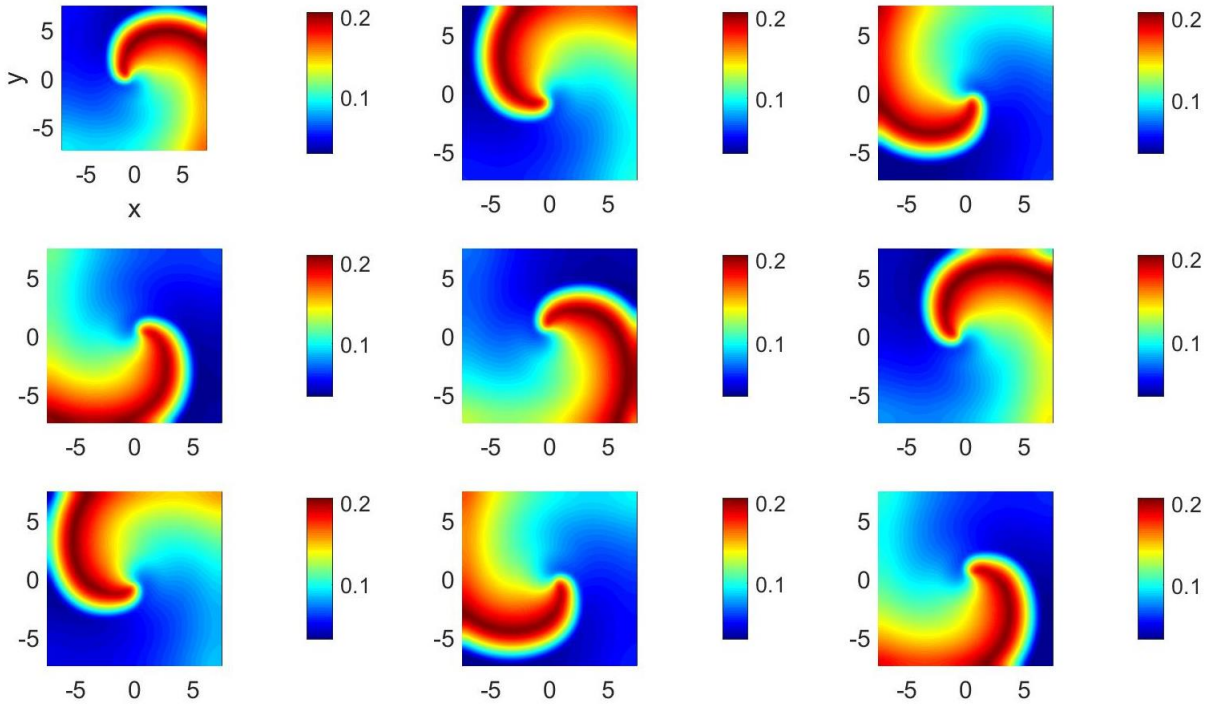

Figure 9. (Color online) $v(t,x,y)$ at (from **left** to **right** and **top** to **bottom**) $t = 50$, 55, 60, 65, 70, 75, 80, 85, and 90 for parameter set 1024.

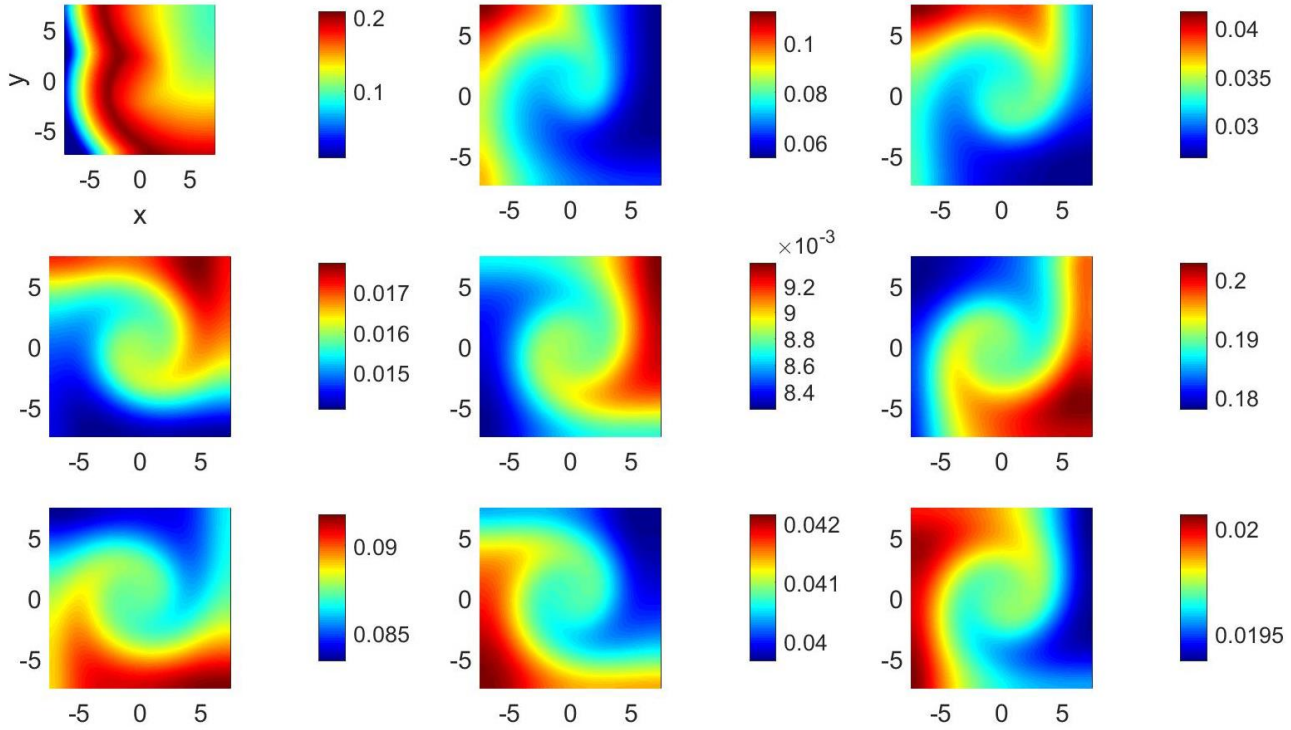

Figure 10. (Color online) $v(t, x, y)$ at (from **left** to **right** and **top** to **bottom**) $t = 50$, 55, 60, 65, 70, 75, 80, 85, and 90 for parameter set 1025.

Figure 9 clearly illustrates the presence of a counter-rotating spiral wave, which is thicker and rotates much more slowly than that exhibited in Figure 2. The reason for this slowdown is that the results in Figure 9 correspond to a clockwise rotating field, which is contrary to the counter-rotating spiral wave, and the vortex diameter is large. No velocity field was used to obtain the results reported in Figure 2.

Although not shown here, analogous results to those in Figure 9 have been obtained for set 1027, corresponding to the same parameters as those of Figure 9 except for $D_{12} = 0.1$, thus indicating once again that the anisotropy of the variable u does not play an important role in the qualitative and quantitative characteristics of the solution to Equation (20).

For the parameters in set 1025, the results presented in Figure 10 are quite different from other results presented previously in this manuscript. For example, the first frame in that figure illustrates a small curvature thick front, whereas the remaining eight frames show vortex-like shapes that remind the reader of the engulfment of fluids in, for example, planar mixing layers (cf., e.g., Figures 3 and 9 in Reference [31]).

4.3. The Effects of Relaxation Times on Wave Propagation

The effects of τ_u and τ_v on the solution were found to be small for relaxation times less than 0.05, which, according to the estimates discussed in this paper, correspond to a velocity along the characteristics equal to $\sqrt{20}$ and $\sqrt{12}$ for u and v, respectively. For the domain considered in this study, whose dimensions in the x and y directions are 15, the times required for the propagation from, say, the left to the right boundary range from 3.35 to 4.33. By way of contrast, the characteristic diffusion times for u and v based on L are 56.25 and 93.75, respectively. These times are clearly much larger than those associated with propagation along the characteristic lines. This means that the effects of the relaxation times are expected to be small and, in fact, they have been found to be small, except in a thin initial layer near $t = 0$ whose time duration is on the order of the relaxation time consistent with the asymptotic analysis of singularly perturbed wave equations, e.g., [32–34].

In order for the characteristic time based on the velocity along the characteristic lines and the diffusion time to be of the same order of magnitude, Equation (19) demands that

$\tau = \mathcal{O}(L^2)$ which, for the domains considered here, implies that $\tau \approx 56.25$, and, for such a large relaxation time, the Taylor series expansion of Equation (5), i.e., Equation (6), is not valid.

5. Conclusions

A time-linearized, three-time-level finite difference method for the numerical solutions of multivariable, multi-dimensional, second-order hyperbolic, advection–reaction–diffusion equations has been presented and applied to analyze the effects of relaxation, convection, and anisotropy on the heat and mass diffusion fluxes in a two-variable, two-dimensional problem. The equations are based on a frame-indifferent constitutive model for the diffusion flux that, for zero relaxation times, reduces to the Fourier law. This model has been formulated for both temperature and species concentrations and can also address the variables of their diffusion fluxes.

It has been shown that the anisotropy of one of the dependent variables plays a very minor role in the numerical solution, whereas the anisotropy of the other variable leads to transitions from spiral waves to fronts of large curvature, and then to fronts of smaller curvature. The solutions corresponding to these fronts have been found to have longer periods than those associated with isotropic diffusion. It has also been found that the concentration peak values of the two dependent variables differ from those obtained for isotropic diffusion.

For small anisotropy in the diffusion tensors and counterclockwise-rotating vortices of small radii, the effect of the velocity field is to stretch and strain the spiral waves, whereas, for clockwise vortices, convection leads to wave compression and deceleration. Similar results to those just described have been found for isotropic diffusion. However, for clockwise-rotating vortices of large diameters in anisotropic media, complex transitions have been observed as the vortex circulation increases. These transitions are characterized by highly distorted spiral waves for small vortex circulations, large curvature fronts for moderate circulations, and wave trapping for large circulations. The wave trapping observed in large-diameter, clockwise-rotating vortical fields exhibits similarities with vortex development and entrainment seen experimentally in non-reactive planar mixing layers.

For large-diameter, counterclockwise-rotating vortices, it has been found that the effects of anisotropy are almost identical at three points located on the main diagonal of the computational square domain employed in the numerical experiments reported here. Only transitions from spiral waves to fronts of large curvatures and then fronts of small curvatures are observed as the vortex circulation increases.

The effects of the relaxation times of the two dependent variables considered in this study are important primarily within an initial layer. This layer's duration is on the order of the largest relaxation time, where the solution undergoes a rapid transition from the initial conditions to those corresponding to parabolic advection–reaction–diffusion equations, consistent with well-known results of the asymptotic analysis of singularly perturbed, second-order hyperbolic equations. This initial adjustment has been solved accurately in the numerical experiments reported here, where a time step two orders of magnitude smaller than the smallest relaxation time was used, and does not have a cumulative effect in time, so that the long-term behaviors of the equations considered in this paper are identical to those for parabolic advection–reaction–diffusion equations.

For the conditions considered in this study, it has also been shown that relaxation effects may be important for large relaxation times, for which the well-known linear relaxation equation is not valid. Therefore, studies based on such large relaxation times may be of academic interest but may not be relevant to heat and mass transport phenomena, which are usually characterized by small relaxation times, although they may be relevant for the modeling of forest fires, virus infections, the spread of epidemics, chemical reactions, biology, ecology, population dynamics, etc.

Funding: This research received no external funding.

Data Availability Statement: Data are contained within the article.

Acknowledgments: This paper was supposed to be an enlarged version of Paper No. 199, entitled "A numerical study of relaxation phenomena in microfluidic reactive–diffusive systems", which was published in the Book of Abstracts of the 14th International Conference on Computational Heat and Mass Transfer (ICCHMT 2023) held in Dusseldorf from 4 to 8 September 2023. An extended version of the two-page abstract is scheduled to appear in Springer's Lecture Notes in Mechanical Engineering. In order to avoid unnecessary duplication, the author decided to not enlarge the above-referred paper that dealt with one-dimensional problems and instead reported the formulation for multi-dimensional, multivariable, hyperbolic advection–reaction–diffusion equations presented in this paper. The author is deeply grateful to Professor Ali C. Benim of Dusseldorf University of Applied Sciences (Germany) for his kindness and help before, during, and after ICCHMT 2023. The author is also grateful to the three referees for their comments on the original manuscript.

Conflicts of Interest: The author declares no conflicts of interest.

References

1. Landau, L.D.; Lifshitz, E.M. *Fluid Mechanics*; Pergamon Press: New York, NY, USA, 1987.
2. Joseph, D.D.; Preziosi, L. Heat waves. *Rev. Mod. Phys.* **1989**, *61*, 41–73. [CrossRef]
3. Joseph, D.D.; Preziosi, L. Addendum to the paper "Heat waves" [Rev. Mod. Phys. 61, 41 (1989)]. *Rev. Mod. Phys.* **1990**, *62*, 375–391. [CrossRef]
4. Murray, J.D. *Mathematical Biology II: Spatial Models and Biomedical Applications*; Springer: New York, NY, USA, 2003.
5. Ritchie, J.S.; Krause, A.L.; Van Gorder, R.A. Turing and wave instabilities in hyperbolic reaction–diffusion systems: The role of second-order time derivatives and cross–diffusion terms on pattern formation. *Ann. Phys.* **2022**, *444*, 169033. [CrossRef]
6. Pourasghar, A.; Chen, Z. Hyperbolic heat conduction and thermoelastic solution of functionally graded CNT reinforced cylindrical panel subjected to heat pulse. *Int. J. Solids Struct.* **2019**, *163*, 117–129. [CrossRef]
7. Rubin, M.A. Hyperbolic heat conduction and the second law. *Int. J. Engng Sci.* **1992**, *30*, 1665–1676. [CrossRef]
8. Christov, C.I. On frame indifferent formulation of the Maxwell–Cattaneo model of finite–speed heat conduction. *Mech. Res. Commun.* **2009**, *36*, 481–486. [CrossRef]
9. Christov, C.I. On the material invariant formulation of Maxwell's displacement current. *Found. Phys.* **2006**, *36*, 1701–1717. [CrossRef]
10. Truesdell, C. *A First Course in Rational Continuum Mechanics*; Academic Press: New York, NY, USA, 1977.
11. Zhmakin, A.I. *Non–Fourier Heat Conduction: From Phase-Lag Models to Relativistic and Quantum Transport*; Springer Switzerland AG: New York, NY, USA, 2023.
12. Williams, F.A. *Combustion Theory*, 2nd ed.; Addison–Wesley Publishing Company: New York, NY, USA, 1985.
13. Vanag, V. K.; Epstein, I.R. Cross–diffusion and pattern formation in reaction–diffusion systems. *Phys. Chem. Chem. Phys.* **2009**, *11*, 897–912. [CrossRef]
14. Shi, J.; Xie, Z.; Little, K. Cross–diffusion induced instability and stability in reaction–diffusion systems. *J. Appl. Anal. Comput.* **2010**, *24*, 95–119. [CrossRef]
15. Carslaw, H.S.; Jaeger, J.C. *Conduction of Heat in Solids*; Oxford University Press: New York, NY, USA, 1959.
16. Bertaglia, G.; Pareschi, L. Hyperbolic models for the spread of epidemics on networks: Kinetic description and numerical methods. *ESAIM Math. Model. Numer. Anal.* **2021**, *55*, 381–407. [CrossRef]
17. Barbera, E.; Currò, C.; Valenti, G. A hyperbolic reaction–diffusion model for the hantavirus infection. *Math. Methods Appl. Sci.* **2028**, *31*, 481–499. [CrossRef]
18. Méndez, V.; Casas–Vázquez, J. Hyperbolic reaction–diffusion model for virus infection. *Int. J. Thermodyn.* **2008**, *11*, 35–38.
19. Méndez, V.; Llebot, J.E. Hyperbolic reaction–diffusion model for a forest fire model. *Phys. Rev. E* **1997**, *56*, 35–38. [CrossRef]
20. Consolo, G.; Curró, C.; Grifó, G.; Valenti, G. Oscillatory periodic pattern dynamics in hyperbolic reaction–advection–diffusion models. *Phys. Rev. E* **2022**, *105*, 034206. [CrossRef] [PubMed]
21. Cho, U.-I.; Eu, B.C. Hyperbolic reaction–diffusion equations and chemical oscillations in the Brussellator. *Phys. D* **1993**, *68*, 351–363. [CrossRef]
22. Al–Ghoul, M.; Eu, B.C. Hyperbolic reaction–diffusion equations and irreversible thermodynamics: Cubic reversible reaction model. *Phys. D* **1996**, *90*, 119–153. [CrossRef]
23. Al–Ghoul, M.; Eu, B.C. Hyperbolic reaction–diffusion equations, patterns, and phase speeds for the Brusselator. *J. Phys. Chem.* **1996**, *100*, 18900–18910. [CrossRef]
24. Zemskov, E.P.; Horsthemke, W. Diffusive instabilities in hyperbolic reaction–diffusion equations. *Phys. Rev. E* **2016**, *93*, 032211. [CrossRef]
25. Ramos, J.I. Numerical methods for nonlinear second-order hyperbolic partial differential equations. I. Time–linearized finite difference methods for 1-D problems. *Appl. Math. Comput.* **2007**, *190*, 722–756. [CrossRef]
26. Greenbaum, A. *Iterative Methods for Solving Linear Systems*; SIAM: Philadelphia, PA, USA 1997.
27. Meurant, G. *Computer Solution of Large Linear Systems*; North-Holland: Amsterdam, The Netherlands, 1999.

28. Saad, Y. *Iterative Methods for Sparse Linear Systems*, 2nd ed.; SIAM: Philadelphia, PA, USA, 2003.
29. Simoncini, V.; Szyld, D.B. Recent computational developments in Krylov subspace methods for linear systems. *Numer. Linear Algebra Appl.* **2007**, *14*, 1–82. [CrossRef]
30. Ramos, J.I. Propagation of spiral waves in anisotropic media: From waves to stripes. *Chaos Solitons Fractals* **2001**, *12*, 1057–1064. [CrossRef]
31. Bernal, L.P.; Roshko, A. Streamwise vortex structure in plane mixing layers. *J. Fluid Mech.* **1986**, *170*, 499–525. S002211208600099X. [CrossRef]
32. Kevorkian, J.; Cole, J.D. *Perturbation Methods in Applied Mathematics*; Springer: New York, NY, USA, 1981.
33. Kevorkian, J.; Cole, J.D. *Multiple Scale and Singular Perturbation Methods*; Springer: New York, NY, USA, 1996.
34. Butuzov, V.F. The angular boundary layer in mixed singularly perturbed problems for hyperbolic equations. *Math. USSR Sb.* **1997**, *33*, 403–425. [CrossRef]

computation

MDPI

Article

The Theory and Computation of the Semi-Linear Reaction–Diffusion Equation with Dirichlet Boundaries

Pius W. M. Chin

Department of Mathematics and Applied Mathematics, Sefako Makgatho Health Sciences University, Medunsa, Ga-Rankuwa, Pretoria 0204, South Africa; pius.chin@smu.ac.za; Tel.: +27-(12)-5213736

Abstract: In this article, we study the semi-linear two-dimensional reaction–diffusion equation with Dirichlet boundaries. A reliable numerical scheme is designed, coupling the nonstandard finite difference method in the time together with the Galerkin in combination with the compactness method in the space variables. The aforementioned equation is analyzed to show that the weak or variational solution exists uniquely in specified space. The a priori estimate obtained from the existence of the weak or variational solution is used to show that the designed scheme is stable and converges optimally in specified norms. Furthermore, we show that the scheme preserves the qualitative properties of the exact solution. Numerical experiments are presented with a carefully chosen example to validate our proposed theory.

Keywords: reaction–diffusion equation; semi-linear equation; nonstandard finite difference method; Galerkin method; optimal rate of convergence

Citation: Chin, P.W.M. The Theory and Computation of the Semi-Linear Reaction–Diffusion Equation with Dirichlet Boundaries. *Computation* **2024**, *12*, 142. https://doi.org/10.3390/computation12070142

Academic Editors: Ali Cemal Benim, Abdulmajeed A. Mohamad, Sang-Ho Suh, Rachid Bennacer, Paweł Oclon and Jan Taler

Received: 6 June 2024
Revised: 4 July 2024
Accepted: 8 July 2024
Published: 11 July 2024

1. Introduction

Many physical and mathematical developments that have taken place recently (due to various chemical as well as diffusion-like systems) in the sciences, ecology, population dynamics, biochemistry and engineering, to mention a few fields, have attracted extensive attention. These physical developments correspond to several phenomena in which chemical substances are transformed into each other. For more on these, see [1,2]. All these activities are modeled to mathematical equations describing semi-linear parabolic partial differential equation, where the reaction–diffusion equation occurs. In this paper, we are concerned with the study of the following two-dimensional semi-linear reaction–diffusion equation of the following type:

$$\frac{\partial u}{\partial t} - \Delta u + (|u|^2 - 1)u = 0, \quad (x,t) \in \Omega \times (0,T) \tag{1}$$

$$u(x,t) = 0 \ \text{ on } \ \partial\Omega \times (0,T) \tag{2}$$

$$u(x,0) = u_0(x) \ \text{ for } \ x \in \Omega \ \ t = 0, \tag{3}$$

where $\Omega \subset \mathbb{R}^2$ is an open-bounded set contained in $\mathbb{R}^2$ with D as a matrix with positive constant and $u : \Omega \longrightarrow \mathbb{R}$ as an unknown scalar function.

In addition to the description of the formation of the semi-linear reaction–diffusion equation stated above, these equations originate naturally in systems consisting of many interesting components in a variety of biological, chemical, physical and population dynamics fields. In certain situations, as in [2], the patterns are seen as phase-field transitional systems. This is a situation in which the phase function u describes the transition between the solid and liquid phases in the solidification process of a material occupying a region Ω. The above reaction–diffusion equation could be seen to be exhibiting a type of Allen–Cahn

equation in [3–5], which is used to describe the motion of anti-phase boundaries in crystalline solids. This has been widely applied to many complex moving interface problems, for example the mixture of two incompressible fluids and the nucleation of solids and vesicle membranes; see [6] for more. Specifically, the Equations (1)–(3) arise in the study of the superconductivity of liquids and have been studied in J. Smoller [7]. A great deal of work has been undertaken on the nonlinear reaction–diffusion equation, and for more on this see [8–12].

The above class of partial differential equations have been analyzed using several methods, such as the fixed node finite difference methods in [13] and the spectral method in [14]. This was followed by some other methods, which have good numerical stability and can be used for multi-dimensional purposes, as presented in [15]. These methods include the method by Sharifi and Rashidian [16], who applied an explicit finite difference associated with extended cubic B-spline collocation method. There is also a method by Wang et al. [17] called the compact boundary value method (CBVM), which is a combination of a compact fourth-order differential method (CFODM) and the P-order boundary value method (POBVM). This method is locally stable and when applied to the equation will obtain a unique solution. Another method is the one by Wu et al. [18], called the variational iteration method (VIM), used for structuring equations, and the Lagrange multipliers and numerical integral formulas are used with this method. Last but not the least is the method by Biazar and Mehriatifan in [19], which solved the equation using the compact finite difference method.

In contrast to the above good methods stated for the analysis of the problem, only very few or none have used the coupling technique as a tool for the analysis of this problem, to the best of this author's knowledge. To this end, we exploited the gap and designed a very reliable and efficient scheme, consisting of the nonstandard finite difference method in time and the Galerkin combined with the compactness method in the space variables (NSFD-GM) in a two-dimensional setting. This method can be used to show that the solution obtained from the semi-linear reaction–diffusion equation exists uniquely. We also proceed to show, using the a priori estimates obtained from the existence of the variational or weak solution, that the designed scheme is stable. The stability of the scheme is further tested for its optimal convergence with the L^2- as well as the H^1-norms to be defined later. Furthermore, we show that the designed scheme (NSFD-GM) preserves or replicates the decaying properties of the exact solution. Numerical experiments are then presented with a carefully chosen example to justify that the numerical results obtained from the above experiments indeed validate the theory presented in the work.

The above method has been used extensively in a one-dimensional situation such as in [20]. It should, however, be noted that the aforementioned one-dimensional case was an extension of the pioneering work in [21], from where the method was initiated in a linear situation over a non-smooth geometry. Our goal in this article was to see whether or not the method could be applicable in a two- or higher-dimensional setting. The relevance of the method could be deduced from the fact that the designed schemes that have in the past emanated from this method preserve or replicate all the qualitative properties of the exact solution of the problems that they have solved. In addition, where the method has been used, it has also performed better than the traditional Euler method. One could also attempt to remark that since real life problems such as this appear mostly in higher dimensional settings, if the method is found to perform exceptionally well, then that will be a remarkable achievement for the method in that framework. The founder of the NSFD method was Mickens [22] and major contributions to the foundation and application to the method can be found in [23–26]. As for the overview of the method, see [27]. The comparison of the finite and nonstandard finite difference methods can be seen in [22].

The organization of this article begins from Section 2, where we briefly outline the notations and tools to be used subsequently in the article. This is followed by Section 3, which addresses the existence and uniqueness of the solution of the problem. We proceed to design the numerical scheme in which convergence analysis is established in Section 4.

Section 5 is then devoted to carrying out the numerical experiments with a carefully chosen example to justify the theory. Conclusions and future remarks are finally stated in Section 6.

2. Notations and Preliminaries

In this section, for the sake of completeness, we gather some important notations with tools such as definitions, concepts and inequalities that will play some important roles in the analysis of the problem. Some of these preliminary tools may duplicate some tools from these papers [20,28–30], the reason being that these papers deal with related subjects that need the same tools. Among these tools are function spaces such as the space $\mathcal{D}(\Omega)$. This space, in summary, is defined as a linear space of infinitely differentiable functions with compact support in the domain Ω, where Ω in our case will be a two-dimensional open set contained in $\mathbb{R}^2$. The above mentioned space $\mathcal{D}(\Omega)$ is followed by the space of distributions $\mathcal{D}'(\Omega)$, which is its pair. The duality pairing of these two spaces is denoted by $\langle \cdot, \cdot \rangle$. In between these two spaces are the $L^p(\Omega)$ spaces which are also essential, and this, in summary, is defined by

$$L^p(\Omega) := \left\{ v : \left(\int_\Omega |v(x)|^p dx \right)^{1/p} < \infty \right\}.$$

for $1 < p < +\infty$. The $L^p(\Omega)$ space is known to be a Banach space with the norm defined by

$$\|v\|_{L^p(\Omega)} = \left(\int_\Omega |v(x)|^p dx \right)^{1/p}. \tag{4}$$

For more on these spaces, see [31–33]. Another very important function space is the Sobolev space, denoted and defined by

$$W^{m,p}(\Omega) := \{ v \in L^p(\Omega) : D^\alpha v \in L^p(\Omega), \text{ for all multi index } |\alpha| \leq m \}. \tag{5}$$

for $m \in \mathbb{N}$ and $p \in \mathbb{R}$ with $1 < p \leq \infty$. The above space (5) with the norm defined by

$$\|v\|_{m,p,\Omega} = \left(\sum_{|\alpha| \leq m} \|D^\alpha v\|_{L^p(\Omega)} \right)^{1/p}, \quad p < \infty \tag{6}$$

or

$$\|v\|_{m,\infty,\Omega} = \sup_{|\alpha| \leq m} \left(ess \sup_{x \in \Omega} |D^\alpha v(x)| \right), \quad p = \infty. \tag{7}$$

which is also a Banach space. When $p = 2$ in the above Sobolev space, the notation $W^{m,2}(\Omega)$ is applied and often denoted by $H^m(\Omega)$ and called a Hilbert space. Most often, we use the superscript $p = 2$ when referring to its norm and semi-norm, especially where there is no ambiguity. See Lions and Magenes [33] for more details. Continuing in the gathering of tools, we would like to introduce another, more general Sobolev space denoted by $H^m[(0,T);X]$, where X is a Hilbert space. The above space, as viewed by Lions and Magenes [33], is defined in summary as the space of square integrable functions taking values from $[0,T]$ to X. The norm of this space is defined by

$$\|v\|_{H^m[(0,T);X]} := \left(\sum_{|\alpha| \leq m} \int_0^T \|D^\alpha v(x)\|_X^2 dt \right)^{1/2}. \tag{8}$$

In view of (8), X could be seen as either L^p or $W^{m,p}$ space and in a particular situation of ours, H_0^1, L^2, L^4 and H_0^m. The following inequalities will be used in this paper: Hölder, Gronwall's, Young's, Poincaré and Gagliador-Nirenburg inequality. For more

inequalities not listed here, we will refer to standard reference materials such as in [31–35] when required.

We conclude the assembly of the tools by introducing the following numerical space, denoted by $\mathcal{V}_h$, needed for the analysis of the discrete problem. This space is finite-dimensional and is defined by

$$\mathcal{V}_h := \Big\{ v_h \in C^0(\bar{\Omega}) : v_h|_{\partial\Omega} = 0, v_h|_{\mathcal{J}} \in P_1, \ \ \forall \mathcal{J} \in \mathcal{J}_h \Big\} \tag{9}$$

where P_1 is the space of a polynomial of a degree less than or equal to 1. $\mathcal{J}_h$, as stated above, will be a regular mesh of the domain Ω, consisting of compatible triangles $\mathcal{J}$ of sizes $h_{\mathcal{J}} < h$. For more details on this see [34]. In view of (9), we observe that, for each $\mathcal{J}_h$, we associate a finite element space $\mathcal{V}$ of a continuous linear piece-wise test function with a value of 1 or zero at every other node of $\mathcal{V}$. That is, if $\{P_j\}_{j=1}^n$ are the interior nodes of $\mathcal{J}_h$, then any function in $\mathcal{V}_h$ is uniquely determined by its values at the point P_j and it should also be noted that $\mathcal{V}_h \subset H_0^1(\Omega)$.

3. The Semi-Linear Reaction–Diffusion Equation

This section is set aside to show that by using Galerkin in combination with the compactness methods, the solution of the two-dimensional semi-linear reaction–diffusion Equations (1)–(3) exits uniquely in the space

$$L^\infty\Big[(0,T);L^2(\Omega)\Big] \cap L^2\Big[(0,T);H_0^1(\Omega)\Big] \cap L^4\Big[(0,T);L^4(\Omega)\Big] \ \text{ and } \ \frac{\partial u}{\partial t} \in L^2\Big[(0,T);H^{-1}(\Omega)\Big] \tag{10}$$

for initial data given in (3). The a priori estimates obtained in the above analysis of the theoretical framework will be crucial to the NSFD-GM numerical scheme, which will be outlined in Section 4. In view of this, we proceed to show this by first stating the following variational or weak problem of the semi-linear reaction–diffusion Equations (1)–(3), finding $u(x,t) \in L^\infty\big[(0,T);L^2(\Omega)\big] \cap L^2\big[(0,T);H_0^1(\Omega)\big] \cap L^4\big[(0,T);L^4(\Omega)\big]$ such that

$$\left\langle \frac{\partial u}{\partial t}, v \right\rangle + \langle \nabla u, \nabla v \rangle + \Big\langle (|u|^2 - 1)u, v \Big\rangle = 0 \tag{11}$$

$$\langle u(x,0), v \rangle = \langle u_0, v \rangle. \tag{12}$$

for all $u_0, v \in H_0^1(\Omega)$. This is undertaken by making use of the orthonormal basis of L^2 functions denoted by $\{e_1, e_2, \cdots, e_m\} \subset H_0^1 \cap H^2(\Omega)$, where $m \in \mathbb{N}$. With these basic functions, we can make use of the test function v spanned by $v \in span\{e_1, e_2, \cdots, e_m\}$ to denote and define the approximation of the solution u of the equation through

$$u_m = \sum_{i=1}^{m} \gamma_i(t) e_i. \tag{13}$$

We can then proceed to apply the above Galerkin framework (13) to the semi-linear reaction–diffusion Equations (1)–(3). The approximation $\{u_m\}, m \in \mathbb{N}$ of the said equation satisfies the following Galerkin system of equations:

$$\frac{\partial u_m}{\partial t} - \Delta u_m + P_m\Big((|u_m|^2 - 1)u_m\Big) = 0, \ \ \text{on} \ \ \Omega \times (0,T) \tag{14}$$

$$u_m(x,t) = 0 \ \ \text{on} \ \ \partial\Omega \times (0,T) \tag{15}$$

$$u(x,0) = P_m u_0 \ \ \text{on} \ \Omega \tag{16}$$

where the above projection P_m denotes the orthogonal projection

$$P_m : H^{-1}(\Omega) \longrightarrow \mathcal{V}_m \subset H^{-1}(\Omega). \tag{17}$$

and $\mathcal{V}_m$ is defined in Equation (9). This means that the operator is extended from $L^2(\Omega)$ into $H^{-1}(\Omega)$ and defined on the $H^{-1}(\Omega)$ by

$$P_m\left(\sum_{k\in m} \gamma_m^k(t)u_k\right) = \sum_{k=1}^{m} \gamma_m^k(t)u_k. \tag{18}$$

At this point, we should state that Equations (14)–(16) are also satisfied, with the discrete solution u_m taking values in the finite dimensional subspace V_m. The connection between the semi-linear reaction–diffusion Equations (1)–(3) and their approximate Galerkin system of Equations (14)–(16) stated above validate the fact that these equations are equivalent, as seen classically in Temam, 1997 [11], and Evans, 1998 [32]. The above connection provides the framework to proceed and shows that the solution of the semi-linear reaction–diffusion equation exists uniquely. This can be achieved thanks to the next Theorem 1.

Theorem 1. *There exists a unique solution u of the semi-linear reaction–diffusion Equations (1)–(3) in the space given in (10), such that the variational solutions of Equations (11) and (12) are satisfied for the initial solution $u_0 \in H_0^1(\Omega)$, with its Dirichlet boundary conditions.*

We will use three subsections to prove this Theorem. These will be Section 3.1, where we will address the uniform approximation of the solution, followed by Section 3.2, where the boundedness of the approximate solution and passage to the limit will be achieved using the compactness method. The uniqueness of the solution of the problem will be shown in Section 3.3.

3.1. Uniform Approximate Solution Estimates of the Equation

To show the uniform approximation estimate of the semi-linear reaction–diffusion equation, we will first consider, here and after, that C will denote all constants independent of m. With this in mind, and $v \in H_0^1(\Omega)$ in Equations (11) and (12), the yield of the variational Equations (14)–(16) will be

$$\frac{1}{2}\frac{d}{dt}\|u_m\|_{L^2}^2 + \|\nabla u_m\|_{L^2}^2 + \int_\Omega \Big(|u_m|^2 u_m - u_m\Big)u_m dx = 0 \tag{19}$$

where $v = u_m$ was set. Proceeding to use the Sobolev embedding Theorem and the fact that $L^4 \subset H^1$, we bound the third term of (19) as follows:

$$\int_\Omega u_m^2(|u_m|^2 - 1)dx \leq \|u_m\|_{L^4}^4 - \|u_m\|_{L^2}^2$$

and introducing it back into Equation (19), yielded

$$\frac{1}{2}\frac{d}{dt}\|u_m\|_{L^2}^2 + \|\nabla u_m\|_{L^2}^2 + \|u_m\|_{L^4}^4 \leq \|u_m\|_{L^2}^2. \tag{20}$$

after taking $D = 1$ for simplicity's sake. Hence, taking the integral of both sides of (20) with respect to the time interval t yields

$$\|u_m\|_{L^2}^2 + \int_0^t \Big[\|\nabla u_m\|_{L^2}^2 + \|u_m(s)\|_{L^2}^4\Big]ds \leq \|u_0\|_{L^2}^2 + \int_0^t \|u_m(s)\|_{L^2}^2 ds. \tag{21}$$

Applying the Gronwall inequalities, keeping only the term $\|u_m(t)\|_{L^2}^2$ on the left-hand side of (21), we obtain

$$\|u_m\|_{L^2}^2 \leq C\Big(\|u_0\|_{L^2}^2\Big)e^T. \tag{22}$$

Using (22) in (21), we find

$$\int_0^t \Big[\|\nabla u_m(s)\|_{L^2}^2 + \|u_m(s)\|_{L^4}^4\Big]ds \leq C\Big(\|u_0\|_{L^2}^2\Big). \tag{23}$$

Hence, in view of the inequalities (22) and (23), this shows that the apprimate solution u_m is uniformly bounded in the space (10). We are now left to estimate the fact that $\left\|\frac{\partial u_m}{\partial t}\right\|_{H^{-1}}$ is also uniformly bounded in (11). To this end, we show, in view of (11),

$$\int_0^T \left|\left\langle \frac{\partial u_m}{\partial t}, v\right\rangle\right| dx \leq \int_0^T |\nabla u_m|_{L^2}^2, |\nabla v|_{L^2}^2 dx + \int_0^T \left|\left\langle u_m(|u_m|^2 - 1), v\right\rangle\right| dx \tag{24}$$

We proceed with (28) to bound the first and second terms of the right-hand side of the inequality, to produce

$$\begin{aligned}\int_0^T \left|\left\langle \frac{\partial u_m}{\partial t}, v\right\rangle\right| dx &\leq \int_0^T |\nabla u_m|_{L^2}^2, |\nabla v|_{L^2}^2 dx + \int_0^T |\langle u_m, v\rangle| dx + \int_0^T |u_m|_{L^4}^3 |v|_{L^2} dx \\ &\leq \int_0^T |\nabla u_m|_{L^2}^2, |\nabla v|_{L^2}^2 dx + \int_0^T |u_m|_{L^4} |v|_{L^2} dx + \int_0^T |u_m|_{L^4}^3 |v|_{L^2} dx \end{aligned} \tag{25}$$

Using the inequalities (22) and (23), the Sobolev embedding Theorem $H^1 \subset L^2$, the supremum over the time interval t and the Gagliardo Nirenberg inequality, the first, second and third terms on the right-hand side of (25) are bounded as follows:

$$\begin{aligned}\int_0^T \left|\left\langle \frac{\partial u_m}{\partial t}, v\right\rangle\right| dx &\leq C_1 + C_2 \sup_{0\leq t\leq T} \|u\|_{L^2}^{1/2} \int_0^T \|\nabla u_m\|_{L^2}^{1/2} \\ &+ C_3 \sup_{0\leq t\leq T} \|u_m\|_{L^2}^{3/2} \int_0^T \|\nabla u_m\|_{L^2}^{3/2} \\ &\leq C \end{aligned} \tag{26}$$

after using the fact that $\|w\|_{H^{-1}} = \sup_{v\in H_0^1} | < w, v > |$ and $\|v\|_{H^1} \leq 1$, and hence we conclude from above that

$$\int_0^T \|\frac{\partial u_m(s)}{\partial t}\|_{H^{-1}} ds \leq C. \tag{27}$$

All the analysis resulting in (22), (23) and (27), above, concludes that the sequence of solutions $\{u_m\}$, $m \in \mathbb{N}$ is uniformly bounded in the following space (10).

3.2. Boundedness and Passage to the Limit of Approximate Solution of the Equation

In view of the analysis of the uniform boundedness of the approximate solution in Section 3.1, we proceed to show that the sequences of solution $\{u_m\}$ will converge strongly to the solution $u(t)$. To this end, we proceed by recalling the fact that we have obtained the following approximate solution $\{u_m\}$ defined on the $[0, T]$:

$$u_m \text{ is uniformly bounded in } L^{\infty}\Big[(0,T);L^2(\Omega)\Big]$$
$$u_m \text{ is uniformly bounded in } L^{2}\Big[(0,T);H_0^1(\Omega)\Big]$$
$$u_m \text{ is uniformly bounded in } L^{4}\Big[(0,T);L^4(\Omega)\Big]$$
$$\frac{\partial u_m}{\partial t} \text{ is uniformly bounded in } L^{2}\Big[(0,T);H^{-1}.(\Omega)\Big]$$

In view of the embedding of

$$H_0^1(\Omega) \hookrightarrow L^2(\Omega) \hookrightarrow H^{-1}(\Omega)$$

by Banach–Alaoglu's Theorem found in [36], there exists a subsequence of u_m still denoted by u_m, such that

$$u_m \longrightarrow u \text{ weakly star in } L^{\infty}\Big[(0,T);L^2(\Omega)\Big]$$
$$u_m \longrightarrow u \text{ weakly in } L^{2}\Big[(0,T);H_0^1(\Omega)\Big]$$
$$u_m \longrightarrow u \text{ weakly in } L^{4}\Big[(0,T);\ L^4(\Omega)\Big]$$
$$\frac{\partial u_m}{\partial t} \longrightarrow \frac{\partial u}{\partial t} \text{ weakly in } L^{2}\Big[(0,T);H^{-1}.(\Omega)\Big]$$

and in view of the following Theorem 2 found in [36], $u_m \longrightarrow u$ strongly in $L^2\big[(0,T);L^2(\Omega)\big]$.

Theorem 2. *Suppose that $X \hookrightarrow Y \hookrightarrow Z$ are Banach spaces in which X, Z are reflexive and X is compactly embedded in Y. Let $1 < p < \infty$. If the functions $w_N : (0,T) \longrightarrow X$ are such that $\{w_N\}$ is uniformly bounded in $L^2[(0,T);X]$ and $\left\{\frac{\partial u}{\partial t}\right\}$ is uniformly bounded in $L^p[(0,T);Z]$, then there is a subsequence that converges strongly in $L^2[(0,T);Y]$.*

With the strong convergence of the approximate solution u_m in $L^2\big[(0,T);L^2(\Omega)\big]$, what remains to be shown now is that the solution satisfies Equation (12). To achieve this, we introduce another test function $\psi(t)$ with values $\psi(0) = 1$ and $\psi(T) = 0$ and also continuously differentiable on the interval $[0,T]$. With this in place, we proceed in view of Equation (19) and the function $\psi(t)$:

$$\left\langle \frac{\partial u_m}{\partial t}, v \right\rangle \psi(t) + \langle \nabla u_m, \nabla v \rangle \psi(t) + \Big\langle u_m(|u_m|^2 - 1), v \Big\rangle \psi(t) = 0. \tag{28}$$

If, in Equation (28), integration by parts with respect to t over the interval $[0,T]$ is applied, then we obtain

$$\begin{aligned} -\int_0^T \Big\langle \frac{u_m}{\partial t}, \psi(t) \Big\rangle v dt + \int_0^T \langle \nabla u_m, \nabla v \psi(t) \rangle dt \quad &+ \quad \int_0^T \Big\langle u_m(|u_m|^2 - 1), v\psi(t) \Big\rangle dt \\ &= \quad \langle u(0), v \rangle \psi(t). \end{aligned} \tag{29}$$

Using Theorem 2, the approximate solution u_m is uniformly bounded. Then, passing to the limit, we have a yield in view of (29) as follows:

$$\begin{aligned} -\int_0^T \Big\langle \frac{u}{\partial t}, \psi(t) \Big\rangle v dt + \int_0^T \langle \nabla u, \nabla v \psi(t) \rangle dt \quad &+ \quad \int_0^T \Big\langle u(|u|^2 - 1), v\psi(t) \Big\rangle dt \\ &= \quad \langle u(0), v \rangle \psi(t). \end{aligned} \tag{30}$$

which holds in particular for $\psi(t) \in \mathcal{D}(0,T)$. This therefore means that the solution u in Equation (30) is satisfield in the distributional sense. Therefore, in view of Equations (28) and (30), this yields

$$\langle u(0) - u_0, v\rangle = 0 \ \ \forall v \in H_0^1(\Omega)$$

and Equation (12) is obtained as required.

3.3. Uniqueness of the Solution of the Equation

We devote this subsection to the uniqueness of the solution of the semi-linear reaction–diffusion Equations (1)–(3). We address this by letting u_1 and u_2 be two solutions of the equations, such that $u := u_1 - u_2$ and $u|_{\partial\Omega} = 0$. Since u satisfies Equations (1) and (2), then $u(0) = u_1(0) - u_2(0) = 0$. In view of this, we proceed, using Equation (1), to obtain

$$\frac{\partial u}{\partial t} - \Delta u + u_1|u_1|^2 - u_1 - (u_2|u_2|^2 - u_2) = 0 \tag{31}$$

from which, after factorizing $|u_1|^2 - |u_2|^2 = (|u_1| + |u_2|)(|u_1| - |u_2|)$ and multiplying throughout by u, we obtain

$$\frac{1}{2}\|u\|_{L^2}^2 + \|\nabla u\|_{L^2}^2 \leq \int_\Omega u||_{L^4}^2\Big(|u_1|^2 + 1\Big)dx + \int_\Omega |u|_{L^4}^2|u_2||u_1|dx + \int_\Omega |u|_{L^4}^2|u_2|^2dx \tag{32}$$

after using Hölder's inequality. Estimating the right hand side of Inequality (32) thanks to the Gagliardo–Nirenberg inequality, we obtain

$$\int_\Omega |u|_{L^4}^2\Big(|u_1|^2 + |u_1||u_2| + |u_2|^2 + 1\Big)dx \leq \frac{1}{2}\|\nabla u\|_{L^2}^2 + \|u\|_{L^2}^2\Big(|u|^2 + |u_1||u_2| + |u_2|^2 + 1\Big)^2 \tag{33}$$

after using the Young inequality. Introducing (33) back into (32) yields

$$\frac{1}{2}\|u\|_{L^2}^2 + \frac{1}{2}\|\nabla u\|_{L^2}^2 \leq C\|u\|_{L^2}^2\mathcal{Y} \tag{34}$$

where $\mathcal{Y} = |u|^2 + |u_1||u_2| + |u_2|^2 + 1$. Integrating the inequality (34) with respect to t over the interval $(0,T)$ and keeping only the term $\|u\|_{L^2}^2$ on the left-hand side yields

$$\|u(t)\|_{L^2}^2 \leq C\|u(0)\|_{L^2}^2 e^{\int_0^T \mathcal{Y}^2 dt} = 0, \ \ \forall t \geq 0$$

after applying the Gronwall inequality. Hence, this proves the uniqueness of the solution of the problem.

4. The Design of the Coupled NSFD-GM Numerical Scheme

Instead of the theoretical analysis of the two-dimensional semi-linear reaction–diffusion equation in Section 3, we apply the a priori estimates obtained from the above section to analyze this section. In view of the complexity that comes from the analysis of the two-dimensional situation of semi-linear equations such as ours, we proceed to use the one-dimensional case in [20] as a reference model to analyze the stability and the convergence results from the designed NSFD-GM numerical scheme. In view of this, we have set aside this section to design and analyze the NSFD-GM numerical scheme mentioned in Section 1. This analysis will be achieved in two subsections, which are Section 4.1, where we will address the stability of the scheme and the optimal convergence of the scheme in both the L^2- as well as the H^1-norms, and Section 4.2, which will show that the scheme preserves the decaying properties of the exact solution. In view of the above three objectives, we start

by stating the discrete version of the variational or weak forms (11) and (12), as follows: find $v_h : [0,T] \longrightarrow \mathcal{V}_h$, and the discrete solution such that

$$\left\langle \frac{\partial u_h}{\partial t}, v_h \right\rangle + \langle \nabla u_h, \nabla v_h \rangle + \left\langle \Big(|u_h|^2 - 1 \Big) u_h, v_h \right\rangle = 0 \tag{35}$$

$$\langle u_h(x,0), v_h \rangle = \langle P_h \rangle, \ \ \forall v_h \in \mathcal{V}_h \tag{36}$$

where P_h is the orthogonal projection onto $\mathcal{V}_h$.

The above discrete form connects us from the continuous to the discrete framework, which is geared toward the analysis of the numerical solution of (35) and (36). The above framework can proceed by assuming the regularity of the solution u of (11) and (12) and the subspace $\mathcal{V}_h \subset H_0^1(\Omega)$, as seen in [34]. Other useful inequalities to be used in this analysis will be

$$\|P_h v - v\| \leq Ch^2 \|v\|_{H^2}, \ \ \text{for} \ \ v \in H_0^1 \cap H^2 \tag{37}$$

where $\|\cdot\|$ is the usual norm in L^2 and H^1 is a standard Sobolev space with some constant C. Also, if u is sufficiently smooth for a closed time interval $[0,T]$, then it is well-known in view of [37] that

$$|u(t) - u_h(t)| \leq C_1(u, C_2, C_3)h^2, \quad \forall t \in [0,T] \tag{38}$$

where C_2 is the bound on U and ∇u with C_3 as the constant in (38).

Setting in place the above desired framework, we continue and let the time step size $t_n = n\Delta t$ for $n = 0, 1, 2, \cdots, \mathbb{N}$ over the time interval $[0,T]$. This then led us to find the NSFD-GM-approximate solution $\left\{U_h^n\right\}$ such that $U_h^n \approx u_h^n$ at each discrete time t_n in the space $\mathcal{V}_h$ for sufficiently smooth functions. The stated approximation permits us to define the NSFD-GM scheme of the semi-linear reaction–diffusion equation as one which consists of a fully discrete solution $U_h^n \in \mathcal{V}_h$ such that for $v_h \in \mathcal{V}_h \subset H_0^1(\Omega)$,

$$\langle \delta_n U_h^n(t), v_h \rangle + \langle \nabla U_h^n, \nabla v_h \rangle + \left\langle U_h^n \Big(|U_h^n|^2 - 1 \Big), v_h \right\rangle \ \ = \ \ 0, \tag{39}$$

$$\langle U_h^n, v_h \rangle = \langle P_h u_0, v_h \rangle, \tag{40}$$

are satisfied, where

$$\delta_n U_h^n = \frac{U_h^n - U_h^{n-1}}{\phi(\Delta t)} \ \ \text{and} \ \ \phi(\Delta t) = \frac{e^{\lambda \Delta t} - 1}{\lambda}. \tag{41}$$

The above new framework needs the following components:

(a) The special and complicated function $\phi(\Delta t)$ where $\lambda > 0$ is in such a way that

$$0 < \phi(\Delta t) < 1 \ \ \text{for} \ \ n = 1, 2, 3, \cdots, N \tag{42}$$

(b) If the nonlinear function $\left(|U_h^n|^2 - 1\right) U_h^n$ is made in such a way that its effect is negligible or even zero, then the scheme (39) will coincide with the exact scheme

$$\left\langle \frac{U_h^{n+1} - U_h^n}{\phi(\Delta t)} \right\rangle + \langle \nabla U_h^n, \nabla v_h \rangle = 0 \tag{43}$$

which, in view of Michens [22], replicates or preserves the decaying-to-zero property of the scheme under investigation; this is actually the main point of the novelty of the method.

4.1. The Stability of the Coupled NSFD-GM Numerical Scheme

In this subsection, we show that the NSFD-GM scheme of (39) and (40) is stable. That is, we show that the numerical solution of the above scheme is uniformly bounded as the following Theorem 3:

Theorem 3. *If we assume that the semi-linear reaction–diffusion equation u in Equations (11) and (12) is regular, then for a given initial solution $U_h^0 \in \mathcal{V}_h$, the numerical solution $U_h^n(t)$ of the scheme (39) and (40) will remain bounded and satisfy the following estimates:*

$$|U_h^0|^2 \quad \leq \quad |U_h^0|^2 + 2\phi(\Delta t)C(\Omega), \tag{44}$$

$$\sum_{n=1}^{N} |U^n - U_h^{n-1}|^2 \quad \leq \quad |U_h^0|^2 + 2\phi(\Delta t)C(\Omega). \tag{45}$$

Proof. We prove the above theorem by first letting $v_h = U_h^n(t)$ in Equation (39) yield

$$\left\langle U_h^n(t) - U_n^{n-1}(t), U_h^n(t) \right\rangle + \phi(\Delta t)\|\nabla U_h^n(t)\|_{L^2}^2 + \phi(\Delta t)\|U_h^n(t)\|_{L^4}^4 - \phi(\Delta t)|U_h^n(t)|_{L^2}^2 = 0$$

from where we have, in view of (20),

$$\left\langle U_h^n(t) - U_n^{n-1}(t), U_h^n(t) \right\rangle + \phi(\Delta t)\|\nabla U_h^n(t)\|_{L^2}^2 + \phi(\Delta t)\|U_h^n(t)\|_{L^4}^4 \leq \phi(\Delta t)\|U_0^1(t)\|_{L^2}^2 \tag{46}$$

It is well-known, in view of the first term of the left-hand side of the inequality (58), that

$$\left\langle U_h^n(t) - U_h^{n-1}(t), U_h^n(t) \right\rangle = \frac{1}{2}|U_h^n|^2 - \frac{1}{2}|U_h^{n-1}|^2 + \frac{1}{2}|U_h^n - U_h^{n-1}|^2.$$

and re-introducing this equality back into (58) yields

$$\begin{aligned} |U_h^n|^2 - |U_h^{n-1}|^2 + |U_h^n - U_h^{n-1}|^2 \quad &+ \quad 2\phi(\Delta t)\|\nabla U_h^n\|_{L^2}^2 + 2\phi(\Delta t)\|U_h^n\|_{L^4}^4 \\ &\leq \quad 2\phi(\Delta t)\|U_h^n\|_{L^2}^2. \end{aligned} \tag{47}$$

Taking the sum to $\mathbb{N}$ of the above inequality (47), we obtain

$$\begin{aligned} |U_h^n|^2 + \sum_{n=1}^{\mathbb{N}} |U_h^n - U_h^{n-1}|^2 \quad &+ \quad 2\phi(\Delta t)\sum_{n=1}^{\mathbb{N}}\|\nabla U_h^n\|_{L^2}^2 + 2\phi(\Delta t)\sum_{n=1}^{\mathbb{N}}\|U_h^n\|_{L^4}^4 \\ &\leq \quad 2\phi(\Delta t)\sum_{n=1}^{\mathbb{N}}\|U_h^n\|_{L^2}^2 + |U_h^0|^2. \end{aligned} \tag{48}$$

In view of (22) and (23), we can immediately read the results (44) and (45) from (48) as required. □

4.2. Optimal Convergence of the Coupled NSFD-GM Numerical Scheme

We devote this subsection to showing that the numerical solution obtained from the NSFD-GM scheme converges optimally in both L^2- and H^1-norms, and also that these solutions replicate or preserve the decay-to-zero properties of the exact solution. To achieve these two objectives, we first state without proof the following results from Shen [38].

Lemma 1. *Let Δt, γ and a_k, b_k, d_k, γ_k for the integer $k \geq 0$ be non-negative numbers such that*

$$a_J + \sum_{k=0}^{J} b_k \Delta t \leq \sum_{k=0}^{J} d_k a_J \Delta t + \sum_{k=0}^{J} \gamma_k \Delta t + \gamma, \quad \forall\, J \geq 0. \tag{49}$$

Suppose that

$$d_k\Delta t < 1 \ \textit{and set} \ \ \sigma_k = (1 - d_k\Delta t)^{-1}, \ \forall \ k \geq 0. \tag{50}$$

Then, we have

$$a_J + \sum_{k=0}^{J} b_k\Delta t \leq \exp\left(\sum_{k=0}^{J} d_k\Delta t\right)\left(\sum_{k=0}^{J} \gamma_k\Delta t + \gamma\right) \ \forall \ J \geq 0. \tag{51}$$

With the above Lemma 1 and NSFD-GM framework in mind, we can then state and prove the error estimate in Theorem 4, next.

Theorem 4. *We assume that Φ_k is a non-negative number and that the continuous and discrete solutions of the semi-linear reaction–diffusion Equations (39) and (40), respectively, exist uniquely and satisfy*

$$\Phi_k\phi(\Delta t) < 1 \ \textit{and} \ \ \sigma_k = (1 - \Phi_k\phi(\Delta t))^{-1}, \ \forall \ k \geq 0.$$

Then, the following error estimate

$$\|u(t_J) - U_h(t_J)\| + \phi(\Delta t)\sum_{k=0}^{J}\left|\nabla(u(t_J) - U_h(t_J))\right|^2 \leq C(t_J)(\phi(\Delta t))^2, \ \ \forall J \geq 0. \tag{52}$$

is satisfied.

Proof. The above Theorem is proved by using the implicit non-standard finite difference method in the time as follows:

$$\frac{U_{n+1} - U_n}{\phi(\Delta t)} = \Delta U_{n+1} + U_{n+1}\Big(1 - |U_{n+1}|^2\Big). \tag{53}$$

In view of the non-standard Taylor's integral Theorem, we find

$$\begin{aligned}\frac{u(t_{n+1} - u(t_n))}{\phi(\Delta t)} &= \frac{\partial u(t_{n+1})}{\partial t} - \frac{1}{2}\int_{t_n}^{t_{n+1}}\frac{\partial^2 u(t)}{\partial t^2}(t_{n+1} - t)dt \\ &= \Delta u(t_{n+1}) + u(t_{n+1})\Big(1 - |u(t_{n+1})|^2\Big) \\ &- \frac{1}{2}\int_{t_n}^{t_{n+1}}\frac{\partial^2 u(t)}{\partial t^2}(t_{n+1} - t)dt. \end{aligned}\tag{54}$$

Subtracting Equation (54) from (53) and noting that $\Theta_n = u(t_n) - U_n$ yields

$$\begin{aligned}\frac{1}{\phi(\Delta t)}[\Theta_{n+1} - \Theta_n, \Theta_{n+1}] &= \Big\langle u^{n+1}\Big(1 - |u^{n+1}|^2\Big) - U_{n+1}\Big(1 - |U_{n+1}|^2\Big), \Theta_{n+1}\Big\rangle \\ &- \|\nabla\Theta_{n+1}\|_{L^2}^2 + \frac{1}{2}\int_{t_n}^{t_{n+1}}\left\langle\frac{\partial^2 u(t)}{\partial t^2}, \Theta_{n+1}\right\rangle(t - t_{n+1})dt \end{aligned}\tag{55}$$

after setting $u^{n+1} = u(t_{n+1})$ and multiplying Equation (53) by Θ_{n+1}. Estimating the first term of the right-hand side of Equation (55), we find

$$\begin{aligned}\int_\Omega\left|\left\langle\Big(u^{n+1}\Big(1 - |u^{n+1}|^2\Big) - U_{n+1}\Big(1 - |U_{n+1}|^2\Big)\Big), \Theta_{n+1}\right\rangle\right|dx &\leq \int_\Omega|\Theta_{n+1}|_{L^4}^2\left|\Big(1 - |u^{n+1}|^2\Big)\right|^2 dx \\ &+ \int_\Omega|\Theta_{n+1}|_{L^4}^2|U_{n+1}|_{H^1}^2 dx \\ &+ \int_\Omega|\Theta_{n+1}|_{L^4}^2|U_{n+2}|_{H^1}|u^{n+1}|dx \end{aligned}\tag{56}$$

after using the fact that $|U_{n+1}|^2 - |u^{n+1}|^2 = (|U_{n+1}| - |u^{n+1}|)(|U_{n+1}| + |u^{n+1}|)$. Estimating each term on the right-hand side of the inequality (56) using Gagliardo–Nirenberg and Young's inequality with the fact that $H^1 \subset L^\infty$ yields the following inequality, beginning with the third term:

$$\int_\Omega |\Theta_{n+1}|_{L^4}^2 |U_{n+1}||u^{n+1}|dx \leq \frac{\epsilon}{2}\|\nabla\Theta_{n+1}\|^2 + \frac{1}{2\epsilon}\|\Theta_{n+1}\|_{L^2}^2\|U_{n+1}\|_{L^\infty}^2\|u^{n+1}\|_{L^2}^2. \tag{57}$$

This is followed by the second term, as follows,

$$\int_\Omega |\Theta_{n+1}|_{L^4}^2 |U_{n+1}|^2 dx \leq \frac{\epsilon}{2}\|\nabla\Theta_{n+1}\|_{L^2}^2 + \frac{1}{2\epsilon}\|\Theta_{n+1}\|_{L^2}^2\|U_{n+1}\|_{L^\infty}^2 \tag{58}$$

and lastly by the first term:

$$\int_\Omega |\Theta_{n+1}|_{L^4}^2 \left|\left(1 - |u^{n+1}|^2\right)\right|^2 dx \leq \frac{\epsilon}{2}\|\nabla\Theta_{n+1}\|_{L^2}^2 + \frac{1}{2\epsilon}\|\Theta_{n+1}\|_{L^2}^2 \left|\left(1 - |u^{n+1}|^2\right)\right|^2 \tag{59}$$

Re-introducing (57)–(59) into inequality (56) yields

$$\begin{aligned} &\int_\Omega \left|\left\langle \left(u^{n+1}\left(1 - |u^{n+1}|^2\right) - U_{n+1}\left(1 - |U_{n+1}|^2\right)\right), \Theta_{n+1}\right\rangle\right| dx \\ \leq\ & \frac{3\epsilon}{2}\|\nabla\Theta_{n+1}\|_{L^2}^2 + \frac{3}{2\epsilon}\|\Theta_{n+1}\|_{L^2}^2\left[|u^{n+1}|_{H^1}^2 + |U_{n+1}|_{H^1}^2 + |U_{n+1}|_{H^1}^2|u^{n+1}|_{H^1}^2 + 1\right] \end{aligned} \tag{60}$$

By estimating the third term of the right-hand side of the inequality (55), we find

$$\left|\frac{1}{2\phi(\Delta t)}\int_{t_n}^{t_{n+1}}\left\langle\frac{\partial^2 u(t)}{\partial t^2}, \Theta_{n+1}\right\rangle(t - t_{n+1})dt\right| \leq \frac{C}{2\phi(\Delta t)}|\nabla\Theta_{n+1}|\int_{t_n}^{t_{n+1}}\left|\frac{\partial^2 u}{\partial t^2}\right||t - t_{n+1}|dt. \tag{61}$$

because according to Poincare inequality, $|\Theta_{n+1}|_{H_0^1} \leq C|\nabla\Theta_{n+1}|_{L^2}$. Using the fact that there exists a function

$$\phi(\Delta t_n) < \phi(\Delta t) < \phi(\Delta t_{n+1}) \ \text{ for } \ t_n < t < t_{n+1}$$

yields

$$\left(\int_{t_n}^{t_{n+1}} |t - t_{n+1}|\right)^{1/2} \leq \phi(\Delta t)(t - t_{n+1})^{1/2} \leq (\phi(\Delta t))^{1/2}.$$

Introducing this and Hölder's inequality in (61), we obtain

$$\left|\frac{1}{2\phi(\Delta t)}\left\langle\frac{\partial^2 u}{\partial t^2}, \Theta_{n+1}\right\rangle(t - t_{n+1})dt\right| \leq \frac{\epsilon}{2}\nabla\Theta_{n+1}|\|_{L^2}^2 + \frac{C}{2\epsilon}\phi(\Delta t)\int_{t_n}^{t_{n+1}}\left|\frac{\partial^2}{\partial t^2}\right|_{H^{-1}}^2 dt, \tag{62}$$

after using Young's inequality for arbitrary $\epsilon > 0$. Re-introducing the inequalities (60) and (62) into (55) produces the following for $\epsilon = 1/2$:

$$\frac{1}{\phi(\Delta t)}[\Theta_{n+1} - \Theta_n, \Theta_{n+1}] + \frac{1}{2}\|\nabla\Theta_{n+1}\|_{L^2}^2 \leq C\|\Theta_{n+1}\|_{L^2}^2\Psi_{n+1} + C\Phi_{n+1}\phi(\Delta t) \tag{63}$$

where

$$\Psi_{n+1} = |U_{n+1}|_{H^1}^2 + |U_{n+1}|_{H^1}^2|u^{n+1}|_{H^1}^2 + ||_{HH^1}^2 + 1$$

and

$$\Phi_{n+1} = \int_{t_n}^{t_{n+1}}\left|\frac{\partial^2 u}{\partial t^2}\right|_{H^{-1}}^2 dt.$$

In view of inequality (63), it is well known that the first term of the left-hand side is

$$(\Theta_{n+1} - \Theta_n, \Theta_{n+1}) = \frac{1}{2}\left[|\Theta_{n+1}|_{L^2}^2 - |\Theta_n|_{L^2}^2 + |\Theta_{n+1} + \Theta_n|_{L^2}^2\right]$$

and introducing this back into inequality (63),

$$|\Theta_{n+1}|_{L^2}^2 - |\Theta_n|_{L^2}^2 + |\Theta_{n+1} - \Theta_n|_{L^2}^2 + \phi(\Delta t)\|\nabla\Theta_{n+1}\|_{L^2}^2 \leq C\phi(\Delta t)\|\Theta_{n+1}\|_{L^2}^2\Psi_{n+1} + C\phi(\Delta t)^2\Phi_{n+1}. \tag{64}$$

Arranging the terms in inequality (64) and setting $a_k = \|\Theta_{n+1}\|_{L^2}^2$ and $b_k = \|\nabla\Theta_{n+1}\|_{L^2}^2$ and summing partially for $k = 0, 1, 2, \cdots, n-1$ and also using the fact that $a_0 = \Theta_0 = u_0 - U_0 = 0$, we obtain

$$a_n + \sum_{k=0}^{n} b_k\phi(\Delta t) \leq \sum_{k=0}^{n} a_k\phi(\Delta t)\Psi_{n+1} + \sum_{k=0}^{n} \phi(\Delta t)^2\Phi_{n+1}. \tag{65}$$

Applying Lemma 1 in inequality (65) yields

$$a_n + \sum_{k=0}^{n} b_k\phi(\Delta t) \leq \exp\left(\sum_{k=0}^{n} \sigma_k\phi(\Delta t)\Psi_{n+1}\right)\left(\sum_{k=0}^{n} \Phi_{n+1}(\phi(\Delta t))^2\right) \tag{66}$$

provided that $\Psi_{n+1}\phi(\Delta t) < 1$ and $\sigma_k = (1 - \Psi_{n+1}\phi(\Delta t))^{-1} \ \ \forall k \geq 0$. Since a_n, b_k, Ψ_{n+1} and Φ_{n+1} are all positive series, then in view of Lemma 1,

$$a_n + \sum_{k=0}^{n} b_k\phi(\Delta t) \leq C(\phi(\Delta t))^2 \tag{67}$$

and the proof of the theorem is completed. □

The error estimate shown above leads to the following optimal rate of convergence in both the L^2- and H^1-norms, as follows.

Theorem 5. *Assuming that the above error estimate in Theorem 4 is satisfied, then the numerical solution of the semi-linear reaction–diffusion scheme (39) and (40) has the following optimal rate of convergence:*

$$\|u(t) - U_h(t)\|_{L^2} \leq C(t)\Big(h^2 + \phi(\Delta t)\Big)$$

using the NSFD-GM method, where $C(t)$ depends on t. Furthermore, the discrete solution $U_h(t)$ replicates all the qualitative properties of the exact solution of the equation under investigation.

Proof. We proceed to prove the above theorem by using the following error decomposition equation:

$$\begin{aligned} \|u(t) - U_h(t)\|_{L^2} &= \|u(t) - P_hu(t) + P_hu(t) - U_h(t)\|_{L^2} \\ &\leq \|\xi_n\|_{L^2} + \|\eta_n\|_{L^2} \end{aligned} \tag{68}$$

where $\|\xi_n\|_{L^2} = \|u(t) - P_hu(t)\|_{L^2}$ and $\|\eta_n\|_{L^2} = \|P_hu(t) - U_h(t)\|_{L^2}$. In view of the above inequality (68), the estimate $\|\xi_n\|_{L^2}$ represents the error inherent in the Galerkin approximation of the linearized reaction–diffusion equation, and that of the estimate $\|\eta_n\|_{L^2}$ is the error caused by the nonlinearity in the problem. The above error decomposition in Equation (68) further leads to the following inequality:

$$\|u(t) - U_h(t)\|_{L^2} \leq C(t_n)h^2 + C(t_n)(\phi(\Delta t))^2, \ \ \forall t \in [t_n, t_{n+1}] \tag{69}$$

after using inequalities (38) and (67). With these inequalities in place, we conclude without difficulty that inequality (69) is indeed optimal.

To complete the preserving of the qualitative properties of the exact solution, we proceed to show, in view of the remark from Mickens [22], that the above scheme was designed for

$$\phi(\Delta t) = \frac{e^{\lambda \Delta t} - 1}{\lambda} \approx \Delta t + O((\Delta t)^2). \tag{70}$$

Based on the above approximation (70), we observe that as $\Delta t \longrightarrow 0$, the function $\phi(\Delta t) \approx \Delta t$. In view of this, we deduced that the numerical schemes (39) and (40) converge point-wise in $\mathcal{V}_h \subset H_0^1(\Omega)$ to the solution u as $\Delta t \longrightarrow 0$ according to the compactness Theorem. We justify this as follows: If we choose the source term of our scheme (39) to be $U_h^0 \in H_0^1(\Omega)$ and $\mathbf{F} \in L^2\big[(0,T); H^{-1}(\Omega)\big]$, then we have

$$\langle \delta_n U_h^n(t), v_h \rangle + \langle \nabla U_h^n, \nabla v_h \rangle + \left\langle U_h^n \Big(|U_h^n|^2 - 1 \Big), v_h \right\rangle = \mathbf{F}. \tag{71}$$

If we, in addition, let the support of $\mathbf{F}$ be very small, so much so that the test function $v_h = 1$ far inside the support, say $\Omega_1 \subset \Omega$ and $\mathbf{F}$, is regular, then integrating Equation (71) over Ω will culminate in the fact that the solution over Ω is equivalent to the point-wise convergence of the scheme (71). In view of [31], the assertion that the scheme NSFD-GM replicates the qualitative properties of the exact scheme (43) is achieved. For more on this, see [20,28–30]. This completes the second part of the proof. □

5. Numerical Experiments

Numerical experiments will be performed in this section to compute the numerical solution of the nonlinear reaction–diffusion Equations (1)–(3). These experiments will be computed over a two-dimensional domain $\Omega = [0,1] \times [0,1]$ and the time interval $[0,T]$. The domain Ω will be regularly discretized into uniform triangular meshes denoted by $\mathcal{J}_h$, where h is the mesh size and the basic functions used will be linear Lagrange-type functions. The mesh size will be defined by $h = \frac{1}{M}$, where M is the number of nodes in the triangulations. The time space $[0,T]$ will be discretized with a step size of Δt. The right-hand side of Equations (1)–(3), denoted by $f(x,t)$, will be determined by introducing a carefully chosen example:

$$u(x_1, x_2, t) = (1 + 2t^2)\cos(2\pi x_1^2)\cos(2\pi x_2^2). \tag{72}$$

We will proceed to use $f(x,t)$ in the NSFD-GM scheme of the semi-linear reaction–diffusion Equation (39) to give the following numerical computable scheme:

$$(M + \phi(\Delta t)A) - \phi(\Delta t)M = f(x,t) + (M + \phi(\Delta t)A) + Mu_0 - \phi(\Delta t)F(u) \tag{73}$$

where

(a) M is the mass matrix;
(b) A is the stiffness matrix;
(c) M_F is the mass matrix with respect to the semi-linear function $F(u)$;
(d) $f(x,t)$ is the prescribed right hand side of the Equation (39).

In view of the above scheme (73), $(M + \phi(\Delta t)A) - \phi(\Delta t)M$ is the Jacobian matrix and $(M + \phi(\Delta t)A) + Mu^{n-1} - \phi(\Delta t)F(u)$ is the Residual vector. With the above scheme, we proceed by evaluating the matrices M, A and M_F locally over a reference element and the basic function v_h. Using this, together with Newton's iterative method using the following initial solution (74), the numerical solution from the scheme can be obtained:

$$u_0 = u(x_1, x_2, 0) = \cos(2\pi x_1^2)\cos(2\pi x_2^2). \tag{74}$$

The above experiments were conducted using the software Matblab 7.100(R2014a). The following specifications were used: $\lambda = 4$, denoting the value of the parameter on the complicated denominator function $\phi(\Delta t)$; the final time $T = 1.0$ and $\Delta t = 0.01$; and M ranging from $40, 80, 120, 160, 200$, and 240 to 280. With the above data, the Newton's iterative method will yield the results in Figures 1–3.

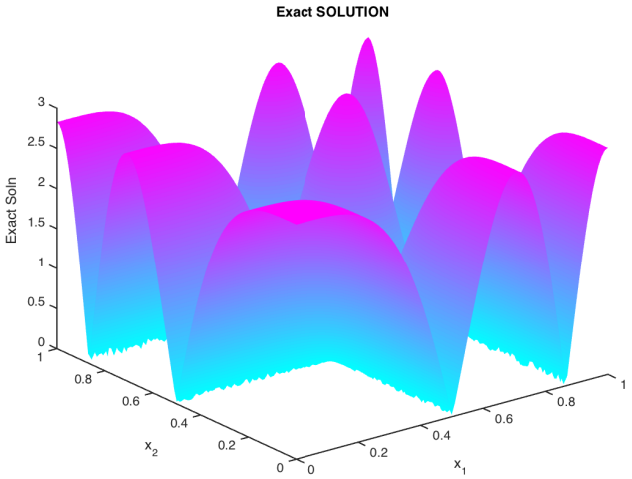

Figure 1. The exact computed solution.

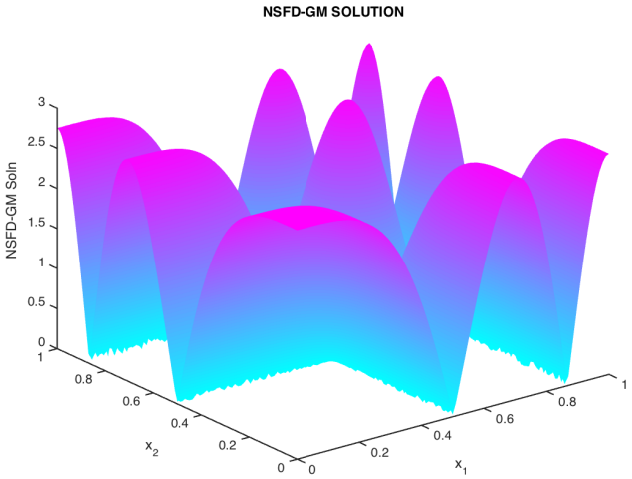

Figure 2. Approximate solution for NSFD-GM scheme.

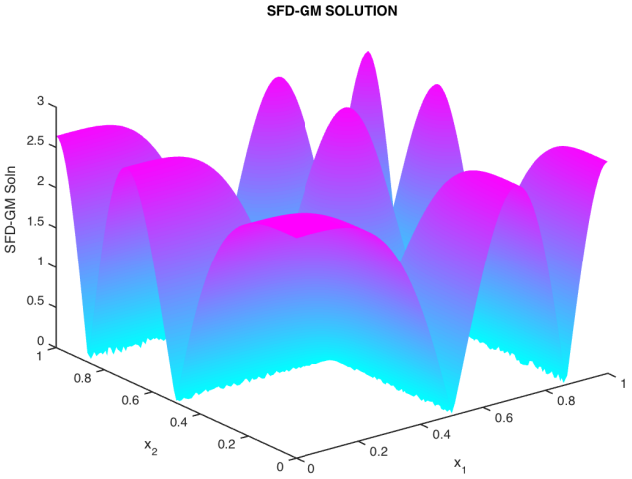

Figure 3. Approximate solution for SFD-GM scheme.

After the figures follow the tabular illustrations of the error and rate of convergence in the solutions, shown in Tables 1 and 2 for a specified value of $T = 1.0$.

Table 1. NSFD-GM error in L^2-norm and error in H^1-norm.

M	Error in L^2-Norm	Rate of L^2	Error in H^1-Norm	Rate of H^1
40	3.0412×10^3		2.1902×10^1	
80	1.2437×10^2	1.29	1.4550×10^1	0.59
120	7.2236×10^3	1.34	1.0955×10^1	0.70
160	4.5851×10^3	1.58	8.6032×10^2	0.84
200	3.1517×10^3	1.68	7.0851×10^2	0.87
240	2.2741×10^3	1.79	6.0239×10^2	0.89
280	1.6993×10^3	1.89	5.2113×10^2	0.94

Table 2. SFD-GM error in L^2-norm and error in H^1-norm.

M	Error in L^2-Norm	Rate of L^2	Error in H^1-Norm	Rate of H^1
40	3.0103×10^2		2.0301×10^1	
80	1.2311×10^2	1.29	1.3209×10^1	0.62
120	7.0352×10^3	1.38	9.6276×10^2	0.78
160	4.4784×10^3	1.57	7.5826×10^2	0.83
200	3.0715×10^3	1.69	6.2586×10^2	0.86
240	2.2203×10^3	1.78	5.3309×10^2	0.88
280	1.6643×10^3	1.89	4.6331×10^2	0.91

Observations 1. *Our expectations were that the rate of convergence in the L^2-norm would be 2 and that in the H^1-norm it would be 1, using both the NSFD-GM and SFD-GM schemes. To our great surprise, the results tended to be approximately 2 and 1 for both the L^2- and H^1-norms, respectively. Even though these values were not far from their expected values, the values of the NSFD-GM scheme in both norms were larger than those from their given counterpart SFD-GM scheme. This advantage of the NSFD-GM scheme over the SFD-GM scheme might be because of the principle of its design, keeping aside its effectiveness, accuracy and viability. It is also well-known and shown in the proof of Theorem 5, above, that the numerical solution from the NSFD-GM scheme exhibits the preservation or replication of the qualitative properties of the exact solution of the problem under investigation. These two reasons are what make the study very interesting, and the properties convince one to consider the NSFD-GM scheme to be a favorite in terms of a fair alternative over a more traditional SFD-GM scheme. The major advantage of the NSFD-GM over the more traditional SFD-GM scheme could be drawn from their rates of convergence, found in the two tables above. These rates of convergence values or results are clear and speak for themselves.*

6. Conclusions and Future Remarks

The design of a reliable scheme consisting of the nonstandard finite difference method in time and the Galerkin combined with the compactness method in the space variables to analyze the semi-linear reaction–diffusion equation is presented in this paper. The analysis of the scheme began with the use of the Galerkin in combination with the compactness method to show that the weak solution of the problem existed uniquely in the space (10). We proceeded using a priori estimates from the existence of the solution process to show that the numerical scheme was stable and converged optimally in the L^2- and H^1-norms. Additionally, it was also shown that the numerical scheme preserves the decaying properties of the exact solution. Finally, with a prescribed example, numerical

experiments were presented to validate the proposed theory. The results obtained from the study speak for themselves, for they were accurate and viable, as expected. In view of the results, the designed scheme could be seen as a fair and a justified alternative to some of the traditional coupling schemes, consisting of the finite difference method in the time, in combination with either the Galerkin or the finite element or even another finite difference method in the space variable itself.

In future, we intend to extend the technique to systems of semi- or quasi-linear parabolic problems such as the ones in [39,40] that have meaning in real life; in addition to this, we would also like to carry out some comparison studies with some similar schemes. We can also try out the technique with hyperbolic problems, as well. Another form of interesting study we would like to conduct is a study of some semi- or quasi-linear problems over non-smooth geometry using weighted Sobolev spaces.

Funding: This research received no external funding.

Data Availability Statement: Data available on request from the authors.

Acknowledgments: The research contained in this article has been supported by Sefako Makgatho Health Sciences University, Medunsa 0204, Ga-rankuwa, Pretoria, South Africa.

Conflicts of Interest: The author declares that they have no known conflicts of interest or personal relationships that could have appeared to influence the work reported in this article.

References

1. Kolmogorov, A.; Petrovski, I.; Piskanov, N. Study of a diffusion equation, that is related to the growth of a quality of matter and its application to a biological problem. *Mosc. Univ. Math. Bull.* **1937**, *1*, 1–26.
2. Newell Alan, C.; Whitehead, J.A. Finite bandwidth, finite amplitude convection. *J. Fluid Mech.* **1969**, *38*, 279–303. [CrossRef]
3. Allen, S.; Cahn, J. Ground state structures in ordered binary alloys with second neighbor interactions. *Acta Metall.* **1972**, *20*, 423–433. [CrossRef]
4. Allen, S.M.; Cahn, J.W. A correction to the ground state of FCC binary ordered alloys with first and second neighbor pairwise interactions. *Scr. Metall.* **1973**, *7*, 1261–1264. [CrossRef]
5. Allen, S.M.; Cahm, J.W. A microscopic theory for antiphase boundary motion and its application to antiphase domain coarsening. *Acta Metall.* **1979**, *27*, 1085–1095. [CrossRef]
6. Chen, X. Generation, propagation and annihilation of metastable patterns. *J. Differ. Equ.* **2004**, *206*, 399–437. [CrossRef]
7. Smoller, J. *Schock Wave and Reaction-Diffusion Equations*; Springer: New York, NY, USA, 1983.
8. Hundsdorfer, W.; Verwer, J. *Numerical Solution of Time-Dependent Advection-Diffusion-Reaction Equations*; Springer Series in Computational Mathematics; Springer: Berlin/Heidelberg, Germany, 2003; Volume 33.
9. Pao, C.V. *Nonlinear Parabolic and Elliptic Eequations*; Plenum Press: New York, NY, USA, 1992.
10. Shen, J.; Yang, X. Numerical approximations of Allen-Cahn and Cahn-Hilliard. *Discrete Contin. Dyn. Syst.* **2010**, *28*, 1669–1691. [CrossRef]
11. Temam, R. *Infinite Dimensional Dynamical System in Mechanics and Physics*; Springer: New York, NY, USA, 1997.
12. Yang, X. Error analysis of stabilized semi-implicit method of Allen-Cahn equation. *Discrete Contin. Dyn. Syst. Ser. B.* **2009**, *11*, 1057–1070. [CrossRef]
13. Macias-Diaz, J.F. On the numerical and structural properties of a logarithmic scheme for diffusion-reaction equations. *Appl. Numer. Math.* **2019**, *140*, 104–114. [CrossRef]
14. Bueno-Orovio, A.; Perez-Garcia, V.M.; Fenton, F.H. Spectral methods for partial differential equations in irregular domains: The spectral smoothed boundary method. *SIAM J. Sci. Comput.* **2006**, *28*, 886–900. [CrossRef]
15. Reitz, R.D. A study of numerical methods for reaction-diffusion equations. *SIAM J. Sci. Stat. Comput.* **1981**, *2*, 95–106. [CrossRef]
16. Sharifi, S.; Rashidinian, T. Collocationme method for convection-reaction-diffusion equation. *J. King Saud Univ.-Sci.* **2019**, *31*, 1115–1121. [CrossRef]
17. Wang, H.; Zhang, C.; Zhou, Y. A class of compact boundary value methods applied to semi-linear reaction-diffusion equations. *Appl. Math. Comput.* **2018**, *325*, 69–81. [CrossRef]
18. Wu, G.; Lee, E.W.M.; Li, G. Numerical solutions of the reaction-diffusion equation. *Int. J. Numer. Methods Heat Fluid Flow* **2015**, *25*, 265–271. [CrossRef]
19. Biazar, J.; Mehrlatifan, M.B. A compact finite difference scheme for reaction-convection-diffusion equation. *Chiang Mac. J. Sci.* **2018**, *45*, 1559–1568.
20. Chin, P.W.M. The analysis of the solution of the Burgers-Huxley equation using the Galerkin method. *Numer. Methods Partial Differ. Equ.* **2023**, *39*, 2787–2807. [CrossRef]

21. Chin, P.W.M.; Djoko, J.K.; Lubuma, J.M.-S. Reliable numerical schemes for a linear diffusion equation on a nonsmooth domain. *Appl. Math. Lett.* **2010**, *23*, 544–548. [CrossRef]
22. Mickens, R.E. *Nonstandard Finite Difference Models of Differential Equations*; World Scientific Publishing: River Edge, NJ, USA, 1994.
23. Anguelov, R.; Lubuma, J.M.-S. Contributions to the mathematics of the nonstandard finite difference method and applications. *Numer. Methods Partial Differ. Equ.* **2001**, *17*, 518–543. [CrossRef]
24. Anguelov, R.; Lubuma, J.M.-S. Nonstandard finite difference method by nonlocal approximation. *Math. Comput. Simul.* **2003**, *61*, 465–475. [CrossRef]
25. Lubuma, J.M.-S.; Mureithi, E.; Terefe, Y.A. Analysis and dynamically consistent numerical scheme for the SIS model and related reaction diffusion equation. *AIP Conf. Proc.* **2011**, *168*, 1404.
26. Lubuma, J.M.-S.; Mureithi, E.W.; Terefe, Y.A. Nonstandard discretization of the SIS Epidemiological model with and without diffusion. *Contemp. Math.* **2014**, *618*, 113.
27. Partidar, K.C. On the use of nonstandard finite difference methods. *J. Differ. Equ. Appl.* **2005**, *11*, 735–758. [CrossRef]
28. Chin, P.W.M. The Galerkin reliable scheme for the numerical analysis of the Burgers'-Fisher equation. *Prog. Comput. Fluid Dyn.* **2021**, *21*, 234–247. [CrossRef]
29. Chin, P.W.M. The analysis of an efficient numerical scheme for the Allen-Cahn equations using the Galerkin method. *Commun. Nonlinear Sci. Numer. Simul.* **2022**, *105*, 106061. [CrossRef]
30. Chin, P.W.M.; Moutsinga, C.R.B.; Adem, K.R. An analysis of the nonstandard finite difference and Galerkin methods as applied to the Huxley equation. *Mathematics* **2024**, *12*, 867. [CrossRef]
31. Adams, A.R. *Sobolev Space*; Academic Press: New York, NY, USA, 1975.
32. Evans, L.C. *Partial Differential Equations. Graduate, Studies in Mathematics*; American Mathematical Society: Providence, RI, USA, 1998; Volume 19.
33. Louis, J.-L.; Magenes, E.; Kenneth, P. *Non-Homogeneous Boundary Value Problems and Applications*; Springer: Berlin/Heidelberg, Germany, 1972; Volume 1.
34. Ciarlet, P.G. *The Finite Element Method for Elliptic Problems*; Elsevier: Amsterdam, The Netherlands, 1978.
35. Temam, R. *Navier-Stokes Equations: Theory and Numerical Analysis*; AMS Chelsea Publishing: Amsterdam, The Netherlands, 1984.
36. Rudin, W. *Functional Analysis*; McGraw-Hill: New York, NY, USA, 1991.
37. Wheeler, M.F. A priori L^2 error estimates for Galerkin approximations to parabolic partial differential equations. *SIAM J. Numer. Anal.* **1973**, *10*, 723–759. [CrossRef]
38. Shen, J. Long time stability and convergence for the fully discrete nonlinear Galerkin methods. *Appl. Anal.* **1990**, *38*, 201–229. [CrossRef]
39. Bondarenko, V.; Markevych, I. Composition method for semi-linear parabolic systems. *Int. J. Appl. Math.* **2024**, *10*, 58. [CrossRef]
40. Sun, T.; Sun, H.-W. A stiff-cut splitting technique for stiff semi-linear systems of differential equations. *Numer. Algorithms* **2024**, *95*, 1387–1412. [CrossRef]

computation

MDPI

Article

Modeling of Heat Flux in a Heating Furnace

Augustín Varga [1], Ján Kizek [2,*], Miroslav Rimár [2], Marcel Fedák [2], Ivan Čorný [2] and Ladislav Lukáč [1]

[1] Department of Thermal Technology and Gas Industry, Institute of Metallurgy, Faculty of Materials, Metallurgy and Recycling, Technical University of Kosice, Letná 9, 042 00 Kosice, Slovakia; augustin.varga@tuke.sk (A.V.); ladislav.lukac@tuke.sk (L.L.)

[2] Department of Process Technique, Faculty of Manufacturing Technologies with a Seat in Presov, Technical University of Kosice, Bayerova 1, 080 01 Presov, Slovakia; miroslav.rimar@tuke.sk (M.R.); marcel.fedak@tuke.sk (M.F.); ivan.corny@tuke.sk (I.Č.)

* Correspondence: jan.kizek@tuke.sk

Abstract: Modern heating furnaces use combined modes of heating the charge. At high heating temperatures, more radiation heating is used; at lower temperatures, more convection heating is used. In large heating furnaces, such as pusher furnaces, it is necessary to monitor the heating of the material zonally. Zonal heating allows the appropriate thermal regime to be set in each zone, according to the desired parameters for heating the charge. The problem for each heating furnace is to set the optimum thermal regime so that at the end of the heating, after the material has been cross-sectioned, there is a uniform temperature field with a minimum temperature differential. In order to evaluate the heating of the charge, a mathematical model was developed to calculate the heat fluxes of the moving charge (slabs) along the length of the pusher furnace. The obtained results are based on experimental measurements on a test slab on which thermocouples were installed, and data acquisition was provided by a TERMOPHIL-stor data logger placed directly on the slab. Most of the developed models focus only on energy balance assessment or external heat exchange. The results from the model created showed reserves for changing the thermal regimes in the different zones. The developed model was used to compare the heating evaluation of the slabs after the rebuilding of the pusher furnace. Changing the furnace parameters and altering the heat fluxes or heating regimes in each zone contributed to more uniform heating and a reduction in specific heat consumption. The developed mathematical heat flux model is applicable as part of the powerful tools for monitoring and controlling the thermal condition of the charge inside the furnace as well as evaluating the operating condition of such furnaces.

Keywords: heat flux; pusher furnace; slab; mathematical model

Citation: Varga, A.; Kizek, J.; Rimár, M.; Fedák, M.; Čorný, I.; Lukáč, L. Modeling of Heat Flux in a Heating Furnace. *Computation* **2023**, *11*, 144. https://doi.org/10.3390/computation11070144

Academic Editor: Ali Cemal Benim

Received: 2 July 2023
Revised: 14 July 2023
Accepted: 14 July 2023
Published: 17 July 2023

1. Introduction

Heating furnaces can be divided into various groups based on selected criteria. One of the criteria is the heating mode, which is determined by the technological requirements. Convective or radiant heating can predominate in the furnace. The importance of the correct heating mode is related to the uniformity of the temperature field within the charge and the heating time. These two factors are crucial for intensifying the heating process and determining the operational economy of such a furnace [1–3].

Among the important types of heating furnaces are pusher furnaces. Pusher furnaces have undergone development, with their geometry and parameters based on technological needs. Various construction types of pusher furnaces have been described by authors in [2] and [3]. An important common factor is the energy consumption for heating the charge. Therefore, possibilities for reducing energy consumption are explored, such as by installing more efficient insulation and refractory materials [4–6]. Another option is to achieve better heat distribution through the installation of new burners [7].

Pusher furnaces are continuous heating furnaces used for heating slabs to the rolling temperature. They feature a floor-level balancing zone, a radiant ceiling, bottom heating, front loading, and front unloading using inclined skids or an unloading machine [3].

Pusher furnaces are used for heating square or rectangular billets for rolling and forging. Furnaces for heating thin material (50–100 mm) with large lengths (up to 12,000 mm) typically have a slight slope, usually around 6–7°, towards the extraction opening to prevent the material from sticking and reduce the required pressing force. The processed materials have the following dimensions: thickness of 40–400 mm, width of 40–2500 mm, length of up to 15,000 mm, and weight of 0.05–40 tons [3,6].

The heating of slabs in pusher furnaces depends on subsequent forming processes and the desired final heating temperature before hot rolling. It is influenced by various factors, especially the type of steel. The temperature should be maintained at approximately 100–150 °C below the solidus curve. The upper limit is constrained by grain growth, the risk of overheating due to thermal stresses, and increased oxidation. The lower limit of heating is determined by the permissible temperature at the end of processing, depending on the steel grade. Pusher furnaces play a crucial role in the rolling process. The furnace must deliver the required quantity of slabs with the desired heating quality within a specified time frame, forming an integral part of the production line [3,6].

The heating of metal in a pusher furnace is a flow process characterized by the movement of heated material through a series of heating zones arranged spatially. Control variables (e.g., zone temperature) are also distributed in space, acting on all slabs simultaneously along the entire length of the heating zone, which are at different thermal states [3,6].

The heating of slabs in a pusher furnace depends on the forming process. This process must be carried out to achieve the following objectives [6]:

- Uniform desired properties along the length of the strip are considered for the rolling direction and transverse direction (yield strength, elongation, toughness);
- The uniform geometric shape of the strip (thickness, width) along its entire length;
- Maximum line performance with minimal energy consumption and minimal material losses [8,9].

The working space of the pusher furnace is divided into several temperature zones. The material passes through four consecutive zones: preheating, heating (upper and lower heating), balancing, and holding zone, where irregularities occurring during material heating are leveled out [3,4,6].

The preheating zone, into which the cold charge enters, serves two main purposes and is characterized by a gradual increase in the flue gas temperature. The first purpose is the slow heating of the pre-rolls up to a temperature of 500 °C, where there is a risk of thermal stress damage to the steel. The charge is heated gradually to avoid an undesirable temperature gradient between the surface and the center of the pre-roll. The second function is the utilization of flue gas heat.

From the preheating zone, the charge proceeds to the heating zone, where the surface of the pre-rolls is rapidly heated to the desired heating temperature. Upon exiting the heating zone, the pre-rolls are unevenly heated, with a significant difference between the surface and center temperatures. The balancing zone is responsible for reducing this temperature difference. It is an important part of the pusher furnace and serves to eliminate shadows during the heating of the pre-rolls on the skids. For rolling purposes, it is required that the temperature gradient along the height of the pre-rolls does not exceed 1 to 3 $K \cdot cm^{-1}$. The power input into the balancing zone is chosen so that the flue gas temperature is 50 to 70 K higher than the heating temperature. The surface temperature remains unchanged, while the center temperature slowly approaches it [1,3,6].

The characteristics of pusher furnaces indicate numerous factors that need to be incorporated into the control of such thermal units.

The authors in [8,9] address the factor of scale in the charge heating process. Appropriate heating parameters allow the formation of deposits to be controlled during the heating process and ensure the predictability of the effects on the material.

For a more complex analysis of the heating process, it is necessary to make an energy and material balance of the charge heating [1]. This is based on data from measurements on heat aggregates, which serve to verify calculations. In many studies, the authors devoted themselves to the creation of balance [10–12] and prediction models [13,14], the basis of which was internal and external heat exchange. Some authors focused on the analysis of furnace work [10,15] and the creation control systems [12,13,16–18] for heating in pusher furnaces. Optimization models [19,20] or, currently, CFD modeling [14,15] are used for the analysis of the work of the thermal aggregate. Another suitable method is work analysis based on heat losses [10], from which the efficiency of the slab heating process is determined. Due to the non-linearity of the parameters of the heated material, it is necessary to apply suitable non-linear equations in the calculations [16,17], which are also part of control and prediction models [12–14,18].

It follows from the works [10–20] that some heat aggregates have a different heating mode, and therefore the mathematical models created are specific.

A big problem with the created models is downtime when removing the heated slabs from the furnace. This is due to a malfunction (technical defect) on the device or in another device during slab processing. In such cases, it is possible to adjust the heating mode using some prediction, control, and control models.

The authors aim to create a mathematical model for evaluating heat fluxes on the massive charge based on temperature profile measurements. The calculation algorithm is based on internal heat exchange. The developed model is intended to serve as a supporting tool for monitoring the duration of the heating process, and the results of the calculations will be used as a basis for intensifying the heating of the charge in the pusher furnace. The created model should be applicable to similar types of charge heating furnaces with moving charges.

2. Materials and Methods

Optimal parameters for heating the slabs in a pusher furnace, including the heating time of the material and specific energy consumption, are dependent on the following factors [1,3]:

1. Temperature field in the furnace working space (heat inputs in individual furnace zones);
2. Composition of the furnace atmosphere (excess combustion air, fuel composition, and fuel combustion);
3. Inlet temperature of the slabs;
4. Slab temperatures above the skids (condition of the furnace cooling system);
5. Type of steel.

These factors significantly influence both the external and internal heat exchange during the slab heating process in pusher furnaces. Conducting a thorough analysis of these factors allows for the identification of key factors that can intensify the slab's heating process.

The internal heat exchange of the slabs is characterized by the temperature field within the slab, while the external heat exchange is determined by the temperature profile in the furnace working space and the heat flux incident on the slab's surface. By evaluating the heat exchange along the length of the furnace during the heating process, temperature measurements taken within the slab between the skids serve as crucial reference data.

In order to enhance slab heating in pusher furnaces, measurements of thermotechnical variables were conducted. The following parameters were measured [1,3]:

- Type and characteristics of the charge material;
- Fuel type, fuel composition, and heat inputs in different furnace zones;
- Quantity of air in each furnace zone and air temperature;
- Furnace temperature in each zone;
- Inlet surface temperature of the charge material;
- The oxygen content of the flue gas at the furnace flue gas outlet;
- Rolling temperature behind the 5th rolling table;

- Quantity of cooling water, as well as inlet and outlet water temperatures;
- Temperatures within the slab.

These measurements provide essential data for understanding and optimizing the slab heating process in pusher furnaces.

To measure the temperature profile inside the material, a test slab made of low-carbon steel 11-375 was utilized. This steel contains a carbon content of up to 0.09% by weight and is accurately defined according to the STN 41-1375 standard [21]. The measurements were carried out with the aim of intensifying the heating of slabs in pusher furnaces. The measurements took place inside the furnace during its operation with the test slab, and the temperatures inside the slab were continuously measured from the entry point into the furnace until its expulsion at the furnace outlet. The measuring device used for these temperature measurements was the data logger TERMOPHIL-stor type 4468/4469 (Ultrakust Electronic GmbH, Gotteszell, Germany), capable of recording data from 6 measuring points. The measuring points within the slab are schematically illustrated in Figure 1. Thermocouples 1–3 were positioned outside the skids at a distance of 650 mm from the right edge of the slab, while thermocouples 4–6 were positioned at a distance of 1300 mm from the right edge of the slab (above the skids). Measurement points 1, 4, 3, and 6 were positioned at a distance of 25 mm from the upper and bottom surfaces of the slab. Measurement points 2 and 5 were positioned in the center of the slab. The selection of measurement locations was specified in order to capture the temperature distribution within the slab, unaffected by the cooling system of the skids, as well as the temperature distribution directly above the skids. This approach enabled the acquisition of more comprehensive insights into the slab heating process.

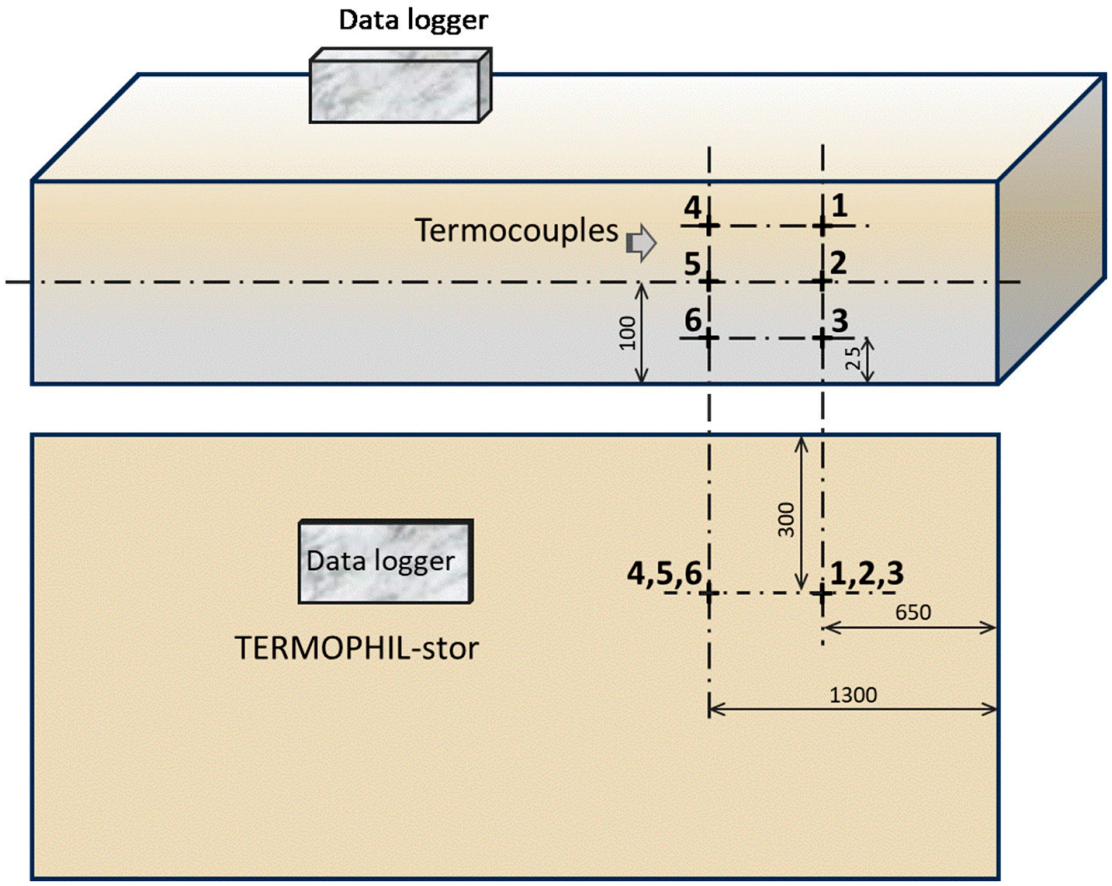

Figure 1. Schematic location of thermocouples at the measuring points in the test slab (side view and top view).

Due to the high temperatures in the furnace, type S thermocouples (PtRh10-Pt) were employed for temperature measurement at the measuring points in the test slab. Type S thermocouples can be used up to a temperature of 1600 °C.

The parameters of the test slab were as follows:

- Dimensions: 8000 × 1540 × 200 mm
- Weight: 15.5 t

The values of the temperatures at all measuring points were registered at one minute intervals.

After the test slab was pushed out of the furnace, the data logger was removed from the slab, and the measurement was completed. By synchronizing the time, a section was marked in the acquired data that corresponded to the actual time the slab stayed in the pusher furnace.

Figure 2 shows the location of the slabs and their movement, which was carried out by a push button at the furnace entrance. At the outlet, the slab slides down the inclined surface onto the roller transport conveyor. The above method of exiting the slabs from the pusher furnace before the reconstruction caused large mechanical shocks when they hit the roller conveyor.

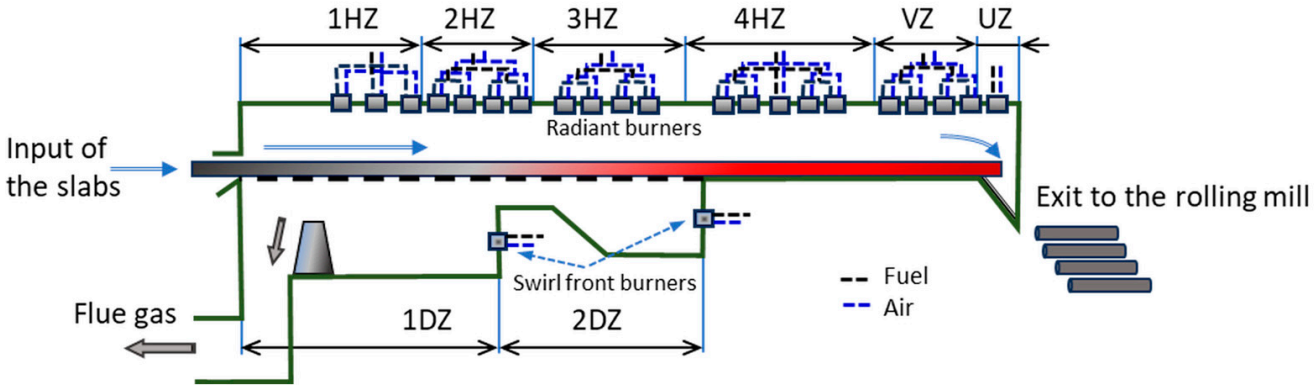

Figure 2. The scheme and the parameters of the pusher furnace before reconstruction. 1HZ, 2HZ, 3HZ, and 4HZ—upper heating zones defined by a group of radiant burners; VZ—balancing zone; UZ—holding zone; and 1DZ and 2DZ—lower heating zones.

The heating of the charge in the pusher furnace is provided by combined heating by overhead radiant and underfloor swirl front burners [7]. For each zone, a separate heating mode is set. In the high-temperature field, the furnace atmosphere is also adjusted to prevent excessive scale formation [4,9]. During heating, scale affects the transfer of the body to the inside of the slab and thus can cause differences in the temperature field across the cross-section of the heated material [6,9].

Figure 3 illustrates the differences between the measured temperatures outside the skids (measuring points 1–3) and directly on the water-cooled skids (measuring points 4–5). The water in the skids creates temperature shadows that need to be eliminated in the balancing zone (VZ).

During the measurement, the residence time of the slab in the furnace was 171 min, with a residence time in the double-sided heating zones of 100 min. The temperatures between the skids reached 1258–1280 °C at the end of the heating process, while above the skids, temperatures ranged from 1244 to 1272 °C. The maximum temperature difference across the thickness of the slab was 42 °C.

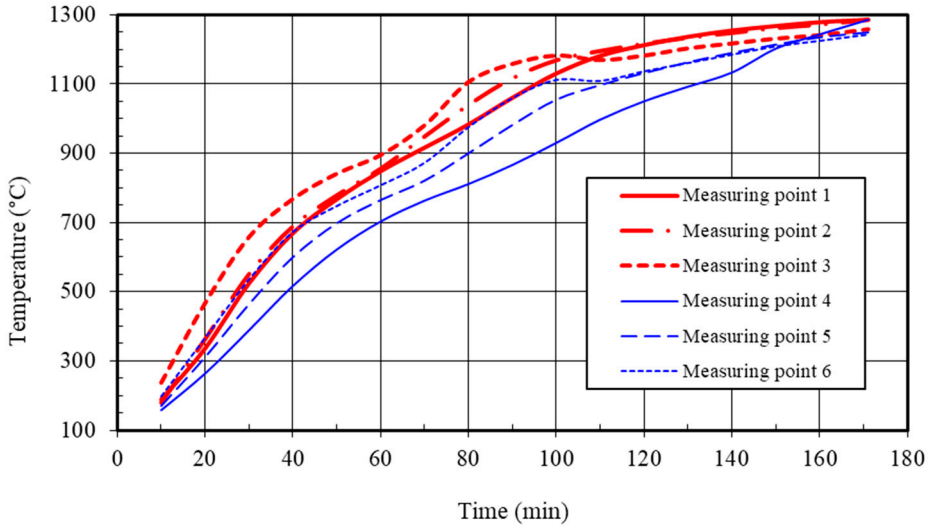

Figure 3. Time-dependent temperature curves before reconstruction (heating time: 171 min).

The analysis of the slab heating process in the pusher furnaces was conducted through comprehensive measurements of furnace operation and temperature profiles in the slabs at various heating times. These measurements subsequently led to the design and implementation of reconstruction, involving adjustments to specific parameters of the pusher furnace. A schematic representation is shown in Figure 4.

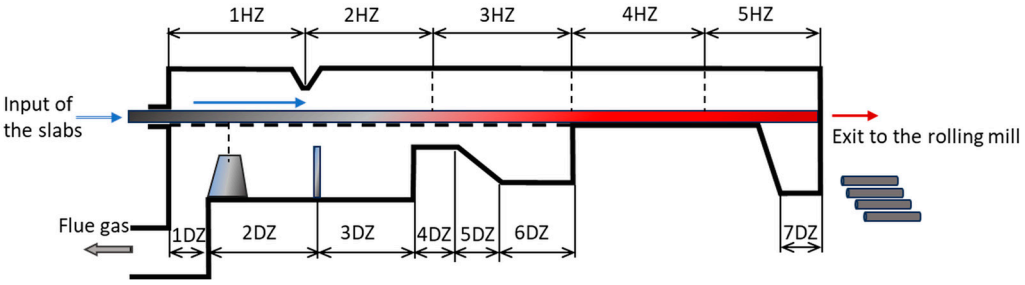

Figure 4. The scheme and the parameters of the pusher furnace after reconstruction.

The main objective of the reconstruction is primarily to reduce the specific energy consumption during heating, improve the quality of slab heating, and reduce losses due to scaling [9]. After the reconstruction of the pusher furnace, the active length of the furnace changed from 32.5 m to 34 m. From the schematic representation in Figure 4, one can also observe the change in the furnace profile in the vault and the lower zone. The added partitions have intensified heat exchange, especially through convection. The flue gases are now forced to flow more around the slabs. The method of slab removal from the furnace has been modified. The insulation of the water-cooled skids and the burner system has been improved.

The furnace reconstruction at its discharge end consists of the elimination of the inclined slips and the prolongation of the furnace nest part. The insulation of the lower face after combustion fuel burners provides higher-quality slab heating, and the temperature difference between the upper and lower slab sides will decrease [3,9].

In order to verify the appropriateness of the changes in the parameters of the pusher furnace, control measurements were carried out using a test slab. The location of the thermocouples in the test slab is shown in Figure 5.

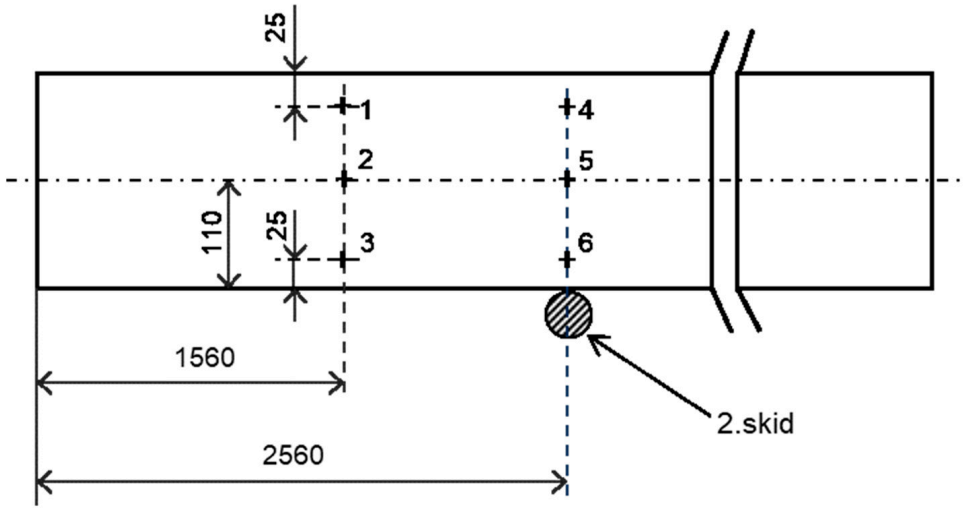

Figure 5. Schematic location of the measuring points in the test slab after the reconstruction of the pusher furnace (side view).

Figure 5 shows the schematic layout of measurement points in the test slab. The material of the used test slab had the same properties as in the case of the pusher furnace before reconstruction, which was low-carbon steel 11-375 [21]. In this case, a test slab with a thickness of 220 mm was employed. The temperature field was recorded at unaffected measurement points 1–3, while the temperature field influenced by the cooling system of the skids was observed at measurement points 4–6.

Figure 6 shows the temperature curves in the test slab at individual measurement points along the length of the furnace. The temperatures indicated in Figure 6 as t_1–t_6 correspond to the respective measuring points 1–6 as illustrated in Figure 5. The heating is set up in such a way that the temperature in the slab increases only in the region of uniform heating, indicated by 20 m. During this heating phase, the surface temperature of the slab reaches approximately 1200 °C. Subsequently, in the following zones during the heating process, the temperature inside the slab equalizes and reaches the desired temperature for rolling.

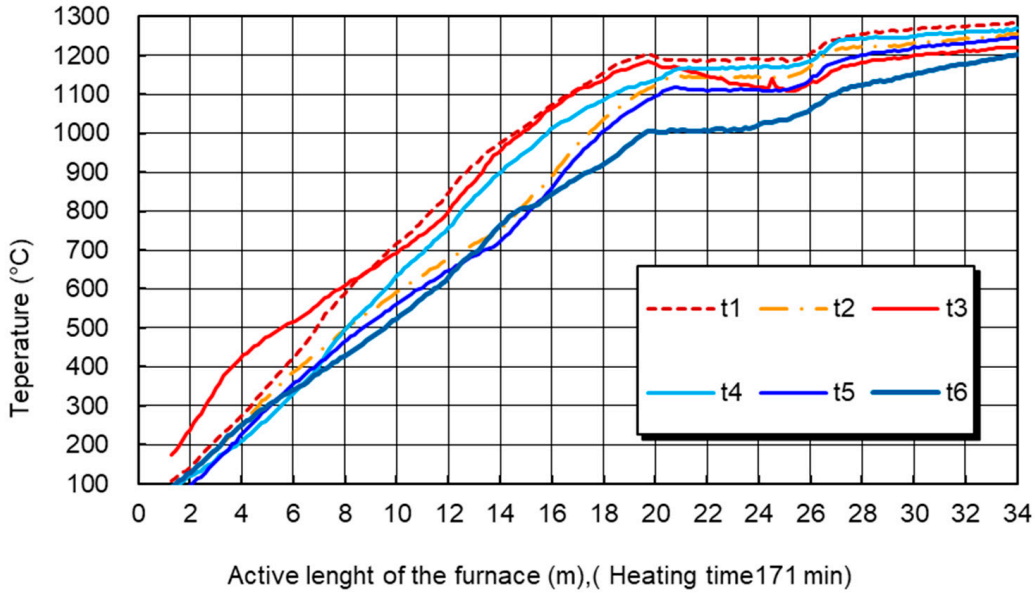

Figure 6. Time-dependent temperature curves after reconstruction (heating time: 171 min).

Determination of Heat Fluxes on the Charge Surface

Knowledge of the course of heat fluxes falling on the charge surface allows charge heating intensification, e.g., Varga [1]. In this work, the authors focused on the solution of internal heat exchange, which was based on the fundamentals of the 1st Fourier law of heat transfer [22–24]. Due to the unsteady heat flux, the 1st Fourier law cannot be applied. Therefore, an alternative solution was sought, which was based on the measured temperatures and the determination of the material's enthalpy. When estimating heat fluxes falling on the charge surface, the way out is the course of the measured temperature in the slab between skids. Since the temperature distribution along the slab height follows a quadratic pattern, the entire temperature profile across the slab cross-section can be determined from just 3 measured values, as described by the following equation:

$$t = k\,x^2 + q\,x + p. \tag{1}$$

The coefficients k, q, and p are obtained by solving Equation (1) for values of 3 temperatures from 3 measuring points (a set of 3 equations of 3 variables).

As the temperature course along the slab cross-section is described by a quadratic equation, the temperature at a certain distance from the slab surface, x_{min}, is minimal at t_{min}.

The t_{min} value is determined from:

$$t_{min} = \frac{dt}{dx} = 0. \tag{2}$$

The distance x_{min} is calculated from Equation (1) when the substitution $t = t_{min}$ is made.

For the calculation of heat fluxes, it is assumed that up to the distance x_{min}, the heat flux from the upper side q_h is effective, and up to the distance $(s - x_{min})$, the heat flux from the lower side q_d is effective. This is clearly illustrated in Figure 7.

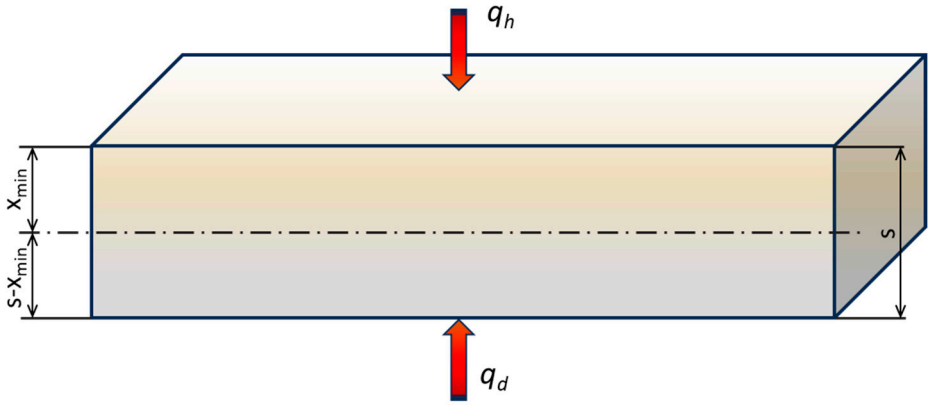

Figure 7. Schematic of the distribution of heat fluxes incident on the surface of the slab from above or below.

The heat fluxes are calculated according to the following equations:

$$q_{h,i} = \left(c_{p\ h,i+1}\,\bar{t}_{h,i+1} - c_{p\ h,i}\,\bar{t}_{h,i}\right)\bar{\rho}_h\,x_{min}\,\Delta\tau, \tag{3}$$

$$q_{d,i} = \left(c_{p\ d,i+1}\,\bar{t}_{d,i+1} - c_{p\ d,i}\,\bar{t}_{d,i}\right)\bar{\rho}_d\,(s - x_{min})\,\Delta\tau, \tag{4}$$

where:

i—time index;

$\Delta\tau$—length of the time interval (s);

$q_{h,i}$ and $q_{d,i}$—the heat flux from the upper side to the lower side (W m^{-2});

$c_{p\ h,i}$—the mean specific heat capacity at the $\bar{t}_{h,i}$ temperature (J·kg^{-1} K^{-1});

$c_{p\ d,i}$—the mean specific heat capacity at the $\bar{t}_{d,i}$ temperature (J·kg^{-1} K^{-1});
$\bar{t}_{h,i+1}$—the mean charge temperature on the thickness x_{min} at time τ_{i+1} (°C);
$\bar{t}_{h,i}$—the mean charge temperature on the thickness x_{min} at time τ_i (°C);
$\bar{t}_{d,i+1}$— the mean charge temperature on the thickness $(s - x_{min})$ at time τ_{i+1} (°C);
$\bar{t}_{d,i}$— the mean charge temperature on the thickness $(s - x_{min})$ at time τ_i (°C);
$\bar{\rho}_h$—charge density at the mean temperature $\frac{\bar{t}_{h,i+1}+\bar{t}_{h,i}}{2}$ in the time interval (τ_i, τ_{i+1}) (kg m^{-3});
$\bar{\rho}_d$—charge density at the mean temperature $\frac{\bar{t}_{d,i+1}+\bar{t}_{d,i}}{2}$ in the time interval (τ_i, τ_{i+1}) (kg m^{-3});
s—slab thickness (m).

The mean charge temperatures from the upper side $\bar{t}_{h,i}$ on the thickness x_{min} and from the lower side $\bar{t}_{d,i}$ on the thickness $(s - x_{min})$ are obtained by solving Equation (1) as follows:

$$\bar{t}_{h,i} = \frac{k\frac{x_{min,i}^3}{3} + q\frac{x_{min,i}^2}{2} + p\, x_{min,i}}{t_{o,i} - t_{min,i}}. \tag{5}$$

To shorten the following equation, substitutions are used:
$a_1 = (s - x_{min})^3$; $a_2 = (s - x_{min})^2$; $a_3 = s - x_{min}$,

$$\bar{t}_{d,i} = \frac{k\frac{a_1}{3} + q\frac{a_2}{2} + p\, a_3}{t_{s,i} - t_{min,i}}, \tag{6}$$

where $t_{o,i}$ represents the temperature of the upper surface of the slab in Equation (5), and $t_{s,i}$ represents the temperature of the lower surface of the slab in Equation (6) (°C).

During the experimental measurements, a slab made of low-carbon steel was used, which exhibits nonlinear thermophysical properties, especially in terms of thermal capacity (c_p). Therefore, it was necessary to establish temperature dependencies for this material. Some of the literature divides the temperature range into smaller intervals and utilizes linearized dependencies in their models. In this case, tabulated values from [25] were employed, and temperature dependencies for the mean specific heat capacity of low-carbon steel with a carbon content of 0.08 mass% were obtained through regression analysis. The temperature dependence of the heat capacity was addressed by employing a 3rd degree polynomial, as outlined in Equation (7), which effectively captured the behaviour of the provided data in [25]. The coefficients necessary for Equation (7) were determined and are presented in Table 1. To enhance the precision of the specific heat capacity calculations, it seemed most appropriate to divide the temperature interval as shown in Table 1.

$$\bar{c}_p = a + b\,\bar{t} + c\,\bar{t}^2 + d\,\bar{t}^3 \tag{7}$$

Table 1. Coefficients for the calculation of the median specific heat capacity, $\bar{c}_p$, (kJ kg^{-1} K^{-1}).

t	a	b	c	d
<800 °C	0.4727	1.67×10^{-4}	-2.654×10^{-7}	5.0107×10^{-10}
≥800 °C	−0.093	2.2962×10^{-3}	-2.1714×10^{-6}	6.66668×10^{-10}

To calculate the density ρ (kg m^{-3}) of low-carbon steel, the following relationship can be used:

$$\rho = 7886,285 - 0,35\,\bar{t}. \tag{8}$$

When deriving Equations (3) and (4) for the heat flux estimation, the law of energy conservation is applied, which means that the charge enthalpy can be changed only due to the heat supplied to the charge surface. From the calculated heat fluxes q_h and q_d the total heat amount falling on the surface unit is determined according to the expression:

$$q = q_h - q_d. \tag{9}$$

From the measured and calculated results obtained, graphical relationships were created.

The correctness of the proposed method for the solution of the heat fluxes is also confirmed by the following calculation:

The change of the specific enthalpy Δi can be estimated according to the expression:

$$\Delta i = c_{p,k}\bar{t}_k - c_{p,\,p}\bar{t}_p, \tag{10}$$

$c_{p,\,p}$—the mean specific heat capacity at the beginning of heating (J kg^{-1} K^{-1});
$c_{p,k}$—the mean specific heat capacity at the end of heating (J kg^{-1} K^{-1});
$\bar{t}_k$—the mean slab temperatures at the end of heating (°C).
$\bar{t}_p$—the mean slab temperatures at the beginning of heating (°C).
The change of enthalpy Δi can be estimated according to the relationship:

$$\Delta i = \sum_{1=1}^{n}(\Delta i_{h,i} + \Delta i_{d,i}), \tag{11}$$

where:

$\Delta i_{h,i}$—change of the charge-specific enthalpy at the heat flux from the upper side for the time interval (J kg^{-1});

$\Delta i_{d,i}$—change of the charge-specific enthalpy at the heat flux from the lower side for the time interval (J kg^{-1}).

For $\Delta i_{h,i}$ and $\Delta i_{d,i}$ the following calculation is applied:

$$\Delta i_{h,i} = \left(c_{p\ h,i+1}\ \bar{t}_{h,i+1} - c_{p\ h,i}\ \bar{t}_{h,i}\right)\frac{x_{min,i}}{s}, \tag{12}$$

$$\Delta i_{d,i} = \left(c_{p\ d,i+1}\ \bar{t}_{d,i+1} - c_{p\ d,i}\ \bar{t}_{d,i}\right)\frac{(s - x_{min,i})}{s}. \tag{13}$$

If we compare the equations for calculating heat fluxes (3) and (4) and the change in enthalpy (12) and (13), the following holds true:

$$\Delta i = \frac{q}{\rho_i\ s\ \Delta\tau}. \tag{14}$$

When comparing the Δi values calculated using Equations (10) and (11), it is observed that there is an approximate difference of 0.5% attributed to calculation inaccuracies. This indicates that the proposed methodology for calculating the heat fluxes falling onto the charge surface from the obtained measurements can be considered accurate. This finding is consistent with the work of Varga [1].

3. Results and Discussion

Based on the mathematical model created and the measured temperatures inside the slab, the results of the heat flux profiles were obtained as a function of the slab heating time in the heating furnace. When performing calculations using the mathematical model, only temperatures outside the skids were considered, as the temperatures inside the slab or the heat dissipation through the water-cooled slides would influence the results, which are not accounted for in this model.

From the processed measurement results, the following graphical dependences have been constructed:

- The temperature courses in the slab in dependence on the duration of before reconstruction and after reconstruction of the pusher furnace;
- The heat flux courses to the slab surface in dependence on the duration of heating before reconstruction and after reconstruction of the pusher furnace.

Figures 8 and 9 show the results for the test slab measurement with a heating time of 187 min. This is because of the heating comparison shown in Figure 3, where the residence time of the slab in the furnace was 171 min.

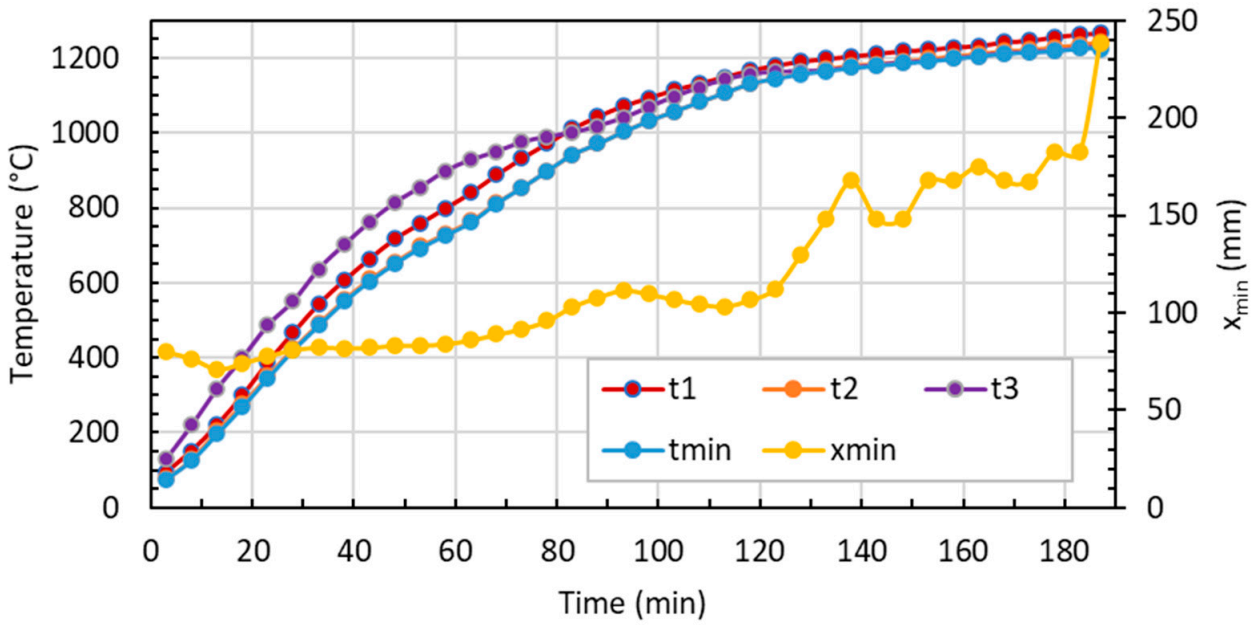

Figure 8. The course of measured temperatures in the slab t_1–t_3 along the length of the furnace and the calculated values t_{min} and x_{min} (before reconstruction).

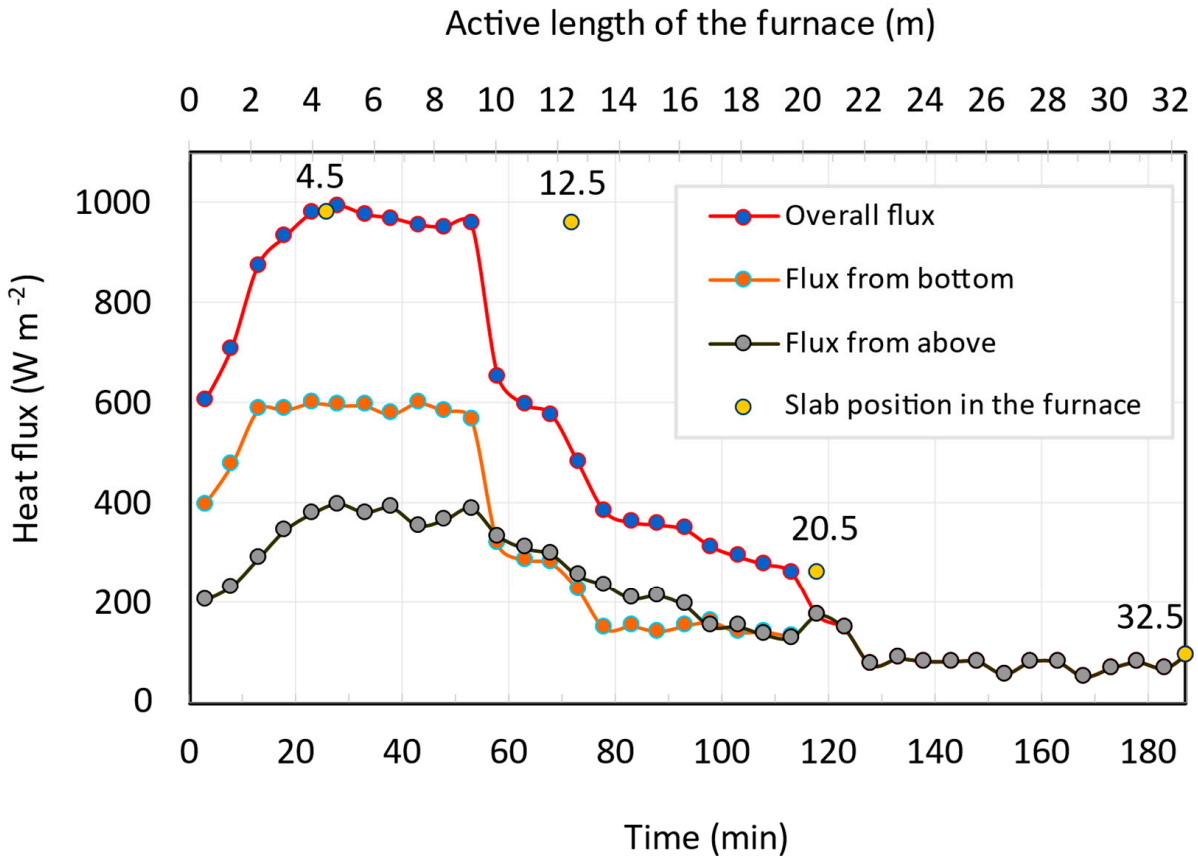

Figure 9. Dependency of calculated heat fluxes along the furnace length as a function of the slab residence time in the pusher furnace (before reconstruction).

In Figure 8, it is possible to observe the temperature rise in the slab during the measurement as well as the calculated minimum temperature t_{min} and the calculated slab

thickness x_{min} needed to calculate the heat fluxes. Temperatures t_1–t_3 correspond to the temperatures at measuring points 1–3 in the slab, which are in Figure 1.

By comparing different residence times in the pusher furnace, it was found that the temperature profiles measured over the furnace length are very similar. From the thermomechanical analysis of the heating of the slabs during the measurements with the test slab (Figures 8 and 9), it follows that there is an increase in heat fluxes from the top and bottom up to a heating time corresponding to a distance of approximately 4 m. In this area of the furnace, there are no burners, and the heat mainly comes from radiation from other parts of the furnace. The increase in heat flux corresponds to an increase in furnace temperatures in that furnace region. In the lower part of the furnace, this distance corresponds to the width of the exhaust flue gas channel.

From Figure 9, it is evident that until a heating time corresponding to the width of 1DZ, the heat fluxes from the bottom are considerably higher than the heat fluxes from the top, which is also reflected in the higher surface temperatures at the bottom, approximately 100 °C higher than the surface temperatures at the top (Figure 9). Furthermore, Figure 9 shows that the heat fluxes in 2DZ are lower than the heat fluxes in the upper zones of that region, resulting in a slight increase in the surface temperatures of the slabs at the bottom compared to the surface temperatures of the slabs at the top (Figure 8). Additionally, Figure 9 indicates that the heat fluxes in 2DZ are lower than the heat fluxes in the upper zones of that region, causing only a slight increase in the surface temperatures of the slabs at the bottom compared to the surface temperatures of the slabs at the top (Figure 8). The surface temperatures of the slabs at the top are higher than those at the bottom at the end of 2DZ, which negatively affects the residence time in 4HZ and VZ, considering only the upper heating method in these zones.

In the 4HZ and VZ regions, the heat fluxes are approximately equal, resulting in only a slight increase in surface temperature at the top. The furnace temperature is relatively uniform throughout this region. Similar results were obtained for low-carbon steels in other measurements.

From this analysis, it can be concluded that such a regime is not suitable in terms of energy consumption. This controlled heating leads to an increased temperature of the exhaust gases leaving the furnace, indicating increased heat losses through the exhaust gases. To reduce specific energy consumption for heating, it is necessary to regulate the heat inputs in individual zones in such a way that:

- The heat fluxes from the bottom and top are approximately equal up to a distance of 1DZ;
- The heat fluxes from the bottom are slightly higher than the heat fluxes from the top in the 2DZ, ensuring higher surface temperatures for the slabs at the bottom and the top at the end of the 2DZ.

To achieve this, it is necessary to reduce the heat input in 1DZ and increase the heat input in 2DZ, resulting in a smoother increase in temperatures in the slab.

Based on measurements of heat inputs in individual zones of the furnace, it can be observed that the heat input in 1DZ was 25.7%, in 1HZ it was 31.4%, and in 2HZ it was 16.6%. Considering that there is a high heat consumption for cooling the skids and other parts of the cooling system in 1DZ, the heat fluxes and surface temperatures of the slabs from the top should be higher than those from the bottom. This fact indicates that significant transfers of heat inputs (or fresh combustion gases) occur through the free spaces between the furnace walls and the charge, from the upper zones to the lower zones. These transfers of heat inputs require studying the flow of combustion gases in the working space of the furnace, depending on the overall furnace regime. Understanding the flow pattern is only possible through a physical furnace model that allows simulation for different furnace heat regime variants or through advanced CFD simulation software [14,15].

Considering that the cooling system of the pusher furnace was not insulated before the reconstruction, there was increased heat consumption, especially in 1DZ and 2DZ. Insulating the cooling system can reduce the heat input in 1DZ and provide the possibility

of increasing the heat input in 2DZ, thus ensuring uniform heating of the slabs up to a distance of approximately 1DZ and slightly increased bottom heating of the slabs in the 2DZ region. Insulating the cooling system and making subsequent adjustments to the furnace heat regime will reduce the overall thermal energy consumption and, therefore, decrease the specific energy consumption for heating the slabs in pusher furnaces. It will also provide a more uniform temperature distribution across the slab section at the end of the heating process and shorten the heating time.

Figure 10 shows the t_1–t_3 temperature time histories corresponding to the temperatures from measurement points 1–3 in the slab according to Figure 5. For the calculation of tmin and xmin, the same calculation methodology was applied as in Figure 8.

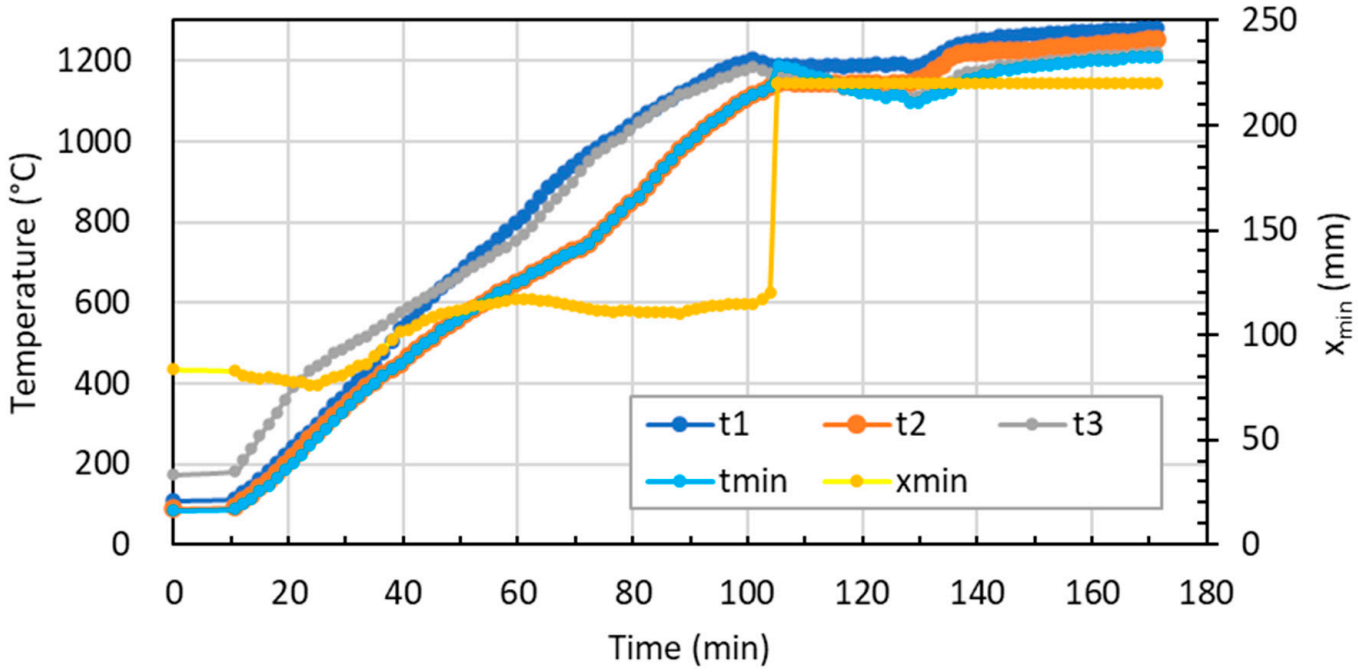

Figure 10. The course of measured temperatures in the slab t_1–t_3 along the length of the furnace and the calculated values t_{min} and x_{min} (after reconstruction).

The comparison of the slab heating curves before reconstruction in Figure 8 and after reconstruction in Figure 10 reveals that the thermal regime of the furnaces after reconstruction is more favorable due to a more uniform temperature rise in the slab area during double-sided heating.

From the comparison of the heat flux curves in Figures 9 and 11, a significant change in the decrease of heat flux in the double-sided heating region can be observed.

Comparing the maximum total heat fluxes, a 63% decrease can be observed, and similarly for the upper (59% decrease) and lower heat fluxes (65% decrease). The mathematical model is applicable for the evaluation of the heating from the internal heat exchange point of view. However, the heat flux drops do not take into account another parameter affecting the specific energy savings. Therefore, it is only an auxiliary but effective tool for more complex mathematical models.

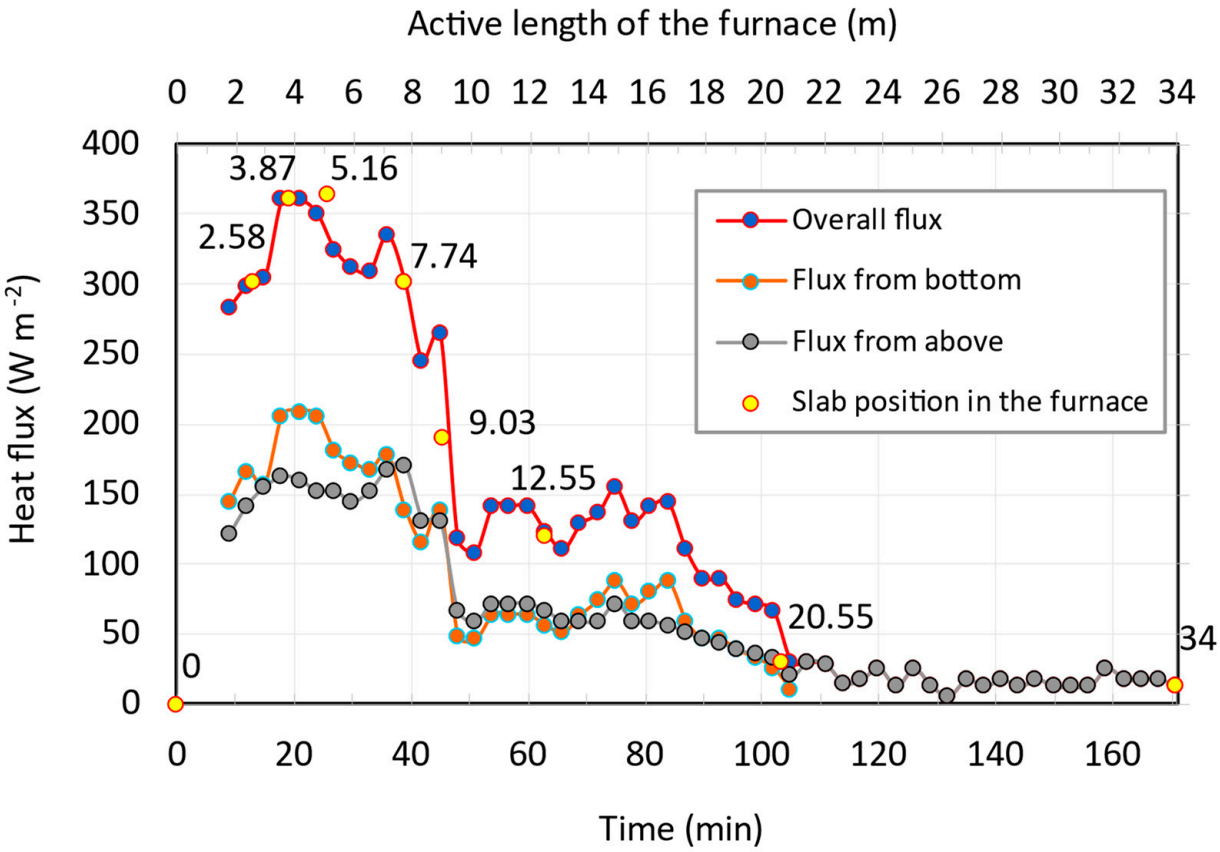

Figure 11. Dependence of calculated heat fluxes along the furnace length as a function of the slab residence time in the pusher furnace (after reconstruction).

4. Conclusions

The mathematical model created for evaluating the thermal regime of pusher furnaces for slab heating prior to rolling provides valuable insights into optimizing the heating process. By combining modern measurement techniques with the mathematical model, important data was gathered to assess the operational state of these furnaces, with a focus on specific energy consumption for slab heating.

The conducted measurements, subsequent calculations, and evaluation of the results have shed light on the fundamental principles of slab heating. They have also highlighted the potential for further improvements in optimizing the slab heating process. These findings pave the way for future research and development efforts aimed at enhancing the efficiency and performance of pusher furnaces.

The utilization of zonal heating in large furnaces, such as pusher furnaces, proves crucial in achieving uniform temperature fields with minimal temperature differences across the material cross-section. This zonal approach allows for the adjustment of thermal regimes in each zone according to the desired parameters, ultimately leading to improved heating performance.

By applying the developed mathematical model, engineers and operators can effectively monitor and control the thermal state of the charge inside the furnace. Additionally, the model serves as a valuable tool for evaluating the operational performance of pusher furnaces, aiding in the reduction of specific energy consumption and overall energy efficiency. The created model can also serve as a predictive tool when changing the parameters of the heated charge or furnace thermal power.

Overall, the findings and insights gained from this research contribute to the advancement of heating technologies in the metallurgical industry, with the potential to drive cost savings, enhance product quality, and minimize environmental impact. Further research

and implementation of optimized heating strategies based on the developed model can lead to significant improvements in the performance and energy efficiency of pusher furnaces for slab heating.

Author Contributions: Conceptualization, A.V. and J.K.; methodology, A.V. and J.K.; software, A.V.; validation, A.V., J.K. and L.L.; formal analysis, M.F.; investigation, M.F.; resources, A.V., J.K. and I.Č.; data curation, A.V.; writing—original draft preparation, J.K., I.Č. and A.V.; writing—review and editing, J.K. and I.Č.; visualization, J.K. and A.V.; supervision, M.R.; project administration, J.K.; funding acquisition, M.R. All authors have read and agreed to the published version of the manuscript.

Funding: The work is supported by the KEGA grant agency under Grant KEGA 023TUKE-4/2021.

Data Availability Statement: The study did not report any data.

Conflicts of Interest: The authors declare no conflict of interest.

References

1. Varga, A. Intensifying the process of heating slabs in pusher furnaces. *Trans. Technol. Univ. Košice* **1992**, *2*, 264–276.
2. Brunklaus, J.H. *Building of Industrial Furnaces*, 2nd ed.; Vulkan-Verlag: Essen, Germany, 1962.
3. Tatič, M.; Lukáč, L.; Súčik, G. *Industrial Furnaces in Metallurgical Secondary Production*, 1st ed.; TU of Košice: Košice, Slovakia, 2021.
4. Tatič, M. Modernization of the pusher furnace lining in VSŽ a.s. *Acta Metall. Slovaca* **1997**, *2*, 469–476.
5. Horbaj, P.; Črnko, J.; Lazić, L. Effect of varying the power and frequency of insulation maintenance on the heat consumption of a pusher furnace. *Hutnícke Listy* **1992**, *47*, 26–28.
6. Kollerova, I. The Study of the Wear of the Pusher Furnace Bottom with Steel Scales. Ph.D. Thesis, Technical University of Ostrava, VŠB Ostrava, Czech Republic, March 2010.
7. Varga, A.; Tatič, M.; Lazić, L. Application of roof radiant burners in large pusher-type furnaces. *Metalurgija* **2009**, *48*, 203–207.
8. Benduch, A.; Boryca, J. The verification of the influence of heating steel charge parameters on the thickness of scale layer. *Adv. Sci. Technol. Res. J.* **2013**, *7*, 1–5. [CrossRef]
9. Kostúr, K. Minimization of costs when heating the slabs in the pusher furnace. *Hutnícke Listy* **1994**, *49*, 43–47.
10. Setiawan, A.F.; Arsana, I.M.; Soeryanto, S. Performance Analysis of Reheating Furnace on Billet Heating Production of Reinforced Iron. In Proceedings of the International Joint Conference on Science and Engineering 2022 (IJCSE 2022), Advances in Engineering Research, Surabaya, Indonesia, 10–11 September 2022.
11. Jaklič, A.; Vode, F.; Koleno, T. Online simulation model of the slab-reheating process in a pusher-type furnace. *Appl. Therm. Eng.* **2007**, *27*, 1105–1114. [CrossRef]
12. Steinboeck, A.; Wild, D.; Kiefer, T.; Kugi, A. A mathematical model of a slab reheating furnace with radiative heat transfer and non-participating gaseous media. *Int. J. Heat Mass Transf.* **2010**, *53*, 25–26. [CrossRef]
13. Feliu Batlle, V.; Rivas Pérez, R.; Castillo, F.; Mora, I.Y. Fractional Order Temperature Control of a Steel Slab Reheating Furnace Robust to Delay Changes. In Proceedings of the 5th IFAC Workshop on Fractional Differentiation and its Applications, FDA'12, Nanjing, China, 14–17 May 2012.
14. Prieler, R.; Mayr, B.; Demuth, M.; Holleis, B.; Hochenauer, C.H. Prediction of the heating characteristic of billets in a walking hearth type reheating furnace using CFD. *Int. J. Heat Mass Transf.* **2016**, *53*, 675–688. [CrossRef]
15. Wang, J.; Liu, Y.; Sundén, B.; Yang, R.; Baleta, J.; Vujanović, M. Analysis of slab heating characteristics in a reheating furnace. *Energy Convers. Manag.* **2017**, *149*, 928–936. [CrossRef]
16. Radhika, S.B.; Nasar, A. Internal Model Control based Preheating Zone Temperature Control for Varying Time Delay Uncertainty of the Reheating Furnace. *Int. J. Sci. Res. (IJSR)* **2015**, *4*, 78–82.
17. Marino, P.; Pignotti, A.; Solis, D. Numerical model of steel slab reheating in pusher furnaces. *Lat. Am. Appl. Res.* **2002**, *32*, 257–261.
18. Marino, P.; Pignotti, A.; Solis, D. Control of Pusher furnaces for steel slab reheating using a numerical model. *Lat. Am. Appl. Res.* **2004**, *34*, 249–255.
19. Andreev, S. System of Energy-Saving Optimal Control of Metal Heating Process in Heat Treatment Furnaces of Rolling Mills. *Machines* **2019**, *7*, 60. [CrossRef]
20. Yang, Z.; Luo, X. Optimal set values of zone modeling in the simulation of a walking beam type reheating furnace on the steady-state operating regime. *Appl. Therm. Eng.* **2016**, *101*, 191–201. [CrossRef]
21. *STN 41 1375*; Steel 11 375 Non-Alloy Steel of The usual Qualities Suitable For Welding For Steel Constructions. Available online: https://docplayer.cz/19932075-Csn-41-1523-nelegovana-konstrukcni-jemnozrnna-11-523-stn-41-1523-ocel-vhodna-ke-svarovani-znacka.html (accessed on 1 July 2023).
22. Rédr, M.; Příhoda, M. *Fundamentals of Thermal Engineering*, 1st ed.; SNTL: Praha, Czech Republic, 1991.
23. Sazima, M.; Kmoníček, V.; Schneller, J. *Heat*, 1st ed.; SNTL: Praha, Czech Republic, 1989.

24. Cengel, Y.; Ghajar, A. *Heat and Mass Transfer: Fundamentals and Applications*, 6th ed.; McGraw Hill: New York, NY, USA, 2019.
25. Hašek, P. *Tables for Thermal Engineering*, 11th ed.; VŠB: Ostrava, Czech Republic, 1980.

computation

MDPI

Article

Mathematical Model and Numerical Method of Calculating the Dynamics of High-Temperature Drying of Milled Peat for the Production of Fuel Briquettes

Natalia Sorokova [1,*], Miroslav Variny [2,*], Yevhen Pysmennyy [1] and Yuliia Kol'chik [3]

[1] Department of Atomic Energy, Institute of Atomic and Thermal Energy, National Technical University of Ukraine "Igor Sikorsky Kyiv Polytechnic Institute", Polytechnic 6, 02000 Kiev, Ukraine
[2] Department of Chemical and Biochemical Engineering, Faculty of Chemical and Food Technology, Slovak University of Technology in Bratislava, Radlinského 9, 812 37 Bratislava, Slovakia
[3] Department of Heat Engineering, Kyiv National University of Construction and Architecture, Povitrofloskyi 31, 03037 Kyiv, Ukraine
* Correspondence: n.sorokova@ukr.net (N.S.); miroslav.variny@stuba.sk (M.V.)

Abstract: Milled peat must be dried for the production of peat fuel briquettes. The current trend in the creation of drying technologies is the intensification of the dehydration process while obtaining a high-quality final product. An increase in the temperature of the drying agent, above 300 °C, significantly accelerates the reaching of the final moisture content of the peat. In the final stage, it is also accompanied by partial thermal decomposition of the solid phase. Its first stage, which is the decomposition of hemicellulose, contributes to a decrease in weight and an increase in the caloric content of the dry residue. The development of high-temperature drying modes consists of determining the temperature and velocity of the drying agent, wherein the duration of the material reaching the equilibrium moisture content will be minimal and the temperature of the material will not rise above the second-stage decomposition temperature of cellulose. This problem can be solved by the mathematical modeling of the dynamics of peat particles drying in the flow. The article presents a mathematical model of heat and mass transfer, phase transitions, and shrinkage during the dehydration of milled peat particles. The equations of the mathematical model were built based on the differential equation of mass transfer in open deformable systems, which, in the absence of deformations, turns into the known equation of state. A numerical method for implementing a mathematical model has been developed. The adequacy of the mathematical model is confirmed by comparing the results of numerical modeling with known experimental data.

Keywords: peat; dynamics of drying; mathematical modeling; heat and mass transfer; phase transitions; thermal destruction

Citation: Sorokova, N.; Variny, M.; Pysmennyy, Y.; Kol'chik, Y. Mathematical Model and Numerical Method of Calculating the Dynamics of High-Temperature Drying of Milled Peat for the Production of Fuel Briquettes. *Computation* **2023**, *11*, 53. https://doi.org/10.3390/computation11030053

Academic Editors: Ali Cemal Benim, Rachid Bennacer, Abdulmajeed A. Mohamad, Paweł Oclon, Sang-Ho Suh and Jan Taler

Received: 6 February 2023
Revised: 3 March 2023
Accepted: 3 March 2023
Published: 6 March 2023

1. Introduction

Most modern solid fuel boilers are able to combust peat briquettes. The use of peat for obtaining solid fuel has great potential in the renewable energy of the countries of Central and Northern Europe. Despite the high initial moisture content and lower calorific value than coal, peat has several advantages. The cost of energy obtained from combustion and gasification plants with high efficiency is lower than the cost of energy obtained from gas and oil. Moreover, the content of sulfur and harmful non-combustible impurities is insignificant compared to coal, fuel oil, and shale. An important part of the technological process of manufacturing fuel briquettes from peat, which determines their quality and cost, is drying. The initial moisture content of peat, which is determined by the ratio of the mass of water held in the pores to the mass of the wet sample, can reach 90%. For the production of high-quality briquettes, their moisture content should be 8–10%. Several methods of drying milled peat are known. The least expensive way is in the open ground under the

influence of solar radiation. Such drying is seasonal, as evidenced by the experimental data presented in [1]. Its intensity significantly depends on weather conditions and the thickness of the peat layer, the duration is significant even for a 4 mm layer, and it is not possible to dry the peat to a low equilibrium moisture content. In [2], the advantages of filtration drying are demonstrated. The main advantage is the possibility of mechanical displacement of moisture (due to pressure gradient) from peat immediately after mining and its environmental friendliness. Dehydration is carried out in a dense layer through which the gas flow moves with temperature $T_{\text{d.a.}}$ = 60–100 °C towards the perforated partition, the space below which is connected to the air suction fan. The power of the fan limits the thickness of the layer of wet material and, accordingly, the productivity of the dryer.

In practice, peat drying is carried out in two stages: after extraction under natural conditions to a moisture content of 45–50%, followed by drying to the final moisture content in aerodynamic or drum-type dryers using a mixture of flue gases and air. The choice of drying temperature depends on the size of the peat particles, their initial moisture content and thermophysical properties, as well as the technical capabilities of the dryer. At the same time, a moderately intensive course of the process (flow temperature $T_{\text{d.a.}}$ = 120–170 °C), and a highly intensive course ($T_{\text{d.a.}}$ = 300–500 °C) can be ensured. In the latter case, flue gases are involved as a drying agent. The high-temperature drying of milled peat particles can be accompanied by the thermal decomposition of the solid phase. The temperature interval at the beginning of the thermal destruction of peat is 160–210 °C [3]. At the same time, the decomposition of hemicellulose begins with the release of oxygen-containing gases and pyrogenetic moisture, which helps to reduce the weight and increase the caloric content of the dry residue [4–7]. The next two stages are characterized by the decomposition of cellulose and lignin and begin [3] in the temperature ranges of 260–340 °C and 315–400 °C, respectively. In the presence of air, the processes of the second and third stages of decomposition are exothermic, accompanied by a rapid increase in temperature and a significant loss of the combustible component of peat; these are undesirable in obtaining quality peat briquettes.

The selection of operating parameters of the drying agent, at which the temperature at any point of the particle will stay below the temperature of the beginning of cellulose decomposition, will ensure effective high-temperature drying. The possibilities of experimental methods for researching transfer processes during the drying of porous materials are limited by determining the average values of their moisture content and temperature. The development of an adequate mathematical model of the dynamics of the milled peat particle drying must account for all the determining factors and the method of its implementation. In this case, it allows studying the range of temperature and concentrations of the components of the bound substance to determine optimal process conditions.

In the mathematical description of interrelated processes of heat and mass transfer and phase transitions in theories of drying, a unified phenomenological approach has not yet been formed [8–19]. Differences in mathematical models are related to the number of involved equations and approaches used to determine the I_V intensity function of phase transitions between the liquid and vapor phases in the internal points of the porous body. In general, the number of transfer equations in a mathematical model is determined by the number of system state parameters to be determined, as well as interphase interaction parameters, in particular the I_V.

In [9], a mathematical model of the low-temperature drying of a peat layer in the soil is presented, assuming that the temperatures in the thin layer of the peat and the surrounding air are the same. The peat layer is considered as a multi-component system containing a solid base, a liquid, and a gas phase. Vapor and air phases are not considered separately. The system of equations contains the mass transfer equation of the gas phase, which considers the filtration transfer and the intensity of the formation of the vapor phase. The filtration rate is determined by Darcy's law, whereas, for the correct determination of the pressure change in the gas phase, it is necessary to have information on the change in the volume fraction of vapor in the vapor-air mixture. The energy transfer equation takes into

account the influence of thermal conductivity, filtration movement in the pores of the gas phase, and the thermal effect of liquid evaporation on the porous peat layer's temperature state. However, in the micropores, there is diffusion transfer of both gas and liquid phases. The liquid phase transfer equation is written under the assumption that the change in liquid concentration occurs only due to evaporation, whereas the expression for the evaporation rate contains the volume concentration of the liquid phase. The article does not contain information about the mathematical model's method of numerical implementation. In addition, filtration transfer, as a rule, is not manifested in drying processes of moderate intensity [10]. In [11], a mathematical model of low-temperature drying of capillary-porous material in sludge is presented. The model is written for the case of diffusion-filtration heat and mass transfer and includes equations of energy transfer and mass transfer of the liquid phase. To determine the effective values of the thermophysical properties of wet sludge, the diffusion coefficient, and the intensity of phase transitions, semi-empirical equations are used. Obtaining these requires a significant amount of experimental information. The effective diffusion coefficient is represented by a polynomial function of the sixth order relative to the mass content of the liquid phase. It is known that the intensity of diffusion processes significantly depends on the temperature [12], which is indirectly taken into account in the presented dependence.

In the mathematical model of drying in a fluidized bed of processed pumpkin pulp [13], the one-hour efficiency of the apparatus for dry product Π per volume unit V of the drying chamber is considered as the desired value. The calculated dependence $\Pi(W,T,V)$ and the empirical equation for the drying rate dW/dt are presented based on experimental data on the drying kinetics. Using the proposed approach to obtain results for other dispersed materials requires new experiments.

In [14], a mathematical model of heat and mass transfer during drying in a fluidized bed of spherical particles of baker's yeast was built, which includes equations of energy transfer and filtration transfer of vapor and liquid phases. The intensity of phase transitions I_V is determined by differentiating the sorption equation. With this approach, the I_V for the case of stationary heat and mass transfer is zero, while during stationary processes, the value of I_V can be of the same order as for non-stationary processes.

In [15], a mathematical model of the dynamics of filtration drying of vegetable raw materials in the period of decreasing velocity was built. This model includes the kinetic equation of mass transfer. It characterizes the velocity of movement of the moisture front inside the particle, the equation for the boundary condition of the third kind at the boundary between the solid body and the heating agent, and the equation for the change in the moisture content of the heating agent along the height of the material layer. For its conclusion, empirical equations were obtained by summarizing experimental data. This allows us to evaluate the interconnection between the moisture content of the material and the gas flow.

The mathematical model of drying dynamics of A.V. Luikov [10,16] for the case of a high-intensity process contains three differential equations—energy, moisture mass transfer, and filtration. The I_V function is determined through the phase transition criterion. It represents the ratio of the change in moisture content of the material due to evaporation to the total change in moisture content due to mass transfer and phase transitions. However, these processes can take place independently of each other. That is why such a technique is represented by the introduction of an additional unknown function, the estimation of which requires conducting physical experiments. It should be noted that the model of A.V. Luikov is quite widely used for the theoretical description of the drying process [17–22]. Therefore, the phase transition criterion is defined for a sufficiently wide range of materials. In [17–21], the solution of the differential equations system of heat and mass transfer is carried out by an analytical method under several assumptions. In [22,23], the expediency of using numerical methods for the simultaneous solution of nonlinear differential transfer equations included in the mathematical model of the drying dynamics of porous materials is demonstrated.

In [24], a mathematical model of the kinetics of high-temperature peat drying is presented. It includes the thermal conductivity equation for a porous particle written in a linear form and the Stefan boundary condition for heat transfer problems with moving boundaries due to phase transitions. At the same time, it is assumed that the change in moisture content W occurs only due to evaporation. The phase transition boundary divides the volume of the particle into a dry region (without the liquid phase) and a wet region (where the moisture content does not change and remains equal to the initial one). Such assumptions are quite controversial from a physical point of view. However, they allow us to use the quasi-stationary method of Leibenzon [25] to solve the problem and obtain curves of changes in the average moisture content.

The paper [23] describes the molecular radiation theory of heat and mass transfer. It is mainly based on the law of particle spectral-radiation intensity by N.I. Nikitenko, which made it possible to mathematically describe the activation processes of evaporation [26] and diffusion transfer [12]. This made it possible to build closed mathematical models of the drying dynamics of consolidated and dispersed capillary-porous materials and colloidal capillary-porous materials and solved several practical problems [8,27,28].

This work presents a mathematical model of high-temperature drying of milled peat. In the final stage, it is accompanied by the initial stage of thermal destruction. The mathematical model includes differential equations of energy and mass transfer of liquid, vapor, and air phases. They are built based on the differential equation of substance transfer (mass, energy, and momentum) for the deformable bodies [23,28]. The mathematical model includes also the following additional equations:

- Darcy's law for calculating the filtration velocities of the phases;
- the equation of state for calculating the pressures of the gas phase components;
- the expression for the capillary pressure of the liquid;
- the formula for the contact surface area of the liquid and gas phases in the pores of the body;
- the thermal-concentration deformation equation;
- the formulas for the intensity of the phase transitions on the outer and inner surfaces of peat particles and the diffusion coefficients of the liquid and gas phases.

During the drying process, under the action of heating when a certain temperature is reached, the process of thermal decomposition of peat begins. In [5,7], the activation nature of the thermal decomposition of the milled peat solid phase is experimentally proved. Processing of the derivatographic studies results [6] of the thermal properties of the milled peat solid residue, using the kinetic model of A.A. Broido [29], made it possible to determine the numerical values of the effective activation energy, A_{ef}, of the bound substance particles. The A_{ef} value [6] for crushed milled peat was included in the mathematical model. A numerical method for calculating a mathematical model has been developed. It allows for the determination of the dynamics of changes in temperature and volume concentrations of the bound substance components in a porous particle, depending on its thermophysical, structural, and geometric characteristics, as well as the parameters of the drying agent. The development of drying modes of porous materials is based on specific calculations. They ensure a reduction in the time of the process and, accordingly, energy resources for its implementation while maintaining the high quality of the final product.

2. Materials and Methods

2.1. Mathematical Model

In a wet state, milled peat is a heterogeneous system that includes a base, in the pores of which liquid, vapor, and air phases are kept. When the system is heated, each component of the substance bound to the base begins to change its concentration as a result of diffusion and filtration mass transfer. This also happens as a result of the phase transition of a liquid to vapor. Peat belongs to the class of colloidal capillary-porous materials [10], the volume of which can decrease several times upon drying. Material shrinkage, in turn, significantly affects the dynamics of transfer processes [8,10,20,23,27,28,30,31]. Particles of milled peat

when crushed have a shape close to spherical [24]. In a drum-type or aerodynamic dryer, the uniform runaround of particles with a flow is achieved. The parameters of the flow along the length of the drying chamber will be kept unchanged. In this case, the mathematical model of diffusion–filtration heat and mass transfer, phase transitions, and deformation during high-temperature drying of milled peat particles is represented by a system of differential Equations (1)–(4):

$$c_{\text{ef}}\left(\frac{\partial T}{\partial t} + w_{\text{ef}\,r}\frac{\partial T}{\partial r}\right) = \frac{1}{r^2}\frac{\partial}{\partial r}\left(\lambda_{\text{ef}} r^2 \frac{\partial T}{\partial r}\right) - LI_V \tag{1}$$

$$\frac{\partial U_{\text{fl}}}{\partial t} + \frac{\partial (w_{\text{fl}\,r} U_{\text{fl}})}{\partial r} = \frac{1}{r^2}\frac{\partial}{\partial r}\left(D_{\text{fl}} r^2 \frac{\partial U_{\text{fl}}}{\partial r}\right) - I_V - \frac{U_{\text{fl}}}{1-\varepsilon_V}\frac{\partial \varepsilon_V}{\partial t} \tag{2}$$

$$\frac{\partial U_{\text{v}}}{\partial t} + \frac{\partial (w_{\text{g}\,r} U_{\text{v}})}{\partial r} = \frac{1}{r^2}\frac{\partial}{\partial r}\left(D_{\text{v}} r^2 \frac{\partial U_{\text{v}}}{\partial r}\right) + I_V - \frac{U_{\text{v}}}{1-\varepsilon_V}\frac{\partial \varepsilon_V}{\partial t} \tag{3}$$

$$\frac{\partial U_{\text{ai}}}{\partial t} + \frac{\partial (w_{\text{g}\,r} U_{\text{ai}})}{\partial r} = \frac{1}{r^2}\frac{\partial}{\partial r}\left(D_{\text{ai}} r^2 \frac{\partial U_{\text{ai}}}{\partial r}\right) - \frac{U_{\text{ai}}}{1-\varepsilon_V}\frac{\partial \varepsilon_V}{\partial t}\,. \tag{4}$$

Here, T—temperature; U_{fl}, U_{v} and U_{ai}—volume concentrations of liquid, steam, and air; t—time; c_{ef}—effective specific volumetric heat capacity of a peat particle, $c_{\text{ef}} = c_b\rho_b\Psi_b + c_{\text{fl}}U_{\text{fl}} + c_v U_v + c_{\text{ai}}U_{\text{ai}}$, c_b, c_{fl}, c_{v} and c_{ai}—specific mass heat capacities of the solid phase, water, steam and air, ρ_b and Ψ_b—density and volume fraction of the solid phase; λ_{ef}—effective thermal conductivity: $\lambda_{\text{ef}} = \lambda_b\Psi_b + \lambda_{\text{fl}}U_{\text{fl}}/\rho_{\text{fl}} + \lambda_v U_v/\rho_v + \lambda_{\text{ai}}U_{\text{ai}}/\rho_{\text{ai}}$; D_{fl}, D_{v} and D_{ai}—diffusion coefficients of liquid, vapor and air phases; I_V—the intensity of phase transitions in the body pores; L—latent heat of phase transitions; ε_V—relative volumetric strain; $w_{\text{ef}r}$—effective rate of filtration of the bound substance along the coordinate r, $w_{\text{ef}r} = \left[w_{\text{fl}r}\, c_{\text{fl}}U_{\text{fl}} + w_{gr}\,(c_v U_v + c_{\text{ai}}U_{\text{ai}})\right]/c_{\text{ef}}$, where $w_{\text{fl}r}$, $w_{\text{gr i}}$—filtration rates of liquid and gas phases.

The diffusion coefficient of the liquid phase is determined by the formula of N.I. Nikitenko [12]: $D_{\text{fl}} = \gamma_{D\text{fl}}[exp(A_D/R_uT) - 1]^{-1}$, where R_u—universal gas constant, A_D—activation energy of diffusion transfer, $\gamma_{D\text{fl}}$—diffusion coefficient. This formula is present in boundary cases, when $A_D/(R_uT) >> 1$ it becomes the empirical Arrhenius formula for solid bodies, and, when $A_D/(R_uT) << 1$ it becomes the Einstein formula for liquid medium. Diffusion coefficients for gas phase components are found according to the well-known formula [32]: $D_v = D_{\text{ai}} = \gamma_{Dv}T^{3/2}/P_{\text{g}}$, where P_{g}—gas phase pressure, $\gamma_{D\text{fl}}$—diffusion coefficient.

The filtration rates of the liquid w_{fl} and gas w_{g} phases are proportional to the pressure gradients of the corresponding phase and can be calculated with Darcy's Equation (5):

$$w_\psi = -\frac{K_0 K_\psi}{\eta_\psi}\nabla P_\psi,\ \psi = \text{fl},\ \text{g}. \tag{5}$$

Here, K_0—total permeability of the medium; K_ψ—relative permeability of the phase ψ; η_ψ—dynamic viscosity coefficient of the phase ψ.

The pressures of the liquid P_{fl} and gas P_{g} phases are calculated through functions U_{fl}, U_{v}, $U_{\text{ai,}}$ and T. For this, the volume fractions of the body Ψ_{b}, liquid Ψ_{fl}, and gas Ψ_{g} in the material are determined according to the following relations: $\Psi_{\text{b}} = 1 - \Pi$, $\Psi_{\text{fl}} = U_{\text{fl}}/\rho_{\text{fl}}$ and $\Psi_{\text{g}} = 1 - \Psi_{\text{b}} - \Psi_{\text{fl}}$, where Π—peat porosity and ρ_{fl}—liquid phase density. The partial densities of steam and air are equal, $\rho_{\text{v}} = U_{\text{v}}/\Psi_{\text{g}}$ and $\rho_{\text{ai}} = U_{\text{ai}}/\Psi_{\text{g}}$, respectively. Partial pressures are found using the equation of state for diluted gases $P_{\text{v}} = \rho_{\text{v}}R_{\text{u}}T/\mu_{\text{v}}$ and $P_{\text{ai}} = \rho_{\text{ai}}R_{\text{u}}T/\mu_{\text{ai}}$. The pressure of the gas mixture will be $P_{\text{g}} = P_{\text{v}} + P_{\text{ai}}$. Liquid phase pressure will be $P_{\text{fl}} = P_{\text{g}} + P_{\text{cap}}$, where the capillary pressure P_{cap} is calculated [8,23] as the average capillary pressure of the liquid. The volume of liquid $dV(r)$, contained in capillaries with a radius from r to $r + dr$ in a unit volume of the body is proportional to the differential function $f(r)$ of the capillary size distribution and the volume fraction $\theta(r)$ of the capillary, which is occupied by liquid: $dV(r) = \theta(r)f(r)dr$. Then, the average value of the capillary

pressure at a given point of the body is represented by an expression similar to the Laplace Equation (6):

$$P_{\text{cap}} = 2\sigma(T) \int_{r_{\min}}^{r_{\max}} \frac{\theta(r)}{r} f(r)dr / \int_{r_{\min}}^{r_{\max}} \theta(r)f(r)dr = \frac{2\sigma(T)}{r*},\ r_{\min} < r* < r_{\max} \tag{6}$$

where $r_{\min}$, $r_{\max}$—minimum and maximum pores radius and *r**—characteristic parameter of pore size dispersion.

The function $\theta(r,t)$ in a capillary of radius r at time t is determined by the expression obtained as the ratio of the cross-sectional area of the capillary occupied by liquid to its total cross-sectional area $\theta(r,t) = \pi\left[r^2 - (r-\delta)^2\right]/\pi r^2 = 2\delta/r - \delta^2/r^2 = 1 - (1-\delta/r)^2$. Where δ is the thickness of the liquid layer on the walls of partially-filled capillaries. It was obtained by the formula for the equilibrium thickness of the condensate layer on a solid surface obtained in [26], Equation (7):

$$\delta = \delta*\overline{\delta} = \delta*\left(1 - \sqrt{1-\varphi}\right) \tag{7}$$

Here, φ—degree of saturation of the steam and gas mixture at a given temperature, $\varphi = P_{\Pi}/P_{\text{H}}(T)$; δ*—the average displacement length of an activated particle in the liquid layer, $\delta^* = A/(\xi n)$. Where A is activation energy at which a liquid particle can move, $\xi = \text{const}$—coefficient of resistance to the particle movement to the free surface of the body, n—density of evaporating molecules, $n = U_{\text{fl}}N_A/\mu$, μ—molar mass, N_A—the Avogadro number; $\overline{\delta} = \delta/\delta*$ when $0 < \delta < \delta*$ and $\overline{\delta} = 1$ when $\delta > \delta*$. The value δ* can be considered as the thickness of the boundary layer. It is adjacent to the free surface of a rather massive, condensed body in which the evaporation process takes place.

The saturation pressure was calculated according to the formula of N.I. Nikitenko [26], Equation (8):

$$P_s = N_P\sqrt{T}[\exp(A/R_uT) - 1]^{-1},\ N_P = \text{const}. \tag{8}$$

The values of A and N_P can be found as a result of the solution of the system of two equations obtained by writing Equation (8) for two points on the saturation line. They correspond to the values of T_1, P_{s1} and T_2, P_{s2} in the table of saturated steam and water, respectively. Formula (8) is valid for liquids of various natures and is quite accurate. This is the case when dividing the temperature interval of the existence of water into two areas $0 < T < 100$ °C and $100 < T < 374$ °C. The maximum errors of calculated and tabular data were: $\Pi_{\max} = 3.4\%$ when $A' = 0.4206 \times 10^8$ J/mol and $N = 0.4361 \times 10^{10}$ kg/(m·s^2·K$^{0.5}$) for the first interval, and $\Pi_{\max} = 2.6\%$ when $A' = 0.3689 \times 10^8$ and $N = 0.8514 \times 10^9$ for the second interval. Here is $A' = AN_A$.

The intensity of liquid evaporation on the outer surface of thorium particles is found as the resulting flow of evaporating and condensing particles [23,26] according to the Formula (9):

$$I = \gamma_{\text{c}}\left\{\varphi_{\text{b}}\left(\exp\left[\frac{A}{R_{\text{u}}\,T|_{\nu=0}}\right] - 1\right)^{-1} - \varphi_{\text{e.m.}}\left(\exp\left[\frac{A}{R_{\text{u}}T_{\text{e.m.}}}\right] - 1\right)^{-1}\right\} \tag{9}$$

Here, γ_{c}—coefficient of evaporation from the surface, $\gamma_{\text{c}} = \varepsilon\rho_{\text{fl}}\delta*/4$; ε—coefficient of evaporation; φ_{b}—moisture content of the body, which can be considered as the relative moisture content of the steam and gas mixture, which, according to the sorption isotherm, corresponds to the volume concentration of the liquid (7): $\varphi_{\text{b}} = \overline{\delta}(2 - \overline{\delta})$.

The intensity of evaporation in the pores of the body is found by the formula that follows from (9) under the condition of local thermodynamic equilibrium of coexisting phases:

$$I_V = \gamma_{\text{c}}\left[\exp\left(\frac{A}{R_{\text{u}}T}\right) - 1\right]^{-1}(\varphi_{\text{b}} - \varphi)S \tag{10}$$

Here, S is the contact area of the liquid and gas phases in the pores of the body unit volume that are not completely filled with liquid. The function S varies from zero, in the case of capillaries completely filled with liquid, to the value of the specific surface of the pores $S_{\max}$ [33] freed from the liquid. This function can be determined based on the equation of the sorption isotherm [23]. According to the equation $\varphi = f_{\varphi}(U_{\text{fl}})$ the relative moisture content of the air φ is found, which corresponds to the volume concentration of the liquid U_{fl} at the considered point of the porous body. Formula (7) determines the average thickness δ of the condensate layer on the surfaces of partially-filled capillaries. During the time interval dt, as a result of the processes of evaporation and heat and mass transfer, the thickness δ will change by the value $d\delta$. This value is found when differentiating (7): $d\delta = \delta^* d\varphi/(2\sqrt{1-\varphi})$. The volume concentration of the liquid will change in the same period of time to $dU_{\text{fl}} = \rho_{\text{fl}} S d\delta$. Here, the expression for the contact area of the phases S is represented by the Equation (11):

$$S = \frac{2\sqrt{1-\varphi_{\text{b}}}}{\rho_{\text{fl}}\delta*}\frac{\partial U_{\text{fl}}}{\partial \varphi_{\text{b}}} \tag{11}$$

The derivative $\partial U_{\text{fl}}/\partial\varphi_{\text{b}}$ is determined by differentiating the desorption isotherm equation. For wood peat, the results on the equilibrium moisture content [10] are rather well-approximated by the equation $U_{\text{fl}} = 0.3U_{\max}(\varphi_{\text{b}}/(1-\varphi_{\text{b}}))^{1/3}$.

The relative volume deformation ε_V is based on the differential equation of the thermal-concentration deformation [23]. In spherical coordinates, for the case of uniform blowing of the body, when there is axial symmetry of the deformation and the radial displacement u_r depends only on the radius r, and there are no displacements u_{φ}, u_{θ} in the directions of φ and θ, the thermal-concentration deformation equation is represented in the following form (12):

$$2\frac{d}{dr}\left(G\frac{du_r}{dr}\right) + \frac{d}{dr}\left(G_1\frac{du_r}{dr}\right) + 2\frac{d}{\partial r}\left(\frac{u_r}{r}\right) + \frac{4G}{r}\left(\frac{du_r}{dr} - \frac{u_r}{r}\right) - \frac{d}{dr}[N(2G+3G_1)] = 0 \tag{12}$$

Here, G, G_1—Lamé coefficients, $G = E_y/[2(1+\nu_{\Pi})]$, $G_1 = E_y\nu_{\Pi}/[(1-2\nu_{\Pi})(1+\nu_{\Pi})]$; ν_{Π}—Poisson's ratio; E_y—modulus of elasticity; N—thermal-concentration function [34,35], which determines the change in the specific volume of a body during its free expansion caused by the processes of thermal conductivity, diffusion, filtration, phase, and chemical transition, $N = \beta_T(T - T_0) + \sum\limits_{\psi}\beta_{\psi}(\omega_{\psi} - \omega_{\psi 0})$. There $\beta_T = (\partial x/\partial T)/x$ and $\beta_{\psi} = (\partial x/\partial\omega_{\psi})/x$ are average coefficients of thermal and concentration expansion in the intervals of temperature [T, T_0] and mass concentration of the component ψ [ω_{ψ}, $\omega_{\psi 0}$]. The function ε_V is related to the normal components ε_{rr}, $\varepsilon_{\varphi\varphi}$, $\varepsilon_{\theta\theta}$ of the deformation tensor ε_{ij} (i, j = 1, 2, 3) by the relation $\varepsilon_V(t) = [1+\varepsilon_{rr}(t)][1+\varepsilon_{\phi\phi}(t)][1+\varepsilon_{\theta\theta}(t)] - 1]$, where $\varepsilon_{rr} = du_r/dr$, $\varepsilon_{\varphi\varphi} = \varepsilon_{\theta\theta} = u_r/r$. If the body is capillary-porous, its shrinkage during drying can be neglected, and $\varepsilon_V = 0$.

The influence of the thermal decomposition of peat on the dynamics of drying is accounted for, given that the processes of thermal destruction, diffusion, and evaporation are activational [3–7,23]. Pyrogenetic water is removed together with the remains of free water and the one bound to the solid phase of peat. As was studied in [5], the beginning of the thermal decomposition stage in the process of milled peat dehydration is characterized by a noticeable decrease in the effective activation energy of moving microparticles. This means there is a diffusion transfer of molecules of a pyrogenetic water mixture, which begins to be released during the thermal decomposition of hemicellulose, and the remains of natural water contained in the peat pores. This transfer will occur when they reach a lower energy level than the activation energy of microparticles of bound water. It has been considered that A.V. Luikov's kinetic equation of drying [10,16] and the kinetic equation of thermal conversion by A.A. Broido [29] have the same structure. This means that the differential equations of substance transfer can be used to adequately describe the dynamics of compatible drying processes and the first stage of thermal decomposition. Thus, the data

on the temperature T_t of the beginning of the thermal decomposition of peat and the values of the effective energy of activation A_{ef} are obtained. Thus, in the process of calculating the dynamics of high-temperature drying based on the mathematical model (1)–(4), as the temperature T_t is reached in individual points of the peat particles, the values of A_{ef} should be included in the formulas for D_{fl}, P_s, I_v and I.

2.2. Single-Valued Condition

While modeling drying processes, it can be assumed that the milled peat was in equilibrium with the surrounding environment before the initial moment of time. Its initial temperature T_0 and pressure P_g of the steam and gas mixture in the internal points of the body are equal to the environmental temperature $T_{e.m.}$ and pressure $P_{e.m.}$, respectively.

The conditions of heat and mass transfer at the boundary $r = 0$ represent the conditions of symmetry of the temperature fields and volume concentrations of the bound substance components, Equation (13):

$$\left.\frac{\partial T}{\partial r}\right|_{r=0} = 0, \ \left.\frac{\partial U_{fl}}{\partial r}\right|_{r=0} = 0, \ \left.\frac{\partial U_v}{\partial r}\right|_{r=0} = 0, \ \left.\frac{\partial U_{ai}}{\partial r}\right|_{r=0} = 0 \tag{13}$$

At the outer boundary $r = R$, there are conditions of the third kind, Equations (14)–(17):

$$\lambda_{ef}\left.\frac{\partial T}{\partial r}\right|_{r=R} + w_{ef\,r}\left.\frac{\partial T}{\partial r}\right|_{r=R} = \alpha(T|_{r=R} - T_{e.m.}) - L\,I|_{r=R} \tag{14}$$

$$D_{fl}\left.\frac{\partial U_{fl}}{\partial r}\right|_{r=R} + \left.\frac{\partial (w_{fl\,r}U_{fl})}{\partial r}\right|_{r=R} = I|_{r=R} \tag{15}$$

$$-D_v\left.\frac{\partial U_v}{\partial r}\right|_{r=R} + \left.\frac{\partial (w_{vr}U_v)}{\partial r}\right|_{r=R} = \gamma_{v,e.m.}\left(U_v|_{r=R} - \rho_{v,e.m.}\psi_v\right) \tag{16}$$

$$U_{ai}|_{r=R} = \frac{P_{e.m.}\psi_g\mu_{ai}}{R_u\,T|_{r=R}} - U_{ai}|_{r=R}\frac{\mu_{ai}}{\mu_v} \tag{17}$$

Expression (16) is obtained from [23] considering the following conditions: when the system enters the equilibrium state $t \to \infty$, parameters $\rho_v = \rho_{v,e.m.}$, $T|_{r=R} = T_{e.m.}$.

The formula for heat transfer in a fluidized bed can be used to determine the heat transfer coefficient α [36]: $Nu = 0.03Pr^{0.33}Re$. The similarity criteria Nu and Re include a diameter of the peat particle that depends on time due to shrinkage.

2.3. Numerical Method of Solution

The system of differential Equations (1)–(4) under boundary conditions (13)–(17), closed by relations (5)–(12), is essentially nonlinear. Its implementation is possible using a numerical method. Equations (1)–(4) contain convective terms, and for their solution, it is advisable to use the explicit three-layer scaling difference circuit of N.I. Nikitenko. [22]. An advantage of this circuit is [27] the simplicity characteristic of all explicit circuits, and, similar to the known implicit circuits, it allows the choosing of arbitrary time steps without deteriorating the accuracy of the solution. In addition, mass transfer Equations (2)–(4) contain terms related to peat shrinkage. To take into account its influence on the required functions, the procedure of splitting the algorithm by physical factors is involved. The difference approximations of the differential Equations (1)–(4) are built on the non-uniform difference grid $r_i = ih$, ($i = 0, 1, \ldots, IK$; $h \neq$ const), $t_n = nl$ ($n = 0, 1, \ldots, l > 0$). There, h is the spatial coordinate step, and l is the time step. At the initial time, the following applies: $h = d/(2 \cdot IK)$, where d is the peat particle diameter (Figure 1).

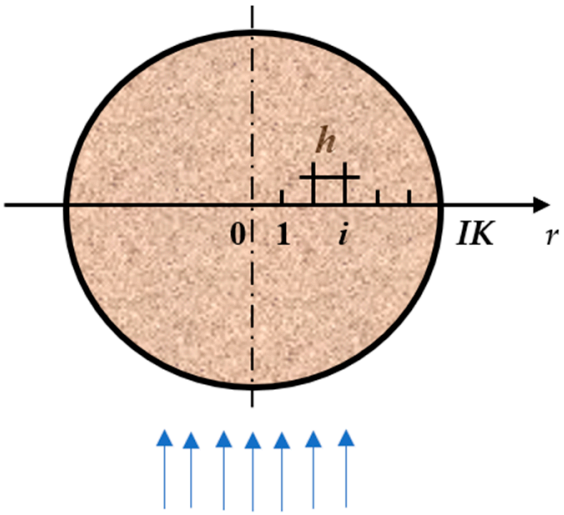

Figure 1. View of the computational domain.

Per the mentioned approach, the difference approximation of the liquid phase transfer Equation (2) is represented by the Equations (18)–(20):

$$\frac{\overline{U}_{\mathrm{fl}_i}^{n+1} - U_{\mathrm{fl}_i}^{n}}{l} = -\left[\left((w_{\mathrm{fl}r}U_{\mathrm{fl}})_{i+1}^{n} - (w_{\mathrm{fl}r}U_{\mathrm{fl}})_{i}^{n}\right) - \left((w_{\mathrm{fl}r}U_{\mathrm{fl}})_{i}^{n} - (w_{\mathrm{fl}r}U_{\mathrm{fl}})_{i-1}^{n}\right)\right] / \left(2h^2\right) \quad (18)$$

$$\begin{gathered}(1+\Omega_{\mathrm{fl}})\frac{\widetilde{U}_{\mathrm{fl}_i}^{n+1} - \overline{U}_{\mathrm{fl}_i}^{n+1}}{l} - \Omega_{\mathrm{fl}}\frac{U_{\mathrm{fl}_i}^{n} - U_{\mathrm{fl}_i}^{n-1}}{l} = \\ = -\left[\left((w_{\mathrm{fl}r}\overline{U}_{\mathrm{fl}})_{i+1}^{n} - (w_{\mathrm{fl}r}\overline{U}_{\mathrm{fl}})_{i}^{n}\right) - \left((w_{\mathrm{fl}r}\overline{U}_{\mathrm{fl}})_{i}^{n} - (w_{\mathrm{fl}r}\overline{U}_{\mathrm{fl}})_{i-1}^{n}\right)\right] / (2h^2) + \\ + \frac{1}{2r_i^2}\left[\left(D_{\mathrm{fl}_{i+1}}r_{i+1}^2 + D_{\mathrm{fl}_i}r_i^2\right)\left(\overline{U}_{\mathrm{fl}_{i+1}}^{n} - \overline{U}_{\mathrm{fl}_i}^{n}\right) - \left(D_{\mathrm{fl}_i}r_i^2 + D_{\mathrm{fl}_{i-1}}r_{i-1}^2\right)\left(\overline{U}_{\mathrm{fl}_i}^{n} - \overline{U}_{\mathrm{fl}_{i-1}}^{n}\right)\right] / h^2 - I_V,\end{gathered} \quad (19)$$

$$\frac{U_{\mathrm{fl}_i}^{n+1} - \widetilde{U}_{\mathrm{fl}_i}^{n+1}}{l} = \frac{\widetilde{U}_{\mathrm{fl}_i}^{n+1}}{1+\varepsilon_V}\frac{{\varepsilon_V}^{n+1} - {\varepsilon_V}^{n}}{l} \quad (20)$$

Equations (3) and (4) are approximated similarly. The differential approximation of the energy Equation (1) based on an explicit scaling difference circuit is represented by two Equations (21) and (22):

$$\frac{\overline{T}_i^{n+1} - T_i^{n}}{l} = -\left[\left((w_{\mathrm{ef}r}T)_{i+1}^{n} - (w_{\mathrm{ef}r}T)_{i}^{n}\right) - \left((w_{\mathrm{ef}r}T)_{i}^{n} - (w_{\mathrm{ef}r}T)_{i-1}^{n}\right)\right] / \left(2h^2\right) \quad (21)$$

$$\begin{gathered}(1+\Omega_{\mathrm{T}})\frac{T_i^{n+1} - \overline{T}_i^{n+1}}{l} - \Omega_{\mathrm{T}}\frac{T_i^{n} - T_i^{n-1}}{l} = \\ = -\left[\left((w_{\mathrm{ef}r}\overline{T})_{i+1}^{n+1} - (w_{\mathrm{ef}r}\overline{T})_{i}^{n+1}\right) - \left((w_{\mathrm{ef}r}\overline{T})_{i}^{n+1} - (w_{\mathrm{ef}r}\overline{T})_{i-1}^{n+1}\right)\right] / (2h^2) + \\ + \frac{1}{c_{\mathrm{ef}}}\left\{\frac{1}{2r_i^2}\left[\left(\lambda_{\mathrm{ef}i+1}r_{i+1}^2 + \lambda_{\mathrm{ef}i}r_i^2\right)\left(\overline{T}_{i+1}^{n+1} - \overline{T}_i^{n+1}\right) - \left(\lambda_{\mathrm{ef}i}r_i^2 + \lambda_{\mathrm{ef}i-1}r_{i-1}^2\right)\left(\overline{T}_i^{n+1} - \overline{T}_{i-1}^{n+1}\right)\right] / h^2 - I_V\right\}\end{gathered} \quad (22)$$

The boundary condition (15) for the surface $r = R$ is represented by the finite difference Equation (23):

$$\begin{gathered}D_{\mathrm{fl}}\frac{U_{\mathrm{fl}IK}^{n+1} - U_{\mathrm{fl}IK-1}^{n+1}}{h} + U_{\mathrm{fl}IK-1}^{n+1}\frac{K_0K_{\mathrm{fl}}}{\eta_{\mathrm{fl}}}\frac{P_{\mathrm{fl}IK}^{n} - P_{\mathrm{fl}IK-1}^{n}}{h} = \\ = \gamma_c\left\{\varphi_{\mathrm{b}IK}\left[\exp\left(\frac{A}{R_u\overline{T}_{IK}^{n}}\right) - 1\right]^{-1} - \varphi_{\mathrm{e.m.}}\left[\exp\left(\frac{A}{R_uT_{\mathrm{e.m.}}}\right) - 1\right]^{-1}\right\}\end{gathered} \quad (23)$$

Similar difference equations approximate the boundary conditions (14), (16), and (17). The approximation error of differential Equations (1)–(4) by difference equations of the form (18)–(20) has the order of $O(l + h^2)$. The weight parameter Ω_ψ (ψ = T, fl, v, ai) allows to increase in the time step, $\Omega_\psi \geq 0$. The necessary conditions for the stability of the difference equations, obtained based on the method of a conditional set of some required functions of the system [22], have the form of inequality (24):

$$l_\psi \leq \left\{ \frac{h}{w_r}; (1 + 2\Omega_\psi) \frac{h^2}{2\nu_\psi} \right\}, \ (\psi = \text{T, fl, v, ai}) \tag{24}$$

where $w_r = w_{efr}$, $\nu_\psi = \lambda_{ef}/c_{ef}$, $\Omega_\psi = \Omega_T$ when ψ = T; $w_r = w_{flr}$, $\nu_\psi = D_{fl}$, $\Omega_\psi = \Omega_{fl}$ when ψ = fl; $w_r = w_{gr}$, $\nu_\psi = D_v$, $\Omega_\psi = \Omega_v$ when ψ = v; $w_r = w_{gr}$, $\nu_\psi = D_{ai}$, $\Omega_\psi = \Omega_{ai}$ when ψ = ai. The calculated time step for the solution of the system (1)–(4) is selected from the condition $l \leq min(l_T; l_{fl}; l_v; l_{ai})$. In accordance with (24), Ω_T, Ω_{fl}, Ω_v and Ω_{ai} are determined after the optional sampling of the difference grid h steps.

2.4. Approbation

To confirm the adequacy of the mathematical model (1)–(4) and the effectiveness of the numerical method, a comparison was made. It consisted of the results of the calculation of the dynamics and kinetics of lowland peat particles drying in the airflow and the results of an experimental study of the peat particles drying kinetics under the same initial conditions. The particles were placed on a mesh surface made of aluminum and evenly blown with atmospheric air with a temperature of $T_{e.m.}$ = 120 °C, at velocity of $w_{e.m.}$ = 1 m/s and moisture content of $d_{e.m.}$ = 10 g/kg of dry air. The shape of the particles was close to spherical with a diameter of 7 mm, the initial temperature was T_0 = 291 K, the initial moisture content—W_0 = 0.97 kg/kg, the porosity—Π = 0.6, the specific surface area $S_{max} = 8 \times 10^5$ m^2/kg. For the calculation, thermophysical parameters of peat were taken [37]: λ_b = 0.08 W/(m·K); c_b = 1970 J/(kg·K); ρ_b = 700 kg/m^3. The activation energy was $A = A_D = 0.4350 \times 10^8$ J/kmol [5]. The constants used in the calculation are presented in Table 1. The constants for the coefficients of diffusion and evaporation from surface are determined by the experimental verification.

Table 1. Values of refined constants.

Name	Meaning
Constants for coefficients of diffusion,	$\gamma_{Dfl} = 0.9 \times 10^{-8}$ m^2/s; $\gamma_{Dv} = 0.134 \times 10^{-4}$ m^2/s;
Coefficient of evaporation from surface,	$\gamma_c = 0.2578 \times 10^{-4}$ kg/(m^2·s);
Total permeability of the medium,	$K_0 = 1 \times 10^{-5}$;
Relative permeability of the fluid,	$K_{fl} = 0.2 \times 10^{-14}$;
Relative permeability of the gas,	$K_g = 1.1 \times 10^{-8}$;
Characteristic parameter of pore size dispersion	$r^* = 1 \times 10^{-8}$ m.

Figure 2 shows the curves of changes over time in the average moisture content of a peat particle, obtained by numerical and physical experiments. It also presents the results of calculating the change in the average temperature of the particle and the temperature on its outer surface. The maximum error of the difference of the values does not exceed 4%. This indicates the possibility of using the developed mathematical model and calculation method to study the dynamics of peat drying in a dispersed state in the aerodynamic layer.

Figure 3 shows the time dependencies of coordinates of spatial nodal points along the peat particle radius. At the beginning of the drying process, the most significant changes in the liquid phase volume concentration, U_{fl}, take place at the outer boundary. Due to shrinkage, the surface area of the external forces tends to decrease. The inner layers of the particle, in which the volume concentration changes more slowly under the action of compressive forces, somewhat reduce their area. At the same time, they increase in their

thickness in such a way that their volume is practically unchanged. As the equilibrium moisture content is approached, a more uniform displacement of the coordinates of the nodal points along the radius of the particle is observed. The shrinkage of the particle was 28%, which corresponds to the data given in [10].

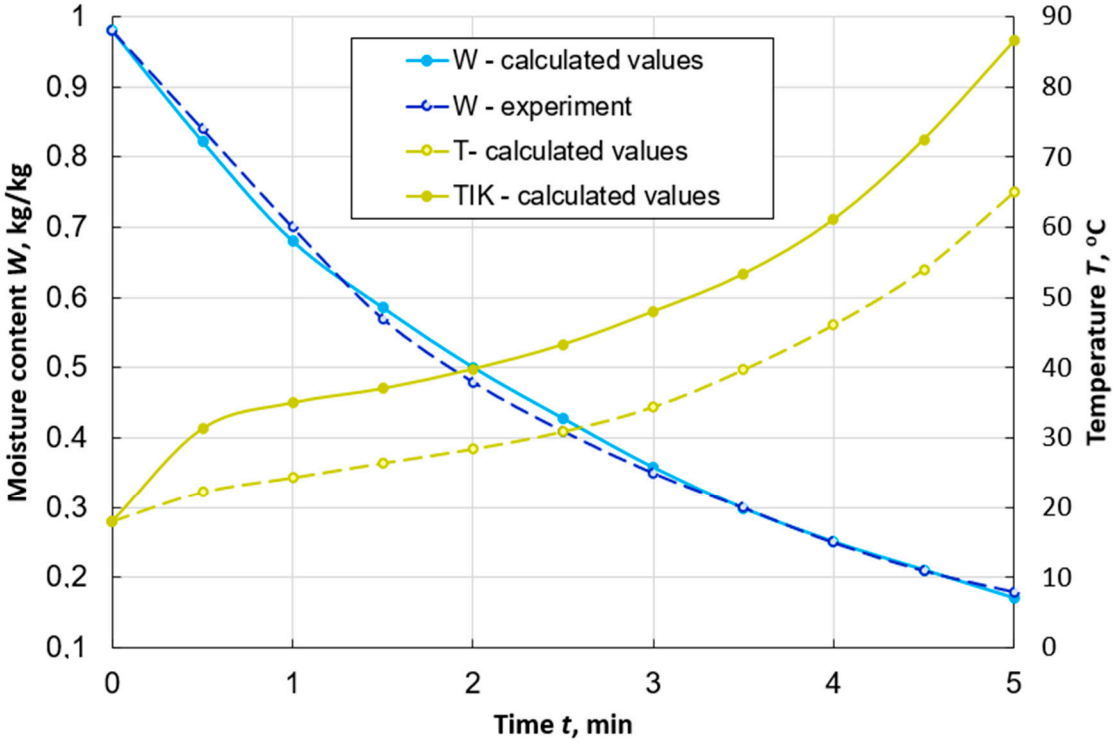

Figure 2. Graphs of changes in the average values of moisture content W and temperature T, as well as the temperature on the surface T_{IK} of a spherical particle of peat with a diameter of $d = 7$ mm during its drying with the flow uniform washing with the following parameters: $T_{\text{e.m.}} = 120$ °C, $w_{\text{e.m.}} = 1$ m/s, $d_{\text{e.m.}} = 10$ g/kg of dry air.

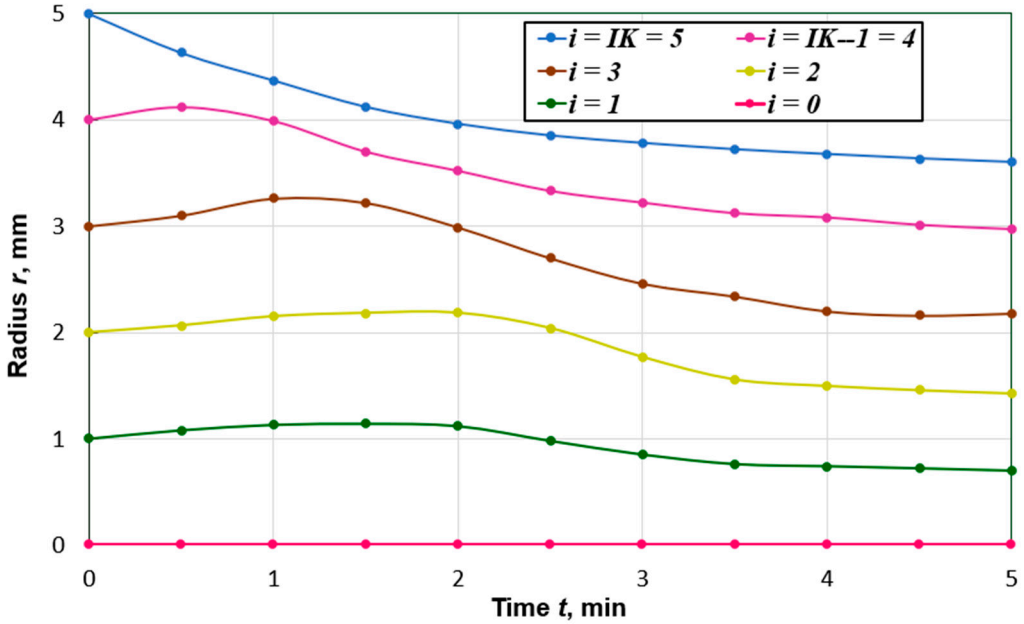

Figure 3. Curves of changes in time of nodal points coordinates $r_i = f(r_i^0, t)$ along the radius of the particle, which at the initial moment of time had the value $r_i^0 = ih^0$, ($i = 0, 1, \ldots, IK$; $IK = 5$).

The temperature of thermal decomposition of peat (lowland peat with average degree of decomposition) was taken [5] as 175 °C. The activation energy of the movement of the bound substance particles, when peat is heated above the temperature of the thermal destruction beginning, is lower than that of the physically and chemically bound water [5] in the temperature range of 28–175 °C and is equal to $A_{ef} = 0.370 \times 10^8$ J/kmol. Accordingly, the intensity of reaching the final peat moisture content with the simultaneous thermal decomposition process will increase. In order to account for the influence of thermal destruction on the dynamics of peat particle dehydration, the calculation program assumed the condition of a local change in the activation energy. The program itself was developed on the basis of the mathematical model (1)–(4) and the numerical method (18)–(22). The abovementioned means that when a temperature of 175 °C is reached at this nodal point of the particle at the given moment of time, in expressions (8)–(10), and for D_{fl}, the value of the activation energies A and A_D changed to the effective A_{ef}. The results of calculating the change over time in the average values of temperature and moisture content of the particle are presented in Figures 4–6. Figures 4–6 also show the results of calculating the temperature change of the surface in contact with the high-temperature flow without taking into account thermal decomposition and taking into account its effect on the duration of dehydration. To exclude the self-ignition of particles, there was a flow of flue gases. When conducting numerical experiments, the temperature of the flow $T_{e.m.}$ and particle size were varied. The flue gases flow velocity was $w_{e.m.} = 4$ m/s.

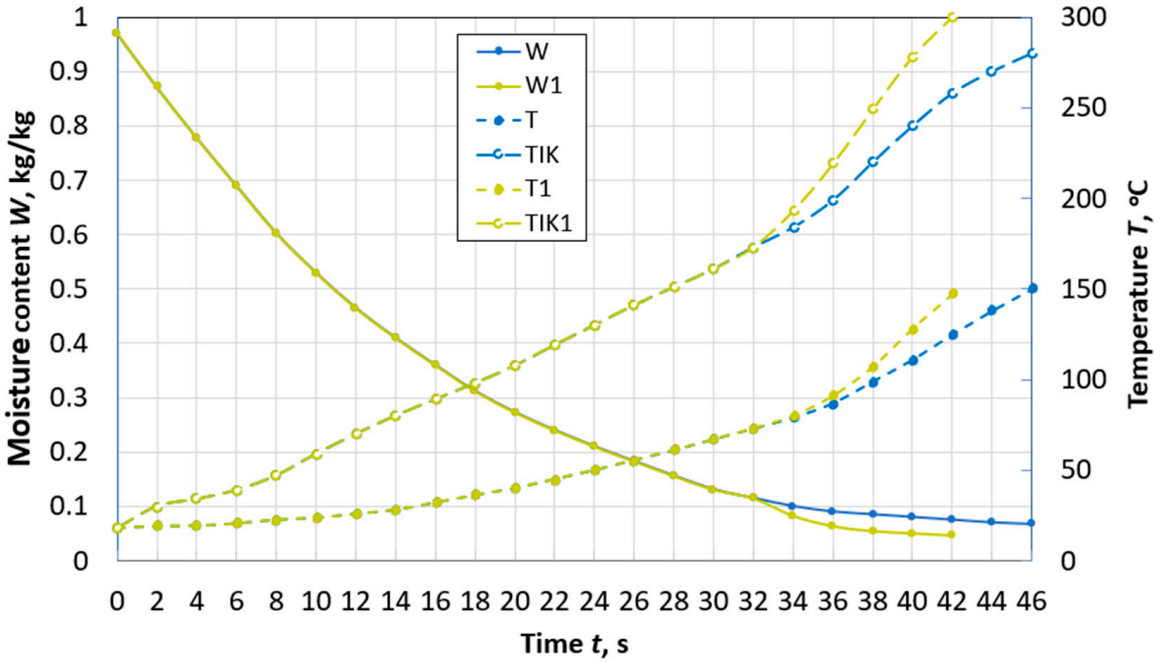

Figure 4. Changes over time in the average moisture content W and temperature T, temperature T_{IK} on the surface of a spherical particle of peat with a diameter of d = 10 mm during drying with and without taking into account thermal destruction ($W1$, $T1$, $T_{IK}1$) in the flow of flue gases with the parameters: $T_{e.m.}$ = 300 °C, $w_{e.m.}$ = 4 m/s, $d_{e.m.}$ = 12 g/kg of dry gas.

At a flow temperature of 300 °C, in a particle with a diameter of 10 mm (Figure 4), thermal destruction begins when its moisture content W is 12%. The time of reaching the moisture content of 8%, accounting for the effect of thermal decomposition, is 27% less than in cases neglecting this process. In addition, an important point in the development of high-temperature drying technologies is the completion of the process before the beginning of the second stage of thermal decomposition. The second stage can begin already at a temperature of 260 °C, and a particle achieves it faster due to the decomposition of hemicellulose.

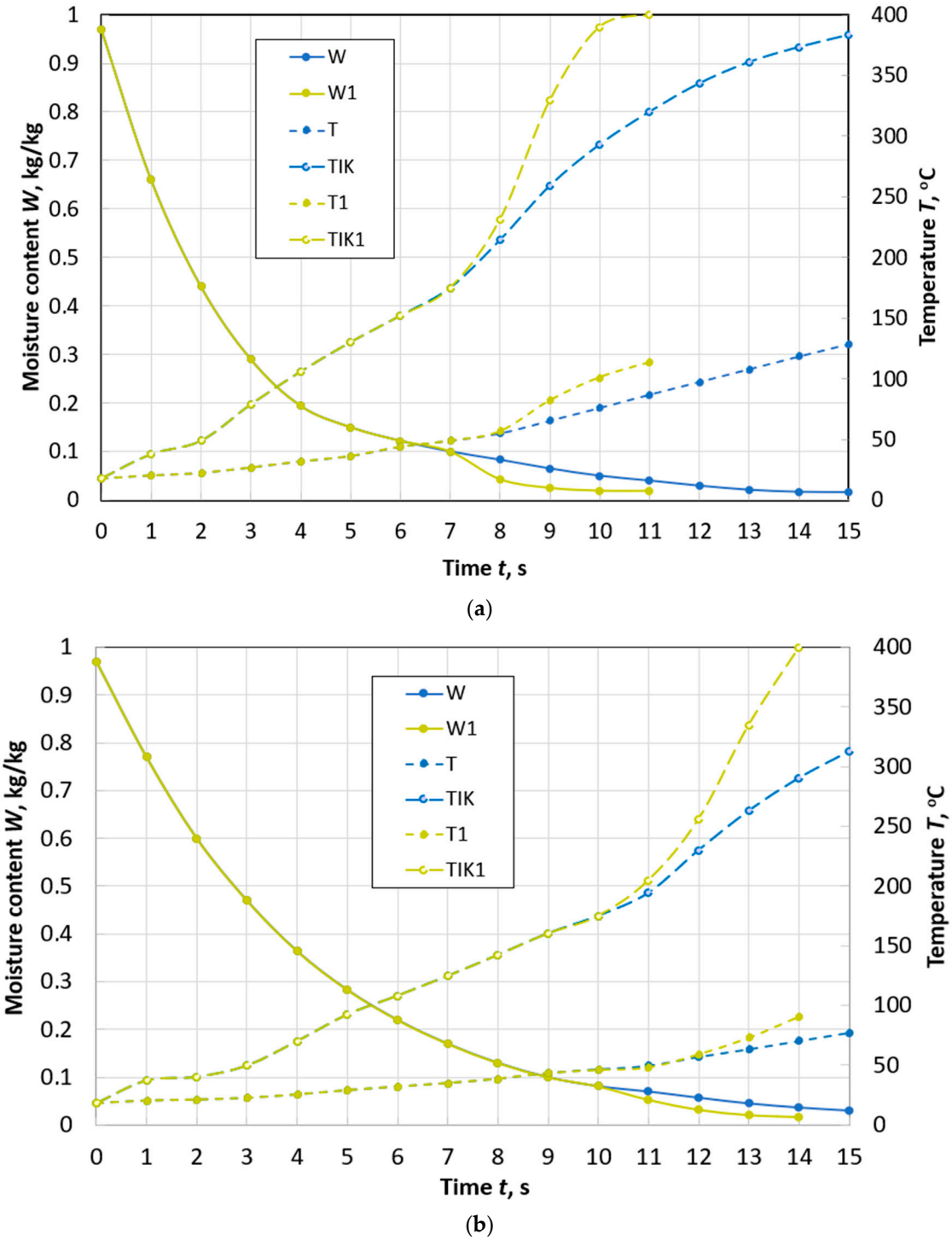

Figure 5. Changes over time in the average values of moisture content W and temperature T, temperature T_{IK} on the surface of a spherical particle of peat with a diameter of d = 10 mm (**a**) and a diameter of d = 13 mm (**b**) during drying with and without taking into account thermal destruction ($W1$, $T1$, $T_{IK}1$) in the flow of flue gases with parameters: $T_{e.m.}$ = 400 °C, $w_{e.m.}$ = 4 m/s, $d_{e.m.}$ = 12 g/kg of dry gas.

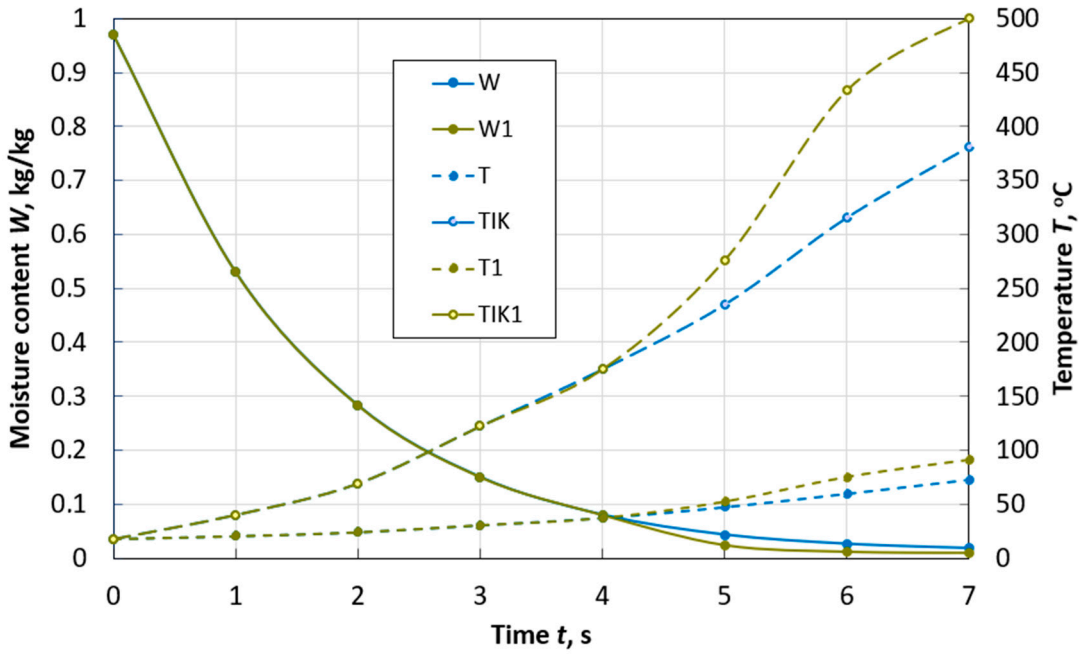

(**a**)

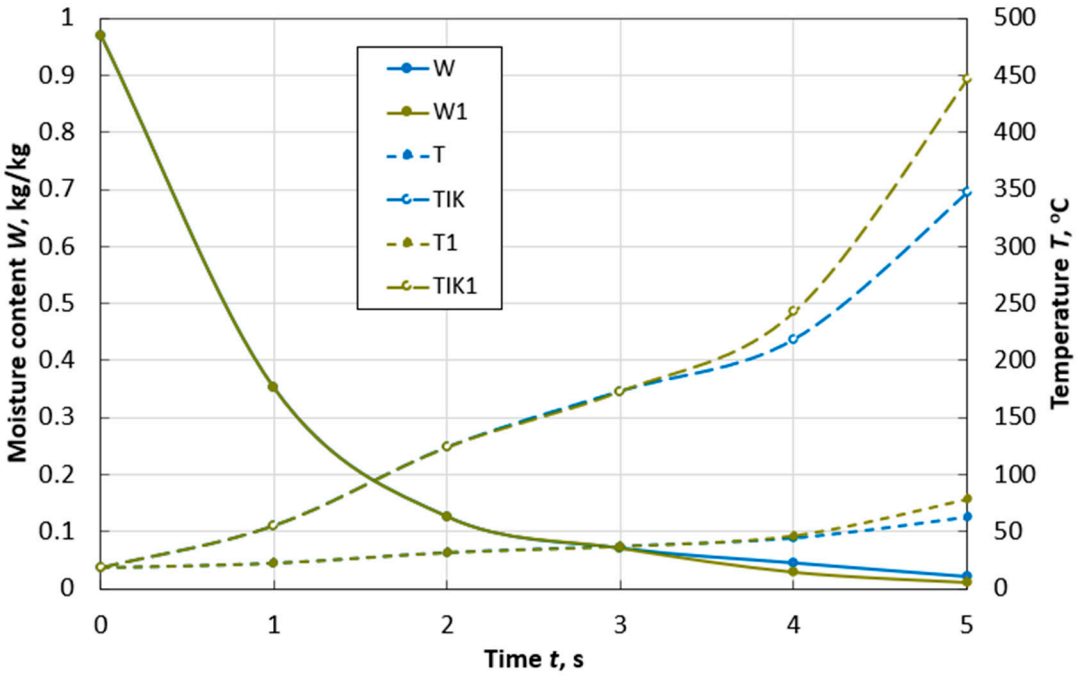

(**b**)

Figure 6. Changes over time in the average values of moisture content W and temperature T, temperature T_{IK} on the surface of a spherical particle of peat with a diameter of d = 10 mm (**a**) and a diameter of d = 13 mm (**b**) during drying with and without taking into account thermal destruction ($W1$, $T1$, $T_{IK}1$) in the flow of flue gases with parameters: $T_{e.m.}$ = 500 °C, $w_{e.m.}$ = 4 m/s, $d_{e.m.}$ = 12 g/kg of dry gas.

When the temperature of the drying agent is increased by 100 °C for a particle of the same size, thermal decomposition begins at a moisture content of W = 10% and the time to reach W = 8% is reduced by almost 3 times (Figure 5a). At the same time, the effect of thermal destruction becomes even more noticeable. The time of the first stage

of decomposition is limited to an interval of 1.5 s, and for a particle with a diameter of 13 mm—to an interval of 2 s (Figure 5b).

At a flow temperature of 500 °C, dehydration occurs so quickly (Figure 6) that the temperature of the thermal destruction's beginning is reached by peat particles of the adopted sizes when they reach a final moisture content of 8%.

The temperature and velocity of the drying agent should be selected based on a number of conditions. Among them, there is the productivity of the technological line for the production of peat briquettes, the technical characteristics of the dryer, the dispersed composition of milled peat, its initial humidity, and the moisture content of the drying agent. The presented mathematical model and the method of its calculation, which are the basis of the computer program, make it possible to account for the influence of all the specified factors and to choose rational parameters of the flow.

3. Discussion

In the technological chain of processing peat into fuel briquettes, the process of dehydration is the most energy-consuming and most decisive for fuel quality. The organization of high-temperature drying of milled peat contributes to solving the issue of energy saving and increasing the calorific value of fuel under the condition of passing the first stage of thermal decomposition [5–7]. The development of effective modes of high-temperature peat drying is possible on the basis of mathematical modeling of the dynamics of heat and mass transfer, phase transitions, and shrinkage under the appropriate conditions of the process. In addition, it is possible when there is information about the kinetic characteristics of thermal destruction in a wide temperature range. The attempt to calculate drying and thermal destruction together was justified by the activation nature of the processes of diffusion, evaporation, and thermal decomposition [3–7,23]. The mathematical model (1)–(4) presented in the work includes the formulas for the diffusion coefficient D_{fl} of the liquid phase, the intensity of evaporation on the outer and inner surfaces of peat particles, and for the saturation pressure. The formulas take into account the dependence of these parameters on temperature and activation energy at each spatial and temporal calculation step. The first stage of thermal destruction is the decomposition of hemicellulose. It is accompanied by the removal of oxygen-containing gases and pyrogenetic moisture and is characterized by a sharp change in the effective activation energy. When peat particles are in contact with a high-temperature flow, the temperature of their outer surface can reach the temperature of thermal decomposition. However, the internal pores will still contain a liquid phase. In this case, the removal of bound water will occur together with pyrogenetic water. This allows us to consider that the proposed approach, when the mathematical model takes into account the simultaneous processes of drying and thermal destruction of peat by means of a local change in the activation energy at the nodal points of the particles, is physically justified.

4. Conclusions

A mathematical model and a numerical method for calculating the dynamics of diffusion–filtration heat and mass transfer, phase transitions, and shrinkage during the dehydration of spherical capillary-porous colloidal peat particles have been developed. This allows the determination of the temperature fields, volume concentrations, and partial pressures of the liquid, vapor, and air phases in the body. Additionally, this allows us to determine the drying time depending on the temperature, moisture content, and velocity of the drying agent, geometric and thermophysical characteristics of the wet body. Physical and numerical experiments were conducted in order to confirm the adequacy of the developed mathematical model and the possibility of its application for the development of peat drying modes. The approach, where the mathematical model takes into account the simultaneous processes of drying and thermal destruction of peat, is proposed. When developing modes of high-temperature peat drying, this allows us to observe the conditions for passing the first stage of thermal destruction and completing the drying process when

the particles reach the temperature at the beginning of the second stage of destruction. This increases the calorific value of fuel peat briquettes.

Author Contributions: Conceptualization, N.S.; methodology, N.S. and M.V.; software, N.S.; validation, N.S. and Y.K.; formal analysis, M.V.; investigation, N.S., M.V. and Y.K.; resources, Y.P. and M.V.; data curation, Y.P.; writing—original draft preparation, N.S.; writing—review and editing, M.V.; visualization, M.V. and Y.K.; supervision, N.S.; project administration, Y.P. and M.V.; and funding acquisition, M.V. and Y.P. All authors have read and agreed to the published version of the manuscript.

Funding: This research received no external funding.

Institutional Review Board Statement: Not applicable.

Informed Consent Statement: Not applicable.

Data Availability Statement: Data is contained within the article.

Conflicts of Interest: The authors declare no conflict of interest.

References

1. Stolbikova, G.E.; Kuporova, A.V. Milled peat drying in case of different size of feed and conditions. *Gorn. Inf. Anal. Byulleten* **2018**, *5*, 65–73. Available online: https://cyberleninka.ru/article/n/osobennosti-sushki-frezernogo-torfa-razlichnoy-udelnoy-zagruzki-i-rezhimov-sushki/viewer (accessed on 12 November 2022). (In Russian) [CrossRef]
2. Kindzera, D.P.; Khanyk, Y.a.M.; Atamanyuk, V.M.; Duleba, V.P. Kinetic of filtration drying of peat. *NU Lviv. Polytech. Chem. Technol. Subst. Appl.* **2002**, *447*, 179–182. Available online: https://ena.lpnu.ua:8443/server/api/core/bitstreams/10659275-4d3c-4960-baf9-d8ae59a11013/content (accessed on 13 November 2022).
3. Smolyaninov, S.I.; Lozbin, V.I.; Ikryn, V.M.; Bblichmaer, Y.A. Features of thermal decomposition of peat according to derivatographic data. *Bull. Tomsk. Polytech. Univ. Geo Assets Eng.* **1976**, *274*, 56–60. Available online: https://cyberleninka.ru/article/n/osobennosti-termicheskogo-razlozheniya-torfa-po-derivatograficheskim-dannym (accessed on 1 December 2022).
4. Mykhailyk, V.A.; Snezhkin, Y.u.F.; Oranska, O.I.; Korinchevska, T.V.; Korinchuk, D.M. Study of the thermal properties of solid residues of milled peat after the humus substances extraction. *Ind. Heat Eng.* **2015**, *37*, 54–64. (In Ukrainian) [CrossRef]
5. Korinchuk, D. Non-isothermal analysis of components of composite fuels based on peat and biomass. *Energy Autom.* **2018**, *1*, 56–71. Available online: http://nbuv.gov.ua/UJRN/eia_2018_1_8 (accessed on 1 December 2022). (In Russian) [CrossRef]
6. Leroy-Cancellieri, V.; Cancellieri, D.; Leoni, E.; Filkov, A.I.; Simeoni, A. A global mechanism for the thermal degradation of peat. In Proceedings of the 4th Fire Behavior and Fuels Conference, St. Petersburg, Russia, 1–4 July 2013; International Association of Wildland Fire: Missoula, MT, USA, 2013.
7. Chen, W.-H.; Kuo, P.-C. Isothermal torrefaction kinetics of hemicellulose, cellulose, lignin and xylan using thermogravimetric analysis. *Energy* **2011**, *36*, 6451–6460. [CrossRef]
8. Nikitenko, N.I.; Snezhkin, Y.F.; Sorokovaya, N.N. Mathematical simulation of heat and mass transfer, phase conversions, and shrinkage for optimization of the process of drying of thermolabile materials. *J. Eng. Phys. Thermophys.* **2005**, *78*, 75–89. [CrossRef]
9. Fil'kov, A.I.; Gladkii, D.A. Mathematical modeling of low-temperature drying of a peat layer. *Tomsk. State Univ. J.* **2012**, *3*, 93–106. (In Russian)
10. Luikov, A.V. *Drying Theory*; Energy: Moscow, Russia, 1968; p. 472. Available online: https://www.twirpx.com/file/1241798/ (accessed on 10 December 2022). (In Russian)
11. Wang, Z.; Wang, Q.; Lai, J.; Liu, D.; Hu, A.; Xu, L.; Chen, Y. Numerical Simulation of Heat and Mass Transfer in Sludge Low-Temperature Drying Process. *Entropy* **2022**, *24*, 1682. [CrossRef]
12. Nikitenko, N.I. Problems of the radiation theory of heat and mass transfer in solid and liquid media. *J. Eng. Phys. Thermophys.* **2000**, *73*, 840–848. [CrossRef]
13. Aleksanyan IYu Titova, L.M.; Nugmanov, A.K. Simulation of the process of drying a dispersed material in a fluidized bed. *Tech. Technol. Food Prod.* **2014**, *3*, 96–102. Available online: https://cyberleninka.ru/article/n/modelirovanie-protsessa-sushki-dispersnogo-materiala-v-kipyaschem-sloe/viewer (accessed on 15 November 2022). (In Russian)
14. Strumillo, C.; Grinchik, N.N.; Kuts, P.S.; Akulich, P.V.; Zbicinski, I. Numerical modeling of nonisothermal moisture transfer in biological colloidal porous materials. *J. Eng. Phys. Thermophys.* **1994**, *66*, 181–190. [CrossRef]
15. Huzova, I.O.; Atamanyuk, V.M. Dynamics of drying processes of plant raw material in the period of decreasing speed. *J. Chem. Technol.* **2022**, *30*, 419–430. Available online: http://chemistry.dnu.dp.ua/article/view/259694 (accessed on 9 December 2022).
16. Luikov, A.V. *Heat and Mass Transfer in Capillary Porous Bodies*; Pergamon Press: Oxford, UK, 1966; pp. 233–303. [CrossRef]
17. Akulich, P.V. *Thermohydrodynamic Processes in Drying Technique*; ITMO: Minsk, Belarus, 2002; p. 268.
18. Kotov, B.I.; Bandura, V.N.; Kalinichenko, R.A. Mathematical modeling and identification of heat and mass transfer in plant dispersed material during drying and heating by an ultra-high frequency electromagnetic field. *Energy Autom.* **2018**, *6*, 35–50. Available online: http://nbuv.gov.ua/UJRN/eia_2018_6_6 (accessed on 3 December 2022).

19. Akulich, P.V.; Slizhuk, D.S. Heat and Mass Transfer in a Dense Layer during Dehydration of Colloidal and Sorption Capillary-Porous Materials under Conditions of Unsteady Radiation-Convective Energy Supply. *Theor. Found. Chem. Eng.* **2022**, *56*, 152–161. [CrossRef]
20. Rudobashta, S.P.; Kartashov, E.M.; Zueva, G.A. Mathematical modeling of convective drying of materials with taking into account their shrinking. *Inzh. Fiz. Zh.* **2020**, *93*, 1394–1401. [CrossRef]
21. Rudobashta, S.P.; Dmitriev, V.M. Investigation of the Diffusion Properties of Plant Capillary-Porous Colloidal Materials with Regard to Their Shrinkage. *J. Eng. Phys. Thermophys.* **2022**, *95*, 1357–1365. [CrossRef]
22. Narang, H.; Wu, F.; Mohammed, A.R. An Efficient Acceleration of Solving Heat and Mass Transfer Equations with the First Kind Boundary Conditions in Capillary Porous Radially Composite Cylinder Using Programmable Graphics Hardware. *J. Comput. Commun.* **2019**, *7*, 267–281. [CrossRef]
23. Nikitenko, N.I.; Snezhkin, Y.u.F.; Sorokovaya, N.N.; Kolchik Yu, N. *Molecular Radiation Theory and Methods for Calculating Heat and Mass Transfer*; Naukova Dumka: Kyiv, Ukraine, 2014; p. 744. Available online: http://ittf.kiev.ua/wp-content/uploads/2016/12/nikitenko.pdf (accessed on 3 December 2022). (In Russian)
24. Sneszkin, Y.F.; Korinchuk, D.N. Modeling of high-temperature drying of peat and biomass in biofuel production technologies. *Sci. Work.* **2017**, *81*, 125–130. Available online: https://sciworks.ontu.edu.ua/en/site/archives/81-1?page=2 (accessed on 15 January 2023). (In Russian)
25. Leibenzon, L.S. *Variational Methods for Solving Problems in the Theory of Elasticity*; Gostekhizdat: Moscow, Russia, 1943; p. 286. (In Russian)
26. Nikitenko, N.I. Investigation of dynamics of evaporation of condensed bodies on the basis of the law of spectral-radiation intensity of particles. *Inzh. Fiz. Zh.* **2002**, *75*, 128–134. [CrossRef]
27. Sorokovaya, N.N.; Snezhkin, Y.F.; Shapar, R.A.; Sorokovoi, R.Y. Mathematical Simulation and Optimization of the Continuous Drying of Thermolabile Materials. *J. Eng. Phys. Thermophys.* **2019**, *92*, 1180–1190. [CrossRef]
28. Sorokova, N.; Didur, V.; Variny, M. Mathematical Modeling of Heat and Mass Transfer during Moisture–Heat Treatment of Castor Beans to Improve the Quality of Vegetable Oil. *Agriculture* **2022**, *12*, 1356. [CrossRef]
29. Broido, A. A Simple, sensitive graphical method of treating thermogravimetric analysis data. *J. Polym. Sci. Part B Polym. Phys.* **1969**, *7*, 1761–1773. [CrossRef]
30. Oostindie, K. *A Simulation Model for the Calculation of Water Balance, Cracking and Surface Subsidence of Clay Soils*; Rep. 47; Winand Staring Centre for Integrated Land, Soil and Water Research: Wageningen, The Netherlands, 1992; p. 65. Available online: https://books.google.com.ua/books/about/FLOCR.html?id=D39jHAAACAAJ&redir_esc=y (accessed on 12 January 2023).
31. Garnier, P.; Perrier, E.; Angulo, A.J.; Baveye, P. Numerical model of 3-dimensional anisotropic deformation and water flow in welling soil. *Soil Sci.* **1997**, *162*, 410–420. [CrossRef]
32. Rudobashta, S.P. *Mass Transfer in Systems with a Solid Phase*; Chemistry: Moscow, Russia, 1980; p. 248. Available online: https://www.libex.ru/detail/book796756.html (accessed on 11 January 2023). (In Russian)
33. Keltsev, N.V. *Fundamentals of Sorption Technology*, 2nd ed.; Chemistry: Moscow, Russia, 1984; p. 590. (In Russian)
34. Nikitenko, N.I. A method for calculating the temperature field by the data of measurement of the deformation of a body. *Inzh. Fiz. Zh.* **1980**, *39*, 281–285.
35. Nikitenko, N.I. Radiation heat conduction mikromechanism. In Proceedings of the First International Conference on Transport Phenomena in Processing, Lancaster, PA, USA, 22–26 March 1992; pp. 1580–1588.
36. Kutateladze, S.S. *Fundamentals of the Theory of Heat Transfer*; Atomizdat: Moscow, Russia, 1979; p. 416. (In Russian)
37. Voznyuk, S.T.; Moshinsky, V.S.; Klymenko, M.O.; Lyko, D.V.; Gneushev, V.O.; Lagodnyuk, O.A.; Voznyuk, N.M.; Kucherova, A.V. *Peat Land Resource of the North-Western Region of Ukraine*; NUWEE: Rivne, Ukraine, 2017; p. 117. Available online: http://ep3.nuwm.edu.ua/id/eprint/7506 (accessed on 11 October 2022). (In Ukrainian)

computation

MDPI

Article

Optimization of the Small Wind Turbine Design—Performance Analysis

Marek Jaszczur [1], Marek Borowski [2], Joanna Halibart [2,*], Klaudia Zwolińska-Glądys [2,*] and Patryk Marczak [1]

[1] Faculty of Energy and Fuels, AGH University of Krakow, al. Adama Mickiewicza 30, 30-059 Kraków, Poland; jaszczur@agh.edu.pl (M.J.); pmarczak@agh.edu.pl (P.M.)
[2] Faculty of Civil Engineering and Resource Management, AGH University of Krakow, al. Adama Mickiewicza 30, 30-059 Kraków, Poland; borowski@agh.edu.pl
* Correspondence: jhalibart@gmail.com (J.H.); kzwolinska@agh.edu.pl (K.Z.-G.)

Abstract: In recent decades, the intensive development of renewable energy technology has been observed as a great alternative to conventional energy sources. Solutions aimed at individual customers, which can be used directly in places where electricity is required, are of particular interest. Small wind turbines pose a special challenge because their design must be adapted to environmental conditions, including low wind speed or variability in its direction. The research study presented in this paper considers the energy efficiency of a small wind turbine with a horizontal axis of rotation. Three key design parameters were analyzed: the shape and inclination of the turbine blades and additional confusor–diffuser shape casings. The tests were carried out for three conceptual variants: a confusor before the turbine, a diffuser after the turbine, and a confusor–diffuser combination. Studies have shown that changing the shape of the blade can increase the analyzed wind turbine power by up to 35%, while changing the blade inclination can cause an increase of up to 16% compared to the initial installation position and a 66% increase in power when comparing the extreme inclination of the blades of the tested turbine. The study has shown that to increase the wind speed, the best solution is to use a confusor–diffuser configuration, which, with increased length, can increase the air velocity by up to 21%.

Keywords: small wind turbine; horizontal-axis wind turbine; diffuser/confusor augmented wind turbine; wind concentrators; computational fluid dynamics

Citation: Jaszczur, M.; Borowski, M.; Halibart, J.; Zwolińska-Glądys, K.; Marczak, P. Optimization of the Small Wind Turbine Design—Performance Analysis. *Computation* **2024**, *12*, 215. https://doi.org/10.3390/computation12110215

Academic Editors: Ali Cemal Benim, Abdulmajeed A. Mohamad, Sang-Ho Suh, Rachid Bennacer, Paweł Oclon and Jan Taler

Received: 1 September 2024
Revised: 16 October 2024
Accepted: 21 October 2024
Published: 25 October 2024

1. Introduction

The increase in greenhouse gas emissions, high energy consumption, and depletion of natural resources are just some crucial factors that contribute to the development of alternative-energy-source technologies. Renewable energy is a fundamental element of the sustainable energy strategy. Due to its inexhaustible potential, its affordability, the reduction in pollution, and the availability of new technologies on the market, renewable energy sources are an interesting alternative to generating energy based on fossil fuels. Among the solutions commonly used and available on the market, there are photovoltaic panels, wind turbines, and hydroelectric power plants. In recent years, wind power plants have gained popularity. Wind potential has long been widely used by humans in everyday life, initially in navigation and as a driving force for windmills used in pumping water systems or mills. Currently, many solutions are available on the market, differing in construction, electrical power, and turbine size.

1.1. Wind Energy

Wind energy has become one of the most dynamically developing industries in recent years. Extensive wind farms are a common element of the landscape of many countries. In addition, more and more wind turbines are being installed on the roofs of buildings or

nearby. The wind turbine is the most important element of every wind power plant that converts the kinetic energy of the wind into useful electrical energy. The design parameters of the turbine determine the properties and power achieved by the wind power plant.

Depending on the position of the axis of rotation of the turbine rotor, Horizontal-Axis Wind Turbines (HAWT) and Vertical-Axis Wind Turbines (VAWT) turbines are distinguished. Currently, the most commonly used solution involves large wind turbine sets with a horizontal axis, where the height can reach a height of up to 100 m. The production of wind power plants depends on the design of the wind turbines and the wind speed. Turbines with a vertical axis of rotation are increasingly being used in urbanized areas, where they are installed directly on buildings. The blades of this design generate less noise, and their main advantage is their independence from changes in the wind direction, as they do not require the use of mechanisms for setting up against the wind direction, unlike turbines with a horizontal axis. This type of construction could operate at low values of wind velocity and is characterized by a simple, easy-to-maintain structure [1].

1.2. Energy Efficiency of Wind Turbines

Wind energy is a widely available source of energy that can be effectively converted into electrical energy using appropriate technologies. Existing mathematical formulas allow the estimation of the electrical power that could be obtained from the operating wind turbine. This formula presents the relationships of the amount of generated energy that can be obtained from the wind under a given wind speed, dependent on the device efficiency resulting from the turbine design. The value of the power P generated from the wind can be estimated from the following formula [2]:

$$P = C_p \cdot \frac{\rho}{2} \cdot A \cdot {v_w}^3 \tag{1}$$

where ρ is the air density (kg/m^3), v_w is the air velocity (m/s), A defines the swept area of the blades (m^2), and C_p denotes the power coefficient.

This equation shows the importance of the wind velocity, which is in the third power. Wind speed is the main factor taken into account in the analysis of wind energy. Doubling the wind speed causes an eight-fold increase in the wind turbine power. The power of the wind turbine also depends on the area swept by the turbine blades, which signifies the advantages of large wind turbine blades. The formula also includes the power coefficient C_p, which expresses the degree of utilization of the total wind power. According to Betz's theory, the maximum possible value of C_p is approximately 59% [3]. The power coefficient depends on the type of wind turbine and changes for a given design, depending on the tip speed ratio (TSR), which expresses the ratio of the velocity of the blade tip to the wind speed [2]. Figure 1 presents the power coefficient C_p values for different wind turbine solutions and the different values of the tip speed ratio (TSR).

1.3. Optimization Solutions to Increase the Efficiency of Wind Turbines

Commercial wind turbines are currently made mostly with a horizontal axis of rotation and with three blades. They constitute about 95% of all installed turbines [4]. A small percentage of the market is covered with wind turbines with a vertical axis of rotation. Currently offered devices are mostly large structures, typically designed and optimized as free-standing devices. Very often, designers or constructors do not consider interactions of the wind turbine with the surrounding constructions. The widespread increased interest in distributed energy is a contribution to scientists' attention to small wind turbines intended for individual purposes. One of the main limitations in domestic application is the low wind speed and high turbulence intensity caused by the roughness of the terrain and existing buildings. An additional challenge is the prediction of the actual efficiency of small wind turbines due to the difficulties in estimating wind conditions in a given location without having detailed measurements [5]. For this reason, research in this area mainly focuses on optimizing the structures used to improve their efficiency in unfavorable conditions.

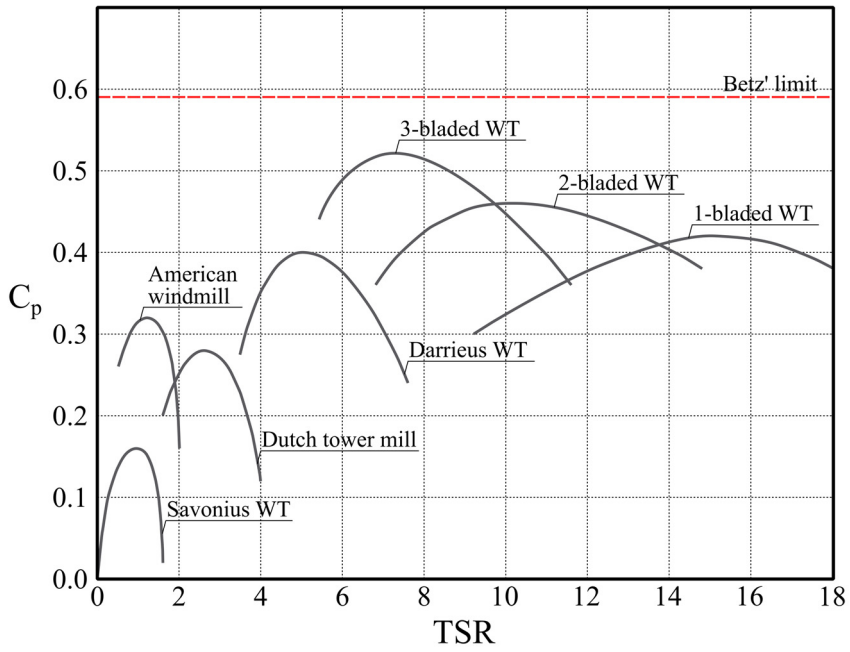

Figure 1. Dependence of the power coefficient C_p on the TSR for different types of wind turbines. Based on [1].

In the literature, several analyses of the shape of blades or rotors and their impact on the obtained power can be found [6–11]. At the design step, it is necessary to consider not only the maximization of efficiency and minimization of the costs of obtained electric energy, but also operational problems such as the start-up velocity and the low wind speed at which the turbine should also operate [10]. Rezaeiha et al. [11] analyzed the effect of the blade pitch angle on the efficiency of a turbine for a VAWT. The results of CFD simulations indicate a clear dependence of the load distribution on the pitch angle, which gives greater possibilities for optimizing the efficiency of the wind turbine.

A good solution for small domestic installations in areas with low and time-varying wind velocity appears to be the application of vertical-axis wind turbines [12,13]. Small vertical-axis wind turbines can be an effective solution, especially for zero-energy buildings and urban models of distributed energy generation. Due to the significant dependence of turbine operation on wind velocity, a thorough environmental analysis is necessary when designing the installation, allowing the selection of an appropriate turbine construction and location. It is particularly crucial to include in the analysis the interactions between winds, buildings, and the topology of the urban area [14–17]. To improve the efficiency of wind turbines, they are most often placed on the roofs of buildings. This allows for reducing the interference related to turbulence caused by the interaction of the wind with the ground and buildings [18]. High turbulence intensity can result in lower energy production as well as higher mechanical stresses on the turbine components [19]. The Savonius turbine analyzed in the wind tunnel [20] showed that high-intensity turbulent flow affects the fluctuations of the loads acting on the turbine blades and consequently impacts the efficiency of the entire device. According to the measurements, for wind speeds below 7 m/s, the energy generated during high-intensity turbulent flow exceeded that obtained with a uniform flow of the same speed. After exceeding the certain velocity of wind, the energy generated for turbulent flow was significantly lower.

Efficiency can be improved by increasing airflow onto the wind turbine rotor. In the literature, several methods can be found to increase airflow, for example, by using "diffuser augmentation". A diffuser-augmented wind turbine (DAWT) has a diffuser installed downstream of the blades or a concentrator upstream to increase the flow speed acting on the blades [3]. There are many ducted or shrouded solutions for wind power applications, especially for small systems for individual users. This interest is mainly related to the

fact that such wind turbines can be significantly more efficient than similar rotors under free-flow conditions [21]. The subject of many studies [22–25] was to analyze the use of additional elements to increase the velocity of the air acting on the rotor, typically in the form of diffusers or concentrators. Bontempo et al. [26] presented a numerical analysis of the rotor enclosed in a profiled shroud. The authors noted that although an additional shroud for an existing turbine increases the turbine efficiency, significantly higher gains can be achieved by designing both the blades and the housing simultaneously to adapt the rotor geometry to the flow characteristics. In the study by Sridhar et al. [27], the authors analyzed the effect of diffuser geometric parameters, including the presence of slits and bleed air holes (the slotted DAWT). Their study showed that both slotted and non-slotted DAWTs obtained higher efficiency than the open wind turbine. Additionally, the slotted diffuser allowed for a 31% increase in air velocity compared to the full casing. Bontempo et al. [28] presents an approach to evaluating the performance of an optimal Joukowsky (free-vortex) rotor enclosed in a duct of general shape. Refaie et al. [29] studied an augmented horizontal-axis wind turbine. The authors analyzed the performance of the wind turbine through numerical investigation and an Archimedes-spiral wind turbine was selected as a test case. The main aim was to specify the optimal design, including additional concentrators, and therefore, to obtain the best performance of wind turbines for urban areas. Teklemariyem et al. [30] investigated the optimization of the geometry of the diffuser to increase airflow through the HAWT rotor. The analysis included different cross-sectional shapes, variable diffuser angles, and the presence of a flange. The obtained results allowed for the selection of a diffuser that would allow for the highest inflow velocity. Similar research was carried out by Shambira et al. [31]. The authors developed a diffuser design optimization model in the context of selecting the most appropriate geometric dimensions to achieve the highest flow velocity. Among the geometric parameters analyzed, in addition to the lengths of individual sections of the concentrator–throat–diffuser set, the diffuser and concentrator angles and flange height were also included. Based on the statistical analysis, it was noted that the concentrator length and diffuser length turned out to be the factors with the greatest influence, resulting in the highest increasing velocity.

This paper focuses on the influence of the design of a small wind turbine on energy efficiency. Among the parameters studied, both the shape and inclination of the rotor blades as well as the use of additional wind-concentrating elements were analyzed. The work was divided into two stages. In the first stage, experimental tests of different blade shapes on the achieved efficiency of the wind turbine were carried out. The angle of the blade was also taken into account during the measurements. In the next step, the influence of the additional aerodynamic shield on the air velocity flowing onto the turbine rotor was analyzed.

2. Materials and Methods

Commercial wind turbines are currently made mostly with a horizontal axis of rotation. One of the main limitations in domestic applications is the low wind speed. HAWTs are characterized by a higher power coefficient C_p but require higher wind speeds than VAWTs. Due to the small amount of data for horizontal-axis wind turbines of small diameter and operation at low wind speeds, the research in this article was focused on such an object.

The basic practical parameter that characterizes a wind turbine, crucial for potential users, is the electrical power that can be generated. Available turbines, especially for individual use, differ significantly in construction, number, as well as the shape of the blades. The experimental study carried out concentrates on measurements of the power generated by wind turbines and includes the effect of the shape of their blades and their inclination on the power and, as a consequence, on obtained wind turbine performance. With the development of computational fluid dynamics (CFD), numerical studies of wind turbines have become increasingly popular and attractive. Simulation studies involve a lower cost than experimental measurements in a wind tunnel. Numerical analyses are used to develop the optimal blade shape and also to determine the performance of the entire

turbine. An interesting issue analyzed using CFD is the impact of additional elements on turbine performance. The numerical analyses described in this article concentrate on evaluating the possibility of increasing the velocity of air coming over the turbine blades. The possibility to increase air velocity is extremely attractive from a wind turbine power perspective. As can be seen in the formula (Equation (1)) for the amount of power generated by a wind turbine, air velocity is one of the most important factors affecting power output because it appears in the formula at the third power. The research presented in this paper is divided into two parts, as described in the previous chapter.

2.1. Experimental Set-Up and Methodology

A research study has been carried out for horizontal-axis wind turbines with a diameter of up to 2 m. The laboratory tests were constructed to determine key turbine parameters under various conditions. The first step of testing consisted of determining the power generated by four different wind turbines, which differ in shape and also in the number of their blades. The second step of testing was performed only for the wind turbine characterized by having the best results from the first step of the evaluation, and this was intended to estimate the effect of the angle of attack of the turbine blades on its basic performance parameters. For the purpose of determining the effect of the angle of attack of the turbine blades, each of the turbine blades was individually rotated using plastic wedges. Wedges with different angles were used in the tests. During the laboratory tests, the turbine's rotational speed and the power generated by the turbines were measured in detail. All tests were carried out at constant wind speed and for various electrical loads of wind turbine generators. Measurements were performed for an air velocity equal to 8 m/s and the maximum rotational speed of the turbine rotor equal to 450 RPM. During the laboratory test, the electrical load was connected to the turbine's electrical generator and its value was set up during the measurements. The laboratory test stand was equipped, among other things, with an inverter-controlled set of 9 fans that were able to simulate wind velocity at the required level of magnitude and profile, as well as with a programming DC electronic load connected to the turbine electric generator RND 320-KEL103. Figure 2 shows the laboratory test stand including the above-described elements.

(**a**) (**b**) (**c**)

Figure 2. The laboratory stand: (**a**) fans' array simulating wind; (**b**) programming DC electronic load; and (**c**) plastic wedge to change blade inclination.

The shape of the turbine blades used in the study is shown in Figure 3.

Figure 3. Rotor turbine blades with different shapes: (**a**) BL1; (**b**) BL2; (**c**) BL3; and (**d**) BL4.

The first type of turbine, indicated as BL1, was characterized by blades with the largest chord, and the rotor used in this test consisted of 5 blades. The results for the second turbine were labeled BL2. This turbine was characterized by three blades and the second-largest chord of the tested blades. The rotors composed of BL3- and BL4-shaped blades were measured as five-bladed wind turbines, with the blades of the BL3 turbine having the smallest chord of all those tested.

2.2. Numerical Simulation Methodology

Numerical analyses were carried out to evaluate the velocity of incoming air in the cross-section of a wind turbine blade assembly. Simulations were carried out with Ansys Fluent 2020 R2 [32,33]. Analyses were performed for different shapes of aerodynamic shields added to the wind turbine constructions. It should be noted that a restriction was applied to the analyzed variants of the elements. The entire assembled system could not extend beyond a cube with a side length of 2000 mm. An additional assumption was that the device must be prepared so that the turbine rotor can be mounted inside a ring with a diameter as large as possible, i.e., of 1950 mm. Due to construction limitations, the length of the ring should be equal to 300 mm, thereby the total length of the aerodynamic shield (confusor or diffuser) can be maximally 1700 mm.

The CFD analyses were performed to verify the effect of the application of additional aerodynamic elements like a confusor or diffuser on the incoming air velocity to the rotor section at a constant wind speed equal to 3.0 m/s. The performed numerical analyses can be divided into two steps. The first step focuses on comparing the obtained velocities in the plane of a hypothetical wind turbine rotor using circle-to-circle and circle-to-square transitions in the diffuser or confusor versions. Figure 4 presents the geometries used in the numerical simulation.

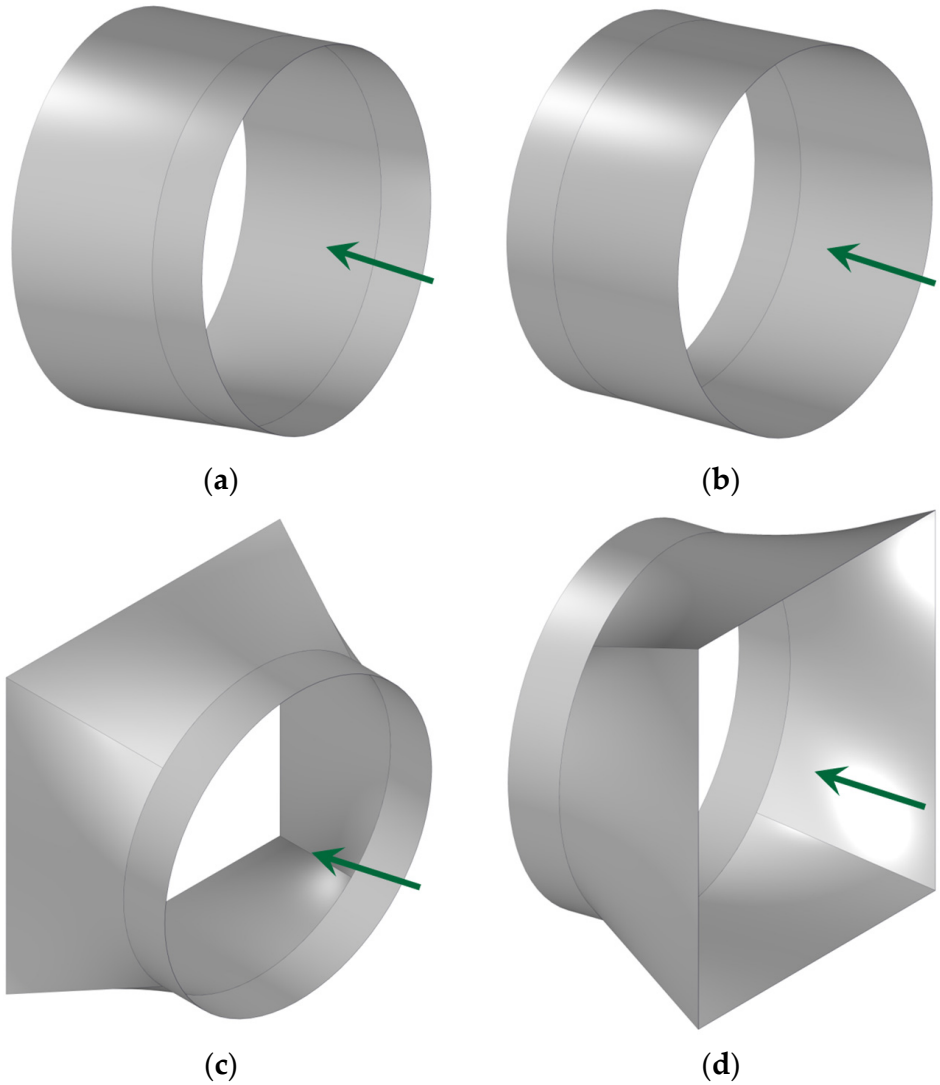

Figure 4. The geometry of the aerodynamic shield with: (**a**) increasing cross-sectional area (diffuser), circle to circle; (**b**) decreasing cross-sectional area (confusor), circle to circle; (**c**) increasing cross-sectional area (diffuser), square to circle; and (**d**) decreasing cross-sectional area (confusor), circle to square. The green arrow indicates the wind direction.

The analyses were carried out for five different lengths of these elements, by the reduction in the confusor or the diffuser length in the analyses. At the first step of the analysis, numerical simulations were used to estimate which one circle–circle or circle–square transition allows higher air velocities just before the rotor section. The second step consisted of evaluating the velocity of incoming air but with the confusor–diffuser configuration integrated into the more favorable version based on the analysis from the first step.

To perform numerical simulations, it is necessary to first prepare a computational model. The model set-up can be divided into three steps. The first step includes preparation of the geometry of the component under analysis and the surrounding environment. The next step is to generate mesh. The final step is the implementation of the required equations to perform calculations and analyze the results. Figure 5 presents the workflow for the simulation of the aforementioned problem, with all key steps highlighted.

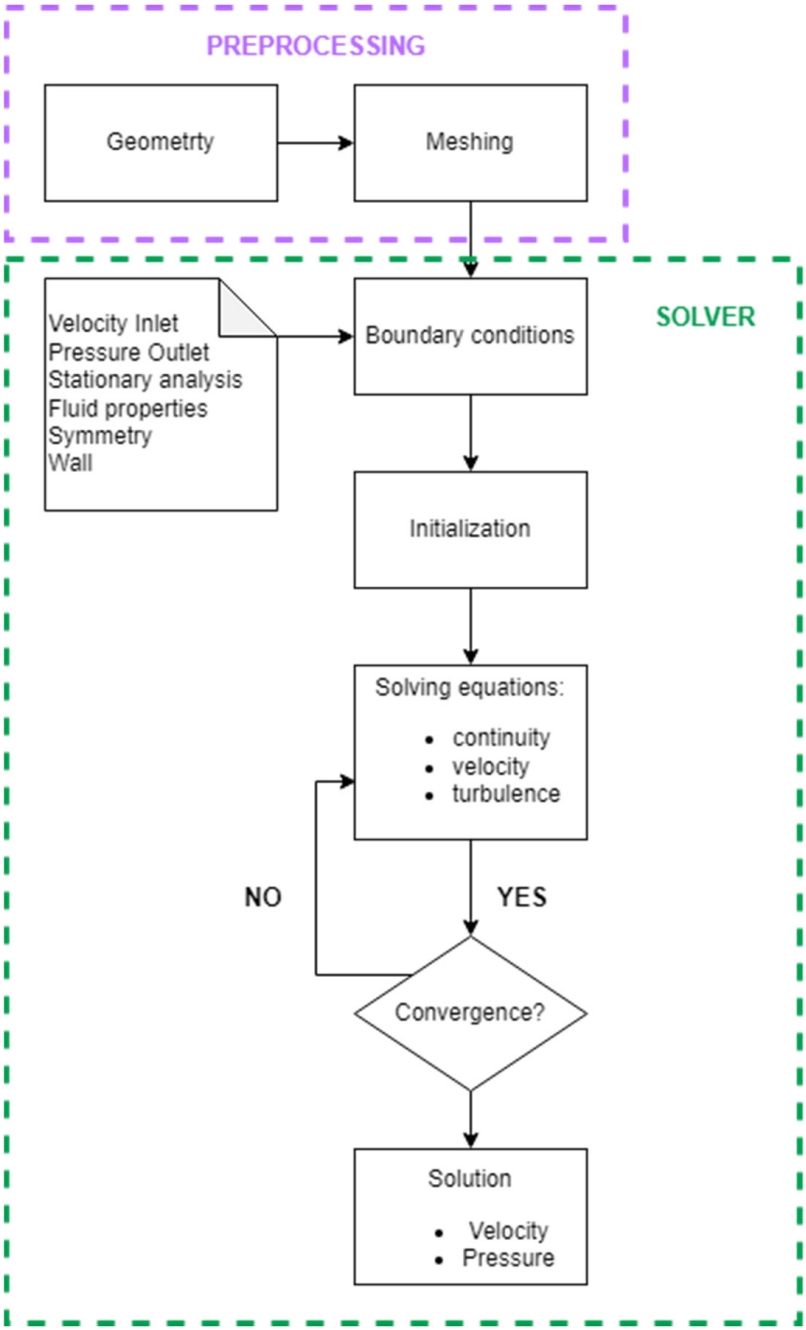

Figure 5. Block scheme of the workflow used for the simulation of the ducts.

To carry out the analyses, 3D models of the geometries were developed; due to their symmetries (geometrical symmetries and boundary condition symmetries), calculations were performed for one-quarter of the model geometry using the symmetry plane—see Figure 6a. The polyhexcore meshes were applied for the analyzed domain [34]—see Figure 6b,c.

In order to properly capture the boundary layer flow, the mesh was refined close to the walls using 20 inflation layers near the walls (first layer thickness set as 0.00015 m with growth ratio 0.272). For all tested cases, the dimensionless wall distance y+ does not exceed 5. Mesh refinement was also applied to the volume around the test element. The test case used a mesh with a size of 600.000 elements. The settings and size of the mesh were selected based on the comparison with two other configurations with a higher number of control volumes, at 1.3 million and 2.4 million, respectively. The difference in average air velocity

was approx. ±0.2% for both cases. Additional refinement with the element size of 0.04 m was applied around the walls of the structure to capture the vortex behavior as well as avoid rapid changes in mesh size through the domain.

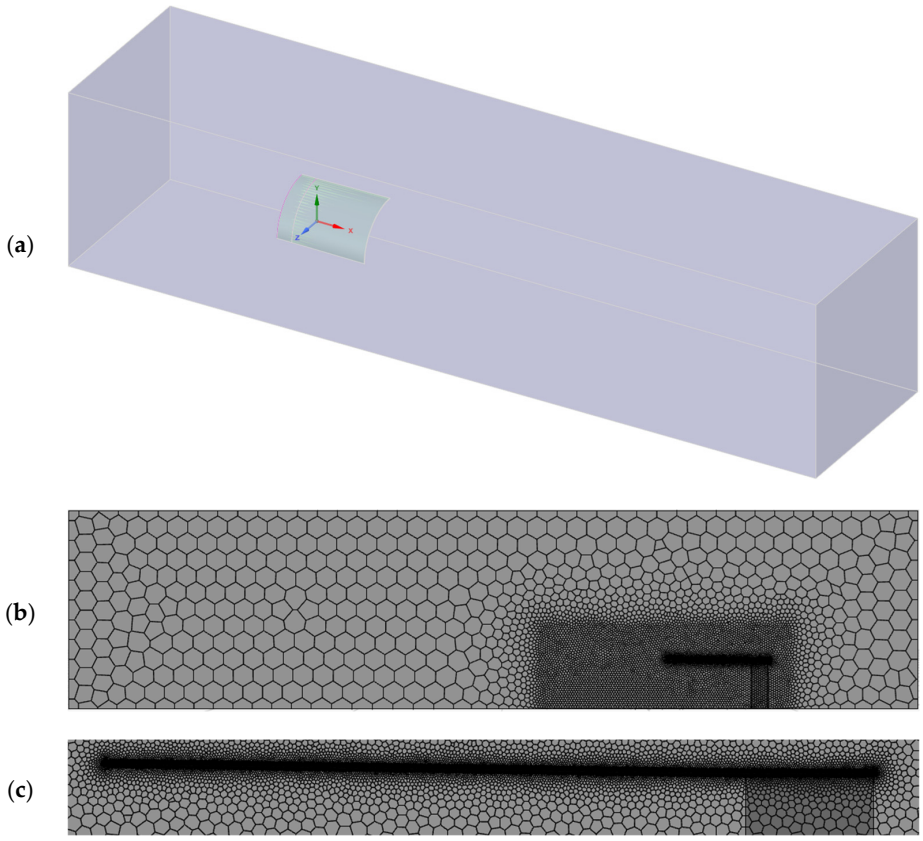

Figure 6. Computational domain: (**a**) geometry; (**b**) mesh—the entire computational domain; and (**c**) mesh—an increase in local mesh density around the wall of the aerodynamic shield.

The k-ω SST turbulence model was used in the simulation [35]. The k-ω SST model is a model that combines the advantages of the k-ε model and the k-ω model. The k-ε model resolves the turbulent flow properly in free flow and the shear layers well and is characterized by low sensitivity to the inlet conditions for quantities describing turbulence. The k-ω model, on the other hand, resolves turbulent flow structures in the boundary layer much better than the k-ε model. The calculation uses a cuboid as the computational domain. At the entrance to the computational domain, the "velocity inlet" boundary condition was used with a constant value equal to 3.0 m/s. The "pressure outlet" boundary condition was applied at the domain exit. For both inlet and outlet, the turbulence intensity was set to 5% and the viscosity ratio to 10. The symmetry condition on the side walls of the domain was used. No-slip boundary conditions were applied on the walls. The pressure-based solver and SIMPLE algorithm were applied. The discretization schemes used for calculation were second-order upwind schemes and for gradient least squares, cell based.

3. Results

3.1. Effect of the Blade Shape and Inclination Angle—Experimental Results

The performance of the small wind turbine with different blade shapes and different numbers of blades was analyzed. Based on the laboratory measurement results, Figure 7 was plotted. It represents the wind turbine power P as a function of the turbine rotational speed.

As the rotational speed increased, the power output increased for all of the tested wind turbines. Once the turning point was reached, the power output began to decrease.

For almost all rotational speeds, the highest values of the power output P were obtained for the five-bladed wind turbine with the largest chord, labeled as BL1. The results obtained for the turbine composed of blade types BL3 or BL4 were very similar, especially for higher rotational speeds, and simultaneously lower than for the turbine composed of blades labeled BL2. The maximum power was achieved at around 350 RPM for all tested configurations. Comparing the values obtained for the individual turbines at this rotational speed, the BL2 turbine produced about 5% less power than the BL1 turbine, the BL3 turbine about 26%, and the BL4 turbine about 35% less power than the BL1 turbine. For a rotational speed of around 400 RPM, the wind turbine with blades labeled BL2 obtained slightly higher performance than the BL1 turbine. The wind turbine with blades BL2 generated approx. 8% higher power than BL1 at this rotational speed, while the BL3 wind turbine had approx. 35% and the BL4 turbine approx. 40% lower power than the five-blade BL1 wind turbine.

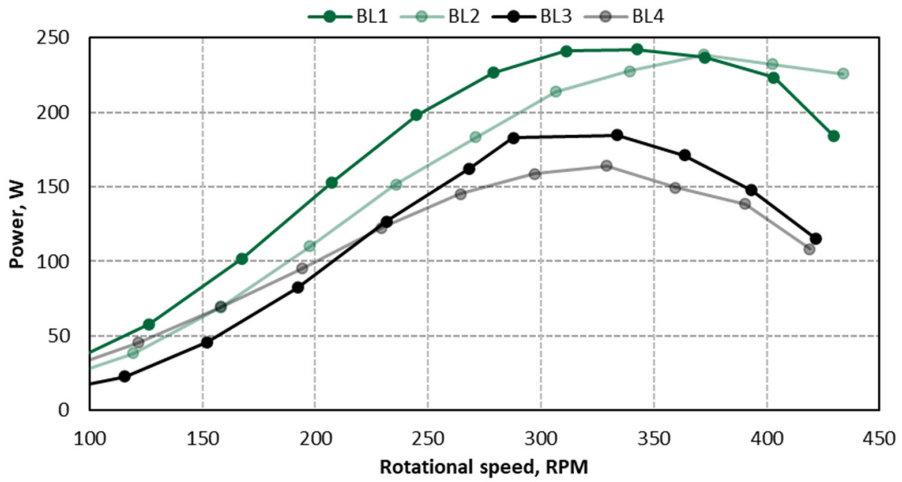

Figure 7. The power output P of the wind turbine as a function of the turbine rotational speed.

Based on the analysis presented above, to evaluate the effect of the blades' inclination angle on the wind turbine power output, a turbine with five blades of the BL1 type was selected. Tests were carried out for no blade inclination (0°) and tilt angles of +3°; +6° (clockwise) as well as −3°, and −6° (counterclockwise), respectively. Figure 8 shows the wind turbine's power output as a function of the turbine rotational speed for the tested inclination angles of the blades BL1.

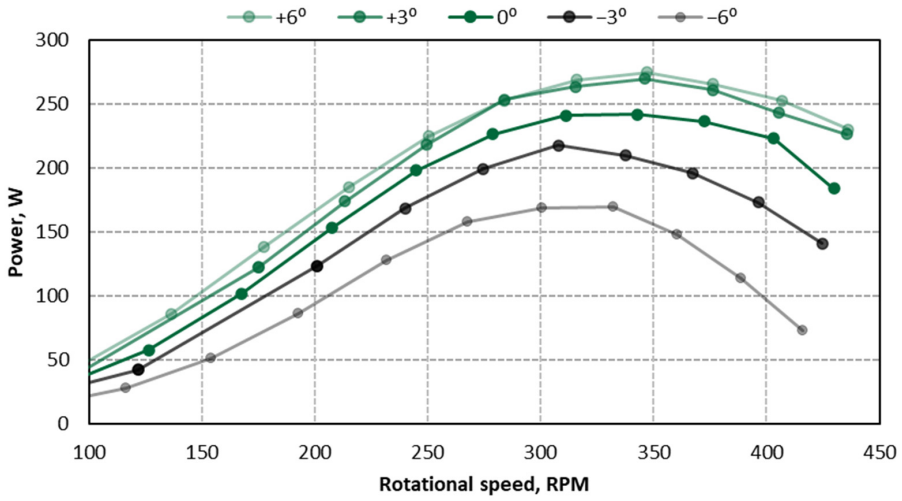

Figure 8. The power output P of the wind turbine as a function of the turbine rotational speed for various inclination angles of wind turbine blades BL1.

It has been found that modification in the inclination angle of the blades in the wind turbine had a significant effect on the power output. By comparing Figures 7 and 8, it is apparent that the BL1 inclination angles of the blades could influence the output power of the turbine more significantly than the shape of the blade. During the analysis, it was evaluated that the highest power outputs were achieved with the blades set at the "+" clockwise angle of attack. For the measurements carried out, the highest power output was obtained for the +6° angle of attack, which resulted in a 16% increase in peak power compared to blades at the base setting and a 66% increase in comparison to blades with the angle of −6°.

3.2. Effect of the Aerodynamic Shield on the Air Velocity in the Rotor Section—Numerical Simulation Results

With numerical research, it is possible to develop a geometry of the aerodynamic shield and assess its ability to increase the average velocity in the rotor cross-sectional plane. As presented in the section describing the research methodology, the numerical analyses began with a comparison of different types of shields dedicated as accessories to wind turbines. In the first stage, the velocity distributions inside and around the aerodynamical shield were compared for four shapes of elements, i.e., two diffusers (circle–circle and circle–square) and two confusors (also circle–circle and circle–square). The results are presented in Figure 9, which contains the velocity distribution in the symmetry plane of the shield for each of the analyzed types of elements for the length L = 666 mm. All drawings were prepared for a common velocity scale.

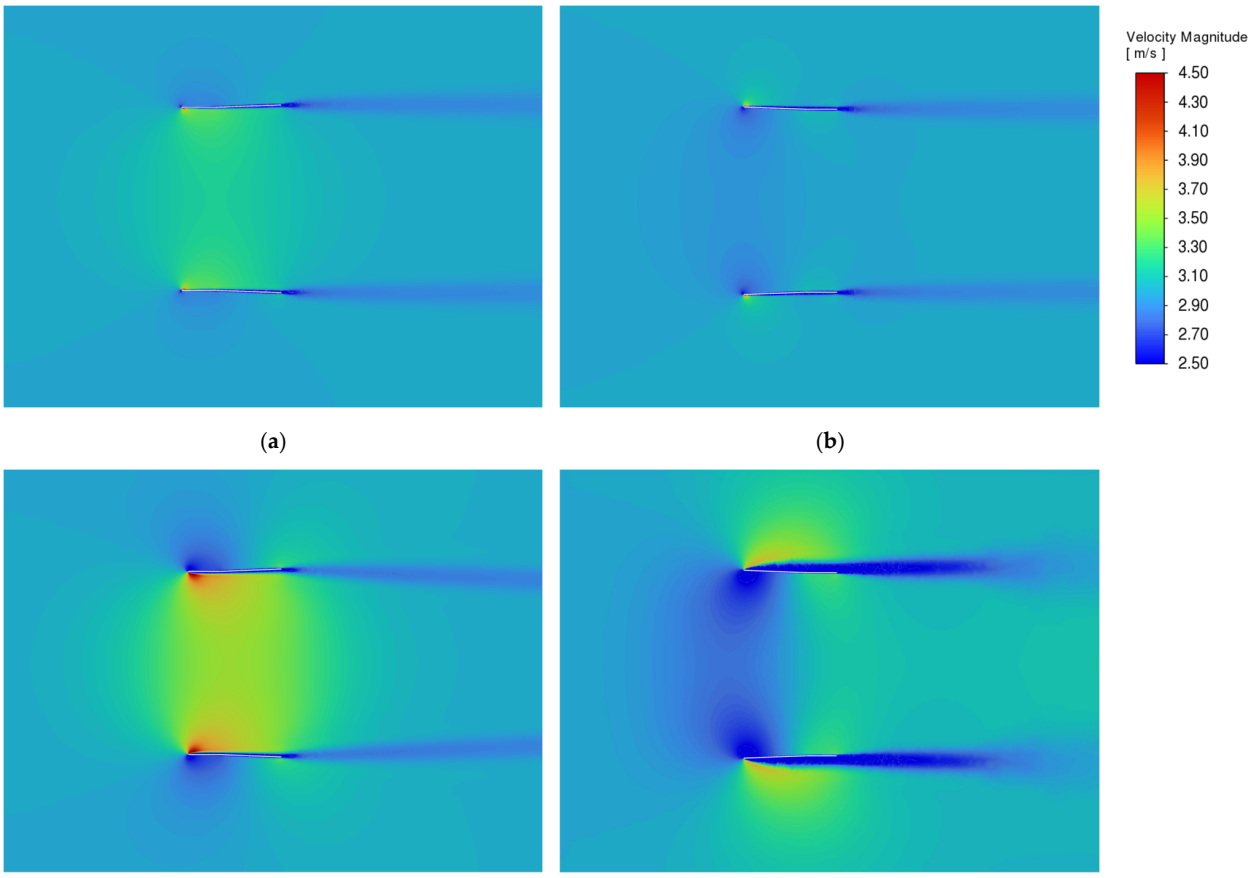

Figure 9. Velocity distribution inside and around the shield for the following configurations: (**a**) diffuser circle-to-circle; (**b**) confusor circle-to-circle; (**c**) diffuser square-to-circle; and (**d**) confusor circle-to-square.

When comparing the velocity distribution in the analyzed configurations, it should be noted that the most important aspect is the velocity in the rotor section. It should be emphasized that in the case of diffusers, this is the section at the beginning of the aerodynamic shield, while in the case of the confusor, it is at its end. As can be seen, for both variable and constant cross-sectional shapes, the diffuser configurations allow for obtaining significantly higher velocity values in the rotor section than the confusor variants. The results for circle-to-circle shapes (Figure 9a,b) show that the flow is more even and without accumulations or local increases in velocity. Changing the shapes, on the other hand, causes local accumulation, and thus a more uneven velocity distribution in the inlet section. Analyzing Figure 9c, i.e., the square-to-circle diffuser, the highest velocities are visible locally at the shield walls. The values there are noticeably higher than any other presented variants. In turn, analyzing Figure 9d, one can observe a low velocity at the inlet of the circle-to-square confusor, also resulting from a much larger cross-section of the cover. However, looking at the rotor sections, an increase in the flow velocity and a fairly uniform flow is visible.

Analogous analyses were performed for other shield lengths. The obtained results can be plotted as a function of the length of the diffuser/confusor in the circle-to-circle and circle-to-square configurations of the aerodynamic shield set-up (see Figure 10).

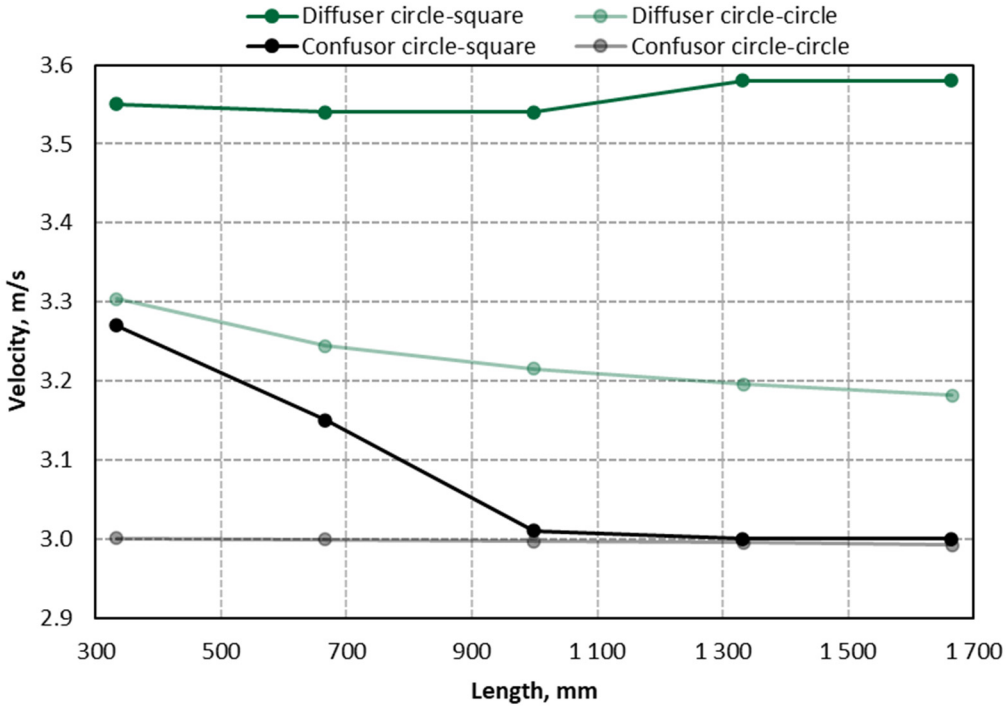

Figure 10. Velocity in a cross section as a function of the diffuser and confusor lengths in the circle-to-circle and circle-to-square configurations.

For the circle-to-square diffuser configuration, increasing the length of this element increases the air velocity in the rotor plane section. For the longest version of the diffuser analyzed, a 1% increase in velocity was obtained compared to that of the diffuser with the smallest length. As can be seen, the increase, although it occurred, is very small. For the circle-to-circle diffuser configuration and both confusors, an increase in their length results in a decrease in air velocity. The velocity reduction of 8% for the confusor circle-to-square configuration, 4% for the diffuser circle-to-circle configuration, and less than 0.5% for the confusor circle-to-circle configuration was observed, respectively. Furthermore, as can be seen in Figure 10, for the diffuser circle-to-square configuration, a higher velocity of 8% was achieved than for the diffuser circle-to-circle configuration. Simultaneously, for the diffuser circle-to-square configuration, it was possible to obtain approximately an 8% higher velocity

than for the diffuser circle-to-circle configuration. For the circle-to-circle configuration, the aerodynamic shield gives lower air velocity values than the circle-to-square variant. These correlations are evident for both the confusor and the diffuser.

The conclusions drawn from the above analysis allowed for the assumption that a combination of these two elements can be a good solution to increase the air velocity in the rotor section of a wind turbine. The set consisted of a module with a decreasing cross-section (confusor) at the inlet, the rotor section, and a module with an increasing cross-section (diffuser) behind it. Since significantly better results were achieved for the circle-to-square cross-section, further analysis was conducted for a combined confusor and diffuser system in the circle-square version. Figure 11 presents an example of geometry used in the numerical simulation.

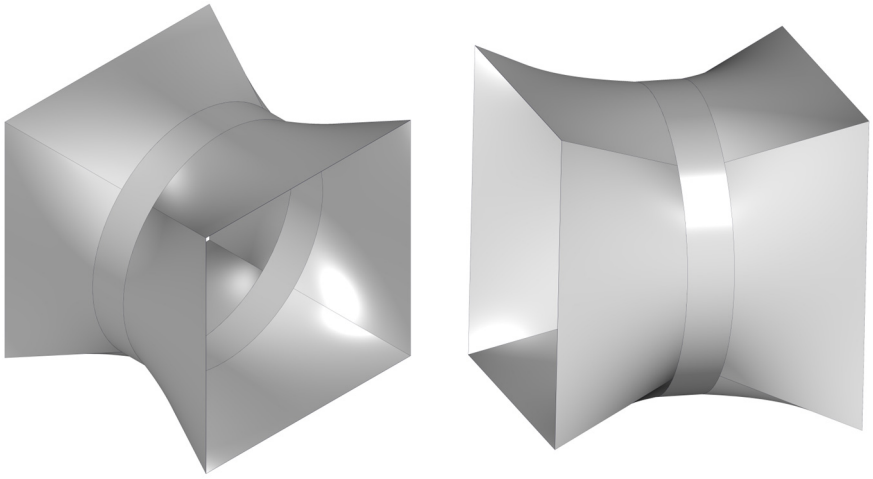

Figure 11. The geometry of the confusor–diffuser configuration used in the numerical simulation.

The calculations performed included various variants differing in the length of individual sections. The analysis was carried out assuming that the total length of the tested system should be 1966 mm. This length already includes the circular ring with a length of 300 mm, which is designed for the rotor. The study focused on four variants with different lengths of the components. The details of the selected variants subject to analysis are presented in Figure 12.

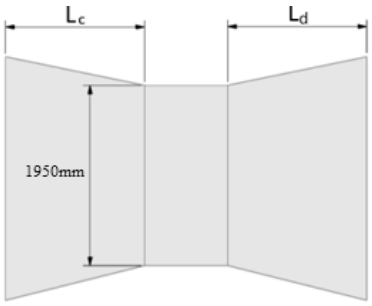

Configuration	CD_1	CD_2	CD_3	CD_4
L_c, mm	111	222	333	833
L_d, mm	1555	1444	1333	833
L_{c+d}, mm	1666	1666	1666	1666
L_{total}, mm	1966	1966	1966	1966

Figure 12. Framework of different variants for the lengths of combined diffuser and confusor elements.

For each of the variants, a geometric model was prepared, which then constituted the basis for the meshing process and numerical calculations. The assumptions and settings adopted were consistent with those used at the analysis stage of the individual elements (diffusers and confusors). Based on the CFD results, the average incoming air velocity into the rotor section of the wind turbine was analyzed. The summary of the values obtained is presented in Figure 13.

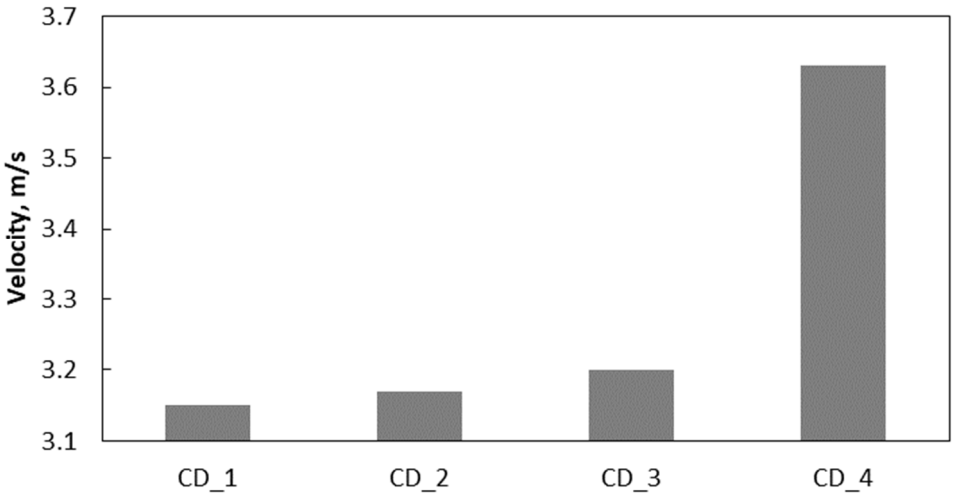

Figure 13. The average velocity in the rotor cross-section for the tested confusor–diffuser (CD) sets (according to Figure 12).

For the configuration labeled CD_4, the air velocity in the analyzed section was the highest. For the longest length of the confusor in the combined confusor and diffuser system, a 13% increase in velocity was obtained compared to the combined confusor and diffuser system with the smallest length of the confusor (CD_1). Lengthening the diffuser part of the combined set increased the velocity at the rotor cross-section. The highest increase in air velocity occurred when the lengths of the confusor and diffuser were the same. The results for configuration that allow for the highest velocity in the rotor section, i.e., CD_4, will be presented in detail below. Figure 14 shows the velocity distribution inside and around the aerodynamic shield CD_4. Figure 14a presents pathlines in the 3D view of the model. The velocity field and velocity vector distribution in the plane of the longitudinal section of the tested element are presented in Figures 14b and 14c, respectively.

As can be seen, the higher velocities are obtained in the middle of the distance between the inlet and outlet of the shield, i.e., in the rotor section. An increase in local velocities closer to the shield walls is also visible. Flow analysis, similar to the example presented, was performed for each configuration included in the research. On this basis, it was possible to assess the flow characteristics and the potential in the context of increasing the speed in the rotor section.

(**a**)

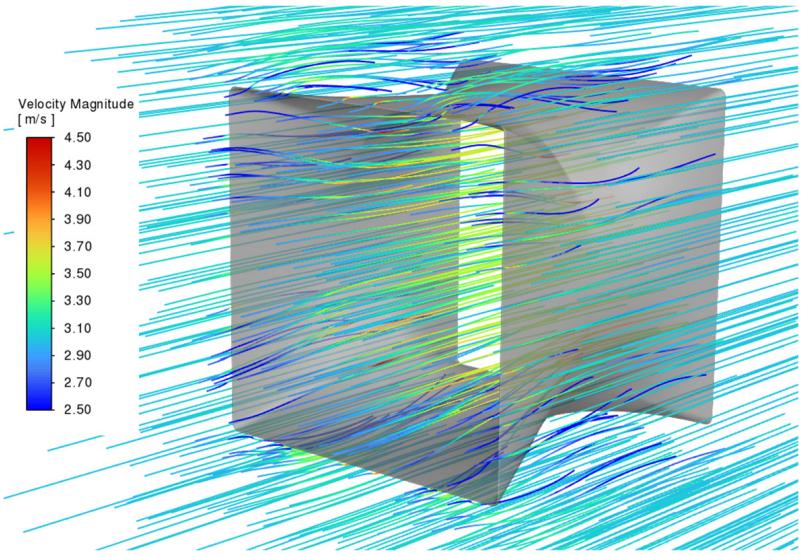

Figure 14. *Cont.*

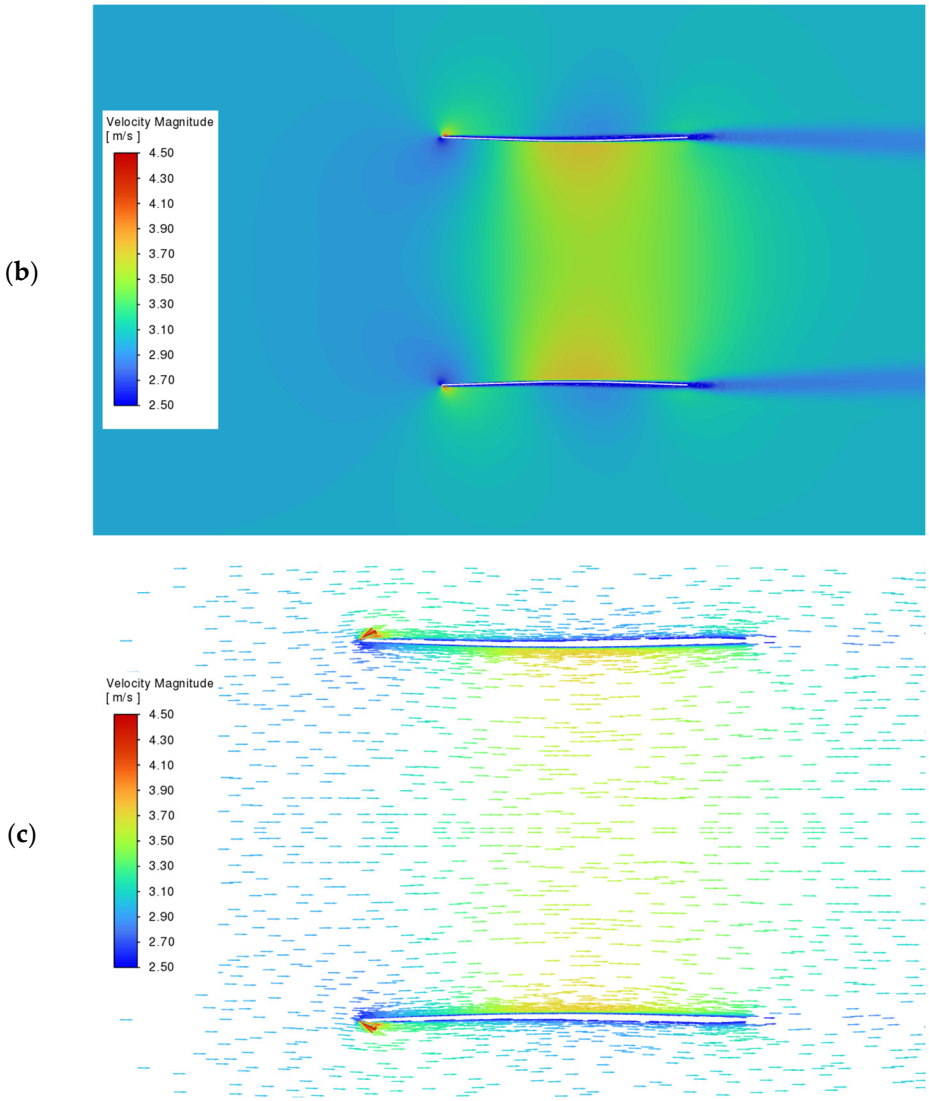

Figure 14. Air velocity inside and around a condenser–diffuser shield CD_4: (**a**) pathlines; (**b**) velocity field; and (**c**) velocity vectors.

To summarize, for a combined system of a confusor and a diffuser with the same length of 833 mm (configuration CD_4), a velocity in the rotor cross-section increases up to approximately 3.63 m/s. For the combined confusor and diffuser system, this translates into a significant air velocity increase of about 21% compared to the incoming air velocity.

4. Discussions

The results of the experimental studies provide important information on the influence of the blade shape and pitch angle on the efficiency of wind turbines. Additionally, numerical simulations allowed us to assess the effectiveness of using additional aerodynamic shields, such as diffusers/confusors, to increase the air velocity flowing through the turbine blades.

4.1. Effect of the Blade Shape and Inclination Angle

The analysis of the experimental results clearly shows that the shape of the blades and the number of blades have a significant influence on the efficiency of the wind turbine. Among the tested configurations, the turbine equipped with five blades with the largest chord (BL1) generated the highest power at almost all rotational speeds. Compared with other configurations, the differences in performance were clear—BL1 obtained about 5%

more power than BL2, 26% more than BL3, and as much as 35% more than BL4. These results show that the appropriate shape of the blades and their number can lead to the improved efficiency of wind turbines.

Another important factor influencing turbine performance was the blade pitch angle. Changing the blade pitch angle of the BL1 blades had a clear effect on the turbine output power. The best results were achieved at an angle of $+6^{\circ}$ (clockwise), which resulted in a power increase of 16% compared to the blades set in the initial position and 66% compared to the blades set at -6°. These results indicate that optimizing the blade pitch angle can significantly improve the performance of wind turbines, even more than modifying the blade shape itself.

4.2. Effect of the Aerodynamic Shield on the Air Velocity in the Rotor Section

Numerical simulations carried out for different aerodynamic shield configurations showed that the use of properly designed diffusers and confusors can significantly affect the air velocity entering the turbine blade section. The results showed that for the diffuser configuration with a circle-to-square transition, extending its length leads to an increase in the air velocity in the rotor plane. The greatest increase in speed, by about 13%, was achieved with the longest version of the confusor combined with a diffuser of the same length. Based on this research, it can be concluded that appropriate optimization of the length and shape of aerodynamic shields can significantly improve the efficiency of wind turbines by increasing the speed of air reaching the blades, which directly translates into greater power generated by the turbine.

5. Conclusions

In this paper, the impact of the design parameters on the power output of a small wind turbine has been analyzed experimentally and using numerical modeling. The shape of the rotor blades and inclination of the rotor blades as well as the use of additional aerodynamic shields were analyzed.

The analysis indicates that the power output of the wind turbine is strongly influenced by the type of blade and the angle of the blades' inclination. The study showed that the best results were obtained by the turbine with blades labeled as BL1. At the same time, the power output for each type of blade depends on the rotational speed. Comparing the values obtained for the individual turbines at a rotational speed of 350 RPM (for most of the tested rotors the maximum power output was achieved around this value), the wind turbines generated approximately 5% to 35% less power, depending on the type of wind turbine blades. The results also indicate the importance of the inclination angle of wind turbine blades. By changing the angle of inclination, up to a 16% increase in power generated by the wind turbine under study was achieved.

The power output of the wind turbine is highly dependent on the wind velocity, as can be deduced by a well-known formula (Equation (1)). Even a small increase in wind velocity can result in significant growth in electrical power. The presented results show that the optimized combined confusor and diffuser set allows for increasing the incoming air velocity on the rotor section. Adequate aerodynamic shapes make wind turbines more efficient and perform better. In the analyzed configuration, an approximate 21% increase in wind speed was observed, resulting in an increase of 77% in wind turbine power output (assuming a constant C_p coefficient).

Author Contributions: Conceptualization, J.H. and K.Z.-G.; methodology, J.H.; software, P.M.; validation, J.H., K.Z.-G. and P.M.; formal analysis, K.Z.-G.; investigation, J.H.; resources, P.M.; data curation, M.J.; writing—original draft preparation, K.Z.-G.; writing—review and editing, M.J. and M.B.; visualization, J.H.; supervision, M.B.; project administration, M.J.; funding acquisition, M.B. All authors have read and agreed to the published version of the manuscript.

Funding: This article was supported by the program "Excellence initiative—research university" for the AGH University of Krakow.

Data Availability Statement: The raw data supporting the conclusions of this article will be made available by the authors on request.

Conflicts of Interest: The authors declare no conflicts of interest.

References

1. Schaffarczyk, A.P. *Introduction to Wind Turbine Aerodynamics*, 3rd ed.; Springer Nature: Cham, Switzerland, 2024.
2. Kalmikov, A. Wind power fundamentals. In *Wind Energy Engineering. A Handbook for Onshore and Offshore Wind Turbines*, 2nd ed.; Letcher, T.M., Ed.; Academic Press: London, UK, 2023.
3. Wood, D. *Small Wind Turbines: Analysis, Design, and Application*; Springer: Berlin/Heidelberg, Germany, 2011.
4. Wolniewicz, K.; Kuczyński, W.; Zagubień, A. *Evaluation of Wind Resources for Horizontal and Vertical Wind Turbine*; Monography of the Faculty of Mechanical Engineering University of Technology: Koszalin, Poland, 2019.
5. James, P.A.B.; Bahaj, A.B.S. Small-scale wind turbines. In *Wind Energy Engineering. A Handbook for Onshore and Offshore Wind Turbines*, 2nd ed.; Letcher, T.M., Ed.; Academic Press: London, UK, 2023.
6. Benim, A.C.; Diederich, M.; Pfeiffelmann, B. Aerodynamic Optimization of Airfoil Profiles for Small Horizontal Axis Wind Turbines. *Computation* **2018**, *6*, 34. [CrossRef]
7. Muhsen, H.; Al-Kouz, W.; Khan, W. Small Wind Turbine Blade Design and Optimization. *Symmetry* **2020**, *12*, 18. [CrossRef]
8. Deghoum, K.; Gherbi, M.T.; Sultan, H.S.; Jameel Al-Tamimi, A.N.; Abed, A.M.; Abdullah, O.I.; Mechakra, H.; Boukhari, A. Optimization of Small Horizontal Axis Wind Turbines Based on Aerodynamic, Steady-State, and Dynamic Analyses. *Appl. Syst. Innov.* **2023**, *6*, 33. [CrossRef]
9. Umar, D.A.; Yaw, C.T.; Koh, S.P.; Tiong, S.K.; Alkahtani, A.A.; Yusaf, T. Design and Optimization of a Small-Scale Horizontal Axis Wind Turbine Blade for Energy Harvesting at Low Wind Profile Areas. *Energies* **2022**, *15*, 3033. [CrossRef]
10. Shen, X.; Yang, H.; Chen, J.; Zhu, X.; Du, Z. Aerodynamic shape optimization of non-straight small wind turbine blades. *Energy Convers. Manag.* **2016**, *119*, 266–278. [CrossRef]
11. Rezaeiha, A.; Kalkman, I.; Blocken, B. Effect of pitch angle on power performance and aerodynamics of a vertical axis wind turbine. *Appl. Energy* **2017**, *197*, 132–150. [CrossRef]
12. Dinh Le, A.; Nguyen Thi Thu, P.; Ha Doan, V.; The Tran, H.; Duc Banh, M.; Truong, V.-T. Enhancement of aerodynamic performance of Savonius wind turbine with airfoil-shaped blade for the urban application. *Energy Convers. Manag.* **2024**, *310*, 118469. [CrossRef]
13. Xu, W.; Li, G.; Zheng, X.; Li, Y.; Li, S.; Zhang, C.; Wang, F. High-resolution numerical simulation of the performance of vertical axis wind turbines in urban area: Part I, wind turbines on the side of single building. *Renew. Energy* **2021**, *177*, 461–474. [CrossRef]
14. Ye, X.; Zhang, X.; Weerasuriya, A.U.; Hang, J.; Zeng, L.; Li, C.Y. Optimum Design Parameters for a Venturi-Shaped Roof to Maximize the Performance of Building-Integrated Wind Turbines. *Appl. Energy* **2024**, *355*, 122311. [CrossRef]
15. Abdelsalam, A.M.; Abdelmordy, M.; Ibrahim, K.; Sakr, I. An investigation on flow behavior and performance of a wind turbine integrated within a building tunnel. *Energy* **2023**, *280*, 128153. [CrossRef]
16. Dilimulati, A.; Stathopoulos, T.; Paraschivoiu, M. Wind turbine designs for urban applications: A case study of shrouded diffuser casing for turbines. *J. Wind Eng. Ind. Aerodyn.* **2018**, *175*, 179–192. [CrossRef]
17. Mao, Z.; Yang, G.; Zhang, T.; Tian, W. Aerodynamic Performance Analysis of a Building-Integrated Savonius Turbine. *Energies* **2020**, *13*, 2636. [CrossRef]
18. Lee, K.-Y.; Tsao, S.-H.; Tzeng, C.-W.; Lin, H.-J. Influence of the vertical wind and wind direction on the power output of a small vertical-axis wind turbine installed on the rooftop of a building. *Appl. Energy* **2018**, *209*, 383–391. [CrossRef]
19. Riziotis, V.A.; Voutsinas, S.G. Fatigue loads on wind turbines of different control strategies operating in complex Terrain. *J. Wind Eng. Ind. Aerodyn.* **2000**, *85*, 211–240. [CrossRef]
20. Wekesa, D.W.; Wang, C.; Wei, Y.; Zhu, W. Experimental and numerical study of turbulence effect on aerodynamic performance of a small-scale vertical axis wind turbine. *J. Wind Eng. Ind. Aerodyn.* **2016**, *157*, 1–14. [CrossRef]
21. Jamieson, P. *Innovation in Wind Turbine Design*, 2nd ed.; Wiley: Hoboken, NJ, USA, 2018.
22. Masukume, P.-M.; Makaka, G.; Mukumba, P. Optimization of the Power Output of a Bare Wind Turbine by the Use of a Plain Conical Diffuser. *Sustainability* **2018**, *10*, 2647. [CrossRef]
23. Watanabe, K.; Ohya, Y.; Uchida, T. Power Output Enhancement of a Ducted Wind Turbine by Stabilizing Vortices around the Duct. *Energies* **2019**, *12*, 3171. [CrossRef]
24. Hwang, P.-W.; Wu, J.-H.; Chang, Y.-J. Optimization Based on Computational Fluid Dynamics and Machine Learning for the Performance of Diffuser-Augmented Wind Turbines with Inlet Shrouds. *Sustainability* **2024**, *16*, 3648. [CrossRef]
25. Alkhabbaz, A.; Yang, H.-S.; Tongphong, W.; Lee, Y.-H. Impact of compact diffuser shroud on wind turbine aerodynamic performance: CFD and experimental investigations. *Int. J. Mech. Sci.* **2022**, *216*, 106978. [CrossRef]
26. Bontempo, R.; Di Marzo, E.M.; Manna, M. Diffuser augmented wind turbines: A critical analysis of the design practice based on the ducting of an existing open rotor. *J. Wind Eng. Ind. Aerodyn.* **2023**, *238*, 105428. [CrossRef]
27. Sridhar, S.; Zuber, M.; Shenoy, S.B.; Kumar, A.; Ng, E.Y.K.; Radhakrishnan, J. Aerodynamic comparison of slotted and non-slotted diffuser casings for Diffuser Augmented Wind Turbines (DAWT). *Renew. Sustain. Energy Rev.* **2022**, *161*, 112316. [CrossRef]

28. Bontempo, R.; Manna, M. The Joukowsky rotor for diffuser augmented wind turbines: Design and analysis. *Energy Convers. Manag.* **2022**, *252*, 114952. [CrossRef]
29. Refaie, A.G.; Abdel Hameed, H.S.; Nawar, M.A.A.; Attai, Y.A.; Mohamed, M.H. Qualitative and quantitative assessments of an Archimedes Spiral Wind Turbine performance augmented by A concentrator. *Energy* **2021**, *231*, 121128. [CrossRef]
30. Teklemariyem, D.A.; Yimer, E.T.; Ancha, V.R.; Zeru, B.A. Parametric study of an empty diffuser geometric parameters and shape for a wind turbine using CFD analysis. *Heliyon* **2024**, *10*, e26782. [CrossRef] [PubMed]
31. Shambira, N.; Makaka, G.; Mukumba, P. Velocity Augmentation Model for an Empty Concentrator-Diffuser-Augmented Wind Turbine and Optimisation of Geometrical Parameters Using Surface Response Methodology. *Sustainability* **2024**, *16*, 1707. [CrossRef]
32. ANSYS. *Fluent Theory Guide*; Release 20.1; ANSYS, Inc.: Canonsburg, PA, USA, 2020. Available online: https://www.ansys.com/products/fluids/ansys-fluent (accessed on 30 April 2024).
33. Marczak, P. Design of a Building Integrated Wind Turbine. Master's Thesis, AGH University of Krakow, Kraków, Poland, 2021. (In Polish).
34. Zore, K.; Sasanapuri, B.; Parkhi, G.; Varghese, A. Ansys Mosaic Poly-Hexcore mesh for high-lift aircraft configuration. In Proceedings of the 21th Annual CFD Symposium, Bangalore, India, 8–9 August 2019.
35. Uchida, T.; Taniyama, Y.; Fukatani, Y.; Nakano, M.; Bai, Z.; Yoshida, T.; Inui, M. A New Wind Turbine CFD Modeling Method Based on a Porous Disk Approach for Practical Wind Farm Design. *Energies* **2020**, *13*, 3197. [CrossRef]

computation

MDPI

Article

Comparative Study of Deflector Configurations under Variable Vertical Angle of Incidence and Wind Speed through Transient 3D CFD Modeling of Savonius Turbine

Hady Aboujaoude [1,*], Guillaume Polidori [1], Fabien Beaumont [1], Sébastien Murer [1], Yessine Toumi [1,2] and Fabien Bogard [1,2]

[1] ITHEMM, University de Reims Champagne-Ardenne, 51100 Reims, France
[2] Pôle de Recherche Châlonnais, Université de Reims Champagne-Ardenne, 51000 Châlons en Champagne, France
* Correspondence: hady.aboujaoude@univ-reims.fr

Abstract: The demand for clean and sustainable energy has led to the exploration of innovative technologies for renewable energy generation. The Savonius turbine has emerged as a promising solution for harnessing wind energy in urban environments due to its unique design, simplicity, structural stability, and ability to capture wind energy from any direction. However, the efficiency of Savonius turbines poses a challenge that affects their overall performance. Extensive research efforts have been dedicated to enhancing their efficiency and optimizing their performance in urban settings. For instance, an axisymmetric omnidirectional deflector (AOD) was introduced to improve performance in all wind directions. Despite these advancements, the effect of wind incident angles on Savonius turbine performance has not been thoroughly investigated. This study aims to fill this knowledge gap by examining the performance of standard Savonius configurations (STD) compared to the basic configuration of the deflector (AOD1) and to the optimized one (AOD2) under different wind incident angles and wind speeds. One key finding was the consistent superior performance of this AOD2 configuration across all incident angles and wind speeds. It consistently outperformed the other configurations, demonstrating its potential as an optimized configuration for wind turbine applications. For instance, at an incident angle of 0°, the power coefficient of the configuration of AOD2 was 61% more than the STD configuration. This ratio rose to 88% at an incident angle of 20° and 125% at an incident angle of 40°.

Keywords: vertical axis wind turbine; transient three-dimensional simulation; CFD simulation; power coefficient; Savonius rotor; aerodynamics; wind deflector

Citation: Aboujaoude, H.; Polidori, G.; Beaumont, F.; Murer, S.; Toumi, Y.; Bogard, F. Comparative Study of Deflector Configurations under Variable Vertical Angle of Incidence and Wind Speed through Transient 3D CFD Modeling of Savonius Turbine. *Computation* **2024**, *12*, 204. https://doi.org/10.3390/computation12100204

Academic Editors: Ali Cemal Benim, Abdulmajeed A. Mohamad, Sang-Ho Suh, Rachid Bennacer, Paweł Oclon and Jan Taler

Received: 7 September 2024
Revised: 9 October 2024
Accepted: 10 October 2024
Published: 14 October 2024

1. Introduction

With the increasing demand for clean and sustainable energy, the exploration of innovative technologies for renewable energy production has become crucial. Among the various available options, the Savonius wind turbine stands out as a promising solution for harnessing wind energy in urban environments. Its distinctive design, simplicity, structural stability, and ability to capture wind energy from all directions make it an ideal choice for areas characterized by complex wind patterns. However, the efficiency of Savonius turbines still needs improvement, which prevents their widespread use. Indeed, the superior power coefficient of the horizontal axis wind speed turbines (HAWT) and the Darrieus-type vertical axis wind turbine (VAWT) contribute significantly to their prevalence in various applications. To overcome this limitation, considerable research efforts have been dedicated to improving their efficiency and optimizing their performance in urban environments. By implementing new techniques, researchers are addressing these limitations with the aim of achieving wider adoption and thus making a significant contribution to a sustainable future. Several articles [1–6] have extensively examined the results of experimental and

numerical research on wind turbines. These numerous studies have focused on enhancing performance by adjusting parameters such as the number of blades [7], the presence of an end plate, the Overlap Ratio (OR), the ratio between the height and diameter of the turbine, the aspect ratio (AR = H/D) [8,9]. The calculated performance criterion is the Cp (the ratio of power provided by the turbine to the wind existing power) (Equation (4)).

For instance, the effect of incorporating upper and lower end plates has led to a 36% increase in the power coefficient Cp with the presence of these plates [10]. Furthermore, the incorporation of an overlap region (OR) between the blades, allowing the wind to circulate backward and generate positive torque, has also been analyzed through comparisons of energy production between turbines with and without the overlap section [11]. Similarly, Sobczak et al. (2018) [12] noted that an AR between 1.0 and 2.0 is a good compromise between performance and compactness. Researchers have also analyzed the pressure distribution on the rotor blades to better understand the areas of low and high pressure that contribute to the overall torque of Savonius turbines [13]. Experimental results highlight the potential for improving the power coefficient by strategically modifying the rotor blade geometry of Savonius turbines [14,15].

Furthermore, another proposed research direction involves innovative external systems to increase airflow towards the turbine and these are reported in Table 1. Researchers initially studied unidirectional wind deflectors to enhance the performance of Savonius turbines in the direction of the dominant wind. They simulated a combination of flat and circular shields, which resulted in achieving a Cp_{max} of 0.243 [1]. A flat deflector facing the turbine yielded a Cp_{max} of 0.34 [16]. Introducing a V-shaped wind concentrator increased power by 19.7% compared to a standard rotor without a deflector [17]. Circular deflectors were also investigated to reduce wind pressure on the convex blade [18]. Concentration deflectors placed upstream of the rotor effectively reduced flow on the return blade, thus minimizing negative torque [19]. Additionally, it was found that guide vanes enhanced rotor performance [3].

Table 1. Research on Savonius deflectors.

Authors	Design	Reported C_{Pmax}	Study	Wind Concentrator
El-Askary et al., 2015 [3]	Curtain design	>0.5	Numerical—2D CFD	Unidirectional
Burçin et al., 2010 [20]	Curtain design	0.38	Experimental—Wind tunnel	Unidirectional
Morcos et al., 1981 [17]	Flat plate shield	0.34	Experimental—Wind tunnel	Unidirectional
Aboujaoude et al., 2022 [21]	Axisymmetric deflector	0.31	Numerical—3D CFD	Axisymmetric multidirectional
Tartuferi et al., 2015 [22]	Curtain design	0.3	Numerical—2D CFD	Self-rotating
Yonghai et al., 2009 [19]	Deflector plate	0.28 *	Numerical—2D CFD	Unidirectional
Alexander et Holownia, 1978 [1]	Flat plate shield	0.24	Experimental—Wind tunnel	Unidirectional
Shaughnessy et Probert, 1992 [18]	V-shaped deflector	<0.12 *	Experimental—Wind tunnel	Unidirectional

The values of CPmax in studies marked with an asterisk * were extrapolated.

Finally, the incorporation of a conveyor-deflector curtain into a conventional Savonius rotor increased the Cp by 0.30 [20]. However, it is important to understand that these improvements are primarily theoretical, given the significant fluctuations in wind direction in urban environments where Savonius wind turbines are intended to be installed. In fact, the proposed deflectors enhanced turbine performance in the predominant wind direction, but conversely, they result in a substantial decrease in performance in all other wind directions. The authors introduced an axisymmetric omnidirectional deflector (AOD) to consider the high turbulence and fluctuating wind direction and speed in urban environments [22]. The initial deflection model (AOD1), a simple truncated cone, showed an average increase in Savonius turbine performance of 25% over the studied peak velocity ratio range and a 30% increase in starting torque in all directions. An optimized model (AOD2) was subsequently developed by the authors to reduce structural fatigue and further increase performance by 20% across the entire range of peak velocities considered [21]. However, the effect of wind incidence angles has not been thoroughly studied in these articles.

The current study aims to fill this gap by examining the performance of a standard Savonius (STD) compared to a Savonius wind turbine with a basic axisymmetric omnidirectional conical deflector (AOD1) and a Savonius wind turbine with an optimized axisymmetric omnidirectional deflector (AOD2) under different wind incidence angles and wind speeds. By accounting for the variability of wind incidence angles in urban environments, this research will contribute to a more comprehensive understanding of Savonius turbine performance and thus to a broader application of their applicability in real-world scenarios.

2. Methodology

2.1. Flow Parameters

In the computational fluid dynamics (CFD) study conducted on the Savonius turbine, various crucial flow parameters were systematically evaluated to analyze and understand its performance characteristics. For this study, three distinct inlet velocities were used, namely 4 m·s^{-1}, 7 m·s^{-1}, and 14 m·s^{-1}. Additionally, six tip speed ratios λ were imposed to comprehensively investigate the turbine's performance across the entire tip speed ratio range, as outlined in Table 2. The tip speed ratio is defined as follows:

$$\lambda = \frac{R\omega}{V_\infty} \tag{1}$$

where R is the radius of the turbine, ω the rotational speed and V_∞ is freestream air speed.

Table 2. Simulation parameters.

Parameters	Description	Unit	Values
λ	Tip speed ratio	Dimensionless	0.2; 0.4; 0.6; 0.8; 1.0
θ	Vertical wind incident angle	Degree	0°; 10°; 20°; 30°; 40°
V_∞	Freestream air speed	m/s	3.5; 7.0; 14.0

This inclusive approach enabled a comprehensive examination of the turbine's efficiency and effectiveness under varying flow conditions and operational parameters. To address the primary focus of this study, which is the impact of wind incident angle (θ), five specific angles were chosen for each simulation, ranging from 0° to 40° with an increment of 10°, as depicted in Figure 1. By carefully considering and manipulating these flow parameters, a detailed analysis of the Savonius turbine's behavior and performance under diverse operating conditions was achieved.

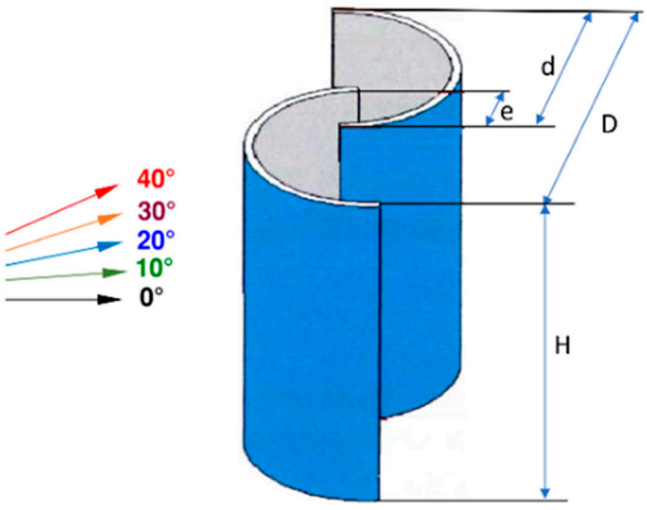

Figure 1. Geometric parameters of the Savonius rotor and the different wind incident angle θ.

2.2. Geometric Details of the Standard Savonius Turbine (STD)

The Savonius rotor studied, devoid of deflectors, comprises a two-blade configuration in line with the suggestions set out in [23], which advocate the use of a two-blade design to improve performance. The aspect ratio AR is set to 1.66 as per the available experimental results conveyed by Blackwell et al. (1977) in order to validate the model. The turbine is chosen to have end plates. As per the literature recommendations [24], the ratio chosen between the diameter of the end plate and the diameter of the turbine is set to 1.1 to benefit from the best performance. The dimensionless gap width is defined by the ratio e/d, see Figure 1. According to [6], the turbine efficiency is optimal for a dimensionless gap width of 0.15. The main geometric parameters impacting the performance of the Savonius rotor are shown in Figure 1 and are defined as follows (Table 3):

Table 3. Turbine dimensions.

Number of Blades	Blade Diameter	Turbine Height	Endplate Diameter	Endplate Height	Dimensionless Gap Width e/d
2	0.5 m	1.5 m	1.0 m	0.01 m	0.15

2.3. Geometric Details of Axisymetric Omnidirectional Deflector (AOD1) and (AOD2)

Wind deflectors applied to Savonius turbines can improve their power coefficient by enhancing the aerodynamic characteristics of the rotor blades. The primary function of the deflector is to redirect and increase the incoming wind flow towards the turbine blades, resulting in improved torque and rotational speed. Additionally, wind deflectors are used to redirect the airflow to the rotor in a way to increase the efficiency of the turbine. The first deflector used as a benchmark in this study is the one developed in [21], specified as axisymetric omnidirectional deflector 1 (AOD1), as shown in Figure 2. The profile consists of a fixed, non-rotating, three-dimensional truncated cone installed above and below the rotating Savonius turbine. The height of the deflector is 75 cm while the small diameter and the big diameter are, respectively, 105 cm and 150 cm. The mounting system of the deflectors is not represented, but it is thought to be completely dissociated and independent from the turbine structure. The second deflector used is an aerodynamically enhanced geometrical shape of AOD1 presented by Aboujaoude et al. [23] based on a convex spline shape deflector with the dimensions presented in Figure 2 and will be referred to as AOD2. This AOD2 spline is defined as a quadratic Bezier curve with three control points represented as black dots in Figure 2a with their relative coordinate dimensions. It showed an improved performance compared with AOD1 [23] along with reduced fatigue and stress on the turbine axis on a wind incident angle θ of 0°.

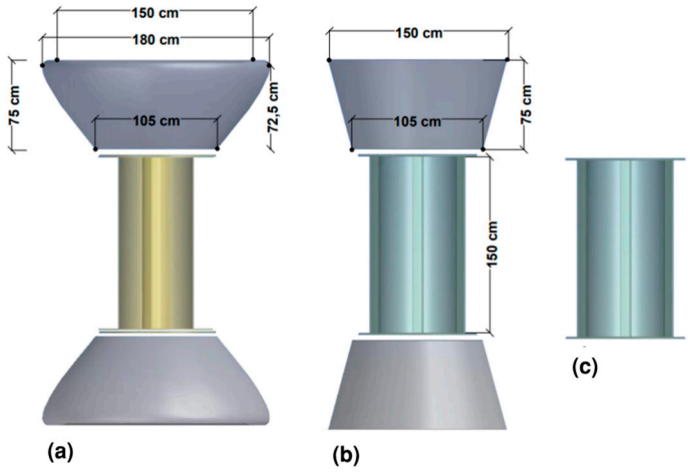

Figure 2. (**a**) AOD2 (optimized cone), (**b**) AOD1 (truncated cone), (**c**) STD (without deflector).

2.4. Computational Domain and Mesh

The computational domain containing a rotor should be sufficiently large to minimize its effect on the performance parameters of the rotor [25]. To analyze the impact of the wind incident angle θ, the inlet boundary was positioned close to the turbine, with an upstream distance of 1 m equivalent to 1 diameter of the rotor. Additionally, considering a maximum wind tested incident angle of 40°, the height of the computational domain was increased to 12 times the rotor diameter (12D) to accurately capture the characteristics of the wake region and, consequently, calculate precisely the torque developed around the turbine axis. The ratio of the frontal cross-sectional area of the rotor and that of the computational domain is known as the blockage ratio. The blockage ratio, which relates the frontal cross-sectional area of the rotor to that of the computational domain, could overestimate the power coefficient (Cp) of a turbine [26]. In our study, we aimed to minimize computational domain boundary effects on the rotor's performance, so a blockage ratio of 0.003125 was chosen to ensure negligible influence. As shown in Figure 3, the downstream distance of the outlet boundary from the rotor domain is set to be 18.5D. The distance between the walls of the computational and the rotor domain is 10D on the left and right side and 12D on the top and bottom side. Considering the blockage ratio requirements, the dimensions of the computational domain were set to 20D × 20D × 24D. The inlet boundary was defined with constant velocity speeds (3.5 $m \cdot s^{-1}$, 7 $m \cdot s^{-1}$, and 14 $m \cdot s^{-1}$) and variable wind incident angles θ ranging from 0° to 40° with an increment angle of 10°. A pressure outlet boundary condition was applied on the right side of the computational domain to enforce the dissipation of airflow at atmospheric pressure outside the computational domain. The remaining sides of the computational domain were set as non-slip wall boundaries. Simulating a system involving a rotating part, such as the turbine rotor in our study, required the use of the sliding meshing method [26]. This method enables separate regions with different meshing requirements for the rotating and stationary subdomains. The stationary subdomain was obtained by extracting the rotating part and the designed deflector from the initial computational domain. The rotating subdomain was then modeled and added as a separate cylinder, as shown in Figure 3. The sliding mesh technique in ANSYS Fluent was utilized to impose the turbine rotation speed for each simulation and monitor the torque developed around the turbine axis. An unstructured mesh consisting of 4 million tetrahedral elements was generated using ANSYS Meshing software (2024 R2 version) (Figure 3). Downstream of the rotor, the mesh was refined to capture wake vortices. Additionally, an inflation mesh with 18 layers of prismatic elements was created around the blades to achieve appropriate (y+) values. The growth ratio used was 1.1 near the walls and 1.2 in the free airsteam to reduce the cell number. The dimensionless height of the first mesh node adjacent to the wall (y+) has a significant impact on the simulation results. To ensure accurate resolution of the viscous sublayer and the torque produced around the turbine axis, a (y+) value below 5 on the blades was targeted. This optimized mesh allowed for an average (y+) value of 1.8 on the turbine surface. The STD model was validated previously by comparing the simulated values of Cp with Blackwell et al. (1977) [2] wind tunnel experiments in the authors' previous published paper [21].

2.5. Governing Equations and Turbulence Models

In CFD studies of Savonius wind turbines, three available techniques for turbulence modelling are used: (a) unsteady Reynolds-averaged Navier–Stokes (URANS), (b) large eddy simulation (LES), and (c) direct numerical simulation (DNS). In the URANS approach, the governing equations are computationally solved for the time-averaged flow behavior along with a suitable turbulence model for the closure of the governing equations. Unlike LES and DNS, the URANS method models all the turbulence scales. While it is less accurate, it is cost effective and less time consuming and provides the accuracy needed in the engineering applications like design optimization and therefore is widely used in wind turbine applications. URANS showed accurate predictions of torque calculation in rotating machinery which is the main parameter used to determine the performance of

turbines [27]. In this approach, the flow properties averaged over time are examined. The URANS momentum and continuity equations are written as follows:

$$\frac{\partial}{\partial t}(\overline{\rho u_i}) + \frac{\partial}{\partial x_j}(\overline{\rho u_i u_j}) = -\frac{\partial \overline{p}}{\partial x_i} + \frac{\partial}{\partial x_j}\left[\mu\left(\frac{\partial \overline{u_i}}{\partial x_j} + \frac{\partial \overline{u_j}}{\partial x_i} - \frac{2}{3}\delta_{ij}\frac{\partial \overline{u_k}}{\partial u_k}\right)\right] + \frac{\partial}{\partial x_j}\left(-\overline{\rho u_i' u_j'}\right) \quad (2)$$

$$\frac{\partial \overline{\rho}}{\partial t} + \frac{\partial}{\partial x_i}(\overline{\rho u_i}) = 0 \quad (3)$$

where $\overline{u_i}$ and u_i' are the mean and fluctuating velocity components (i = 1, 2, 3), ρ is the fluid density, μ the molecular viscosity, p is the pressure, and the function δ_{ij} is defined as $\delta_{ij} = \begin{cases} 1, i = j \\ 0, i \neq j \end{cases}$. The Reynolds stress term $-\overline{\rho u_i' u_j'}$ is modeled by the k-ω SST two equation turbulence model which was found to be the most appropriate for wind turbine applications. The flow is considered as incompressible where the density is constant, and the molecular viscosity is also considered as constant.

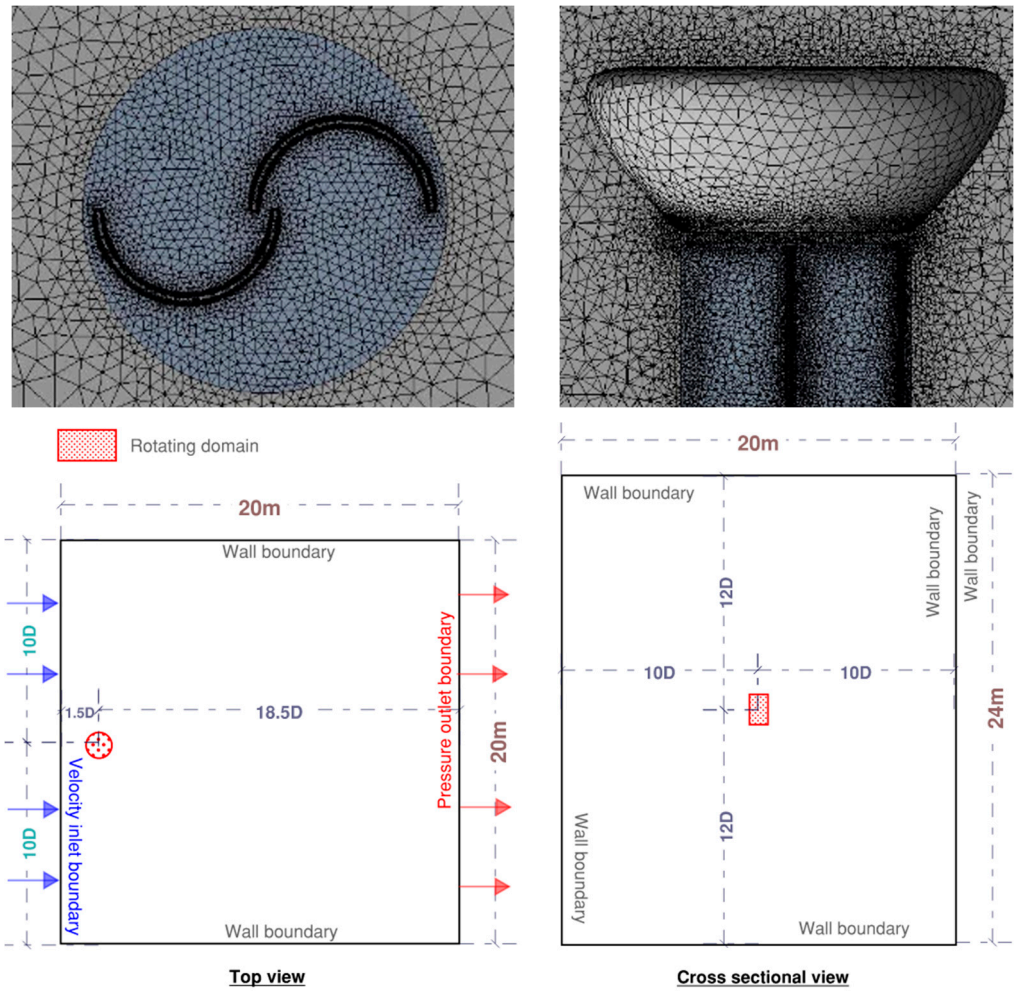

Figure 3. Computational domain and mesh cross sections used.

The typical k-ω model works well for wall-bounded flows, but not for free-shear flows. The SST k-ω model is an extensively used model that combines the features of k-ω and k-ϵ models. It showed accurate prediction for rotating applications such as the vertical axis wind turbine compared to experimental values [28,29].

It has been used and validated by many researchers for modelling the Reynolds stress in the vertical axis wind turbine simulations.

2.6. Solver Settings

Numerical simulations were carried out using the commercial CFD software ANSYS Fluent (2024 R2 version), employing the finite volume method. Given the computationally intensive nature of the transient 3D CFD simulations, steps were taken to reduce simulation time. This involved reducing the mesh count and employing larger time steps. To achieve these computational time reductions, a hybrid algorithm scheme was implemented, as recommended by [23]. This hybrid approach combined a segregated algorithm with a pressure-based coupling. The pressure-based coupled algorithm, while providing greater accuracy and fewer divergences compared to the segregated algorithm, is computationally demanding. However, it enables the use of a coarser mesh and prevents divergence at the beginning of the simulation. To leverage the benefits of both schemes, the hybrid algorithm initially employs a coarser mesh along with the pressure-based coupled algorithm for the first three iterations, see Figure 4. Afterward, it switches to the segregated algorithm to further optimize computational time. Additionally, a second-order upwind scheme was employed to enhance solution stability and accuracy, particularly for the convective terms. Table 4 sums up the CFD parameters.

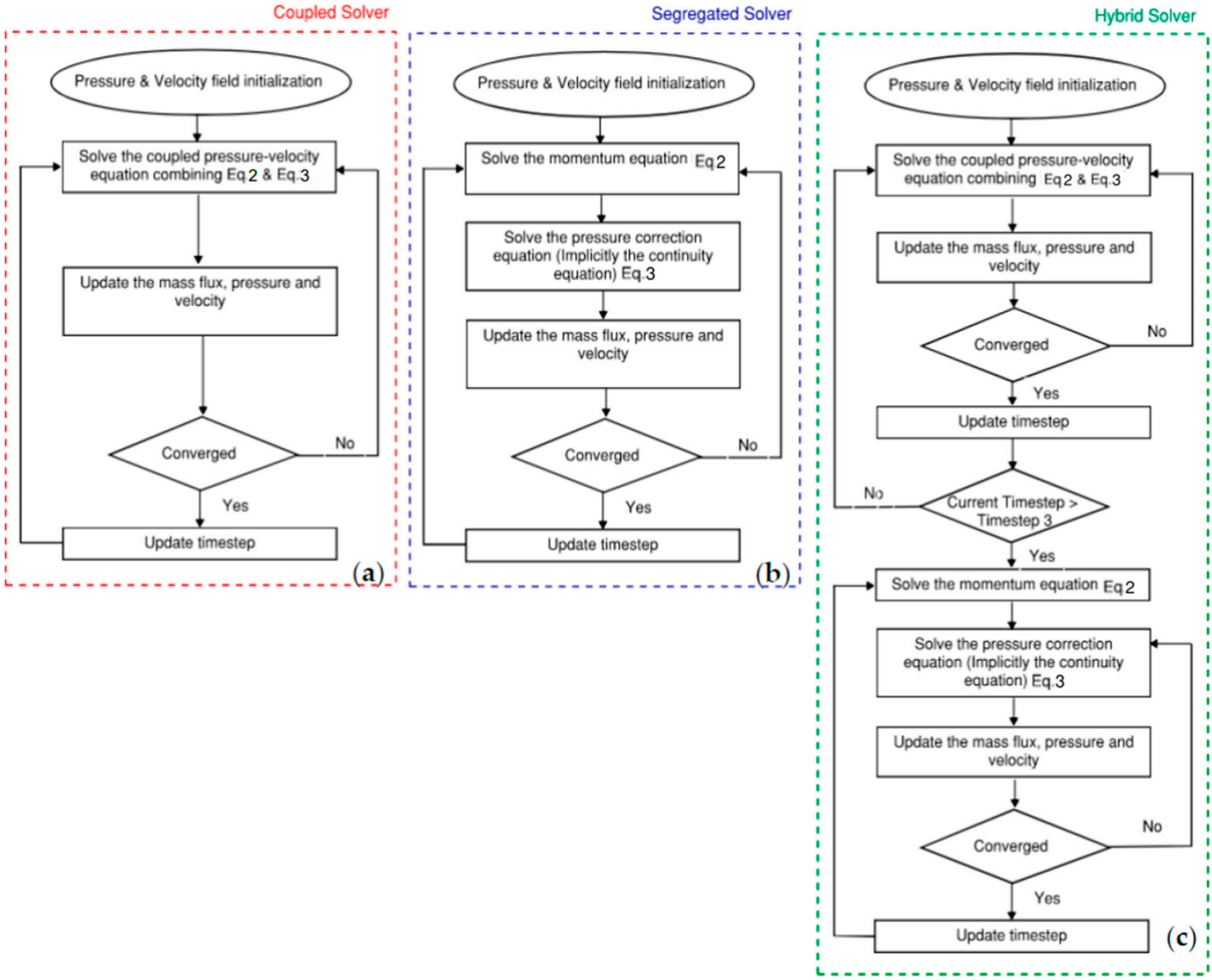

Figure 4. Solver's algorithm. (**a**) Coupled solver algorithm. (**b**) Segregated solver algorithm. (**c**) Hybrid solver scheme [23].

Table 4. CFD parameters and settings.

Parameters	Method or Specification
Solver Type	Transient
Turbulence Model	kw-SST
Solution Method	Hybrid solver using Pressure Coupled and Simple Algorithms
Timestep	1°
Residual Criteria	10–4 for the continuity and 10–6 for all the other parameters
Rotational Model	Sliding mesh technique
Spatial discretization: Gradient	Least square cell based
Spatial discretization: Pressure	Second order
Momentum, Turbulence Kinetic Energy & Specific Dissipation Rate	Second order upwind
Transient Formulation	Second order implicit

3. Results

3.1. Mesh and Timestep Sensitivity Analysis

A mesh sensitivity analysis was carried out on the STD type turbine configuration to ensure grid independency using four meshes with different y+ values and cell sizes. The number of cells varied from 0.5 million to 8.0 million across the four different grids. Figure 5 sums up the variations in Cp values with tip speed ratio for the four grids. It can be observed that the 8-million-cell grid has quite similar results as the 4-million-cell grid for all the values of λ. For this study, the 4-million-cell grid is selected for the subsequent study to reduce the computational cost and provide good accuracy. The maximum courant number in this study is fixed at 0.8. The averaging of torque and power coefficients is performed for three values of rotations of 0.5°, 1.0°, and 2.0° per time step. Table 5 shows the averaged torque coefficient for three values of the time step considered. The variation between 2.0° per time step and 1.0° per time step rotation is 2.4%. However, the variation between 1.0° per time step and 0.5° per time step is 0.8%. Therefore, a time step of 1.0° is selected for simulations.

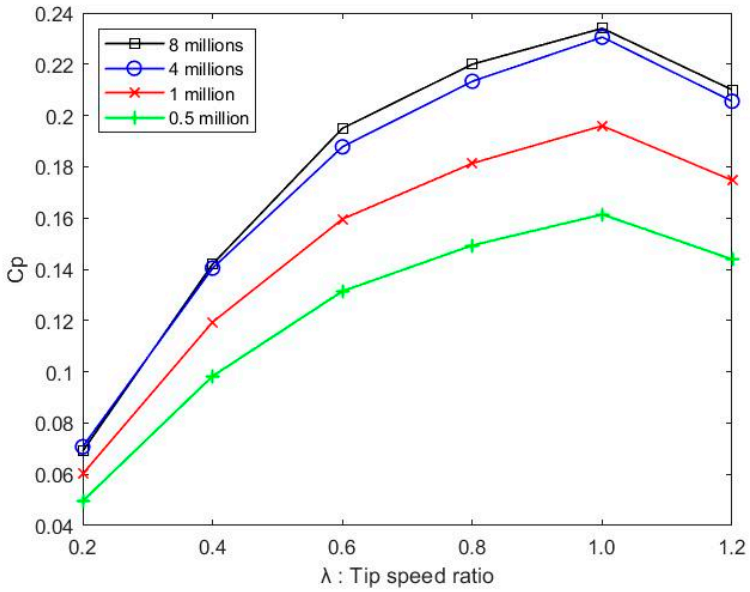

Figure 5. Power coefficient for different meshes.

Table 5. Power coefficient using different timesteps.

Rotation Angle per Time Step	Cp at λ = 1.0
0.5°	0.2307
1°	0.2305
2°	0.225

3.2. Incidence Angle Effect on Power Coefficient on Various Configurations at a Wind Speed of 7 m·s^{-1}

3.2.1. Power Coefficient

The variation of wind speed and direction in urban environments and on high-rise buildings is significant due to turbulence. Savonius turbines, commonly installed in these locations, often operate under conditions where both the wind speed and direction are changing. Although VAWT turbines have the advantage of being able to harvest wind energy from any direction, the vertical wind incidence angle θ still significantly affects their performance. The numerical and experimental investigations provided in the literature consider θ = 0°. This simplified assumption, while helpful for initial understanding, does not represent real-world urban conditions. To fill this knowledge gap, 75 cases of 3D unsteady numerical simulation were launched to monitor the performance variations of these Savonius turbine configurations under various θ.

The power coefficient defined by (Equation (4)), is a key indicator of the wind turbine performance and is widely used in the literature as a basis for comparison between novel turbine designs and standard configurations or between numerical and experimental results. Similarly, in this study, Cp is used to compare the different configuration performances.

$$C_P = \frac{T\omega}{0.5\rho V_\infty^3 DH} \tag{4}$$

where T is the torque developed around the axis of the wind turbine, ω is the rotational speed of the wind turbine, ρ is the air density, V_∞ is the air velocity, D is the diameter of the wind turbine and H is its height.

Figure 6 retraces the Cp values of each of the configuration STD, AOD1, and AOD2 versus the tip speed ratio λ. In addition, and to monitor the impact of the vertical incidence angle on the performance, separate curves were plotted for each θ.

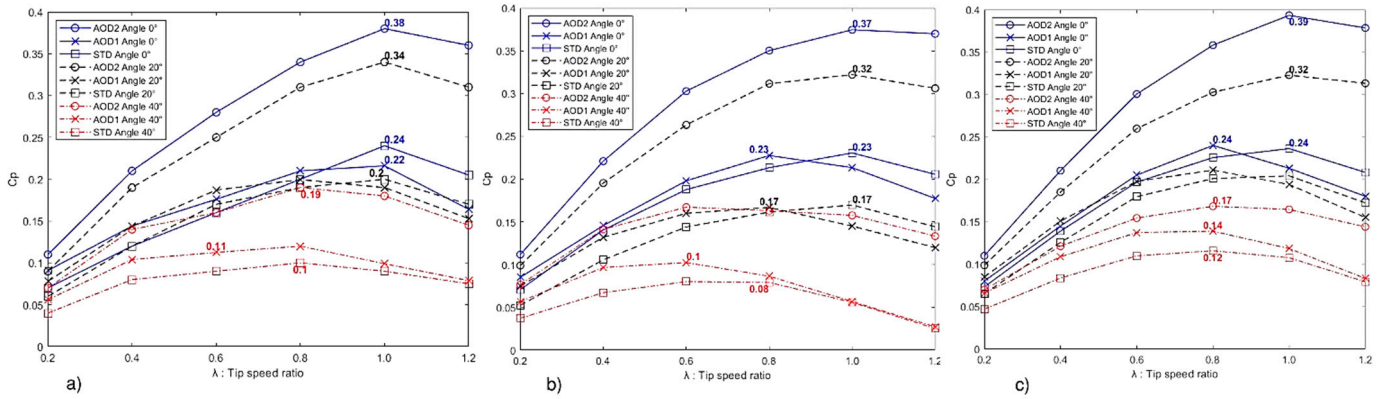

Figure 6. Power coefficient of different turbine configurations (STD, AOD1, and AOD2) under varying incidence angle and tip speed ranges. (**a**) Wind speed of 3.5 m·s^{-1}, (**b**) wind speed of 7 m·s^{-1}, (**c**) wind speed of 14 m·s^{-1}.

Analysis of the simulation Cp values revealed a distinct overall pattern.

A negative correlation exists between turbine performance (Cp) and vertical wind incidence angle θ for all the configurations. This phenomenon is attributable to the fact that the Savonius turbine's rotational energy is derived from the drag forces exerted on

its blades. As θ increases, the resulting drag force exerted on the turbine blade decrease,s while the lift force exerted on the deflector and the end plate increases. Obviously, at θ = 0° the conversion of the wind kinetic energy to drag force is at its maximum.

As shown in Figure 6, this is true for all configurations and for all inlet wind speeds (3.5 m/s, 7 m/s, and 14 m/s).

Another key finding was the consistent superior performance of the AOD2 configuration across all incidence angles. The simulation results show that AOD2 significantly surpasses AOD1 and STD. Notably, even at a wind incidence angle of 30°, AOD2's power coefficient remains higher than the best-case power coefficient of STD at 0°.

To delve deeper into the deflectors' impact, we introduced a parameter called PIR (performance increase ratio) defined by Equation (5) below:

$$PIR_{\theta}^{AOD2|STD} = \left[\frac{C_p^{\theta}(AOD2)}{C_p^{\theta}(STD)} - 1 \right] \quad (5)$$

where $C_p^{\theta}(AOD2)$ and $C_p^{\theta}(STD)$ are the power coefficient of the respective configurations at specific vertical wind incident θ.

It was observed that $PIR_{\theta}^{AOD2|STD}$ is directly correlated with θ. For instance, while $PIR_{\theta=0^{\circ}}^{AOD2|STD} = 62\%$, $PIR_{\theta=10^{\circ}}^{AOD2|STD} = 78\%$, $PIR_{\theta=20^{\circ}}^{AOD2|STD} = 89\%$, $PIR_{\theta=30^{\circ}}^{AOD2|STD} = 102\%$ and $PIR_{\theta=40^{\circ}}^{AOD2|STD} = 187\%$.

As depicted in Figure 7, a direct correlation exists between the increase in θ and the PIR. Notably, this increase becomes progressively more pronounced at higher values of θ. In simpler terms, the anticipated energy gain from using the AOD2 deflector compared to the standard turbine is even more significant in turbulent settings like urban areas. As a result, the seasonal energy harvested by the AOD2 configuration cannot be reflected solely by the power coefficient at 0 = 0° as per the state of the art. A more precise methodology would be to estimate the wind incidence angle yearly profile and to integrate the energy as per the angle-specific power coefficient. This would account for the additional gain in performance at higher θ and could eventually impact the decision of installing the AOD2 deflector.

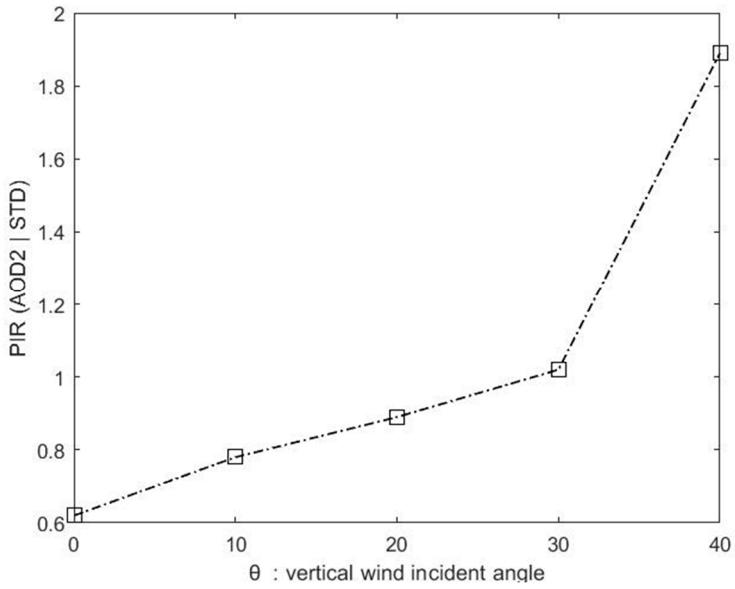

Figure 7. Performance increase ratio $PIR_{\theta}^{AOD2|STD}$ curve versus θ.

On another note, it was observed that the AOD1 configuration exhibited improved performance as the angle of incidence increased, while the STD configuration showcased superior performance over AOD1 at higher turbine speeds. These observations provide

valuable insights into the performance characteristics of the different turbine configurations under varying incidence angle and tip speed ranges.

The simulations also revealed interesting trends regarding the optimal tip speed ratio λ for each setup. Both the STD and AOD2 configurations achieved their maximum Cp at θ = 0° for a wind incident speed of 7 $m \cdot s^{-1}$, and at a turbine tip speed ratio of λ = 1.0. On the other hand, the AOD1 configuration exhibited its best performance at a lower turbine speed, λ = 0.8, indicating its suitability for specific operational conditions. Furthermore, and for all configurations, as θ increased, the maximum power coefficient Cp was achieved at lower turbine tip speed ratio λ and hence turbine rotational velocities. This effect was more pronounced in the AOD1 configuration. At θ = 40°, the Cpmax of the AOD1 configuration occurred within the λ = 0.6 range. In contrast, the Cpmax of the STD and AOD2 configurations fell within the λ = 0.8 range at the same incidence angle.

3.2.2. Pressure Contours and Streamlines

Pressure contours, a well-established technique in computational fluid dynamics (CFD), are instrumental in elucidating the aerodynamic forces acting upon a body. By meticulously analyzing these contours, we can glean valuable insights into the deflector's influence on the Savonius turbine's performance. As delineated in Equation (4), the power coefficient is primarily defined by the product of the torque exerted around the turbine axis and its rotational speed. The torque calculation is intrinsically linked to the differential pressure exerted on both the concave and convex facets of the turbine blades.

Figure 8 illustrates the total pressure contour results within both the horizontal plane (z = 0) and the vertical plane (y = 0), in conjunction with the velocity streamlines (y = 0) as derived from our CFD simulations. These simulations were conducted at a tip speed ratio of λ = 1.0 and an inlet wind speed of 7 m/s.

A comparative analysis of the pressure contours within the horizontal plane at θ = 0° for the STD (Figure 8a) and AOD2 (Figure 8d) configurations reveals distinct patterns. The AOD2 configuration exhibits a significantly more pronounced pressure gradient, as evidenced by the contrasting color distribution on both sides of the driving blade. This heightened pressure differential translates into a substantial enhancement of torque development and, consequently, a notable increase in power coefficients, as previously observed in Section 3.2.

It is imperative to note that when scrutinizing the color contrast, the regions farthest from the turbine's axis exert the most significant influence. This aligns with the torque definition, which is the product of force and distance from the center, thereby emphasizing the pivotal role of the peripheral regions in torque generation. On the other hand, while comparing the wake region in the velocity streamlines (Figure 8c,f), the recirculation region in the AOD2 configuration seems way more developed. This translates into lower wake pressure zone as seen in the vertical plane Figure 8e compared to Figure 8b.

The observed performance enhancement is attributable to the deflector mechanism. The deflector effectively redirects the airflow towards the rotor, resulting in an augmented mass flow rate of air traversing the turbine, as evidenced by the velocity streamlines depicted in Figure 8f.

When θ = 40°, the pressure contours and velocity streamlines of the AOD2 configuration exhibit patterns comparable to those observed at θ = 0° within the wake region. Nevertheless, the diminished pressure values at the turbine inlet are a consequence of the mass flow rate bypassing the turbine through the upper deflector at elevated velocities, resulting in a reduction of the power coefficient from 0.37 to 0.17. This phenomenon gives rise to minor recirculation vortices atop the deflector. Moreover, a visual inspection of the velocity streamlines in Figure 8l unequivocally demonstrates the deflector's continued efficacy in redirecting a portion of the flow towards the turbine.

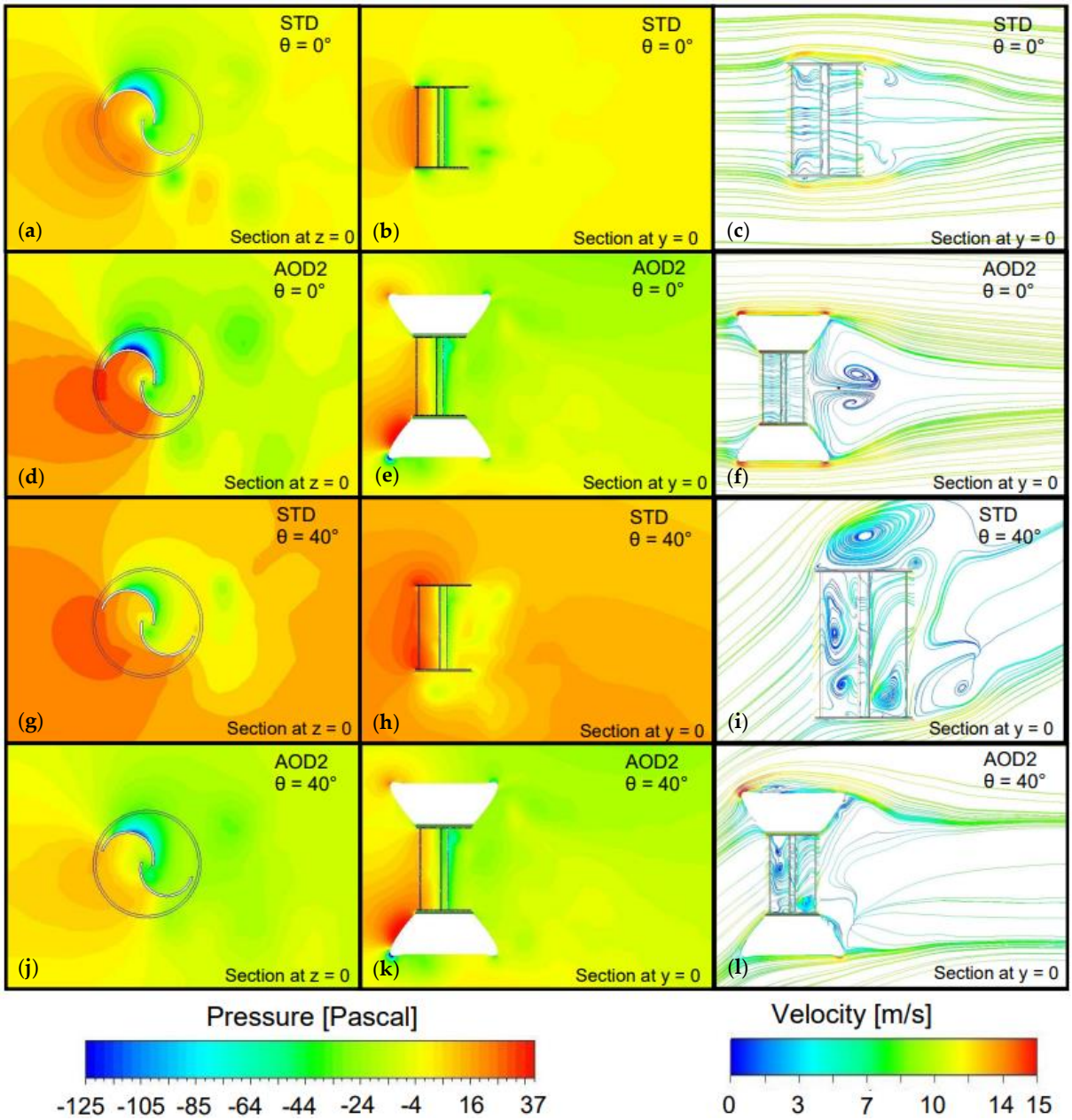

Figure 8. Pressure contour and velocity streamlines for STD and AOD2 at 7 m·s^{-1} wind speed for λ = 1.0. (**a**) STD horizontal plane pressure contour at z = 0 at θ = 0°, (**b**) STD vertical plane pressure contour at y = 0 at θ = 0°, (**c**) STD vertical plane velocity streamlines at y = 0 at θ = 0°, (**d**) AOD2 horizontal plane pressure contour at z = 0 at θ = 0°, (**e**) AOD2 vertical plane pressure contour at y = 0 at θ = 0°, (**f**) AOD2 vertical plane velocity streamlines at y = 0 at θ = 0°, (**g**) STD horizontal plane pressure contour at z = 0 at θ = 40°, (**h**) STD vertical plane pressure contour at y = 0 at θ = 40°, (**i**) STD vertical plane velocity streamlines at y = 0 at θ = 40°, (**j**) AOD2 horizontal plane pressure contour at z = 0 at θ = 40°, (**k**) AOD2 vertical plane pressure contour at y = 0 at θ = 40°, (**l**) AOD2 vertical plane velocity streamlines at y = 0 at θ = 40°.

Conversely, for the STD configuration, a substantial alteration in pressure contour behavior is observed when θ is adjusted to 40°. The turbine operates at an elevated inlet pressure while generating a diminished torque around its axis. These pronounced pressure gradients, induced by the modification of θ, are also implicated in the heightened structural stresses encountered by turbines deployed in urban environments. Figure 8i illustrates a disrupted wake region characterized by the formation of large-scale recirculating eddies

atop the end plate at $\theta = 40^{\circ}$. These eddies function as obstacles to the perpendicular wind flow, resulting in a reduction of its velocity around the turbine. The end plate, while not significantly redirecting the wind flow, contributes to the generation of flow separation at the turbine's apex.

3.3. Effect of Different Incoming Wind Speed on the Turbine Performance for Different Incidence Angles

To comprehensively investigate the impact of wind speed on turbine performance across various incidence angles (θ), three-dimensional CFD URANS simulations were conducted for wind speeds of 3.5 m/s^{-1}, 7 m/s^{-1}, and 14 m/s^{-1}. The power coefficient (Cp) results are summarized in Figure 6a–c. At $\theta = 0^{\circ}$, the primary objective was to corroborate the findings of prior research [2] on the Savonius STD configuration, which established a correlation between Cp and the tip speed ratio (λ) rather than the incident wind speed or Reynolds number. As evident in Figure 6, this conclusion was validated, with the Cp of the STD turbine exhibiting comparable values across different wind speeds. Minor deviations can be attributed to inherent CFD simulation errors. Notably, the implementation of the external wind deflector in the AOD1 and AOD2 configurations did not alter these observations, as their Cp values also demonstrate comparable trends. However, a noteworthy observation is the enhanced Cpmax of the STD configuration at $\theta = 40^{\circ}$ for the 14 m/s^{-1} wind speed scenario. Here, the calculated Cpmax is 0.12 compared to 0.08 at 7 m/s^{-1}, exceeding the margin of potential CFD errors. This anomaly necessitates further investigation to elucidate the underlying mechanism

4. Conclusions and Perspectives

Overall, the simulations conducted in this study provide enlightening information on the impact of the incidence angle on the power coefficient of Savonius turbines through the STD, AOD1, and AOD2 configurations. This study fills the knowledge gap by examining the turbine performance under different wind incidence angles and wind speeds. The urban turbines are usually installed in urban areas and on the roof of the buildings where θ is never constant and is rarely 0°. The AOD2 outperformed the STD and AOD1 configurations due to its aerodynamical optimized shape by avoiding the creation of eddies and redirecting the air into the center of the turbine rotor. The performance increase was correlated with the increase in the incidence angle showing a 61% Cp_{max} increase for $\theta = 0^{\circ}$ and 125% increase at $\theta = 40^{\circ}$ compared to the standard STD model. In addition, the pressure gradients exhibited by the AOD2 model were significantly lower compared to the STD configuration. This reduction in pressure gradients translates to less structural fatigue, ultimately extending the turbine operational lifespan. These findings contribute to a more comprehensive understanding of turbine performance in urban environments with high turbulence and varying wind incidence angle. The high gain in performance encourages the installation of an AOD2-type deflector on new and existing Savonius turbine installations. On the other hand, the paper highlights that the state of art in the methodology of the deflector design is not relevant in urban areas for VAWT turbines. The main key performance indicator in the assessment of the turbine performance Cp and thus the benefit from installing the deflectors is only assessed at $\theta = 0^{\circ}$. As shown in this study, the benefit from AOD2 configuration is double at $\theta = 40^{\circ}$. In view of the predominant vertical wind incidence angle θ at the specific site installation location, this valuable information could lead to a change in the decision regarding the installation or not of the configuration.

Despite the valuable conclusions of this study, there are important limitations related to the CFD simulations. Unlike the 2D simulations, 3D transient URANS CFD studies have shown good correlation with experiments as they can capture the effects of the fluid flow on the total height of the turbine; however, results were not validated experimentally through wind tunnel experiments. The deflector-mounting system is not considered in the model, which could impact the airflow depending on its final design. On another note,

the study is specific to AOD1 and AOD2 designs and the Savonius turbine and the results could not be generalized to other deflectors or the Darrieus turbine.

Author Contributions: Conceptualization, H.A.; methodology, H.A.; validation, F.B. (Fabien Bogard), G.P., F.B. (Fabien Beaumont), Y.T. and S.M.; formal analysis, H.A.; investigation, H.A.; writing—original draft preparation, H.A.; writing—review and editing, F.B. (Fabien Bogard); supervision, G.P.; project administration, H.A. All authors have read and agreed to the published version of the manuscript.

Funding: This research received no external funding.

Data Availability Statement: Data available upon request.

Acknowledgments: The authors wish to thank the Communauté d'Agglomération de Châlons en Champagne (France) and the Pôle de Recherche Châlonnais for their material support.

Conflicts of Interest: The authors declare no conflict of interest.

References

1. Alexander, A.; Holownia, B. Wind tunnel tests on a savonius rotor. *J. Ind. Aerodyn.* **1978**, *3*, 343–351. [CrossRef]
2. Blackwell, B.F.; Sheldahl, R.E.; Feltz, L.V. *Wind Tunnel Performance Data for Two and Three Bucket Savonius Rotor*; Sandia National Laboratories Report, SAND76-0l30; Sandia Laboratories: Springfield, VA, USA, 1977.
3. El-Askary, W.A.; Nasef, M.H.; Abdelhamid, A.A.; Gad, H.E. Harvesting wind energy for improving performance of Savonius rotor. *J. Wind Eng. Ind. Aerodyn.* **2015**, *139*, 8–15. [CrossRef]
4. Ferrari, G.; Federici, D.; Schito, P.; Inzoli, F.; Mereu, R. CFD study of Savonius wind turbine: 3D model validation and parametric analysis. *Renew. Energy* **2017**, *105*, 722–734. [CrossRef]
5. Renato, R.; Roberto, R.; Sergio, M.; Daniele, V. Experimental study on a Savonius wind rotor for street lighting systems. *Appl. Energy* **2016**, *161*, 143–152. [CrossRef]
6. Fujisawa, N. On the torque mechanism of Savonius rotors. *J. Wind. Eng. Ind. Aerodyn.* **1991**, *40*, 277–292. [CrossRef]
7. Frederikus, W.; Andy, S.; Hadi, S. An Experimental Study on the Performance of Savonius Wind Turbines Related With The Number Of Blades. *Energy Procedia* **2015**, *68*, 297–304. [CrossRef]
8. Thiyagaraj, J.; Rahamathullah, I.; Anbuchezhiyan, G.; Barathiraja, R.; Ponshanmugakumar, A. Influence of blade numbers, overlap ratio and modified blades on performance characteristics of the savonius hydro-kinetic turbine. *Mater. Today Proc.* **2021**, *46*, 4047–4053. [CrossRef]
9. Payambarpour, S.A.; Amir, F.; Franco, M. Investigation of deflector geometry and turbine aspect ratio effect on 3D modified in-pipe hydro Savonius turbine: Parametric study. *Renew. Energy* **2020**, *148*, 44–59. [CrossRef]
10. Jeon, K.S.; Jeong, J.I.; Pan, J.-K.; Ryu, K.-W. Effects of end plates with various shapes and sizes on helical Savonius wind turbines. *Renew. Energy* **2015**, *79*, 167–176. [CrossRef]
11. Akwa, J.V.; Vielmo, H.A.; Petry, A.P. A review on the performance of Savonius wind turbines. *Renew. Sustai. Energy Rev.* **2012**, *16*, 3054–3064. [CrossRef]
12. Sobczak, K. Numerical investigations of an influence of the aspect ratio on the Savonius rotor performance. *J. Phys. Conf. Ser.* **2018**, *1101*, 012034. [CrossRef]
13. Tong, Z.; Dietmar, R. Numerical study of detailed flow field and performance of Savonius wind turbines. *Renew. Energy* **2013**, *51*, 373–381. [CrossRef]
14. Al Absi, S.M.; Jabbar, A.H.; Mezan, S.O.; Al-Rawi, B.A.; Al_Attabi, S.T. An experimental test of the performance enhancement of a Savonius turbine by modifying the inner surface of a blade. *Mater. Today Proc.* **2021**, *42*, 2233–2240. [CrossRef]
15. Kamoji, M.A.; Kedare, S.B.; Prabhu, S.V. Experimental investigations on single stage modified Savonius rotor. *Appl. Energy* **2009**, *86*, 1064–1073. [CrossRef]
16. Morcos, S.; Khalafallah, M.; Heikel, H. The effect of sheilding on the aerodynamic performance of Savonius wind turbines. *ASME* **1981**, *2*, 2037–2040.
17. Shaughnessy, B.M.; Probert, S.D. Partially-Blocked Savonius Rotor. *Appl. Energ.* **1992**, *43*, 239–249. [CrossRef]
18. Yonghai, H.; Zhengmin, T.; Shanshan, W. A new type of VAWT and blade optimization. In Proceedings of the International Technology and Innovation Conference 2009 (ITIC 2009), Xi'an, China, 12–14 October 2009.
19. Burçin, D.A.; Mehmet, A. The use of a curtain design to increase the performance level of a Savonius wind rotors. *Renew. Energy* **2010**, *35*, 821–829. [CrossRef]
20. Tartuferi, M.; Alessandro, V.; Montelpare, S.; Ricci, R. Enhancement of Savonius wind rotor aerodynamic performance: A computational study of new blade shapes and curtain systems. *Energy* **2015**, *79*, 371–384. [CrossRef]
21. Aboujaoude, H.; Bogard, F.; Beaumont, F.; Murer, S.; Polidori, G. Aerodynamic Performance Enhancement of an Axisymmetric Deflector Applied to Savonius Wind Turbine Using Novel Transient 3D CFD Simulation Techniques. *Energies* **2023**, *16*, 909. [CrossRef]

22. Aboujaoude, H.; Beaumont, F.; Murer, S.; Polidori, G.; Bogard, F. Aerodynamic performance enhancement of a Savonius wind turbine using an axisymmetric deflector. *J. Wind. Eng. Ind. Aerodyn.* **2022**, *220*, 104882. [CrossRef]
23. Ross, I.; Altman, A. Wind tunnel blockage corrections: Review and application to Savonius vertical-axis wind turbines. *J. Wind. Eng. Ind. Aerodyn.* **2011**, *99*, 523–538. [CrossRef]
24. Saha, U.K.; Thotla, S.; Maity, D. Optimum design configuration of Savonius rotor through wind tunnel experiments. *J. Wind. Eng. Ind. Aerodyn.* **2008**, *96*, 1359–1375. [CrossRef]
25. Svetlana, M. Performance of a Savonius Wind Turbine in Urban Sites Using CFD Analysis. Thesis, University of VAASA, Vaasa, Finland, 2016.
26. Modi, V.J.; Fernando, M.S.U.K. On the performance of the Savonius wind turbine. *J. Sol. Energy Eng.* **1989**, *111*, 71–81. [CrossRef]
27. Duc, M.B.; The, H.T.; Van, K.P.; Le, A.D. Predicting aerodynamic performance of savonius wind turbine: An application of generalized k-ω turbulence model. *Ocean. Eng.* **2023**, *286*, 115690. [CrossRef]
28. Rezaeiha, A.; Montazeri, H.; Blocken, B. On the accuracy of turbulence models for CFD simulations of vertical axis wind turbines. *Energy* **2019**, *180*, 838–857. [CrossRef]
29. Alom, N.; Saha, U.K.; Dean, A. In the quest of an appropriate turbulence model for analyzing the aerodynamics of a conventional Savonius (S-type) wind rotor. *J. Renew. Sustain. Energy* **2021**, *13*, 023313. [CrossRef]

computation

MDPI

Article

Performance Rating and Flow Analysis of an Experimental Airborne Drag-Type VAWT Employing Rotating Mesh

Doğan Güneş and Ergin Kükrer *

Mechanical Engineering Department, Istanbul Bilgi University, Eyüp, Istanbul 34060, Türkiye; dogan.gunes@bilgi.edu.tr
* Correspondence: ergin.kukrer@bilgi.edu.tr

Abstract: This paper presents the results of a performance analysis conducted on an experimental airborne vertical axis wind turbine (VAWT), specifically focusing on the MAGENN Air Rotor System (MARS) project. During its development phase, the company claimed that MARS could generate a power output of 100 kW under wind velocities of 12 m/s. However, no further information or numerical models supporting this claim were found in the literature. Extending our prior conference work, the main objective of our study is to assess the accuracy of the stated rated power output and to develop a comprehensive numerical model to analyze the airflow dynamics around this unique airborne rotor configuration. The innovative design of the solid model, resembling yacht sails, was developed using images in the related web pages and literature, announcing the power coefficient (Cp) as 0.21. In this study, results cover 12 m/s wind and flat terrain wind velocities (3, 5, 6, and 9 m/s) with varying rotational velocities. Through meticulous calculations for the atypical blade design, optimal rotational velocities and an expected Tip Speed Ratio (TSR) of around 1.0 were determined. Introducing the Centroid Speed Ratio (CSR), which is the ratio of the sail blade centroid and the superficial wind velocities for varied wind speeds, the findings indicate an average power generation potential of 90 kW at 1.4 rad/s for 12 m/s and approximately 16 kW at a 300 m altitude for a 6 m/s wind velocity.

Keywords: airborne vertical axis wind turbine (VAWT); MAGENN air rotor system (MARS); unsteady computational analysis; rotating mesh; power coefficient (Cp)

Citation: Güneş, D.; Kükrer, E. Performance Rating and Flow Analysis of an Experimental Airborne Drag-Type VAWT Employing Rotating Mesh. *Computation* **2024**, *12*, 77. https://doi.org/10.3390/computation12040077

Academic Editors: Ali Cemal Benim, Rachid Bennacer, Abdulmajeed A. Mohamad, Paweł Oclon, Sang-Ho Suh and Jan Taler

Received: 11 March 2024
Revised: 1 April 2024
Accepted: 6 April 2024
Published: 8 April 2024

1. Introduction

Renewable energy plays a crucial role in meeting the growing need for sustainable and eco-friendly power solutions on a global scale. Notably, in the European Union (EU), the final energy consumption from renewable sources reached a substantial 23.0% share in 2022, according to stats [1,2]. To strengthen this commitment, EU Directive 2023/2413 sets a target of achieving a 45% share by 2030, with a particular emphasis on harnessing wind and solar energy resources [3]. Within the broader spectrum of renewable sources, wind energy has emerged as a significant contributor, acknowledged for its role as one of the cleanest and readily available forms of power. In this context, airborne wind energy systems have been further developed to harvest winds at atmospheric levels beyond traditional wind turbines [4].

Airborne Wind Energy Systems (AWESs) represent an emerging frontier in renewable energy innovation. These systems, distinguished by their capacity to capture high-altitude winds through aerial structures or tethered devices, represent a departure from conventional ground-based wind energy solutions. Their primary objective is to harness the more robust and consistent wind resources found at higher altitudes. Bechtle et al.'s study [5] evaluates wind resources in the EU for 300, 1000, and 1500 m altitudes over seven years, revealing available power between 40 and 1600 W/m^2 with wind velocities ranging from 2.4 to 10.9 m/s.

AWESs are classified based on the position of the generator as Ground-Gen and Fly-Gen systems, or by types as drag-type or lift-type wind turbines [4,6]. In the Ground-Gen category, electricity generator alternator systems are positioned on the ground, whereas in the Fly-Gen category, the entire generator assembly is airborne, and the electricity generated is conveyed to the ground through tethered wires.

Drag-type airborne wind turbines utilize the drag force on their blades to extract energy from the wind. This type of turbine includes configurations such as the Savonius wind turbine, which is a vertical axis wind turbine (VAWT) with a drag-type design. Savonius turbines are notable for their self-starting nature thanks to their high torque at lower speeds. This feature makes them suitable for conditions with low wind speeds [7]. However, despite high starting torque, Savonius turbines have lower efficiency compared to Darrieus turbines, which are typical lift-type airborne wind turbines [8]. Lift-type turbines operate based on the lift force generated by their airfoil-shaped blades and are characterized by their vertical orientation that can harness wind energy from any direction without the need for a yaw mechanism.

In this context, AWESs offer several advantages over traditional ground-based wind turbines. Primarily, airborne systems can access higher altitudes where the wind is generally stronger and more consistent, leading to increased energy production [4,5]. This is supported by the fact that AWESs aim to harness wind energy beyond the altitude of traditional windmills in stronger and more steady winds using tethered wings [9]. Furthermore, a substantial reduction in mass is provided compared to conventional wind turbines, potentially resulting in economic efficiencies [10]. These advantages position AWESs as a promising technology for the future of wind energy generation.

Yet, AWESs face several key challenges and limitations in practical implementation compared to traditional wind turbines. Firstly, they rely on consistent and predictable wind patterns for optimal performance, making them less suitable for areas with highly unpredictable or intermittent winds. Additionally, AWESs require sophisticated tether management systems to ensure safe operation, as tether wear, entanglement, and breakage can pose significant operational risks. Moreover, altitude restrictions, airspace regulations, and aviation safety concerns limit the potential power generation capacity of AWESs. The complexity of control systems needed to manage airborne components, optimize power generation, and ensure stability adds another layer of challenge. AWES technology is still in its early stages of development, requiring further advancements, research, and testing to address key challenges and improve performance and reliability for widespread adoption.

Addressing the above-mentioned challenges requires targeted research efforts and innovative methodologies. Key research gaps include developing advanced control algorithms to optimize tethered flight paths and power generation efficiency. An improved understanding of aerodynamics and turbulence in high-altitude wind regimes is essential for designing robust and efficient AWES configurations. Advanced computational models and simulation tools can aid in predicting system behavior and optimizing design parameters. As technology advances, the performance of airborne wind turbines requires an extensive investigation and rigorous research effort to fully establish their feasibility and potential.

1.1. Literature Survey

The literature covers a range of research on AWES. A comprehensive review of AWESs, highlighting their various technologies, such as flying tethered wings or aircraft designed to access high-altitude winds, was provided by Cherubini et al. [4]. Their study categorized prototypes developed by universities and companies worldwide based on system architecture, highlighting both proven hardware configurations and potential future implementations. Gerrie et al. [11] presented recent experimental and computational results for three-bladed Darieus and three-bladed Savonius VAWTs. The computational results demonstrate a significant difference from the experimental results, with an order of magnitude discrepancy. Furthermore, the experimental power coefficient findings are notably low.

The authors conclude that further experiments employing models representing changes in design parameters may be required as significant differences are observed between experimental results and simulations.

A number of other publications [12–21] have also focused on improving the performance of either Savonius, Daerius, or hybrid VAWTs using different approaches in design. However, it is important to note that while these turbines are practical for harnessing wind energy at low altitudes, the total energy produced is relatively low. The power coefficient for drag-type VAWT turbines ranges from 0.2 to 0.35. The area covered by the turbine is small, and the wind speed at low altitudes is very low (3–5 m/s at an altitude of 80 m). Scientists have conducted experiments and developed models at extremely high speeds, up to 12–14 m/s, to attract attention.

Noronha and Munishamaih [22] developed and manufactured a prototype Horizontal Axis Airborne Wind Turbine (HAWT), in which a rotor is housed in a helium-filled enclosure and is also elevated by a spherical balloon. The prototype was tested under field conditions at a number of altitudes. The turbine produced 250 W at an average wind velocity of 6 m/s, with a power coefficient (Cp) of 0.25. The consistency between the experimental and computational results was evaluated in their study using the sliding mesh method in the numerical model (the mesh is stationary, and a superficial rotation effect is added to the rotor [23]). The results were in agreement with the experimental results. Ali and Kim [24] studied a detailed analysis of the power conversion performance of airborne wind turbines under unsteady loads. Their study utilized the computational fluid dynamics (CFD) analysis of a 2.51 m blade radius with a 6.5 tip speed ratio and 18 m/s wind speed for high-altitude offshore applications.

Several significant projects have been carried out regarding AWESs. One remarkable project application is the Buoyant Airborne Turbine (BAT) developed by Altaeros Energies, an MIT start-up [25]. BAT proposes around twice the performance of ground-based wind turbines at altitudes around 600 m, where the expected wind power density rises to 1200 (W/m^2).

Another significant project is Omnidea's LEMAP project [26], based on the Magnus effect of the airborne rotor, which consists of a tethered cylindrical unit filled with helium gas. The Magnus effect enables the generation of lift and propulsion force through the rotation of bodies, such as cylinders or rotors, in a fluid medium. This phenomenon has been a subject of interest in designing and controlling airborne wind energy systems, particularly those utilizing the Magnus effect for harnessing wind power. A thorough recent review by Seifert [27] explains the historical foundation and various applications of the Magnus effect. This effect has also been extensively studied and applied in the context of ship propulsion, particularly in the development of rotor ships such as Flettner's Baden–Baden ship [27,28]. The computational studies of Gowree and Prince [29] and Milutinović et al. [30] are also noteworthy in this respect.

This study investigates the MAGENN Air Rotor System (MARS) project, a novel experimental drag-type vertical axis wind turbine (VAWT), and its performance assessment in various flat terrain conditions. Further analysis of our work was presented at ICCHMT 2023 [31].

1.2. MAGENN Air Rotor System (MARS)

MARS is a novel airborne rotor designed and patented by Frederick D. Ferguson [32]. The airborne rotor design is presented in Figure 1. The figure illustrates the rotor, a cylindrical structure with a base diameter of 45 ft (13.7 m) and a length of 100 ft (30.5 m), which is filled with helium. As the interior of the structure is filled with helium, MARS, together with the Alteros's BAT and Omnidea's LEMAP projects, falls into the lighter-than-air category, with its sail-like wings, central disc, and bulky body. The rotor is expected to have a positive lift force due to not only the helium-filled body but also the spinning of the cylindrical zeppelin. The rotating cylinder design of the airborne rotor-type wind turbine aims to obtain a positive lift from the Magnus effect by increasing the elevation

of the helium-filled rotor to high altitudes (300–600 m). The rotor is set to rise with the lift produced by initial rotation at lower altitudes obtained by increasing lift. The central disk maintains the motion perpendicular to the wind, and the corresponding diameter of the disk is 23.16 m. The rotor design is further addressed in detail in our previous publications [31,33].

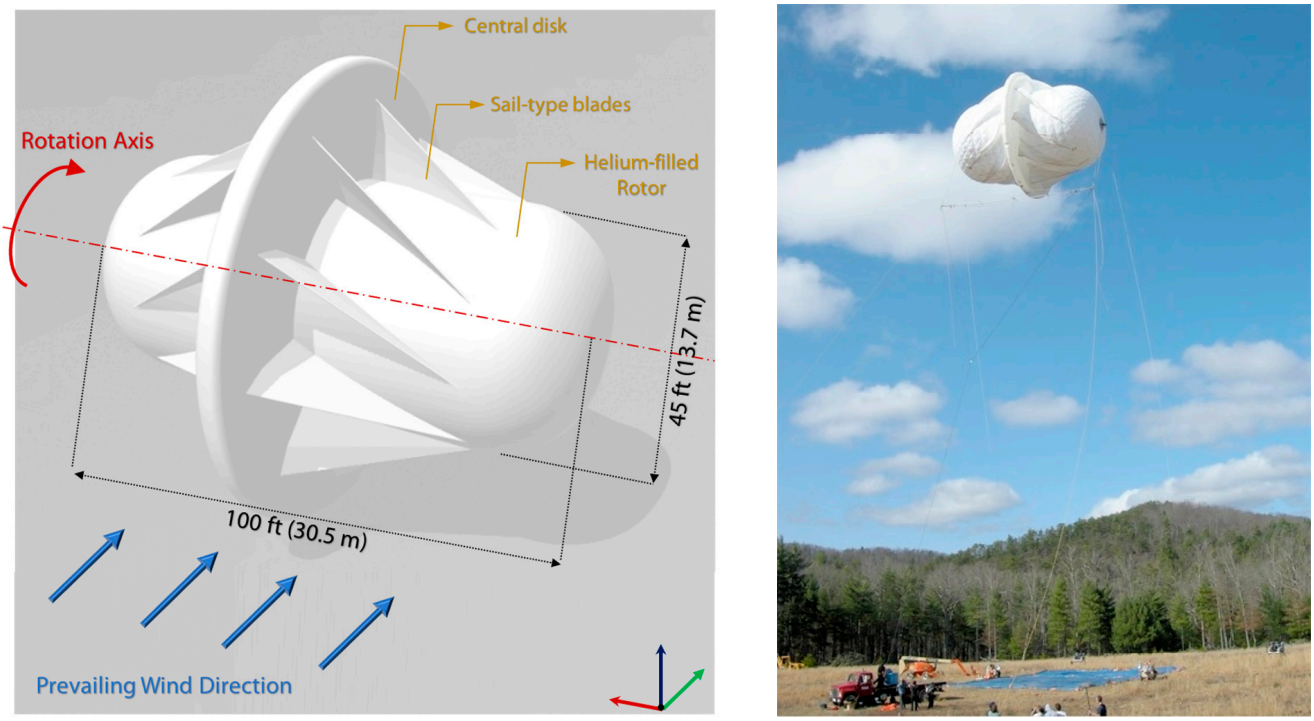

(**a**) (**b**)

Figure 1. MARS Drag-Type VAWT Airborne Rotor. (**a**) Developed solid model. (**b**) Experimental Wind Turbine by MAGENN [34].

1.3. Scope and Novelty of the Study

During the development phase, the company claimed that MARS had a power output of 100 kW for a 12 m/s wind velocity [34]. Although this 100 kW-rated power output in 12 m/s wind velocity is also mentioned in Chaudhari's study [35], there is no clear information on the subject, and the existence of a numerical model is controversial. The only reference is that three different prototypes of MARS were tested for performance in the VIGYAN wind tunnel. One of the prototype tests by VIGYAN Inc. is presented in Figure 2 [36]. However, no explicit experimental data or results are presented elsewhere.

In this context, the aim of our investigation, building on our previous work [31,33], is to evaluate the accuracy of the stated rated power output for this novel design and to develop a numerical model of the airflow around this airborne rotor configuration. Our work presented at the ICCHMT 2023 Conference [31] reported the extreme superficial wind velocity results of 12 m/s, which is in line with the rated wind velocity for the company. However, according to the EU wind atlas [37], the average wind speed is not close to 12 m/s. The wind velocities reach their maximum at limited locations, with values of around 10 to 11 m/s [5,37]. Therefore, our extended analysis for superficial wind velocities of 3, 5, 6, and 9 m/s are investigated in this paper. A summary of results is presented to assess the performance analysis of the airborne drag-type VAWT for rating purposes, assuming acceptable wind speed velocities on flat terrain. In this way, our study aims to provide valuable insights into the design, development, and applications of airborne rotor systems, highlighting their potential in the field of renewable energy and transportation.

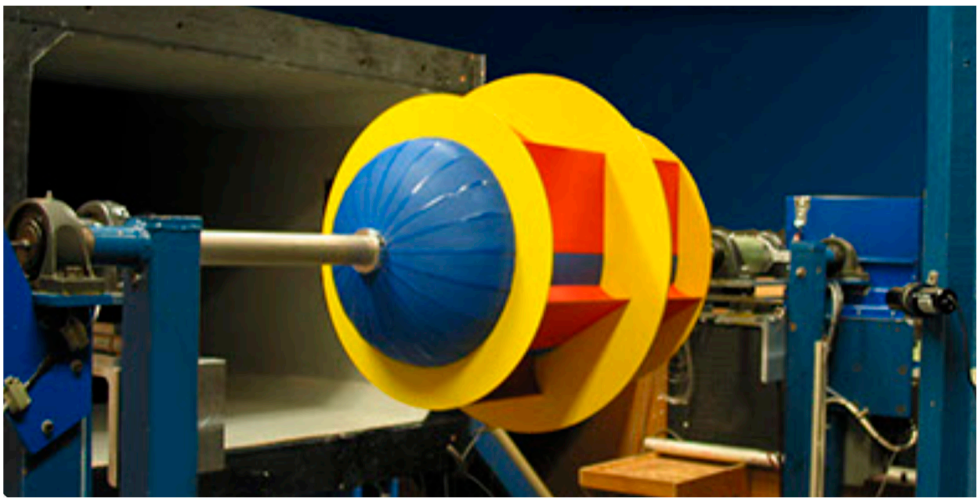

Figure 2. MARS prototype wind tunnel testing by VIGYAN Inc. [36].

2. Materials and Methods

In this section, we elaborate on the materials and methods employed in our study to facilitate a comprehensive investigation and analysis. Specifically, we outline the development of a solid model for the experimental airborne turbine, followed by the construction of a numerical model derived from this solid representation.

2.1. Computational Solution Domain Properties

The computational solution domain is established based on the physical scale and operational parameters of the novel wind turbine system, as illustrated in Figure 1. The dimensions mentioned in this section are derived from patents and references issued by the company [32,34,35]. The cylindrical rotor has a base diameter of 13.7 m (45 feet), with the blade tip height extending 11.58 m (36 feet) from the axis. Additionally, the central disk ensures motion perpendicular to the wind, with a corresponding diameter of 23.16 m.

For computational fluid dynamics (CFD) analysis, the three-dimensional (3D) solid model was imported into ANSYS Workbench, where the mesh structure was generated using ANSYS Meshing. Subsequently, the numerical model was solved by selecting the appropriate models within the Fluent module [23].

The computational solution domain is organized into a multi-zone configuration to support numerical analysis and facilitate mesh rotation with the rotor. This setup includes two rectangular zones and one cylindrical zone, as illustrated in Figure 3. The large rectangular zone spans dimensions of 450 $\times$ 400 $\times$ 130 m, as depicted. Within this rectangular area, there are designated sub-rectangular and cylindrical regions for adjusting mesh density and aiding rotational computations. The rotor, which has a diameter of 13.7 m (Figure 1), is located at the center of the cylindrical area with a diameter of 90 m.

In the domain, a careful initial adaptation of the mesh structure along the solution procedure is employed to generate a detailed mesh structure for the solution procedures. In total, over 1.2 million nodes and 6.5 million tetrahedral elements are constructed for mesh generation. The validity and quality of the mesh are evaluated through an analysis of mesh skewness and orthogonal quality. The results reveal an average skewness of 0.2, while the orthogonal quality is assessed at 0.8. Additionally, targeted mesh adaptation is implemented for regions prone to high turbulence and proximity to walls. Notably, Figure 3 illustrates the denser mesh structures strategically positioned near the rotor wall and sections of the flow domain where turbulence levels are anticipated to be elevated.

A moving Reference Frame (MRF) approach with sliding mesh is utilized for the rotating cylinder zone (Figure 3), while the remaining domain meshes are stationary. Although it requires significant computational resources, this method is widely regarded as the most precise for forecasting flow in multiple moving reference frames. Therefore,

it is commonly employed in such CFD models of airborne rotors [16,38]. In the sliding mesh methodology, the adjacent zones move relative to each other along the mesh interface, facilitating rotation without the need for cell alignment. This approach is particularly advantageous in accommodating the inherently unsteady flow conditions encountered in the simulation.

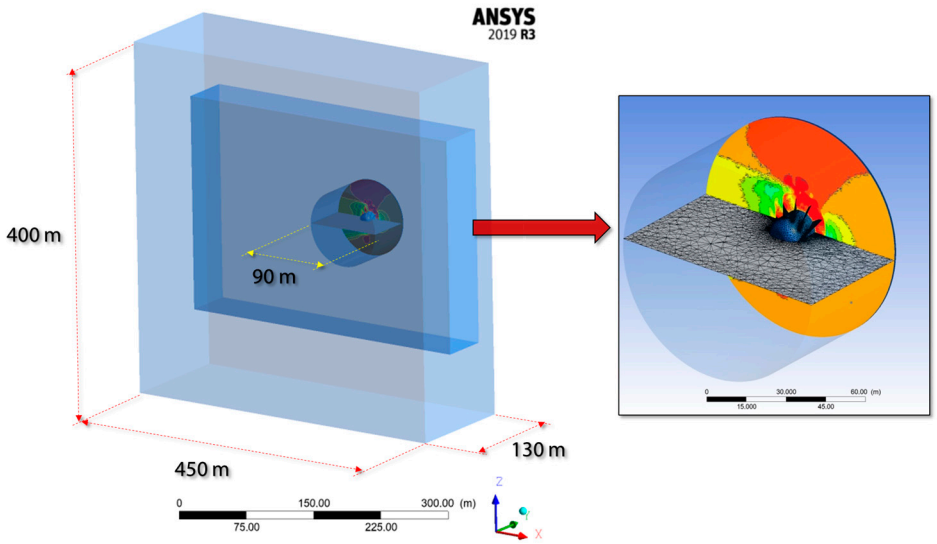

Figure 3. Multi-zone solution domain with the rotating cylinder zone housing the rotor.

To ensure continuous flow, a time-dependent solution procedure is implemented using a moving reference frame as a link between the stationary and rotating zones, given the transient nature of the flow. Hence, we employed unsteady Reynolds Averaged Navier–Stokes (RANS), incorporating a sliding boundary condition for the rotating cylinder. The cylindrical enclosure mesh was assigned different rotational speeds to conduct a parametric study. Specifically, the rotational speed varied to Ω = 0.36 rad/s for V = 3 m/s wind velocity; 0.65 rad/s for V = 5 m/s, 0.7 and 0.8 rad/s for V = 6 m/s; 1.0, 1.06 and 1.1 rad/s for V = 9 m/s; and, finally, 1.2 and 1.4 rad/s for V = 12 m/s.

In the numerical setup, the boundary condition for the prevailing wind direction cross-section of the rectangular domain was designated as velocity inlet, ensuring the entry of air into the computational domain across flat terrain wind velocities ranging from 3 to 12 m/s. Meanwhile, the other outer surfaces of the computational domain are specified as symmetry boundary conditions.

The initial computations commenced with a time step of 0.001 s, ensuring the development of a sufficiently accurate flow field. Subsequently, the time step was progressively increased to 0.002 s, and occasionally to 0.003 and/or 0.005 s, adhering to the Levi–Friedrich–Courant criterion to maintain the Courant number (CFL) below 1 (CFL << 1). Maintaining a CFL value below 1 ensures numerical stability and time-step validation. Time-step validation was verified by monitoring the CFL value to ensure its consistency below this threshold. This adaptive time-step strategy enables efficient computation while upholding numerical stability [39].

Our study covers a range of wind speeds, from 3 m/s to 12 m/s, resulting in varying characteristic Reynolds numbers, ranging from Re = 2.2×10^6 to 18.8×10^6, depending on the wind velocity. To model turbulence, we employed the realizable k-ε turbulence model in the solver. Additionally, second-order models were used for pressure, momentum, turbulent kinetic energy, and dissipation rate equations.

2.2. Performance Parameters

- Available wind power, force, and moment relations

Turbine performance is assessed on the basis of various specific performance parameters. The available wind power (E_{wind}) for a given wind velocity refers to the energy potential that can be harnessed from the kinetic energy of the moving air mass. It represents the maximum amount of power that can be extracted by a wind turbine operating under ideal conditions at a specific wind velocity of V. This available power is determined by the wind velocity and the area intercepted by the turbine rotor, as expressed in Equation (1). It is a crucial parameter used for assessing the feasibility and efficiency of wind energy conversion systems, offering insights into the renewable energy potential of a geographical location or wind resource.

$$E_{wind} = \frac{1}{2}\rho A V^3 \tag{1}$$

For superficial flow velocities (V) of 3, 5, 6, 9, and 12 m/s, the oncoming total energy to the rotor (E_{wind}) is calculated as 5.3, 24.5, 42.2, 142.6, and 338 kW, respectively. The cross-sectional area (A) is considered in the calculations as the total cross-sectional area perpendicular to the flow cross-section, as shown in Figure 1.

The aerodynamic forces acting on wind turbine rotors (F_{wind}) are critical in determining their operational performance. The relation for the superficial forces that are acting on the rotor due to wind is presented in Equation (2).

$$F_{wind} = \frac{1}{2}\rho A V^2 \tag{2}$$

These forces cause periodic and fluctuating aerodynamic loads on the rotor body and blades, directly impacting the overall performance of the wind turbine. To quantify these effects, the aerodynamic forces are integrated over the length of the blade to determine the instantaneous forces and moments acting on the rotor body and the blades (M_{wind}). Understanding these aerodynamic forces is essential for assessing the performance, efficiency, and structural integrity of wind turbines, ultimately maximizing their power output and reliability.

Furthermore, the energy generation potential of the rotor is directly related to the moment exerted on the blades, as depicted in Equation (3). The available wind force moment (M_{wind}) is calculated by multiplying the calculated superficial force (F_{wind}) by the characteristic length (L).

$$M_{wind} = \frac{1}{2}\rho A V^2 L \tag{3}$$

- Performance-related coefficients in airborne wind turbines

In the context of rating airborne wind turbines, the lift coefficient (Cl), drag coefficient (Cd), and power coefficient (Cp) are essential performance parameters that are directly related to the efficiency and power generation of these systems.

The lift coefficient is the ratio of total superficial forces and the lift forces acting on the body of the rotor, as presented in Equation (4).

$$Cl = \frac{F_l}{\frac{1}{2}\rho A V^2} \tag{4}$$

The lift coefficient (Cl) holds significant importance in the context of airborne wind turbines due to its direct influence on the aerodynamic performance and efficiency of these systems. Lift force is also directly related to the Magnus effect, as explained in the previous sections. A higher lift coefficient implies greater lift force production for a given wind speed, leading to enhanced turbine performance and improved power generation capabilities, especially for kite-type or lift-type airborne wind turbines.

On the other hand, the drag coefficient (Cd) represents the dimensionless parameter that quantifies the aerodynamic drag experienced by the turbine body and its components

relative to the airflow. It is defined as the ratio of the drag force acting on the turbine to the dynamic pressure of the airflow, as expressed by Equation (5).

$$Cd = \frac{F_d}{\frac{1}{2}\rho A V^2} \tag{5}$$

In AWESs, the power coefficient (Cp) is the most significant parameter used to assess the system's efficiency and power generation capabilities. It represents the ratio of the actual power generated by the turbine to the maximum possible power that could be extracted from the wind, given ideal conditions. The power coefficient is presented in Equation (6).

$$Cp = \frac{Actual\ power\ generated}{Max.\ possible\ power} = Cm\frac{R_{blade}\Omega}{V} = \mathrm{Cm}\lambda \tag{6}$$

Cp is directly dependent on the rotational velocities and, therefore, the moment developed on the blades. The power coefficient is directly proportional to the moment coefficient (Cm) and tip speed ratio (TSR), denoted as λ. TSR is the ratio of the characteristic moment arm length (R_{blade}) multiplied by the rotational speed of the blade (Ω) to the corresponding wind velocity (V), and it is calculated using Equation (7).

$$\text{Tip Speed Ratio(TSR)} = \lambda = \frac{R_{blade}\Omega}{V} \tag{7}$$

However, as illustrated in Figure 4, the characteristic length for the moment calculation varies due to the sail-type and triangular area in our study.

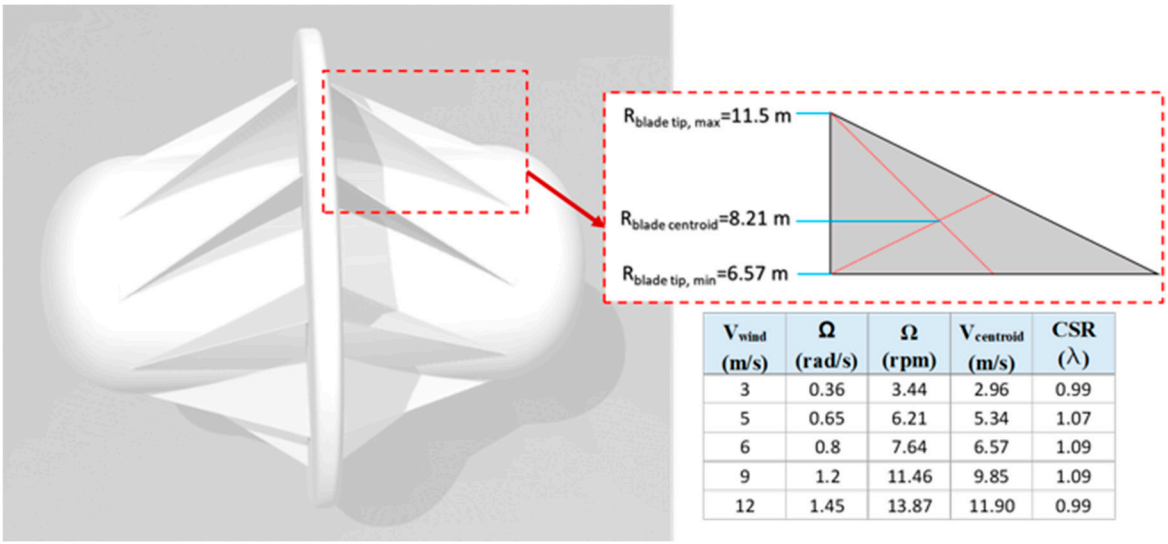

V_{wind} (m/s)	Ω (rad/s)	Ω (rpm)	$V_{centroid}$ (m/s)	CSR (λ)
3	0.36	3.44	2.96	0.99
5	0.65	6.21	5.34	1.07
6	0.8	7.64	6.57	1.09
9	1.2	11.46	9.85	1.09
12	1.45	13.87	11.90	0.99

Figure 4. Solid model of the airborne wind turbine showing the centroid of the sail-type blade structure with Centroid Speed Ratios (CSRs) for selected wind and rotational velocities.

The tip of the blade on the cylindrical surface of the rotor ($R_{blade\ tip,\ min}$) is 6.57 m from the center, while the outermost point of the blade ($R_{blade\ tip,\ max}$) is 11.5 m from the center. Considering the triangular shape of the blade, the characteristic length is chosen as the centroid of the sail (8.21 m), as depicted in the figure. For this reason, the tip speed ratio will now be referred to as the Centroid Speed Ratio (CSR) throughout the manuscript.

Figure 3 also presents the rotational velocity (Ω), centroid velocity ($V_{centroid}$), and CSR values corresponding to the flat terrain wind velocities (V_{wind}) in our parametric study.

3. Results

In the three-dimensional domain, all computations are conducted for specified wind velocities of 3, 5, 6, 9, and 12 m/s using ANSYS Fluent 19.R3 and 21.R2 modules. The rotational speed of the rotor (and, accordingly, the cylindrical rotating mesh zone) is set based on the CSR values, which are addressed in Figure 4. To ensure the development and stability of the flow in the solution area, particularly in the wake behind the rotor, we considered results after the rotor completed three rotations. Subsequently, data were collected on the drag coefficient (Cd), lift coefficient (Cl), moment coefficient (Cm), power coefficient (Cp), and power per unit time, along with the corresponding angular position of the rotor. The results are presented and addressed separately for each flat terrain wind velocity.

- The 3 m/s wind velocity results

Our initial set of results is derived from a flat terrain wind velocity of 3 m/s, which is applicable within heights ranging from 0 to 50 m, as per the European Wind Atlas [37]. Utilizing Equation (7) with a wind velocity of 3 m/s and a corresponding rotational velocity of 0.36 rad/s (equivalent to 3.438 rpm), the centroid speed ratio is calculated to be 0.985.

The numerical results obtained are plotted in Figure 5a, illustrating the flow-related parameters per degree. These parameters were described in detail in the earlier sections. Furthermore, velocity magnitude and static pressure distributions on the rotor and in the flow field are obtained. The velocity magnitude and static pressure contours are presented in Figures 5b and 5c, respectively. For a clearer observation of the flow field and the section after the rotor, an XZ midplane was defined in the contour plots precisely at the center point of the rotor.

Figure 5a illustrates that the total power generated (in kW) peaks every 36 degrees due to the presence of 10 blades distributed along the 360-degree circumference. The cross-sectional area perpendicular to the flow varies with the position of the blade, repeating every 36 degrees owing to the utilization of a time-dependent transient solution. However, since the wind turbine analyzed in our study is of the drag type, the condition where the cross-sectional area is tangentially perpendicular to the centerline experiences the greatest drag, resulting in the highest power extraction. It is noteworthy that as the blade rotates in the direction of the force applied by the drag, the drag acting on the blade diminishes, consequently reducing the extracted power. This cycle repeats at every 36 degrees.

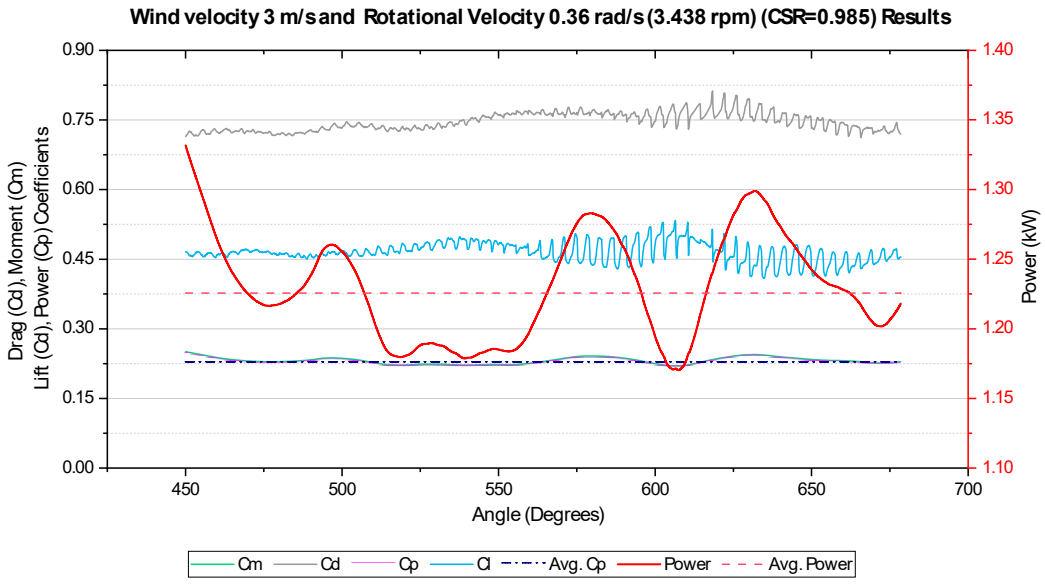

(**a**)

Figure 5. *Cont.*

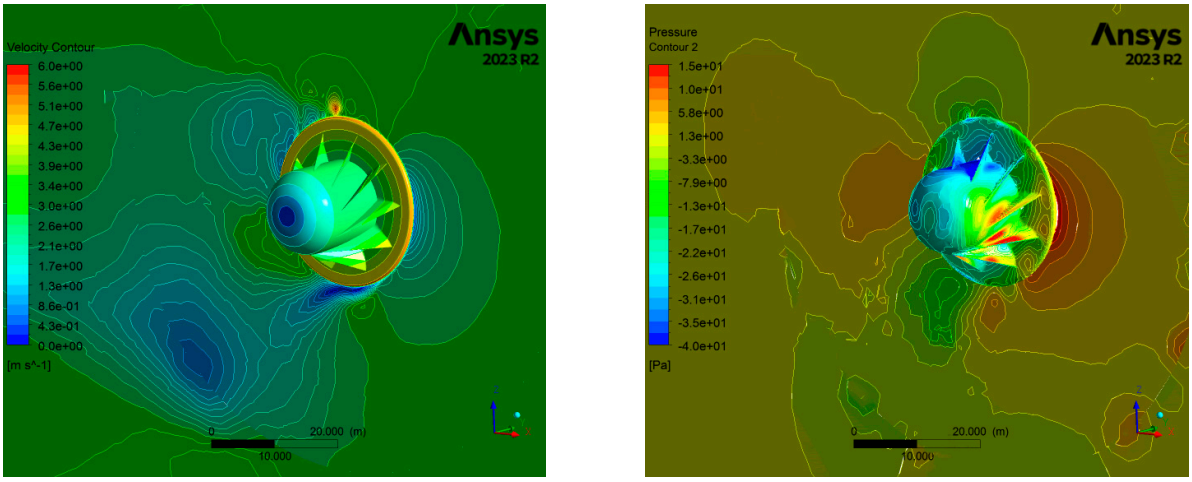

(**b**) (**c**)

Figure 5. Results for wind velocity of 3 m/s and rotational speed of 0.36 rad/s (equivalent to 3.438 rpm): (**a**) Drag, lift, moment, and power coefficients; (**b**) Velocity magnitude contours; (**c**) Static pressure distribution.

The cycle, however, does not exactly follow an identical pattern of repeated peaks and troughs for a result of 3 m/s. This variation primarily arises from the flow instability due to the low speed and the constant evolution of wakes in the rear area of the rotor cross-section. The wakes behind the flow are clearly visible in the velocity contours presented in Figure 5b. While a wake develops from the bottom to the rear of the rotor, superficial velocities in the domain and on the rotor reach 6 m/s in the upper sections.

The drag coefficient on the rotor varies between 0.72 and 0.80, while the lift coefficient varies between 0.42 and 0.52. At an air velocity of 3 m/s, the average power produced is 1.22 kW out of a total potential power of 5.4 kW. Therefore, the ratio of these two terms, the average power coefficient, is found to be 0.228.

- The 5 m/s wind velocity results

Secondly, results were obtained for a flat terrain wind velocity of 5 m/s. According to the European Wind Atlas, a wind velocity of 5 m/s is commonly observed at altitudes ranging from 50 to 100 m [37]. At this velocity, the rotational velocity was determined to be 0.65 rad/s (equivalent to 6.207 rpm). Consequently, the Centroid Speed Ratio (CSR) value was calculated as 1.067.

The results for a wind velocity of 5 m/s are presented in Figure 6a for power and performance coefficients, and in Figures 6b and 6c for velocity and pressure coefficients, respectively.

The estimated power generation and drag coefficient shown in Figure 6a exhibit greater stability and cyclic behavior compared to the wind velocity of 3 m/s. Specifically, the estimated power generation varies between 6 and 7.5 kW. With the available potential power calculated at 24.9 kW for 5 m/s wind velocity, the average power coefficient is determined to be 0.277 for this case. Additionally, the lift coefficient fluctuates between 0.50 and 0.70, and the drag coefficient is observed to range from 0.38 to 0.45.

In the contour plots presented in Figure 6b,c, it is evident that the wake forms and translates in the upper rear part of the rotor compared to the results obtained at a 3 m/s wind velocity. The velocity magnitudes increase up to 10 m/s in the outer diameter of the cylindrical disc and in the upper top sections of the rotor. Upon analyzing the static pressure, positive pressure is found on the blade surfaces as expected.

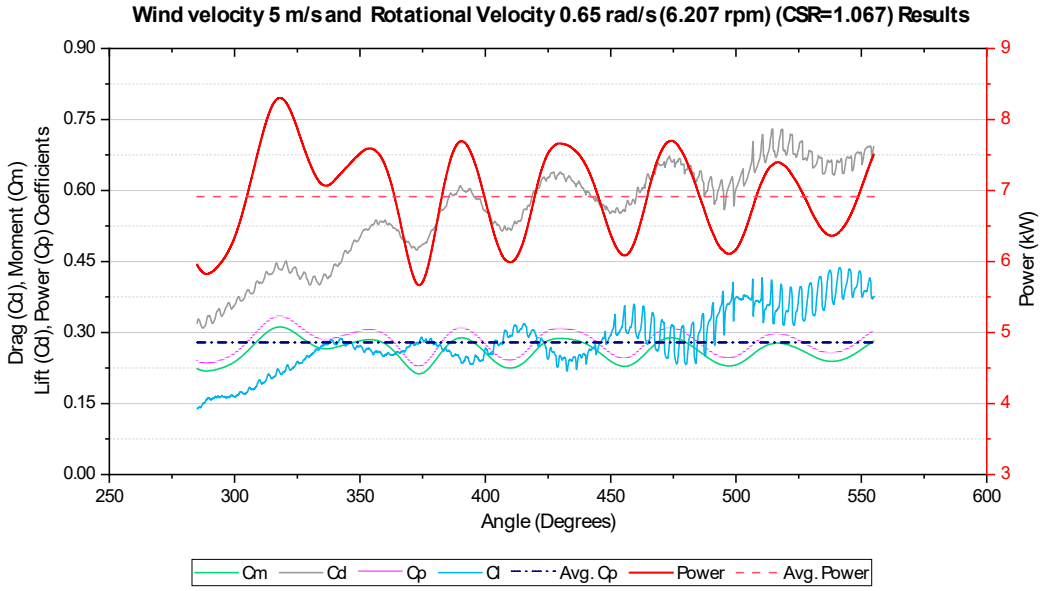

(**a**)

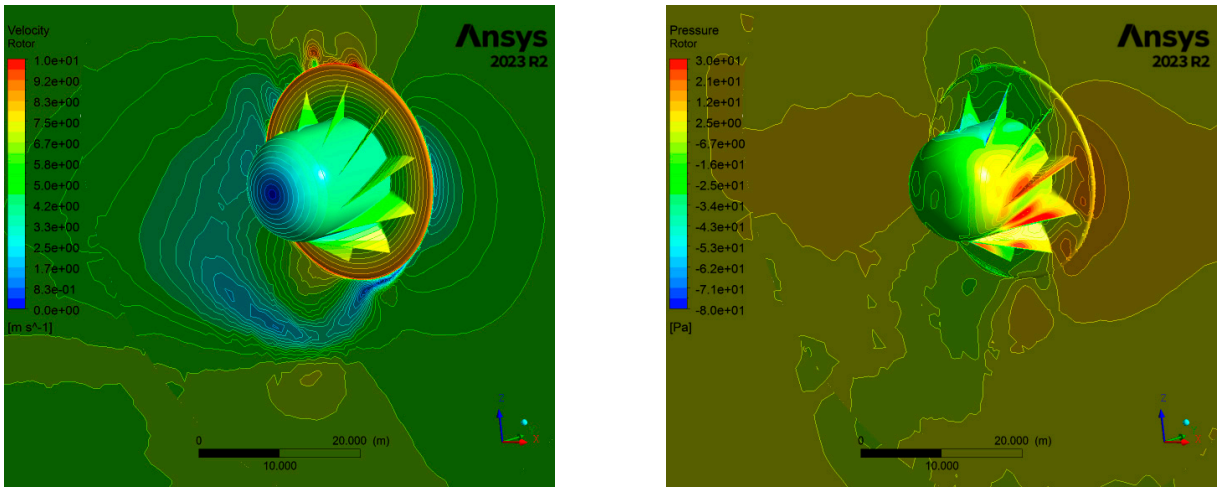

(**b**) (**c**)

Figure 6. Results for wind velocity of 5 m/s and rotational speed of 0.65 rad/s (equivalent to 6.207 rpm): (**a**) Drag, lift, moment, and power coefficients; (**b**) Velocity magnitude contours; (**c**) Static pressure distribution.

- The 6 m/s wind velocity results

Our study presents two sets of results for the Centroid Speed Ratio (CSR) and rotational speed corresponding to a superficial wind velocity of 6 m/s. Wind velocities of 6 m/s are commonly observed on a large scale, ranging from 100 m to 150 m altitudes with reference to ground in Europe [37]. The first set of results consists of a CSR value of 0.958, achieved with a rotational velocity of 0.70 rad/s (equivalent to 6.685 rpm). These results for CSR = 0.958 are comprehensively presented in Figure 7.

Analyzing the variation of performance parameters in Figure 7a concerning time and the instantaneous position of the rotor reveals that the estimated power potential ranges from 8 to 9.5 kW. Considering the total harvestable power of 43.1 kW, these values correspond to relatively low power coefficient values (Cp = 0.198).

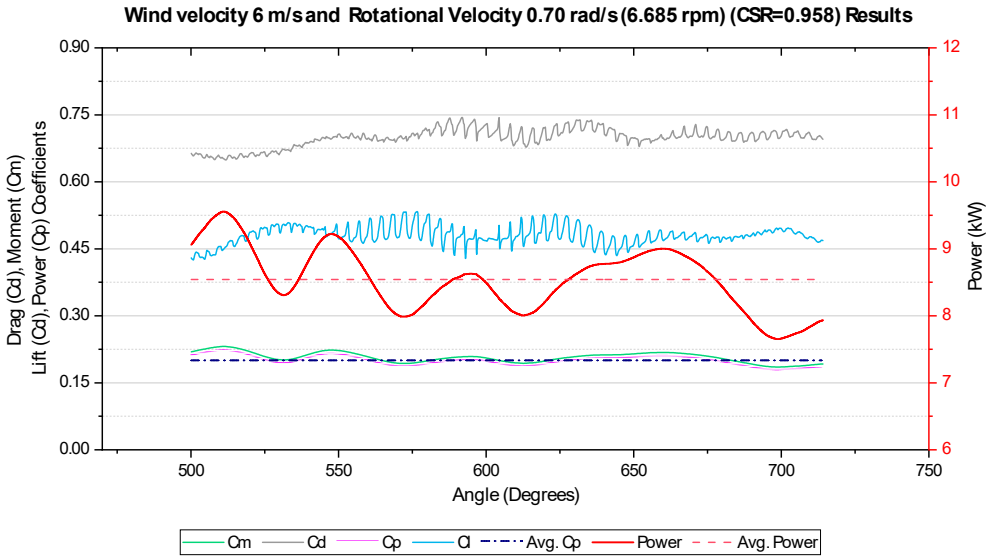

(**a**)

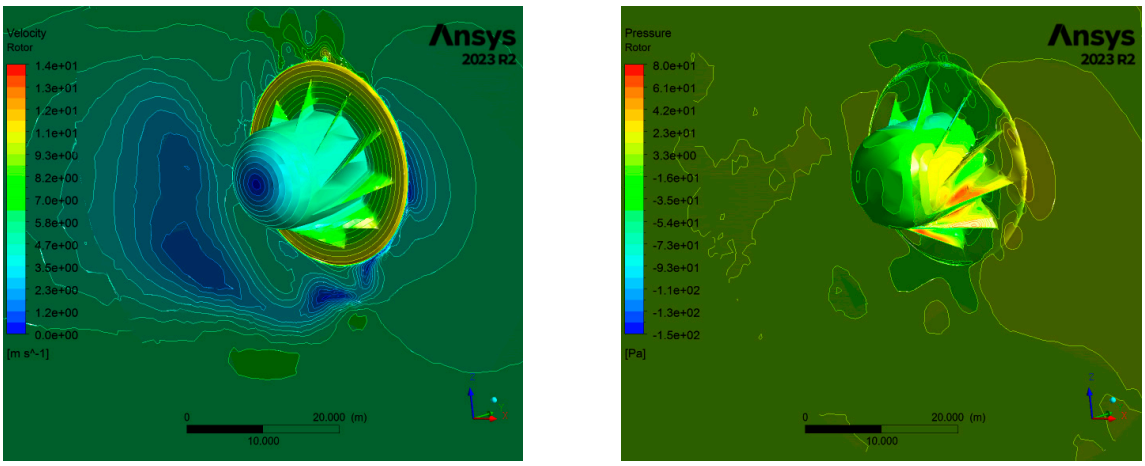

(**b**) (**c**)

Figure 7. Results for wind velocity of 6 m/s and rotational speed of 0.7 rad/s (equivalent to 6.685 rpm): (**a**) Drag, lift, moment, and power coefficients; (**b**) Velocity magnitude contours; (**c**) Static pressure distribution.

Therefore, a further case for a 6 m/s flat terrain velocity was assessed as a new scenario by incrementally increasing the rotational speed to explore instances with a higher Center Speed Ratio (CSR). The condition with a rotational velocity of 0.80 rad/s, applicable to the case with CSR = 1.094, was evaluated, and the results are similarly presented in Figure 8.

According to the results depicted in Figure 8, the instantaneous power obtained for a wind velocity of 6 m/s and a rotational speed of 0.8 rad/s ranges between 16.0 and 17.5 kW. The coefficient of performance (Cp) notably increased compared to the results obtained at 0.7 rad/s, averaging 0.384. The drag coefficient remained consistent with an average of 0.70, while the lift coefficient exhibited a slight increase due to the higher rotation speed, rising from the 0.43–0.45 range to 0.48.

The contour results reveal that, at lower rotational speeds for the same air velocity, the wake typically forms and translates in the upper rear part of the rotor. However, with increasing rotational speed, the wake may shift and become more pronounced in specific areas behind the rotor. Additionally, the wake extends further downstream due to the increased momentum of the airflow passing through the rotor.

These changes in the wake characteristics also influence the pressure distribution in the surrounding airflow. Examination of the static pressure demonstrates variations, often resulting in positive pressure observed on the blade surfaces, as expected. Specifically, for the 6 m/s results, this positive pressure ranges from 70 to 80 Pa, indicating the aerodynamic forces acting on the rotor blades.

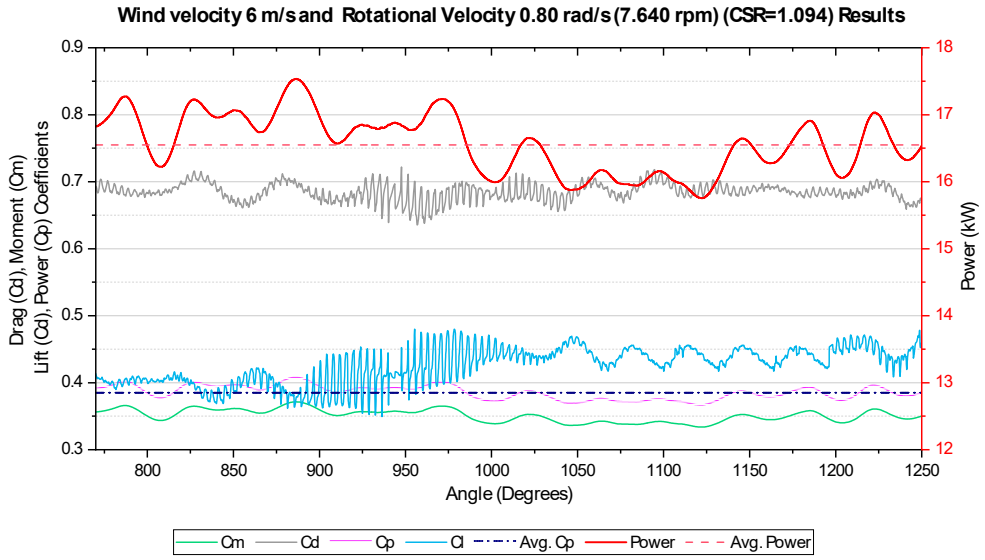

(**a**)

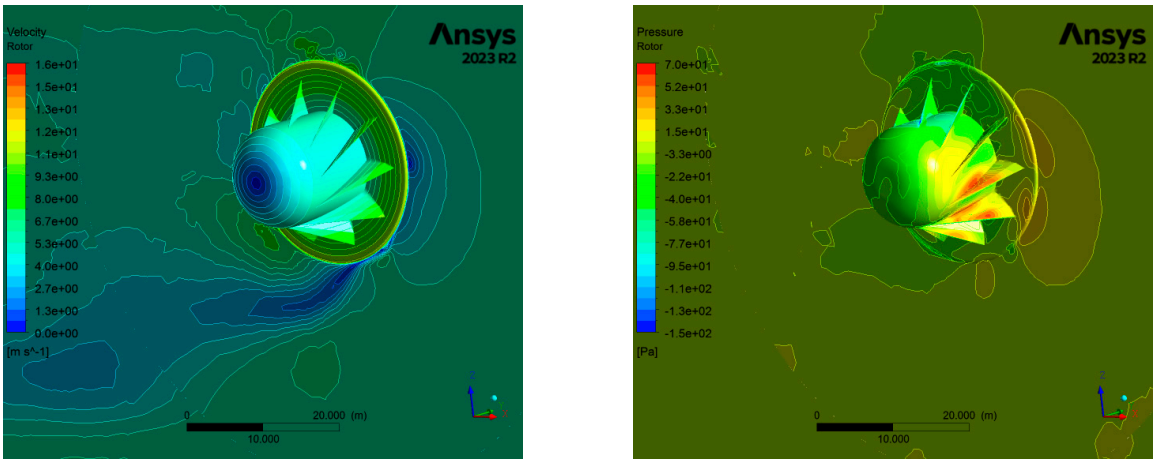

(**b**) (**c**)

Figure 8. Results for wind velocity of 6 m/s and rotational speed of 0.8 rad/s (equivalent to 7.640 rpm): (**a**) Drag, lift, moment, and power coefficients; (**b**) Velocity magnitude contours; (**c**) Static pressure distribution.

- The 9 m/s wind velocity results

In this section, we present the results obtained for a wind velocity of 9 m/s. Wind velocities of 9 m/s are achievable onshore during specific periods, particularly at heights of 150 to 200 m and above ground level. Conversely, for offshore applications, this wind speed is commonly encountered, especially in regions like the North Sea [37]. Wind speeds of this magnitude offer considerable energy potential, with a total harvestable energy estimated at 142 kW.

In this context, initial analyses were conducted with a rotational speed of 1.06 rad/s (equivalent to 10.12 rpm), corresponding to a Centroid Speed Ratio (CSR) of 1.00. The resulting outputs are presented in Figure 9.

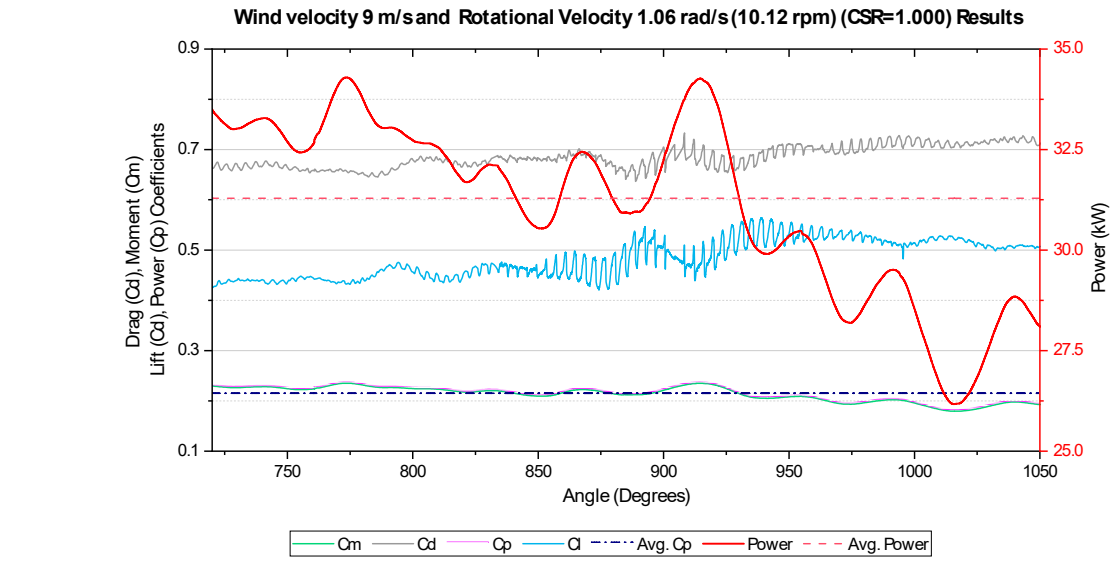

(**a**)

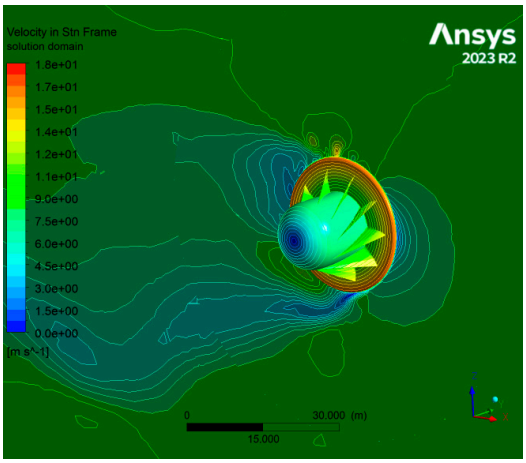

(**b**)

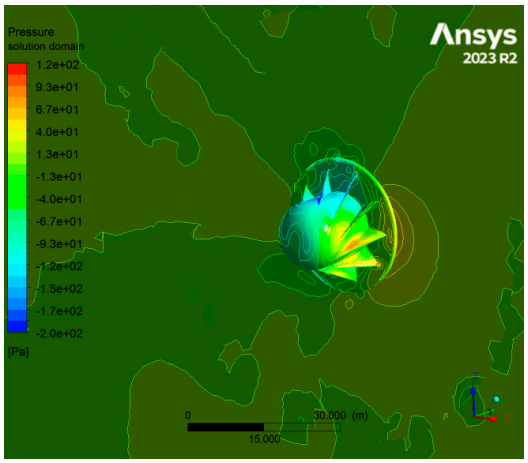

(**c**)

Figure 9. Results for wind velocity of 9 m/s and rotational speed of 1.06 rad/s (equivalent to 10.12 rpm): (**a**) Drag, lift, moment, and power coefficients; (**b**) Velocity magnitude contours; (**c**) Static pressure distribution.

For a rotational velocity of 1.06 rad/s, it is observed that the obtainable energy varies widely, ranging from 26 to 33 kW, with an average of 31.3 kW. Consequently, the power coefficient is calculated to be 0.213. The drag coefficient remains consistent at 0.70, as observed in previous results.

A wide range of velocities is observed on the rotor surfaces, reaching up to 18 m/s. Additionally, the static pressure is measured at −200 Pa on the rear blade surfaces and at 120 Pa on the front surfaces.

The case involving a rotational speed of 1.20 rad/s (rpm) for the same wind speed is analyzed as a subsequent step. The corresponding CSR value calculated for this case is 1.095. The results obtained for a rotation speed of 1.20 rad/s are presented in Figure 10.

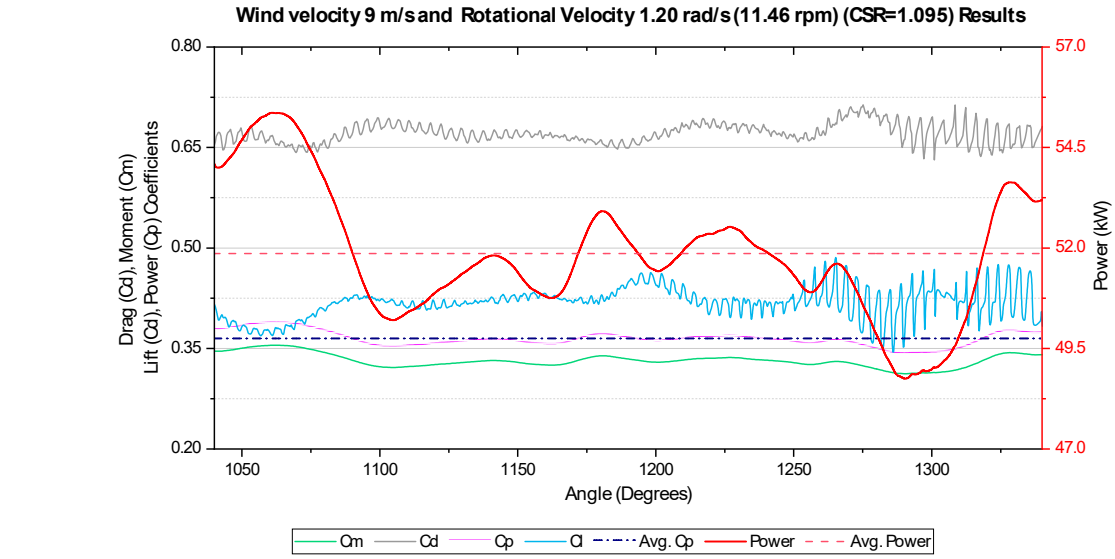

(**a**)

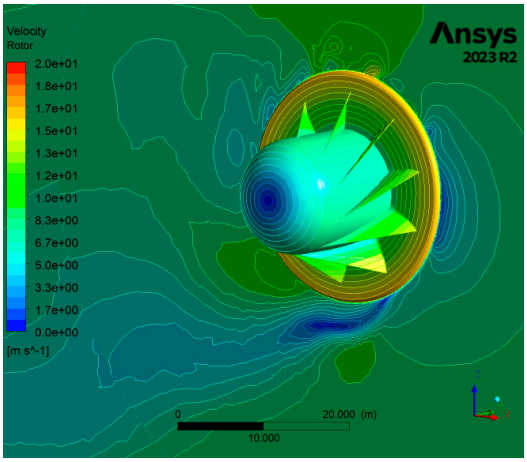

(**b**)

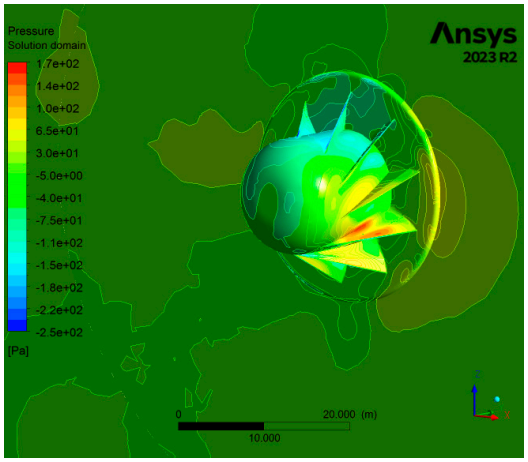

(**c**)

Figure 10. Results for wind velocity of 9 m/s and rotational speed of 1.20 rad/s (equivalent to 11.46 rpm): (**a**) Drag, lift, moment, and power coefficients; (**b**) Velocity magnitude contours; (**c**) Static pressure distribution.

As depicted in Figure 10, an increase in rotational velocity leads to a significant rise in the power coefficient, reaching 0.364, similar to the previous case. The estimated power obtained ranges between 48 and 55 kW. The drag coefficient remains constant at 0.70, while the lift coefficient stabilizes at approximately 0.40.

Similarly to the observations at 6 m/s, the heightened rotational speed causes a further downstream extension of the wake due to the increased momentum of the airflow passing through the rotor.

Furthermore, it was observed that as the rotational speed increased, the static pressure on the front surface of the rotor blades exceeded 170 Pa.

- The 12 m/s wind velocity results

In our study, we evaluated the results for wind speed conditions of 12 m/s as the highest wind velocity scenario by extending our previous conference work [31]. Wind speeds of 12 m/s can typically be observed in regions with favorable wind conditions, such as coastal areas or elevated terrains (>300 m above ground level). However, the

availability of such high wind speeds may vary depending on the geographical location, local topography, and weather patterns.

A wind speed of 12 m/s is considered relatively high and falls within the category of strong winds. According to the Beaufort scale [40], which classifies wind speeds based on observed effects on land and sea, 12 m/s corresponds to a Beaufort scale force of 6, indicating strong breeze conditions. Notably, such strong breeze conditions are unlikely to persist stably for extended periods.

However, despite the infrequency of stable 12 m/s wind conditions, it was essential to evaluate the performance of wind energy systems under such circumstances. This is particularly significant considering that the MARS airborne rotor system manufacturer provided estimated power output figures based on the rated 12 m/s wind speed. Therefore, in our study, we tested scenarios where 12 m/s wind speeds occur and analyzed the results accordingly.

For a wind velocity of 12 m/s, the results obtained for a rotational speed of 1.20 rad/s (11.46 rpm) are depicted in Figure 11.

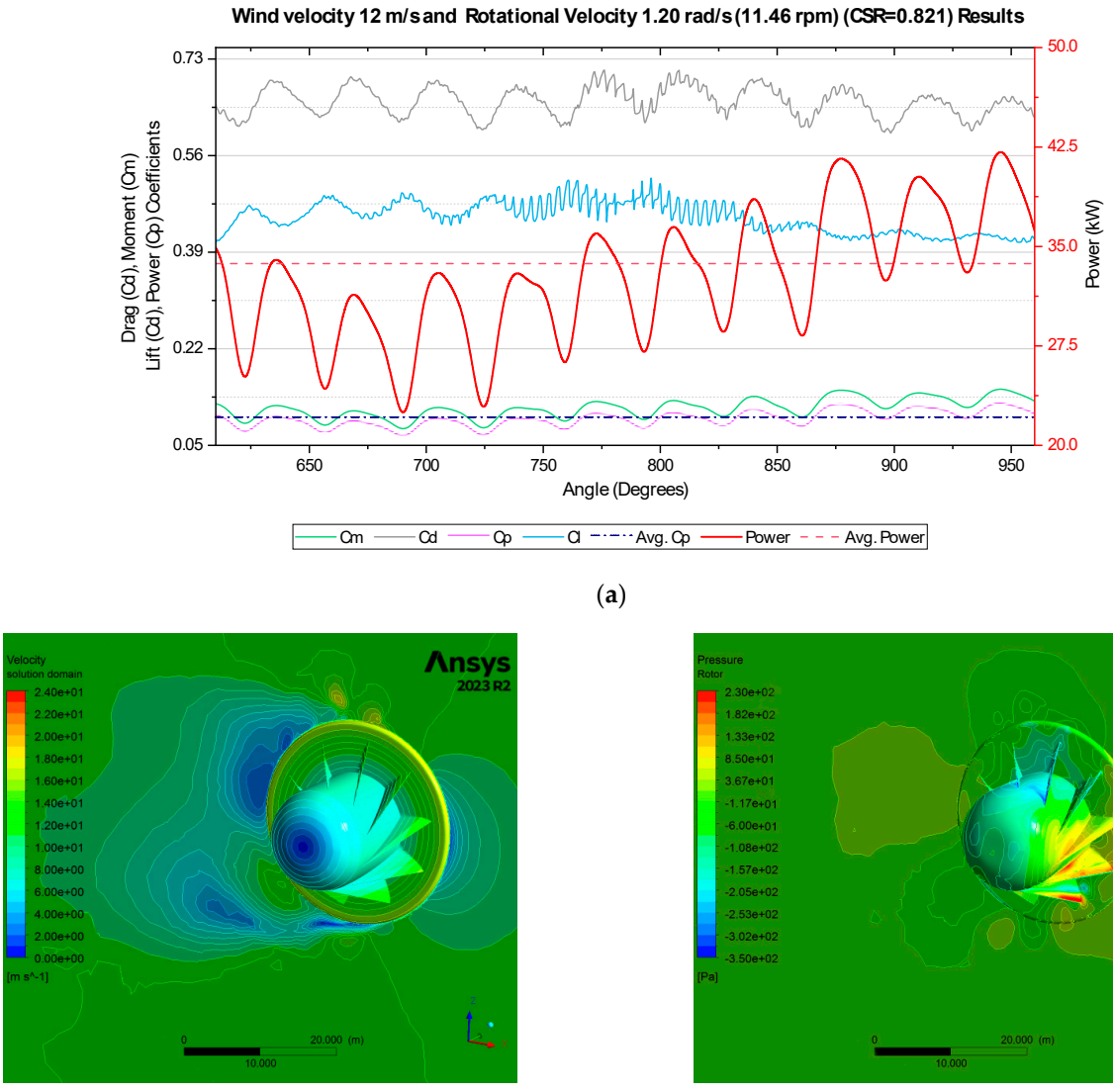

Figure 11. Results for wind velocity of 12 m/s and rotational speed of 1.20 rad/s (equivalent to 11.46 rpm): (**a**) Drag, lift, moment, and power coefficients; (**b**) Velocity magnitude contours; (**c**) Static pressure distribution.

For a wind velocity of 12 m/s and a rotational speed of 1.20 rad/s (corresponding to CSR = 0.821), the power generation results exhibit a wide range, spanning from 23 to 43 kW. The average calculated power is 33.7 kW, which is relatively low considering the potential energy of 12 m/s air, estimated at 345 kW. The power coefficient is indirectly determined to be 0.098, marking the lowest value in our study. Therefore, to explore cases with higher CSR values, the scenario involving a rotational speed of 1.45 rad/s (CSR = 0.992) was also examined, and the results are illustrated in Figure 12.

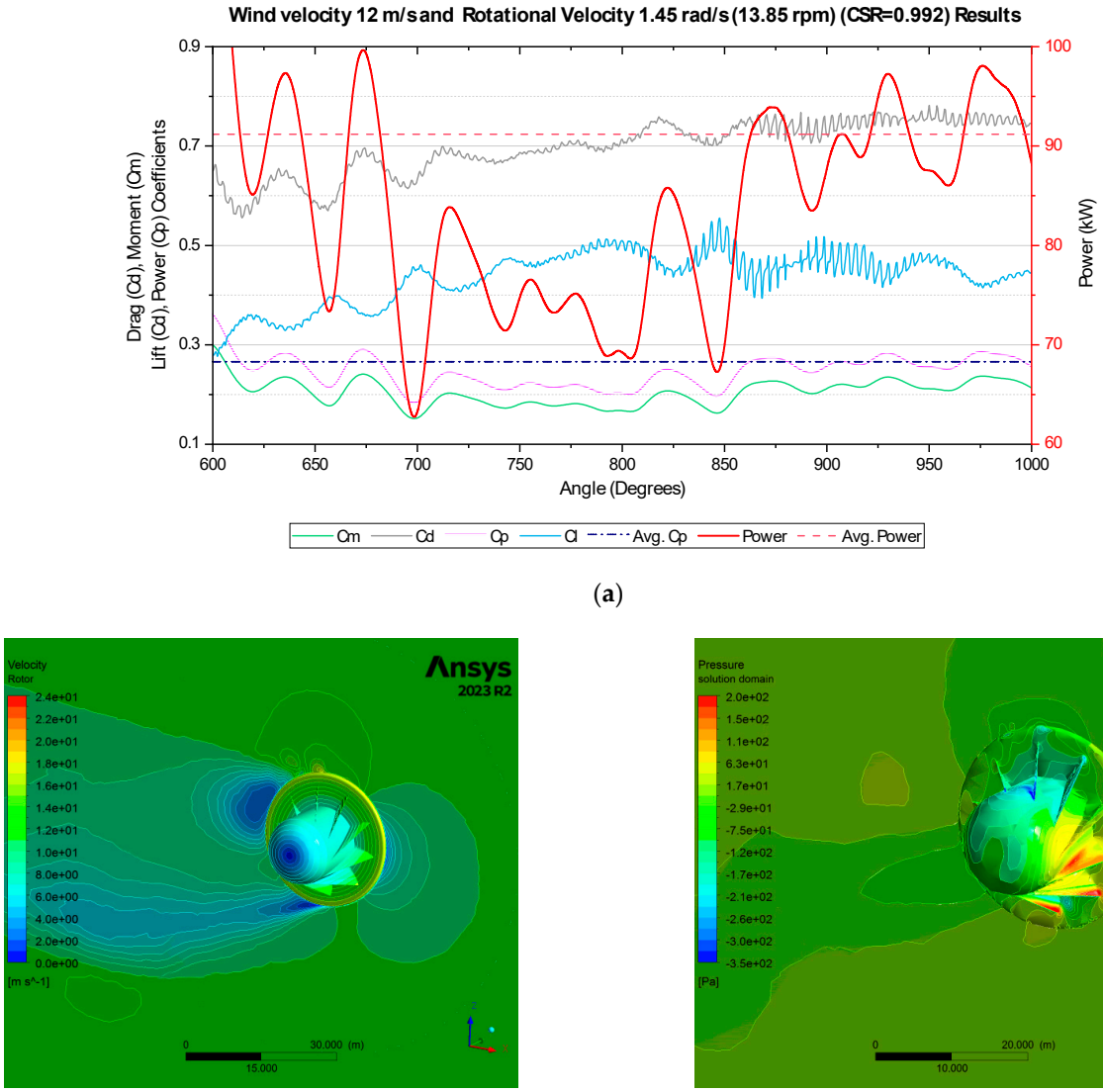

Figure 12. Results for wind velocity of 12 m/s and rotational speed of 1.45 rad/s (equivalent to 13.85 rpm): (**a**) Drag, lift, moment, and power coefficients; (**b**) Velocity magnitude contours; (**c**) Static pressure distribution.

As anticipated, the increase in rotational speed corresponded to a rise in potential power output. The estimated power generation ranged between 70 and 100 kW, aligning with the rated energy output of 100 kW provided by the patented manufacturer of the MAGENN Airborne Rotor System (MARS). However, it is worth noting that achieving stable wind speeds of 12 m/s poses a significant challenge for the project.

Furthermore, with higher wind speeds and rotation rates, the lift coefficient exceeded the 0.50 threshold, slightly surpassing values observed in previous cases, which typically

ranged between 0.40 and 0.45. Similarly, the drag coefficient also showed a slight increase, hovering slightly above 0.70.

Another noteworthy observation from the contour plots is the elongation of the wake behind the rotor with increasing wind speed. This phenomenon arises from the accelerated airflow, creating a larger disturbed air zone downstream, which persists longer. This correlation between wind speed and wake behavior underscores the complex nature of airflow dynamics around airborne rotor systems.

4. Discussion

In this paper, we conducted an in-depth analysis of the potential performance of an airborne vertical axis wind turbine (VAWT) under maximum rating wind velocities of up to 12 m/s, considering flat terrain wind speed conditions up to approximately 300 m height. This study aimed to evaluate the performance characteristics of this novel VAWT design across a range of wind speeds, from 3 m/s to 12 m/s. The results of our analysis are summarized in Table 1 below, including the average power production and average power coefficient of the rotor at each wind velocity.

Table 1. Possible average power production and average power coefficient of the rotor for selected wind and rotational velocities.

Wind Velocity (m/s)	Rotational Velocity (rpm)	Average Power Coefficient (Cp)	Available Power (kW)	Possible Average Power Production (kW)
3	3.44	0.228	5.4	1.22
5	6.21	0.277	24.9	6.91
6	6.68	0.198	43.1	8.54
6	7.64	0.384	43.1	16.55
9	10.12	0.213	142.6	31.29
9	11.46	0.364	142.6	51.86
12	11.46	0.098	345.0	33.70
12	13.85	0.264	345.0	91.18

In addition, the power coefficient (Cp) curves at different Centroid Speed Ratios (CSRs) under the same wind velocities are presented in Figure 13.

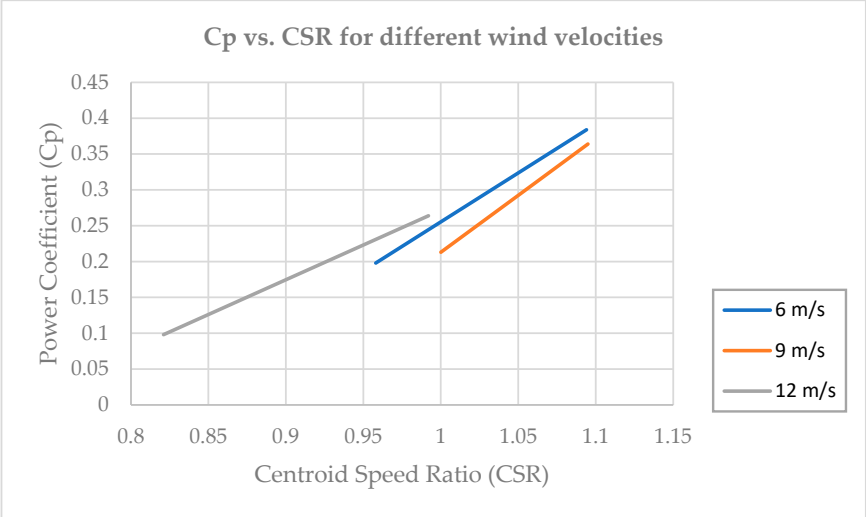

Figure 13. Power coefficient (Cp) curves at different Centroid Speed Ratios (CSRs) under the same flow velocity.

The results demonstrate a clear relationship between wind velocity, rotational velocity, and the performance of the MAGENN airborne wind turbine system. Notably, the average power coefficient (Cp) varies between 0.1 and 0.38 across different wind and rotational velocities, with the highest power generation potential observed at a wind speed of 12 m/s and a rotational speed of 13.85 rpm, resulting in an average power production of 91.18 kW.

This study also presents wake and vorticity characteristics under various flow conditions and Reynolds numbers through contours. The findings indicate that, at lower rotational speeds and consistent air velocities, the wake predominantly forms and moves in the upper rear section of the rotor. However, as the rotational speed increases, the wake may shift and intensify in specific regions behind the rotor. Furthermore, the wake extends farther downstream due to the heightened momentum of airflow passing through the rotor. Nevertheless, conducting a more comprehensive analysis of wake and vorticity is planned for future studies.

Validity of the Results

The comparison with existing studies provides a valuable framework for assessing the validity of our results. Our findings, which demonstrate favorable performance compared to similar investigations on Savonius Drag-Type Vertical Wind Turbines, align well with the literature. Specifically, Gerrie et al. [11] reported Cp values ranging from 0.12 to 0.14, Al-Gburi et al. [15] reported a range from 0.10 to 0.21, Mohamed et al. [21] reported a range from 0.10 to 0.25, Shukla et al. [14] reported a range from 0.23 to 0.27, and Alom et al. [41] reported a range from 0.11 to 0.33. However, it is crucial to acknowledge that each study involves a unique geometry, conditions, and experimental setups, which can influence the observed outcomes. Despite these differences, the consistency of our results with the broader body of literature on wind turbine performance gives credibility to our findings. Further research and validation efforts, including experimental verification when feasible, would enhance the robustness and reliability of our conclusions.

5. Conclusions

The computational analysis conducted in this study offers valuable insights into the performance characteristics of a novel airborne vertical axis wind turbine (AVAWT) system across varying wind conditions. Our findings not only highlight the complex interactions between wind speed, rotational speed, and turbine performance but also provide several opportunities for researchers and developers in the field of airborne wind energy.

One significant implication of this research is the identification of optimal operating conditions for maximizing energy extraction efficiency. The cyclic behavior observed in power generation, characterized by peaks at specific rotor positions, underscores the importance of adjusting rotational speed to optimize power output. This presents an opportunity for further research into advanced control strategies and optimization algorithms aimed at dynamically adjusting rotor speed to adapt to changing wind conditions in real time, thereby enhancing overall system efficiency.

In this study, we carried out a comprehensive evaluation of the performance of a vertical axis wind turbine (VAWT) airborne wind turbine system inspired by the innovative design resembling yacht sails. By using information from related websites and literature, which reported a power coefficient (Cp) of 0.21, we aimed to validate and extend these initial claims. Through meticulous computational analysis, we investigated the performance of the turbine across a spectrum of wind speeds and rotational velocities. Our findings revealed a dynamic range of average power coefficients (Cp) spanning from 0.1 to 0.38, underscoring the versatility and adaptability of the turbine system under diverse operating conditions. Notably, the highest power generation potential was observed at a wind speed of 12 m/s and a rotational speed of 13.85 rpm, culminating in an impressive average power production of 91.18 kW.

Moreover, our analysis of wake formation and translation behind the rotor highlights the need for further research to minimize power losses due to wake interference. Wake

and vortex structures could be further explored to mitigate the adverse effects of wake turbulence on downstream turbines. Additionally, experimental validation of the numerical results could further enhance the reliability and accuracy of the predictive models.

In conclusion, this study contributes to the ongoing efforts to harness the vast potential of airborne wind energy as a sustainable and renewable energy source. By addressing key research challenges and identifying opportunities for innovation, this research lays the foundation for the continued development and commercialization of different types of airborne wind turbine systems.

Author Contributions: Conceptualization, D.G.; methodology, D.G.; software, D.G. and E.K.; validation, D.G. and E.K.; formal analysis, D.G. and E.K.; investigation, D.G. and E.K.; resources, D.G.; data curation, D.G. and E.K.; writing—original draft preparation, D.G. and E.K.; writing—review and editing, D.G. and E.K.; visualization, D.G. and E.K. All authors have read and agreed to the published version of the manuscript.

Funding: This research received no external funding.

Data Availability Statement: The data presented in this study are available on reasonable requests from the corresponding author.

Conflicts of Interest: The authors declare no conflicts of interest.

References

1. European Union-Eurostat Share of Energy from Renewable Sources. Available online: https://ec.europa.eu/eurostat/databrowser/view/nrg_ind_ren/default/bar?lang=en (accessed on 4 February 2024).
2. Worku, M.Y. Recent Advances in Energy Storage Systems for Renewable Source Grid Integration: A Comprehensive Review. *Sustainability* **2022**, *14*, 5985. [CrossRef]
3. EUR-Lex Directive (EU) 2023/2413 of the European Parliament and of the Council of 18 October 2023 Amending Directive (EU) 2018/2001, Regulation (EU) 2018/1999 and Directive 98/70/EC as Regards the Promotion of Energy from Renewable Sources, and Repealing Council. Available online: https://eur-lex.europa.eu/legal-content/EN/TXT/?uri=OJ:L_202302413 (accessed on 4 February 2024).
4. Cherubini, A.; Papini, A.; Vertechy, R.; Fontana, M. Airborne Wind Energy Systems: A Review of the Technologies. *Renew. Sustain. Energy Rev.* **2015**, *51*, 1461–1476. [CrossRef]
5. Bechtle, P.; Schelbergen, M.; Schmehl, R.; Zillmann, U.; Watson, S. Airborne Wind Energy Resource Analysis. *Renew. Energy* **2019**, *141*, 1103–1116. [CrossRef]
6. Diehl, M. Airborne Wind Energy: Basic Concepts and Physical Foundations. In *Airborne Wind Energy*; Ahrens, U., Diehl, M., Schmehl, R., Eds.; Springer: Berlin/Heidelberg, Germany, 2013; pp. 3–22. ISBN 978-3-642-39965-7.
7. Puspitasari, D.; Sahim, K. Effect of Savonius Blade Height on the Performance of a Hybrid Darrieus-Savonius Wind Turbine. *J. Mech. Eng. Sci.* **2019**, *13*, 5832–5847. [CrossRef]
8. Zhou, T.; Rempfer, D. Numerical Study of Detailed Flow Field and Performance of Savonius Wind Turbines. *Renew. Energy* **2013**, *51*, 373–381. [CrossRef]
9. Zgraggen, A.U.; Fagiano, L.; Morari, M. Real-Time Optimization and Adaptation of the Crosswind Flight of Tethered Wings for Airborne Wind Energy. *IEEE Trans. Control Syst. Technol.* **2015**, *23*, 434–448. [CrossRef]
10. Trevisi, F.; Croce, A.; Riboldi, C.E.D. Flight Stability of Rigid Wing Airborne Wind Energy Systems. *Energies* **2021**, *14*, 7704. [CrossRef]
11. Gerrie, C.; Islam, S.Z.; Gerrie, S.; Turner, N.; Asim, T. 3D CFD Modelling of Performance of a Vertical Axis Turbine. *Energies* **2023**, *16*, 1144. [CrossRef]
12. Ferrari, G.; Federici, D.; Schito, P.; Inzoli, F.; Mereu, R. CFD Study of Savonius Wind Turbine: 3D Model Validation and Parametric Analysis. *Renew. Energy* **2017**, *105*, 722–734. [CrossRef]
13. Didane, D.H.; Bajuri, M.N.A.; Manshoor, B.; Boukhari, M.I. Performance Investigation of Vertical Axis Wind Turbine with Savonius Rotor Using Computational Fluid Dynamics (CFD). *CFD Lett.* **2022**, *14*, 116–124. [CrossRef]
14. Shukla, A.; Alom, N.; Saha, U.K. Spline-Bladed Savonius Wind Rotor with Porous Deflector: A Computational Investigation. *J. Braz. Soc. Mech. Sci. Eng.* **2022**, *44*, 444. [CrossRef]
15. Al-Gburi, K.A.H.; Al-Quraishi, B.A.J.; Alnaimi, I.; Tan, F.B.; Al-Safi, E.S.; Otto, M.; Hansen, L.; Abdulkareem, K.; Al-Gburi, H.; Abdulameer, B.; et al. Experimental and Simulation Investigation of Performance of Scaled Model for a Rotor of a Savonius Wind Turbine. *Energies* **2022**, *15*, 8808. [CrossRef]
16. Mohamed, M.H.; Alqurashi, F.; Ramadan, A.; Thévenin, D. Enhancement Attempts for a Three-Bladed Savonius Turbine Performance. *Front. Energy Res.* **2022**, *10*, 797868. [CrossRef]
17. Ramarajan, J.; Jayavel, S. Performance Study of Savonius Vertical Axis Wind Turbine with Slotted Blades. In Proceedings of the Fluid Mechanics and Fluid Power (Vol. 1); Bhattacharyya, S., Chattopadhyay, H., Eds.; Springer: Singapore, 2023; pp. 447–452.

18. Moreno-Armendáriz, M.A.; Ibarra-Ontiveros, E.; Calvo, H.; Duchanoy, C.A. Integrated Surrogate Optimization of a Vertical Axis Wind Turbine. *Energies* **2021**, *15*, 233. [CrossRef]
19. Trisakti, M.; Halim, L.; Arthaya, B.M. Power Coefficient Analysis of Savionus Wind Turbine Using CFD Analysis. In Proceedings of the International Conference on Mechatronics, Robotics and Systems Engineering (MoRSE), Bali, Indonesia, 4–6 December 2019; pp. 24–29.
20. Bishnoi, A.K.; Dewan, A.; Singh, T.P. Aerodynamic Characteristics of Elliptical Bladed Savonius Wind Turbine Rotor: A Computational Study Using Different Turbulence Models. *AIP Conf. Proc.* **2023**, *2786*, 20008.
21. Abdelaziz, K.R.; Nawar, M.A.A.; Ramadan, A.; Attai, Y.A.; Mohamed, M.H. Performance Assessment of a Modified of Savonius Rotor: Impact of Sine and Conical Blade Profiles. *Energy* **2023**, *272*, 127172. [CrossRef]
22. Noronha, N.P.; Munishamaih, K. Performance Assessment of a Balloon Assisted Micro Airborne Wind Turbine System. *Energy Harvest. Syst.* **2021**, *8*, 63–71. [CrossRef]
23. ANSYS. Ansys Fluent Rotating Machinery Modeling. Available online: https://www.ansys.com/services/training-center/fluids/ansys-cfd-fluent-and-cfx-rotating-machinery-modeling (accessed on 17 November 2023).
24. Ali, Q.S.; Kim, M.-H. Power Conversion Performance of Airborne Wind Turbine under Unsteady Loads. *Renew. Sustain. Energy Rev.* **2022**, *153*, 111798. [CrossRef]
25. MIT News Office High-Flying Turbine Produces More Power. Available online: https://news.mit.edu/2014/high-flying-turbine-produces-more-power-0515 (accessed on 7 February 2024).
26. OMNIDEA. Long Endurance Medium Altitude Platform (LEMAP). Available online: https://omnidea.net/lemap.omnidea.net/index.php/project-overview (accessed on 7 February 2024).
27. Seifert, J. A Review of the Magnus Effect in Aeronautics. *Prog. Aerosp. Sci.* **2012**, *55*, 17–45. [CrossRef]
28. Lv, J.; Lin, Y.; Zhang, R.; Li, B.; Yang, H. Assisted Propulsion Device of a Semi-Submersible Ship Based on the Magnus Effect. *Pol. Marit. Res.* **2022**, *29*, 33–46. [CrossRef]
29. Gowree, E.R.; Prince, S.A. A Computational Study of the Aerodynamics of a Spinning Cylinder in a Cross Flow of High Reynolds Number. In Proceedings of the 28th International Congress of the Aeronautical Sciences, Brisbane, Australia, 23–28 September 2012; Grant, I., Ed.; pp. 1–10.
30. Milutinović, M.; Čorić, M.; Deur, J. Operating Cycle Optimization for a Magnus Effect-Based Airborne Wind Energy System. *Energy Convers. Manag.* **2015**, *90*, 154–165. [CrossRef]
31. Kükrer, E.; Güneş, D. Flat Terrain Performance Rating Analysis of a Novel Airborne Rotor-Type Vertical Axis Wind Turbine (VAWT) by Applying Three-Dimensional Rotating Mesh Unsteady RANS Simulation Method. In *Lecture Notes in Mechanical Engineering*; Springer: Dusseldorf, Germany, 2023.
32. Ferguson, F.D. Systems and Methods for Tethered Wind Turbines. Patent No. 8,148,838, 17 August 2010.
33. Güneş, D.; Kükrer, E.; Aydoğdu, T. Computational Performance Analysis of an Airborne Rotor-Type Electricity Generator Wind Turbine. *E3S Web Conf.* **2019**, *128*, 09007. [CrossRef]
34. Wind Atlas MAGENN Floating Wind Generators Take Advantage of High Altitude Winds. Available online: https://newatlas.com/magenn-mars-floating-wind-generator/11109/ (accessed on 8 February 2024).
35. Chaudhari, R. Electric Energy Generation by Magenn Air Rotor System (MARS). *Int. J. Comput. Sci. Netw.* **2015**, *4*, 2277–5420.
36. VIGYAN. Wind Tunnels Rotor Test Cell. Available online: https://vigyan.com/rotor-test-cell.html (accessed on 8 February 2024).
37. NEWA. New European Wind Atlas. Available online: https://map.neweuropeanwindatlas.eu/ (accessed on 17 November 2023).
38. Alaimo, A.; Esposito, A.; Messineo, A.; Orlando, C.; Tumino, D. 3D CFD Analysis of a Vertical Axis Wind Turbine. *Energies* **2015**, *8*, 3013–3033. [CrossRef]
39. Trivellato, F.; Raciti Castelli, M. On the Courant–Friedrichs–Lewy Criterion of Rotating Grids in 2D Vertical-Axis Wind Turbine Analysis. *Renew. Energy* **2014**, *62*, 53–62. [CrossRef]
40. Wheeler, D.; Wilkinson, C. From Calm to Storm: The Origins of the Beaufort Wind Scale. *Mar. Mirror* **2004**, *90*, 187–201. [CrossRef]
41. Alom, N.; Kolaparthi, S.C.; Gadde, S.C.; Saha, U.K. Aerodynamic Design Optimization of Elliptical-Bladed Savonius-Style Wind Turbine by Numerical Simulations. In Proceedings of the ASME 2016 35th International Conference on Ocean, Offshore and Arctic Engineering, Busan, Republic of Korea, 19–24 June 2016.

computation

MDPI

Article

Hydraulic Performance Optimization of a Submersible Drainage Pump

Md Rakibuzzaman [1,2,*], Sang-Ho Suh [3,*], Hyung-Woon Roh [4], Kyung Hee Song [5], Kwang Chul Song [5] and Ling Zhou [1]

[1] National Research Center of Pumps, Jiangsu University, Zhenjiang 212013, China; lingzhou@ujs.edu.cn
[2] Department of Mechanical Engineering, International University of Business Agriculture and Technology, Dhaka 1230, Bangladesh
[3] School of Mechanical Engineering, Soongsil University, Seoul 06978, Republic of Korea
[4] IVAI Ltd., Gangseo-gu, Seoul 157-754, Republic of Korea; rohlee@ivai.co.kr
[5] Daeyoung Power Pump, Hwaseong City 445-861, Gyoenggi-do, Republic of Korea; dew322@dypump.co.kr (K.H.S.); kcsong813@dypump.co.kr (K.C.S.)
* Correspondence: rakibuzzaman@iubat.edu (M.R.); suhsh@ssu.ac.kr (S.-H.S.)

Abstract: Small submersible drainage pumps are used to discharge leaking water and rainwater in buildings. In an emergency (e.g., heavy rain or accident), advance monitoring of the flow rate is essential to enable optimal operation, considering the point where the pump operates abnormally when the water level is increased rapidly. Moreover, pump performance optimization is crucial for energy-saving policy. Therefore, it is necessary to meet the challenges of submersible pump systems, including sustainability and pump efficiency. The final goal of this study was to develop an energy-saving and highly efficient submersible drainage pump capable of performing efficiently in emergencies. In particular, this paper targeted the hydraulic performance improvement of a submersible drainage pump model. Prior to the development of driving-mode-related technology capable of emergency response, a way to improve the performance characteristics of the existing submersible drainage pump was found. Disassembling of the current pump followed by reverse engineering was performed instead of designing a new pump. Numerical simulation was performed to analyze the flow characteristics and pump efficiency. An experiment was carried out to obtain the performance, and it was validated with numerical results. The results reveal that changing the cross-sectional shape of the impeller reduced the flow separation and enhanced velocity and pressure distributions. Also, it reduced the power and increased efficiency. The results also show that the pump's efficiency was increased to 5.56% at a discharge rate of 0.17 m^3/min, and overall average efficiency was increased to 6.53%. It was concluded that the submersible pump design method is suitable for the numerical designing of an optimized pump's impeller and casing. This paper provides insight on the design optimization of pumps.

Keywords: submersible pump; computational fluid dynamics; experiment; impeller shape; flow balance block; optimum model

Citation: Rakibuzzaman, M.; Suh, S.-H.; Roh, H.-W.; Song, K.H.; Song, K.C.; Zhou, L. Hydraulic Performance Optimization of a Submersible Drainage Pump. *Computation* **2024**, *12*, 12. https://doi.org/10.3390/computation12010012

Academic Editor: Sergey A. Karabasov

Received: 18 November 2023
Revised: 7 December 2023
Accepted: 8 January 2024
Published: 10 January 2024

1. Introduction

This study focused on the performance improvement of submersible drainage pumps. Submersible drainage pumps are divided into two categories. One is referred to as "large submersible pumps", which are used for drainage (rainwater) pumping stations, and the other is known as "small submersible pumps", which are used in buildings. Small submersible drainage pumps are used for draining from buildings when leakage and rainwater flow into the basement [1–3]. The TRL (Technology Readiness Level) of submersible drainage pumps is 7–9, and it is a situation from which no unique technology will arise. Existing technology patents also utilize technology used in other fields. According to patent acquisition, vibration sensors are installed on the pump shaft to solve the blocking

phenomenon caused by foreign substances and vibration problems caused by, e.g., cavitation. The shape of the impeller can be changed without impacting performance to prevent the clogging of foreign substances or improve existing monitoring technologies. Pump efficiency is a significant energy-saving policy factor [4,5]. If pump efficiency increases, a significant amount of energy will be saved.

Due to the complicated, implicit relationship between hydraulic performance and the complex geometry shape of impeller passages, the study of optimization and the inverse problem of the submersible pump is moving slowly [6,7]. Shi et al. [8] started to design a new submersible pump for deep wells with the computational fluid dynamics (CFD) technique. They achieved sufficient pump efficiency compared with that of traditional pumps. Zhu et al. [9] investigated a mechanistic model for improving system performance with gas–liquid flow in a submersible pump. Manivannan [10] conducted a study on the computational fluid dynamics of a mixed-flow pump to predict the flow pattern inside the impeller. Different parameters and optimization techniques were used to obtain optimal output for the pump impeller numerically [11]. The pump impeller head was optimized using various optimization algorithms to reduce frictional loss during pump operation [12]. Using an inverse design, Zangeneth et al. [13] investigated using a mixed-flow pump for suppressing secondary flows. Afterwards, they [14] performed an experimental study to confirm the validity of the model pump. Kim et al. [15] attempted to improve suction performance and efficiency by optimizing a mixed-flow pump with the CFD technique. Another researcher [16] studied the suction performance improvement of mixed-flow pumps. The result exhibited that the specific speed and shape of the pump's impeller greatly influence the suction performance.

Yan et al. [17] investigated a CFD-based pump redesign of a centrifugal to improve efficiency and decrease unsteady radial forces. The CFD method was applied to study the effect of the volute and the number of impeller blades and trailing-edge modification of pumps [18,19]. Qian et al. [20] adopted the Plackett–Buram test design method for the performance optimization of multistage centrifugal pumps. The results showed a significantly impacted pump axial force and hydraulic performance when considering the blade exit angle, outlet diameter, blade wrap angle, etc. Liu et al. [21] studied the RBF neural network and particle swarm optimization method to improve the performance of submersible well pumps. They found that the pressure gradient in the impeller was increased, and the pressure amplitude of the impeller was significantly reduced. Ling Bai et al. [22] highlighted the performance improvement of an EPS impeller based on the Taguchi approach and found that the front and rear shrouds of the impeller meridian significantly affect the ESP performance. Chen et al. [23] studied performance improvement of a mixed-flow pump based on the entropy production method. They found that the geometric and hydrodynamic parameters greatly influenced the pump's energy characteristics. Suh et al. [24] optimized impeller and suction performance to increase the hydraulic efficiency of a mixed-flow pump. Jeon et al. [25] conducted a study on a regenerative pump impeller and enhanced the model's efficiency by numerical simulation and design of experiments (DoE). Siddique et al. [26] investigated the impeller design optimization of a centrifugal pump by numerically enhancing the pump head and significantly reducing the input power. Shim et al. [27] presented a study on enhancement flow recirculation and cavitation of a centrifugal pump by controlling the meridional profile of the blade. Yang et al. [28] investigated multistage ESP to improve hydraulic performance using the Taguchi optimization method. The Taguchi method was a remarkably handy tool for optimizing the ESP. Arocena et al. [29] designed and analyzed the intake structure of a submersible pump numerically. Wei et al. [30] investigated the influence of impeller gap drainage width on the performance of a low-specific-speed centrifugal pump, and the results revealed that using a smaller gap width could significantly improve the performance. Han et al. [31] presented the influence of various impeller blade outlet angles on the performance of a high-speed ESP using experimental and computational methods. It was found that the impeller vane exit angle had a significant effect on the pump performance

curve. Tong et al. [32] conducted axial flow pump performance analysis experimentally and numerically. The results showed that a higher head led to increased pump rotation speed. Fakher et al. [33] studied the efficiency improvement of an electric submersible pump. They replaced the conventional motor with a permanent magnetic one to achieve prolonged ESP mean failure. The flow patterns inside an electrical submersible pump are presented using CFD and compared with visualization experiments [34]. However, the study did not show whether optimizing the shape of the pump casing and impeller can improve the hydraulic performance in a single-stage submersible drainage pump.

Therefore, this study focused especially on the hydraulic performance optimization of a centrifugal-type submersible drainage pump as a development target. To improve our understanding of the flow characteristics inside pumps, existing and developed pumps' performances were analyzed through simulations and experiments. Moreover, this study was intended to provide a basic design of the pump shape to enhance the performance of significant parts, manufacture parts and conduct pump tests using 3D printing technology. In addition, primary research findings were patented based on the developed technology.

2. Materials and Methods

2.1. Pump Dimensions and 3D Model

Three-dimensional scanning was performed to accurately obtain the dimensions of the pump casing and impeller to be analyzed. For this purpose, a DWE-08B submersible drainage pump was disassembled, as shown in Figure 1. The exact dimensions of the pump were required for analysis through computational methods. Of the pump components, only the significant parts of the pump impeller and casing were scanned using a noncontact portable 3D scanner (Creaform 50, with a tolerance of 1/100, Creaform, Lévis, QC, Canada). The software generated the three-dimensional geometrical shape and imported it to CAD software (ANSYS-ICEM (21R2)) for cleaning.

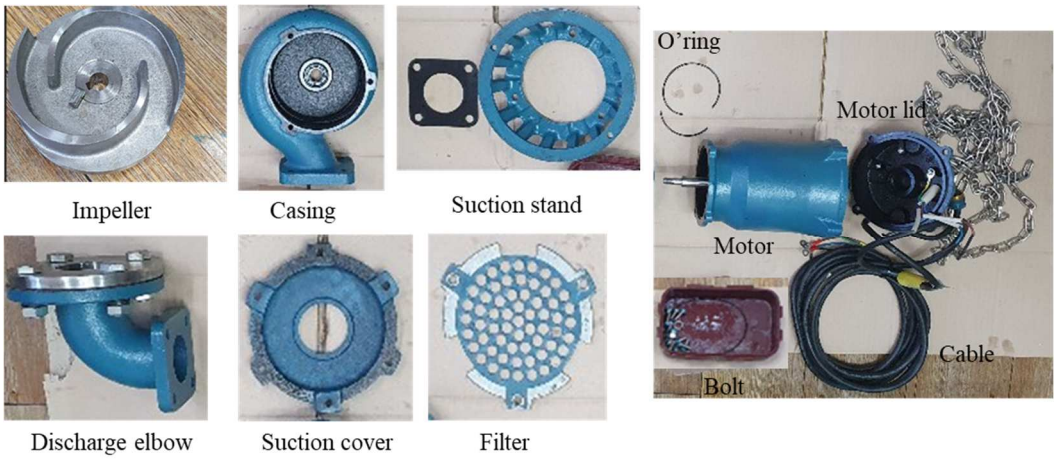

Figure 1. Disassembling the submersible drainage pump (DWE-08).

This study used ANSYS-ICEM commercial software to clean-scan 3D geometry and create an .STP file. Figure 2 shows an assembly and disassembly drawing of the vertical semi-open-type submersible pump (model—DWE-08B). Figure 3 illustrates the cross-sectional view of the main components of the pump. Table 1 presents the major design dimensions of the pump impeller and the casing obtained from the pump company's catalog.

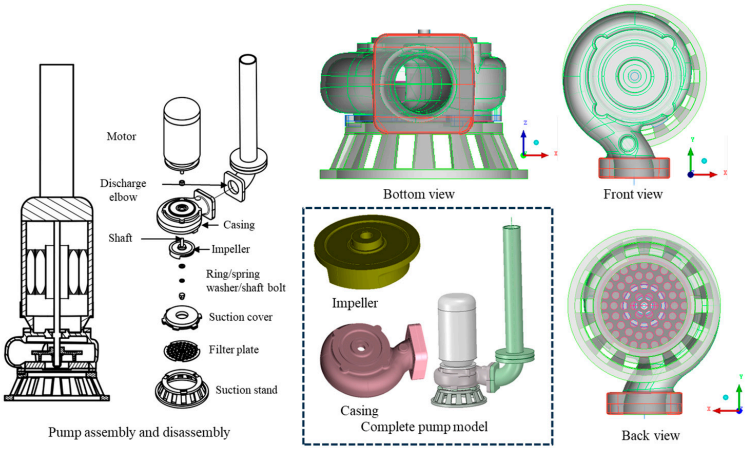

Figure 2. Assembly and disassembly drawing of the submersible drainage pump (DWE-08B) and different views.

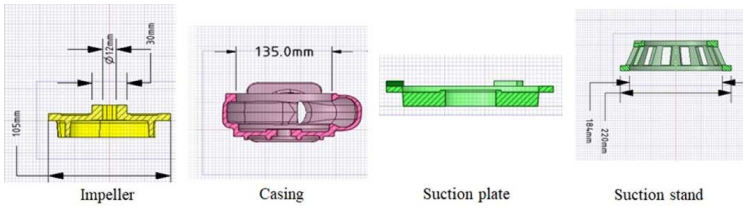

Figure 3. Cross-sectional view of the pump's key components.

Table 1. Original submersible pump model (DWE-08B) design parameters.

Description	Power	Flow Rate	Head	Impeller			Casing		
				Blades	D1	D2	Flow Path Height	Inlet Height	Outlet Dia.
Model	**H.P.**	**m^3/min**	**m**	**No.**	**mm**	**mm**	**mm**	**mm**	**mm**
DWE-08B	1	0.16	10	2	25	105	54	135	60

2.2. Specifications of the Submersible Pump

The pump company only provided the major pump specifications. Figure 4 illustrates the various pump models' performance curves. The DWE-08B model performance data are represented in the black curve with a circle and red line. Table 2 shows the submersible pump's data, as presented in the pump company's catalog [2]. Specific points of the subject pump were determined from the record. Figure 5 illustrates the hydraulic performance optimization procedure.

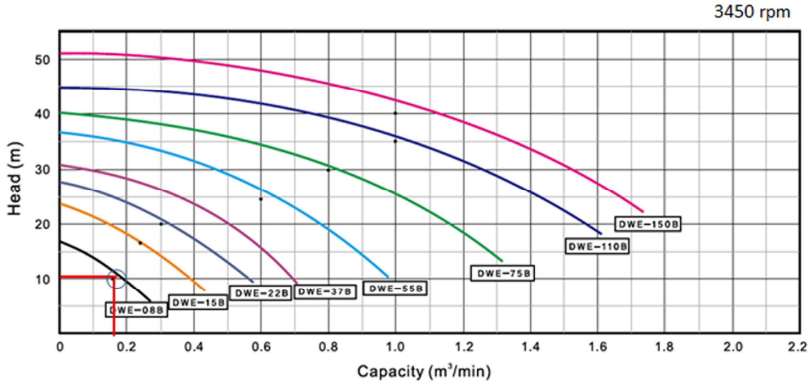

Figure 4. Hydraulic performance curve of various submersible pumps [2].

Table 2. Submersible pump performance data [2].

Model	Outlet Height (mm)	Power (H.P.)	Flow Rate (m^3/min)	Head (m)
DWE-08B	50	1	0.16	10

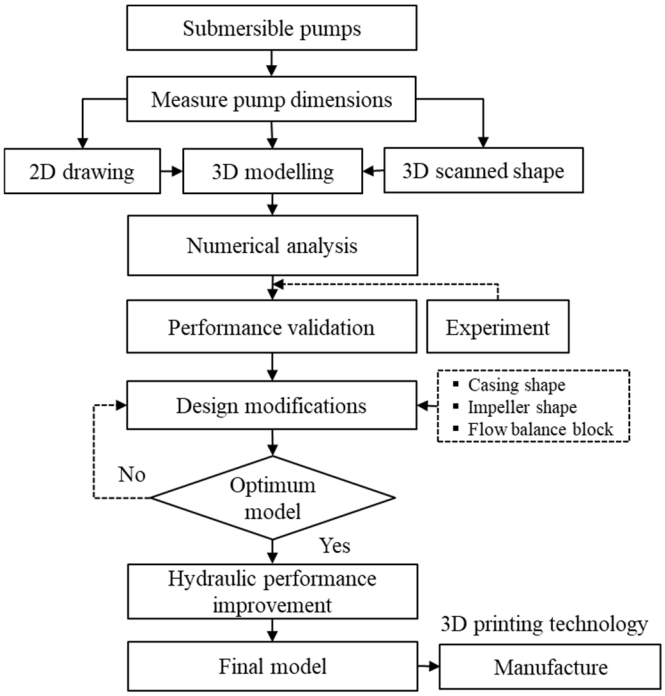

Figure 5. Procedure for hydraulic performance optimization of the submersible drainage pump.

2.3. Computational Domain and Boundary Conditions

The ANSYS ICEM-CFX commercial software (21R2, ANSYS Inc., Canonsburg, PA, USA, 2021) based on the finite volume method was utilized for grid generation and analysis of the pump. Then, unconstructed tetrahedral meshing grids were created, as shown in Figure 6. Changing the number of meshing grids confirms the grid dependency [35]. Table 3 shows the various pump meshing grids performance and relative errors. The proposed total meshed grids had 272,563 nodes and 1,374,829 elements.

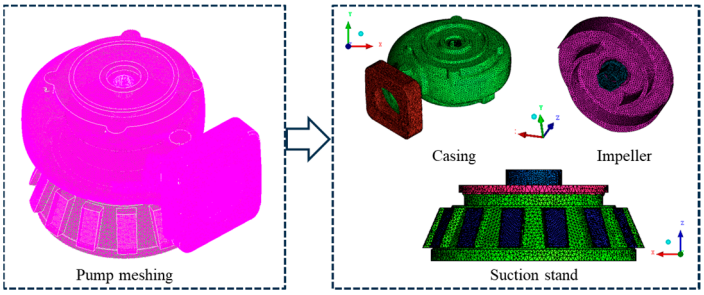

Figure 6. Submersible pump meshing grids used for computation.

Table 3. Meshing grids of the DWE-08 submersible pump.

Description	Elements	Nodes	Head (m)	Relative Error (%)
Model 1	205,962	1,241,365	9.824	-
Model 2	272,563	1,374,829	9.871	0.47842
Model 3	532,924	2,733,319	9.853	0.18235
Model 4	1,085,683	5,648,730	9.816	0.37552

To run the computer simulation, this study accounted for the Reynolds Average Navier–Stokes (RANS) equations for calculating the flow analysis of the pump [36]. The following assumptions were considered: (i) incompressible, (ii) steady-state flow and (iii) turbulence model. The fluid was assumed to be Newtonian fluid, and the thermophysical properties were constant with temperature. Under the assumptions of incompressible and steady state, the governing equations of the continuity and momentum equations (known as Navier–Stokes) are expressed as [36,37]

$$\frac{\partial u_i}{\partial x_i} = 0 \tag{1}$$

$$\rho\left(\frac{\partial u_i}{\partial t} + u_j\frac{\partial u_i}{\partial x_j}\right) = -\frac{\partial p}{\partial x_i} + \frac{\partial \tau_{ij}}{\partial x_j} + S \tag{2}$$

In the above equations, u_i represents the velocity vector, x is the component of the position vector, p is the scalar pressure, ρ is the density of the fluid, τ_{ij} designates the stress tensor, S is the source term, and i and j represent tensor notations.

To calculate the turbulent flow, eddy viscosity was added. The SST (shear stress transport turbulence) model was considered to calculate the fluid's turbulent shear stress [38,39]. The standard k-ω model was originally developed by Wilcox [38]. The k-ω-based SST model was developed by Menter [39] and can be used to effectively blend the robust and accurate formulation of the model in the near-wall region. This model is widely applicable in turbomachinery and pumps and can also predict the onset of flow separation under an adverse pressure gradient. Therefore, the SST model was chosen for the current application. Turbulent viscosity μ_t was determined by solving two-transport equations: turbulent energy k and the turbulence frequency ω. The two k-ω-based equations can be expressed as

k-equation:

$$\rho\frac{\partial k}{\partial t} + \rho u_j\frac{\partial k}{\partial x_j} = \frac{\partial}{\partial x_j}\left[\left(\mu + \frac{\mu_t}{\sigma_k}\right)\right]\frac{\partial k}{\partial x_j} + P_k - \rho\beta^* k\omega + P_{kb} \tag{3}$$

ω-equation:

$$\rho\frac{\partial \omega}{\partial t} + \rho u_j\frac{\partial \omega}{\partial x_j} = \frac{\partial}{\partial x_j}\left[\left(\mu + \frac{\mu_t}{\sigma_\omega}\right)\right]\frac{\partial \omega}{\partial x_j} + \alpha\frac{\omega}{k}P_{\ k} - \rho\beta\omega^2 + P_{\omega b} \tag{4}$$

The turbulent eddy viscosity μ_t was calculated from

$$\mu_t = \rho\frac{k}{max(\omega, S{\cdot}F_2)} \tag{5}$$

where P_{kb} and $P_{\omega b}$ are the shear production of turbulence, S is the invariant measure of the strain rate, and F_2 is a blending function that restricts the limiter to the wall boundary layer defined by

$$F_2 = tanh\left[max\left(\frac{2\sqrt{k}}{\beta^*\omega y};\ \frac{500\mu}{\rho y^2\omega}\right)\right]^2 \tag{6}$$

The first SST blending function is formulated as

$$F_1 = tanh\left[min\left\{max\left(\frac{\sqrt{k}}{\beta^*\omega y};\ \frac{500\mu}{\rho y^2\omega}\right);\ \frac{4\rho k}{CD_{k\omega}\sigma_{\omega 2}y^2}\right\}\right]^4 \tag{7}$$

where y is the distance to the nearest wall, and $CD_{k\omega}$ is the positive part of the cross-diffusion term, i.e.,

$$CD_{k\omega} = max\left(2\rho\frac{1}{\sigma_{\omega 2}\omega}\frac{\partial k}{\partial x_j}\frac{\partial \omega}{\partial x_j},\ 10^{-10}\right) \tag{8}$$

The turbulence model coefficients are given as

$$\alpha = 0.55,\ \beta = 0.075,\ \beta^* = 0.09,\ \sigma_k = 2.0,\ \sigma_\omega = 2.0$$

In this work, the boundary conditions used for the simulation were mass flow rate as the inlet and 0 Pa as the pressure outlet. All boundary walls were assumed to be smooth walls with no-slip conditions. A frozen rotor operating at a specific rotational speed of 3450 rpm was selected for steady-state, incompressible flow analysis. Figure 7 represents the boundary conditions for numerical analysis of the DWE-08 pump domain. The velocity and pressure residual value was 1×10^{-5}, controlled by convergence criteria.

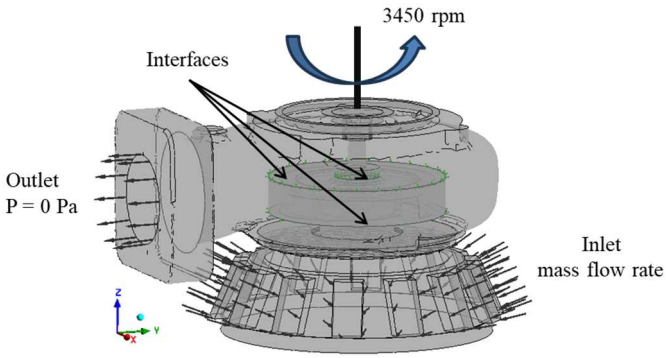

Figure 7. Boundary conditions of the computational domain.

3. Results and Discussion

Section 3.1 provides the pump performance validation of the computed data. Section 3.2 describes the performance analysis of the submersible pump under different operating conditions. Additionally, design modifications of the casing and impeller are illustrated in Section 3.3. Moreover, Section 3.4 presents the pump's hydraulic performance improvement and optimum model.

3.1. Verification of the Numerical Results

An experimental setup was constructed for comparison with the computed data to verify the reliability of the test pump that the test facility employed to meet the KSB 6321 and ISO 5198 standards [40,41]. The measurement sensors used in the test pump to obtain the test data allowed a standard deviation of ±2%. The test environmental working fluid temperature and relative humidity were 13 ± 1 °C and 32 ± 5%, respectively.

The hydraulic performance parameters such as head, volume flow rate, power and efficiency are sufficient for comparing the measured with the calculated data. The equations for pump head, energy and efficiency are expressed as

$$H = \frac{p_2 - p_1}{\rho g} + \frac{V_2^2 - V_1^2}{2g} + (z_2 - z_1) \tag{9}$$

$$P = \omega T \tag{10}$$

$$\eta = \frac{\rho g Q H}{\omega T} \tag{11}$$

where H represents the pump head in m, p is the static pressure of the pump in N/m^2, V is the velocity of the pump in m/s, z is the elevation of the pump in m, P is the shaft

power in kW, Q is the volumetric flow rate in m^3/min, ω is the rotational speed in rad/s, T is the toque in N·m, ρ is the working fluid density in kg/m^3, and g is the gravitational acceleration in m/s^2, respectively. Subscripts 1 and 2 denote the inlet and outlet sections of the pump.

Figure 8 presents the experimental measurement data tested by the KTC (Korea Testing Certification Institute) at the pump test facility center. By examining the results in Figure 8, it can be seen that when the flow-specific point (volumetric flow rate) was 0.165 m^3/min, the total head was 10 m, and the overall efficiency was only 32.14%, which was not the same as the pump efficiency. Because the test pump was in the water and could not measure the torque, the motor's power factor (0.78) must be considered in comparing it with the experimental results. In addition, the catalog's performance data, test data and analysis data were all presented for each outcome. When comparing all data, the average head error value was only 0.0456%, the power average error was only 0.0808%, and the efficiency average error was only 0.0617%. The head and efficiency differences were only 0.07% and 10.18% at the design flow rate. The lower difference was observed at the higher flow rate of the pump. The standard deviation of the pump head was 0.046%, the power was 0.0047%, and the rotational speed was 1.54%. At the 95% confidence limit, the normal distribution of the test pump was measured, revealing that the uncertainty of the pump head was H ± 0.00989 m, the discharge rate was Q ± 0.00178 m^3/min, the power was P ± 0.0102 kW, and the rotational speed was N ± 3.298 rpm.

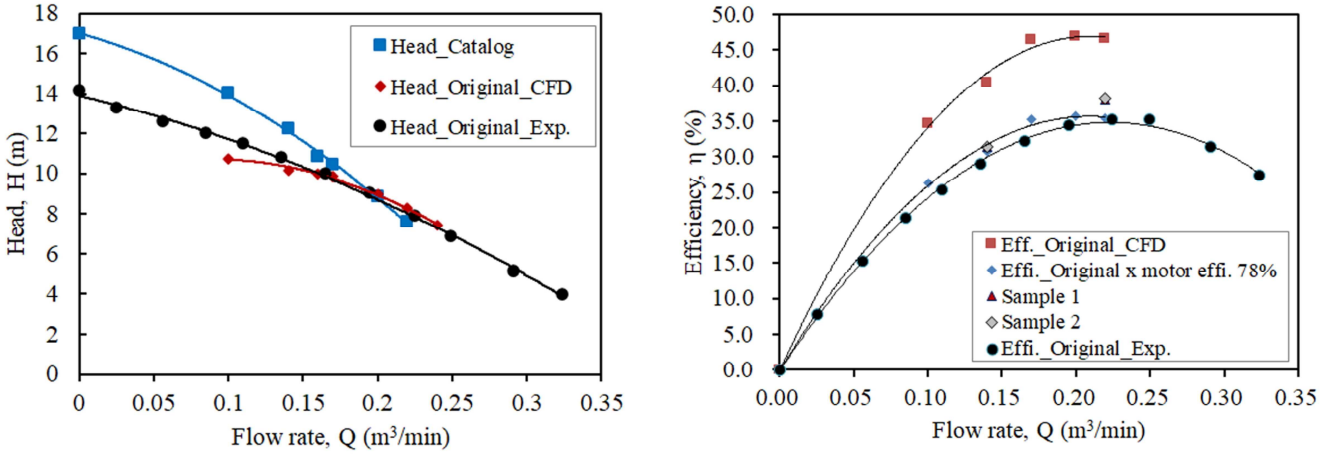

(**a**) (**b**)

Figure 8. Performance comparison between the experiment and computational results for the submersible pump: (**a**) head vs. flow rate and (**b**) efficiency vs. flow rate (experimental uncertainty in N ± 3.298 rpm, Q ± 0.00178 m^3/min, H ± 0.0989 m and P ± 0.0102 kW).

First, looking at Figure 8a, there is a clear difference between the test and catalog results. As observed from the H-Q curve, the analysis results agree relatively well with the experimental data, except for the low flow rate. The two results do not match well in the low-flow region due to the influence of the grid and y+. Therefore, we decided it would be best to exclude or modify the catalog data. In comparing this with the test value, it was found that the test results are well matched when considering the motor power factor of 0.78, as mentioned in the shaft power report. The values of Samples 1 and 2 in Figure 8b are the efficiencies mentioned in the high-efficiency energy equipment report. Moreover, in this study, the mechanical losses of the submersible pump were not taken into consideration in the numerical analysis.

3.2. Performance Analysis

Additionally, this study analyzed the flow pattern inside the pump and velocity distributions at the design flow rate. Figure 9 shows the velocity vectors and velocity

streamline distribution of the pump. As can be observed, the flow recirculates in the pump discharge region, where the energy dissipates, resulting in significant pump losses. The flow separation in the casing caused relatively large vortices at the outlet of the pump casing. Also, the clearance gap between the pump volute and impeller was large (more than 2 mm). This clearance gap flow creates vortices that separate from the impeller blade and reduce local pressure. Also, the impeller was located in the casing at the bottom of the pump, as shown in Figure 10. Henceforth, changing the impeller's center further reduced the pump's efficiency. Therefore, a CFD-based design modification study and research analyzing the behavior of the flow in various geometries are needed to enhance pump performance.

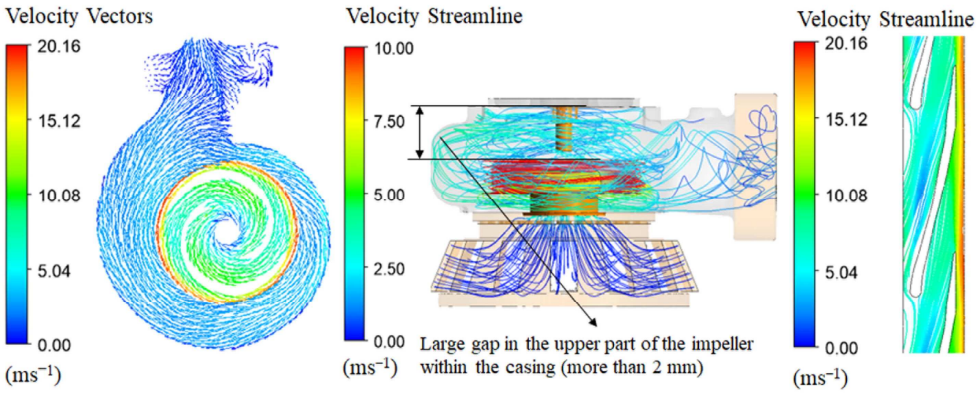

Figure 9. Velocity distributions analysis inside the casing: (**a**) velocity vectors; (**b**) velocity streamlines; (**c**) blade-to-blade velocity streamlines.

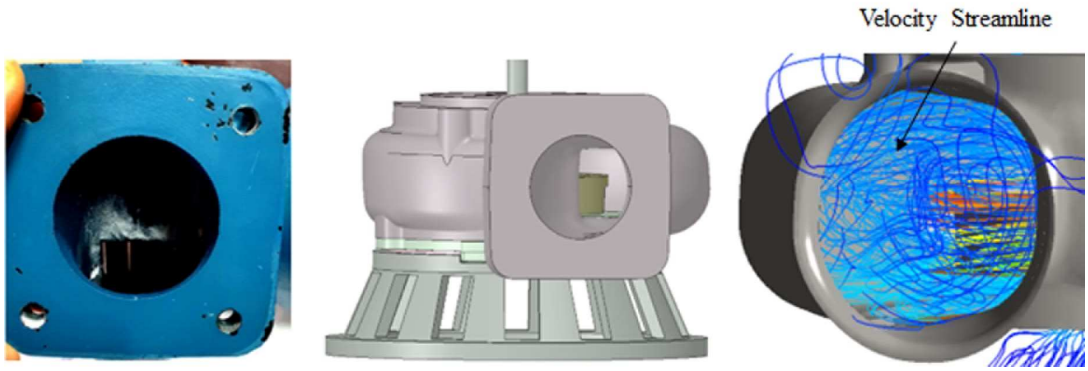

Figure 10. The position of the impeller inside the casing of the pump.

Based on the experimental and simulation results, we determined that there is a possibility of increasing efficiency by using an efficient pump motor and designing or shaping the part where the loss occurs. The use of an efficient pump motor was outside the scope of this study; this study examined the cause of the decrease in efficiency and found a way to supplement the design of the pump components. It was noted from the loss analysis of the pump that the mechanical loss, the ratio of impeller loss to casing, and inlet loss were also high [42]. The efficiency of the DWE-08B pump ranged from 30% to 40%, which is not an optimal performance condition. Of course, since the impeller was a semi-open type, it was less efficient than the closed type, but its efficiency was comparatively low compared with other pumps. Therefore, this study considered improving the efficiency to create the optimal design of the impeller and casing, suggesting improvements in the geometry of the two components.

3.3. Design Modifications of the Casing and Impeller

In this study, two shapes that can reduce the large gap in the upper region of the pump impeller were proposed and analyzed to optimize the shape of the casing. Model 1 was created with a reduced flow path compared with the original model; model 2 was created with a cochlear (tubular) flow passage in the intact casing. Figure 11 shows the casing shape change model.

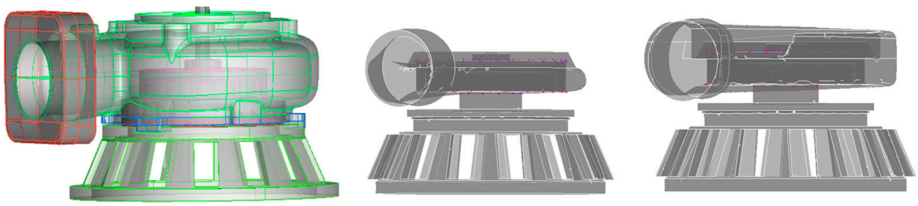

(a) Original model (b) Model 1 (c) Model 2

Figure 11. Casing shape change model: (**a**) original model; (**b**) model 1 (**c**) model 2.

Figure 12 displays the comparison of velocity streamlines for the casing shape change model. As shown in Figure 12, the fluid flow formed a streamlined shape, eliminating the idle space at the top; the fluid flow at the outlet of the pump casing was discharged without swirling using a guide rib. Figure 13 shows the performance comparison for the casing shape change model. Table 4 presents the pump efficiency of the casing shape change models. By changing the casing shape, the relative efficiency was improved by up to 4~5%.

However, it is difficult to make a new one with die and casting; therefore, an in-depth investigation is a prerequisite for optimization. We applied the optimization plan of the casing shape to prevent the need for wood-shaped and casting work. One method involves attaching a simple installable member to the pump casing to reduce the space. Optimizing the casing shape utilizes an approach of changing the casing shape using a flow balance block (FBB), which can be easily installed. Here, we employed an FBB instead of the casing shape change model. Figure 14 shows the flow balance block model. We utilized an FBB to reduce secondary and friction losses where the flow in the casing was stagnant.

Table 4. Comparison of pump efficiency for casing shape change model.

Flow Rate (m^3/min)	Original (%)	Model 1 (%)	Model 2 (%)	Efficiency Improvement (%)	
				Model 1	Model 2
0.10	34.593	40.542	38.904	5.949	4.311
0.14	40.420	48.358	45.474	7.938	5.054
0.16	45.415	50.687	49.230	5.272	3.815
0.17	46.375	51.513	49.301	5.138	2.926
0.20	46.921	52.826	52.357	5.905	5.436
0.22	46.562	53.487	52.221	6.925	5.659

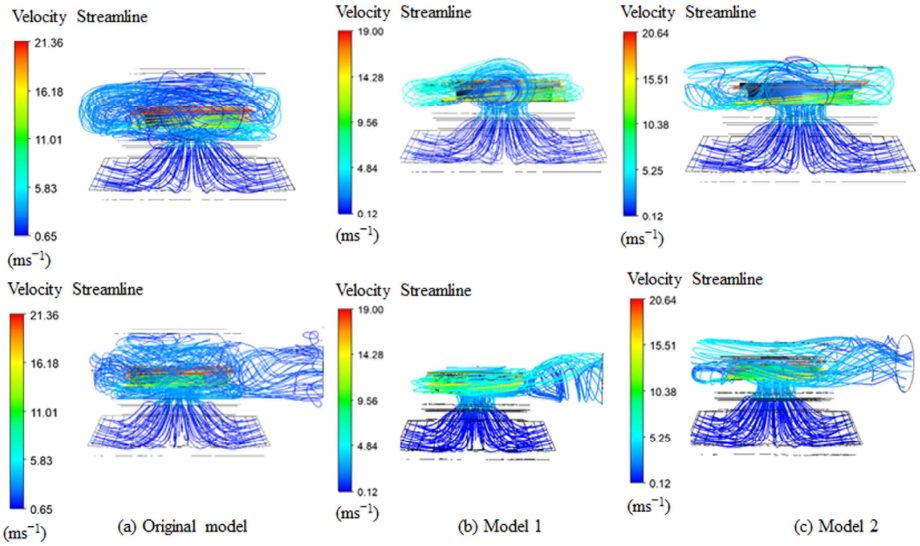

Figure 12. Velocity streamline comparison for shape change model: (**a**) original model; (**b**) model 1; (**c**) model 2.

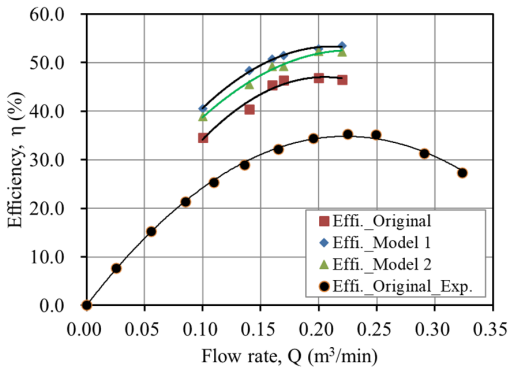

Figure 13. Performance comparison for casing shape change model.

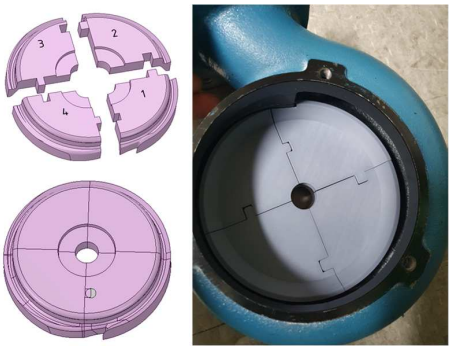

Figure 14. Flow balance block model.

Also, we modified the three different shapes of the impeller. Impeller 1's vanes were created diagonal (oblique line) in the basic model. Impeller 2 had an extended tip compared with Impeller model 1. Impeller model 3's vanes were thicker compared with the vanes of the basic model. Figure 15 shows the impeller shape change model. The impeller shape change involved inclining the vane to improve the flow in front of the rear shroud. These pump simulation data were compared to assess the performance characteristics of the different impeller shapes to improve the efficiency of the original model.

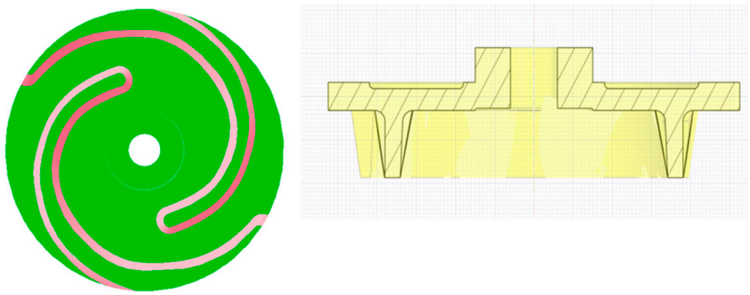

Figure 15. Impeller shape model 1.

Furthermore, Figure 16 illustrates the pressure and velocity streamline distribution in other planes of the pump impeller. As observed, the flow losses could be reduced by improving the streamline in the lower area (planes 1, 2) via a change in the impeller shape. Figure 17 shows the performance comparison of various impeller shape change models. The result shows that changing the shape of the impeller increased the pump efficiency. Hence, changing the impeller shape reduces the shaft power and increases the efficiency to 5.56% by preventing flow disturbance. Therefore, this study found the impeller shape change model 1 optimal for manufacturing.

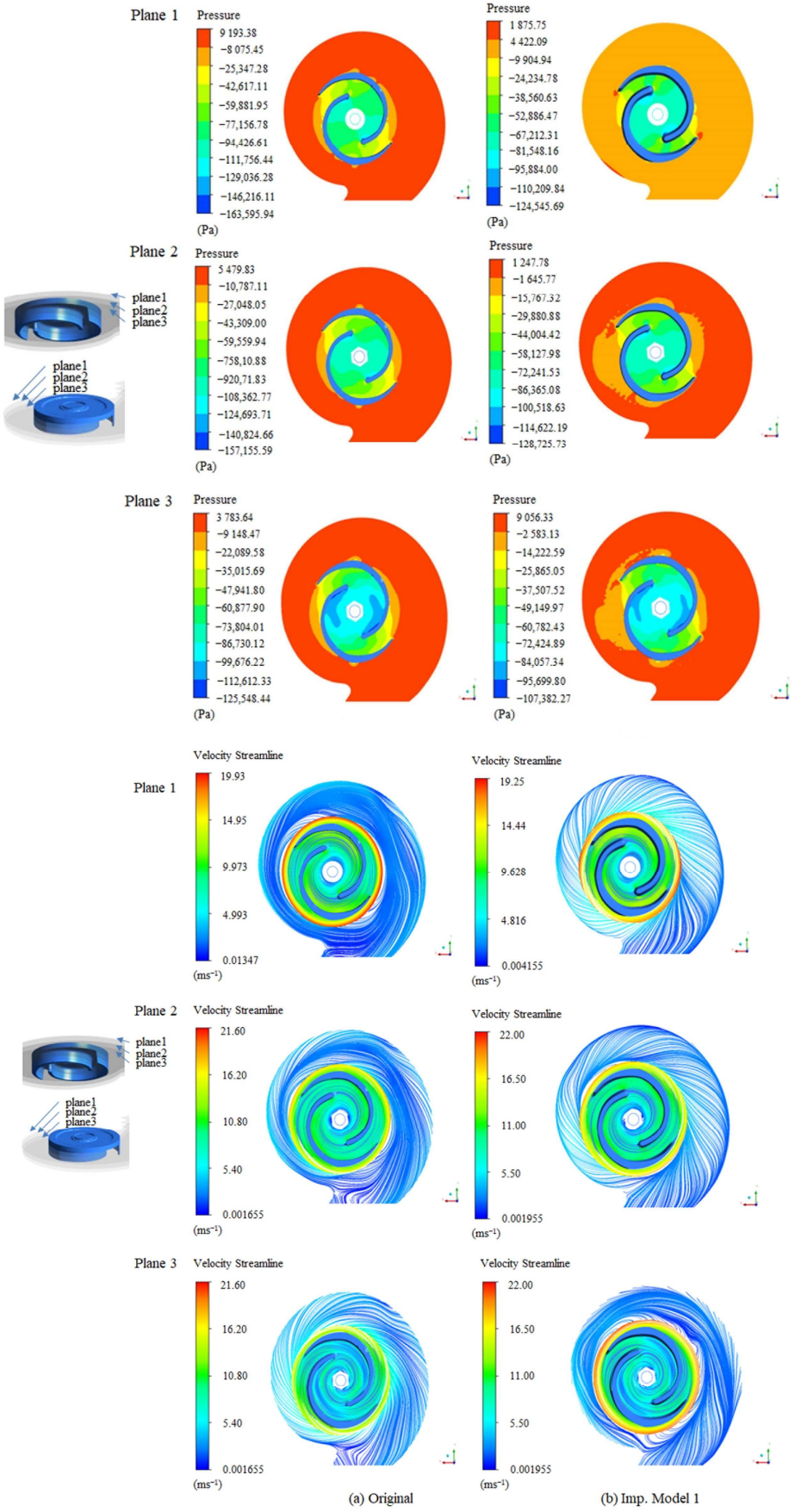

Figure 16. Pressure and velocity streamline distribution in different planes: (**a**) original impeller; (**b**) impeller model 1.

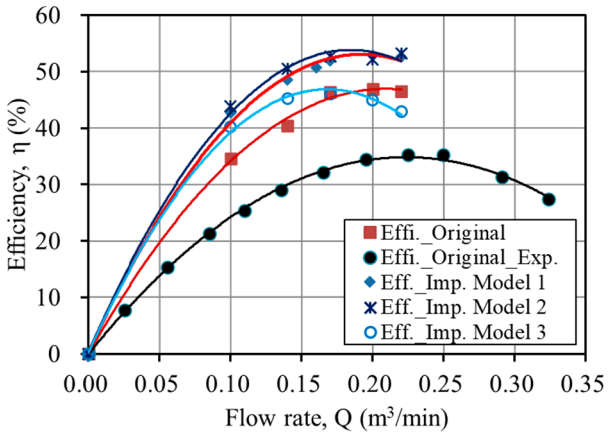

Figure 17. Performance comparison of impeller shape change models.

3.4. Optimum Model

The existing model's performance analysis and modification of the casing and impeller were reviewed. This study examined the flow around the impeller of the current model and devised a strategy to increase efficiency. The pump efficiency was significantly increased to 49.30%, less than 2.64% of that of the modified impeller, by modifying the casing shape at a 0.17 m^3/min flow rate. Also, changing the impeller shape of the pump enhanced the internal pressure distribution and reduced the flow separation at the discharge side and its efficiency. The design flow rate of the pump was shifted from 0.16 m^3/min to 0.17 m^3/min.

Moreover, the efficiency increased to 5.56% at 0.17 m^3/min, and the average efficiency increased to 6.27%. It is understood that changing the shape of the impeller and casing is the best solution to improving a pump's performance [43]. Figure 18 shows the cross-sectional view of the original and newly designed impellers. Therefore, impeller shape change model 1 was considered optimal for manufacture.

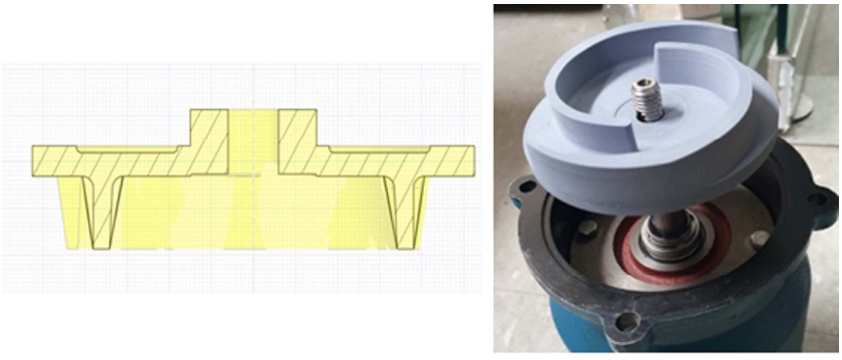

Figure 18. Cross-sectional view of the optimum model: (**a**) impeller model 1; (**b**) manufactured model.

4. Conclusions

Hydraulic performance optimization in a submersible pump was performed. A new pump impeller and flow balance block were designed, computational simulation was performed, parts were manufactured, and experiments were conducted. The results of this study on performance improvement are summarized as follows:

(a) The test data verified the computed results, confirming the pump's performance.
(b) We modified the casing and impeller shape to improve hydraulic performance and used a flow balance block to reduce the inner space of the pump.
(c) Changing the impeller shape reduced the power and increased efficiency, which can prevent flow disturbance. The attachment of the flow balance block increased the efficiency in the flow area more significantly than the operating point.

(d) The flow separation inside the pump was significantly improved and increased pump performance by up to 5.56% at the design flow rate.
(e) This research obtained two Korean patents based on the identified performance improvement results.
(f) Further studies should consider conducting a performance test for the shape change model for a submersible pump.

5. Patents

Impeller for submersible pump (patent no.: 20-2021-0001433) and centrifugal submersible pump (patent no.: 10-2021-0058374). http://engpat.kipris.or.kr/engpat/searchLogina.do?next=MainSearch (17 November 2023).

Author Contributions: M.R. conceived and designed the study, analyzed the results, wrote the paper and edited the draft; S.-H.S. contributed to project administration and conceptualization and supervised the work; H.-W.R. managed resources, conducted the experiment and edited the draft; K.H.S. contributed to fund acquisitions and resources for the work; K.C.S. contributed to the experiment; and L.Z. advised on project work. All authors have read and agreed to the published version of the manuscript.

Funding: This research was funded by the Daeyoung Power Pump Co., Ltd., for the promotion of science.

Data Availability Statement: The study did not report any data.

Acknowledgments: This research was supported by Daeyoung Power Pump.

Conflicts of Interest: The authors declare no conflicts of interest.

References

1. Dabade, S.P.; Gajendragadkar, J. Design, Modelling and CFD Analysis of Submersible Vertical Turbine Pump (Polder Pump). In Proceedings of the National Conference on Recent Trends in Mechanical Engineering, Sangli, India, 28–29 April 2016.
2. Daeyoung Power Pump Catalog (DWE-Submersible Pump), Daeyoung Power Pump Co., Ltd., Korea. Available online: http://www.dypump.co.kr/eng/sub02/view.php?id=95&ca_id=50&page= (accessed on 8 May 2023).
3. Takacs, G. *Electrical Submersible Pumps Manual: Design, Operations and Maintenance*; Gulf Professional Publishing: Burlington, MA, USA, 2009; ISBN 9781856175579.
4. Suh, S.-H.; Rakibuzzaman; Kim, K.-W.; Kim, H.-H.; Yoon, I.S.; Cho, M.-T. A Study on Energy Saving Rate for Variable Speed Condition of Multistage Centrifugal Pump. *J. Therm. Sci.* **2015**, *24*, 566–573. [CrossRef]
5. Kaya, D.; Yagmur, E.A.; Yigit, K.S.; Kilic, F.C.; Eren, A.S.; Celik, C. Energy Efficiency in Pumps. *Energy Convers. Manag.* **2008**, *49*, 1662–1673. [CrossRef]
6. Goto, A.; Nohmi, M.; Sakurai, T.; Sogawa, Y. Hydrodynamic Design System for Pumps Based on 3-D CAD, CFD, and Inverse Design Method. *J. Fluids Eng. Trans. ASME* **2002**, *124*, 329–335. [CrossRef]
7. Parrondo-Gayo, J.L.; González-Pérez, J.; Fernández-Francos, J. The Effect of the Operating Point on the Pressure Fluctuations at the Blade Passage Frequency in the Volute of a Centrifugal Pump. *J. Fluids Eng. Trans. ASME* **2002**, *124*, 784–790. [CrossRef]
8. Shi, W.-D.; Lu, W.-G.; Wang, H.-L.; Li, Q.-F. Research on the Theory and Design Methods of the New Type Submersible Pump for Deep Well. In Proceedings of the ASME 2009 Fluids Engineering Division Summer Meeting, Vail, CO, USA, 2–6 August 2009; pp. 1–7.
9. Zhu, J.; Zhang, J.; Zhu, H.; Zhang, H.Q. A Mechanistic Model to Predict Flow Pattern Transitions in Electrical Submersible Pump under Gassy Flow Condition. In Proceedings of the SPE Artificial Lift Conference and Exhibition—Americas, The Woodlands, TX, USA, 28–30 August 2018. [CrossRef]
10. Manivannan, A. Computational Fluid Dynamics Analysis of a Mixed Flow Pump Impeller. *Int. J. Eng. Sci. Technol.* **2011**, *2*, 200–206. [CrossRef]
11. Ragoth Singh, R.; Nataraj, M. Parametric Study and Optimization of Pump Impeller by Varying the Design Parameter Using Computational Fluid Dynamics. *Int. Rev. Mech. Eng.* **2012**, *6*, 1581–1585.
12. Ajay, A.J.; Stephen, S.E.A.; Smart, D.S.R. Shape Optimization of Submersible Pump Impeller Design. In Proceedings of the 2017 First International Conference on Recent Advances in Aerospace Engineering (ICRAAE), Coimbatore, India, 3–4 March 2017; Volume 8, pp. 56–69. [CrossRef]
13. Zangeneh, M.; Goto, A.; Takemura, T. Suppression of Secondary Flows in a Mixed-Flow Pump Impeller by Application of Three-Dimensional Inverse Design Method: Part 1-Design and Numerical Validation. *ASME J. Turbomach.* **1996**, *118*, 536–543. [CrossRef]

14. Goto, A.; Takemura, T.; Zangeneh, M. Suppression of Secondary Flows in a Mixed-Flow Pump Impeller by Application of 3d Inverse Design Method: Part 2-Experimental Validation. In Proceedings of the ASME 1994 International Gas Turbine and Aeroengine Congress and Exposition, The Hague, Netherlands, 13–16 June 1994; Volume 1, pp. 536–543. [CrossRef]
15. Kim, S.; Lee, K.Y.; Kim, J.H.; Choi, Y.S. A Numerical Study on the Improvement of Suction Performance and Hydraulic Efficiency for a Mixed-Flow Pump Impeller. *Math. Probl. Eng.* **2014**, *2014*, 269483. [CrossRef]
16. Kim, S.; Kim, Y.I.; Kim, J.H.; Choi, Y.S. Design Optimization for Mixed-Flow Pump Impeller by Improved Suction Performance and Efficiency with Variables of Specific Speeds. *J. Mech. Sci. Technol.* **2020**, *34*, 2377–2389. [CrossRef]
17. Yan, P.; Chu, N.; Wu, D.; Cao, L.; Yang, S.; Wu, P. Computational Fluid Dynamics- Based Pump Redesign to Improve Efficiency and Decrease Unsteady Radial Forces. *J. Fluids Eng. Trans. ASME* **2017**, *139*, 011101. [CrossRef]
18. Baun, D.O.; Flack, R.D. Effects of Volute Design and Number of Impeller Blades on Lateral Impeller Forces and Hydraulic Performance. *Int. J. Rotating Mach.* **2003**, *9*, 145–152. [CrossRef]
19. Wu, D.; Yan, P.; Chen, X.; Wu, P.; Yang, S. Effect of Trailing-Edge Modification of a Mixed-Flow Pump. *J. Fluids Eng. Trans. ASME* **2015**, *137*, 101205. [CrossRef]
20. Qian, C.; Luo, X.; Yang, C.; Wang, B. Multistage Pump Axial Force Control and Hydraulic Performance Optimization Based on Response Surface Methodology. *J. Brazilian Soc. Mech. Sci. Eng.* **2021**, *43*, 136. [CrossRef]
21. Liu, Z.M.; Gao, X.G.; Pan, Y.; Jiang, B. Multi-Objective Parameter Optimization of Submersible Well Pumps Based on RBF Neural Network and Particle Swarm Optimization. *Appl. Sci.* **2023**, *13*, 8772. [CrossRef]
22. Bai, L.; Yang, Y.; Zhou, L.; Li, Y.; Xiao, Y.; Shi, W. Optimal Design and Performance Improvement of an Electric Submersible Pump Impeller Based on Taguchi Approach. *Energy* **2022**, *252*, 124032. [CrossRef]
23. Chen, J.; Wang, M.; Bao, Y.; Chen, X.; Xia, H. Mixed-Flow Pump Performance Improvement Based on Circulation Method. *Front. Energy Res.* **2023**, *11*, 1177437. [CrossRef]
24. Suh, J.W.; Yang, H.M.; Kim, Y.I.; Lee, K.Y.; Kim, J.H.; Joo, W.G.; Choi, Y.S. Multi-Objective Optimization of a High Efficiency and Suction Performance for Mixed-Flow Pump Impeller. *Eng. Appl. Comput. Fluid Mech.* **2019**, *13*, 744–762. [CrossRef]
25. Jeon, S.Y.; Kim, C.K.; Lee, S.M.; Yoon, J.Y.; Jang, C.M. Performance Enhancement of a Pump Impeller Using Optimal Design Method. *J. Therm. Sci.* **2017**, *26*, 119–124. [CrossRef]
26. Siddique, H.; Mrinal, K.R.; Samad, A. Optimization of a Centrifugal Pump Impeller by Controlling Blade Profile Parameters. In Proceedings of the ASME Turbo Expo 2016: Turbomachinery Technical Conference and Exposition, Seoul, South Korea, 13–17 June 2016; American Society of Mechanical Engineers: Seoul, South Korea, 2016; pp. 1–8.
27. Shim, H.S.; Kim, K.Y.; Choi, Y.S. Three-Objective Optimization of a Centrifugal Pump to Reduce Flow Recirculation and Cavitation. *J. Fluids Eng. Trans. ASME* **2018**, *140*, 091202. [CrossRef]
28. Yang, Y.; Zhou, L.; Hang, J.; Du, D.; Shi, W.; He, Z. Energy Characteristics and Optimal Design of Diffuser Meridian in an Electrical Submersible Pump. *Renew. Energy* **2021**, *167*, 718–727. [CrossRef]
29. Arocena, V.M.; Abuan, B.E.; Reyes, J.G.T.; Rodgers, P.L.; Danao, L.A.M. Numerical Investigation of the Performance of a Submersible Pump: Prediction of Recirculation, Vortex Formation, and Swirl Resulting from off-Design Operating Conditions. *Energies* **2021**, *14*, 5082. [CrossRef]
30. Wei, Y.; Yang, Y.; Zhou, L.; Jiang, L.; Shi, W.; Huang, G. Influence of Impeller Gap Drainage Width on the Performance of Low Specific Speed Centrifugal Pump. *J. Mar. Sci. Eng.* **2021**, *9*, 106. [CrossRef]
31. Han, C.; Liu, J.; Yang, Y.; Chen, X. Influence of Blade Exit Angle on the Performance and Internal Flow Pattern of a High-Speed Electric Submersible Pump. *Water* **2023**, *15*, 2774. [CrossRef]
32. Tong, Z.; Yuan, Y.; Zhang, C.; Zhang, Z.; Zhang, Y. Performance Analysis and Experimental Verification of Hydraulic Driven Axial Flow Pumps. *J. Mech. Sci. Technol.* **2023**, *37*, 2941–2947. [CrossRef]
33. Fakher, S.; Khlaifat, A.; Nameer, H. Improving Electric Submersible Pumps Efficiency and Mean Time between Failure Using Permanent Magnet Motor. *Upstream Oil Gas Technol.* **2022**, *9*, 100074. [CrossRef]
34. Zhu, J.; Zhu, H.; Zhang, J.; Zhang, H.Q. A Numerical Study on Flow Patterns inside an Electrical Submersible Pump (ESP) and Comparison with Visualization Experiments. *J. Pet. Sci. Eng.* **2019**, *173*, 339–350. [CrossRef]
35. Kim, H.-H.; Rakibuzzaman, M.; Kim, K.; Suh, S.-H. Flow and Fast Fourier Transform Analyses for Tip Clearance Effect in an Operating Kaplan Turbine. *Energies* **2019**, *12*, 264. [CrossRef]
36. Ansys Inc. *ANSYS-CFX (CFX Introduction, CFX Reference Guide, CFX Tutorials, CFX-Pre User's Guide, CFX-Solver Manager User's Guide, Theory Guide), Release 21.00R2, USA 2021*; Ansys Inc.: Bloomington, MN, USA, 2021.
37. Anderson, D.A.; Tannehill, J.C.; Pletcher, R.H. *Computational Fluid Mechanics and Heat Transfer*; Taylor & Francis: Washington DC, USA, 1984.
38. David, C. *Wilcox Turbulence Modeling for CFD*, 1st ed.; DCW Industries, Inc.: La Cañada Flintridge, CA, USA, 1994.
39. Menter, F.R. Two-Equation Eddy-Viscosity Turbulence Models for Engineering Applications. *AIAA J.* **1994**, *32*, 1598–1605. [CrossRef]
40. *KS B 6301*; Testing Methods for Centrifugal Pumps, Mixed Flow Pumps and Axial Flow Pumps, National Standard. Korean Standards Association: Seoul, Korea, 2015.
41. *ISO 5198*; Centrifugal, Mixed Flow and Axial Pumps-Code for Hydraulic Performance Tests-Precision Class. International Standard: Geneva, Switzerland, 1987.

42. Douglas, J.F.; Gasiorek, J.; Swaffield, J. *Fluid Mechanics*, 4th ed.; Prantise Hall: Upper Saddle River, NJ, USA, 2001.
43. Rakibuzzaman, M.; Suh, S.H.; Kim, H.H.; Ryu, Y.; Kim, K.Y. Development of a Hydropower Turbine Using Seawater from a Fish Farm. *Processes* **2021**, *9*, 266. [CrossRef]

computation

MDPI

Article

Numerical Method for Predicting Transient Aerodynamic Heating in Hemispherical Domes

Arif Cem Gözükara [1,*] and Uygar Ateş Ceylan [2]

[1] Aselsan Inc. MGEO Business Sector, Ankara 06750, Turkey
[2] Atlas Copco Airpower NV, Boomsesteenweg 957, 2610 Antwerp, Belgium; uygarates.ceylan@atlascopco.com
* Correspondence: cgozukar@aselsan.com

Abstract: In this research, a streamlined numerical approach designed for the quick estimation of temperature profiles across the finite thickness of a hemispherical dome subjected to aerodynamic heating is introduced. Hemispherical domes, with their advantageous aerodynamic, structural, and optical properties, are frequently utilized in the front sections of objects traveling at supersonic velocities, including missiles or vehicles. The proposed method relies on one-dimensional analyses of fluid dynamics and flow characteristics to approximate the local heat flux across the exterior surface of the dome. By calculating these local heat flux values, it is also possible to predict the temperature variations within the thickness of the dome by employing the finite difference technique, to solve the heat conduction equation in spherical coordinates. This process is iterated over successive time intervals, to simulate the entire flight duration. Unlike traditional Computational Fluid Dynamics (CFD) simulations, the proposed strategy offers the benefits of significantly lower computational time and resource demands. The primary objective of this work is to provide an efficient numerical tool for evaluating aerodynamic heating impact and temperature gradients on hemispherical domes under specific conditions. The effectiveness of the proposed method will be validated by comparing the temperature profiles derived for a standard flight scenario against those obtained from 2-D axisymmetric transient CFD simulations performed using ANSYS-Fluent 2022 R2.

Keywords: aerodynamic heating; numerical method; hemispherical dome

Citation: Gözükara, A.C.; Ceylan, U.A. Numerical Method for Predicting Transient Aerodynamic Heating in Hemispherical Domes. *Computation* **2024**, *12*, 162. https://doi.org/10.3390/computation12080162

Academic Editors: Ali Cemal Benim, Abdulmajeed A. Mohamad, Sang-Ho Suh, Rachid Bennacer, Paweł Oclon and Jan Taler

Received: 19 June 2024
Revised: 29 July 2024
Accepted: 3 August 2024
Published: 12 August 2024

1. Introduction

In this section, the problem of aerodynamic heating will be introduced. The motivation behind focusing on the hemispherical nose shape for the investigation will be explained. In addition, the proposed numerical method will be presented, in terms of its advantageous features compared to existing Computational Fluid Dynamics (CFD) simulations.

1.1. Motivation

The phenomenon known as aerodynamic heating occurs when a body is subjected to high-speed airflows, causing it to heat up due to the conversion of kinetic energy into heat as a result of compression and friction. This heat is then transferred to the body through the boundary layer. This subject has been of significant importance in the design of high-speed vehicles for over 70 years, with studies demonstrating that bodies with blunted nose shapes undergo lower rates of heat transfer compared to those with sharper nose shapes [1–5]. Among these shapes, the hemispherical nose is of particular interest, due to its beneficial properties, in terms of aerodynamics, mechanics, and optics when exposed to high-speed flows. This design is notably utilized in external stores and missiles, serving various functions, such as window, optical path lens, or radome [6–8].

In supersonic flight, aerodynamic heating becomes particularly pronounced, especially near the stagnation point, at which heat generation is primarily due to the direct

compression of air. Along the sides of the missile or vehicle, viscous forces in the boundary layer are the dominant source of heat generation. This effect is not only a structural concern but also affects the performance of optical systems, as the thermal characteristics of materials, including the optical components and the dome, change during flight. This transient behavior can degrade the optical system's performance, making precise thermal management crucial [9,10].

The exploration of aerodynamic heating began with experimental and theoretical studies in the 1950s and 60s, later evolving to include numerical simulations with the advent of computation technology, leading to the development of various in-house codes. These codes have incorporated advanced methodologies, such as the axisymmetric analogue, Lees' formulations, and DeJarnette, and Davis's approximate techniques for streamline distribution [10,11]. Industry codes like HABP [12], MINIVER [13], AEROHEAT [14], INCHES [15], CBAERO [16], and HATLAP [17] have enhanced the fidelity of calculations for surface streamlines, pressure, and heating formulations, often comparing favorably with more complex simulations, such as viscous shock layer models and comprehensive CFD simulations. Notably, AEROHEAT includes a unique equivalent boundary layer method that involves a direct solution of a boundary layer specific to each streamline [10]. While these in-house codes offer deep insights and precision, their varied methodologies and restricted availability have limited their widespread usage in broader research and industrial contexts [18,19].

Recent advancements in commercial CFD tools have enabled the simulation of aerodynamic heating more accurately with high fidelity. However, most high-speed missiles have a relatively short flight time, and simulating them with conventional CFD tools remains challenging, due to the transient nature of heat transfer [9]. This work introduces a streamlined numerical approach that aims to bridge the gap between accuracy, efficiency, and availability for specific cases and conditions that will be discussed in detail. Unlike prior studies that have focused on either detailed CFD simulations or specific industrial contexts with limited availability, the proposed method utilizes an open source, one-dimensional approach for rapid predictions, tailored for real-time applications in the conceptual design of high-speed missiles. This study stands out by combining the practicality of quick estimations with a level of precision that approaches more elaborate methods, making it a useful tool for preliminary design assessments where resource constraints are significant. The proposed method, akin to other specialized in-house codes, has its set of limitations and advantages, which will be further discussed in this paper.

1.2. Advantages of the Developed Methodology

The primary benefit of this technique lies in its efficiency, offering significant time savings compared to simulations performed by widespread commercial CFD tools. This new approach allows for quick approximations of aerothermal heating and temperature variations across the dome, achieving reasonable accuracy in a fraction of the time required by conventional finite volume- or finite element-based solvers. Employing this numerical tool, particularly during the initial phases of design, enables the prediction of aerodynamic heating effects on hemispherical structures with an acceptable level of accuracy. The adoption of this technique accelerates the evaluation process for such thermal conditions, thereby reducing the interval between successive design modifications. A thorough and stable simulation of a missile's complete flight, which would conventionally take several days to compute using conventional finite volume- or finite element-based solvers (excluding time spent on pre- and post-processing), could see a dramatic reduction in the required computational time, contingent upon the missile's total flight duration and the specific flight scenario involved. The current study is focused and specific to hemispherical dome geometry. One of its main advantages, compared to similar algorithms [9,20], can be referred to as the calculation of local heat flux and temperature distribution in a stagnation region and its vicinity by using a specific semi-empirical correlation tailored for hemispheres.

2. Methodology

In this part, the proposed methodology will be detailed alongside the constraints specific to this approach. Following this, the outcomes derived from these computations will be presented, in comparison with the results from standard CFD simulations. For these comparisons, the results from transient finite-volume CFD simulations are employed since experimental results related to aerodynamic heating of finite-thickness hemispheres in the literature are of limited availability. Further sections will investigate the details of the CFD model employed for these comparative analyses. A hypothetical flight scenario is adapted within this study, to evaluate the efficacy of the proposed method developed. The profile of the Mach number applied is described as follows:

$$M_\infty(t) = \begin{cases} 0.219t^{1.2} & \text{for } t \leq 9.0, \\ 7.4911e^{-0.1t} & \text{for } t > 9.0, \end{cases} \tag{1}$$

where $M_\infty(t)$ is the freestream Mach number at time t, and t is the time variable in seconds.

Similarly, the altitude change is defined by

$$h(t) = 3.1411t^2 + 93.744t, \tag{2}$$

where $h(t)$ is the altitude at time t.

In order to determine the freestream flow conditions at the flight altitude, Equations (1) and (2) are used together with the 1976 U.S. Standard Atmosphere data [21]. Figure 1 shows the profile of both the Mach number and the altitude as a function of time:

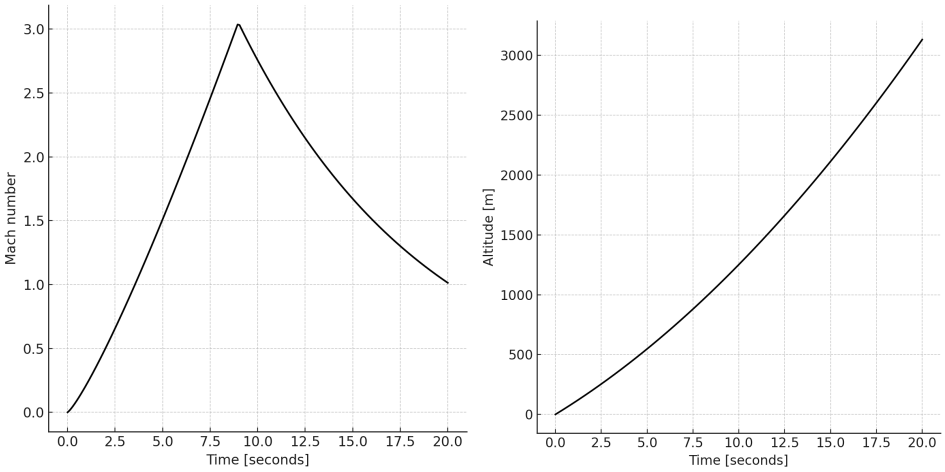

(**a**) (**b**)

Figure 1. The Mach number (**a**) and altitude (**b**) profiles that summarize the flight scenario.

The proposed methodology's first step is calculating the local flow and fluid properties at the outer edge of the boundary layer around the hemispherical dome. The second step is calculating the local heat transfer coefficient values by utilizing the flow properties and the correlation proposed by Beckwith and Gallagher [1]. In the third step, using local heat transfer coefficients and flow properties, the heat conduction within the shell of the hemispherical dome is solved by the finite difference method, to obtain the temperature distribution. These steps are repeated in a time-iterative manner, to simulate the full flight. The calculation procedure involves the determination of the heat transfer coefficient at the current time step by using the dome surface temperature distribution obtained from the previous time step and the flow properties calculated at the current time step. This calculation structure is summarized in Figure 2:

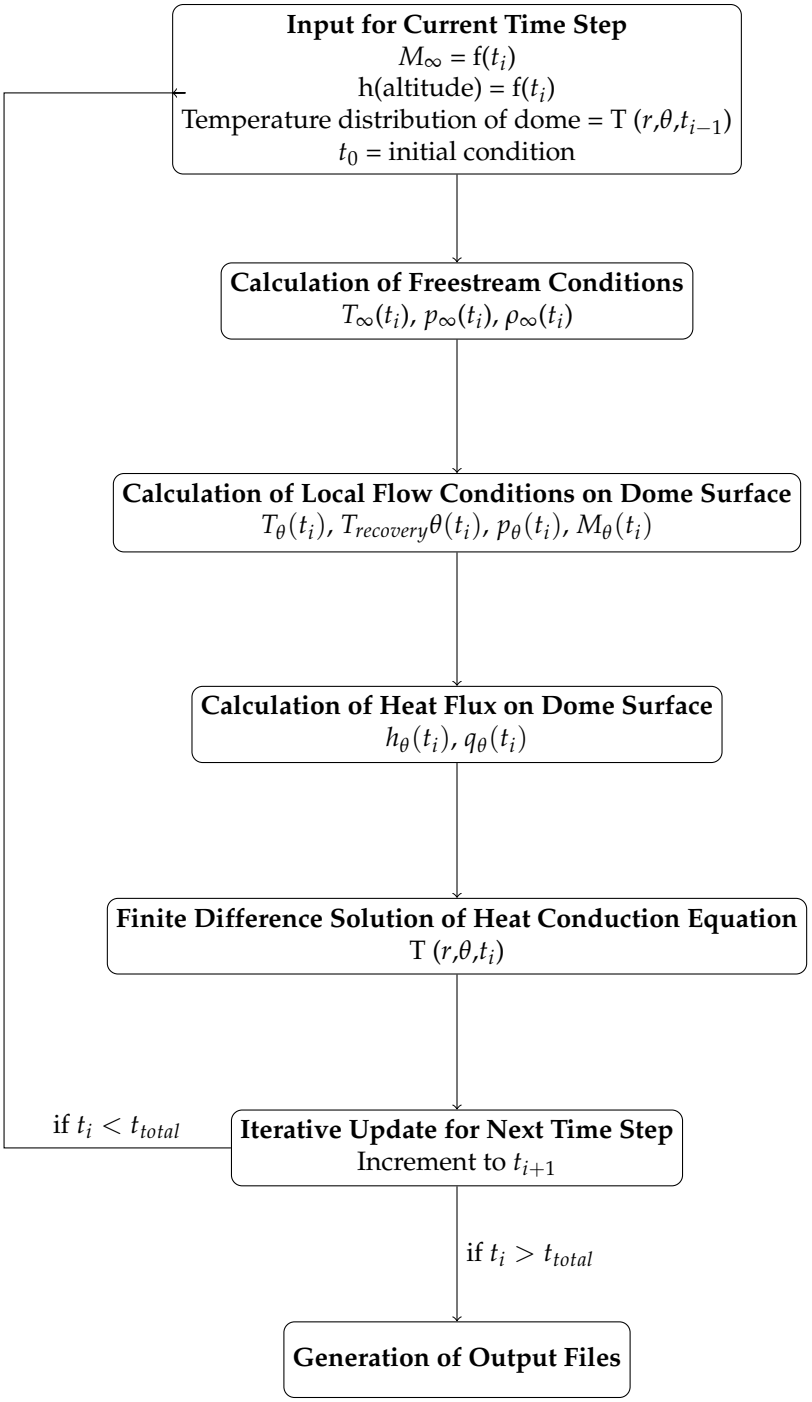

Figure 2. The diagram shows the step-by-step process, starting with the initial conditions and freestream calculations, followed by the local flow and heat flux computations. It includes the solution of the heat conduction equation and the iterative updates for each time step, ending with the output generation. The iterations cease upon reaching the total flight time (t_{total}).

2.1. Flow Properties

Throughout the flight of the missile, variations in altitude and velocity require the evaluation of changing flow properties over time. The method introduced calculates these flow properties using isentropic flow relations. For subsonic flow conditions, free stream and stagnation point properties are evaluated, while for the supersonic flow conditions properties behind the shock are also used.

The determination of the local heat transfer coefficient is a critical aspect of the current numerical model, as these coefficients directly influence the prediction of heat flux across the hemispherical dome's surface. The correlation employed within the scope of this study was proposed by Beckwith and Gallagher [1], and it was modified to account for supersonic flow conditions, based on the derivations outlined by Anderson [22]. The methodology of this study adapts this correlation, to account for the varying Mach numbers, atmospheric conditions, and characteristics specific to hemispherical domes subject to high-speed flows. Additionally, the coefficients are recalculated at each time step, to reflect the dynamic changes in flow conditions during flight. This iterative updating is essential for capturing transient thermal behavior accurately, allowing the model to adapt to the rapid changes in environmental conditions that affect aerodynamic heating. The total temperature, pressure, and, density values are calculated by using isentropic flow relations for subsonic and supersonic conditions. During the iterations flow variables at the edge of the boundary layer are required for heat transfer coefficient calculations. For subsonic flow conditions, the variables at the edge of the boundary layer are calculated by using the freestream flow properties. On the other hand for supersonic flow conditions flow properties outside the boundary layer are calculated by utilizing normal shock relations. The temperature, pressure, density, and Mach number behind the shock wave along the stagnation streamline for supersonic conditions can be expressed as follows, respectively:

$$\frac{T_2}{T_\infty} = (1 + \frac{2\gamma}{1+\gamma}(M_\infty^2 - 1))^{\frac{2+(\gamma-1)M_\infty^2}{(\gamma+1)M_\infty^2}}, \tag{3}$$

where T_2 is the temperature immediately after the shock, T_∞ is the freestream temperature, and γ is the specific heat ratio,

$$\frac{p_2}{p_\infty} = 1 + \frac{2\gamma}{\gamma+1}(M_\infty^2 - 1), \tag{4}$$

where p_2 is the pressure immediately after the shock, and where p_∞ is the freestream pressure,

$$\frac{\rho_2}{\rho_\infty} = \frac{(\gamma+1)M_\infty^2}{2+(\gamma-1)M_\infty^2}, \tag{5}$$

where ρ_2 is the density immediately after the shock, and where ρ_∞ is the freestream density,

$$M_2 = \sqrt{\frac{1 + \frac{\gamma-1}{2}M_\infty^2}{\frac{\gamma M_\infty^2 - (\gamma-1)}{2}}}. \tag{6}$$

where M_2 is the Mach number immediately after the shock.

Following this initial step, the method proceeds to determine the flow properties, such as the pressure distribution at the hemisphere's external, the velocity distribution at the edge of the boundary layer, the coefficient of the heat transfer, and the heat flux around the hemisphere's external surface. The local velocity at the edge of the boundary layer around the hemisphere is calculated by utilizing modified Newtonian theory given by [22], ideal gas law, and isentropic flow relations. The relevant equations are presented as follows:

$$p_\theta = p_0 sin^2\theta + p_\infty cos^2\theta, \tag{7}$$

where p_θ is the local pressure at angle θ, p_0 is the stagnation point pressure, p_∞ is the freestream pressure, and θ is the angular position from the stagnation point,

$$u_\theta = \sqrt{\gamma\frac{p_0}{\rho_0}[\frac{2}{\gamma-1}[(\frac{p_\theta}{p_0})^{\frac{\gamma-1}{\gamma}} - 1]]}, \tag{8}$$

where u_θ is the local flow velocity at angle θ, γ is the specific heat ratio, and ρ_0 is the stagnation point density,

$$T_\theta = \frac{T_0}{(1 + \frac{\gamma-1}{2} M_\theta^2)}, \tag{9}$$

where T_θ is the local temperature at angle θ, T_0 is the stagnation temperature, and M_θ is the local Mach number at angle θ.

Using the relation introduced by van Driest [5], the recovery temperature distribution around the outer surface can be expressed as

$$T_{recovery\theta} = T_\theta (1 + Pr_\theta^{\frac{1}{3}} \frac{\gamma - 1}{2} M_\theta^2), \tag{10}$$

where $T_{recovery\theta}$ is the recovery temperature at angle θ, and where Pr_θ is the Prandtl number at angle θ.

The calculation of these properties enables the determination of the local heat transfer coefficient through the employment of the correlation provided by Beckwith and Gallagher [1]. The correlation is used for the calculation of the local heat transfer coefficient distribution in the turbulent boundary layer on the outer surface of the hemispherical dome. This correlation is obtained by applying Reynolds analogy to Falkner's expression for skin friction on a flat plate and combining this expression with the stagnation point heat transfer relation which is based on dimensionless stagnation point velocity gradient [3,23,24]:

$$h_{w\theta} = 0.0157 Pr_w [\frac{u_\theta p_\theta r_s \theta}{u_{\theta ref} p_{\theta ref} r_s \theta_{ref}}]^{\frac{5}{14}} (\frac{\rho_{w_\theta ref} u_{\theta ref} r_s \theta_{ref}}{\mu_w \theta_{ref}})^{\frac{5}{14}}, \tag{11}$$

where $h_{w\theta}$ is the local heat transfer coefficient calculated for the angular position θ, Pr_w is the Prandtl number at the wall temperature, r_s is the radius of the sphere, μ_w is the dynamic viscosity at wall temperature, and "ref" denotes the reference conditions determined at a reference angular position, specifically at $\theta = 90^\circ$,

$$q_{w\theta} = h_{w\theta} (T_{recovery\theta} - T_{w\theta}). \tag{12}$$

where $q_{w\theta}$ is the heat flux calculated for the angular position theta θ, and $T_{w\theta}$ is the wall temperature at the angular position theta θ.

The angular position of interest is θ, and its depiction can be found in Figure 3. It is also important to underline that variations in the ψ direction are disregarded, due to the model's axisymmetrical nature used in the computations. In addition to the axisymmetry of the geometry, the flow is also assumed to be symmetrical since the dome is expected to reach its highest temperature under symmetrical flow conditions. Under these conditions, a two-dimensional heat conduction equation will be solved, together with one-dimensional flow calculations for determining the temperature distribution within the dome thickness, as illustrated in Figure 3:

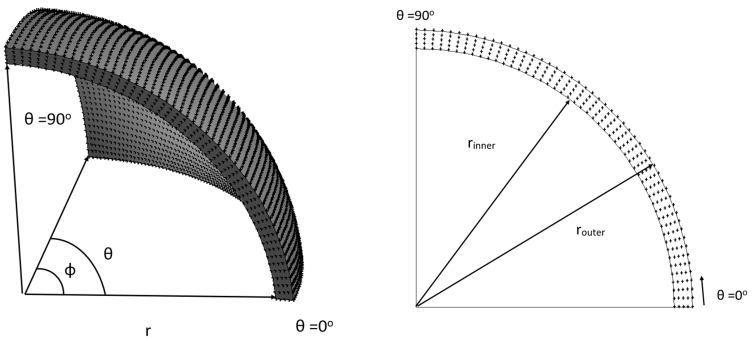

Figure 3. 3D representation of the hemispherical dome (**left**); 2D representation of the domain of interest (**right**).

2.2. Governing Equations and Boundary Conditions

The temperature profiles within and on the hemisphere's surfaces are derived from solving the two-dimensional heat conduction equation in spherical coordinates:

$$\rho_s c_{ps} \frac{\partial T_S}{\partial t} = \frac{1}{r^2} \frac{\partial}{\partial r} \left(k_s r^2 \frac{\partial T_s}{\partial r} \right) + \frac{1}{r^2 \sin\theta} \frac{\partial}{\partial \theta} \left(k_s \sin\theta \frac{\partial T_s}{\partial \theta} \right), \tag{13}$$

where ρ_s is the density and c_{ps} is the specific heat at constant pressure of the sphere material,T_S is the temperature within the sphere, k_s is the thermal conductivity of the sphere material, r is the radial, and θ is the angular coordinate.

Heat exchange with the ambient air occurs at the outer boundary of the sphere's solid domain. Therefore, the heat flux caused by aerodynamic heating will be applied to the outer surface of the solid domain ($r = r_{outer}$ $0^\circ \leq \theta \leq 90^\circ$):

$$-k_s \frac{\partial T_s}{\partial r} = q_{w\theta} = h_{w\theta} \left(T_{\text{recovery }\theta} - T_{w\theta} \right), \tag{14}$$

where $q_{w\theta}$ is the heat flux at the wall at angle θ, $h_{w\theta}$ is the heat transfer coefficient at the wall at angle θ, $T_{\text{recovery }\theta}$ is the recovery temperature at angle θ, $T_{w\theta}$ is the wall temperature at angle θ, and r_{outer} is the outer radius of the hemisphere.

The inner boundary ($r = r_{inner}$ $0^\circ \leq \theta \leq 90^\circ$) is assumed to be adiabatic:

$$-k_s \frac{\partial T_s}{\partial r} = 0, \tag{15}$$

where r_{inner} is the inner radius of the hemisphere.

Similarly, the symmetry axis ($\theta = 0^\circ$ $r_{inner} \leq r \leq r_{outer}$) and the shoulder boundary ($\theta = 90^\circ$ $r_{inner} \leq r \leq r_{outer}$) are assumed to be adiabatic:

$$-k_s \frac{\partial T_s}{\partial \theta} = 0. \tag{16}$$

2.3. Finite Difference Approach

The finite difference method was selected for its robustness and straightforward implementation in handling the heat conduction equation in spherical coordinates. The proposed method is particularly advantageous in this context, due to its ability to accommodate complex boundary conditions and variable material properties, which are essential in accurately simulating the transient heat response of hemispherical domes under aerodynamic heating. It allows for a clear and intuitive representation of the physical problem, facilitating easier debugging and validation of the numerical model. The proposed method also scales efficiently on modern computational platforms, ensuring that the simulations remain feasible even when extended to three-dimensional scenarios in future work.

In practice, the finite difference method will be employed, with ghost nodes introduced to implement the boundary conditions with second-order spatial precision. The representation of the ghost nodes can be seen in Figure 4.

Central differences are utilized for the calculation of second-order spatial derivatives, while the forward difference approximates the time derivative, achieving second-order spatial accuracy and first-order temporal accuracy. For the outer boundary ($r = r_{outer}$, $0^\circ \leq \theta \leq 90^\circ$), the equation is discretized as

$$h_{w\theta} \left(T_{\text{recovery }\theta} - T_s^n(N,m) \right) = -k_s \frac{T_s^n(N+1,m) - T_s^n(N-1,m)}{2\Delta r}, \tag{17}$$

where N and m are the indices in the radial and angular directions in the numerical grid, respectively. The superscript n stands for the iteration in time.

Finally, the time step is chosen based on the CFL condition, to ensure the stability of the solution:

$$\Delta t \leq \frac{1}{2\alpha_s}\left(\frac{1}{\Delta r^2}+\frac{1}{(r\Delta\theta)^2}\right), \tag{18}$$

where Δt is the time step, Δr and $\Delta\theta$ are the spatial steps in the radial and angular directions, and α_s is the thermal diffusivity of the sphere material.

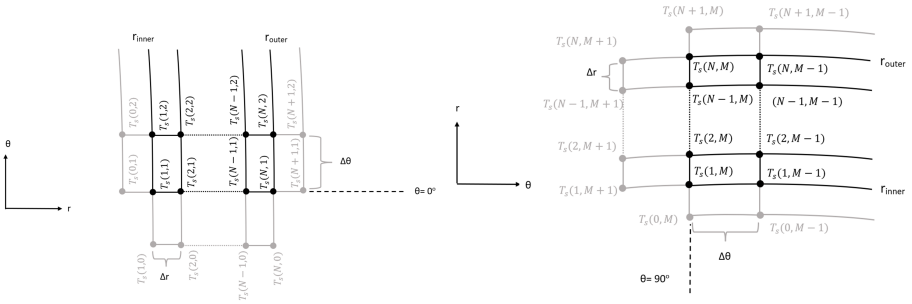

(**a**) (**b**)

Figure 4. The visualization of the nodes used in finite-difference solution. The configuration of the points at the (**a**) symmetry axis boundary, (**b**) shoulder boundary.

2.4. Multidimensional CFD Simulations as the Comparison Case

To evaluate the accuracy of the introduced method, a two-dimensional Unsteady Reynolds-Averaged Navier–Stokes (URANS) simulation was conducted. The simulation's computational domain included both the dome section and its surrounding flow field. In this Computational Fluid Dynamics (CFD) setup, a finite-thickness cylinder with an identical radius and a length of 3 m was positioned following the hemisphere. The dome itself had a radius of 0.36 m and a thickness of 0.004 m. The flow domain and the missile geometry are presented in Figure 5. To discretize the domain for simulation, a structured mesh composed of 1.2 million elements was employed, as depicted in Figure 6. The turbulence was modeled using the k–ω–SST model. A pressure-based, coupled solver was utilized for the simulations. The simulations also accounted for conjugate heat transfer between the dome and the flow, employing second-order schemes for both spatial and temporal discretization. The dome's wall boundaries were treated with a no-slip condition and were considered perfectly smooth. Within the dome, the buoyancy effects were disregarded, and radiative heat transfer was not accounted for in these simulations.

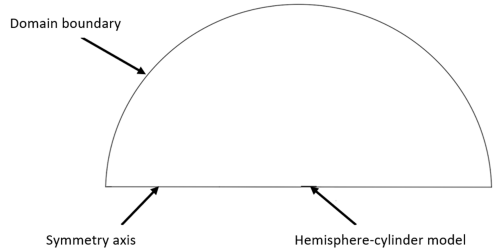

(**a**) 2-D axisymmetric computational domain.

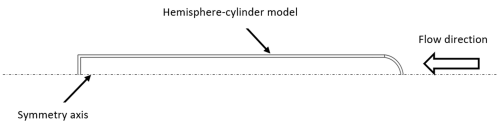

(**b**) 2-D axisymmetric hemisphere-cylinder model.

Figure 5. The computational domain and hemisphere-cylinder model used for CFD simulations.

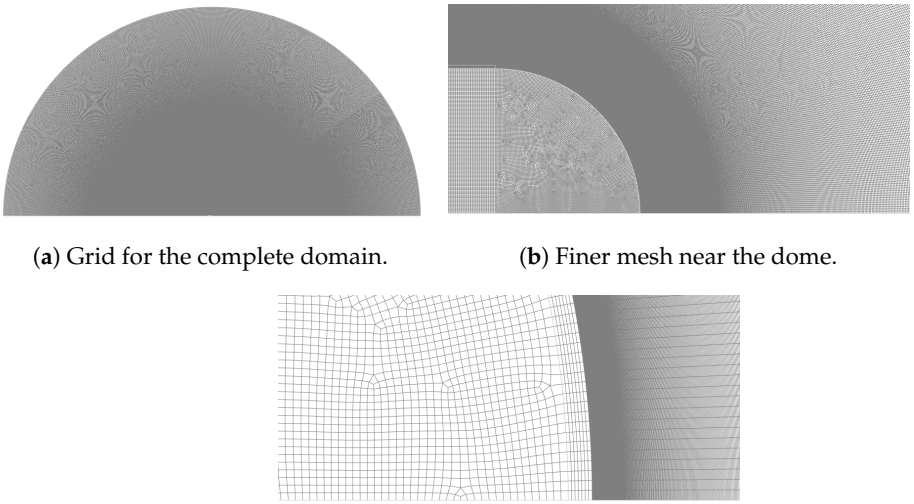

(**a**) Grid for the complete domain.

(**b**) Finer mesh near the dome.

(**c**) Finer mesh near the dome.

Figure 6. The mesh used for the CFD analysis.

2.5. Limitations and Assumptions

Employing the specified geometrical details and properties, the proposed methodology enables the calculation of local heat transfer coefficients for hemispherical domes, utilizing established correlation found in the literature. However, the proposed numerical method is based on some assumptions and has its own limitations, which are listed below:

- Air is assumed to be a perfect gas.
- The temperature and pressure change with altitude according to the 1976 U.S. Standard Atmosphere data.
- Shock–boundary layer interactions and flow separation cannot be considered in the calculations.
- The dynamic viscosity of air is assumed to vary with temperature according to Sutherland's Law.
- Thermal conductivity and the ratio of specific heats of air are assumed to be constant.
- The thermophysical properties of the dome solid material are assumed to be constant.
- The flow is considered to be entirely turbulent in both the CFD simulations and the analytical models.

3. Results and Discussion

The variation of the maximum temperature at the outer surface of the hemisphere over time was plotted for the specified flight scenario, and it can be observed in Figure 7. Comparing the maximum temperature values derived from both the CFD simulations and the developed numerical approach alongside the variation of the recovery temperature reveals that there is a quite reasonable correlation between the outcomes of the proposed method and the CFD simulations throughout the heating phase. This phase was identified as the initial 13 s of flight, during which the recovery temperature exceeded the maximum outer temperature of the dome. However, a discrepancy in the results from the proposed method and the CFD simulations became apparent during the cooling phase, when the recovery temperature fell below the maximum outer temperature of the dome. This suggests that the heat flux estimations made by the numerical approach were slightly lower than those from the CFD simulations, particularly in the cooling phase, when the velocity of the flow is reduced due to deceleration.

The subsequent aspect of the comparative analysis focused on the temperature distributions across the outer and inner surfaces of the dome, as showcased in Figure 8. Here, the temperature profiles on the dome's outer and inner surfaces at 5, 10, 15, and 20 s of the

flight are demonstrated. Echoing the trends observed in the maximum temperature graph in Figure 7, the temperature profiles derived from both the numerical and CFD simulations show significant alignment up to the 15 s mark, with discrepancies becoming more evident at 20 s. A notable similarity in these findings is the temperature difference between areas near the stagnation point and the shoulder area ($\theta \approx 90^{\circ}$) of the dome. The heat flux on the outer boundary was estimated utilizing an adapted correlation from turbulent flat plate flow. This method tended to underestimate temperatures at the stagnation point by up to 15% compared to the results obtained from the CFD simulations. Discrepancies observed near the dome's shoulder in the numerical findings versus the CFD simulations are also noteworthy. The proposed method tended to overestimate temperature values in this region, as it was based on modified Newtonian theory, which is incapable of capturing flow separation effects. The separation that may occur in regions close to the shoulder cannot be modeled accurately with the current approach. Therefore, the temperature values estimated by the proposed method were higher than the temperature values obtained from CFD simulations.

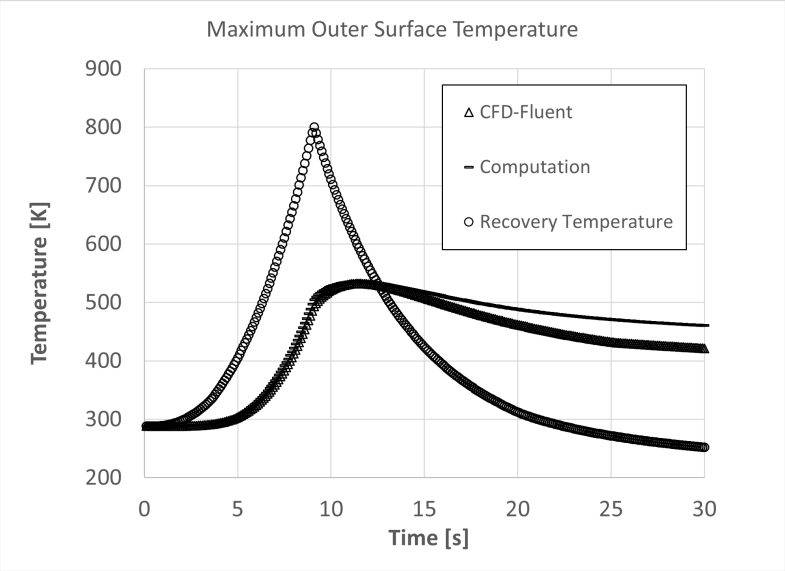

Figure 7. Time history of the maximum outer surface and recovery temperature during flight.

In conclusion, the outcomes derived from the numerical approach are in good agreement with those from the CFD simulations, exhibiting a maximal variation of about 15%. This variance is notably evident in the stagnation area and its surroundings for the majority of the flight's duration. As mentioned earlier, due to the inability of the correlation to capture the separation effects, the differences between temperature distribution near the shoulder were also visible. Moreover, these temperature discrepancies became more pronounced during the cooling phase, when the recovery temperature fell beneath the maximum surface temperature, likely due to the presence of adverse pressure gradient during the reduction of velocity, which caused flow separation. Even though the observed discrepancy may be significant, it is crucial to consider that this level of accuracy is particularly noteworthy, given the substantial reduction in computational resources and time required by the proposed method compared to CFD simulations. In the context of aerothermal analysis, where experimental or simulation methods often struggle to deliver reliable results within reasonable time frames, the proposed numerical approach potentially offers a highly effective and efficient alternative that could be useful during the preliminary design phase.

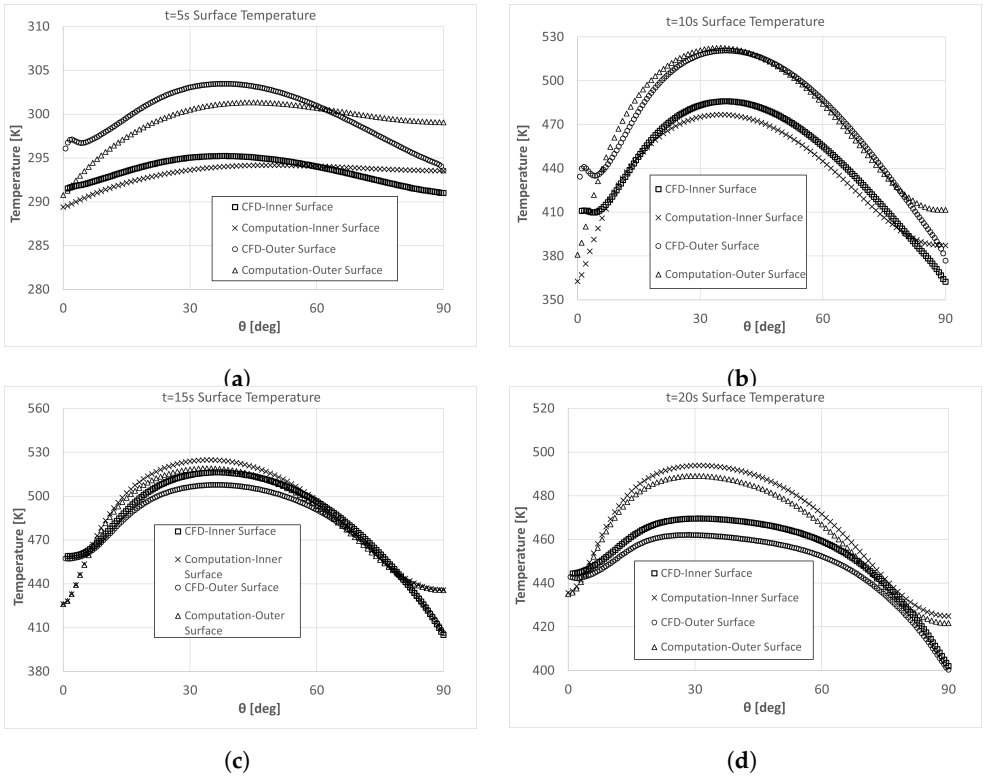

Figure 8. Inner and outer temperature distributions for (**a**) 5 (**b**) 10 (**c**) 15 (**d**) 20 s of flight.

4. Conclusions

The proposed methodology provided results that were in good agreement with those from CFD simulations, delivering temperature profiles across hemispherical domes with a reasonable degree of accuracy. The efficiency of the proposed methodology is a significant advantage over the traditional CFD simulations. The proposed method requires merely 180 s on a single CPU to model 30 s of flight, compared to the extensive computational demands of conventional CFD, which requires approximately 88,473,600 CPU seconds. This efficiency is achieved without compromising the accuracy to an unacceptable extent, making it highly valuable for preliminary design phases and real-time simulations.

The calculations with the numerical model were conducted on a single CPU. In contrast, the CFD simulations were conducted on a High-Performance Computing (HPC) cluster. This stark difference in computational requirements underscores the practicality and resourcefulness of the proposed method. While the CFD approach potentially offers higher accuracy, the proposed method provides a rapid and reasonably accurate alternative that can significantly accelerate the design and analysis process. Such rapid calculation capabilities prove invaluable during the preliminary design phase of missiles and in identifying critical points. Additionally, this system offers flexibility, potentially incorporating enhancements, such as the transition from laminar to turbulent flow, variations in the angle of attack, and the impact of surface roughness without significantly increasing computational load or altering the fundamental model.

Future Directions for Method Improvement

While the proposed methodology demonstrates significant efficiency and reasonable accuracy, several areas for potential enhancement have been identified. Addressing these limitations in future work could further improve the reliability and applicability of this numerical approach.

The current model assumes fully turbulent flow conditions. However, incorporating a model to simulate the transition from laminar to turbulent flow could enhance accuracy. This addition would allow the model to better capture the thermal and fluid dynamics in a broader range of flight conditions. In addition, the model assumes an axisymmetric flow

with a zero angle of attack and sideslip angle. Extending the model to include variations in these angles could provide more comprehensive predictions for different flight scenarios. This enhancement would be particularly useful for simulating real-world scenarios where the missile or vehicle may not always travel perfectly aligned with the flow. Furthermore, improvements in the accuracy and efficiency of the code could be achieved by improving the numerical accuracy by transforming the equations solved [25].

Additionally, the capability of modeling more complex geometries, such as ogive nose and 3D wing profiles, could be explored. These profiles are commonly used in aerospace applications, due to their favorable aerodynamic characteristics. The ogive nose profile is utilized for reducing drag and improving performance in supersonic regimes, whereas the 3D wing profile is investigated mostly for optimizing lift-to-drag ratios and handling characteristics in varying flight conditions [26–28]. Extending the model to include these shapes could enhance its applicability to a wider range of aerospace vehicles. Moreover, to handle more complex geometries and model deforming boundaries, methods such as the immersed boundary method [29] or the immersed finite element method [30] could be employed. These methods can be particularly useful for simulating phenomena like ablation, where the outer surface nodes undergo deformation. If needed, CPU parallelization could also be implemented in the code, to address computational needs introduced by modeling complex phenomenon and geometries. Finally, experimental validation with relevant geometry might be added to the numerical model, to benchmark and refine its predictions against real-world data, similar to the study of Duarte et al. [9]. The parametric system identification method, as outlined in the aforementioned study, aims to integrate experimental data into the mathematical framework of aerodynamic heating, to estimate the average heat transfer coefficient. This approach involves adjusting the calculated final temperatures, to align with known experimental temperature data, thereby estimating the heat flux.

Author Contributions: Both authors have contributed equally to the conceptualization, methodology, software, validation, formal analysis, investigation, data curation, original draft preparation, review and editing, and visualization. Supervision is provided exclusively by A.C.G. All authors have read and agreed to the published version of the manuscript.

Funding: The authors declare that this research received no external funding.

Data Availability Statement: The data utilized in this study were specifically created and represented for the purposes of this research. These data are not publicly archived but are available from the corresponding author upon request and permission.

Conflicts of Interest: Author Arif Cem Gözükara was employed by the company Aselsan, Inc., and author Uygar Ateş Ceylan was employed by Atlas Copco Airpower NV. Both authors declare that the research was conducted in the absence of any commercial or financial relationships that could be construed as a potential conflict of interest, and that the content of the article is in agreement with their respective employers.

References

1. Beckwith, E.I.; Gallagher, J.J. *Heat Transfer and Recovery Temperatures on a Sphere with Laminar, Transitional and Turbulent Boundary Layers, at Mach Numbers of 2.00 and 4.15*; Technical Note 4125; NACA (National Advisory Committee for Aeronautics): Langley Field, VA, USA, 1959.
2. Chauvin, L.T.; Maloney, J.P. *Experimental Convective Heat Transfer to a 4-Inch and 6-Inch Hemisphere at Mach Numbers from 1.62 to 3.04*; Research memorandum; NACA (National Advisory Committee for Aeronautics): Langley Field, VA, USA, 1954.
3. Reshotko, E.; Cohen, C.B. *Heat Transfer at the Forward Stagnation Point of Blunt Bodies*; Technical Note 3513; NACA (National Advisory Committee for Aeronautics), Lewis Flight Propulsion Laboratory: Cleveland, OH, USA, 1955.
4. Stine, H.A.; Wanlass, K. *Theoretical and Experimental Investigation of Aerodynamic-Heating and Isothermal Heat-Transfer Parameters on a Hemispherical Nose with Laminar Boundary Layer at Supersonic Mach Numbers*; Technical Note 3344; NACA (National Advisory Committee for Aeronautics), Ames Aeronautical Laboratory: Santa Clara, CA, USA, 1954.
5. Van Driest, E.R. The Problem of Aerodynamic Heating. In *Aeronautical Engineering Review*; Institute of the Aeronautical Sciences: Los Angeles, CA, USA, 1956; pp. 26–41.
6. Kouroupis, J.B. Flight capabilities of high-speed-missile radome materials. *Johns Hopkins APL Tech. Dig.* **1992**, 13, 3.

7. Trotta, P. Precision conformal optics technology program. *Proc. SPIE-Int. Soc. Opt. Eng.* **2001**, *4375*, 96–107.
8. Yu, J.; Fan, Z. The correction of dynamic aero-optical aberration of optical dome at different altitudes using wavefront coding. *Optik* **2022**, *252*, 168535. [CrossRef]
9. Duarte, G.F.R.; Silva, M.G.d.; Castro, B.d.M. Aerodynamic Heating of Missile/Rocket—Conceptual Design Phase. In Proceedings of the 20th International Congress of Mechanical Engineering (COBEM 2009), ABCM, Gramado, RS, Brazil, 15–20 November 2009.
10. Martinelli, S.K.; Braun, R.D. Centerline Heating Methodology for use in Preliminary Design Studies. In *Special Problems Report*; AE8900 MS Special Problems Report; Guggenheim School of Aerospace Engineering, Georgia Institute of Technology: Atlanta, GA, USA, 2010.
11. DeJarnette, F.R.; Davis, R.M. *A Simplified Method of Calculating Laminar Heat Transfer over Bodies at an Angle of Attack*; Technical Report NASA TN-4720; NASA: Washington, DC, USA, 1968.
12. Smyth, D.N.; Loo, H.C. *Analysis of Static Pressure Data from 1/12-Scale Model of the YF-12A. Volume 3: The MARK IVS Supersonic-Hypersonic Arbitrary Body Program, User's Manual*; Technical Report NASA-CR-151940; NASA: Washington, DC, USA, 1981.
13. McDonnell Douglas Corporation. A Miniature Version of the JA70 Aerodynamic Heating Computer Program H800 (MINIVER); Technical Report MDC 60642; McDonnell Douglas Corporation: St. Louis, MO, USA, 1972.
14. Zoby, E.; Simmonds, A.L. Engineering Flowfield Method with Angle-of-Attack Applications. *J. Spacecr. Rocket.* **1985**, *22*, 398–404. [CrossRef]
15. Riley, C.J.; DeJarnette, F.R.; Zoby, E.V. Surface Pressure and Streamline Effects on Laminar Heating Calculations. *J. Spacecr. Rocket.* **1990**, *27*, 9–14. [CrossRef]
16. Kinney, D.J. Aero-Thermodynamics for Conceptual Design. In Proceedings of the 42nd AIAA Aerospace Sciences Meeting and Exhibit, Reno, NV, USA, 5–8 January 2004; Number AIAA-2004-31-962.
17. Jain, A.; Hayes, J. Hypersonic Pressure, Skin-Friction, and Heat Transfer Distributions on Space Vehicles: Planar Bodies. *AIAA J.* **2004**, *42*, 2060–2068. [CrossRef]
18. Hollis, B.R.; Horvath, T.J.; Berry, S.A.; Hamilton, H.H.; Thompson, R.A.; Alter, S.J. X-33 Computational Aeroheating Predictions and Comparisons with Experimental Data. In Proceedings of the 33rd AIAA Thermophysics Conference, Norfolk, VA, USA, 28 June–1 July 1999; pp. 99–3559.
19. Quinn, R.D.; Gong, L. *Real-Time Aerodynamic Heating and Surface Temperature Calculations for Hypersonic Flight Simulation*; Technical Memorandum NASA TP-2914; NASA (National Aeronautics and Space Administration), Ames Research Center: Edwards, CA, USA, 1990.
20. Şimşek, B.; Uslu, S.; Ak, M.A. Validation of Aerodynamic Heating Prediction Tool. *IsÄ± Bilim. Tek. Derg.* **2020**, *40*, 53–63.
21. *NOAA-S/T 76-1562*; U.S. Standard Atmosphere, 1976. Technical Report; NOAA: Washington, DC, USA; NASA: Washington, DC, USA; USAF: Washington, DC, USA, 1976.
22. Anderson, J.D., Jr. *Hypersonic And High Temperature Gas Dynamics*; AIAA: Reston, VA, USA, 2006.
23. Falkner, V.M. A New Law for Calculating Drag: The Resistance of a Smooth Flat Plate With Turbulent Boundary Layer. *Aircr. Eng.* **1943**, *XV*, 65–69. [CrossRef]
24. Mangler, W. *Compressible Boundary Layers on Bodies of Revolution*; Technical Report 47; Office of the Publication Board, Department of Commerce: Washington, DC, USA, 1946.
25. Temimi, H.; Ben-Romdhane, M.; Baccouch, M.; Musa, M. A two-branched numerical solution of the two-dimensional Bratu's problem. *Appl. Numer. Math.* **2020**, *153*, 202–216. [CrossRef]
26. Conlan-Smith, C.; Ramos-GarcÃa, N.; Sigmund, O.; Andreasen, C.S. Aerodynamic Shape Optimization of Aircraft Wings Using Panel Methods. *AIAA J.* **2020**, *58*, 3765–3776. [CrossRef]
27. Javadhpour, S.; Rahmati, B.; Khorasani Nezhad, E.; Maryami, R. Optimization of Radar Cross Section and Drag Coefficient of Ogive Nose Using the NSGA-II Algorithm. *J. Radar* **2019**, *7*, 53–63.
28. Mayo, E.E.; Weisskopf, G.A.; Hutton, C.I. *Nose Optimization Study, Part I: Comparative Performance of Tangent Ogive and Conical Noses*; Technical Report; Goddard Space Flight Center: Washington, DC, USA, 1965.
29. Peskin, C. The immersed boundary method. *Acta Numer.* **2002**, *11*, 479–517. [CrossRef]
30. Zhang, L.; Gay, M. Immersed finite element method for fluid-structure interactions. *J. Fluids Struct.* **2007**, *23*, 839–857. [CrossRef]

computation

MDPI

Article

Air–Water Two-Phase Flow Dynamics Analysis in Complex U-Bend Systems through Numerical Modeling

Ergin Kükrer [1,2,*] and Nurdil Eskin [1]

[1] Faculty of Mechanical Engineering, Istanbul Technical University, Beyoglu, Istanbul 34437, Türkiye; eskinn@itu.edu.tr
[2] Mechanical Engineering Department, Istanbul Bilgi University, Eyüp, Istanbul 34060, Türkiye
* Correspondence: ergin.kukrer@bilgi.edu.tr

Abstract: This study aims to provide insights into the intricate interactions between gas and liquid phases within flow components, which are pivotal in various industrial sectors such as nuclear reactors, oil and gas pipelines, and thermal management systems. Employing the Eulerian–Eulerian approach, our computational model incorporates interphase relations, including drag and non-drag forces, to analyze phase distribution and velocities within a complex U-bend system. Comprising two horizontal-to-vertical bends and one vertical 180-degree elbow, the U-bend system's behavior concerning bend geometry and airflow rates is scrutinized, highlighting their significant impact on multiphase flow dynamics. The study not only presents a detailed exposition of the numerical modeling techniques tailored for this complex geometry but also discusses the results obtained. Detailed analyses of local void fraction and phase velocities for each phase are provided. Furthermore, experimental validation enhances the reliability of our computational findings, with close agreement observed between computational and experimental results. Overall, the study underscores the efficacy of the Eulerian approach with interphase relations in capturing the complex behavior of the multiphase flow in U-bend systems, offering valuable insights for hydraulic system design and optimization in industrial applications.

Keywords: air–water two phase flows; U-bend; Eulerian–Eulerian approach; interphase relations; void-fraction

Citation: Kükrer, E.; Eskin, N. Air–Water Two-Phase Flow Dynamics Analysis in Complex U-Bend Systems through Numerical Modeling. *Computation* **2024**, *12*, 81. https://doi.org/10.3390/computation12040081

Academic Editors: Ali Cemal Benim, Rachid Bennacer, Abdulmajeed A. Mohamad, Paweł Oclon, Sang-Ho Suh and Jan Taler

Received: 8 March 2024
Revised: 6 April 2024
Accepted: 10 April 2024
Published: 12 April 2024

1. Introduction

Gas–liquid two-phase flows, characterized by the simultaneous transport of gas and liquid phases within various flow components, represent a fundamental yet challenging phenomenon critical to a wide range of industrial applications. These applications span a broad spectrum, including nuclear reactors [1,2], oil and gas pipelines [3–5], bio/chemical processes [6,7], and thermal management systems [8]. A comprehensive understanding and characterization of two-phase flow phenomena is necessary due to the critical role that the dynamic interaction between gas and liquid phases within flow components plays in determining system behavior, performance, and safety.

In many applications, flow components can have a range of geometries. Multiphase flow can occur in various configurations, including ducts and straight channels [9], U-bends [10,11], manifolds with collectors [12,13], or expansion/contraction sections [14,15]. Industrial flow systems comprise components of varying geometries, leading to singularities and complexities that require comprehensive analysis. Among the flow components, bends and elbows are of particular interest in many studies due to the centrifugal forces, changes in pressure and velocity gradients, and the associated secondary flow conditions. The dynamics of multiphase flows in bends are influenced by factors such as boundary conditions, flow regimes and interfaces, and the distribution of phases within the flow.

Zahedi and Rad [16] examine two-phase flows in 90-degree horizontal bends, focusing on parameters such as volume fraction, velocity, pressure, turbulence intensity, and

swirling intensity using the volume of fluids (VOF) approach. Kim et al. [17] assess the impact of the geometric characteristics of 90-degree bends and determine that the presence of the elbow significantly influences both the distribution of local parameters and their evolution. Dutta et al.'s study [18] explores flow separation for high Re numbers in horizontally oriented bends, while Mazumder and Siddique [19] and Aung and Yuwono [20] investigate the two-phase characteristics of horizontal to vertical orientation by employing the Eulerian approach. Abhari et al. [21] conduct a study in horizontal 90-degree elbows but for a large diameter pipe (1.1 m). Qiao et al.'s [22] study evaluates the void fraction and velocity profile development in a 90-degree vertical elbow through a combination of measurements and numerical analysis. Measurements at the elbow reveal the generation of a secondary flow due to centripetal forces and pressure gradients in the direction of the inner curvature.

Limited studies in the literature have also been conducted on 180-degree return bends (U-bends) with various orientations, highlighting a gap in the current research landscape beyond investigations on 90-degree bends. While some of the research has explored the flow regimes and characteristics [23–25] and heat transfer enhancements [26–28] in 180-degree bends, comprehensive studies on the influence of bend geometry on two and three-dimensional flow dynamics in such configurations are scarce. Furthermore, most of the studies focus solely on pressure drop characteristics [23,25,27]. However, understanding the dynamics of two-phase flows in different bend configurations is crucial for various industrial applications of hydraulic systems. The presence of multiple flow regimes, such as stratified, annular, or slug flow, along with the centrifugal forces induced by the bend, significantly influences phase distribution, flow velocities, and heat transfer characteristics. Therefore, there is a clear research gap in understanding the detailed flow patterns and scour behavior in those complex geometries, necessitating more in-depth investigations to enhance our knowledge of multiphase flows in these challenging geometries.

Based on the literature survey, most of the studies have focused solely on unidirectional (upward/downward) or vertical/horizontal orientations, treating bends and elbows as individual sections. In contrast, our study investigates the air–water two-phase flow in a complete U-bend, comprising two horizontal-to-vertical (upward and downward) 90-degree bends and one vertical 180-degree elbow. This comprehensive approach allows us to model the entire bend as a cohesive system, mirroring real-world applications. Expanding upon our preliminary work presented at the 14th International Conference on Computational Heat, Mass, and Momentum Transfer (ICCHMT 2023) [29], where we introduced the concept of transient two-phase modeling in U-bends, this extended study includes a parametric analysis of airflow rates of 30, 35, and 40 L/min. Our numerical model employs separate equations for each phase by leveraging the Eulerian–Eulerian approach and providing a grounded framework for the separated flow model. The robust computational model developed in our study facilitates a comprehensive assessment of two-phase flow dynamics in complex pipeline applications, encompassing both horizontal and vertical orientations. Additionally, experimental validation conducted at Istanbul Technical University Hydraulic Laboratories confirms the reliability of our computational results, demonstrating good agreement between numerical simulations and experimental data.

2. Materials and Methods

This section provides a detailed description of the computational model used to analyze an air–water two-phase flow in a sophisticated U-bend system. The geometry of the system, solid model, mesh structure, boundary conditions, and numerical model setup are elaborated upon to offer a clear understanding of the methodology employed in the study to simulate the complex flow behavior within the U-bend configuration.

2.1. Geometry of Computational Model

The complete flow domain model is constructed by assembling the injector, upstream, U-bend, and downstream sections, as depicted in Figure 1.

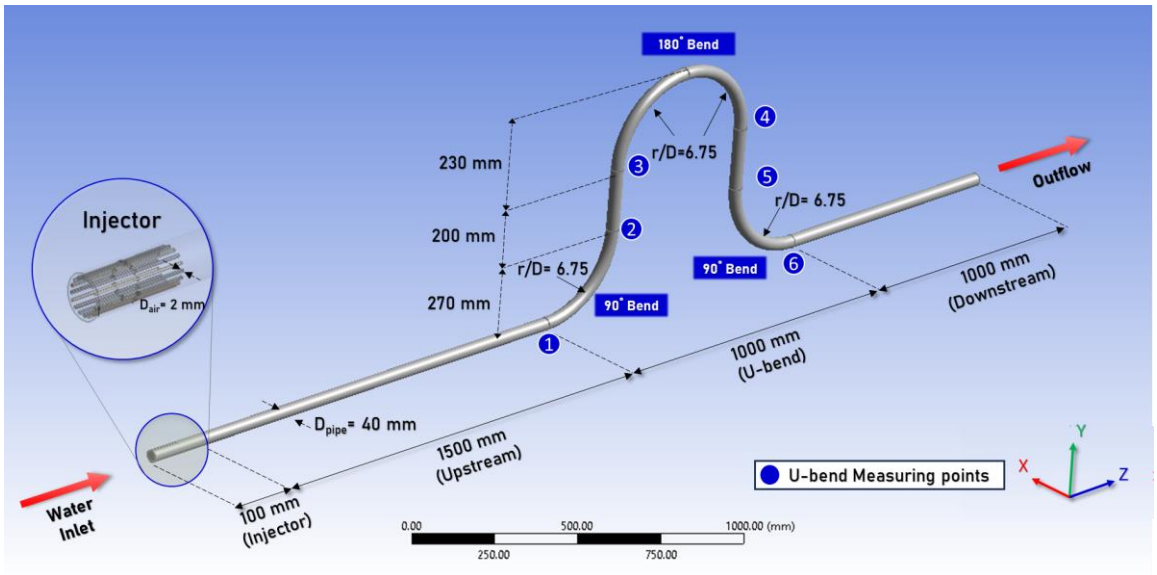

Figure 1. Constructed solid model with detailed U-bend system geometry.

The dimensions of the model utilized in this study were specifically designed to be consistent with the physical setup outlined in our previously published studies [10,29,30]. The flow domain initiates at the inlet cross-section of a cylindrical pipe with a diameter of D_{pipe} = 40 mm, where two-phase air–water flow conditions are introduced via the circular air injector. The injector provides air injection into the water flow through nozzles located at 16 equally spaced points around the circumference. As illustrated in the figure, each air pipe has a hydraulic diameter of D_{air} = 2 mm and extends 100 mm into the flow domain. This extension of the pipe into the flow domain establishes a separate domain for the air phase to develop. In the numerical model, the inner surfaces of the extended part are designated as inflow to prevent any flow disturbance, while the inlet cross-sections are individually configured as air inlets.

Following the injector section, a 1500-mm-long horizontal section called the upstream section is constructed. This section allows for observing the air–water flow development before entering the test section, which includes the U-bend geometry. In the upstream region, the flow reaches fully developed conditions prior to entering the U-bend section. Fully developed conditions are identified based on the hydrodynamic characteristics of the determined flow regime becoming evident. The flow regime for our phase characteristics and physical conditions is established as plug flow by employing commonly used flow regime maps of horizontal liquid–gas flows outlined in Baker's [31] and Hewitt and Robert's [32] studies. In our previous and experimental investigations, we confirmed that the transition to plug flow is achieved within the upstream region. This enables us to examine the two-phase flow characteristics under fully developed multiphase conditions for both phases. We observed that the bubbles are clustered in the upper portion of the pipe as plugs, exhibiting characteristics indicative of plug flow towards the end of the upstream region. This aspect is further explored in our experimental study [10].

The U-bend section initiates with a 90° vertical upward elbow featuring a curvature ratio of r/D = 6.75 (r = 270 mm, D = 40 mm), following the upstream segment. It is then followed by a further 200mm vertical upward section, diverging our work from previous works investigating the U-bend effect in the literature. Typically, U-bends are constructed solely as 180-degree return bends [25,28,31,32]. However, in our study, we also examine the pre-effect of the 90-degree upward and downward elbows on the two-phase flow, in addition to the effect of the 180-degree return U-bend. The 180-degree bend features a curvature ratio of r/D = 5.75 (r = 230 mm, D = 40 mm). After passing through the U-bend, the flow moves symmetrically downwards towards the last 90° bend (transitioning from

a vertical to a horizontal orientation) with a curvature ratio of r/D = 6.75. Later, the flow proceeds to the pipe outflow along the downstream section.

2.2. Mesh Structure and Design Parameters

The meshing for the fluid domain comprises high-resolution tetrahedral-based elements, a common practice in flow and two-phase flow simulations due to their effectiveness in handling complex geometries [33]. In this study, we adopted a tetrahedral-weighted mesh with a finer element size to model the complex geometry of the injector and U-bend more accurately and consistently. The complete model is composed of more than 4.1 million nodes and 2.8 million elements, with a mesh size set at 1×10^{-5} m, and the maximum allowed mesh size is 4×10^{-3} m. The mesh size is selected in compliance with the bubble diameters calculated at the outlet of the injector. The bubble diameter at the outlet of the injector is calculated using the relation developed by Kunii and Levenspiel [34] based on the variables, which are the volumetric flow rate and the diameter of the air nozzles. The mean bubble size estimated is 1 mm to 5 mm, as was also investigated in our previous experimental results [10].

The mesh skewness and orthogonal quality study are utilized to assess mesh quality. The average skewness is determined to be 0.22, while the orthogonal quality is evaluated at 0.78. Figure 2 illustrates the generated mesh structure of the injector and bend sections.

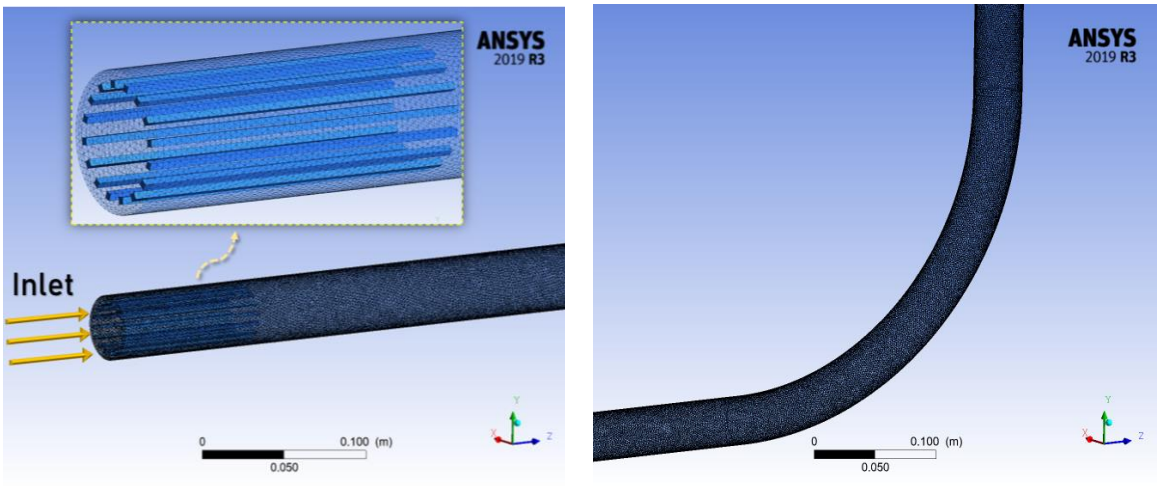

(**a**) (**b**)

Figure 2. The mesh structure of the (**a**) injector and (**b**) bend sections.

As shown in Figure 2a, the inlet cross-sectional area is defined as a velocity-inlet boundary condition for each phase. Meanwhile, the side areas of the rectangular cross-section of the air domain are specified as interior flow boundaries. The remaining pipe walls are set as no-slip boundary conditions. The boundary condition is chosen as a pressure outlet at the outlet section located at the end of the downstream segment, as the pipe discharges into a tank that is open to the atmosphere.

The water phase is designated as the primary phase for computational modeling, and the volumetric water flow rate is set at 180 L/min. The design parameters for the water phase are detailed in Table 1.

In the calculations, all thermal properties of the water phase are determined based on the average temperature of 24 °C. The mass flux rate and superficial velocity are computed considering the pipe diameter, which is 40 mm (0.04 m). Additionally, the Reynolds Number (Re) for the liquid phase is calculated as 1.04×10^6 (»3500), indicating that the water flow regime is turbulent.

Table 1. Design parameters for water phase.

Definition	Symbol		Unit
Density	ρ_w	997.3	kg/m^3
Dynamic viscosity	μ_w	0.0009107	kg/m·s
Volumetric flow rate	$\dot{Q}_w$	180	L/min
Mass flux rate	G_w	2380.9	kg/m^2s
Superficial velocity	j_w	2.4	m/s

On the other hand, the secondary phase is designated as air to represent the gas phase. The volumetric airflow rate is varied at 30, 35, and 40 L/min to conduct a parametric study. The air is distributed to the injector section through sixteen capillary pipes placed around the pipe circumference at equal angles. Design conditions for the air phase are presented in Table 2.

Table 2. Design parameters for air phase.

Definition	Symbol		Unit
Density	ρ_a	1.196	kg/m^3
Dynamic viscosity	μ_a	0.0000183	kg/m·s
Volumetric flow rate	$\dot{Q}_a$	30; 35; 40	L/min
Mass flux rate	G_a	0.479; 0.559; 0.639	kg/m^2s
Superficial velocity	j_a	0.622; 0.725; 0.829	m/s

2.3. Numerical Model

The volume of fluid (VOF), mixture, and Eulerian models are commonly used numerical methods for simulating multiphase flows. While the VOF model is employed to analyze interfaces between phases, it can be computationally expensive and struggles with resolving thin interfaces and complex interfacial dynamics. In contrast, the mixture model treats multiphase flow as a single continuous mixture, rendering it suitable for dispersed flows but limited in accurately capturing phase segregation and interface dynamics. Despite their utility, both models exhibit weaknesses in representing strong phase interactions, often necessitating more advanced modeling approaches for precise predictions. On the other hand, the Eulerian Model, particularly the Eulerian–Eulerian approach, has attracted significant attention in multiphase flow modeling due to its effectiveness in simulating complex scenarios. Hence, the Eulerian model will be further elaborated in this study.

2.3.1. Eulerian Model

The Eulerian model is among the most comprehensive approaches for multiphase modeling. Developed based on the separated flow model theory, it treats the properties of each phase separately, solving the governing equations independently for each phase.

The volume fraction (α) is determined by solving the continuity equation. Equation (1) addresses the continuity equation per phase.

$$\frac{\partial}{\partial t}\left(a_q \rho_q\right) + \nabla\left(\alpha_q \rho_q \vec{u}_q\right) = \sum_{p=1}^{n}\left(m_{pq} - m_{qp}\right) + S_q \quad (1)$$

On the right-hand side of Equation (1), the terms m_{pq} and m_{qp} represent mass transfer terms, while S_q denotes the source term. By default, the source term is typically zero, but it can be adjusted based on user input.

Equation (2) introduces the momentum equation solved for the Eulerian model, incorporating the interphase relations.

$$\begin{array}{c}\left(\alpha_q \rho_q \vec{u}_q\right) + \nabla\left(\alpha_q \rho_q \vec{u}_q^{\,2}\right) = -\alpha_q \nabla p + \nabla \cdot \tau_q + \alpha_q \rho_q \vec{g} + \\ \sum_{p=1}^{n}\left(K_{pq}\left(\vec{u}_p - \vec{u}_q\right) + m_{pq}\vec{u}_{pq} - m_{qp}\vec{u}_{qp}\right) + \\ \left(\vec{F}_q + \vec{F}_{lift,q} + \vec{F}_{wl,q} + \vec{F}_{vm,q} + \vec{F}_{td,q}\right)\end{array} \quad (2)$$

On the right-hand side of Equation (2), the first three terms relate to pressure, friction, and buoyancy forces, respectively. Subsequently, drag forces are accounted for in terms of interfacial and mass transfer forces. In the last part of the equation, various non-drag forces are included. As depicted, the momentum equation comprehensively addresses interphase momentum exchange and bubble interactions, incorporating various non-drag terms such as external forces (F_q), lift ($F_{lift,q}$), wall lubrication ($F_{wl,q}$), virtual mass ($F_{vm,q}$), and turbulent dispersion ($F_{td,q}$) forces. These interactions are elaborated upon in detail in the following section.

- Interphase Momentum Exchange Relations

The Eulerian approach is particularly suitable for situations where detailed insights into phase interactions are essential. Known for its robustness and computational efficiency [35], it has been widely employed across diverse applications, demonstrating its capability to accurately capture the complexities of interphase relations [36].

Interphase relations in two-phase flows are categorized under drag and non-drag forces and are critical for modeling the dynamics and behavior of complex systems. Drag forces, resulting from the relative motion between phases, play a significant role in shaping the distribution, dispersion, and mixing of phases within the flow domain. These forces are typically classified based on flow conditions and phase properties, with factors such as viscosity and bubble size influencing their strength. The magnitude of drag force is notably affected by the shape and interfacial area of the dispersed phase. For our analysis, we adopted the Tomiyama drag model [37], which is well-suited for accommodating various bubble sizes and shapes and is commonly utilized in the literature.

Non-drag forces, on the other hand, introduce additional complexity to the system and include lift, wall lubrication, virtual mass, and turbulent dispersion forces. Lift forces, for instance, can induce the ascent of gas bubbles or descent of liquid droplets, while surface-tension-related forces like wall lubrication tend to minimize interface surface area, impacting phenomena such as droplet formation and coalescence. In our study, we incorporated the Hosokawa et al. model [38] for wall lubrication, the Tomiyama et al. [37] lift model for lift forces, the Drew et al. [39] model for virtual mass forces, and the Bertodano model [40] for turbulent dispersion forces to accurately capture bubble interactions as non-drag forces.

2.3.2. Numerical Setup

Numerical modeling of the two-phase flow was carried out utilizing ANSYS Fluent (v19.R3) in this study. Following the import of the solid model and the provision of the appropriate mesh structure, the Fluent module was employed for flow analysis.

The multiphase solver selected is the Eulerian method solver, as described previously. In this setup, water is defined as the primary phase, while air is defined as the secondary phase. The specifications for both phases are outlined in Tables 1 and 2, as previously addressed.

For discretization, a cell-based least squares method was selected for pressure, offering advantages in convergence and accuracy, particularly with unstructured meshes. Conversely, a first-order upwind discretization scheme was employed for pressure, momentum, turbulent kinetic energy, and turbulent dissipation rate.

Furthermore, pressure–velocity coupling played a crucial role in modeling the interaction between pressure and velocity fields. Algorithms were utilized to ensure that the changes in pressure affected velocity, adhering to the continuity equation. In this context, the phase-coupled option was utilized, allowing the velocities of each phase to be independently solved based on the respective pressures.

As far as turbulence is concerned, the realizable k–ε turbulence model was employed, which is known for its ability to accurately predict turbulent characteristics and flow behavior in complex scenarios while maintaining lower computational loads and high calculation accuracy [41].

In transient simulations, the timestep is set to 1×10^{-4} s (0.1 ms), which is in line with the experimental acquisition time determined using the Nyquist sampling theorem. Further details on the sampling rate investigation can be found in [10,30]. The simulation is run over an extended flow time, with local two-phase results saved as an output file for each timestep. Cell Courant numbers are maintained below 1.0 throughout the simulation, averaging between 0.6 and 0.8.

3. Results and Discussion

The numerical results are presented in terms of local air void fraction (α_{air}) and phase velocities.

3.1. Local Air Void Fraction

The air void fraction (α_{air}) is determined locally for all points in the flow domain of the developed numerical model. The rendering of air volume fraction in the flow domain was plotted within the range of 0.00–1.00 (or 0–100% as a percentage) for visualization. Figure 3 illustrates the air volume fraction rendered for different airflow rates in our study. In the figure, the transparent sections represent the water phase ($\alpha_{air} = 0$), while the opaque sections ($\alpha_{air} > 0$) depict the air phase and the corresponding air void fraction.

As depicted in Figure 3, similar flow types and regimes are observed for all three airflow rates. These results align closely with the flow map regimes discussed in the earlier sections and corroborate the experimental findings and observations. Notably, the injected bubbles in the circumferential direction complete their horizontal development along the upstream section. The gas phase is notably concentrated in the vertical upper diameter of the pipe, forming extended air chords, signifying the completion of flow development by the end of the upstream. This configuration characterizes a distinct plug flow regime. Upon entering the first 90-degree bend from horizontal to vertical orientation, these elongated air chords fragment into individual slugs, also known as Taylor bubbles. This breakup phenomenon primarily originates from the bend's effect, which generates higher centripetal forces at the outer radius compared to the inner radius, leading to bubble fragmentation post-bend, as noted by Qiao et al. [22]. Consequently, bubble breakup in the curvature direction becomes more pronounced at elevated gas flow rates, aligning with observations from the previous literature [18]. Furthermore, the bubbles tend to migrate further toward the center of the pipe as the airflow rate increases. The cross-sectional average void fractions corresponding to the present airflow rates were measured at 12.7%, 18.0%, and 22.7%, respectively.

After the initial 90-degree bend, the flow advances through a straight 200 mm riser section before reaching the 180-degree U-bend, as detailed in the geometry section. In this part of the flow, the presence of Taylor bubbles becomes notably pronounced. The liquid phase covers the entire outer wall, while the gas phase occupies the inner center, creating a local annular flow pattern. This observation holds practical significance, especially in heat transfer applications, where it can enhance heat transfer to the liquid phase along the outer wall and optimize heat exchanger designs.

As the downward vertical movement commences after the U-bend, the influence of body forces acting on the phases becomes significantly more pronounced in this section. In the downward segment, buoyancy forces act opposite to the flow direction for the gas

phase. Consequently, the body forces in this region cause the liquid phase to concentrate towards the outer curvature diameter, resulting in the capture of air bubbles between the accelerating liquid phase and the inner wall of the pipe. This phenomenon leads to higher void fractions of the accumulated gas phase. However, it is observed that the effect of gas phase accumulation can be mitigated by increasing the airflow rate. The maximum local void fraction at the outer radius was found to be 82%, 81%, and 78% for 30, 35, and 40 L/min airflow rates, respectively.

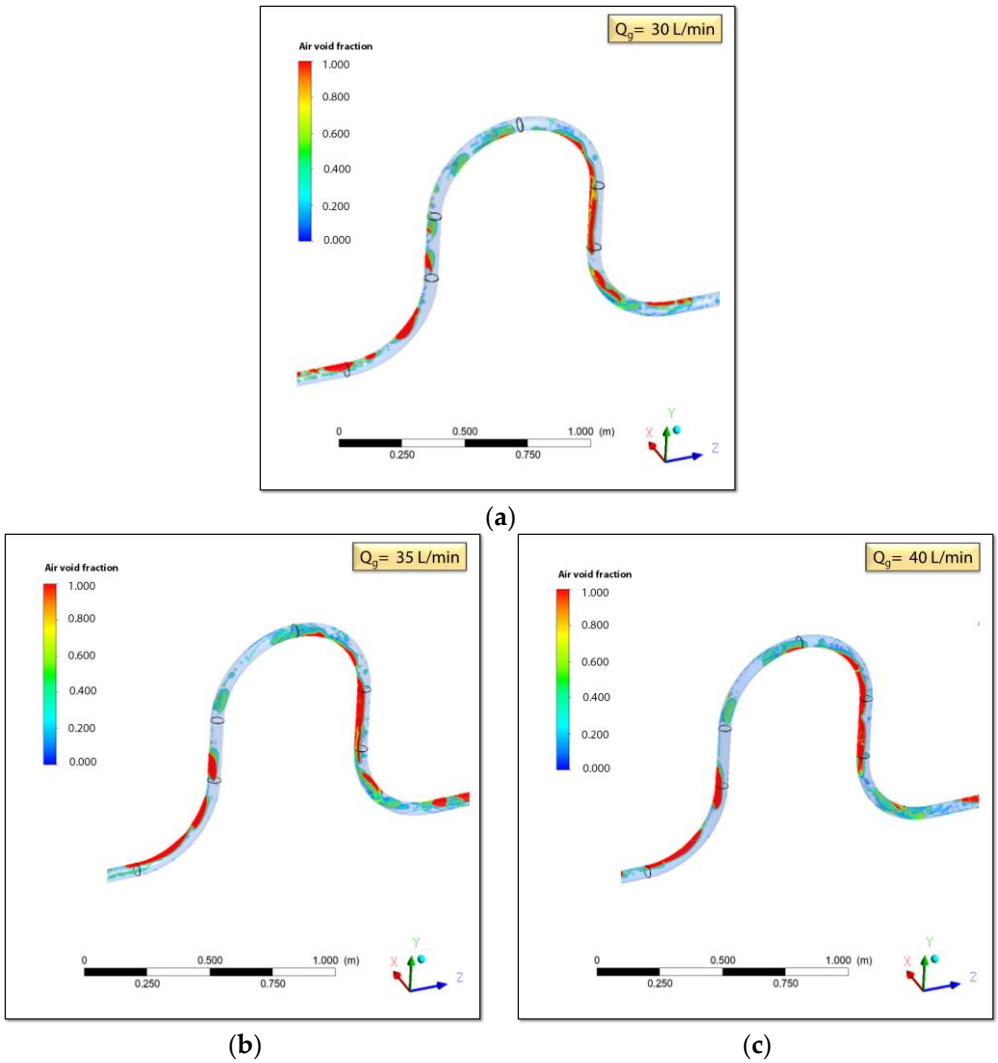

Figure 3. Volume rendered local void fractions of U-bend for (**a**) 30 L/min, (**b**) 35 L/min, and (**c**) 40 L/min airflow rates.

A turbulence effect is observed following the final 90-degree bend, leading to a local transition to churn flow after the last elbow. This transition is attributed to the increased water velocity impacting the bottom of the wall and the centrifugal effect generated by the elbow. However, it is noteworthy that the bubbles clustered once again in the upper section, resembling plugs, and the effects of turbulence diminished significantly in the downstream section.

3.2. Phase Velocity

Since the Eulerian–Eulerian model, based on separated flow theory, is utilized for the multiphase model, the phase velocity equations are solved independently for air and water. Hence, the phase velocities are determined separately throughout the flow domain in the

numerical model. Consequently, the velocities of the air and water phases in the U-bend domain were visualized using volume rendering. Figures 4 and 5 show the water and air phase velocity contours in the U-bend for the parametric airflow rates, respectively.

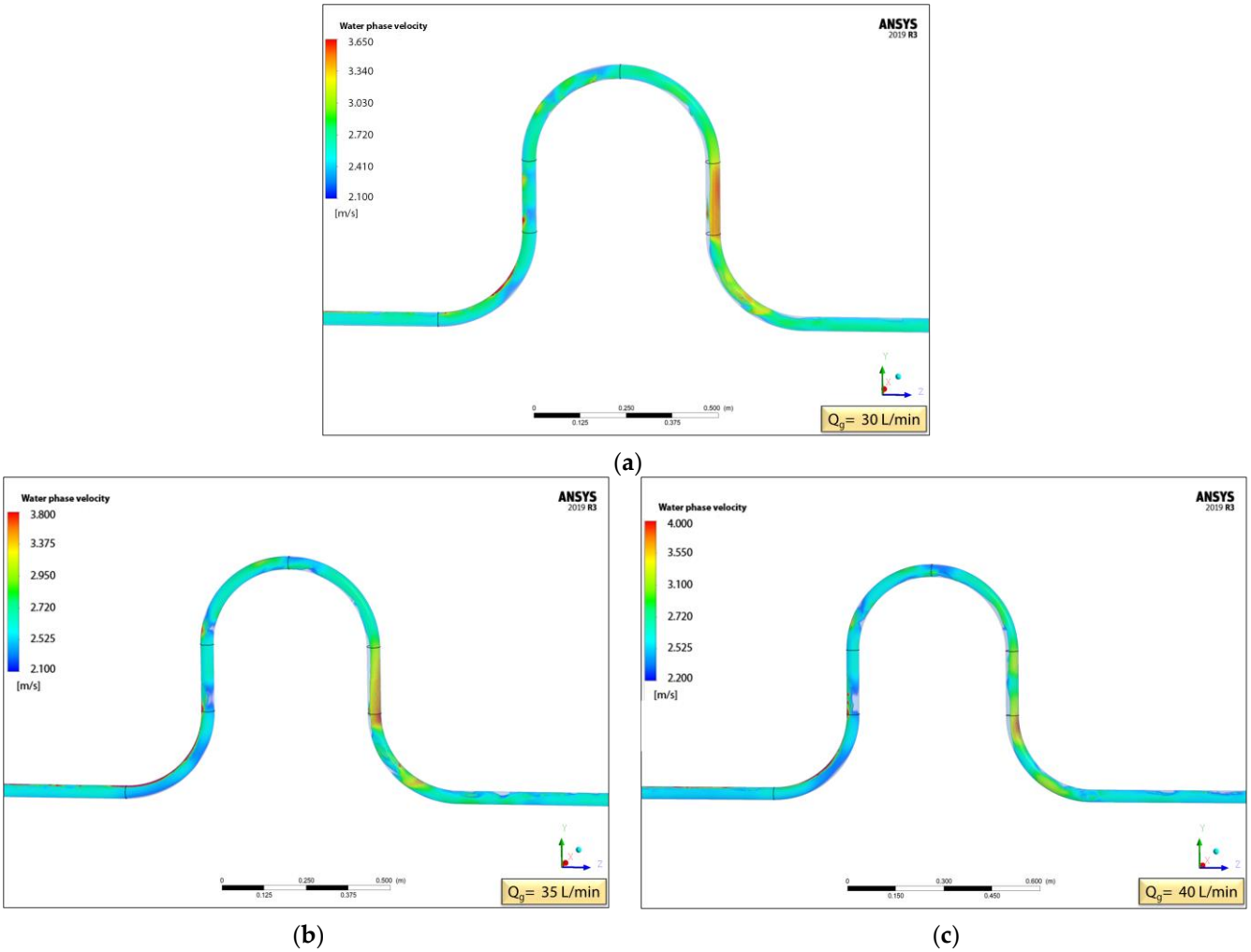

Figure 4. Volume rendered local water phase velocities in U-bend for (**a**) 30 L/min, (**b**) 35 L/min, and (**c**) 40 L/min airflow rates.

In the vertical upward flow, the local water phase velocity decreases to 2.1 to 2.2 m/s for airflow rates of 30, 35, and 40 L/min, owing to the influence of body forces on the water phase. Conversely, the local air velocity increases to approximately 4.0–4.5 m/s due to buoyancy forces acting on the Taylor bubbles.

At the first upward bend, the average local bubble velocities at the outer radius are locally found to be 3.1 m/s for 30 L/min, 4.1 m/s for 35 L/min, and 4.5 m/s for 40 L/min. This observation underscores the substantial impact of the volumetric airflow rate on the phase velocities in the upward flow. Conversely, the water phase velocity is significantly reduced in the upward flow due to body forces acting on the water phase. Accordingly, the local average phase velocities are found to be between 2.5 and 2.7 m/s.

Upon examining the downward vertical flow, it is observed that the local water phase velocities increase up to 3.7 m/s. As indicated by the local void fraction results, air bubbles are trapped between the accelerating liquid phase and the inner wall of the pipe in the downward flow. Consequently, Figures 4 and 5 demonstrate that the water phase is accelerated, particularly in the 200 mm straight section of the downward flow, as the trapped air restricts the cross-sectional area of the pipe. Investigation into the local velocity of the air phase in the downward direction reveals a stagnation point in the pipe sections

of the inner radius where air is trapped, while in the pipe sections of the outer radius, a few bubbles can be seen drifting with the flowing water. Additionally, turbulent flow is noticed at the very end of the U-bend.

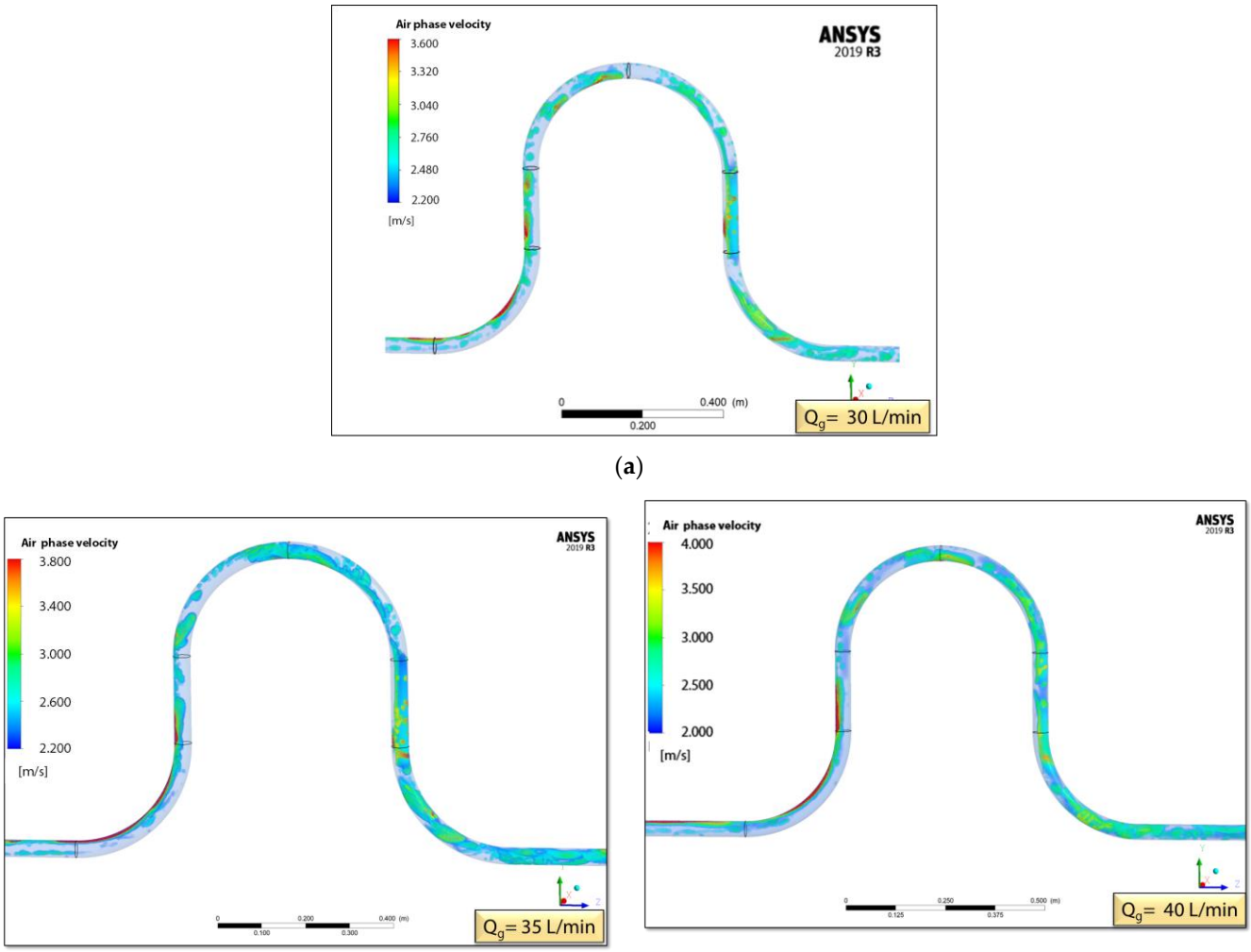

Figure 5. Volume rendered local air phase velocities in U-bend for (**a**) 30 L/min, (**b**) 35 L/min, and (**c**) 40 L/min airflow rates.

While the average cross-sectional velocity increases in the vertical upward segment due to the influence of buoyancy forces on the bubbles, the average velocities decrease in the 180-degree U-bend section due to bubble breakup from chord form and their migration towards the central section. In the last elbow, U-bend-4, the bubble velocities were notably reduced to below 2.0 m/s across the majority of the cross-section.

3.3. Validation of the Results

The computational results of the developed model are validated by comparing the numerical results obtained for an airflow rate of 30 L/min with the experimental data. The controlled experiments were conducted at Istanbul Technical University Hydraulics Laboratory under precisely the same conditions as those described in the numerical setup. The experimental setup layout and equipment are presented in Figure 6, which is addressed more comprehensively in our other studies [10].

On the water side, represented in the blue color in Figure 6, a magnetic-type flow meter was utilized to monitor the water volumetric flow rate, maintained at 180 L/min as specified in Table 1. The accuracy of the device is estimated at 0.5% of the reading, with

uncertainties up to ±0.48 and ±1.32 L/min [10]. On the other hand, for the air side, the volumetric airflow rate is measured by a rotameter with an accuracy of ±2.1 L/min and uncertainty levels ranging from ±2.12 to ±2.22 L/min.

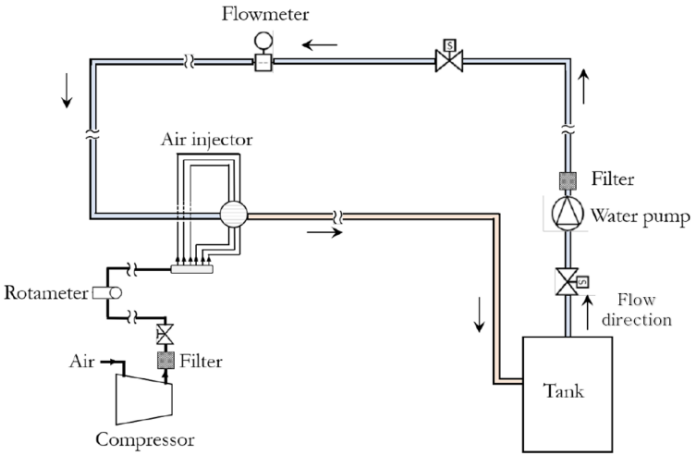

Figure 6. Experimental setup layout.

In the experiments, the local void fractions at six predefined measuring points within the test section, as depicted in Figure 1, were measured using an advanced optical probe over an extended duration. The uncertainty level associated with the optical probe measurements is evaluated as ±7% [10]. Figure 7 illustrates the axial development of void fractions for the predefined measuring points, comparing experimental and numerical results.

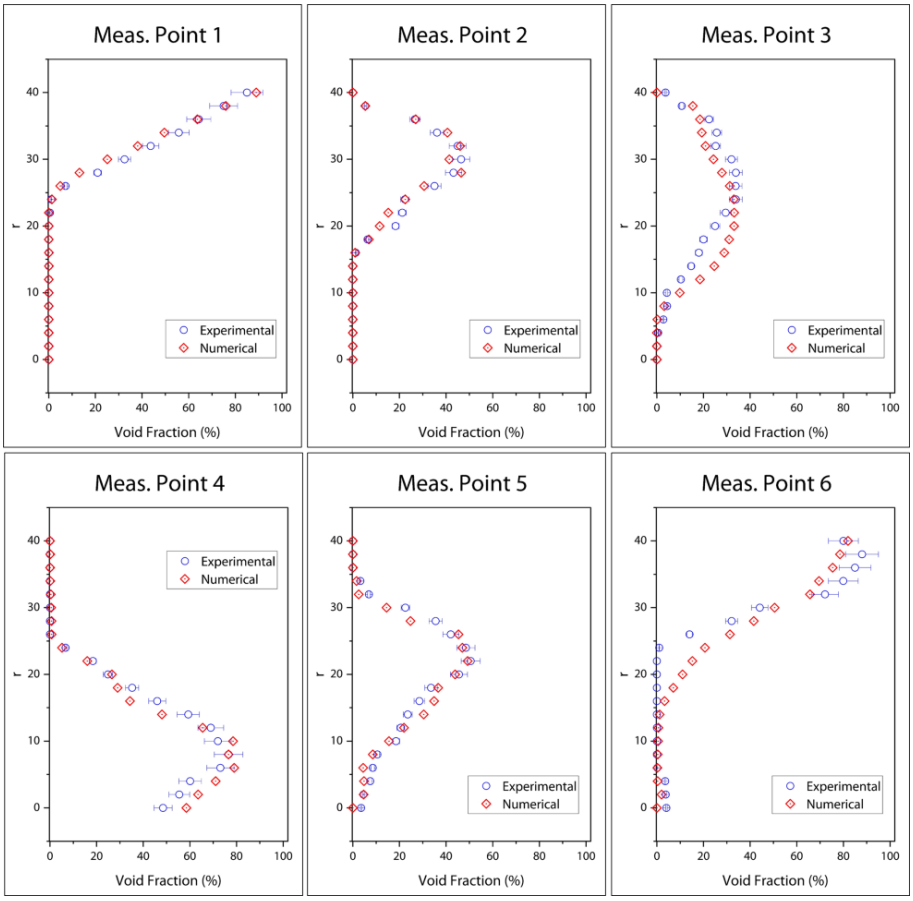

Figure 7. Validation of numerical results with experimental results.

The numerical data were obtained from the model by placing virtual probes at the same locations as the experimental measuring points. As depicted in the figures, the trends of the numerical and experimental results are similar, indicating good agreement between the two datasets.

4. Conclusions

Through our comprehensive investigation, this study provides valuable insights into the complex behavior of the air–water two-phase flow within a complete U-bend configuration, encompassing two horizontal-to-vertical 90-degree bends and one vertical 180-degree elbow. We were able to analyze the intricate interplay between drag and non-drag forces, shedding light on the dynamics of phase distribution and phase velocities within the U-bend by employing the Eulerian–Eulerian approach in our computational model. Our findings emphasize several key points:

- The observed flow patterns, including the development of plug flow, the formation of Taylor bubbles with local annular flow, and the transition to churn flow, underscore the significant influence of bend geometry and airflow rates on multiphase flow behavior.
- Bubbles form extended chords and elongated bubbles as plugs due to density variations in the upstream region. However, these chords break up upon entering the first vertical 90-degree bend, transitioning into single slugs or Taylor bubbles. This phenomenon is driven by the critical role of body forces and buoyancy effects on bubble interactions. Thus, employing interphase relations is significant in terms of computational accuracy.
- In the downward vertical flow, local water phase velocities accelerate, influenced by body forces. Taylor bubbles get trapped between the accelerating liquid phase and the inner wall, leading to significant air accumulation and a detected void fraction of 85% in the inner cross-section of the wall. However, it is found that the gas phase accumulation effect can be reduced by increasing the airflow rate. It may be worthwhile to consider increasing the flow rate of the gas phase to avoid air accumulations for practical applications, including such U-bends.
- A turbulence effect, leading to a local transition to churn flow, is observed after the last elbow, driven by increased water velocity impacting the bottom of the wall and the centrifugal effect of the elbow. However, bubble clustering reoccurs in the upper section, resembling plugs, and turbulence effects diminish in the downstream section.
- The Eulerian–Eulerian approach (separated flow theory) yields reasonable results to predict the flow characteristics of air–water flow in elbows, as appropriate sub-models for phase interactions are employed.

The results presented in this study provide implications for future applications and assist further studies that can address the findings for different piping systems and elbows commonly used in practical applications in the industry under various design conditions. The validation of our numerical model against the experimental data reaffirms its reliability and applicability in practical engineering scenarios. Further investigations will aim to explore pressure-drop relations to extend this advanced multiphase flow research in such complex geometries.

Author Contributions: Methodology, E.K. and N.E.; supervision, N.E.; software, E.K.; validation, E.K.; formal analysis, E.K. and N.E.; investigation, E.K. and N.E.; resources, E.K. and N.E.; data curation, E.K. and N.E.; writing—original draft preparation, E.K.; writing—review and editing, E.K. and N.E.; visualization, E.K. All authors have read and agreed to the published version of the manuscript.

Funding: This paper is produced based on the Ph.D. dissertation and supported by the Research Fund of the Istanbul Technical University under project number: 42451.

Data Availability Statement: The data presented in this study are available on reasonable requests from the corresponding author.

Conflicts of Interest: The authors declare no conflicts of interest.

References

1. Miwa, S.; Hibiki, T. Inverted Annular Two-Phase Flow in Multiphase Flow Systems. *Int. J. Heat Mass Transf.* **2022**, *186*, 122340. [CrossRef]
2. Khasawneh, K.; Moon, J.; Ko, Y.; Jeong, J.J.; Yun, B. Experimental Study on Local Droplet Parameters in a Deformed 2 × 2 Rod Bundle under Air-Water Annular-Mist Flow. *Int. J. Multiph. Flow* **2023**, *160*, 104374. [CrossRef]
3. Li, C.; Zhu, Y.; Wang, J.; Liu, W.; Fang, L.; Zhao, N. Mass Flow Rate Measurement of Gas-Liquid Two-Phase Flow Using Acoustic-Optical-Venturi Mutisensors. *Flow Meas. Instrum.* **2023**, *90*, 102314. [CrossRef]
4. Figueiredo, M.M.F.; Goncalves, J.L.; Nakashima, A.M.V.; Fileti, A.M.F.; Carvalho, R.D.M. The Use of an Ultrasonic Technique and Neural Networks for Identification of the Flow Pattern and Measurement of the Gas Volume Fraction in Multiphase Flows. *Exp. Therm. Fluid Sci.* **2016**, *70*, 29–50. [CrossRef]
5. Hansen, L.S.; Pedersen, S.; Durdevic, P. Multi-Phase Flow Metering in Offshore Oil and Gas Transportation Pipelines: Trends and Perspectives. *Sensors* **2019**, *19*, 2184. [CrossRef]
6. Dollet, B.; Marmottant, P.; Garbin, V. Bubble Dynamics in Soft and Biological Matter. *Annu. Rev. Fluid Mech.* **2019**, *51*, 331–355. [CrossRef]
7. Xu, Y.; Wang, L.; Wang, Y.; Qian, Y.; Wang, H.; Xu, Y.; Yang, X. Gas-Liquid Flow Pattern Identification and Bubble Characteristics Analysis in a Static Mixer Based HiPOxTM Reactor. *Chem. Eng. Sci.* **2023**, *267*, 118269. [CrossRef]
8. Başaran, A. Experimental Investigation of R600a as a Low GWP Substitute to R134a in the Closed-Loop Two-Phase Thermosyphon of the Mini Thermoelectric Refrigerator. *Appl. Therm. Eng.* **2022**, *211*, 11850. [CrossRef]
9. Zade, S.; Costa, P.; Fornari, W.; Lundell, F.; Brandt, L. Experimental Investigation of Turbulent Suspensions of Spherical Particles in a Square Duct. *J. Fluid Mech.* **2018**, *857*, 748–783. [CrossRef]
10. Kükrer, E.; Eskin, N. Experimental Assessment of Local Void Fraction and Flow Development in a U-Bend Piping System for Air-Water Two-Phase Flow. *Int. J. Multiph. Flow* **2023**, *169*, 104610. [CrossRef]
11. Cao, Z.; Zhang, H.; Mei, H.; Yan, G.; Chu, W.; Wang, Q. Numerical Study on R32 Flow Condensation in Horizontally Oriented Tubes with U-Bends. *Energies* **2022**, *15*, 4799. [CrossRef]
12. Croquer, S.; Vieiro, J.; Chacon, C.; Asuaje, M. CFD Multi-Phase Flow Analysis Across Diverging Manifolds: Application in the Oil-Gas Industry. In Proceedings of the ASME 2014 International Mechanical Engineering Congress and Exposition, Montreal, QC, Canada, 14–20 November 2014; ASME: Montreal, QC, Canada, 2014.
13. Vist, S.; Pettersen, J. Two-Phase Flow Distribution in Compact Heat Exchanger Manifolds. *Exp. Therm. Fluid Sci.* **2004**, *28*, 209–215. [CrossRef]
14. Dong, W.; Yao, L.; Luo, W. Numerical Simulation of Flow Field of Submerged Angular Cavitation Nozzle. *Appl. Sci.* **2023**, *13*, 613. [CrossRef]
15. Deniz, E.; Eskin, N. Hydrodynamic Characteristics of Two-Phase Flow through Horizontal Pipe Having Smooth Expansion. *J. Therm. Sci. Technol.* **2015**, *35*, 1–9.
16. Zahedi, R.; Babaee Rad, A. Numerical and Experimental Simulation of Gas-Liquid Two-Phase Flow in 90-Degree Elbow. *Alexandria Eng. J.* **2021**, *61*, 2536–2550. [CrossRef]
17. Kim, S.; Park, J.H.; Kojasoy, G.; Kelly, J.M.; Marshall, S.O. Geometric Effects of 90-Degree Elbow in the Development of Interfacial Structures in Horizontal Bubbly Flow. *Nucl. Eng. Des.* **2007**, *237*, 2105–2113. [CrossRef]
18. Dutta, P.; Saha, S.K.; Nandi, N.; Pal, N. Numerical Study on Flow Separation in 90° Pipe Bend under High Reynolds Number by K-ε Modelling. *Eng. Sci. Technol. Int. J.* **2016**, *19*, 904–910. [CrossRef]
19. Mazumder, Q.H.; Siddique, S.A. CFD Analysis of Two-Phase Flow Characteristics in a 90 Degree Elbow. *J. Comput. Multiph. Flows* **2011**, *3*, 165–175. [CrossRef]
20. Aung, N.Z.; Yuwono, T. Computational Fluid Dynamics Simulations of Gas-Liquid Two-Phase Flow Characteristics through a Vertical to Horizontal Right Angled Elbow. *ASEAN J. Sci. Technol. Dev.* **2013**, *30*, 1–16. [CrossRef]
21. Abhari, M.N.; Ghodsian, M.; Vaghefi, M.; Panahpur, N. Experimental and Numerical Simulation of Flow in a 90° bend. *Flow Meas. Instrum.* **2010**, *21*, 292–298. [CrossRef]
22. Qiao, S.; Zhong, W.; Wang, S.; Sun, L.; Tan, S. Numerical Simulation of Single and Two-Phase Flow across 90° Vertical Elbows. *Chem. Eng. Sci.* **2021**, *230*, 116185. [CrossRef]
23. Sharma, M.; Ravi, P.; Ghosh, S.; Das, G.; Das, P.K. Hydrodynamics of Lube Oil-Water Flow through 180° Return Bends. *Chem. Eng. Sci.* **2011**, *66*, 4468–4476. [CrossRef]
24. El-Behery, S.M.; Hamed, M.H.; El-Kadi, M.A.; Ibrahim, K.A. CFD Prediction of Air-Solid Flow in 180° Curved Duct. *Powder Technol.* **2009**, *191*, 130–142. [CrossRef]
25. De Oliveira, P.M.; Barbosa, J.R. Pressure Drop and Gas Holdup in Air-Water Flow in 180° Return Bends. *Int. J. Multiph. Flow* **2014**, *61*, 83–93. [CrossRef]

26. Dhanasekaran, T.S.; Wang, T. Numerical Model Validation and Prediction of Mist/Steam Cooling in a 180-Degree Bend Tube. *Int. J. Heat Mass Transf.* **2012**, *55*, 3818–3828. [CrossRef]
27. Domanski, P.A.; Hermes, C.J.L. An Improved Correlation for Two-Phase Pressure Drop of R-22 and R-410A in 180° Return Bends. *Appl. Therm. Eng.* **2008**, *28*, 793–800. [CrossRef]
28. Aliyu, A.M.; Almabrok, A.A.; Baba, Y.D.; Lao, L.; Yeung, H.; Kim, K.C. Upward Gas–Liquid Two-Phase Flow after a U-Bend in a Large-Diameter Serpentine Pipe. *Int. J. Heat Mass Transf.* **2017**, *108*, 784–800. [CrossRef]
29. Kükrer, E.; Eskin, N. Transient Computational Fluid Dynamics Modeling of Air-Water Two-Phase Flow for Elbows. In *Lecture Notes in Mechanical Engineering*; Springer: Berlin/Heidelberg, Germany, 2024.
30. Kükrer, E. *Analysis of Non-Boiling Gas-Liquid Two-Phase Flow through Flow Components: Experimental Investigation and Numerical Modelling*; Istanbul Technical University (ITU): Istanbul, Turkey, 2023.
31. Almabrok, A.A.; Aliyu, A.M.; Baba, Y.D.; Lao, L.; Yeung, H. Void Fraction Development in Gas-Liquid Flow after a U-Bend in a Vertically Upwards Serpentine-Configuration Large-Diameter Pipe. *Heat Mass Transf.* **2018**, *54*, 209–226. [CrossRef]
32. Dassler, C.; Janoske, U. Experimental Investigation of Single- and Two-Phase Pressure Drop in Slender Rectangular 180° Return Bends. *Exp. Therm. Fluid Sci.* **2019**, *103*, 126–132. [CrossRef]
33. Antepara, O.; Balcázar, N.; Oliva, A. Tetrahedral Adaptive Mesh Refinement for Two-Phase Flows Using Conservative Level-Set Method. *Int. J. Numer. Methods Fluids* **2021**, *93*, 481–503. [CrossRef]
34. Kunii, D.; Levenspiel, O. *Fluidization Engineering*, 2nd ed.; Butterworth–Heinemann: Oxford, UK, 1991; ISBN 978-0-08-050664-7.
35. Benim, A.C.; Deniz Canal, C.; Boke, Y.E. Computational Investigation of Oxy-Combustion of Pulverized Coal and Biomass in a Swirl Burner. *Energy* **2022**, *238*, 121852. [CrossRef]
36. Wu, Y.; Liu, D.; Ma, J.; Chen, X. Three-Dimensional Eulerian–Eulerian Simulation of Coal Combustion under Air Atmosphere in a Circulating Fluidized Bed Combustor. *Energy Fuels* **2017**, *31*, 7952–7966. [CrossRef]
37. Tomiyama, A. Struggle with Computational Bubble Dynamics. *Multiph. Sci. Technol.* **1998**, *10*, 369–405. [CrossRef]
38. Hosokawa, S.; Tomiyama, A.; Misaki, S.; Hamada, T. Lateral Migration of Single Bubbles Due to the Presence of Wall. In Proceedings of the American Society of Mechanical Engineers, Fluids Engineering Division, Montreal, QC, Canada, 14–18 July 2002; FED: Montreal, QC, Canada, 2002; Volume 257.
39. Drew, D.; Cheng, L.; Lahey, R.T. The Analysis of Virtual Mass Effects in Two-Phase Flow. *Int. J. Multiph. Flow* **1979**, *5*, 233–242. [CrossRef]
40. Lopez de Bertodano, M.A. Two Fluid Model for Two-Phase Turbulent Jets. *Nucl. Eng. Des.* **1998**, *179*, 65–74. [CrossRef]
41. Wang, W.; Sun, Y.; Wang, B.; Dong, M.; Chen, Y. CFD-Based Erosion and Corrosion Modeling of a Pipeline with CO_2-Containing Gas–Water Two-Phase Flow. *Energies* **2022**, *15*, 1694. [CrossRef]

computation

MDPI

Article

Computational Fluid Dynamics Analysis of Varied Cross-Sectional Areas in Sleep Apnea Individuals across Diverse Situations

W. M. Faizal *, C. Y. Khor, Suhaimi Shahrin, M. H. M. Hazwan, M. Ahmad, M. N. Misbah and A. H. M. Haidiezul

Faculty of Mechanical Engineering & Technology, University Malaysia Perlis, 02600 Arau, Perlis, Malaysia; cykhor@unimap.edu.my (C.Y.K.); suhaimishahrin@unimap.edu.my (S.S.); hazwanhanid@unimap.edu.my (M.H.M.H.); masniezam@unimap.edu.my (M.A.); mnur@unimap.edu.my (M.N.M.); haidiezul@unimap.edu.my (A.H.M.H.)

* Correspondence: wanmohd@unimap.edu.my; Tel.: +60-124-524-518

Abstract: Obstructive sleep apnea (OSA) is a common medical condition that impacts a significant portion of the population. To better understand this condition, research has been conducted on inhaling and exhaling breathing airflow parameters in patients with obstructive sleep apnea. A steady-state Reynolds-averaged Navier–Stokes (RANS) approach and an SST turbulence model have been utilized to simulate the upper airway airflow. A 3D airway model has been created using advanced software such as the Materialize Interactive Medical Image Control System (MIMICS) and ANSYS. The aim of the research was to fill this gap by conducting a detailed computational fluid dynamics (CFD) analysis to investigate the influence of cross-sectional areas on airflow characteristics during inhale and exhale breathing in OSA patients. The lack of detailed understanding of how the cross-sectional area of the airways affects OSA patients and the airflow dynamics in the upper airway is the primary problem addressed by this research. The simulations revealed that the cross-sectional area of the airway has a notable impact on velocity, Reynolds number, and turbulent kinetic energy (TKE). TKE, which measures turbulence flow in different breathing scenarios among patients, could potentially be utilized to assess the severity of obstructive sleep apnea (OSA). This research found a vital correlation between maximum pharyngeal turbulent kinetic energy (TKE) and cross-sectional areas in OSA patients, with a variance of 29.47%. Reduced cross-sectional area may result in a significant TKE rise of roughly 10.28% during inspiration and 10.18% during expiration.

Keywords: CFD; breathing disorders; turbulent kinetic energy; obstructive sleep apnea; real patient

Citation: Faizal, W.M.; Khor, C.Y.; Shahrin, S.; Hazwan, M.H.M.; Ahmad, M.; Misbah, M.N.; Haidiezul, A.H.M. Computational Fluid Dynamics Analysis of Varied Cross-Sectional Areas in Sleep Apnea Individuals across Diverse Situations. *Computation* **2024**, *12*, 16. https://doi.org/10.3390/computation12010016

Academic Editors: Ali Cemal Benim, Rachid Bennacer, Abdulmajeed A. Mohamad, Paweł Oclon, Sang-Ho Suh and Jan Taler

Received: 10 December 2023
Revised: 12 January 2024
Accepted: 12 January 2024
Published: 17 January 2024

1. Introduction

Obstructive sleep apnea (OSA) substantially impacts the sleep quality of affected individuals. In recent times, scholars have directed their attention toward exploring the influence of body characteristics on this condition and its effects on individuals with OSA. Their studies have shed light on the importance of considering various body characteristics in comprehending the phenomenon of OSA. Wang et al. [1] discovered that the weight of a patient contributes significantly to the occurrence and impact of OSA. These findings were the same as those of Tham [2], who demonstrated that obesity significantly contributes to the onset and development of obstructive sleep apnea (OSA). Nonetheless, notable enhancements in managing obstructive sleep apnea (OSA) can be achieved by promoting substantial weight loss within the range of approximately 7% to 11%. In the case of neonates, the underdeveloped nature of their nasal cavity significantly influences the configuration of their airways. More precisely, the lack of an inferior meatus in neonates hinders airflow through the inferior regions, resulting in an uneven distribution of airflow [3]. Modena et al. [4] discovered that even slight changes in hip-to-waist ratio, neck circumference, and body mass

index (BMI) can impact the likelihood of developing obstructive sleep apnea syndrome (OSAS). Higher values in these variables are associated with a greater risk of developing OSAS. While it is important to acknowledge the limitations in published studies, it has been shown that behavioral, pharmacological, and surgical interventions can facilitate weight loss, leading to improvements in the severity of OSAS, reversal of common comorbidities, and enhanced quality of life [5]. After weighing the evidence, feasibility, and acceptability of these interventions, the expert panel strongly advised implementing a comprehensive lifestyle intervention for individuals with obstructive sleep apnea (OSA) who are overweight or obese. This intervention should encompass (1) adoption of a low-calorie diet [6], (2) engagement in exercise or increased physical activity [7], and (3) receiving behavioral guidance [8]. This holistic approach aims to address various aspects of lifestyle to enhance overall well-being and manage the specific challenges associated with OSA in individuals with higher body weight. Managing weight loss is suggested through potential strategies such as increasing physical activity through exercise and adopting a reduced-calorie diet. However, implementing these approaches is contingent upon the individual's specific circumstances. In some instances, pharmacological therapy or bariatric surgery may be considered appropriate options for patients requiring additional assistance with weight loss [9]. In inpatient populations, the upper airway length tends to be longer. It exhibits a robust correlation with body weight. An increase in body weight results in significant fat infiltration within the tongue, inducing the downward movement of the hyoid. This situation, in turn, elongates the airway in affected individuals. The correlation between the apnea–hypopnea index (AHI) and the airway length, along with the size of the tongue, is prominently evident [10]. Unexpectedly, there are substantial distinctions between healthy males and patients in terms of both the distance parameter "h" and the angle near the occipital bone. These variations arise from the diverse backward tilt angles, and both parameters exhibit a robust correlation with the AHI. In patients, the downward movement of the hyoid bone and the tilted head contribute to 67.4–80.5 percent and 19.5–32.6 percent of the lengthening of the airway. Furthermore, there is a strong correlation between the size of the parapharyngeal fat pad and the AHI [11].

As a result, the cross-sectional area's information about the cavity and airways may affect the severity of OSA in patients. Faizal et al. [12] recognize turbulent kinetic energy (TKE) as a valuable tool for understanding various medical disorders, including OSA. Turbulent kinetic energy (TKE) was employed to assess the state of turbulent flow within the upper airway and to compute the energy balance of the airflow. This measurement provides insights into turbulence and energy distribution characteristics within the airway system. Elevated turbulent kinetic energy (TKE) within the upper airway can lead to tissue vibration during breathing, potentially triggering sleep apnea. Moreover, TKE has been used to explore the airflow dynamics of the upper airway and anatomy, contributing to the development of virtual reality surgery for sleep-disordered breathing (SDB) [13].

Furthermore, airway stenosis reduces the airways' cross-sectional area by narrowing them, hindering airflow into the lungs. Various diseases can cause airway stenosis [14], such as infection, a chronic inflammatory disease [15], trauma, and cancer. The stenosis airway correction is typically achieved by endoscopic or open surgery to expand the lumen. Various factors, including individual anatomy, larynx and trachea functionality, patient-related considerations, and the availability of facilities, play a role in influencing the surgical procedure. In cases of airway stenosis, utilizing a 50 percent helium–oxygen mixture during high-frequency jet ventilation results in an 18 percent increase in minute volume. This increase is achieved with airway pressures equal to or lower than those generated using 100 percent oxygen [16]. Simulation analysis allows for a better understanding of the airflow patterns in airways affected by stenosis, particularly concerning various disease conditions [17]. Velocity profile and pressure drops are the popular parameters used in the simulation analysis. The particle distribution during the inhale and exhale breathing can also be visualized in the numerical method.

Examining the flow dynamics in the upper airway offers valuable insights for addressing sleep apnea and respiratory illnesses. Employing CFD simulations and particle image velocimetry experiments allows for visualizing the inhalation and exhalation flow patterns [18]. The "glottal jet" phenomenon is less apparent at higher flow rates, and the separation zone is smaller during inhalation. Nevertheless, the peak velocity observed was notably lower than the inhalation phase. The flow patterns in the tracheal region remained unchanged by the exhalation breathing modes [18]. Simulating the inhalation and exhalation patterns aids in visualizing and comprehending particle movement within the human airway. The nonstationary flow was represented by a steady flow, replacing the asymmetric cycle simulation. The volumetric flow rates encompassed maximum and average rates during inhalation [19]. Utilizing CFD simulation, with wall motion guided by magnetic resonance imaging, during both inhalation and exhalation offers novel perspectives on the authentic flow dynamics of breathing. The dynamic motion of the airway has the potential to generate physiologically realistic outcomes in the CFD simulation [20].

This study aims to explore turbulent airflow in the pharyngeal airway among individuals diagnosed with OSA, highlighting both inhalation and exhalation and examining the impact of cross-sectional areas in diverse OSA patients. To the best of the authors' knowledge, there is a notable absence of research concerning the influence of cross-sectional areas in various OSA patients. Hence, a notable research gap exists, especially in the simulation modeling analysis. Therefore, this study primarily explores body characteristics to comprehend the OSA phenomenon. However, it lacks the thorough investigation needed to elucidate the complexities of airflow, which is essential for a comprehensive understanding of OSA. The novelty of the research lies in its comprehensive airflow reaching the critical cross-sectional area. The TKE increase in the human upper airway (HUA) segment significantly surpassed other segments in the control scenario. The study revealed a strong correlation between maximum pharyngeal turbulent kinetic energy (TKE) and cross-sectional areas among patients with OSA.

2. Materials and Methods

In this investigation, a CFD simulation was performed to model the upper human airway, specifically customized to suit the characteristics of the study's subjects. The primary emphasis was on patients with OSA, considering the diverse cross-sectional areas of their upper airways. The objective was to examine the airflow patterns during both inhalation and exhalation. The three-dimensional HUA simulation models were created based on the CT-Scan data. ANSYS Fluent was utilized in the CFD simulation to create mesh elements, model the flow behavior, and define the boundary conditions. The grid sensitivity test was carried out to ensure that there was no grid effect on the simulation model. The solver applied in the simulation was also compared with that of the previous study. A detailed discussion of the methodology is presented in the following subsections.

2.1. Subject

The HUA's specific geometry was extracted using volunteer OSA patient subjects based on data availability, as detailed in Table 1. Written informed consent was provided by patients, and the study adhered to the principles of the Declaration of Helsinki regarding research involving human subjects. The research was approved by the Universiti Malaysia Perlis Research Ethics Committee, Perlis, Malaysia, with the reference UniMAP/PTNC(P&I)/JKETIKA (10/11/2021). As shown in Figure 1, 431 frames with a slice thickness of 0.3 mm were used to scan the subject's upper airway using an i-CAT Cone Beam 3D Dental Imaging System (version 3.1.62 supplied by Imaging Science International, Hatfield, PA, USA). The description of the airway boundary is established by applying a threshold based on the intensity of the gray image in the CT scan images. As detailed in previous research, these images were acquired while the patient was in an awake position, lying down and facing upward, as described in the previous work [21]. Each CT scan comprises 534 pixels $\times$ 534 pixels, with a pixel spacing of 0.3 mm $\times$ 0.3 mm. These CT scan

images were stored in the Digital Imaging and Communications in Medicine (DICOM) format. Subsequently, these images were brought into the MIMICS software (version 15.0; Materialise, Leuven, Belgium), a three-dimensional (3D) medical image processing tool. The Hounsfield-unit-based image segmentation of the hypopharyngeal airway (HUA) was conducted on the DICOM image series to delineate the 3D airway region. Following this, the 3D volume of the pharyngeal airway was generated and exported to facilitate the creation of the 3D model mesh.

Table 1. General characteristics of OSA patient.

	Responder 1	**Responder 2**
Sex	Female	Male
Age (years)	33	44
BMI (kg/m^2)	28.5	25.42
OSA Level	12.5 (Mild)	27.1 (Moderate)

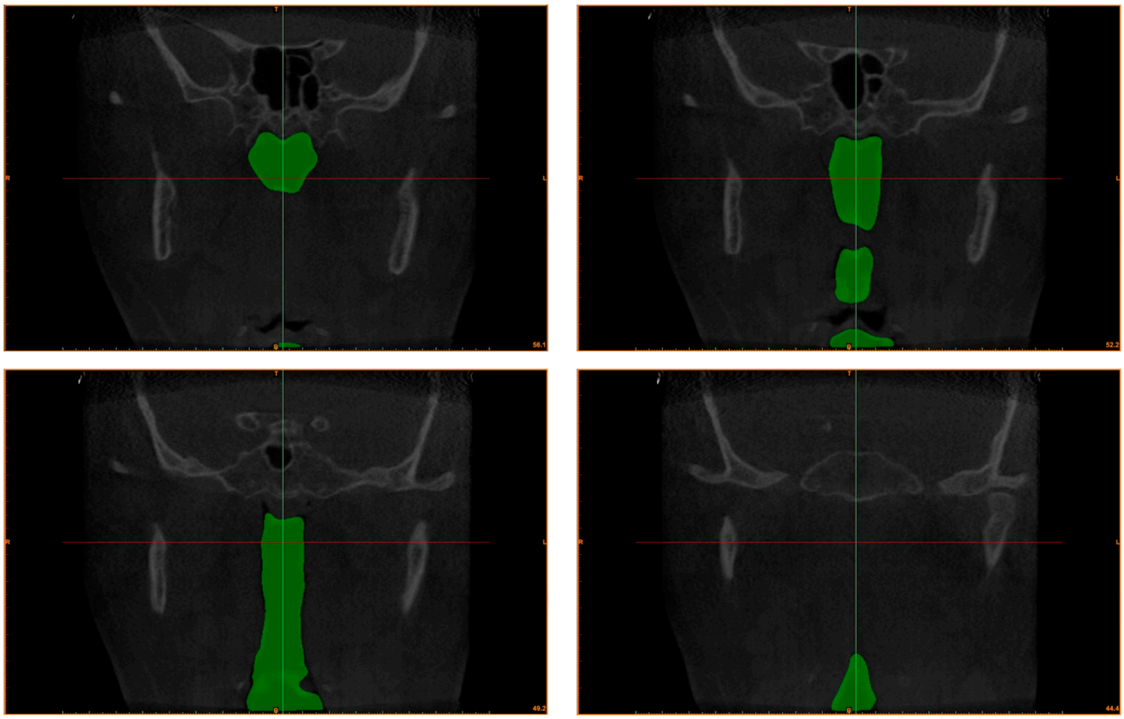

Figure 1. CT scan images of the OSA upper airway cavity.

The boundary conditions for the 3D model were established based on the model's surface, as indicated in Figure 2. The approach employed in this study integrates computational fluid dynamics (CFD) modeling with the segmentation of obtained computed tomography scans (CT scans). The CT scan image of the patient served as the foundation for creating the domain. The designated locations of P6 and P1 were employed to specify the inlet and outlet boundary conditions for inhalation to focus on the flow simulation. The model, initially created using MIMICS software, was then transferred to 3-Matic (version 15.0; Leuven, Belgium) to construct the airway's wall mesh. Afterwards, the preprocessor, ICEM (ANSYS Inc., Canonsburg, PA, USA), generated unstructured tetrahedral meshes for the airway volume. A similar meshing technique used in our previous work [12] was applied in the current study. The pharyngeal airway surfaces were meshed with a maximum face size of 2.0 mm. The mesh's size range spans from 2 mm to a minimum of 0.002 mm. Inflation was applied around the wall boundary of the pharyngeal airway mesh to enhance simulation accuracy. The y+ approach, which represents a dimensionless distance, was employed to estimate the initial thickness of the boundary layer. This esti-

mation corresponds to a near-wall cell size of 0.272, providing a measure of the proximity of the computational grid to the physical wall in the simulation. With a skewness value of 0.2142, indicating excellent cell quality within the recommended range of 0–0.25 by ANSYS, the mesh sensitivity grid study was conducted using various grid scales on the 3D airway model.

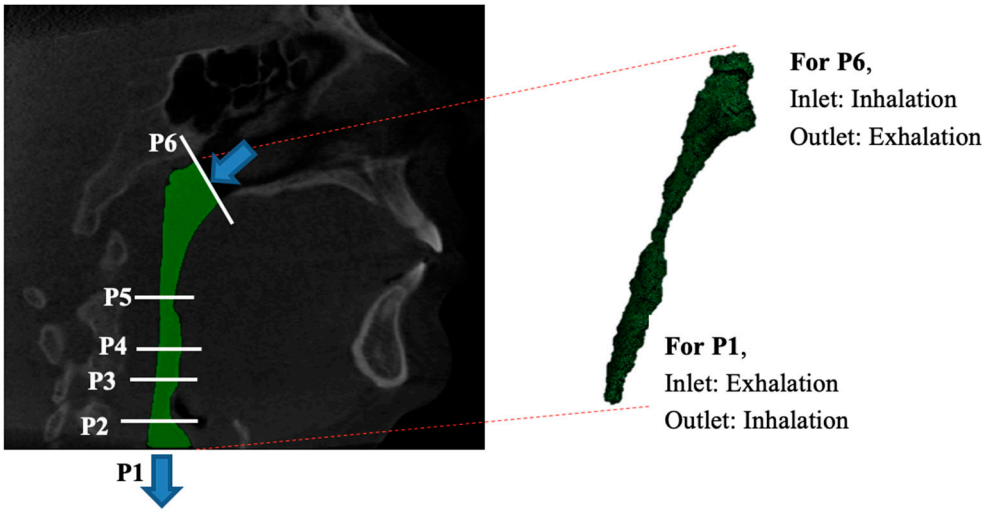

Figure 2. The lateral perspective of the meshed airway model of the upper airway. The CT scan's anatomically designated points, denoted as P1, P2, P3, P4, P5, and P6, correspond to specific locations: (P6) nasal choanae level; (P5) minimum cross-section area; (P4) tip of uvula; (P3 and P2) laryngopharynx; and (P1) base of epiglottis—representing the outlet of the computational fluid dynamics (CFD) model.

The steady-state turbulent model is the most established technique for modeling respiratory flows in the CFD analysis [22–24]. This study used ANSYS Fluent, which employs finite volume methods with fitted grids, to compute steady-state turbulent airflow in the airway. The assumption of a uniform velocity profile during breathing was made. The axial velocity was perpendicular to the flow inlet, specifically the nasopharynx [22,25]. Light breathing conditions were modeled at the inlet for both scenarios. The simulation incorporated a volume flow rate of 7.5 L/min [26]. The outlet was characterized by an average gauge pressure of 0 Pa, and a turbulent intensity of 10% was considered representative of the actual conditions [27].

Furthermore, the current study has limitations, such as considering the uniform breathing velocity. The airway geometry was scanned while the subject was awake and in an upright position. This study also excludes the sleep study, respiratory stage, and tongue control. The airway model was considered rigid in the simulation, and any influences stemming from soft tissue were ignored.

2.2. Numerical Modeling

The distinctive nature of the pharyngeal airway contributes to variations in airflow characteristics. Therefore, the simulation analysis employed a steady-state Reynolds-averaged Navier–Stokes (RANS) formulation, utilizing the k–ω shear stress transport (SST) turbulence model with low Reynolds number correction to compute the flow field in the pharyngeal airway for patients with obstructive sleep apnea (OSA). The popular k–ω SST turbulence model was considered in this work instead of the k–ϵ model due to the greater accuracy of the former in viscous near-wall region treatment while considering the effects of the adverse pressure gradient [28]. The SST model is recommended for high-accuracy boundary layer simulations, necessitating a very high grid resolution near the boundary [26]. The rigid model of the upper airway with a static wall was considered in the simulation without considering the fluid–structure interaction aspects. The assumption

of a rigid model helps explore the effect of airway narrowing on a deformable airway's performance [28].

The simulation analysis considered and solved the continuity equation (Equation (1)) and momentum equation (Equation (2)) to describe the motion of incompressible airflow. However, a minimal temperature change was observed in the airway during this study. Thus, the energy equation and gravitational force were neglected.

$$\nabla \vec{v} = 0 \tag{1}$$

$$\rho u_i \frac{\partial u_j}{\partial x_i} = -\frac{\partial P}{\partial x_i} + \frac{\partial}{\partial x_i}\left[\mu\left(\frac{\partial u_i}{\partial x_j} + \frac{\partial u_j}{\partial x_i}\right) - \rho\overline{u_i' u_j'}\right] \tag{2}$$

where u is the velocity, and i and j represents the Cartesian coordinates. An advection scheme employing a second-order upwind discretization scheme was selected. Convergence of results was deemed achieved when the residual level reached the predefined target of 1×10^{-6}.

2.3. TKE Model and Turbulent Reynolds Number

The Reynolds-averaged Navier–Stokes (RANS) equations describe the average flow field quantities over time in fluid dynamics, particularly turbulent flows. The turbulence closure problem in RANS involves introducing additional equations or models to account for the effects of turbulence.

$$u' = \sqrt{\frac{1}{N_i}\sum_{i=1}^{N}(u_i - \overline{u})^2} \tag{3}$$

where N represents the number of samples in the signal incorporated in the ANSYS simulation, and the equation for the fluctuation component is equally applicable to the velocity signals v and w. With these fluctuation components (u', v', and w'), it is then possible to model the TKE as:

$$\frac{\partial(\rho k)}{\partial t} + \frac{\partial(\rho u_j k)}{\partial x_j} = \frac{\partial}{\partial x_j}\left[\left(\mu + \frac{\mu_t}{\sigma_k}\right)\frac{\partial k}{\partial x_j}\right] - \rho\varepsilon + P_k - \beta^*\rho k \tag{4}$$

with density (ρ); turbulent kinetic energy (k), also known as TKE; fluctuation velocity (u_j); viscosity (μ); turbulent viscosity (μ_t); turbulent Prandtl number for k ((σ_k); dissipation rate of turbulent kinetic energy (ε); production of turbulent kinetic energy (P_k); turbulent kinetic energy dissipation constant (β^*). By employing this equation, the velocity fluctuation utilized in the computation of TKE around the HUA can aid in assessing the severity of breathing blockage within the HUA. In comparison, kinetic energy (KE) is defined as:

$$KE = \frac{1}{2}\rho\left(u^2 + v^2 + w^2\right) \tag{5}$$

where u, v, and w are the phase-averaged velocity. The definition of the turbulent Reynolds number, $\mathrm{Re_y}$, is shown in Equation (6):

$$Re_y = \frac{Kinectic\ Energy}{Work\ of\ friction} = \frac{KE}{W} \tag{6}$$

The balance of *KE* is given in Equation (5), while the work friction force, *W*, is given in Equation (7):

$$W = \iiint_v \tau_{ij} dV \tag{7}$$

where τ_{ij} represents the total shear stress component, encompassing both molecular and turbulent friction, acting on the surface of the integration volume, dV.

2.4. Grid Sensitivity and Solver Verification

A grid sensitivity test has been conducted to assess grid sensitivity before advancing to solver verification, varying the total number of elements. Five numbers of elements ranging from 371 k to 3.29 million for the Responder 1 model and 383 k to 4.77 million for the Responder 2 model were compared for the grid sensitivity test. The simulation result converged at 1.29 million elements for the Responder 1 model with a deviation of 0.25% compared to 3.29 million elements and for Responder 2 converged at 1.8 million elements with a deviation of 0.31% compared to 4.77 million elements, as shown in Figure 3. Thus, the 3D simulation model with 1.29 million and 1.8 million elements for model Responders 1 and 2, respectively, was considered in this study. The dimensionless normal distance between the wall (or airway surface) and the closest mesh cell in the viscous sublayer is represented by the wall unit (y+). The y+ value was less than 1 for all individuals over the domain. This situation was enough to resolve the mesh model near wall flow dynamics for Responders 1 and 2, which are 0.04223 and 0.04831, respectively. After this, the research underwent solver verification, a process detailed in our prior publication [29], as shown in Figure 4. Using the solver (RANS k−ω SST), the current results showed an almost similar trend to the previous experimental and simulation results as mentioned in Figure 4. Thus, the results indicated that the RANS k−ω SST solver is validated for the current study, and the prediction using this solver is reliable.

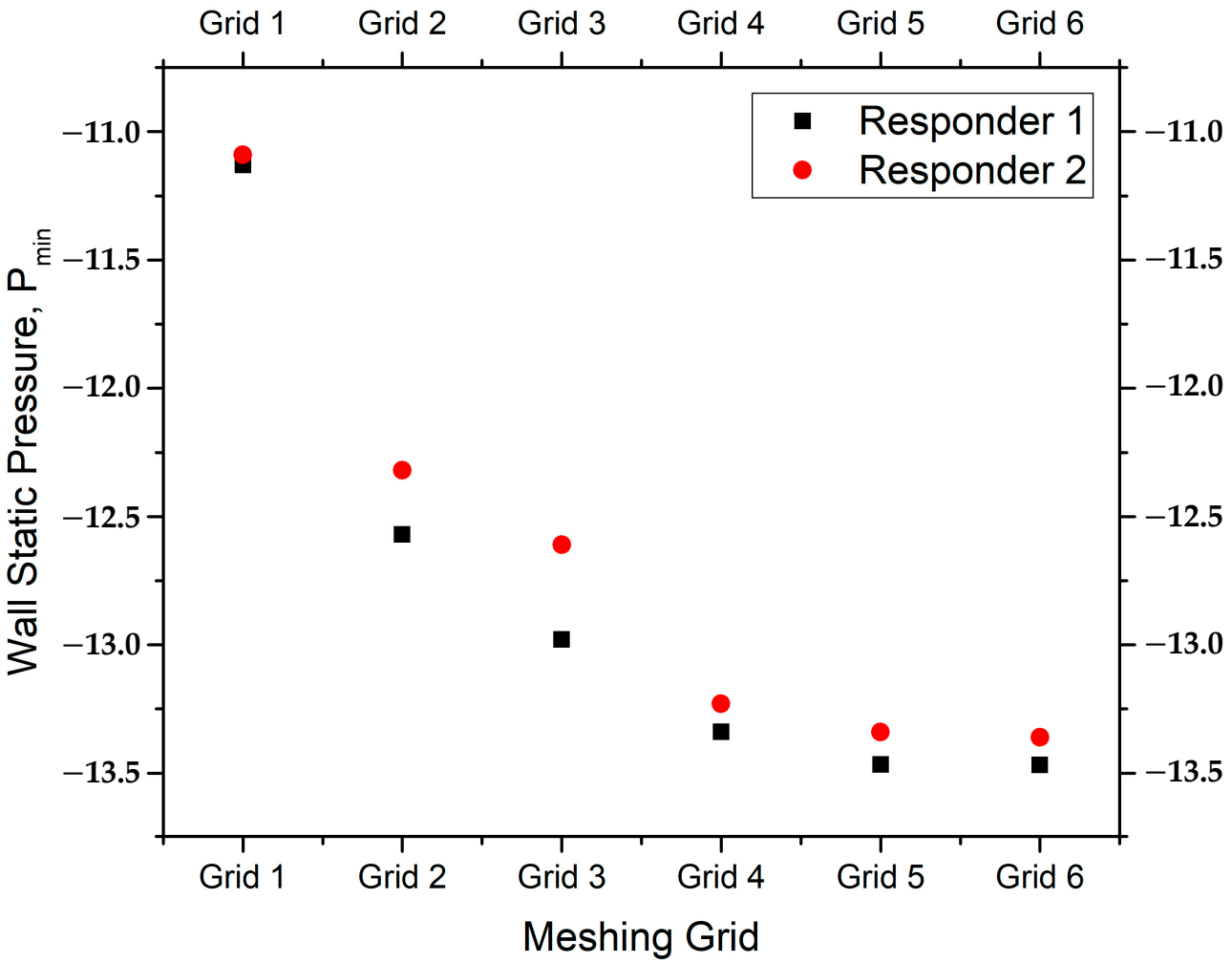

Figure 3. The grid sensitivity test on the various grid sizes for Responders 1 and 2.

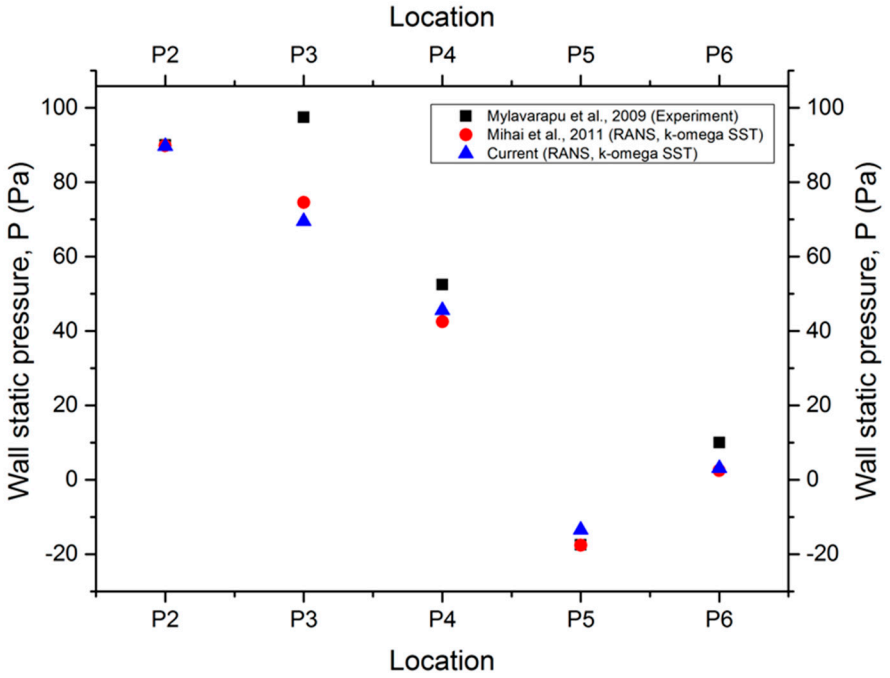

Figure 4. Solver verification with previous simulation and experimental results by Mylavarapu et al. [30] and Mihai et al. [31].

3. Results and Discussion

3.1. Cross-Sectional Area

In Figure 5, the hypopharyngeal airway (HUA) cross-sectional area changes are depicted across thirty-four planes in the z-direction (i.e., flow direction). The representation highlights that for Responder 1, the patient exhibits a minimum cross-sectional area of 7.68 mm^2 at a distance of 28 mm, while for Responder 2 it is 5.42 mm^2 at a distance of 31 mm from the inlet. The different cross-sectional areas between Responders 1 and 2 are around 29%. Figure 5 shows that both responders have different cross-sectional areas of the upper airway within 25–35 mm, which may be attributed to the individual features of the OSA patient's airway. Thus, the current study is significant in providing the airflow pattern to help medical practitioners individualize the OSA treatment based on underlying mechanisms. The narrowing of the cross-sectional area impacts the fluidity of the airflow as it traverses through the hypopharyngeal airway (HUA). TKE was used to explain this study's significant result to reveal the flow characteristics of the HUA because of the cross-sectional area.

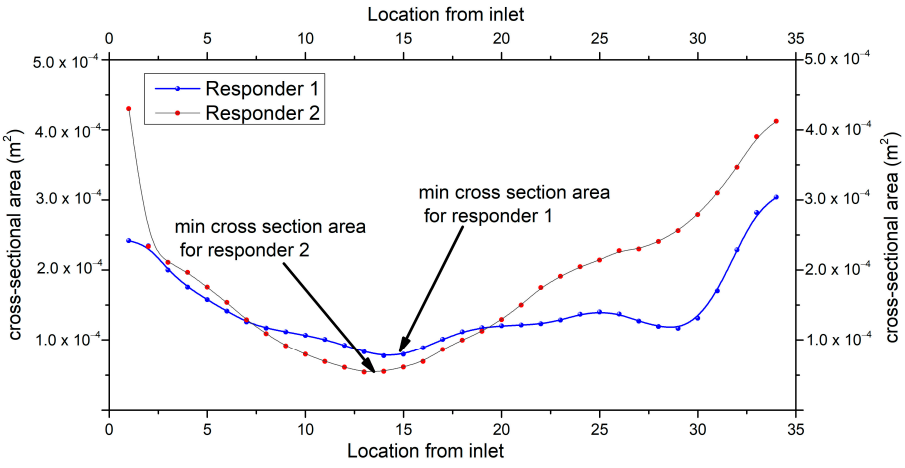

Figure 5. The generation of the cross-sectional area along the airflow direction in the airway model.

Moreover, Zhao et al. [32] demonstrated the significance of correlation analysis by revealing that pharyngeal volume and upper airway cross-sectional area were useful markers for screening sleep apnea patients. The discoveries by Lin et al. [33] endorse the notion that alterations in the cross-sectional configuration of the upper airway exert a substantial influence on airway resistance. The modification in the shape of the upper airway's cross-section can offer crucial clinical insights into an individual's patterns of upper airway collapse. Ryu et al. [34] recently completed an airway simulation to examine geometrical implications. Based on the computed results, they developed a model to anticipate the flow characteristics that cause contraction of the upper airway in sleep apnea patients.

3.2. Static Pressure

Figure 6 illustrates the static pressure (unit: Pa) exerted on the airway wall throughout the inhalation and exhalation phases, featuring distinct responders (i.e., cross-sectional areas). The simulation results discovered the maximum axial velocity and minimum static pressure in the small cross-sectional regions [27]. In terms of mechanism, the genioglossus is influenced by a locally medicated working effective reflex system that responds to negative pharyngeal pressure and central respiratory drive.

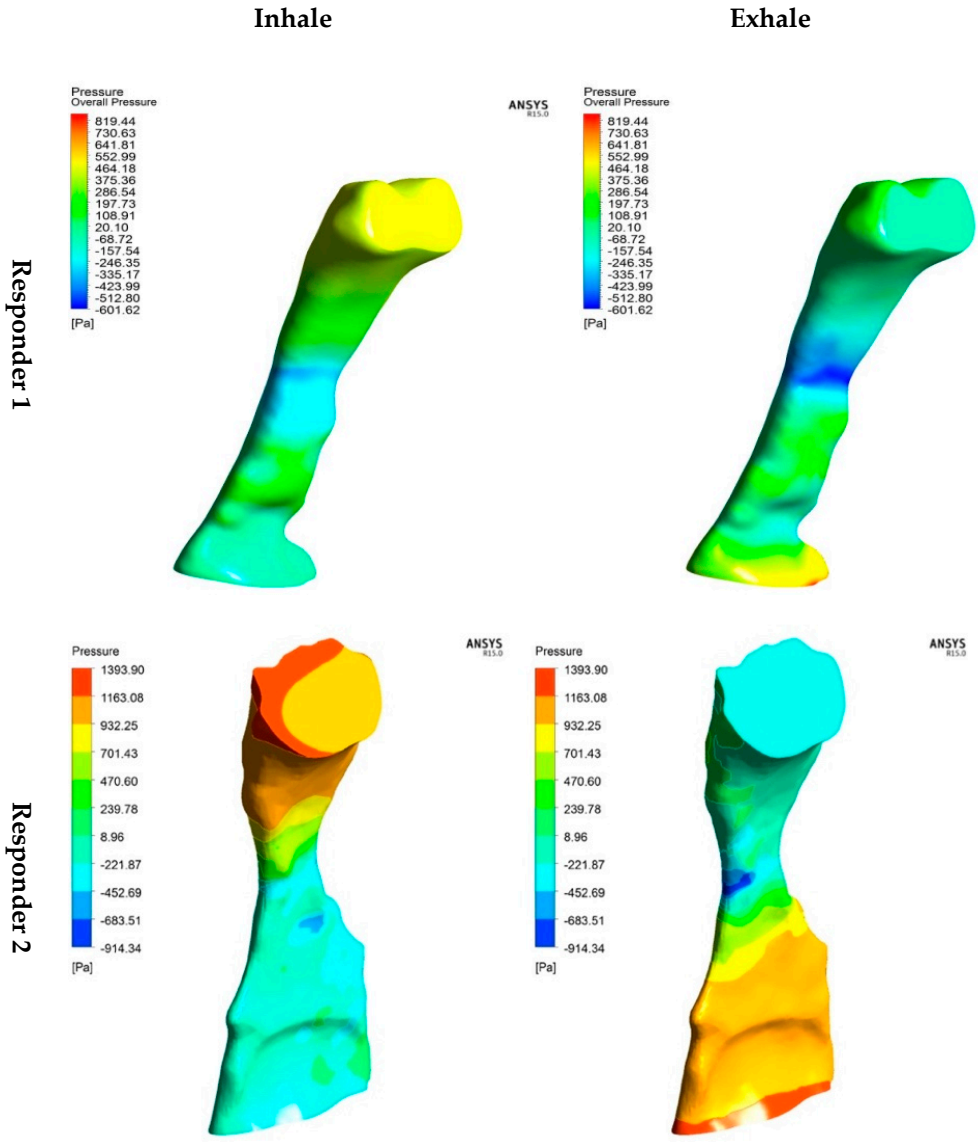

Figure 6. Contour of the static pressure exerted on the airway wall during inhaling and exhaling.

One such mechanism is activated in response to rapid changes in negative extrapharyngeal pressure, which causes the sub-atmosphere or suction pressure to increase. Indeed, advancing our comprehension of the neuroanatomy associated with the genioglossus negative pressure reflex and hypoglossal motor muscles has revealed the widespread presence of inhibitory inputs influencing the genioglossus. Nonetheless, while the responsiveness of the genioglossus muscles may be reduced during sleep compared to wakefulness, the muscles respond to sustained negative pressure.

3.3. Velocity

The velocity fluctuation exhibits a randomized direction, exerting a high magnitude that impacts the obstruction in the breathing area, as depicted in Figure 7. At the narrow cross-sectional breathing area, there is a notable low pressure. The obstructed regions primarily exhibit high wall shear stress, contributing to elevated turbulent energy near the wall. A recent investigation found that shear stress generates fluctuating velocity, leading to heightened turbulent energy in this region. The variations in velocity and turbulent flow near the wall induce vibrations, concurrently generating snoring and compromising the genioglossus function. Consequently, the severity of snoring correlates with turbulent energy. Over time, persistent snoring can diminish tissue strength in the pharyngeal region, potentially causing tissue collapse or laxity because of the gravitational effects when the patient is in a supine position. This scenario becomes a factor in the development of sleep apnea.

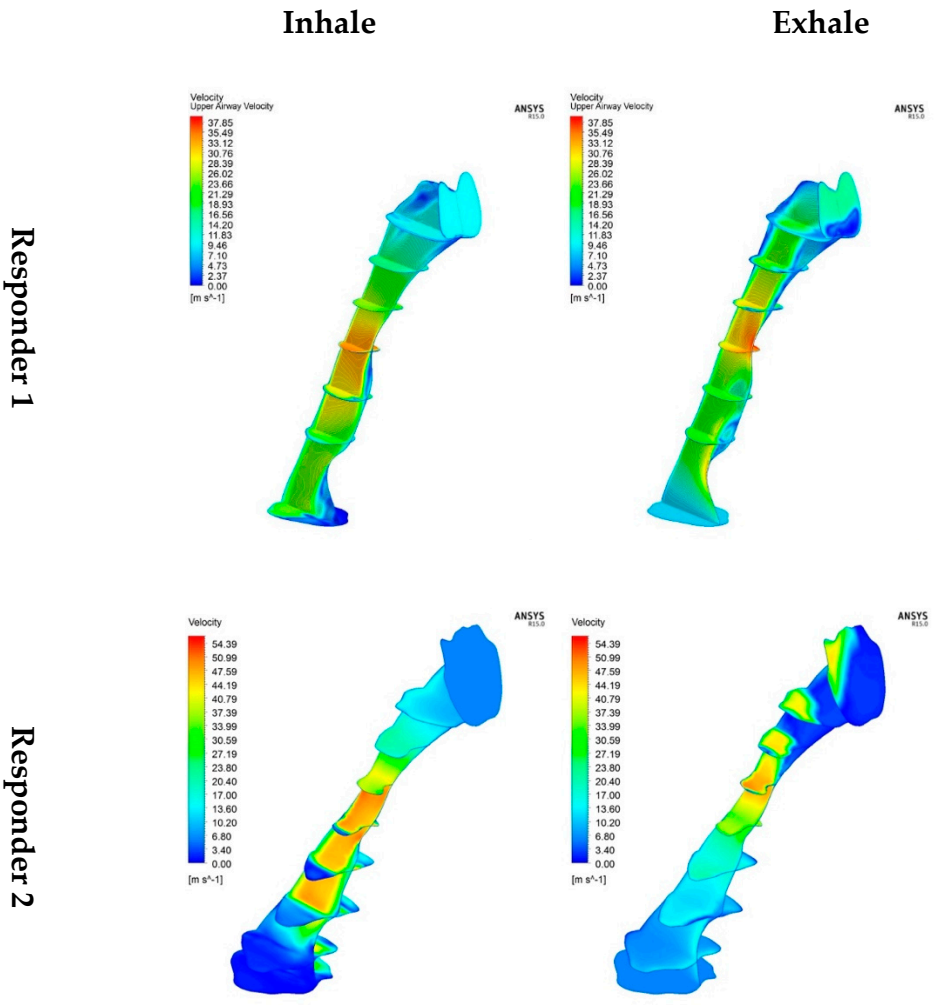

Figure 7. Contour of upper airway velocity magnitude on the airway wall during inhale and exhale breathing.

3.4. Turbulent Reynolds Number

Figure 7 shows the pattern of the turbulent Reynolds number for both responders and considers inhalation and exhalation breathing. It is noticed that after the critical cross-sectional area HUA, the flow pattern becomes turbulent. The maximum Re_y for Responder 1 during inhalation and exhalation is 2398.44 and 1417.66, respectively. However, for Responder 2, the inhalation and exhalation Re_y values are 3022.45 and 2134.13, respectively. The simulation results show that the Re_y value of Responder 2 is higher than that of Responder 1. The difference between the two respondents is nearly 26.0% for inhaling and 50.5% for exhaling. This comparison reveals a reduced cross-sectional area in the airway (Responder 2), which led to increased airflow deterioration during inhalation and exhalation. The intensity of turbulent flow blocks the smooth airway during breathing, either during inhalation or exhalation. After the critical cross-sectional area, this turbulent condition will block the airway during breathing. The results revealed that the turbulent Reynolds number of both responders occurred after the area contraction during inhalation and exhalation breathing. The different cross-sectional areas between Responders 1 and 2 contribute to the different turbulence intensities after the critical cross-sectional area.

Nevertheless, during exhalation as shown in Figure 8, the occurrence of turbulence becomes more sophisticated. In the plane pattern after the inlet, the airflow already has higher turbulence than the inhalation breathing condition. Thus, the TKE was considered further to explain the airflow characteristics in the current study. It indicated that the expression of the turbulent Reynolds number is insufficient to measure or determine the severity of OSA as a new method.

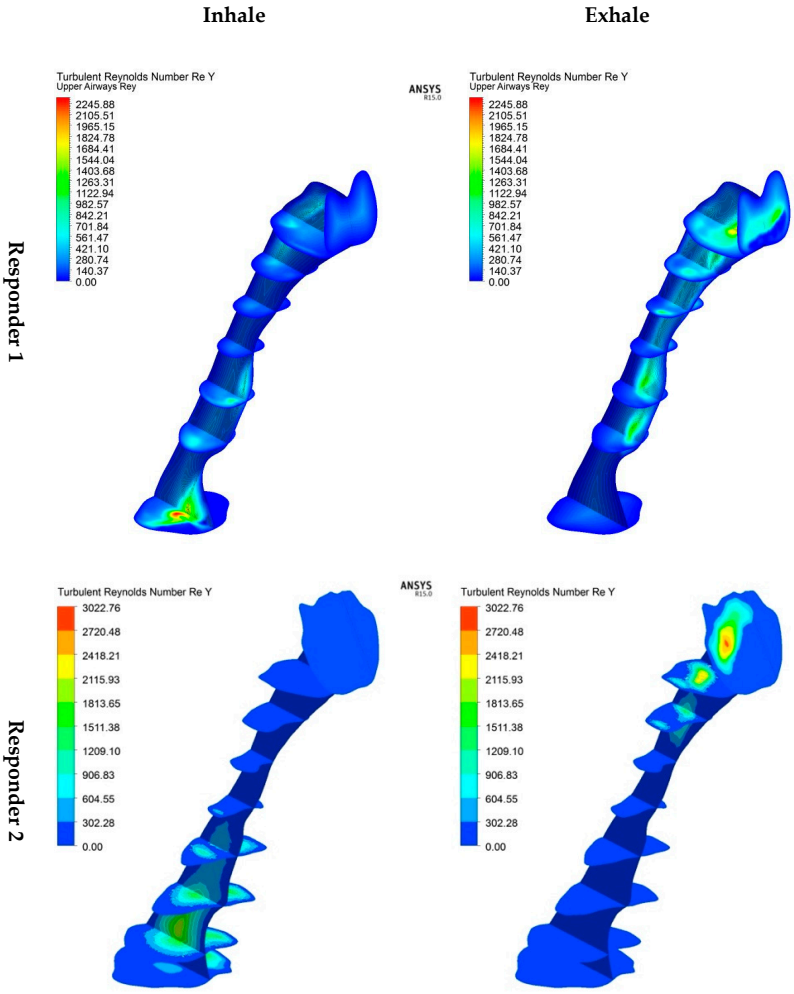

Figure 8. Contour of Re_y at the center plane for inhale breathing and exhale breathing.

The correlation between the cross-sectional areas and turbulent Reynolds numbers can be measured, as expressed in Figure 9. The results revealed that the changes in turbulent Reynolds numbers of both responders occur after the area contraction during inhalation and exhalation breathing. This phenomenon corresponds to the velocity magnitude as discussed in Section 3.3. The different cross-sectional areas between Responders 1 and 2 contribute to the different turbulence intensities after the critical cross-sectional area. During inhalation, the turbulent behavior in airflow becomes more evident after the cross-sectional area of the upper airway for both responders. However, during exhalation, the occurrence of turbulence becomes more sophisticated. This phenomenon shows that in the pattern of the plane after the inlet, the airflow already has high turbulence compared to the inhalation breathing condition. This observation indicated that the expression of the turbulent Reynolds number is insufficient to measure or determine the severity of OSA as a new method. Thus, the turbulent kinetic energy was considered further to explain the airflow characteristics in the current study.

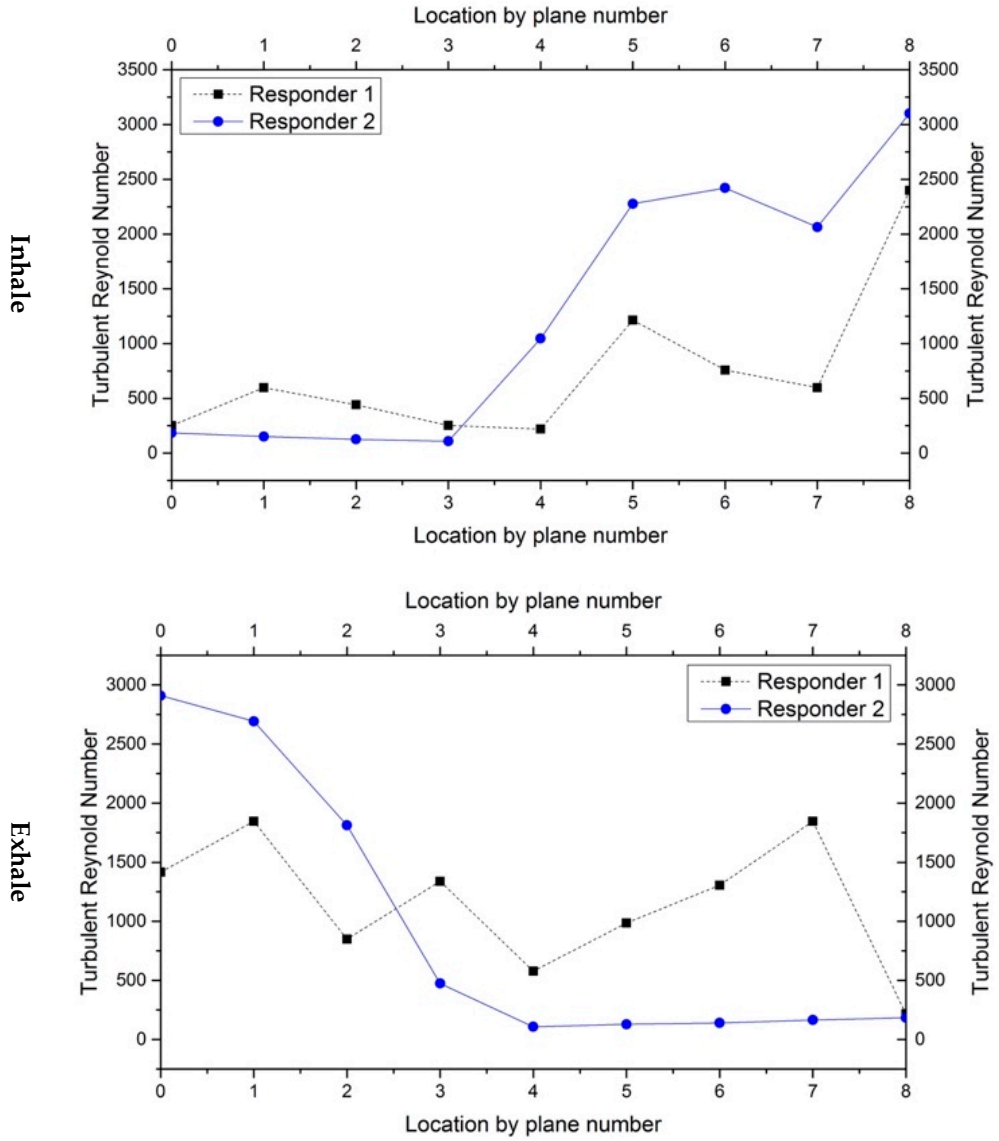

Figure 9. Turbulent Reynolds number trend for inhalation and exhalation for Responders 1 and 2.

3.5. Turbulent Kinetic Energy

Figure 10 illustrates the TKE contour resulting from the velocity fluctuation, as outlined in Equation (4). The turbulent Reynolds number (Re_y) was computed using Equation (6),

following the methodology established by Guangchu et al. [35]. In the airway, the predominant motion of airflow is attributed to energy in turbulent flow. Therefore, employing TKE is appropriate for describing vortices and quantifying turbulence levels. The outcomes reveal elevated TKE concentrated in the region following the narrow passage for both breathing conditions. Moreover, the formation of a jet stream was noted in the pharyngeal airway. The influence of this jet stream phenomenon on the wall probably resulted in the remodeling of velocity near the airway wall. The recirculation phenomenon induces the occurrence of TKE at high-velocity fluctuation.

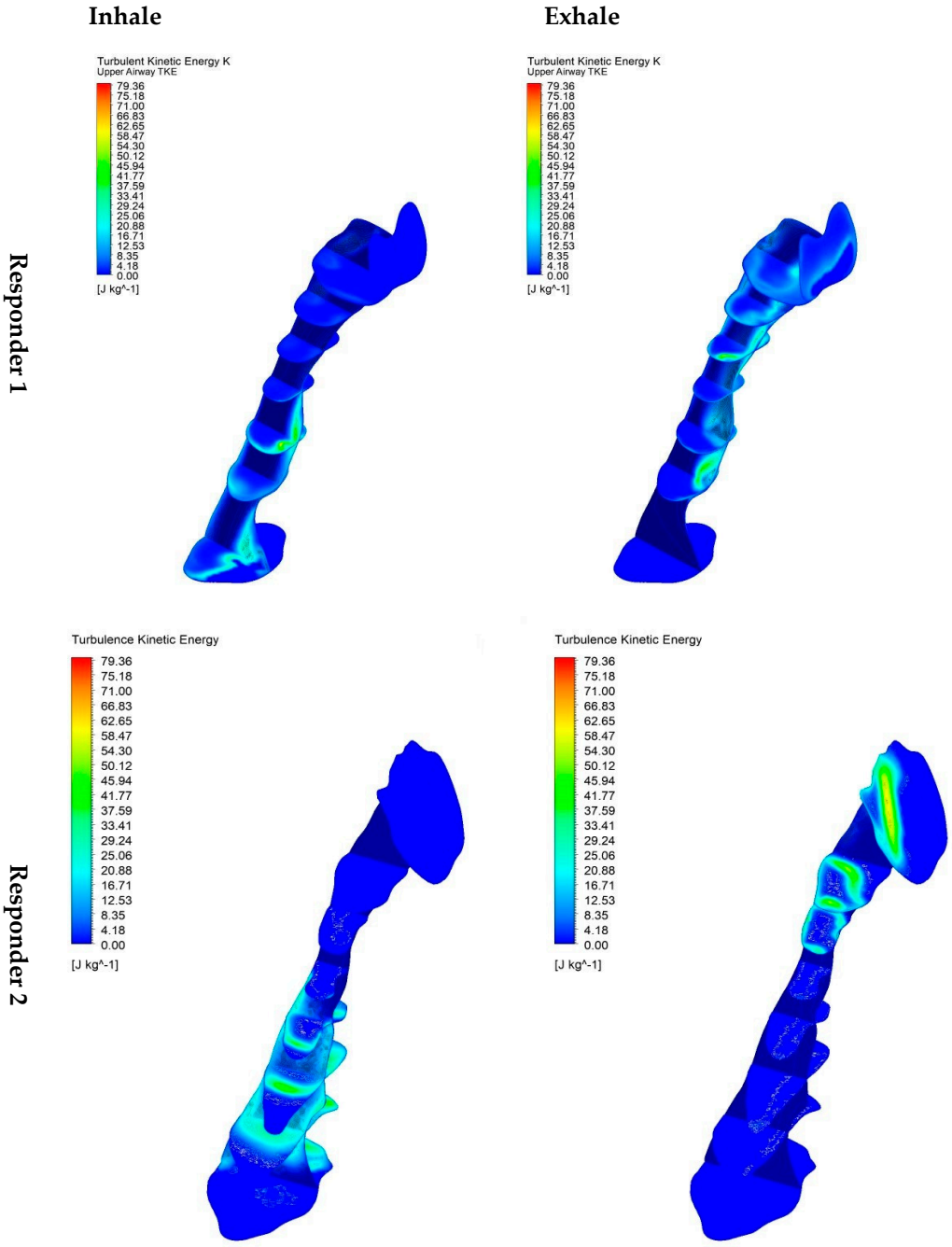

Figure 10. TKE contour of the upper airway at the center plane for inhale and exhale breathing conditions.

During inspiration, there is an increase in velocity from the inlet to the maximum value in the nasopharynx. In this stage, a high-velocity jet and increased turbulent kinetic

energy exist. Examining backflow and vortex downstream of the nasopharynx emphasizes the importance of the negative pressure gradient arising from the sudden expansion in the cross-sectional area. Throughout both inspiration and expiration, the model predicts localized areas of high TKE near the airway wall and the downstream jet. This phenomenon contributes to the relatively moderate pressure recovery in the jet expansion. The increased kinetic energy and dissipative energy loss upstream cause a decrease in pharyngeal luminal pressure during inspiration. Reduced luminal pressure reduces the cross-sectional area of the segment in hypotonic and extremely compliant pharynxes.

Figure 11 compares the turbulent kinetic energy of both responders during inhalation and exhalation breathing. The turbulent kinetic energy trends during breathing corresponded with the turbulent Reynolds number. In contrast, the sudden changes in TKE were spotted after the contraction area of the airway. The sudden increase and decrease in turbulent kinetic energy are found from Plane 3 to Plane 4 for both responders. The results show that the variations from Plane 3 to Plane 4 of Responder 2 are more than those of Responder 1. This situation is attributed to the critical cross-sectional area of Responder 2 being smaller than Responder 1. A smaller cross-sectional area showed variations in inhalation and exhalation before and after the narrowed area. Thus, it revealed that the critical cross-sectional area of the airway significantly affects the airflow characteristics of breathing, leading to the obstruction of sleep apnea.

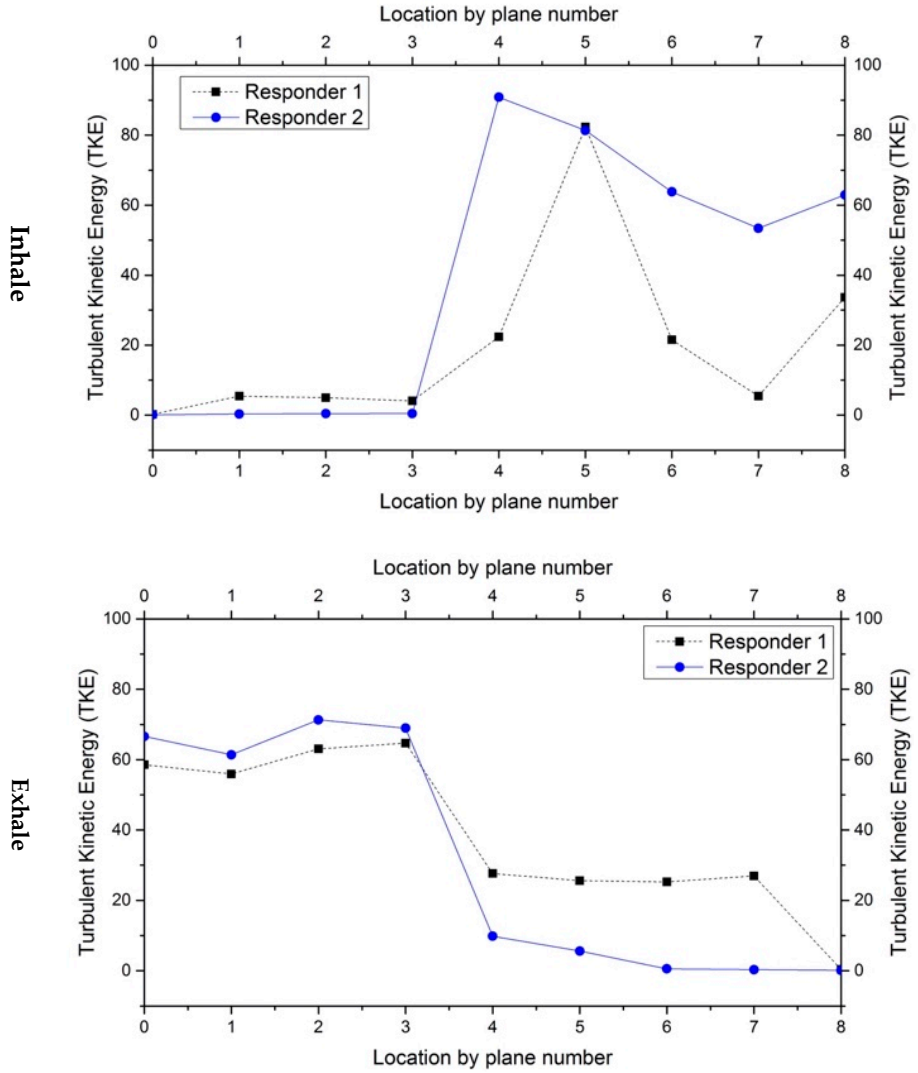

Figure 11. Turbulent kinetic energy trend for inhalation and exhalation for Responders 1 and 2.

The correlation between maximum pharyngeal TKE and cross-sectional area can be shown in relation to the OSA patient (Responders 1 and 2), respectively. The difference in cross-sectional areas was estimated at 29.47%. Reducing the cross-sectional area may increase TKE by almost 10.28% during inspiration and 10.18% for expiration (Table 2). The TKE increase was several-fold higher in the HUA after the critical cross-sectional area than in other segments in the control case.

Table 2. Comparison table between Responder 1 and Responder 2 during inhale and exhale breathing.

		Responder 1	**Responder 2**	**Diff (%)**
Cross-sectional area		7.68 mm^2	5.42 mm^2	29.47%
TKE	Inhale	82.37	90.84	10.28%
	Exhale	64.72	71.31	10.18%

4. Conclusions

The CFD method successfully simulates the flow characteristic during inhale and exhale breathing of OSA patients. The breathing condition has been considered in the simulations to study the impact of the cross-sectional area with different OSA patients. This study involved creating a 3D model of the pharyngeal airway using DICOM images and applying a solver verification to ensure the reliability of the computational model. ANSYS Fluent was utilized to set flow conditions, generate mesh, and conduct simulations, including a grid sensitivity test. It emphasized the significance of turbulent kinetic energy (TKE) in assessing obstructive sleep apnea (OSA) severity, highlighting its association with airflow characteristics. The research uncovered a substantial link between maximum pharyngeal TKE and cross-sectional areas in OSA patients, revealing that reduced cross-sectional areas could significantly increase TKE during inspiration and expiration. Decreasing the cross-sectional area could lead to a nearly 10.28% increase in TKE during inspiration and a 10.18% increase during expiration. This finding underscores the crucial role of TKE in understanding and evaluating OSA. Additionally, visualizing turbulent airflow patterns in individuals with pharyngeal airway irregularities provided valuable insights into potential factors contributing to OSA severity. These findings demonstrate how modeling can establish a specific patient's cross-sectional area and the underlying cause of hypopharyngeal airway (HUA) collapse. Thus, this information can be helpful to identify the most suitable treatment solution for OSA. The simulation results contribute to the profound understanding of the airflow patterns in the upper airway of OSA patients and facilitate individualizing OSA treatment based on underlying airflow mechanisms.

Author Contributions: W.M.F. designed the research, reviewed and revised the manuscript, approved the final manuscript as submitted, and obtained funding for the project. C.Y.K. analyzed and discussed the results and drafted and revised the manuscript. S.S. collected the data and carried out the research. M.H.M.H., M.A., M.N.M. and A.H.M.H. reviewed and revised the manuscript and approved the final manuscript as submitted. All authors have read and agreed to the published version of the manuscript.

Funding: This study was funded by the Ministry of Higher Education Malaysia (Ref. No: FRGS/1/2020/TK0/UNIMAP/03/26).

Data Availability Statement: The datasets used and analyzed during the current study are available from the corresponding author upon reasonable request.

Conflicts of Interest: The authors declare no competing interests.

References

1. Wang, J.; Zhao, Y.; Yang, W.; Shen, T.; Xue, P.; Yan, X.; Chen, D.; Qiao, Y.; Chen, M.; Ren, R.; et al. Correlations between obstructive sleep apnea and adenotonsillar hypertrophy in children of different weight status. *Sci. Rep.* **2019**, *9*, 11455. [CrossRef] [PubMed]
2. Tham, K.W.; Lee, P.C.; Lim, C.H. Weight Management in Obstructive Sleep Apnea: Medical and Surgical Options. *Sleep Med. Clin.* **2019**, *14*, 143–153. [CrossRef]

3. Corda, J.V.; Shenoy, B.S.; Ahmad, K.A.; Lewis, L.; Prakashini, K.; Khader, S.M.A.; Zuber, M. Nasal airflow comparison in neonates, infant and adult nasal cavities using computational fluid dynamics. *Comput. Methods Programs Biomed.* **2022**, *214*, 106538. [CrossRef] [PubMed]
4. Modena, D.A.O.; Cazzo, E.; Candido, E.C.; Baltieri, L.; Silveira, L.; Almeida, A.M.N.; Gobato, R.C.; Chaim, E.A. Obstructive sleep apnea syndrome among obese individuals: A cross-sectional study. *Rev. Assoc. Med. Bras.* **2017**, *63*, 862–868. [CrossRef]
5. Randerath, W.; Bassetti, C.L.; Bonsignore, M.R.; Farre, R.; Ferini-Strambi, L.; Grote, L.; Hedner, J.; Kohler, M.; Martinez-Garcia, M.A.; Mihaicuta, S.; et al. Challenges and perspectives in obstructive sleep apnoea: Report by an ad hoc working group of the Sleep Disordered Breathing Group of the European Respiratory Society and the European Sleep Research Society. *Eur. Respir. J.* **2018**, *52*, 1702616. [CrossRef]
6. Carberry, J.C.; Amatoury, J.; Eckert, D.J. Personalized Management Approach for OSA. *Chest* **2018**, *153*, 744–755. [CrossRef]
7. Suzuki, M. Obstructive sleep apnea—Consideration of its pathogenesis. *Auris Nasus Larynx* **2022**, *49*, 313–321. [CrossRef] [PubMed]
8. Passali, D.; Passali, F.M.; Cambi, J.; Bellussi, L. Role of adenotonsillectomy in OSAS children and behavioural disturbance. *Otolaryngol. Pol.* **2013**, *67*, 187–191. [CrossRef]
9. Hudgel, D.W.; Patel, S.R.; Ahasic, A.M.; Bartlett, S.J.; Bessesen, D.H.; Coaker, M.A.; Fiander, P.M.; Grunstein, R.R.; Gurubhagavatula, I.; Kapur, V.K.; et al. The Role of Weight Management in the Treatment of Adult Obstructive Sleep Apnea. An Official American Thoracic Society Clinical Practice Guideline. *Am. J. Respir. Crit. Care Med.* **2018**, *198*, e70–e87. [CrossRef]
10. Lin, H.C.; Friedman, M. Volumetric Tongue Reduction for Obstructive Sleep Apnea. *Sleep Med. Clin.* **2019**, *14*, 59–65. [CrossRef]
11. Lin, H.; Xiong, H.; Ji, C.; Wang, C.; Li, Y.; An, Y.; Li, G.; Guo, J.; Huang, X.; Zhang, H.; et al. Upper airway lengthening caused by weight increase in obstructive sleep apnea patients. *Respir. Res.* **2020**, *21*, 272. [CrossRef]
12. Faizal, W.M.; Ghazali, N.N.N.; Khor, C.Y.; Zainon, M.Z.; Badruddin, I.A.; Kamangar, S.; Ibrahim, N.B.; Razi, R.M. Computational Analysis of Airflow in Upper Airway under Light and Heavy Breathing Conditions for a Realistic Patient Having Obstructive Sleep Apnea. *Comput. Model. Eng. Sci.* **2021**, *128*, 583–604. [CrossRef]
13. Vinha, P.P.; Thuler, E.R.; de Mello-Filho, F.V. Effects of surgically assisted rapid maxillary expansion on the modification of the pharynx and hard palate and on obstructive sleep apnea, and their correlations. *J. Craniomaxillofac. Surg.* **2020**, *48*, 339–348. [CrossRef]
14. Klopper, G.J.; Adeniyi, O.V.; Stephenson, K. Adolescent and adult laryngotracheal stenosis: A review. *Egypt. J. Otolaryngol.* **2021**, *37*, 36. [CrossRef]
15. Yang, I. TLR4 Asp299Gly polymorphism is not associated with coronary artery stenosis. *Atherosclerosis* **2003**, *170*, 187–190. [CrossRef]
16. Buczkowski, P.W.; Fombon, F.N.; Russell, W.C.; Thompson, J.P. Effects of helium on high frequency jet ventilation in model of airway stenosis. *Br. J. Anaesth.* **2005**, *95*, 701–705. [CrossRef]
17. Cheng, T.; Carpenter, D.; Cohen, S.; Witsell, D.; Frank-Ito, D.O. Investigating the effects of laryngotracheal stenosis on upper airway aerodynamics. *Laryngoscope* **2018**, *128*, E141–E149. [CrossRef]
18. Xu, X.; Wu, J.; Weng, W.; Fu, M. Investigation of inhalation and exhalation flow pattern in a realistic human upper airway model by PIV experiments and CFD simulations. *Biomech. Model. Mechanobiol.* **2020**, *19*, 1679–1695. [CrossRef]
19. Ganimedov, V.L.; Muchnaya, M.I. Numerical simulation of particle deposition in the human nasal cavity. *Thermophys. Aeromechanics* **2020**, *27*, 303–312. [CrossRef]
20. Bates, A.J.; Schuh, A.; Amine-Eddine, G.; McConnell, K.; Loew, W.; Fleck, R.J.; Woods, J.C.; Dumoulin, C.L.; Amin, R.S. Assessing the relationship between movement and airflow in the upper airway using computational fluid dynamics with motion determined from magnetic resonance imaging. *Clin. Biomech.* **2019**, *66*, 88–96. [CrossRef]
21. Chan, A.S.; Sutherland, K.; Schwab, R.J.; Zeng, B.; Petocz, P.; Lee, R.W.; Darendeliler, M.A.; Cistulli, P.A. The effect of mandibular advancement on upper airway structure in obstructive sleep apnoea. *Thorax* **2010**, *65*, 726–732. [CrossRef]
22. Powell, N.B.; Mihaescu, M.; Mylavarapu, G.; Weaver, E.M.; Guilleminault, C.; Gutmark, E. Patterns in pharyngeal airflow associated with sleep-disordered breathing. *Sleep Med.* **2011**, *12*, 966–974. [CrossRef] [PubMed]
23. Chang, K.K.; Kim, K.B.; McQuilling, M.W.; Movahed, R. Fluid structure interaction simulations of the upper airway in obstructive sleep apnea patients before and after maxillomandibular advancement surgery. *Am. J. Orthod. Dentofac. Orthop.* **2018**, *153*, 895–904. [CrossRef] [PubMed]
24. Haghnegahdar, A.; Zhao, J.; Kozak, M.; Williamson, P.; Feng, Y. Development of a hybrid CFD-PBPK model to predict the transport of xenon gas around a human respiratory system to systemic regions. *Heliyon* **2019**, *5*, e01461. [CrossRef]
25. Schendel, S.; Powell, N.; Jacobson, R. Maxillary, mandibular, and chin advancement: Treatment planning based on airway anatomy in obstructive sleep apnea. *J. Oral. Maxillofac. Surg.* **2011**, *69*, 663–676. [CrossRef] [PubMed]
26. Wakayama, T.; Suzuki, M.; Tanuma, T. Effect of Nasal Obstruction on Continuous Positive Airway Pressure Treatment: Computational Fluid Dynamics Analyses. *PLoS ONE* **2016**, *11*, e0150951. [CrossRef] [PubMed]
27. Mylavarapu, G.; Mihaescu, M.; Fuchs, L.; Papatziamos, G.; Gutmark, E. Planning human upper airway surgery using computational fluid dynamics. *J. Biomech.* **2013**, *46*, 1979–1986. [CrossRef]
28. Wilcox, D.C. Reassessment of the scale-determining equation for advanced turbulence models. *Am. Inst. Aeronaut. J.* **1988**, *26*, 1299–1310. [CrossRef]

29. Faizal, W.M.; Ghazali, N.N.N.; Khor, C.Y.; Zainon, M.Z.; Ibrahim, N.B.; Razif, R.M. Turbulent Kinetic Energy of Flow during Inhale and Exhale to Characterise the Severity of Obstructive Sleep Apnea Patient. *Comput. Model. Eng. Sci.* **2023**, *136*, 43–61. [CrossRef]
30. Mylavarapu, G.; Murugappan, S.; Mihaescu, M.; Kalra, M.; Khosla, S.; Gutmark, E. Validation of computational fluid dynamics methodology used for human upper airway flow simulations. *J. Biomech.* **2009**, *42*, 1553–1559. [CrossRef]
31. Mihaescu, M.; Mylavarapu, G.; Gutmark, E.J.; Powell, N.B. Large eddy simulation of the pharyngeal airflow associated with obstructive sleep apnea syndrome at pre and post-surgical treatment. *J. Biomech.* **2011**, *44*, 2221–2228. [CrossRef]
32. Zhao, Y.; Li, X.; Ma, J. Combined application of pharyngeal volume and minimal cross-sectional area may be helpful in screening persons suspected of obstructive sleep apnea (OSA). *Sleep Breath.* **2022**, *26*, 243–250. [CrossRef] [PubMed]
33. Lin, H.; Wang, C.; Zhang, H.; Xiong, H.; Li, Z.; Huang, X.; Ji, C.; Xian, J.; Huang, Y. Threshold of the upper airway cross-section for hypopnea onset during sleep and its identification under waking condition. *Respir. Res.* **2019**, *20*, 280. [CrossRef] [PubMed]
34. Ryu, S.; Kim, J.H.; Yu, H.; Jung, H.D.; Chang, S.W.; Park, J.J.; Hong, S.; Cho, H.J.; Choi, Y.J.; Choi, J.; et al. Diagnosis of obstructive sleep apnea with prediction of flow characteristics according to airway morphology automatically extracted from medical images: Computational fluid dynamics and artificial intelligence approach. *Comput. Methods Programs Biomed.* **2021**, *208*, 106243. [CrossRef]
35. Hu, G.; Grossman, B. The computation of massively separated flows using compressible vorticity confinement methods. *Comput. Fluids* **2006**, *35*, 781–789. [CrossRef]

computation

MDPI

Article

Natural Convection Fluid Flow and Heat Transfer in a Valley-Shaped Cavity

Sidhartha Bhowmick [1], Laxmi Rani Roy [1], Feng Xu [2] and Suvash C. Saha [3,*]

[1] Department of Mathematics, Jagannath University, Dhaka 1100, Bangladesh; dr.sidhartha@math.jnu.ac.bd (S.B.); lrroy.jnu@gmail.com (L.R.R.)
[2] School of Civil Engineering, Beijing Jiaotong University, Beijing 100044, China; fxu@bjtu.edu.cn
[3] School of Mechanical and Mechatronic Engineering, University of Technology Sydney, Sydney, NSW 2007, Australia
* Correspondence: suvash.saha@uts.edu.au

Abstract: The phenomenon of natural convection is the subject of significant research interest due to its widespread occurrence in both natural and industrial contexts. This study focuses on investigating natural convection phenomena within triangular enclosures, specifically emphasizing a valley-shaped configuration. Our research comprehensively analyses unsteady, non-dimensional time-varying convection resulting from natural fluid flow within a valley-shaped cavity, where the inclined walls serve as hot surfaces and the top wall functions as a cold surface. We explore unsteady natural convection flows in this cavity, utilizing air as the operating fluid, considering a range of Rayleigh numbers from Ra = 10^0 to 10^8. Additionally, various non-dimensional times τ, spanning from 0 to 5000, are examined, with a fixed Prandtl number (Pr = 0.71) and aspect ratio (A = 0.5). Employing a two-dimensional framework for numerical analysis, our study focuses on identifying unstable flow mechanisms characterized by different non-dimensional times, including symmetric, asymmetric, and unsteady flow patterns. The numerical results reveal that natural convection flows remain steady in the symmetric state for Rayleigh values ranging from 10^0 to 7×10^3. Asymmetric flow occurs when the Ra surpasses 7×10^3. Under the asymmetric condition, flow arrives in an unsteady stage before stabilizing at the fully formed stage for $7 \times 10^3 <$ Ra $< 10^7$. This study demonstrates that periodic unsteady flows shift into chaotic situations during the transitional stage before transferring to periodic behavior in the developed stage, but the chaotic flow remains predominant in the unsteady regime with larger Rayleigh numbers. Furthermore, we present an analysis of heat transfer within the cavity, discussing and quantifying its dependence on the Rayleigh number.

Keywords: unsteady flow; natural convection; valley-shaped cavity; bifurcations; heat transfer

Citation: Bhowmick, S.; Roy, L.R.; Xu, F.; Saha, S.C. Natural Convection Fluid Flow and Heat Transfer in a Valley-Shaped Cavity. *Computation* **2024**, *12*, 146. https://doi.org/10.3390/computation12070146

Academic Editors: Ali Cemal Benim, Abdulmajeed A. Mohamad, Sang-Ho Suh, Rachid Bennacer, Paweł Oclon and Jan Taler

Received: 4 June 2024
Revised: 11 July 2024
Accepted: 12 July 2024
Published: 14 July 2024

1. Introduction

The study of natural convection within confined spaces has attracted considerable attention from scientists due to its widespread applicability across various disciplines [1,2]. Researchers have utilized different types of enclosures with diverse boundary conditions as experimental setups to investigate natural convection, aiming to deepen our understanding of heat transfer mechanisms and fluid dynamics. This interest stems from the multitude of applications where natural convection phenomena are integral, spanning fields such as geophysics, building insulation, geothermal reservoir management, and industrial separation processes. However, the complexity of the Earth's surface, characterized by irregular geometries highly influenced by slanted terrains, poses challenges for traditional geometric configurations. Despite the prevalence of irregular shapes in both natural and industrial settings, natural convection remains a subject of ongoing study owing to its significance in understanding fluid flow behavior. While much research has focused on natural convection within conventional square or rectangular enclosures due to their simplicity [3,4], the investigation of natural convection within triangular-shaped cavities holds particular

importance as it contributes significantly to our understanding of phenomena such as Rayleigh–Bénard convection [5,6]. Recently, Cui et al. [7] focused on the study of mixed convection and heat transfer in an arc-shaped cavity with inner heat sources under the conditions of bottom heating and top wall cooling. Chuhan et al. [8] examined the thermal behavior of a power law fluid in a plus-shaped cavity as a result of natural convection, taking into account the Darcy number and magnetohydrodynamics. Sarangi et al. [9] explored the heat loss induced by radiation and persistently laminar natural convection in a solar cooker cavity with a rectangular or trapezoidal cavity.

Enhancing our understanding of natural convection flows holds paramount importance in improving predictions of heat transfer and facilitating flow control mechanisms. Researchers intrigued by this phenomenon can investigate detailed explanations of buoyancy-induced natural convection flows [10]. Natural convection near a thermal boundary is often idealized as flow adjacent to a thermally well-conducted infinite or semi-infinite flat plate, leading to the formation of Rayleigh–Bénard convection. Studies by Manneville and Bodenschatz et al. [11,12] provide comprehensive insights into Rayleigh–Bénard instability findings, whereas Sparrow and Husar [13] focus on exploring Rayleigh–Bénard convection on inclined flat plates. Investigating cavities with vertical and horizontal temperature gradients reveals two distinct natural or free convection flow scenarios. While natural convection is predominantly studied in rectangular or square cavities due to their simplicity, Batchelor's [14] research offers a significant understanding of natural convection flows within differentially heated cavities, particularly emphasizing the influence of conduction on heat transfer, especially at low Rayleigh numbers. As the Rayleigh number exceeds a threshold, convection controls the flow dynamics. Early studies have primarily examined stable natural convection flows [15–17]. The intriguing phenomenon of baroclinity, engendered by the thermal vertical wall, instigates spontaneous convection flows within the interior cavity through viscous shear under symmetric conditions [18]. At lower Rayleigh numbers, the thermal boundary layer proximal to the wall remains steady, while convective instability induces discrete traveling waves as the Rayleigh numbers increase [18]. Recent studies have delved into the dynamics and transient nature of transient natural convection flows, building upon earlier investigations [19,20]. These findings contribute to our understanding of the complex interplay between thermal gradients and fluid dynamics within confined spaces, shedding light on the transient behaviors inherent to natural convection phenomena. Recent research indicates the occurrence of baroclinity-induced spontaneous convection flows and turbulent Rayleigh–Bénard convection [21]. Rahaman et al. [22,23] explore transitional natural convection flows in a trapezoidal enclosure heated from below, supported by numerical investigations, further enriching our comprehension of this complex phenomenon.

Natural convection flows within cavities featuring inclined walls have attracted considerable attention due to their prevalence and ease of observation [24]. Specifically, investigations into the natural convection flows within triangular cavities have revealed their significant enhancement of Rayleigh–Bénard convection, as documented in prior studies [5,6]. Extensive research explores the characteristics and heat transfer mechanisms of natural convection flows within attic-shaped cavities characterized by temperature gradients between the bottom surface and the inclined borders [25–31]. Notably, studies by Asan and Namli [25,26] and Salman [27] have examined the instability and bifurcations of natural convection flow solutions in triangular cavities, revealing empirical evidence showcasing the profound influence of the aspect ratio and Rayleigh number on both the temperature and flow fields. Analytical findings indicate that as the Rayleigh numbers increase, the aspect ratios decrease, leading to the occurrence of multiple vortex flow patterns. Poulikakos and Bejan [29] investigated heat transmission and natural convection flows within attic spaces during night or winter conditions, establishing scaling relationships and engaging in discussions regarding natural convection flow dynamics [30]. Flack [31] elucidated heat transport dynamics using the Nusselt number–Rayleigh number relationship, while Holtzman et al. [32] observed the transition from symmetric to asymmetric

flow patterns with increasing Grashof numbers, identifying a Pitchfork bifurcation based on experimental data. Furthermore, Lei et al. [33] provided evidence of the existence of transient natural convection flows within attic cavities, further enriching our understanding of this complex phenomenon.

The evolution of flow under sudden heating and cooling undergoes three distinct stages: early, transitional, and steady or quasi-steady [33]. It has been observed that lower Rayleigh numbers result in heating across the entire flow zone rather than the splitting of the thermal boundary layer, with layer separation occurring as the Rayleigh numbers increase. Particularly in scenarios of rapid cooling, the thickness of the thermal boundary layer exceeds the vertical distance from the center of the inclined surface to the horizontal bottom, especially at lower Rayleigh numbers. The thermal boundary layer stabilizes prior to cavity cooling as the Rayleigh numbers increase, with fluid passing the sloping surface and contacting the bottom tip before entering the interior. Attic heat transmission has been studied under thermal stimuli by Saha et al. [34–38]. Additionally, researchers have investigated the behavior and heat transfer dynamics of natural convection flows in wedge-shaped cavities, serving as models for various shallow-water bodies with inclined bottom surfaces, such as reservoir sidearms and seashores. As described by Lei and Patterson [39–41], convective flow within wedges undergoes three stages from isothermal and stationary states. Mao et al. [42–44] argued that the horizontal location of the wedge determines the primary heat transfer mode and flow status for varying Rayleigh numbers, with different flow regimes observed in the shallow littoral zone. Bednarz et al. [45] explored natural convection flows within reservoir-shaped cavities, observing the formation of two heating boundary layers: inflow at the bottom and unstable reflux below the water for different Grashof values. Understanding natural convection flows in V-shaped cavities is crucial, given their prevalence in both natural and industrial systems [46–57]. Kenjeres [58] quantified the heat transfer and turbulent natural convection fluxes in V-shaped cavities, noting that upslope flow increases with rising Rayleigh numbers. Kimura et al. [59] utilized angled V-shaped channel open chambers to calculate heat transfer dynamics.

The flow pattern and heat transfer quantities have been meticulously measured in previous studies [30,31]. Despite the detailed examinations conducted, natural convection flows within an attic or a wedge-shaped triangular cavity may not accurately depict the flow dynamics in a V-shaped cavity over time. Given their natural occurrence, natural convection flows within V-shaped triangular enclosures with opposing boundary conditions have been deemed worthy of thorough investigation. Bhowmick et al. [60–62] investigated the transition from symmetric steady flow to asymmetric unsteady flow in a V-shaped triangular enclosure, where heating occurred from below and cooling from above. It was observed that different fluids exhibit distinct movement behaviors. Despite witnessing the transition from regular to chaotic flow in the valley-shaped cavity heated from below, the mechanisms driving unsteady flow in such cavities remain unclear. To the best of the authors' knowledge, no study has examined the unsteady flow structures present at various times in the valley-shaped cavity. Moreover, there is a need for further quantitative analysis of the dynamics of heat transfer in such configurations.

This literature review highlights the significance of investigating unsteady natural convection in V-shaped cavities for air, providing valuable insights into the flow patterns, transition processes, and heat transfer phenomena in such systems. However, a comprehensive understanding of the intricate physics governing unsteady flow mechanisms within V-shaped cavities remains imperative. Analysis of the existing literature reveals a dearth of studies focusing on characterizing unsteady flow structures at different non-dimensional times within V-shaped cavities. To address this gap, the present study aims to examine unsteady flow in a valley-shaped cavity through two-dimensional numerical simulations, considering air with Rayleigh numbers ranging from 10^0 to 10^8, a Prandtl number of 0.71, and an aspect ratio of 0.5. The impact of various Ra and τ values on the flow structure, heat transfer, and transient flow characteristics in the fully formed stage of the valley-shaped cavity are covered in this study. This research contributes to existing knowledge

by enhancing our understanding of how fluid characteristics affect flow behavior and transition processes. The evolution of flow mechanisms and changes within the cavity are elucidated using the temperature and velocity differences over time. Such insights are crucial for enhancing the energy efficiency of engineering applications and optimizing the design of thermal systems like heat exchangers and cooling systems. Consequently, this study is poised to make a novel contribution to the field, offering distinct and valuable conclusions that will benefit specialists engaged in modeling and experimentation on flow over complex geometries.

2. Numerical Model Formulations

The primary objective of this study is to analyze the characteristics of natural convection flows in a triangular cavity with a valley-shaped configuration. To achieve this, a two-dimensional numerical simulation approach is employed. The physical model and its corresponding boundary conditions are visually represented in Figure 1. In order to rectify the singularity present at the connection between the top and inclined walls, a strategic adjustment is made by removing an appropriate amount of substance from both the top corners. Specifically, 4% of the length is carefully extracted in the form of minuscule points. It should be noted that this minor adjustment does not exhibit any discernible impact on the mechanics of fluid flow and heat transfer, as indicated by previous studies [18,20–24,29–31]. The dimensions of the cavity are defined as follows: the horizontal length is $2L$, and the height is H, where $L = 2H$ and the ratio $A = H/L = 0.5$. At time $T = T_0$, the fluid inside the cavity is initially at a uniform temperature and not in motion. At a given temperature of $T_c = T_0 - \Delta T/2$ and $T_h = T_0 + \Delta T/2$, respectively, the top and inclined walls undergo instantaneous cooling and heating processes. In every given circumstance, all the boundaries are motionless.

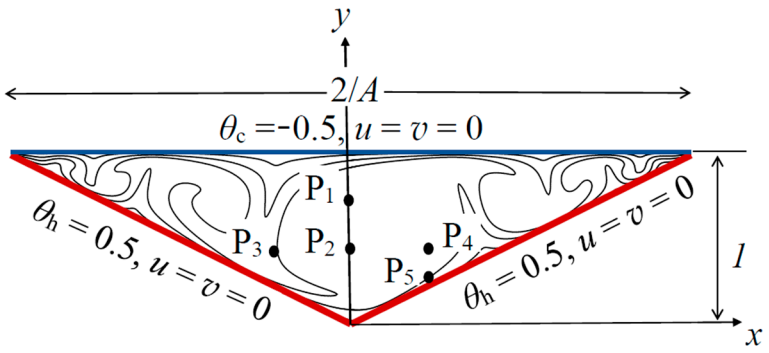

Figure 1. Physical domain and non-dimensional boundary conditions with the figuring points P_1 (0, 0.825), P_2 (0, 0.46), P_3 (−0.5, 0.5), P_4 (0.5, 0.5), and P_5 (0.5, 0.255), which are applied in the following figures.

This study analyses two-dimensional natural convection flows within a valley-shaped enclosure. The governing equations employed in this investigation are presented below, utilizing the Boussinesq approximation as a simplifying assumption [62].

$$\frac{\partial U}{\partial X} + \frac{\partial V}{\partial Y} = 0, \tag{1}$$

$$\frac{\partial U}{\partial t} + U\frac{\partial U}{\partial X} + V\frac{\partial U}{\partial Y} = -\frac{1}{\rho}\frac{\partial P}{\partial X} + \nu\left(\frac{\partial^2 U}{\partial X^2} + \frac{\partial^2 U}{\partial Y^2}\right), \tag{2}$$

$$\frac{\partial V}{\partial t} + U\frac{\partial V}{\partial X} + V\frac{\partial V}{\partial Y} = -\frac{1}{\rho}\frac{\partial P}{\partial Y} + \nu\left(\frac{\partial^2 V}{\partial X^2} + \frac{\partial^2 V}{\partial Y^2}\right) + g\beta(T - T_0), \tag{3}$$

$$\frac{\partial T}{\partial t} + U\frac{\partial T}{\partial X} + V\frac{\partial T}{\partial Y} = \kappa\left(\frac{\partial^2 T}{\partial X^2} + \frac{\partial^2 T}{\partial Y^2}\right). \tag{4}$$

U and V in the equations, respectively, represent the horizontal and the vertical flow rates. For a two-dimensional coordinate system:

- P is the pressure;
- ρ is the density;
- t is the time;
- T is the temperature, at time T_0, where $T_0 = (T_c + T_h)/2$, the fluid medium in the triangular cavity is isothermally stationary.

The dimensionless variables utilized are as follows:

$$x = \frac{X}{H},\ y = \frac{Y}{H},\ u = \frac{UH}{\kappa \mathrm{Ra}^{\frac{1}{2}}},\ v = \frac{VH}{\kappa \mathrm{Ra}^{\frac{1}{2}}},\ p = \frac{PH^2}{\rho \kappa^2 \mathrm{Ra}},\ \theta = \frac{T - T_\infty}{T_h - T_c}, \tau = \frac{t\kappa \mathrm{Ra}^2}{H^2}. \quad (5)$$

In the aforementioned equations, the variables v, x, y, p, τ, and θ represent the normalized counterparts of U, V, X, Y, P, t, and T, respectively. The three governing variables, the aspect ratio (A), Prandtl number (Pr), and Rayleigh number (Ra), have an impact on the enclosure's natural convectional flows (view [6] for further details), which are best described as follows:

$$A = \frac{H}{L},\ \mathrm{Pr} = \frac{\nu}{\kappa},\ \mathrm{Ra} = \frac{g\beta(T_h - T_c)H^3}{\nu\kappa}\ . \quad (6)$$

The above dimensionless variables are added, and then Equations (1)–(4) become (for more information, see [61]):

$$\frac{\partial u}{\partial x} + \frac{\partial v}{\partial y} = 0\ , \quad (7)$$

$$\frac{\partial u}{\partial \tau} + u\frac{\partial u}{\partial x} + v\frac{\partial u}{\partial y} = -\frac{\partial p}{\partial x} + \frac{\mathrm{Pr}}{\mathrm{Ra}^{\frac{1}{2}}}\left(\frac{\partial^2 u}{\partial x^2} + \frac{\partial^2 u}{\partial y^2}\right), \quad (8)$$

$$\frac{\partial v}{\partial \tau} + u\frac{\partial v}{\partial x} + v\frac{\partial v}{\partial y} = -\frac{\partial p}{\partial y} + \frac{\mathrm{Pr}}{\mathrm{Ra}^{\frac{1}{2}}}\left(\frac{\partial^2 v}{\partial x^2} + \frac{\partial^2 v}{\partial y^2}\right) + \mathrm{Pr}\theta\ , \quad (9)$$

$$\frac{\partial \theta}{\partial \tau} + u\frac{\partial \theta}{\partial x} + v\frac{\partial \theta}{\partial y} = \frac{\mathrm{Pr}}{\mathrm{Ra}^{\frac{1}{2}}}\left(\frac{\partial^2 \theta}{\partial x^2} + \frac{\partial^2 \theta}{\partial y^2}\right). \quad (10)$$

The present study used a finite-volume Navier–Stokes solver [62], Fluent 15.0 in ANSYS, to model natural convection within a valley-shaped cavity. The principles of mass conservation, momentum conservation, and energy conservation are the foundations of the computational model that is used to simulate unsteady natural convection flow in an air cavity. The continuity equation, the Navier–Stokes equations, and the energy equations have all been solved using finite volume methods after the appropriate numerical techniques have been applied. The non-uniform 2D mesh system is created with the help of the commercial software ICEM 15.0, and the numerical results have been displayed graphically with the help of the post-processing program TECPLOT 360.

The governing Equations (7)–(10) are solved by means of a finite volume technique using the SIMPLE method, which is thoroughly explained in reference [63] and Saha [64]. The numerical procedure for the SIMPLE method is shown in Figure 2.

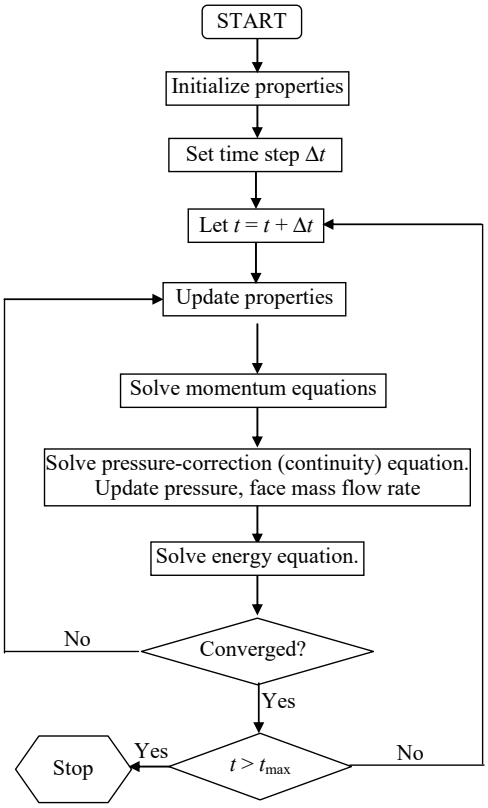

Figure 2. Flowchart of the SIMPLE method for transient flow.

3. Grid Dependency Test

The mesh and time step dependence of the largest Rayleigh number (Ra = 10^8) for the Prandtl number (Pr = 0.71) and aspect ratio (A = 0.5) was investigated in the present inquiry. Three symmetrical, non-uniform meshes were employed in the test, with dimensions of 600 × 100, 800 × 150, and 1200 × 200. These meshes were designed to have finer grids near the boundaries and coarser grids in the inner zone. The 800 × 150 mesh underwent a 3% expansion, ranging from a minimum width of 0.00025 near the wall to a maximum width of 0.02 in the inside. Figure 3 illustrates the time series of the Nusselt number at the right wall of the cavity. The data were obtained using different meshes and time steps for a Rayleigh number of 10^8. The Nusselt numbers obtained from the different meshes and time steps show uniformity during the initial stage, along with some divergence during the mature stage. In addition, Table 1 provides a calculation and list of the average Nusselt numbers during the fully developed stage. Based on the analysis conducted, it has been determined that the variations in outcomes observed across the different meshes and time steps are within the acceptable threshold of 2%. Taking this into consideration, the numerical simulation in this study used a mesh size of 800 × 150 and a time step of 0.0025.

Table 1. Nusselt numbers (Nu) for different grids and time steps.

Mesh and Time Step	Average Nu	Difference
600 × 100 and $\Delta\tau$ = 0.0025	121.63	1.94%
800 × 150 and $\Delta\tau$ = 0.00125	122.47	1.27%
800 × 150 and $\Delta\tau$ = 0.0025	124.04	-
1200 × 200 and $\Delta\tau$ = 0.0025	122.95	0.87%

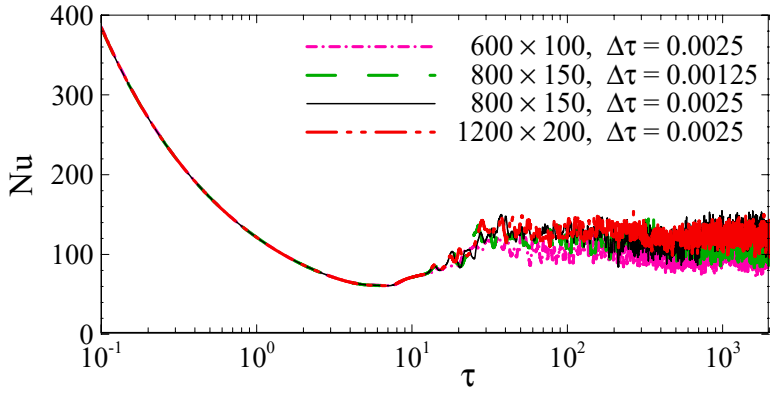

Figure 3. Nusselt numbers time series at the right inclined wall in the valley-shaped cavity for Ra = 10^8 with definite grids and time steps.

4. Validation

Figure 4 compares the laboratory experiment conducted by Holtzman et al. [32] with the current numerical results for additional confirmation. In contrast to the triangular cavity in this study, it is vertically inverted and the Rayleigh numbers have been employed in place of the corresponding Grashof numbers. In comparison to the experimental results in Figure 4b for the Rayleigh numbers Ra = 3.5 × 10^3, Figure 4d for Ra = 7 × 10^3, and Figure 4f for Ra = 7 × 10^4, the numerical results depicting the symmetric flow for Ra = 7 × 10^3 in Figure 4a and the asymmetric flow for Ra = 1.2 × 10^4, and Ra = 10^5 in Figure 4c,e are accurate. As indicated by Xu et al. [18] and Patterson and Armfield [20], the presence of inconsistencies between numerical Ra values and experimental Ra findings gives rise to a notable contradiction: if the numerical findings and experiment results are accurate, the experimental Rayleigh number is approximately 1.5 to 2.5 times the numerical Rayleigh number. The numerical methods utilized in this research can be used to depict a transitional flow in a triangular cavity, as the experimental and computational results are identical.

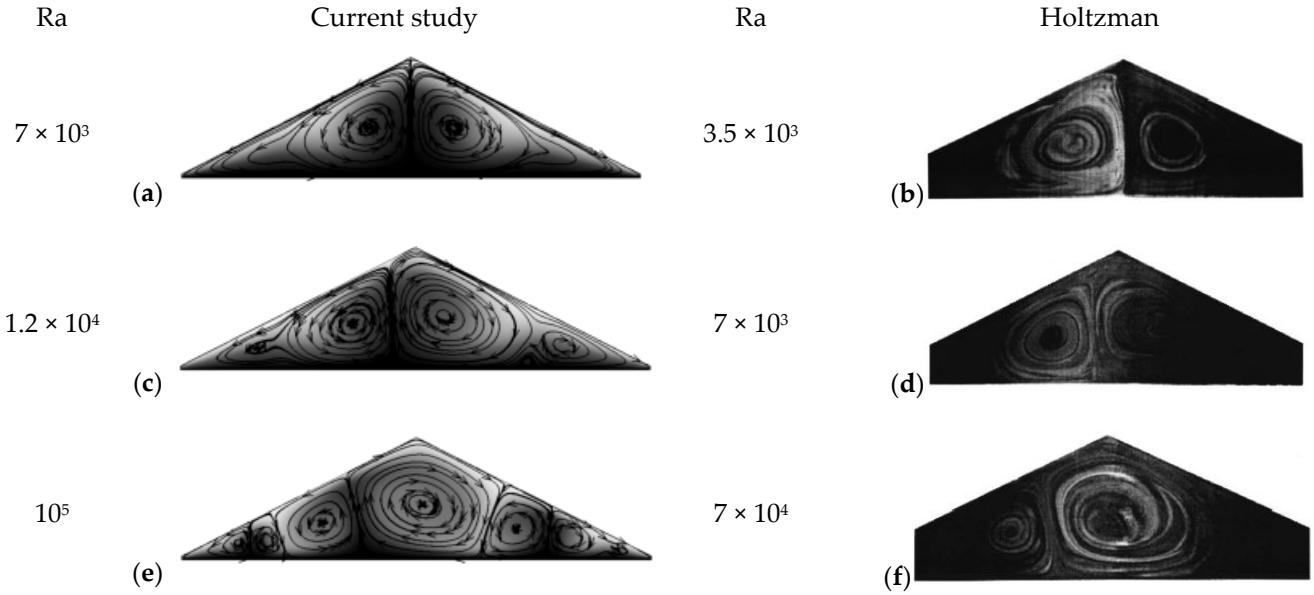

Figure 4. Comparison of the experimental results of Holtzman (**b**,**d**,**f**) [32] for different Rayleigh numbers with the current study (**a**,**c**,**e**).

5. Numerical Results and Discussion

The subsequent section provides an explanation of the primary characteristics of the fluid flows within a V-shaped cavity, wherein the flow is stimulated by heat from the

inclined walls and dissipated by cooling from the top wall. The analysis focuses on a range of Rayleigh numbers, spanning from Ra = 10^0 to 10^8, a Prandtl number, Pr = 0.71, and an aspect ratio, A = 0.5. Various non-dimensional times are considered to comprehensively examine the flow growth phenomenon. In this work, a 2D numerical simulation has been conducted. According to the numerical simulations, the evolution of the flow for these Rayleigh numbers in different times from τ = 0 to 5000 may be split into symmetric flow, asymmetric flow and unsteady flow.

To produce the simulation results, we used high-performance computing facilities with 64 processors, with which it took 15 days for a small Ra = 10^5 and 20 days for a large Ra = 10^8 for non-dimensional time, τ = 5000 with time step size, $\Delta\tau$ = 0.0025.

5.1. Symmetric Flow

It was discovered that for Ra = 10^0, 10^1 and 10^2, the transitional flow development with non-dimensional time did not exhibit an increasing or decreasing plume, which indicates that for those Rayleigh numbers, the flow exhibited an ongoing level of stability due to the prevailing influence of conduction dominance. In this study, the results for Ra = 10^0, 10^1 and 10^2 at τ = 0, 0.1, 0.5, 1 and 2000 are included in Figure 5. Initially, at τ = 0, the temperature is constant, and at this time, there is no fluid flow in the cavity. Fluid flows develop when the inclined walls are suddenly heated and the top wall is suddenly cooled. In Figure 5, the temperature rapidly changes for a small Ra = 10^0 and 10^1 at τ = 0.1 and becomes symmetric, but for Ra = 10^2, it becomes symmetric at τ = 0.5 and this symmetric tendency is observed from τ = 0.5 to 2000. For all the Ra and τ values, the cavity contains a pair of symmetrical cells. Convective flows exhibit relatively low magnitudes, with the cells having a prevailing conduction dominance that provides stability.

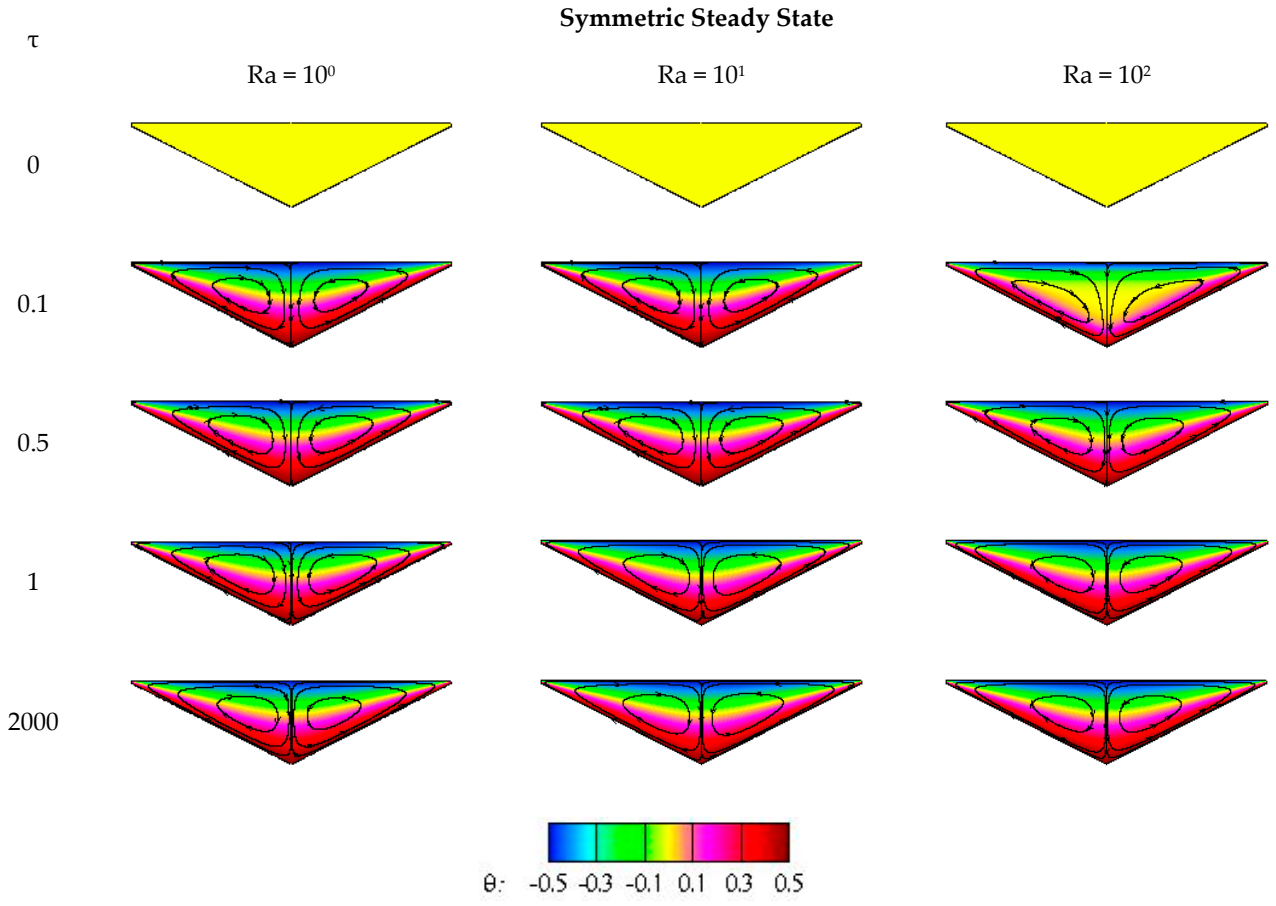

Figure 5. Streamlines and isotherms at various non-dimensional time intervals, τ, and different small Rayleigh numbers, Ra, for the symmetric steady state.

5.2. Asymmetric Flow

The flow of different Rayleigh numbers of Ra = 10^3, 7×10^3 and 2×10^4 is shown in Figure 6 on the basis of the time with the displayed streamlines and isotherms. Initially, at $\tau = 0$, the temperature is constant and no fluid moves in the cavity. Fluid flows start when the inclined walls are suddenly heated and the top wall is suddenly cooled. In Figure 6, the temperature gradually changes for Ra = 10^3 and 7×10^3 at $\tau = 0.1$ and becomes symmetric, whereas for Ra = 2×10^4, it becomes symmetric at $\tau = 1$. In the initial stage, when $\tau = 1$, the steady flows for all the Rayleigh numbers are symmetric. The cavity has two symmetric cells. Since the cells have a conduction dominance that keeps them eternally stable, convective flows are really extremely low. The baroclinity near the inclined walls produces viscous shear, which induces natural convection flows in the fundamental symmetric state, but as time passes, the flow for Ra = 7×10^3 and 2×10^4 starts becoming gradually asymmetric. As the figure shows, in the initial transitional stage at $\tau = 1$, the convection in Ra = 7×10^3 and 2×10^4 is increased, although it is not sufficiently strong to disrupt the symmetric flow structure (see Figure 7), while the convection in Ra = 10^3 remains static. Though there are only two cells when Ra = 10^3 and Ra = 7×10^3, four cells occur in the cavity for Ra = 2×10^4 at $\tau = 10$. That is, aside from symmetric break, the Rayleigh number causes an increase in the number of cells in the cavity. It should be noted that depending on the initial perturbations, any one of the two cells may be bigger and advance into the cavity. The convection of Ra = 10^3 is found to be constant and weak in all the subsequent stages of time, like $\tau = 100$, 1000, 2000 and 4000, but the convection in Ra = 7×10^3 becomes stronger slowly in $\tau = 100$, 1000, 2000 and 4000, though it is not enough to break the symmetric state. On the other hand, for Ra = 2×10^4, the convection grows so strongly that it breaks the symmetrical structure and creates more than two new cells, which is evident at $\tau = 100$, and the flow becomes asymmetric (in Figure 7). Six cells are present for Ra = 2×10^4 at $\tau = 100$ and 1000. Depending on the initial perturbations, one of the two cells at $\tau = 1000$ becomes larger and dominates the other cell in the cavity, moving toward the cavity's center. At $\tau = 2000$, the number of cells decreases to five, and this trend persists until $\tau = 4000$. Upon careful examination, it is evident that during the further development stage, the asymmetric flow has attained a state of equilibrium commonly referred to as a steady-state situation. The transition from a symmetric to an asymmetric state, occurring within the range of Ra = 7×10^3 to Ra = 2×10^4, can be understood as a supercritical Pitchfork bifurcation. This transformation is driven by the onset of Rayleigh–Bénard instability. It is seen that there is more circulation of cells and that the flow pattern is becoming continually asymmetric.

Figure 7 depicts the time series of the temperature and velocity for Ra = 10^3, Ra = 7×10^3, and Ra = 2×10^4 at different points P_1, P_2, and P_5. The fluid within the valley-shaped cavity initially exhibits isothermal and stationary behavior. The cooling and heating of the top wall and the inclined walls occur simultaneously, with a non-dimensional temperature denoted as θ_c for the top wall and θ_h for the inclined walls. Figure 7a demonstrates that there is no difference in temperature between any of the points P_1 and P_2, and temperature is different at point P_5 in the early stage for a small Ra = 10^3. As a result of the passage of time, the temperature increases and decreases at the three different points in the transitional period. Finally, there is no temperature fluctuation in the completely developed stage, and then the flow becomes steady. For more accuracy of the flow steadiness, here, we have used non-dimensional times from 0 to 5000. In Figure 7d, initially, the velocity is zero; as the time increases, the velocity remains the same at points P_1 and P_2; and at point P_5, the velocity increases and finally becomes constant. Similar consequences have been seen in Figure 7b,e. The figures clearly indicate that the flow within the cavity is in a state of steady symmetry. From this, it would seem that the flow is always steady at symmetric states. Now, in Figure 7c, the temperature decreases suddenly and then increases at points P_1 and P_2 during the transitional period and finally stabilizes at the completely developed stage. At point P_5, there are no changes because of its position. However, the velocity (Figure 7f)

clearly overshoots suddenly and then becomes constant in the completely formed stage, and it indicates that the flow becomes an asymmetric steady state for Ra = 2×10^4.

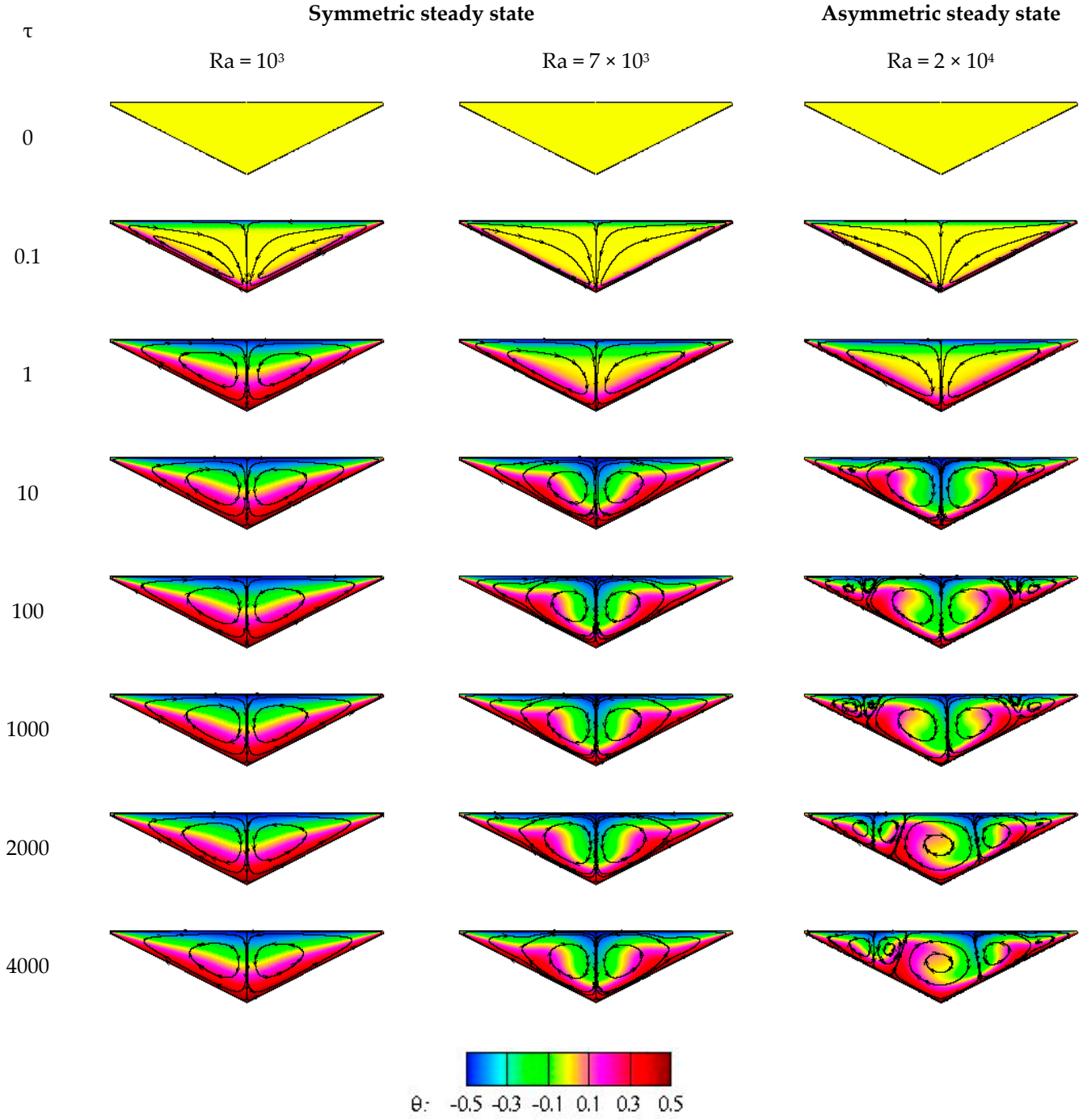

Figure 6. Streamlines and isotherms at various non-dimensional time intervals for the steady-state Rayleigh numbers, Ra = 10^3, Ra = 7×10^3 and Ra = 2×10^4.

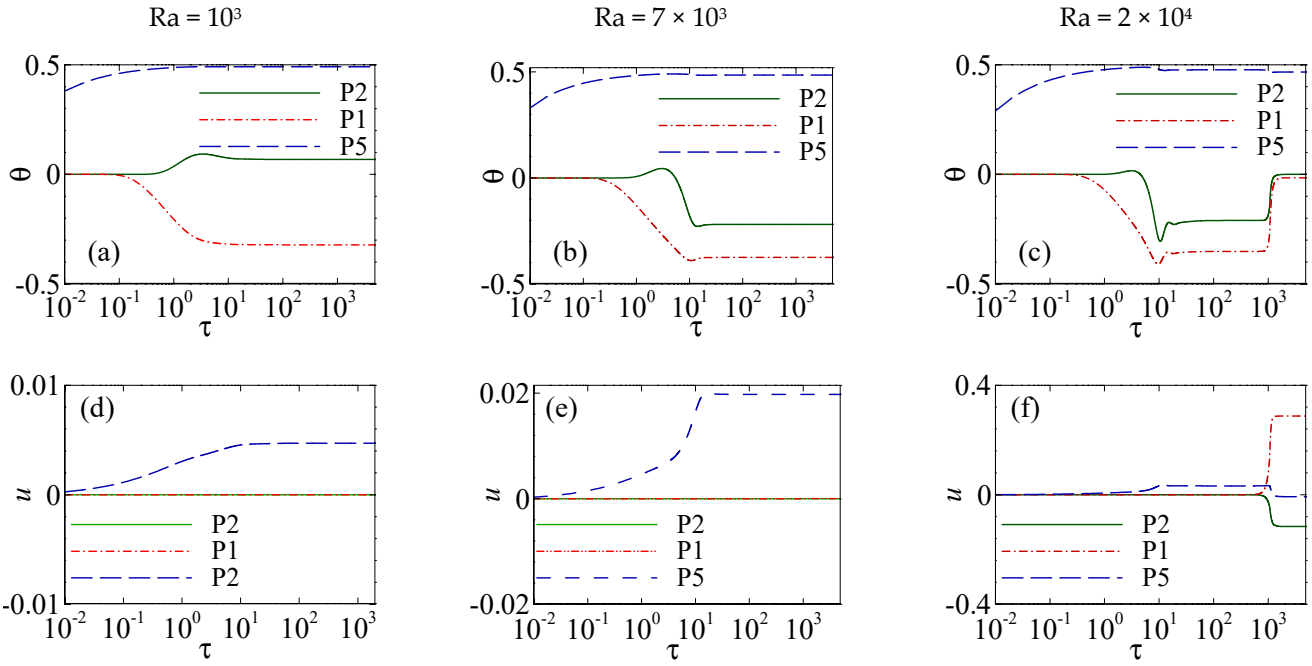

Figure 7. Times series of the temperature and velocity at three distinct points, P_1 (0, 0.825), P_2 (0, 0.46) and P_5 (0.5, 0.255), for (**a**,**d**) when Ra = 10^3, for (**b**,**e**) when Ra = 7×10^3, and for (**c**,**f**) when Ra = 2×10^4.

5.2.1. Pitchfork Bifurcation

Figure 8 illustrates the isotherms and streamlines corresponding to a Rayleigh number of Ra = 10^4. Figure 8a demonstrates the continued presence of clear symmetry in the flow at Ra = 7×10^3. At Ra = 10^4 and Ra = 1.3×10^4, the flow shows asymmetry, as depicted in Figure 8b,c. It is to be noted that depending on the initial perturbations, any one of the two cells might grow bigger and move toward the cavity. When the Rayleigh number reaches a value of Ra = 1.3×10^4, as depicted in Figure 8c, an additional cell emerges in the top-right region of the cavity (depending on the initial perturbations), and such an asymmetric flow configuration becomes more clearly evident as being the value of the Rayleigh number increases. That is, aside from the symmetric break, the Rayleigh number is responsible for the growing number of cells within the cavity. For instance, Figure 8b has four cells for Ra = 10^4, whereas Figure 8c has five cells for Ra = 1.3×10^4. The transition observed around Ra = 10^4, where a symmetric state transforms to an asymmetric state, can be characterized as a supercritical Pitchfork bifurcation, which happens when Rayleigh–Bénard instability begins to occur.

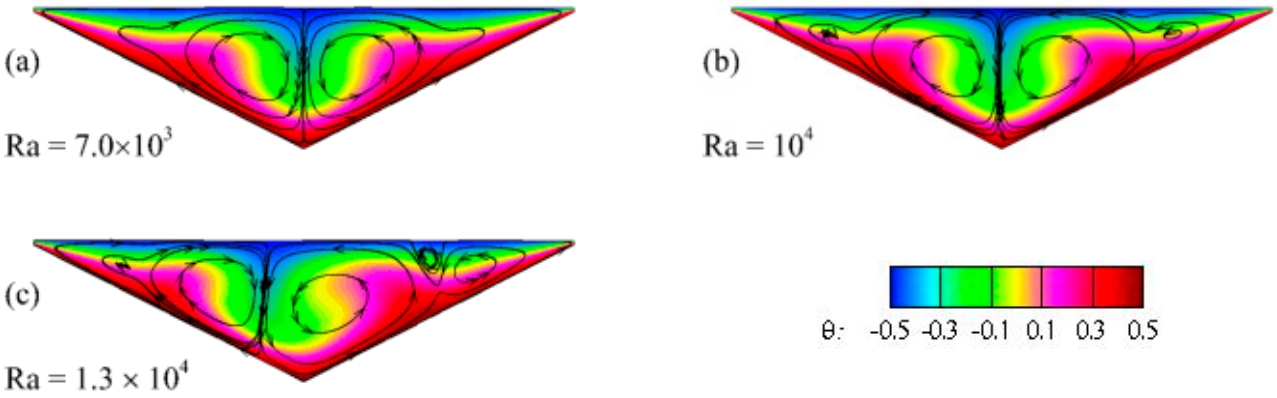

Figure 8. Streamlines and isotherms at Ra = 7×10^3, Ra = 10^4, and Ra = 1.3×10^4.

Table 2 presents the *x*-velocity at point P_2 (0, 0.46) for various Rayleigh numbers (Ra = 10^1 to 10^6) to comprehend the transition from a symmetric to an asymmetric state during the fully developed stage (τ = 2000) of the Pitchfork bifurcation. For Ra values less than or equal to 7.5×10^3, the *x*-velocity is nearly zero due to the symmetry of the flow. Once the Rayleigh number reaches or exceeds 7.6×10^3, the cell's polarity shifts to positive when the *x*-velocity increases and negative when the x-velocity decreases.

Table 2. Velocities in the *x*-direction for different Rayleigh numbers at point P_2 (0, 0.46).

Rayleigh Number	Velocity
10^1	0
10^2	0
10^3	0
7.5×10^3	0
7.6×10^3	$\pm 9.47 \times 10^{-5}$
10^4	$\pm$0.00669
1.2×10^4	$\pm$0.0557
1.5×10^4	$\pm$0.09
10^5	$\pm$0.096
10^6	$\pm$0.0993

At the initial stage at τ = 0, the temperature is constant, as depicted in Figure 9. The figure indicates that the flows are symmetric and continuous in the early stage at τ = 1 for Ra = 5×10^4, Ra = 10^5 and Ra = 10^6. The Pitchfork bifurcation causes the flow to intensify over time and eventually become asymmetric. The graphs show the asymmetric streamlines and isotherms at Rayleigh numbers Ra = 5×10^4, Ra = 10^5 and Ra = 10^6 at the transitional stages (τ = 100 and 800). It is undoubtedly interesting that the flow oscillates for a considerable amount of time with a higher Rayleigh number. In this figure, for all the Ra values, the flows in the valley-shaped cavity are asymmetric and steady with the passing of time. For a higher Ra = 10^6, the flow becomes asymmetric and steady at τ = 800, whereas Ra = 5×10^4 and Ra = 10^5 take more time to reach the asymmetric steady-state situation.

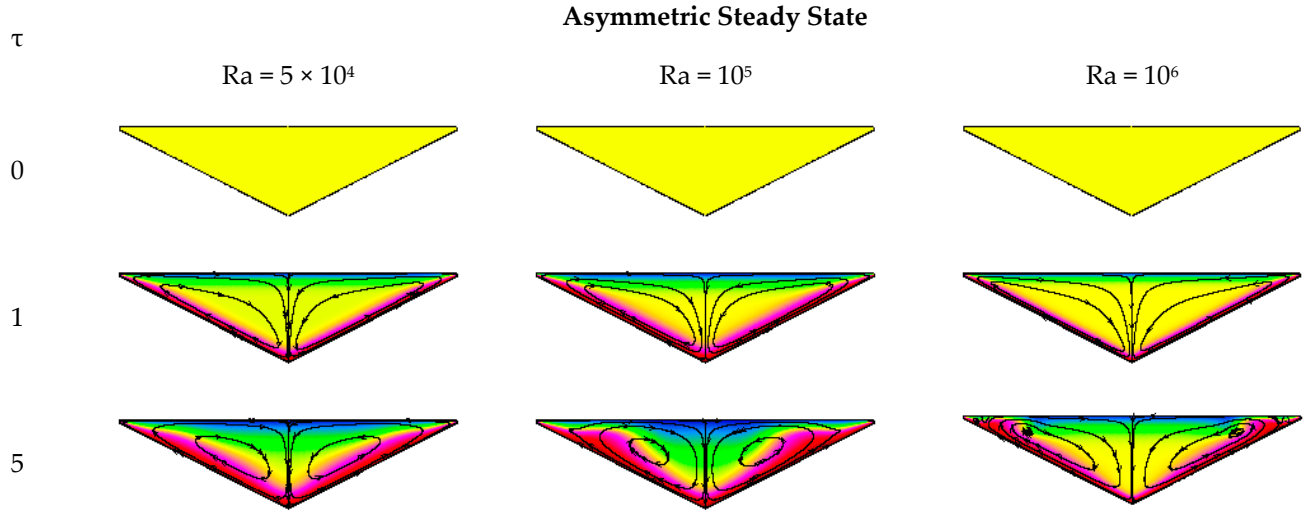

Figure 9. *Cont.*

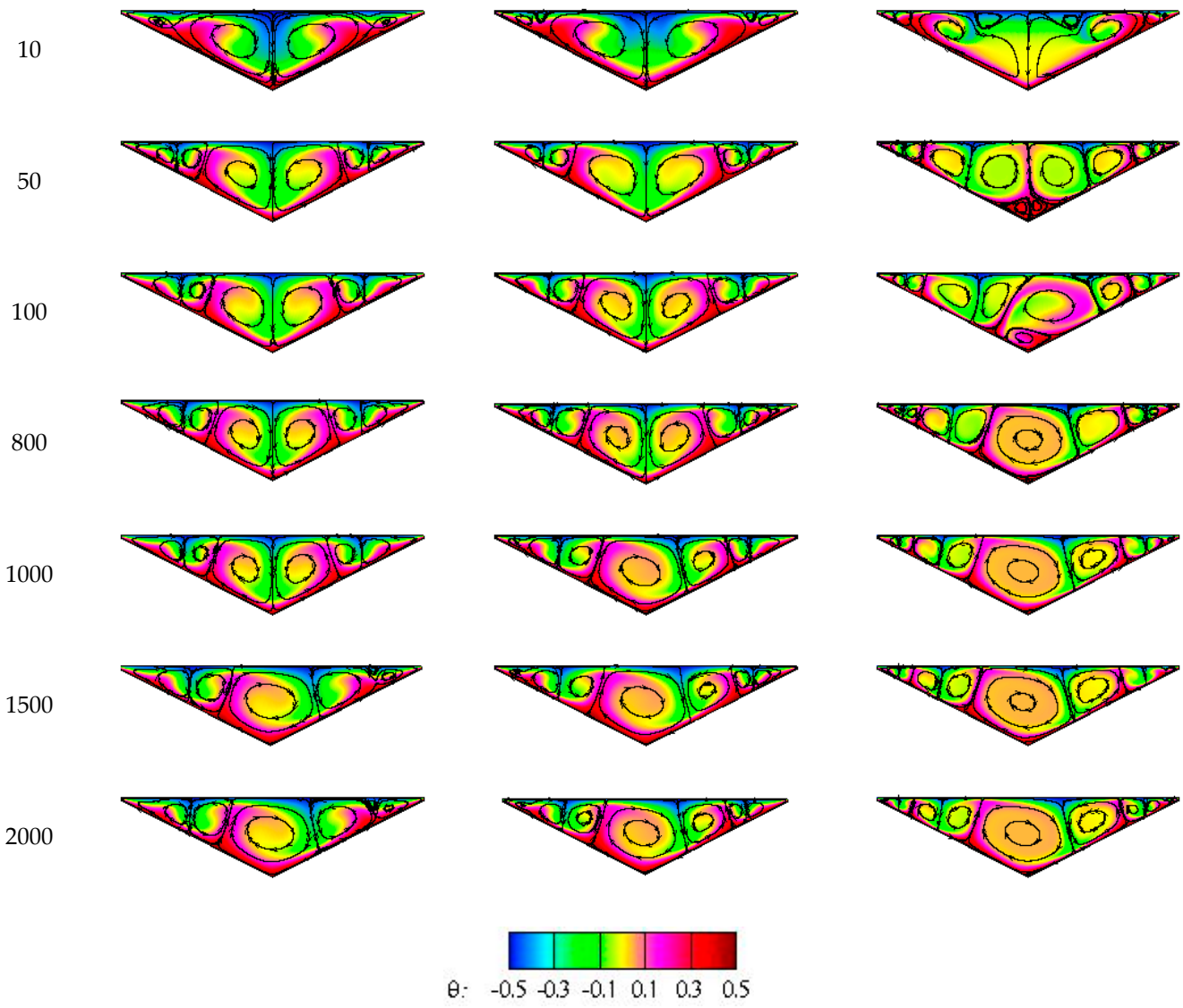

Figure 9. Streamlines and isotherms at various non-dimensional time intervals for Ra = 5 × 10^4, Ra = 10^5 and Ra = 10^6.

Clearly, the temperature and velocity effect on the flow in the cavity with time, as has been calculated in Figure 10 for more precision at a range of Rayleigh numbers and various points. Figure 10a,b demonstrate that, at first, the temperatures are uniform at points P_1 and P_2, but point P_5 is located close to the heated wall (see Figure 1), which causes it to heat up more quickly than the other points in the early stage. As time goes on, the temperature in the transitional stage first drops and then rises, ultimately achieving its constant point in the fully developed stage, when there are no longer any temperature variations. Also, from Figure 10d,e, it is clearly seen that the velocity increases with the passing of time. The velocity overshoots in the transitional period before becoming stable in the fully developed stage. Figure 10c shows that the temperature increases in the transitional stage and becomes stable in the fully developed stage. In contrast, the velocity in Figure 10f fluctuates during the transitional period before becoming constant during the last stage. The preceding figures and analyses indicate that in an asymmetric state, the flow becomes unsteady in the transitional period and then steady in the fully developed stages.

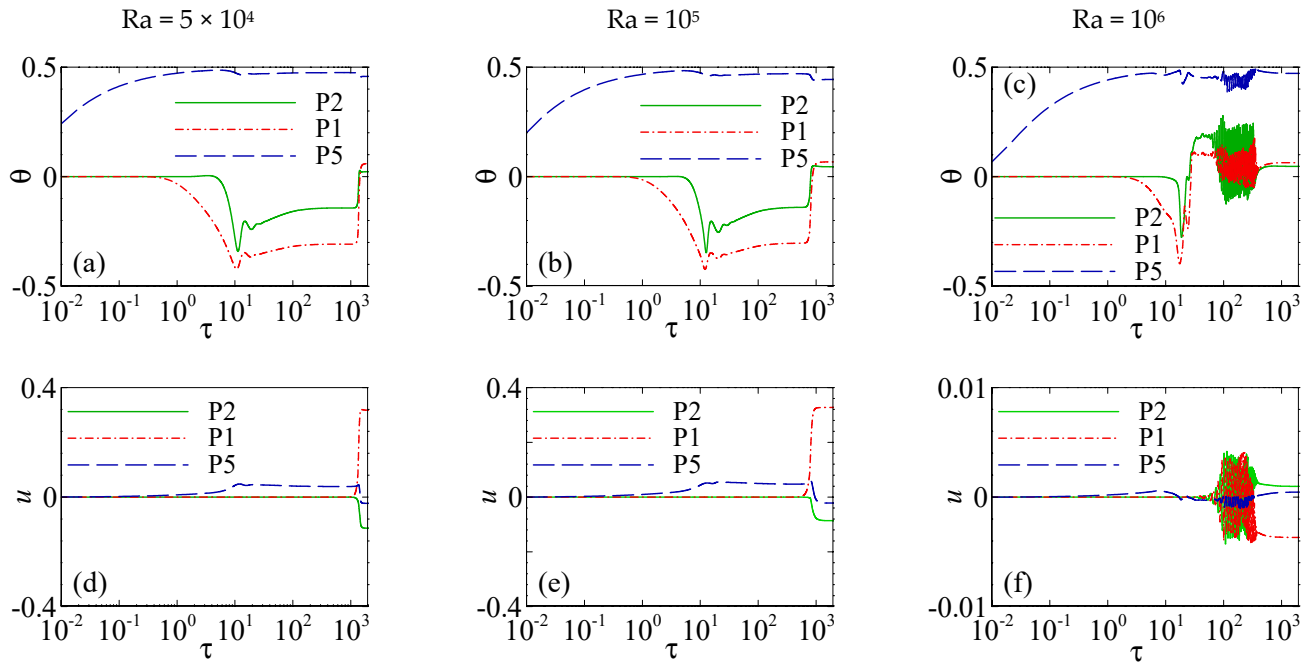

Figure 10. Times series of the temperature and velocity at three distinct points, P_1 (0, 0.825), P_2 (0, 0.46), and P_5 (0.5, 0.255), for (**a**,**d**) when Ra = 5 × 10^4, for (**b**,**e**) when Ra = 10^5, and for (**c**,**f**) when Ra = 10^6.

5.2.2. Other Bifurcations

For higher Rayleigh numbers, the asymmetric isotherms and streamlines are depicted in Figure 11. It is evident that when the Rayleigh number increases, several types of further bifurcations occur, leading to an increase in the number of cells, as seen in Figure 11. In Figure 11a, there are two cells in the cavity. With the increase in the Ra, we see in Figure 11b that the cell number becomes four; in Figure 11c, the cell number is five. For instance, the cell number increases from six at a Rayleigh number of 5 × 10^4 in Figure 11d to more than six, as shown in Table 3. Figure 11 demonstrates that when the Rayleigh number rises, more new tiny cells develop in the left or right side of the cavity. However, a single large cell consistently persists at the center of the cavity. This indicates that the flow configuration within the cavity becomes increasingly complex for an asymmetric steady state when the Rayleigh number rises.

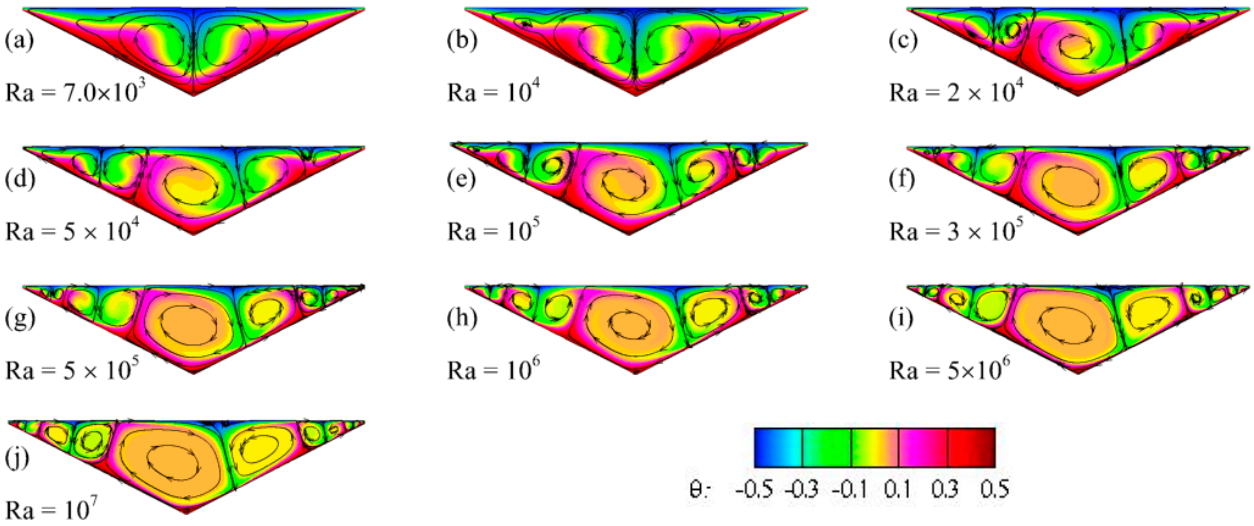

Figure 11. At the fully developed stage, streamlines and isotherms for various Rayleigh numbers.

Table 3. Number of cells with corresponding Rayleigh numbers.

Rayleigh Number	Number of Cells
7×10^3	2
10^4	4
2×10^4	5
5×10^4	6
10^5	7
3×10^5	9
5×10^5	10
10^6	11
5×10^6	13
10^7	15

Table 3 shows that the Rayleigh number and the number of cells are linked. The Rayleigh number increased from 7×10^3 to 10^7 as the number of bifurcations increased from two to fifteen cells. For Ra values between 10^4 and 10^7, it is clear that there is a nearly linear link between the number of cells and the Ra.

5.3. Unsteady Flow

An asymmetric flow structure is created as a consequence of a Pitchfork bifurcation that arises during the later stages of the transitional period. As already noted, the numerical simulation experiences a Pitchfork bifurcation early on. Figure 12 displays the streamlines and isotherms for Ra = 10^7, Ra = 5×10^7, and Ra = 10^8 to better study the flow at greater Rayleigh numbers for different times. In Figure 12, initially at $\tau = 0$, the temperature is constant for all the Ra values. The figure depicts that the fluids are symmetric for all the Rayleigh numbers when $\tau = 1$, but as time passes, when $\tau = 5$, they become asymmetric and create two additional tiny cells in the cavity at the right and left upper corners. With increasing cell numbers, all the Ra values at $\tau = 10$ in Figure 12 exhibit the same flow pattern. When $\tau = 50$ for Ra = 10^7, a tiny cell appears in the top center of the two largest cells in the cavity, but for Ra = 5×10^7 and Ra = 10^8 at $\tau = 50$, the steady flow breaks and becomes unsteady. In Figure 11, the flow is more convoluted for Ra = 5×10^7 and Ra = 10^8 at $\tau = 50$, even though it is still constant, and the biggest cell has a few smaller cells at its upper right and left side. This indicates that between Ra = 10^7 and 5×10^7, there is a Hopf bifurcation (see [19] for details on the bifurcation). When Ra = 10^7, the asymmetric steady state remains similar at all the subsequent transitional, developed transitional and fully developed stages when τ = 100, 1000, 1500 and 2000, respectively. The observed trends remain consistent during both the developed transitional stage (τ = 1000 and 1500) and the completely developed stage (τ = 2000) for two distinct Rayleigh numbers, namely Ra = 5×10^7 and Ra = 10^8. But as τ rises, as shown in Figure 12 for Ra = 10^8 at $\tau = 2000$, both cells grow in the middle of the two largest cells. The largest central cell exhibits a right-to-left movement. The unsteady flow becomes more and more complex due to its lack of stability.

Over time, the temperature series has been followed and analyzed spectrally to gain an understanding of the unsteady flow at higher Rayleigh numbers. Figure 13 displays the temperature variation over time and the power spectral densities according to various Ra values. Figure 13a demonstrates a steady flow throughout the fully established stage for Ra = 10^7, while Figure 13b exhibits periodic flow for Ra = 5×10^7. Additionally, Figure 13c displays the temperature power spectral density located in Figure 13b. The periodic flow's fundamental frequency, with harmonic modes, is $f_p = 0.397$. The periodic flow changes as the Rayleigh number rises. This indicates the occurrence of one more bifurcation for which a periodic solution transforms into another. As the Rayleigh number continues to rise, the unstable flow becomes chaotic, as seen in Figure 13d, which depicts the fully developed stage for Ra = 10^8. According to Figure 13e, the unique frequency with harmonic modes vanishes for Ra = 10^8, while the flow is chaotic but unstable at the fully developed stage.

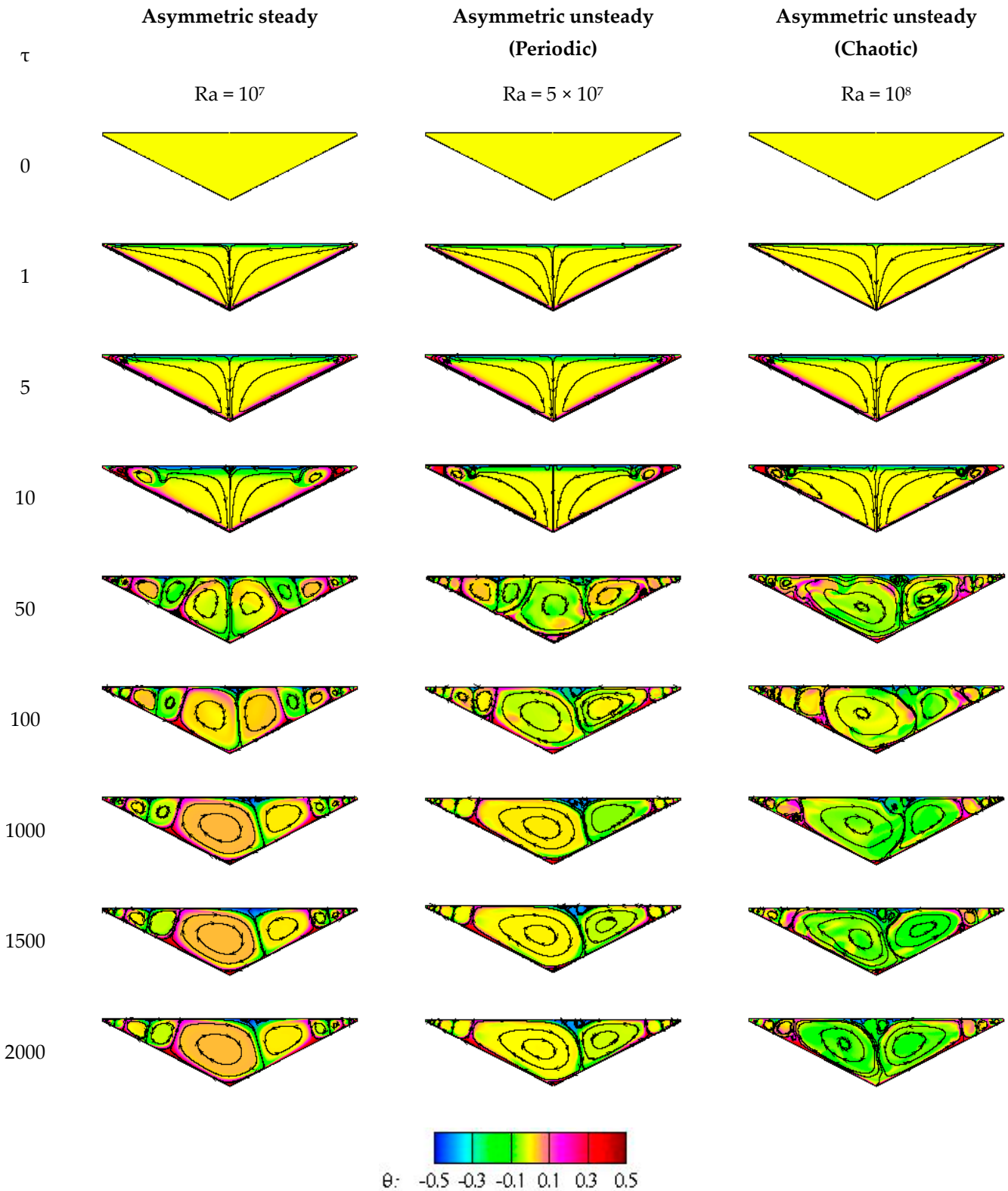

Figure 12. Streamlines and isotherms at various non-dimensional time intervals for distinct higher Rayleigh numbers: Ra = 10^7, Ra = 5×10^7 and Ra = 10^8.

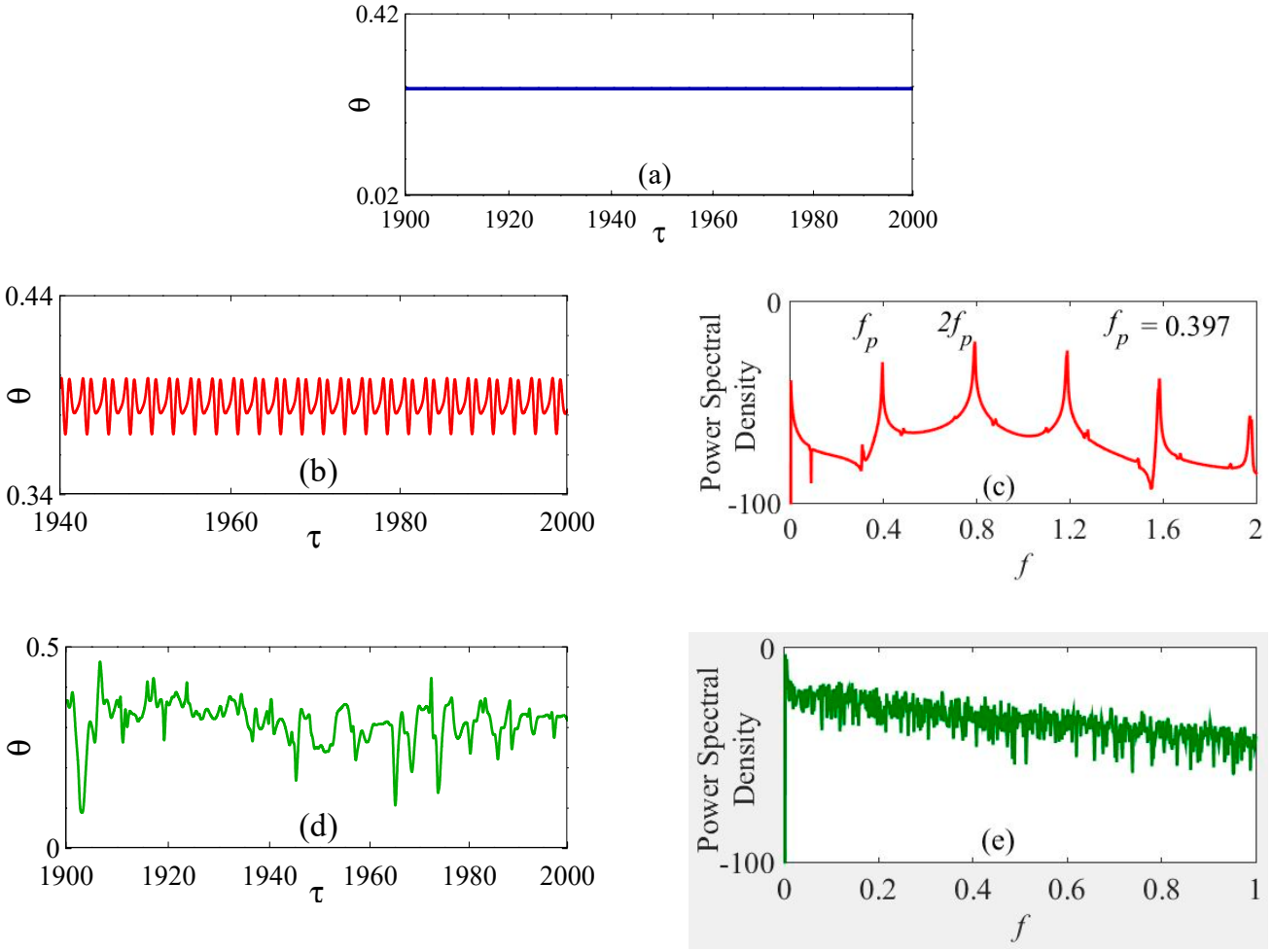

Figure 13. A time series of the temperature at the completely developed stage and the power spectral density at point P_5 (0.5, 0.255) (**a**) for Ra = 10^7, (**b**,**c**) for Ra = 5×10^7, and (**d**,**e**) for Ra = 10^8.

Figure 14 depicts a time series analysis of the temperature as well as the velocity at three distinct points, P1, P2, and P5, with higher Rayleigh numbers, specifically Ra = 10^7, 5×10^7 and 10^8. Because the temperature is initially isothermal and constant in Figure 14a–c, it is the same at various stages in the early stage for greater Rayleigh numbers. In the transitional period, the temperature fluctuates with the time for each Ra in Figure 14. In the advanced stage of development, as Figure 14a shows, the temperature becomes constant; that is, there are no changes in the temperature, but in Figure 14b, we see that it becomes periodic. In Figure 14c, with the time increases, the flow becomes chaotic and more complex in the fully developed stage. However, the velocity (Figure 14d–f) starts off at zero and changes as time moves on during the transitional stage. Figure 14d–f all show that the flow is stable in the developed stage, periodic in Figure 14e, and chaotic in Figure 14f. In addition, most importantly, it seems that the flow of a periodic state changes from a periodic one to a chaotic one at a stage of transition. Furthermore, in a chaotic state, the flow is constantly chaotic at the transitional stage and at the developed stages.

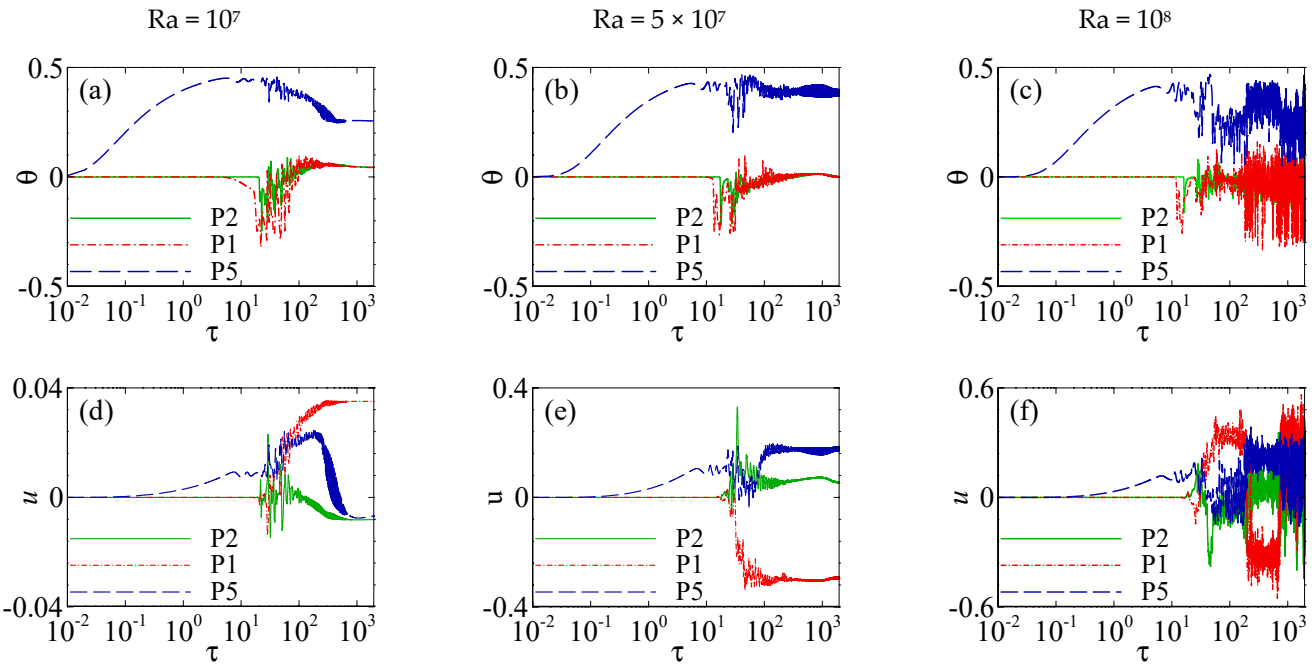

Figure 14. Times series of the temperature and velocity at three distinct points, P_1 (0, 0.825), P_2 (0, 0.46) and P_3 (0.5, 0.255), for (**a**,**d**) when Ra = 10^7, for (**b**,**e**) when Ra = 5×10^7, and for (**c**,**f**) when Ra = 10^8.

5.3.1. Hopf Bifurcation

Figure 15 displays the streamlines and isotherms for Ra = 10^7 and Ra = 2×10^7 to allow for a more in-depth analysis of the flow in the case of greater Rayleigh numbers. Figure 15a illustrates the more complicated flows throughout the fully developed stage for Ra = 10^7, even though it is still steady. However, a deeper inspection of the numerical results reveals that more than two tiny cells alternately occur; as a result, the flow becomes unsteady for Ra = 2×10^7 in the fully developed stage. This indicates that there is a Hopf bifurcation between Ra = 10^7 and 2×10^7.

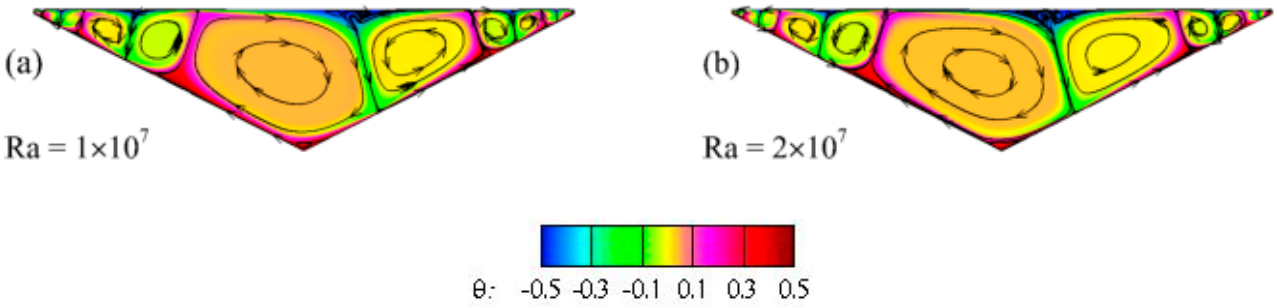

Figure 15. Streamlines and isotherms at Ra = 10^7 and Ra = 2×10^7.

Figure 16 shows the attractors with values ranging from τ = 300 to 2000 for Ra = 10^7 and τ = 1000 to 1500 for Ra = 5×10^7 at the defining point P_1 (0, 0.825) in order to facilitate an understanding of the Hopf bifurcation, which takes place during the transition from the steady state to the periodic stage. Figure 16a illustrates that the u-θ plane curve reaches a specific value when Ra = 10^7. Figure 16b displays a limit cycle for Ra = 5×10^7. As a result, when Ra = 5×10^7, a Hopf bifurcation takes place (for further information on the Hopf bifurcation, see [65]).

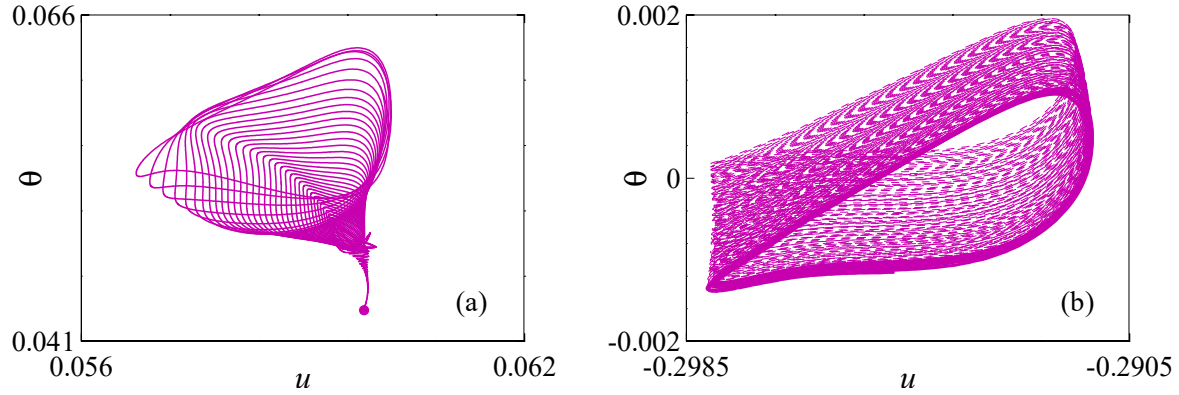

Figure 16. The limit point and limit cycle for (**a**) Ra = 10^7, and for (**b**) Ra = 5×10^7 on the plane of u-θ at point P_1 (0, 0.825).

5.3.2. Chaotic

Figure 17a illustrates that the two cells in the upper right portion of the biggest cell become bigger precisely as the Rayleigh number increases. The biggest cell in the center likewise travels across the right as well as the left sides when Ra = 10^8, as seen in Figure 17b. The unsteady flow becomes increasingly complicated, which is known as chaotic.

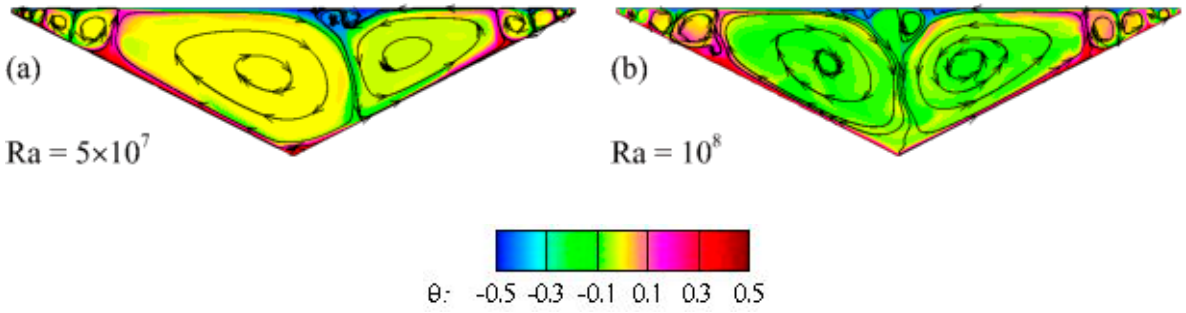

Figure 17. Streamlines and isotherms at Ra = 5×10^7 and Ra = 10^8.

Figure 18 shows the trajectories through the stage space in the u-θ plane at point P_5 (0.5, 0.255) for Ra = 5×10^7 and 10^8 in order to more clearly illustrate how the periodic condition changes to a chaotic state. The observed limit cycle depicted in Figure 18a demonstrates the periodic nature of the unsteady flow at a Rayleigh number of Ra = 5×10^7. This finding aligns with the information presented in Figure 16 and further supports the existence of a limit cycle. In Figure 18b, the trajectory for Ra = 10^8 shows that the periodic flow changes to chaotic, which takes place between Ra = 5×10^7 and 10^8. For a detailed explanation of the stage-space trajectories, see [66].

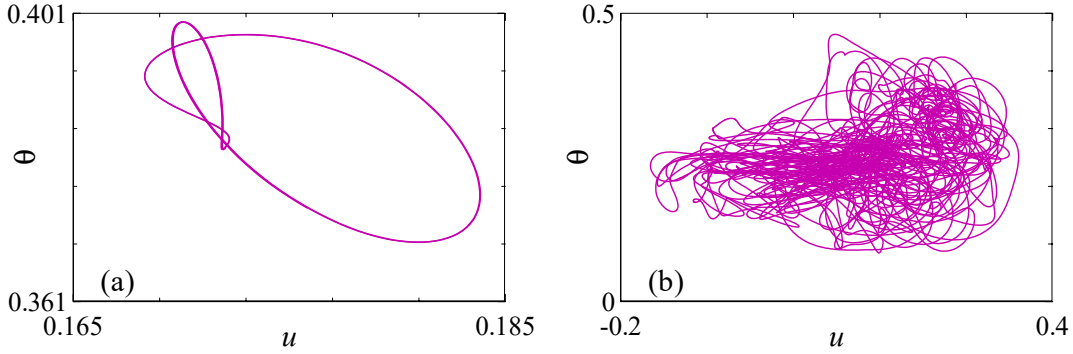

Figure 18. Temperature and x-velocity trajectories in the stage space for the values of Ra = 5×10^7 and Ra = 10^8 at the point P_5 (0.5, 0.255).

5.4. Temperature and Velocity

Figure 19 displays the temperature and velocity at designated points P_1 (0, 0.825) over time across various Rayleigh numbers. This information is provided to help understand the formation of natural convection flow patterns within the cavity in response to sudden heating from the inclined walls and cooling from the top wall. The simulations were conducted using various Rayleigh numbers, ranging from Ra = 10^0 to 10^8. An observation was made about the various fluctuating flow properties throughout a range of Rayleigh numbers. Figures 5, 6, 9 and 12 depict the isotherms and corresponding streamlines for various Rayleigh numbers, specifically focusing on the case where $A = 0.5$. The observed numerical outcomes for the various Ra values, as depicted in Figure 19, exhibit discernible changes. At the lowest Rayleigh number, convective flow instabilities may first be seen. However, the number of waves and the unsteadiness increase with increasing Rayleigh numbers. Based on the symmetry and continuous flow, it is expected that the flow is weaker and displays symmetric behavior at Ra = 10^3. During the transitional stage of fluid flow, it is observed that the flow develops asymmetrically for the Rayleigh numbers of Ra = 10^4, 10^5, and 10^6. However, as the flow progresses toward the fully developed stage, it stabilizes. Finally, the flow changes into periodic and chaotic states at Ra = 10^7 and Ra = 10^8, respectively, as shown in Figure 19a. As illustrated in Figure 19b, a similar characteristic can also be seen in the x-velocity at the point P_1.

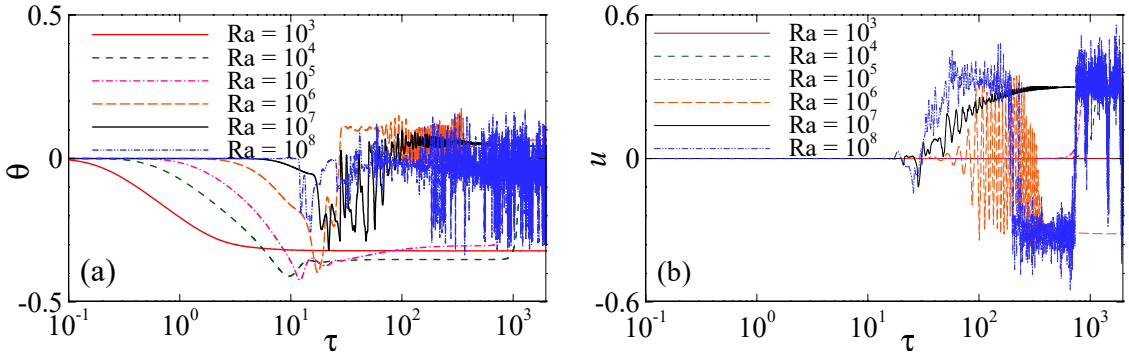

Figure 19. (**a**) Temperature time series and (**b**) x-velocity time series for different Rayleigh numbers at point P_1 (0, 0.825).

5.5. Heat Transfer

During the transitional stage, convective heat transfer dominates in the V-shaped cavity. Convective heat transfer is enhanced by the irregular fluctuations and vortices that encourage fluid mixing. For air, the Nusselt number that expresses the proportion of convective to conductive heat transfer is examined. The Nusselt number Nu [60–62] is defined as:

$$Nu = \frac{1}{ln} \int_{ln}^{\frac{\partial \theta}{\partial n}} ds. \tag{11}$$

In accordance with Figure 20a, a time series representation has been provided to illustrate the average Nusselt number associated with the inclined wall. This particular measurement has been employed to quantify the amount of heat transfer occurring across the cavity wall. It is important to highlight that Figure 20b additionally presents the representation of the Nu after being normalized by $Ra^{1/4}$. The presence of a significant temperature difference between the fluid and the wall may contribute to the substantial heat transfer phenomenon. Consequently, it is expected that a large value of the Nusselt number (Nu) is observed. The observed phenomenon can be attributed to the simultaneous application of heating and cooling to both the inclined walls and the top wall. Figure 20b illustrates how, as time moves on, throughout the beginning stage, the Nu dramatically decreases, and throughout the fully devolved stage, it gradually attains a value that is either constant or oscillatory, and this value is determined by the Rayleigh number. This

is similar to those in Figure 13, where the Nusselt number oscillates for Ra $\geq 5 \times 10^7$ but remains constant for Ra = 10^7. In contrast to those in Figure 20a, it is obvious that the Nu versus the curves in Figure 20b collapse together. As a result, Nu~$Ra^{1/4}$ scaling works effectively, considering the current set of Ra values. Figure 20b demonstrates that $NuRa^{-1/4}$ almost maintains a constant value of 1.473 as the Rayleigh number rises, although somewhat decreasingly.

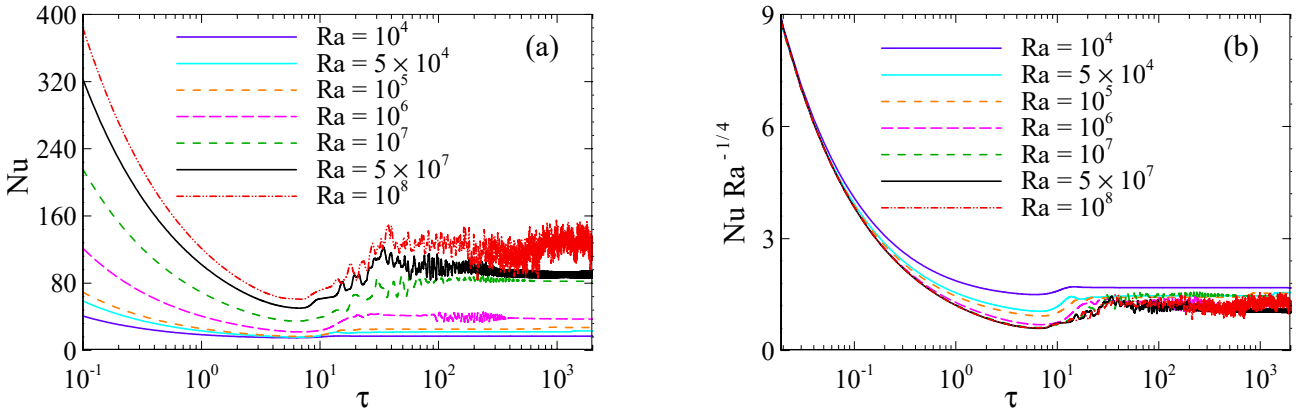

Figure 20. (**a**) The Nusselt number and (**b**) the normalized Nusselt number time series for several kinds of Rayleigh numbers.

6. Conclusions

The current investigation delves into the numerical exploration of unsteady 2D natural convection flows within a valley-shaped cavity filled with water, where heating occurs along the inclined walls while cooling is facilitated through the top wall. The study encompasses a broad spectrum of Rayleigh numbers ranging from Ra = 10^0 to 10^8, under the Prandtl number Pr = 0.71 and the aspect ratio A = 0.5, spanning various non-dimensional times from τ = 0 to τ = 5000. The research delineates the diverse flow structures evolving within the cavity over time and scrutinizes the relationship between heat transfer dynamics and Rayleigh numbers.

Analysis reveals that the progression of natural convection flows manifests in three discernible stages: an initial stage, a transitional stage, and a fully developed stage, following the sudden application of heating through inclined walls and cooling through the top wall. This study examines the symmetric, asymmetric, and unsteady flow patterns characterizing these stages, supported by numerical findings. Specifically, the investigation primarily focuses on elucidating the flow mechanisms across all the stages. It is observed that natural convection flows remain steady at the symmetric state for Rayleigh numbers ranging from Ra = 10^0 to 7×10^3. Beyond Ra > 7×10^3, flows exhibit asymmetry. Furthermore, during the asymmetric state, the flow transitions into an unsteady regime in the transitional stage before stabilizing at the fully developed stage for 7×10^3 < Ra < 10^7. This study highlights that periodic unsteady flows evolve into chaotic states during the transitional stage, reverting to periodic behavior in the developed stage at Ra = 5×10^7, while at higher Rayleigh numbers like Ra = 10^8, the chaotic flow remains predominant in the unsteady regime.

Additionally, the investigation discusses the notable bifurcations observed in the fully developed states. Detailed analyses, including the power spectral density and stage space trajectories for Pr = 0.71, are provided. Numerical studies elucidate the intricacies of heat transfer and demonstrate the influence of the Rayleigh number on both the Nusselt number and flow rate dynamics.

Author Contributions: Conceptualization, S.B. and S.C.S.; investigation, L.R.R.; methodology, L.R.R.; project administration, S.C.S.; software, L.R.R.; supervision, S.B. and S.C.S.; validation, L.R.R.; writing—original draft, S.B. and L.R.R.; writing—review and editing, F.X. and S.C.S. All authors have read and agreed to the published version of the manuscript.

Funding: This research received no external funding.

Data Availability Statement: No data is used in this study. Use of Artificial Intelligence: During the preparation of this work, we used ChatGPT in order to improve the language and readability.

Conflicts of Interest: The authors declare no conflict of interest.

Nomenclature

κ	thermal diffusivity
τ	non-dimensional time
$\Delta\tau$	non-dimensional time step
θ	non-dimensional temperature
ν	kinematic viscosity
ρ	Density
β	thermal expansion coefficient
A	aspect ratio
g	gravitational acceleration
Gr	Grashof number
L	half length of the cavity
H	height of the cavity
k	thermal conductivity
l	inclined wall length
n	non-dimensional coordinate normal to the inclined wall
ln	non-dimensional length of the inclined wall
Nu	Nusselt number
P	Pressure
p	non-dimensional pressure
Pr	Prandtl number
Ra	Rayleigh number
Ra_c	critical Rayleigh number for the break of the symmetric state
T	dimensional temperature
T_0	initial temperature
T_c	cold top wall temperature
T_h	hot inclined wall temperature
t	Time
ΔT	temperature difference
U, V	velocity components
u, v	the non-dimensional velocity components
X, Y	coordinates in the horizontal and vertical
x, y	the non-dimensional coordinates in the horizontal and vertical

References

1. Gill, E. The boundary-layer regime for convection in a rectangular cavity. *J. Fluid Mech.* **1966**, *26*, 515–536. [CrossRef]
2. Prandtl, L. *Essentials of Fluid Dynamics*; Blackie: London, UK, 1952; pp. 422–425.
3. Ravi, M.R.R.; Henkes, R.A.W.M.; Hoogendoorn, C.J. On the high-Rayleigh-number structure of steady laminar natural-convection flow in a square enclosure. *J. Fluid Mech.* **1994**, *262*, 325–351. [CrossRef]
4. Xu, F.; Patterson, J.C.; Lei, C. An experimental study of the unsteady thermal flow around a thin fin on a sidewall of a differentially heated cavity. *Int. J. Heat Fluid Flow* **2008**, *29*, 1139–1153. [CrossRef]
5. Cui, H.; Xu, F.; Saha, S.C. Transition to unsteady natural convection flow in a prismatic enclosure of triangular section. *Int. J. Therm. Sci.* **2017**, *111*, 330–339. [CrossRef]
6. Saha, S.C.; Khan, M.M.K. A review of natural convection and heat transfer in attic-shaped space. *Energy Build.* **2011**, *43*, 2564–2571. [CrossRef]
7. Cui, H.; An, H.; Wang, W.; Han, Z.; Hu, B.; Xu, F.; Liu, Q.; Saha, S.C. Numerical Study of Mixed Convection and Heat Transfer in Arc-Shaped Cavity with Inner Heat Sources. *Appl. Sci.* **2023**, *13*, 1029. [CrossRef]

8. Chuhan, I.S.; Li, J.; Guo, Z.; Yaqub, M.; Manan, M.A. Heat Transfer Investigation in Plus-Shaped Enclosure Using Power Law Fluid: A Finite Element Approach. *Appl. Sci.* **2023**, *13*, 11042. [CrossRef]
9. Sarangi, A.; Sarangi, A.; Sahoo, S.S.; Mallik, R.K.; Awad, M.M. Conjugate Radiation and Convection Heat Transfer Analysis in Solar Cooker Cavity Using a Computational Approach. *Energies* **2023**, *16*, 3868. [CrossRef]
10. Gebhart, B.; Jaluria, Y.; Mahajan, R.L.; Sammakia, B. *Buoyancy-Induced Flows and Transport*; Hemisphere: Washington, DC, USA, 1988.
11. Manneville, P. Rayleigh-Bénard convection, thirty years of experimental, theoretical, and modeling work, Dynamics of spatio-temporal cellular structures. In *Dynamics of Spatio-Temporal Cellular Structures: Henri Bénard Centenary Review*; Springer: New York, NY, USA, 2006; Volume 207, pp. 41–65.
12. Bodenschatz, E.; Pesch, W.; Ahlers, G. Recent developments in Rayleigh Benard convection. *Annu. Rev. Fluid Mech.* **2000**, *32*, 709–778. [CrossRef]
13. Sparrow, E.M.; Husar, R.B. Longitudinal vortices in natural convection flow on inclined plates. *J. Fluid Mech.* **1969**, *37*, 251–255. [CrossRef]
14. Batchelor, G.K. Heat transfer by free convection across a closed cavity between vertical boundaries at different temperatures. *Q. Appl. Math.* **1954**, *12*, 209–233. [CrossRef]
15. Eckert, E.R.G.; Carlson, W.O. Natural convection in an air layer enclosed between two vertical plates at different temperatures. *Int. J. Heat Mass Transf.* **1961**, *2*, 106–120. [CrossRef]
16. Elder, J.W. Laminar free convection in a vertical slot. *J. Fluid Mech.* **1965**, *23*, 77–98. [CrossRef]
17. Xu, F.; Patterson, J.C.; Lei, C. An experimental study of the coupled thermal boundary layers adjacent to a partition in a differentially heated cavity. *Exp. Therm. Fluid Sci.* **2014**, *54*, 12–21. [CrossRef]
18. Xu, F.; Patterson, J.C.; Lei, C. Transient natural convection flows around a thin fin on the sidewall of a differentially heated cavity. *J. Fluid Mech.* **2009**, *639*, 261–290. [CrossRef]
19. Patterson, J.C.; Imberger, J. Unsteady natural convection in a rectangular cavity. *J. Fluid Mech.* **1980**, *100*, 65–86. [CrossRef]
20. Patterson, J.C.; Armfield, S.W. Transient features of natural convection in a cavity. *J. Fluid Mech.* **1990**, *219*, 469–497. [CrossRef]
21. De, A.K.; Eswaran, V.; Mishra, P.K. Scaling of heat transport and energy spectra of turbulent Rayleigh-Bénard convection in a large-aspect-ratio box. *Int. J. Heat Fluid Flow* **2017**, *67*, 111–124. [CrossRef]
22. Rahaman, M.M.; Bhowmick, S.; Mondal, R.N.; Saha, S.C. Unsteady natural convection in an initially stratified air-filled trapezoidal enclosure heated from below. *Processes* **2022**, *10*, 1383. [CrossRef]
23. Rahaman, M.M.; Bhowmick, S.; Mondal, R.N.; Saha, S.C. A Computational Study of Chaotic Flow and Heat Transfer within a Trapezoidal Cavity. *Energies* **2023**, *16*, 5031. [CrossRef]
24. Princevac, M.; Fernando, H.J.S. Morning breakup of cold pools in complex terrain. *J. Fluid Mech.* **2008**, *616*, 99–109. [CrossRef]
25. Asan, H.; Namli, L. Laminar natural convection in a pitched roof of triangular cross-section: Summer day boundary conditions. *Energy Build.* **2000**, *33*, 69–73. [CrossRef]
26. Asan, H.; Namli, L. Numerical simulation of buoyant flow in a roof of triangular cross-section under winter day boundary conditions. *Energy Build.* **2001**, *33*, 753–757. [CrossRef]
27. Salmun, H. Convection patterns in a triangular domain. *Int. J. Heat Mass Transf.* **1995**, *38*, 351–362. [CrossRef]
28. Salmun, H. The stability of a single-cell steady-state solution in a triangular enclosure. *Int. J. Heat Mass Transf.* **1995**, *18*, 363–369. [CrossRef]
29. Poulikakos, D.; Bejan, A. The fluid dynamics of an attic space. *J. Fluid Mech.* **1983**, *131*, 251–269. [CrossRef]
30. Poulikakos, D.; Bejan, A. Natural convection experiments in a triangular enclosure. *J. Heat Transf.* **1983**, *105*, 652–655. [CrossRef]
31. Flack, R.D. The experimental measurement of natural convection heat transfer in triangular enclosures heated or cooled from below. *J. Heat Transf.* **1980**, *102*, 770–772. [CrossRef]
32. Holtzman, G.A.; Hill, R.W.; Ball, K.S. Laminar natural convection in isosceles triangular enclosures heated from below and symmetrically cooled from above. *J. Heat Transf.* **2000**, *122*, 485–491. [CrossRef]
33. Lei, C.; Armfield, S.W.; Patterson, J.C. Unsteady natural convection in a water-filled isosceles triangular enclosure heated from below. *Int. J. Heat Mass Transf.* **2008**, *51*, 2637–2650. [CrossRef]
34. Saha, S.C.; Lei, C.; Patterson, J.C. Natural convection in a triangular enclosure subject to periodic thermal forcing. In Proceedings of the 13th International Heat Transfer Conference, Sydney, Australia, 13–18 August 2006.
35. Saha, S.C.; Lei, C.; Patterson, J.C. Effect of aspect ratio on natural convection in attics subject to periodic thermal forcing. *Anziam J.* **2007**, *48*, C618–C632. [CrossRef]
36. Saha, S.C.; Patterson, J.C.; Lei, C. Natural convection in attic-shaped spaces subject to sudden and ramp heating boundary conditions. *Heat Mass Transf.* **2010**, *46*, 621–638. [CrossRef]
37. Saha, S.C.; Patterson, J.C.; Lei, C. Natural convection in attics subject to instantaneous and ramp cooling boundary conditions. *Energy Build.* **2010**, *42*, 1192–1204. [CrossRef]
38. Saha, S.C.; Patterson, J.C.; Lei, C. Natural convection and heat transfer in attics subject to periodic thermal forcing. *International J. Therm. Sci.* **2010**, *49*, 1899–1910. [CrossRef]
39. Lei, C.; Patterson, J.C. Natural convection in a reservoir sidearm subject to solar radiation: Experimental observations. *Exp. Fluids* **2002**, *32*, 590–599. [CrossRef]

40. Lei, C.; Patterson, J.C. Unsteady natural convection in a triangular enclosure induced by absorption of radiation. *J. Fluid Mech.* **2002**, *460*, 181–209. [CrossRef]
41. Lei, C.; Patterson, J.C. Natural convection in a reservoir sidearm subject to solar radiation: A two-dimensional simulation. *Numer. Heat Transf.* **2002**, *42*, 13–32. [CrossRef]
42. Mao, Y.; Lei, C.; Patterson, J.C. Unsteady natural convection in a triangular enclosure induced by absorption of radiation—A revisit by improved scaling analysis. *J. Fluid Mech.* **2009**, *622*, 75–102. [CrossRef]
43. Mao, Y.; Lei, C.; Patterson, J.C. Unsteady near-shore natural convection induced by surface cooling. *J. Fluid Mech.* **2010**, *642*, 213–233. [CrossRef]
44. Mao, Y.; Lei, C.; Patterson, J.C. Characteristics of instability of radiation-induced natural convection in shallow littoral waters. *Int. J. Therm. Sci.* **2010**, *49*, 170–181. [CrossRef]
45. Bednarz, T.P.; Lei, C.; Patterson, J.C. A numerical study of unsteady natural convection induced by iso-flux surface cooling in a reservoir model. *Int. J. Heat Mass Transf.* **2009**, *52*, 56–66. [CrossRef]
46. Whiteman, C.D. Breakup of temperature inversions in deep mountain valleys: Part I. Observations. *J. Appl. Meteorol.* **1982**, *21*, 270–289. [CrossRef]
47. Roach, W.T.; Brown, R.; Caughey, S.J.; Garland, J. The physics of radiation fog: Part I: A field study. *Q. J. R. Meteorol. Soc.* **1976**, *102*, 313–333.
48. Pilie, R.J.; Mack, E.J.; Kocmond, W.C.; Rogers, C.W.; Eadie, W.J. The life cycle of valley fog. Part I: Micrometeorological characteristics. *J. Appl. Meteorol.* **1975**, *14*, 347–363. [CrossRef]
49. Fuzzi, S.; Facchini, M.C. The Po Valley fog experiment 1989, an overview. *Tellus* **1992**, *44B*, 448–468. [CrossRef]
50. Jiusto, J.E.; Lala Grieser, J.G.G. *Radiation Fog Field Programs Recent Studies*; Publication no. 869; Atmospheric Sciences Research Center, State University of New York (ASRC, SUNY): New York, NY, USA, 1983.
51. Zihua, L.; Limin, Z.; Qinghong, Z. The physical structure of the winter fog in Chongqing metropolitan area and its formation process. *Acta Meteorol. Sin.* **1994**, *8*, 316–328.
52. Haiden, T.; Whiteman, C.D. Katabatic flow mechanisms on a low-angle slope. *J. Appl. Meteorol.* **2005**, *44*, 113–126. [CrossRef]
53. Catalano, F.; Cenedese, A. High-resolution numerical modeling of thermally driven slope winds in a valley with strong capping. *Am. Meteorol. Soc.* **2010**, *49*, 1859–1880. [CrossRef]
54. Clark, P.A.; Hopwood, W.P. One-dimensional site-specific forecasting of radiation fog. Part 1: Model formulation and idealized sensitivity studies. *Meteorol. Appl.* **2001**, *8*, 279–286. [CrossRef]
55. Baumbach, G.; Vogt, U. Experimental determination of the effect of mountain-valley breeze circulation on air pollution in the vicinity of Freiburg. *Atmos. Environ.* **1999**, *33*, 4019–4027. [CrossRef]
56. Lehner, M.; Gohm, A. Idealized simulations of daytime pollution transport in a steep valley and its sensitivity to thermal stratification and surface albedo. *Bound.-Layer Meteorol.* **2010**, *134*, 327–351. [CrossRef]
57. Liu, H.; Liang, B.; Zhu, F.; Zhang, B.; Sang, J. Water-tank experiment on the thermal circulation induced by the bottom heating in an asymmetric valley. *Adv. Atmos. Sci.* **2004**, *21*, 536–546. [CrossRef]
58. Kenjeres, S. Heat transfer enhancement induced by wall inclination in turbulent thermal convection. *Phys. Rev. E* **2015**, *92*, 053006. [CrossRef]
59. Kimura, F.; Noguchi, T.; Kitamura, K. Fluid flow and heat transfer of natural convection around heated V-shaped cavity. *Mech. Eng. J.* **2016**, *3*, 16–00330. [CrossRef]
60. Bhowmick, S.; Saha, S.C.; Qiao, M.; Xu, F. Transition to a chaotic flow in a V-shaped triangular cavity heated from below. *Int. J. Heat Mass Transf.* **2019**, *128*, 76–86. [CrossRef]
61. Bhowmick, S.; Xu, F.; Molla, M.M.; Saha, S.C. Chaotic phenomena of natural convection for water in a V-shaped enclosure. *Int. J. Therm. Sci.* **2022**, *176*, 107526. [CrossRef]
62. Bhowmick, S.; Xu, F.; Zhang, X.; Saha, S.C. Natural convection and heat transfer in a valley-shaped cavity filled with initially stratified water. *Int. J. Therm. Sci.* **2018**, *128*, 59–69. [CrossRef]
63. Patankar, S.V. *Numerical Heat Transfer and Fluid Flow*; Hemisphere Publishing Corporation: New York, NY, USA, 1980.
64. Saha, S.C. Natural Convection Adjacent to an Inclined Flat Plate and in an Attic Space under Various Thermal Forcing Conditions. Ph.D. Thesis, School of Engineering and Physical Sciences, Townsville, Australia, 2009.
65. Drazin, P.G. *Introduction to Hydrodynamic Stability*; Cambridge University Press: Cambridge, UK, 2002.
66. McLaughlin, J.B.; Orszag, S.A. Transition from periodic to chaotic thermal convection. *J. Fluid Mech.* **1982**, *122*, 123–142. [CrossRef]

computation

MDPI

Article

Accelerating Conjugate Heat Transfer Simulations in Squared Heated Cavities through Graphics Processing Unit (GPU) Computing

César Augusto Borges da Silva Reis [1], Daniel Botezelli [1], Arthur Mendonça de Azevedo [1], Elisan dos Santos Magalhães [1,*] and Aristeu da Silveira Neto [2]

[1] Applied Thermal Engineering Laboratory, Energy Department, Aeronautics Institute of Technology—ITA, São José dos Campos 12228-900, Brazil; arthurama@ita.br (A.M.d.A.)
[2] School of Mechanical Engineering, Federal University of Uberlândia—UFU, Uberlandia 38400-902, Brazil; aristeus@ufu.br
* Correspondence: elisan@ita.br

Abstract: This research develops an innovative framework for accelerating Conjugate Heat Transfer (CHT) simulations within squared heated cavities through the application of Graphics Processing Units (GPUs). Although leveraging GPUs for computational speed improvements is well recognized, this study distinguishes itself by formulating a tailored optimization strategy utilizing the CUDA-C programming language. This approach is specifically designed to tackle the inherent challenges of modeling squared cavity configurations in thermal simulations. Comparative performance evaluations reveal that our GPU-accelerated framework reduces computation times by up to 99.7% relative to traditional mono-core CPU processing. More importantly, it demonstrates an increase in accuracy in heat transfer predictions compared to existing CPU-based models. These results highlight not only the technical feasibility but also the substantial enhancements in simulation efficiency and accuracy, which are crucial for critical engineering applications such as aerospace component design, electronic device cooling, and energy system optimization. By advancing GPU computational techniques, this work contributes significantly to the field of thermal management, offering a potential for broader application and paving the way for more efficient, sustainable engineering solutions.

Keywords: CUDA; Conjugate Heat Transfer; GPU; CUDA-C; computational time reduction

Citation: da Silva Reis, C.A.B.; Botezelli, D.; de Azevedo, A.M.; dos Santos Magalhães, E.; da Silveira Neto, A. Accelerating Conjugate Heat Transfer Simulations in Squared Heated Cavities through Graphics Processing Unit (GPU) Computing. *Computation* **2024**, *12*, 106. https://doi.org/10.3390/computation12050106

Academic Editors: Ali Cemal Benim, Rachid Bennacer, Abdulmajeed A. Mohamad, Paweł Oclon, Sang-Ho Suh and Jan Taler

Received: 30 March 2024
Revised: 9 May 2024
Accepted: 13 May 2024
Published: 19 May 2024

1. Introduction

The early exploration into Conjugate Heat Transfer (CHT) problems by Perelman [1] highlighted the complexity of solving heat conduction equations for solid bodies and their surrounding fluids simultaneously. Further advancements were made by Luikov et al. [2], who developed analytical methods to address convective heat transfer issues, acknowledging the crucial role of heat propagation in solids in contact with moving fluids. In the mid-1970s, Chida and Katto [3] utilized vectorial dimensional analysis to propose new dimensionless groups that encapsulate the conjugate nature of heat transfer. The impact of porous media within cavities on heat transfer was experimentally explored by Seki et al. [4]. Inaba and Fukuda [5] conducted a groundbreaking study on the effects of water's density inversion near 4 °C within inclined square cavities, revealing unique natural convection patterns that deviate significantly from those observed in traditional Boussinesq fluids. The late 1980s saw Ho and Yih [6] numerically investigate the attenuated heat transfer rates in air-filled rectangular cavities with partitions. Frederick and Valencio [7] studied natural convection in square cavities with conducting partitions, demonstrating the significant impact of partition. These pioneering studies collectively provide a comprehensive foundation for the ongoing exploration of conjugated heat transfer phenomena, particularly

in configurations involving square cavities and conducting solids, including the effect of geometry and thermal properties on convective heat transfer mechanisms.

The exploration of CHT within square cavities has seen notable advancements over the last decade, characterized by innovative methodologies and diverse applications. For instance, Alkhalid et al. [8] studied buoyancy-driven rarefied gas dynamics within conjugate cavities, examining the effects of cavity aspect ratios, conductivity ratios, and tilt angles. Alsabery et al. [9] demonstrated the potential of nanofluids to significantly enhance thermal management through heatline visualization. Khatamifar et al. [10] optimized partitioned square cavities for improved thermal management. Gijon-Rivera et al. [11] simulated CHT in rooms with glazed windows, modeled as square cavities. Chen et al. [12] introduced a novel lattice Boltzmann approach, tackling the modeling complexities associated with fluid-porous interfaces. Alvarado-Juarez et al. [13] characterized thermal mechanisms in solar receivers, showcasing the crucial role of radiatively participating media in thermal analysis.

The acceleration of CHT problem resolutions through the use of GPUs has been a significant area of research over the last decade. Klimeš and Stetina [14] presented a fully three-dimensional GPU-based heat transfer and solidification model for the continuous casting of steel, highlighting the necessity for rapid computation in real-time applications like casting control and optimization. Zhang et al. [15] presented a GPU-assisted finite element methodology for the modeling and analysis of bio-heat transfer processes in thermal ablation treatment, demonstrating computational performance improvements of up to 55.3 times with GPU acceleration. Narang et al. [16] explored the use of GPUs for accelerating the numerical solution of heat and mass transfer equations, demonstrated drastic performance enhancements, and highlighted the potential of GPUs in speeding up complex simulations. Silvestri and Pecnik [17] implemented a fast Monte Carlo algorithm on GPUs for radiative heat transfer in turbulent flows; the study achieved significant speed-ups, enabling accurate solutions for radiative heat transfer that can be coupled to direct numerical simulations of turbulent flows. Dugast et al. [18] demonstrated an efficient GPU-based thermal process simulator for laser powder bed fusion additive manufacturing; the paper proposed a matrix-free preconditioned conjugate gradient algorithm, resulting in significant computational speedups. Luo et al. [19] focused on the heat transfer in a porous brick roof filled with phase change materials; the numerical study employed a GPU-accelerated multiple-relaxation-time Lattice Boltzmann Method to investigate thermal buffering capacity, demonstrating the efficiency of GPU acceleration in simulating complex thermal phenomena. Gou and Shen [20] introduced a new GPU-based CFD-DEM model designed to simulate gas–solid flow involving large numbers of particles and complex geometries. They developed an innovative coupling strategy between the CFD and DEM GPU-based solvers, which enhanced both the efficiency and stability of simulations, reaching 95.6% simulation time reduction. Wang et al. [21] utilized the Lattice Boltzmann Method to simulate thermal convective flows, demonstrating its effectiveness in handling complex boundary conditions and providing a comparative benchmark for our GPU-accelerated approach.

GPU computing has become increasingly pivotal in CFD due to its ability to significantly accelerate complex simulations. GPUs are being leveraged for their superior parallel processing capabilities, allowing for faster computation of large-scale simulations. Narang et al. [16] exemplify this; in their study, GPUs facilitated the efficient acceleration of heat and mass transfer equations, showcasing the potential for rapid processing in real-time applications. In terms of integration with traditional methods, there is a growing trend of integrating GPU computing with traditional computational methods like the FVM to enhance computational efficiency while maintaining accuracy. This integration is highlighted in studies such as those by Moukalled et al. [22], which discuss the adaptation of FVM for GPU implementation. Furthermore, researchers are focusing on developing and optimizing solvers that are specifically designed for GPU architectures. For instance, Silvestri and Pecnik [17] implemented a fast GPU Monte Carlo algorithm for radiative heat transfer,

which showed significant computational speed-ups. This method serves as another validation point for the efficiency of GPU utilization in complex simulations. These studies exemplify the potent combination of GPU acceleration and CHT analysis, demonstrating the significant computational advantages and broad application potential of this approach in engineering and scientific research. With the advancement in GPU technologies, there is an increased focus on conducting real-time simulations and visualizations of complex fluid dynamics scenarios. This application is crucial for industries where real-time data and feedback are essential for operational success and safety. As computational demands grow, there is also a concurrent focus on making GPU computing more sustainable and energy efficient. This involves developing algorithms that not only run faster but also consume less power, aligning with global sustainability goals.

This work investigates the application of GPU technologies to accelerate CHT simulations within squared heated cavities, focusing on increased parallel computing capabilities to reduce the computational time. The goal is to formulate a comprehensive methodology that not only addresses the specifics of GPU computing but also the unique challenges presented by square heated cavity configurations. In summary, this paper aims to bridge the gap between the computational demands of high-fidelity CHT simulations and the capabilities of contemporary computing hardware by leveraging GPU acceleration. Given the importance of accurate and efficient thermal management in various engineering applications, the development of optimized computational strategies is imperative. This work presents a novel approach that combines the parallel processing power of GPUs with advanced numerical methods to significantly enhance the speed of CHT simulations without compromising accuracy. By showcasing the application of this technology in squared heated cavity configurations, the work highlights the potential for widespread adoption and further innovation in the simulation of complex thermal phenomena.

The GPU simulations were conducted using an inhouse code developed in CUDA-C and operated on a MSI Nvidia™ GeForce® RTX™ 4090 graphic card (made in Hsinchu, Taiwan), equipped with 24 GB of video memory. Additionally, this CUDA® code was run on a desktop PC powered by an Intel® Core™ i9 12900KF processor (made in Hillsboro, Oregon, United States of America). Figure 1 presents the general numerical fluid solution developed utilizing both CPU and GPU capabilities.

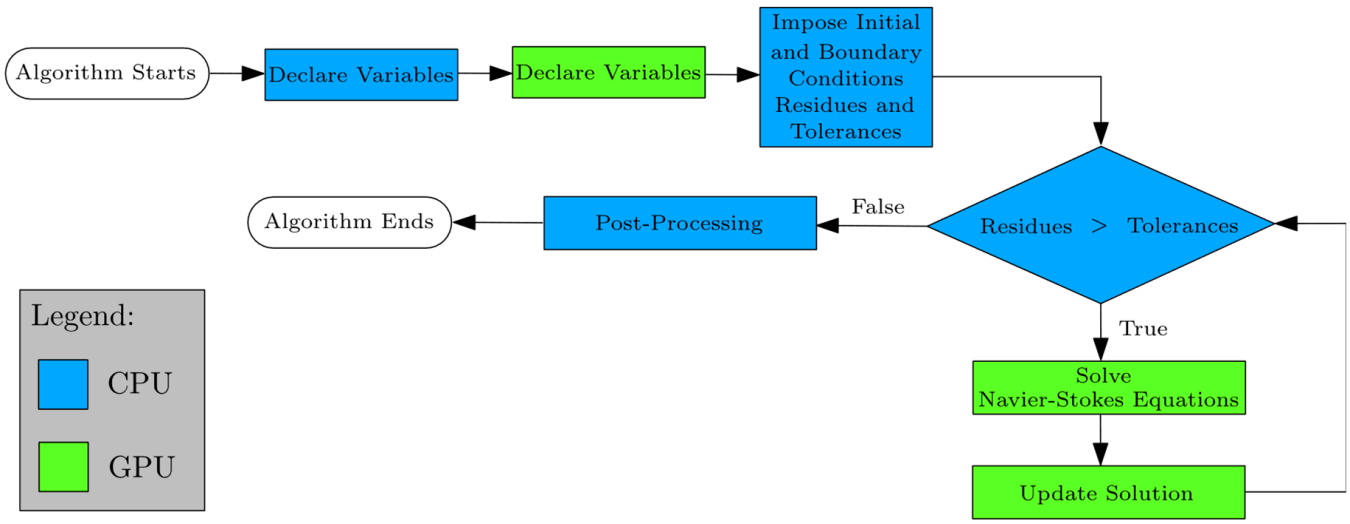

Figure 1. Flowchart of the developed CUDA-C language code.

2. Materials and Methods

2.1. Mathematical Model

Computational Fluid Dynamics (CFD) problems typically involve solving sets of partial differential equations (PDEs) that describe the behavior of fluid flow. The governing

equations for CHT, for instance, include the simultaneous solution of the Navier–Stokes equations and the Energy-Transport Balance equation [22].

The conservation of mass, known as the continuity equation, considering that the flow is incompressible, is expressed as

$$\nabla \cdot \mathbf{v} = 0 \tag{1}$$

where $\mathbf{v}$ is the velocity vector.

The linear momentum conservation, in turn, considering Equation (1) and the fluid viscosity being constant, can be written as

$$\frac{\partial}{\partial t}[\rho_f \mathbf{v}] + \nabla \cdot \left\{\rho_f \mathbf{v}\mathbf{v}\right\} = -\nabla p + \mu \nabla^2 \mathbf{v} + \mathbf{f}_b \tag{2}$$

where ρ_f is the fluid density, t is the time, p is the fluid pressure, μ is the fluid viscosity coefficient, and $\mathbf{f}_b$ is the body forces vector.

Finally, the energy-transport balance, in terms of temperature, is given by

$$\frac{\partial}{\partial t}\left(\rho_f c T\right) + \nabla \cdot \left[\rho_f c \mathbf{v} T\right] = \nabla \cdot [k \nabla T] + Q^T \tag{3}$$

where c is the specific heat, T is the temperature, k is the thermal conductivity, and Q^T is the source term.

Considering the Boussinesq approximation, the equation for density becomes

$$\rho_f = \rho_{f,\infty}[1 - \beta(T - T_\infty)] \tag{4}$$

where T_∞ is the environment temperature, $\rho_{f,\infty}$ is the fluid density at T_∞, and β is the volume expansion coefficient.

2.2. Boundary and Initial Conditions

2.2.1. Lid-Driven Cavity

Figure 2 shows the scheme for a classical problem, the Lid-Driven Cavity. It involves a square cavity filled with an ideal gas, with the top lid moving at a constant speed while the other walls remain stationary. This movement creates complex flow patterns within the cavity due to the shear forces at the moving boundary. The primary interest in this problem lies in understanding how the fluid moves, how vortices develop within the cavity, and how these vortices evolve with changes in the speed of the lid and the viscosity of the fluid. This configuration is particularly relevant for applications involving lubrication technologies and microfluidic devices, where fluid shear and boundary layer interactions are critical. The specific conditions were chosen to simulate typical microscale flow environments, enabling the study of shear-driven flow patterns, which is essential for optimizing device performance. For this case, Table 1 presents all boundary and initial conditions used in this simulation case.

Table 1. Boundary and initial conditions for Lid-Driven Cavity.

Boundary/Initial Conditions	Description
$u = 1.0$ m/s	horizontal velocity at top lid
$u = 0$ m/s	horizontal velocity at bottom, left. and right faces
$v = 0$ m/s	vertical velocities for all faces
$\partial p/\partial x = 0$ N/m^3	pressure gradient for vertical faces
$\partial p/\partial y = 0$ N/m^3	pressure gradient for horizontal faces
$g_y = 9.81$ m/s^2	vertical gravitational acceleration
$p\ (t = 0) = p_0$ [N/m^2]	initial pressure condition

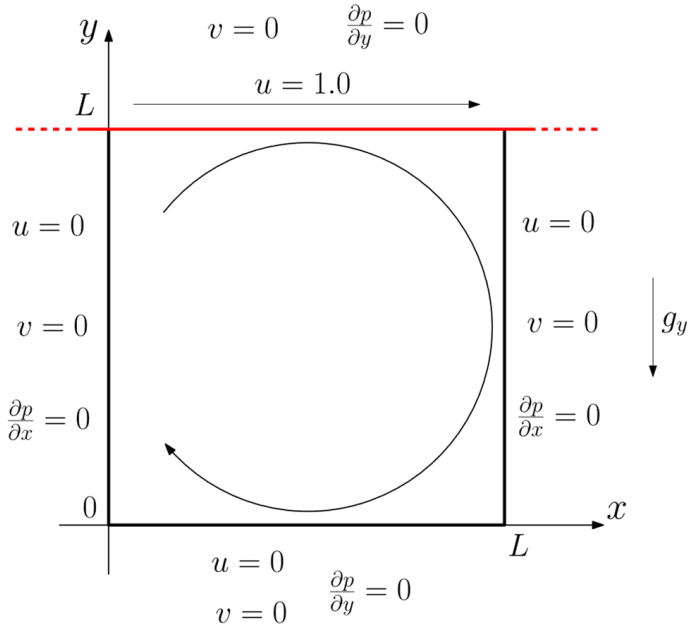

Figure 2. Scheme and boundary conditions for the simulations of Lid-Driven Cavity.

2.2.2. Natural Convection in a Square Cavity

Figure 3 presents the scheme for a square cavity subject to natural convection inside. In this scenario, a fluid-filled square cavity typically has vertical walls at different temperatures, causing the fluid near the hot wall to heat up, decrease in density, and rise, while the fluid near the cold wall cools down, increases in density, and sinks. This creates a circulating motion of the fluid within the cavity, known as a convection current. The simplicity of the square cavity model makes it ideal for studying fundamental aspects of convection without the complexities of external influences. The prescribed boundary and initial conditions mimic real-world conditions, where convection is crucial for heat dissipation, thereby aiding in the design of efficient heat exchangers and cooling systems. Table 2 presents all boundary and initial conditions used in this simulation case.

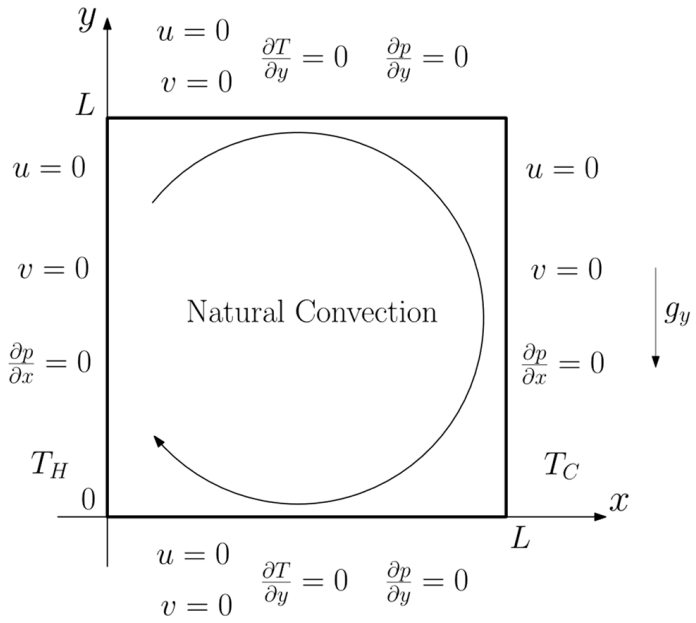

Figure 3. Square cavity subject to natural convection.

Table 2. Boundary and initial conditions for Natural Convection in a Square Cavity.

Boundary/Initial Conditions	Description
$u = 0$ m/s	horizontal velocity for all faces
$v = 0$ m/s	vertical velocity for all faces
$\partial T/\partial y = 0$ K/m	insulation at top and bottom faces
$\partial p/\partial x = 0$ N/m^3	pressure gradient for vertical faces
$\partial p/\partial y = 0$ N/m^3	pressure gradient for horizontal faces
T_H and T_C [K]	prescript temperature ($T_H > T_C$)
$T\ (t = 0) = T_0$ [K]	initial condition

In this case, the authors considered an ideal gas as a fluid inside the cavity.

2.2.3. Conjugate Heat Transfer

Figure 4 presents the scheme for a square cavity with a solid block inside, where U and V are the zero horizontal and vertical dimensionless velocities; $\partial T_{\text{dimless}}/\partial y = 0$ is the horizontal face insulation; $\partial p_{\text{dimless}}/\partial x = 0$ and $\partial p_{\text{dimless}}/\partial y = 0$ are the zero dimensionless pressure gradients at the vertical and horizontal faces, respectively; $T_{H,\text{dimless}}$ and $T_{C,\text{dimless}}$ are prescript dimensionless temperatures; and $T_{\text{dimless}}\ (T = 0) = 0.5$ is the initial dimensionless temperature. The boundary conditions for the CHT simulations, involving a square cavity with a solid block inside, are crucial for understanding the thermal interactions in industrial applications such as electronic component cooling and reactor safety assessments. The chosen conditions aim to closely represent the thermal behavior observed in systems where solid-structure and fluid interactions determine the overall thermal management efficiency. This is essential for evaluating the effectiveness of various material properties and configurations in real-life engineering applications.

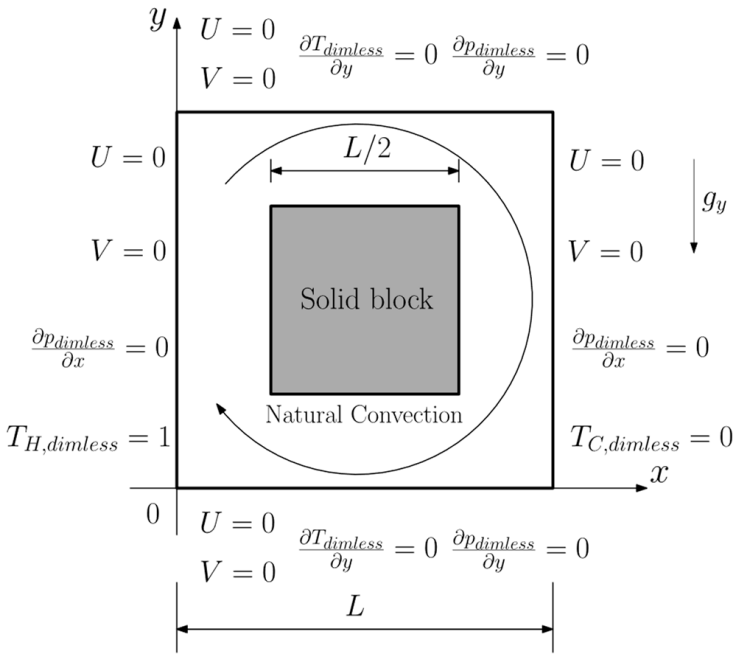

Figure 4. Square cavity with solid block inside.

In this case, the authors considered that the fluid inside of cavity is an ideal gas. Furthermore, the governing equations are made dimensionless according to [23]. Then,

$$(X, Y) = \frac{(x, y)}{L} \tag{5}$$

where x and y are Cartesian coordinates, X and Y are dimensionless Cartesian coordinates, and L is the square cavity dimension.

$$(U, V) = \frac{(u, v)}{\alpha / L} \tag{6}$$

where u and v are the horizontal and vertical velocities, respectively; U and V are the horizontal and vertical dimensionless velocities, respectively; and α is the thermal diffusivity.

$$p_{\text{dimless}} = \frac{(p + \rho g_y y)}{(\alpha / L)^2} \tag{7}$$

where p_{dimless} is the dimensionless pressure, and g_y is the gravity acceleration.

$$T_{\text{dimless}} = \frac{T - T_C}{T_H - T_C} \tag{8}$$

where T_{dimless} is the dimensionless temperature, and T_H and T_C are the temperatures of the heated and cooled faces, respectively.

2.3. Numerical Model

In this section, the authors detail the numerical methodologies employed to solve the governing equations. The Fractional Step Method (FSM) was selected due to its robustness in handling the coupling between velocity and pressure fields in fluid dynamics simulations. FSM effectively splits the Navier–Stokes equations into simpler sub-steps, allowing for more stable and accurate solutions by treating the momentum and continuity equations separately. This method is particularly advantageous in complex flow simulations, where precision in pressure-velocity coupling is crucial.

Additionally, the Finite Volume Method (FVM) was applied due to its high fidelity in discretizing the governing equations on structured meshes. FVM conserves fluxes across control volume boundaries, ensuring conservation of mass, momentum, and energy, which is essential for accurately capturing the nuanced behaviors of thermal and flow fields in natural convection scenarios. By using FVM, it is possible to achieve detailed spatial discretization and gain precise control over the numerical diffusion, which is particularly important in the study of thermal transport in fluid systems.

The displaced mesh approach complements these methods by addressing the staggered arrangement of velocity components, which helps in reducing numerical errors associated with grid alignment. The co-located arrangement of pressure and temperature fields on the same mesh, alongside the staggered velocity fields, enhances the stability and accuracy of our simulation framework, particularly in handling the complex boundary layers and thermal gradients observed in natural convection within square cavities.

Figure 5a illustrates the mesh within a rectangular domain, segmented into volumes known as finite volumes, with each featuring its respective nodes positioned at the domain's center. This mesh configuration specifically accounts for the nodes associated with pressure and temperature. Given the presence of boundary conditions, the introduction of ghost cells is deemed necessary. As depicted in Figure 5b, the mesh representing the vertical component of the velocity field is displaced upwards, while the mesh for the horizontal component is shifted to the right.

The numerical solution consists of use the SIMPLE (Semi-Implicit Method for Pressure Linked Equations) Algorithm in three stages to solve Navier–Stokes equations. If the problem involves a temperature field, it is necessary to solve the Energy-Transport Balance Equation. The process begins by calculating the initial conditions for velocity and pressure to estimate the velocity field. Then, the linear system is solved using the Successive Over-Relaxation (SOR) method, aimed at determining pressure correction values. If a temperature field is present, the Energy-Transport Balance Equation must be solved

explicitly. This iterative process continues until the convergence criterion is met, based on the residue value representing mass conservation in the discretized volumes.

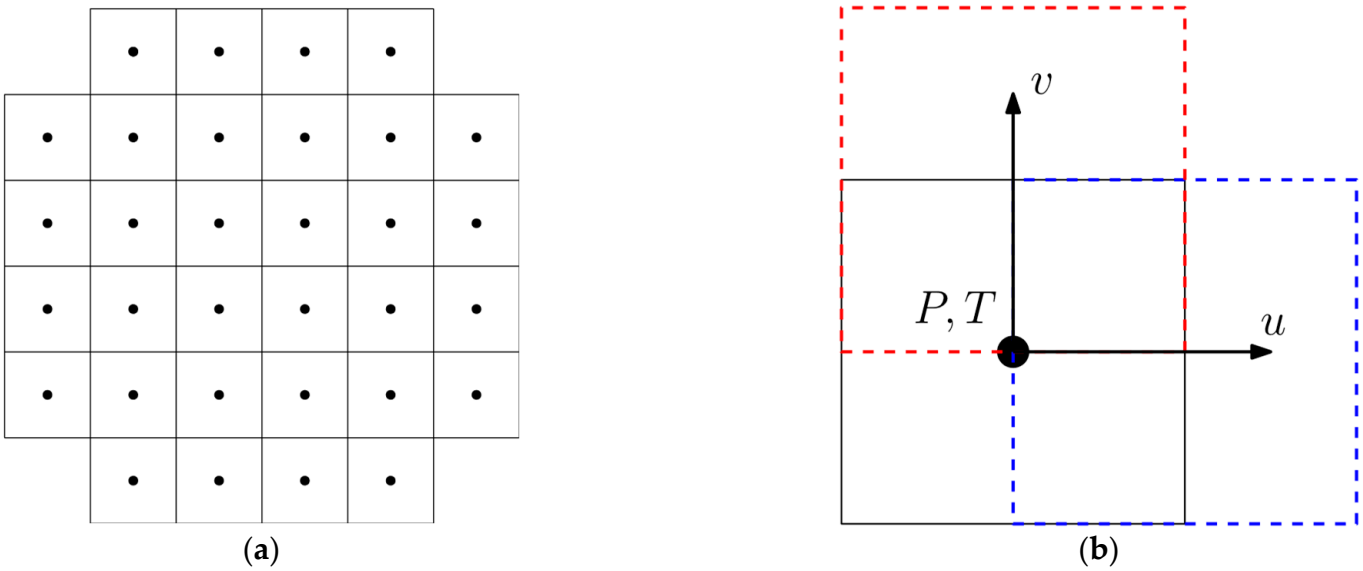

Figure 5. Mesh model illustration: (**a**) square domain mesh for the pressure and the temperature with the ghost cells in the boundaries; (**b**) scheme of displaced mesh for the vertical and horizontal components of the velocity field, the vertical volume component is highlighted in red, and the horizontal volume component is highlighted in blue.

Equation (9) represents the linear system to solve the estimated velocity field and the pressure correction.

$$a_P P_P^{'} = a_E P_E^{'} + a_W P_W^{'} + a_N P_N^{'} + a_S P_S^{'} + S \tag{9}$$

where the subscript P is the center of the control volume (CV); the subscripts E (east), W (west), N (north), and S (south) are the CV neighbors of P; and S is the source term.

The SOR method, in turn, can be written as

$$a_E P_E^{'} + a_W P_W^{'} + a_N P_N^{'} + a_S P_S^{'} + S = R \tag{10}$$

Substituting Equation (10) in Equation (9), we obtain

$$a_P P_P^{'} = R \tag{11}$$

The value of pressure correction of the central node can be obtained using Equation (11), and its value of the next iteration can be calculated using Equation (12).

$$P_P^{'e+1} = P_P^{'e} + \kappa W_P \tag{12}$$

where the superscript e is the index of the pressure iteration, and W_P is the correction.

Hence, the iterative solution of the linear system can be written as

$$a_P \left(P_P^{'e+1} + \kappa W_P \right) = R \tag{13}$$

$$W_P = \frac{R}{a_P} - P_P^{'e+1} \tag{14}$$

Finally, the solution for the pressure correction can be written as

$$P_P^{\prime e+1} = \frac{P_P^{\prime e} + \kappa \frac{R}{a_P}}{1+\kappa} \tag{15}$$

With the estimated velocity field and the pressure correction, the update for these can be written as

$$P = P' + P_0 \tag{16}$$

$$u = u' + u_0 \tag{17}$$

$$v = v' + v_0 \tag{18}$$

where P is the pressure correction, and u and v are horizontal and vertical velocity fields updates.

In scenarios involving CHT problems, there are two distinct domains: a solid and a fluid. The numerical solution for each domain is computed independently. However, these domains exchange information at the interface, such as heat flux or temperature, ensuring a cohesive solution across the boundary between the solid and fluid regions.

Figure 6 illustrates the partitioned domain model utilizing the CHT problem approach. Within this model, I_1 and I_2 represent the information exchanged between the solid and fluid domains. I_1 corresponds to the heat flux at the interface between the fluid and solid, derived from the calculations performed in the solid domain. Conversely, I_2 represents the temperature at the same location, determined based on the fluid domain's results and then transferred to the solid domain. This bidirectional exchange—where one domain contributes heat flux and the other temperature—is crucial for achieving stable and convergent numerical model results.

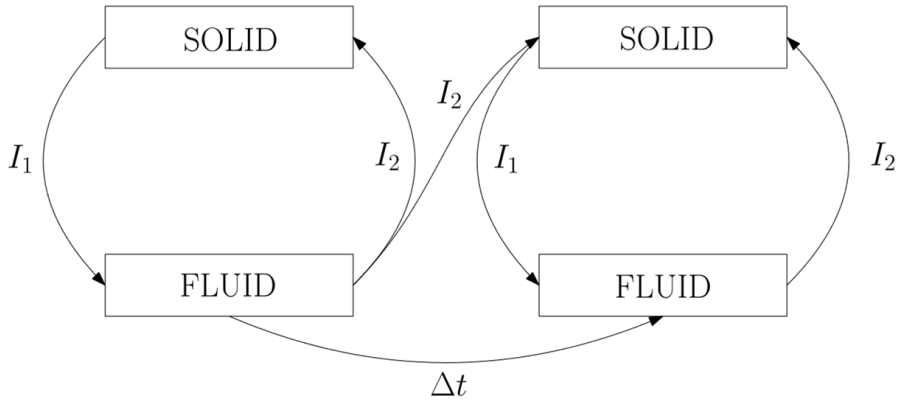

Figure 6. Partitioned domain model with the sequence adopted in the CHT problem.

Equations (19) and (20) represent the information I_1 and I_2, respectively.

$$q_{\text{fw}}^i = \beta_q q_{\text{fw}}^{i-1} + (1-\beta_q) q_{\text{sw}}^i \tag{19}$$

$$T_{\text{sw}}^{i+1} = \beta_T T_{\text{sw}}^i + (1-\beta_T) T_{\text{fw}}^i \tag{20}$$

The parameters β_q and β_T in Equations (19) and (20) are sub-relaxation parameters, and the stability of the numerical model depends of the choice of these.

3. Results and Discussion

This section presents findings for three distinct scenarios: the Lid-Driven Cavity, Natural Convection in a Square Cavity, and the CHT Problem. For each case, the validation

of the GPU computational approach was conducted against the existing literature, which utilized alternative methodologies. Additionally, this section will highlight the mesh convergence observed in the numerical model when processed via GPU, particularly exemplifying this through the Lid-Driven Cavity case with a Reynolds number of 1000. Finally, an analysis of the CPU's performance in simulating the problem addressed in this paper will be provided.

3.1. Lid-Driven Cavity

In this CFD study, the numerical solutions were obtained for four distinct scenarios. In each scenario, the cavity's upper boundary is subjected to a velocity of 1.0 m/s, while the remaining boundaries of the square geometry, measuring 1 m $\times$ 1 m, maintain consistent boundary conditions according Figure 2. The variable parameter in this investigation is the Reynolds number, which is set to 100, 400, 1000, and 3200 for each case. Figure 7 presents the streamlines of the velocity field in Lid-Driven Cavity simulations across a range of Reynolds numbers. The mesh configuration for all cases is 150 $\times$ 150.

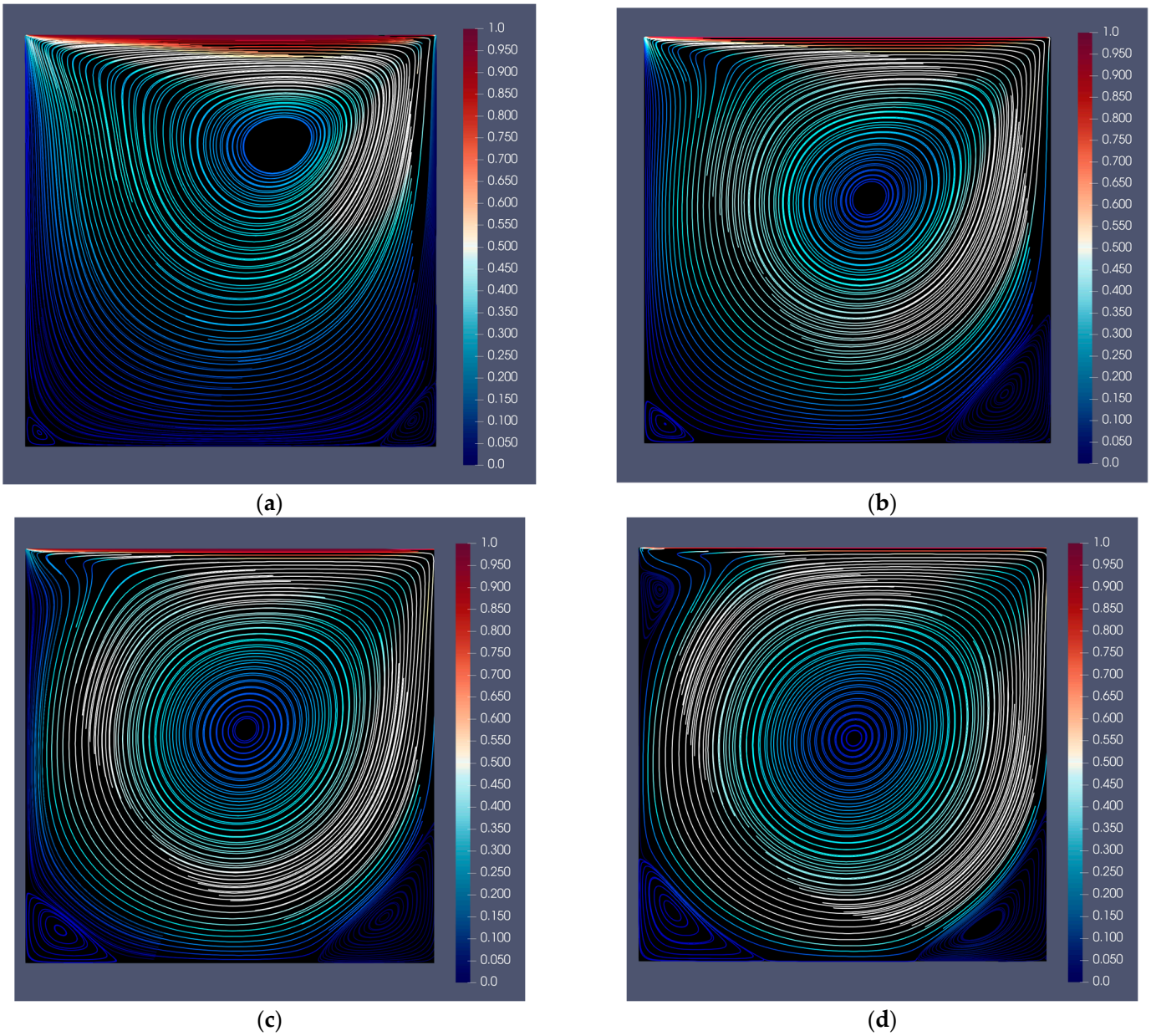

Figure 7. Streamlines of the velocity field in Lid-Driven Cavity simulations across a range of Reynolds numbers (Re): (**a**) Re = 100, (**b**) Re = 400, (**c**) Re = 1000, and (**d**) Re = 3200.

A significant observation from the results of the first three cases is the presence of three recirculation zones within the cavity. There is a large recirculation region dominating the space, accompanied by two smaller recirculation areas in the bottom corners. As the Reynolds number increases, as seen in Figure 7a–c, the intensity of the recirculation in these corner regions becomes more pronounced. Furthermore, Figure 7d reveals an additional recirculation zone emerging in the upper left corner of the cavity, in addition to the similar recirculation regions observed in each case. Figures 8 and 9 present the comparison results among this work and Guia et al. [24]. In this comparison, the authors present the vertical velocity at x = 0.5 m and the horizontal velocity at y = 0.5 m across a range of Reynolds numbers, Re = {100, 400, 1000, 3200}.

The results for each scenario, corresponding to their respective Reynolds numbers, closely align with those reported by Ghia [24]. This similarity underscores the accuracy of the methodology employed in this study.

3.2. Natural Convection in a Square Cavity

The second scenario involves Natural Convection in a Square Cavity, with the dimensions being 1.0 m $\times$ 1.0 m. Here, the Rayleigh number serves as the variable parameter across four cases, set to 10^3, 10^4, 10^5, and 10^6. The gravitational acceleration, consistent in all cases and directed along the y-axis, is 9.81 m/s^2. Parameters such as dynamic viscosity, specific mass, specific heat, dissipation constant, and the adjustable boundary conditions on the cavity's vertical walls are fine-tuned to yield the Rayleigh number. For the horizontal walls, the boundary conditions remain consistent across all cases, characterized by a heat flux equal to zero, according Figure 3. Furthermore, the authors considered the fluid as an ideal gas, and $\beta = 1/T_0$, where T_0 is the reference temperature. Figure 10 presents the isothermal lines results of Natural Convection in a Square Cavity across a range of Rayleigh numbers.

It is clear that with a low Rayleigh number, the isothermal lines tend to be vertical, with little detour in the horizontal direction. With the increase of this dimensionless parameter, the isothermal lines, when near the vertical walls, show a large inclination in relation to the horizontal direction; when distant from the vertical walls, they clearly show a horizontal direction. This means that with a low Rayleigh number, the heat flux does not have zero relation to the horizontal direction, and with the increase of the Rayleigh number, the heat flux in the horizontal direction can be null, with the exception of near the vertical walls. Table 3 presents the comparison of the present work and other works [21,25,26] for the Nusselt number at the vertical wall across a range of Rayleigh numbers.

Table 3. Comparison results for the Nusselt number at the vertical wall across a range of Rayleigh numbers.

Rayleigh Number	$\mathbf{10^3}$	$\mathbf{10^4}$	$\mathbf{10^5}$	$\mathbf{10^6}$
Santos [26]	1.1180	2.2460	4.5270	8.8600
Duarte [25]	1.0720	2.0900	4.3900	8.9010
Wang et al. [21]	1.1180	2.2450	4.5220	8.8270
Present study	1.0755	2.1447	4.3506	8.3725

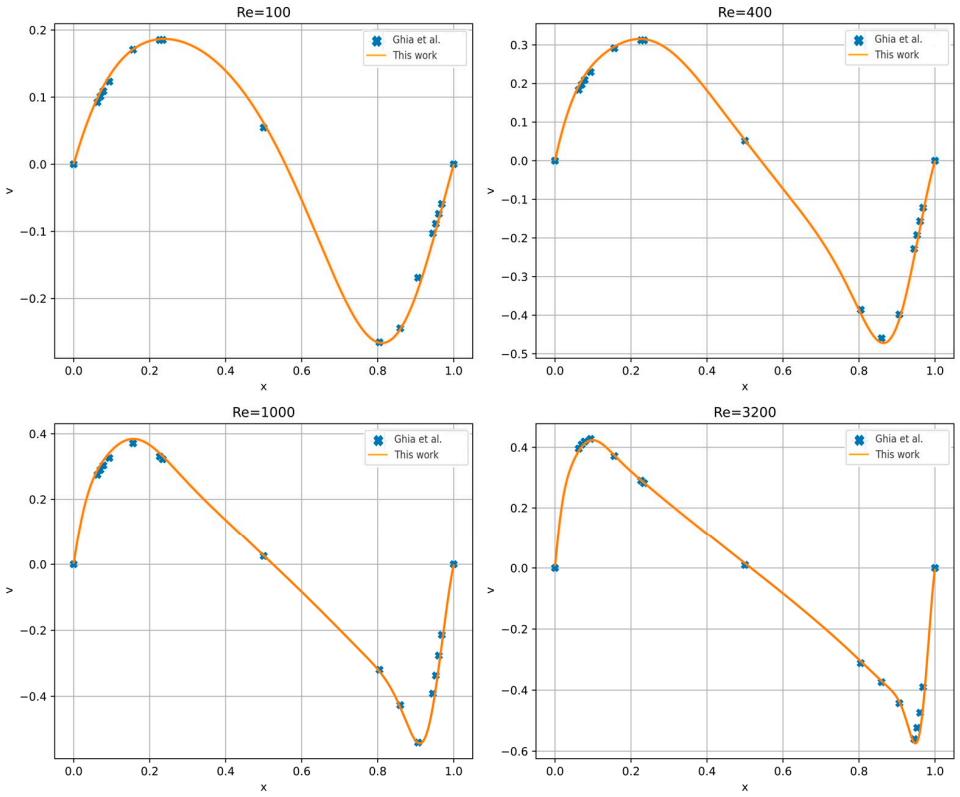

Figure 8. Comparison results for vertical velocity at x = 0.5 m across a range of Reynolds numbers, Re = {100, 400, 1000, 3200} [26].

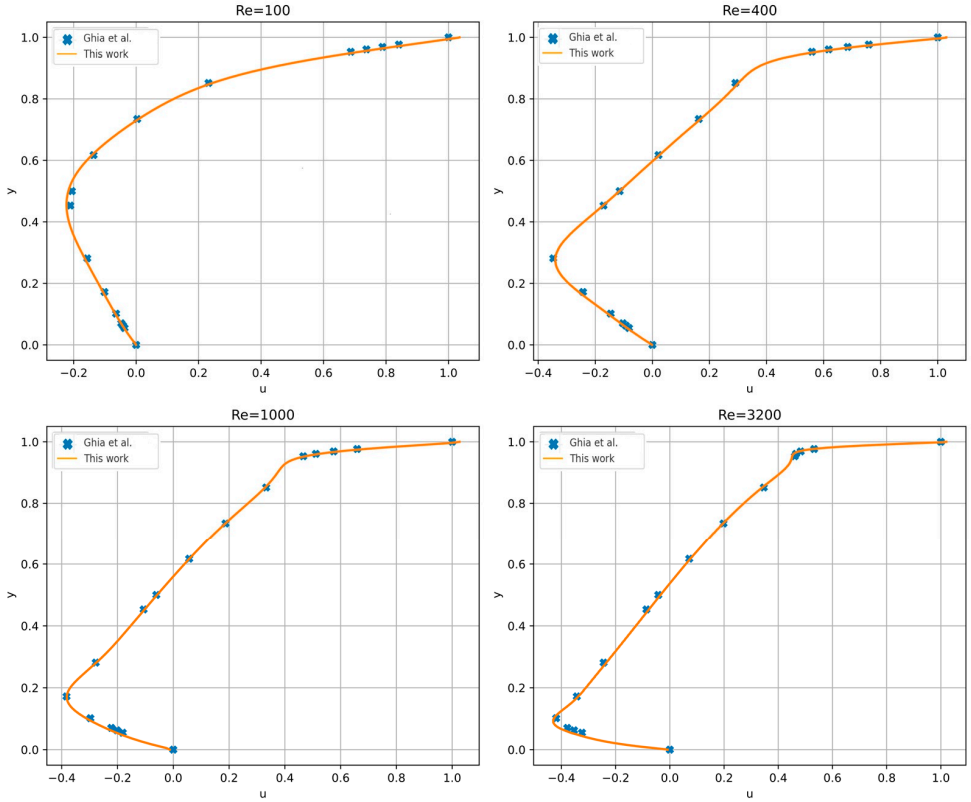

Figure 9. Comparison results for the horizontal velocity at y = 0.5 m across a range of Reynolds numbers, Re = {100, 400, 1000, 3200} [26].

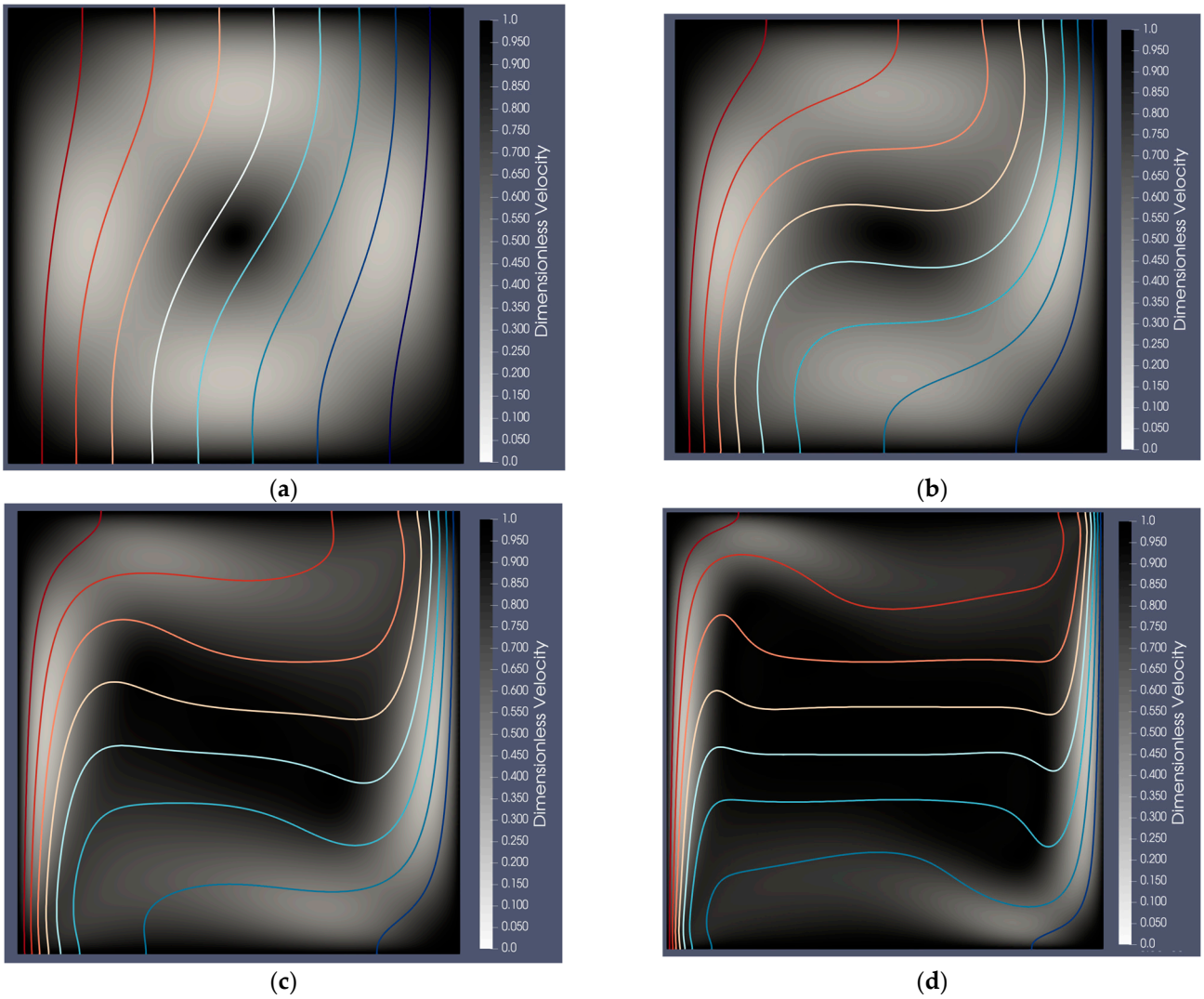

Figure 10. Isothermal lines of Natural Convection in a Square Cavity simulations across a range of Rayleigh numbers (Ra): (**a**) Ra = 10^3, (**b**) Ra = 10^4, (**c**) Ra = 10^5, and (**d**) Ra = 10^6.

Reviewing Table 3 in the context of this study compared to others, it is evident that the numerical model achieves a close approximation to previous works, albeit with a slight deviation in the case of a Rayleigh number equal to 10^6. While the initial hypothesis attributed the discrepancy primarily to the application of a single iteration of the SIMPLE algorithm, several other aspects could also influence the outcome. In terms of numerical stability and convergence, the use of a single iteration of the SIMPLE algorithm might not sufficiently capture the complex interactions between buoyancy forces and thermal gradients at such a high Rayleigh number. This high value intensifies the non-linearities due to increased convective heat transfer, possibly requiring multiple iterations for the algorithm to achieve a stable and accurate solution. On the other hand, the chosen mesh resolution might not be adequate for capturing the finer details of the flow and temperature fields at high Rayleigh numbers. A grid independence study could reveal whether a denser mesh could help in reducing the observed discrepancy by providing a more refined spatial discretization. In terms of physical modeling assumptions such as the Boussinesq approximation, which simplifies the density variations to be solely a function of temperature, these might not hold perfectly at higher temperature differentials. Deviations could also arise from boundary layer approximations or simplifications in the properties of the fluid used in the simulations. Finally, the SIMPLE algorithm itself, while robust for a wide range of applications, has limitations in handling the highly dynamic and complex flow patterns that emerge at very

high Rayleigh numbers. Exploring alternative algorithms or more advanced iterations within the SIMPLE framework could provide insights into the sensitivity of the results to the numerical method employed.

3.3. Conjugate Heat Transfer

The final analysis discussed in this paper necessitates the nondimensionalization of the equations governing both the fluid and solid domains, with the approach for the solid domain detailed by [26]. This study focuses on a square cavity of dimensions L × L, containing a concentric solid body with dimensions 0.5 L × 0.5 L. Within the fluid domain, the assumption is that the fluid behaves as an ideal gas. Two scenarios were simulated: the first with a dimensionless thermal conductivity ratio k* set to 0.2, representing the ratio of the solid's dimensionless thermal conductivity to that of the fluid, and the second with k* = 5.0. The mesh resolution for the entire system, encompassing both the solid and fluid, was set to 201 × 201. Figure 11 presents the isothermal lines of CHT simulations. Furthermore, Table 4 presents a comparison of the present work and other works [26,27] for the Nusselt number at the vertical wall for the CHT problem.

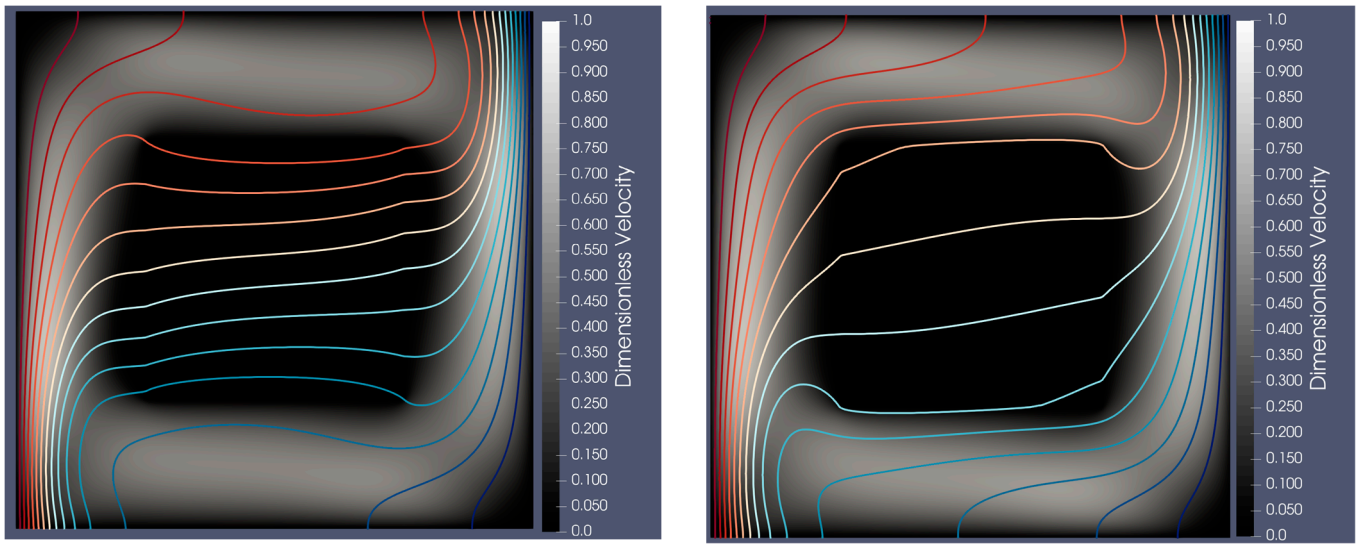

(**a**) (**b**)

Figure 11. Isothermal lines of CHT simulations for (**a**) *k** = 0.2 and (**b**) *k**= 5.0.

Table 4. Comparison results for the Nusselt number at the vertical wall for the CHT problem.

Thermal Conductivity Ratio (k*)	**0.2**	**5.0**
Present study	4.6167	4.3112
Santos [26]	4.6000	4.3320
House et al. [27]	4.6260	4.3220

For k^* = 0.2 (Figure 11a), the isotherms bend around the square, indicating that it has a lower thermal conductivity compared to the surrounding medium, acting as a thermal resistance. This results in a noticeable 'shadowing' effect downstream of the square, which creates regions of lower temperature gradients. For k^* = 5.0 (Figure 11b), although the square still influences the temperature field, the isotherms are less disturbed by its presence. This could imply that the square's thermal conductivity is closer to that of the surrounding medium or that the overall system has a higher thermal diffusivity, allowing for a more uniform temperature distribution despite the presence of the square. The curvature of the isotherms near the boundaries and the square's edges in both cases suggests a complex interaction between conductive and convective heat transfer mechanisms. The nature of

this interaction is likely to depend on the thermal properties of the materials involved as well as the boundary conditions of the system.

The data presented in Table 4 illustrate the high accuracy of the simulation outcomes achieved using GPU processing. This demonstrates that, in addition to its efficiency in terms of processing time, GPU-based simulation also delivers precise results. The findings from GPU-accelerated CHT simulations are significant not only in terms of computational efficiency but also for their potential applications in real-world engineering problems, such as enhanced thermal management in aerospace and automotive industries, energy systems optimization, and electronic cooling systems.

3.4. Mesh Convergence

The analysis presents mesh convergence in the Lid-Driven Cavity problem at a Reynolds umber of 1000, employing simulations across mesh resolutions of 25 × 25, 50 × 50, 100 × 100, and 200 × 200. The L_2 norm was calculated to compare the 50 × 50 mesh against the 25 × 25, the 100 × 100 against the 50 × 50, and finally, the 200 × 200 mesh compared to the 100 × 100. Figure 12a,b compares the results from all four mesh configurations with those reported by Ghia [24]. On the other hand, Figure 12c shows the L2 norm as a function of the number of cells.

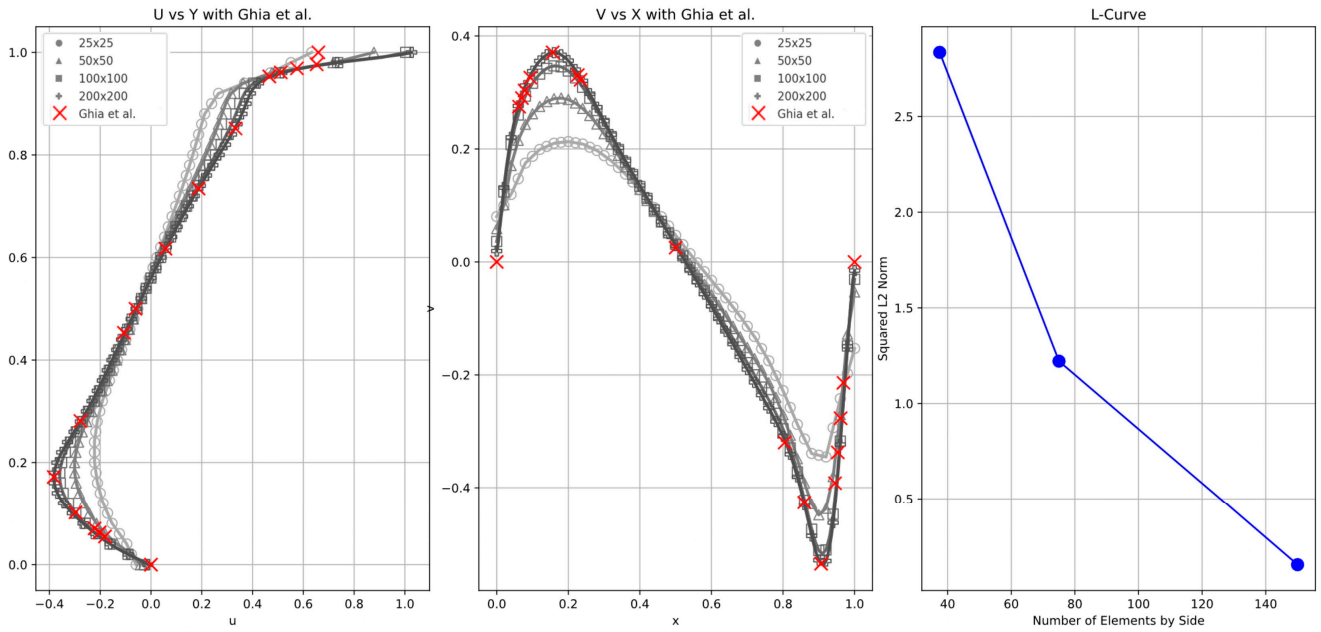

Figure 12. Mesh convergence test for the Lid-Driven Cavity with Re = 1000: (**a**) vertical velocity results, (**b**) horizontal velocity results, and (**c**) L_2 norm [26].

3.5. Simulation Performance

To evaluate the computational performance of GPU processing, three simulations were conducted, each incorporating variations of a specific dimensionless parameter. These simulations achieved results closely matching those found in the literature, which were obtained using conventional CPU-based methodologies. Notably, the use of GPU processing in this study resulted in a substantial reduction in simulation time, achieving a 99.7% decrease compared to mono-core CPU processing.

In the case of the Lid-Driven Cavity problem, which involves complex flow structures and high Reynolds numbers (notably at 1000 and 3200), GPU processing provided results that closely approximated those reported by Ghia [24]. This underscores the significant time-saving benefits of utilizing GPUs for such simulations.

The study also explored Natural Convection in a Square Cavity, a scenario that introduces an additional equation for heat transport and involves varying Rayleigh numbers. Here too, GPU-accelerated algorithms delivered results that aligned well with findings from other research, demonstrating the GPU's effectiveness in handling complex problems.

Furthermore, the final simulation addressed a more intricate issue of solid–fluid interaction, where the heat flux varies across the physical domain. The outcomes from this simulation, consistent with established physics, underscore the potential of GPU technology. With appropriate application, GPUs can offer a cost-effective means to solve complex problems with greater fidelity to real-world phenomena. Despite achieving significant computational time reductions (up to 99.7% compared to mono-core CPU processing) and maintaining high fidelity, the research acknowledges potential limitations such as model assumptions, boundary condition dependencies, and hardware-specific performance. These factors could affect the generalizability and scalability of the findings. Addressing these uncertainties through expanded validation, sensitivity analysis, and testing across different hardware setups is suggested for future research to further establish the robustness and applicability of GPU-accelerated thermal simulations in engineering.

4. Conclusions

This research elucidates the substantial computational advantages and precision achievable through GPU acceleration in simulating CHT within squared heated cavities. By leveraging the parallel processing capabilities of GPUs and employing the CUDA-C programming language, the study found an up to 99.7% reduction in computation time compared to traditional mono-core CPU processing, without compromising accuracy. This work provides a novel and optimized framework for conducting high-fidelity CHT simulations, addressing both the computational demands and the specific challenges posed by squared heated cavity configurations. The findings underscore the potential of GPU acceleration to significantly enhance simulation speeds while maintaining high levels of accuracy, offering a valuable resource for future research and application in thermal simulations across various engineering domains. The effective utilization of GPU technology, as demonstrated in this study, marks a significant step forward in the efficient and accurate modeling of complex thermal phenomena, contributing to the advancement of thermal management strategies in engineering applications.

Author Contributions: Conceptualization, C.A.B.d.S.R., E.d.S.M. and A.d.S.N.; methodology, C.A.B.d.S.R., A.M.d.A., E.d.S.M. and A.d.S.N.; software, D.B., A.M.d.A. and E.d.S.M.; validation, C.A.B.d.S.R. and D.B.; formal analysis, C.A.B.d.S.R., A.M.d.A. and E.d.S.M.; investigation, A.M.d.A. and E.d.S.M.; resources, C.A.B.d.S.R. and E.d.S.M.; data curation, C.A.B.d.S.R. and D.B.; writing—original draft preparation, C.A.B.d.S.R., A.M.d.A., E.d.S.M. and A.d.S.N.; writing—review and editing, C.A.B.d.S.R., A.M.d.A. and E.d.S.M.; visualization, C.A.B.d.S.R., D.B., A.M.d.A., E.d.S.M. and A.d.S.N.; supervision, E.d.S.M. and A.d.S.N.; project administration, E.d.S.M. and A.d.S.N.; funding acquisition, E.d.S.M. All authors have read and agreed to the published version of the manuscript.

Funding: This research was funded by the Conselho Nacional de Desenvolvimento Científico e Tecnológico (CNPq, an agency of the ministry of Science, Technology, Innovations, and Communications of Brazil, under the grant 402673/2021–2) and by Petróleo Brasileiro S.A. (PETROBRAS, a Brazilian multinational company).

Data Availability Statement: The data presented in this study are available on request from the corresponding author.

Conflicts of Interest: The authors whose names are listed in this work certify that they have NO affiliations with or involvement in any organization or entity with any financial interest (such as honoraria; educational grants; participation in speakers' bureaus; membership, employment, consultancies, stock ownership, or other equity interest; and expert testimony or patent-licensing arrangements), or non-financial interest (such as personal or professional relationships, affiliations, knowledge, or beliefs) in the subject matter or materials discussed in this manuscript.

Abbreviations

Table of Acronyms

CFD	Computational Fluid Dynamics	FVM	Finite Volume Method
CHT	Conjugate Heat Transfer	GPU	Graphics Processing Unit
CPU	Central Processing Unit	PDE	Partial Differential Equations
CV	Control Volume	SIMPLE	Semi-Implicit Method for Pressure Linked Equations
CUDA	Compute Unified Device Architecture	SOR	Successive Over-Relaxation
FSM	Fractional Step Method		

Table of Symbols

α	thermal diffusivity	(m^2/s)	T_H	heated face temperature	(K)
β	volume expansion coefficient	(1/K)	T_∞	reference temperature	(K)
c	specific heat	(J/kgK)	T_C	cooled face temperature	(K)
$\mathbf{f}_b$	body forces vector	(N)	T_H	heated face temperature	(K)
g_y	gravity acceleration	(m/s^2)	$T_{dimless}$	dimless. temperature	(-)
k	thermal conductivity	(W/mK)	t	time	(s)
L	square cavity dimension	(m)	u	horizontal velocity	(m/s)
μ	fluid viscosity coefficient	(Pa·s)	U	dimless. horizontal velocity	(-)
∇	Nabla Operator	(-)	v	vertical velocity	(m/s)
p	fluid pressure	(Pa)	$\mathbf{v}$	velocity vector	(m/s)
$p_{dimless}$	dimless. fluid pressure	(-)	V	dimless. vertical velocity	(-)
Q^T	source term	(W/m^3)	V_c	volume of the control volume	(m^3)
ρ_f	fluid density	(kg/m^3)	x and y	Cartesian coordinates	(m)
$\rho_{f,\infty}$	fluid density at T_∞	(kg/m^3)	X and Y	dimless. Cartesian coord.	(-)
T	temperature	(K)			

References

1. Perelman, T.L. On Conjugated Problems of Heat Transfer. *Int. J. Heat Mass. Transf.* **1961**, *3*, 293–303. [CrossRef]
2. Luikov, A.V.; Aleksashenko, V.A.; Aleksashenko, A.A. Analytical Methods of Solution of Conjugated Problems in Convective Heat Transfer. *Int. J. Heat Mass. Transf.* **1971**, *14*, 1047–1056. [CrossRef]
3. Chida, K.; Yoshiro, K. Study on Conjugate Heat Transfer by Vectorial Dimensional Analysis. *Int. J. Heat Mass. Transf.* **1976**, *19*, 453–460. [CrossRef]
4. Seki, N.; Fukusako, S.; Inaba, H. Heat Transfer in a Confined Rectangular Cavity Packed with Porous Media. *Int. J Heat Mass. Transf.* **1978**, *21*, 985–989. [CrossRef]
5. Inaba, H.; Fukuda, T. Natural Convection in an Inclined Square Cavity in Regions of Density Inversion of Water. *J. Fluid Mech.* **1984**, *142*, 363–381. [CrossRef]
6. Ho, C.J.; Yih, Y.L. Conjugate Natural Convection Heat Transfer in an Air-Filled Rectangular Cavity. *Int. Commun. Heat Mass. Transf.* **1987**, *14*, 91–100. [CrossRef]
7. Frederick, R.L.; Valencio, A. Heat Transfer in a Square Cavity with a Conducting Partition on Its Hot Wall. *Int. Commun. Heat Mass. Transf.* **1989**, *16*, 347–354. [CrossRef]
8. Alkhalidi, A.; Kiwan, S.; Al-Kouz, W.; Alshare, A. Conjugate Heat Transfer in Rarefied Gas in Enclosed Cavities. *Vacuum* **2016**, *130*, 137–145. [CrossRef]
9. Alsabery, A.I.; Chamkha, A.J.; Saleh, H.; Hashim, I. Heatline Visualization of Conjugate Natural Convection in a Square Cavity Filled with Nanofluid with Sinusoidal Temperature Variations on Both Horizontal Walls. *Int. J. Heat Mass. Transf.* **2016**, *100*, 835–850. [CrossRef]
10. Khatamifar, M.; Lin, W.; Armfield, S.W.; Holmes, D.; Kirkpatrick, M.P. Conjugate Natural Convection Heat Transfer in a Partitioned Differentially-Heated Square Cavity. *Int. Commun. Heat Mass. Transf.* **2017**, *81*, 92–103. [CrossRef]
11. Gijón-Rivera, M.; Xamán, J.; Álvarez, G. Conjugate Heat Transfer Analysis in a Glazed Room Modeled as a Square Cavity. *Heat Transf. Eng.* **2018**, *39*, 120–140. [CrossRef]
12. Chen, S.; Gong, W.; Yan, Y. Conjugate Natural Convection Heat Transfer in an Open-Ended Square Cavity Partially Filled with Porous Media. *Int. J. Heat Mass. Transf.* **2018**, *124*, 368–380. [CrossRef]
13. Alvarado-Juárez, R.; Montiel-González, M.; Villafán-Vidales, H.I.; Estrada, C.A.; Flores-Navarrete, J. Experimental and Numerical Study of Conjugate Heat Transfer in an Open Square-Cavity Solar Receiver. *Int. J. Therm. Sci.* **2020**, *156*, 106458. [CrossRef]
14. Klimeš, L.; Štětina, J. A Rapid GPU-Based Heat Transfer and Solidification Model for Dynamic Computer Simulations of Continuous Steel Casting. *J. Mater. Process Technol.* **2015**, *226*, 1–14. [CrossRef]
15. Zhang, J.; Hills, J.; Zhong, Y.; Shirinzadeh, B.; Smith, J.; Gu, C. GPU-accelerated finite element modeling of bio-heat conduction for simulation of thermal ablation. *J. Mech. Med. Biol.* **2018**, *18*, 1840012. [CrossRef]

16. Narang, H.; Wu, F.; Mohammed, A.R. An Efficient Acceleration of Solving Heat and Mass Transfer Equations with the Second Kind Boundary Conditions in Capillary Porous Composite Cylinder Using Programmable Graphics Hardware. *J. Comput. Commun.* **2018**, *06*, 24–38. [CrossRef]
17. Silvestri, S.; Pecnik, R. A Fast GPU Monte Carlo Radiative Heat Transfer Implementation for Coupling with Direct Numerical Simulation. *J. Comput. Phys. X* **2019**, *3*, 100032. [CrossRef]
18. Dugast, F.; Apostolou, P.; Fernandez, A.; Dong, W.; Chen, Q.; Strayer, S.; Wicker, R.; To, A.C. Part-Scale Thermal Process Modeling for Laser Powder Bed Fusion with Matrix-Free Method and GPU Computing. *Addit. Manuf.* **2021**, *37*, 101732. [CrossRef]
19. Luo, Z.; Xu, H.; Lou, Q.; Feng, L.; Ni, J. GPU-Accelerated Lattice Boltzmann Simulation of Heat Transfer Characteristics of Porous Brick Roof Filled with Phase Change Materials. *Int. Commun. Heat Mass. Transf.* **2020**, *119*, 104911. [CrossRef]
20. Gou, D.; Shen, Y. GPU-Accelerated CFD-DEM Modeling of Gas-Solid Flow with Complex Geometry and an Application to Raceway Dynamics in Industry-Scale Blast Furnaces. *Chem. Eng. Sci.* **2024**, *294*, 120101. [CrossRef]
21. Wang, J.; Wang, D.; Lallemand, P.; Luo, L.-S. Lattice Boltzmann Simulations of Thermal Convective Flows in Two Dimensions. *Comput. Math. Appl.* **2013**, *65*, 262–286. [CrossRef]
22. Moukalled, F.; Mangani, L.; Darwish, M. *The Finite Volume Method in Computational Fluid Dynamics. An Advanced Introduction with OpenFOAM and Matlab*; Springer: Berlin/Heidelberg, Germany, 2012; Volume 113, ISBN 9783319168739.
23. Zhao, F.Y.; Liu, D.; Tang, G.F. Conjugate Heat Transfer in Square Enclosures. *Heat Mass. Transf. /Waerme-Und Stoffuebertragung* **2007**, *43*, 907–922. [CrossRef]
24. Ghia, U.; Ghia, K.N.; Shin, C.T. High-Re Solutions for Incompressible Flow Using the Navier-Stokes Equations and a Multigrid Method. *J. Comput. Phys.* **1982**, *48*, 387–411. [CrossRef]
25. Duarte, B.A.D.F. *Modelagem de Mudança de Fase Em Escoamentos Não-Isotérmicos: Um Modelo Matemático, Numérico e Com-Putacional Para Substâncias Puras*; Universidade Federal de Uberlândia: Uberlândia, Brazil, 2017.
26. Santos, G.M.D. *Transferência Térmica Conjugada Utilizando Fronteira Imersa Para Solução de Problemas Bidimensionais*; Universidade Federal de Uberlândia: Uberlândia, Brazil, 2022.
27. House, J.M.; Beckermann, C.; Smith, T.F. Effect of a centered conducting body on natural convection heat transfer in an enclosure. *Numer. Heat Transf. Part. A-Appl.* **1990**, *18*, 213–225. [CrossRef]

computation

MDPI

Article

An Implementation of LASER Beam Welding Simulation on Graphics Processing Unit Using CUDA

Ernandes Nascimento [1,*], Elisan Magalhães [1], Arthur Azevedo [1], Luiz E. S. Paes [2] and Ariel Oliveira [1]

[1] Aeronautics Institute of Technology—ITA, São José dos Campos 12228-900, SP, Brazil; elisan@ita.br (E.M.); arthurama@ita.br (A.A.); arielafmo@ita.br (A.O.)
[2] Faculty of Mechanical Engineering, Federal University of Uberlândia—UFU, Uberlândia 38410-337, MG, Brazil; luiz.paes@ufu.br
* Correspondence: ernandes@ita.br

Abstract: The maximum number of parallel threads in traditional CFD solutions is limited by the Central Processing Unit (CPU) capacity, which is lower than the capabilities of a modern Graphics Processing Unit (GPU). In this context, the GPU allows for simultaneous processing of several parallel threads with double-precision floating-point formatting. The present study was focused on evaluating the advantages and drawbacks of implementing LASER Beam Welding (LBW) simulations using the CUDA platform. The performance of the developed code was compared to that of three top-rated commercial codes executed on the CPU. The unsteady three-dimensional heat conduction Partial Differential Equation (PDE) was discretized in space and time using the Finite Volume Method (FVM). The Volumetric Thermal Capacitor (VTC) approach was employed to model the melting-solidification. The GPU solutions were computed using a CUDA-C language in-house code, running on a Gigabyte Nvidia GeForce RTX™ 3090 video card and an MSI 4090 video card (both made in Hsinchu, Taiwan), each with 24 GB of memory. The commercial solutions were executed on an Intel® Core™ i9-12900KF CPU (made in Hillsboro, Oregon, United States of America) with a 3.6 GHz base clock and 16 cores. The results demonstrated that GPU and CPU processing achieve similar precision, but the GPU solution exhibited significantly faster speeds and greater power efficiency, resulting in speed-ups ranging from 75.6 to 1351.2 times compared to the CPU solutions. The in-house code also demonstrated optimized memory usage, with an average of 3.86 times less RAM utilization. Therefore, adopting parallelized algorithms run on GPU can lead to reduced CFD computational costs compared to traditional codes while maintaining high accuracy.

Keywords: Nvidia CUDA®; CUDA-C code; GPU processing; finite volume method; LASER beam welding

Citation: Nascimento, E.; Magalhães, E.; Azevedo, A.; Paes, L.E.S.; Oliveira, A. An Implementation of LASER Beam Welding Simulation on Graphics Processing Unit Using CUDA. *Computation* **2024**, *12*, 83. https://doi.org/10.3390/computation12040083

Academic Editors: Ali Cemal Benim, Abdulmajeed A. Mohamad, Sang-Ho Suh, Rachid Bennacer, Paweł Oclon and Jan Taler

Received: 16 March 2024
Revised: 11 April 2024
Accepted: 13 April 2024
Published: 17 April 2024

1. Introduction

Numerical techniques to find approximated solutions instead of exact ones were found to be helpful in various fields of science, engineering, physics, and many other disciplines where mathematical models were used to describe real-world phenomena. Over the past 60 years, as noted by Thomée V. [1], the research and development of computational methods have successfully addressed numerous engineering problems, including heat transfer and fluid flow. As a result, the field of Computational Fluid Dynamics (CFD) became an essential part of the modern industrial design process [2].

Numerical algorithms involve iterative processes, where an initial guess is refined through successive calculations to approach the true solution. The process continues until a predefined convergence criterion is met. Still, the processing efficiency and solution accuracy are strongly related to the hardware capacity and software optimization. For instance, the electronic connections between processor and memory units may limit the data throughput. Therefore, it is important to evaluate the Random Access Memory (RAM) and Video Random Access Memory (VRAM) implementations in terms of operational

speeds [GHz] [3]. The RAM device may be defined as the main computer memory used to store and process data, being placed at the computer's motherboard. Conversely, GPUs possess a distinct and non-removable type of memory known as VRAM, which is directly integrated into the graphics card. In GPU processing platforms such as CUDA®, RAM is often referred to as host machine memory, while VRAM is termed device memory [4].

Over the past few decades, many commercial CFD packages have been developed. However, most are designed to perform computations based on CPU processors. With the advent of high-performance computing, parallelized numerical methods have become increasingly important. When parallel computing is employed, calculations are distributed among multiple processors or cores to efficiently solve large-scale problems. In such conditions, the computational cost is often decreased compared to sequential computation via CPUs.

A subject of industrial interest is yield stress fluids, which do not deform until the yield stress is exceeded. In the case of flow into a narrow eccentric annulus, this type of phenomenon can be decomposed into multiple long-thin flows. The nonlinearity in the governing equations requires substantial calculations, so the Lagrangian algorithm is often applied. Medina Lino et al. (2023) [5] proposed implementing a non-Newtonian Hele–Shaw flow to model the displacement of Herschel–Bulkley fluids in narrow eccentric annuli. They utilized the CUDA® Fortran language to accelerate calculations compared to CPU processing. The calculations run in an NVIDIA GeForce® RTX™ 2080 Ti were up to 40 times faster than the simulations run in an Intel® Core™ I7 3770 processor.

Continuing in the field of fluid flow modeling, Xia et al. (2020) [6] developed a CUDA-C language GPU-accelerated package for simulation of flow in nanoporous source rocks with many-body dissipative particle dynamics. The authors demonstrated through a flow simulation in realistic shale pores that the CPU counterpart requires 840 Power9 cores to rival the performance delivered by the developed package with only four Nvidia V100 GPUs. More recently, Viola et al. (2022) [7] applied CUDA to perform GPU-accelerated simulations of the Fluid–structure–electrophysiology Interaction (FSEI) in the left heart. The resulting GPU-accelerated code can solve a single heartbeat within a few hours (ranging from three to ten hours depending on the grid resolution), running on a premises computing facility consisting of a few GPU cards. These cards can be easily installed in a medical laboratory or hospital, thereby paving the way for a systematic Computational Fluid Dynamics (CFD)-aided diagnostic approach.

Simulations in the field of computational biomedicine have also been accelerated with the aid of GPU processing. The desire to create a three-dimensional virtual human as a digital twin of one's physiology has led to the development of simulations using the CUDA® computing platform as a means of reducing processing time. For example, the HemeLB solver, which is based on the lattice Boltzmann method, is widely utilized for simulating blood flow using real patient images. Zacharoudiou et al. (2023) [8] utilized the method's strong scaling capability to adapt their algorithm for execution on a GPU architecture using CUDA-C language. Indeed, such scalability extends to a higher level of parallelism for GPU codes compared to CPU codes. When comparing computations using an equivalent number of GPU and CPU threads, computations using the GPU were still up to 85 times faster. The authors compared different settings of supercomputers.

Applying the GPU for calculations may also facilitate the achievement of more detailed and realistic simulations. In 2021, O'Connor and Rogers [9] adapted and implemented the open-source DualSPHysics code to run on a GPU. This adaptation was aimed at achieving more reliable simulations of coupled interactions between free-surface flows and flexible structures, addressing concerns that frequent use of reduced models may lead to erroneous assumptions. The execution time needed to perform the calculations using an NVIDIA™ Tesla® V100 GPU and an Intel® Xeon™ E5 2690 were compared. The GPU outperformed the CPU for all numbers of particles investigated. However, the speed-up was proportional to the number of particles. Thus, when dealing with a small number of particles, the speed-up

on the GPU was relatively low. As the number of particles increased, so did the speed-up, reaching up to 50 times faster on the GPU.

In addition to fluid flow, some authors also use numerical models computed through GPUs to investigate heat transfer. For example, Satake et al. (2012) [10] performed optimizations of a GPU-accelerated heat conduction equation by a programming of CUDA Fortran from an analysis of a Parallel Thread Execution (PTX) file. Before implementing the proposed code corrections, CUDA-C exhibited a speed 1.5 times faster than by CUDA Fortran. Later, Klimeš and Štětina (2015) [11] employed the Finite Difference Method (FDM) to perform three-dimensional simulations with solidification modeling. The results demonstrated that the GPU implementation outperformed CPU-based simulations by 33–68 times when utilizing a single Nvidia Tesla C2075 GPU to execute kernels. This considerable speed-up was enough to enable the application of their method in real-time scenarios. Szénási (2017) [12] solved the Inverse Heat Conduction Problem (IHCP) using NVLink capable power architecture between the host and devices. This implementation (running on four GPUs) was about 120 times faster than a traditional CPU implementation using 20 cores.

Continuing the literature review in GPU-based computational methods in heat transfer, Semenenko et al. (2020) [13] simulated conductive stationary heat transfer on a two-dimensional domain to compare the performance of CPU and GPU architectures. Their study was performed through several simulations using various hardware configurations, including four different GPUs: AMD Radeon™ RX VEGA® 56, NVIDIA GeForce® GTX™ 1060, NVIDIA GeForce® GTX™ 860 m, and NVIDIA Tesla™ M40®. It also utilized five Intel® Core™ i7 CPU processors: 3630 QM, 4720 HQ, 6700 K, 7700, and 7820 HQ. Different numbers of mesh elements were simulated. The results indicated that with an increase in the number of elements in the mesh, GPU calculations were faster compared to those on the CPU. Across all configurations considered, the GPU was, on average, 9 to 11 times faster than the CPU.

Convective and radiative heat transfers can also be studied using parallel computing. For instance, Taghavi et al. (2021) [14] performed simulations of convective heat transfer in nanofluids inside a sinusoidal wavy channel. The authors solved the tridiagonal matrices obtained through the Spline Alternating Direction Implicit (SADI) technique using the Parallel Thomas Algorithm (PTA) on the GPU and the classic Thomas algorithm on the CPU, respectively. Implementing this high-order method on the GPU significantly reduced the computing time. The simulations could be performed up to 18.32 times faster on a GeForce® GTX™ 970 than on an Intel® Core™ i7 5930K processor. Additionally, the Monte Carlo, Runge–Kutta, and ray tracing methods were combined to simulate radiative heat transfer in a graded-index (GRIN) medium. Despite providing high precision, such sequential computations often require a significant amount of computational time.

Shao et al. (2021) [15] developed two- and three-dimensional models optimized for graded-index (GRIN) media using parallel computing on GPUs to enhance processing. Computational times were compared between GPU implementations using an NVIDIA GeForce® GTX™ 1080 Ti and CPU implementations using the Intel® Core™ i7 8750H and the Xeon™ Gold 5120 processors. In the two-dimensional model, the GPU demonstrated a speed-up of over 43 times and 5 times compared to the equivalent CPU implementation using a single core and six CPU cores, respectively. In the three-dimensional case, the GPU was 35 times and 2 times faster than the CPU, considering a single core and 14 CPU cores sequentially.

As discussed in the previous literature review, crucial contributions have made possible the acceleration of computational processing times through the application of GPU parallelization in several fields of engineering research. The CPU-based processing has been investigated for over fifty years, while GPU processing methods are still in early development, having been a research focus for nearly fifteen years. Hence, there is ample opportunity to explore new parallelized methods and specific studies for better addressing the GPU capabilities. For instance, in previous work, Azevedo et al. (2022) [16] compared nonlinear and constant thermal properties approaches applied for estimating the

temperature in LASER Beam Welding (LBW) simulations. The authors conducted a detailed study on the temperature gradient, its influence on thermocouple positioning, and a methodology to evaluate thermal properties convergence. However, the results were not extensively compared in terms of processing performance, energy, optimization and accuracy to well-established commercial code solutions. Therefore, in the present research, the advantages and drawbacks of an implementation of LASER Beam Welding (LBW) simulation using CUDA were investigated. The developed numerical solution utilizes CPU and GPU runtime code functions, along with multithreaded GPU parallelization, as illustrated in Figure 1.

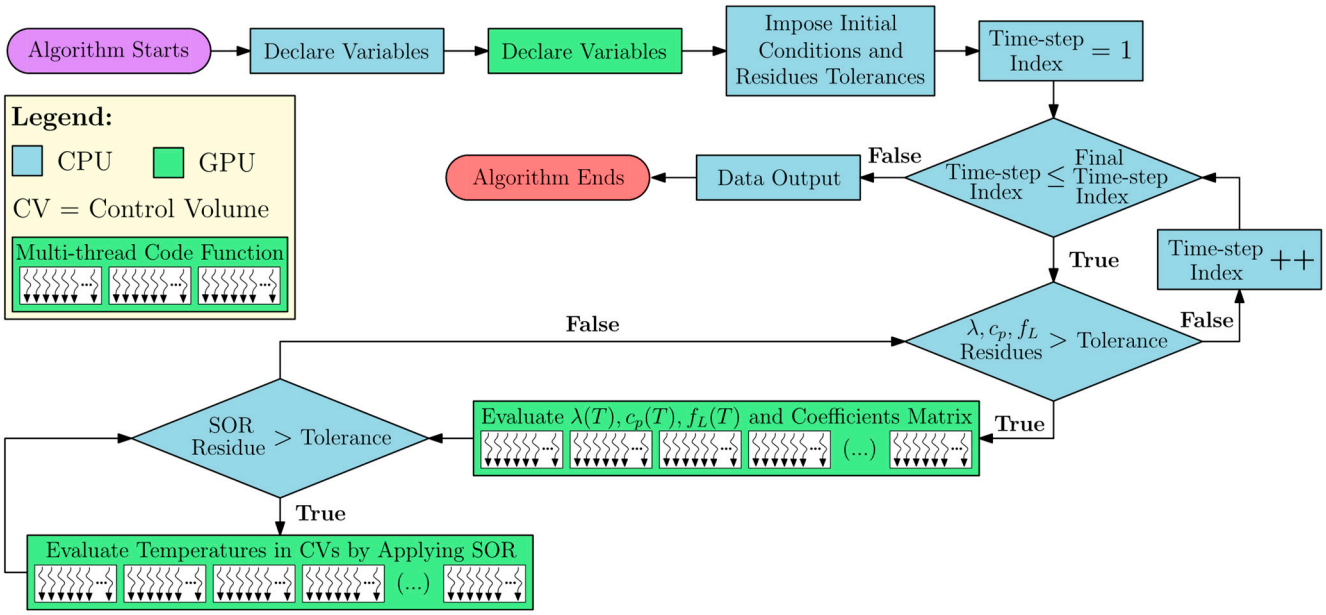

Figure 1. Developed CUDA-C language code flowchart.

The investigation was conducted through the application of the heat conduction Partial Differential Equation (PDE) with a transient total enthalpy term to model the LBW process. The latter is needed to account for the phase change (melting) according to the Volumetric Thermal Capacitor (VTC) approach [17]. The equations were discretized in space and time over a three-dimensional domain by applying the Finite Volume Method (FVM). The heat losses through convection at the boundaries of the domain were accounted for using Newton's law of cooling and the losses through radiation were calculated by applying the Stefan–Boltzmann law. A Gaussian conical profile models the welding heat source. The effects of implementing constant and temperature-dependent thermophysical properties for the specimen's material were evaluated. The GPUs simulations were performed in an in-house code written in CUDA-C language and run in an Nvidia™ Geforce® RTX™ 3090 and a Geforce® RTX™ 4090, both with 24 GB of video memory. A parallelized form of the Successive Over-Relaxation (SOR) solver was used to find the solution of the linear system of equations. The CUDA® code, as well as the three other top-rated CPU-based commercial codes, were executed on a desktop PC equipped with an Intel® Core™ i9 12900KF processor. The temperature profiles simulated using equivalent solutions produced by GPU and CPU were compared, as well as the computational performance in terms of processing time, energy consumption, cost efficiency, and memory usage. The enhanced performance demonstrated in the research results highlights the significant potential for GPUs to replace CPUs in CFD applications.

2. Materials and Methods

2.1. The Laser Beam Welding (LBW) Simulation

The Laser Beam Welding (LBW) technique is a high-precision process that makes use of a concentrated light beam to join metals together. The method yields high-quality welds due to a low Heat Affected Zone (HAZ) resultant from the high precision of the laser and the accurate control over the welding parameters, thus minimizing distortions and retaining much of the material's original mechanical properties. The technique also offers easy automation, which results in a high-speed manufacturing process, as the laser generates enough heat to rapidly move across the workpiece. The positive final characteristics of the LBW joint and its versatility contributed to a significant increase in the method's popularity in the last few years. For instance, LBW is currently by far the most simulated welding technique present in recent scientific publications [18]. The previous simulation of the process allows for various advantages such as optimization of the technique through new modeling and parameters tuning [19], enhanced materials selection [20], the prediction of the final weld bead mechanical characteristics [21,22], and the estimation of involved parameters through inverse analysis [23–25]. Hence, the present computational performance analysis was performed by simulating an LBW process conducted by an automated LASER head focused on an SAE 1020 steel specimen. The welding process and its geometrical parameters and thermophysical considerations are schematized in Figure 2, where L_x, L_y, and L_z are the specimen lengths at x, y, and z directions, respectively, L_w is the weld bead length, u is the LASER head velocity, T_∞ is the ambient temperature, q''_{rad} is the rate of heat loss by radiation per unit area, and q''_{con} is the rate of heat loss by convection per unit area. The values for each LBW parameter are tabulated in Table 1.

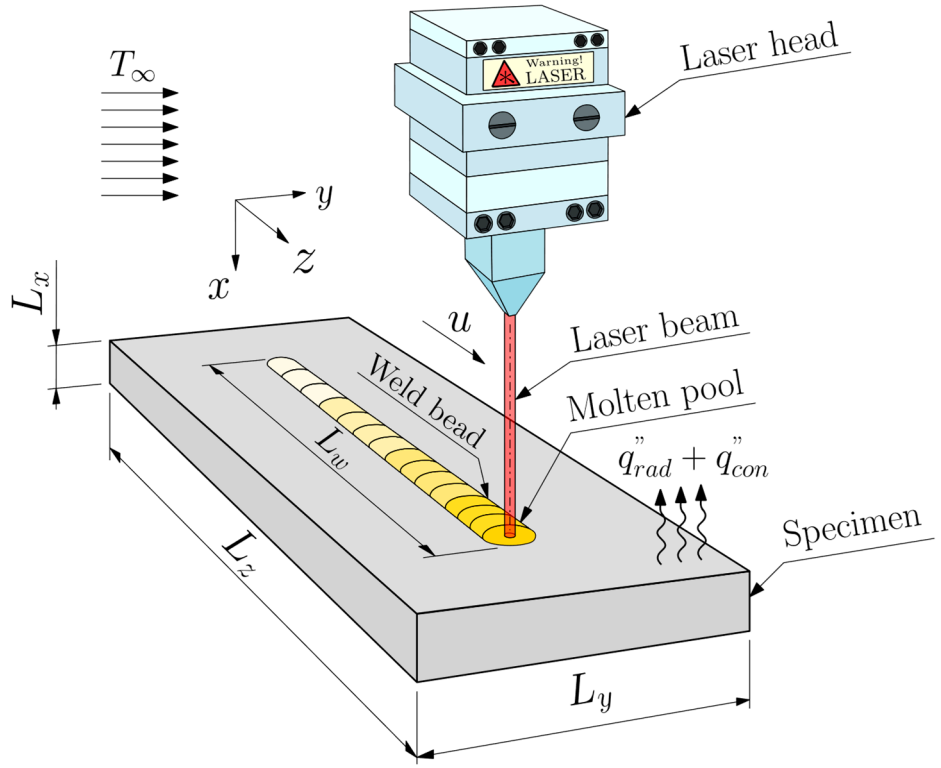

Figure 2. Simulated LASER Beam Welding (LBW) process schematics, parameters, and thermal modeling.

Table 1. LBW process parameters.

Parameter	Values
Ambient temperature (T_∞) [°C]	20.0
LASER head velocity (u) [mm/min]	3000.0

Table 1. *Cont.*

Parameter	Values
Sample length at x-direction (L_x) [mm]	9.5
Sample length at y-direction (L_y) [mm]	20.0
Sample length at z-direction (L_z) [mm]	40.0
Weld bead length (L_w) [mm]	30.0

2.2. Mathematical Model

A transient three-dimensional heat conduction equation physically governs the simulated welding process. The phenomenon may be modeled through a PDE with a volumetric heat generation term aimed at quantifying the heat input and a transient term written as a function of the total enthalpy to account for the metal phase change. Hence, the final governing equation may be written as follows [26]:

$$\underbrace{\frac{\partial}{\partial x}\left(\lambda\frac{\partial T}{\partial x}\right)+\frac{\partial}{\partial y}\left(\lambda\frac{\partial T}{\partial y}\right)+\frac{\partial}{\partial z}\left(\lambda\frac{\partial T}{\partial z}\right)}_{\text{Three}-\text{dimensional heat conduction}}+\dot{g}=\underbrace{\frac{\partial H}{\partial t}}_{\substack{\text{Transient}\\ \text{term}}} \tag{1}$$

where x, y, and z are the cartesian coordinates, λ is the nonlinear thermal conductivity, T is the temperature, $\dot{g}$ is the volumetric heat source rate, and t is the physical time. The total enthalpy term, H, can be mathematically written as [27]:

$$H=\underbrace{\rho\int_0^T c_p(\varphi)d\varphi}_{\substack{\text{Portion related to}\\ \text{the sensible heat}}}+\underbrace{\rho f_L(T)L_f}_{\substack{\text{Portion related to}\\ \text{the latent heat}}} \tag{2}$$

where ρ is the density, c_p is the specific heat at constant pressure, f_L is the temperature-dependent liquid mass fraction function, φ is the generic integration variable, and L_f is the latent heat of fusion. The total enthalpy term was solved through a partial implementation of the Volumetric Thermal Capacitor (VTC) method [17]. A linear temperature-dependent function was applied to model the materials' fusion. This equation may be written as follows [25]:

$$f_L(T)=\begin{cases}0 \text{ if } T<T_m\\ 1 \text{ if } T>T_m\end{cases}, 0<f_L<1 \text{ if } T=T_m \tag{3}$$

where T_m is the melting temperature. The heat losses by convection and radiation were calculated based on Newton's law of cooling and the Stefan–Boltzmann law, respectively. The final heat loss equation may be written as follows [28]:

$$q_L''=-\lambda\frac{\partial T}{\partial \eta}=\underbrace{h(T)(T-T_\infty)}_{\substack{\text{Newton}'\text{s law}\\ \text{of cooling}}}+\underbrace{\sigma\phi_{rad}(T)\left(T^4-T_\infty^4\right)}_{\text{Stefan Boltzmann law}} \tag{4}$$

where η is the direction normal to the surface, $h(T)$ is the temperature-dependent convection heat transfer coefficient, σ is the Stefan–Boltzmann constant, and ϕ_{rad} is the material's emissivity.

2.3. Moving Heat Source

The automated LASER head heat source was modeled as a constant velocity mobile Gaussian whole conical volumetric profile, implemented here as tuned, and reviewed in previous work [18,29]. The heat distribution may be mathematically written as

$$\dot{g} = \frac{Q_w}{0.460251 h_p R^2} e^{-\frac{4.5(z-ut)^2}{R^2}} e^{-\frac{4.5(y-L_y/2)^2}{R^2}} \left(1 - \frac{x^{1/2}}{h_p^{1/2}}\right) \quad (5)$$

where Q_w is the LASER heat source power, h_p is the height of penetration, R is the welding radius, and u is the LASER head velocity. The applied heat source model and its geometrical parameters are schematized in Figure 3.

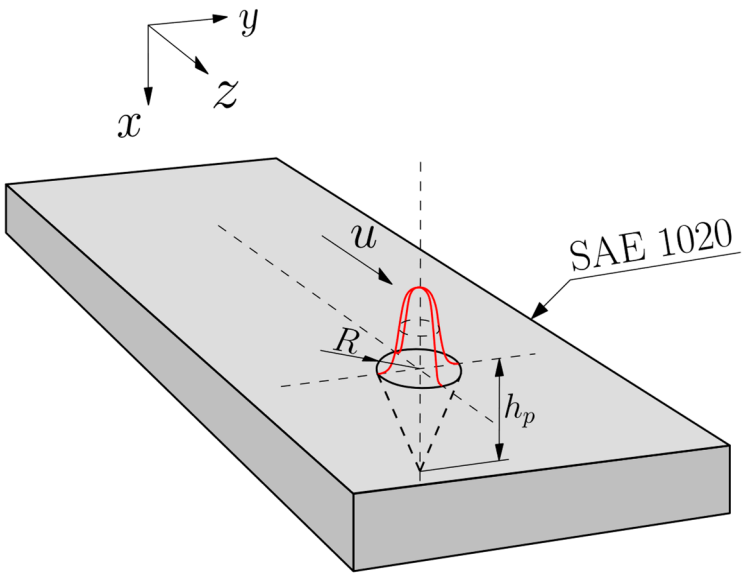

Figure 3. Gaussian whole conical volumetric heat source profile.

The heat source model parameters are tabulated in Table 2.

Table 2. Gaussian whole conical heat source model parameters.

Parameter	Values
Height of penetration (h_p) [mm]	1.65
LASER power (Q_w) [W]	800.0, 1200.0
Welding radius (R) [mm]	0.5

2.4. Post Processing, Spatial and Temporal Meshes Independencies

The four probe points, P_1 to P_4, were positioned transversally to the weld bead to allow for measurement and comparison of the resultant temperature fields simulated by each code run. Instead of parallel to the welding direction, the transverse positioning of the probe points allows for an enhanced numerical convergence analysis by avoiding a similar shape to all the curves. This alternative displacement results in a different temperature magnitude of the curves as well as the different peak times caused by the thermal inertia variance resultant from the smaller (P_1) and larger distances (P_3 and P_4) between the reading points and the heat core. The cartesian coordinates for each probe point are presented in Table 3 and its positions in the specimen are illustrated in Figure 4.

Table 3. Probe points three-dimensional cartesian coordinates.

Coordinates	P_1	P_2	P_3	P_4
x [mm]	9.5	9.5	9.5	9.5
y [mm]	10.0	11.0	12.0	13.0
z [mm]	20.0	20.0	20.0	20.0

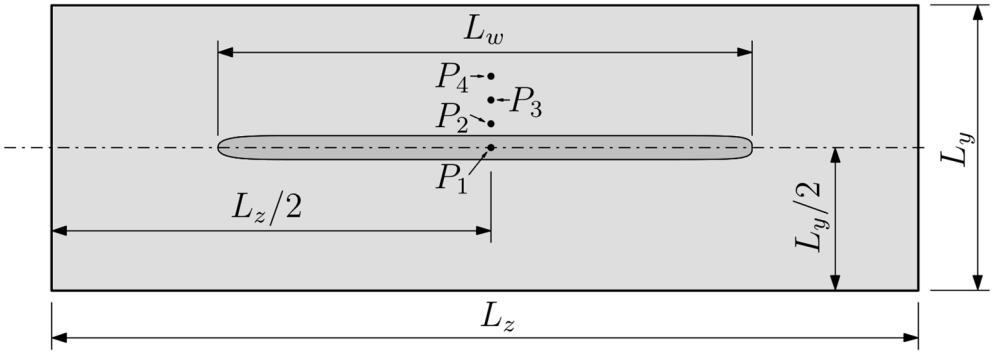

Figure 4. Applied temperature probe points (P_i) positioning.

A mesh size independence study was performed to ensure results independent of spatial refinement. The simulated domain was built as a uniform orthogonal structured grid. The resultant temperature fields became independent of mesh refinement at nearly 3,000,000 total nodes, distributed in nearly equal proportion to the specimen lengths at each dimension. Hence, a final mesh with 3,203,904 total nodes was instead used (82 × 148 × 264 nodes, at x, y, and z, respectively), resulting in an added design safety factor of approximately 6.797%. The average absolute errors (E_{avg}) [%] between a very refined mesh (G_7) and the other investigated cases (G_n) are tabulated in Table 4, where N_x, N_y, and N_z are the number of nodes at x, y, and z directions, respectively, and N_T is the total number of nodes.

Table 4. Average absolute error (E_{avg}) [%] between mesh size G_7 and others for probe points P_1 and P_2.

Mesh (G_n)	$N_x \times N_y \times N_z$ = Total Nodes (N_T)	P_1—Error (E_{avg}) [%]	P_2—Error (E_{avg}) [%]
G_1	24 × 48 × 82 = 94,464	27.608	25.787
G_2	9 × 58 × 113 = 190,066	3.867	3.642
G_3	37 × 74 × 137 = 375,106	3.296	3.792
G_4	46 × 95 × 177 = 773,490	0.785	0.812
G_5	62 × 126 × 208 = 1,624,896	1.811	1.540
G_6	82 × 148 × 264 = 3,203,904	0.029	0.157
G_7	111 × 172 × 325 = 6,204,900	-	-

A time-step size independence analysis was also conducted to investigate the temperature fields dependency on the temporal grid refinement. The results became independent of time-step size for values smaller than 2.5×10^{-3} [s]. However, the values of 1.0×10^{-3} and 2.5×10^{-5} s were instead applied. These values were intercalated, depending on the combination of input parameters, in direct proportion to the applied heat source power [W]. Time-step size values larger than 2.5×10^{-5} [s] will result in solver failure for some of the commercial codes in the analysis when a 1200 [W] heat source power or more is applied.

2.5. Material Properties

The welded material in the simulated LBW process is the SAE 1020 steel. Variations between constant and temperature-dependent thermal properties were applied for the specific heat (c_p) and the thermal conductivity (λ) to verify the quality of the CUDA® in-house code resultant data in both cases. The corresponding values of the properties at 20 °C were fixed and applied whenever constant properties were used. The thermophysical properties of

the SAE 1020 steel specimen are exposed in Table 5. The temperature-dependent behaviors of the specific heat (c_p) (input units in Kelvin) and the thermal conductivity (λ) (input units in Celsius degrees) are depicted in Figure 5.

Table 5. SAE 1020 steel alloy thermophysical properties.

Thermal Properties (SAE 1020)	Values/Equations
Density (ρ) [kg/m^3]	7731.3
Emissivity (ϕ_{rad})	0.8
Latent heat of fusion (L) [kJ/kg]	247.0
Melting temperature (T_m) [°C]	1450.0
Specific heat (c_p) [J/kg·K]	$c_p(T) = 3.298 \times 10^2 e^{1.509 \times 10^{-3} T}$
Thermal conductivity (λ) [W/m·K]	$\lambda(T) = 2.5 \times 10^{-5} T^2 - 0.053T + 57.2$

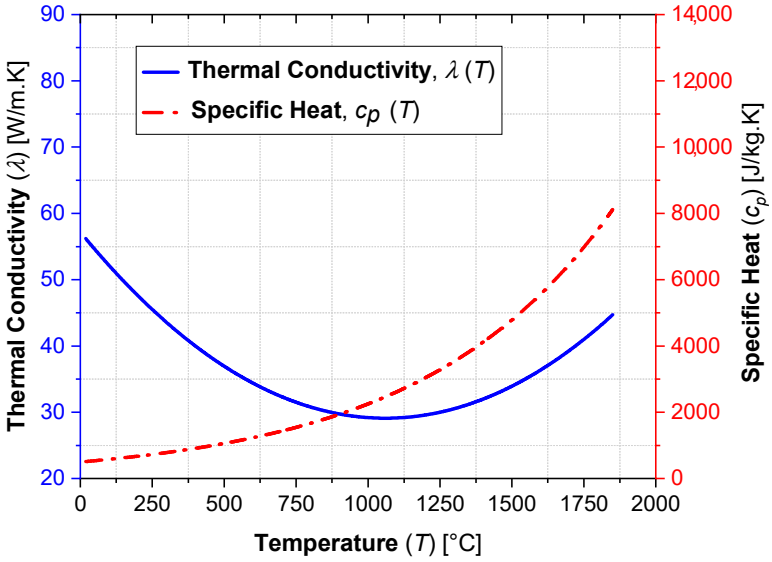

Figure 5. Specific heat (c_p) [J/kg·K] and thermal conductivity (λ) [W/m·K] behavior as a function of temperature (T) [°C].

2.6. Simulation Parameters

Despite all the commercial code solutions using multigrid techniques, the Successive Over-relaxation (SOR) parallelized solver was applied in the GPU solution without using multigrid techniques. All the simulations were performed with a first-order scheme temporal discretization. An energy residual convergence criterion was applied to all cases, and the threshold was set to 1.0×10^{-5}. Finally, the simulation parameters are presented in Table 6.

Table 6. Simulated cases parameters.

Parameter	Values
Temporal discretization	First-order scheme
Time-step (Δt) [s]	1.0×10^{-3} and 2.5×10^{-5}
Simulation total time (t_{Tot}) [s]	2.5
Solver convergence criterion	Energy residual
Residual threshold	1.0×10^{-5}

3. Results and Discussion

3.1. LBW Temperature Fields

The first analysis was conducted with the aim of verifying the accuracy of the GPU solution and its code behavior when constant or temperature-dependent thermal properties

are applied. As there is a notable drop in thermal conductivity (λ) values when the temperature increases (as in Figure 5), the LASER power (Q_w) was firstly reduced to 800.0 [W] to avoid excessively high temperatures when constant properties are applied. The curves presented in Figure 6 illustrate the temperature fields for the CUDA® code and commercial solutions through probe points P_1 to P_4. The average absolute error (E_{avg}) [%] between the GPU code and each commercial solution is included in Table 7. The maximum error reached was 3.746% between the CUDA® code and the commercial code #2 for probe point P_3. However, the equivalent measurements probed at the other commercial codes returned values with much better agreement.

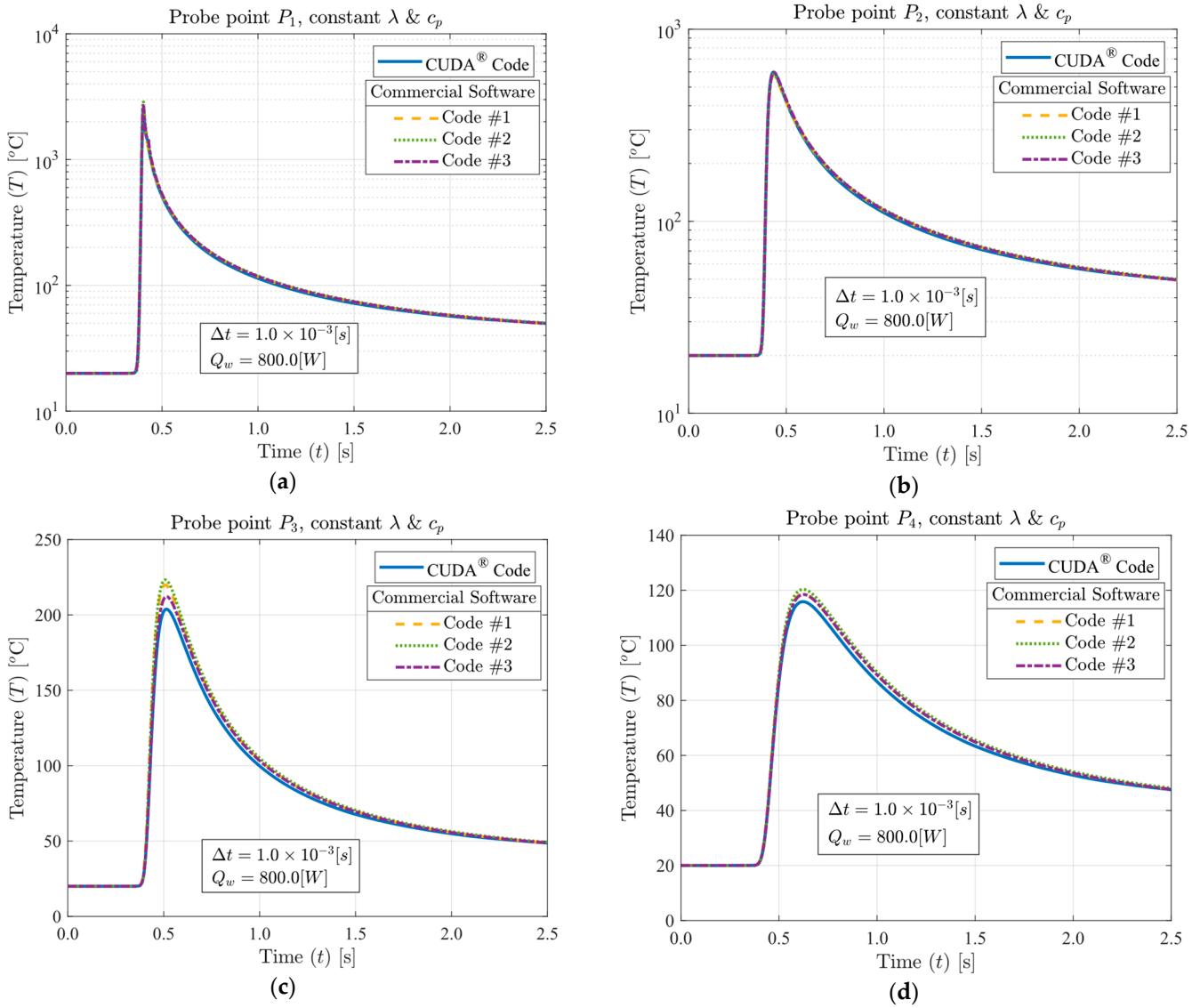

Figure 6. Temperature (T) [°C] as a function of time (t) [s] for 800 [W] LASER power (Q_w), 1.0×10^{-3} [s] time-step size (Δt), constant λ, constant c_p and (**a**) Probe point P_1, (**b**) Probe point P_2, (**c**) Probe point P_3, (**d**) Probe point P_4.

Table 7. Average absolute error (E_{avg}) [%] between CUDA® and each processing code (#n) as a function of probe point (P_n) for constant λ and constant c_p.

	Average Absolute Error (E_{avg}) [%]		
Probe Point/Solution	**Commercial Code #1**	**Commercial Code #2**	**Commercial Code #3**
P_1	2.070	3.051	2.180
P_2	1.530	2.456	1.810
P_3	2.843	3.746	2.065
P_4	1.678	2.582	1.575

Applying temperature-dependent thermal properties caused the temperatures at probe point P_1 to drop nearly 55.6%. The resultant temperature fields are illustrated in Figure 7. The overall good matching between the GPU and the commercial solutions was kept, and the maximum average absolute error was 2.756% at probe point P_3 for CUDA® and commercial code #2. The average absolute error (E_{avg}) values are presented in Table 8. The first two sets of results evidenced that the higher the thermal gradient achieved, the higher the errors involved in all code solutions.

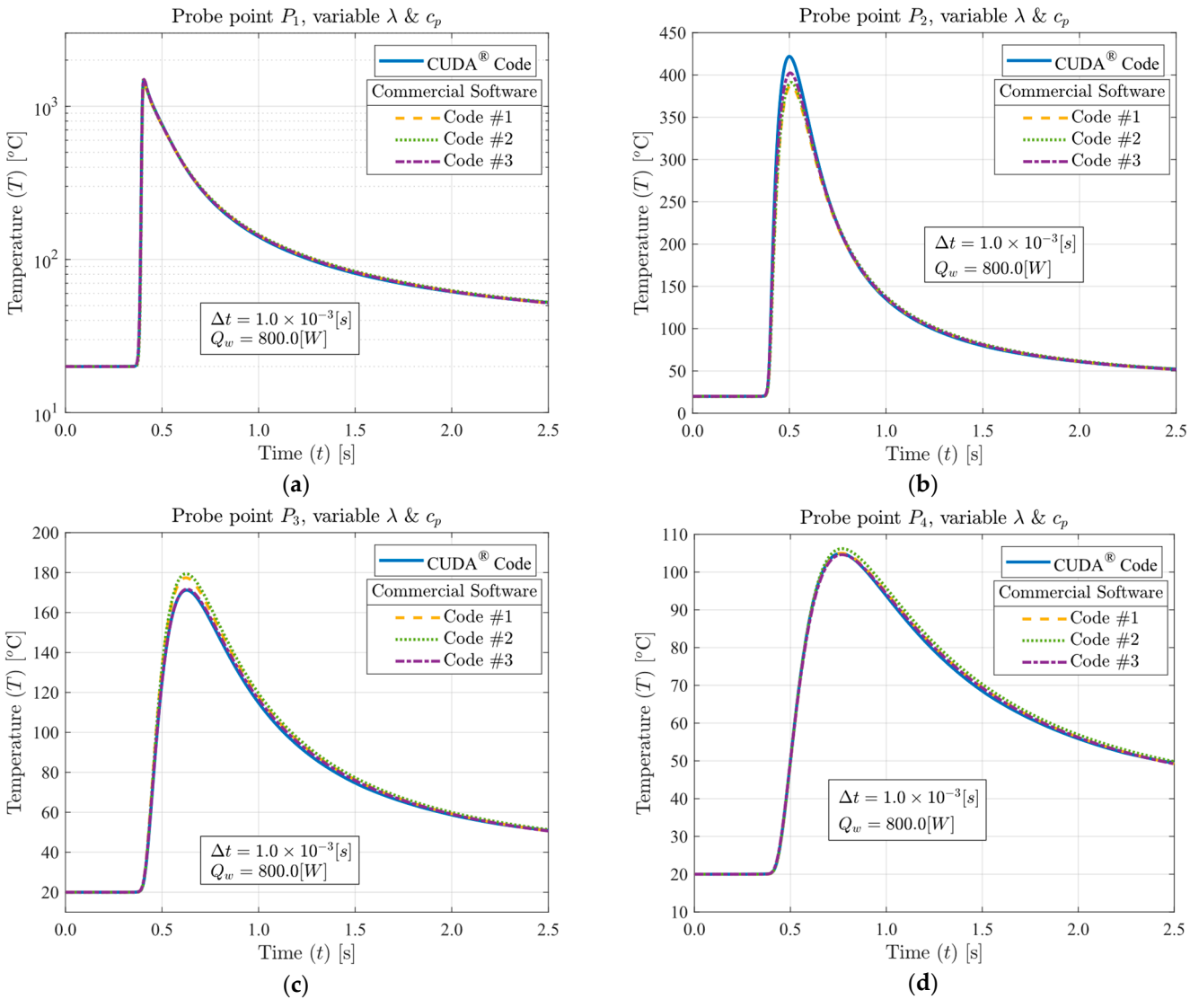

Figure 7. Temperature (T) [°C] as a function of time (t) [s] for 800 [W] LASER power (Q_w), 1.0×10^{-3} [s] time-step size (Δt), variable λ, variable c_p and (**a**) Probe point P_1, (**b**) Probe point P_2, (**c**) Probe point P_3, (**d**) Probe point P_4.

Table 8. Average absolute error (E_{avg}) [%] between CUDA® and each processing code (#n) as a function of probe point (P_n) for variable λ, variable c_p and 800 [W] LASER power (Q_w).

	Average Absolute Error (E_{avg}) [%]		
Probe Point/Solution	**Commercial Code #1**	**Commercial Code #2**	**Commercial Code #3**
P_1	1.059	2.149	0.929
P_2	1.475	2.280	1.092
P_3	1.768	2.756	0.863
P_4	0.635	1.521	0.600

The temperature field investigation was finalized by increasing the LASER power (Q_w) to 1200.0 [W] and applying temperature-dependent thermal properties to better address the precision of the applied phase change modeling. For the sake of brevity, only the temperature curves for probe points P_1 and P_2 were plotted, as in Figure 8. Here, the maximum absolute average error (E_{avg}) observed was 4.617% at probe point P_3 for commercial code #2. The calculated error values are presented in Table 9. As expected, the increase in thermal gradient magnitude resulted in higher error values at probe point P_1 compared to the errors presented in Table 8.

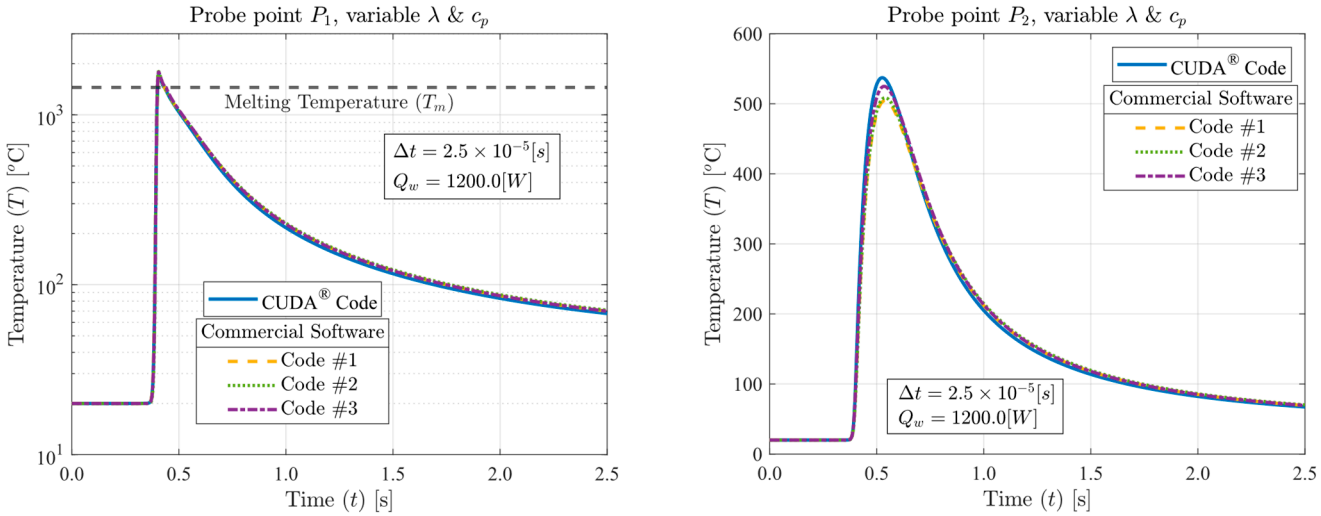

Figure 8. Temperature (T) [°C] as a function of time (t) [s] for 1200 [W] LASER power (Q_w), 2.5×10^{-5} [s] time-step size (Δt), variable λ, variable c_p and (**a**) Probe point P_1, (**b**) Probe point P_2.

Table 9. Average absolute error (E_{avg}) [%] between CUDA® and each processing code (#n) as a function of probe point (P_n) for variable λ, variable c_p and 1200 [W] LASER power (Q_w).

	Average Absolute Error (E_{avg}) [%]		
Probe Point/Solution	**Commercial Code #1**	**Commercial Code #2**	**Commercial Code #3**
P_1	3.291	4.615	2.539
P_2	3.076	4.248	1.976
P_3	3.497	4.617	1.117
P_4	1.996	2.937	1.487

3.2. CUDA® vs. Variable CPU Processing Nodes

The investigation was continued by analyzing the change in computational performance of the commercial solutions through the variation of the number of CPU parallel processing nodes (N_p). The consumer-available codes were set to run in three, five, and seven CPU processing nodes. The CUDA® code is a GPU parallelized solution; thus, it runs on only one CPU processing node. The overall performance of all solutions is included

in the bar charts of Figure 9 for an LBW simulated case with 800 [W] LASER power (Q_w), 1.0×10^{-3} [s] time-step size (Δt), variable λ, and variable c_p. The computational time (τ_c) [min] as a function of the number of CPU parallel processing nodes (N_p) is exposed in Figure 9a. Figure 9b shows the total speed-up reached (χ) [$\times$ (times)] at each GPU solution as a function of the computational code/hardware. The analysis revealed that commercial code #3 has an optimum number of CPU processing nodes (N_p) equal to 7, whereas the other codes are faster for N_p equal to 5. Although for the particular LBW problem simulated here, the variation of N_p often results in little difference in the computational time (τ_c), the optimum values for each software were used in the next analyses. The highest decrease in the computational time was nearly 26.34% for commercial code #3 when switching from N_p equals 3 to 7. Finally, the simulation was executed on an RTX™ 4090 to further enrich the investigation, resulting in a processing time 38.14% faster than that of the RTX™ 3090.

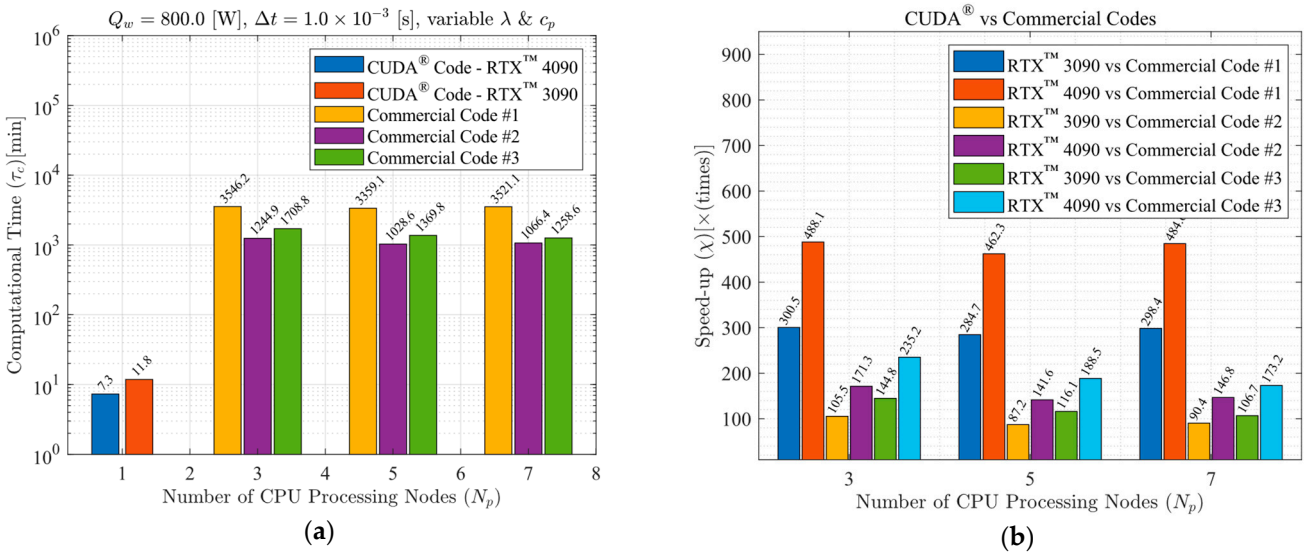

Figure 9. Processing performance comparison for 800 [W] LASER power (Q_w), 1.0×10^{-3} [s] time-step size (Δt), variable λ and variable c_p: (**a**) computational time (τ_c) [min] versus number of CPU processing nodes (N_p), (**b**) total speed-up reached (χ) [$\times$ (times)] as a function of applied code/hardware.

3.3. Processing Performance vs. Mesh Size

The GPU solution was investigated in terms of processing performance as a function of mesh refinement. Here, the computational grid sizes G_4, G_5, and G_6 were simulated for 800 [W] LASER power (Q_w), 1.0×10^{-3} [s] time-step size (Δt), variable λ, variable c_p, and optimum N_p. The overall computational performance of all analyzed codes is presented in Figure 10. Figure 10a illustrates the computational time (τ_c) [min] as a function of the number of mesh total nodes (N_T). The total speed-up reached (χ) [$\times$ (times)] as a function of computational code/hardware is shown in Figure 10b. It is possible to observe a nearly linear direct proportionality between the number of mesh total nodes (N_T) and the required computational time (τ_c) to complete the simulation, with some exceptions noted for commercial code #1. The resultant speed-ups achieved ranged from 75.6 (between CUDA® and commercial code #3, for the 773,490 total nodes mesh) to 1351.2 times (between CUDA® and commercial code #1, for the 773,490 total nodes mesh).

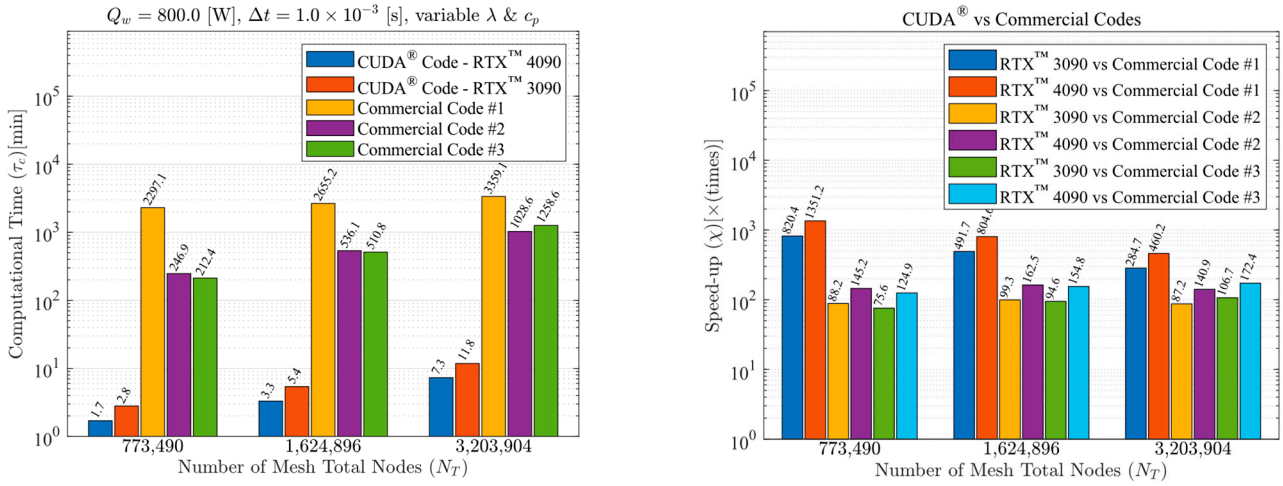

(**a**) (**b**)

Figure 10. Processing performance comparison for 800 [W] LASER power (Q_w), 1.0×10^{-3} [s] time-step size (Δt), variable λ and variable c_p: (**a**) computational time (τ_c) [min] versus number of mesh total nodes (N_T), (**b**) total speed-up reached (χ) [× (times)] as a function of applied code/hardware.

3.4. Processing Hardware Energy Consumption

An electricity consumption analysis was performed to study the GPU solution in terms of energy efficiency and to ensure no possibility of increasing environmental damages due to the use of GPU simulations. Hence, the numerical solutions had their respective hardware monitored during an LBW simulation case with 800 [W] LASER power (Q_w), 1.0×10^{-3} [s] time-step size (Δt), variable λ, and variable c_p. The commercial solutions were rerun in the optimum number of CPU parallel processing nodes (N_p) (5, 5, and 7 for commercial codes #1, #2, and #3, respectively). The general energy efficiency of the tested solutions is presented in Figure 11. Figure 11a illustrates the processing hardware electric power (P_E) [W] as a function of computational time (τ_c) [s], whereas Figure 11b exposes the processing hardware electricity consumption (ε_T) [kWh] as a function of applied code/hardware. The CUDA® code simulations yield an average of only 5% CPU utilization, and thus, its central processor's power consumption is nearly the same as that of an idle computer. It is important to highlight that the present analysis only accounts for the main processing hardware electricity consumption. Hence, the total computer consumption is significantly higher than the values shown. The investigation evidenced that the GPU solutions required an average of 83.24 times less electrical energy.

The analysis was continued by conducting a cost efficiency study on the energy consumption of the numerical solutions provided by the applied computing methodologies. Here, the investigation was performed based on the electricity rates of where the research was developed (Brazil, city of São José dos Campos) and where it was first exposed (Germany, city of Düsseldorf) in mid-2023. The electricity rates used in the calculations were obtained straight from local energy distribution companies, EDP Brasil and Stadtwerke Düsseldorf. In mid-2023, Brazilian energy rates were governed by the green flag pricing, and hence, the cost per kWh for a commercial low voltage installation (B3 classification) yields the sum between the cost of the electrical energy and the cost for the usage of the distribution system (BRL 0.27614 and BRL 0.37743, respectively). The calculation then totals USD 0.13642 by the commercial conversion rate of BRL 4.791 per dollar (1 August 2023). According to Stadtwerke Düsseldorf, a similar installation would result in EUR 0.3030 per kWh, resulting in a rate of USD 0.33231 by the commercial conversion rate of EUR 1.097 per dollar (1 August 2023). All the monetary quantities were defined here according to the ISO4217 standard [30]. The electricity rates per kilowatt hour may be easily rechecked at each local provider's website. The overall processing hardware electricity cost per simulation (C_s) [USD] as a function of computational code/hardware is shown

in Figure 12. The GPU solutions yielded an average cost per simulation 80.57 times lower than the average cost required by the commercial codes (regardless of the country).

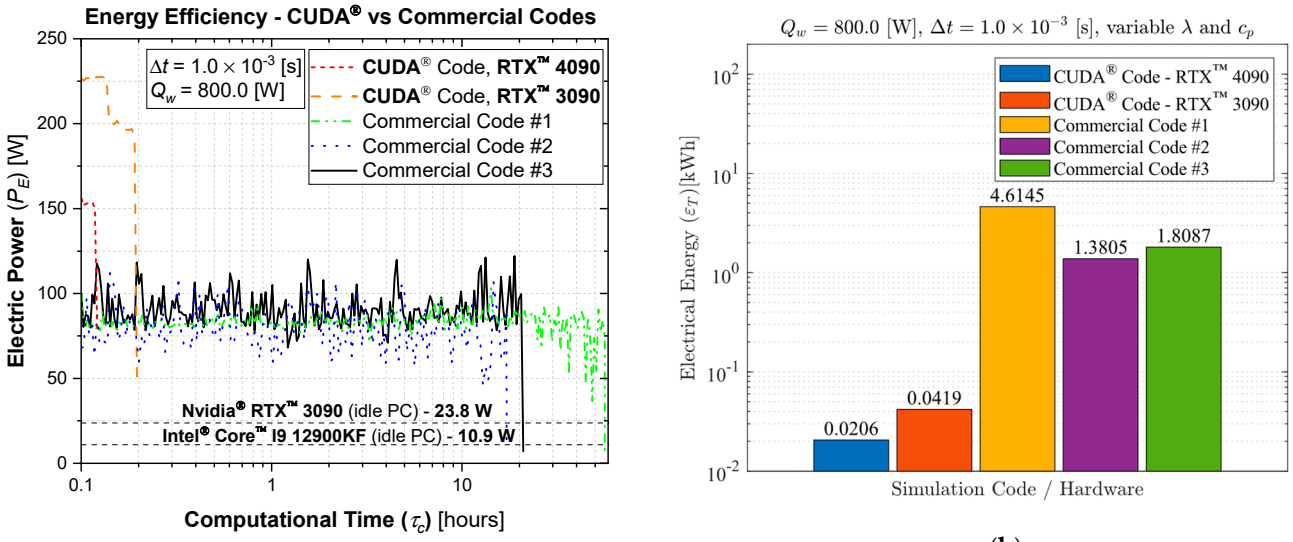

Figure 11. CUDA® vs. commercial codes energy efficiency comparison for 800 [W] LASER power (Q_w), 1.0×10^{-3} [s] time-step size (Δt), variable λ and variable c_p: (**a**) processing hardware electric power (P_E) [W] as a function of computational time (τ_c) [s], (**b**) processing hardware total electricity consumption (ε_T) [kWh] as a function of applied code/hardware.

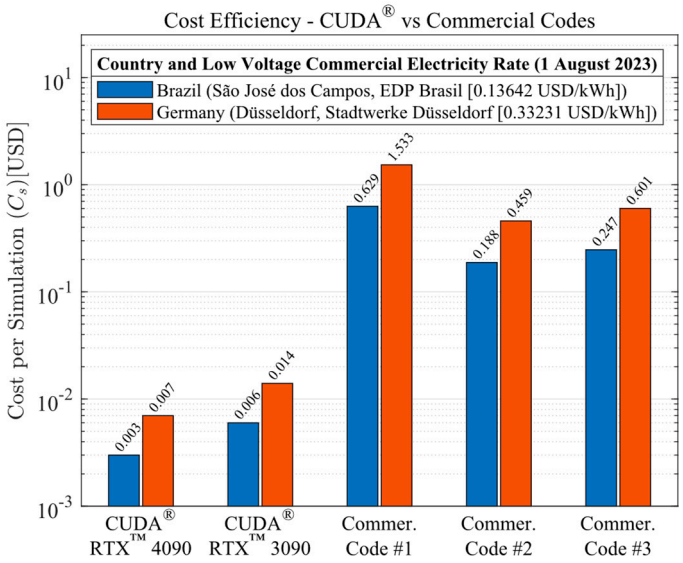

Figure 12. Cost per simulation (C_s) [USD] as a function computational code/hardware for the Brazilian (São José dos Campos, SP, Brazil) electricity rate [USD] and Germany (Düsseldorf) electricity rate [USD] in mid-2023.

3.5. Code Optimization

The GPU solution was investigated in terms of code optimization through a memory usage analysis. This study was performed by comparing the allocated RAM and VRAM at each code during the solution of the LBW problem. The host computer had all apps removed from startup, and the machine was restarted at every new simulation to clean its memory and ensure that each code was running alone. The overall memory performance of the implemented codes is illustrated in Figure 13. The memory usage (M_u) as a function of simulated physical phenomenon time (t) is shown in letter (a) and represents the system's

total memory usage during simulation (the sum between the operational system and each running code). The average net memory usage ($\overline{M_u\prime}$) was calculated by subtracting the idle PC operational system's memory consumption from each code's average total memory usage value. The CUDA® code was run directly from the Integrated Development Environment (IDE); hence, its RAM memory usage is inevitably summed with the RAM of the GPU simulation code, which is consequently considerably smaller than shown. In spite of that fact, the CUDA® solution still presented an excellent code optimization since its memory usage is by far the lowest among all analyzed codes. The GPU code requires nearly four times less RAM than the average net usage between the three commercial solutions (13.402 GB). The CUDA® solution also offers the advantage of nearly zero memory usage fluctuation, keeping its consumption approximately constant from simulation start to finish.

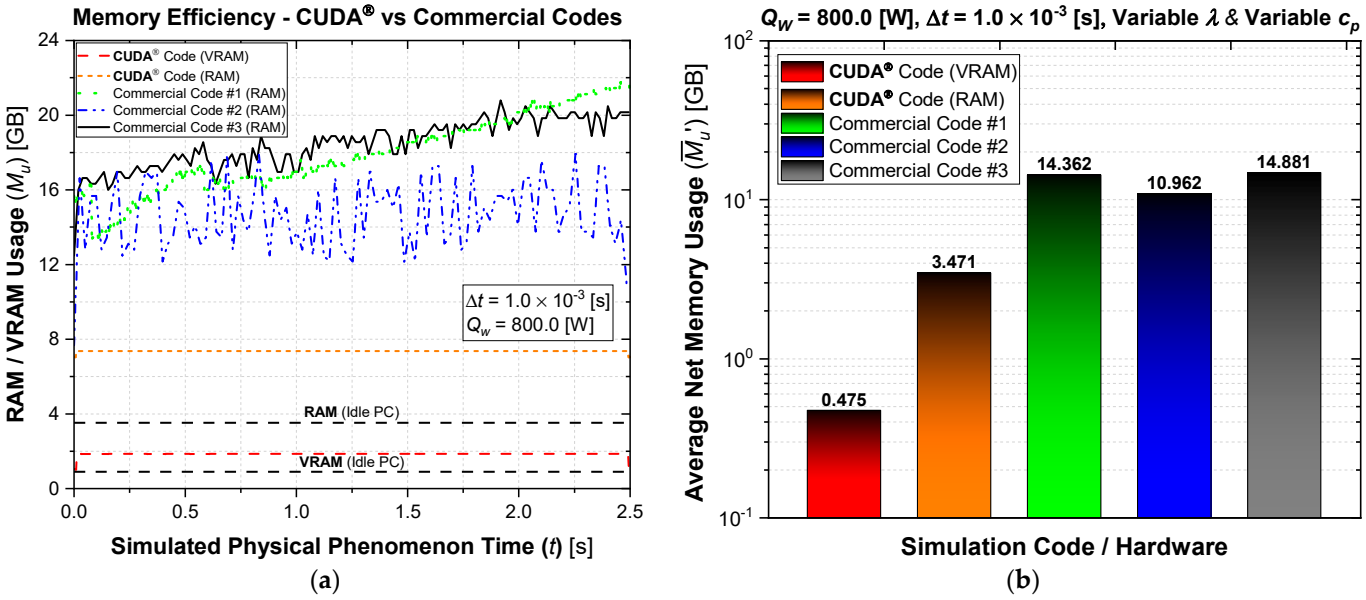

Figure 13. Code memory optimization for 800 [W] LASER power (Q_w), 1.0×10^{-3} [s] time-step size (Δt), variable λ and variable c_p: (**a**) memory usage (M_u) [GB] as a function of simulated physical phenomenon time (t) [s], (**b**) average net memory usage ($\overline{M_u\prime}$) [GB] as a function of simulated code.

4. Conclusions

A computational performance analysis of a GPU LASER beam welding implementation using CUDA® was conducted. The applied methodology involved calculating temperature-dependent thermal properties, the temperature-dependent liquid mass fraction function, the coefficients matrix, and the final temperatures of each control volume through multi-thread parallelization. These code functions were executed on the GPU to achieve high-scale parallelism. The CPU was then utilized to coordinate the sequence of execution of all code functions and handle memory management. The results of this implementation were compared to output data from three top-rated commercial codes, assessing accuracy, processing performance, energy consumption, cost efficiency, and code optimization. The GPU solutions demonstrated vast potential in reducing CFD costs and time. The performance investigation yielded speed-ups ranging from 75.6 to 1351.2 times faster than the commercial solutions. This study also demonstrated that each commercial code has an optimum number of CPU parallel processing nodes (N_p) that may vary with the type of physics simulated, mesh, number of chip physical cores, and other parameters (for the cases in the present study, N_p = 5, 5, and 7, for commercial codes #1, #2, and #3, respectively). The double precision capability of modern graphics cards was evidenced through their calculations, resulting in an accuracy similar to that of the CPU solutions. Some of the cutting-edge GPU chips have similar or higher Thermal Design Power (TDP) than high-performance CPUs, but end up consuming far less electricity due to the ability to

execute higher parallel processing scaling and thus finishing tasks much faster. As a matter of fact, the investigation revealed that the proposed GPU solutions required an average of 83.24 times less electrical energy in comparison to the commercial codes. In terms of budget, this higher energy efficiency of the GPU solutions resulted in an average cost per simulation 80.57 times lower than the average cost required by the commercial codes (regardless of the country). The in-house code also demonstrated optimized RAM and VRAM usage, averaging 3.86 times less RAM utilization in comparison to the commercial CFD solutions. Lastly, the primary drawbacks of implementing CFD simulations using CUDA® are the heightened coding complexity and the necessity of a CUDA-compatible graphics card. Future work will involve code enhancements through adopting an unstructured multigrid approach.

Author Contributions: Conceptualization, E.N. and E.M.; methodology, E.N., E.M. and A.A.; software, E.M., A.A. and E.N.; validation, A.A.; formal analysis, E.N. and A.A.; investigation E.N. and A.A.; resources, E.M.; data curation, E.N. and A.A.; writing—original draft preparation, E.N., A.O. and L.E.S.P.; writing—review and editing, E.N., A.A. and A.O.; visualization, E.N., E.M., A.A., L.E.S.P. and A.O.; supervision, E.M. and L.E.S.P.; project administration, E.M. and L.E.S.P.; funding acquisition, E.M. All authors have read and agreed to the published version of the manuscript.

Funding: This research was funded by the Coordenação de Aperfeiçoamento de Pessoal de Nível Superior (CAPES, an agency of the ministry of education of Brazil, under the grant 88887.512576/2020–00), by the Conselho Nacional de Desenvolvimento Científico e Tecnológico (CNPq, an agency of the ministry of Science, Technology, Innovations, and Communications of Brazil, under the grant 402673/2021–2) and by Petróleo Brasileiro S.A. (PETROBRAS, a Brazilian multinational company).

Data Availability Statement: The data presented in this study are available on request from the corresponding author.

Acknowledgments: The authors would like to thank the Brazilian Ministry of Defense, the Brazilian Airforce (FAB), and the GAP-SJ group for providing food support for the researchers of the Aeronautics Institute of Technology—ITA.

Conflicts of Interest: The authors declare no conflict of interest.

References

1. Thomée, V. From Finite Differences to Finite Elements. *J. Comput. Appl. Math.* **2001**, *128*, 1–54. [CrossRef]
2. Moukalled, F.; Mangani, L.; Darwish, M. *The Finite Volume Method in Computational Fluid Dynamics*; Fluid Mechanics and Its Applications; Springer International Publishing: Cham, Switzerland, 2016; Volume 113, ISBN 978-3-319-16873-9.
3. Pappas, C.; Moschos, T.; Alexoudi, T.; Vagionas, C.; Pleros, N. 16-Bit (4 × 4) Optical Random Access Memory (RAM) Bank. *J. Light. Technol.* **2023**, *41*, 949–956. [CrossRef]
4. Choi, J.; You, H.; Kim, C.; Young Yeom, H.; Kim, Y. Comparing Unified, Pinned, and Host/Device Memory Allocations for Memory-Intensive Workloads on Tegra SoC. *Concurr. Comput.* **2021**, *33*, e6018. [CrossRef]
5. Medina Lino, I.L.; Carrasco-Teja, M.; Frigaard, I. GPU Computing of Yield Stress Fluid Flows in Narrow Gaps. *Theor. Comput. Fluid Dyn.* **2023**, *37*, 661–680. [CrossRef]
6. Xia, Y.; Blumers, A.; Li, Z.; Luo, L.; Tang, Y.-H.; Kane, J.; Goral, J.; Huang, H.; Deo, M.; Andrew, M. A GPU-Accelerated Package for Simulation of Flow in Nanoporous Source Rocks with Many-Body Dissipative Particle Dynamics. *Comput. Phys. Commun.* **2020**, *247*, 106874. [CrossRef]
7. Viola, F.; Spandan, V.; Meschini, V.; Romero, J.; Fatica, M.; de Tullio, M.D.; Verzicco, R. FSEI-GPU: GPU Accelerated Simulations of the Fluid–Structure–Electrophysiology Interaction in the Left Heart. *Comput. Phys. Commun.* **2022**, *273*, 108248. [CrossRef]
8. Zacharoudiou, I.; McCullough, J.W.S.; Coveney, P.V. Development and Performance of a HemeLB GPU Code for Human-Scale Blood Flow Simulation. *Comput. Phys. Commun.* **2023**, *282*, 108548. [CrossRef]
9. O'Connor, J.; Rogers, B.D. A Fluid–Structure Interaction Model for Free-Surface Flows and Flexible Structures Using Smoothed Particle Hydrodynamics on a GPU. *J. Fluids Struct.* **2021**, *104*, 103312. [CrossRef]
10. Satake, S.; Yoshimori, H.; Suzuki, T. Optimizations of a GPU Accelerated Heat Conduction Equation by a Programming of CUDA Fortran from an Analysis of a PTX File. *Comput. Phys. Commun.* **2012**, *183*, 2376–2385. [CrossRef]
11. Klimeš, L.; Štětina, J. A Rapid GPU-Based Heat Transfer and Solidification Model for Dynamic Computer Simulations of Continuous Steel Casting. *J. Mater. Process. Technol.* **2015**, *226*, 1–14. [CrossRef]
12. Szénási, S. Solving the Inverse Heat Conduction Problem Using NVLink Capable Power Architecture. *PeerJ Comput. Sci.* **2017**, *3*, e138. [CrossRef]

13. Semenenko, J.; Kolesau, A.; Starikovičius, V.; Mackūnas, A.; Šešok, D. Comparison of GPU and CPU Efficiency While Solving Heat Conduction Problems. *Sci. Future Lith.* **2020**, *12*, 1–5. [CrossRef]
14. Taghavi, S.M.H.; Akbarzadeh, P.; Mahmoodi Darian, H. SADI Approach Programming on GPU: Convective Heat Transfer of Nanofluids Flow inside a Wavy Channel. *J. Therm. Anal. Calorim.* **2021**, *146*, 31–46. [CrossRef]
15. Shao, J.; Zhu, K.; Huang, Y. A Fast GPU Monte Carlo Implementation for Radiative Heat Transfer in Graded-Index Media. *J. Quant. Spectrosc. Radiat. Transf.* **2021**, *269*, 107680. [CrossRef]
16. de Azevedo, A.M.; Magalhães, E.d.S.; da Silva, R.G.D.; Lima e Silva, S.M.M.d. A Comparison between Nonlinear and Constant Thermal Properties Approaches to Estimate the Temperature in LASER Welding Simulation. *Case Stud. Therm. Eng.* **2022**, *35*, 102135. [CrossRef]
17. de Azevedo, A.M.; Magalhães, E.d.S. The Volumetric Thermal Capacitor Method for Nonlinear Heat Transfer in Phase-Change Materials. *Int. Commun. Heat Mass Transf.* **2023**, *142*, 106672. [CrossRef]
18. Nascimento, E.J.G.; dos Santos Magalhães, E.; dos Santos Paes, L.E. A Literature Review in Heat Source Thermal Modeling Applied to Welding and Similar Processes. *Int. J. Adv. Manuf. Technol.* **2023**, *126*, 2917–2957. [CrossRef]
19. Unni, A.K.; Vasudevan, M. Determination of Heat Source Model for Simulating Full Penetration Laser Welding of 316 LN Stainless Steel by Computational Fluid Dynamics. *Mater. Today Proc.* **2021**, *45*, 4465–4471. [CrossRef]
20. Behúlová, M.; Babalová, E. Numerical Simulation of Temperature Fields during Laser Welding–Brazing of Al/Ti Plates. *Materials* **2023**, *16*, 2258. [CrossRef]
21. Deng, P.; Xiang, S.; Ran, Q.; Tan, Y.-B.; Liu, F. Influence of Heat Input on Microstructure and Mechanical Properties of Laser Welding GH4169 Bolt Assembly—Numerical and Experimental Analysis. *Adv. Eng. Mater.* **2023**, *25*, 2300309. [CrossRef]
22. Kumar, B.; Bag, S.; Ruhul Amin, M. Evaluation of Phase Transformation Strain and Its Influence on Residual Stress Generation in Laser Welded Ti–6Al–4V Alloy. *J. Manuf. Sci. Eng.* **2022**, *144*, 121002. [CrossRef]
23. Dourado da Silva, R.G.; Magalhães, E.d.S.; Marcondes Lima e Silva, S.M. Modified Nonlinear Function Specification and Temperature Moving Sensor to Estimate the Heat Supply in a Welding Process. *Int. J. Therm. Sci.* **2021**, *162*, 106780. [CrossRef]
24. Dourado da Silva, R.G.; dos Santos Magalhães, E.; de Lima e Silva, S.M.M.; dos Santos Paes, L.E.; Pereira, M. Estimating the Absorption Efficiency in a Laser Welding Process Using a Nonlinear Inverse Problem Method. *Int. J. Therm. Sci.* **2023**, *183*, 107846. [CrossRef]
25. Magalhães, E.d.S. A Quadrilateral Optimization Method for Non-Linear Thermal Properties Determination in Materials at High Temperatures. *Int. J. Heat Mass Transf.* **2021**, *181*, 121857. [CrossRef]
26. Versteeg, H.K.; Malalasekera, W. *An Introduction to Computational Fluid Dynamics*, 2nd ed.; Pearson Education Limited: Harlow, UK, 2007.
27. Crank, J. *Free and Moving Boundary Problems*; Clarendon Press: Oxford, UK, 1984; Volume 1.
28. Bergman, T.L.; Lavine, A.S.; Incropera, F.P.; Dewitt, D.P. *Fundamentals of Heat and Mass Transfer*, 7th ed.; John Wiley & Sons: Hoboken, NJ, USA, 2011.
29. Magalhães, E.d.S.; Paes, L.E.d.S.; Pereira, M.; da Silveira, C.A.; Pereira, A.d.S.P.; Lima e Silva, S.M.M. A Thermal Analysis in Laser Welding Using Inverse Problems. *Int. Commun. Heat Mass Transf.* **2018**, *92*, 112–119. [CrossRef]
30. *ISO 4217:2015*; Codes for the Representation of Currencies and Funds. ISO: 2015. International Organization for Standardization. Available online: https://www.iso.org/iso-4217-currency-codes.html (accessed on 11 March 2024).

computation

MDPI

Article

Analysis of a Novel Method for Generating 3D Mesh at Contact Points in Packed Beds

Daniel F. Szambien, Maximilian R. Ziegler, Christoph Ulrich and Roland Scharf *

Institut für Kraftwerkstechnik und Wärmeübertragung, Gottfried Wilhelm Leibniz Universität Hannover, An der Universität 1, 30823 Garbsen, Germany

* Correspondence: scharf@ikw.uni-hannover.de; Tel.: +49-511-762-14251

Abstract: This study comprehensively analyzes the impact of the novel HybridBridge method, developed by the authors, for generating a 3D mesh at contact points within packed beds within the effective thermal conductivity. It compares HybridBridge with alternative methodologies, highlights its superiority and outlines potential applications. The HybridBridge employs two independent geometry parameters to facilitate optimal flow mapping while maintaining physically accurate effective thermal conductivity and ensuring high mesh quality. A method is proposed to estimate the HybridBridge radius for a defined packed bed and cap height, enabling a presimulative determination of a suitable radius. Numerical analysis of a body-centered-cubic unit cell with varied HybridBridges is conducted alongside previous simulations involving a simple-cubic unit cell. Additionally, a physically based resistance model is introduced, delineating effective thermal conductivity as a function of the HybridBridge geometry and porosity. An equation for the HybridBridge radius, tailored to simulation parameters, is derived. Comparison with the unit cells and a randomly packed bed reveals an acceptable average deviation between the calculated and utilized radii, thereby streamlining and refining the implementation of the HybridBridge methodology.

Keywords: computational fluid dynamics; contact points; packed bed; effective thermal conductivity; mesh generation; heat transfer

Citation: Szambien, D.F.; Ziegler, M.R.; Ulrich, C.; Scharf, R. Analysis of a Novel Method for Generating 3D Mesh at Contact Points in Packed Beds. *Computation* **2024**, *12*, 89. https://doi.org/10.3390/computation12050089

Academic Editors: Ali Cemal Benim, Abdulmajeed A. Mohamad, Sang-Ho Suh, Rachid Bennacer, Paweł Oclon and Jan Taler

Received: 25 March 2024
Revised: 26 April 2024
Accepted: 28 April 2024
Published: 30 April 2024

1. Introduction

The versatility of packed beds in the energy and process industries knows virtually no bounds. Their remarkable ratio of surface area to volume renders them indispensable in myriad applications, serving as separators or as chemical reactors across diverse designs, as illustrated in [1]. Simultaneously, packed beds play pivotal roles in thermodynamic processes such as the cooling of cement clinker or in drying processes, for example within the natural gas storage.

Spanning from powder beds hosting dust-sized particles to pebble beds with pronounced boundary effects, their size distribution encompasses a broad spectrum. From a process engineering perspective, precision in describing transport phenomena within packed beds is paramount. Such precision facilitates the more accurate design of apparatuses and the optimization of existing processes. Consequently, packed beds have been subject to decades of intensive study employing experimental and analytical methods. With the burgeoning advancement in microelectronics, computer-aided techniques, particularly numerical simulations, have gained prominence in recent years.

These simulations offer a distinct advantage in visualizing heat and mass transfer within packed beds and other complex geometries. They have the capacity to incorporate local variables that significantly influence transport processes. Various modelling approaches, each with differing levels of complexity, find applicability in this domain.

For instance, the categorization proposed by Tsotsas [2] offers a valuable means of differentiation. While not inherently tied to numerical methodologies, this classification

aids in achieving a more nuanced characterization. Tsotsas [2] delineates between homogeneous modelling and heterogeneous modelling. In homogeneous modelling, the fluid and solid phases are amalgamated, enabling the description of the packed bed solely through a characteristic transport parameter, such as the effective thermal conductivity k_{eff}. Conversely, heterogeneous modelling involves coupling the fluid phase of the packed bed to the solid phase through an additional coupling parameter. In the case of heat transfer, this coupling parameter is known as the heat transfer coefficient.

The heterogeneous methodologies mentioned above can further be categorized based on the level of geometry resolution. When particles are not explicitly modelled in their spatial arrangement, it is referred to as a porous media model. This approach can enhances modelling accuracy in comparison to homogeneous methods.

In contrast, heterogeneous particle-resolved simulations, such as those based on the finite volume method, aim to depict physical processes within packed beds with maximum fidelity. Nevertheless, generating the computational mesh for such simulations presents a significant challenge. This challenge stems from the contact points among particles themselves and between particles and the enclosing reactor walls. The nature of these points of contact can vary depending on the shapes and arrangements of the particles. In the simplest scenario, featuring a packed bed of monodisperse spherical particles with no consideration for particle elasticity, all contact points manifest as point contacts. Point contacts are characterised by infinitesimally small contact areas between the spheres.

In practical applications, meshing point contacts often lead to the creation of highly skewed cells, potentially triggering convergence issues. Alternatively, one may resort to utilizing very small cells to address this challenge. However, this approach inevitably inflates the number of cells within the model, consequently prolonging computation times.

In transient simulations, this extensive local refinement, coupled with adherence to the Courant–Friedrichs–Lewy condition—which mandates smaller predefined time steps for stability—further compounds the computation burden. This combination of factors can significantly escalate computation times.

To circumvent these challenges, a prevalent approach involves altering the spheres to eliminate point contact. When outlining the scientific consensus numerous approaches for consideration can be found. One group of methods, known for their simplicity in implementation, are the global methods, which modify the entire sphere. A widely employed technique, especially in earlier studies (e.g., [3–5]), involves reducing the sphere size, commonly referred to as the gaps method. In contrast, the overlaps method, introduced by Guardo et al. [6], involves enlarging the spheres to create overlaps. However, both these global methods have drawbacks, notably their potential to induce significant alterations in key parameters of packed beds, such as the porosity ε.

To address this limitation, local methods were developed, focusing on modifying spheres solely in the vicinity of the contact point. Two such methods are the bridges method introduced by Ookawara et al. [7] and the caps method proposed by Eppinger et al. [8]. In the bridges method, the spheres are connected to each other with bridges by enlarging the contact point. Conversely, the caps method, involves removing a portion of each sphere at the contact point, akin to cutting off a cap. These techniques are applicable not only to spherical particles but also to non-spherical ones. For instance, Eppinger and Wehinger [9] and Kutscherauer et al. [10] have extended the original caps method to accommodate diverse particle geometries.

With appropriate specifications, both of the local methods presented here are well-suited for the particle-resolved simulations of (spherical) packed beds. However, they share a common drawback in that they may not always accurately represent the effective thermal conductivity of the bed, or may do so only with significant additional effort.

In the caps method, the creation of an artificial fluid gap between contacting spheres may result in an underestimation of the thermal conductivity. Conversely, the bridges method tends to overestimate heat conduction. While this overestimation can be mitigated by introducing a third pseudophase as a bridge material, as demonstrated by

Dixon et al. [11] or Wehinger et al. [12], such an approach requires substantial additional implementation effort and is notably detached from physical reality.

To address these issues, alternative strategies have been proposed. For instance, one can utilize very small bridges in the bridges method, as explored in [13], or significantly reduce the gap size in the caps method, as demonstrated in [10]. However, it is important to note that these adjustments do not offer a systematic and universally applicable solution to the contact point problem.

Henceforth, Szambien et al. [14], introduced the so-called HybridBridge method in their previous work. This method ingeniously amalgamates the advantages of both the caps and bridges techniques, allowing the effective thermal conductivity of the packed bed to remain intact and providing a reliable contact point modification. Thus, whenever the effective thermal conductivity is dominated by the thermal conduction between the spheres, the HybridBridge method offers an advantage over conventional local methods.

The aim of this work is to explain the theory of the HybridBridge in more detail and to investigate the effect of the HybridBridge on the effective thermal conductivity when used for particle-particle contact points. In addition, an initial approximate a priori approach for the design of the HybridBridge's geometry is proposed.

2. Materials and Methods

2.1. Theoretical Context

In principle, the effective thermal conductivity K_x of flowed-through packed beds can be divided into two parts: one that depends on the Péclet number (in the case of heat transfer, the following applies: $Pe = Re\,Pr$) and a non-flow-through share dominated by the effective thermal conductivity of the non flown-through packed bed $k_{\mathrm{eff}} = f\left(k_{\mathrm{p}}, k_{\mathrm{f}}, \dots\right)$. For K_x, with x representing either axial or radial direction, the following applies [15,16]:

$$\frac{K_x}{k_{\mathrm{f}}} = \frac{k_{\mathrm{eff}}}{k_{\mathrm{f}}} + \frac{Pe_0}{C_x}. \tag{1}$$

In this equation

$$Pe_0 = w_0\,\rho_{\mathrm{f}}\,c_{p,\mathrm{f}}\,d_{\mathrm{p}}/k_{\mathrm{f}} \tag{2}$$

is the Péclet number of the empty tube and C_x is a specific constant.

When the influence of k_{eff} predominates, the contact points between particles can exert a significant impact on heat transfer. This scenario arises, for instance, when Pe_0 values are small, as indicated by Equation (1). Furthermore Aichlmayr and Kulacki [17], as well as Hsu et al. [18], stated that the influence of contact points may become important when the thermal conductivity of the particles k_{p} is substantially greater than that of the fluid k_{f}.

When conducting numerical investigations on a packed bed with a notable k_{eff} ensuring an accurate modeling of k_{eff} becomes imperative. The innovative new HybridBridge method has been introduced for this purpose. The rationale underlying the introduction of the HybridBridge is best illustrated by the following example:

In this scenario we compare the standard bridges method and the conventional caps method between two monosized particles with the radius r_{p}. Both modifications utilize identical radii ($r_{\mathrm{b}} = r_{\mathrm{c}}$). We use the predefined height of the cap h_{c} to calculate its radius:

$$r_{\mathrm{c}} = \sqrt{r_{\mathrm{p}}^2 - (r_{\mathrm{p}} - h_{\mathrm{c}})^2)}. \tag{3}$$

The radius r_{c} is selected to be sufficiently small to ensure that the flow in the context under consideration remains unaffected. The following assumption is made: the velocity within the fluid gap of the cap is set to exactly zero, as illustrated in [9]. Consequently, in this specific scenario, both methods give identical results for flow computations. However, when it comes to heat conduction between the particles, they exhibit notably divergent behaviour. While the bridges method tends to induce excessively high heat flows, the caps method tends to result in disproportionately low heat conduction.

As previously noted in the introduction, this issue can be avoided by the introduction of a pseudo phase as a bridge or by a reduction in the size of the bridge or cap. However, it is important to note that, due to the physical circumstances, the caps method can never provide a perfect representation of heat conduction. This limitation stems from the nature of surface contact.

As an alternative, it is possible to create a parallel arrangement of thermal resistances consisting of the high thermal conductivity k_p solid phase and the low thermal conductivity k_f stagnant fluid phase. This arrangement can effectively replicate the thermal resistance exhibited by the third pseudophase or that observed in real packed beds.

By adopting the simplest symmetrical geometry and appropriate phase assignment, the continuity of both phases can be seamlessly maintained without interruption. This concept aligns precisely with the HybridBridge methodology we have introduced: a solid centred cylinder encompassed by a concentric hollow fluid cylinder. Figure 1 illustrates a comparison between conventional methods and the new HybridBridge approach.

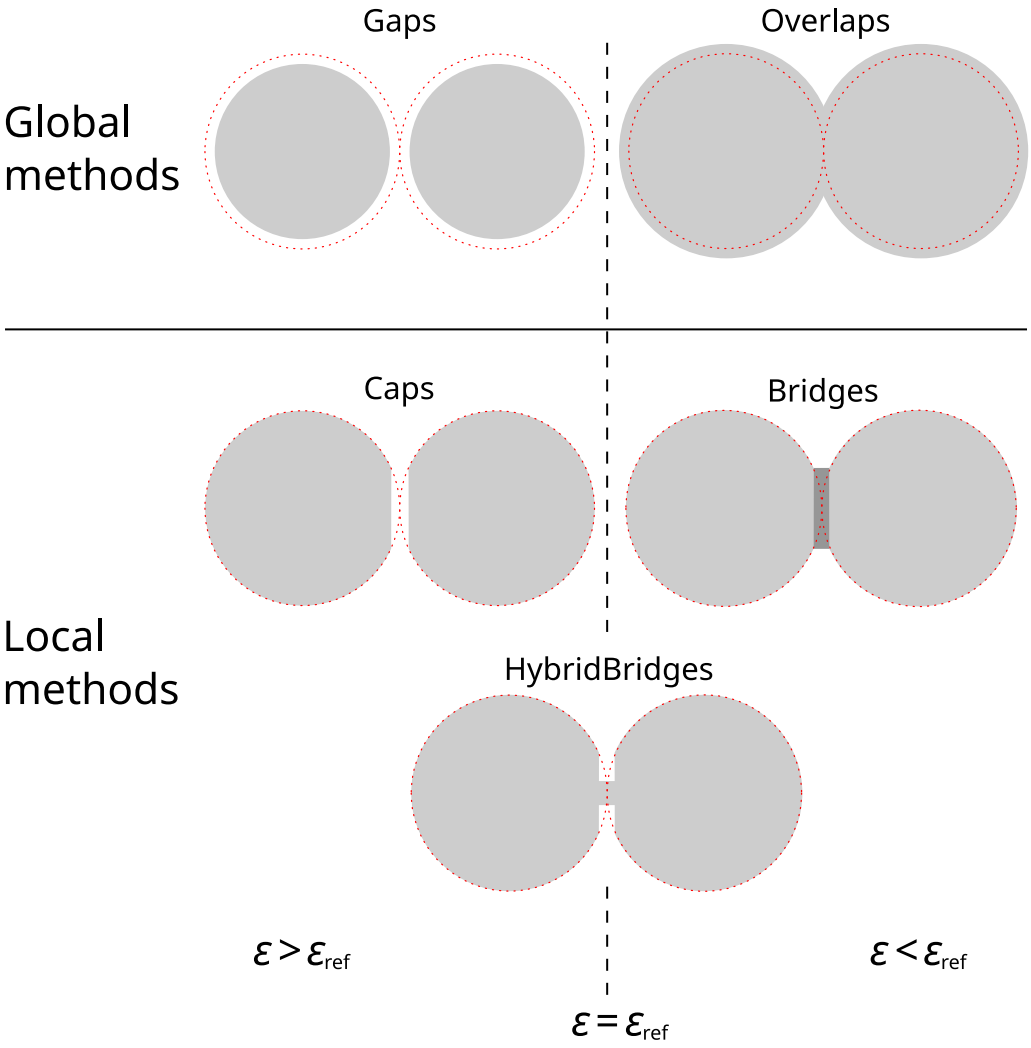

Figure 1. Comparison of conventional contact point modification methods with the novel HybridBridge method. The white areas represent the fluid phase, the different shades of grey represent the solid phases. The red circles represent the circumferences of the original spheres.

In our prior research [14], we have demonstrated the meshing advantages offered by the HybridBridge. Based on our assessments, the mesh quality closely aligns with that of conventional caps. Additionally, significantly larger cells can be employed, and a reduced number of cells suffices when compared to conventional bridges with an equivalent radius.

For fitting geometrical parameters, a replication of the effective thermal conductivity according to the Zehner–Bauer–Schlünder Model was achievable. Demonstration of real-world applicability of the Hybrid Bridge method has been successful.

The HybridBridge thus unites the advantages of both conventional methods: the meshing behavior of the caps method and the representation of thermal conductivity of the bridge method.

2.2. Geometrical Description

Unlike the conventional methods presented, HybridBridge contains two independent geometry parameters the height of the cap h_c and the radius of the bridge r_b, as shown in Figure 2. This dual-parameter setup enables control over two overarching properties of the packed bed. The initial objective is to ensure precise flow simulation by selecting an appropriate cap height h_c. Subsequently, achieving the desired effective thermal conductivity becomes feasible by selecting a suitable bridge radius r_b. Values for estimating the order of magnitude for h_c of the HybridBridge can be found in the literature [9,10] but must be adjusted to the individual packed bed and flow regime. An option to calculate the corresponding radius r_b will be introduced later in the paper (see Equation (16)).

Alternatively, adjustment of the effective thermal conductivity k_{eff} in combination with the porosity ε is also feasible. Herein lies a unique aspect of the HybridBridge method. Unlike conventional approaches, the HybridBridge method theoretically enables the preservation of the true porosity while modifying the contact points. Moreover, the alteration in porosity associated with the HybridBridge is consistently less pronounced compared to that of conventional caps of the equivalent height.

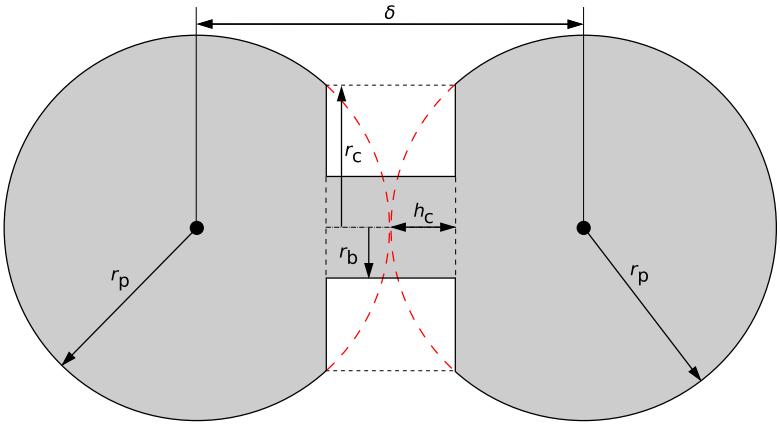

Figure 2. Schematic representation of the geometrical parameters of a HybridBridge between two monosized spheres. In order to provide a clearer overview, the HybridBridge is shown larger than it should be used in practice.

Furthermore, the HybridBridge can be regarded as a versatile local method for contact point modification. It inherently encompasses both the conventional bridges method (for $r_b = r_c$) as well as the conventional caps method (for $r_b = 0$) as special cases of the HybridBridge method. The simultaneous availability of both conventional methods represents a significant advantage when implementing the HybridBridge in a workflow for meshing a numerical model. At the same time, this versatility ensures, that the usage of the HybridBridge method is as least as advantageous as conventional methods for any packed beds.

2.3. Analysis of a Body-Centred Cubic Unit Cell

Szambien et al. [14] investigated how various parameters of HybridBridge geometry impact the effective thermal conductivity within a unit cell structured in a simple-cubic (sc) grid arrangement. Initial insights into how the HybridBridge geometry adapts to the

actual thermal conductivity k_{eff} of the scrutinized packed bed emerged from analyzing the results of this particular unit cell.

The simple-cubic lattice arrangement epitomizes the most basic unit cell. Moreover, heat conduction was assumed to occur in one direction only, running parallel to one of the main grid axis, traversing from midpoint to midpoint of the two spheres. Hence, within this unit cell, a solitary contact point enables the flow of heat. It is important to highlight that the assumption of one-dimensional heat conduction pertains exclusively to the modelling of effective thermal conductivity and the associated homogeneous perception of the packed bed. Within the numerical simulation model of unit cells, heat propagation is inherently three-dimensional. Consequently, it is deduced that heat flows occurring at interfaces perpendicular to the macroscopically imposed temperature gradient, as dictated by boundary conditions, are excluded.

The simple-cubic (sc) grid structure is characterized by a small number of contact points that affect heat conduction. Consequently, this unit cell tends to underestimate heat conduction compared to a realistically random packed bed. To address this discrepancy, in this work, we have carried out a numerical investigation of a unit cell featuring a body-centred-cubic (bcc) grid structure. In line with the aforementioned assumptions, this arrangement has a coordination number of 8 [19]. All eight contact points had to be modified with HybridBridge to ensure realistic heat conduction. No contact points were disregarded as irrelevant in this process.

To ensure a fair comparison with the simple-cubic grid, we adopted identical parameters for the simulation process. These simulation parameters are summarized in Table 1, while a qualitative representation can be observed in Figure 3. To generate the necessary .stl file we once more utilized our Python [20,21] tool in conjunction with Salome [22]. The numerical simulation was executed employing chtMultiRegionFoam within OpenFOAM (refer to [23,24]). The underlying mesh was generated using snappyHexMesh.

Table 1. Parameters of the unit cell with relevant initial and boundary values.

Specification			**Particle**	**Fluid**
Radius	in mm		10	—
Material			1.4301	dry air
k	in W/(m K)		15	0.026
Velocity	in m/s		—	0
Pressure	in Pa		—	101,300
Temperature	in K	internal field	273.15	273.15
		surface cold side	273.15	273.15
		surface hot side	283.15	283.15

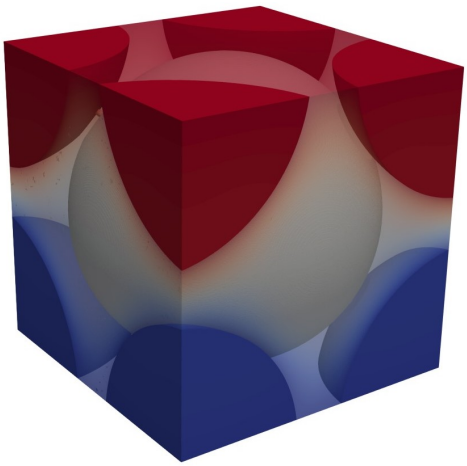

Figure 3. Body-centered-cubic unit cell with a qualitative temperature profile, red color indicates hotter temperatures and blue color indicates cooler temperatures.

2.4. Dimensioning of the HybridBridge

For achieving a high-quality multiphase particle-resolved numerical simulation of heat transport within packed beds, accurate modelling of heat conduction, as previously elucidated, is paramount. When applying the HybridBridge method for treating contact points, it becomes imperative to meticulously select the radius of the bridge r_b in relation to the height of the caps h_c. The effective thermal conductivity k_{eff} can be used to design the appropriate radius. To achieve this, the heterogeneous CFD model has to be homogenized. The homogenization of the model is based on Fourier's Law of thermal conduction:

$$\dot{q} = -k\,\mathrm{grad}(T). \tag{4}$$

This equation must give the same results as the heterogeneous CFD model.

To determine the appropriate bridge radius r_b, one must have knowledge of the target value for the effective thermal conductivity k_{eff}. This can be gleaned from a suitable model for the effective thermal conductivity, such as the model of Zehner, Bauer and Schlünder [25] or from experimental results.

This specification must be complemented with an understanding of how the geometry parameters of the HybridBridge influence the system. For this purpose, we conducted an extensive array of particle-resolved numerical simulations for unit cells (uc) both within the scope of this study and in our previous work [14].

Here, we computed the resulting values of the effective thermal conductivity of the unit cell, denoted as $k_{eff,uc}$ for various HybridBridges. From Equation (4), $k_{eff,uc}$ of the unit cell for a steady state is given by

$$k_{eff,uc} = \frac{\delta_{uc}\left(\dot{Q}_{Air,in} + \dot{Q}_{p,in}\right)}{A_{uc}\left(T_{hot} - T_{cold}\right)} = \frac{\delta_{uc}\left(\dot{Q}_{Air,out} + \dot{Q}_{p,out}\right)}{A_{uc}\left(T_{hot} - T_{cold}\right)}. \tag{5}$$

with the cross-sectional area $A_{uc} = (1.01 \cdot 2\,r_p)^2$ of the unit cell and their height $\delta_{uc} = 2\,r_p$. The heat flows $\dot{Q}$ are taken from the converged numerical simulations. Leveraging these unit cell results, we aim to derive an equation for the approximate estimation of the bridge radius.

3. Results

3.1. Assessment of the Body-Centred-Cubic Unit Cell

Figure 4 illustrates the effective thermal conductivity values, k_{eff}, derived utilizing Equation (5), alongside numerical simulation of the body-centered-cubic unit cell, incorporating various HybridBridge geometries. For comparison, the data corresponding to the simple-cubic unit cell, as presented in our earlier study [14], is provided in Figure 5. Both figures collectively demonstrate the HybridBridge's capacity to encompass a wide spectrum of effective thermal conductivities within numerical simulations.

Upon comparing the ratios of the effective thermal conductivities for the simple-cubic and body-centered-cubic unit cells, as illustrated in Figure 6, surprisingly it can be observed that the following approximation holds true:

$$\frac{k_{eff,bcc}}{k_{eff,sc}} \approx 2$$

Given that this observation holds across all examined HybridBridge geometries, it can be concluded that the HybridBridge exerts the most significant influence on the effective thermal conductivity k_{eff} in the conducted simulations. The factor of 2 can be explained by the number of HybridBridges per unit cell:

Starting with the simple-cubic unit cell, it is evident that the mean heat flux represented as $\dot{q}_m$ remains identical for two identical unit cells. This straightforward observation underscores that altering the surface area by linking several unit cells in parallel does not affect the mean heat flux.

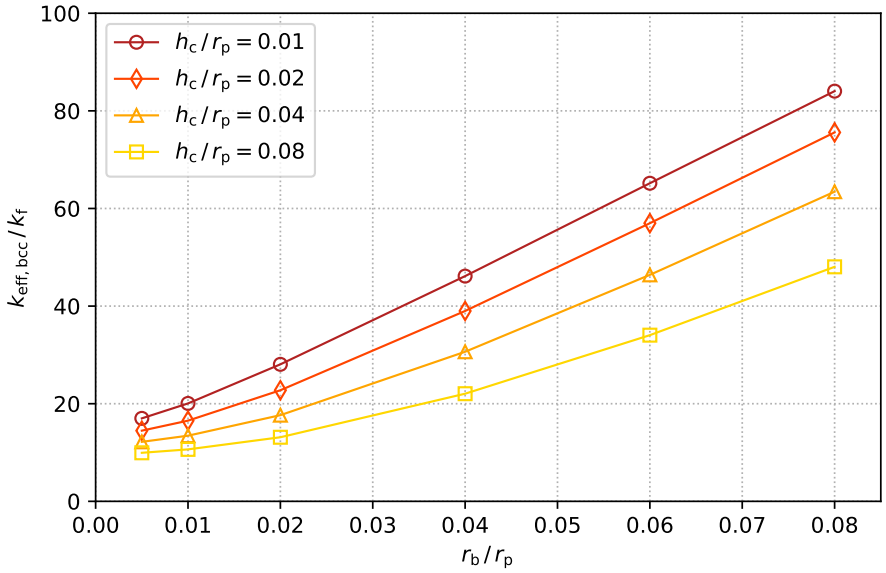

Figure 4. Effective thermal conductivity k_{eff} of the HybridBridge with various ratios of h_c/r_p for a body-centred-cubic arrangement of monodisperse spheres.

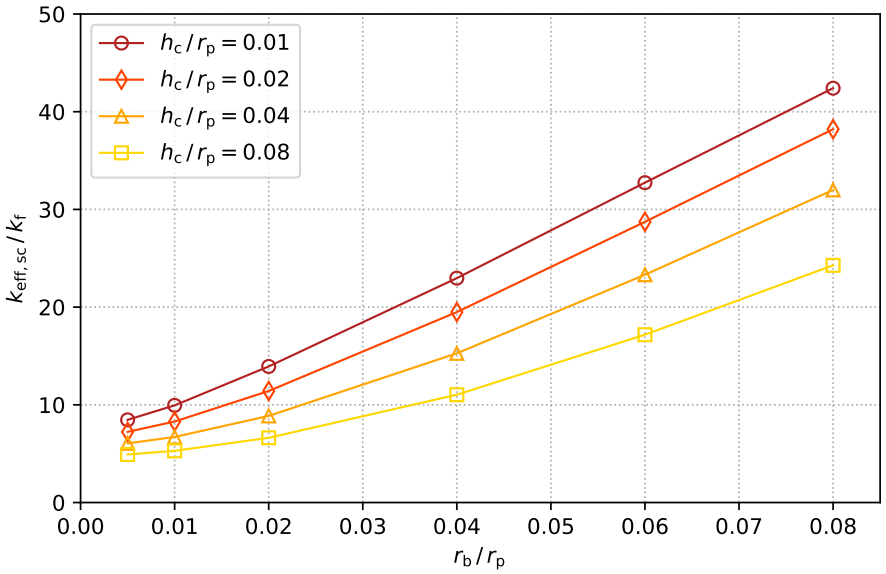

Figure 5. Effective thermal conductivity k_{eff} of the HybridBridge with various ratios of h_c/r_p for a simple-cubic arrangement of monodisperse spheres. Results taken from Szambien et al. [14].

A similar analysis applies to the sequential alignment along the main direction of heat flow of two unit cells. Due to symmetry considerations, the gradient remains identical for both unit cells, resulting in an identical total gradient along the two unit cells. Consequently, the heat flow or mean heat flux remains identical when these two unit cells are aligned under the appropriate boundary conditions. These considerations further justify the use of a unit cell.

Moreover, in addition Figure 6, examination of the temperature profile within the unit cell (refer to Figure 3) reveals that the HybridBridge, or its corresponding contact point, significantly influences the total heat flow. This dominance stems from the substantial disparity between the thermal conductivities of the phases and the notably high thermal resistance at the contact point compared to the particle interior.

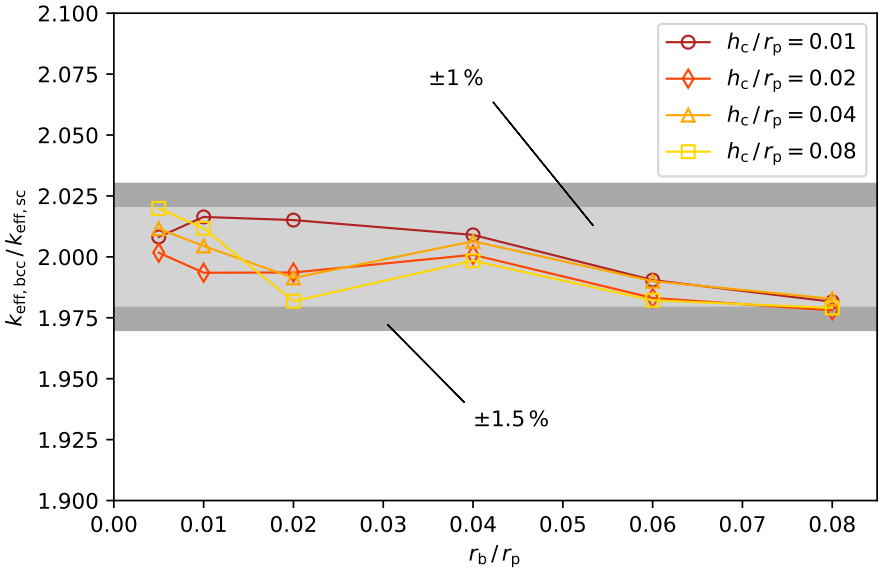

Figure 6. Ratios of the effective thermal conductivities k_{eff} for body-centred-cubic (bcc) grid structure to simple-cubic (sc) grid structure.

Considering all three factors, it becomes evident that $\dot{q}_{\mathrm{m}}$ is unaffected by changes in A or δ, but rather influenced by the number of HybridBridges per unit cell. It is crucial to differentiate whether the HybridBridges are arranged in parallel or in series with respect to the main direction of heat conduction. For clarification: A parallel connection describes the number of HybridBridges denoted as $n_{\mathrm{HB,A}}$, on a plane parallel to A, whereas a serial connection counts the number of such parallel planes, denoted as $n_{\mathrm{HB},\,\delta}$, aligned along δ.

A straightforward resistance analysis of the HybridBridge reveals that $\dot{q}_{\mathrm{m}}$ is directly proportional to $n_{\mathrm{HB,A}}$ and inversely proportional to $n_{\mathrm{HB},\,\delta}$. Likewise, considering Equation (4), k_{eff} is proportional to $n_{\mathrm{HB,A}}$ and inversely proportional to $n_{\mathrm{HB},\,\delta}$. Applying this analysis to the body-centred-cubic unit cell yields the following result:

$$k_{\mathrm{eff,bcc}} \approx \frac{n_{\mathrm{HB,A}}}{n_{\mathrm{HB},\,\delta}} k_{\mathrm{eff,sc}} \approx \frac{4}{2} k_{\mathrm{eff,sc}} \approx 2\,k_{\mathrm{eff,sc}}. \tag{6}$$

The subsequent relationship between $k_{\mathrm{eff,sc}}$ and k_{eff} can be generalized to encompass the utilization of HybridBridge in any packed bed. For illustration we can state the descriptive equation

$$k_{\mathrm{eff}} \approx k_{\mathrm{eff,sc}} \frac{n_{\mathrm{HB},A}}{A\,/\,A_{\mathrm{sc}}} \frac{\delta\,/\,\delta_{\mathrm{sc}}}{n_{\mathrm{HB},\delta}} \tag{7}$$

3.2. Predesign of the HybridBridge Geometry

As demonstrated earlier, the influence of the geometry of the HybridBridge on the effective thermal conductivity k_{eff} can be traced back to the results of the simple-cubic unit cell. Hence, we will formulate an approximate representation for $k_{\mathrm{eff,sc}}$ drawing upon the insights garnered from the simple-cubic unit cell results.

To address this objective, we have crafted a straightforward thermal resistance model that is as close as possible to the physical situation. This adaptable model can be fine-tuned to align with CFD findings by adjusting empirical parameters. The model is based on the following equation:

$$k_{\mathrm{eff,sc}} = \frac{\delta_{\mathrm{sc}}}{R_{sc}\,A_{\mathrm{sc}}}. \tag{8}$$

In this equation δ_{sc} and A_{sc} represent the dimensions of the simple-cubic unit cell, visually depicted in Figure 7. The equations governing the calculation of the total resistance R_{sc} are the following:

$$\frac{1}{R_{sc}} = \frac{1}{R_{HB} + R_{0,ser}} + \frac{1}{R_{0,par}} \tag{9}$$

$$\frac{1}{R_{HB}} = \frac{1}{R_b} + \frac{1}{R_c} \tag{10}$$

$$R_b = \frac{2\,h_c}{k_b\,A_b} \tag{11}$$

$$R_c = \frac{2\,h_c}{k_c\,A_c} \tag{12}$$

$$A_b = \pi\,r_b^2 \tag{13}$$

$$A_c = (\pi\,r_c^2) - A_b \tag{14}$$

The graphical representation of the resistance network is provided in Figure 7. The resistance $R_{0,ser}$ encompasses all the resistance connected in series with the HybridBridge, including those of the two hemispheres. The resistance $R_{0,par}$ amalgamates all resistances that are parallel to the HybridBridge, such as those pertaining to heat conduction through the fluid outside the generated cap region.

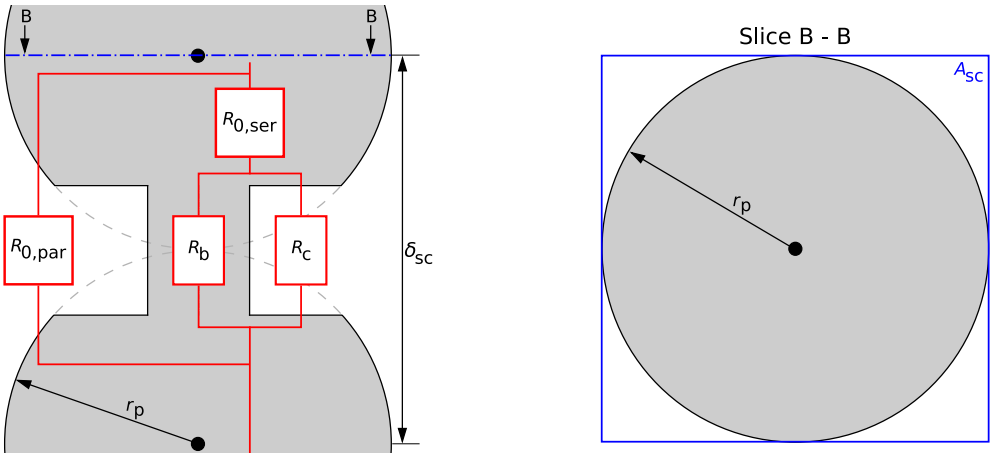

Figure 7. Schematic representation of the main dimensions of the simple-cubic unit cell with the proposed resistance network model. Analogous to Figure 2, the HybridBridge is shown larger than it should be used in practice.

$R_{0,par}$ and $R_{0,ser}$ are empirical values crucial for refining the accuracy of this simplified modelling approach. These values are determined through fitting the outcomes of the numerical model. For this purpose, h_c and r_b from the simulations performed (see Figure 5) were used in Equations (8)–(14) while adding missed fixed values from Table 1. The resulting relationship calculates values of k_{eff} for a given HybridBridge Geometry as a function of $R_{0,par}$ and $R_{0,ser}$. By calculating the deviation between values of k_{eff}, obtained using the procedure described, and the corresponding numerically computed values for

k_{eff}, the optimal values of $R_{0,\text{par}}$ and $R_{0,\text{ser}}$ were determined using the least squares method. The least squares method yields the following values:

$$\begin{aligned} R_{0,\text{par}} &= 550.00\,\frac{\text{K}}{\text{W}} \\ R_{0,\text{ser}} &= \ 46.64\,\frac{\text{K}}{\text{W}}. \end{aligned}$$

Based on the findings presented in from Section 3.1 it is plausible to interpolate between the two unit cells using the contact points. However, determining the precise locations of these contact points is not always feasible, or conducting an analysis of their positions in relation to the main heat conduction direction can be excessively time-consuming. Hence, porosity emerges as a viable criterion for interpolation, as it correlates with the number of contact points, evident from the coordination number. This relationship is expressed as follows:

$$k_{\text{eff}} = k_{\text{eff,sc}} \left(\frac{\varepsilon_{\text{sc}} - \varepsilon}{\varepsilon_{\text{sc}} - \varepsilon_{\text{bcc}}} + 1 \right) \tag{15}$$

The incorporation of the porosity of the simple-cubic unit cell $\varepsilon_{\text{sc}} = 0.476$ [19] and the porosity of the body-centered-cubic unit cell $\varepsilon_{\text{bcc}} = 0.320$ [19] yields the following for $0.320 \leq \varepsilon \leq 0.476$.

$$k_{\text{eff}} = k_{\text{eff,sc}} \left(\frac{0.476 - \varepsilon}{0.156} + 1 \right).$$

Now, we aim to derive a functional relationship using Equations (8)–(15) to approximate the radius of the HybridBridge for a given packed bed (ε and k_{eff} given) and a selected cap radius.

To maintain the function's complexity within manageable bounds, all predefined values for the examined unit cells from Table 1 have already been set and roughly consolidated, except those required for a dimensionless context. The transformations are partially based on [26]. The equation is presented below:

$$r_{\text{b}} = r_{\text{p}} \left(\frac{0.00174\, h_{\text{c}}/r_{\text{p}} \ \cdot \ \beta}{\varepsilon + 0.00356\, k_{\text{eff}}/k_{\text{f}} - 0.632} \right)^{\frac{1}{2}} \tag{16}$$

with

$$\beta = \left[h_{\text{c}}/r_{\text{p}} \left(\varepsilon + 0.00356\, k_{\text{eff}}/k_{\text{f}} - 0.632 \right) - 6.10\, \varepsilon - 0.194\, k_{\text{eff}}/k_{\text{f}} + 3.85 \right].$$

To validate this equation, simulation results for both unit cells were used. The calculated bridge radius was compared with the radius used in the underlying CFD model. For $r_{\text{b}}/r_{\text{p}} \geq 0.01$, the average deviation is about 7%. Notably, the deviation increases significantly for $r_{\text{b}}/r_{\text{p}} = 0.005$. Across all simulation runs, including $r_{\text{b}}/r_{\text{p}} = 0.005$, the average deviation between the calculated and utilized radii is slightly below 20%.

For a real packed bed with $r_{\text{b}}/r_{\text{p}} = 0.02$, investigated in [14], the equation yielded $r_{\text{b}}/r_{\text{p}} = 0.01653$ for the relative bridge radius. This results in a deviation of 17.3%. To ascertain porosity, we employed our MATLAB [27] tool, capable of numerically computing porosity for geometrically defined beds, both in general and with local resolution in the axial and radial directions. The porosity of the examined packed bed was determined to be $\varepsilon = 0.402$.

Accounting for all eventualities with a single equation is impractical due to the multitude of variables influencing the effective thermal conductivity k_{eff}. Models such as that proposed by Zehner, Bauer and Schlünder (e.g., [25]), illustrate the complexity inherent in this problem. Moreover, the wide variety of geometries and material combinations found in packed beds further complicate the issue.

The objective of Equation (16) is not to describe the effective thermal conductivity k_{eff} with a single equation, but to offer a method for implementing the new HybridBridge

method in a more focused manner. Consequently, the formal validation of this equation is restricted to the packed bed parameters outlined in this work. The generalizability of Equation (16) cannot be reliably estimated due to the inherent variability in such systems. However, it is essential to note that this limitation is specific for Equation (16) alone. Regarding the resistance model in general, there is no evidence to suggest that it cannot be used to predesign the HybridBridge with other packed bed parameters.

Users are encouraged to test Equation (16) for their specific applications. Should the attained accuracy fail to meet the specified requirements, it is advisable to derive a more suitable empirical equation from our proposed resistance model, following the structure of Equation (16). This iterative process allows for refinement tailored to the intricacies of individual applications, ensuring optimal performance.

4. Discussion

The new HybridBridge method, introduced in [14], has undergone a thorough analysis. This method aims to address the contact point problem, ensuring that the effective thermal conductivity remains consistent with physical specifications while minimizing the impact of particle modifications on flow dynamics.

The theoretical framework demonstrates the potential advantages of the HybridBridge method over other local techniques, particularly evident for small Péclet numbers and significant ratios of particle thermal conductivity to fluid thermal conductivity $\left(k_\mathrm{p}/k_\mathrm{f}\right)$. Furthermore, we have established the plausibility that the HybridBridge method typically induces a lesser alteration in porosity compared to conventional caps methods. In our previous work [14] we have illustrated that larger cells and thus a smaller number of cells using the HybridBridge method is sufficient to achieve comparable mesh quality to the conventional bridges method. This underscores the HybridBridge's reliability in addressing the contact point problem across a broader range of scenarios than traditional methods could offer.

The comprehensive geometrical description highlights that the HybridBridge method inherently encompasses both the conventional bridges and caps methods as special cases. This simplifies its integration into workflow, as several local methods become available through the adoption of the HybridBridge approach.

Through an analysis of the body-centered-cubic unit cell, we have rectified a limitation in our prior work, where the porosity, and consequently the coordination number, was lower than observed in many real cases of randomly packed beds. We have specified how the HybridBridge can be adapted to physical reality using a homogenization approach and experimental values or models for the effective thermal conductivity k_eff.

Given that the HybridBridge method involves two independent geometric parameters and aims for a more accurate representation of the effective thermal conductivity, k_eff, the implementation effort required is greater compared to conventional methods. The primary challenge lies in the difficulty of designing the appropriate bridge radius for the given effective thermal conductivity and cap height prior to simulation.

Through a comprehensive assessment of our recent simulations involving both the body-centered-cubic and simple-cubic unit cells, we have outlined an initial methodology for the a priori design of the HybridBridge, intended for numerical simulations. This involved the development of a semi-empirical resistance model tailored to the effective thermal conductivity of the simple-cubic unit cell. Subsequently, we extended the applicability of this model to other packed beds by leveraging insights from the body-centered-cubic unit cell, employing interpolation techniques across varying porosities and their corresponding coordination numbers.

Building upon this model approach, we derived an equation to approximate the bridge radius. To validate the accuracy of this equation, we compared the calculated radius against the radius employed in unit cells and a previously examined randomly packed bed. The mean deviation was found to be less than 20%, which is deemed satisfactory for the model's intended purpose.

It is crucial to note that while this equation provides a valuable tool for estimating the bridge radius, it cannot be directly applied to other packed beds without adjustments and validation to the specific parameters of each individual bed under investigation. However, the underlying resistance network model approach remains unaffected and is applicable to other packed beds.

A potential avenue for future research is suggested: building upon the investigation into the impact of diverse lattice arrangements, coordination numbers, and porosities, it would be beneficial to extend the study to encompass various material combinations. In addition, the HybridBridge method should be extended to other forms of contact. This expanded scope will facilitate a deeper understanding of the possibilities and hurdles associated with the innovative HybridBridge method of contact point modification, enabling a more nuanced and targeted application of the HybridBridge approach.

Author Contributions: The authors have contributed to the work as follows: conceptualization, D.F.S., M.R.Z., C.U. and R.S.; methodology, D.F.S., M.R.Z., C.U. and R.S.; software, D.F.S., M.R.Z. and C.U.; validation, D.F.S.; formal analysis, D.F.S., M.R.Z. and R.S.; investigation, D.F.S., M.R.Z. and C.U.; resources, D.F.S., M.R.Z. and R.S.; data curation, D.F.S.; writing—original draft preparation, D.F.S. and M.R.Z.; writing—review and editing, D.F.S., M.R.Z. and R.S.; visualization, D.F.S. and M.R.Z.; supervision, R.S.; project administration, D.F.S.; funding acquisition, R.S. All authors have read and agreed to the published version of the manuscript.

Funding: Funded by the Deutsche Forschungsgemeinschaft (DFG, German Research Foundation)—INST 187/742-1 FUGG; INST 187/592-1 FUGG.

Data Availability Statement: The raw data supporting the conclusions of this article will be made available by the authors on request.

Conflicts of Interest: The authors declare no conflicts of interest. The funders had no role in the design of the study; in the collection, analyses, or interpretation of data; in the writing of the manuscript; or in the decision to publish the results.

Abbreviations

The following abbreviations are used in this manuscript:

b	bridge
bcc	body-centered-cubic
c	cap
CFL	Courant–Friedrichs–Lewy
eff	effective
f	fluid
g	gap
HB	HybridBridge
p	particle
par	parallel
uc	unit-cell
s	solid
sc	simple-cubic
ser	serial
x	radial or axial coordinate

References

1. Eigenberger, G.; Ruppel, W. Catalytic Fixed–Bed Reactors. In *Ullmann's Encyclopedia of Industrial Chemistry*; Wiley-VCH, Ed.; Wiley-VCH: Weinheim, Germany, 2012. [CrossRef]
2. Tsotsas, E. Über die Wärme- und Stoffübertragung in durchströmten Festbetten: Experimente, Modelle, Theorien. Habilitation Thesis, VDI-Verlag, Düsseldorf, Germany, 1990; pp. 7–16.
3. Dixon, A.G.; Nijemeisland, M. CFD as a Design Tool for Fixed-Bed Reactors. *Ind. Eng. Chem. Res.* **2001**, *40*, 5246–5254. [CrossRef]
4. Romkes, S.; Dautzenberg, F.; van den Bleek, C.; Calis, H. CFD modelling and experimental validation of particle-to-fluid mass and heat transfer in a packed bed at very low channel to particle diameter ratio. *Chem. Eng. J.* **2003**, *96*, 3–13. [CrossRef]

5. Bai, H.; Theuerkauf, J.; Gillis, P.A.; Witt, P.M. A Coupled DEM and CFD Simulation of Flow Field and Pressure Drop in Fixed Bed Reactor with Randomly Packed Catalyst Particles. *Ind. Eng. Chem. Res.* **2009**, *48*, 4060–4074. [CrossRef]
6. Guardo, A.; Coussirat, M.; Larrayoz, M.A.; Recasens, F.; Egusquiza, E. CFD Flow and Heat Transfer in Nonregular Packings for Fixed Bed Equipment Design. *Ind. Eng. Chem. Res.* **2004**, *43*, 7049–7056.+. [CrossRef]
7. Ookawara, S.; Kuroki, M.; Street, D.; Ogawaa, K. High-fidelity DEM-CFD modeling of packed bed reactors for process intensification. In Proceedings of the European Congress of Chemical Engineering (ECCE-6), Copenhagen, Denmark, 16–20 September 2007.
8. Eppinger, T.; Seidler, K.; Kraume, M. DEM-CFD simulations of fixed bed reactors with small tube to particle diameter ratios. *Chem. Eng. J.* **2011**, *166*, 324–331. [CrossRef]
9. Eppinger, T.; Wehinger, G.D. A Generalized Contact Modification for Fixed–Bed Reactor CFD Simulations. *Chem. Ing. Tech.* **2021**, *93*, 143–153. [CrossRef]
10. Kutscherauer, M.; Böcklein, S.; Mestl, G.; Turek, T.; Wehinger, G.D. An improved contact modification routine for a computationally efficient CFD simulation of packed beds. *Chem. Eng. J. Adv.* **2022**, *9*, 100197. [CrossRef]
11. Dixon, A.G.; Nijemeisland, M.; Stitt, E.H. Systematic mesh development for 3D CFD simulation of fixed beds: Contact points study. *Comput. Chem. Eng.* **2013**, *48*, 135–153. [CrossRef]
12. Wehinger, G.D.; Fütterer, C.; Kraume, M. Contact Modifications for CFD Simulations of Fixed-Bed Reactors: Cylindrical Particles. *Ind. Eng. Chem. Res.* **2017**, *56*, 87–99. [CrossRef]
13. Bu, S.; Wang, J.; Sun, W.; Ma, Z.; Zhang, L.; Pan, L. Numerical and experimental study of stagnant effective thermal conductivity of a graphite pebble bed with high solid to fluid thermal conductivity ratios. *Appl. Therm. Eng.* **2020**, *164*, 114511. [CrossRef]
14. Szambien, D.F.; Ulrich, C.; Ziegler, M.R.; Maaß, N.P.; Scharf, R. A Novel Method for Generating 3D Mesh at Contact Points in Packed Beds. In Proceedings of the 14. International Conference on Computational Heat and Mass Transfer (ICCHMT2023), Düsseldorf, Germany, 4–8 September 2023.
15. Yagi, S.; Kunii, D. Studies on effective thermal conductivities in packed beds. *AIChE J.* **1957**, *3*, 373–381. [CrossRef]
16. Tsotsas, E. M7 Wärmeleitung und Dispersion in durchströmten Schüttungen. In *VDI-Wärmeatlas*; Stephan, P., Kabelac, S., Kind, M., Mewes, D., Schaber, K., Wetzel, T., Eds.; Springer Vieweg: Berlin/Heidelberg, Germany, 2019; pp. 1753–1772. [CrossRef]
17. Aichlmayr, H.T.; Kulacki, F.A. The Effective Thermal Conductivity of Saturated Porous Media. *Adv. Heat Transf.* **2006**, *39*, 377–460. [CrossRef]
18. Hsu, C.T.; Cheng, P.; Wong, K.W. Modified Zehner-Schlunder models for stagnant thermal conductivity of porous media. *Int. J. Heat Mass Transf.* **1994**, *37*, 2751–2759. [CrossRef]
19. von Seckendorff, J.; Hinrichsen, O. Review on the structure of random packed-beds. *Can. J. Chem. Eng.* **2021**, *99*, S703–S733. [CrossRef]
20. van Rossum, G. *Python Reference Manual: Report CS-R9525*; Centrum Wiskunde & Informatica: Amsterdam, The Netherlands, 1995.
21. Anaconda, Inc. *Anaconda Individual Edition 2021.05*; Anaconda, Inc.: Austin, TX, USA, 2021.
22. Open CASCADE. *Salome: The Open Source Platform for Numerical Simulation. SALOME Version 9.10.0*; Open CASCADE: Issy-Les-Moulineaux, France, 2023.
23. Greenshields, C. *OpenFOAM v9 User Guide*; The OpenFOAM Foundation: London, UK, 2021.
24. Weller, H.G.; Tabor, G.; Jasak, H.; Fureby, C. A tensorial approach to computational continuum mechanics using object-oriented techniques. *Comput. Phys.* **1998**, *12*, 620–631. [CrossRef]
25. Tsotsas, E. M11 Wärmeleitfähigkeit von Schüttschichten. In *VDI-Wärmeatlas*; Stephan, P., Kabelac, S., Kind, M., Mewes, D., Schaber, K., Wetzel, T., Eds.; Springer Vieweg: Berlin/Heidelberg, Germany, 2019; pp. 1831–1843._30. [CrossRef]
26. Wolfram Alpha LLC. *Wolfram|Alpha*; Wolfram Research, Inc.: Champaign, IL, USA, 2024.
27. The MathWorks Inc. *MATLAB Version: 9.9.0. (R2020b)*; MathWorks Inc.: Natick, MA, USA, 2020.

computation

MDPI

Article

Numerical Estimation of Nonlinear Thermal Conductivity of SAE 1020 Steel

Ariel Flores Monteiro de Oliveira [1], Elisan dos Santos Magalhães [1,*], Kahl Dick Zilnyk [1], Philippe Le Masson [2] and Ernandes José Gonçalves do Nascimento [1]

[1] Instituto Tecnológico de Aeronáutica—ITA, São José dos Campos 12228-900, Brazil; arielafmo@ita.br (A.F.M.d.O.); zilnyk@ita.br (K.D.Z.); ernandes@ita.br (E.J.G.d.N.)
[2] IRDL, Université de Bretagne-Sud—UBS, CNRS 6027, Rue de Saint Maudé, 56100 Lorient, France; philippe.le-masson@univ-ubs.fr
* Correspondence: elisan@ita.br

Abstract: Thermally characterizing high-thermal conductivity materials is challenging, especially considering high temperatures. However, the modeling of heat transfer processes requires specific material information. The present study addresses an inverse approach to estimate the thermal conductivity of SAE 1020 relative to temperature during an autogenous LASER Beam Welding (LBW) experiment. The temperature profile during LBW is computed with the aid of an in-house CUDA-C algorithm. Here, the governing three-dimensional heat diffusion equation is discretized through the Finite Volume Method (FVM) and solved using the Successive Over-Relaxation (SOR) parallelized iterative solver. With temperature information, one may employ a minimization procedure to assess thermal properties or process parameters. In this work, the Quadrilateral Optimization Method (QOM) is applied to perform estimations because it allows for the simultaneous optimization of variables with no quantity restriction and renders the assessment of parameters in unsteady states valid, thereby preventing the requirement for steady-state experiments. We extended QOM's prior applicability to account for more parameters concurrently. In Case I, the optimization of the three parameters that compose the second-degree polynomial function model of thermal conductivity is performed. In Case II, the heat distribution model's gross heat rate (Ω) is also estimated in addition to the previous parameters. Ω [W] quantifies the power the sample receives and is related to the process's efficiency. The method's suitability for estimating the parameters was confirmed by investigating the reduced sensitivity coefficients, while the method's stability was corroborated by performing the estimates with noisy data. There is a good agreement between the reference and estimated values. Hence, this study introduces a proper methodology for estimating a temperature-dependent thermal property and an LBW parameter. As the performance of the present algorithm is increased using parallel computation, a pondered solution between estimation reliability and computational cost is achieved.

Keywords: inverse heat conduction problem (IHCP); numerical estimation; thermal conductivity; quadrilateral optimization method (QOM); simultaneous assessment; GPU processing; CUDA-C

Citation: de Oliveira, A.F.M.; Magalhães, E.d.S.; Zilnyk, K.D.; Le Masson, P.; Nascimento, E.J.G.d. Numerical Estimation of Nonlinear Thermal Conductivity of SAE 1020 Steel. *Computation* **2024**, *12*, 92. https://doi.org/10.3390/computation12050092

Academic Editors: Ali Cemal Benim, Abdulmajeed A. Mohamad, Sang-Ho Suh, Rachid Bennacer, Paweł Oclon and Jan Taler

Received: 26 March 2024
Revised: 24 April 2024
Accepted: 1 May 2024
Published: 4 May 2024

1. Introduction

Mathematical modeling is an essential tool for enhancing industrial processes, both for process control and product quality. Modeling heat transfer processes requires knowledge of the process parameters, the environmental attributes to define the boundary conditions, and the material characteristics, such as size, to define the domain and the thermophysical properties to adequately describe the heat transfer. In addition, the use of temperature-dependent properties substantially influences the validity of the simulation outcomes [1]. However, the materials properties are dictated by their chemical composition and the spatial arrangement of their components. Thus, such properties usually oscillate, given small

differences in composition [2]. This fact hinders cataloging the properties of all materials, as new ones are being developed at different materials engineering branches [3–7].

There are direct approaches for attaining thermophysical properties. Besides consulting data series such as the Thermophysical Properties of Matter (TPRC), one may also measure such properties experimentally. Some thermal characterization methods consist of the guarded hot plate (GHP) [8,9], the LASER flash method [10,11], and the comparative fluxmetric method (CFM) [12]. However, precise material characterization usually involves large amounts of unknown parameters, which may vary with the temperature gradient. Also, the literature regarding low-temperature range and low-thermal conductivity materials is vast, but most approaches entail materials in the solid state. Indeed, there is a gap regarding metals at high temperatures, i.e., temperatures close to the melting point, because the data acquirement may be hampered due to the interactions between the specimen and its container, for example [13].

Then, inverse approaches are being extensively used to fill such a gap in obtaining the data on thermophysical properties. In this case, the inverse heat transfer problems (IHTPs) are applied to estimate unknown parameters of the thermal process, given temperature data inside or on the surface of the domain. The temperature information may be retrieved from numerical experiments, which determine the temperature based on a mathematical model, or from laboratory experiments, which usually focus on measuring the temperature field in specific points of a thermally excited sample [14,15]. Several areas of thermal engineering benefit from the inverse technique. For example, one may cite the estimation of the thermal conductivity of polymeric materials [16], the attainment of the unknown functional form of a time-dependent heat transfer coefficient [17], and the estimation of the thermal conductivity and volumetric heat capacity of living tissue using a recent noninvasive measurement method [18]. In addition, there are IHTP applications in food science and engineering for assessing process parameters, for example, the energy consumption during baking [19] or temperature-dependent food properties such as moisture diffusivity [20].

Besides the previous examples regarding the attainment of parameters from experimental or numerical temperatures, several different methods exist to optimize the parameters of interest. In [21], the authors acquired the numerical temperature of a metal sample interacting with a LASER pulse through the commercial software ANSYS Fluent ®. After validating the model with laboratory experiments, the authors applied the Levenberg–Marquardt (LM) technique to optimize four LASER pulse parameters: the power of the LASER pulse, the dimensionless shape parameter of the heat source distribution, and the beginning and end times of its interaction with the sample. The inverse algorithm was implemented by applying GNU Octave and ANSYS Fluent software packages. Another approach is to combine artificial intelligence with inverse heat conduction problems. In [22], the authors propose a proportional-integral-derivative (PID) inverse algorithm to perform the real-time estimation of the boundary heat flux in an unsteady heat conduction problem. To address the lack of adaptive ability of the latter method, the authors introduce the single neural adaptive PID (SNA-PID) [23]. Such a method is capable of adaptively adjusting the weights of the PID parameters and is more robust regarding signal interferences than the classical PID method. Both AI approaches comprise inverse the estimate of boundary heat flux involved in a numerical experiment governed by a one-dimensional transient heat diffusion equation, given the numerical data computed at a single position. Bayesian techniques, namely Gauss–Newton minimization regarding the maximum a posteriori objective function and the Markov chain Monte Carlo method application in the simultaneous assessment of the thermal diffusivity and thermal conductivity of a metallic sample were proved to be accurate [13]. Herein, the experimental setting based on the front-face flash method with contactless transient flux measurements of thermally excited metallic samples was modeled. The forward problem was solved through the Finite Element Method (FEM) with the aid of COMSOL Multiphysics® 4.3b, while the inverse problem analytical solution was implemented using MATLAB®. The Broydon–Fletcher–Goldfarb–Shanno (BFGS) technique consists of the minimization of an error square function,

given the difference between the numerical and experimental temperatures. The latter approach could be successfully applied to attain the thermal profile from the estimated heat rate during Gas Tungsten Arc Welding (GTAW) [24]. Afterward, the methodology was applied to determine the cooling rate at the Fused Zone (FZ), Heat-Affected Zone (HAZ), and Base Metal (BM). The authors implemented the direct and inverse models in an authorial C++ software [25].

The main limitation of the previously reviewed works lies in properly optimizing the solution of inverse heat transfer problems by driving the forward model through an efficient optimization tool. Therefore, the present study showcases the application of a methodology developed to estimate a temperature-dependent thermal property by carefully balancing the solution between estimation reliability and computational cost, thereby addressing the gap in the literature. The applied multivariable optimization technique is the Quadrilateral Optimization Method (QOM) previously proposed by Magalhães [26], which enables the estimation of temperature-dependent thermal properties described by math functions. This inverse method was specifically developed to determine material thermal properties at elevated temperatures. A key advantage of the QOM is its ability to estimate parameters in unsteady states, eliminating the need for steady-state experiments. In the present work, the QOM functionality was extended to enable the simultaneous estimation of a higher number of parameters. The extension also allows for estimating different quantities other than thermal properties.

In this work, the QOM is applied to acquire the nonlinear thermal conductivity of an SAE 1020 sample and the heat input provided by the LASER during a LASER Beam Welding (LBW) process. The solution to the forward problem described in Section 2.1 is achieved using an in-house CUDA-C algorithm to attain the reference temperature evolution during 2.0 s of experiment. Here, the three-dimensional heat diffusion equation is discretized through the Finite Volume Method (FVM), and the thermal conductivity function used to model the property evolution with temperature presents a second-degree polynomial form. With possession of the temperature data, the QOM is applied to minimize an objective function, considering different combinations of the parameters of interest. Two cases are studied. In Case I, we optimize the three parameters that compose the thermal conductivity function. In Case II, we optimize the gross heat rate provided by the LASER, along with the thermal conductivity. Implementing the method in a parallelized structure allows the computations to be performed at an acceptable time, reducing computational costs compared to those of sequential approaches. Further information about the inverse technique and details about its application in the estimation of thermal conductivity are given in Sections 2.2 and 2.3. Once the numerical data used as reference are noiseless, the study of the method's suitability for estimating the parameters given noisy data is delineated in Section 2.4. Section 3 describes the methods used in the sensitivity analysis and discusses the results of the reduced coefficients. The study of the sensitivity allows for the calibration of the number of time steps that regularize the objective function. Both accuracy and computational time are pondered to attain the optimal time steps. Such investigation is explained in Section 4. Afterward, we discuss in Section 5 the method's stability introduced in Section 2.4. After assuring the method is qualified to perform the estimations, the estimation results and the comparison between the numerical temperatures computed given reference and estimated parameters are presented in Section 6.

2. Materials and Methods

2.1. The Forward Model

The assessment of temperature-dependent thermal conductivity is an ill-posed inverse problem. In this instance, the baseline for the estimates is the temperature field during the LASER beam welding of steel SAE 1020. The nonlinear three-dimensional heat diffusion equation may describe the transient heat transfer during the process as follows:

$$\frac{\partial}{\partial x}\left(\lambda(T)\frac{\partial T}{\partial x}\right)+\frac{\partial}{\partial y}\left(\lambda(T)\frac{\partial T}{\partial y}\right)+\frac{\partial}{\partial z}\left(\lambda(T)\frac{\partial T}{\partial z}\right)+\dot{g}=\frac{\partial H(T)}{\partial t} \tag{1}$$

where x, y, and z are the cartesian coordinates, $\lambda(T)$ is the nonlinear thermal conductivity, T is the temperature, $\dot{g}$ is the generated heat source, H is the nonlinear enthalpy function, and t is the time. H is used to model the phase change and may be expressed as follows:

$$H = (1-f)\int_0^{T_m} \rho c_{p,s} dT + f\int_{T_m}^{T} \rho c_{p,l} dT + \rho f L \tag{2}$$

where f is the fraction of solid, defined by the Heaviside step function; T_m is the melting temperature; ρ is the specific mass; $c_{p,s}$ and $c_{p,l}$ are the nonlinear specific heat of the solid and liquid material, respectively; and L is the fusion latent heat.

The heat source assumes a Gaussian distribution above the sample surface. However, the barrier effect suffered by the LASER beam decreases the heat flux distribution as the penetration increases up to the coordinate h. In this case, the volumetric generated heat distribution ($\dot{g}$) may be written as follows:

$$\dot{g} = \frac{\Omega}{0.46hR^2} e^{-\frac{4.5(x-ut)^2}{R^2}} e^{-\frac{4.5(y-L/2)^2}{R^2}} \left(1 - \frac{z^{1/2}}{h^{1/2}}\right) \tag{3}$$

where Ω (=1000 W) is the gross heat rate; R (=0.50 mm) is the weld bead radius; u (=0.05 m/s) is the welding velocity; L (=40.00 mm) is the sample width (along the y-axis); and x, y, and z are the coordinates in the respective Cartesian axis. Such values are defined by calibrating the experimental configuration so the simulated and the experimentally observed weld bead geometry match [27].

The model considers boundary conditions of convection and radiation at the sample surfaces, described by the following:

$$-\lambda \frac{\partial T}{\partial n}\bigg|_U = h(T)(T - T_\infty) + \sigma\varepsilon(T)(T^4 - T_\infty^4) \tag{4}$$

where n is the normal direction on the domain boundaries, $h(T)$ is the convection heat transfer function, T_∞ (=20 °C) is the environment temperature, and σ is the Stefan–Boltzmann constant. The inferior surface of the specimen had its convection coefficient calculated through the empirical correlations of a heated inverted horizontal flat plate [28]. In the side surfaces, the correlation for a vertical flat plate was used [29]. Lastly, the free jet model for forced convection was applied to the top surface [29].

An in-house algorithm written in CUDA-C language solves Equation (1) by discretizing it through the Finite Volume Method (FVM) to achieve the temperature profile during LBW. The equation is applied over the domain depicted in Figure 1. The point P_0 (0,0,0) represents the origin of the domain. The heat source is pointed at P_1 (5,10,0) at the beginning of the experiment and moves 30 mm along the x-axis until point P_2 (35,10,0). The dotted lines stand for the sample centerline, which coincides with the joint centerline. In addition, the blue and red arrows are placed in the specimen's surfaces subjected to heat loss by natural and forced convection, sequentially, as specified after Equation (4). Here, the heat loss in the posterior surface is omitted for the sake of clarity.

As shown in Equations (1) and (4), the thermophysical properties of the material are required to compute the temperature of the sample. Such inputs are temperature-dependent and accounted for as temperature functions with specific behavior. Regarding SAE 1020, the reference thermal conductivity data represented by the blue dots Figure 2. were retrieved from Clain et al. [30]. They may be modeled as a second-degree polynomial function of temperature, depicted as the orange dashed line, which is mathematically represented as $\lambda(T) = 2.5 \times 10^{-5}T^2 - 5.3 \times 10^{-2}T + 57.2$. The maximum error between the reference information and the polynomial fitting is less than 4.5%, despite the outlier at circa 780 °C. Indeed, the steel presents an allotropic transformation near this temperature. In this model, the authors chose not to model such behavior with no prejudice toward the

predicted temperature field for the sake of algorithm simplification and computational time savings.

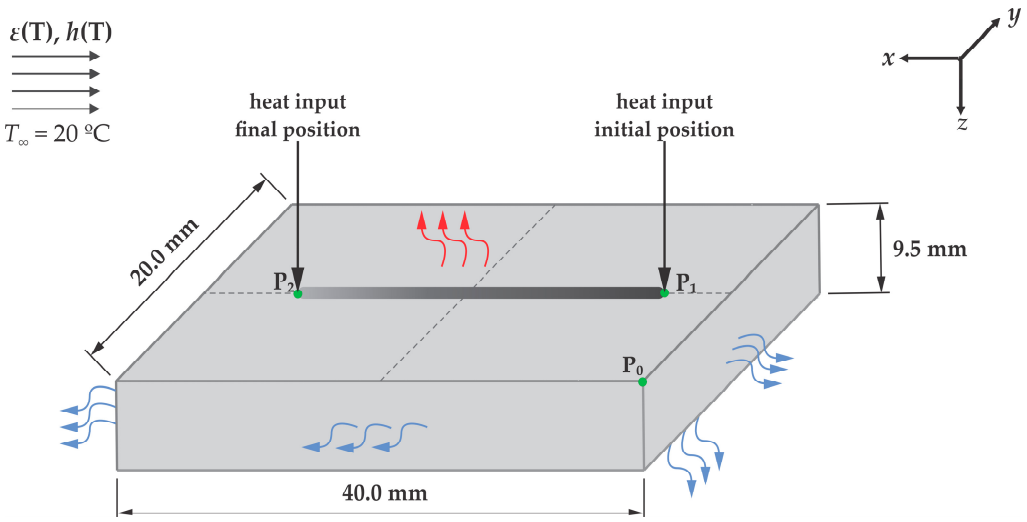

Figure 1. Three-dimensional scheme of the simulated LBW process.

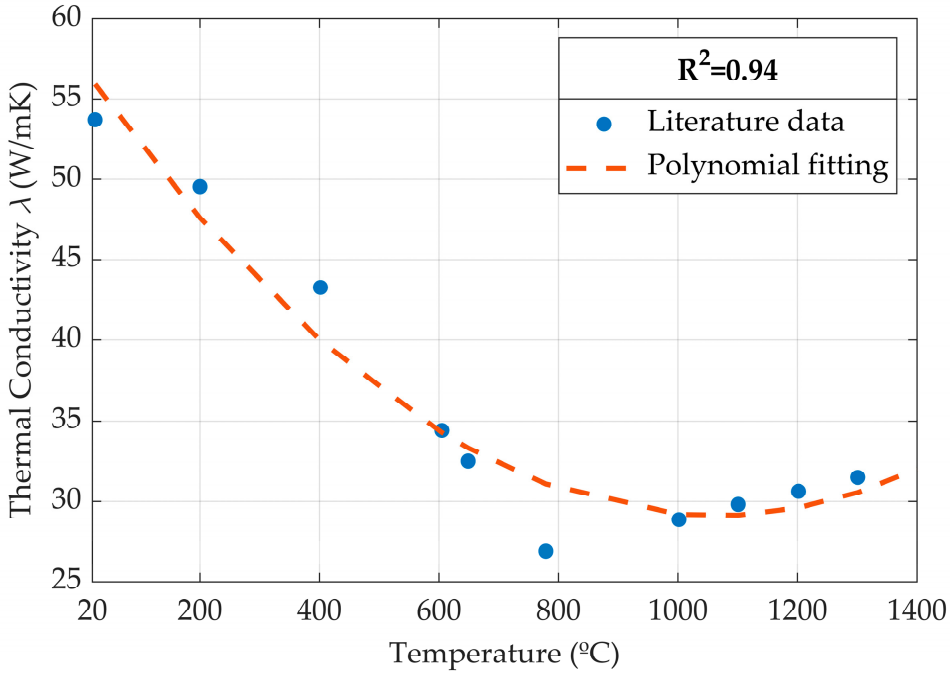

Figure 2. Polynomial fitting of the nonlinear thermal conductivity function for SAE 1020.

A uniform orthogonal structured mesh with 225,000 total nodes (100 × 50 × 45 nodes, at x, y, and z, respectively) was applied in the solution of the forward model. The Finite Volume Method (FVM) system of equations was solved using the Successive Over-Relaxation (SOR) parallelized iterative solver. An energy residual convergence criterion was applied to all cases, and the threshold was set to 1.0×10^{-5}. The applied simulation parameters are presented in Table 1.

Table 1. Simulation parameters.

Parameter	Values
Temporal discretization	First-order scheme
Time-step (Δt) [s]	1.0×10^{-3}
Solver convergence criterion	Energy residual
Residual threshold	1.0×10^{-5}

Solving the forward model through the in-house CUDA-C algorithm allows for the obtainment of the temperature profile shown in Figure 3. Each curve stands for the temperature evolution at a different point of the sample surface. The algorithm runs for an experiment period of 2.0 s, divided into 1.0 millisecond time steps. The thermocouples are placed at the same sample surface where the heat is applied (plane *xy*). The spots of temperature acquisition are exhibited in Table 2.

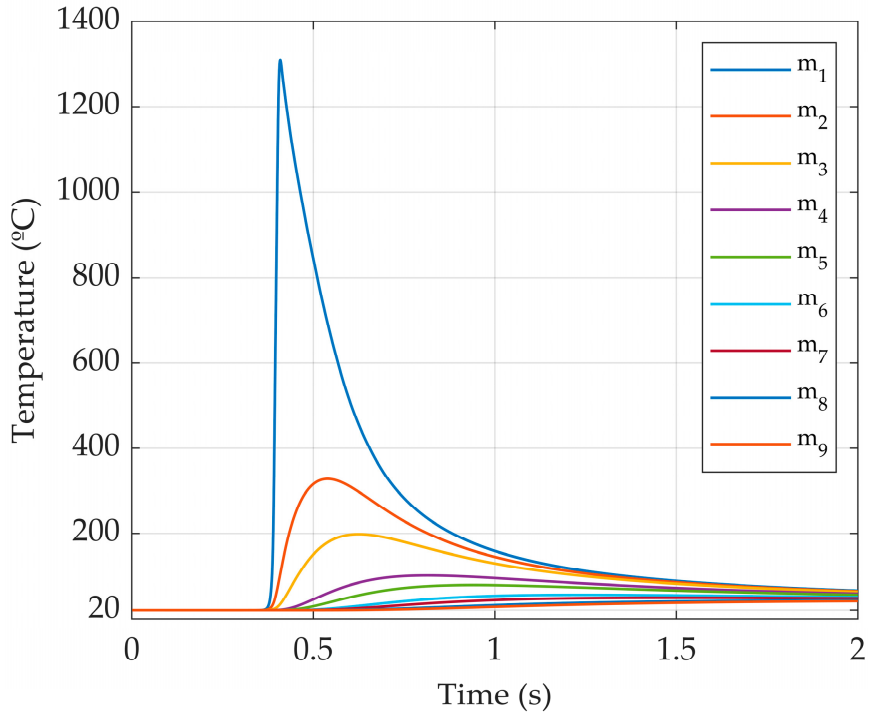

Figure 3. Temperature evolution with the time during the autogenous LBW of SAE 1020.

Table 2. Thermocouple positioning.

Sensor	m1	m2	m3	m4	m5	m6	m7	m8	m9
x (mm)	20.0	20.0	20.0	20.0	20.0	20.0	20.0	20.0	20.0
y (mm)	10.0	9.0	8.0	7.0	6.0	5.0	4.0	3.0	2.0
z (mm)	0	0	0	0	0	0	0	0	0

The forward model applied in this work underwent a rigorous verification process [31] to assess the quality of the resulting temperature fields. The verification steps involved investigations regarding the accuracy, computational performance, energy consumption, cost efficiency, and code memory optimization of the in-house CUDA-C code.

2.2. The Inverse Problem

The QOM developed by Magalhães [26] is an optimization method that allows for the assessment of more than one variable concurrently by minimizing an objective function (F) given by the sum of squares of the difference between the simulated (T') and reference

(T) temperatures. Moreover, F is minimized in a future time step rather than the present one to increase F sensitivity through the Future Time Regularization (FTR) [32]. This regularization technique expands the Function Specification Method developed by Beck et al. [33]. Thus, the regularized objective function may be described by the following:

$$F = \sum_{p=0}^{r} \sum_{m=1}^{N} (T'_{m,p} - T_{m,p})^2 \tag{5}$$

where r is the number of time steps adopted, p is related to the time step position, N is the total number of thermocouples, and m is the thermocouple number.

Here, T is the numerical temperature computed using reference values of the assessed parameters, and T' is the numerical temperature calculated using algorithm guesses, i.e., possible values of the parameters of interest. To define the values of each guess, the method divides a specified domain into 3^κ equally distributed points, where κ is the number of parameters being assessed. Such a domain is addressed as the search domain and comprises all the possible linear combinations between the parameters, being limited by the maximum and minimum values each estimated parameter may assume. Then, the objective function is evaluated for each guess. The closer the assessed parameters are to the reference values, the closer T' is to T, and, consequently, the objective function is lower. Therefore, the evaluation of F supports the definition of the pivot point G_p, being the guess that presents the minor objective function. A new set of 3^κ guesses is distributed around the pivot point, following pre-defined convergence criteria, which decreases the domain at each interaction. The convergence process continues until the maximum number of interactions is reached. All the calculations are performed in an in-house CUDA-C code. In this case, the QOM algorithm proceeding may be summarized as follows:

1. Initialize the number of variables (κ), convergence rate (τ), search domain bounds, maximum number of interactions, and number of time steps of the FTR;
2. First division: evaluate the search domain bounds to define the initial guess vector **G** of equally spaced guesses within the domain;
3. Settling the pivot point G_p: evaluate the objective function for each guess. The guess that presents the minimum F is defined as G_p;
4. Redistribution: evaluate τ and G_p to redefine **G** with guesses equally far from G_p.
5. Convergence: repeat steps 3 and 4 to decrease the domain at each interaction until the maximum number of interactions is reached.

The size of the initial domain division mentioned in step 2 may be determined for the general parameter ξ as follows:

$$\Delta\xi = \frac{\xi_1 - \xi_0}{4} \tag{6}$$

where the subscripts 0 and 1 represent the minimum and maximum value the parameter ξ may assume, i.e., the search domain bounds.

As previously stated, the subsequent divisions of the domain are related to the pivot point instead of the upper and lower bounds as described in Equation (6). for the first division. In this instance, the size of the domain division ($\Delta\xi$) decreases at each interaction by a factor c, given by the following:

$$c_j = \prod^{j} (1 - \tau)^{\kappa - 1} \tag{7}$$

where j is the counter for the interactions.

The convergence process continues until the maximum number of interactions is reached. At this point, the algorithm returns the combination of parameters of interest that present the lesser F, being the closest to the real values, as the difference between the temperature computed using such parameters (T') and the reference temperature (T) is the minimum. An algorithm scheme is presented in Figure 4 for illustrative purposes.

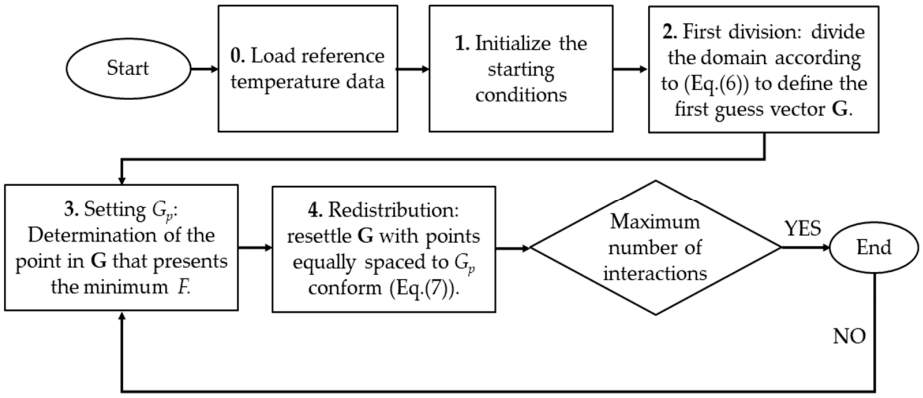

Figure 4. Schematized procedure for the QOM algorithm.

2.3. QOM Applied to the Thermal Conductivity Estimate

Initially, the Quadrilateral Optimization Method is applied to simultaneously define the coefficients of the nonlinear thermal conductivity function of SAE 1020 (Case I). Then, the gross heat rate Ω used in the calculus of the heat distribution described in Equation (3) is estimated along with the nonlinear thermal conductivity function (Case II). To estimate the thermal conductivity using the heat transfer model described in Section 2.1, it is necessary to define all the parameters of the function that describes the nonlinear thermal conductivity. The reference thermal conductivity for SAE 1020 portrayed in Figure 2 may be represented by Equation (8).

$$\lambda(T) = 2.5 \times 10^{-5} T^2 - 5.3 \times 10^{-2} T + 57.2 \tag{8}$$

Equation (9) shows the general form of $\lambda(T)$, where the coefficients of the second-degree polynomial function (α, β, and γ) are real numbers that vary according to the sample composition. Hence, for the steel SAE 1020, the goal values the method should find for Equation (9) parameters α, β, and γ are 2.5×10^{-5}, -5.3×10^{-2}, and 57.2, respectively.

$$\lambda(T) = \alpha T^2 - \beta T + \gamma \tag{9}$$

Moreover, the estimation of the gross heat rate (Ω) along with the thermal conductivity function parameters requires the expansion of the algorithm so it minimizes all parameters concurrently. Such a parameter is constant (=1000 W), with no need for a function to model its behavior. In such a condition, four variables must be minimized at the same time. Regarding Ω, the goal value of 1000 W is obtained by the calibration of the forward model once it corresponds to the heat absorbed by the sample, given in Watts. Table 3 shows the definition of the search domain for estimating the thermal conductivity function parameters and the gross heat rate and summarizes the reference values. Besides defining the search domain, the method requires the convergence rate and maximum number of interactions. This work adopts τ = 0.5 and 16 interactions.

Table 3. Conductivity function parameters and gross heat rate search domain.

Variable	Lower Bound	Upper Bound	Reference
α	2.0×10^{-5}	3.0×10^{-5}	2.5×10^{-5}
β	-6.0×10^{-2}	-5.0×10^{-2}	-5.3×10^{-2}
γ	40	80	57.2
Ω	500	1500	1000

In the search domain for Case I, the thermal conductivity function is within the three-dimensional plane defined by α, β, and γ, limited by the upper and lower bounds for each parameter. Hence, κ = 3, as there are three parameters of interest. For Case II, κ = 4 (α, β, γ, and Ω). For better clarification, we elucidate the search domain for Case I. In Figure 5,

the edges defined by α, β, and γ are represented in red, blue, and green, respectively. For instance, point A coordinates are (α_1, β_1, and γ_1), which correspond to (3.0×10^{-5}, -5.0×10^{-2}, 80), according to Table 3. The gray dotted lines show the initial division of the domain into 4^3 equal cuboids. The divisions within the domain are omitted for better delineation. The inner cuboids dimensions are calculated by Equation (6).

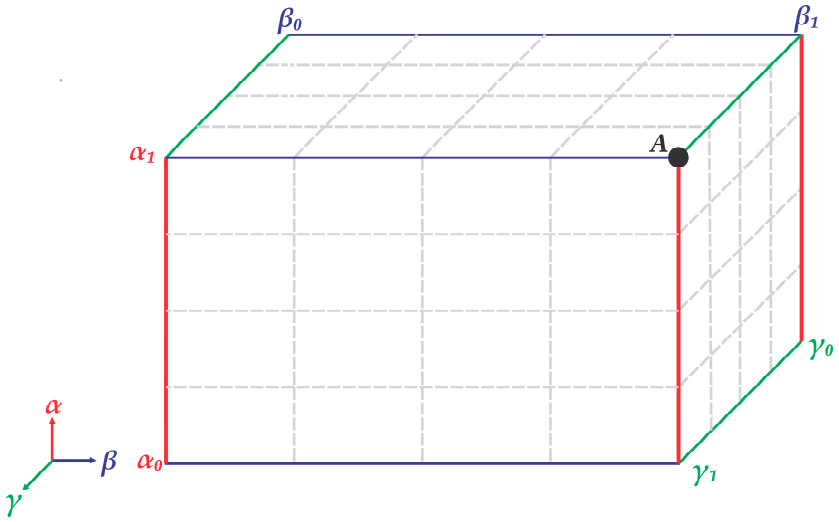

Figure 5. Three-dimensional search domain for the thermal conductivity function parameters.

The guess vector **G** is defined by the divisions of the search domain, which correspond to specific combinations of α, β, and γ. When estimating three variables, each **G** is composed of 27 guesses, defined by the coordinates of the inner vertexes of the domain division. When estimating four parameters, 81 guesses are needed to account for the linear combinations between the parameters.

2.4. Input Data with Added Noise

The theory of linear propagation of uncertainty was applied in this work to extend the investigation and address the capabilities of the QOM when the input data contains added uncertainties and noise. Applying the theory of linear propagation of uncertainty results in [26]

$$U^2 = U_{S'}^2 + U_T^2 + U_{QOM}^2 \tag{10}$$

where U is the global uncertainty, $U_{S'}$ is the uncertainty associated with experimental sensors, U_T is the numerical thermal model uncertainty, and U_{QOM} is the uncertainty related to the QOM approach. The $U_{S'}$ uncertainty term encompasses the temperature sensor positioning and the data acquisition system errors, as well as the thermal contact resistances involved in the measurements. The U_T uncertainty includes the FVM, the solver truncation, and the numerical (rounding) errors. The U_{QOM} term comprises the FTR uncertainty.

3. Sensitivity Analysis

In parameter estimation, it is necessary to investigate how expressive the parameter being assessed is for the calculated results. This investigation allows the verification of the method's suitability for estimating such a parameter. The output from the forward model presented in Section 2.1 is the temperature profile during autogenous LBW. In light of this, this work evaluates the significance of temperature variation given a disturbance in the parameters α, β, γ, and Ω by analyzing the evolution of the sensitivity coefficients with time. The sensitivity coefficients may be obtained through the partial derivative of the temperature with respect to a specified parameter [34]. However, the unknown parameters may differ regarding the units or magnitude order. Hence, in order to standardize the coefficients, the

reduced sensitivity coefficient (S) may be obtained by Equation (11), considering the assessment of the generic parameter X. In this instance, S is given in degrees Celsius.

$$S = X\frac{\partial T}{\partial X} \tag{11}$$

Equation (11) represents the effect of the parameter X over the temperature, considering the temperature is acquired in one location. However, the direct model computes the temperature in the nine spots introduced in Table 2. Such configuration may be accounted for by summing the coefficients for every sensor as follows:

$$Sn = \sum_{n=1}^{N} X\frac{\partial T}{\partial X} \tag{12}$$

where Sn is the sensitivity coefficient for N sensors, and N is the number of thermocouples. In this case, $N = 9$.

We consider the significance of the temperature variation, given a 1% deviation in the model parameters, obtained by the central derivative of Equation (12), described by Equation (13).

$$Sn = \sum_{n=1}^{N} X\frac{T\left(X + X \times 10^{-2}\right) - T\left(X - X \times 10^{-2}\right)}{2X \times 10^{-2}} \tag{13}$$

3.1. Sensitivity of the Thermal Conductivity Function Parameters (α, β, and γ)

The significance of the temperature variation given a 1% disturbance in parameters α, β, and γ from the thermal conductivity function described in Equation (9) are portrayed in Figure 6. For all the parameters, the reduced sensitivity coefficient is equal or close to 0 from the beginning of the experiment until circa 0.200 s. The null values occur because there is no significant temperature variation during this period, so $T = T_\infty = 20$ °C despite the parameters variations. After the constant period, Sn assumes positive values for about 0.1 s before dropping significantly. It corresponds to the pre-heating when the sample is subjected to a slight heat loss by convection, given the low temperature of the shielding gas jet. The sample temperature at all the considered spots should be greater than 20 °C when the coefficients start decreasing, assuming negative values from circa 0.400 s. Besides this behavior, every parameter investigated exerts significant influence on the temperature computed during the experiment, given the magnitudes of Sn. The most significant Sn values for α, β, and γ are -23.88, -51.75, and -86.02, respectively. Such values are found from 0.540 to 0.640 s. Therefore, the method is sensitive enough to assess the thermal conductivity function parameters, considering the temperature acquired by the nine sensors at the positions determined in Table 2.

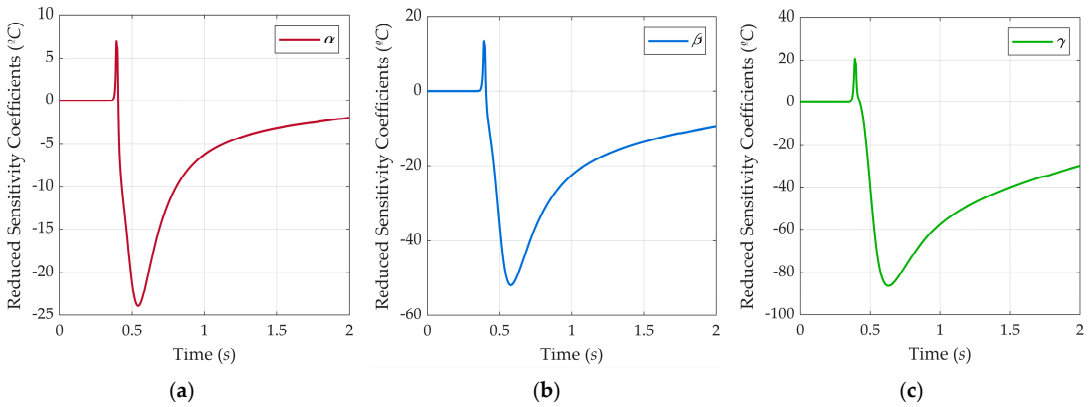

Figure 6. Evolution of the thermal conductivity function parameters' reduced sensitivity coefficients (Sn) with time. (**a**) α; (**b**) β; (**c**) γ.

3.2. Sensitivity of the Gross Heat Rate (Ω)

Figure 7 shows the evolution of the reduced sensitivity coefficient with the time for the gross heat rate. The parameter Ω exerts no influence on the temperature for the initial 0.300 s, corresponding to the period where the temperature difference is irrelevant. After that, the temperature variation given Ω increases at an enhanced rate for circa 0.1 s, and then the rate decreases. As previously stated, this time corresponds to the sample cooling by the action of the shielding gas, enhancing the heat transfer due to a more significant thermal gradient between the sample once its temperature is lower than 20 °C. When the sample temperature exceeds room temperature, the thermal gradient decreases, and so does the efficiency of the heat source. The most significant *Sn* for the gross heat rate is 111.7 °C, found at 0.573 s. The coefficients presented considerable values until the experiment ended.

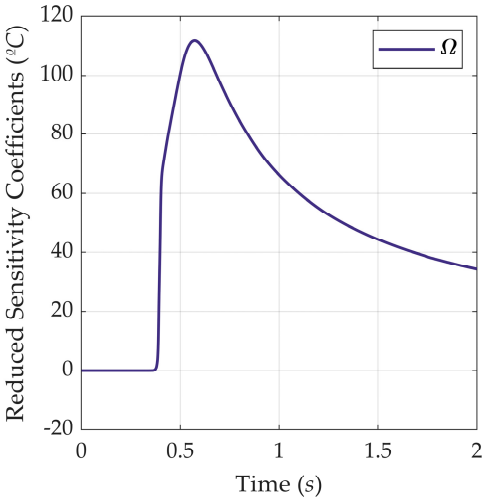

Figure 7. Evolution of the gross heat rate reduced sensitivity coefficients (*Sn*) with time.

4. Future Time Regularization (FTR) Analysis

The objective function sensitivity is enhanced by the *FTR*, so *F* is calculated as described in Equation (5). Here, one may not calibrate the reference temperature *T*, which is constant in time and location, nor the numerical temperature *T′*, once the values result from the guesses automatically defined by the code. In this circumstance, one may attain more exact estimates by adjusting the number of time steps *r* or the number of thermocouples *N* or both. In order to evaluate the effect of different *r* on the assessments, this work considers the *N* constant (=9) once the *Sn* calculated using this thermocouple configuration presents acceptable values, as shown in Figures 6 and 7.

Therefore, different numbers of time steps were applied to perform the estimates using the QOM. Here, the investigation of the relationships between *r*, the assessments accuracy, and the computational time required aims to attain the optimum number of time steps that should be considered for the parameter calculations. Considering the *Sn* calculated for α, β, γ, and Ω, it is possible to affirm the need for a considerable temperature variation so the method is sensitive enough to perform the estimates. In this case, the time considered for the calculations should be greater than the initial period where the temperature is comparable to 20 °C. The temperature profile depicted in Figure 3 implies that the temperature surpasses 20 °C close to 0.300 s. In order to determine the exact point in time where $T > 20$ °C for all the sensors, it is necessary to define such a point for the sensor placed farther away from the heat source. If the temperature at this point is greater than 20 °C during heating, the temperature at the other considered locations will also exceed 20 °C. Hence, Figure 8 shows the temperature profile for sensor m9 from 0 to 0.4 s. Here, the temperatures for the sensors m1 to m8 are omitted because the thermocouple m9 is farther from the heat source than the other sensors. The intersection between the dashed

lines delimits the point in time from which the temperature assumes values greater than 20 °C. Therefore, more than 0.308 s should be used for the estimates. Moreover, it is possible to observe that the cooling caused by the shielding gas is less than 0.01 °C at this point.

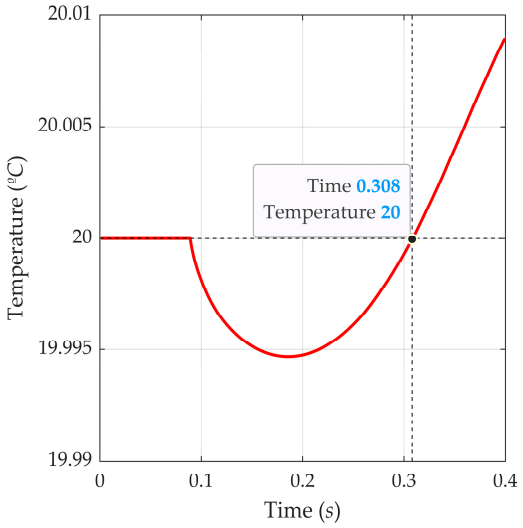

Figure 8. Temperature profile at sensor m9 during 0.4 s.

The time and time step size ratio gives the number of time steps r. As the temperature is calculated at points 0.001 s from each other, r is given by the following:

$$r = \frac{t}{0.001} \tag{14}$$

So, to consider times over 0.308 s, one should apply r bigger than 308 to compute the objective function. Figure 9 highlights the Sn evolution for α, β, and γ from 0.3 to 0.6 s to guarantee the period Sn assumes considerable values. One may notice that the coefficients for all the parameters are unsuitable for the estimations at 0.308 s remaining close to 0 up to 0.350 s. To ensure that Sn is greater than the possible noise in the temperature data, we consider an absolute Sn of at least 5 °C appropriate. The α and β Sn are comparable to -5 °C at 0.410 s. However, the γ Sn passes such a value at 0.443 s. As all the parameters are appraised simultaneously, the lesser appropriate r is 443.

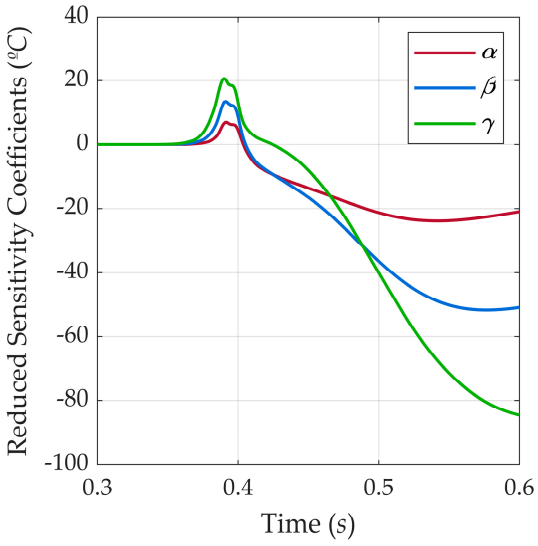

Figure 9. Evolution of the reduced sensitivity coefficients (Sn) with time from 0.3 to 0.6 s for α, β, and γ.

In light of this, r values ranging from 450 to 900 were considered. The estimates obtained using the QOM, the reference values, and the error percentages are shown in Table 4. Also, the last column of the table refers to the objective function F obtained given the respective combination of α, β, and γ pondered by r. Such an assumption allows for the comparison of the data, disregarding the number of points summed. If the accuracy for each parameter was considered independently, the best r configuration would be 900 for α, 550 for β, and 800 or 850 for γ. However, by observing $\overline{F}$, it is possible to obtain the combination of α, β, and γ, for which the computed temperature is closer to the reference temperature. As all the parameters are assessed simultaneously, r = 450 should be applied.

Table 4. Effect of the number of time steps in the estimates results.

	α		β		γ		$\overline{F}$
Reference	$\mathbf{2.50 \times 10^{-5}}$		$\mathbf{-5.30 \times 10^{-2}}$		**57.20**		
	Value ($\times\mathbf{10^{-5}}$)	**Error (%)**	**Value** ($\times\mathbf{10^{-2}}$)	**Error (%)**	**Value**	**Error (%)**	
r = 450	2.54	−1.7	−5.62	−6.1	59.9	−4.7	**0.69**
r = 500	2.54	−1.7	−5.62	−6.1	59.9	−4.8	1.16
r = 550	2.54	−1.7	−5.61	**−5.9**	59.7	−4.4	2.06
r = 600	2.54	−1.7	−5.65	−6.5	59.9	−4.7	5.35
r = 650	2.54	−1.7	−5.66	−6.8	59.9	−4.7	9.49
r = 700	2.54	−1.7	−5.65	−6.5	59.7	−4.3	11.22
r = 750	2.54	−1.7	−5.65	−6.5	59.6	−4.3	13.31
r = 800	2.54	−1.7	−5.65	−6.5	59.6	**−4.2**	14.85
r = 850	2.54	−1.7	−5.65	−6.5	59.6	**−4.2**	16.00
r = 900	2.51	**−0.4**	−5.65	−6.5	59.7	−4.4	23.50

In addition, the relationship between the computational time (t) required to perform the estimates and r is portrayed in Figure 10. In this period, the algorithm computes 432 times the direct model, given different combinations of α, β, and γ, and compares the results with the reference temperature to minimize the objective function, which is also calculated 432 times. Observing a linear proportion between the computational time required for the estimates and r is possible. The time varies because more or less temperature data are considered in the estimates. The dashed line stands for the linear trendline of the relationship between r and the time, described by Equation (15), with an R^2 of 0.9994. The computational time ranges from 2760 to 5820 ± 60 s. Thus, one should choose 450 r to estimate the thermal conductivity function parameters, as the estimates accuracy and computational time are satisfactory.

$$t = 6.8436r - 365.4545 \quad (15)$$

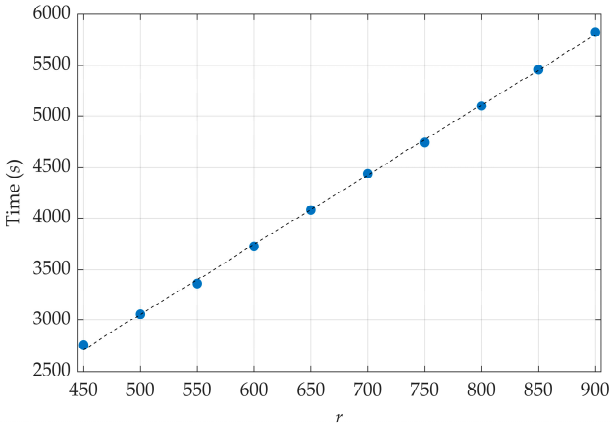

Figure 10. Computational time for estimating α, β, and γ using the QOM with different r configurations.

Moreover, it is also possible to use r = 450 for Case II, given the expressive Sn for Ω until 0.450 s. The initial evolution of Sn with time is highlighted in Figure 11 for 0.300 to 0.450 s. The Sn exceeds 5 °C at 0.387 s, increasing to 83.6 °C at 0.450 s.

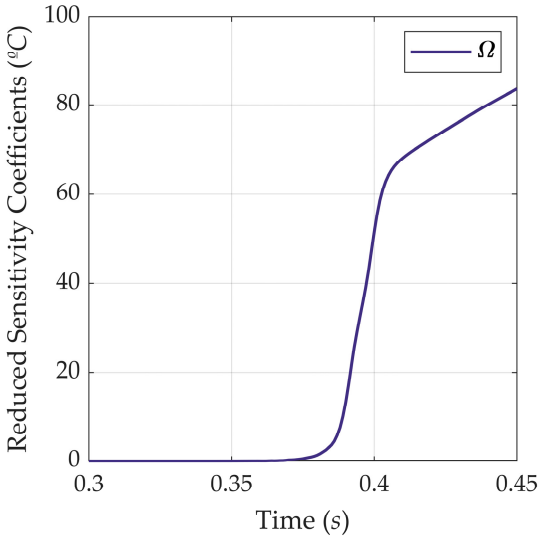

Figure 11. Evolution of the reduced sensitivity coefficients (Sn) with time from 0.3 to 0.45 s for Ω.

5. Effect of Measurement Errors on the Estimated Results

Acquiring the temperature field using a numerical model implies no noise, measurement errors, or uncertainties once the computations are exact. However, experimental data could be used as a baseline for estimating materials thermal properties through the QOM, and possible temperature measurement errors may be enhanced in the estimation result, resulting in the method's instability [23]. In this case, evaluating if the algorithm would return comparable results for noisy data is necessary. Hence, the QOM was applied to assess the parameters α, β, γ, and Ω given a disturbed temperature profile, as described in Section 2.4. The noise was added to the reference temperature profile (Figure 3) to verify if the method would return comparable results. A standard deviation of 10% was considered.

MATLAB® was used to add normalized random errors to the reference temperature. Such data were implemented in the algorithm as the reference temperature, considering the optimum r of 450. The results obtained by the QOM are shown in Table 5 for Cases I and II, as well as the error percentages for each parameter. One may notice that the errors remained lower than the imposed standard deviation for every parameter. Regarding Case I, there is a remarkable similarity between the values estimated with noisy data (Table 5) and the reference temperature (Table 4). This fact corroborates that the method is robust enough to perform the estimates, even if there is noise in the input data.

Table 5. Estimated parameters and errors associated with noisy data.

Parameter		α	β	γ	Ω
Goal value		2.50×10^{-5}	-5.30×10^{-2}	57.20	1000
Case I	QOM result	2.54×10^{-5}	-5.62×10^{-2}	59.9	--
	Error (%)	1.7	6.1	4.7	--
Case II	QOM result	2.50×10^{-5}	-5.44×10^{-2}	62.2	1071
	Error (%)	0.0	2.7	8.8	7.1

6. Estimation Results

The estimations were performed by implementing the starting conditions described in Table 6. The results are presented in Sections 6.1 and 6.2 for Cases I and II, respectively.

Table 6. QOM algorithm parameters used in the estimations.

Parameter	Value	
	Case I	**Case II**
κ	3	4
Points in **G**	27	81
τ	0.5	0.5
Search domain bounds	See Table 3.	
Maximum number of interactions	16	16
r	450	450

6.1. Case I: Nonlinear Thermal Conductivity Function

The estimated thermal conductivity in function of the temperature may be expressed as follows:

$$\lambda(T) = 2.5 \times 10^{-5} T^2 - 5.6 \times 10^{-2} T + 59.9 \quad (16)$$

Note that such values for the parameters α, β, and γ were obtained when applying the optimal r configuration discussed in Section 4. When implementing Equation (16) in the direct model, the calculated temperature presents no significant deviations from the reference temperature during the experiment period at all thermocouples. Figure 12 shows good agreement between the data. In this matter, the numerical temperature profiles computed with the reference nonlinear thermal conductivity are represented by the solid lines, while the dotted lines depict the numerical temperature profiles acquired using the estimated nonlinear thermal conductivity function.

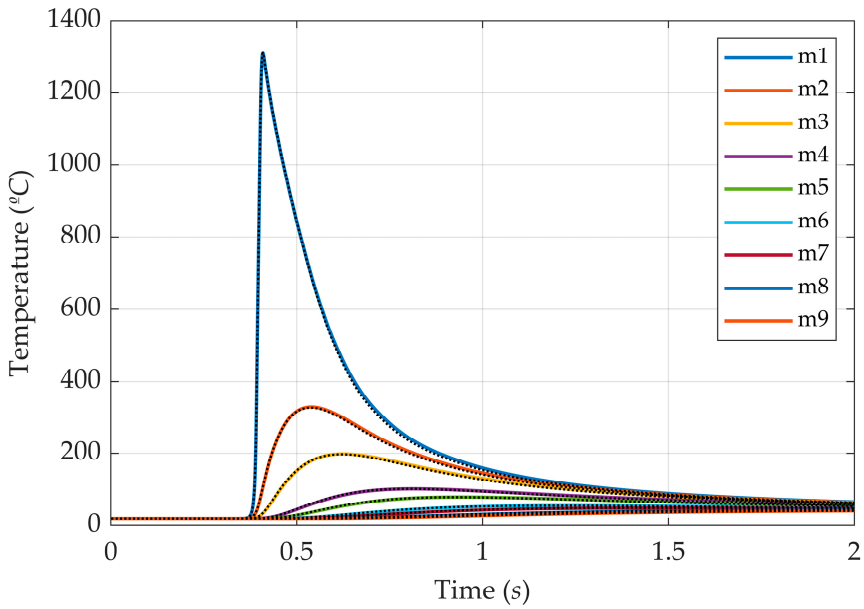

Figure 12. Comparison between the numerical temperature profiles computed using the reference and the estimated nonlinear thermal conductivity function (Case I).

The relative error further analyzes the corroboration for the good agreement between the temperature. Table 7 describes the maximum deviation in percentages between the temperatures calculated when implementing Equations (8) and (16). It is possible to notice that the deviation is homogeneous for all the temperature acquisition spots, with an average of 2.46%.

Table 7. Most expressive deviations between the numerical temperature profiles computed using the reference and the estimated $\lambda(T)$ in terms of percent error.

Sensor	m1	m2	m3	m4	m5	m6	m7	m8	m9
Error (%)	2.19	2.78	2.88	2.84	2.74	2.46	2.29	2.00	1.97

6.2. Case II: Nonlinear Thermal Conductivity Function and Gross Heat Rate

The results obtained using the QOM to assess α, β, γ, and Ω and their respective error percentages are shown in Table 8.

Table 8. Results attained for Case II applying 450 *r*.

Reference	α		β		γ		Ω	
	2.50×10^{-5}		-5.30×10^{-2}		57.20		1000	
	Value ($\times 10^{-5}$)	Error (%)	Value ($\times 10^{-2}$)	Error (%)	Value	Error (%)	Value	Error (%)
$r = 450$	2.57	2.8	-5.56	4.97	57.7	1.0	1071	7.1

Hence, the nonlinear thermal conductivity may be approximated by the following:

$$\lambda(T) = 2.6 \times 10^{-5} T^2 - 5.6 \times 10^{-2} T + 57.8 \quad (17)$$

The dotted lines of Figure 13 represent the temperatures calculated using Equation (17) and $\Omega = 1071$ W. It is possible to observe that the temperatures computed with the estimated thermal conductivity slightly overestimate the reference temperatures (solid lines). This tendency is found because the gross heat rate is 71 W greater than the reference value, so more heat is being provided to the sample, increasing its temperature. Regarding the peak temperatures, the more significant deviation is found at sensor m4, corresponding to less than 5% of the reference temperature. Hence, the estimated values of α, β, γ, and Ω are acceptable.

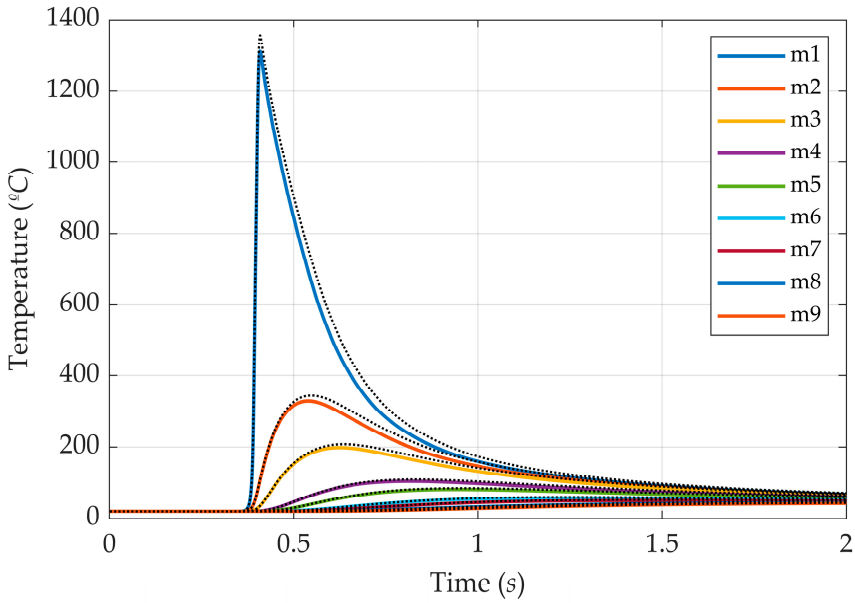

Figure 13. Comparison between the numerical temperature profiles computed using the reference and the estimated nonlinear thermal conductivity function and the gross heat rate (Case II).

The magnitudes of the overestimates are depicted in Table 9, which shows the most significant error percentages when using Equations (8) and (17) to attain the temperature field. The error percentages are inversely proportional to the thermocouple distance to the heat source. As the overestimate is mainly due to the greater heat input, such a tendency emphasizes the more significant Ω effect in the temperatures calculated at positions near the heat source. Indeed, the temperature computed at m1 directly reflects the Ω magnitude. However, such an overestimate should not interfere with the experiment results, as it is insufficient to cause steel's phase or microstructural changes during all experimental periods.

Table 9. Most expressive deviations between the numerical temperature profiles computed using the reference and the estimated $\lambda(T)$ and Ω in terms of percent error.

Sensor	**m1**	**m2**	**m3**	**m4**	**m5**	**m6**	**m7**	**m8**	**m9**
Error (%)	11.09	8.65	7.54	6.14	5.57	4.69	4.31	3.82	3.60

7. Conclusions

This work proposes an inverse method for estimating the thermal conductivity and gross heat rate during an autogenous LASER Beam Welding experiment. Two cases are considered. In Case I, we assess the three parameters that compose the second-degree conductivity function of temperature. In Case II, the gross heat rate related to the heat distribution is also estimated, in addition to the nonlinear thermal conductivity function. The temperature field is acquired by solving the three-dimensional heat diffusion equation using an in-house CUDA-C code. Such a language is also used to implement the inverse method. A gradient descendent technique called the Quadrilateral Optimization Method (QOM) is applied to optimize the parameters. The method's suitability for Cases I and II is investigated by considering the sensitivity of the temperature for every parameter of interest and the stability of the method when performing the assessments from noisy data. After assuring the method is sensitive enough, we evaluate the effect of the number of time steps used in the regularization technique to optimize the estimates considering accuracy and computational time. The primary outcomes may be summarized as follows:

1. The method is sensitive enough to provide precise estimates of the nonlinear thermal conductivity function and the gross heat rate simultaneously. The estimates consider nine points of temperature acquisition (see Table 2) during a 2.0 s experiment.
2. The method sensitivity may be enhanced by calibrating the parameter r of the Future Time Regularization (FTR). The effect of r on the computational time and estimate accuracy was investigated. The optimum r that minimizes the computational time and presents considerable accuracy is 450.
3. The comparison between the simulated temperature using reference and estimated values showed that the estimated parameters could be used as input data to calculate the heat transfer during SAE 1020 LBW. In Case I, the error remained lower than 3%. Case II presents more significant error percentages mainly due to the sensitivity of Ω. The values decrease from 11% with the sensor distance to the heat source.
4. The computational time required for the estimates using 450 r is 46 $\pm$ 1 min and 99 $\pm$ 1 min for Cases I and II, respectively. In the former case, the direct model is calculated 432 times; in the latter case, the direct model is calculated 1296 times.

The results presented in this work emphasize the extent to which the QOM may be applied for IHTPs by performing the novel estimation of three and four parameters simultaneously, including both a thermophysical property and a process parameter. The main gaps of the adopted procedure consist of the requirement to know the functional form that best suits the modelization of property evolution with temperature. Also, the authors chose not to model the austenite decomposition of steel during solidification. One may also find slight differences when estimating the properties during the heating and cooling of

the sample. Future works will address such behavior by considering different functions to model the thermal conductivity under determined temperature ranges. In addition, we intend to investigate the method's sensitivity further by analyzing the amount and location of the thermocouples.

Author Contributions: Conceptualization, A.F.M.d.O. and E.d.S.M.; methodology, A.F.M.d.O., E.d.S.M. and P.L.M.; software, A.F.M.d.O., E.d.S.M. and E.J.G.d.N.; validation, A.F.M.d.O.; formal analysis, A.F.M.d.O.; investigation, A.F.M.d.O.; writing—original draft preparation, A.F.M.d.O.; writing—review and editing, A.F.M.d.O., E.d.S.M., P.L.M., K.D.Z. and E.J.G.d.N.; supervision, E.d.S.M., P.L.M. and K.D.Z.; project administration, E.d.S.M.; funding acquisition, E.d.S.M. All authors have read and agreed to the published version of the manuscript.

Funding: This research was funded by the Coordenação de Aperfeiçoamento de Pessoal de Nível Superior (CAPES) and by Petróleo Brasileiro S.A. (PETROBRAS).

Data Availability Statement: The data presented in this study are available on request from the corresponding author.

Acknowledgments: The authors would like to thank the Brazilian Ministry of Defense, the Brazilian Airforce (FAB), and the Aeronautics Institute of Technology (ITA).

Conflicts of Interest: The authors declare no conflicts of interest. The funders had no role in the design of the study; in the collection, analyses, or interpretation of data; in the writing of the manuscript; or in the decision to publish the results.

References

1. Yan, S.; Meng, Z.; Chen, B.; Tan, C.; Song, X.; Wang, G. Prediction of Temperature Field and Residual Stress of Oscillation Laser Welding of 316LN Stainless Steel. *Opt. Laser Technol.* **2022**, *145*, 107493. [CrossRef]
2. Zhao, S.; Sun, X.; Li, Z.; Xie, W.; Meng, S.; Wang, C.; Zhang, W. Simultaneous Retrieval of High Temperature Thermal Conductivities, Anisotropic Radiative Properties, and Thermal Contact Resistance for Ceramic Foams. *Appl. Therm. Eng.* **2019**, *146*, 569–576. [CrossRef]
3. Belokon, Y.; Hrechanyi, O.; Vasilchenko, T.; Krugliak, D.; Bondarenko, Y. Development of New Composite Materials Based on TiN–Ni Cermets during Thermochemical Pressing. *Results Eng.* **2022**, *16*, 100724. [CrossRef]
4. Panmanee, P.; Okhawilai, M.; Mora, P.; Jubsilp, C.; Karagiannidis, P.; Rimdusit, S. Development of a New Birthing Model Material Based on Silicone Rubber/Natural Rubber Blend. *Polym. Test.* **2023**, *117*, 107849. [CrossRef]
5. Peng, G.; Sun, Y.; Zhang, Q.; Yang, Q.; Shen, W. A Collaborative Design Platform for New Alloy Material Development. *Adv. Eng. Inform.* **2022**, *51*, 101488. [CrossRef]
6. Balandin, A.A.; Zaitsev-Zotov, S.V.; Grüner, G. Charge-Density-Wave Quantum Materials and Devices-New Developments and Future Prospects. *Appl. Phys. Lett.* **2021**, *119*, 17041. [CrossRef]
7. Wardak, C.; Morawska, K.; Pietrzak, K. New Materials Used for the Development of Anion-Selective Electrodes—A Review. *Materials* **2023**, *16*, 5779. [CrossRef] [PubMed]
8. Rottmann, M.; Beikircher, T.; Ebert, H.P. Thermal Conductivity of Evacuated Expanded Perlite Measured with Guarded-Hot-Plate and Transient-Hot-Wire Method at Temperatures between 295 K and 1073 K. *Int. J. Therm. Sci.* **2020**, *152*, 106338. [CrossRef]
9. Jannot, Y.; Remy, B.; Degiovanni, A. Measurement of Thermal Conductivity and Thermal Resistance with a Tiny Hot Plate. *High Temp. -High Press.* **2010**, *39*, 11–31.
10. Katz, M.D.; Katz, I.M. Evaluation of the Laser-Flash Method and Its Errors for Determining of Materials Thermal Diffusivity at High Temperatures. *MATEC Web Conf.* **2017**, *110*, 5. [CrossRef]
11. Nishi, T.; Shibata, H.; Ohta, H.; Waseda, Y. Thermal Conductivities of Molten Iron, Cobalt, and Nickel by Laser Flash Method. *Metall. Mater. Trans. A* **2003**, *34*, 2801–2807. [CrossRef]
12. Jannot, Y.; Meulemans, J.; Schick, V.; Capp, M.; Bargain, I. A Comparative Fluxmetric (CFM) Method for Apparent Thermal Conductivity Measurement of Insulating Materials at High Temperature. *Int. J. Thermophys.* **2020**, *41*, 94. [CrossRef]
13. Lamien, B.; Le Maux, D.; Courtois, M.; Pierre, T.; Carin, M.; Le Masson, P.; Orlande, H.R.B.; Paillard, P. A Bayesian Approach for the Estimation of the Thermal Diffusivity of Aerodynamically Levitated Solid Metals at High Temperatures. *Int. J. Heat Mass Transf.* **2019**, *141*, 265–281. [CrossRef]
14. Reddy, K.S.; Jayachandran, S. Investigations on Design and Construction of a Square Guarded Hot Plate (SGHP) Apparatus for Thermal Conductivity Measurement of Insulation Materials. *Int. J. Therm. Sci.* **2017**, *120*, 136–147. [CrossRef]
15. El-Sharkawy, A.A.; Dessouky, M.T.; Abousehly, A.M.; Raafat, A. Thermal Properties Investigation of Inhomogeneous Ternary Alloy (Se–Te–S) Using Flash Method Technique. *Int. J. Thermophys.* **2020**, *41*, 25. [CrossRef]
16. Farahani, S.D.; Kisomi, M.S. Experimental Estimation of Temperature-Dependent Thermal Conductivity Coefficient by Using Inverse Method and Remote Boundary Condition. *Int. Commun. Heat Mass Transf.* **2020**, *117*, 104736. [CrossRef]

17. Mohebbi, F.; Sellier, M. Estimation of Functional Form of Time-Dependent Heat Transfer Coefficient Using an Accurate and Robust Parameter Estimation Approach: An Inverse Analysis. *Energies* **2021**, *14*, 5073. [CrossRef]
18. Yue, K.; Zhang, X.; Yu, F. Simultaneous Estimation of Thermal Properties of Living Tissue Using Noninvasive Method. *Int. J. Thermophys.* **2007**, *28*, 1470–1489. [CrossRef]
19. Ravula, S.R.; Arepally, D.; Datta, A.K. Estimation of the Energy Requirement of Bread during Baking by Inverse Heat Transfer Method. *J. Therm. Anal. Calorim.* **2023**, *148*, 13297–13311. [CrossRef]
20. Cevoli, C.; Panarese, V.; Catalogne, C.; Fabbri, A. Estimation of the Effective Moisture Diffusivity in Cake Baking by the Inversion of a Finite Element Model. *J. Food Eng.* **2020**, *270*, 109769. [CrossRef]
21. Łapka, P.; Pietrak, K.; Kujawińska, M.; Malesa, M. Development and Validation of an Inverse Method for Identification of Thermal Characteristics of a Short Laser Pulse. *Int. J. Therm. Sci.* **2020**, *150*, 106240. [CrossRef]
22. Wan, S.; Xu, P.; Wang, K.; Yang, J.; Li, S. Real-Time Estimation of Thermal Boundary of Unsteady Heat Conduction System Using PID Algorithm. *Int. J. Therm. Sci.* **2020**, *153*, 106395. [CrossRef]
23. Wan, S.; Wang, K.; Xu, P.; Huang, Y. Numerical and Experimental Verification of the Single Neural Adaptive PID Real-Time Inverse Method for Solving Inverse Heat Conduction Problems. *Int. J. Heat Mass Transf.* **2022**, *189*, 122657. [CrossRef]
24. dos Santos Magalhães, E.; de Carvalho, S.R.; Silva, S.M.M.L.E. The Use of Non-Linear Inverse Problem and Enthalpy Method in GTAW Process of Aluminum. *Int. Commun. Heat Mass Transf.* **2015**, *66*, 114–121. [CrossRef]
25. Magalhães, E.D.S.; Correa, E.O.; Silva, A.L.F.L.E.; Silva, S.M.M.L.E. Microstructural Analysis in GTA Aluminum Alloy Welding Using Inverse Problems. *Appl. Therm. Eng.* **2016**, *100*, 333–339. [CrossRef]
26. Magalhães, E. dos S. A Quadrilateral Optimization Method for Non-Linear Thermal Properties Determination in Materials at High Temperatures. *Int. J. Heat Mass Transf.* **2021**, *181*, 121857. [CrossRef]
27. de Oliveira, A.F.M.; Magalhães, E.D.S.; Paes, L.E.D.S.; Pereira, M.; da Silva, L.R. A Thermal Analysis of LASER Beam Welding Using Statistical Approaches. *Processes* **2023**, *11*, 25. [CrossRef]
28. Çengel, Y.A.; Ghajar, A.J. *Heat and Mass Transfer: Fundamentals and Applications*, 4th ed.; McGraw-Hill Science/Engineering/Math: New York, NY, USA, 2010.
29. Bergman, T.L.; Lavine, A.S.; Incropera, F.P.; Dewitt, D.P. *Fundamentals of Heat and Mass Transfer*, 7th ed.; John Wiley & Sons: Hoboken, NJ, USA, 2011.
30. Clain, F.M.; Teixeira, P.R.D.F.; Araújo, D.B.D. Two Heat Source Models to Simulate Welding Processes with Magnetic Deflection. *Soldag. E Insp.* **2017**, *22*, 99–113. [CrossRef]
31. Nascimento, E.; Magalhães, E.; Azevedo, A.; Paes, L.E.S.; Oliveira, A. An Implementation of LASER Beam Welding Simulation on Graphics Processing Unit Using CUDA. *Computation* **2024**, *12*, 83. [CrossRef]
32. Magalhães, E.D.S.; Anselmo, B.D.C.S.; Lima e Silva, A.L.F.D.; Lima e Silva, S.M.M. Time Traveling Regularization for Inverse Heat Transfer Problems. *Energies* **2018**, *11*, 15. [CrossRef]
33. Beck, J.V.; Blackwell, B.; Haji-Sheikh, A. Comparison of Some Inverse Heat Conduction Methods Using Experimental Data. *Int. J. Heat Mass Transf.* **1996**, *39*, 3649–3657. [CrossRef]
34. Taktak, R.; Beck, J.V.; Scott, E.P. Optimal Experimental Design for Estimating Thermal Properties of Composite Materials. *Int. J. Heat Mass Transf.* **1993**, *36*, 2977–2986. [CrossRef]

computation

MDPI

Article

Analytical and Numerical Investigation of Two-Dimensional Heat Transfer with Periodic Boundary Conditions

İrem Bağlan [1] and Erman Aslan [2,*]

[1] Department of Mathematics, Kocaeli University, TR-41380 Kocaeli, Türkiye; isakinc@kocaeli.edu.tr
[2] Department of Mechanical Engineering, Kocaeli University, TR-41380 Kocaeli, Türkiye
* Correspondence: erman.aslan@kocaeli.edu.tr; Tel.: +90-262-303-3414

Abstract: A two-dimensional heat diffusion problem with a heat source that is a quasilinear parabolic problem is examined analytically and numerically. Periodic boundary conditions are employed. As the problem is nonlinear, Picard's successive approximation theorem is utilized. We demonstrate the existence, uniqueness, and constant dependence of the solution on the data using the generalized Fourier method under specific conditions of natural regularity and consistency imposed on the input data. For the numerical solution, an implicit finite difference scheme is used. The results obtained from the analytical and numerical solutions closely match each other.

Keywords: quasilinear parabolic equation; periodic boundary condition; generalized Fourier method; finite difference method

check for updates

Citation: Bağlan, İ.; Aslan, E. Analytical and Numerical Investigation of Two-Dimensional Heat Transfer with Periodic Boundary Conditions. *Computation* **2024**, *12*, 11. https://doi.org/10.3390/computation12010011

Academic Editors: Ali Cemal Benim, Rachid Bennacer, Abdulmajeed A. Mohamad, Paweł Oclon, Sang-Ho Suh and Jan Taler

Received: 8 November 2023
Revised: 7 December 2023
Accepted: 2 January 2024
Published: 10 January 2024

1. Introduction

The investigation of a mathematical model has broad implications for a great number of important applications, such as chemical diffusions [1,2], heat conduction problems, [3–5], population dynamics [6], thermoelasticity [7], medical science, electrochemistry [8], engineering, and control theory. This necessitates the analysis of two-dimensional parabolic partial differential equations with nonlocal boundary conditions [9–11].

The heat diffusion equation is one of the two-dimensional quasilinear parabolic problems. It is employed to determine temperature distribution in every region of the domain at desired time for conduction heat transfer problems. Heat transfer by conduction involves temperature differences in a solid or stationary fluid. Information on temperature distribution in a solid can be utilized to determine structural integrity through assessing thermal stresses, expansions, deflections, and cracks. The evaluation and propagation of granite thermal stresses and thermal cracks with time are shown in Figure 1 [12]. The temperature distribution can also be used to optimize the thickness of an insulating material or to determine the compatibility of the material with special coatings or adhesives used [13].

Initial and boundary conditions are required for solving the two-dimensional quasilinear parabolic problem, such as the heat diffusion equation. Some of boundary conditions for the heat diffusion equation, Dirichlet (or first kind) determines the fixed temperature at surfaces. For example, the surface is very close to this when it comes into contact with a melting solid and/or a boiling liquid. In both cases, heat transfer occurs at the surface, whereas the surfaces remain at the temperature of phase-changing process [13]. Neumann (or the second type) corresponds to the presence of constant heat flux on the surface. This heat flux is related to the temperature at the surface according to Fourier's law and can be accomplished by bonding a thin electric heater to the surface. A special case of this situation corresponds to a perfectly insulated or adiabatic surface. A periodic boundary condition is combined with Dirichlet and Neumann boundary conditions [14], and it is set to isolate repeating temperature distribution in the solution's domain [15].

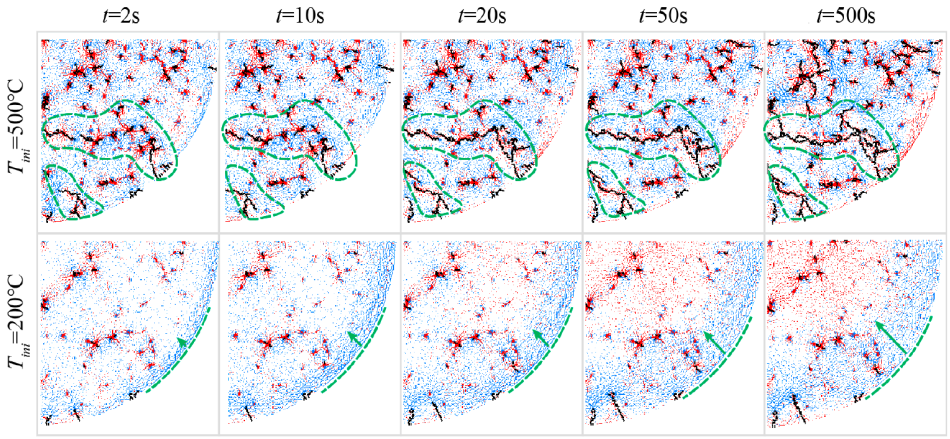

Figure 1. Evaluation and propagation of granite thermal stress field and thermal cracks [12].

The periodic boundary condition, a special case of the nonlocal boundary [16] condition, is used in the present investigation. Generally, the periodic boundary condition is often employed in numerical simulations and mathematical models. Additionally, the periodic boundary condition results from many important applications in heat transfer, fluid dynamics, life sciences, and used lunar theory [14,17,18].

There are analytical methods available for solving two-dimensional quasilinear parabolic problems. One of these methods is the Fourier method. Baglan and Kanca analytically solved the two-dimensional quasilinear parabolic problem (heat diffusion) with an inverse coefficient and a heat source using the Fourier method [14,19]. The two-dimensional heat diffusion equation with time-dependent thermal conductivity and a heat source problem is analytically solved with the Fourier method by the same authors [20]. Additionally, similar analytical solutions for fractional diffusion equations can be found in the literature [21–23].

In order to solve the two-dimensional quasilinear parabolic problem, several numerical methods are available, such as the finite difference method [24,25], the finite element method [26,27], the finite volume method [28], and the lattice Boltzmann methods [15,29,30]. Denghan solved the one-dimensional heat diffusion equation numerically using the finite difference method [31]. In this study, three different schemes were employed, namely, the backward time-centered space (BTCS) implicit scheme, the implicit Crandall's method, the forward time-centered space (FTCS) explicit scheme, and the Dufort–Frankel three-level techniques. The Crank–Nicolson implicit scheme is used to numerically solve the one-dimensional heat diffusion equation with an inverse coefficient by Baglan et al. [32]. Kanca and Baglan numerically solved the two-dimensional heat diffusion equation with periodic boundary conditions [20]. An implicit finite difference scheme is used for numerical solutions. Hamila et al. [33] investigated the effects of changes in thermal conductivity on several transient heat transfer problems using the lattice Boltzmann methods (LBM). Benchmark problems containing conduction and/or radiation with constant thermal conductivity were calculated and simulated. The heat diffusion equation was solved numerically by exclusively using the lattice Boltzmann methods. The numerical results closely aligned with the available results in the literature.

The finite difference method is one of the existing numerical methods considered in the present investigation that can be applied to solve partial differential equations. The finite difference method is based on the discretization of differential equations through finite difference equations. Finite difference approximations have algebraic forms and relate the value of a dependent variable at one point in the solution region to the values at some neighboring points. Using Taylor series is the most usual way to construct these approximations. The numerical method recommended here is the implicit finite difference method. This method supports second order accuracy in the spatial grid sizes and first order time grid size. The explicit finite scheme has a restriction of determining time step

size due to stability requirements for the numerical solution of the two-dimensional heat diffusion equation.

In the present paper, we establish the existence, uniqueness, and continuous dependence of the solution on the data. We derive the analytical solution by the Fourier Method and Picard's successive approximation for the two-dimensional heat diffusion problem with periodic boundary conditions [14,19,20]. For the numerical solution, we employ an implicit finite difference approximation. The numerical solution demonstrates good agreement with the analytical solution.

This problem is nonlinear. Obtaining an analytical solution for a nonlinear problem is only possible through a few methods, namely, the Fourier Method, the maximum principle method, and/or the operation method. The periodic boundary condition used in the problem poses a challenging condition, and analytically solving this boundary condition is very difficult. Generally, in the literature, there are very few analytical solutions for problems that are both nonlinear and have periodic boundary conditions. As mentioned before, we utilized the Fourier method along with the Picard's successive approximation for our analytical solution. We compared this analytical solution with a numerical solution, highlighting the novelty of our study.

2. The Problem with Periodic Boundary Conditions

Let us examine the two-dimensional, quasilinear heat diffusion problem with the heat source given below,

$$\frac{\partial T}{\partial \tau} = \frac{\partial^2 T}{\partial \alpha^2} + \frac{\partial^2 T}{\partial \beta^2} + h(\alpha, \beta, \tau, T), \tag{1}$$

with the initial condition,

$$T(\alpha, \beta, 0) = \phi(\alpha, \beta), \alpha \in [0, \pi], \beta \in [0, \pi], \tag{2}$$

and with the periodic boundary conditions,

$$\begin{array}{l} T(0, \beta, \tau) = T(\pi, \beta, \tau), \beta \in [0, \pi], \tau \in [0, \Upsilon] \\ T(\alpha, 0, \tau) = T(\alpha, \pi, \tau), \alpha \in [0, \pi], \tau \in [0, \Upsilon], \end{array} \tag{3}$$

$$\begin{array}{l} T_\alpha(0, \beta, \tau) = T_\alpha(\pi, \beta, \tau), \beta \in [0, \pi], \tau \in [0, \Upsilon] \\ T_\beta(\alpha, 0, \tau) = T_\beta(\alpha, \pi, \tau), \alpha \in [0, \pi], \tau \in [0, \Upsilon]. \end{array} \tag{4}$$

Studies involving equations similar to the heat diffusion equation we solved in our work can be found in the literature [13,14,19,20,32]. In Equations (1)–(4), where T is temperature distribution, h is a source function, α and β represent the direction, and τ and Υ are time and maximum time, respectively. The domain size is π for the α and β directions. ϕ is the initial condition. A schematic figure of the problem with boundary conditions is shown in Figure 2.

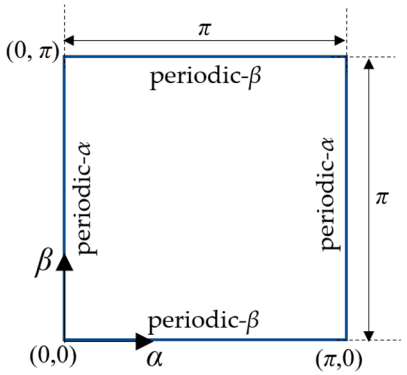

Figure 2. Schematic figure of the problem with boundary conditions.

$$\begin{aligned} T(\alpha,\beta,\tau) &= \tfrac{T_0(\tau)}{4} + \sum_{r,s=1}^{\infty} T_{crs}(\tau)\cos(2r\alpha)\cos(2s\beta) + \sum_{r,s=1}^{\infty} T_{scrs}(\tau)\sin(2r\alpha)\cos(2s\beta) \\ &+ \sum_{r,s=1}^{\infty} T_{csrs}(\tau)\cos(2r\alpha)\sin(2s\beta) + \sum_{r,s=1}^{\infty} T_{srs}(\tau)\sin(2r\alpha)\sin(2s\beta). \end{aligned} \tag{5}$$

where the Fourier coefficients:

$$T_0(\tau) = T_0(0) + \frac{4}{\pi^2}\int_0^t\int_0^\pi\int_0^\pi h(\alpha,\beta,\tau,T)d\alpha d\beta d\tau,$$

$$T_{crs}(\tau) = T_{crs}(0)e^{-\int_0^t[(2r)^2+(2s)^2]dt} + \frac{4}{\pi^2}\int_0^t\int_0^\pi\int_0^\pi e^{-\int_\tau^t[(2r)^2+(2s)^2]dt} h(\alpha,\beta,\tau,T)\cos(2r\alpha)\cos(2s\beta)d\alpha d\beta d\tau,$$

$$T_{csrs}(\tau) = T_{csrs}(0)e^{-\int_0^t[(2r)^2+(2s)^2]dt} + \frac{4}{\pi^2}\int_0^t\int_0^\pi\int_0^\pi e^{-\int_\tau^t[(2r)^2+(2s)^2]dt} h\left(\alpha,\beta,\tau,T^{(N)}\right)\cos(2r\alpha)\sin(2s\beta)d\alpha d\beta d\tau,$$

$$T_{scrs}(\tau) = T_{scrs}(0)e^{-\int_0^t[(2r)^2+(2s)^2]dt} + \frac{4}{\pi^2}\int_0^t\int_0^\pi\int_0^\pi e^{-\int_\tau^t[(2r)^2+(2s)^2]dt} h(\alpha,\beta,\tau,T)\sin(2r\alpha)\cos(2s\beta)d\alpha d\beta d\tau,$$

$$T_{srs}(\tau) = T_{srs}(0)e^{-\int_0^t[(2r)^2+(2s)^2]dt} + \frac{4}{\pi^2}\int_0^t\int_0^\pi\int_0^\pi e^{-\int_\tau^t[(2r)^2+(2s)^2]dt} h(\alpha,\beta,\tau,T)\sin(2r\alpha)\sin(2s\beta)d\alpha d\beta d\tau.$$

Then, we obtain the solution:

$$\begin{aligned} T(\alpha,\beta,\tau) &= \tfrac{1}{4}\left(\varphi_0 + \tfrac{4}{\pi^2}\int_0^t h_0(\tau,T)d\tau\right) \\ &+ \sum_{r,s=1}^{\infty}\left(\varphi_{crs} + \tfrac{4}{\pi^2}\int_0^t e^{-\int_\tau^t[(2r)^2+(2s)^2]dt} h_{crs}(\tau,T)d\tau\right)\cos(2r\alpha)\cos(2s\beta) \\ &+ \sum_{r,s=1}^{\infty}\left(\varphi_{csrs} + \tfrac{4}{\pi^2}\int_0^t e^{-\int_\tau^t[(2r)^2+(2s)^2]dt} h_{csrs}(\tau,T)d\tau\right)\cos(2r\alpha)\sin(2s\beta) \\ &+ \sum_{r,s=1}^{\infty}\left(\varphi_{scrs} + \tfrac{4}{\pi^2}\int_0^t e^{-\int_\tau^t[(2r)^2+(2s)^2]dt} h_{scrs}(\tau,T)d\tau\right)\sin(2r\alpha)\cos(2r\beta) \\ &+ \sum_{r,s=1}^{\infty}\left(\varphi_{srs} + \tfrac{4}{\pi^2}\int_0^t e^{-\int_\tau^t[(2r)^2+(2s)^2]dr} h_{srs}(\tau,T)d\tau\right)\sin(2r\alpha)\sin(2s\beta) \end{aligned} \tag{6}$$

where h_0, h_{crs}, h_{csrs}, h_{scrs}, and h_{srs} are the Fourier coefficients of the source function.

3. Analytical Solution of the Problem

Let us assume the following rules for the functions used in the problem:

(A) $\varphi(\alpha,\beta)C^{1,1}([0,\pi]\times[0,\pi])$,

Let L be constant, $\|\varphi\| \le L$,

$$\varphi(0,\beta) = \varphi(\pi,\beta),\ \varphi_\alpha(0,\beta) = \varphi_\alpha(\pi,\beta),$$

$$\varphi(\alpha,0)=\varphi(\alpha,\pi),\varphi_{\beta}(\alpha,0)=\varphi_{\beta}(\alpha,\pi).$$

(B) Let $h(\alpha,\beta,\tau,v)$ have the following properties:

$$\left|\frac{\partial h(\alpha,\beta,\tau,T)}{\partial\alpha}-\frac{\partial h(\alpha,\beta,\tau,\overline{T})}{\partial\alpha}\right|\leq b(\alpha,\beta,\tau)\left|T-\overline{T}\right|,$$

$$\left|\frac{\partial h(\alpha,\beta,\tau,T)}{\partial\beta}-\frac{\partial h(\alpha,\beta,\tau,\overline{T})}{\partial\beta}\right|\leq b(\alpha,\beta,\tau)\left|T-\overline{T}\right|,$$

$$\left|\frac{\partial h(\alpha,\beta,\tau,T)}{\partial\alpha\partial\beta}-\frac{\partial h(\alpha,\beta,\tau,\overline{T})}{\partial\alpha\partial\beta}\right|\leq b(\alpha,\beta,\tau)\left|T-\overline{T}\right|,$$

where

$$b(\alpha,\beta,\tau)\in L_2, b(\alpha,\beta,\tau)\geq 0,$$

$$b(\alpha,\beta,\tau)\in C^{1,1,0}[0,\pi],$$

$$h(\alpha,\beta,\tau,T)|_{\alpha=0}=h(\alpha,\beta,\tau,T)|_{\alpha=\pi},$$

$$h_{\alpha}(\alpha,\beta,\tau,T)|_{\alpha=0}=h_{\alpha}(\alpha,\beta,\tau,T)|_{\alpha=\pi},$$

$$h_{\beta}(\alpha,\beta,\tau,T)\big|_{\beta=0}=h_{\beta}(\alpha,\beta,\tau,T)\big|_{\beta=\pi},$$

$$h_{\alpha\beta}(\alpha,\beta,\tau,T)\big|_{\alpha=0}=h_{\alpha\beta}(\alpha,\beta,\tau,T)\big|_{\alpha=\pi},$$

$$h_{\alpha\beta}(\alpha,\beta,\tau,T)\big|_{\beta=0}=h_{\alpha\beta}(\alpha,\beta,\tau,T)\big|_{\beta=\pi}.$$

and where $b(\alpha,\beta,\tau)$ is the Lipschitz coefficient.

Definition 1.

$$\{T(\tau)\}=\{T_0(\tau),T_{crs}(\tau),T_{csrs}(\tau),T_{scrs}(\tau),T_{srs}(\tau)\},$$

$$\max_{0\leq t\leq T}\frac{|T_0(\tau)|}{4}+\sum_{r,s=1}^{\infty}\left(\begin{array}{c}\max\limits_{0\leq t\leq T}|T_{crs}(\tau)|+\max\limits_{0\leq t\leq T}|T_{csrs}(\tau)|\\+\max\limits_{0\leq t\leq T}|T_{scrs}(\tau)|+\max\limits_{0\leq t\leq T}|T_{srs}(\tau)|\end{array}\right)<\infty,$$

$$\|T(\tau)\|=\max_{0\leq t\leq T}\frac{|T_0(\tau)|}{4}+\sum_{r,s=1}^{\infty}\left(\begin{array}{c}\max\limits_{0\leq t\leq T}|T_{crs}(\tau)|+\max\limits_{0\leq t\leq T}|T_{csrs}(\tau)|\\+\max\limits_{0\leq t\leq T}|T_{scrs}(\tau)|+\max\limits_{0\leq t\leq T}|T_{srs}(\tau)|\end{array}\right).$$

is called Banach (B) norm.

Problem (1)–(4) is a nonlinear problem; therefore, an iterative method should be employed to determine the existence, uniqueness, and convergence of the problem. The solution using the Picard Successive Iteration method is as follows.

Theorem 1. *Let the assumptions (A)–(B) be satisfied, then the problem has a unique solution.*

Proof. As an iteration for the problem.

$$T_0{}^{(N+1)}(\tau) = T_0{}^{(0)}(0) + \frac{4}{\pi^2}\int_0^t\int_0^\pi\int_0^\pi h\Big(\alpha,\beta,\tau,T^{(N)}\Big)d\alpha d\beta d\tau,$$

$$T_{crs}{}^{(N+1)}(\tau) = T_{crs}{}^{(0)}(0)e^{-\int_0^t[(2r)^2+(2s)^2]dt} + \frac{4}{\pi^2}\int_0^t\int_0^\pi\int_0^\pi e^{-\int_\tau^t[(2r)^2+(2s)^2]dt}h\Big(\alpha,\beta,\tau,T^{(N)}\Big)\cos(2m\alpha)\cos(2n\beta)d\alpha d\beta d\tau,$$

$$T_{csrs}{}^{(N+1)}(\tau) = T_{csrs}{}^{(01)}(0)e^{-\int_0^t[(2r)^2+(2s)^2]dt} + \frac{4}{\pi^2}\int_0^t\int_0^\pi\int_0^\pi e^{-\int_\tau^t[(2r)^2+(2s)^2]dt}h\Big(\alpha,\beta,\tau,T^{(N)}\Big)\cos(2r\alpha)\sin(2s\beta)d\alpha d\beta d\tau,$$

$$T_{scrs}{}^{(N+1)}(\tau) = T_{scrs}{}^{(0)}(0)e^{-\int_0^t[(2r)^2+(2s)^2]dt} + \frac{4}{\pi^2}\int_0^t\int_0^\pi\int_0^\pi e^{-\int_\tau^t[(2r)^2+(2s)^2]dt}h\Big(\alpha,\beta,\tau,T^{(N)}\Big)\sin(2r\alpha)\cos(2s\beta)d\alpha d\beta d\tau,$$

$$T_{srs}{}^{(N+1)}(\tau) = T_{srs}{}^{(0)}(0)e^{-\int_0^t[(2r)^2+(2s)^2]dt} + \frac{4}{\pi^2}\int_0^t\int_0^\pi\int_0^\pi e^{-\int_\tau^t[(2r)^2+(2s)^2]dt}h\Big(\alpha,\beta,\tau,T^{(N)}\Big)\sin(2r\alpha)\sin(2s\beta)d\alpha d\beta d\tau.$$

where N is the iteration number.

By applying the Cauchy, Bessel, and Hölder inequalities and the Lipschitz condition, we have

$$\begin{aligned}\left\|T^{(1)}(\tau)\right\| &= \max_{0\le t\le T}\frac{\left|T_0^{(1)}(\tau)\right|}{4} + \sum_{r,s=1}^{\infty}\begin{pmatrix}\max\limits_{0\le t\le T}\left|T_{crs}^{(1)}(\tau)\right| + \max\limits_{0\le t\le T}\left|T_{csrs}^{(1)}(\tau)\right| \\ +\max\limits_{0\le t\le T}\left|T_{scrs}^{(1)}(\tau)\right| + \max\limits_{0\le t\le T}\left|T_{srs}^{(1)}(\tau)\right|\end{pmatrix} \\ &\le \frac{|\varphi_0(\tau)|}{4} + \sum_{r,s=1}^{\infty}|\varphi_{crs}(\tau)| + |\varphi_{csrs}(\tau)| + |\varphi_{scrs}(\tau)| + |\varphi_{srs}(\tau)| \\ &+\left(\frac{2\pi^2\sqrt{T}+3\sqrt{T}}{3\pi^2}\right)\|b(\alpha,\beta,\tau)\|\left\|T^{(0)}(\tau)\right\| + \left(\frac{2\pi^2\sqrt{T}+3\sqrt{T}}{3\pi^2}\right)M.\end{aligned} \tag{7}$$

where φ_0, φ_{crs}, φ_{csrs}, φ_{scrs}, and φ_{scs} are the Fourier coefficients of the source function. M presents the arbitrary constant.

From the theorem, $T^{(0)}(\tau) \in B$.

Applying for the step N,

$$\begin{aligned}\left\|T^{(N+1)}(\tau)\right\| &= \max_{0\le t\le T}\frac{\left|T_0^{(N)}(\tau)\right|}{4} + \sum_{r,s=1}^{\infty}\begin{pmatrix}\max\limits_{0\le t\le T}\left|T_{crs}^{(N)}(\tau)\right| + \max\limits_{0\le t\le T}\left|T_{csrs}^{(N)}(\tau)\right| \\ +\max\limits_{0\le t\le T}\left|T_{scrs}^{(N)}(\tau)\right| + \max\limits_{0\le t\le T}\left|T_{srs}^{(N)}(\tau)\right|\end{pmatrix} \\ &\le \frac{|\varphi_0(\tau)|}{4} + \sum_{r,s=1}^{\infty}|\varphi_{crs}(\tau)| + |\varphi_{csrs}(\tau)| + |\varphi_{scrs}(\tau)| + |\varphi_{srs}(\tau)| \\ &+\left(\frac{2\pi^2\sqrt{T}+3\sqrt{T}}{3\pi^2}\right)\|b(\alpha,\beta,\tau)\|\left\|T^{(N)}(\tau)\right\| + \left(\frac{2\pi^2\sqrt{T}+3\sqrt{T}}{3\pi^2}\right)M.\end{aligned} \tag{8}$$

We receive $T^{(N)}(\tau) \in B$ since $T^{(N+1)}(\tau) \in B$.

Let us show that $T^{(N+1)}(\tau)$ is converged for $N \to \infty$.

$$\begin{aligned}
\left\|T^{(1)}-T^{(0)}\right\| &\le \tfrac{1}{4}\left(\tfrac{4}{\pi^2}\int_0^t\int_0^\pi\int_0^\pi\Big[h(\alpha,\beta,\tau,T^{(0)})-h(\alpha,\beta,\tau,0)\Big]e^{-\int_\tau^t[(2r)^2+(2s)^2]dt}d\alpha d\beta d\tau\right)\\
&+\tfrac{1}{4}\left(\tfrac{4}{\pi^2}\int_0^t\int_0^\pi\int_0^\pi[h(\alpha,\beta,\tau,0)]e^{-\int_\tau^t[(2r)^2+(2s)^2]dt}d\alpha d\beta d\tau\right)\\
&+\sum_{r,s=1}^{\infty}\tfrac{4}{\pi^2}\int_0^t\int_0^\pi\int_0^\pi\Big[h(\alpha,\beta,\tau,T^{(0)})-h(\alpha,\beta,\tau,0)\Big]e^{-\int_\tau^t[(2r)^2+(2s)^2]dt}\cos(2r\alpha)\cos(2s\beta)d\alpha d\beta d\tau\\
&+\sum_{r,s=1}^{\infty}\tfrac{4}{\pi^2}\int_0^t\int_0^\pi\int_0^\pi[(\alpha,\beta,\tau,0)]e^{-\int_\tau^t[(2r)^2+(2s)^2]dt}\cos(2r\alpha)\cos(2s\beta)d\alpha d\beta d\tau\\
&+\sum_{r,s=1}^{\infty}\tfrac{4}{\pi^2}\int_0^t\int_0^\pi\int_0^\pi\Big[h(\alpha,\beta,\tau,T^{(0)})-h(\alpha,\beta,\tau,0)\Big]e^{-\int_\tau^t[(2r)^2+(2s)^2]dt}\cos(2r\alpha)\sin(2s\beta)d\alpha d\beta d\tau\\
&+\sum_{r,s=1}^{\infty}\tfrac{4}{\pi^2}\int_0^t\int_0^\pi\int_0^\pi[h(\alpha,\beta,\tau,0)]e^{-\int_\tau^t[(2r)^2+(2s)^2]dt}\cos(2r\alpha)\sin(2s\beta)d\alpha d\beta d\tau\\
&+\sum_{r,s=1}^{\infty}\tfrac{4}{\pi^2}\int_0^t\int_0^\pi\int_0^\pi\Big[h(\alpha,\beta,\tau,T^{(0)})-h(\alpha,\beta,\tau,0)\Big]e^{-\int_\tau^t[(2r)^2+(2s)^2]dt}\sin(2r\alpha)\cos(2s\beta)d\alpha d\beta d\tau\\
&+\sum_{r,s=1}^{\infty}\tfrac{4}{\pi^2}\int_0^t\int_0^\pi\int_0^\pi[h(\alpha,\beta,\tau,0)]e^{-\int_\tau^t[(2r)^2+(2s)^2]dt}\sin(2r\alpha)\cos(2s\beta)d\alpha d\beta d\tau\\
&+\sum_{r,s=1}^{\infty}\tfrac{4}{\pi^2}\int_0^t\int_0^\pi\int_0^\pi\Big[h(\alpha,\beta,\tau,T^{(0)})-h(\alpha,\beta,\tau,0)\Big]e^{-\int_\tau^t[(2r)^2+(2s)^2]dt}\sin(2r\alpha)\sin(2s\beta)d\alpha d\beta d\tau\\
&+\sum_{r,s=1}^{\infty}\tfrac{4}{\pi^2}\int_0^t\int_0^\pi\int_0^\pi[h(\alpha,\beta,\tau,0)]e^{-\int_\tau^t[(2r)^2+(2s)^2]dt}\sin(2r\alpha)\sin(2s\beta)d\alpha d\beta d\tau.
\end{aligned}$$

By applying the Cauchy, Bessel, and Hölder inequalities and the Lipschitz condition, we have

$$\left\|T^{(1)}(\tau)-T^{(0)}(\tau)\right\| \le \left(\frac{2\pi^2\sqrt{T}+3\sqrt{T}}{3\pi^2}\right)\|b(\alpha,\beta,\tau)\|\left\|T^{(0)}(\tau)\right\| + \left(\frac{2\pi^2\sqrt{T}+3\sqrt{T}}{3\pi^2}\right)M, \quad (9)$$

where let $A = \left(\frac{2\pi^2\sqrt{T}+3\sqrt{T}}{3\pi^2}\right)\|b(\alpha,\beta,\tau)\|\left\|T^{(0)}(\tau)\right\| + \left(\frac{2\pi^2\sqrt{T}+3\sqrt{T}}{3\pi^2}\right)M$.

Applying for the step N,

$$\left\|T^{(N+1)}(\tau)-T^{(N)}(\tau)\right\| \le \left(\frac{2\pi^2\sqrt{T}+3\sqrt{T}}{3\pi^2}\right)^{(N)}\frac{A}{\sqrt{N!}}\|b(\alpha,\beta,\tau)\|^{(N)}. \quad (10)$$

We obtain $T^{(N+1)}(\tau)\to T^{(N)}(\tau)$.

Let us show that $T^{(N+1)}(\tau)\to T(\tau)$ is converged for $N\to\infty$.

By applying the Cauchy, Bessel, and Hölder inequalities and the Lipschitz condition, we have

$$\begin{aligned}
\left\|T(\tau)-T^{(N+1)}(\tau)\right\| &\le \left(\tfrac{2\pi^2\sqrt{T}+3\sqrt{T}}{3\pi^2}\right)\|b(\alpha,\beta,\tau)\|\left\|T(\tau)-T^{(N+1)}\right\|\\
&+\left(\tfrac{2\pi^2\sqrt{T}+3\sqrt{T}}{3\pi^2}\right)\|b(\alpha,\beta,\tau)\|\left\|T^{(N+1)}(\tau)-T^{(N)}\right\| + \left(\tfrac{2\pi^2\sqrt{T}+3\sqrt{T}}{3\pi^2}\right)M.
\end{aligned} \quad (11)$$

From the Gronwall's inequality,

$$\left\|T(\tau)-T^{(N+1)}(\tau)\right\|^2 \leq \frac{A^2}{\sqrt{N!}}\left(\frac{2\pi^2\sqrt{T}+3\sqrt{T}}{3\pi^2}\right)^2\|b(\alpha,\beta,\tau)\|^{2N}\exp\left(\frac{2\pi^2\sqrt{T}+3\sqrt{T}}{3\pi^2}\right)^2\|b(\alpha,\beta,\tau)\|^2. \tag{12}$$

From Equation (12), we receive $T^{(N+1)}(\tau)\to T(\tau)$.

To show the uniqueness, we receive two solutions for the problem $\{T(\tau), U(\tau)\}$.

By applying the Cauchy, Bessel, and Hölder inequalities and the Lipschitz condition, we have

$$\|T(\tau)-U(\tau)\| \leq \left(\frac{2\pi^2\sqrt{T}+3\sqrt{T}}{3\pi^2}\right)\|b(\alpha,\beta,\tau)\|\|T(\tau)-U(\tau)\| + \left(\frac{2\pi^2\sqrt{T}+3\sqrt{T}}{3\pi^2}\right)M.$$

From the Gronwall's inequality,

$$\|T(\tau)-U(\tau)\|^2 \leq 0\times\exp\left(\frac{2\pi^2\sqrt{T}+3\sqrt{T}}{3\pi^2}\right)^2\|b(\alpha,\beta,\tau)\|^2. \tag{13}$$

We receive $T(\tau)=U(\tau)$. □

4. Stability of Solution

Theorem 2. *Let the assumptions (A)–(B) be satisfied. Then, the problem is constantly dependent on the data.*

Proof.

$$\begin{aligned}
T-\overline{T} &= \tfrac{(\varphi_0-\overline{\varphi_0})}{4}+\sum_{r,s=1}^{\infty}\varphi_{crs}e^{-\int_\tau^t[(2r)^2+(2s)^2]dt}\cos(2r\alpha)\cos(2s\beta)+\sum_{r,s=1}^{\infty}\overline{\varphi_{crs}}e^{-\int_\tau^t[(2r)^2+(2s)^2]dt}\cos(2r\alpha)\cos(2s\beta)\\
&+\sum_{r,s=1}^{\infty}\varphi_{csrs}e^{-\int_\tau^t[(2r)^2+(2s)^2]dr}\cos(2r\alpha)\sin(2s\beta)+\sum_{r,s=1}^{\infty}\overline{\varphi_{csrs}}e^{-\int_\tau^t[(2r)^2+(2s)^2]dt}\cos(2r\alpha)\sin(2s\beta)\\
&+\sum_{r,s=1}^{\infty}\varphi_{scrs}e^{-\int_\tau^t[(2r)^2+(2s)^2]dt}\sin(2r\alpha)\cos(2s\beta)+\sum_{r,s=1}^{\infty}\overline{\varphi_{scmn}}e^{-\int_\tau^t[(2r)^2+(2s)^2]dt}\sin(2r\alpha)\cos(2s\beta)\\
&+\sum_{r,s=1}^{\infty}\varphi_{srs}e^{-\int_\tau^t[(2r)^2+(2s)^2]dt}\sin(2r\alpha)\sin(2r\beta)+\sum_{r,s=1}^{\infty}\overline{\varphi_{smn}}e^{-\int_\tau^t[(2r)^2+(2s)^2]dt}\sin(2r\alpha)\sin(2s\beta)\\
&+\tfrac{1}{4}\begin{pmatrix}\frac{4}{\pi^2}\int_0^t\int_0^\pi\int_0^\pi\left[h(\alpha,\beta,\tau,T)-h(\alpha,\beta,\tau,\overline{T})\right]\\ e^{-\int_\tau^t[(2r)^2+(2s)^2]dt}d\alpha d\beta d\tau\end{pmatrix}\\
&+\sum_{r,s=1}^{\infty}\tfrac{4}{\pi^2}\int_0^t\int_0^\pi\int_0^\pi\left[h(\alpha,\beta,\tau,T)-h(\alpha,\beta,\tau,\overline{T})\right]e^{-\int_\tau^t[(2r)^2+(2s)^2]dt}\cos(2r\alpha)\cos(2s\beta)d\alpha d\beta d\tau\\
&+\sum_{r,s=1}^{\infty}\tfrac{4}{\pi^2}\int_0^t\int_0^\pi\int_0^\pi\left[h(\alpha,\beta,\tau,T)-h(\alpha,\beta,\tau,\overline{T})\right]e^{-\int_\tau^t[(2r)^2+(2s)^2]dt}\cos(2r\alpha)\sin(2s\beta)d\alpha d\beta d\tau\\
&+\sum_{r,s=1}^{\infty}\tfrac{4}{\pi^2}\int_0^t\int_0^\pi\int_0^\pi\left[h(\alpha,\beta,\tau,T)-h(\alpha,\beta,\tau,\overline{T})\right]e^{-\int_\tau^t[(2r)^2+(2s)^2]dt}\sin(2r\alpha)\cos(2s\beta)d\alpha d\beta d\tau\\
&+\sum_{r,s=1}^{\infty}\tfrac{4}{\pi^2}\int_0^t\int_0^\pi\int_0^\pi\left[h(\alpha,\beta,\tau,T)-h(\alpha,\beta,\tau,\overline{T})\right]e^{-\int_\tau^t[(2r)^2+(2s)^2]dt}\sin(2r\alpha)\sin(2s\beta)d\alpha d\beta d\tau.
\end{aligned}$$

By applying the Cauchy, Bessel, and Hölder inequalities and the Lipschitz condition, we have

$$\begin{aligned}\|T-\overline{T}\| &\leq \tfrac{\|\varphi_0-\overline{\varphi_0}\|}{4}+\sum_{r,s=1}^{\infty}\|\varphi_{crs}-\overline{\varphi_{crs}}\|+\|\varphi_{csrs}-\overline{\varphi_{csrs}}\|+\|\varphi_{scrs}-\overline{\varphi_{scrs}}\|+\|\varphi_{srs}-\overline{\varphi_{srs}}\|\\ &+\left(\tfrac{2\pi^2\sqrt{T}+3\sqrt{T}}{3\pi^2}\right)\|b(\alpha,\beta,\tau)\|\|T(\tau)-\overline{T}(\tau)\|+\left(\tfrac{2\pi^2\sqrt{T}+3\sqrt{T}}{3\pi^2}\right)\|b(\alpha,\beta,\tau)\|M,\end{aligned}$$

$$\|\theta-\overline{\theta}\|=\frac{\|\varphi_0-\overline{\varphi_0}\|}{4}+\sum_{r,s=1}^{\infty}\|\varphi_{crs}-\overline{\varphi_{crs}}\|+\|\varphi_{csrs}-\overline{\varphi_{csrs}}\|+\|\varphi_{scrs}-\overline{\varphi_{scrs}}\|+\|\varphi_{srs}-\overline{\varphi_{srs}}\|.$$

From the Gronwall's inequality,

$$\|T-\overline{T}\|^2\leq\|\theta-\overline{\theta}\|^2\times\exp\left(\frac{2\pi^2\sqrt{T}+3\sqrt{T}}{3\pi^2}\right)^2\|b(\alpha,\beta,\tau)\|^2. \tag{14}$$

From Equation (14), $\theta\to\overline{\theta}$. Then, $T\to\overline{T}$. □

5. Numerical Method for Problem

The analytical solution described above, which involves Fourier series, is itself an approximate solution. To validate this approximate solution using another approximate method, namely, the numerical method, we performed a numerical solution following the analytical solution.

In this section, we use an implicit finite difference approximation [14,27,28] of the discretized problems (1)–(4);

$$\frac{1}{\Delta\tau}\left(T_{i,j}^{k+1}-T_{i,j}^{k}\right)=\frac{1}{\Delta\alpha^2}\left(T_{i-1,j}^{k+1}-2T_{i,j}^{k+1}+T_{i+1,j}^{k+1}\right)+\frac{1}{\Delta\beta^2}\left(T_{i,j-1}^{k+1}-2T_{i,j}^{k+1}+T_{i,j+1}^{k+1}\right)+f_{i,j}^{k+1}, \tag{15}$$

$$T_{i,j}^{0}=\varphi_i, \tag{16}$$

$$\begin{aligned}T_{1,j}^{k}&=T_{n\alpha,j}^{k}\\ T_{i,1}^{k}&=T_{i,n\beta},^{k}\end{aligned} \tag{17}$$

$$\begin{aligned}T_{n\alpha,j}^{k}&=\tfrac{T_{2,j}^{k}-T_{n\alpha-1,j}^{k}}{2}\\ T_{i,n\beta}^{k}&=\tfrac{T_{i,2}^{k}-T_{i,n\beta-1}^{k}}{2},\end{aligned} \tag{18}$$

where the computational domain $[0,\pi]\times[0,\pi]\times[0,\tau]$ is discretized as follows:

$\alpha_i=i(\Delta\alpha-1)$, $i=1,2,\ldots\ldots,n\alpha$, $\beta_j=j(\Delta\beta-1)$, $j=1,2,\ldots\ldots,n\beta$, $\tau_k=k\Delta\tau$, and $k=0,1,\ldots\ldots,n$.

Where $\Delta\alpha=\pi/n\alpha$, $\Delta\beta=\pi/n\beta$, and $\Delta\tau=\tau/n$ are the space α direction, space β direction, and time steps, respectively. nx, ny, and n are three positive integers.

$T_{i,j}^{k}=T(\alpha_i,\beta_j,\tau_k)$, and $f_{i,j}^{k}=T(\alpha_i,\beta_j,\tau_k)$.

In order to define periodic boundary conditions (Equations (17) and (18)) for the implicit finite difference scheme, a one-dimensional schematic figure with numerical meshes is represented in Figure 3. Point-1 and point-nα are the boundary points of the one-dimensional solution domain. When determining spatial discretization with a finite difference scheme, the used finite difference formulations are defined as

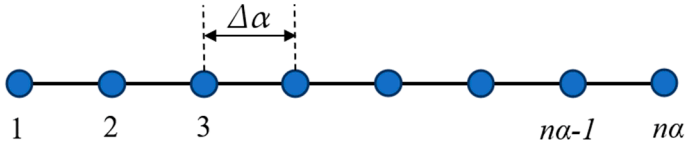

Figure 3. One-dimensional schematic figure with numerical meshes.

$$\ldots = r_\alpha \begin{bmatrix} T_{n\alpha} - 2T\alpha_1 + T_2 \\ T_1 - 2T\alpha_2 + T_3 \\ \ldots \\ T_{n\alpha-1} - 2T\alpha_{n\alpha} + T_1 \end{bmatrix}, \tag{19}$$

where $r_\alpha = \Delta\tau/\Delta\alpha^2$, and the coefficient matrix can be rewritten for one-dimensional solution domain.

$$r_\alpha \begin{bmatrix} -2 & 1 & 0 & \ldots & 0 & 1 \\ 1 & -2 & 1 & 0 & \ldots & 0 \\ & \ddots & \ddots & \ddots & & \\ & & \ddots & \ddots & \ddots & \\ 0 & \ldots & 0 & 1 & -2 & 1 \\ 1 & 0 & \ldots & 0 & 1 & -2 \end{bmatrix}, \tag{20}$$

This one-dimensional formulation and coefficient matrix can be extended to a two-dimensional solution domain. A two-dimensional schematic figure with numerical meshes (9 finite difference meshes) is represented in Figure 4. Of course, a matrix is constructed for 9 finite difference meshes; therefore, the matrix size is 9×9. Point-1, -2, and -3 are periodic with Point-7, -8, and -9, respectively, in the β-direction. Point-1, -4, and -7 are periodic with -3, -6, and -9, respectively, at the α direction. The coefficient matrix can be written as

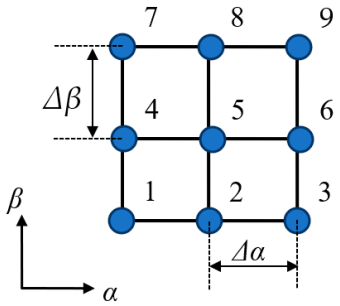

Figure 4. Two-dimensional schematic figure with numerical meshes.

$$\begin{bmatrix} -\left(1+2r_\alpha+2r_\beta\right) & r_\alpha & r_\alpha & r_\beta & 0 & 0 & r_\beta & 0 & 0 \\ r_\alpha & -\left(1+2r_\alpha+2r_\beta\right) & r_\alpha & 0 & r_\beta & 0 & 0 & r_\beta & 0 \\ r_\alpha & r_\alpha & -\left(1+2r_\alpha+2r_\beta\right) & 0 & 0 & r_\beta & 0 & 0 & r_\beta \\ r_\beta & 0 & 0 & -\left(1+2r_\alpha+2r_\beta\right) & r_\alpha & r_\alpha & r_\beta & 0 & 0 \\ 0 & r_\beta & 0 & r_\alpha & -\left(1+2r_\alpha+2r_\beta\right) & r_\alpha & 0 & r_\beta & 0 \\ 0 & 0 & r_\beta & r_\alpha & r_\alpha & -\left(1+2r_\alpha+2r_\beta\right) & 0 & 0 & r_\beta \\ r_\beta & 0 & 0 & r_\beta & 0 & 0 & -\left(1+2r_\alpha+2r_\beta\right) & r_\alpha & r_\alpha \\ 0 & r_\beta & 0 & 0 & r_\beta & 0 & r_\alpha & -\left(1+2r_\alpha+2r_\beta\right) & r_\alpha \\ 0 & 0 & r_\beta & 0 & 0 & r_\beta & r_\alpha & r_\alpha & -\left(1+2r_\alpha+2r_\beta\right) \end{bmatrix}, \tag{21}$$

where $r_\beta = \Delta\tau/\Delta\beta^2$. If a large number of meshes are used, the matrix can be extended in a same way. For example, if we have 20 meshes in both the α and β directions, our matrix size will be 400×400, the total number of elements in the matrix is 160,000, and our matrix can be constructed in the same manner to define points of periodic boundary conditions and points of inner (no periodic boundary condition points).

The methods that are described above were implemented in-house using finite difference code via the FORTRAN Programming language. The obtained results were visualized using the program Tecplot 360 [34].

Example 1. *Consider the heat diffusion problem with heat sources (1)–(4):*

The temperature distribution is given as

$$T(\alpha, \beta, \tau) = e^{\tau^2}(5 + \cos 2\alpha + \cos 2\beta),$$

with the heat source,

$$h(\alpha, \beta, \tau) = 2e^{\tau^2}(\tau + 2)(\cos 2\alpha + \cos 2\beta),$$

and with the initial condition,

$$\phi(\alpha, \beta) = 5 + \cos 2\alpha + \cos 2\beta.$$

We determined the time step size to be $\Delta\tau = 0.005s$. The discretization of spaces or mesh sizes in the α and β directions are considered equal ($\Delta\alpha = \Delta\beta$). To determine mesh sizes in the α and β directions, a grid independence study was conducted. For the grid-independence study, fifteen different grid resolutions are used.

In the α and β directions, the same numbers of grid were used because of the equal grid size ($\Delta\alpha = \Delta\beta$) being considered. In Figure 5, two different grid resolutions are illustrated among fifteen different resolutions. The displayed grid numbers are 2500 and 6400. For every grid resolution, we observed an area-weighted averaged value of temperature for the whole solution domain. Figure 6 shows the grid-independent study of area-weighted averaged value of temperature. According to Figure 6, the mesh number of 6400 is taken as the grid independent mesh number. In this case, eighty grids are used for the α and β directions; therefore, our mesh size for the α and β directions is obtained as 0.03926875 m.

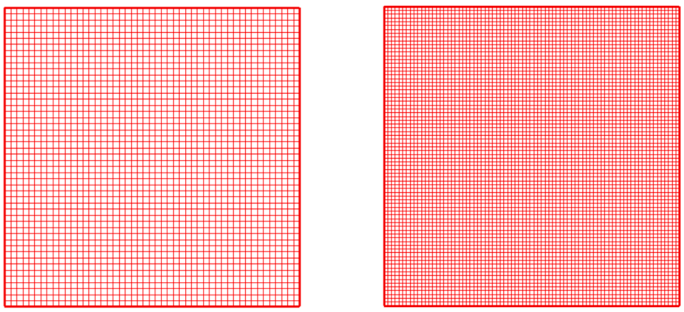

Figure 5. Two different grid resolutions.

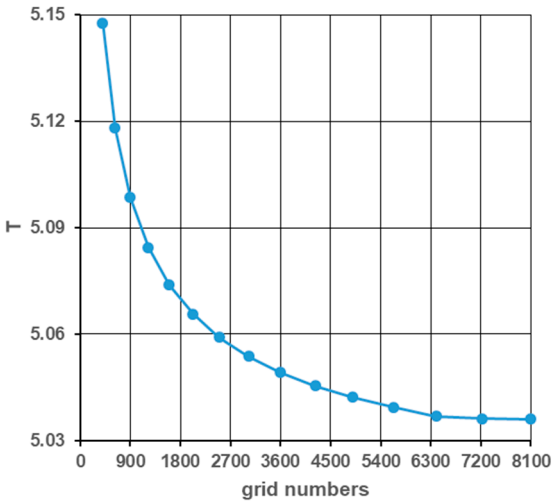

Figure 6. Grid independence study of area-weighted averaged value of temperature.

Figure 7 shows the (a) exact and (b) numerical solutions for the temperature with the time at 0.1 s. The exact and numerical solutions are paraboloidal. Maximum and minimum temperature values are observed at corners and at the middle of the solution domain, respectively. Due to periodic boundary conditions at the side of solution domain, temperatures are the same at the side of the solution domain. Also, the exact and numerical solutions are quite similar.

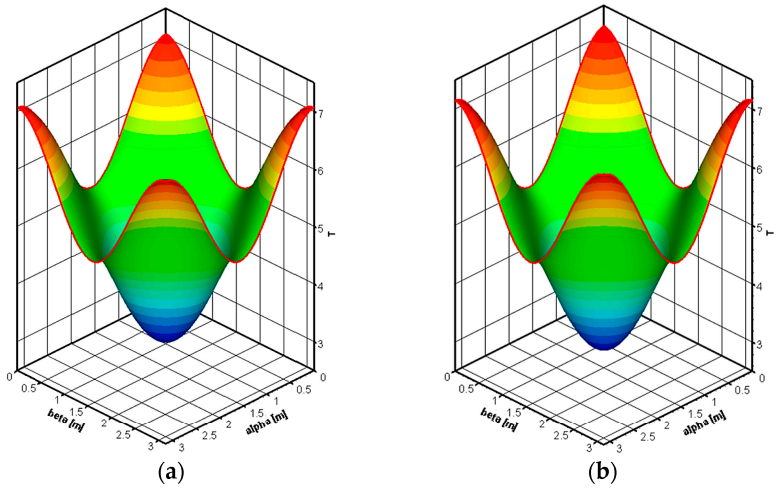

Figure 7. The (**a**) exact and (**b**) numerical solutions for $T(\alpha, \beta, 0.1\text{ s})$.

Figure 8 depicts the (a) absolute error and (b) relative absolute error for the temperature with the time at 0.1 s. Absolute error is defined as the absolute value of the difference between the exact solution value and the numerical solution. According to Figure 7a, the maximum absolute error is observed at center of the solution domain, and the absolute error is higher at the corners of the solution domain. At the center of the solution domain, an approximate absolute error of 0.1 is observed. The relative absolute error is the ratio of the absolute error to the exact solution. The magnitude of the absolute error in terms of the exact solution is determined using the relative absolute error. Similar to the absolute error, the maximum relative error, which is 0.03, is observed at the center of the solution domain. At the corners of the solution domain, the relative absolute error is in the order of 0.01. As time progresses, the absolute error and relative absolute error remain in the same order, and these errors are reasonable.

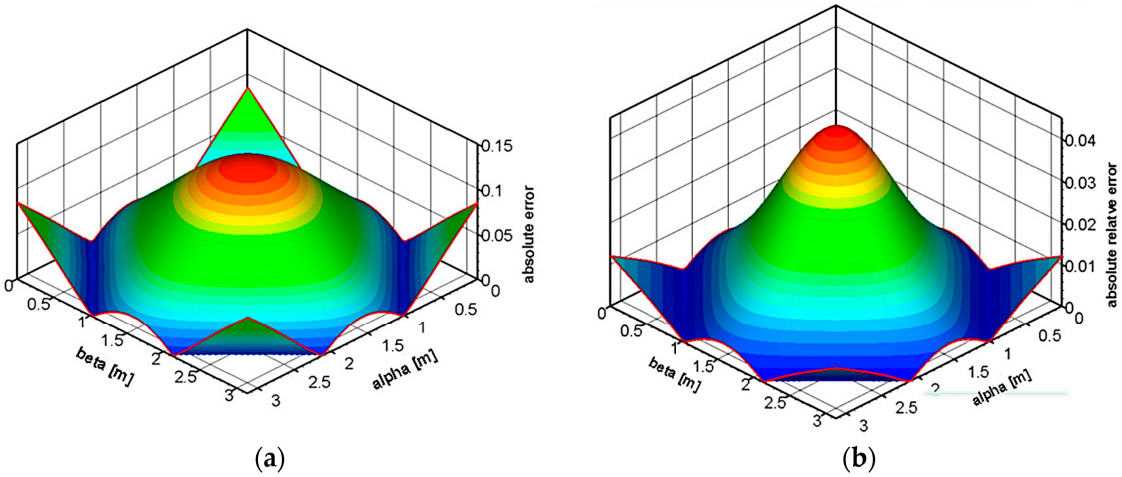

Figure 8. The (**a**) absolute error and (**b**) relative absolute error of $T(\alpha, \beta, 0.1\text{ s})$.

Figure 9 presents the numerical predictions of the temperature distributions at the times (a) 0.1 s, (b) 0.25 s, and (c) 0.5 s. As one can see, the temperature distributions at these specific times are paraboloid. The concavity of the paraboloid increases with time. The minimum and the maximum values of the temperature appear at the center and corners of the solution domain, respectively, at all times.

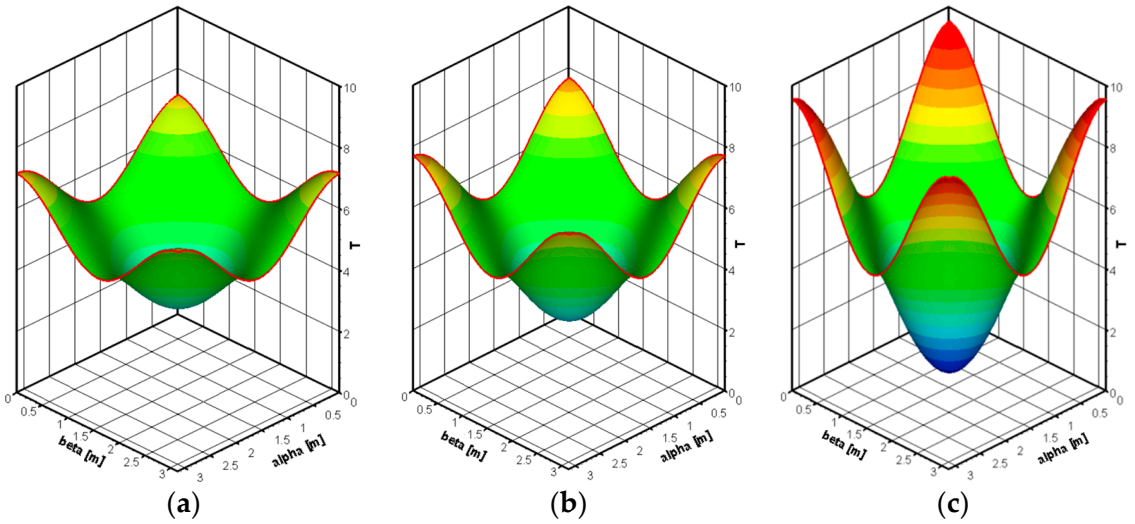

Figure 9. Numerical predictions of T distributions at times (**a**) 0.1 s, (**b**) 0.25 s, and (**c**) 0.5 s.

In order to visualize all time intervals in a single figure, Figure 10 illustrates the temperature distribution over a time range from 0 s to 0.5 s. Paraboloids are not shown in this representation. Maximum and minimum temperature values are observed at the corners and center of the solution domain, respectively, at all times. Additionally, with increasing time, the temperature values of the corners increase, and the temperature values of the centers decrease.

Fundamentally, this study has focused on the analytical and numerical solution of a two-dimensional, time-dependent system with heat generation. However, it has not extensively delved into the specific applications of this problem. Nevertheless, the results obtained from this problem could be applied in a suitable context by other researchers.

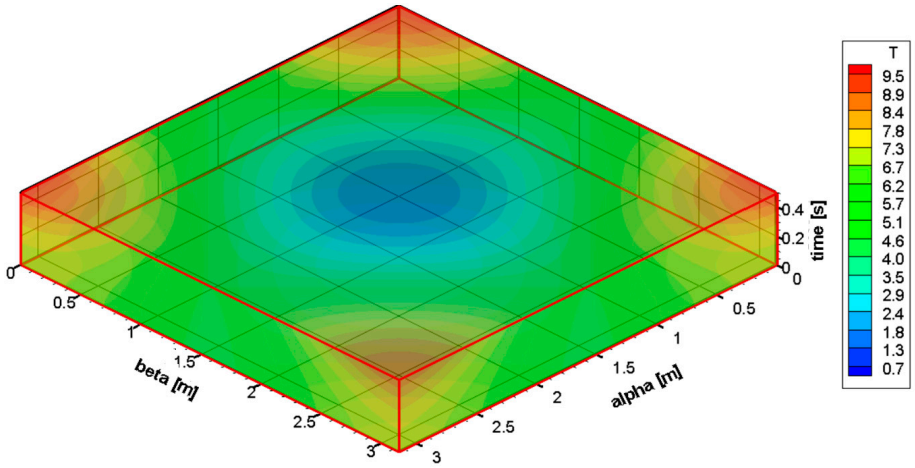

Figure 10. Distribution of temperature over a time range from 0 s to 0.5 s.

6. Limitations and Future Scope

This problem is characterized by specific limits and assumptions, constituting a time-dependent, two-dimensional heat diffusion problem with a heat source and periodic boundary conditions. Due to the applied periodic boundary conditions, temperature distributions at the edges and corners of the solution domain are found to be identical. In systems with heat generation, the temperature profile at a specific time tends to exhibit a parabolic shape. As time progresses, the slope of this parabolic nature also increases.

For future studies, this problem can be expanded into three dimensions, enabling an investigation into the influence of the third dimension on heat diffusion. As an analytical

solution method, the maximum principle and/or the operation method may be considered in future work. For numerical solutions, various schemes can be employed in the finite difference method, or alternative methods such as the finite volume method and the lattice Boltzmann methods could be explored.

7. Conclusions

An analytical and numerical investigation of a two-dimensional heat diffusion problem with a heat source has been conducted. This problem is a quasi-linear parabolic problem, and we used an initial condition and a periodic boundary condition to determine the temperature in the solution domain. Due to the problem being nonlinear, Picard's successive approximation theorem is used. Under certain conditions of natural regularity and consistency imposed upon the input data, we establish the existence, uniqueness, and constant dependence of the solution on the data using the generalized Fourier method. An implicit finite difference scheme is employed for the numerical solution. The number of numerical meshes, where results do not change, is determined according to the grid independence study. In light of the analytical and numerical solution, the distribution of the temperature forms a paraboloid at a certain time. With increasing time, the concavity of the parabola increases. At the time of 0.1 s, the maximum absolute error and relative error occur in the middle of the solution domain at 0.1 and 0.03, respectively. Therefore, we can conclude that the analytical solution and numerical solutions are closely aligned. Also, with increasing time, the degrees of absolute and relative absolute remain the same. For future studies, extending the problem to three dimensions can investigate the influence of the third dimension on heat diffusion. Analytically, considering the maximum principle and/or the operation method is an option. Numerically, exploring various schemes in the finite difference method or alternative methods, such as finite volume and the lattice Boltzmann methods, is possible.

Author Contributions: Conceptualization, İ.B. and E.A.; methodology, İ.B.; software, E.A.; validation, E.A; formal analysis, İ.B.; investigation, İ.B. and E.A.; resources, İ.B.; data curation, E.A.; writing—original draft preparation, E.A.; writing—review and editing, İ.B. and E.A.; visualization, E.A.; supervision, İ.B.; All authors have read and agreed to the published version of the manuscript.

Funding: This research received no external funding.

Data Availability Statement: Data are contained with this article.

Conflicts of Interest: The authors declare no conflicts of interest.

Nomenclature

$\varphi(\alpha,\beta)$	is the initial temperature.
$\varphi_0(\tau)$, $\varphi_{crs}(\tau)$, $\varphi_{csrs}(\tau)$, $\varphi_{scrs}(\tau)$, $\varphi_{srs}(\tau)$	are the Fourier coefficients of initial condition.
$T(\alpha,\beta,\tau)$	is the temperature distribution.
$h(\alpha,\beta,\tau,T)$	is a source function.
$h_0(\tau)$, $h_{crs}(\tau)$, $h_{csrs}(\tau)$, $h_{scrs}(\tau)$, $h_{srs}(\tau)$	are the Fourier coefficients of source function.
$T_0(\tau)$, $T_{crs}(\tau), T_{csrs}(\tau), T_{scrs}(\tau), T_{srs}(\tau)$	are the Fourier coefficients.
M	is an arbitrary constant.
$b(\alpha,\beta,\tau)$	is a Lipschitz coefficient.
L_2	is a converged space.
N	is an iterative number.

References

1. Permikin, D.V.; Zverev, V.S. Mathematical model on surface reaction diffusion in the presence of chemical reaction. *Int. J. Heat Mass Transf.* **2013**, *57*, 215–221. [CrossRef]
2. Tredenick, E.C.; Farewell, T.W.; Forster, W.A. Modeling of diffusion of a hydrophilic ionic fertilizer in plant cuticles: Surfactant and hygroscopic effects. *Front. Plant Sci.* **2018**, *9*, 1888. [CrossRef] [PubMed]
3. Canon, J.R. The solution of the heat equation subject to the specification of energy. *Q. Appl. Math.* **1963**, *21*, 155–160. [CrossRef]

4. Canon, J.R. Determination of an unknown heat source from overspecified boundary data. *SIAM J. Numer. Anal.* **1968**, *5*, 275–286. [CrossRef]
5. Zhu, Q.; Tran, H.; Yang, H. Heat conduction: Mathematical modeling and experimental data. *J. Emerg. Investig.* **2021**, *4*, 1–4. [CrossRef] [PubMed]
6. Venkatesha, P.; Eunice, G.B.; Akshaya, B.; Arya Kumari, S. Mathematical modeling of population growth. *Int. J. Sci. Eng. Manag.* **2017**, *2*, 117–121.
7. Avey, M.; Fantuzzi, N.; Sofiyev, A. Mathematical modeling and analytical solution of thermoelectric stability problem of functionally graded nanocomposite cylinders within different theories. *Mathematics* **2022**, *10*, 1081. [CrossRef]
8. Turnbull, A.; Ferriss, D.H. Mathematical modelling of the electrochemistry in corrosion fatigue cracks in structural steel cathodically protected in sea water. *Corros. Sci.* **1986**, *26*, 601–628. [CrossRef]
9. Dehghan, M. Implicit locally one-dimensional methods for two-dimensional diffusion with a non-local boundary condition. *Math. Comput. Simul.* **1999**, *49*, 331–349. [CrossRef]
10. Siddique, M. Solving two-dimensional diffusion equations with nonlocal boundary conditions by a special class of Padé approximants. *Syst. Cybern. Inform.* **2010**, *8*, 23–29.
11. Mohebbi, A. A numerical algorithm for determination of a control parameter in two-dimensional parabolic inverse problems. *Acta Math. Appl. Sin. Engl. Ser.* **2015**, *31*, 213–224. [CrossRef]
12. Li, Q.; Yin, T.; Li, X.; Shu, R. Experimental and numerical investigation on thermal damage of granite subjected to heating and cooling. *Mathematics* **2021**, *9*, 3027. [CrossRef]
13. Bergmann, T.L.; Lavine, A.S.; Incropera, F.P.; Dewitt, D.P. *Fundamentals of Heat and Mass Transfer*, 7th ed.; John Wiley & Sons: Danver, MA, USA, 2011.
14. Baglan, I.; Kanca, F. Two-dimensional inverse quasilinear parabolic problems with periodic boundary conditions. *Appl. Anal.* **2019**, *98*, 1549–1565. [CrossRef]
15. Mohamad, A.A. *Lattice Boltzmann Method Fundamentals and Engineering Applications with Computer Codes*, 2nd ed.; Springer: London, UK, 2019.
16. Afshar, S.; Soltanalizadeh, B. Solution of the two-dimensional second-order diffusion equation with nonlocal boundary conditions. *Int. J. Pure Appl. Math.* **2014**, *94*, 119–131. [CrossRef]
17. Rao, Y.; Zhang, Y.; Xu, Y.; Ke, H. Experimental study and numerical analysis of heat transfer enhancement and turbulent flow over shallowly dimples channel surfaces. *Int. J. Heat Mass Transf.* **2020**, *160*, 120195. [CrossRef]
18. Hill, G.W. On the part of the motion of the lunar perigee which is a function of the mean motions of the sun and moon. *Acta Math* **1886**, *8*, 1–36. [CrossRef]
19. Kanca, F.; Baglan, I. Solution of the boundary-value problem of heat conduction with parabolic conditions. *Ukr. Math. J.* **2020**, *72*, 232–245. [CrossRef]
20. Kanca, F.; Baglan, I. Analysis for two-dimensional inverse quasilinear parabolic problem by Fourier Method. *Inverse Probl. Sci. Eng.* **2021**, *29*, 1912–1945. [CrossRef]
21. Yasmin, H.; Aljahdaly, N.F.; Saeed, A.M.; Shah, R. Probing families of optical soliton solutions in fractional perturbed Radhakrishnan-Kundu-Lakshmanan model with improved versions of extended direct algebraic method. *Fractal Fract.* **2023**, *7*, 512. [CrossRef]
22. Yasmin, H.; Aljahdaly, N.F.; Saeed, A.M.; Shah, R. Investigating families of solution solutions for the complex structured coupled fractional Biswas-Arshed model in Birefringent fibers using a novel analytical technique. *Fractal Fract.* **2023**, *7*, 491. [CrossRef]
23. Yasmin, H.; Aljahdaly, N.F.; Saeed, A.M.; Shah, R. Investigating symmetric soliton solutions for the fractional coupled Konno-Onno system using improved versions of a novel analytical technique. *Mathematics* **2023**, *11*, 2686. [CrossRef]
24. Morton, K.W.; Mayers, D.F. *Numerical Solution of Partial Differential Equation*, 2nd ed.; Cambridge University Press: Cambridge, UK, 2005.
25. Dmitriev, V.G.; Danilin, A.N.; Popova, A.R.; Pshenichnova, N.V. Numerical analysis of deformation characteristics of elastic inhomogeneous rotational shells at arbitrary displacements and rotating angles. *Computation* **2022**, *10*, 184. [CrossRef]
26. Benim, A.C.; Zinser, W. Investigation into finite element analysis of confined turbulent flows using a k-ε model of turbulence. *Compt. Methods Appl. Mech. Eng.* **1985**, *51*, 507–523. [CrossRef]
27. Benim, A.C. Finite element analysis of confined turbulent swirling flows. *Int. J. Num. Meth. Fluids* **1990**, *11*, 697–717. [CrossRef]
28. Versteeg, H.K.; Malalasekera, W. *An Introduction to Computational Fluid Dynamics*, 2nd ed.; Pearson, Prentice Hall: London, UK, 2007.
29. Chen, S.; Doolen, G.D. Lattice Boltzmann method for fluid flows. *Annu. Rev. Fluid Mech.* **1998**, *30*, 329–364. [CrossRef]
30. Succi, S. *The Lattice Boltzmann Equation for Fluid Dynamics and Beyond*; Oxford University Press: Oxford, UK, 2001.
31. Denghan, M. Efficient techniques for the second-order parabolic equation subject to nonlocal specifications. *Appl. Num. Math.* **2005**, *12*, 39–62. [CrossRef]
32. Baglan, I.; Kanca, F.; Mishra, V.N. Determination of an unknown heat source from integral overdetermination condition. *Iran J. Sci. Technol. Trans. Sci.* **2018**, *42*, 1373–1382. [CrossRef]
33. Hamila, R.; Chaabane, R.; Askri, F.; Jemni, A.; Nasrallah, S.B. Lattice Boltzmann method for heat transfer problems with variable thermal conductivity. *Int. J. Heat Technol.* **2017**, *35*, 313–324. [CrossRef]
34. Tecplot Inc. *Tecplot 360 2008 Release 1*; Tecplot Inc.: Bellevue, WA, USA, 2007.

computation

MDPI

Article

Overlapping Grid-Based Spectral Collocation Technique for Bioconvective Flow of MHD Williamson Nanofluid over a Radiative Circular Cylindrical Body with Activation Energy

Musawenkosi Patson Mkhatshwa

Department of Mathematics and Applied Mathematics, University of Limpopo, Private Bag X1106, Sovenga 0727, South Africa; patsonmkhatshwa@gmail.com; Tel.: +27-15-268-2906

Abstract: The amalgamation of motile microbes in nanofluid (NF) is important in upsurging the thermal conductivity of various systems, including micro-fluid devices, chip-shaped micro-devices, and enzyme biosensors. The current scrutiny focuses on the bioconvective flow of magneto-Williamson NFs containing motile microbes through a horizontal circular cylinder placed in a porous medium with nonlinear mixed convection and thermal radiation, heat sink/source, variable fluid properties, activation energy with chemical and microbial reactions, and Brownian motion for both nanoparticles and microbes. The flow analysis has also been considered subject to velocity slips, suction/injection, and heat convective and zero mass flux constraints at the boundary. The governing equations have been converted to a non-dimensional form using similarity variables, and the overlapping grid-based spectral collocation technique has been executed to procure solutions numerically. The graphical interpretation of various pertinent variables in the flow profiles and physical quantities of engineering attentiveness is provided and discussed. The results reveal that NF flow is accelerated by nonlinear thermal convection, velocity slip, magnetic fields, and variable viscosity parameters but decelerated by the Williamson fluid and suction parameters. The inclusion of nonlinear thermal radiation and variable thermal conductivity helps to enhance the fluid temperature and heat transfer rate. The concentration of both nanoparticles and motile microbes is promoted by the incorporation of activation energy in the flow system. The contribution of microbial Brownian motion along with microbial reactions on flow quantities justifies the importance of these features in the dynamics of motile microbes.

Keywords: Williamson nanofluid; motile microorganisms; nonlinear convection; nonlinear radiation; activation energy; cylindrical surface; overlapping grid; bivariate spectral local linearisation method

Citation: Mkhatshwa, M.P. Overlapping Grid-Based Spectral Collocation Technique for Bioconvective Flow of MHD Williamson Nanofluid over a Radiative Circular Cylindrical Body with Activation Energy. *Computation* **2024**, *12*, 75. https://doi.org/10.3390/computation12040075

Academic Editors: Ali Cemal Benim, Abdulmajeed A. Mohamad, Sang-Ho Suh, Rachid Bennacer, Paweł Oclon and Jan Taler

Received: 7 March 2024
Revised: 1 April 2024
Accepted: 3 April 2024
Published: 5 April 2024

1. Introduction

Investigation of non-Newtonian fluidic models is a subject of curiosity for many researchers because of their nature, engineering, and industrial solicitations, including polymeric melt, crystal growing, dilute polymer solutions, drilling muds, cosmetic products, foods, coated sheets, and glass blowing. From a previous analysis, it is clear that many constitutional correlations have been put forward to flaunt the knotty traits of non-Newtonian fluids. Such entrenchment emerges from the view that the indispensable features of non-Newtonian liquids cannot be scrutinized using the classical Navier–Stokes equations, which are solely applicable to determine Newtonian fluid traits. Numerous researchers have investigated the behaviour of non-Newtonian fluids through various geometrical configurations. Among these geometries we have cylindrical surfaces, which play a significant role in polymer processing systems. Nazar et al. [1] investigated mixed convective flow of micropolar fluids through a horizontal circular cylinder for the case of constant surface temperature. Madhavi et al. [2–4] and Gaffar et al. [5] scrutinized third-grade fluid flow through a horizontal cylinder surface. Gaffar et al. [6] also explored boundary layer flow

and the heat relocation of tangent hyperbolic fluid across a horizontal circular cylindrical body with first-order thermal and velocity slip. Nagaraj et al. [7] investigated flow and heat relocation in non-Newtonian Eyring–Powell fluids over a horizontal circular cylindrical surface by taking into account suction/blowing and heat convective boundary constraints. Zokri et al. [8] studied the flow of non-Newtonian Jeffrey fluids over a horizontal circular cylinder in the company of mixed convection and viscous heating effects.

The non-Newtonian fluid model for Williamson fluids was introduced by Williamson [9], and it has been confirmed to be among the predominantly crucial non-Newtonian fluids due to its low viscosity and higher shear rate. In particular, the Williamson fluid model predicts that the effective viscosity will decline monotonically with an elevation in the shear rate and vice versa. This pseudo-plastic fluid deportment is one instance of the various ways in which this non-Newtonian liquid might be usable in modern technology and industry. The applicability of Williamson fluid in technologies and industries has generated a major effect on manufacturing processes. Thus, many scholars have been involved in the exploration of features of Williamson fluids in the improvement of the thermal features of this fluid. However, just like any other non-Newtonian fluid, the Williamson fluid is still incapable of fulfilling the demand for superior extremity heat transport due to its dissatisfying thermal conductivity. To upsurge thermal conductivity as well as enhance heat transport performance, the theory of adding nanoparticles (NPs) into the non-Newtonian fluid has proven to be one of the more contemporaneously innovative concepts in the recent past years. The mixture of NPs and the host fluid is called a nanofluid (NF) [10]. Various models have been put forward to scrutinize NFs, of which the Buongiorno NF model [11] is one of them. The Buongiorno [11] NF model is a two-phase model that focuses on Brownian motion and thermophoresis impacts, and this model plays a significant role when the movement of NPs remarkably impacts the fluid flow. Another notable model is the Tiwari–Das NF model [12], which is a single-phase model that is concerned with studying the volume fraction of NPs. Rashad et al. [13] used the Buongiorno NF model to analyze the combined convection flow of a Newtonian NF across a horizontal circular cylinder immersed in a penetrable medium with heat-convective boundary conditions. Using the Tiwari–Das NF model, Zokri [14] also studied the mixed convection flow of Jeffrey NFs past a horizontal cylinder by accounting for suction/injection and heat convective boundary constraints. Merkin [15] initiated the study of fluid flow moving through a horizontal circular cylinder with mixed convection, and many studies were reported thereafter. Mixed convection plays a major role in enhancing the thermal features of heat transport. It also accounts for the general instance of convection that takes place in various industrial and technological solicitations including electronic device cooling, solar energy storage, drying technology, food processing, and float glass manufacturing.

In many engineering, technological, and industrial processes, the disparity between the surface and ambient (free stream) temperatures need not be small. In the instance of huge temperature variations, the fluid and heat transfer features are remarkably influenced. In such instances, accounting for linear Boussinesq approximation and classical linear Rosseland approximation in the fluid and heat transport equations, respectively, is inadequate, and that can lead to a reduction in the quality of the results. Consequently, it is mandatory to account for nonlinear Boussinesq approximations and nonlinear Rosseland thermal radiation in such instances so that accurate results are achieved. Practical examples of nonlinear thermal convection include engineering, geophysical, and astrophysical flows. On the other hand, nonlinear Rosseland heat radiation plays a fundamental role in manufacturing processes with larger temperature differences. EL-Zahar et al. [16] employed the modified Tiwari–Das NF to investigate the magnetized mixed convective flow of hybrid NFs across a horizontal circular cylindrical surface by considering nonlinear thermal radiation. Basha et al. [17] used the Buongiorno NF model to analyze the mixed convection flow of tangent hyperbolic NFs through a horizontal circular cylinder by accounting for nonlinear Boussinesq estimation. Activation energy (AE) is the minimal quantity of energy needed by chemical reactants to go through a chemical reaction. Mass transport procedures

together with chemical reactions with Arrhenius AE emerge in areas of chemical engineering and food processing. Huang [18] studied free convective flow via a horizontal circular cylindrical surface immersed in a penetrable medium with AE and suction/injection.

Bioconvection is a phenomenon whereby the flow and thermal features of the fluid are impacted by the existence of microbes. Bioconvection flows emerge in various fascinating solicitations in environmental systems, fuel cells, and biological polymer synthesis [19]. The upward swimming microorganisms give rise to unstable density stratification, and because of that, bioconvection takes place in the fluid. In other words, bioconvection is compelled by instability that emerges due to self-propelled microorganisms swimming to and interacting with NPs and buoyancy [20–23]. The amalgamation of bioconvection and NF has yielded some exceptional results in micro-fluidic devices such as micro-channels and micro-rectors. Kuznestov and Avramenko [24] initiated the use of NPs to scrutinize the bioconvection of gyrotactic microorganisms. Hill and Pedly [25] provided a review study of the hydrodynamics of bioconvection. Through the use of Navier–Stokes equations, Allouit et al. [26] investigated the bioconvection of gyrotactic microorganisms via a vertical cylinder. Mallikarjuna [27] scrutinized the mixed bioconvective flow of a NF containing gyrotatic microorganisms from a vertical slender cylindrical surface. Rashad et al. [28] investigated mixed the bioconvective flow of a Newtonian NF comprising gyrotactic microbes through a horizontal circular cylinder in the company of heat-convective and zero mass flux boundary conditions.

The literature review, particularly investigations by Rashad et al. [13,28], reveals that there is no study on the bioconvective flow of non-Newtonian Williamson NFs in thermal and mass relocation mechanisms over a cylindrical surface with the following research gaps that result in the novelties of the present analysis.

- The complex rheology features of Williamson materials are examined using the modified Buongiorno NF model in the presence of an applied magnetic field, porous media, and variable fluid viscosity.
- Nonlinear Boussinesq approximation and nonlinear Rosseland thermal radiation are incorporated in the momentum and energy equations, respectively, to cater for large temperature differences.
- Heat generation/assimilation and variable thermal conductivity are incorporated in the heat equation for the characterization of energy transfer mechanisms.
- The modified Arrhenius AE, chemical and microbial reactions, NP and microbial Brownian diffusions are considered in the NP concentration and motile microorganism equations for characterization of mass and motile microbes transfer mechanisms.

The main objective of the current analysis is to scrutinize the bioconvective flow, heat, mass, and motile microbes transfer features of the magnetized Williamson NF model containing motile gyrotactic microbes through a horizontal circular cylindrical surface encased in a porous medium. The consequences of nonlinear thermal convection, nonlinear heat radiation, heat generation/assimilation, varying fluid attributes, AE with chemical and microbial reactions, and Brownian motion for both NPs and motile microbes are further elaborated as novelties. There has been limited research conducted on the influence of microbial Brownian motion in conjunction with microbial reactions on fluid flow properties [29,30]. Moreover, the entire flow analysis has been subjected to first-order velocity slips, suction/injection, and heat-convective and zero mass flux constraints at the boundary. The consideration of mixed convective flow of non-Newtonian NF through a heated horizontal cylinder plays a fundamental role in geological, technological, and industrial processes including the thermal recuperation of oil, geothermal reservoirs, insulating wires, drag reduction, thrust bearing, assessment of aquifers, and underground nuclear waste storage. An efficient and accurate overlapping grid-based multi-domain bivariate spectral local linearization method (OMD-BSLLM) [31–33] is executed to procure approximate solutions to the complex fluid flow model. The impact of various pertinent variables on the flow profiles and physical quantities of engineering attentiveness is scrutinized through graphical representations.

2. Mathematical Modeling

We contemplate the two-dimensional, laminar, steady, incompressible, and viscous nonlinear mixed convective boundary layer flow of Williamson NFs comprising gyrotactic microbes that swim from a horizontal circular cylindrical surface immersed in a porosity medium. The pictorial representation of the flow model and the physical coordinate system is depicted in Figure 1, where a is the radius of the cylinder. The $\bar{x}$ and $\bar{y}$ coordinates are, respectively, measured alongside the surface of the cylinder, resuming from the lower stagnation point, and normal to the cylinder. The uniform magnetic field intensity is enforced parallel to the fluid movement. Fluctuations in density for the buoyant expression are established by utilizing non-linear Boussinesq estimation, and the basic fluid and NPs are in a thermal equilibrium state. The surface of the cylinder is heated via convection from the heated fluid at the temperature T_f, which produces a heat transport coefficient h_f. The cylinder's surface is maintained at a constant temperature T_f, which is assumed to be greater than the free stream (ambient) temperature $(T_f > T_\infty)$ for the warmed surface (aiding flow) and lower than the ambient temperature $(T_f < T_\infty)$ for the cooled surface (reversing flow). The velocity of the external flow is represented by $\bar{u}_e(\bar{x}) = U_\infty \sin\left(\frac{\bar{x}}{a}\right)$, where U_∞ is the ambient velocity. The surface of the cylinder is also maintained at a uniform density of motile microbes n_w, whereas the uniform NP volume fraction and density of motile microbes far-off from the cylindrical surface are signified by φ_∞ and n_∞, respectively. Due to the absence of agglomeration and accumulation of NPs, the NF suspension is dilute (i.e homogeneous dispersion is attained). Furthermore, it is presumed that NPs have no impact on the direction and velocity of the gyrotactic microbes' swimming. It is worth noting that the velocity for motile microbes, NPs, and the basic fluid is the same. For the characterization of heat transportation, features of nonlinear thermal radiation, heat sink/source, and variable thermal conductivity are involved in the heat (energy) equation. However, for the characterization of mass and motile microbes transportation, features of AE, chemical and microbial reactions, and NP and microbial Brownian motions are invoked in the equations of NP species concentration and motile microbe density conservation. In view of the aforementioned presuppositions, the entire fundamental equations of the flow problem take the form [13,28].

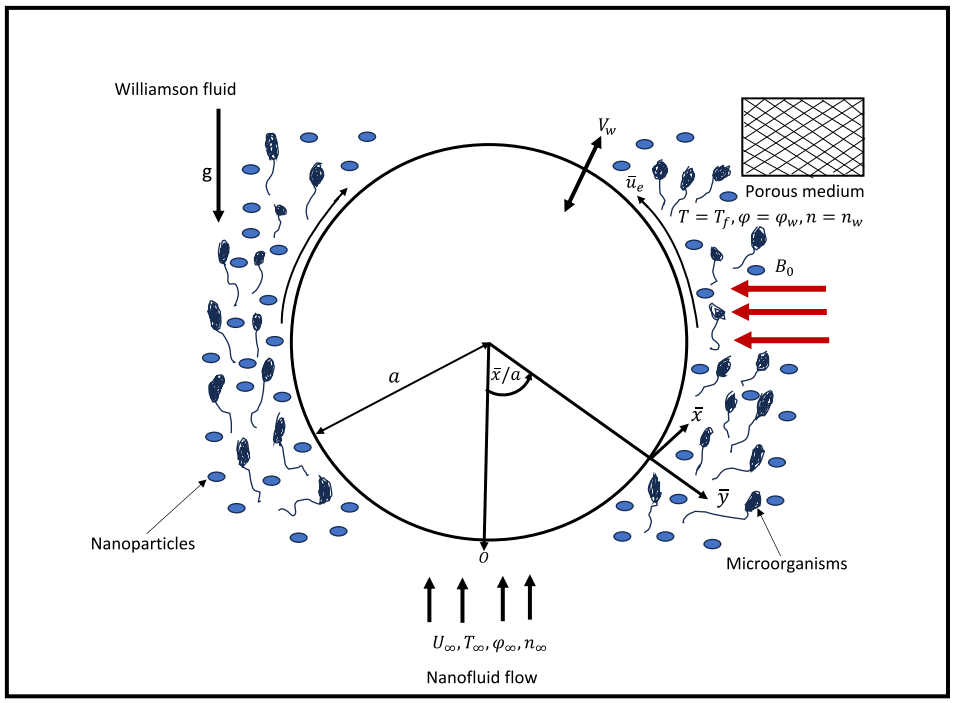

Figure 1. Flow model and physical coordinate system.

$$\frac{\partial \bar{u}}{\partial \bar{x}} + \frac{\partial \bar{v}}{\partial \bar{y}} = 0, \tag{1}$$

$$\rho_{f\infty}\left(\bar{u}\frac{\partial \bar{u}}{\partial \bar{x}} + \bar{v}\frac{\partial \bar{u}}{\partial \bar{y}}\right) = \rho_{f\infty}\bar{u}_e\frac{d\bar{u}_e}{d\bar{x}} + \frac{\partial}{\partial \bar{y}}\left(\mu(T)\frac{\partial \bar{u}}{\partial \bar{y}}\right) + \sqrt{2}\Gamma\frac{\partial}{\partial \bar{y}}\left(\mu(T)\frac{\partial \bar{u}}{\partial \bar{y}}\right)\frac{\partial \bar{u}}{\partial \bar{y}}$$
$$+\left(\sigma B_0^2 + \frac{\mu(T)}{k_p}\right)(\bar{u}_e - \bar{u}) + g\left[(1-\varphi_\infty)\rho_{f\infty}\left\{\beta_0(T-T_\infty) + \beta_1(T-T_\infty)^2\right\}\right]\sin\left(\frac{\bar{x}}{a}\right)$$
$$-g(\rho_p - \rho_{f\infty})(\varphi - \varphi_\infty)\sin\left(\frac{\bar{x}}{a}\right) - g(\rho_{m\infty} - \rho_{f\infty})\gamma(n - n_\infty)\sin\left(\frac{\bar{x}}{a}\right), \tag{2}$$

$$\bar{u}\frac{\partial T}{\partial \bar{x}} + \bar{v}\frac{\partial T}{\partial \bar{y}} = \frac{1}{\rho C_p}\frac{\partial}{\partial \bar{y}}\left(\kappa(T)\frac{\partial T}{\partial \bar{y}}\right) + \frac{Q_0(T-T_\infty)}{\rho C_p} - \frac{1}{\rho C_p}\frac{\partial q_r}{\partial \bar{y}}$$
$$+\tau\left[D_B\frac{\partial \varphi}{\partial \bar{y}}\frac{\partial T}{\partial \bar{y}} + D_n\frac{\partial n}{\partial \bar{y}}\frac{\partial T}{\partial \bar{y}} + \frac{D_T}{T_\infty}\left(\frac{\partial T}{\partial \bar{y}}\right)^2\right], \tag{3}$$

$$\bar{u}\frac{\partial \varphi}{\partial \bar{x}} + \bar{v}\frac{\partial \varphi}{\partial \bar{y}} = D_B\frac{\partial^2 \varphi}{\partial \bar{y}^2} - k_r^2\left(\frac{T}{T_\infty}\right)^p\exp\left(-\frac{E_b}{k_B T}\right)(\varphi - \varphi_\infty) + \frac{D_T}{T_\infty}\frac{\partial^2 T}{\partial \bar{y}^2}, \tag{4}$$

$$\bar{u}\frac{\partial n}{\partial \bar{x}} + \bar{v}\frac{\partial n}{\partial \bar{y}} + \frac{bW_c}{\varphi_\infty}\frac{\partial}{\partial \bar{y}}\left(n\frac{\partial \varphi}{\partial y}\right) = D_n\frac{\partial^2 n}{\partial \bar{y}^2} - k_m^2\left(\frac{T}{T_\infty}\right)^p\exp\left(-\frac{E_b}{k_B T}\right)(n - n_\infty) + \frac{D_T}{T_\infty}\frac{\partial^2 T}{\partial \bar{y}^2}, \tag{5}$$

where $\bar{u}$ and $\bar{v}$ are velocity segments along the $\bar{x}-$ and $\bar{y}-$ axes, $\rho_f, \rho_p, \rho_{f\infty}$, and $\rho_{m\infty}$ represent the density of the fluid, NPs, base fluid, and microbes, Γ is the material constant, σ signifies electrical conductivity, B_0 stands for the intensity of the magnetic field, $\mu(T)$ stands for the dynamic viscosity that varies with temperature, $\kappa(T)$ indicates thermal conductivity that varies with temperature, g represents acceleration due to gravity, k_p is the penetrability of the porous medium, β_0 and β_1 signify linear and nonlinear volumetric thermal expansion coefficients, γ is the average volume of the motile microbes, Q_0 stands for the heat sink/source coefficient, C_p represents the specific heat capacity, τ signifies the NF heat capacity ratio, D_T is the thermophoretic diffusion coefficient, D_B is the Brownian motion factor, D_n is the coefficient of motile microbes diffusion, k_r^2 and k_m^2 are the chemical and microbial reaction rates, k_B is the Boltzmann constant, p is the fitted rate constant, E_b is the coefficient of AE, b is the chemotaxis constant, and W_c is the speed of the swimming cell. It is notable that the third term of the momentum boundary layer equation introduces the non-Newtonian fluid's behaviour, while the fourth term represents contributions from the porous media and magnetic field. The remaining three terms on the right-hand side of the momentum equation account for buoyancy forces due to temperature variations, NP concentration, and motile microbes. In the heat equation, the second and third terms on the right-hand side capture the contributions from heat generation/absorption and thermal radiation flux based on the Rosseland approximation. However, the last term addresses the impact of nanoparticles on the thermal behavior of the fluid, encompassing phenomena such as thermophoresis and NP and microbial Brownian motions. The second term of the NP concentration and motile microbes equations incorporates the effects of AE, chemical reactions, and microbial reactions. With regard to the Rosseland diffusion approximation, the radiative flux is furnished as [34,35]

$$q_r = -\frac{4\sigma^*}{3k^*}\frac{\partial T^4}{\partial \bar{y}} = -\frac{16\sigma^* T^3}{3k^*}\frac{\partial T}{\partial \bar{y}}, \tag{6}$$

where k^* represents the Rosseland extinction coefficient, σ^* signifies the Stefan–Boltzmann constant, and the term $\frac{16\sigma^* T^3}{3k^*}$ is called radiative conductivity. Since features of first-order velocity slip, uniform suction/injection velocity, and thermal convective and zero mass flux conditions are considered at the boundary, the appropriate physical boundary conditions for the flow problem under consideration are given by

$$\bar{u} = N_0\frac{\partial \bar{u}}{\partial \bar{y}}, \quad \bar{v} = V_w, \quad -\kappa\frac{\partial T}{\partial \bar{y}} = h_f\left(T_f - T\right), \quad D_B\frac{\partial \varphi}{\partial \bar{y}} + \frac{D_T}{T_\infty}\frac{\partial T}{\partial \bar{y}} = 0, n = n_w, \text{at } \bar{y} = 0,$$
$$\bar{u} \to \bar{u}_e(\bar{x}), \quad T \to T_\infty, \quad \varphi \to \varphi_\infty, n \to n_\infty, \quad \text{as } \bar{y} \to \infty, \tag{7}$$

where V_w is the mass suction/injection velocity and N_0 is the first-order velocity slip factor.

In view of Rashad et al. [13,28], the external flow velocity $\bar{u}_e(\bar{x})$ for the boundary layer equations takes the form $\bar{u}_e(\bar{x}) = U_\infty \sin\left(\frac{\bar{x}}{a}\right)$, where U_∞ is the free stream velocity. The next dimensionless variables are adopted in order to aid in the attainment of the numerical solutions [28]

$$\xi = \frac{\bar{x}}{a},\ \eta = \sqrt{Re}\left(\frac{\bar{y}}{a}\right),\ u = \frac{\bar{u}}{U_\infty},\ v = \sqrt{Re}\left(\frac{\bar{v}}{U_\infty}\right),\ u_e(\xi) = \frac{\bar{u}_e(\bar{x})}{U_\infty},$$
$$\theta(\xi,\eta) = \frac{T - T_\infty}{T_f - T_\infty},\ \phi(\xi,\eta) = \frac{\varphi - \varphi_\infty}{\varphi_\infty},\ \chi(\xi,\eta) = \frac{n - n_\infty}{n_w - n_\infty}, \tag{8}$$

where $Re = \frac{aU_\infty}{\nu_\infty}$ signifies the Reynolds number, $T = T_\infty[1 + (\theta_f - 1)\theta(\xi,\eta)]$ with $\theta_f = \frac{T_f}{T_\infty}$ being the surface temperature excess ratio. The correctness of the NF flow and the rate of heat transmission can be achieved by considering the temperature-variant fluid viscosity and heat conductance. Consequently, the fluid velocity follows an exponential variation with temperature and the thermal conductivity fluctuates linearly with temperature, respectively, as follows [36–39]

$$\mu(T) = \mu_\infty e^{-\alpha\theta}, \quad \kappa(T) = \kappa_\infty(1 + \beta\theta), \tag{9}$$

where α is the viscosity variation parameter and β ($\beta > 0$ for fluids such as air and water, $\beta < 0$ for fluids such as lubricant oil) is the temperature-variant thermal conductivity parameter. Applying the non-dimensional variables into Equations (1)–(5), we obtain the next non-similar PDEs

$$\frac{\partial u}{\partial \xi} + \frac{\partial v}{\partial \eta} = 0, \tag{10}$$

$$u\frac{\partial u}{\partial \xi} + v\frac{\partial u}{\partial \eta} = u_e\frac{du_e}{d\xi} + e^{-\alpha\theta}\left(\frac{\partial^2 u}{\partial \eta^2} - \alpha\frac{\partial \theta}{\partial \eta}\frac{\partial u}{\partial \eta}\right)\left(1 + \Lambda\frac{\partial u}{\partial \eta}\right)$$
$$+\left(M + \varepsilon e^{-\alpha\theta}\right)(u_e - u) + \lambda\left(\theta + \Omega\theta^2 - Nr\phi - Rb\chi\right)\sin\xi, \tag{11}$$

$$u\frac{\partial \theta}{\partial \xi} + v\frac{\partial \theta}{\partial \eta} = \frac{1}{Pr}\left[\frac{\partial^2 \theta}{\partial \eta^2} + \beta\theta\frac{\partial^2 \theta}{\partial \eta^2} + \beta\left(\frac{\partial \theta}{\partial \eta}\right)^2\right] + \frac{4Rd}{3Pr}\left\{\frac{\partial \theta}{\partial \eta}\left[(\theta_f - 1)\theta + 1\right]^3\right\}'$$
$$+Nb\frac{\partial \theta}{\partial \eta}\frac{\partial \phi}{\partial \eta} + Nn\frac{\partial \theta}{\partial \eta}\frac{\partial \chi}{\partial \eta} + Nt\left(\frac{\partial \theta}{\partial \eta}\right)^2 + Q\theta, \tag{12}$$

$$u\frac{\partial \phi}{\partial \xi} + v\frac{\partial \phi}{\partial \eta} = \frac{1}{Sc}\frac{\partial^2 \phi}{\partial \eta^2} - K_c\left[1 + (\theta_f - 1)\theta\right]^p \exp\left(\frac{-E}{1 + (\theta_f - 1)\theta}\right)\phi + \frac{1}{Sc}\frac{Nt}{Nb}\frac{\partial^2 \theta}{\partial \eta^2}, \tag{13}$$

$$Sb\left(u\frac{\partial \chi}{\partial \xi} + v\frac{\partial \chi}{\partial \eta}\right) + Pe\left[\frac{\partial \chi}{\partial \eta}\frac{\partial \phi}{\partial \eta} + (\chi + \omega)\frac{\partial^2 \phi}{\partial \eta^2}\right] = \frac{\partial^2 \chi}{\partial \eta^2}$$
$$-K_m Sb\left[1 + (\theta_f - 1)\theta\right]^p \exp\left(\frac{-E}{1 + (\theta_f - 1)\theta}\right)\chi + \frac{Nt}{Nn}\frac{\partial^2 \theta}{\partial \eta^2}, \tag{14}$$

and the corresponding boundary conditions change to

$$u = \delta\frac{\partial u}{\partial \eta}, v = \frac{V_w Re^{1/2}}{U_\infty}, \frac{\partial \theta}{\partial \eta} = -Bi[1 - \theta],\ Nb\frac{\partial \phi}{\partial \eta} + Nt\frac{\partial \theta}{\partial \eta}, \chi = 1 \quad \text{at } \eta = 0,$$
$$u \to u_e, \theta \to 0, \phi \to 0, \chi \to 0 \quad \text{as } \eta \to \infty, \tag{15}$$

The flow parameters appearing in Equations (10)–(14) are explicated as magnetic field parameter $M = \frac{\sigma B_0^2 a}{U_\infty \rho_{f\infty}}$, Williamson fluid parameter $\Lambda = \frac{\sqrt{2}\Gamma Re^{1/2}U_\infty}{a}$, Prandtl number $Pr = \frac{\mu_\infty C_p}{\kappa_\infty}$, thermal radiation parameter $Rd = \frac{4\sigma^* T_\infty^3}{k^* \kappa_\infty}$, heat source/sink parameter $Q = \frac{Q_0 a}{U_\infty \rho_{f\infty} C_p}$, porosity parameter $\varepsilon = \frac{a\nu_\infty}{k_p U_\infty}$, velocity slip parameter $\delta = \frac{Re^{1/2}N_0}{a}$, thermal Biot number $Bi = \frac{h_f a}{Re^{1/2}\kappa_\infty}$, buoyancy ratio parameter $Nr = \frac{(\rho_p - \rho_{f\infty})\varphi_\infty}{(1-\varphi_\infty)\rho_{f\infty}\beta_0(T_f - T_\infty)}$, bioconvection Rayleigh number $Rb = \frac{(\rho_{m\infty} - \rho_{f\infty})\gamma(n_w - n_\infty)}{(1-\varphi_\infty)\rho_{f\infty}\beta_0(T_f - T_\infty)}$, nonlinear convection parameter $\Omega = \frac{\beta_1(T_f - T_\infty)}{\beta_0}$, NP Brown-

ian motion parameter $Nb = \frac{\tau D_B \varphi_\infty}{\nu_\infty}$, microbial Brownian motion parameter $Nn = \frac{\tau D_n (n_w - n_\infty)}{\nu_\infty}$, thermophoresis parameter $Nt = \frac{\tau D_T (T_f - T_\infty)}{\nu_\infty T_\infty}$, Schmidt number $Sc = \frac{\nu_\infty}{D_B}$, bioconvection Schmidt number $Sb = \frac{\nu_\infty}{D_n}$, AE parameter $E = \frac{Eb}{k_B T_\infty}$, chemical reaction rate parameter $K_c = \frac{ak_r^2}{U_\infty}$, bioconvection Peclet number $Pe = \frac{bWc}{D_n}$, bioconvection constant $\omega = \frac{n_\infty}{(n_w - n_\infty)}$, microbial reaction rate parameter $K_m = \frac{ak_m^2}{U_\infty}$, and mixed convection parameter $\lambda = \frac{(1-\varphi_\infty) g \beta_0 (T_f - T_\infty) a}{U_\infty^2} = \frac{Gr}{Re^2}$ with $Gr = \frac{(1-\varphi_\infty) g \beta_0 (T_f - T_\infty) a^3}{\nu_\infty^2}$ being the Grashof number.

Equations (9)–(14), along with boundary conditions (15), can be expressed in dimensionless form by assuming that $\Psi = \xi f(\xi, \eta), \theta = \theta(\xi, \eta), \phi = \phi(\xi, \eta)$, and $\chi = \chi(\xi, \eta)$ [13,28], where Ψ signifies the dimensionless stream function given by $u = \frac{\partial \Psi}{\partial \eta}$ and $v = -\frac{\partial \Psi}{\partial \xi}$. Thus, the continuity equation is automatically satisfied and the momentum, energy, NP concentration, and microorganism equations convert into

$$e^{-\alpha\theta}\left(f''' - \alpha\theta' f''\right)\left(1 + \Lambda\xi f''\right) - f'^2 + ff'' + \left(M + \varepsilon e^{-\alpha\theta}\right)\left(\frac{\sin\xi}{\xi} - f'\right) + \frac{\sin\xi\cos\xi}{\xi} + \lambda\left(\theta + \Omega\theta^2 - Nr\phi - Rb\chi\right)\frac{\sin\xi}{\xi} = \xi\left(f'\frac{\partial f'}{\partial \xi} - f''\frac{\partial f}{\partial \xi}\right), \quad (16)$$

$$\frac{1}{Pr}\left(\theta'' + \beta\theta\theta'' + \beta\theta'^2\right) + \frac{4Rd}{3Pr}\left\{\theta'\left[(\theta_f - 1)\theta + 1\right]^3\right\}' + f\theta' + Nb\theta'\phi' + Nn\theta'\chi' + Nt\theta'^2 + Q\theta = \xi\left(f'\frac{\partial \theta}{\partial \xi} - \theta'\frac{\partial f}{\partial \xi}\right), \quad (17)$$

$$\frac{1}{Sc}\phi'' + f\phi' - K_c(1 + (\theta_f - 1)\theta)^p \exp\left(\frac{-E}{1 + (\theta_f - 1)\theta}\right)\phi + \frac{Nt}{ScNb}\theta'' = \xi\left(f'\frac{\partial \phi}{\partial \xi} - \phi'\frac{\partial f}{\partial \xi}\right), \quad (18)$$

$$\chi'' + Sbf\chi' - K_m Sb(1 + (\theta_f - 1)\theta)^p \exp\left(\frac{-E}{1 + (\theta_f - 1)\theta}\right)\chi - Pe\left[\phi'\chi' + (\chi + \omega)\phi''\right] + \frac{Nt}{Nn}\theta'' = Sb\xi\left(f'\frac{\partial \chi}{\partial \xi} - \chi'\frac{\partial f}{\partial \xi}\right), \quad (19)$$

with accompanying boundary conditions

$$f' = \delta f'', \quad f = f_w, \quad \theta' = -Bi[1 - \theta], \quad Nb\phi' + Nt\theta' = 0, \quad \chi = 1 \quad \text{at } \eta = 0,$$
$$f' \to \frac{\sin\xi}{\xi}, \quad \theta \to 0, \quad \phi \to 0, \quad \chi \to 0, \quad \text{as } \eta \to \infty, \quad (20)$$

where $f_w = -\frac{V_w Re^{1/2}}{U_\infty}$ is the suction parameter when $f_w > 0$ or the injection (blowing) parameter when $f_w < 0$. It is noteworthy that near the lower stagnation point of the cylinder (i.e., $\xi \approx 0$), $\frac{\sin\xi}{\xi} \approx 1$, $\frac{\sin\xi\cos\xi}{\xi} \approx 1$, and Equations (16)–(19) reduce to the subsequent system of ordinary differential equations (ODEs):

$$e^{-\alpha\theta}\left(f''' - \alpha\theta' f''\right)\left(1 + \Lambda\xi f''\right) - f'^2 + ff'' + \left(M + \varepsilon e^{-\alpha\theta}\right)(1 - f') + 1 + \lambda\left(\theta + \Omega\theta^2 - Nr\phi - Rb\chi\right) = 0, \quad (21)$$

$$\frac{1}{Pr}\left(\theta'' + \beta\theta\theta'' + \beta\theta'^2\right) + \frac{4Rd}{3Pr}\left\{\theta'\left[(\theta_f - 1)\theta + 1\right]^3\right\}' + f\theta' + Nb\theta'\phi' + Nn\theta'\chi' + Nt\theta'^2 + Q\theta = 0, \quad (22)$$

$$\phi'' + Scf\phi' - K_c Sc(1 + (\theta_f - 1)\theta)^p \exp\left(\frac{-E}{1 + (\theta_f - 1)\theta}\right)\phi + \frac{Nt}{Nb}\theta'' = 0, \quad (23)$$

$$\chi'' + Sbf\chi' - Pe\left[\phi'\chi' + (\chi + \omega)\phi''\right] + \frac{Nt}{Nn}\theta'' - K_m Sb(1 + (\theta_f - 1)\theta)^p \exp\left(\frac{-E}{1 + (\theta_f - 1)\theta}\right)\chi = 0, \quad (24)$$

and the boundary conditions diminish to

$$f' = \delta f'', \quad f = f_w, \quad \theta' = -Bi[1 - \theta], \quad Nb\phi' + Nt\theta' = 0, \quad \chi = 1 \quad \text{at } \eta = 0,$$
$$f' \to 1, \quad \theta \to 0, \quad \phi \to 0, \quad \chi \to 0, \quad \text{as } \eta \to \infty. \quad (25)$$

The significant physical quantities of engineering attentiveness are the local wall friction factor $C_f(\xi)$, local Nusselt number $Nu(\xi)$, and local density number of motile

microorganisms $Nm(\xi)$ that can be derived using the transformations described above, and expressed in dimensionless form as follows:

$$\begin{aligned} C_f(\xi) &= Re^{1/2}\frac{\tau_w}{\rho_{f\infty}U_\infty^2} = e^{-\alpha\theta(\xi,0)}\left[\xi f''(\xi,0) + \frac{\Lambda}{2}\xi^2(f''(\xi,0))^2\right], \\ Nu(\xi) &= Re^{-1/2}\frac{aq_w}{k_\infty(T_f - T_\infty)} = -\left[1 + \beta\theta(\xi,0) + \frac{4}{3}Rd(1 + (\theta_f - 1)\theta(\xi,0))^3\right]\theta'(\xi,0), \\ Nm(\xi) &= Re^{-1/2}\frac{am_w}{D_n(n_w - n_\infty)} = -\chi'(\xi,0), \end{aligned} \tag{26}$$

where $\tau_w = \mu(T)\left[\frac{\partial\bar{u}}{\partial\bar{y}} + \frac{\Gamma}{\sqrt{2}}\left(\frac{\partial\bar{u}}{\partial\bar{y}}\right)^2\right]_{\bar{y}=0}$ (surface shear stress), $q_w = -\left[\left(\kappa(T) + \frac{16\sigma^*}{3k^*}T^3\right)\frac{\partial T}{\partial\bar{y}}\right]_{\bar{y}=0}$ (surface heat flux) and $m_w = -\left(\frac{\partial n}{\partial\bar{y}}\right)_{\bar{y}=0}$ (surface mass flux).

3. Solution Method

Numerical solutions for the non-dimensional PDEs (16)–(19) along with boundary conditions (20) have been determined by applying OMD-BSLLM. This numerical method has been successfully implemented in solving dimensional PDEs for some boundary layer flow problems with different degrees of non-linearity and complexity [31–33]. The choice of the numerical scheme for the present flow problem is justified by the following merits:

- The numerical approach is remarkably accurate, convergent, stable, and resource-efficient when solving problems in both smaller and larger computational domains.
- The numerical method uses fewer number of grid nodes and iterations to achieve results with good spectral accuracy.
- This numerical method is well-structured, straightforward, and versatile to program in various computer software such as Matlab and Mathematica.
- The scheme produces a less dense matrix system due to the use of the overlapping grid approach.

The numerical procedure for obtaining the numerical solutions to the present problem using the OMD-BSLLM is discussed in detail in the following section. The method is applied to linear equations, therefore it is necessary to begin by linearising the nonlinear equations using one of the linearisation techniques available in the literature. To this end, the algorithm called local linearisation method (LLM) is applied in the linearisation of the nonlinear terms in the dimensionless PDEs (16)–(19). The LLM algorithm was identified by Motsa et al. [40–42] as an efficient method for solving coupled systems of nonlinear ODEs and PDEs that model boundary layer flow problems. The LLM algorithm used in the simplification and decoupling of Equations (16)–(19) is summarized in Appendix A. The resulting linear iterative scheme is as follows:

$$a_{0,r}f'''_{r+1} + a_{1,r}f''_{r+1} + a_{2,r}f'_{r+1} + a_{3,r}f_{r+1} + a_{4,r}\frac{\partial f'_{r+1}}{\partial\xi} + a_{5,r}\frac{\partial f_{r+1}}{\partial\xi} = a_{6,r}, \tag{27}$$

$$b_{0,r}\theta''_{r+1} + b_{1,r}\theta'_{r+1} + b_{2,r}\theta_{r+1} + b_{3,r}\frac{\partial\theta_{r+1}}{\partial\xi} = b_{4,r}, \tag{28}$$

$$\phi''_{r+1} + c_{1,r}\phi'_{r+1} + c_{2,r}\phi_{r+1} + c_{3,r}\frac{\partial\phi_{r+1}}{\partial\xi} = c_{4,r}, \tag{29}$$

$$\chi''_{r+1} + e_{1,r}\chi'_{r+1} + e_{2,r}\chi_{r+1} + e_{3,r}\frac{\partial\chi_{r+1}}{\partial\xi} = e_{4,r}, \tag{30}$$

where $r+1, r$ represent current and previous iterations, and the variable coefficients have been obtained using the LLM approach (see Appendix B). The next step involves discussing the decomposition of the time domain $\xi \in [0, \xi_F]$, which is the solution domain for the di-

mensionless PDEs. The time interval $0 \leq \xi \leq \xi_F$ is then segmented into ϖ non-overlapping sub-domains indicated as follows:

$$\Delta_\iota = [\xi_\iota, \xi_{\iota-1}], 0 = \xi_0 < \xi_1 < ..... < \xi_{\varpi-1} < \xi_\varpi = \xi_F, \iota = 1, 2, 3, ..., \varpi, \tag{31}$$

where each sub-domain is further partitioned into $N_{\bar{\xi}} + 1$ Chebyshev collocation points (see Figure 2). The PDEs are solved in the ϖ non-overlapping sub-domains $[\xi_\iota, \xi_{\iota-1}]$ by starting with the easily calculated initial solutions in the first sub-interval (Δ_1). These initial solutions, which are initial conditions for the first interval, are obtained by solving the system of ODEs (21)–(24). For the remaining sub-domains, we use the solutions produced at the last grid point of each sub-interval as initial conditions for the next sub-interval. This means that the solution at the last grid point of Δ_ι is used as an initial condition in $\Delta_{\iota+1}$. In accordance with the validity of the spectral collocation method (SCM), which is in the interval $[-1, 1]$, the decomposed domain $[\xi_\iota, \xi_{\iota-1}]$ has to be transformed to $[-1, 1]$ using the following linear transformation:

$$\bar{\xi} = \frac{2}{\xi_{\iota-1} - \xi_\iota}\xi - \frac{\xi_\iota + \xi_{\iota-1}}{\xi_\iota - \xi_{\iota-1}}, \ \xi \in [\xi_{\iota-1}, \xi_\iota], \ \hat{\xi} \in [-1, 1], \ \iota = 1, 2, 3, ..., \varpi. \tag{32}$$

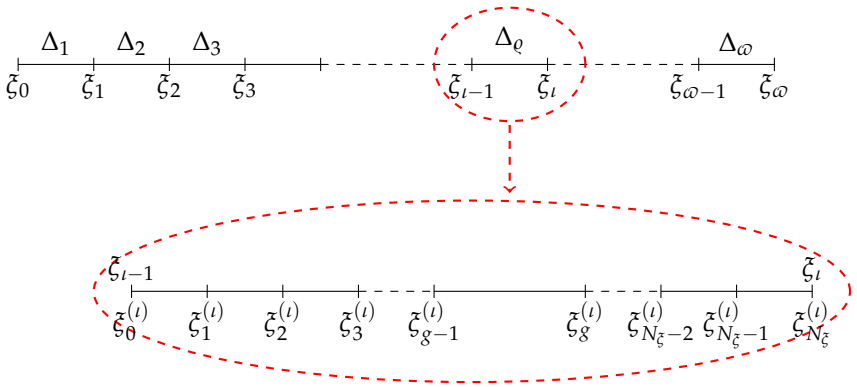

Figure 2. Dividing the time solution domain into ϖ non-overlapping sub-intervals.

Because of this transformation, we now have a new collocation variable $\bar{\xi} \in [-1, 1]$, which is defined as [43]

$$\{\bar{\xi}_j\}_{j=0}^{N_{\bar{\xi}}} = \cos\left(\frac{j\pi}{N_{\bar{\xi}}}\right). \tag{33}$$

The complete grid in the time variable (ξ) takes the following order:

$$\left\{0 = \xi_{N_{\bar{\xi}}}^{(1)}, ..., \xi_0^{(1)} = \xi_{N_{\bar{\xi}}}^{(2)}, ..., \xi_0^{(\iota-1)} = \xi_{N_{\bar{\xi}}}^{(\iota)}, ..., \xi_0^{(\varpi)} = \xi_F, ..., 2 \leq \iota \leq \varpi\right\}. \tag{34}$$

Next, we discuss domain decomposition for the spatial variable η. Unlike the variable ξ, which is defined in the finite domain $[0, \xi_F]$, the space variable η is specified in the semi-finite domain $[0, \infty)$. In order to apply the method, this semi-finite domain has to be truncated to a finite domain $[0, K_\infty]$, where K_∞ is a finite value that is handpicked with the intention that it conforms to the far field boundary constraints. The resulting truncated domain is then divided into ς overlapping sub-domains indicated as

$$J_\vartheta = [\eta_0^{(\vartheta)}, \eta_{N_\eta}^{(\vartheta)}], \ \vartheta = 1, 2, 3, ..., \varsigma, \tag{35}$$

where each sub-domain is subsequently partitioned into $N_\eta + 1$ Chebyshev collocation points (see Figure 3). Yang et al. [44] reported that using a different number of collocation points in the various sub-intervals can lead to difficulties in the implementation of the

method. In addition to that condition, the length for each sub-domain must be kept the same for all sub-domains, especially if a linear transformation is utilized. This length is given by $L = \frac{K_\infty}{\varsigma+(1-\varsigma)(1-\cos\frac{\pi}{N_\eta})/2}$ (see Appendix C). Again, the decomposed domain $[\eta_0^{(\vartheta)}, \eta_{N_\eta}^{(\vartheta)}]$ has to be transformed to $[-1,1]$ as well, using the following linear mapping:

$$\bar{\eta} = \frac{2}{\eta_{N_\eta}^{(\vartheta)} - \eta_0^{(\vartheta)}}\eta - \frac{\eta_{N_\eta}^{(\vartheta)} + \eta_0^{(\vartheta)}}{\eta_{N_\eta}^{(\vartheta)} - \eta_0^{(\vartheta)}}, \tag{36}$$

and because of this transformation, we have a new collocation variable $\bar{\eta} \in [-1,1]$, which is defined as

$$\{\bar{\eta}_i\}_{i=0}^{N_\eta} = \cos\left(\frac{i\pi}{N_\eta}\right). \tag{37}$$

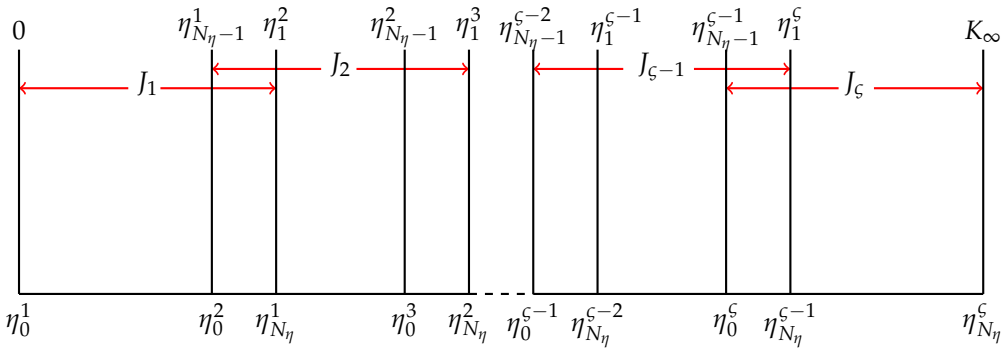

Figure 3. Dividing the spatial solution domain into ς overlapping sub-intervals.

The complete grid in the space variable (η) takes the following order:

$$\left\{0 = \eta_{N_\eta}^{(1)}, ..., \eta_1^{(1)} = \eta_{N_\eta}^{(2)}, \eta_0^{(1)} = \eta_{N_\eta-1}^{(2)}, ..., \eta_1^{(\vartheta-1)} = \eta_{N_\eta}^{(\vartheta)}, \eta_0^{(\vartheta-1)} = \eta_{N_\eta-1}^{(\vartheta)}, ..., \eta_0^{(\varsigma)} = K_\infty,\ 2 \le \vartheta \le \varsigma\right\}. \tag{38}$$

The numerical solutions at different time intervals can be differentiated using $\overset{(\iota)}{f}$, $\overset{(\iota)}{\theta}$, $\overset{(\iota)}{\phi}$, and $\overset{(\iota)}{\chi}$. We remark that for the time variable, equations are solved independently in each sub-domain, but for the space variable, equations are solved contemporaneously across the whole domain of integration. Thus, the linearised iterative scheme (27)–(30) takes the form

$$a_{0,r}\frac{\partial^3 \overset{(\iota)}{f}_{r+1}}{\partial\eta^3} + a_{1,r}\frac{\partial^2 \overset{(\iota)}{f}_{r+1}}{\partial\eta^2} + a_{2,r}\frac{\partial \overset{(\iota)}{f}_{r+1}}{\partial\eta} + a_{3,r}\overset{(\iota)}{f}_{r+1} + a_{4,r}\frac{\partial}{\partial\eta}\left(\frac{\partial \overset{(\iota)}{f}_{r+1}}{\partial\xi}\right) + a_{5,r}\frac{\partial \overset{(\iota)}{f}_{r+1}}{\partial\xi} = a_{6,r}, \tag{39}$$

$$b_{0,r}\frac{\partial^2 \overset{(\iota)}{\theta}_{r+1}}{\partial\eta^2} + b_{1,r}\frac{\partial \overset{(\iota)}{\theta}_{r+1}}{\partial\eta} + b_{2,r}\overset{(\iota)}{\theta}_{r+1} + b_{3,r}\frac{\partial \overset{(\iota)}{\theta}_{r+1}}{\partial\xi} = b_{4,r}, \tag{40}$$

$$\frac{\partial^2 \overset{(\iota)}{\phi}_{r+1}}{\partial\eta^2} + c_{1,r}\frac{\partial \overset{(\iota)}{\phi}_{r+1}}{\partial\eta} + c_{2,r}\overset{(\iota)}{\phi}_{r+1} + c_{3,r}\frac{\partial \overset{(\iota)}{\phi}_{r+1}}{\partial\xi} = c_{4,r}, \tag{41}$$

$$\frac{\partial^2 \overset{(\iota)}{\chi}_{r+1}}{\partial\eta^2} + e_{1,r}\frac{\partial \overset{(\iota)}{\chi}_{r+1}}{\partial\eta} + e_{2,r}\overset{(\iota)}{\chi}_{r+1} + e_{3,r}\frac{\partial \overset{(\iota)}{\chi}_{r+1}}{\partial\xi} = e_{4,r}, \tag{42}$$

In the first interval (Δ_1), the initial conditions $\overset{(1)}{f}(0,\eta)$, $\overset{(1)}{\theta}(0,\eta)$, $\overset{(1)}{\phi}(0,\eta)$, and $\overset{(1)}{\chi}(0,\eta)$ are used to obtained numerical solutions $\overset{(1)}{f}(\xi,\eta)$, $\overset{(1)}{\theta}(\xi,\eta)$, $\overset{(1)}{\phi}(\xi,\eta)$, and $\overset{(1)}{\chi}(\xi,\eta)$. Then, for the remaining time sub-intervals ($\Delta_\iota, \iota = 2,3,4,...,\varpi$), the continuity conditions are given as

$$\overset{(\iota)}{f}_{r+1}(\xi_{\iota-1},\eta) = \overset{(\iota-1)}{f}_{r+1}(\xi_{\iota-1},\eta), \overset{(\iota)}{\theta}_{r+1}(\xi_{\iota-1},\eta) = \overset{(\iota-1)}{\theta}_{r+1}(\xi_{\iota-1},\eta), \tag{43}$$

$$\overset{(\iota)}{\phi}_{r+1}(\xi_{\iota-1},\eta) = \overset{(\iota-1)}{\phi}_{r+1}(\xi_{\iota-1},\eta), \overset{(\iota)}{\chi}_{r+1}(\xi_{\iota-1},\eta) = \overset{(\iota-1)}{\chi}_{r+1}(\xi_{\iota-1},\eta), \tag{44}$$

are used to generate numerical solutions $\overset{(\iota)}{f}(\xi,\eta)$, $\overset{(\iota)}{\theta}(\xi,\eta)$, $\overset{(\iota)}{\phi}(\xi,\eta)$, and $\overset{(\iota)}{\chi}(\xi,\eta)(\iota = 2,3,...,\varpi)$ in the other sub-intervals. The procedure for generating the numerical solution is carried out by approximating the desired solutions, such as $f(\xi,\eta)$, using the bivariate Lagrange interpolating polynomial that appears as

$$\overset{(\iota)}{f}(\xi,\eta) \approx \overset{(\iota)}{F}(\xi,\eta) = \sum_{h=0}^{N_\eta}\sum_{l=0}^{N_\xi} \overset{(\iota)}{F}(\eta_h,\xi_l)L_h(\eta)L_l(\xi). \tag{45}$$

For each space sub-domain J_ϑ, the first, second, and n^{th}order derivative matrices in the spatial direction are evaluated at the collocation points $(\bar{\xi}_i,\bar{\eta}_j)$ for $j = 0,1,2,...,N_{\bar{\xi}}$ as follows [33]:

$$\frac{\partial \overset{(\iota)}{f}}{\partial\eta}(\bar{\eta}_i,\xi_j) = \mathbf{D}\overset{(\iota)}{\mathbf{F}}_j, \frac{\partial^2 \overset{(\epsilon)}{f}}{\partial\eta^2}(\bar{\eta}_i,\xi_j) = \mathbf{D}^2\overset{(\iota)}{\mathbf{F}}_j, \frac{\partial^n \overset{(\epsilon)}{f}}{\partial\eta^n}(\bar{\eta}_i,\xi_j) = \mathbf{D}^n\overset{(\iota)}{\mathbf{F}}_j, \tag{46}$$

where the Chebyshev differential matrix $\mathbf{D} = \frac{2}{L}\bar{\mathbf{D}}$, and $\bar{\mathbf{D}}$ in the standard Chebyshev differential matrix of the first order with dimension $(N_\eta+1)\times(N_\eta+1)$. However, the matrix $\mathbf{D}$ has dimension $(M_\eta+1)\times(M_\eta+1)$, where $M_\eta = N_\eta + (N_\eta-1)(\varsigma-1)$ is the combination of all collocation points used in the whole spatial region. On the other hand, $\overset{(\iota)}{\mathbf{F}}_j = \left[\overset{(\iota)}{f}(\eta_0^{(\vartheta)},\xi_j), \overset{(\iota)}{f}(\eta_1^{(\vartheta)},\xi_j), \overset{(\iota)}{f}(\eta_2^{(\vartheta)},\xi_j),..., \overset{(\iota)}{f}(\eta_{N_\eta}^{(\vartheta)},\xi_j)\right]^T$ is the matrix-vector function with dimension $(N_\eta+1)\times 1$. We note that the $n^{th}(n>1)$ derivative matrix is obtained via matrix multiplication. For each time sub-interval Δ_ι, the first-order derivative matrix in the time direction is evaluated at the collocation points $(\bar{\xi}_i,\bar{\eta}_j)$ for $i = 0,1,2,3,...,N_\eta$ as [33]

$$\frac{\partial \overset{(\iota)}{f}}{\partial\xi}(\bar{\eta}_i,\xi_j) = \sum_{l=0}^{N_{\bar{\xi}}} d_{j,l}\overset{(\iota)}{\bar{\mathbf{F}}}_l \tag{47}$$

where $d_{j,l} = \frac{2}{\bar{\xi}_\iota - \bar{\xi}_{\iota-1}}\bar{d}_{j,l}(j,l = 0,1,2,3,...,N_{\bar{\xi}})$, and $\bar{d}_{j,l}$ in the standard Chebyshev differential matrix of the first order with dimension $(N_{\bar{\xi}}+1)\times(N_{\bar{\xi}}+1)$. It is noteworthy that the matrix-vector function $\overset{(\iota)}{\bar{\mathbf{F}}}_l$ has dimension $(M_\eta+1)\times 1$, since it accounts for the solution in the entire spatial domain. A similar procedure is utilized in the approximation of the other unknown functions $\theta(\xi,\eta),\phi(\xi,\eta),\chi(\xi,\eta)$, and their corresponding derivatives at the collocation points $(\bar{\xi}_i,\bar{\eta}_j)$. Because of the execution of the overlapping grid strategy, the Chebyshev differential matrix $\mathbf{D}$ contains many zero elements and becomes less dense, and the structure of the matrix is illustrated in [32,33,38,39] (see Appendix D). The crucial idea behind the use of SCM lies in the approximation of continuous derivatives with discrete derivatives. Consequently, by replacing the continuous derivatives in Equations (39)–(42) with the discrete derivatives discussed in the previous paragraphs and making use of the initial conditions, we obtain

$$\left[a_{0,r}\mathbf{D}^3 + a_{1,r}\mathbf{D}^2 + a_{2,r}\mathbf{D} + a_{3,r}\right]\overset{(\iota)}{\bar{\mathbf{F}}}_{i,r+1} + a_{4,r}\sum_{j=0}^{N_\xi-1} d_{i,j}\mathbf{D}\overset{(\iota)}{\bar{\mathbf{F}}}_{j,r+1} + a_{5,r}\sum_{j=0}^{N_\xi-1} d_{i,j}\overset{(\iota)}{\bar{\mathbf{F}}}_{j,r+1} = \overset{(\iota)}{\mathbf{R}}_{1,i,r}, \tag{48}$$

$$\left[b_{0,r}\mathbf{D}^2 + b_{1,r}\mathbf{D} + b_{2,r}\right]\overset{(\iota)}{\bar{\Theta}}_{i,r+1} + b_{3,r}\sum_{j=0}^{N_\xi-1} d_{i,j}\overset{(\iota)}{\bar{\Theta}}_{j,r+1} = \overset{(\iota)}{\mathbf{R}}_{2,i,r}, \tag{49}$$

$$\left[\mathbf{D}^2 + c_{1,r}\mathbf{D} + c_{2,r}\right]\overset{(\iota)}{\bar{\Phi}}_{i,r+1} + c_{3,r}\sum_{j=0}^{N_\xi-1} d_{i,j}\overset{(\iota)}{\bar{\Phi}}_{j,r+1} = \overset{(\iota)}{\mathbf{R}}_{3,i,r}, \tag{50}$$

$$\left[\mathbf{D}^2 + e_{1,r}\mathbf{D} + e_{2,r}\right]\overset{(\iota)}{\bar{\chi}}_{i,r+1} + e_{3,r}\sum_{j=0}^{N_\xi-1} d_{i,j}\overset{(\iota)}{\bar{\chi}}_{j,r+1} = \overset{(\iota)}{\mathbf{R}}_{4,i,r}, \tag{51}$$

where the right-hand side of the equations are explicated as $\overset{(\iota)}{\mathbf{R}}_{1,i,r} = a_{6,r} - a_{4,r}d_{i,N_\xi}\mathbf{D}\overset{(\iota)}{\bar{\mathbf{F}}}_{N_\xi} - a_{5,r}d_{i,N_\xi}\overset{(\iota)}{\bar{\mathbf{F}}}_{N_\xi}$, $\overset{(\iota)}{\mathbf{R}}_{2,i,r} = b_{4,r} - b_{3,r}d_{i,N_\xi}\overset{(\iota)}{\bar{\Theta}}_{N_\xi}$, $\overset{(\iota)}{\mathbf{R}}_{3,i,r} = c_{4,r} - c_{3,r}d_{i,N_\xi}\overset{(\iota)}{\bar{\Phi}}_{N_\xi}$, and $\overset{(\iota)}{\mathbf{R}}_{4,i,r} = e_{4,r} - e_{3,r}d_{i,N_\xi}\overset{(\iota)}{\bar{\chi}}_{N_\xi}$. The matching boundary constraints are also evaluated at the collocation points, and they take the form

$$\begin{aligned}
&\overset{(\iota)}{f}_{r+1}(\eta_{M_\eta},\xi_i) = f_w,\ \sum_{h=0}^{M_\eta}\mathbf{D}_{M_\eta,h}\overset{(\iota)}{f}_{r+1}(\eta_h,\xi_i) - \delta\sum_{h=0}^{M_\eta}\mathbf{D}^2_{M_\eta,h}\overset{(\iota)}{f}_{r+1}(\eta_h,\xi_i) = 0,\ \overset{(\iota)}{\chi}_{r+1}(\eta_{M_\eta},\xi_i) = 1,\\
&\sum_{h=0}^{M_\eta}\mathbf{D}_{M_\eta,h}\overset{(\iota)}{f}_{r+1}(\eta_h,\xi_i) - Bi\,\overset{(\iota)}{\theta}_{r+1}(\eta_{M_\eta},\xi_i) = -Bi,\\
&\sum_{h=0}^{M_\eta}\mathbf{D}_{M_\eta,h}\overset{(\iota)}{\phi}_{r+1}(\eta_h,\xi_i) + \frac{Nt}{Nb}\sum_{h=0}^{M_\eta}\mathbf{D}^2_{M_\eta,h}\overset{(\iota)}{\theta}_{r+1}(\eta_h,\xi_i) = 0,\\
&\sum_{h=0}^{M_\eta}\mathbf{D}_{0,h}\overset{(\iota)}{f}_{r+1}(\eta_h,\xi_i) = \frac{\sin\xi_i}{\xi_i},\quad \overset{(\iota)}{\theta}_{r+1}(\eta_0,\xi_i) = 0,\quad \overset{(\iota)}{\phi}_{r+1}(\eta_0,\xi_i) = 0,\quad \overset{(\iota)}{\chi}_{r+1}(\eta_0,\xi_i) = 0.
\end{aligned} \tag{52}$$

In the form of an $N_\xi(M_\eta+1)\times N_\xi(M_\eta+1)$ matrix arrangement, Equation (48) takes the form

$$\begin{bmatrix}
\mathbf{A}_{0,0} & \mathbf{A}_{0,1} & \mathbf{A}_{0,2} & \cdots & \mathbf{A}_{0,N_\xi-1}\\
\mathbf{A}_{1,0} & \mathbf{A}_{1,1} & \mathbf{A}_{1,2} & \cdots & \mathbf{A}_{1,N_\xi-1}\\
\vdots & \vdots & \ddots & \vdots & \\
\mathbf{A}_{N_\xi-1,0} & \mathbf{A}_{N_\xi-1,1} & \mathbf{A}_{N_\xi-1,2} & \cdots & \mathbf{A}_{N_\xi-1,N_\xi-1}
\end{bmatrix}\begin{bmatrix}\overset{(\iota)}{\bar{\mathbf{F}}}_0\\ \overset{(\iota)}{\bar{\mathbf{F}}}_1\\ \vdots\\ \overset{(\iota)}{\bar{\mathbf{F}}}_{N_\xi-1}\end{bmatrix} = \begin{bmatrix}\overset{(\iota)}{\mathbf{R}}_{1,0}\\ \overset{(\iota)}{\mathbf{R}}_{1,1}\\ \vdots\\ \overset{(\iota)}{\mathbf{R}}_{1,N_\xi-1}\end{bmatrix}, \tag{53}$$

where

$$\begin{aligned}
&\mathbf{A}_{i,i} = a_{0,r}\mathbf{D}^3 + a_{1,r}\mathbf{D}^2 + a_{2,r}\mathbf{D} + a_{3,r}\mathbf{I} + a_{4,r}d_{i,i}\mathbf{D} + a_{5,r}d_{i,i}\mathbf{I},\ i = j,\\
&\mathbf{A}^{(1)}_{i,j} = a_{4,r}d_{i,j}\mathbf{D} + a_{5,r}d_{i,j}\mathbf{I},\ i \neq j,
\end{aligned} \tag{54}$$

$$\begin{bmatrix}
a_{\zeta,r}(\eta_0,\xi_i) & & & \\
& a_{\zeta,r}(\eta_1,\xi_i) & & \\
& & \ddots & \\
& & & a_{\zeta,r}(\eta_{M_\eta},\xi_i)
\end{bmatrix},\ \zeta = 0,1,2,3,4,5, \tag{55}$$

and $\mathbf{I}$ is an $(M_\eta+1)\times(M_\eta+1)$ unit matrix. The additional equations will also give a similar matrix arrangement of the same dimension. The resulting discrete boundary conditions are incorporated into the main diagonal sub-blocks of each matrix system to yield a new system of linear algebraic equations. The later matrix system is then solved iteratively, resuming with initial approximations that are picked in such a way that they

conform to the boundary conditions. The compact form of matrix Equations (48)–(51) is given by

$$\begin{bmatrix}(1)\\ \mathbf{A}\end{bmatrix}\begin{bmatrix}\mathbf{F}\end{bmatrix} = \begin{bmatrix}\mathbf{R}_1\end{bmatrix}, \begin{bmatrix}(2)\\ \mathbf{A}\end{bmatrix}\begin{bmatrix}\mathbf{\Theta}\end{bmatrix} = \begin{bmatrix}\mathbf{R}_2\end{bmatrix}, \begin{bmatrix}(3)\\ \mathbf{A}\end{bmatrix}\begin{bmatrix}\mathbf{\Phi}\end{bmatrix} = \begin{bmatrix}\mathbf{R}_3\end{bmatrix}, \begin{bmatrix}(4)\\ \mathbf{A}\end{bmatrix}\begin{bmatrix}\boldsymbol{\chi}\end{bmatrix} = \begin{bmatrix}\mathbf{R}_4\end{bmatrix}. \quad (56)$$

The functions used as initial guesses are given by

$$f_0(\eta) = f_w + \frac{1}{1+\delta}\left(e^{-\eta} - 1\right) + \eta,\ \theta_0(\eta) = \frac{Bi}{1+Bi}e^{-\eta}, \phi_0(\eta) = -\frac{NtBi}{Nb(1+Bi)}e^{-\eta}, \chi_0(\eta) = e^{-\eta}. \quad (57)$$

4. Results and Discussion

A comprehensive parametric study is carried out and numerical results are reported in this section through graphs. The numerical computation is performed for each parameter by assigning fixed values to other related parameters as $\xi = \frac{\pi}{2}$ [13,28], $\omega = 0.2$ [28], $Rb = 0.1$ [28],$Nt = 0.1$ [13,28], $Nb = 0.3$ [13,28], $Sc = 10$ [13,28], $Pe = 1$ [28], $Sb = 1$ [28], $Nr = 0.5$ [13,28], $Pr = 6.8$ [28], $\delta = 0.5$ [4], $K_c = 2$ [18], $Bi = 5$ [13,28], $K_m = 2, M = 0.5$ [4, 17],
f_w [18]$= 0.5$, $Rd = 0.5$ [17], $\theta_f = 1.1$ [16], $\Lambda = 1$ [17], $\varepsilon = 1$ [28], $\beta = 0.5$ [37], $Q = 0.2$ [37], $\alpha = 0.3$ [39], $E = 2$ [18], $p = 0.2$ [18], $\Omega = 0.1$ [17], $\lambda = 5$ [13,28], and $Nn = 0.2$ [29]. To corroborate the correctness of the present numerical method, the results for the heat transfer rate $-\theta'(0)$ were contrasted against those disclosed by Merkin [15], Nazar et al. [1], Rashad et al. [13], Rashad et al. [28], and Zahar et al. [16] in Table 1. Table 1 demonstrates that the numerical values in all considered cases were in substantial coherence. Hence, the selection of the present overlapping grid-based numerical scheme can be rationalized.

Table 1. Comparison of $-\theta'(0)$ when $Pr = 1, \theta_f = 1, Bi \to \infty, \xi = \beta = \alpha = f_w = M = \Lambda = Rd = Q = \varepsilon = \delta = Nr = Rb = \Omega = Nb = Nn = Nt = Sc = Sb = E = K_c = Pe = K_m = \omega = p = 0$.

λ	**Merkin** [15]	**Nazar et al.** [1]	**Rashad et al.** [13]	**Rashad et al.** [28]	**Zahar et al.** [16]	**Present Results**
−1.75	0.4199	0.4205	0.4202	0.4202	0.4198	0.4199516
−1.50	0.4576	0.4601	0.4579	0.4579	0.4573	0.4573551
−1.00	0.5067	0.5080	0.5068	0.5068	0.5067	0.5066785
−0.50	0.5420	0.5430	0.5421	0.54201	0.5421	0.5420654
0.00	0.5705	0.5710	0.5706	0.5706	0.5705	0.5704700
0.50	0.5943	0.5949	0.5947	0.5947	0.5945	0.5945339
0.88	0.6096	0.6112	0.6111	0.6111	0.6108	0.6107615
0.89	0.6110	0.6116	0.6114	0.6114	0.6112	0.6111687
1.00	0.6158	0.6160	0.6160	0.6160	0.6154	0.6155872
2.00	0.6497	0.6518	0.6518	0.6518	0.6515	0.6514920
5.00	0.7315	0.7320	0.7319	0.7319	0.7315	0.7315104

The convergence of the OMD-BSLLM is tracked by monitoring the solution errors, as defined in [32]. These errors represent solution-based discrepancies and quantify the number of accurate digits in the approximate solutions at the r-th iteration level. If the numerical scheme is converging, it is anticipated that the error norms will decrease as the number of iterations increases. Figure 4 illustrates the evolution of the solution errors for the approximate numerical solutions of $f(\eta, \xi), \theta(\eta, \xi), \phi(\eta, \xi)$, and $\chi(\eta, \xi)$ over iterations in both MD-BSLLM and OMD-BSLLM. The consistent reduction in all solution errors suggests that the numerical methods converge. Full convergence is considered attained when the convergence plots start to level off. It is evident that complete convergence is reached after approximately five iterations for all solutions in the MD-BSLLM approach and six iterations for all solutions in the OMD-BSLLM technique, with solution errors approaching 10^{-8} and 10^{-12} in the MD-BSLLM scheme and OMD-BSLLM technique, respectively. The minimal

errors observed with the OMD-BSLLM approach validate its superior accuracy compared to the MD-BSLLM scheme. The precision of the overlapping grid-based scheme (OMD-BSLLM) can be assessed by evaluating the residual errors, as defined in [32]. These errors quantify how closely the numerical solutions approximate the true solution of the PDEs (16)–(19). Figure 5 is plotted to demonstrate residual error graphs at different time levels for both OMD-BSLLM and MD-BSLLM (no overlapping) schemes. In all the graphs, it is clear that each graph displays sufficiently small residual errors, and that is an indication of good accuracy in both numerical schemes. The accuracy is also noted to be uniform throughout the time domain, and that is one of the benefits of using the multi-domain approach in the implementation of SCM. Nevertheless, the OMD-BSLLM scheme proves to be more accurate than the MD-BSLLM approach in all the graphs. Furthermore, using more overlapping sub-domains with a smaller number of spatial collocation points yields more precision in the OMD-BSLLM approach.

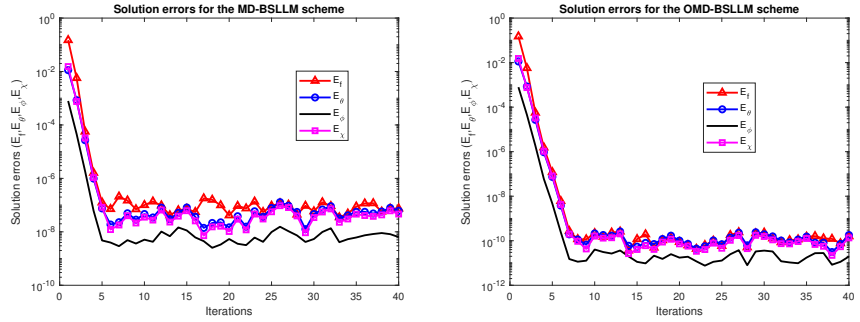

(**a**) (**b**)

Figure 4. Comparison of solution errors (E_f, E_θ, E_ϕ, and E_χ) when $N_{\bar{\xi}} = 5$ and $\varpi = 20$. (**a**) Solution errors against iterations for the MD-BSLLM ($\varsigma = 1, N_\eta = 100$). (**b**) Solution errors against iterations for the OMD-BSLLM ($\varsigma > 1, N_\eta = 10$).

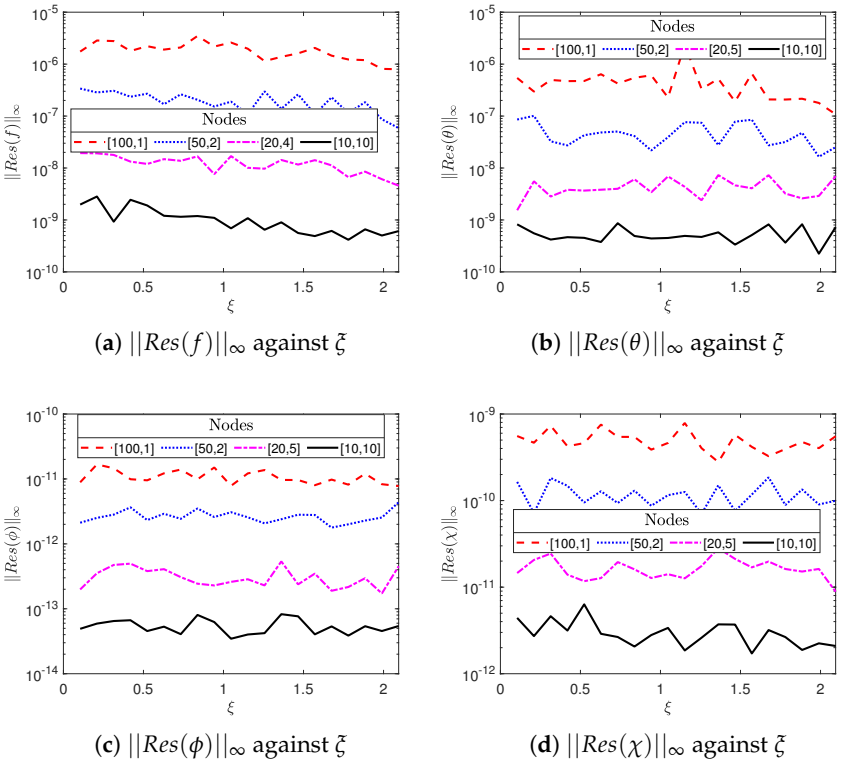

(**a**) $||Res(f)||_\infty$ against $\bar{\xi}$ (**b**) $||Res(\theta)||_\infty$ against $\bar{\xi}$

(**c**) $||Res(\phi)||_\infty$ against $\bar{\xi}$ (**d**) $||Res(\chi)||_\infty$ against $\bar{\xi}$

Figure 5. Comparison of residual error approximations for the case of MD-BSLLM ($\varsigma = 1$) and OMD-BSLLM ($\varsigma > 1$) when $N_{\bar{\xi}} = 5$ and $\varpi = 20$ for different nodes ($[N_\eta, \varsigma] = [100, 1], [50, 2], [20, 5], [10, 10]$).

The stability of the OMD-BSLLM scheme is assessed by analyzing the condition numbers of the coefficient matrices associated with the system of linear algebraic equations that need to be solved. The condition number of the matrix gauges the degree of sensitivity of the solution to variations in the input data and to the round-off errors incurred during the solution process. The condition numbers for the coefficient matrices $(\overset{(1)}{\mathbf{A}}, \overset{(2)}{\mathbf{A}}, \overset{(3)}{\mathbf{A}}, \overset{(4)}{\mathbf{A}})$ are presented in Table 2 when the number of collocation points and overlapping sub-intervals are varied. The overlapping grid-based numerical scheme is noted to yield small condition numbers compared to the non-overlapping grid-based scheme. The use of the overlapping grid approach results in coefficient matrices that are better conditioned compared to those generated by the non-overlapping grid-based calculations. The small condition numbers observed with the overlapping grid-based scheme indicate that the problem is well-conditioned, suggesting that the matrix representing the problem is not close to being singular. This characteristic is desirable as it ensures the stability, accuracy, and reliability of the numerical solution to the problem. As the number of overlapping sub-intervals increases and the number of space collocation points decreases, the condition numbers also decrease. This trend suggests that maximizing the number of overlapping sub-intervals while reducing the number of space collocation points further enhances the stability and accuracy of the numerical solutions. These findings affirm that the OMD-BSLLM scheme is the preferred numerical method for solving fluid flow problems akin to the one addressed in the current study.

Table 2. Condition numbers for varying nodes $[N_\eta, \varsigma]$.

ς	N_η	M_η	Cond $(\overset{(1)}{\mathbf{A}})$	Cond $(\overset{(2)}{\mathbf{A}})$	Cond $(\overset{(3)}{\mathbf{A}})$	Cond $(\overset{(4)}{\mathbf{A}})$
1 (MD-BSLLM)	100	100	1.4518640e+10	6.0399799e+06	2.5107303e+06	3.1173003e+06
2 (OMD-BSLLM)	50	99	1.7962336e+09	1.2883089e+06	5.4063508e+05	6.6439084e+05
4 (OMD-BSLLM)	25	97	2.4075014e+08	2.7726519e+05	1.1971839e+05	1.4291087e+05
5 (OMD-BSLLM)	20	96	1.2646992e+08	1.6967207e+05	7.4692771e+04	8.7440012e+04
10 (OMD-BSLLM)	10	91	1.6621778e+07	3.7796142e+04	1.9268267e+04	1.9579885e+04
20 (OMD-BSLLM)	5	81	1.7880098e+06	9.4107769e+03	7.4254531e+03	4.6950726e+03
25 (OMD-BSLLM)	4	76	8.0984196e+05	6.3770832e+03	6.1905704e+03	2.9795539e+03

For brevity, the consequences of other flow parameters such as ε, Bi, Nr, Λ, Rb, Nb, Nt, Pe, Pr, Sc, and Sb on the fluid flow attributes and design quantities of engineering attentiveness have been omitted in the current study. This is because the contributions of these flow parameters are similar to the ones that were adequately discussed in Rashid et al. [13,28] in the scenario of Newtonian fluids and the absence of variable fluid properties, nonlinear heat convection, magnetic field, heat sink/source, nonlinear thermal radiation, bioconvection Brownian diffusion, activation energy, chemical and microbial reactions, suction/injection, and first-order velocity slips. The current study seeks to extend the works of Rashid et al. [13,28] by analyzing, from a mathematical point of view, the fluid flow properties, heat, mass, and motile microbe transfer phenomena when the above features are incorporated in the present bioconvection flow model. Figures 6–20 illustrate the impact of various parameters stemming from the aforementioned novel features, including the Williamson fluid (Λ), nonlinear convection (Ω), suction $(f_w > 0)$, velocity slip (δ), variable viscosity (α), magnetic field (M), thermal radiation (Rd), temperature ratio (θ_f), variable thermal conductivity (β), heat source $(Q > 0)$, chemical reaction (K_c), AE (E), microbial reaction (K_m), microbial Brownian motion (Nn), and motile microbe (ω) parameters, on dimensionless velocity (f'), temperature (θ), NP concentration (ϕ), density of motile microbes (χ), wall friction factor (C_f), Nusselt number (Nu), and density number of motile microbes (Nm). These pertinent parameters are chosen in the ranges: Λ = 0, 1, 2, 3; Ω = 0.1, 0.5, 1, 1.5; f_w = 0.1, 0.3, 0.5, 0.8; δ = 0.1, 0.3, 0.5, 0.8; α = 0.1, 0.5, 1, 1.5; M = 0.1, 1, 5, 10; Rd = 0.3, 0.6, 1, 1.5; θ_f = 1.1, 1.3, 1.5, 1.8; 0.1, 0.5, 1, 1.5; Q = 0.1, 0.3, 0.5, 0.8; K_c = 0.1, 1, 2, 3, 5; E = 0, 1, 2, 3; K_m = 0.1, 1, 3, 5; Nn = 0.2, 0.3, 0.5, 0.8; and ω = 0.1, 0.3, 0.5, 0.8. The selected range of values for the present model align with those commonly found in a typical nanofluid. For parameters exhibiting a broad spectrum, we

opted for values that ensured the stability of the numerical scheme. Figure 6 is plotted to demonstrate the impact of the Williamson fluid parameter (Λ) and nonlinear thermal convection parameter (Ω) on the dimensionless velocity. From Figure 6a, it is clear that velocity dissemination is diminished with increasing values of Λ. The variable Λ signifies the ratio of Williamson fluid relaxation time to retardation time. When the Williamson fluid parameter gets larger, the relaxation time of the fluid is noted to be lifted. As a result, resistance in the fluid flow direction is produced, which in turn reduces the NF velocity. Basically, because of the high relaxation time, fluid particles take more time to migrate to their original position; thus, fluid viscosity is improved and the velocity of the fluid particles is diminished. Conversely, velocity dissemination is accelerated with mounting values of Ω. For larger Ω, the disparity between the surface and free stream (ambient) temperatures $(T_f - T_\infty)$ is increased, instigating a rise in the fluid velocity.

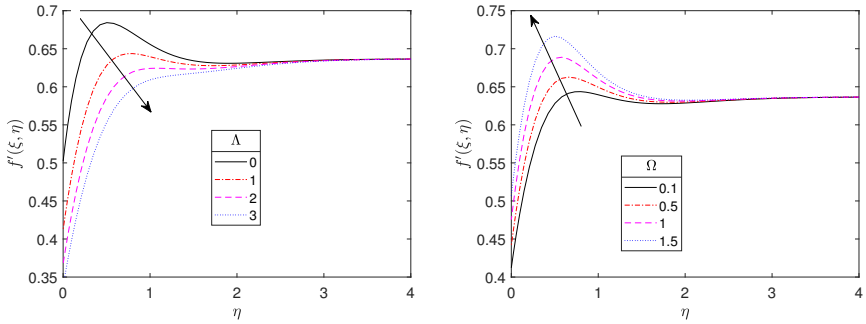

(**a**) Ramification of Λ on $f'(\xi,\eta)$ (**b**) Ramification of Ω $f'(\xi,\eta)$

Figure 6. Dimensionless velocity profiles.

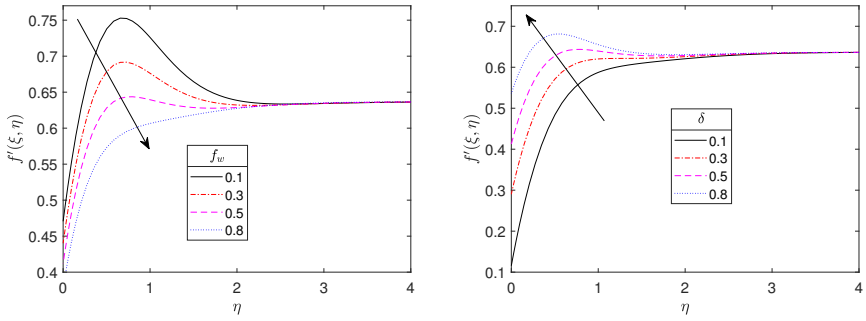

(**a**) Ramification of f_w on $f'(\xi,\eta)$ (**b**) Ramification of δ on $f'(\xi,\eta)$

Figure 7. Dimensionless velocity profiles.

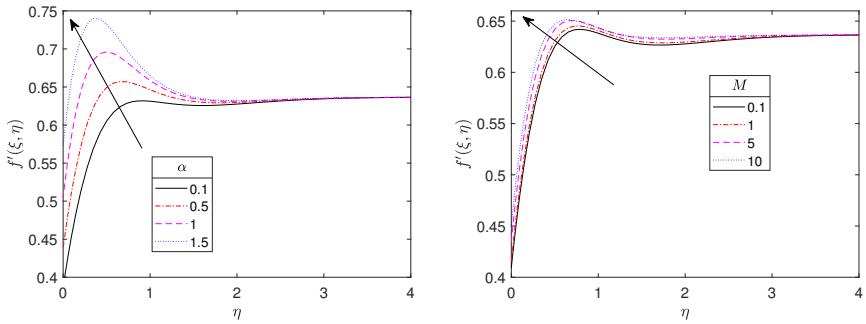

(**a**) Ramification of α on $f'(\xi,\eta)$ (**b**) Ramification of M on $f'(\xi,\eta)$

Figure 8. Dimensionless velocity profiles.

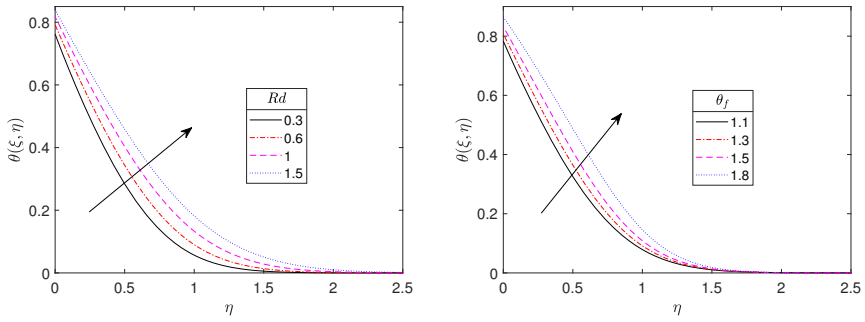

(**a**) Ramification of Rd on $\theta(\xi, \eta)$ (**b**) Ramification of θ_f on $\theta(\xi, \eta)$

Figure 9. Dimensionless temperature profiles.

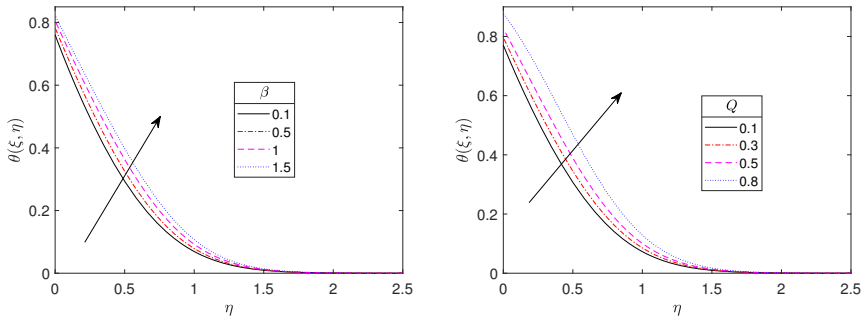

(**a**) Ramification of β on $\theta(\xi, \eta)$ (**b**) Ramification of Q on $\theta(\xi, \eta)$

Figure 10. Dimensionless temperature profiles.

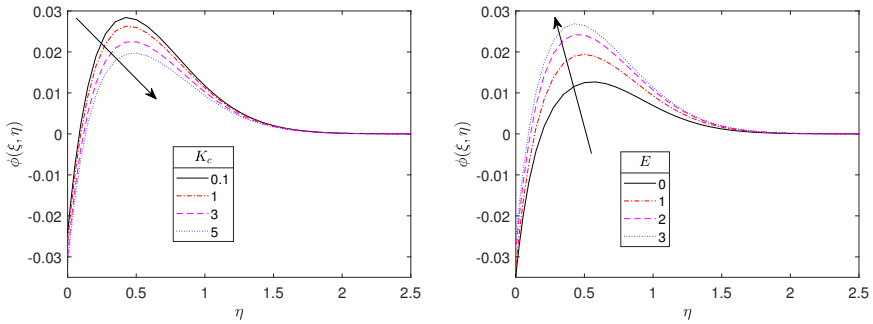

(**a**) Ramification of K_c on $\phi(\xi, \eta)$ (**b**) Ramification of E on $\phi(\xi, \eta)$

Figure 11. Dimensionless nanoparticle concentration profiles.

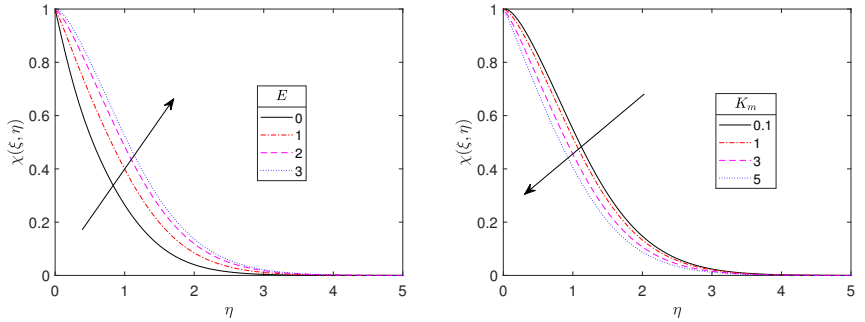

(**a**) Ramification of E on $\chi(\xi, \eta)$ (**b**) Ramification of K_m on $\chi(\xi, \eta)$

Figure 12. Dimensionless density of the motile microbe profiles.

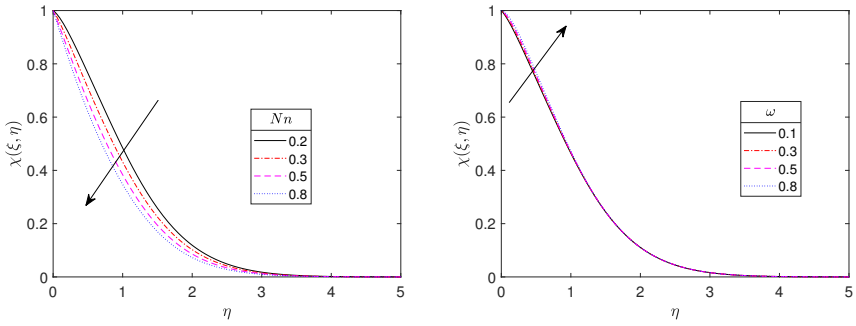

(**a**) Ramification of N_n on $\chi(\xi,\eta)$ (**b**) Ramification of ω on $\chi(\xi,\eta)$

Figure 13. Dimensionless density of the motile microbe profiles.

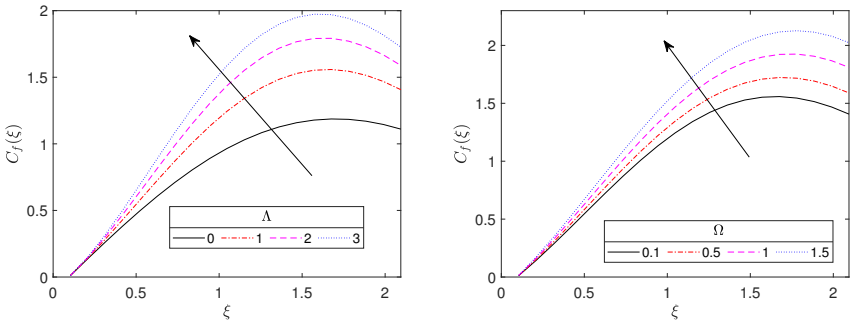

(**a**) Ramification of Λ on $C_f(\xi)$ (**b**) Ramification of Ω on $C_f(\xi)$

Figure 14. Dimensionless surface drag coefficient.

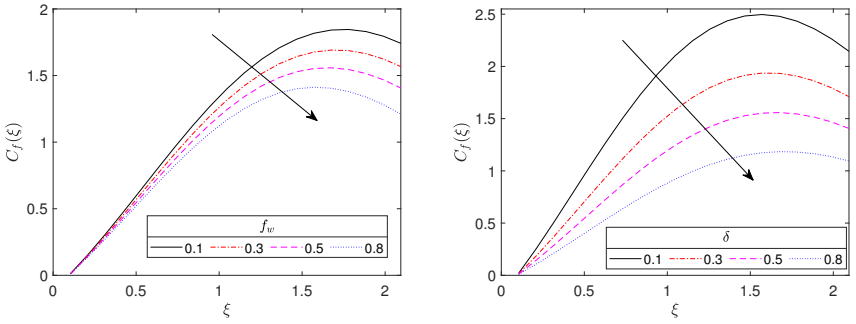

(**a**) Ramification of f_w on $C_f(\xi)$ (**b**) Ramification of δ on $C_f(\xi)$

Figure 15. Dimensionless surface drag coefficient.

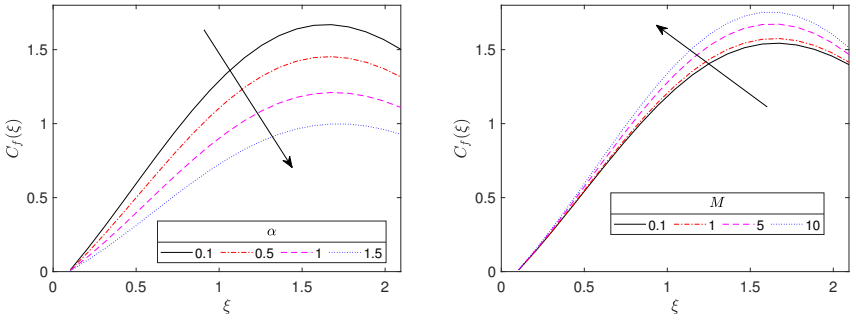

(**a**) Ramification of α on $C_f(\xi)$ (**b**) Ramification of M on $C_f(\xi)$

Figure 16. Dimensionless surface drag coefficient.

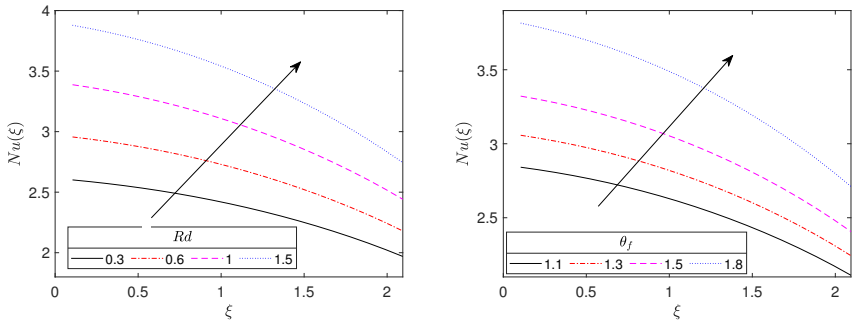

(**a**) Ramification of Rd on $Nu(\xi)$ (**b**) Ramification of θ_f on $Nu(\xi)$

Figure 17. Dimensionless Nusselt number.

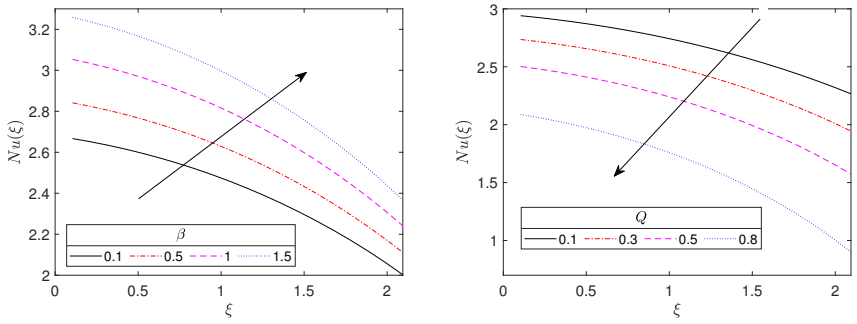

(**a**) Ramification of β on $Nu(\xi)$ (**b**) Ramification of Q on $Nu(\xi)$

Figure 18. Dimensionless Nusselt number.

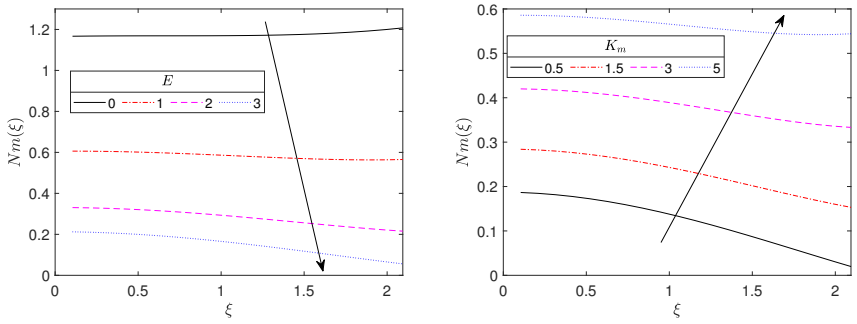

(**a**) Ramification of E on $Nm(\xi)$ (**b**) Ramification of K_m on $Nm(\xi)$

Figure 19. Dimensionless density number of the motile microbes.

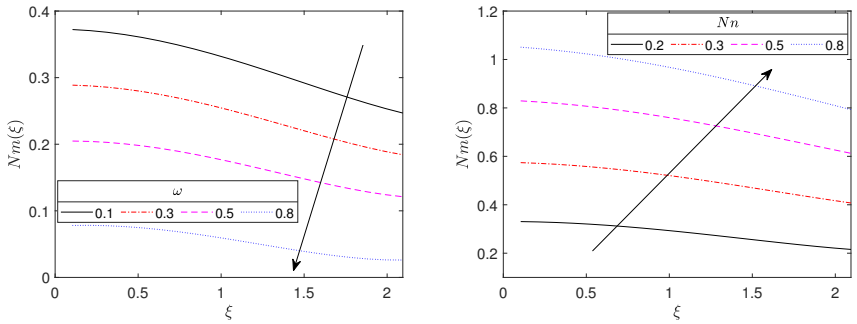

(**a**) Ramification of ω on $Nm(\xi)$ (**b**) Ramification of N_n on $Nm(\xi)$

Figure 20. Dimensionless density number of the motile microbes.

The consequence of the suction parameter $(f_w > 0)$ and first-order velocity slip parameter (δ) on the velocity dissemination is portrayed in Figure 7. Figure 7a demonstrates that the velocity boundary layer's thickness is diminished with the mounting values of the suction parameter. This deportment is owed to the fact that suction upshot plays a fundamental role in the removal of the fluid from the flow system; thus, momentum boundary layer thickness is remarkably decelerated. Figure 7b shows that dimensionless velocity is maximized with the growing velocity slip variable. This is on account of the acceleration in the fluid flow and the corresponding momentum boundary layer thickness as the velocity slip effect is increased. The acceleration of the fluid velocity component with improved velocity slip impact was also disclosed by Gaffar et al. [6] and Prasad et al. [45] in the absence of microbes.

The variation of dimensionless velocity against the transverse coordinate (η) when the variable viscosity parameter (α) and the applied magnetic field parameter (M) are varied is illustrated in Figure 8. It is clear that the velocity field is improved with rising values of the variable viscosity parameter (see Figure 8a). Physically, increasing values of α tend to augment the temperature variation $(T_f - T_\infty)$, consequently, the Williamson fluid bond is weakened and the intensity of the dynamic viscosity of the non-Newtonian material is minimized. As a result, the momentum boundary layer thickness is improved, and the fluid velocity is also accelerated. On the other hand, the dimensionless velocity of our nonlinear mixed convective flow is seen to be increased with mounting values of applied magnetic field parameter. This behaviour is opposite to that of the free convective flows (see Gaffar et al. [6]), where the velocity is declined by rising values of M. From a physics perspective, in an electrically conducting fluid, the magnetic field operating in a transverse direction to the geometry generates a resistive force known as the Lorentz force. The resulting Lorentz force inhibits the velocity of the fluid, as is evident in the free convective flows. In the present problem, it is noteworthy that the velocity component portrays the mounting behaviour because of the existence of nonlinear mixed convection. The similar behaviour is adequately explained by Basha et al. [17] in the absence of gyrotactic microorganisms.

Figure 9 presents the effect of the thermal radiation parameter (Rd) and surface temperature excess ratio (θ_f) on the dimensionless temperature curves. From the first figure, it is noted that the temperature curve is enhanced by rising values of the thermal radiation parameter. This is because increments in thermal radiation energize the boundary layer and upsurge the heat radiation energy; consequently, both the fluid temperature and thermal boundary layer width are also improved. The Rosseland radiation absorption is enhanced by the rising values of the heat radiation parameter Rd; thus, radiative heat transmission rate to the fluid is upsurged, leading to an improvement in the temperature dispersion. On the other hand, the non-dimensional temperature is also increased by the escalating values of the temperature ratio parameter since the parameter θ_f improves the fluid's thermal state. From a physics point of view, the greater values of the surface temperature excess ratio imply an upsurge in the temperature difference $(T_f - T_\infty)$, consequently, the temperature of the fluid is elevated. Figure 10 illustrates the ramifications of the variable thermal conductance parameter (β) and heat generation parameter $(Q > 0)$ on the temperature curves. Figure 10a reveals that the temperature curve improves with the escalation in β, which is owed to the excess amount of heat transmitted from the surface of the cylinder to the fluid. The parameter β is directly proportional to the temperature difference. As a result, an elevation in the variable thermal conductance parameter causes a remarkable potential for thermal energy to convey more heat energy to the NPs, instigating a rise in the fluid temperature. Figure 10b shows that temperature distribution mounts with the rising values of the heat source parameter. It is worth pointing out that $Q > 0$ represents the amount of heat produced within the system during the fluid flow. Thus, an increment in Q means that more heat is absorbed by the fluid, leading to an enhancement in the thermal boundary layer's thickness and fluid temperature.

Figure 11 reveals the impact of the non-dimensional AE parameter (E) and chemical reaction rate parameter (K_c) on the non-dimensional NP species concentration distributions.

From Figure 11a, it is clear that increasing the non-dimensional chemical reaction rate lessens the thickness of the non-dimensional concentration dissemination. The thinning in the non-dimensional species concentration dissemination is continuously occurring in conjunction with an enlarged non-dimensional concentration gradient. On the other hand, the rise in the non-dimensional AE impact decreases the non-dimensional wall concentration gradient. The physical justification for such a behaviour is that high AE slows down the chemical reaction process. As a result, both the non-dimensional species concentration profiles (see Figure 11b) and the thickness of the concentration boundary layer improve, leading to a reduction in the non-dimensional wall concentration gradient.

The impact of the AE parameter (E) and microbial reaction rate parameter (K_m) on the non-dimensional density of the motile microbes is portrayed in Figure 12. It is perceived from Figure 12a that the density of the motile microbes is reinforced by the rising values of the AE parameter. Since the microbial reaction process is improved by using AE, the motile microbe concentration profile is augmented to a greater extent. On the other hand, Figure 12b illustrates that the density of motile microbes declines with the augmenting values of the microbial reaction rate parameter. With an elevation in K_m, the microorganisms' diffusivity shrinks, for which less motile microorganism transfer occurs. In this phenomenon, the concentration of motile microorganisms drops as the values of K_m increase.

Figure 13 reveals the non-dimensional microorganism concentration dissemination for the different values of the motile microbe parameter (ω) and microbial Brownian motion parameter (Nn). It is worth pointing out that the microbial Brownian motion is implied by the unrestricted mobility and unpredictable behaviour of motile microbes. The decline in the gyrotactic microorganism concentration profile for high Nn indicates fewer motile microbes for the reaction (see Figure 13a). From a physics point of view, when Nn gets larger, the random collision between motile microbes increases, which leads to a reduction in motile microorganism transfers. As a result, an elevation in Nn resembles a decrement in the motile microbe concentration characteristics. In the other figure, there is an enhancement in the magnitude of motile microbes, in particular near the wall of the cylinder, when the bioconvection constant is raised. From formula $\omega = \frac{n_\infty}{n_w - n_\infty}$, we note that the motile microbe constant correlates the ambient density of the motile microbes to the density difference across the boundary layer. When ω upsurges, there is a larger density gradient across the boundary layer regime, which promotes the propulsion of motile microbes from the surface to the bulk flow. This results in an enhancement in the density of the motile microbes, in particular near the wall of the cylinder.

The ramification of the Williamson fluid parameter (Λ) and nonlinear thermal convection coefficient (Ω) on the wall friction factor is disclosed in Figure 14. Figure 14a demonstrates that the surface drag coefficient is a decreasing function of the changing Williamson fluid parameter. Larger values of Λ imply that a long relaxation time is needed to yield excess fluid movement resistance, thus increasing the skin friction factor. Figure 14b shows that wall shear stress is also improved with a rise in the nonlinear temperature parameter since an upsurge in Ω raises the density of the fluid flow, which in turn augments resistance to the flow. Figure 15 illustrates the upshots of the suction parameter $(f_w > 0)$ and velocity slip parameter (δ) on the surface drag coefficient. It is perceived from Figure 15a that a greater suction parameter leads to a decrement in the skin friction factor. This demonstrates that an improvement in the cylinder surface's porosity causes an increment in the fluid flow resistance. In the other figure, surface shear stress is also diminished by increasing the values of δ, since the fluid flow is decelerated along the cylinder when δ is raised. As noted in Prasad et al. [45], there is progressive movement in the peak shear stress locations far away from the lower stagnation when δ is elevated. Thus, the repercussion of the wall slip is noted to be significant on the boundary layer features of the Williamson fluid flow from the horizontal cylinder.

Figure 16 highlights the consequences of the variable viscosity parameter (α) and applied magnetic field parameter (M) on the wall friction factor. From the first figure, it is

clear that the skin friction factor is reduced by the rise in α because of a lower resistance to flow on the cylinder surface. When there is less resistance to flow, the fluid moves more freely along the surface, causing a reduction in the shear stress and skin friction coefficient. On the other hand, a rise in the magnetic field parameter augments the surface drag coefficient. This is because the Lorentz force monitors the rate at which the fluid particles tend to move; thus, the drag coefficient increases at the level of the cylinder's surface.

The upshots of the heat radiation parameter (Rd) and temperature ratio parameter (θ_f) on the dimensionless Nusselt number are depicted in Figure 17. From Figure 17a, it is clear that the elevation in Rd suggests a prominent increment in the local Nusselt number. This deportment is in harmony with the fact that heat transportation becomes superior with the radiation effect. Figure 17b illustrates that the heat transfer rate escalates with increment in the surface temperature excess ratio since the presence of the temperature ratio parameter $\theta_f = \frac{T_f}{T_\infty}$ contributes towards enhancement of the temperature of the fluid.

Figure 18 illustrates the distribution of the local Nusselt number for various variable thermal conductance (β) and heat generation parameters $(Q > 0)$. The local Nusselt number is enhanced by rising values of β as seen in Figure 18a. This behaviour is due to the fact that the cylinder distributes additional heat by intensifying β, which in turn accelerate the heat distribution in the system as well as the rate of heat transport. Figure 18b demonstrates that escalation in Q gives rise to higher Nusselt numbers. This is because the mechanisms of heat source produce a layer of warmed fluid near the cylindrical surface; thus, the temperature of the fluid surpasses the temperature of the cylinder's surface.

The variation in the dimensionless local density number of the motile microbes with the AE parameter (E) and microbial reaction parameter (K_m) is depicted in Figure 19. It is evident that the density number of motile microbes drops when the dimensionless AE parameter is increased. This signifies that as the Reynolds number escalates, the diffusion rate prevails over the motile microbe transfer rate. The lower the density number of motile microbes, the more AE there is. Higher AE implies that more energy is needed for the motile microbes to have a fruitful collision. On the other hand, the density number of motile microorganisms is noted to be remarkably enhanced by strong motile microbial reactions. Figure 20 elucidates the impact of the bioconvection constant (ω) and microbial Brownian motion parameter (Nn) on the density number of motile microbes. Figure 20a reveals that as Nn augments, the density number of motile microbes is enhanced. This might be attributed to the fact that motile microbes in the Williamson fluid are moving haphazardly. The other figure demonstrates that the motile microbe transfer rate is reduced with the growing values of the motile microbes parameter.

5. Concluding Remarks

A mathematical model has been described for the bioconvective flow of magneto-Williamson NF comprising motile microbes through a radiative horizontal circular cylinder in a porous medium with nonlinear Boussinesq approximation, heat generation/assimilation, variable fluid properties, AE, chemical and microbial reactions, and Brownian motion for both NPs and motile microorganisms. The modified Buongiorno NF model is employed, and the problem is modeled subject to velocity slip, suction/injection, and heat-convective and zero mass flux boundary conditions. Using appropriate similarity transformations, a non-dimensional partial differential boundary value problem has been derived for the transport features. The resulting coupled partial differential equation system has been solved numerically with appropriate boundary conditions at the wall and in the free stream, using an overlapping grid-based SCM that employs the local linearisation technique to deal with non-linearity in the flow problem. The findings confirmed that the overlapping grid-based numerical scheme should be the most preferred numerical method for solving flow problems similar to the one considered in the current work. The remaining prominent numerical results of the present investigation are recapitulated as follows:

- Nonlinear thermal convection, velocity slip, magnetic field, and variable viscosity parameters accelerate NF motion, while the Williamson fluid and suction parameters decelerate the fluid flow.
- The surface drag coefficient is lifted for the Williamson fluid, nonlinear convection, and magnetic field parameters, but decays for suction, velocity slip, and variable viscosity.
- The NF temperature and heat relocation rate are enhanced by rising thermal radiation, temperature ratio, and fluctuating thermal conductivity parameters.
- The inclusion of AE assists in raising concentrations of NPs and motile microbes.
- The incorporation of microbial reactions and Brownian motion contributes to a rise in motile microbes transfer rate and a reduction in the density of motile microbes.

In the near future, the current problem can be extended to the bioconvection flow of other non-Newtonian fluid models by considering the Tiwari–Das nanofluid model with other features such as electro-magnetohydrodynamics, viscous dissipation, Joule heating, and microbial growth. To optimize thermal processes, analysis of entropy generation will also be studied.

Funding: This research received no external funding.

Informed Consent Statement: Not applicable.

Data Availability Statement: The data presented in this study are available on request from the corresponding author.

Conflicts of Interest: The author declares no conflicts of interest.

Abbreviations

The following abbreviations are used in this manuscript:

Latin Symbols

$\bar{u}, \bar{v}$	Dimensional velocity segments along $\bar{x}-$ and $\bar{y}-$axis (m s^{-1})
$\bar{u}_e$	velocity of the external flow (m s^{-1})
U_∞	Free stream (ambient) velocity (m s^{-1})
V_w	Mass suction/injection velocity (m s^{-1})
k_r^2, k_m^2	Chemical and microbial reaction rates (s^{-1})
a	Radius of the cylinder (m)
k_B	Boltzmann constant (eV K^{-1})
Q_0	Heat source/sink coefficient (W m^{-3} K^{-1})
N_0	First order velocity slip factor (m s^{-1})
T	Fluid temperature (K)
T_f, T_∞	Surface and free stream temperature (K)
b	Chemotaxis constant (m)
k^*	Mean absorption variable (m^{-1})
m_w	surface motile microbes flux (kg m^{-2} s^{-1})
n	Motile microbes concentration (kg m^{-3})
n_w, n_∞	Surface and free stream concentrations of motile microbes (kg m^{-3})
D_B	Brownian motion factor (m^2 s^{-1})
C_p	Specific heat capacity (J kg^{-1} K^{-1})
D_T	Thermophoretic diffusion coefficient (m^2 s^{-1})
q_w	Surface heat flux (W m^{-2})
W_c	Maximum cell swimming speed (m s^{-1})
g	Acceleration due to gravity (m s^{-2})
D_n	Diffusivity of motile microbes (m^2 s^{-1})
E_b	Coefficient of activation energy (eV)
B_0	Magnetic field strength (kg s^{-2} A^{-1})

Latin Symbols

k_p	permeability of the porous medium (m^2)
u, v	Non-dimensional velocity components (m s^{-1})
Gr	Grashof number
Bi	Thermal Biot number
Nu	Local Nusselt number
C_f	Skin friction vcoefficient
Nm	Local density number of motile microbes
p	fitted rate constant
Nb, Nn	NP and microbes Brownian diffusion parameters
M	Magnetic field parameter
Sc	Schmidt number
K_c, K_n	Chemical and microbes reaction rate parameters
Pe	bioconvection Peclet number
h_f	Heat transfer coefficient
f_w	Suction/blowing parameter
Re	Local Reynolds number
f	Dimensionless stream function
Q	Heat generation/absorption parameter
Rb	Bioconvection Rayleigh number
Pr	Prandtl number
Nr	Buoyancy ratio parameter
E	non-dimensional activation energy parameter
Rd	Thermal radiation parameter
Nt	Thermophoresis force constant
Sb	Bioconvection Schmidt number

Greek Symbols

γ	Average volume of motile microbes (kg m^{-3})
β_0, β_1	Linear and nonlinear volumetric thermal expansion coefficients (K^{-1})
κ	Thermal conductivity (W m^{-1} K^{-1})
ν	Kinematic viscosity (m^2 s^{-1})
μ	Dynamic viscosity (kg m^{-1} s^{-1})
θ, ϕ, χ	Dimensionless temperature, NP species and microbes concentration
φ	NP volume fraction (kg m^{-3})
τ_w	Wall shear stress (kg m^{-1} s^{-2})
σ^*	Stefan-Boltzmann constant (1.3807×10^{-23} J K^{-1})
σ	Electrical conductivity (S m^{-1})
ρ	Density (kg m^{-3})
φ_∞	Ambient NP volume fraction (kg m^{-3})
Ψ	Stream function (m^2 s^{-1})

Subscripts

w, ∞	Wall and ambient conditions

Greek Symbols

θ_f	Temperature ratio parameter
η	Pseudo-similarity variable
Λ	Williamson fluid parameter
Γ	Material constant
Ω	nonlinear convection parameter
ε	Porosity parameter
ω	Difference variable of microbes concentration
α	Viscosity variation parameter
β	Variable thermal conductivity parameter
τ	Nanofluid heat capacity ratio
λ	Mixed convection parameter
δ	Velocity slip parameter
ξ	Stream-wise (transverse) coordinate

Superscripts

f, p, m	Fluid, NP and motile microbes

Appendix A. LLM Algorithm

1. Solve for f in the first equation assuming that θ, ϕ and χ are known from previous iteration. $\rightarrowtail f_{r+1}$.
2. Considering that f_{r+1} is now known, solve for θ in the second equation, assuming that ϕ and χ are known from previous iteration. $\rightarrowtail \theta_{r+1}$.
3. Considering that f_{r+1} and θ_{r+1} are now known, solve for θ in the third equation, assuming that χ is known from previous iteration. $\rightarrowtail \phi_{r+1}$.
4. Lastly, considering that f_{r+1}, θ_{r+1} and ϕ_{r+1} are now known, solve for θ in the last equation. $\rightarrowtail \chi_{r+1}$.

Appendix B. Variable Coefficients Obtained Using the LLM Approach

$$a_{0,r} = e^{-\alpha\theta_r} + \Lambda\xi e^{-\alpha\theta_r} f_r'',\ a_{1,r} = f_r - \alpha\theta_r' e^{-\alpha\theta_r} + \Lambda\xi e^{-\alpha\theta_r} f_r''' - 2\alpha\Lambda\xi\theta_r' f_r'' e^{-\alpha\theta_r} + \xi\frac{\partial f_r}{\partial\xi},$$

$$a_{2,r} = -2f_r' - (M + \varepsilon e^{-\alpha\theta_r}) - \xi\frac{\partial f_r'}{\partial\xi}, a_{3,r} = f_r'', a_{4,r} = -\xi f_r', a_{5,r} = \xi f_r'', a_{6,r} = f_r f_r'' - f_r'^2$$

$$-M\frac{\sin\xi}{\xi} - \varepsilon e^{-\alpha\theta_r}\frac{\sin\xi}{\xi} - \frac{\sin\xi\cos\xi}{\xi} + \Lambda\xi f_r'' f_r''' e^{-\alpha\theta_r} - \alpha\Lambda\xi\theta_r' f_r''^2 e^{-\alpha\theta_r} - \xi f_r'\frac{\partial f_r'}{\partial\xi} + \xi f_r''\frac{\partial f_r}{\partial\xi}$$

$$-\lambda(\theta_r + \Omega\theta_r^2 - Nr\phi_r - Rb\chi_r)\frac{\sin\xi}{\xi}, b_{0,r} = 1 + \beta\theta_r + \frac{4}{3}Rd + 4(\theta_f - 1)Rd\theta_r + 4(\theta_f - 1)^2 Rd\theta_r^2$$

$$+\frac{4}{3}Rd(\theta_f - 1)^3\theta_r^3, b_{1,r} = Prf_r + 2\beta\theta_r' + 8Rd(\theta_f - 1)\theta_r' + 16Rd(\theta_f - 1)^2\theta_r\theta_r' + 8Rd(\theta_f - 1)^3\theta_r^2\theta_r'$$

$$+NbPr\phi_r' + NnPr\chi_r' + 2NtPr\theta_r' + Pr\xi\frac{\partial f_r}{\partial\xi}, b_{2,r} = \beta\theta_r'' + 4Rd(\theta_f - 1)\theta_r'' + 8Rd(\theta_f - 1)^2\theta_r\theta_r''$$

$$+4Rd(\theta_f - 1)^3\theta_r''\theta_r^2 + 8Rd(\theta_f - 1)^2\theta_r'^2 + 8Rd(\theta_f - 1)^3\theta_r\theta_r'^2 + PrQ, b_{3,r} = -Pr\xi f_r', b_{4,r} =$$

$$4Rd(\theta_f - 1)\left[\theta_r\theta_r'' + 2(\theta_f - 1)\theta_r''\theta_r^2 + (\theta_f - 1)^2\theta_r''\theta_r^3 + \theta_r'^2 + 4(\theta_f - 1)\theta_r\theta_r'^2 + 3(\theta_f - 1)^2\theta_r^2\theta_r'^2\right]$$

$$+\beta\theta_r\theta_r'' + \beta\theta_r'^2 + NtPr\theta_r'^2, c_{1,r} = Scf_r + Sc\xi\frac{\partial f_r}{\partial\xi}, c_{3,r} = -Sc\xi f_r', \quad c_{4,r} = -\frac{Nt}{Nb}\theta_r'', c_{2,r} =$$

$$-ScK_c(1 + (\theta_f - 1)\theta_r)^p \exp\left(\frac{-E}{(1 + (\theta_f - 1)\theta_r)}\right), e_{1,r} = Sbf_r - Pe\phi_r' + Sb\xi\frac{\partial f_r}{\partial\xi}, e_{2,r} = -Pe\phi_r''$$

$$-SbK_m(1 + (\theta_f - 1)\theta_r)^p \exp\left(\frac{-E}{(1 + (\theta_f - 1)\theta_r)}\right),\ e_{3,r} = -Sb\xi f_r',\ e_{4,r} = Pe\omega\phi_r'' - \frac{Nt}{Nn}\theta_r''. \tag{A1}$$

Appendix C. Derivation of the Length of Each Sub-Interval (L)

To ascertain the length of individual sub-intervals, we observe that the entire length of the spatial domain is specified by

$$\begin{aligned} K_\infty &= 2L - \varrho + (2L - 2\varrho)\left(\frac{\varsigma}{2} - 1\right) \\ &= 2L - \varrho + (L - \varrho)(\varsigma - 2) \\ &= \varrho(1 - \varsigma) + \varsigma L, \end{aligned} \tag{A2}$$

where ϱ represents the distance of overlap between two adjacent sub-intervals. It is important to highlight that ϱ equals the difference between η_0 and η_1 (i.e., $\varrho = \eta_0 - \eta_1$). When examining the first interval J_1, where $\eta \in [0, \eta^1_{N_\eta}]$, we can establish the length $L = \eta^1_{N_\eta}$. Utilizing the linear transformation

$$\eta = \frac{L}{2}\bar{\eta} + \frac{\eta^1_{N_\eta}}{2}, \tag{A3}$$

facilitates the conversion of the interval $[0, \eta^1_{N_\eta}]$ into $[-1, 1]$. Therefore, by employing the Gauss–Lobatto collocation points $\bar{\eta}_i = \cos\left(\frac{\pi i}{N_\eta}\right)$, where $i = 0, 1, 2, ..., N_\eta$, we acquire

$$\begin{aligned} \eta_0 - \eta_1 &= \frac{L}{2}(\bar{\eta}_0 - \bar{\eta}_1) \\ &= \frac{L}{2}\left(1 - \cos\frac{\pi}{N_\eta}\right). \end{aligned} \tag{A4}$$

As a result, Equation (A2) is transformed into

$$K_\infty = \frac{L}{2}\left(1 - \cos\frac{\pi}{N_\eta}\right)(1 - \varsigma) + \varsigma L, \tag{A5}$$

and rearranging the formula given in Equation (A5) to solve for L, we acquire

$$L = \frac{K_\infty}{\varsigma + (1 - \varsigma)(1 - \cos\frac{\pi}{N_\eta})/2}. \tag{A6}$$

Appendix D. The Structure of Chebyshev Differentiation Matrix (D)

$$\mathbf{D} = \begin{bmatrix} \overset{(\varsigma)}{D}_{0,0} & \overset{(\varsigma)}{D}_{0,1} & \cdots & \overset{(\varsigma)}{D}_{0,N_\eta-1} & \overset{(\varsigma)}{D}_{0,N_\eta} & & & & & & & \\ \overset{(\varsigma)}{D}_{1,0} & \overset{(\varsigma)}{D}_{1,1} & \cdots & \overset{(\varsigma)}{D}_{1,N_\eta-1} & \overset{(\varsigma)}{D}_{1,N_\eta} & & & & & & & \\ \ddots & \ddots & \ddots & \ddots & \ddots & & & & & & & \\ \overset{(\varsigma)}{D}_{N_\eta-1,0} & \overset{(\varsigma)}{D}_{N_\eta-1,1} & \cdots & \overset{(\varsigma)}{D}_{N_\eta-1,N_\eta-1} & \overset{(\varsigma)}{D}_{N_\eta-1,N_\eta} & & & & & & & \\ & & & \overset{(\varsigma-1)}{D}_{1,0} & \overset{(\varsigma-1)}{D}_{1,1} & \cdots & \overset{(\varsigma-1)}{D}_{1,N_\eta-1} & \overset{(\varsigma-1)}{D}_{1,N_\eta} & & & & \\ & & & \overset{(\varsigma-1)}{D}_{2,0} & \overset{(\varsigma-1)}{D}_{2,1} & \cdots & \overset{(\varsigma-1)}{D}_{2,N_\eta-1} & \overset{(\varsigma-1)}{D}_{2,N_\eta} & & & & \\ & & & \ddots & \ddots & \ddots & \ddots & \ddots & & & & \\ & & & \overset{(\varsigma-1)}{D}_{N_\eta-1,0} & \overset{(\varsigma-1)}{D}_{N_\eta-1,1} & \cdots & \overset{(\varsigma-1)}{D}_{N_\eta-1,N_\eta-1} & \overset{(\varsigma-1)}{D}_{N_\eta-1,N_\eta} & & & & \\ & & & & & & \ddots & \ddots & & & & \\ & & & & & & \overset{(1)}{D}_{1,0} & \overset{(1)}{D}_{1,1} & \cdots & \overset{(1)}{D}_{1,N_\eta-1} & \overset{(1)}{D}_{1,N_\eta} \\ & & & & & & \overset{(1)}{D}_{2,0} & \overset{(1)}{D}_{2,1} & \cdots & \overset{(1)}{D}_{2,N_\eta-1} & \overset{(1)}{D}_{2,N_\eta} \\ & & & & & & \ddots & \ddots & \ddots & \ddots & \ddots \\ & & & & & & \overset{(1)}{D}_{N_\eta,0} & \overset{(1)}{D}_{N_\eta,1} & \cdots & \overset{(1)}{D}_{N_\eta,N_\eta-1} & \overset{(1)}{D}_{N_\eta,N_\eta} \end{bmatrix}, \tag{A7}$$

References

1. Nazar, R.; Amin, N.; Pop, I. Mixed convection boundary-layer flow from a horizontal circular cylinder in micropolar fluids: Case of constant wall temperature. *Int. J. Numer. Methods Heat Fluid Flow* **2003**, *13*, 86–109. [CrossRef]

2. Madhavi, K.; Nagendra, N.; Raju, G.S.S.; Prasad, V.R. Non-similarity transformations of MHD flow of third-grade fluid over a horizontal circular cylinder in the presence of radiation and suction. *Int. J. Innov. Res. Sci. Eng. Technol.* **2017**, *6*, 73–79.
3. Madhavi, K.; Nagendra, N.; Raju, G.S.S.; Prasad, V.R. Heat transfer analysis of MHD non-Newtonian fluid over a horizontal circular cylinder with Biot number effect. *Res. J. Sci. Technol.* **2017**, *9*, 395–399. [CrossRef]
4. Madhavi, K.; Prasad, V.R.; Gaffar, S.S.; Venkatadri, K. Entropy analysis of third-grade MHD convection flows from a horizontal cylinder with slip. *Arch. Mech. Eng.* **2018**, *65*, 417–440.
5. Gaffar, S.A.; Prasad, V.R.; Reddy, P.R.; Khan, B.M.H. Radiative flow of third grade non-Newtonian fluid from a horizontal circular cylinder. *Nonlinear Eng.* **2019**, *8*, 673–687. [CrossRef]
6. Gaffar, S.A.; Prasad, V.R.; Beg, O.A. Computational analysis of magnetohydrodynamic free convection flow and heat transfer on non-Newtonian tangent hyperbolic fluid from a horizontal circular cylinder with partial slip. *Int. J. Appl. Comput. Math.* **2015**, *1*, 651–675. [CrossRef]
7. Nagaraja, L.; Reddy, M.S.; Reddy, M.S.N. Heat transfer in non-Newtonian fluid past horizontal circular cylinder in non-Darcy porous medium with suction/injection effects. *Indian J. Sci. Technol.* **2017**, *10*, 1–7. [CrossRef]
8. Zokri, S.M.; Arifin, N.S.; Mohamed, M.K.A.; Kasim, A.R.M.; Mohammad, N.F.; Salleh, M.Z. Mathematical model of mixed convection boundary layer flow over a horizontal circular cylinder filled in a Jeffrey fluid with viscous dissipation effect. *Sains Malays.* **2018**, *47*, 1607–1615. [CrossRef]
9. Williamson, R.V. The flow of psedoplastic materials. *Ind. Eng. Chem.* **1929**, *21*, 1108–1111. [CrossRef]
10. Choi, S.U.S.; Eastman, J.A. Enhancing thermal conductivity of fluids with nanoparticles. *ASME Fluids Eng. Div.* **1995**, *23*, 99–106.
11. Buongiorno, J. Convective transport in nanofluids. *J. Heat Transfer* **2006**, *128*, 240–250. [CrossRef]
12. Tiwari, R.J.; Das, M.K. Heat transfer augmentation in a two-sided lid-driven differentially heated square cavity utilizing nanofluids. *Int. J. Heat Mass Transf.* **2007**, *50*, 2002–2018. [CrossRef]
13. Rashad, A.M.; Chamkha, A.J.; Modather, M. Mixed convection boundary-layer flow past a horizontal circular cylinder embedded in a porous medium filled with a nanofluid under convective boundary condition. *Comput. Fluids* **2013**, *86*, 380–388. [CrossRef]
14. Zokri, S.M.; Salleh, M.Z.; Arifin, N.S.; Kasim, A.R.M. Lower stagnation point flow of convectively heated horizontal circular cylinder in Jeffrey nanofluid with suction/injection. *J. Adv. Res. Fluid Mech. Therm. Sci.* **2020**, *76*, 135–144. [CrossRef]
15. Merkin, J.H. Mixed convection from a horizontal circular cylinder. *Int. J. Heat Mass Transf.* **1977**, *20*, 73–77. [CrossRef]
16. Zahar, E.R.; Rashad, A.M.; Saad, W.; Seddek, L.F. Magneto-hybrid nanofluids flow via mixed convection past radiative circular cylinder. *Sci. Rep.* **2020**, *10*, 10494. [CrossRef] [PubMed]
17. Basha, H.T.; Sivaraj, R.; Prasad, V.R.; Beg, O.A. Entropy generation of tangent hyperbolic nanofluid flow over a circular cylinder in the presence of nonlinear Boussinesq approximation: A non-similar solution. *J. Therm. Anal. Calorim.* **2021**, *143*, 2273–2289. [CrossRef]
18. Huang, C.-J. Arrhenius activation energy effect on free convection about a permeable horizontal cylinder in porous media. *Transp. Porous Media* **2019**, *128*, 723–740. [CrossRef]
19. Das, K.; Duari, P.R.; Kundu, P.K. Nanofluid bioconvection in presence of gyrotactic microorganisms and chemical reaction in a porous medium. *J. Mech. Sci. Technol.* **2015**, *29*, 4841–4849. [CrossRef]
20. Bees, M.; Hill, N.A. Wavelengths of bioconvection patterns. *J. Exp. Biol.* **1997**, *200*, 1515–1526. [CrossRef]
21. Kuznetsov, A. Nanofluid bioconvection: Interaction of microorganisms oxytactic up-swimming, nanoparticle distribution, and heating/cooling from below. *Theor. Comput. Fluid Dyn.* **2012**, *26*, 291–310. [CrossRef]
22. Pedley, T.J. Gyrotaxis in uniform vorticity. *J. Fluid Mech.* **2015**, *762*, R6. [CrossRef]
23. Khan, S.U.; Al-Khaled, K.; Aldabesh, A.; Awais, M.; Tlili, I. Bioconvection ow in accelerated couple stress nanoparticles with activation energy: Biofuel applications. *Sci. Rep.* **2021**, *11*, 3331. [CrossRef]
24. Kuznetsov, A.V.; Avramenko, A.A. Effect of small particles on this stability of bioconvection in a suspension of gyrotactic microorganisms in a layer of finite depth. *Int. Commun. Heat Mass Transf.* **2004**, *31*, 1–10. [CrossRef]
25. Hill, N.A.; Pedley, T.J. Bioconvection. *Fluid Dyn. Res.* **2005**, *37*, 1–20. [CrossRef]
26. Alloui, Z.; Nguyen, T.H.; Bilgen, E. Bioconvection of gravitactic microorganisms in a vertical cylinder. *Int. Commun. Heat Mass Transf.* **2005**, *32*, 739–747. [CrossRef]
27. Mallikarjuna, B.; Rashad, A.M.; Chamkha, A.; Abdou, M.M.M. Mixed bioconvection flow of a nanofluid containing gyrotactic microorganisms past a vertical slender cylinder. *Front. Heat Mass Transf.* **2018**, *10*, 1–10. [CrossRef]
28. Rashad, A.M.; Nabwey, H.A. Gyrotactic mixed bioconvection flow of nanofluid past a circular cylinder with convective boundary condition. *J. Taiwan Inst. Chem. Eng.* **2019**, *99*, 9–17. [CrossRef]
29. Dhlamini, M.; Mondal, H.; Sibanda, P.; Motsa, S.; Sachin, S. A mathematical model for bioconvection flow with activation energy for chemical reaction and microbial activity. *Pramana-J. Phys.* **2022**, *96*, 112. [CrossRef]
30. Mkhatshwa, M.P. Bioconvective flow of fourth-grade nanofluid via a stretchable porous surface with microbial activity and activation energy. *Case Stud. Therm. Eng.* **2023**, *51*, 103526. [CrossRef]
31. Mkhatshwa, M.P.; Motsa, S.S.; Sibanda, P. Overlapping multi-domain bivariate spectral method for non-Darcian mixed convection chemically reacting flow of micropolar fluid over a flat surface in porous media. *J. Appl. Anal. Comput.* **2021**, *11*, 1–25.
32. Mkhatshwa, M.P. Overlapping grid spectral collocation approach for electrical MHD bioconvection Darcy–Forchheimer flow of a Carreau–Yasuda nanoliquid over a periodically accelerating surface. *Heat Transf.* **2022**, *51*, 1468–1500. [CrossRef]

33. Mkhatshwa, M.P.; Khumalo, M. Double diffusion and Hall effects on MHD sinusoidal natural convection flow of silver water-based nanofluid from a porous vertical plate. *Partial Differ Equ. Appl. Math.* **2023**, *7*, 100516. [CrossRef]
34. Raptis, A. Radiation and free convection flow through a porous medium. *Int. Comm. Heat Transf.* **1998**, *25*, 289–295. [CrossRef]
35. Hakiem, M.A.; Rashad, A.M. Effect of radiation on non-Darcy free convection from a vertical cylinder embedded in a fluid saturated porous medium with a temperature-dependent viscosity. *J. Porous Media* **2007**, *10*, 209–218.
36. Oyelakin, I.S.; Sibanda, P. Analysis of exponentially varying viscosity and thermal conductivity on a tangent hyperbolic fluid. *SeMA J.* **2020**, *77*, 257–273. [CrossRef]
37. Mkhatshwa, M.P.; Khumalo, M. Irreversibility scrutinization onEMHD Darcy–Forchheimer slip flow of Carreau hybrid nanofluid through a stretchablesurface in porous medium with temperature-variant properties. *Heat Transf.* **2023**, *52*, 395–429. [CrossRef]
38. Mkhatshwa, M.P.; Motsa, S.S.; Sibanda, P. MHD mixed convective radiative flow of Eyring-Powell fluid over an oscillatory stretching sheet using bivariate spectral method on overlapping grids. *Heat Transf.* **2021**, *50*, 655–687. [CrossRef]
39. Mkhatshwa, M.P.; Motsa, S.S.; Sibanda, P. MHD bioconvective radiative flow of chemically reactive Casson nanofluid from a vertical surface with variable transport properties. *Int. J. Ambient Energy* **2020**, *43*, 3170–3188. [CrossRef]
40. Motsa, S.S. A new spectral local linearization method for nonlinear boundary layer flow problems. *J. Applied Math.* **2013**, *2013*, 423628. [CrossRef]
41. Motsa, S.S. On the practical use of the spectral homotopy analysis method and local linearisation method for unsteady boundary-layer flows caused by an impulsively stretching plate. *Numer. Algorithms* **2014**, *66*, 865–883. [CrossRef]
42. Motsa, S. On the new bivariate local linearisation method for solving coupled partial differential equations in some applications of unsteady fluid flows with heat and mass transfer. In *Mass Transfer—Advancement in Process Modelling*; InTech: Vienna, Austria, 2015.
43. Trefethen, L.N. *Spectral Methods in MATLAB*; SIAM: Philadelphia, PA, USA, 2000.
44. Yang, H.H.; Seymour, B.R.; Shizgal, B.D. A Chebyshev pseudospectral multi-domain method for steady flow past a cylinder up to $Re = 150$. *Comput. Fluids* **1994**, *23*, 829–851. [CrossRef]
45. Prasad, V.R.; Rao, A.S.; Reddy, N.B.; Beg, O.A. Modelling laminar transport phenomena in a Casson rheological fluid from an isothermal sphere with partial slip in a non-Darcy medium. *Thoret. Appl. Mech.* **2013**, *40*, 469–510. [CrossRef]

computation

MDPI

Article

Hybrid Nanofluid Flow over a Shrinking Rotating Disk: Response Surface Methodology

Rusya Iryanti Yahaya [1], Norihan Md Arifin [1,2,*], Ioan Pop [3], Fadzilah Md Ali [1,2] and Siti Suzilliana Putri Mohamed Isa [1,4]

[1] Institute for Mathematical Research, Universiti Putra Malaysia, Serdang 43400, Malaysia; rusyairyanti@gmail.com (R.I.Y.); fadzilahma@upm.edu.my (F.M.A.); ctsuzilliana@upm.edu.my (S.S.P.M.I.)
[2] Department of Mathematics and Statistics, Universiti Putra Malaysia, Serdang 43400, Malaysia
[3] Department of Mathematics, Babeş-Bolyai University, 400084 Cluj-Napoca, Romania; popm.ioan@yahoo.co.uk
[4] Centre of Foundation Studies for Agricultural Science, Universiti Putra Malaysia, Serdang 43400, Malaysia
* Correspondence: norihana@upm.edu.my

Abstract: For efficient heating and cooling applications, minimum wall shear stress and maximum heat transfer rate are desired. The current study optimized the local skin friction coefficient and Nusselt number in Al_2O_3-Cu/water hybrid nanofluid flow over a permeable shrinking rotating disk. First, the governing equations and boundary conditions are solved numerically using the bvp4c solver in MATLAB. Von Kármán's transformations are used to reduce the partial differential equations into solvable non-linear ordinary differential equations. The augmentation of the mass transfer parameter is found to reduce the local skin friction coefficient and Nusselt number. Higher values of these physical quantities of interest are observed in the injection case than in the suction case. Meanwhile, the increase in the magnitude of the shrinking parameter improved and reduced the local skin friction coefficient and Nusselt number, respectively. Then, response surface methodology (RSM) is conducted to understand the interactive impacts of the controlling parameters in optimizing the physical quantities of interest. With a desirability of 66%, the local skin friction coefficient and Nusselt number are optimized at 1.528780016 and 0.888353037 when the shrinking parameter (λ) and mass transfer parameter (S) are -0.8 and -0.6, respectively.

Keywords: disk; hybrid nanofluid; RSM; shrinking; suction/injection

Citation: Yahaya, R.I.; Arifin, N.M.; Pop, I.; Ali, F.M.; Isa, S.S.P.M. Hybrid Nanofluid Flow over a Shrinking Rotating Disk: Response Surface Methodology. *Computation* **2024**, *12*, 141. https://doi.org/10.3390/computation12070141

Academic Editors: Ali Cemal Benim, Abdulmajeed A. Mohamad, Sang-Ho Suh, Rachid Bennacer, Paweł Oclon and Jan Taler

Received: 28 June 2024
Revised: 6 July 2024
Accepted: 8 July 2024
Published: 10 July 2024

1. Introduction

Rotating machinery, gas turbine rotators, and thermal power generating systems are among the numerous practical applications of the classical rotating-disk flow [1]. The Navier–Stokes equations for rotating-disk flow were first presented by Von Kármán [2]. In this study, Von Kármán's transformations were introduced to reduce the partial differential equations into a system of ordinary differential equations. Later, these equations were employed in various rotating-disk flow problems. Ayano et al. [3] did a numerical computation on magnetohydrodynamics (MHD) nanofluid flow over a stretching rotating disk with Brownian motion, thermophoresis, and gyrotactic microorganisms. Von Kármán's transformations were employed in this study, and the increased stretching parameter was found to reduce the temperature profile. Meanwhile, the augmentation of the thermophoresis and Brownian motion enhanced and reduced the concentration profile. Then, the unsteady flow of nanofluid over a stretching rotating disk with variable viscosity, Brownian motion, and thermophoresis was analyzed by Sharma et al. [4]. It was found that the increased stretching rate promoted fluid flow in the radial direction and enhanced horizontal velocity. Puneeth et al. [5] then examined the unsteady flow over a permeable stretching rotating disk. It was observed that a high nanoparticle volume fraction improved and reduced the temperature and velocity profiles of the nanofluid.

Researchers have also examined the rotating-disk flow of hybrid nanofluids containing the dispersion of two different nanoparticles. Rashid et al. [6] analyzed the MHD hybrid nanofluid flow over a rotating disk with Brownian motion and thermophoresis. It was noted that the hybrid nanofluid possessed better thermal conductivity than the nanofluid. Moreover, the augmentation of the magnetic field reduced axial and tangential velocities while increasing the surface drag. Meanwhile, thermophoresis and nanoparticle volume fraction enhanced the heat transfer performance. Alkuhayli [7] extended this study with thermal radiation and heat source/sink. The enhancement of the thermal radiation and variable thermal conductivity parameters was found to have boosted the temperature profile and local Nusselt number. Further extension of this study was made by Kumar et al. [8], who considered the electromagnetohydrodynamic flow over a stretching rotating disk with an irregular heat source, Arrhenius energy, and non-linear radiation. The increment in the electric parameter was noted to reduce the skin friction coefficient and enhance the heat transfer rate. Meanwhile, Kulkarni [9] found that the heat transfer rate increased with the sphericity of the nanoparticles in hybrid nanofluid flow over a permeable rotating disk with mixed convection, magnetic field, and slip. Lone et al. [10] then analyzed the MHD flow of Al_2O_3-Cu/water hybrid nanofluid over a rotating disk with velocity slip, zero mass flux, and convective boundary conditions. Next, Khashi'ie et al. [11] conducted a stability analysis on multiple solutions obtained in MHD hybrid nanofluid flow over a permeable stretching/shrinking rotating disk with heat generation. The findings revealed that only the first and second solutions were stable and physically significant, while the third solution was unstable. In addition, only the suction parameter enhanced the heat transfer performance of the hybrid nanofluid. Vijay and Sharma [12] then studied the Soret and Dufour effects on MHD hybrid nanofluid flow over a permeable decelerating rotating disk. Later, Abu Bakar et al. [13] analyzed the unsteady flow of Al_2O_3-Cu/water hybrid nanofluid over an inclined, shrinking, rotating disk with thermal radiation and velocity slip. Similarly, only the first solution was found to be stable, while the second solution was unstable. The nanoparticle volume fraction, radiation, and shrinking parameters increased the heat transfer rate. Recently, the rotating-disk flow of ternary and tetra hybrid nanofluids, consisting of three and four different nanoparticles dispersed in a base fluid, was also analyzed by researchers (see Ali et al. [14], Singh et al. [15], and Patgiri and Paul [16]). In addition, researchers have also incorporated machine learning approaches to study fluid flow over a rotating disk (see Ali et al. [17] and Kumar et al. [18]).

Moreover, researchers have also included statistical analysis to improve theoretical investigations of fluid flow over a rotating disk. A sophisticated statistical tool called the response surface methodology (RSM) is commonly employed to analyze the effects and significance of various controlling parameters on specified responses. The optimal conditions at which to achieve the desired response can also be estimated using the RSM. Mehmood et al. [19] utilized the RSM to optimize the local skin friction coefficients and Nusselt number in MHD nanofluid flow past a stretched rotating disk with entropy generation and autocatalytic chemical reaction. Both physical quantities of interest were found to be optimized by the higher value of the magnetic parameter. Then, Shafiq et al. [20] considered the Darcy–Forchheimer flow of nanofluid past a stretched rotating disk with thermal radiation. Based on the RSM and sensitivity analysis, the local Nusselt number was most sensitive towards the solid volume fraction, followed by the radiation parameter and Biot number. Later, Mathew et al. [21] examined the effects of magnetic field and stratification in bioconvective stagnation-point flow over a stretched rotating disk. This study employed the RSM to investigate the relationship between the magnetic field, thermal stratification, the nanoparticle volume fraction of magnetite, and the velocity ratio parameter and the heat transfer rate. The thermal stratification and magnetic field parameters were found to have a negative correlation with the heat transfer rate. Recently, the RSM was utilized by Hussain et al. [22] to optimize the MHD nanofluid flow past a rotating disk with thermal radiation and Joule heating. Meanwhile, Khashi'ie et al. [23] found through the RSM that the magnetic and suction parameters significantly affected the skin friction coefficient in

unsteady hybrid nanofluid flow over a rotating disk with heat generation. In the meantime, the heat transfer rate was affected by the magnetic, suction, and heat generation parameters.

Due to the scarcity of rotating-disk flow studies that combine numerical and statistical investigations, the current research will focus on these approaches to analyze the flow and heat transfer performance in Al_2O_3-Cu/water hybrid nanofluid flow past a shrinking rotating disk. The surface is assumed to be permeable to allow for suction/injection. Partial differential equations and boundary conditions governing this flow problem will be solved numerically using the bvp4c solver in MATLAB. Then, RSM will be executed to analyze the interaction of mass transfer with shrinking parameters and their significance in optimizing the physical quantities of interest. The current study aims to fill the existing literature gap and offer a better understanding of the impacts of mass transfer and shrinking parameters on the considered flow problem.

2. Mathematical Formulation

The working fluid contains alumina (Al_2O_3) and copper (Cu) nanoparticles dispersed in water. This combination is chosen because Cu nanoparticles offer high thermal conductivity, Al_2O_3 nanoparticles exhibit good inertness, and water is widely available. Moreover, an experimental study by Siddiqui et al. [24] demonstrated that an Al_2O_3-Cu/water hybrid nanofluid with a 50:50 mixing ratio resulted in an overall enhanced hydrothermal property with improved thermal conductivity and better stability. Meanwhile, the correlations and values of thermophysical properties for the Al_2O_3-Cu/water hybrid nanofluid are based on Takabi et al. [25] and Oztop and Abu-Nada [26]. At a low-volume concentration of this hybrid nanofluid, the correlations proposed by Takabi et al. [25] were found to be in good agreement with the experiment results presented by Suresh et al. [27]. Following this, a low-volume concentration of Cu and Al_2O_3 nanoparticles is used in the current study (i.e., $\phi_{Al_2O_3} = \phi_{Cu} = 0.02$).

Meanwhile, the flow configuration is described using cylindrical coordinates (r, φ, z) and velocity components (u, v, w), respectively. The schematic representation is depicted in Figure 1.

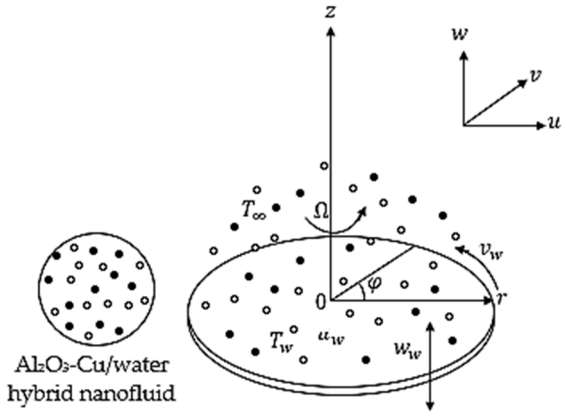

Figure 1. Schematic diagram of the flow problem.

The fluid is assumed to flow in the region $z \geq 0$ over an infinite rotating disk with a uniform shrinking rate a in the radial direction r; angular velocity Ω; mass flux velocity $w_w = \sqrt{\Omega \nu_{bf}} S$ with mass transfer parameter S and kinematic viscosity of base fluid ν_{bf}; and constant temperature T_w. Meanwhile, the surrounding hybrid nanofluid is assumed to have a temperature of T_∞, with $T_w > T_\infty$ for a hot disk. In the current study, the flow is considered to be steady and axisymmetric (i.e., $\partial/\partial\varphi = 0$ for all variables).

Following the stated assumptions, the governing equations and boundary conditions for the laminar, incompressible Newtonian hybrid nanofluid flow are as follows [28,29]:

$$\frac{\partial u}{\partial r} + \frac{u}{r} + \frac{\partial w}{\partial z} = 0, \tag{1}$$

$$u\,\frac{\partial\, u}{\partial\, r} + w\,\frac{\partial\, u}{\partial\, z} - \frac{v^2}{r} = \frac{\mu_{hnf}}{\rho_{hnf}}\left[\frac{1}{r}\frac{\partial u}{\partial r} - \frac{u}{r^2} + \frac{\partial^2 u}{\partial\, r^2} + \frac{\partial^2 u}{\partial\, z^2}\right], \tag{2}$$

$$u\,\frac{\partial\, v}{\partial\, r} + w\,\frac{\partial\, v}{\partial\, z} + \frac{u\,v}{r} = \frac{\mu_{hnf}}{\rho_{hnf}}\left[\frac{1}{r}\frac{\partial v}{\partial r} - \frac{v}{r^2} + \frac{\partial^2 v}{\partial\, r^2} + \frac{\partial^2 v}{\partial\, z^2}\right], \tag{3}$$

$$u\,\frac{\partial\, v}{\partial\, r} + w\,\frac{\partial\, v}{\partial\, z} + \frac{u\,v}{r} = \frac{\mu_{hnf}}{\rho_{hnf}}\left[\frac{1}{r}\frac{\partial v}{\partial r} - \frac{v}{r^2} + \frac{\partial^2 v}{\partial\, r^2} + \frac{\partial^2 v}{\partial\, z^2}\right], \tag{4}$$

$$u\,\frac{\partial\, T}{\partial\, r} + w\,\frac{\partial\, T}{\partial\, z} = \frac{k_{hnf}}{\left(\rho\, C_p\right)_{hnf}}\left[\frac{1}{r}\frac{\partial T}{\partial r} + \frac{\partial^2 T}{\partial\, r^2} + \frac{\partial^2 T}{\partial\, z^2}\right], \tag{5}$$

$$\left.\begin{array}{c} u = u_w = ar,\quad v = v_w = \Omega\, r,\quad w = w_w,\quad T = T_w \quad \text{at}\quad z = 0 \\ u \to 0,\quad v \to 0,\quad T \to T_\infty \quad \text{as}\quad z \to \infty \end{array}\right\}. \tag{6}$$

In these equations, the subscript hnf denotes hybrid nanofluid, μ is the dynamic viscosity, ρ is the density, k is the thermal conductivity, C_p is the specific heat, T is the temperature, and p is the pressure. Then, these partial differential equations are subjected to the following Von Kármán's transformations [2]:

$$\left.\begin{array}{c} u = \Omega\, r f(\eta),\quad v = \Omega\, r g(\eta),\quad w = \sqrt{\Omega\,\nu_{bf}}\, h(\eta),\quad \theta(\eta) = \frac{T - T_\infty}{T_w - T_\infty} \\ p - p_\infty = 2\,\mu_{bf}\,\Omega\, P(\eta),\quad \eta = z\sqrt{\frac{\Omega}{\nu_{bf}}} \end{array}\right\} \tag{7}$$

to form the following non-linear ordinary differential equations and boundary conditions:

$$2\, f + h' = 0, \tag{8}$$

$$\frac{\mu_{hnf}/\mu_{bf}}{\rho_{hnf}/\rho_{bf}} f'' - h f' - f^2 + g^2 = 0, \tag{9}$$

$$\frac{\mu_{hnf}/\mu_{bf}}{\rho_{hnf}/\rho_{bf}} g'' - h\, g' - 2fg = 0, \tag{10}$$

$$\frac{k_{hnf}/k_{bf}}{\left(\rho\, C_p\right)_{hnf}/\left(\rho\, C_p\right)_{bf}} \theta'' - Prh\, \theta' = 0, \tag{11}$$

$$\left.\begin{array}{c} g(0) = 1,\quad f(0) = \lambda,\quad h(0) = S,\quad \theta(0) = 1 \\ g(\eta) \to 0,\quad f(\eta) \to 0,\quad \theta(\eta) \to 0 \quad as \quad \eta \to \infty \end{array}\right\}, \tag{12}$$

where '$\prime$' denotes differentiation with respect to η; bf refers to the base fluid; f, g, and h are the radial, tangential, and axial velocities; $\lambda = a/\Omega$ is the shrinking parameter; S is the mass transfer parameter with $S < 0$ for injection and $S > 0$ for suction; and $Pr = \left(\mu\, C_p\right)_{bf}/k_{bf}$ is the Prandtl number. According to Turkyilmazoglu [28], the fluid pressure can be determined by integrating Equation (4), and the resulting pressure equation is decoupled from the flow field. Since the interest of the current study is to analyze the flow and thermal fields of the hybrid nanofluid, the pressure function can be neglected.

Then, the physical quantities of interest are the skin friction coefficient (C_f) and Nusselt number (Nu_r) [28]:

$$C_f = \frac{\mu_{hnf}\sqrt{\left[\left(\frac{\partial u}{\partial z} + \frac{\partial w}{\partial \varphi}\right)_{z=0}\right]^2 + \left[\left(\frac{\partial v}{\partial z} + \frac{1}{r}\frac{\partial w}{\partial \varphi}\right)_{z=0}\right]^2}}{\rho_{bf}\,(\Omega\, r)^2},$$

$$Nu_r = \frac{r\, k_{nf}}{k_{bf}\,(T_w - T_\infty)}\left(-\frac{\partial T}{\partial z}\right)_{z=0},$$

which result in the following:

$$Re_r^{1/2} C_f = \frac{\mu_{hnf}}{\mu_{bf}}\sqrt{[f'(0)]^2 + [g'(0)]^2}, \quad Re_r^{-1/2} Nu_r = -\frac{k_{hnf}}{k_{bf}}\theta'(0), \tag{13}$$

where $Re_r^{1/2} C_f$ is the local skin friction coefficient; $Re_r^{-1/2} Nu_r$ is the local Nusselt number; and $Re_r = \frac{\Omega r^2}{\nu_{bf}}$ is the local Reynolds number. Here, an increase in the angular velocity can raise the local Reynolds number.

3. Response Surface Methodology (RSM)

Box and Wilson [30] introduced an experimental design-based approach, incorporating statistical and mathematical techniques, called the response surface methodology (RSM). The RSM can be used to model, analyze, and optimize a system containing dependent (response) and independent parameters. The relationship between the response and independent parameters can be described as follows [31]:

$$\text{Response} = F(X_1, X_2, X_3, \ldots, X_N) \pm E, \tag{14}$$

where F is the unknown function of response with $X_1, X_2, X_3, \ldots, X_N$ as independent parameters; and E is the random experimental error assumed to have a zero mean. Meanwhile, the general quadratic model is

$$\text{Response} = c_0 + \sum_{i=1}^{N} c_i x_i + \sum_{i=1}^{N} c_{ii} x_i^2 + \sum_{i=1}^{N-1}\sum_{j=i+1}^{N} c_{ij} x_i x_j, \tag{15}$$

with c_0, c_i, c_{ii}, and c_{ij} representing the intercept, linear, quadratic, and bilinear two-factor terms, respectively.

The current study utilizes the RSM and face-centered central composite design to investigate the significance of the mass transfer and shrinking parameters on the local skin friction coefficient and Nusselt number, as well as the optimal settings of these parameters to minimize and maximize the responses. Therefore, the mass transfer and shrinking parameters are denoted as the independent parameters, and the local skin friction coefficient and Nusselt number are the responses. The independent parameters are labeled as A and B and are assigned with actual and coded values, as shown in Table 1. The ranges for the actual values are taken based on the numerical investigation conducted in the current study.

Table 1. The actual and coded values of the independent parameters.

Independent Parameter	Symbol	Level		
		Low (−1)	Medium (0)	High (1)
λ	A	−1.0	−0.9	−0.8
S	B	−0.6	−0.1	0.4

The central composite design is the most commonly used response surface design to determine the coefficients of the quadratic model. According to Bhattacharya [32], the

central composite design has the benefit of estimating the non-linear relationship between the independent parameters and the response, as well as the ability to provide maximum information with minimal experimental data, and fewer experiments are needed to predict the quadratic term in a quadratic model. The central composite design is comprised of several types, including the face-centered type. The face-centered central composite design requires three levels of each factor or independent parameter (i.e., -1, 0, 1) with $2^N + 2N + C$ experiments. Here, N is the number of independent parameters; 2^N denotes the factorial points; $2N$ denotes the axial points; and C denotes the center points. As stated by Sahoo and Barman [33], the center points may vary from three to six. In this current study, with $N = 2$ and $C = 5$, a total of 13 runs are carried out. The respective responses, calculated using MATLAB for each run, are then tabulated in Table 2. Meanwhile, Figure 2 presents the flowchart of the numerical and statistical procedures involved in the current study.

Table 2. Experimental design and response values.

Runs	Coded Values		Actual Values		Responses	
	A	**B**	λ	S	$Re_r^{1/2}Cf$ **(Response 1)**	$Re_r^{-1/2}Nu_r$ **(Response 2)**
1	-1	-1	-1.0	-0.6	1.803245471	0.232133118
2	1	-1	-0.8	-0.6	1.529299905	0.975650061
3	-1	1	-1.0	0.4	1.475361873	0.000000014
4	1	1	-0.8	0.4	1.229514429	0.000001138
5	-1	0	-1.0	-0.1	1.642240690	0.000228587
6	1	0	-0.8	-0.1	1.380007580	0.004928016
7	0	-1	-0.9	-0.6	1.659170147	0.525530320
8	0	1	-0.9	0.4	1.346068736	0.000000126
9	0	0	-0.9	-0.1	1.504436107	0.001106468
10	0	0	-0.9	-0.1	1.504436107	0.001106468
11	0	0	-0.9	-0.1	1.504436107	0.001106468
12	0	0	-0.9	-0.1	1.504436107	0.001106468
13	0	0	-0.9	-0.1	1.504436107	0.001106468

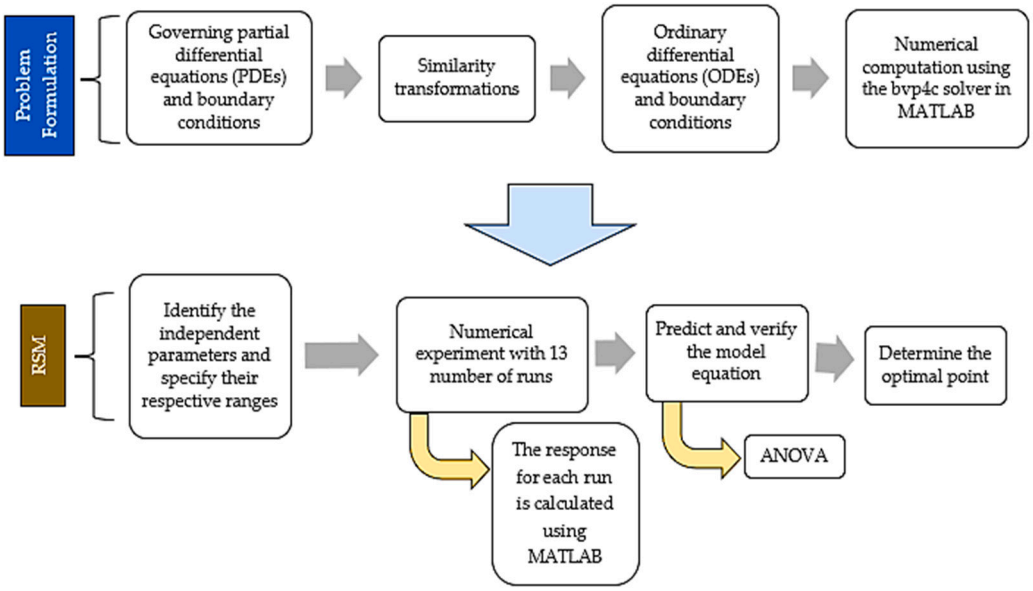

Figure 2. Flowchart of the numerical and statistical procedures.

4. Results and Discussion

The boundary value problem (8)–(12) is numerically solved using the bvp4c solver in MATLAB, and the algorithm is presented in Supplementary Materials. A comparison of

results is made to validate the correctness of the mathematical approach employed in this current study. For $\phi_{hnf} = 0$, the boundary value problem reduces into a classical viscous fluid flow problem, and the numerical results can be compared with those computed by Rashidi et al. [34] and Turkyilmazoglu [28]. These previous studies utilized the shooting and spectral Chebyshev collocation methods, respectively. Despite the difference in computation techniques, the results generated by the bvp4c solver are in close agreement with the previous studies (see Table 3). Furthermore, by assuming the finite value of the free stream boundary condition (i.e., $\eta \to \infty$) to be $\eta_{\max} = 10$, all profiles acquired in this investigation approach the free stream boundary conditions (12) asymptotically. Therefore, it enhances confidence in the reliability of the numerical findings.

Table 3. Comparison of results for $\phi_{Al_2O_3} = \phi_{Cu} = S = \lambda = 0$ and $Pr = 6.2$.

	Rashidi et al. [34]	**Turkyilmazoglu [28]**	**Present Study**
$f'(0)$	0.510186	0.51023262	0.510232394
$-g'(0)$	0.61589	0.61592201	0.615921866
$-\theta'(0)$	-	0.93387794	0.933877577

The effects of shrinking and mass transfer parameters on the velocity and temperature profiles are presented in Figure 3. The radial, tangential, and axial velocities are denoted by $f(\eta)$, $g(\eta)$, and $h(\eta)$, respectively. As observed in Figure 3a, the radial velocity profile of the hybrid nanofluid decreases with the augmentation of the mass transfer parameter and the magnitude of the shrinking parameter. However, the opposite behavior is observed at some distance from the disk. As the disk is assumed to have a no-slip condition and to shrink in the radial direction, the radial velocity of the hybrid nanofluid near the disk decreases as the magnitude of the shrinking parameter increases. The shrinking effects towards the fluid velocity are shown to be diminished at some distance away from the disk (see Figure 3a). Meanwhile, the shrinking of the disk does not affect the tangential and axial velocities of the hybrid nanofluid. The tangential velocity of the hybrid nanofluid continues to increase throughout the boundary layer when the mass transfer parameter and magnitude of the shrinking parameter increase (see Figure 3b). Figure 3c demonstrates that the axial velocity profile near the disk rises with both the mass transfer parameter and the magnitude of the shrinking parameter. As the mass transfer occurs in the axial direction, the fluid velocity increases with the mass transfer parameter. Meanwhile, the radial velocity near the disk, shown in Figure 3a, decreases due to fluid removal from the boundary by suction ($S > 0$). The increment in the mass transfer parameter and magnitude of the shrinking parameter then enhances the temperature profile, as shown in Figure 3d.

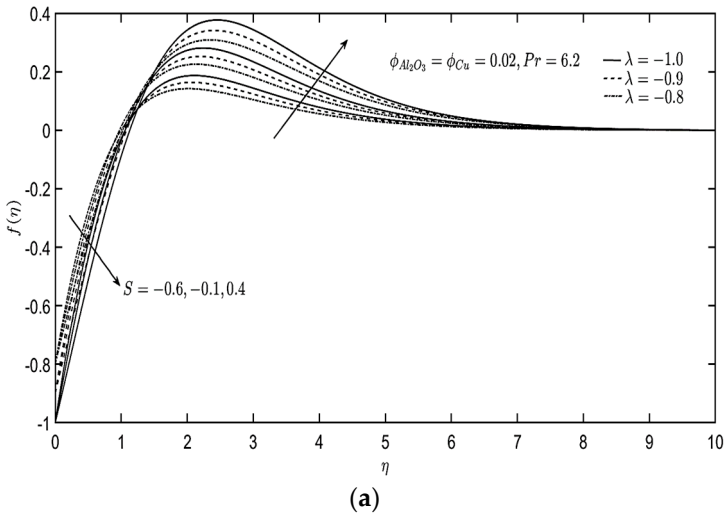

(**a**)

Figure 3. *Cont.*

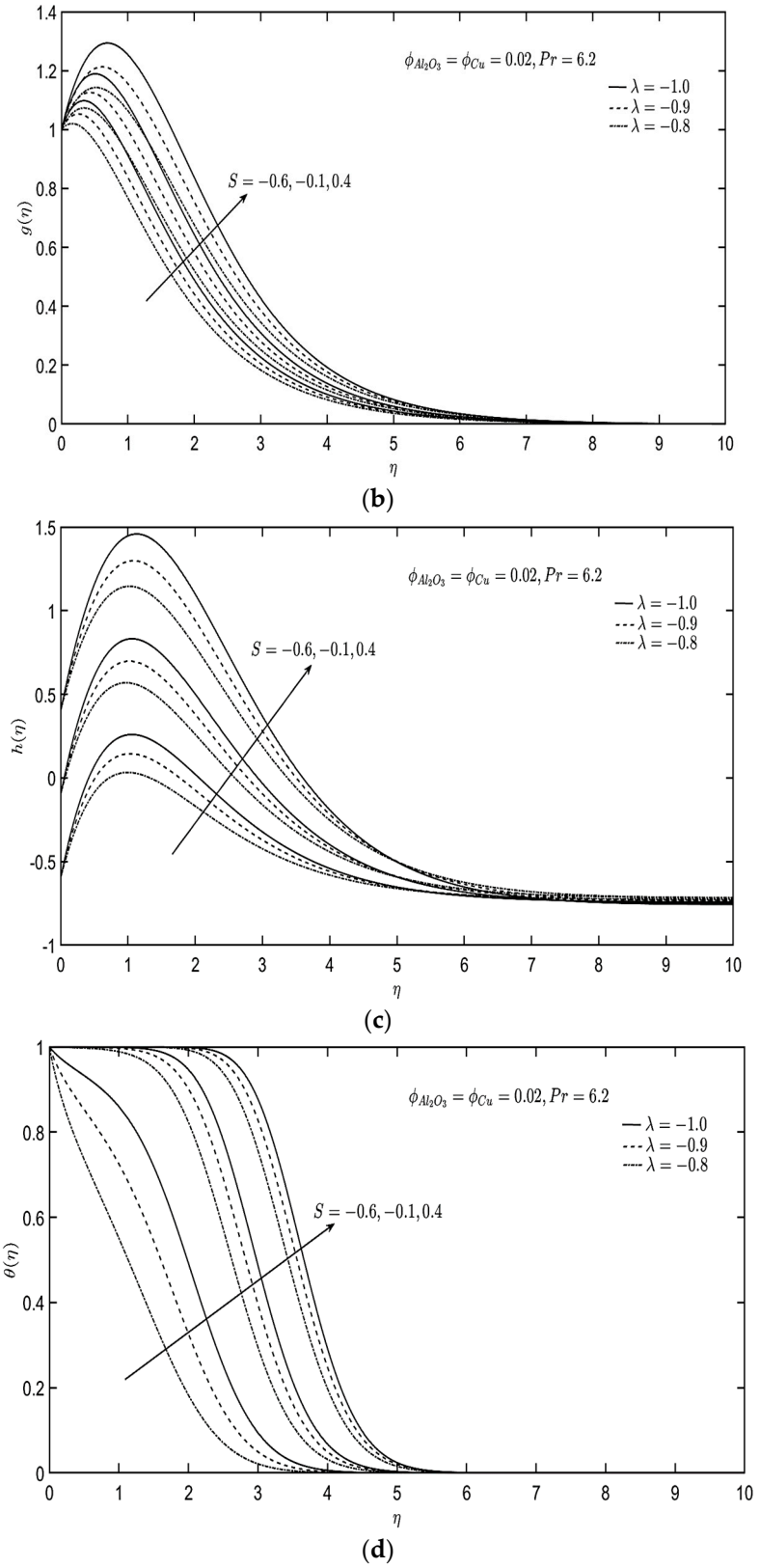

Figure 3. The profiles of (**a**) radial velocity, (**b**) tangential velocity, (**c**) axial velocity, and (**d**) temperature with various values of λ and S.

Next, the effects of shrinking and mass transfer parameters on the local skin friction coefficient and Nusselt number are illustrated in Figure 4. The enhancement of the mass transfer parameter is found to reduce the local skin friction coefficient and Nusselt number

in Figure 4a,b, respectively. Meanwhile, the increment in the magnitude of the shrinking parameter raises the local skin friction coefficient, as shown in Figure 4a. Thus, the wall shear stress rises with the increase in the magnitude of the shrinking parameter. In contrast, the local Nusselt number diminishes as $|\lambda|$ increases. The observed behavior may be due to the reduction of the surface area available for heat transfer. Hence, it causes the heat transfer rate between the disk and hybrid nanofluid to decrease. Moreover, it can be noted that the values of the local skin friction coefficient and Nusselt number for the injection case ($S < 0$) are higher than the suction case ($S > 0$).

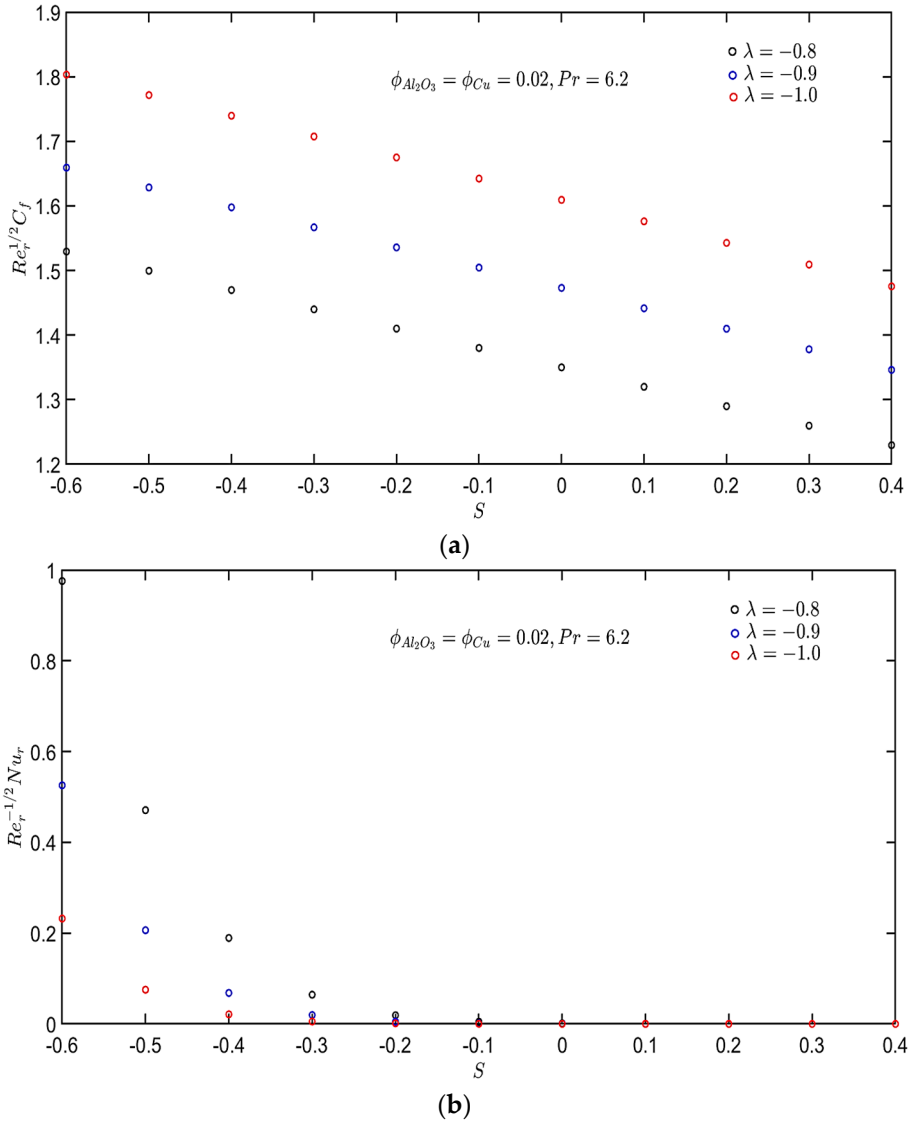

Figure 4. The profiles of (**a**) local skin friction coefficient and (**b**) local Nusselt number with various values of λ and S.

Meanwhile, the interacting impacts of the shrinking and mass transfer parameters on the physical quantities of interest are analyzed using the RSM in Minitab. The correlations between the independent parameters and the responses are given by the following:

$$\text{Response 1} = c_0 + c_1\text{A} + c_2\text{B} + c_{11}\text{AA} + c_{22}\text{BB} + c_{12}\text{AB}, \tag{16}$$

$$\text{Response 2} = c_0 + c_1\text{A} + c_2\text{B} + c_{11}\text{AA} + c_{22}\text{BB} + c_{12}\text{AB}. \tag{17}$$

The significance of each term in Equations (16) and (17) are identified through the analysis of variance (ANOVA). The results are presented in Tables 4 and 5.

Table 4. Analysis of variance for Response 1.

Source	DF	Adj SS	Adj MS	F-Value	*p*-Value
Model	5	0.249759313	0.049951863	174774.611709837	0.000000000
Linear	2	0.249435660	0.124717830	436370.320105496	0.000000000
A	1	0.101927475	0.101927475	356630.043436460	0.000000000
B	1	0.147508184	0.147508184	516110.596774533	0.000000000
Square	2	0.000126277	0.000063139	220.913397825	0.000000474
AA	1	0.000124396	0.000124396	435.243856915	0.000000146
BB	1	0.000008884	0.000008884	31.084684334	0.000837291
2-Way Interaction	1	0.000197376	0.000197376	690.591542539	0.000000030
AB	1	0.000197376	0.000197376	690.591542539	0.000000030
Error	7	0.000002001	0.000000286		
Lack-of-Fit	3	0.000002001	0.000000667	*	*
Pure Error	4	0.000000000	0.000000000		
Total	12	0.249761314			

The symbol * denotes the value is too small.

Table 5. Analysis of variance for Response 2.

Source	DF	Adj SS	Adj MS	F-Value	*p*-Value
Model	5	1.000087703	0.200017541	29.206710770	0.000150454
Linear	2	0.594033446	0.297016723	43.370603881	0.000113785
A	1	0.093304904	0.093304904	13.624451749	0.007745032
B	1	0.500728543	0.500728543	73.116756012	0.000059439
Square	2	0.267850314	0.133925157	19.555851501	0.001363026
AA	1	0.001069278	0.001069278	0.156136818	0.704502971
BB	1	0.216321666	0.216321666	31.587451304	0.000798846
2-Way Interaction	1	0.138203943	0.138203943	20.180643085	0.002824322
AB	1	0.138203943	0.138203943	20.180643085	0.002824322
Error	7	0.047938393	0.006848342		
Lack-of-Fit	3	0.047938393	0.015979464	*	*
Pure Error	4	0.000000000	0.000000000		
Total	12	1.048026096			

The symbol * denotes the value is too small.

The symbol * denotes the value is too small.

According to Alhadri et al. [35], a term is statistically significant if its *p*-value is less than 0.05. Based on Tables 4 and 5, all terms are significant for correlation (16), while the term AA can be removed from correlation (17) as its *p*-value is greater than 0.05. After eliminating the insignificant term, a second ANOVA is carried out for Response 2. Then, the following new correlations, containing only the significant terms, are obtained:

$$\text{Response 1} = 1.50443 - 0.130338\text{A} - 0.156795\text{B} + 0.006711\text{AA} - 0.001794\text{BB} + 0.007025\text{AB}, \quad (18)$$

$$\text{Response 2} = 0.0015 + 0.1247\text{A} - 0.2889\text{B} + 0.2874\text{BB} - 0.1859\text{AB}. \quad (19)$$

Based on Equations (18) and (19), the term B is seen to have a negative correlation with Response 1 and Response 2. Hence, the increment in the mass transfer parameter has an unfavorable impact on the local skin friction coefficient and Nusselt number. These findings agree with the results obtained in Figure 4.

Then, the interactive impacts between the shrinking and mass transfer parameters can be analyzed through the surface and contour plots displayed in Figures 5 and 6. Based

on Figure 5, the increase in A and B reduces Response 1. The higher and medium levels of shrinking parameter (A) and mass transfer parameter (B) are observed to produce low values of $Re_r^{1/2}C_f$ (Response 1). The maximum $Re_r^{1/2}C_f$ (Response 1) occurs at low levels of these independent parameters. Meanwhile, Figure 6 shows that lower levels of the mass transfer parameter (B) and higher levels of the shrinking parameter (A) produce high values of $Re_r^{-1/2}Nu_r$ (Response 2). However, at the moderate level of mass transfer parameter (B), the increment in the shrinking parameter (A) has no significant effect on $Re_r^{-1/2}Nu_r$ (Response 2).

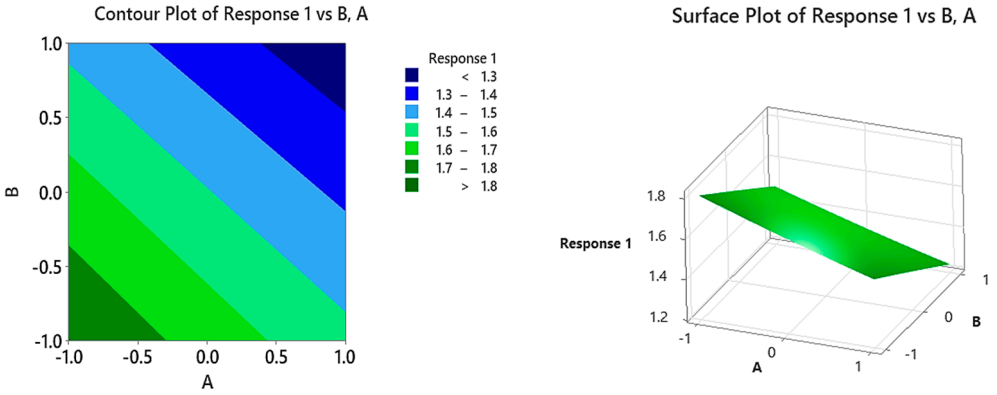

Figure 5. Contour and surface plots for Response 1.

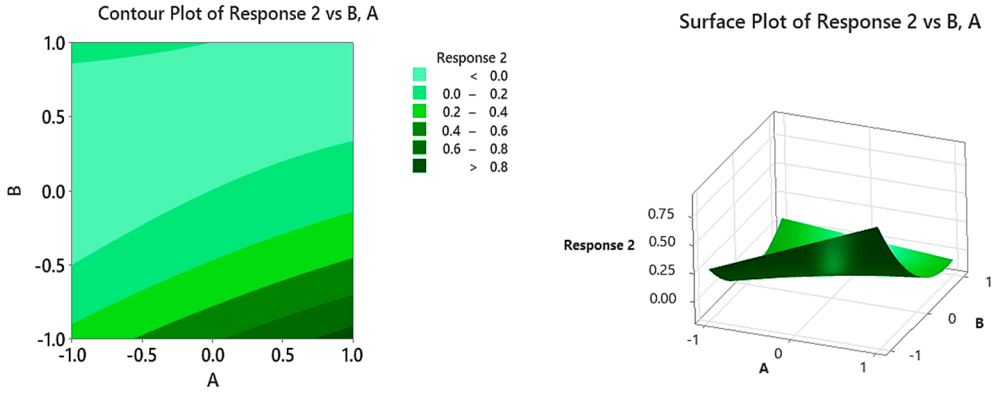

Figure 6. Contour and surface plots for Response 2.

Next, optimization is conducted to minimize and maximize the local skin friction coefficient and Nusselt number, respectively. The local skin friction coefficient is related to the wall shear stress. A low skin friction coefficient is sought to reduce energy consumption in most applications. Meanwhile, a high heat transfer rate, represented by the local Nusselt number, is desired for better heat transfer performance in cooling or heating processes. The composite desirability assesses how the configurations of the independent parameters optimize a given set of responses. The desirability is measured on a scale from zero to one. A value of zero signifies that one or more responses exceed their permissible limits, whereas a value of one represents the optimal scenario. Therefore, in the present investigation, the optimization can be observed by examining the composite desirability.

Table 6 presents the optimization result for the local skin friction coefficient and Nusselt number. The minimum local skin friction coefficient (Response 1) and maximum local Nusselt number (Response 2) can be achieved by setting the shrinking parameter (A) and mass transfer parameter (B) at high and low levels, respectively. With a desirability of 66% at $\lambda = -0.8$ and $S = -0.6$, the local skin friction coefficient is minimized at 1.528780016, while the local Nusselt number is maximized at 0.888353037. Hence, the lowest magnitude of the shrinking parameter and lowest mass transfer parameter optimized the physical

quantities of interest in the current flow problem. Different behavior may be observed for other controlling parameters and flow conditions ranges.

Table 6. Optimization of responses.

Solution	A	B	Response 2 Fit	Response 1 Fit	Composite Desirability
1	1	−1	0.888353037	1.528780016	0.659986551

5. Conclusions

The current study analyzes the rotating-disk flow of a hybrid nanofluid. The disk is considered to shrink in the radial direction and is permeable to allow for suction/injection. The local skin friction coefficient and Nusselt number for this flow problem are optimized using the RSM. First, the governing equations for the flow problem, consisting of differential equations and boundary conditions, are presented and solved using the bvp4c solver in MATLAB. Then, the Minitab 21 software is utilized to perform the RSM. The results are outlined as follows:

1. As the mass transfer parameter and the magnitude of the shrinking parameter ($|\lambda|$) increase, the radial velocity profile of the hybrid nanofluid near the disk decreases.
2. The increment in the mass transfer parameter and the magnitude of the shrinking parameter improves the profiles of tangential velocity, axial velocity, and temperature.
3. The local skin friction coefficient and Nusselt number diminish with the increase in the mass transfer parameter. The injection case demonstrates higher values of these physical quantities of interest than the suction case.
4. The increment in the magnitude of the shrinking parameter enhances the local skin friction coefficient and reduces the local Nusselt number.
5. Based on the RSM, low values of $Re_r^{1/2}C_f$ are produced at higher and medium levels of shrinking parameter (λ) and mass transfer parameter. Meanwhile, the highest value of $Re_r^{1/2}C_f$ is observed at low levels of these independent parameters.
6. High values of $Re_r^{-1/2}Nu_r$ occur at lower levels of the mass transfer parameter and higher levels of the shrinking parameter.
   The local Nusselt number is not significantly impacted by the increase in the shrinking parameter at the moderate level of the mass transfer parameter.
7. With a desirability of 66%, the local skin friction coefficient is minimized at 1.528780016, while the local Nusselt number is maximized at 0.888353037 when $\lambda = -0.8$ and $S = -0.6$.

The current study can be extended to other types of hybrid nanofluids, such as non-Newtonian hybrid nanofluids, carbon nanotubes hybrid nanofluids, and ternary hybrid nanofluids. In addition, the complex non-linear interaction of various controlling parameters in this flow problem can be further analyzed using a sophisticated machine learning technique known as the artificial neural network (ANN).

Supplementary Materials: The following supporting information can be downloaded at: https://www.mdpi.com/article/10.3390/computation12070141/s1.

Author Contributions: Conceptualization, I.P.; methodology, I.P. and R.I.Y.; validation, I.P. and N.M.A.; formal analysis, R.I.Y.; writing—original draft preparation, R.I.Y. and I.P.; writing—review and editing, N.M.A. and I.P.; supervision, N.M.A., F.M.A. and S.S.P.M.I.; funding acquisition, N.M.A. All authors have read and agreed to the published version of the manuscript.

Funding: This research was funded by Universiti Putra Malaysia, grant number GP-GPB 9711400.

Data Availability Statement: The original contributions presented in the study are included in the article/Supplementary Materials, further inquiries can be directed to the corresponding author/s.

Conflicts of Interest: The authors declare no conflicts of interest. The funders had no role in the design of the study; in the collection, analyses, or interpretation of data; in the writing of the manuscript; or in the decision to publish the results.

References

1. Gamachu, D.; Ibrahim, W. Mixed Convection Flow of Viscoelastic Ag-Al_2O_3/Water Hybrid Nanofluid Past a Rotating Disk. *Phys. Scr.* **2021**, *96*, 125205. [CrossRef]
2. Kármán, T.V. Über Laminare Und Turbulente Reibung. *ZAMM J. Appl. Math. Mech. Z. Angew. Math. Mech.* **1921**, *1*, 233–252. [CrossRef]
3. Ayano, M.S.; Otegbeye, O.; Mathunjwa, J.S. Numerical Simulation Of Nanofluid Flow Due To A Stretchable Rotating Disk. *Theor. Appl. Mech.* **2023**, *50*, 55–72. [CrossRef]
4. Sharma, K.; Vijay, N.; Bhardwaj, D.; Jindal, R. Flow of Water Conveying Fe_3O_4 and Mn–$ZnFe_2O_4$ Nanoparticles over a Rotating Disk: Significance of Thermophoresis and Brownian Motion. *J. Magn. Magn. Mater.* **2023**, *574*, 170710. [CrossRef]
5. Puneeth, V.; Aly, E.H.; Pop, I. Nanofluid Flowing over a Rotating Disk That Is Stretching and Permeable: An Unsteady Model. *Int. J. Mod. Phys. B* **2023**, *37*, 23502491. [CrossRef]
6. Rashid, A.; Dawar, A.; Ayaz, M.; Islam, S.; Galal, A.M.; Gul, H. Homotopic Solution of the Chemically Reactive Magnetohydrodynamic Flow of a Hybrid Nanofluid over a Rotating Disk with Brownian Motion and Thermophoresis Effects. *ZAMM Z. Angew. Math. Mech.* **2023**, *103*, e202200262. [CrossRef]
7. Alkuhayli, N.A.M. Heat Transfer Analysis of a Hybrid Nanofluid Flow on a Rotating Disk Considering Thermal Radiation Effects. *Case Stud. Therm. Eng.* **2023**, *49*, 103131. [CrossRef]
8. Kumar, P.; Poonia, H.; Areekara, S.; Sabu, A.S.; Mathew, A.; Ali, L. Significance of Irregular Heat Source and Arrhenius Energy on Electro-Magnetohydrodynamic Hybrid Nanofluid Flow over a Rotating Stretchable Disk with Nonlinear Radiation. *Numer. Heat. Transf. A Appl.* **2024**, *85*, 1866–1888. [CrossRef]
9. Kulkarni, M. Mixed Convective Magnetized GO-MoS_2/H_2O Hybrid Nanofluid Flow about a Permeable Rotating Disk. *Asia Pac. J. Chem. Eng.* **2023**, *18*, e2923. [CrossRef]
10. Lone, S.A.; Anwar, S.; Raizah, Z.; Almusawa, M.Y.; Saeed, A. A Theoretical Investigation of the MHD Water-Based Hybrid Nanofluid Flow over a Convectively Heated Rotating Disk Surface with Velocity Slips and Zero Mass Flux Conditions. *Eur. Phys. J. Plus* **2023**, *138*, 1–14. [CrossRef]
11. Khashi'ie, N.S.; Waini, I.; Zainal, N.A.; Hamzah, K.; Arifin, N.M.; Pop, I. Multiple Solutions and Stability Analysis of Magnetic Hybrid Nanofluid Flow Over a Rotating Disk with Heat Generation. *J. Adv. Res. Fluid. Mech. Therm. Sci.* **2023**, *102*, 59–72. [CrossRef]
12. Vijay, N.; Sharma, K. Magnetohydrodynamic Hybrid Nanofluid Flow over a Decelerating Rotating Disk with Soret and Dufour Effects. *Multidiscip. Model. Mater. Struct.* **2023**, *19*, 253–276. [CrossRef]
13. Abu Bakar, S.; Pop, I.; Md Arifin, N. Unsteady Flow of Hybrid Nanofluid over a Permeable Shrinking Inclined Rotating Disk with Radiation and Velocity Slip Effects. *Neural Comput. Appl.* **2024**, *36*, 11525–11544. [CrossRef]
14. Ali, F.; Zaib, A.; Khan, M.I.; Alzahrani, F.; Eldin, S.M. Irreversibility Analysis in Stagnation Point Flow of Tri-Hybrid Nanofluid over a Rotating Disk; Application of Kinetic Energy. *J. Indian. Chem. Soc.* **2023**, *100*, 100873. [CrossRef]
15. Singh, S.P.; Kumar, M.; Yaseen, M.; Rawat, S.K. Ternary Hybrid Nanofluid ($TiO_2-SiO_2-MoS_2$/Kerosene Oil) Flow over a Rotating Disk with Quadratic Thermal Radiation and Cattaneo-Christov Model. *J. Cent. S. Univ.* **2023**, *30*, 1262–1278. [CrossRef]
16. Patgiri, B.; Paul, A. Inspection of Viscoelastic Ag+Cu+Fe_3O_4+Al_2O_3/Kerosene Oil Tetra-Hybrid Nanofluid Flow across a Stretchable Rotating Disk with Exponentially Varying Viscosity. *J. Taibah Univ. Sci.* **2024**, *18*, 2336327.
17. Ali, I.; Gul, T.; Khan, A. Unsteady Hydromagnetic Flow over an Inclined Rotating Disk through Neural Networking Approach. *Mathematics* **2023**, *11*, 1893. [CrossRef]
18. Varun Kumar, R.S.; Kumar, R.N.; Ben Ahmed, S.; Madhu, J.; Verma, A.; Punith Gowda, R.J. Unsteady Flow of a Ternary Nanofluid over a Slow-Rotating Disk Subject to Uniform Suction and Backpropagated Neural Network. *Numer. Heat Transf. Part B Fundam.* **2023**, 1–21. [CrossRef]
19. Mehmood, T.; Ramzan, M.; Howari, F.; Kadry, S.; Chu, Y.M. Application of Response Surface Methodology on the Nanofluid Flow over a Rotating Disk with Autocatalytic Chemical Reaction and Entropy Generation Optimization. *Sci. Rep.* **2021**, *11*, 4021. [CrossRef]
20. Shafiq, A.; Sindhu, T.N.; Al-Mdallal, Q.M. A Sensitivity Study on Carbon Nanotubes Significance in Darcy–Forchheimer Flow towards a Rotating Disk by Response Surface Methodology. *Sci. Rep.* **2021**, *11*, 8812. [CrossRef]
21. Mathew, A.; Areekara, S.; Sabu, A.S. Significance of Magnetic Field and Stratification Effects on the Bioconvective Stagnation-Point Flow of Ferro-Nanofluid over a Rotating Stretchable Disk: Four-Factor Response Surface Methodology. *J. Indian Chem. Soc.* **2022**, *99*, 100615. [CrossRef]
22. Hussain, S.; Ali, A.; Rasheed, K.; Pasha, A.A.; Algarni, S.; Alqahtani, T.; Irshad, K. Application of Response Surface Methodology to Optimize MHD Nanofluid Flow over a Rotating Disk with Thermal Radiation and Joule Heating. *Case Stud. Therm. Eng.* **2023**, *52*, 103715. [CrossRef]

23. Khashi'ie, N.S.; Waini, I.; Hamzah, K.B.; Mukhtar, M.F.; Kasim, A.R.M.; Arifin, N.M.; Pop, I. Numerical Solution and Statistical Analysis of the Unsteady Hybrid Ferrofluid Flow with Heat Generation Subject to a Rotating Disk. *ZAMM J. Appl. Math. Mech. Z. Angew. Math. Mech.* **2023**, *103*, e202200384. [CrossRef]
24. Siddiqui, F.R.; Tso, C.Y.; Chan, K.C.; Fu, S.C.; Chao, C.Y.H. On Trade-off for Dispersion Stability and Thermal Transport of Cu-Al_2O_3 Hybrid Nanofluid for Various Mixing Ratios. *Int. J. Heat Mass Transf.* **2019**, *132*, 1200–1216. [CrossRef]
25. Takabi, B.; Gheitaghy, A.M.; Tazraei, P. Hybrid Water-Based Suspension of Al_2O_3 and Cu Nanoparticles on Laminar Convection Effectiveness. *J. Thermophys. Heat Trans.* **2016**, *30*, 523–532. [CrossRef]
26. Oztop, H.F.; Abu-Nada, E. Numerical Study of Natural Convection in Partially Heated Rectangular Enclosures Filled with Nanofluids. *Int. J. Heat Fluid Flow* **2008**, *29*, 1326–1336. [CrossRef]
27. Suresh, S.; Venkitaraj, K.P.; Selvakumar, P.; Chandrasekar, M. Synthesis of Al_2O_3-Cu/Water Hybrid Nanofluids Using Two Step Method and Its Thermo Physical Properties. *Colloids Surf. A Physicochem. Eng. Asp.* **2011**, *388*, 41–48. [CrossRef]
28. Turkyilmazoglu, M. Nanofluid Flow and Heat Transfer Due to a Rotating Disk. *Comput. Fluids* **2014**, *94*, 139–146. [CrossRef]
29. Yin, C.; Zheng, L.; Zhang, C.; Zhang, X. Flow and Heat Transfer of Nanofluids over a Rotating Disk with Uniform Stretching Rate in the Radial Direction. *Propuls. Power Res.* **2017**, *6*, 25–30. [CrossRef]
30. Box, G.E.P.; Wilson, K.B. On the Experimental Attainment of Optimum Conditions. *J. R. Stat. Soc. Ser. B (Methodol.)* **1951**, *13*, 1–38. [CrossRef]
31. Mahanthesh, B.; Thriveni, K.; Rana, P.; Muhammad, T. Radiative Heat Transfer of Nanomaterial on a Convectively Heated Circular Tube with Activation Energy and Nanoparticle Aggregation Kinematic Effects. *Int. Commun. Heat Mass Transf.* **2021**, *127*, 105568. [CrossRef]
32. Bhattacharya, S. Central Composite Design for Response Surface Methodology and Its Application in Pharmacy. In *Response Surface Methodology in Engineering Science*; IntechOpen: London, UK, 2021.
33. Sahoo, P.; Barman, T.K. ANN Modelling of Fractal Dimension in Machining. In *Mechatronics and Manufacturing Engineering*; Woodhead Publishing: Cambridge, UK, 2012.
34. Rashidi, M.M.; Abelman, S.; Mehr, N.F. Entropy Generation in Steady MHD Flow Due to a Rotating Porous Disk in a Nanofluid. *Int. J. Heat Mass Transf.* **2013**, *62*, 515–525. [CrossRef]
35. Alhadri, M.; Raza, J.; Yashkun, U.; Lund, L.A.; Maatki, C.; Khan, S.U.; Kolsi, L. Response Surface Methodology (RSM) and Artificial Neural Network (ANN) Simulations for Thermal Flow Hybrid Nanofluid Flow with Darcy-Forchheimer Effects. *J. Indian Chem. Soc.* **2022**, *99*, 100607. [CrossRef]

computation

MDPI

Article

Boundary Layer Stagnation Point Flow and Heat Transfer over a Nonlinear Stretching/Shrinking Sheet in Hybrid Carbon Nanotubes: Numerical Analysis and Response Surface Methodology under the Influence of Magnetohydrodynamics

Nazrul Azlan Abdul Samat [1,2], Norfifah Bachok [1,3,*] and Norihan Md Arifin [1,3]

[1] Department of Mathematics and Statistics, Faculty of Science, Universiti Putra Malaysia, Serdang 43400, Selangor, Malaysia; nazrul_lan@usas.edu.my (N.A.A.S.); norihana@upm.edu.my (N.M.A.)
[2] Department of Management, Faculty of Management and Information Technology, Universiti Sultan Azlan Shah, Kuala Kangsar 33000, Perak, Malaysia
[3] Institute of Mathematical Research, Faculty of Science, Universiti Putra Malaysia, Serdang 43400, Selangor, Malaysia
* Correspondence: norfifah@upm.edu.my

Abstract: The present study aims to offer new numerical solutions and optimisation strategies for the fluid flow and heat transfer behaviour at a stagnation point through a nonlinear sheet that is expanding or contracting in water-based hybrid nanofluids. Most hybrid nanofluids typically use metallic nanoparticles. However, we deliver a new approach by combining single- and multi-walled carbon nanotubes (SWCNTs-MWCNTs). The flow is presumptively steady, laminar, and surrounded by a constant temperature of the ambient and body walls. By using similarity variables, a model of partial differential equations (PDEs) with the magnetohydrodynamics (MHD) effect on the momentum equation is converted into a model of non-dimensional ordinary differential equations (ODEs). Then, the dimensionless first-order ODEs are solved numerically using the MATLAB R2022b bvp4C program. In order to explore the range of computational solutions and physical quantities, several dimensionless variables are manipulated, including the magnetic parameter, the stretching/shrinking parameter, and the volume fraction parameters of hybrid and mono carbon nanotubes. To enhance the originality and effectiveness of this study for practical applications, we optimise the heat transfer coefficient via the response surface methodology (RSM). We apply a face-centred central composite design (CCF) and perform the CCF using Minitab. All of our findings are presented and illustrated in tabular and graphic form. We have made notable contributions in the disciplines of mathematical analysis and fluid dynamics. From our observations, we find that multiple solutions appear when the magnetic parameter is less than 1. We also detect double solutions in the shrinking region. Furthermore, the increase in the magnetic parameter and SWCNTs-MWCNTs volume fraction parameter increases both the skin friction coefficient and the local Nusselt number. To compare the performance of hybrid nanofluids and mono nanofluids, we note that hybrid nanofluids work better than single nanofluids both in skin friction and heat transfer coefficients.

Keywords: boundary layer; hybrid CNTs; nonlinear stretching/shrinking sheet; magnetohydrodynamics; RSM

Citation: Samat, N.A.A.; Bachok, N.; Arifin, N.M. Boundary Layer Stagnation Point Flow and Heat Transfer over a Nonlinear Stretching/Shrinking Sheet in Hybrid Carbon Nanotubes: Numerical Analysis and Response Surface Methodology under the Influence of Magnetohydrodynamics. *Computation* **2024**, *12*, 46. https://doi.org/10.3390/computation12030046

Academic Editors: Ali Cemal Benim, Abdulmajeed A. Mohamad, Sang-Ho Suh, Rachid Bennacer, Paweł Oclon and Jan Taler

Received: 1 February 2024
Revised: 20 February 2024
Accepted: 1 March 2024
Published: 3 March 2024

1. Introduction

The need to enhance the transmission of heat over various surfaces of devices has continued to escalate in thermal management systems. Traditionally, base fluids such as water and kerosene work as heat transfer media (HTM) in order to transport heat to the environment. With rising industrial requirements to transfer heat at a faster rate, the innovative idea of mixing nanoparticles (NPs) with a base fluid has encouraged researchers to explore the most effective combinations for the preparation of nanofluids (NFs).

Because NPs have a large surface area with a nanometre scale of size, the investigations into the manipulation of NPs using experimental, theoretical, and numerical methods have still been ongoing since Choi's pioneering work [1] in this area. The fruitful development in nanotechnology has led to scientists not just suspending single types of NPs with a base fluid but successfully inventing two different types of NPs working with the base fluid. This process produces a new HTM called hybrid nanofluids (HNFs). The addition of HNFs to the flow has significantly improved the flow by promising a high thermal conductivity and, hence, increasing the heat-transmitting process in many applications. Turcu et al. [2] were reported as the first team to produce HNFs by combining NPs from carbon-based and non-metal materials. Reddy et al. [3] enumerated the possible uses of HNFs in numerous fields, including heat exchangers, engine cooling, and solar collectors.

The excellent achievement of HNFs in their narratives can be debated when it comes to determining the most effective amalgamation of NPs. Despite the inherent advantages of HNFs over traditional fluids in terms of heat transfer enhancement, the selection of an appropriate nanoparticle match for heat transfer enhancement in HNFs has been a subject of ongoing assessment and discussion. Concerning this challenge, Devi and Devi, Khashi'ie et al. and Khashi'ie et al. [4–6] recommended that researchers vary the mixture of NPs in order to produce the most productive HNFs that could potentially improve the flow and heat transfer behaviour.

Among the best ways to synthesise HNFs is by applying carbon-based materials. Sajid et al. [7] reported that Turcu and his team [2] became the first group to use multi-walled carbon nanotubes (MWCNTs), which are one of the nanoparticles from carbon-based particles that act as the main nanoparticles in HNFs. As CNT materials were identified as suitable materials for environmental applications by Navrotskaya et al. [8], demand for producing HNFs from these materials has increased significantly in nanotechnology. The increase in applying CNTs in HNFs is also supported, notably, by other relevant explorations of CNTs, which found them to contain excellent physical and thermal characteristics. However, there has been less discussion on the experimental and theoretical study of hybrid-based carbon nanotubes, especially in suspending single and multi-walled carbon nanotubes (SWCNTs and MWCNTs) as potential HNFs. The studies conducted by Hanaya et al., Sulochana et al., Aladdin et al. and Tabassum et al. [9–12] were identified in the literature as actively investigating the feasibility of manipulating hybrid SWCNTs and MWCNTs in order to study flow and heat transfer behaviour over different geometrical surfaces. From their research, all of them concluded that hybrid SWCNTs and MWCNTs performed better than single nanofluids, either SWCNTs or MWCNTs.

The boundary layer analysis near bodies of different geometrical shapes plays a vital role in investigating the flow behaviour of certain fluids. Svorcan et al.'s findings [13] suggest that studying the boundary layer has the potential to aid in the development of highly efficient boundary layer control devices. Due to the high application of shrinking and stretching sheets in cooling systems, researchers have focused attention on these surfaces. In a considerable proportion of the literature, most studies have explored these bodies, taking into account that the boundary velocity varies linearly with the fluid flow. Shateyi et al., Lund et al., Rosca et al., Dinarvand et al. and Samat et al. [14–18] were among the groups that studied the flow characteristics of a sheet linearly moved that was either stretching or shrinking using various mathematical models. In their models, it was assumed that the sheet moved at a linear velocity at the speed of the boundary layer. From our survey, the majority of researchers have been motivated by Crane et al.'s [19] study on the linear velocity along the stretched surface. However, realistically, it is important to explore the nonlinear variation of velocity over these surfaces, as emphasised by Vajravelu et al. [20]. According to Nayakar et al. [21], a stretching or shrinking sheet that moves at a nonlinear velocity will employ at least a quadratic function velocity along the x-axis in a two-dimensional Cartesian coordinate system. The current understanding of the nonlinear velocity change occurring in an expanding or contracting sheet is considered insufficient for

comprehensive discourse. This topic needs to be looked into more in the future, especially when it comes to investigating non-Newtonian fluid flow behaviour, like HNFs.

A search of the literature has revealed that the current works of flow over shrinking and stretching sheets have put NFs and HNFs in the spotlight. One of the numerous studies on flow in nanofluids was conducted by Rahman et al., Ragupathi et al. and Saranya et al. [22–24]. By taking the effect of magnetohydrodynamics into account in nanofluid flow over a nonlinear shrinking and stretching sheet, they analysed the possible region of non-unique solutions. They reported that the shrinking case contributed to producing multiple solutions while stretching only executed a single solution. The other attempt performed by Mahabaleshwar et al. [25] explained the thermal radiation and mass transpiration reactions in the boundary layer flow of nanofluids containing carbon nanotubes (CNTs) past linear shrinking and stretching sheets, and they found the existence of dual solutions in the skin friction coefficient.

Aly and his team [26] chose to look at the stagnation point flow of HNFs across a sheet that is either stretching or shrinking at a linear velocity because they had some interesting data from HNFs studies. They chose copper and alumina oxide (Cu-Al_2O_3) as the main composition of HNFs, cooperating with water. They found that the duality solution appeared for defined parameters, and HNFs worked better than single nanofluids both in heat transfer and skin friction coefficients. The different positions of the stretching or shrinking sheet were scrutinised numerically by Khan et al. [27] by dealing with the vertical stretching or shrinking sheet. They observed that the process of separating the boundary layer became slower when the suction parameter increased. Although multidisciplinary research has been carried out on stretching/shrinking sheets, to date, the exploration of the flow of hybrid CNTs over a nonlinear sheet has not yet been organised by any researchers. Additionally, up to now, more work has been conducted on making models of how HNFs flow over a sheet that is linearly stretching or shrinking. Examples include the work by Zainal et al., Waini et al. and Jawad et al. [28–30].

The examination of stagnation point flow is currently the most extensively researched area pertaining to the flow characteristics across a surface that is undergoing either stretching or shrinking due to a wide range of industrial processes. In Merkin et al.'s [31] study, they found that the stagnation point was present on all body surfaces, regardless of whether they were subjected to stretching or shrinking. In the stagnation area, as seen in Figure 1, the fluid particles encountered a state of rest velocity in the vicinity of the stretching or shrinking sheet. According to Merkin et al. [31], this phenomenon offers a high transmission rate of heat in this region.

Magnetohydrodynamics (MHD) plays a crucial role in the improvement of many applications, including nuclear reactors, accelerators, and generators. Alekseev et al. and Ragupathi et al. [32,33] describe that MHD is used to explain the motion of electrically conducting and incompressible fluids in the presence of a magnetic field. To the best of our knowledge, not much research has been performed on computing the contribution of the numeric value and properties of the electrical conductivity of nanoparticles that are used in numerical studies that look into how MHD affects fluid dynamics. The comprehensive depiction of the MHD impact on flow motion may be hindered if computational analysis fails to include the electrical conductivity of nanoparticles in the model. The investigation of boundary layer CNTs with an MHD effect was carried out by Mahabaleshwar et al. [34]. This team discovered that MHD produced a positive impact on the fluid flow when the flow passed through a linearly stretching or shrinking sheet. A recent study was undertaken by Mahesh and his colleagues [35], whereby they analysed the flow of carbon nanotubes (CNTs) in the boundary layer over a sheet that is either linearly extending or contracting. The research was performed under the influence of MHD. When the performance of SWCNTs and MWCNTs was compared, it was found that both types of nanotubes had better velocity profiles when the MHD level went up. However, to date, no investigation has yet been conducted on the boundary layer flow of hybrid CNTs (SWCNTs-MWSCNTs) across a nonlinear stretching or shrinking sheet in the presence of the MHD effect.

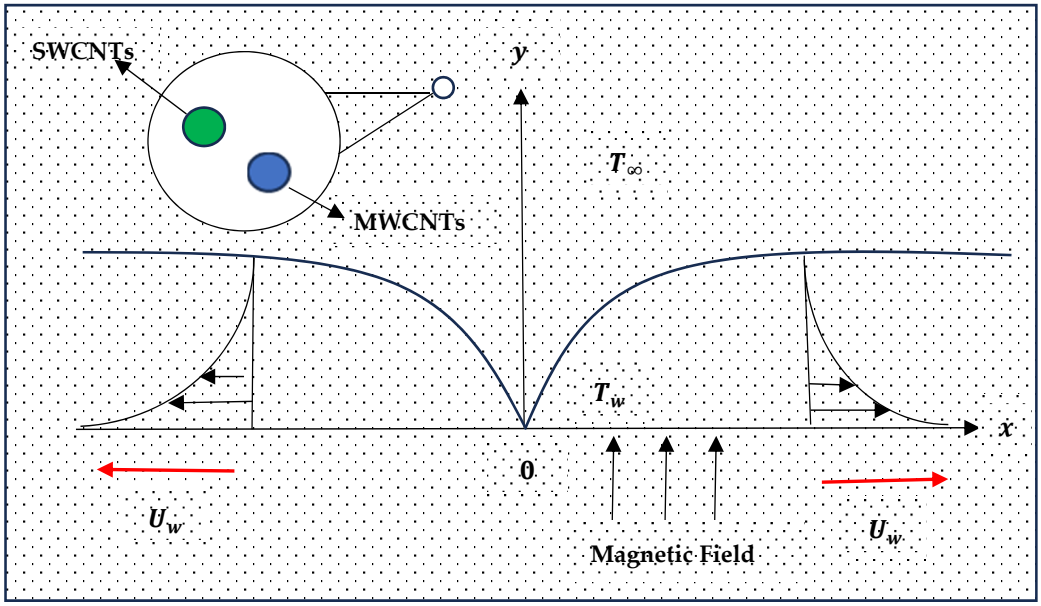

(**a**) Nonlinear Stretching Sheet

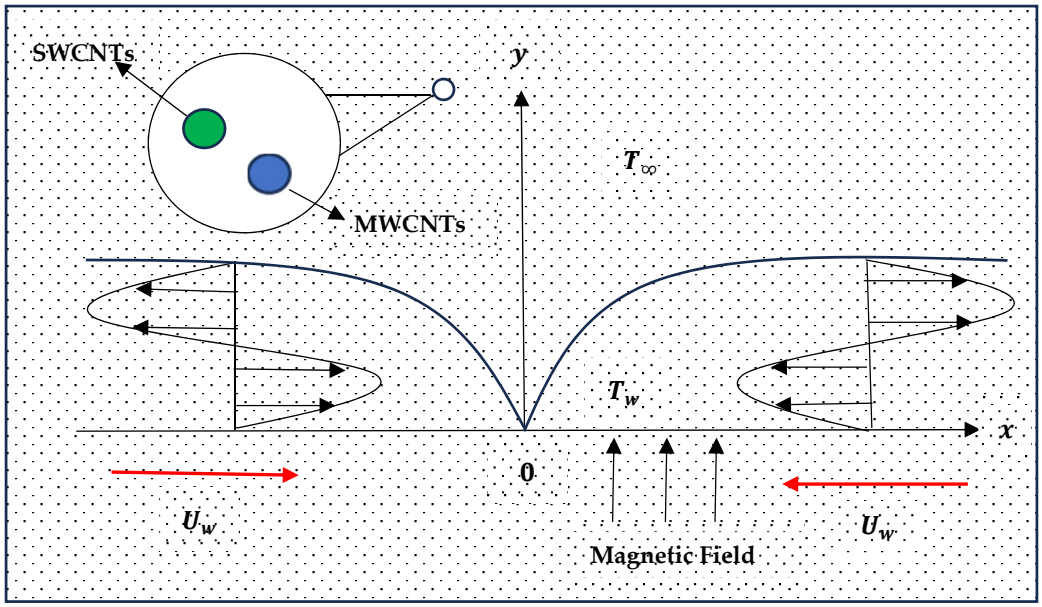

(**b**) Nonlinear Shrinking Sheet

Figure 1. The schematic model of stagnation point flow over nonlinear (**a**) stretching sheet and (**b**) shrinking sheet.

Motivated by the above studies, our team is planning to extend the original idea proposed by Anuar et al. [36]. The previous work by Anuar et al. [36] presented the analysis of HNFs on different forms of nonlinear velocity over stretching or shrinking sheets. They reported that the greater the value of the polynomial function n, the greater the contribution of detaching the boundary layer at a faster pace. However, this team did not use CNTs and performed optimisation procedures. In this study, we improve Anuar et al.'s model [36] by examining the impact of the MHD effect on the fluid flow characteristics and conducting an optimisation of the heat transfer. To build a different model from others, the MHD effect in that equation is counted together with the effect of the electrical conductivity of CNTs and water. Specifically, we use HNFs differently from the previous model by considering HNFs based on CNTs as the basis of our investigation. The decision made to enhance the prior model has a substantial impact on the new numerical outcome and the flow

behaviour of HNFs. The use of MHD has found widespread application in several fields. Reddy et al. [3] have shown that this mechanism significantly influences the magnetic and electrical conductivity characteristics of fluid behaviour. In developing our model, we are taking a different approach from Jaafar et al.'s work [37] in order to investigate the MHD effect on the momentum equation and employ similarity variables that were suggested by Anuar et al. [36] before. In order to develop a highly effective model, our study focuses on the concept of MHD, as discussed in the article by Jaafar et al. and Khashi'ie et al. [37,38]. Because Jaafar et al.'s model [37] did not take the flow at stagnation points into account and Khashi'ie et al. [38] studied a moving plate, our study, which is MHD-influenced, differs from that of Jaafar et al. and Khashi'ie et al. [37,38].

In creating the model, we adhere to the suggestion of Zafar et al. [39] since it is based on the assumption of flow in the laminar phase. Hence, the mathematical study of this model is conducted based on the Tiwari and Das model. Zafar et al. [39] concluded that utilising the Tiwari and Das model was the best option for illustrating the uniform fluid flow of nanofluids compared to other models.

For the purpose of ascertaining the most ideal magnetic parameter for this model, we provide a novel approach to quantifying the maximum heat transfer rate. To achieve optimal heat transfer, we use the response surface methodology (RSM) with the desirability function approach to design the numerical experiment. The use of the RSM approach has not been implemented in the models previously mentioned. The face-centred composite design (CCF) is employed to build a design of experiment (DOE) that incorporates other possible controllable factors. The objective of this DOE is to maximise the heat transmission capacity using a quadratic regression model. Matsui's study [40] indicates that the quadratic regression model is more adaptable than the linear regression model for assessing the interplay of several factors and responses to predict the best values of these interactions. To conduct the numerical analysis, we use the bvp4c function built in MATLAB, whereas the RSM analysis is carried out using Minitab. Since the integration of numerical approaches with RSM has garnered very little attention from scholars, this is an opportunity for further exploration of this combination. Both the numerical and RSM strategies that are built into this model may contribute to a comprehensive knowledge of the relationship between computational and experimental studies.

2. Formulation of the Model

2.1. Mathematical Formulation

In order to govern the boundary layer equations, which are organised into nonlinear partial differential equations (PDEs), we establish the following assumptions:

- The flow experiences an incompressible, steady, and laminar flow without a slip effect.
- The flow is described in two-dimensional (2D) space, with x and y acting as the axes on the cartesian coordinates.
- The sheet is extended and contracted with the free stream velocity $U_\infty(x)$ and the stretching or shrinking velocity $U_w(x)$.
- The terms $U_\infty(x)$ and $U_w(x)$ can be written as $U_\infty(x) = ax^n$ and $U_w(x) = bx^n$, where a, b and n are positive constants, such that $a, b > 0$ and $n > 1$.
- The sheet is surrounded by the constant surface temperature T_w and the constant ambient hybrid CNT nanofluids temperature T_∞.
- Temperature does not affect the thermophysical properties of hybrid CNTs.
- The size of SWCNTs and MWCNTs is not varied, and there is no issue of agglomeration in the flow.

To design our model, Anuar et al.'s study [36] is adopted, and the effect of the magnetic field on the strength B_0 in the dimensionless unit is taken into consideration in the flow, where $B_0^2 x^{n-1} = B^2$. However, the influence of an induced magnetic field is neglected. By setting u and v as the velocity components that are dependent on x and y, our model with specific boundary conditions is defined as follows:

$$\frac{\partial u}{\partial x} + \frac{\partial v}{\partial y} = 0, \tag{1}$$

$$u\frac{\partial u}{\partial x} + v\frac{\partial u}{\partial y} = U_\infty \frac{dU_\infty}{dx} + \frac{\mu_{hnf}}{\rho_{hnf}}\frac{\partial^2 u}{\partial y^2} + \frac{\sigma_{hnf}}{\rho_{hnf}}B^2(U_\infty - u), \tag{2}$$

$$u\frac{\partial T}{\partial x} + v\frac{\partial T}{\partial y} = \alpha_{hnf}\frac{\partial^2 T}{\partial y^2}, \tag{3}$$

subjected to

$$\begin{gathered} u = U_w,\ v = 0,\ T = T_w \text{ at } y = 0, \\ u \to U_\infty,\ T \to T_\infty \text{ as } y \to \infty. \end{gathered} \tag{4}$$

The variables u and v in Equations (1)–(4) represent the component velocities that are dependent on the Cartesian coordinates x and y. These components are written in non-dimensional units using the following equations:

$$u = \frac{\partial \psi}{\partial y},\ v = -\frac{\partial \psi}{\partial x}. \tag{5}$$

The terms μ_{hnf}, ρ_{hnf} and σ_{hnf} in Equation (2) indicate the dynamic viscosity, density and electrical conductivity of hybrid CNT nanofluids, while α_{hnf} in Equation (3) illustrates the thermal diffusivity of hybrid CNT nanofluids.

2.2. Non-Dimensional Similarity Ordinary Equations

To reduce the complexity of solving the above model, we introduce several similarity variables that were employed by Anuar et al. [36]. These variables play a vital role in transforming the PDEs system into the non-dimensional ordinary differential equations (ODEs) model. Crank [41] asserts that by converting PDEs into ODEs, it is possible to examine the physical system of fluid flow and heat transfer using a less complex system. This claim was supported by Burden and Faires [42] who said that ODEs are more numerically stable than PDEs. The introduction of these similarity variables can be deployed in the following expressions:

$$\eta = \left(\frac{b(n+1)}{2\nu_f}\right)^{\frac{1}{2}} y x^{\frac{n-1}{2}},\ \psi = \left(\frac{2b\nu_f}{n+1}\right)^{\frac{1}{2}} x^{\frac{n+1}{2}} f(\eta),\ T = T_\infty + (T_w - T_\infty)\theta(\eta). \tag{6}$$

By inserting Equation (6) into Equations (2)–(5), we discover the following system of ordinary differential equations (ODEs).

$$A_1 f''' + ff'' - A_2\left(f'^2 - 1\right) + A_3 A_4\left(1 - f'\right) = 0, \tag{7}$$

$$\frac{1}{\mathrm{Pr}} A_5 \theta'' + f\theta' = 0, \tag{8}$$

subject to boundary conditions:

$$\begin{gathered} f'(\eta) = \varepsilon,\ f(\eta) = 0,\ \theta(\eta) = 1, \text{ at } \eta = 0, \\ f'(\eta) \to 1,\ \theta(\eta) \to 0\ , \text{ as } \eta \to \infty. \end{gathered} \tag{9}$$

The term A_i, for $i = 1, 2, 3, 4, 5$ can be recorded as below:

$$A_1 = \frac{\mu_{hnf}/\mu_f}{\rho_{hnf}/\rho_f},\ A_2 = \left(\frac{2n}{n+1}\right),\ A_3 = \frac{\sigma_{hnf}/\sigma_f}{\rho_{hnf}/\rho_f},\ A_4 = \frac{2M}{n+1},\ A_5 = \frac{k_{hnf}/k_f}{\left(\rho C_p\right)_{hnf}/\left(\rho C_p\right)_f}, \tag{10}$$

where n, M and $\varepsilon = a/b$ are the nonlinear, magnetic and stretching/shrinking velocity parameters, respectively, in dimensionless units. f and θ are functions of η. Hence, we can differentiate f with respect to η to obtain f', f'' and f''', and differentiate θ with respect to η to obtain θ' and θ''. Referring to Jaafar et al. and Khashi'ie et al. [37,38], the term M in Equation (10) can be denoted as $M = \frac{\sigma_f}{\rho_f}\frac{B_0^2}{b}$. To measure the physical quantities that can be applied in studying the application of the model, we define the local skin friction coefficient, C_f, and the local Nusselt number, N_{ux}, in the following equations:

$$C_f = \frac{\tau_w}{\rho_f U_\infty^2}, \tag{11}$$

and

$$Nu_x = \frac{xq_w}{k_f(T_w - T_\infty)}, \tag{12}$$

where τ_w and q_w represent the surface shear stress and the surface heat flux, respectively. The terms τ_w and q_w can be written as

$$\tau_w = \mu_{hnf}\left(\frac{\partial u}{\partial y}\right), \text{at } y = 0, \tag{13}$$

and

$$q_w = -k_{hnf}\left(\frac{\partial T}{\partial y}\right), \text{at } y = 0. \tag{14}$$

Applying the similarity variables from Equation (6), we obtain the reduced skin friction and heat transfer coefficients, respectively, in Equations (15) and (16) as follows:

$$C_f Re_x^{1/2} = A_6 f''(0), \tag{15}$$

and

$$Nu_x Re_x^{-1/2} = A_7 \theta'(0), \tag{16}$$

where $A_6 = \left(\mu_{hnf}/\mu_f\right)((n+1)/2)^{1/2}$ and $A_7 = \left(-k_{hnf}/k_f\right)((n+1)/2)^{1/2}$. We use the thermophysical properties of A_1, A_2, A_3, A_4, A_5, A_6 and A_7 from Xue's model (thermal conductivity), Maxwell's model (electrical conductivity), Devi and Devi's model and Bazbouz et al. [43]. The mathematical correlation of the thermal conductivity of hybrid CNTs in this model is also drawn from the most up-to-date research on hybrid CNTs conducted by Aladdin et al. [11] and Haider et al. [44]. The correlations and specific numeric values for the physical properties can be viewed in Tables 1 and 2.

Table 1. The thermophysical characteristics and correlations of hybrid CNTs dispersed in water.

Characteristics	Correlations
Viscosity	$\mu_{hnf} = \frac{\mu_f}{(1-\phi_{SWCNT})^{2.5}(1-\phi_{MWCNT})^{2.5}}$
Density	$\rho_{hnf} = (1-\phi_{MWCNT})\left[(1-\phi_{SWCNT})\rho_f + \phi_{SWCNT}\rho_{SWCNT}\right] + \phi_{MWCNT}\rho_{MWCNT}$
Heat Capacity	$(\rho C_p)_{hnf} = (1-\phi_{MWCNT})\left[(1-\phi_{SWCNT})(\rho C_p)_f + \phi_{SWCNT}(\rho C_p)_{SWCNT}\right] + \phi_{MWCNT}(\rho C_p)_{MWCNT}$
Thermal Conductivity	$k_{hnf} = \left(\frac{(1-\phi_{MWCNT})+2\phi_{MWCNT}\left(\frac{k_{MWCNT}}{k_{MWCNT}-k_{nf}}\right)\ln\left(\frac{k_{MWCNT}+k_{nf}}{k_{nf}}\right)}{(1-\phi_{MWCNT})+2\phi_{MWCNT}\left(\frac{k_{nf}}{k_{MWCNT}-k_{nf}}\right)\ln\left(\frac{k_{MWCNT}+k_{nf}}{k_{nf}}\right)}\right)k_{nf}$, $k_{nf} = \left(\frac{(1-\phi_{SWCNT})+2\phi_{SWCNT}\left(\frac{k_{SWCNT}}{k_{SWCNT}-k_f}\right)\ln\left(\frac{k_{SWCNT}+k_f}{k_f}\right)}{(1-\phi_{SWCNT})+2\phi_{SWCNT}\left(\frac{k_f}{k_{SWCNT}-k_f}\right)\ln\left(\frac{k_{SWCNT}+k_f}{k_f}\right)}\right)k_f$
Electrical Conductivity	$\sigma_{hnf} = \left(\frac{\sigma_{MWCNT}+2\sigma_{nf}-2\phi_{MWCNT}(\sigma_{nf}-\sigma_{MWCNT})}{\sigma_{MWCNT}+2\sigma_{nf}+\phi_{MWCNT}(\sigma_{nf}-\sigma_{MWCNT})}\right)\sigma_{nf}$, $\sigma_{nf} = \left(\frac{\sigma_{SWCNT}+2\sigma_f-2\phi_{SWCNT}(\sigma_f-\sigma_{SWCNT})}{\sigma_{SWCNT}+2\sigma_f+\phi_{SWCNT}(\sigma_f-\sigma_{SWCNT})}\right)\sigma_f$

Table 2. The thermophysical characteristics of hybrid CNTs and water at room temperature.

Characteristics	Nanoparticles		Base Fluid
	SWCNTs	MWCNTs	Water
Density, ρ (kg m^{-3})	2600	1600	997.1
Heat Capacity, C_p (J kg^{-1} K^{-1})	425	796	4179
Thermal Conductivity, k (W m^{-1} K^{-1})	6600	3000	0.613
Electrical Conductivity, σ (S m^{-1})	1.0×10^8	3.5×10^6	5.0×10^{-2}

2.3. Numerical Procedure

For the purpose of being able to numerically solve Equations (7)–(9), the higher-order dimensionless ODEs are altered into first-order ODEs. This approach allows for the model to be entered into the bvp4c function in MATLAB. The transformation process is initiated by establishing the following equations:

$$\begin{gathered} f = y(1),\ f' = y(2),\ f'' = y(3), \\ \theta = y(4),\ \theta' = y(5). \end{gathered} \tag{17}$$

Therefore, the higher orders of dimensionless f''' and θ'' are expressed as follows:

$$\begin{gathered} f''' = -\tfrac{1}{A_1}((y(1)y(3)) - A_2((y(2)y(2)) - 1) + A_3A_4(1 - y(2))), \\ \theta'' = -\tfrac{\mathrm{Pr}}{A_5}((y(1)y(5))). \end{gathered} \tag{18}$$

The boundary conditions pointed out in Equation (9) turn into these mathematical expressions:

$$\begin{gathered} ya(1) = 0,\ ya(2) - \varepsilon = 0,\ ya(4) - 1 = 0, \text{ at } \eta = 0, \\ yb(2) - 1 = 0,\ yb(4) = 0, \text{ as } \eta \to \infty. \end{gathered} \tag{19}$$

2.4. Optimisation Procedure

To conduct the optimisation procedures, we apply the Response Surface Methodology (RSM). According to Myres et al. [45], the adoption of RSM can boost the efficiency of experimental and numerical operations by offering optimum solutions based on statistical and mathematical concepts. Researchers such as Benim et al. [46] successfully manipulated the RSM to optimise the aerofoil profiles in wind turbines.

To begin the optimisation process, we first identify three factors or parameters that have the potential to impact the heat transfer performance. According to Equations (7)–(10), the volume fraction, magnetic and nonlinear parameters are selected as the elements in the input set. These parameters are recognised as the most significant inputs that may contribute to the model's performance. Additionally, the Tiwari and Das model emphasises that the volume parameter is the key factor in determining the fluid flow and heat transmission characteristics. Adhering to this model in developing the mathematical model has become the main reason for choosing this parameter as part of the input set. The matrix of these factors with different levels is illustrated in Table 3. Table 3 is organised according to the relative limitations of each parameter. $[+1] = [1]$ stands for the highest level, $[0]$ for the middle level and $[-1]$ for the lowest level. Numerical simulations are used to produce the output responses of hybrid (y_{hCNT}) and mono (y_{CNT}) CNTs nanofluids by systematically altering the values of the factors. We also utilise a face-centred central composite design (CCF) to create an experimental design, with the number of trials N calculated using the formula below:

$$N = 2^F + 2F + C, \tag{20}$$

where F and C are the number of factors and the centre point, respectively.

Table 3. Different levels of values of independent variables (factors).

Factors		
ϕ_{hmf} or ϕ_{nf} $[x_1]$	M $[x_2]$	n $[x_3]$
0.03 [+1]	0.3 [+1]	5.0 [+1]
0.02 [0]	0.2 [0]	3.5 [0]
0.01 [−1]	0.1 [−1]	2.0 [−1]

Note: The symbol [] denotes a coded component.

After screening the factors and their output variables, we develop the multivariate quadratic regression equations by modifying the quadratic model expressed previously by Myres et al. [45] in order to investigate the relationship between factors and their response variables. These equations are also formed to optimise the heat transfer for both hybrid and mono CNT nanofluids. The regression models of (y_{hCNT}) and (y_{CNT}) are written as follows:

$$y_{hCNT} = \beta_0 + \beta_1\phi_{hnf} + \beta_2 M + \beta_3 n + \beta_4\phi_{hnf}^2 + \beta_5 M^2 + \beta_6 n^2 + \beta_7\phi_{hnf}M + \beta_8\phi_{hnf}n + \beta_9 Mn + \epsilon, \quad (21)$$

and

$$y_{CNT} = \beta_0 + \beta_1\phi_{nf} + \beta_2 M + \beta_3 n + \beta_4\phi_{nf}^2 + \beta_5 M^2 + \beta_6 n^2 + \beta_7\phi_{nf}M + \beta_8\phi_{nf}n + \beta_9 Mn + \epsilon. \quad (22)$$

The terms β_0, β_i, $i = 1, 2, 3$, β_j, $j = 4, 5, 6$, β_k, $k = 7, 8, 9$ and ϵ represent the mean value, the linear coefficients, the interaction between factors coefficients, the quadratic coefficients and the error term, respectively. The mathematical formulation of Equations (21) and (22), which include quadratic components, can be helpful in our analysis to determine the optimal amount of the heat transfer coefficient. According to Myres et al. [45], a quadratic model is suitable for fitting the process of an optimal issue. To determine the value of coefficients in Equations (21) and (22), we use the analysis of variance (ANOVA). The ANOVA data for the y_{hCNT} and y_{CNT} models are computed with the aid of the Minitab program.

3. Results and Discussions

3.1. Numerical Solutions

To validate the programming code developed in the bvp4c function (MATLAB), we compare the data with Anuar et al.'s model [36]. By setting $\phi_{SWCNT} = \phi_{MWCNT} = M = 0$, $n = 1$, $\varepsilon = -1.1$, and Pr= 0.7, the model produces the reduced skin friction $f''(0)$ and the reduced heat transfer $-\theta'(0)$ as displayed in Table 4. The results presented in Table 4 indicate that the current model and the previous model are in good agreement. The result of this agreement gives us the opportunity to commence our investigation by examining the effects of magnetic fields on the heat transfer and flow characteristics of the hybrid CNTs.

Table 4. Comparison between the current model and Anuar et al.'s model [36].

	$f'(0)$		$-\theta'(0)$	
n	**Anuar et al.'s Model [36]**	**The Present Solution**	**Anuar et al.'s Model [36]**	**The Present Solution**
1	1.1867	1.1867	0.1828	0.1828

In order to examine the effect of the magnetic parameter M on the flow separation, it is necessary to identify the region in which the duality solution occurs. It is possible to predict the point at which the boundary layer separates from the surface using the dual solution. We assume that the upper solution (the first solution) and the lower solution (the second solution) are the attached and separated flow solutions, respectively. To investigate this region, we set M to vary from 0 to 0.2 and $-1.5 < \varepsilon < 1.5$. The Waqas et al. model [47] serves as a guide for changing the variable M. The other parameters are kept at constant values, where $Pr = 6.2$, $\phi_1 = \phi_{SWCNT} = 0.01$, $\phi_2 = \phi_{MWCNT} = 0.01$ and $n = 2$. The first

solution (solid line) and the second solution (dash line) appear when $\varepsilon_c \leq \varepsilon < 0$, where ε is in shrinking mode and ε_c represents the critical point of producing the dual solutions. These phenomena are visually represented in Figure 2. An additional observation that can be made from this figure is that the boundary layer delays being separated as M increases. Increasing n also results in a noticeable lag in the detachment of boundary layers, as displayed in Figure 3. The aforementioned outcomes are produced through the configuration of various values for n and ε while holding all other variables constant. From Figures 2 and 3, the rise of M and n contributes to the widening range of $f''(0)$ and $-\theta'(0)$.

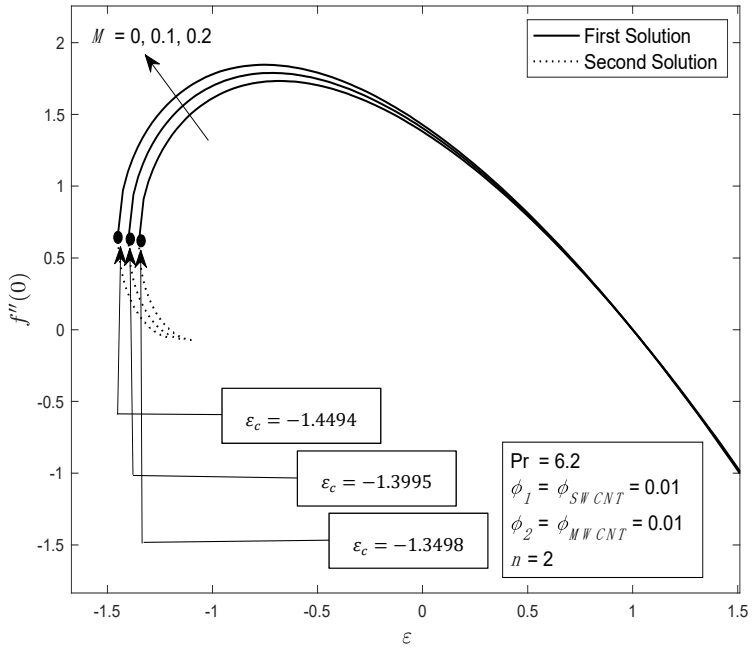

(**a**)

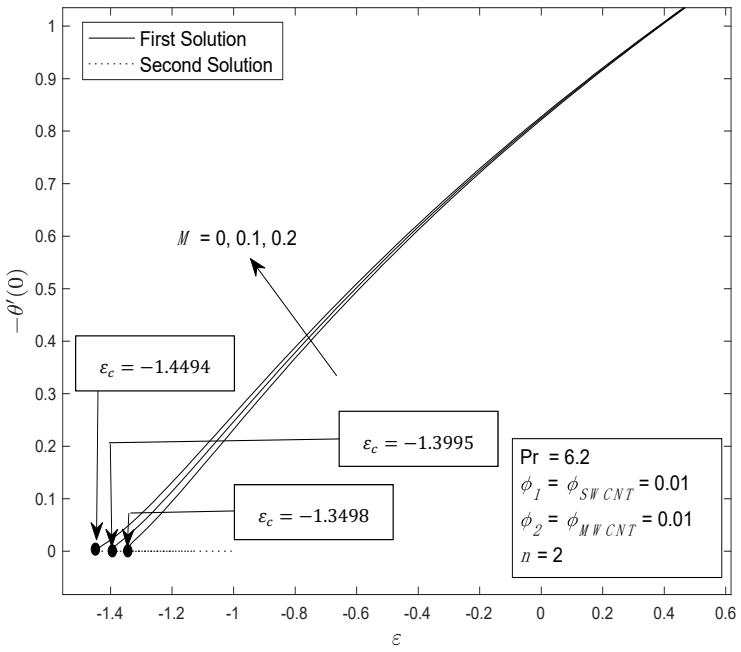

(**b**)

Figure 2. Variation of solutions (**a**) $f''(0)$; (**b**) $-\theta'(0)$ using different values of ε and M in hybrid SWCNTs-MWCNTs water-based nanofluids.

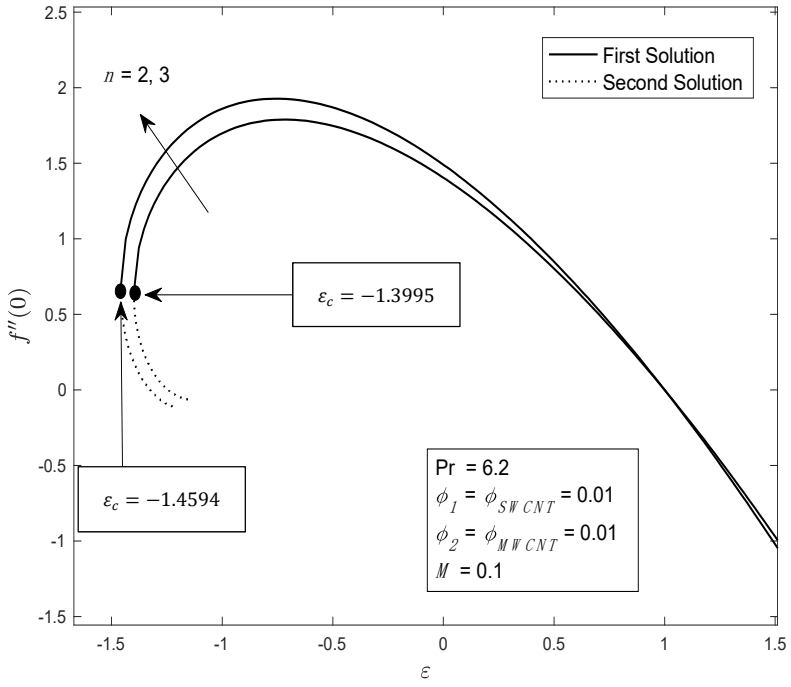

(**a**)

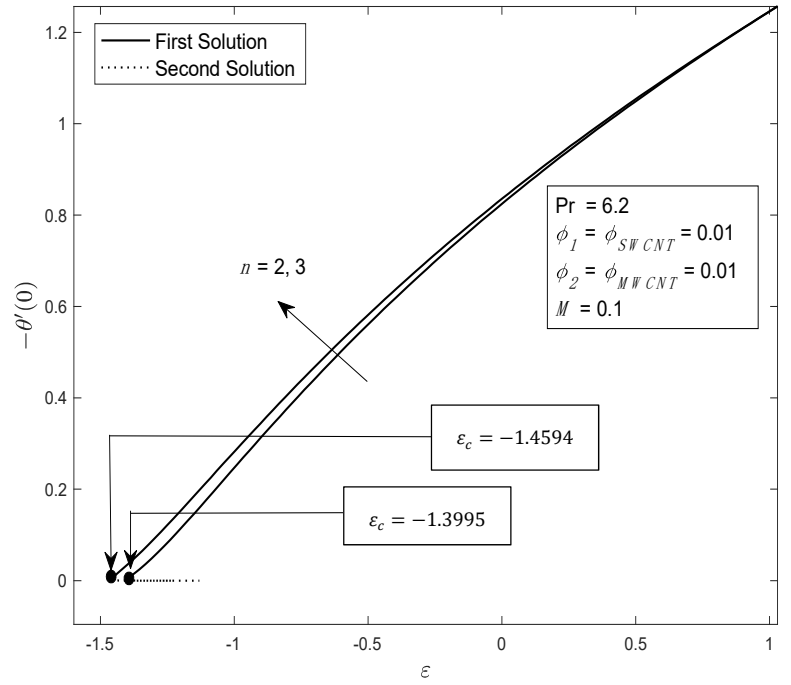

(**b**)

Figure 3. Variation of solutions (**a**) $f''(0)$; (**b**) $-\theta'(0)$ using different values of ε and n in hybrid SWCNTs-MWCNTs water-based nanofluids.

The variations in velocity $f'(\eta)$ and temperature $\theta(\eta)$ profiles for hybrid CNTs nanofluids resulting from the modifications in M and n can be demonstrated in Figures 4 and 5, respectively. In Figure 4, the value of M is modified from 0 to 0.2, while in Figure 5, the value of n is adjusted from 2 to 4. We noticed that both figures (4 and 5) generate the dual solution when the sheet moves at stretching velocity ($\varepsilon < 0$), where the first solution

is thinner than the second solution. Figures 4 and 5 also provide strong evidence that the profiles asymptotically meet the boundary constraints specified in Equation (9). The velocity profile $f'(\eta)$ for the first solution has an increasing trend as the values of M and n grow. But the rise in the values of M and n leads to a distinct pattern in the profile of $f'(\eta)$ for the second solution. To illustrate the thermal boundary layer of the first solution, we discover that an increase in M and n results in a drop in $\theta(\eta)$. However, the value of $\theta(\eta)$ for the second solution gets higher as a consequence of the increase in M.

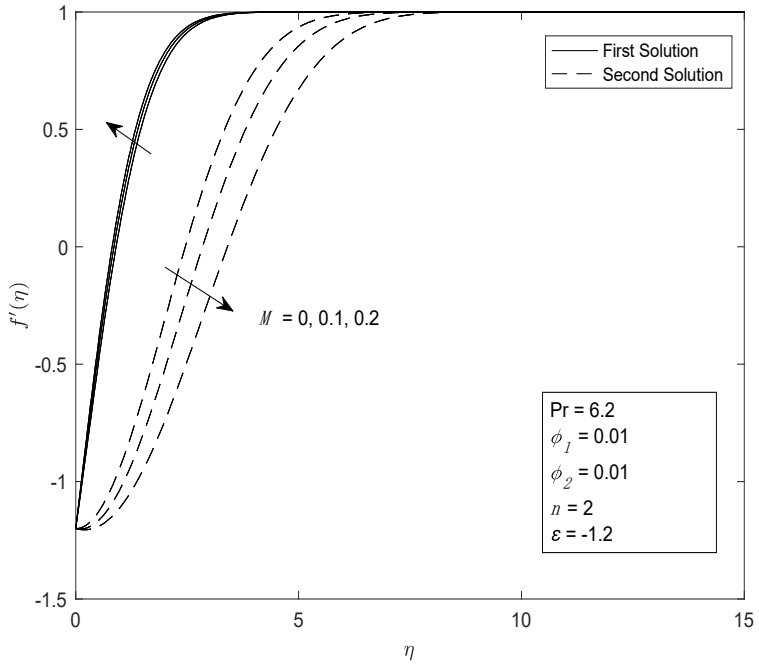

(**a**)

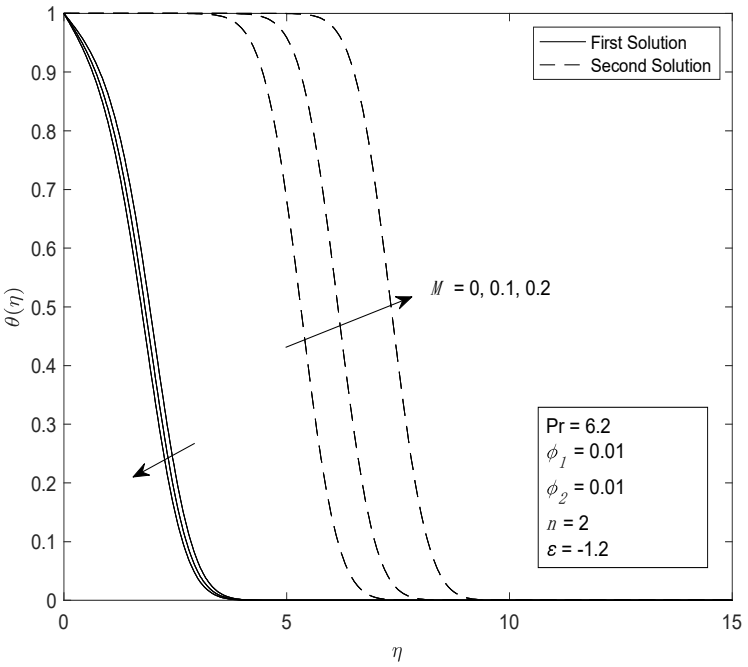

(**b**)

Figure 4. Variation of solutions (**a**) velocity; (**b**) temperature profiles using different values of M in hybrid SWCNTs-MWCNTs water-based nanofluids.

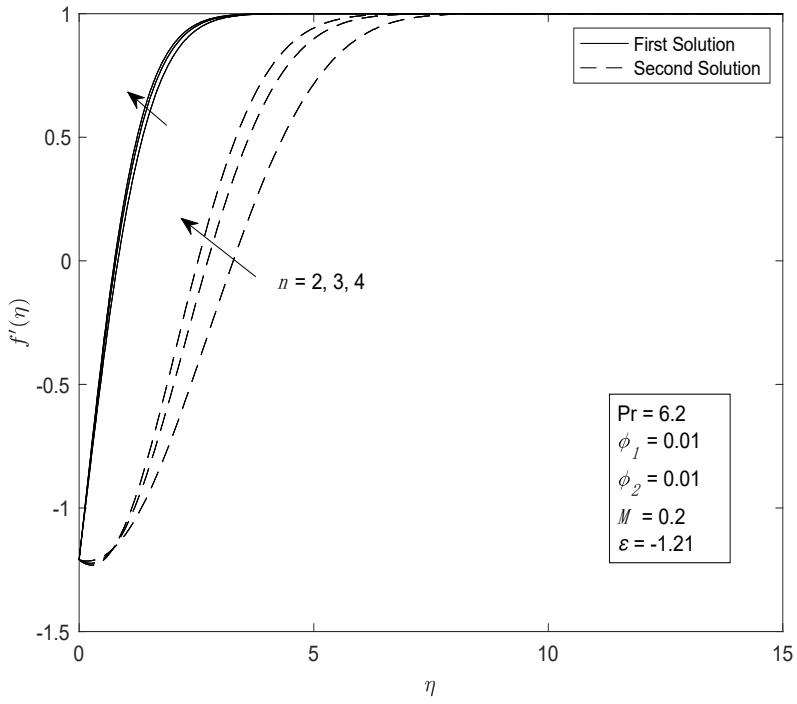

(**a**)

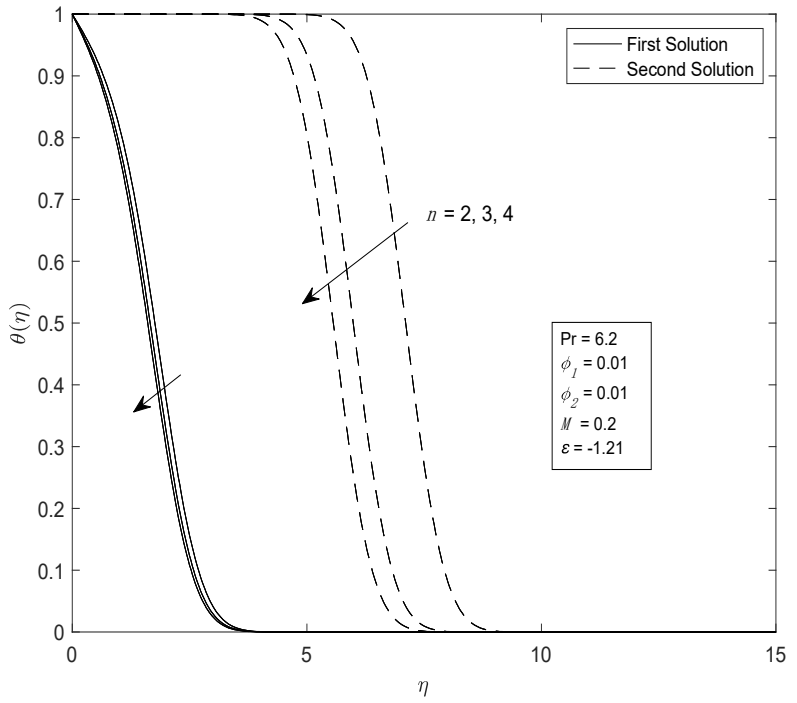

(**b**)

Figure 5. Variation of solutions (**a**) velocity; (**b**) temperature profiles using different values of n in hybrid SWCNTs-MWCNTs water-based nanofluids.

The performance of hybrid CNTs both for the skin friction and heat transfer rate under the impact of M, $\phi_1 = \phi_{SWCNT}$, and $\phi_2 = \phi_{MWCNT}$ are discussed in Figure 6. The values of M are set at 0, 0.1 and 0.2, while ϕ_1 and ϕ_2 vary from 0 to 0.1. The values of ϕ_1 and ϕ_2 undergo modifications at low concentrations, as shown by Kumar et al. [48]. They believe that the performance of the transfer is effectively enhanced under low-concentration conditions. The

other parameters are held constant, with $Pr = 6.2$, $\varepsilon = 0.5$ and $n = 2$. Based on this figure, we identified that the rise in M, ϕ_1 and ϕ_2 triggers a boost in both the skin friction and heat transfer coefficients. Prior research conducted by Sun et al. [49] demonstrated the enhancement of heat transfer resulting from the application of a magnetic field. According to Shah et al. [50], they stated that the magnetic field induces an increase in heat transfer via the action of Lorentz forces.

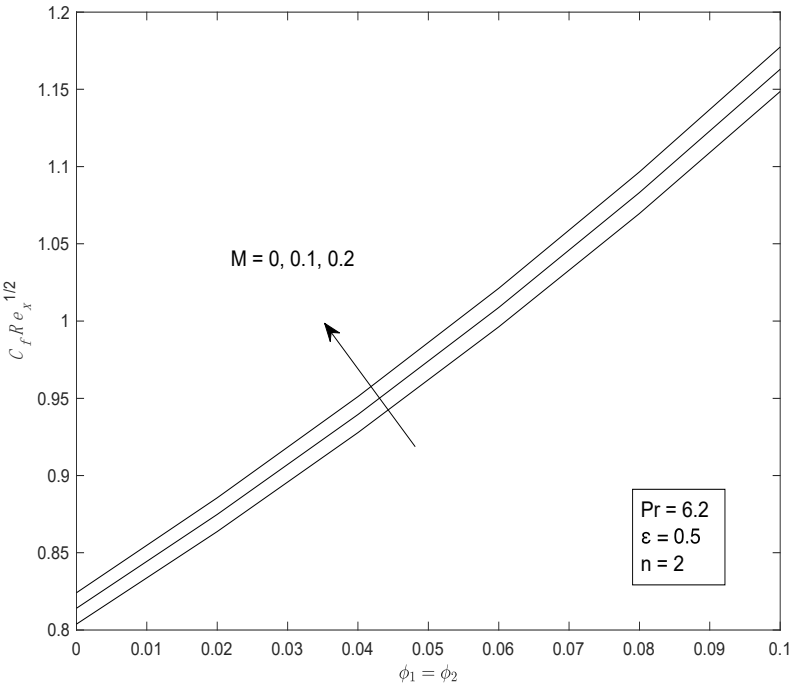

(**a**)

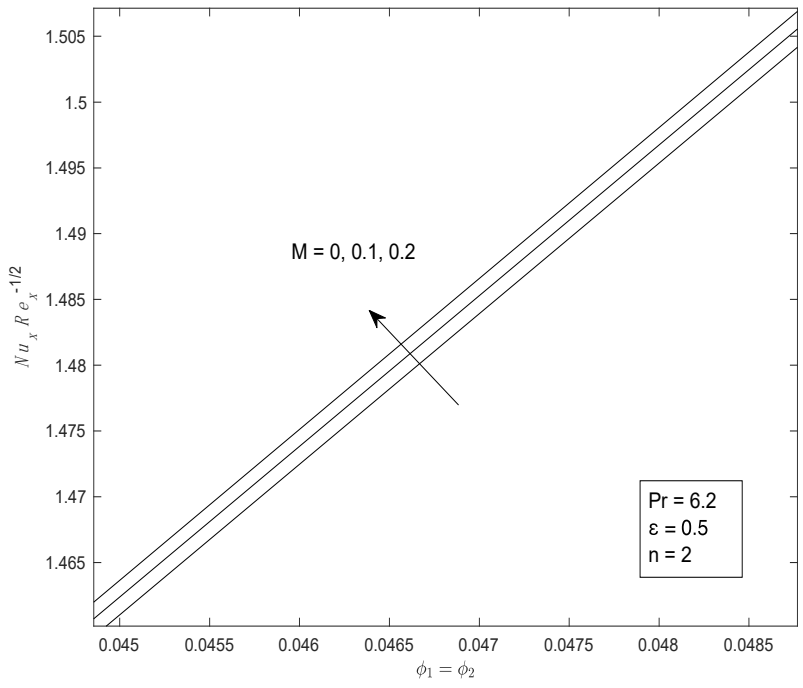

(**b**)

Figure 6. Variation of solutions (**a**) skin friction; (**b**) heat transfer coefficients using different values of M and ϕ in hybrid SWCNTs-MWCNTs water-based nanofluids.

With the goal of evaluating the performance of hybrid carbon nanotubes (CNTs) nanofluids with mono-CNTs nanofluids in terms of skin friction and heat transfer, we conduct investigations utilising various values of ϕ_1, ϕ_2 and M. To choose the most suitable nanoparticles that effectively act as mono-CNTs, we adhere to Samat et al.'s model [51]. They found that SWCNTs were better at transferring heat than MWCNTs. This means that SWCNTs represent mono-CNTs. By leaving Pr at 6.2 and $n = 2$, we can discover from Figures 7 and 8 that the skin friction and heat transfer coefficients for hybrid CNTs nanofluids and mono-CNTs nanofluids both rise. Furthermore, hybrid carbon nanotubes (CNTs) nanofluids exhibit superior performance compared to mono-CNTs nanofluids in terms of both skin friction and heat transfer coefficients.

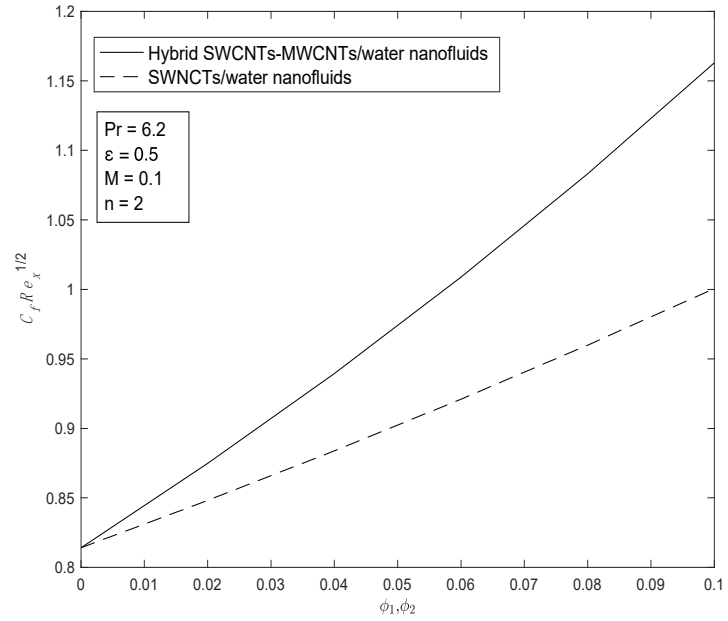

(**a**)

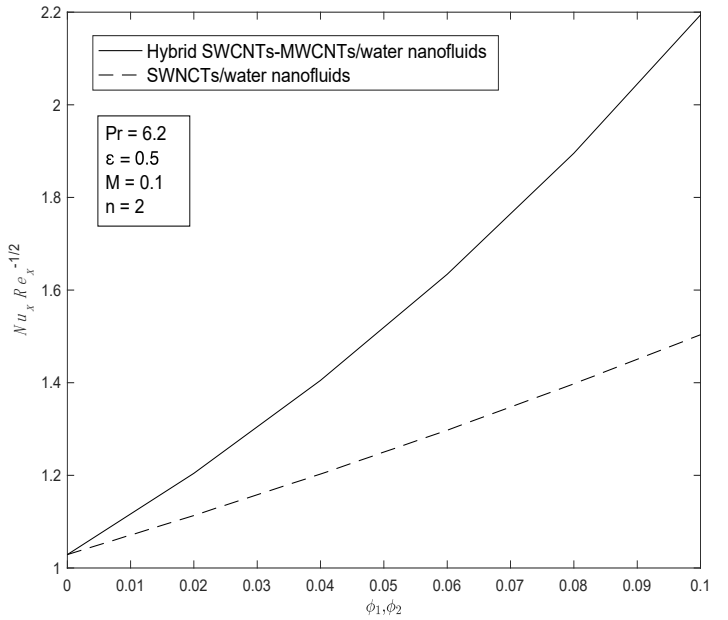

(**b**)

Figure 7. Comparison performance of hybrid CNTs and mono CNTs in (**a**) skin friction; (**b**) heat transfer coefficients using different values of $\phi_1 = \phi_{SWCNT}$ and $\phi_2 = \phi_{MWCNT}$.

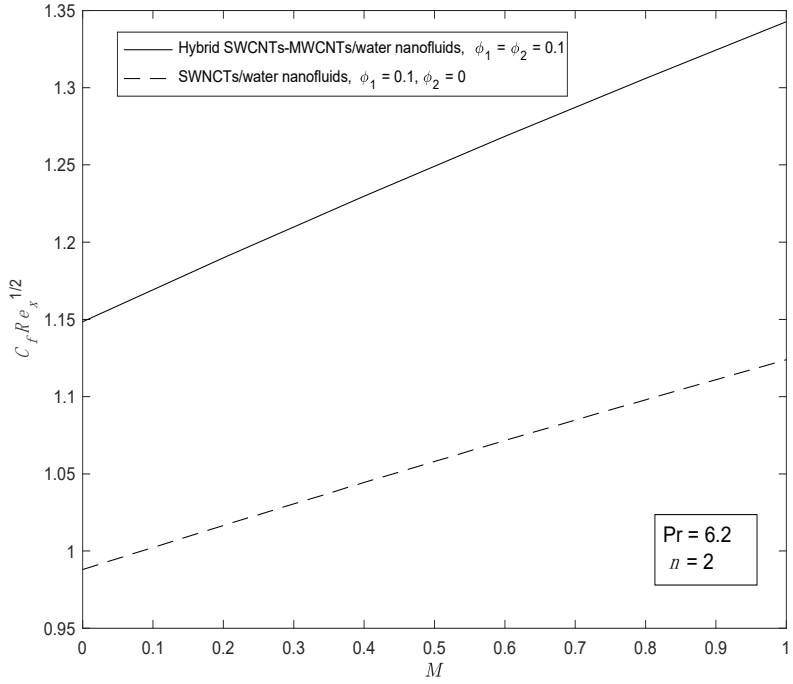

(**a**)

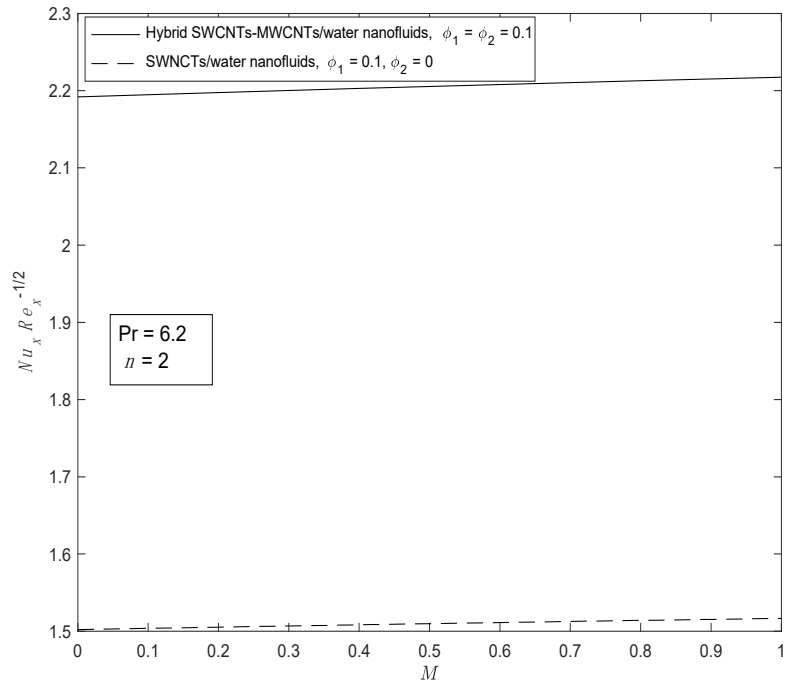

(**b**)

Figure 8. Comparison performance of hybrid CNTs and mono CNTs in (**a**) skin friction; (**b**) heat transfer coefficients using different values of M.

3.2. RSM

In order to compute the numerical values of the responses y_{hCNT} and y_{CNT}, we employ a mixture of several parameter levels, including ϕ_{hnf}, ϕ_{nf}, M and n. The distribution of various values of these independent variables and their corresponding responses is shown in Table 5. Employing Equation (20) with $F = 3$, $C = 6$, we perform 20 trials. The numerical findings arranged in Table 5 are tested using the analysis of variance (ANOVA) in Minitab.

Table 5. Design of experiment of heat transfer in hybrid CNTs and mono CNTs with water-based nanofluids.

Runs	Uncoded Parameters			Coded Parameters			Responses	
	ϕ_{hnf} or ϕ_{nf}	M	n	x_1	x_2	x_3	y_{hCNT}	y_{CNT}
1	0.01	0.1	2.0	−1	−1	−1	1.3641	1.3112
2	0.03	0.1	2.0	1	−1	−1	1.5940	1.4178
3	0.01	0.3	2.0	−1	1	−1	1.3666	1.3136
4	0.03	0.3	2.0	1	1	−1	1.5972	1.4204
5	0.01	0.1	5.0	−1	−1	1	1.9425	1.8673
6	0.03	0.1	5.0	1	−1	1	2.2699	2.0190
7	0.01	0.3	5.0	−1	1	1	1.9440	1.8687
8	0.03	0.3	5.0	1	1	1	2.2719	2.0206
9	0.01	0.2	3.5	−1	0	0	1.6795	1.6145
10	0.03	0.2	3.5	1	0	0	1.9627	1.7457
11	0.02	0.1	3.5	0	−1	0	1.8153	1.6782
12	0.02	0.3	3.5	0	1	0	1.8174	1.6801
13	0.02	0.2	2.0	0	0	−1	1.4766	1.3650
14	0.02	0.2	5.0	0	0	1	2.1016	1.9428
15	0.02	0.2	3.5	0	0	0	1.8164	1.6791
16	0.02	0.2	3.5	0	0	0	1.8164	1.6791
17	0.02	0.2	3.5	0	0	0	1.8164	1.6791
18	0.02	0.2	3.5	0	0	0	1.8164	1.6791
19	0.02	0.2	3.5	0	0	0	1.8164	1.6791
20	0.02	0.2	3.5	0	0	0	1.8164	1.6791

The ANOVA results in analysing the heat transfer coefficients for hybrid CNTs and mono CNTs are displayed in Tables 6 and 7 and Figures 9–14. Both models, y_{hCNT} and y_{CNT}, are considered well-fitting models as their residuals are normally distributed. According to Myres et al. [45], the model is statistically significant if the P-value of the sources is less than 0.05. Since the P-values of the several inputs in Tables 6 and 7 exceed 0.05, we exclude these factors when establishing the reduced models for hybrid CNTs and mono CNTs. The reduced models for hybrid CNTs and mono CNTs are constructed in Tables 8 and 9, respectively.

Table 6. Analysis of variance for the full model of heat transfer in hybrid CNTs with water-based nanofluids.

Source	DF	Adj SS	Adj MS	F-Value	p-Value
Model	9	1.18411	0.131568	158,942.79	0.000
Linear	3	1.17631	0.392102	473,685.11	0.000
x1	1	0.19576	0.195760	236,491.30	0.000
x2	1	0.00001	0.000013	15.30	0.003
x3	1	0.98053	0.980533	1,184,548.72	0.000
Square	3	0.00307	0.001022	1234.95	0.000
x1 × x1	1	0.00006	0.000061	73.81	0.000
x2 × x2	1	0.00000	0.000000	0.00	0.952
x3 × x3	1	0.00205	0.002048	2473.55	0.000
2-Way Interaction	3	0.00474	0.001580	1908.33	0.000
x1 × x2	1	0.00000	0.000000	0.17	0.691
x1 × x3	1	0.00474	0.004738	5724.07	0.000
x2 × x3	1	0.00000	0.000001	0.75	0.408
Error	10	0.00001	0.000001		
Lack-of-Fit	5	0.00001	0.000002	*	*
Pure Error	5	0.00000	0.000000		
Total	19	1.18412			

Note: The symbol * indicates that the data is too small.

Table 7. Analysis of variance for the full model of heat transfer in mono CNTs with water-based nanofluids.

Source	DF	Adj SS	Adj MS	*F*-Value	*p*-Value
Model	9	0.881473	0.097941	611,438.84	0.000
Linear	3	0.877407	0.292469	1,825,856.01	0.000
x1	1	0.042015	0.042015	262,298.05	0.000
x2	1	0.000010	0.000010	60.93	0.000
x3	1	0.835382	0.835382	5,215,209.04	0.000
Square	3	0.003047	0.001016	6340.68	0.000
x1 × x1	1	0.000002	0.000002	14.26	0.004
x2 × x2	1	0.000000	0.000000	0.00	0.962
x3 × x3	1	0.001748	0.001748	10,915.25	0.000
2-Way Interaction	3	0.001019	0.000340	2119.83	0.000
x1 × x2	1	0. 000000	0.000000	0.15	0.711
x1 × x3	1	0.001018	0.001018	6356.36	0.000
x2 × x3	1	0.000000	0.000000	3.00	0.114
Error	10	0.000002	0.000000		
Lack-of-Fit	5	0.000002	0.000000	*	*
Pure Error	5	0.00000	0.000000		
Total	19	0.881475			

Note: The symbol * indicates that the data is too small.

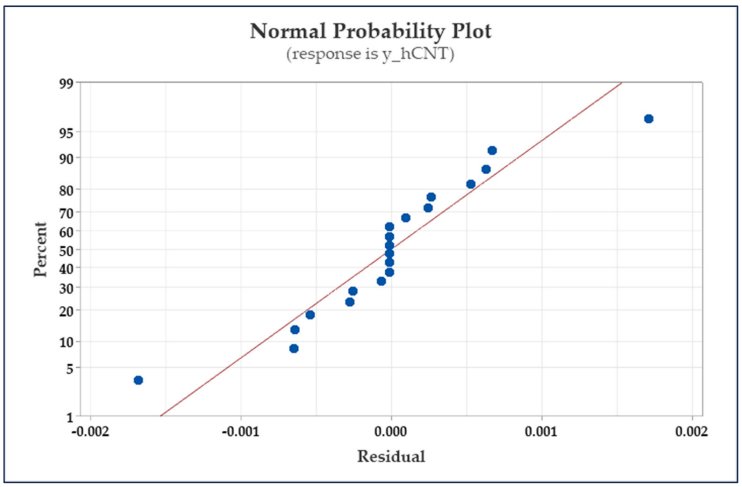

(**a**)

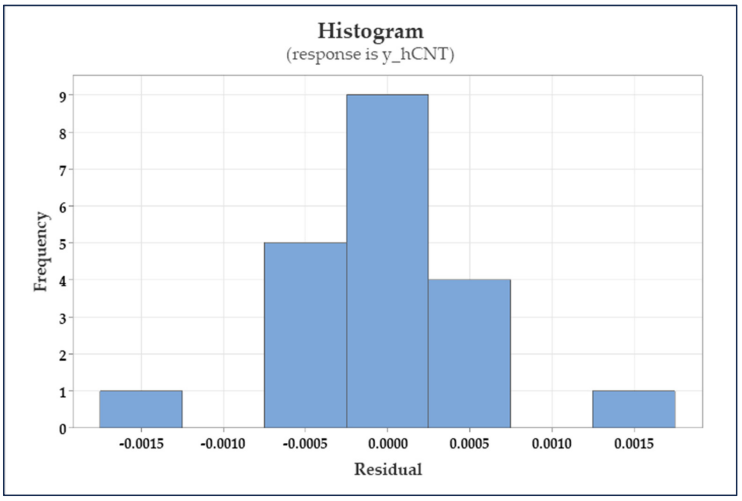

(**b**)

Figure 9. (**a**) Normal probability plot; (**b**) residual histogram for hybrid CNTs.

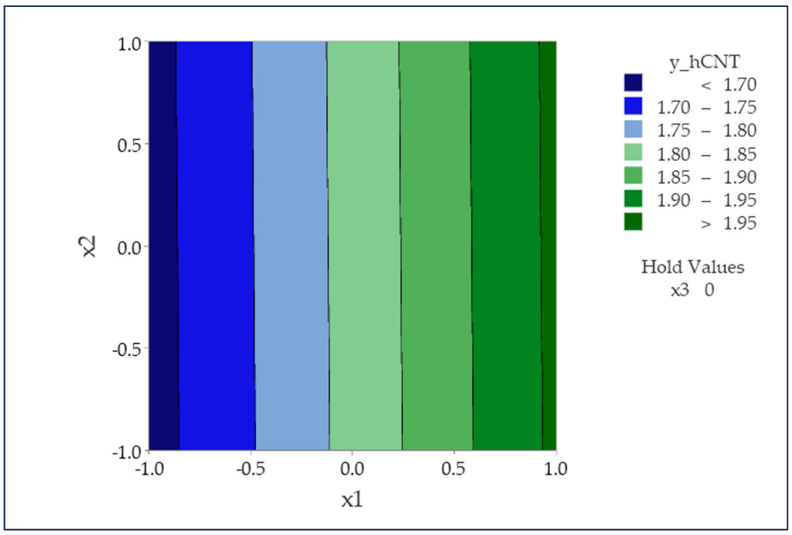

(**a**)

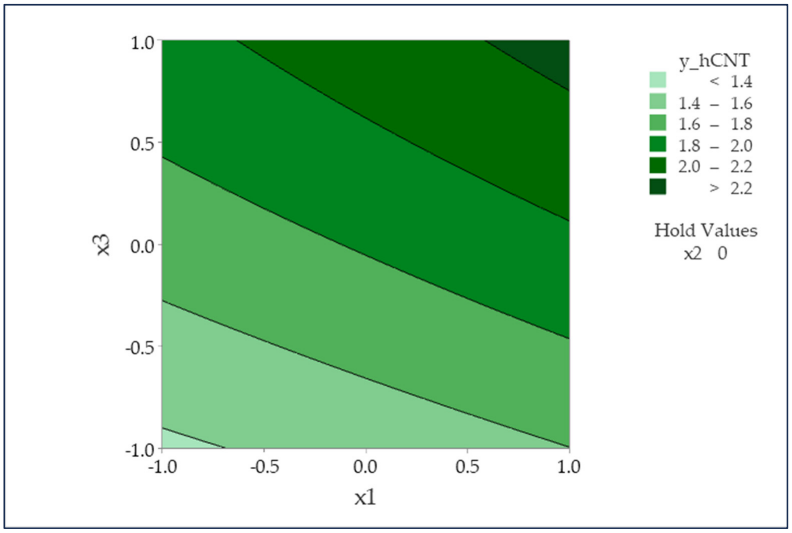

(**b**)

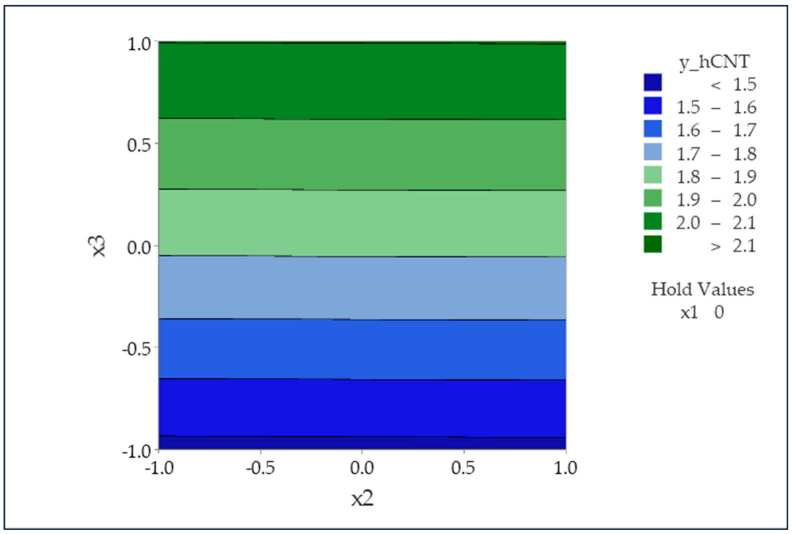

(**c**)

Figure 10. Contour plots for the interaction of (**a**) x_1 and x_2; (**b**) x_1 and x_3; (**c**) x_2 and x_3 for hybrid CNTs.

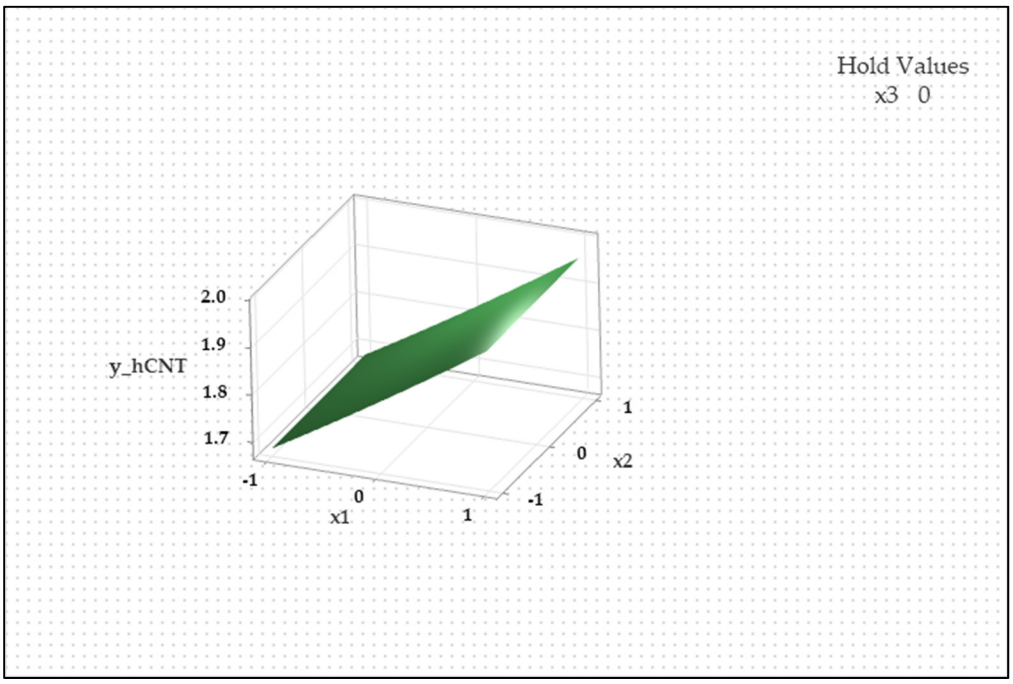

(**a**)

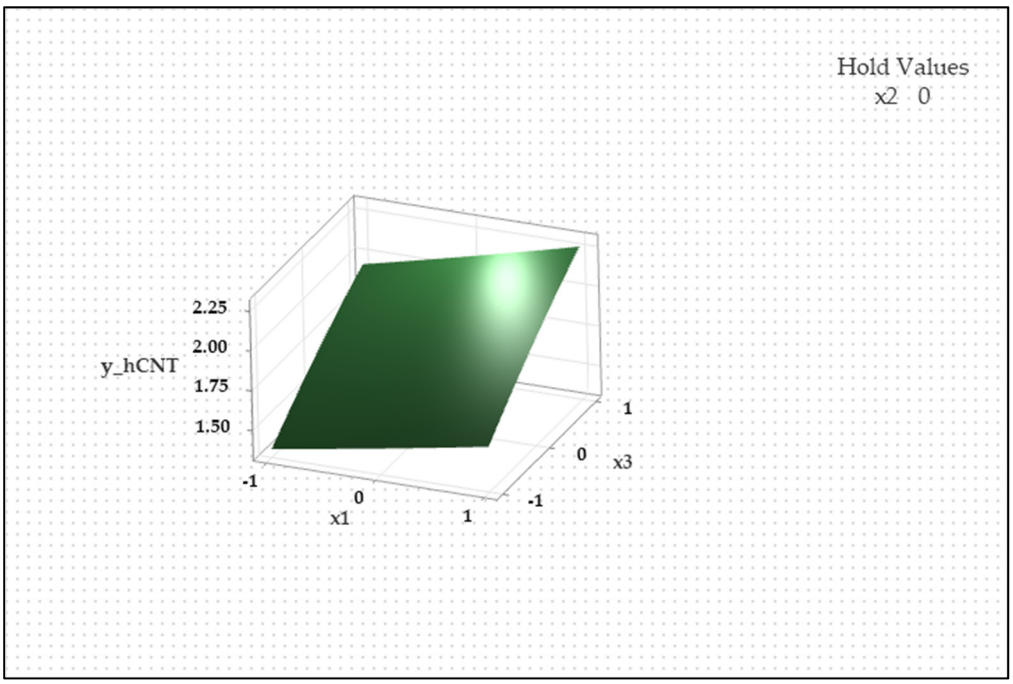

(**b**)

Figure 11. *Cont*.

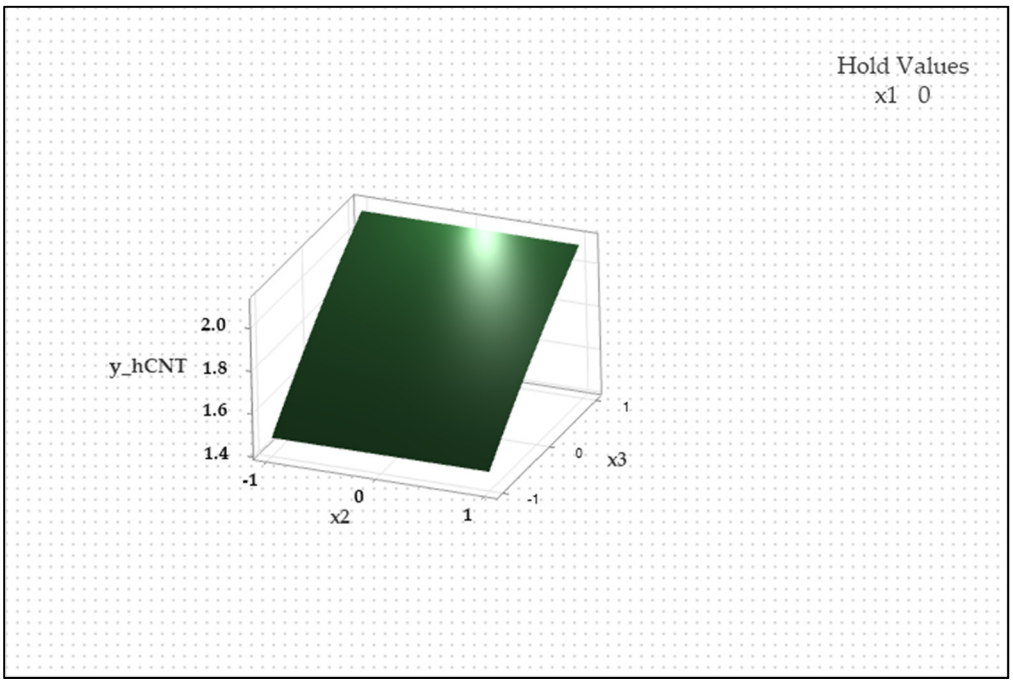

(**c**)

Figure 11. Surface plots for the interaction of (**a**) x_1 and x_2; (**b**) x_1 and x_3; (**c**) x_2 and x_3 for hybrid CNTs.

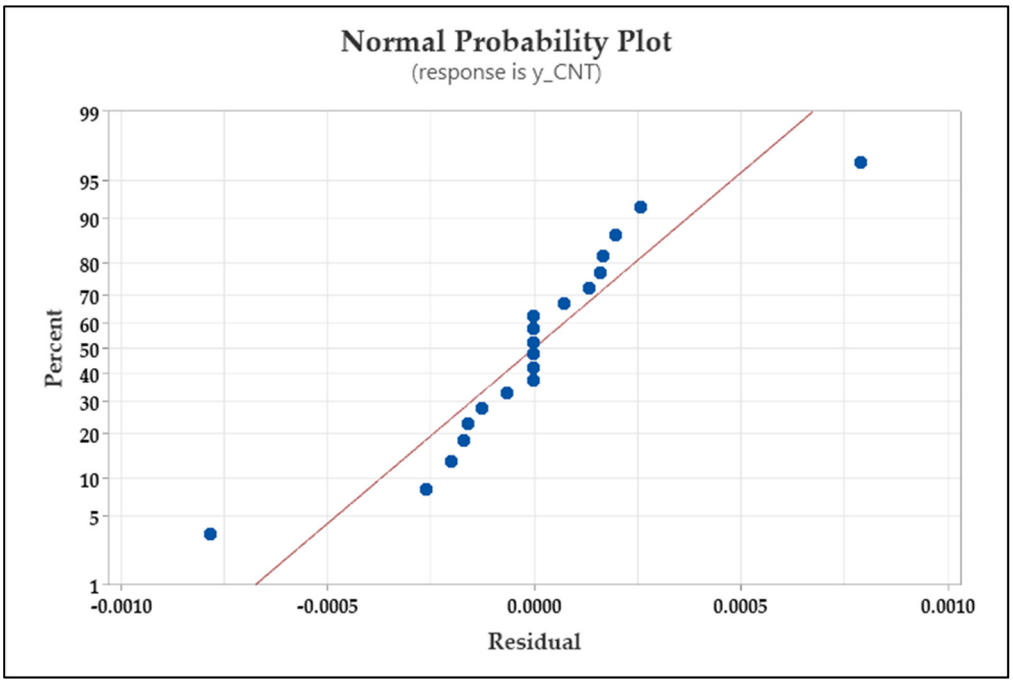

(**a**)

Figure 12. *Cont.*

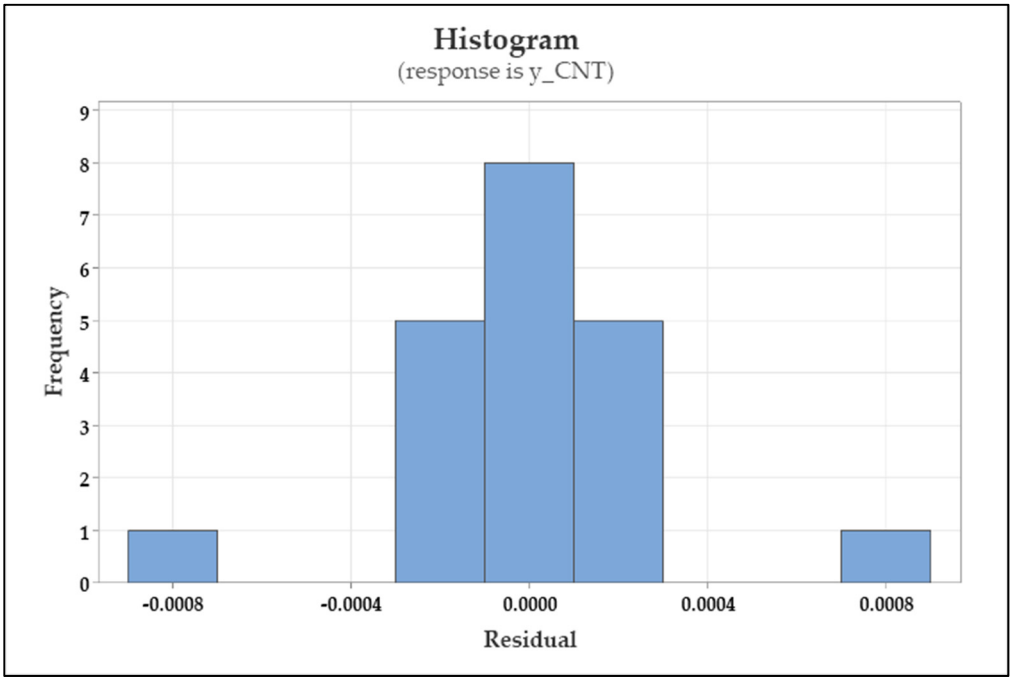

(**b**)

Figure 12. (**a**) Normal probability plot; (**b**) residual histogram for mono CNTs.

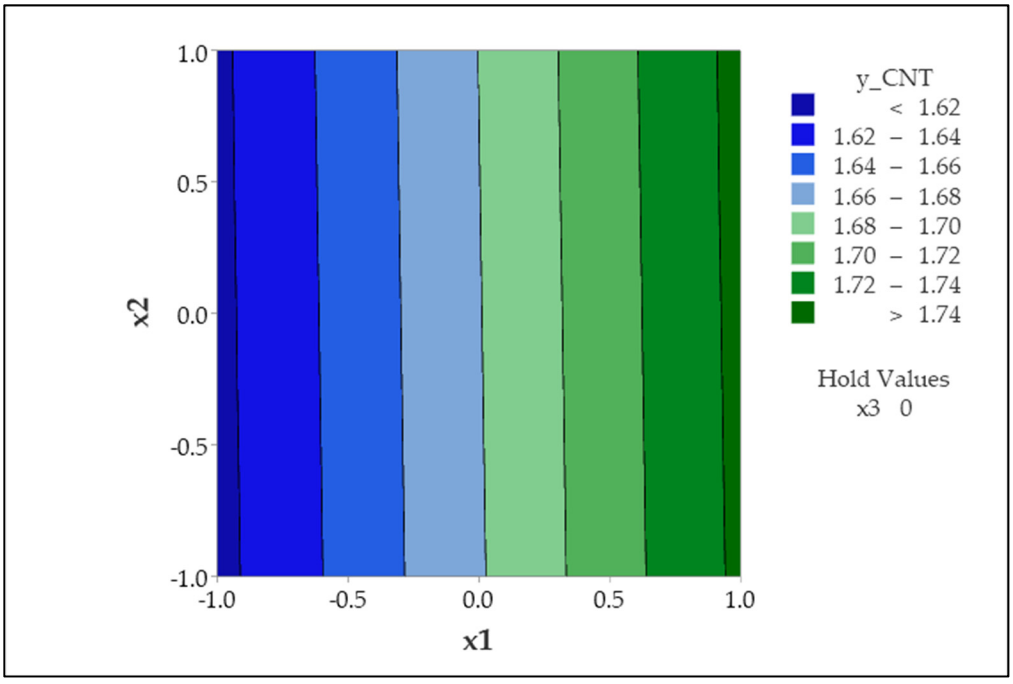

(**a**)

Figure 13. *Cont.*

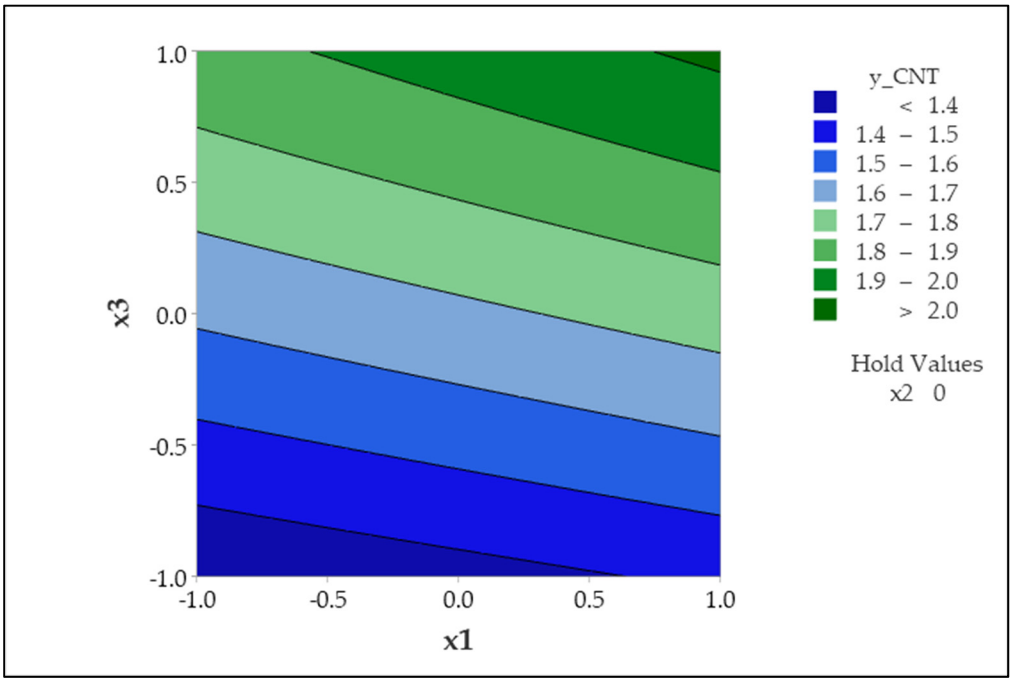

(**b**)

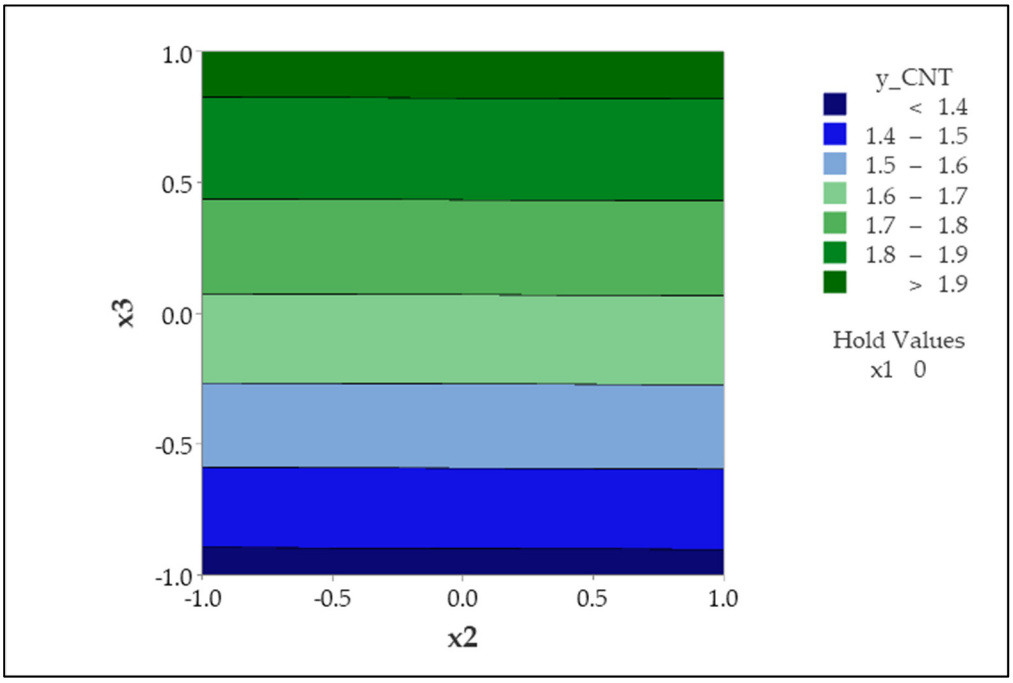

(**c**)

Figure 13. Contour plots for the interaction of (**a**) x_1 and x_2; (**b**) x_1 and x_3; (**c**) x_2 and x_3 for mono CNTs.

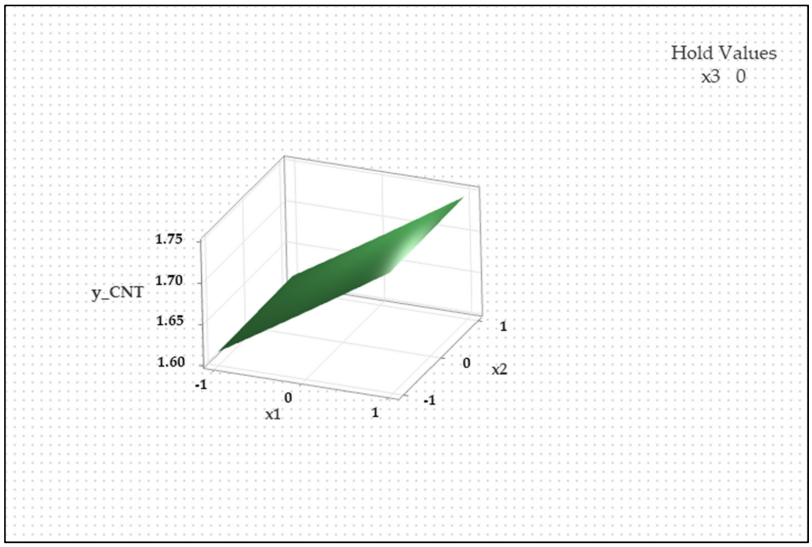

(**a**)

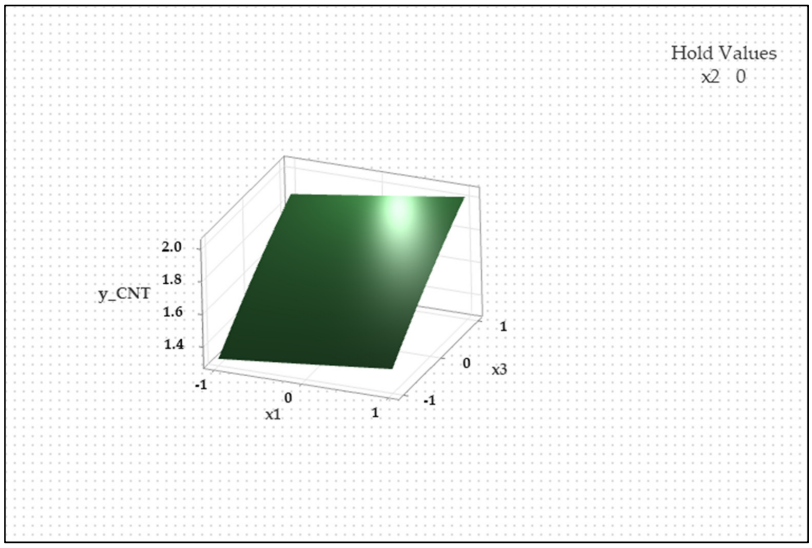

(**b**)

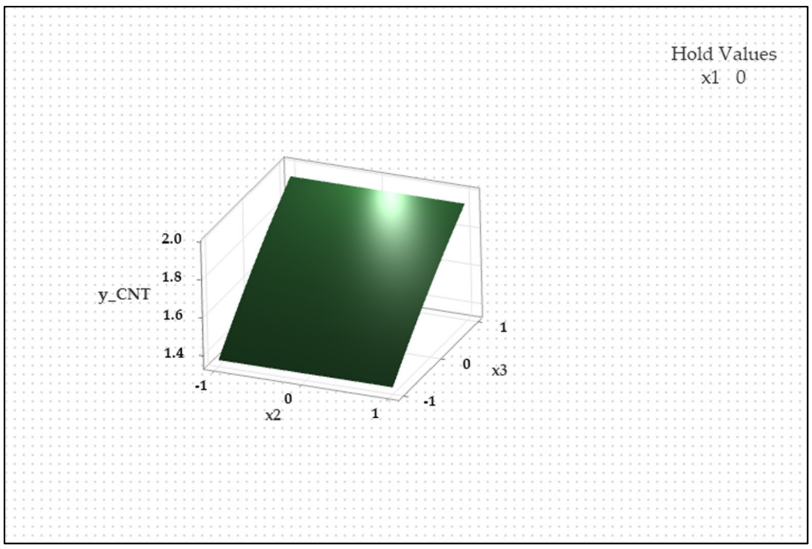

(**c**)

Figure 14. Surface plots for the interaction of (**a**) x_1 and x_2; (**b**) x_1 and x_3; (**c**) x_2 and x_3 for mono CNTs.

Table 8. Analysis of variance for the reduced model of heat transfer in hybrid CNTs with water-based nanofluids.

Source	DF	Adj SS	Adj MS	*F*-Value	*p*-Value
Model	6	1.18411	0.197352	283,895.82	0.000
Linear	3	1.17631	0.392102	564,049.09	0.000
x1	1	0.19576	0.195760	281,606.29	0.000
x2	1	0.00001	0.000013	18.22	0.001
x1	1	0.98053	0.980533	1,410,522.77	0.000
Square	2	0.00307	0.000071	2205.80	0.000
x1 × x1	1	0.00006	0.000061	101.72	0.000
x3 × x3	1	0.00205	0.002385	3430.59	0.000
2-Way Interaction	3	0.00474	0.004738	6816.04	0.000
x1 × x3	1	0.00474	0.004738	6816.04	0.000
Error	13	0.00001	0.000001		
Lack-of-Fit	8	0.00001	0.000001	*	*
Pure Error	5	0.00000	0.000000		
Total	19	1.18412			

Note: The symbol * indicates that the data is too small.

Table 9. Analysis of variance for the reduced model of heat transfer in mono CNTs with water-based nanofluids.

Source	DF	Adj SS	Adj MS	*F*-Value	*p*-Value
Model	6	0.881473	0.146912	907,150.03	0.000
Linear	3	0.877407	0.292469	1,805,932.91	0.000
x1	1	0.042015	0.042015	259,435.95	0.000
x2	1	0.000010	0.000010	60.26	0.000
x3	1	0.835382	0.835382	5,158,302.53	0.000
Square	2	0.003047	0.001532	9407.24	0.000
x1 × x1	1	0.000003	0.000003	16.25	0.001
x3 × x3	1	0.002035	0.002035	12,567.25	0.000
2-Way Interaction	1	0.001018	0.001018	6287.00	0.000
x1 × x3	1	0.001018	0.001018	6287.00	0.000
Error	13	0.000002	0.000000		
Lack-of-Fit	8	0.000002	0.000000	*	*
Pure Error	5	0.000000	0.000000		
Total	19	0.881475			

Note: The symbol * indicates that the data is too small.

After removing these terms, the ANOVA results in Tables 8 and 9 show that all the sources have *p*-values less than 0.05. As a consequence, the reduced models fit statistically to produce the optimal solution for heat transfer y_{hCNT} and y_{CNT}. Therefore, we have productively formulated the final quadratic regression equations of the heat transfer for hybrid CNTs in Equation (23) and mono CNTs in Equation (24). The equations are written as follows:

$$y_{hCNT} = 1.81639 + 0.129914\phi_{hnf} + 0.001125M + 0.313135n + 0.004701\phi_{hnf}^2 - 0.027299n^2 + 0.024337\phi_{hnf}n, \quad (23)$$

$$y_{CNT} = 1.67915 + 0.064819\phi_{nf} + 0.000988M + 0.289030n + 0.000907\phi_{nf}^2 - 0.025219n^2 + 0.011281\phi_{nf}n. \quad (24)$$

The satisfactory outcomes shown in Tables 8 and 9 also enable the determination of the ideal solutions for heat transmission in both kinds of nanofluids. Utilising the response optimizer, the rate of heat transfer for hybrid CNTs and mono CNTs is maximised when ϕ_{hnf}, ϕ_{nf}, M and n are at their highest values. With a composite desirability value of 100%, Tables 10 and 11 reveal that hybrid CNTs have excellent heat transmission performance compared to individual CNTs. In terms of heat transfer, this result shows that the RSM has successfully confirmed the previous computational findings. These findings show that hybrid carbon nanotubes (CNTs) are better than mono CNTs.

Table 10. The optimal solution of heat transfer in hybrid CNTs with water-based nanofluids.

Solution	ϕ_{hnf}	M	n	y_{hCNT} Fit	Composite Desirability
1	1	1	1	2.27230	1

Table 11. The optimal solution of heat transfer in mono CNTs with water-based nanofluids.

Solution	ϕ_{nf}	M	n	y_{CNT} Fit	Composite Desirability
1	1	1	1	2.02095	1

4. Conclusions

The investigation of hybrid CNTs flow and heat transfer past a nonlinear stretching or shrinking sheet is successfully performed using the numerical and RSM approaches under the influence of magnetohydrodynamic effects. The model is developed by taking the magnetic and volume fractions of hybrid and mono CNTs, nonlinear, and shrinking or stretching parameters as the leading variables in non-dimensionless units. The similarity equations in the form of non-dimensional ordinary differential equations are solved using the similarity variables method. The bvp4C MATLAB function is employed to numerically compute the first order of the ODEs system. By referring to the mathematical model and using the numerical experiment data, the design of the heat transfer coefficients both for hybrid CNTs and mono CNTs is statistically optimised in Minitab. The design of this optimisation procedure involves three parameters and twenty simulation runs. The findings show that:

- The multiple solution is generated when the sheet moves nonlinearly in the shrinking region where $\varepsilon_c \leq \varepsilon < 0$.
- The boundary layer of the first solution is thinner than that of the second solution.
- The model may provide a couple of solutions when the magnetic parameter is below 1.
- The magnetic and non-linear parameters delay the occurrence of boundary layer separation and expand the range of potential solutions for the reduced skin friction $f''(0)$ and the reduced heat transfer $-\theta'(0)$.
- The magnetic and hybrid CNTs volume fraction parameters enhance the favourable effect on skin friction and heat transfer coefficients.
- To maximise the heat transfer rate, the magnetic, nonlinear, and hybrid CNTs volume fractions are set at their greatest values.
- Hybrid CNTs are superior to mono CNTs for the skin friction coefficient.
- The numerical analysis and response surface methodology demonstrate that hybrid CNTs are better than mono CNTs with regard to the heat transfer rate.

5. Future Works

Due to some limitations in this model, there are several recommendations to extend the model in the future. They are as follows:

- The investigation of hybrid nanofluids flow-based carbon nanotubes over a nonlinear stretching/shrinking sheet under an unsteady flow case.
- The study of hybrid carbon nanotube flow across a nonlinear stretching/shrinking sheet using the 3-Dimension (3D) flow approach.
- The examination of hybrid nanofluids flow-based carbon nanotubes over a nonlinear stretching/shrinking sheet with distinct effects, including velocity and thermal slip effects.
- The exploration of hybrid carbon nanotube flow past different geometric configurations, such as a Riga plate.

The suggestions mentioned above for future research could potentially improve the comprehension of the fluid motion and heat transfer characteristics of hybrid nanofluids, particularly for hybrid carbon nanotubes.

Author Contributions: N.A.A.S. contributed to the research concept, the design of the study, the preparation of materials, data collection, the analysis of findings, and the writing of the first draft of the article. N.B. validated the research concept, the design of the study, the preparation of materials, data collection, the analysis of findings, and the review of the first draft of the article. N.M.A. validated the research concept and the design of the study. All authors have read and agreed to the published version of the manuscript.

Funding: This research received no external funding.

Data Availability Statement: The data presented in this study are available on request from the corresponding author.

Acknowledgments: We would like to extend our deepest gratitude to the Malaysian Ministry of Higher Education (MOHE) throughout this journey to complete this article. We also express our gratitude for all the positive and encouraging reviews and comments.

Conflicts of Interest: The authors declare no conflicts of interest.

Abbreviations

Nomenclature

Pr	Prandtl number
T	Constant temperature
U	Constant velocity
M	Dimensionless magnetic parameter
n	Dimensionless nonlinear parameter
Nu_x	Local Nusselt number
Re_x	Local Reynolds number
C_f	Skin friction coefficient
Res	Response
u, v	Velocity components
x, y	Cartesian coordinates system
B_0	Dimensionless magnetic strength
CNTs	Carbon nanotubes
f	Dimensionless function
F	The number of factors
C	Center points

Subscripts

w	Condition on the sheet wall
∞	Ambient condition
hnf	Hybrid nanofluids
nf	Nanofluids
f	Base fluid
nf	Nanofluids
hnf	Hybrid Nanofluids
$SWCNT$	Single-walled carbon nanotubes
$MWCNT$	Multi-walled carbon nanotubes
1	Single-walled carbon nanotubes
2	Multi-walled carbon nanotubes
CNT	Mono-carbon nanotubes
$hCNT$	Hybrid carbon nanotubes

Greek Symbols

α	Thermal diffusivity
μ	Dynamic viscosity
ρ	Density
θ	Dimensionless temperature
ψ	Dimensionless stream function
η	Dimensionless thickness
C_p	Specific heat for base fluid
β	Regression coefficients
k	Thermal conductivity
ν	Kinematic viscosity
ϕ	Dimensionless nanoparticles volume fraction
ε	Dimensionless stretching/ shrinking parameter
ε_c	Critical value
ϵ	Error term

References

1. Choi, U.S. Enhancing Thermal Conductivity of Fluids with Nanoparticles, Developments and Application of Non-Newtonian Flows. *ASME J. Heat Transf.* **1995**, *66*, 99–105.
2. Turcu, R.; Darabont, A.L.; Nan, A.; Aldea, N.; Macovei, D.; Bica, D.; Vekas, L.; Pana, O.; Soran, M.L.; Koos, A.; et al. New Polypyrrole-Multiwall Carbon Nanotubes Hybrid Materials. *J. Optoelectron. Adv. Mater.* **2006**, *8*, 643–647.
3. Reddy, V.S.; Kandasamy, J.; Sivanandam, S. Stefan Blowing Impacts on Hybrid Nanofluid Flow over a Moving Thin Needle with Thermal Radiation and MHD. *Computation* **2023**, *11*, 128. [CrossRef]
4. Devi, S.P.A.; Devi, S.S.U. Numerical Investigation of Hydromagnetic Hybrid Cu-Al_2O_2/Water Nanofluid Flow over a Permeable Stretching Sheet with Suction. *Int. J. Nonlinear Sci. Numer. Simul.* **2016**, *17*, 24–257. [CrossRef]
5. Khashi'ie, N.S.; Arifin, N.M.; Nazar, R.; Hafidzuddin, E.H.; Wahi, N.; Pop, I. Magnetohydrodynamics (MHD) Axisymmetric Flow and Heat Transfer of a Hybrid Nanofluid Past a Radially Permeable Stretching/Shrinking Sheet with Joule Heating. *Chin. J. Phys.* **2020**, *64*, 251–263. [CrossRef]
6. Khashi'ie, N.S.; Hafidzuddin, E.H.; Md Arifin, N.; Wahi, N. Stagnation Point Flow of Hybrid Nanofluid over a Permeable Vertical Stretching/Shrinking Cylinder with Thermal Stratification Effect. *CFD Lett.* **2021**, *12*, 80–94.
7. Sajid, M.U.; Ali, H.M. Thermal Conductivity of Hybrid Nanofluids: A Critical Review. *In. J. Heat Mass Transf.* **2018**, *126*, 211–234. [CrossRef]
8. Navrotskaya, A.G.; Aleksandrova, D.D.; Krivoshapkina, E.F.; Sillanpaa, M.; Krivoshapkin, P.V. Hybrid Materials Based on Carbon Nanotubes and Nanofibers for Environmental Applications. *Front. Chem.* **2020**, *8*, 00546. [CrossRef]
9. Al-Hanaya, A.M.; Sajid, F.; Abbas, N. Effect of SWCNT and MWCNT on the Flow of Micropolar Hybrid Nanofluid over a Curved Stretching Surface with Induced Magnetic Field. *Sci. Rep.* **2020**, *10*, 8488. [CrossRef]
10. Sulochana, C.; Kumar, T.P. Heat Transfer of SWCNT-MWCNT Based Hybrid Nanofluid Boundary Layer Flow with Modified Thermal Conductivity Model. *J. Adv. Res. Fluid Mech. Therm. Sci.* **2022**, *92*, 13–24. [CrossRef]
11. Aladdin, N.A.L.; Bachok, N. Duality Solutions in Hydromagnetic Flow of SWCNT-MWCNT/Water Hybrid Nanofluid over Vertical Moving Slender Needle. *Mathematics* **2021**, *9*, 2927. [CrossRef]
12. Tabassum, R.; Al-Zubaidi, A.; Rana, S.; Mehmood, R.; Saleem, S. Slanting Transport of Hybrid (MWCNTs-SWCNTs/H_2O) Nanofluid Upon a Riga Plate with Temperature Dependent Viscosity and Thermal Jump Condition. *Int. Commun. Heat Mass Transf.* **2022**, *135*, 106165. [CrossRef]
13. Svorcan, J.; Wang, J.M.; Griffin, K.P. Current State and Future Trends in Boundary Layer Control on Lifting Surfaces. *Adv. Mech. Eng.* **2022**, *14*, 1–23. [CrossRef]
14. Shateyi, S.; Muzara, H. On The Numerical Analysis of Unsteady MHD Boundary Layer Flow of Williamson Fluid over a Stretching Sheet and Heat and Mass Transfers. *Computation* **2020**, *8*, 55. [CrossRef]
15. Lund, L.A.; Omar, Z.; Khan, I.; Sherif, E.S.M. Dual Solutions and Stability Analysis of Aa Hybrid Nanofluid over a Stretching/Shrinking Sheet Executing MHD Flow. *Symmetry* **2020**, *12*, 276. [CrossRef]
16. Rosca, N.C.; Rosca, A.V.; Aly, E.H.; Pop, I. Flow and Heat Transfer Past a Stretching/Shrinking Sheet Using Modified Buongiorno Nanoliquid Model. *Mathematics* **2021**, *9*, 3047. [CrossRef]
17. Dinarvand, S.; Yousefi, M.; Chamkha, A.J. Numerical Simulation of Unsteady Flow toward a Stretching/Shrinking Sheet in Porous Medium Filled with a Hybrid Nanofluid. *J. Appl. Comput. Mech.* **2022**, *8*, 11–20.
18. Samat, N.A.A.; Bachok, N.; Arifin, N.M. The Significant Effect of Hydromagnetic on Carbon Nanotubes Based Nanofluids Flow and Heat Transfer Past a Porous Stretching/Shrinking Sheet. *J. Adv. Res. Fluid Mech. Therm. Sci.* **2023**, *106*, 51–64.
19. Crane, L.J. Flow Past a Stretching Plate. *J. Appl. Math. Phys.* **1970**, *21*, 645–647. [CrossRef]
20. Vajravelu, K.; Mukhopadhyay, S. Flow Past a Shrinking Sheet. In *Fluid Flow, Heat and Mass Transfer at Bodies of Different Shapes: Numerical Solutions*, 1st ed.; Vajravelu, K., Mukhopadhyay, S., Eds.; Academic Press: Cambridge, UK, 2016; pp. 47–76.
21. Nayakar, S.; Mahabaleshwar, U.; Vinaykumar, P.; Lorenzini, G.; Baleanu, D. Nonlinear Stretching/Shrinking Cooling of a Sheet Involving an MHD Walters' Liquid B with Suction. *Math. Model. Eng. Probl.* **2019**, *6*, 343–348. [CrossRef]
22. Abd Rahman, N.H.; Bachok, N.; Rosali, H. MHD Stagnation Point Flow over a Nonlinear Stretching/Shrinking Sheet in Nanofluids. *J. Adv. Res. Fluid Mech. Therm. Sci.* **2020**, *76*, 139–152. [CrossRef]
23. Ragupathi, P.; Saranya, S.; Hakeem, A.K.A. Second-Order Slip and Thermal Jump Effects on MHD Flow of Nanosecond Grade Fluid Flow Over a Stretching Sheet. In *Advances in Fluid Dynamics. Selected Proceedings of the International Conference on Applications of Fluid Dynamics (ICAFD 2018)*; Springer: Singapore, 2021; pp. 457–467.
24. Saranya, S.; Ragupathi, P.; Al-Mdallal, Q. Analysis of Bio-Convective Heat Transfer over an Unsteady Curved Stretching Sheet Using the Shifted Legendre Collocation Method. *Case Stud. Therm. Eng.* **2022**, *39*, 102433. [CrossRef]
25. Mahabaleshwar, U.S.; Sneha, K.N.; Souayeh, B. Flow Due to a Porous Stretching/Shrinking Sheet with Thermal Radiation and Mass Transpiration. *Heat Tranf.* **2022**, *51*, 5441–5546. [CrossRef]
26. Aly, E.M.; Pop, I. MHD Flow and Heat Transfer Near Stagnation Point over a Stretching/Shrinking Surface with Partial Slip and Viscous Dissipation: Hybrid Nanofluid Versus Nanofluid. *Powder Technol.* **2020**, *367*, 192–205. [CrossRef]
27. Khan, U.; Zaib, A.; Bakar, S.A.; Ishak, A. Stagnation-Point Flow of a Hybrid Nanoliquid over a Non-Isothermal Stretching/Shrinking Sheet with Characteristics of Inertial and Microstructure. *Case Stud. Therm. Eng.* **2021**, *26*, 101150. [CrossRef]
28. Zainal, N.A.; Waini, I.; Khashi'ie, N.S.; Kasim, A.R.M.; Naganthran, K.; Nazar, R.; Pop, I. Stagnation Point Hybrid Nanofluid Flow Past a Stretching/Shrinking Sheet Driven by Arrhenius Kinetics and Radiation Effect. *Alex. Eng. J.* **2023**, *68*, 29–38. [CrossRef]

29. Waini, I.; Ishak, A.; Pop, I. Hybrid Nanofluid Flow and Heat Transfer Past a Permeable Stretching/Shrinking Surface with a Convective Boundary Condition. *J. Phys. Conf. Ser.* **2019**, *1366*, 012022. [CrossRef]
30. Jawad, M.; Jan, R.; Boulaaras, S.; Amin, I.; Shah, N.A.; Idris, S.A. Unsteady Electrohydrodynamic Stagnation Point Flow of Hybrid Nanofluid Past a Convective Heated Stretch/Shrink Sheet. *Adv. Math. Phys.* **2021**, *2021*, 6229706. [CrossRef]
31. Merkin, J.H.; Pop, I. Stagnation Point Flow Past a Stretching/Shrinking Sheet Driven by Arrhenius Kinetics. *Appl. Math. Comput.* **2018**, *337*, 583–590. [CrossRef]
32. Alekseev, V.; Tang, Q.; Vasilyeva, M.; Chung, E.T.; Efendiev, Y. Mixed Generalized Multiscale Finite Element Method for a Simplified Magnetohydrodynamics Problem in Perforated Domains. *Computation* **2020**, *8*, 58. [CrossRef]
33. Ragupathi, P.; Saranya, S.; Hakeem, A.K.A.; Ganga, B. Numerical Analysis on the Three-Dimensional Flow and Heat Transfer of Multiple Nanofluids Past a Riga Plate. *J. Phys. Conf. Ser.* **2021**, *1850*, 012044. [CrossRef]
34. Mahabaleshwar, U.S.; Sneha, K.N.; Chan, A.; Zeidan, D. An Effect of MHD Fluid Flow Heat Transfer Using CNTs with Thermal Radiation and Heat Source/Sink Across a Stretching/Shrinking Sheet. *Int. Commun. Heat Mass Transf.* **2022**, *135*, 106080. [CrossRef]
35. Mahesh, R.; Mahabaleshwar, U.S.; Sofos, F. Influence of Carbon Nanotube Suspensions on Casson Fluid Flow over a Permeable Shrinking Membrane: An Analytical Approach. *Sci Rep.* **2023**, *13*, 3369. [CrossRef] [PubMed]
36. Anuar, N.S.; Bachok, N.; Md Arifin, N.; Rosali, H. Numerical Solution of Stagnation Point Flow and Heat Transfer over a Nonlinear Stretching/Shrinking Sheet in Hybrid Nanofluid: Stability Analysis. *J. Adv. Res. Fluid Mech. Therm. Sci.* **2020**, *76*, 85–98. [CrossRef]
37. Jaafar, A.; Waini, I.; Jamaludin, A.; Nazar, R.; Pop, I. MHD Flow and Heat Transfer of a Hybrid Nanofluid Past a Nonlinear Surface Stretching/Shrinking with Effects of Thermal Radiation and Suction. *Chin. J. Phys.* **2022**, *79*, 13–27. [CrossRef]
38. Khashi'ie, N.S.; Arifin, N.M.; Pop, I. Magnetohydrodynamics (MHD) Boundary Layer Flow of Hybrid Nanofluid over a Moving Plate with Joule Heating. *Alex. Eng. J.* **2022**, *61*, 1938–1945. [CrossRef]
39. Zafar, M.; Sakidin, H.; Sheremet, M.; Dzulkarnain, I.B.; Hussain, A.; Nazar, R.; Khan, J.A.; Irfan, M.; Said, Z.; Afzal, F.; et al. Recent Development and Future Prospective of Tiwari and Das Mathematical Model in Nanofluid Flow for Different Geometries: A Review. *Processes* **2023**, *11*, 834. [CrossRef]
40. Matsui, H. Quadratic Regression for Functional Response Models. *Econom. Stat.* **2020**, *13*, 125–136. [CrossRef]
41. Crank, J. *The Mathematics of Diffusion*, 2nd ed.; Oxford University Press: New York, NY, USA, 1975.
42. Burden, R.L.; Faires, J.D. *Numerical Analysis*, 9th ed.; Cengage Learning: Boston, MA, USA, 2010.
43. Bazbouz, M.B.; Aziz, A.; Copic, D.; Volder, M.D.; Welland, M.E. Fabrication of High Specific Electrical Conductivity and High Ampacity Carbon Nanotube/Copper Composite Wires. *Adv. Electro. Mater.* **2021**, *7*, 202001213. [CrossRef]
44. Haider, S.M.A.; Ali, B.; Wang, Q.; Zhao, C. Rotating Flow and Heat Transfer of Single-Wall Carbon Nanotube and Multi-Wall Carbon Nanotube Hybrid Nanofluid with Base Fluid Water over a Stretching Sheet. *Energies* **2022**, *15*, 6060. [CrossRef]
45. Myres, R.H.; Montgomery, D.C.; Anderson-Cook, C.M. *Response Surface Methodology: Process and Product Optimization Using Designed Experiments*, 3rd ed.; John Wiley & Sons: Hoboken, NJ, USA, 2009.
46. Benim, A.C.; Diederich, M.; Pfeiffelmann, B. Aerodynamic Optimization of Airfoil Profiles for Small Horizontal Axis Wind Turbines. *Computation* **2018**, *6*, 34. [CrossRef]
47. Waqas, H.; Wakif, A.; Al-Mdallal, Q.; Zaydan, M.; Farooq, U.; Hussain, M. Significance of Magnetic Field and Activation Energy on the Features of Stratified Mixed Radiative-Convective Couple-Stress Nanofluid Flows with Motile Microorganisms. *Alex. Eng. J.* **2022**, *61*, 1425–1436. [CrossRef]
48. Kumar, J.P.; Umavathi, J.C.; Dhone, A.S. Forced Convection of Magnetohydrodynamic (MHD)—Boundary Layer Flow Past Thin Needle with Variable Wall Temperature Using Casson Nanofluid. *J. Nanofluids* **2023**, *12*, 271–279. [CrossRef]
49. Sun, B.; Guo, Y.; Yang, D.; Li, H. The Effect of Constant Magnetic Field on Convective Heat Transfer of Fe_3O_4/Water Magnetic Nanofluid in Horizontal Circular Tubes. *Appl. Therm. Eng.* **2020**, *171*, 114920. [CrossRef]
50. Shah, Z.; Hajizadeh, M.R.; Ikramullah; Alreshidi, N.A.; Deebani, W.; Shutaywi, M. Entropy Optimization and Heat Transfer Modeling for Lorentz Forces Effect on Solidification of NEPCM. *Int. Commun. Heat Mass Transf.* **2020**, *117*, 104715. [CrossRef]
51. Samat, N.A.A.; Bachok, N.; Arifin, N.M. Carbon Nanotubes (CNTs) Nanofluids Flow and Heat Transfer under MHD Effect over a Moving Surface. *J. Adv. Res. Fluid Mech. Therm. Sci.* **2023**, *103*, 165–178. [CrossRef]

computation

MDPI

Article

Residential Sizing of Solar Photovoltaic Systems and Heat Pumps for Net Zero Sustainable Thermal Building Energy

Shafquat Rana [1], Uzair Jamil [2], Nima Asgari [1], Koami S. Hayibo [1], Julia Groza [3] and Joshua M. Pearce [1,3,*]

[1] Department of Electrical & Computer Engineering, Western University, London, ON N6A 5B9, Canada; srana63@uwo.ca (S.R.); nasgari@uwo.ca (N.A.); khayibo@uwo.ca (K.S.H.)
[2] Department of Mechanical and Material Engineering, Western University, London, ON N6A 5B9, Canada; ujamil@uwo.ca
[3] Ivey Business School, Western University, London, ON N6G 0N1, Canada; jgroza@uwo.ca
* Correspondence: joshua.pearce@uwo.ca

Abstract: To enable net zero sustainable thermal building energy, this study develops an open-source thermal house model to couple solar photovoltaic (PV) and heat pumps (HPs) for grid-connected residential housing. The calculation of both space heating and cooling thermal loads and the selection of HP is accomplished with a validated Python model for air-source heat pumps. The capacity of PV required to supply the HPs is calculated using a System Advisor Model integrated Python model. Self-sufficiency and self-consumption of PV and the energy imported/exported to the grid for a case study are provided, which shows that simulations based on the monthly load profile have a significant reduction of 43% for energy sent to/from the grid compared to the detailed hourly simulation and an increase from 30% to 60% for self-consumption and self-sufficiency. These results show the importance of more granular modeling and also indicate mismatches of PV generation and HP load based on hourly simulation datasets. The back-calculation PV sizing algorithm combined with HP and thermal loads presented in this study exhibited robust performance. The results indicate this approach can be used to accelerate the solar electrification of heating and cooling to offset the use of fossil fuels in northern climates.

Keywords: photovoltaic; heat pump; residential; net zero; building energy; solar energy

Citation: Rana, S.; Jamil, U.; Asgari, N.; Hayibo, K.S.; Groza, J.; Pearce, J.M. Residential Sizing of Solar Photovoltaic Systems and Heat Pumps for Net Zero Sustainable Thermal Building Energy. *Computation* **2024**, *12*, 126. https://doi.org/10.3390/computation12060126

Academic Editors: Ali Cemal Benim, Abdulmajeed A. Mohamad, Sang-Ho Suh, Rachid Bennacer, Paweł Oclon and Jan Taler

Received: 1 May 2024
Revised: 6 June 2024
Accepted: 8 June 2024
Published: 17 June 2024

1. Introduction

Access to energy is crucial in determining social-economic development and reducing poverty [1] as modern societies depend on abundant and low-cost energy [2]. Unfortunately, the energy sector is also the largest emitter of greenhouse gases (GHGs) [3], which are driving climate change and the concomitant negative externalities for humanity and nature [4]. For example, in Canada, the energy sector emitted 80% of the total GHG emissions [5] and Canadian per capita emissions are some of the highest in the world [6]. To rectify this, Canada has made a commitment to aggressively reduce GHG emissions by passing the Net-Zero Emission Accountability Act, with the mandate to reach net zero emissions by 2050 [7]. To reach zero emissions, the residential sector is of particular interest because building energy use is responsible for 17% of the GHG emissions in Canada [5] and residential buildings are under the control of consumers/citizens [8,9]. For the energy use in residential buildings space, heating, and domestic hot water demand account for 63.6% and 17.2% of energy consumption in average Canadian homes, respectively [10]. Thermal energy demands also drive energy use in the residential sector outside of Canada, as about 27% of the world's total energy consumption is used by residential structures [11].

One of the solutions to the energy/emissions challenge is the deployment of renewable energy sources, which can meet rising energy demands without harming the environment by replacing scarce and unsustainable fossil fuels [12,13]. Among renewable energy sources, solar photovoltaic (PV) systems have gained prominence due to their environmentally

friendly, clean and safe operations [14]. Since its commercial development a few decades ago, the growth of power generation utilizing PV technology has been sustained and increased [15]. PV accounted for 2.6% of the world's electricity generation in 2019 and is projected to provide 25% of the energy required by 2050 [16]. Additionally, it is anticipated that integrated PV buildings will provide 40% of this energy [16]. In recent years, solar energy has radically dropped in price [15] and been employed at accelerating rates [17], making it one of the most rapidly growing sources of energy supply globally [18]. PV systems can be deployed for stand-alone operation in residential homes economically [19–21]; sizing such systems can be complicated because of the need for battery storage [22–26]. Recent work has even used artificial neural networks (ANNs) and metaheuristic methods [27], which are computationally demanding [28] but reliable techniques that provide a techno-economic solution to determine appropriate sizing [29]. Stand-alone PV systems, however, are the minority as most residential PV systems are grid-tied [30].

Although the value of solar electricity is often higher than the net metered rate [31], residential solar customers may be credited far lower than the net metered rate [32]. In such instances, it is economically optimal for the residential solar customer to self-consume, that is, to use their higher-value solar energy rather than feed it back to the grid. Nicoletti et al. [33], have shown it is challenging to guarantee high self-consumption with just the installation of the PV system alone. PV coupled with electric storage increases the ability for self-consumption but is generally costly [34]. Another approach, which has recently gained economic viability in North America is to use PV-powered heat pumps (HPs) [35–37]. PV coupled with HPs can also increase the self-sufficiency and self-consumption rates of households, becoming a source of local flexibility [38,39]. Electrically powered HPs efficiently serve both space/water heating and cooling, making them superior to conventional heaters as they also function as air conditioners during the summer [40]. Due to the great thermodynamic efficiency of HPs and the potential to use renewable electricity as a source of energy, they are currently the most promising technology for reducing the carbon footprint of the heat supply while fostering the integration of renewable energy in buildings [41]. For example, solar PV technology with HPs can reduce residential building GHG emissions by up to 50% immediately [36]. Several studies perform sizing of HPs for different objectives [42–44] along with numerous heat pump designs that consider the available heat source (such as air, earth, or water) and the way the heat is delivered to the building. (e.g., ducted air, ductless air, hydronic) [45].

HPs can be broadly categorized into two groups: ground-source heat pumps (GSHP), often known as geothermal heat pumps, and air-source heat pumps (ASHP). GSHPs are generally more efficient and have more installation cost than ASHPs [46]. In GSHP, with a coefficient of performance (COP) equal to 2.94 at $-17.7\ ^{\circ}C$ [47], the ground heat exchanger's (GHE) design is frequently the most important factor in determining performance and economics [48–50]. The drilling prices of GSHPs are also an added cost that makes the capital expense much higher than the ASHP [51]. One of the ways to reduce the cost of GSHPs is to use horizontal GHE; however, this approach requires more land area and thus is not suitable for all residential applications. According to Lim et al. [52], only 61% of residences in the U.S. can install GSHPs; of those that can, 8% must utilize the more expensive vertical GHE. Beyond installation costs, it is challenging to make a single HP design proposal for an entire region [53], due to the significant relationships between climate, geology, energy prices, fuel prices, and inflation rates [54].

By eliminating the requirement for GHE, ASHPs offer a stronger economic proposition than GSHPs, and in recent years the technology has advanced to be a competitive alternative in cold areas [55]. Lowering the minimum operating temperatures and reducing auxiliary heat have been accomplished using new refrigerants, ejectors, and dual-stage compression [56]. The COP of air-to-air heat pumps normally ranges between 2 and 5.4 at $8\ ^{\circ}C$ [57] and can fall to a meager 1.04 at $-21\ ^{\circ}C$ [58]; testing on commercial models has shown that it can reach 1.5 [59]. Thus, the economic competitiveness of ASHP varies by geography and application, just as GSHP. The economics, however, have recently shifted in

favor of HPs. According to the latest International Energy Agency (IEA) analysis, global sales of HPs grew by 11% in 2022, with Europe's HP sales growing by nearly 40%, whereas in 2023 in the U.S. HP sales exceeded gas furnaces for the first time [60]. Dated studies of only a few years on Canadian buildings [61,62] showed that ASHPs are more expensive than natural gas in most places, with milder climates being the most promising. More recent results, however, have shown that PV-powered ASHPs are economical in Canada [35]. Similarly, in the northern U.S. Padovani et al. [36] showed that the electrification of the heating system by combining PV and HPs can be economical at the residential level for replacing propane and other studies have shown the same for natural gas [35,37]. HPs achieve up to 66% secondary energy savings and up to 84% in GHG reductions [63].

If PV systems are to also cover thermal loads, these have a great influence on the sizing of the PV [64]. Determining the amount of energy needed to provide thermal loads in buildings today is challenging as it depends on a variety of factors like the kind of construction materials and their coefficients of heat transfer, outside and indoor temperatures, humidity, the number of occupants, lightning and human behavior [65,66]. In addition, the optimal sizing of the PV+HP system depends on various other parameters i.e., solar radiation, and variable solar electricity costs that are sensitive to initial costs of every component of the system. Although much work has been done on sizing PV systems to meet non-thermal electric loads, comparatively less work has focused on the use of solar-powering heat pumps for heating and cooling thermal loads.

This study aims to develop an open-source thermal house model to be coupled to solar PV and HP models for grid-connected residential housing. This model provides hourly and monthly thermal load profiles that are used to observe how the import and export of electricity to/from the grid changes based on different load profiles for optimally sized solar PV systems used to run optimally sized HPs. After briefly reviewing the literature, the calculation of the thermal loads (i.e., both space heating and cooling) is made to provide the selection of HPs. This is done using the black box model developed in Python for an air-source heat pump to meet thermal loads for a one-story grid-connected residential building model for both space heating and cooling and validated by using the Hourly Analysis Program 5.11 (HAP) [67]. Finally, the capacity of PV required to supply the HP is calculated using the System Advisor Model (SAM) integrated Python model [68]. The novelty of this approach is a PV model which has been introduced to select the system developed for an optimal power supply considering both heating and cooling load requirements of the HP. This model provides details about the import/export of electricity to/from the grid, self-consumption, and self-sufficiency, and how they change based on hourly and monthly load profiles. A case study is presented for Ontario Canada, but the model can be used for other geographical regions globally. The results are presented and discussed in the context of accelerating the solar electrification of heating and cooling to offset the use of fossil fuels.

2. Background

For all PV system-sizing calculations, input data (system specifications, meteorological data, load demand data), system models, simulation techniques and formulated objective functions are typically the four key components of numerical techniques [69]. Analytical techniques [70] generate a simple formula that specifies the size of PV systems to achieve desired system reliabilities. This method's main advantage is its simple computations, while its main drawback is the difficulty of predicting the coefficients of mathematical models and the dependence of these models on location [21,71]. With purely electrical residential PV systems, there are a wide variety of PV simulation tools to match simple electric loads [72] which includes ESP-r [73], SolarGIS (PV Planner) [74], SolarDesignTool [75], Aurora Solar Software [76], PVSYST [77], SolarPro [78] and others. To solve the general issue of PV sizing for more complex systems involving thermal loads, various software programs, including TRNSYS [79], RETScreen [80], SAM [68], HOMER [81], IHOGA [82] and HYBRID2 [83], have been developed to determine the PV system's optimal size [84,85]. The most well-known software for PV scaling of complex systems is RETscreen and HOMER [86,87]

although many authors write MATLAB code for the optimization of PV size [26,88]. The vast majority of these tools are adequate for net metered systems, but as many utilities do not net meter [89] and there is a trend away from net metering [32,90] more complex calculations are necessary to optimize the economic return of a PV system.

For PV+HP systems, the dimensioning of all the components is carried out considering economic criteria [91] and therefore it is necessary to analyze the whole system together, as the size chosen for one of these components inevitably affects the size of the others. For example, Angenendt et al. [92] used different operating strategies to perform optimization of PV+HP+battery system component size and the results showed a great economic impact on the cost associated with the operation. Beck et al. [93] analyzed the combined size of PV and heat pumps under different scenarios and found that the size of the PV field and the electrical storage are significantly influenced by the electrical load profiles, while the choice of heat pump is almost completely independent of scenario assumptions. These articles do not consider the impact on summer behavior and thus space cooling loads. Other studies have also analyzed the dimensioning of the heat pump coupled with PV systems [93–95]. Lyden et al. [95] designed the heat pump size based on the different tariffs and assumed predictive control. These articles, however, did not focus on the sizing of the PV system. Energy simulations were carried out by Dongellini et al. [96] using an air–water heat pump (AWHP) that only provides a portion of the building's thermal demand while the remaining portion is delivered by the boiler. The study highlights the significance of appropriate design by showing that the performance is highly related to HP sizing.

Air–water HPs are systems that are frequently utilized to offer space heating and cooling in the Mediterranean region. The optimal dimensioning of components for cold climate locations, where cooling is not necessary, is the subject of the research works listed so far. Space cooling is a crucial factor to take into account in areas with temperate climates [97]. The quantity of electrical energy needed by the HP during the summer must be considered while choosing the best dimensions. Nicoletti et al. [33] used EnergyPlus to carry out energy simulations for obtaining data for the combined sizing of PV-battery and air–water HP systems considering both heating and cooling demand. Baghoolizadeh et al. [2] simulated a building model in cities with different climatic conditions using EnergyPlus to optimize the energy loads and their costs for both heating and cooling loads. In the literature, combined optimal dimensioning is only used for cold areas with low cooling demand. In warm climate sites where it is necessary to consider both the winter and summer building–plant behavior, there is a gap in the literature about the joint dimensioning of these systems. Therefore, in this study, the sizing of PV is done conducted on both the HP specification and all the thermal loads (both heating and cooling).

3. Methodology

A one-story residential house located in London, Ontario, Canada, is first modeled to calculate the energy required for space heating and cooling load for the house to select the desired system. To have precise and hourly data, the considered system is validated at each step. The validation of the house model is done by using HAP V 5.11. (Hourly Analysis Program) software, whereas the PV system is modeled by a SAM-integrated Python model, which is used in the calculation of the PV size required to run the HP loads and supply the house heating/cooling loads. Since the PV system depends on the meteorological data from [98], the system model can be implemented in different locations. The flowchart for the methodology is shown in Figure 1.

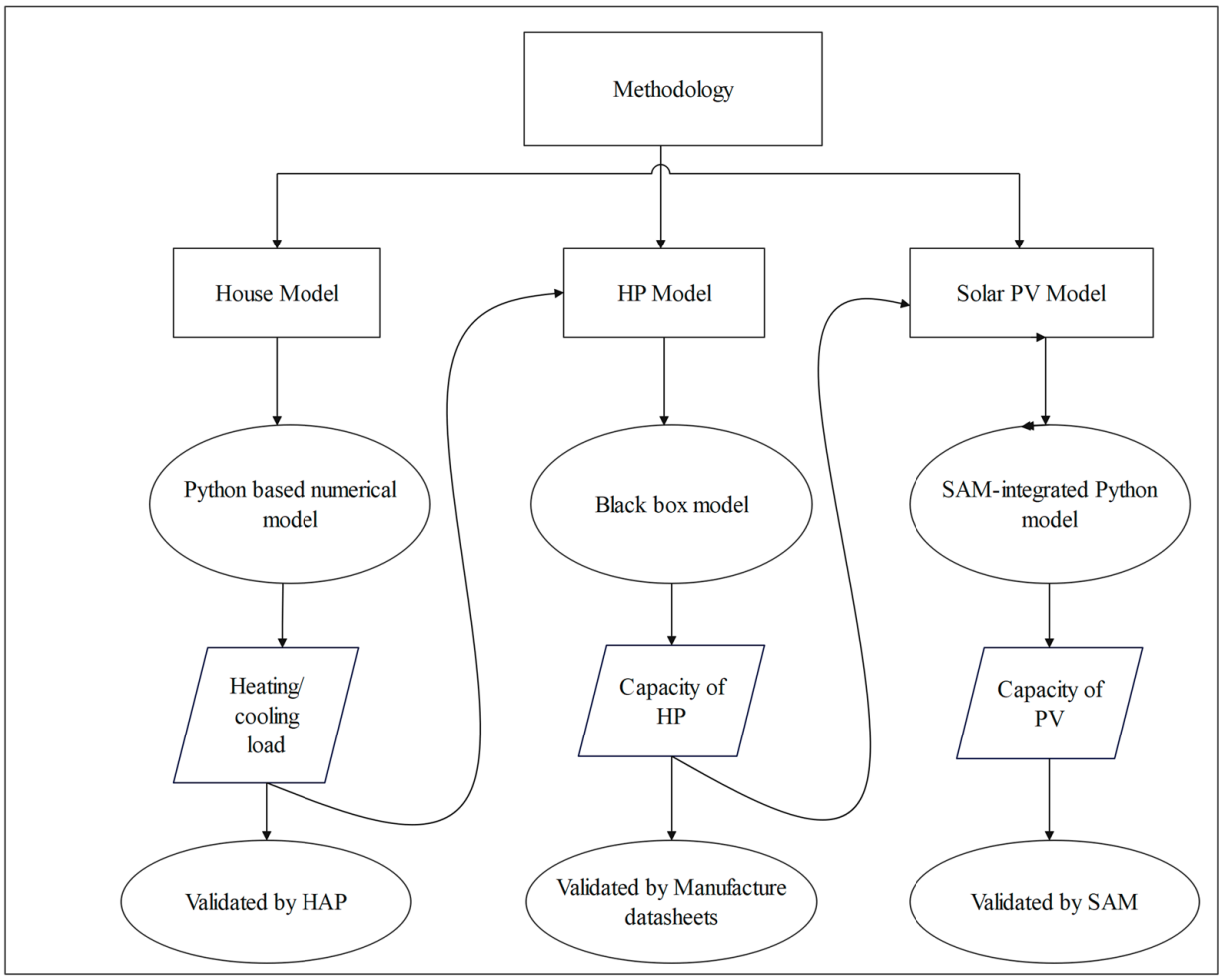

Figure 1. Flowchart showing the proposed methodology.

3.1. Calculation of Heating/Cooling Loads

The walls, ceiling, floor, people, lighting system, electrical equipment, air infiltration, doors, and windows all contribute to energy losses in the house that affect the cooling and heating loads. The calculation for thermal loads is first done using the heat transfer principles provided in the book *Heating, Ventilating, and Air Conditioning: Analysis and Design (HVAC)* [99] and then validated using HAP V 5.11. (Hourly Analysis Program). Only the waste heat produced by the most energy-demanding electrical applications, i.e., oven, microwave, and refrigerator, are considered in the model. Moreover, cooling loads of people, lighting as well as infiltration are also included. The detailed calculation for the heating/cooling loads can be found in the OSF depository [100]. The load calculation is done for a one-bed one-bath one-story house without a basement considering the effect of thermal losses from the roof and floor. Figure 2 illustrates the schematic of the House+HP+PV system.

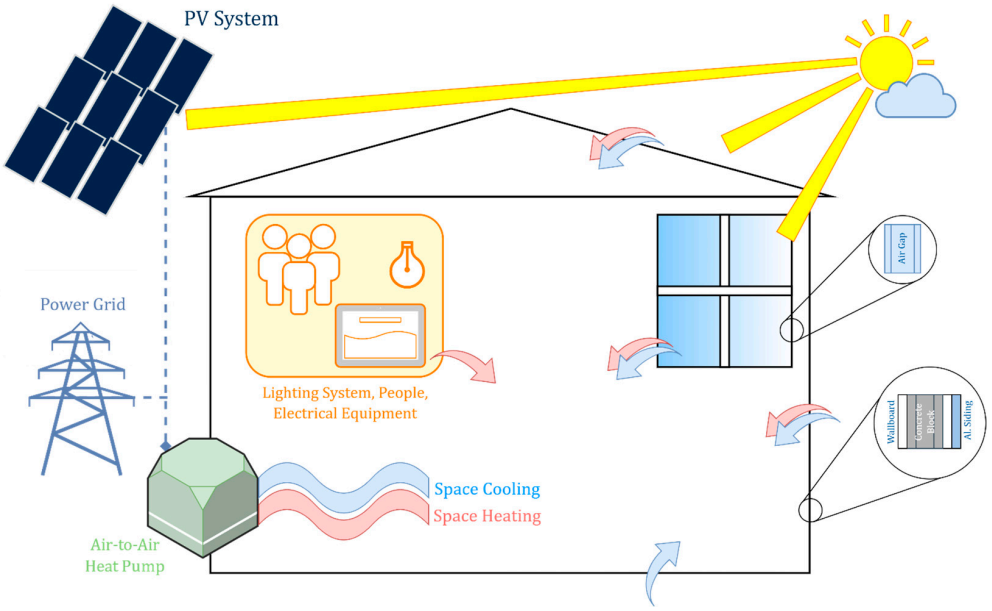

Figure 2. Schematic of the house+HP+PV system.

3.1.1. Heating Load Calculations

The heating calculation model is developed for the whole house. The first step is to determine the areas for walls, windows, doors, and floors that are exposed to the outside—these are the surfaces where heat transfer will take place and hence affect the heating load. The area for each space is determined by measuring the distance of walls and selecting a suitable scale based on the dimensions provided in the floor plans (scale: 1 cm = 1.5 m). The plan view and dimensions of the main level of the house are shown in Figure 3. Further, the calculation of the surface areas of heat transfer walls for each space of the main level is shown in Table 1.

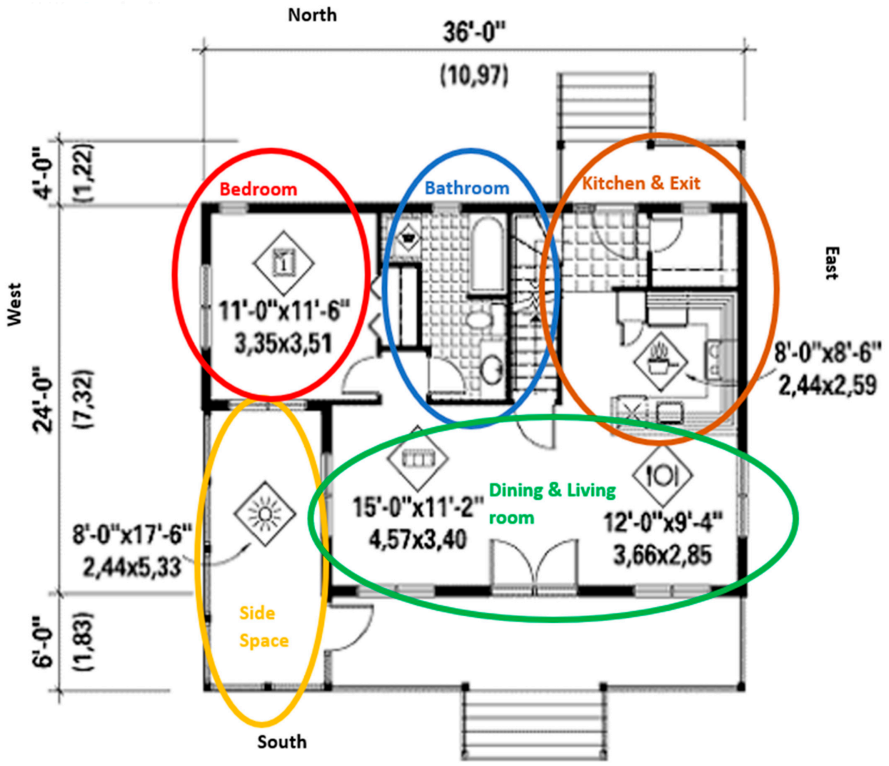

Figure 3. Floor plan of the house.

Table 1. Calculated surface areas and perimeter of the house plan.

Space Area/Perimeter	Direction	Bedroom	Bathroom	Kitchen and Exit	Dining and Living	Side Space
Wall (m^2)	North	8.36	6.16	8.95	–	141.7
	West	6.40	–	–	–	–
	East	–	–	10.60	5.57	26.60
	South	–	–	–	11.09	63
Window (m^2)	North	0.40	6.16	0.40	–	–
	West	2.71	–	–	–	–
	East	–	–	–	2.74	–
	South	–	–	–	2.74	–
Roof (m^2)	–	15.78	7.82	20.86	27.97	139.40
Door (m^2)	North	–	–	1.89	–	–
	South	–	–	–	3.90	–
Floor slab (m)	–	7.34	2.71	9.14	11.40	9.60

Once the areas of walls, windows, doors, perimeter of floors, etc., contributing to heat transfer are determined for each space, the overall heat transfer coefficient (U) for walls, windows, doors, roofs and floors in each space is then calculated. The block diagram in Figure 4 shows the further heating-calculation process and all the formulas required are given in Table 2.

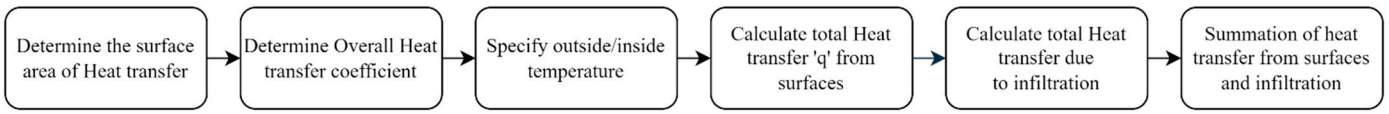

Figure 4. Block diagram for heating load calculations.

Table 2. Required heat transfer equations for heating load calculations [99].

Overall heat transfer coefficient		
$q = U_{tot} \cdot A \cdot \Delta t$	$U_{tot} = \frac{1}{R_{tot}}$	$R_{tot} = R_{ori} - R_{brick} + R_{insulating\ board}$
$q_{floor} = HLC_{edge} \cdot P \cdot \Delta t$		
Conduction		
$q_{Cond} = -k \cdot A \cdot \frac{dt}{dx} = -\frac{t_2 - t_1}{R'}$	$R' = \frac{x_2 - x_1}{kA} = \frac{\Delta x}{kA}$	$R = \frac{\Delta x}{k}$
Convection		
$q_{conv} = h \cdot A \cdot \left(t_f - t_w\right) = \frac{t_f - t_w}{R'}$	$R' = \frac{1}{hA}$	$R = \frac{1}{h}$
Heat transfers due to infiltration		
$\mathrm{I} = \mathrm{V} \cdot A_{fl} \cdot \mathrm{H} \cdot \mathrm{ACH}$	$\dot{m} = \frac{\mathrm{I}}{v \times 3600}$	
$q\prime_s = \dot{m} \cdot C_p \cdot \Delta t$	$q\prime_l = \dot{m} \cdot (W_i - W_o) \cdot h_{fg}$	$q_i = q\prime_s + q\prime_l$

The following assumptions are made about the structure of house, materials used and design conditions:

- Walls: The value of unit thermal resistances is provided in Table 5-4a (construction 2) of the HVAC book [99]. This value can be determined by using thermal conductivity (k) for each material.
    - Construction 2 is taken for the project with a slight change. Aluminum siding backed with a 0.375 in (9.5 mm) insulating board is incorporated in place of the brick whose conductance is taken as 3.123 $W/m^{2\circ}C$. These are installed in the space of reflective air space and constitute 20% of the space.
    - Two resistances are calculated, one considering reflective air space and one considering vertical furring instead of reflective air space. Since vertical fur-

ring only corresponded with 20%, the U value determined from resistances is multiplied by 0.2, while other resistance is multiplied by 0.8.
    - U_{tot} for walls = 0.6814 W/m^2-°C.
    - U_{tot} for roof = 0.2839 W/m^2-°C (Example 5-2 from HVAC book [99]).
    - For a 0.15 m concrete floor with an average thermal conductivity of 1.7 W/mK, fully covered by an insulation material with a thermal resistance of 0.88 m^{2}K/W on the ground with thermal conductivity of 0.1152 W/mK (London, Ontario) [67], the edge heat loss coefficient (HLC_{edge}) for the floor slab is 0.8304 W/m°C [99,101].
- The height of north and west facing windows are 0.914 m and 1.829 m. While the height of the door is considered 2.134 m.
- For doors and windows
    - All windows and doors are assumed to be double glazed with 0.0127 m air space (wood/vinyl).
- Inside temperature, i.e., space temperature, which is to be maintained inside the house, is assumed to be 22.22 °C; i.e., the set point temperature and outside temperature (t_o) is taken as −14.2 °C.
- For infiltration:
    - To determine the latent heat transfer, the humidity ratio for inside conditions (W_i) and humidity ratio for outside conditions (W_o) are ascertained. These are determined through a psychrometric chart [102] at an inside temperature of 22.22 °C and assuming a 30% relative humidity and meteorological data for ambient conditions. The relative humidity might change for indoors which will change the humidity ratio accordingly.
    - For our calculations, Wi is taken as 0.005 kg(w)/kg(a), hg is found to be 2,541,150 J/kg and h_f is found to be 93,040 J/kg.
    - The amount of infiltration for space of the residential building air is considered as 0.5 air change per hour (*ACH*).

Further, the value of sensible heating load from the heat transfer surfaces and infiltration are added to ascertain the total sensible heating loads for individual spaces.

3.1.2. Cooling Load Calculations

The cooling load calculation block diagram is shown in Figure 5 and the formulas are presented in Table 3 following the Radiant Time Series Method (RTSM) [99]. The first step is to determine the sol-air temperature, which is an equivalent temperature that eliminates the requirement to model convection for the outdoor air, radiation to the ground and sky, and solar radiation separately. This simplifies the calculations as a single heat transfer between an equivalent (sol-air) temperature and the surface temperature then can be calculated. Solar intensities are required as input to calculate sol-air temperature. Next, heat gains are ascertained for windows (using solar intensities—referred to as solar heat gain) and for exterior surfaces of the space (using sol-air temperature—referred to as conduction heat gain). Conduction heat gain is calculated for windows as well. Lighting, equipment, people, and infiltration heat gains are then estimated. All the calculations performed are on an hourly basis. The cooling loads are then segregated into radiative and convective components. The radiative components are processed further through an appropriate radiant time series before being added into convective components to come up with the final cooling loads. Figure 5 shows the process of cooling load calculations.

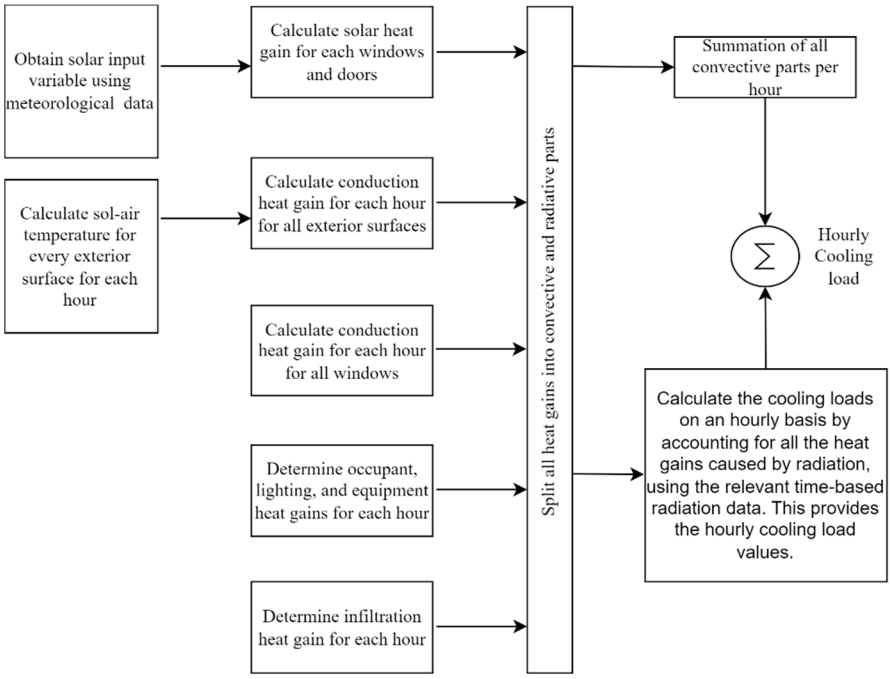

Figure 5. Block diagram for cooling load calculations.

Table 3. Required heat transfer equations for cooling load calculations.

Temperature	
$t\prime_o = T - DR \cdot X$	$t_e = t\prime_o + \frac{\alpha \cdot G_t}{h_t} - \frac{\epsilon \delta R}{h_t}$
Solar heat gain	
$q_{SHG} = \left(SHGC_{gD} A_{sl,g} + SHGC_f A_{sl,f}\right) \cdot G_D + \left(SHGC_{gd} A_g + SHGC_f A_f\right) \cdot G_d$	
$SHGC_f = a_f^s \left(\frac{U_f A_{f\prime}}{h_f A_{surf}}\right)$	
Conduction	
$q_{cond,window} = \left(U_f A_f + U_g A_g\right) \cdot (t_o - t_i)$	$q'_{cond,\frac{wall}{roof}} = \sum_{n=0}^{23} Y_{pn} \left(t_{e,j} - t_{rc}\right)$
$q_{cond,\frac{wall}{roof}} = A_j q'_{cond,\frac{wall}{roof}}$	
Heat transfers due to infiltration	
$q_{in} = m_a \cdot C_p \cdot (t_o - t_i) = \frac{Q \cdot C_p}{v_o} (t_o - t_i)$	
Radiant Time Series	
$q_{cooling\ load} = \sum_{n=0}^{23} r_n \left(q_{e,j}\right)$	

The following assumptions are made about the structure of the house, materials used and design conditions:

- All the required data mentioned below are taken from the HVAC handbook [99].
  - The design dry bulb temperature for the day (T) and daily range (DR) (which is the difference between the average maximum and average minimum for the hottest month of a location) are, respectively, taken from National Renewable Energy Laboratories (NREL) [98] and HVAC book [99]. The daily range is taken as 18.5 °F. The design temperatures and daily ranges are also provided in Appendix B (Table B-1) of HVAC handbook [99].
  - The hourly incident solar radiation is ascertained from NREL [98].
  - For determining the solar heat gain constant for diffuse (d) and direct radiation (D), Table 7-3 from the HVAC handbook [99] is used.

- The periodic response factors are available in Table 8-18 in the HVAC book [99]. Wall 1 and Roof 1 are considered for calculations, while radiant time factors from Table 8-28 are assumed. The radiant time factors for low-weight, medium-weight, and heavy-weight buildings are available in Table 8-21 in the HVAC Book [99].
- Heat transfer through the floor for cooling load calculations is neglected.

- From Table 8-2 in the HVAC book [99], the sensible and latent heat gain for occupants can be estimated. However, the sensible and latent heat gain for occupants is taken as 73.27 W and 58.61 W, respectively, from the HVAC Book [99] (Table 8-2 moderately active office work or standing, light work, walking).
- $\frac{e\delta R}{h_o}$ is a constant in Table 3 [99] and is normally selected as -13.8 °C for horizontal surfaces and -17.7 °C for vertical surfaces.
- The heat gain from lighting is considered as 21.5 W/m^2 [99].
- The heat gain from equipment (refrigerator, microwave, and oven) is taken as 4.8 kW [99].
- The sensible and latent load associated with infiltration is determined in a similar manner as for heating load calculations. For the calculations, the specific volume of outdoor air is considered as 0.89 m^3/Kg. Humidity ratio values are taken as 85 °F outdoor temperature and 72 °F indoor temperature, which is the set point temperature for cooling load calculations.
- The cooling load essentially represents the incumbent energy removal rate to maintain the desired temperature and humidity in a space. It typically differs from heat gain because radiation from interior surfaces and direct solar radiation entering through openings does not immediately warm the air inside. Instead, this radiant energy is absorbed by floors, walls, and furniture, primarily cooled through convection as they reach temperatures higher than the room air. Only when this energy is transferred to the air by convection does it contribute to the cooling load. The thermal inertia of the building resists changes in temperature, maintaining a stable internal climate by absorbing and slowly releasing heat energy over time. The thermal properties of the structure and interior objects determine the thermal lag, influencing the relationship between heat gain and the cooling load. The heat emitted by people and equipment operates similarly. The radiant energy portion generated by lights, equipment, or individuals is temporarily stored in the surroundings. Energy directly transferred into the air by lights and people, eventually transferred by the surroundings, becomes part of the cooling load. As the RTSM employs a radiant time series for the radiative segments of heat gain, designers need to categorize all heat gains into radiative and convective components. The radiative-convective splits for the heat gain are shown in Table 4.

Table 4. Radiative-convective heat gain.

	Radiative (%)	**Convective (%)**
Wall, window	63	37
Roof	84	16
People	70	30
Lighting	67	33
Equipment	20	80
Window solar	90	10
Infiltration	0	100

3.2. Black Box Heat Pump (BBHP) Model

The black box heat pump model is developed using the datasheet of the Goodman Air-Air heat pump for both heating and cooling operation modes [103]; a supervised regression learning model was developed in Python to export the mathematical functions for COP of heat pumps with a nominal capacity range of 18,000–60,000 BTU/h. As Li et al. [104] have

proposed correlations for load demand and COP of an air-conditioning heat pump, it is expected that the regressions of COP would be a second-degree polynomial as a function of indoor and ambient temperatures.

3.2.1. Heating Mode

The correlation of COP is dependent on ambient temperature (T) in (°C) as Equation (1):

$$COP_{heating} = b_0 + b_1 T + b_2 T^2 \quad (1)$$

The coefficients b_0–b_2 are extracted using the polynomial curve fitting technique and are shown for all rated capacities of GSZ16 Goodman Heat Pumps in Table 5 for heating mode. The fitting curve of heating COP for an 18,000 BTU/h heat pump is shown in Figure 6a.

Table 5. Coefficients of polynomial correlations of COP in heating mode.

Rated Capacity (BTU/h)	COP Coefficients			
	b_0	b_1	b_2	R^2
18,000	3.202	0.0887	0.000386	99.55
24,000	3.202	0.08879	0.000348	99.53
30,000	3.232	0.09092	−0.00048	99.11
36,000	3.197	0.08875	0.000523	99.66
42,000	3.093	0.0737	0.000217	99.44
48,000	3.273	0.08474	−0.00024	99.13
60,000	2.967	0.07639	0.000272	99.43

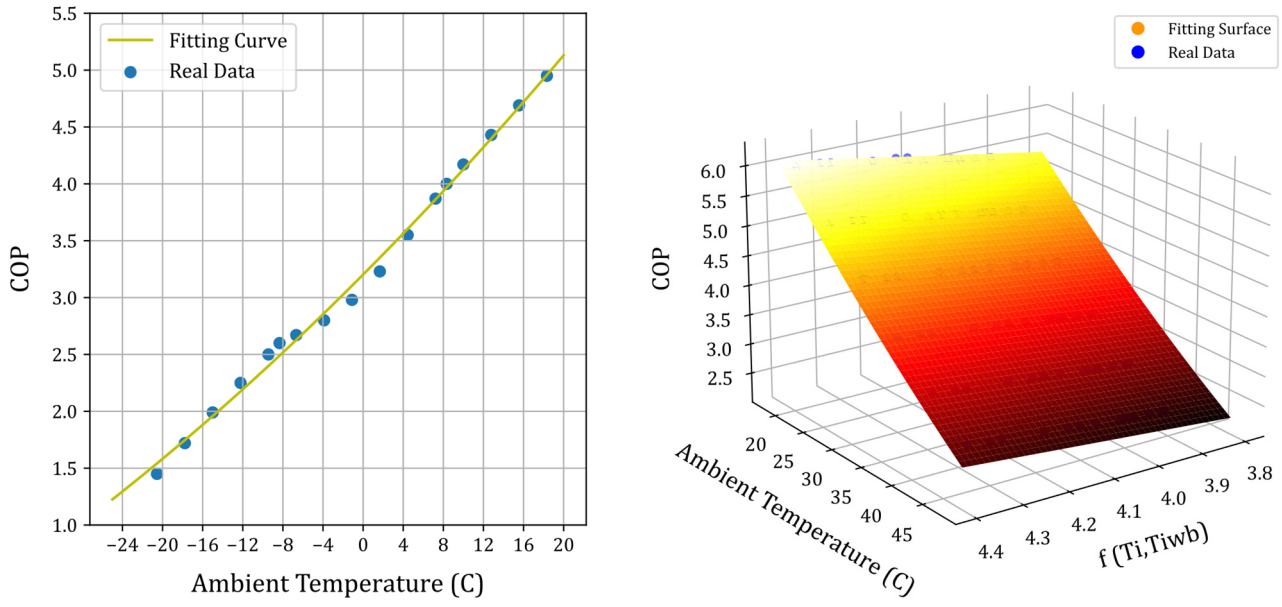

(**a**) (**b**)

Figure 6. Fitting curves of COP for 18,000 BTU/h heat pump: (**a**) heating mode, (**b**) cooling mode.

3.2.2. Cooling Mode

The manufacturer's datasheets for cooling mode were prepared based on the variations of ambient temperature and indoor dry bulb and wet bulb temperatures [103]. To be able to illustrate the fitting surfaces in 3D plots, the cooling capacity and COP correlations were developed as a function of ambient temperature and another second-degree polynomial, as shown in Table 6 which is itself is a function of indoor temperatures. Figure 6b presents the

fitting surface for COP of an 18,000 BTU/h heat pump in cooling mode. The COP of the cooling mode is obtained using Equation (2).

$$COP_{cooling} = b_o + b_1 T_i + b_2 T_{iwb} + b_3 T_o + b_4 T_i T_{iwb} + b_5 T_i T_o + b_6 T_{iwb} T_o + b_7 T_i^2 + b_8 T_{iwb}^2 + b_9 T_o^2 + b_{10} T_i^2 T_o + b_{11} T_{iwb}^2 T_o + b_{12} T_i T_{iwb} T_o \quad (2)$$

Table 6. Coefficients of polynomial correlations of COP in cooling mode.

		Rated Capacity (BTU/h)						
		18,000	**24,000**	**30,000**	**36,000**	**42,000**	**48,000**	**60,000**
Coefficients of COP	b_0	10.45648	9.14469	10.80332	10.66776	11.1678	10.7799	10.48214
	b_1	−0.11064	0.012049	−0.13687	−0.12536	−0.14811	−0.12931	−0.12989
	b_2	−0.21069	−0.21788	−0.18697	−0.19849	−0.208	−0.1978	−0.18888
	b_3	−0.17693	−0.15915	−0.18717	−0.18142	−0.19111	−0.18515	−0.18156
	b_4	−0.00038	-5×10^{-5}	−0.00024	−0.00012	8.46×10^{-5}	−0.00013	−0.00014
	b_5	0.001363	−0.00014	0.001632	0.001463	0.001723	0.001535	0.001532
	b_6	0.002596	0.002523	0.002229	0.002317	0.002419	0.002348	0.002227
	b_7	0.002739	−0.0001	0.003153	0.002864	0.003197	0.002939	0.00295
	b_8	0.008582	0.008251	0.007745	0.007893	0.00789	0.00791	0.007562
	b_9	0.000623	0.000609	0.000722	0.000671	0.000727	0.000694	0.000706
	b_{10}	-3.4×10^{-5}	1.16×10^{-6}	-3.8×10^{-5}	-3.3×10^{-5}	-3.7×10^{-5}	-3.5×10^{-5}	-3.5×10^{-5}
	b_{11}	−0.00011	-9.6×10^{-5}	-9.2×10^{-5}	-9.2×10^{-5}	-9.2×10^{-5}	-9.4×10^{-5}	-8.9×10^{-5}
	b_{12}	7.73×10^{-6}	9.2×10^{-7}	4.63×10^{-6}	2.34×10^{-6}	-1.6×10^{-6}	2.54×10^{-6}	2.61×10^{-6}
	R^2	99.96	99.98	99.97	99.98	99.98	99.98	99.98

When the maximum heating (cooling) demand of a house on the coldest (warmest) day of the year is calculated, the size of the HP can be determined. After selecting the heat pump, its COP correlation is used to calculate the power consumption. The same correlations of the selected heat pump on the other days of the year will be used to calculate the power consumption as well.

3.3. Solar PV Sizing

The solar PV system sizing is performed using a new design approach proposed in a recent study [40] to calculate the optimal size of PV for supplying the residential thermal load. This new approach relies on the strength of SAM [68] developed by NREL [68] and uses the flexibility of a Python implementation of SAM [105,106] to design and evaluate the performance of a PV system coupled with a load.

SAM is generally capable of evaluating the generation potential of a PV system with a known DC power rating. In this research, however, the energy consumption (electricity load of HP in kW) and operating hours are known, and the PV DC power rating needs to be calculated. To achieve this, a reverse calculation approach is applied. This approach involves calculating the actual PV system size by considering the total load demand (in this context, the power demanded by HP), local weather data, and system losses. The back-calculation code is integrated with the Python version of SAM, which extracts all the necessary data for simulation. The details of this method along with the required inputs are provided in [40].

Based on solar irradiation data and the hourly power consumption of the HP, the PV capacity is estimated using Equation (3). It is important to note that this estimation relies on approximations, as the average irradiation and certain losses are variable and dependent on ambient and operating conditions. Equation (4) is then used to calculate the number of PV modules required.

In these equations, $P_{estimated}$ represents the estimated total PV power in kW, P_{hp} is the hourly average HP consumption in kW, I_s is the daily average solar irradiation in kWh/m^{2}day, n and η are, respectively, the number of hours in a day (24) and the combined efficiency factor (between 0 and 1, both excluded) of all the PV system components (as-

sumed as 0.5 in this study), and N denotes the number of PV modules, while P_m represents the individual module power in W. Once the estimated number of modules is determined, the annual AC energy estimate is obtained by running the Python implementation of SAM. This estimated annual AC energy is then compared to the actual AC energy required, which is calculated using Equation (5):

$$P_{estimated} = \frac{P_{hp} \cdot n}{I_s \cdot \eta} \tag{3}$$

$$N = \frac{P_{estimated} \times 1000}{P_m} \tag{4}$$

$$E_{act.needed} = P_{hp} \cdot n \cdot n' \tag{5}$$

In this equation, $E_{act.needed}$ is the actual annual AC energy required in kWh, and n' represents the number of days (365 in this study). The results obtained from the back-calculation algorithm are used to design a realistic PV system for residential houses in London, Ontario, Canada. The PV modules and inverters are selected to match the lifetime energy demand of the house to the lifetime energy production of the PV. The loss values used in this study were taken from SAM and the PV was considered fixed tilt with an optimal inclination angle of 34° for annual production. The 34°-tilt angle has been shown in past studies to be the optimal inclination for non-tracking PV systems in London, ON [107]. The total energy produced by the PV, the energy sent to and taken from the grid, and the system's self-consumption and self-sufficiency are the metrics used to assess the performance of the residential PV system.

A distributed energy system's energy performance can be assessed locally using two metrics: self-consumption (SC(%)) and self-sufficiency (SS(%)) [108]. Self-consumption measures the proportion of locally consumed energy that is generated on-site relative to the total energy generated locally. In this research, self-consumption is determined as the discrepancy between the energy produced by the PV system and the energy exported to the grid, divided by the total energy generated by the PV, as expressed in Equation (6) [108]. Likewise, self-sufficiency is computed by dividing the difference between the energy generated by the PV system and the energy sent to the grid by the total load consumption, as demonstrated in Equation (7) [108].

$$SC = \frac{E_{PV} - E_{to-grid}}{E_{PV}} \times 100 \tag{6}$$

$$SS = \frac{E_{PV} - E_{to-grid}}{E_L} \times 100 \tag{7}$$

3.4. Limited Data PV System Sizing

The main challenge for sizing PV and conducting energy performance analysis is data availability [109]. Therefore, a specific case was investigated by considering a limited data scenario to further the analysis in this study. In this scenario, it was considered that only monthly data were available for the user, which are usually the data provided to the users by utilities. To reproduce the monthly energy-consumption data, the hourly data generated in this study was aggregated monthly. Starting from the monthly energy value, the following procedure was adopted to generate hourly values.

The data-disaggregation process used here relied on a previous study that examined the statistical distribution of HVAC energy loads in residential buildings. According to the study's findings, the energy-consumption model of a house is on average a Gaussian [110]. This concept was applied here by generating Gaussian hourly data from the monthly energy. First, the monthly energy is averaged to find the average daily energy for each month.

Then, average daily energy is distributed on a Gaussian curve centered on the middle of the day (noon) as shown in Equation (8) to obtain hourly values.

$$E_{hourly} = k \times \frac{1}{\sigma\sqrt{2\pi}} \exp\left(-\frac{(hod-\mu)^2}{2\sigma^2}\right) \quad (8)$$

where E_{hourly} (kWh) is the hourly energy of the system, σ is the standard deviation of the distribution, hod (h) is the hour of the day (0 to 23) for which the calculation is performed, μ (h) is the time of the day around which the gaussian is centered (12 pm or noon in this study) and k is a constant scale factor that is applied to the distribution to ensure the sum of the hourly energy equals the average daily energy. The standard deviation and the mean value can be adjusted to suit the most common load profile in a specific geographical area. In this study, the standard deviation was set at 2. For each month, all days are considered to have the same load profile. The generated Gaussian hourly data are then used to size the PV system as described in the section above.

4. Results

4.1. Validation

By contrasting the simulation results obtained from HAP software V 5.11. for the same residential house and the mathematically modelled ones, the performance of the house model was validated for the heating load. For the same input meteorological data, the comparative results are exported for heating load on the coldest day of the year. The total sensible heating load is found to be 8499 W, while the total latent heating load is found to be 367 W. The values of sensible and latent heating load from HAP are found to be 7890 W and 368 W, respectively. The difference between the sensible loads is approximately 7.16%, whereas for latent heating loads it is 0.3%. The present model, however, provides a more conservative estimate. The maximum cooling load (sensible) for an hour is 10,741 W. For the same hour, the maximum latent cooling load is determined as 956 W. The model is validated using data from McQuiston et al. [99].

Similarly, the validation of the BB HP model is done using the manufacture datasheet of the GSZ16 series Goodman Air-Air heat pump. The average deviation of the correlated results for heating COP with the datasheet of the manufacturer is found to be 2.5%, whereas the average deviation of the correlated results for cooling COP is 1.3%.

4.2. Heating/Cooling Load Demand

The total heating load requirement for the house on the coldest day is obtained at 7695 W from the simulation. Similarly, the maximum cooling load for an hour is ascertained at 11,277 W. In this study, the heating and cooling load for the proposed house model on a monthly, daily, and hourly basis is also obtained from the simulation results.

4.2.1. Monthly Load Demand

The average monthly heating and cooling load demand for the house in London, Ontario, Canada, was calculated and is shown in Figure 7. The load calculations are performed on an hourly basis.

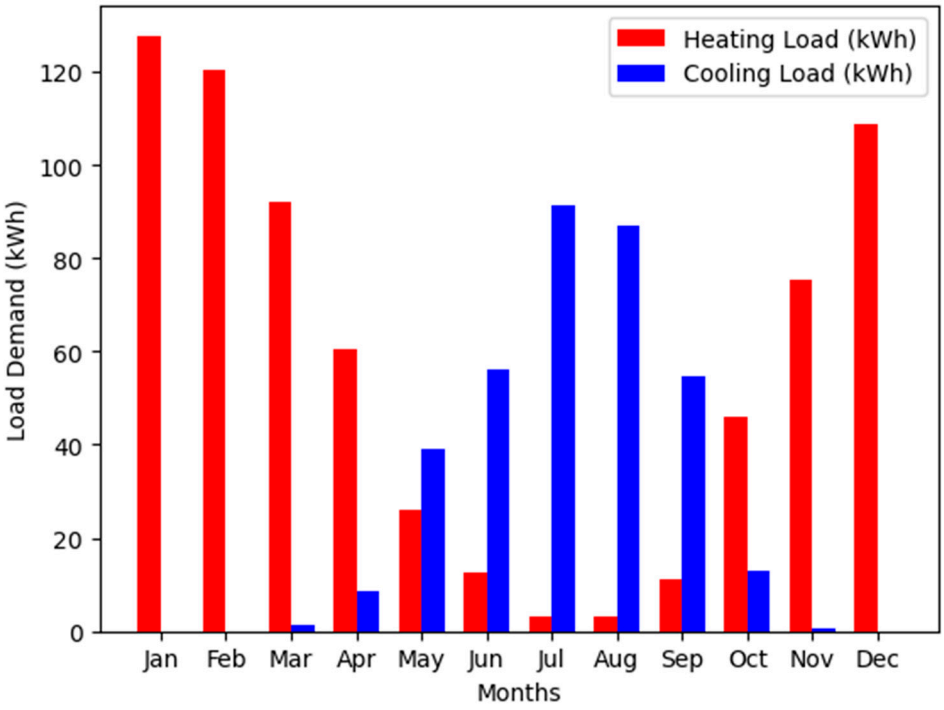

Figure 7. Comparison of average monthly load demand profile for heating and cooling.

4.2.2. Daily Load Demand

Figure 8 shows the average daily heating and cooling load demand of the house throughout the year. The total heating load requirement for the house on the coldest day occurs on the 48th day of the year, i.e., 17 February. Similarly, the maximum total cooling load occurs on the 212th day of the year, i.e., 31 July. Here, the daily average cooling demand is less than the daily average heating demand. The daily load can be one of the parameters for the system modelling giving more precise data than the monthly average.

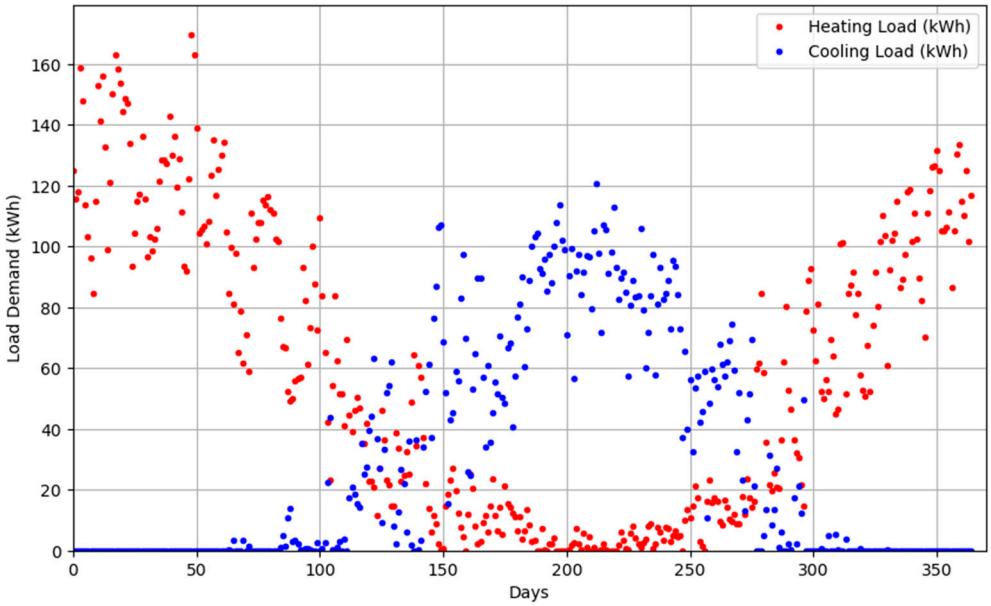

Figure 8. Comparison of average daily load demand profile for heating and cooling.

4.2.3. Hourly Load Demand

The hourly load data are also obtained and used for further modelling of the system. Figure 9 shows the hourly heating and cooling demand of the house throughout the year. The maximum heating load is 7695 W, which occurs on 17 February at 4 am while the maximum cooling load comes out to be 11,277 W on 31 July at 5 pm. The BBHP and PV sizing models rely on hourly data and predominantly employ the BTU/h capacity parameter, which is widely recognized for its common usage and precision. Figure 10 shows the hourly–monthly heating loads, of the proposed house to have a detailed analysis of the pattern and variation of load with time. The average air temperature used for calculation is shown in Figure 11 whereas Figure 12 shows the hourly-monthly cooling loads for the proposed system

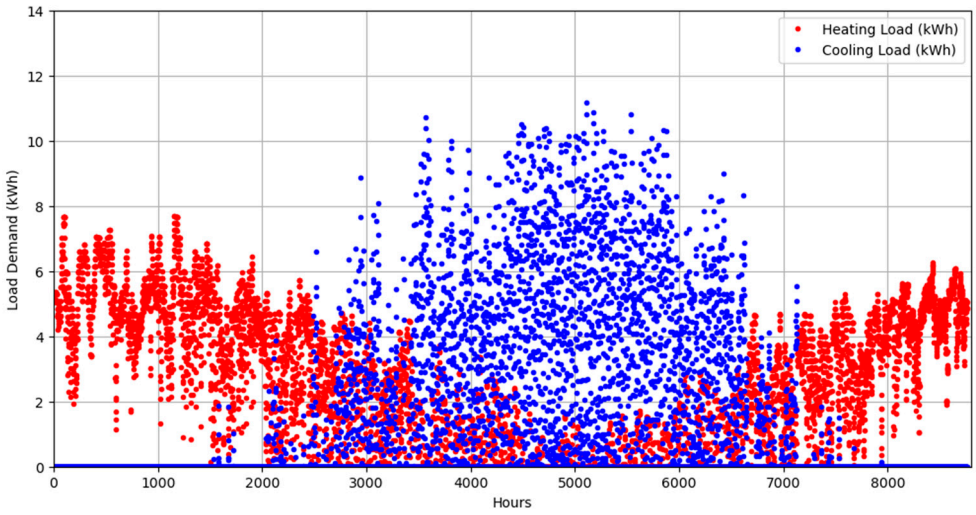

Figure 9. Comparison of average hourly load demand profile for heating and cooling.

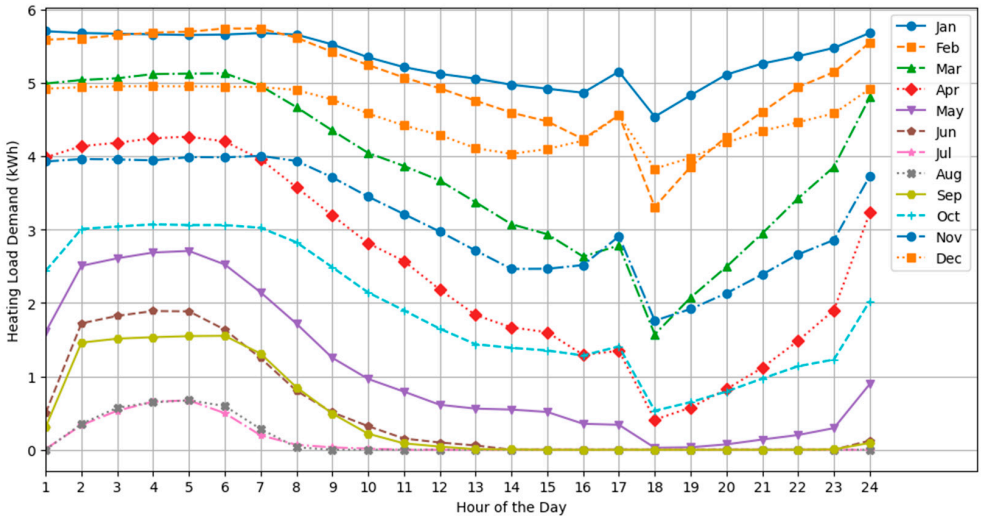

Figure 10. Hourly–monthly load profile for net heating load.

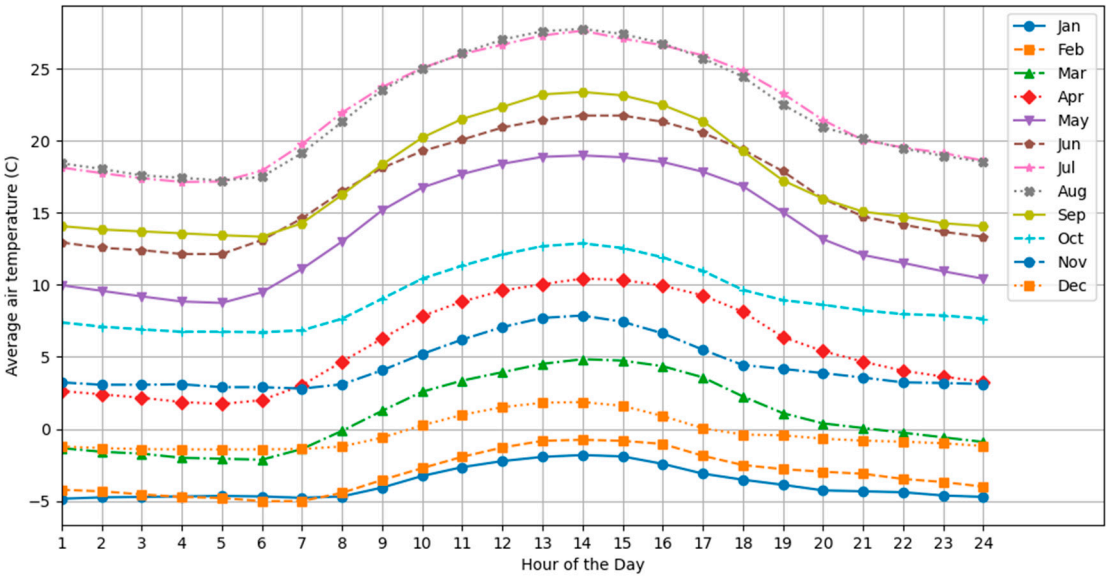

Figure 11. Hourly–monthly average air temperature for heating load.

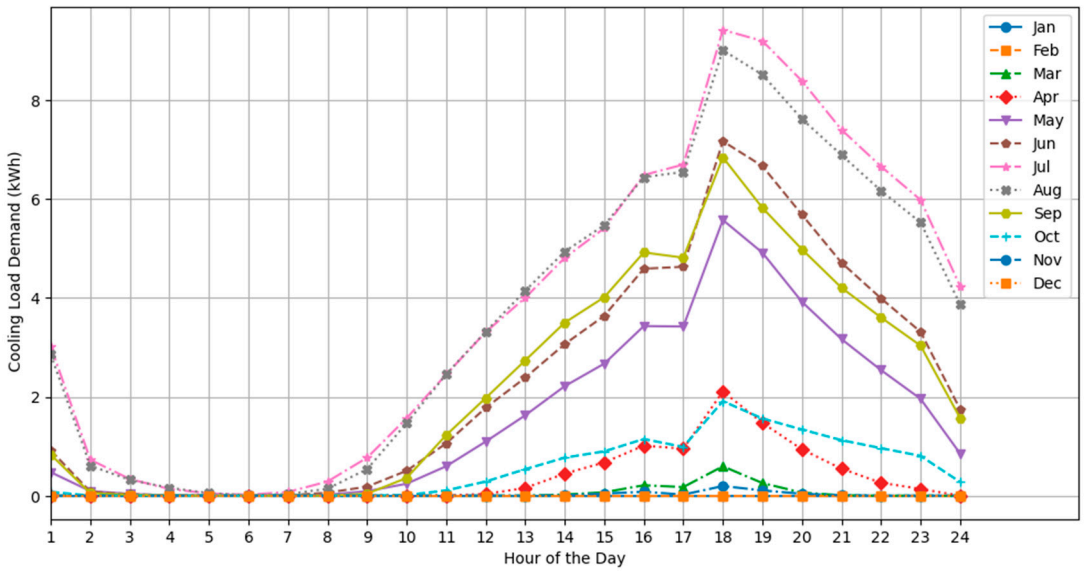

Figure 12. Hourly–monthly load profile for net cooling load.

4.3. Sizing of Heat Pump

Based on the hourly heating/cooling load of the proposed model, the sizing (capacity) of the heat pump is found separately for heating and cooling loads, and the COP of the heat pump is calculated. It is found that based on the maximum heating and cooling load at the coldest and hottest day, the HP required from the manufacture datasheet of the Goodman HP model is 0301B series with a capacity of 30,000 BTU/h and 0421B with a capacity of 42,000 BTU/h, respectively. The COP for the heating load in the manufacturing datasheet for 0301B ranges from 4.73 to 1.01; however, the COP calculated on the worst day, i.e., the coldest day using Equation (1) is 2.05. Similarly, for the cooling load, the manufacturing datasheet for 0421B ranges from 6.09 to 2.52; however, the EER calculated on the worst day, i.e., the hottest day using Equation (2) is 4.42. The seasonal COP/EER for heating and cooling mode is shown in Table 7, whereas the seasonal EER (SEER) is obtained by dividing cooling energy output in BTU with the electrical energy input in Wh obtained over a season. The detailed calculations for calculating EER and SEER are available in the OSF depository [100].

Table 7. COP and EER of the proposed heat pumps on the worst day of the year and seasonal, respectively.

	COP/EER	**SCOP/SEER**
Heat pump	**On Worst day**	**On Worst day**
Heating Mode	2.06	3.14
Cooling Mode	4.42	5.06

4.4. Sizing of Solar PV

The back-calculation algorithm yielded a PV capacity necessary to support the proposed residential house model of 6.88 kW. Using this theoretical PV capacity, a real PV system made up of specific modules with a rated power of 6.85kW was designed in SAM using the parameters in Table 8, resulting in a negligible deviation of 0.44%. The simulation results, as presented in Table 9, show that the energy fed into the grid and the energy drawn from the grid are closely aligned. The design aims to keep these values as similar as possible to minimize grid electricity costs, especially in areas with net-metering or value of solar quantification for grid-connected PV systems [31]. According to Table 9, the system's self-consumption is 30.02%, meaning that 30.02% of the energy generated by the PV system is utilized on-site by the heat pump during its lifetime. Additionally, the self-sufficiency of the system is 30.06%, indicating that 30.06% of the energy required by the heat pump is met by the PV system over its lifetime. Here, the electric load of the house in addition to the HP is not considered.

Table 8. Parameters of the designed PV system in SAM.

Parameters	**Value**
System Type	Residential
Total PV Capacity (kWp)	6.88
PV Module	SunPower SPR-M430-H-AC
Module Efficiency (%) [111]	22.3
Module DC Rating (Wp)	429.6
Number of Modules	16
DC/AC Ratio	0.99
Inverter Capacity (kW)	7.21
Number of Inverters	1
Number of Strings	2
Modules per Strings	8
Azimuth (°)	180
Tilt Angle (Optimal tilt angle in London ON)	34
Soiling Losses (%) [68]	5
DC Losses (%) (Default SAM values) [68]	4.44
Location	London ON

Table 9. Lifetime simulation results of the PV-ASHP in SAM showing the energy performance of the PV system using the thermal model data in this study and the Gaussian distribution data for limited load data scenarios.

Parameters	**Thermal Model Data**	**Gaussian Distribution Data**
Estimated PV Rating (kW)	6.85	6.85
Real PV Rating (kW)	6.88	6.88
Load Demand (MWh)	218.57	218.57
PV Energy (MWh)	221.03	221.03
Energy to Grid (MWh)	154.69	88.66
Energy from Grid (MWh)	152.22	86.19
Self-Consumption (%)	30.02	59.89
Self-Sufficiency (%)	30.06	60.56

Figure 13 illustrates the annual energy performance over the lifetime of the air-source HP model and PV generation. The PV system generates surplus energy compared to the load demand during the initial 14 years, but less energy in the last 9 years. The decline in PV energy generation is attributed to an annual PV degradation rate of 0.5% [31], while the HP load is considered constant over the lifetime of the system. This difference is offset by the simultaneous increase in self-consumption and decrease in self-sufficiency as the system matures.

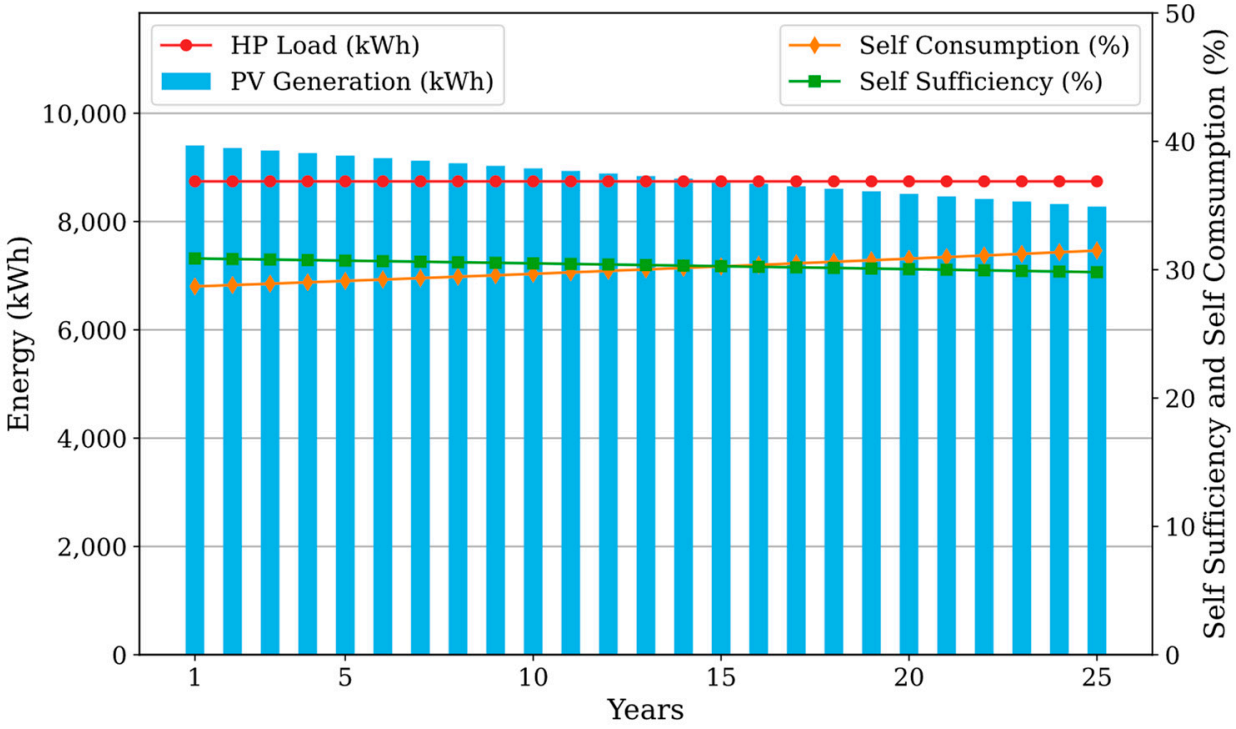

Figure 13. Twenty-five-year lifetime annual energy performance results of the proposed residential house with air-source heat pump.

In Figure 14, the PV generation and HP load for the initial year of the residential house equipped with ASHP are shown. In Figure 14a, the data reveal the daily fluctuations in PV generation in relation to the HP load. The peak load and peak PV generation do not consistently coincide, underscoring the need for grid connectivity in the system. Figure 14b illustrates a noteworthy inverse relationship between self-consumption and self-sufficiency. Self-consumption reaches its peak during the winter months, particularly in January and December (68% and 48%, respectively), while self-sufficiency is notably higher during the summer (50% in July). Figure 14c depicts the monthly patterns in PV energy generation and monthly load requirements. Additionally, it shows the energy supplied to and drawn from the grid. Energy drawn from the grid is highest in the winter, moderately high in summer, and lower during the transitional seasons of spring and autumn. Conversely, energy sent to the grid is less during the winter and highest in the summer.

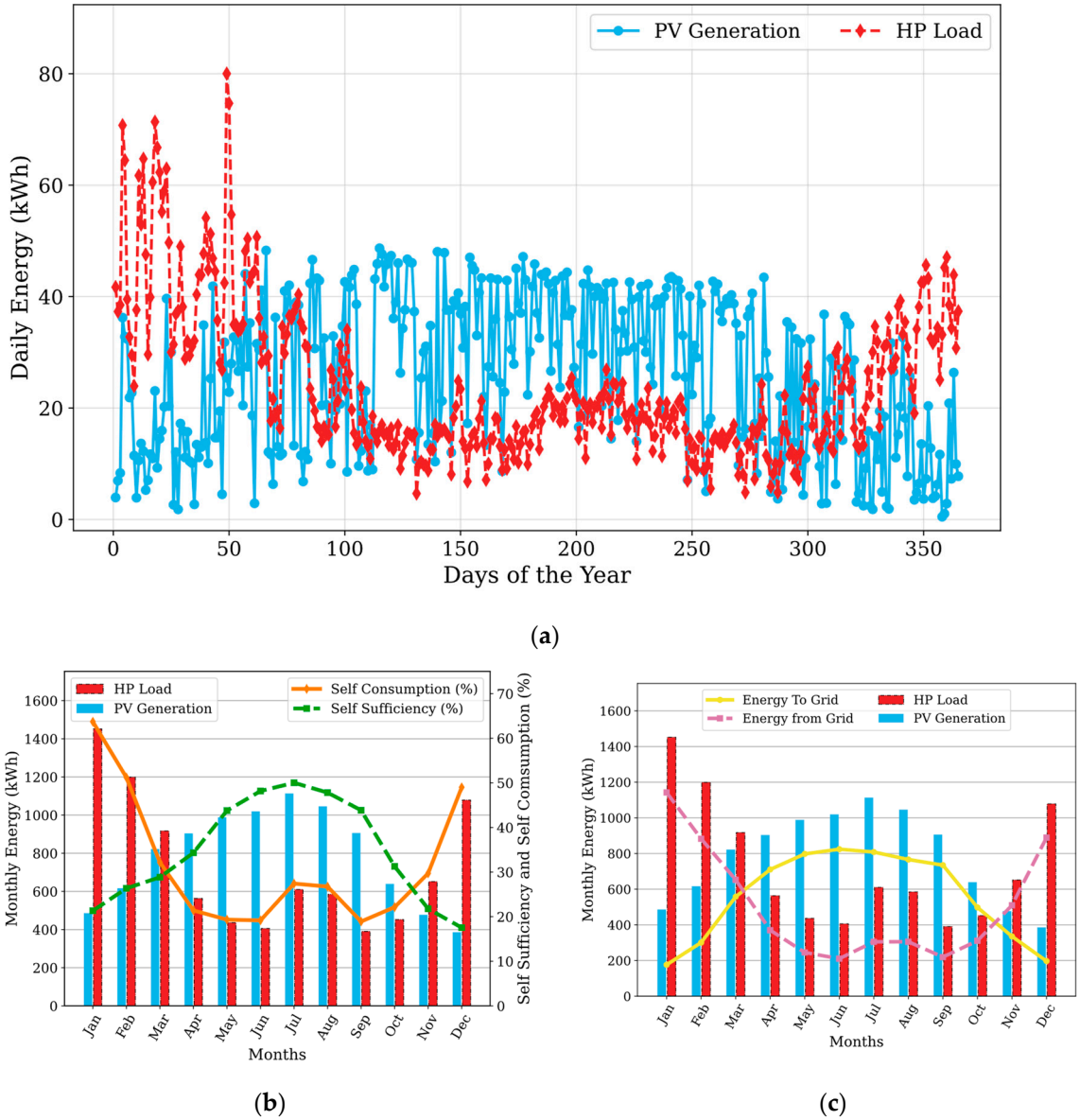

Figure 14. Year 1 energy performance results of proposed residential house with ASHP: (**a**) Daily PV energy generation and load demand. (**b**) Monthly PV generation, load demand, self-consumption, and self-sufficiency. (**c**) Monthly PV generation, load demand, energy to the grid, and energy from the grid.

To verify the opposite trend operation of the PV system observed in the summer and winter, the result for the warmest day (a, b) and the coldest day of the year (c, d) is shown in Figure 15. The warmest day was July 31, while the coldest day was February 17. As depicted in Figure 15a, PV self-consumption and self-sufficiency both reach 100%, but at different time intervals. On the warmest day, PV generation peaks in the middle of the day, while the heat pump load reaches its peak at 5 pm, as shown in Figure 15b. This leads to a mismatch in peak load timings between the PV system generation and the heat pump load during the summer. In contrast, on February 17, the heat pump load was elevated during the nighttime due to a significant drop in winter temperatures, resulting in increased heating demands. The PV generation, however, reaches its peak in the middle of the day, causing a peak load timing discrepancy between the PV system generation and the heat pump load during the winter as well. The plots in Figure 15c confirm these findings, showing the opposite behavior of self-sufficiency and self-consumption during the morning and nighttime hours.

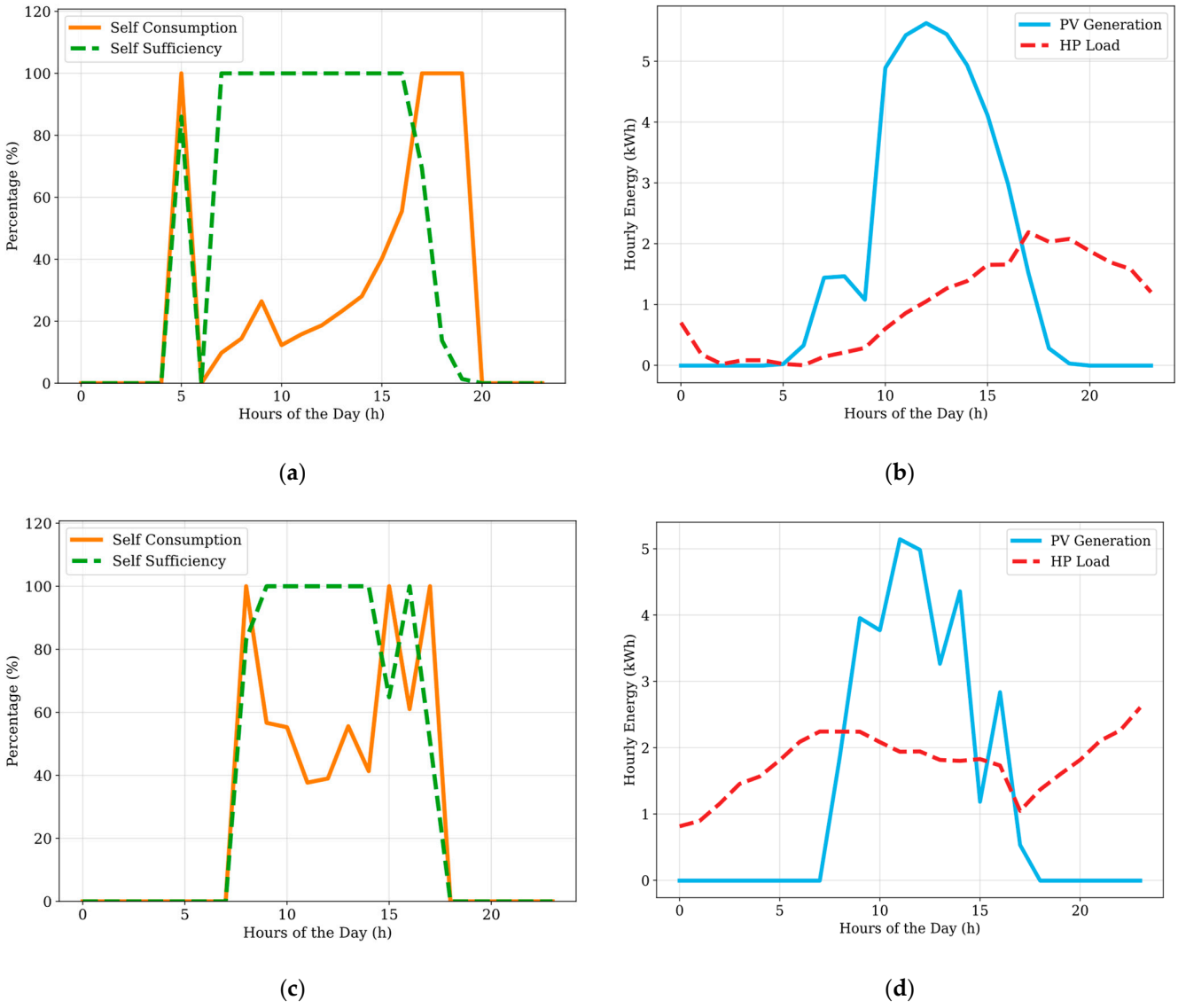

Figure 15. Energy performance results of the warmest day (July 31) and the coldest day (February 17) of the study period: (**a**) Self-sufficiency and self-consumption on the warmest day. (**b**) PV generation and HP load for the warmest day. (**c**) Self-sufficiency and self-consumption on the coldest day. (**d**) PV generation and HP load for the coldest day.

Similarly, for the spring and fall equinoxes which occur on 21 March and 22 September, respectively, energy performance results are shown in Figure 16. Figure 16a,c shows the self-sufficiency and self-consumption on the spring and fall equinoxes, which is 100% during slightly different time intervals. Figure 16b,d shows the variation in PV system generation and HP load during the day and night. It can be seen that HP load demand is comparatively less than PV generation, which shows energy supplied to the grid is greater during spring and fall in Figure 14b,c.

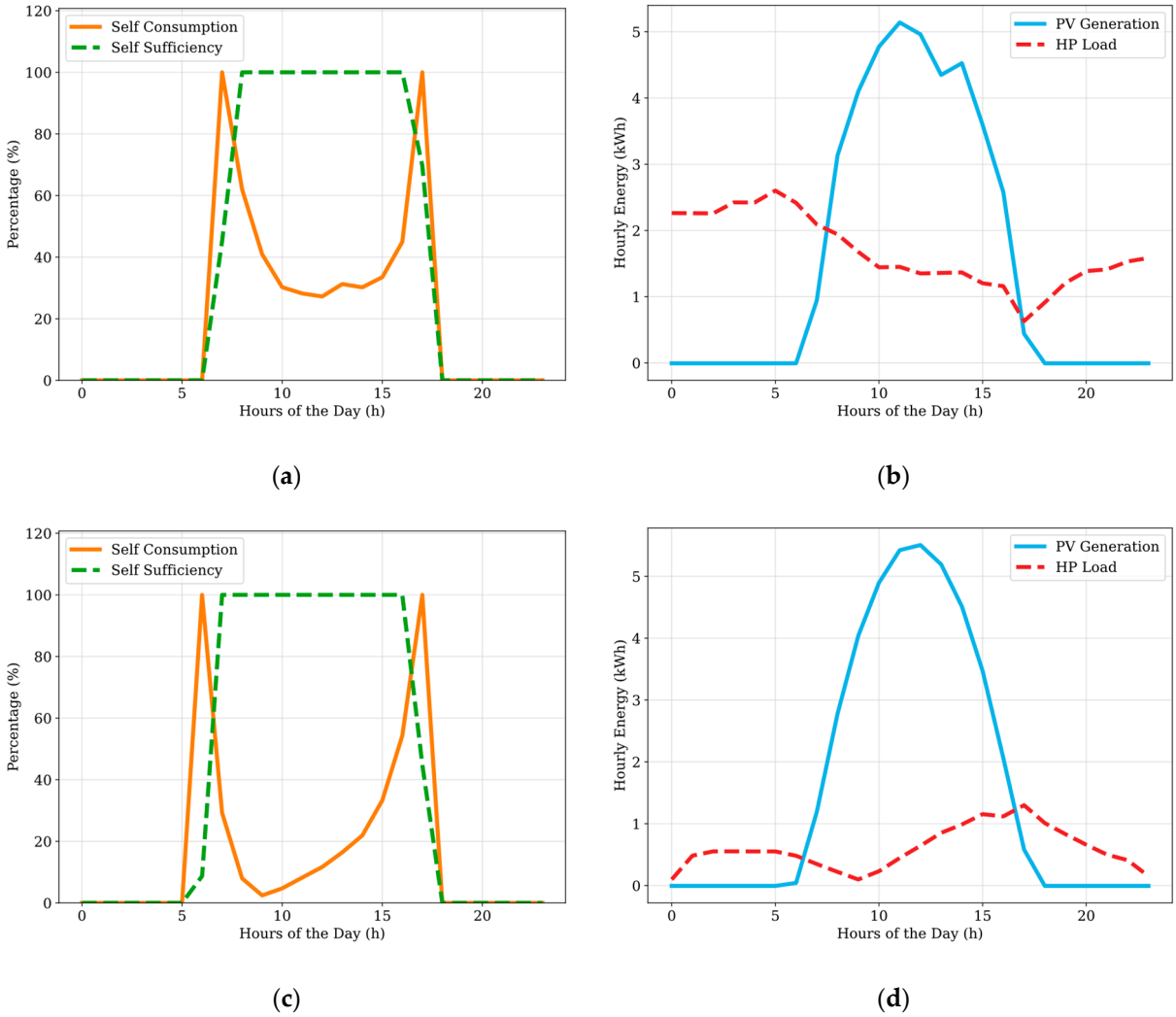

Figure 16. Energy performance results of the spring equinox (March 21) and the fall equinox (September 22) of the study period: (**a**) Self-sufficiency and self-consumption on the spring equinox. (**b**) PV generation and HP load for the spring equinox. (**c**) Self-sufficiency and self-consumption on the fall equinox. (**d**) PV generation and HP load for the fall equinox.

4.5. Impacts of the Limited Data Model on PV Sizing

When the PV system is designed using the Gaussian data model, the estimated PV rating, the real PV rating, the load demand, and the PV energy generation remain unchanged over the system's lifetime compared to the hourly data model, as shown in Table 9. These results are expected because the PV size is designed to ensure the overall annual PV energy generation matches the total annual heat pump load. There is, however, a significant change in the other parameters in Table 9. A significant reduction is observed in the energy sent to the grid (from 154.7 to 88.7 MWh) and the energy taken from the grid (from 152.2 to 86.2 MWh), representing close to a 43% decrease. On the other hand, the self-consumption and self-sufficiency values have increased significantly. More specifically, self-consumption and self-sufficiency both doubled in value (from 30% to 60%).

Figure 17 compares the monthly energy sent and taken from the grid for the hourly data model and the Gaussian data model. The comparison between the hourly data model and the Gaussian data model emphasizes the importance of collecting accurate data for heat pumps in residential buildings. Even though the limited model data predicts the same PV size as the hourly data, it may skew the economic analysis by underestimating the amount of electricity taken and sent to the grid.

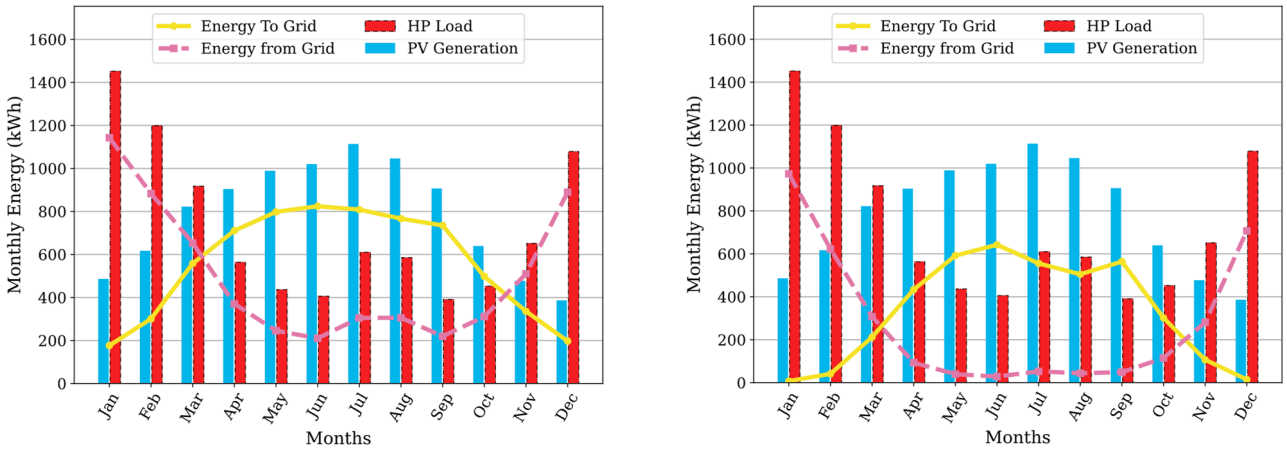

Figure 17. Comparison of the energy sent to the grid and the energy received from the grid using two different load data models. (**a**) hourly data model proposed in this study. (**b**) Gaussian model generated from unique monthly data.

5. Discussion

The size of the PV system plays a crucial role in determining the economic viability, feasibility, and extent of adoption [69]. Thus, designing optimal systems sizing is essential for achieving reliability and the highest degree of cost-effectiveness [19,20,112]. Existing studies provide combined sizing of PV+HP systems in cold climates [64,92,93,113,114], by only considering the heating load of the house neglecting the cooling load. Similarly, other studies focus on sizing PV and battery systems without including the HP sizing [115–117], or only focus on the sizing of HP systems [94–96,118]. In contrast, this study presents a mathematical model for heat pump sizing as well as a straightforward PV sizing method, shedding light on the potential of PV-powered heat pumps for residential housing based on both heating and cooling loads with stepwise sizing of the system, providing the basis for the economic analysis of the system based on the load profile and importance of coupling thermal energy storage to the PV+HP system. The house model is validated with HAP and the HP model with the manufactural datasheets and presents the reliability of these models for future techno-economic optimizations under the circumstances of any possible locations. The heating and cooling load demand for the house is obtained by developing an open-source Python model of the house as it gives more flexibility in terms of customization to the users as compared to HAP software. HAP has limitations in terms of customization, and users are typically bound to the offered features i.e., it takes default values for certain parameters whereas the proposed model parameters can be modified as required giving an advantage for unique or specialized simulations.

The open-source house model, including the heating/cooling loads that can be regulated by the users, is developed and well-defined. The simulation results are obtained on an hourly, daily, and monthly basis. Although monthly data provides seasonal variations and trends with an understanding of monthly energy consumption, it may not provide short-term variations within the month. Daily load data simulations, however, provide more details than monthly load data but still lack the granularity of hourly load simulations. Hourly load data simulation is also useful for understanding the impact of diurnal and seasonal change; however, it requires more computational time and detailed input data. Since the sizing of one component can affect the other it is therefore necessary to analyze the mutual influence to appropriately size the whole system and this is achieved in this study by hourly simulation data. The system sizing based on hourly simulations provides more precise results compared to monthly for understanding energy consumption and PV self-consumption and self-sufficiency on specific days which is used for import/export of

electricity to/from the grid providing especially for economic studies and evaluating peak loads which are shown in this study. Furthermore, the open-source black box air-air heat pump model is developed based on the Goodman manufacturers' datasheet and hourly load of the house. The COP and EER of the proposed HP model 0301B series on the coldest and for 0421B on the warmest day are 2.06 and 4.42 respectively. This underscores the need to correctly select the situation that the optimization is run for in the system.

The maximum size of PV required to provide the power to run the heat pump to supply the residential thermal loads is estimated as 6.88 kW. The PV system is designed in SAM with an aim to minimize the grid electricity costs and the emissions from the residential sectors, aligning with the overarching goal of achieving net zero energy consumption. Therefore, in this study, PV power generated over the year, monthly, and on the coldest/warmest day as well as on the spring/fall equinox is also presented with self-consumption and self-sufficiency of PV as well as energy sent to/from the grid to provide clarity. By integrating these analyses, the study not only addresses immediate energy needs but also contributes to the larger objective of sustainable energy practices and achieving a net zero energy footprint for the residential sector. Residential sectors account for energy use amounting to 20% of energy consumption in Ontario [119], where 40% of emissions come from space and water heating [120], i.e., an average home in London emits 10.5 tons of carbon emission each year [120]. To reduce these emissions and achieve Canada's net zero energy goal [7], the data obtained for energy sent to/from the grid will give us a reference to fulfill our missing targets. It also highlights the change in energy sent to/from the grid based on the hourly and monthly load profile, which is an important consideration when it comes to an economic analysis of the system model.

It is also shown in this study referring to the coldest, warmest, spring and fall equinox day of the year that there is a peak time mismatch for maximum PV generation and peak-time HP load as shown in Figure 15b; PV generation peaks in the middle of the day, while the heat pump load reaches its peak at 5 pm for summer. Similarly, on February 17, the heat pump load is elevated during the nighttime due to a significant drop in winter temperatures, resulting in increased heating demands. The PV generation, however, reaches its peak in the middle of the day, causing a peak load timing discrepancy during the winter as well, as shown in Figure 15d. Similar trends are also seen on the spring and fall equinoxes as shown in Figure 16b,d. Thus, maintaining the reliability on the grid during these periods is critical. This, however, opens future opportunities to store the excess PV energy generated during these mismatch periods in thermal energy-storage systems (i.e., thermal batteries) to increase the reliability of system models and decrease the dependence on the grid.

One of the limitations of this study pertains to the use of only the Gaussian model to generate the hourly data from the monthly energy. The main argument for using another model was to show the importance of generating accurate hourly data on PV system sizing in residential buildings' heat pump applications. The results have, expectedly, revealed the importance of hourly data for PV-HP energy performance and economic analysis. Future work is required to investigate the impact of changing the mean and standard deviation of the normal distribution on the PV performance. This could result in proposing an optimal distribution model that matches the hourly data generated in this study. Further studies are also required to investigate other types of statistical distributions for the heat pump load [121]. These results can be further improved by incorporating non-HP electric loads into the full system with sizing. Future work can also include the optimization of this model based on the other constraints, i.e., space and specific economic limitations. These results can also be used further to size the backup system for the model, for example, integration of a thermal storage system; i.e., developing an optimal thermal battery (TB) model that can store the excess energy from the solar PV during the generation in the off-peak time period and use it during the peak time period so the need for electricity from the grid can be minimized. Thermal batteries can allow the storing of this excess energy which can be used when necessary, thus minimizing the energy supply–demand mismatch occurring due to the integration of renewable resources [122]. Moreover, this thermal battery model

should also be sized accordingly based on the economics and size of the whole system, which again raises the need for economic analysis of the PV+HP+TB system. The technical, economical, and environmental benefits of integrating PV+HP with thermal energy storage have been identified by many researchers, including peak shaving, enhancing system overall efficiency, economic and energy savings, demand-side management, and emission mitigation [123]. Further studies are required to obtain the performance analysis, different system configurations and control strategies of the PV+HP+TB system as presented in [124] for the PV+HP system with integration of thermal and electrical energy storage. Along with this, the strategy needs to store energy in the TB system to be developed with a detailed thermodynamic model of the heat pump to optimize the size of TB and obtain its charging and discharging capability. Further, the study can also include electrical loads and domestic hot water demand throughout the year and optimize the system together making it more sustainable, leading to the net zero energy goal. This also opens the scope of carrying out economic efficiency and environmental impact studies to calculate yearly carbon tax/reduction compared to conventional fossil fuel systems.

6. Conclusions

This study outlines the sizing of the solar PV and HP based on the hourly and monthly heating and cooling loads of the residential house. The code written for each system model is open source and is available for other residential PV+HP models for different locations. Here, the heat pump model developed selects the heat pump based on the heating and cooling load of the house, giving an optimal HP size for the required house. The sizing of the PV system is such that the power generated is used to supply HP on an annual basis based on heating and cooling loads, the weather, and location data. Self-sufficiency and self-consumption of PV and the energy taken and fed to the grid are provided, which shows that the simulation based on the monthly load profile has a significant reduction of 43% for energy sent to/from the grid compared to the detailed hourly simulation and an increase from 30% to 60% for self-consumption and self-sufficiency. It also highlights the mismatch of PV system generation and HP load based on hourly simulation datasets for specific days in each season, i.e., the warmest and coldest day as well as spring and fall equinox. In future work, these datasets can be used to further economic analysis and design backup systems and/or reduce dependence on the grid with the help of optimal load management. The back-calculation PV-sizing algorithm combined with HP and thermal loads presented in this study exhibited robust performance and can be seamlessly used alongside other PV performance-analysis software tools like SAM. In the case study, the algorithm precisely determined the required PV size to meet the demands of the proposed residential house, which roughly doubles the size of a PV system targeted at meeting conventional plug loads. These results are easily integrated into the SAM to provide PV system designs for the combined house and heat pump. The algorithm's flexibility positions it as a valuable tool for enabling solar electrification of both space heating and cooling.

Author Contributions: Conceptualization, J.M.P.; methodology, S.R., U.J., N.A., K.S.H., J.G. and J.M.P.; software, S.R., U.J., N.A., K.S.H. and J.G.; validation, S.R., U.J., N.A., K.S.H., J.G. and J.M.P.; formal analysis, S.R., U.J., N.A., K.S.H., J.G. and J.M.P.; investigation, S.R., U.J., N.A., K.S.H., J.G. and J.M.P.; resources, J.M.P.; data curation, S.R., U.J., N.A., K.S.H. and J.G.; writing—original draft preparation, S.R., U.J., N.A., K.S.H., J.G. and J.M.P.; writing—review and editing, S.R., U.J., N.A., K.S.H., J.G. and J.M.P.; visualization, S.R., U.J., N.A. and K.S.H.; supervision, J.M.P.; funding acquisition, J.M.P. All authors have read and agreed to the published version of the manuscript.

Funding: This research was supported by the Western University Carbon Solutions Grant, the Natural Sciences and Engineering Research Council of Canada, and the Thompson Endowment.

Data Availability Statement: All data is available on the Open Science Framework https://osf.io/msrgk/.

Conflicts of Interest: The authors declare no conflicts of interest. The funders had no role in the design of the study; in the collection, analysis or interpretation of data; in the writing of the manuscript; or in the decision to publish the results.

Nomenclature

Abbreviations	
ACH	Air Change per Hour
ANN	Artificial Neural Network
ASHP	Air Source Heat Pump
AWHP	Air–Water Heat Pump
COP	Coefficient of Performance
E	Energy
EER	Energy Efficiency Ratio
HAP	Hourly Analysis Program
HP	Heat pump
HVAC	Heating, Ventilation and Air Conditioning
GHE	Ground Heat Exchanger
GHG	Greenhouse Gas
GSHP	Ground Source Heat Pump
NREL	National Renewable Energy Laboratories
PV	Photovoltaics
SAM	System Advisor Model
SC	Self-consumption
SS	Self-sufficiency
SHG	Solar Heat Gain
SHGC	Solar Heat Gain Constant
Latin symbols	
dt/dx	Temperature gradient across the heat transfer surface
A	Area normal to the direction of heat transfer (m^2)
A_{fl}	Area of floor (m^2)
A_f	Area of frame (m^2)
$A_{f\prime}$	Projected surface area of frame (m^2)
A_g	Area of glazing (m^2)
A_{surf}	Actual surface area of the frame incorporating the depth at which the glass is placed inside the frame (m^2)
α	Absorptivity
a_f^s	Solar absorptivity of exterior frame surface (W/m^2)
C	Conductance ($W/(m^2K)$)
C_p	Specific heat of infiltrated air (kJ/(kg-K))
DR	Daily range
G_D	Direct irradiance (W/m^2)
G_t	Incident solar radiation (W/m^2)
h	Convective heat transfer coefficient ($W/(m^2{}^\circ C)$)
h_f	Overall exterior surface conductance (1/(Ohmm))
h_t	Combined convection and conduction coefficient ($W/(m^2C)$)
H	Height of ceiling (m)
h_{fg}	Latent heat of vaporization (J/Kg)
I	Infiltration (m^3/s)
k	Thermal conductivity ($W/(m^\circ C)$)
$\dot{m}$	Mass flow rate (kg/s)
q	Heat transfer rate (W)
$q\prime$	Conduction heat flux (W/m^2)
$q\prime_l$	Latent heat transfer (W)
$q\prime_s$	Sensible heat transfer (W)
R	Thermal unit resistance ((m^2 °C)/W)
$R\prime$	Resistance (°C/W)
$t\prime$	Hourly temperature (°C)
t_e	Hourly Sol-air temperature (°C)

t_f	Temperature of fluid in contact with heat transfer surface (°C)
t_w	Temperature of heat transfer surface (°C)
Δt: ($t_o - t_i$)	Difference between indoor and outdoor dry bulb temperature (°C)
T	Ambient temperature (°C)
U	Overall heat transfer coefficient
V	Space volume (m^3)
v	Specific Volume (m^3/kg)
W	Humidity ratio
X	Percentage (%)
Subscripts and superscripts	
Cond	Conduction
Conv	Convection
D	Direct radiation
d	Diffuse radiation
f	Frame
g	Glazing
i	Inside
iwb	Inside wet bulb
in	Infiltration
o	Outside
ori	Original
L	Load
sl	Sunlit area
tot	Total

References

1. Dincer, I.; Rosen, M.A.; Ahmadi, P. *Optimization of Energy Systems*; John Wiley & Sons: Hoboken, NJ, USA, 2017; ISBN 1-118-89443-X.
2. Baghoolizadeh, M.; Rostamzadeh-Renani, R.; Rostamzadeh-Renani, M.; Toghraie, D. A Multi-Objective Optimization of a Building's Total Heating and Cooling Loads and Total Costs in Various Climatic Situations Using Response Surface Methodology. *Energy Rep.* **2021**, *7*, 7520–7538. [CrossRef]
3. USEPA. O Sources of Greenhouse Gas Emissions. Available online: https://www.epa.gov/ghgemissions/sources-greenhouse-gas-emissions (accessed on 20 September 2023).
4. IPCC. *The Evidence Is Clear: The Time for Action Is Now. We Can Halve Emissions by 2030*; IPCC: Geneva, Switzerland, 2022.
5. Environment and Climate Change Canada. Greenhouse Gas Sources and Sinks in Canada: Executive Summary. 2022. Available online: https://www.canada.ca/en/environment-climate-change/services/climate-change/greenhouse-gas-emissions/sources-sinks-executive-summary-2022.html (accessed on 4 July 2023).
6. Canada: CO2 Emissions per Capita 1970–2022. Available online: https://www.statista.com/statistics/1290653/per-capita-emissions-in-canada/ (accessed on 20 September 2023).
7. Canada, S. Net-Zero Emissions by 2050. Available online: https://www.canada.ca/en/services/environment/weather/climatechange/climate-plan/net-zero-emissions-2050.html (accessed on 11 July 2023).
8. Dubois, G.; Sovacool, B.; Aall, C.; Nilsson, M.; Barbier, C.; Herrmann, A.; Bruyère, S.; Andersson, C.; Skold, B.; Nadaud, F.; et al. It Starts at Home? Climate Policies Targeting Household Consumption and Behavioral Decisions Are Key to Low-Carbon Futures. *Energy Res. Soc. Sci.* **2019**, *52*, 144–158. [CrossRef]
9. Gandzeichuk, I. Council Post: Smart Homes: Reducing Carbon Footprint and Expenses. Available online: https://www.forbes.com/sites/forbestechcouncil/2021/12/10/smart-homes-reducing-carbon-footprint-and-expenses/ (accessed on 11 July 2023).
10. Canada.ca. Heating Equipment for Residential Use. Available online: https://natural-resources.canada.ca/energy-efficiency/products/heating-equipment-for-residential-use/13740 (accessed on 25 February 2023).
11. Zhang, C.; Nielsen, E.; Fan, J.; Furbo, S.; Li, Q. Experimental Investigation on a Combined Solar and Ground Source Heat Pump System for a Single-Family House: Energy Flow Analysis and Performance Assessment. *Energy Build.* **2021**, *241*, 110958. [CrossRef]
12. El Hannach, M.; Ahmadi, P.; Guzman, L.; Pickup, S.; Kjeang, E. Life Cycle Assessment of Hydrogen and Diesel Dual-Fuel Class 8 Heavy Duty Trucks. *Int. J. Hydrogen Energy* **2019**, *44*, 8575–8584. [CrossRef]
13. Mahjoob, A.; Ahmadi, P.; Afsaneh, H.; Vojdani, M.; Mortazavi, M. System Sizing and Transient Simulation of a Solar Photovoltaic Off-Grid Energy System in Various Climates with Air Heat Pumps. *Sustain. Energy Technol. Assess.* **2022**, *54*, 102788. [CrossRef]
14. Karayel, G.K.; Javani, N.; Dincer, I. Green Hydrogen Production Potential for Turkey with Solar Energy. *Int. J. Hydrogen Energy* **2022**, *47*, 19354–19364. [CrossRef]
15. Matasci, S. *How Solar Panel Cost & Efficiency Change Over Time*; EnergySage: Boston, MA, USA, 2022.

16. Masson, G. 2018 Snapshot of Global Photovoltaic Markets. Report IEA PVPS T1-33: 2018. 2018. Available online: https://apvi.org.au/wp-content/uploads/2018/04/IEA_PVPS-A_Snapshot_of_Global_PV-1992-2017.pdf (accessed on 20 September 2023).
17. Ahmadi, P.; Khoshnevisan, A. Dynamic Simulation and Lifecycle Assessment of Hydrogen Fuel Cell Electric Vehicles Considering Various Hydrogen Production Methods. *Int. J. Hydrogen Energy* **2022**, *47*, 26758–26769. [CrossRef]
18. Mertens, K. *Photovoltaics: Fundamentals, Technology, and Practice*; John Wiley & Sons: Hoboken, NJ, USA, 2018; ISBN 1-119-40104-6.
19. Al-Falahi, M.D.; Jayasinghe, S.D.G.; Enshaei, H. A Review on Recent Size Optimization Methodologies for Standalone Solar and Wind Hybrid Renewable Energy System. *Energy Convers. Manag.* **2017**, *143*, 252–274. [CrossRef]
20. Goel, S.; Sharma, R. Performance Evaluation of Stand Alone, Grid Connected and Hybrid Renewable Energy Systems for Rural Application: A Comparative Review. *Renew. Sustain. Energy Rev.* **2017**, *78*, 1378–1389. [CrossRef]
21. Okoye, C.O.; Solyalı, O. Optimal Sizing of Stand-Alone Photovoltaic Systems in Residential Buildings. *Energy* **2017**, *126*, 573–584. [CrossRef]
22. Shukla, A.K.; Sudhakar, K.; Baredar, P. Design, Simulation and Economic Analysis of Standalone Roof Top Solar PV System in India. *Sol. Energy* **2016**, *136*, 437–449. [CrossRef]
23. Al-Salaymeh, A.; Al-Hamamre, Z.; Sharaf, F.; Abdelkader, M.R. Technical and Economical Assessment of the Utilization of Photovoltaic Systems in Residential Buildings: The Case of Jordan. *Energy Convers. Manag.* **2010**, *51*, 1719–1726. [CrossRef]
24. Khatib, T.; Mohamed, A.; Sopian, K. A Review of Photovoltaic Systems Size Optimization Techniques. *Renew. Sustain. Energy Rev.* **2013**, *22*, 454–465. [CrossRef]
25. Sidrach-de-Cardona, M.; Lopez, L.M. A Simple Model for Sizing Stand Alone Photovoltaic Systems. *Sol. Energy Mater. Sol. Cells* **1998**, *55*, 199–214. [CrossRef]
26. Kazem, H.A.; Khatib, T.; Sopian, K. Sizing of a Standalone Photovoltaic/Battery System at Minimum Cost for Remote Housing Electrification in Sohar, Oman. *Energy Build.* **2013**, *61*, 108–115. [CrossRef]
27. Muhsen, D.H.; Nabil, M.; Haider, H.T.; Khatib, T. A Novel Method for Sizing of Standalone Photovoltaic System Using Multi-Objective Differential Evolution Algorithm and Hybrid Multi-Criteria Decision Making Methods. *Energy* **2019**, *174*, 1158–1175. [CrossRef]
28. Ridha, H.M.; Gomes, C.; Hizam, H.; Ahmadipour, M.; Heidari, A.A.; Chen, H. Multi-Objective Optimization and Multi-Criteria Decision-Making Methods for Optimal Design of Standalone Photovoltaic System: A Comprehensive Review. *Renew. Sustain. Energy Rev.* **2021**, *135*, 110202. [CrossRef]
29. Amara, S.; Toumi, S.; Salah, C.B.; Saidi, A.S. Improvement of Techno-Economic Optimal Sizing of a Hybrid off-Grid Micro-Grid System. *Energy* **2021**, *233*, 121166. [CrossRef]
30. Do Grid-Tied Photovoltaic Systems Really Have an Advantage? Available online: https://www.greenbuildingadvisor.com/article/do-grid-tied-photovoltaic-systems-really-have-an-advantage (accessed on 11 October 2023).
31. Hayibo, K.S.; Pearce, J.M. A Review of the Value of Solar Methodology with a Case Study of the U.S. VOS. *Renew. Sustain. Energy Rev.* **2021**, *137*, 110599. [CrossRef]
32. The Role of Net Metering in the Evolving Electricity System | National Academies. Available online: https://www.nationalacademies.org/our-work/the-role-of-net-metering-in-the-evolving-electricity-system (accessed on 19 July 2023).
33. Nicoletti, F.; Cucumo, M.A.; Arcuri, N. Cost Optimal Sizing of Photovoltaic-Battery System and Air–Water Heat Pump in the Mediterranean Area. *Energy Convers. Manag.* **2022**, *270*, 116274. [CrossRef]
34. O'Shaughnessy, E.; Cutler, D.; Ardani, K.; Margolis, R. Solar plus: A Review of the End-User Economics of Solar PV Integration with Storage and Load Control in Residential Buildings. *Appl. Energy* **2018**, *228*, 2165–2175. [CrossRef]
35. Pearce, J.M.; Sommerfeldt, N. Economics of Grid-Tied Solar Photovoltaic Systems Coupled to Heat Pumps: The Case of Northern Climates of the U.S. and Canada. *Energies* **2021**, *14*, 834. [CrossRef]
36. Padovani, F.; Sommerfeldt, N.; Longobardi, F.; Pearce, J.M. Decarbonizing Rural Residential Buildings in Cold Climates: A Techno-Economic Analysis of Heating Electrification. *Energy Build.* **2021**, *250*, 111284. [CrossRef]
37. Sommerfeldt, N.; Pearce, J.M. Can Grid-Tied Solar Photovoltaics Lead to Residential Heating Electrification? A Techno-Economic Case Study in the Midwestern U.S. *Appl. Energy* **2023**, *336*, 120838. [CrossRef]
38. Pena-Bello, A.; Schuetz, P.; Berger, M.; Worlitschek, J.; Patel, M.K.; Parra, D. Decarbonizing Heat with PV-Coupled Heat Pumps Supported by Electricity and Heat Storage: Impacts and Trade-Offs for Prosumers and the Grid. *Energy Convers. Manag.* **2021**, *240*, 114220. [CrossRef]
39. Battaglia, M.; Haberl, R.; Bamberger, E.; Haller, M. Increased Self-Consumption and Grid Flexibility of PV and Heat Pump Systems with Thermal and Electrical Storage. *Energy Procedia* **2017**, *135*, 358–366. [CrossRef]
40. Asgari, N.; Hayibo, K.S.; Groza, J.; Rana, S.; Pearce, J.M. *Greenhouse Applications of Solar Photovoltaic Driven Heat Pumps in Northern Environments*; Western University: London, ON, Canada, 2024; *under review*.
41. Bloess, A.; Schill, W.-P.; Zerrahn, A. Power-to-Heat for Renewable Energy Integration: A Review of Technologies, Modeling Approaches, and Flexibility Potentials. *Appl. Energy* **2018**, *212*, 1611–1626. [CrossRef]
42. Rana, S.; Sommerfeldt, N.; Pearce, J.M. *Best Practices of Techno-Economic Methods for Solar Photovoltaic Coupled Heat Pump Analysis in Cold Climates*; Western University: London, ON, Canada, 2024; *under review*.
43. Heidarinejad, M.; Mattise, N.; Dahlhausen, M.; Sharma, K.; Benne, K.; Macumber, D.; Brackney, L.; Srebric, J. Demonstration of Reduced-Order Urban Scale Building Energy Models. *Energy Build.* **2017**, *156*, 17–28. [CrossRef]

44. Jin, H.; Spitler, J.D. A Parameter Estimation Based Model of Water-to-Water Heat Pumps for Use in Energy Calculation Programs. *ASHRAE Trans.* **2002**, *108*, 3.
45. Staffell, I.; Brett, D.; Brandon, N.; Hawkes, A. A Review of Domestic Heat Pumps. *Energy Environ. Sci.* **2012**, *5*, 9291–9306. [CrossRef]
46. Emily Air Source vs Ground Source Heat Pumps (GSHPs). Available online: https://www.boreholesolutions.co.uk/blog/air-source-vs-ground-source-heat-pumps-gshps/ (accessed on 21 May 2024).
47. Ground-Source versus Air-Source Heat Pumps. Dandelion Energy. Available online: https://dandelionenergy.com/ground-source-vs-air-source-heat-pumps (accessed on 7 July 2023).
48. Casasso, A.; Sethi, R. Efficiency of Closed Loop Geothermal Heat Pumps: A Sensitivity Analysis. *Renew. Energy* **2014**, *62*, 737–746. [CrossRef]
49. Cho, H.; Choi, J.M. The Quantitative Evaluation of Design Parameter's Effects on a Ground Source Heat Pump System. *Renew. Energy* **2014**, *65*, 2–6. [CrossRef]
50. Guo, Y.; Zhang, G.; Zhou, J.; Wu, J.; Shen, W. A Techno-Economic Comparison of a Direct Expansion Ground-Source and a Secondary Loop Ground-Coupled Heat Pump System for Cooling in a Residential Building. *Appl. Therm. Eng.* **2012**, *35*, 29–39. [CrossRef]
51. Lazzarin, R. Heat Pumps and Solar Energy: A Review with Some Insights in the Future. *Int. J. Refrig.* **2020**, *116*, 146–160. [CrossRef]
52. Lim, T.H.; De Kleine, R.D.; Keoleian, G.A. Energy Use and Carbon Reduction Potentials from Residential Ground Source Heat Pumps Considering Spatial and Economic Barriers. *Energy Build.* **2016**, *128*, 287–304. [CrossRef]
53. Aditya, G.R.; Mikhaylova, O.; Narsilio, G.A.; Johnston, I.W. Comparative Costs of Ground Source Heat Pump Systems against Other Forms of Heating and Cooling for Different Climatic Conditions. *Sustain. Energy Technol. Assess.* **2020**, *42*, 100824. [CrossRef]
54. Nguyen, H.V.; Law, Y.L.E.; Alavy, M.; Walsh, P.R.; Leong, W.H.; Dworkin, S.B. An Analysis of the Factors Affecting Hybrid Ground-Source Heat Pump Installation Potential in North America. *Appl. Energy* **2014**, *125*, 28–38. [CrossRef]
55. Baxter, V.D.; Groll, E.; Sikes, K. *IEA HPT Annex 41 Cold Climate Heat Pumps—Final Report (HPT-AN41-1)*; IEA Heat Pump Centre: London, UK, 2017.
56. Zhang, L.; Jiang, Y.; Dong, J.; Yao, Y. Advances in Vapor Compression Air Source Heat Pump System in Cold Regions: A Review. *Renew. Sustain. Energy Rev.* **2018**, *81*, 353–365. [CrossRef]
57. Natural Resources Canada. Heating and Cooling with a Heat Pump. Available online: https://natural-resources.canada.ca/energy-efficiency/energy-star-canada/about/energy-star-announcements/publications/heating-and-cooling-heat-pump/6817 (accessed on 7 July 2023).
58. Zhang, Y.; Ma, Q.; Li, B.; Fan, X.; Fu, Z. Application of an Air Source Heat Pump (ASHP) for Heating in Harbin, the Coldest Provincial Capital of China. *Energy Build.* **2017**, *138*, 96–103. [CrossRef]
59. Kegel, M.; Sager, J.; Thomas, M.; Giguere, D.; Sunye, R. Performance Testing of Cold Climate Air Source Heat Pumps. In Proceedings of the 12th IEA Heat Pump Conference 2017, Rotterdam, The Netherlands, 15–18 May 2017; pp. 15–18.
60. Global Heat Pump Sales Continue Double-Digit Growth—Analysis. Available online: https://www.iea.org/commentaries/global-heat-pump-sales-continue-double-digit-growth (accessed on 7 July 2023).
61. Asaee, S.R.; Ugursal, V.I.; Beausoleil-Morrison, I. Techno-Economic Feasibility Evaluation of Air to Water Heat Pump Retrofit in the Canadian Housing Stock. *Appl. Therm. Eng.* **2017**, *111*, 936–949. [CrossRef]
62. Udovichenko, A.; Zhong, L. Techno-Economic Analysis of Air-Source Heat Pump (ASHP) Technology for Single-Detached Home Heating Applications in Canada. *Sci. Technol. Built Environ.* **2020**, *26*, 1352–1370. [CrossRef]
63. Kegel, M.; Tamasauskas, J.; Sunye, R.; Giguère, D. Heat Pumps in the Canadian Residential Sector. In Proceedings of the 11th IEA Heat Pump Conference, Montreal, QC, Canada, 12–16 May 2014.
64. Fischer, D.; Lindberg, K.B.; Madani, H.; Wittwer, C. Impact of PV and Variable Prices on Optimal System Sizing for Heat Pumps and Thermal Storage. *Energy Build.* **2016**, *128*, 723–733. [CrossRef]
65. Zaya, N.E.; Hassan, L.H.; Bilgil, H. Mathematical Modeling for Prediction of Heating and Air-Conditioning Energies of Multistory Buildings in Duhok City. *Acad. J. Nawroz Univ.* **2018**, *7*, 153–167. [CrossRef]
66. Ashrae, A.H.F.; Atlanta, G. American Society of Heating. *Refrig. Air-Cond. Eng.* **2009**, *1*, 17.1–17.32.
67. Hourly Analysis Program | Carrier Carrier Commercial North America. Available online: https://www.carrier.com/commercial/en/us/software/hvac-system-design/hourly-analysis-program/ (accessed on 7 June 2023).
68. Freeman, J.M.; DiOrio, N.A.; Blair, N.J.; Neises, T.W.; Wagner, M.J.; Gilman, P.; Janzou, S. *System Advisor Model (SAM) General Description (Version 2017.9.5)*; NREL/TP--6A20-70414; National Renewable Energy Laboratory: Golden, CO, USA, 2018; p. 1440404.
69. Ibrahim, I.A.; Khatib, T.; Mohamed, A. Optimal Sizing of a Standalone Photovoltaic System for Remote Housing Electrification Using Numerical Algorithm and Improved System Models. *Energy* **2017**, *126*, 392–403. [CrossRef]
70. Ibrahim, H.; Anani, N. Evaluation of Analytical Methods for Parameter Extraction of PV Modules. *Energy Procedia* **2017**, *134*, 69–78. [CrossRef]
71. Egido, M.; Lorenzo, E. The Sizing of Stand Alone PV-System: A Review and a Proposed New Method. *Sol. Energy Mater. Sol. Cells* **1992**, *26*, 51–69. [CrossRef]

72. Solar Photovoltaic Software—Appropedia, the Sustainability Wiki. Available online: https://www.appropedia.org/Solar_photovoltaic_software (accessed on 11 July 2023).
73. ESP-r. Available online: https://web.archive.org/web/20200202174513/http://www.esru.strath.ac.uk:80/Programs/ESP-r.htm (accessed on 20 September 2023).
74. s.r.o, © Solargis Solargis: pvPlanner. Available online: https://solargis.info/pvplanner/#tl=Google:hybrid&bm=satellite (accessed on 20 September 2023).
75. Solar, L. Generate Solar Permit Packages in Minutes | Lyra Solar. Available online: https://get.solardesigntool.com/ (accessed on 20 September 2023).
76. Aurora Solar: The World's #1 Solar Design Software. Available online: https://aurorasolar.com/ (accessed on 20 September 2023).
77. PVsyst—Logiciel Photovoltaïque. Available online: https://www.pvsyst.com/ (accessed on 20 September 2023).
78. Laplace Systems Co., Ltd. Available online: https://www.lapsys.co.jp/english/products/pro.html (accessed on 20 September 2023).
79. Welcome | TRNSYS: Transient System Simulation Tool. Available online: https://www.trnsys.com/ (accessed on 11 April 2023).
80. RETScreen. Available online: https://www.deassociation.ca/retscreen (accessed on 26 May 2023).
81. HOMER—Hybrid Renewable and Distributed Generation System Design Software. Available online: https://www.homerenergy.com/ (accessed on 20 September 2023).
82. iHOGA/MHOGA—Simulation and Optimization of Stand-Alone and Grid-Connected Hybrid Renewable Systems. Available online: https://ihoga.unizar.es/en/ (accessed on 20 September 2023).
83. Hybrid2 | Wind Energy Center. Available online: https://www.umass.edu/windenergy/research/topics/tools/software/hybrid2 (accessed on 20 September 2023).
84. Connolly, D.; Lund, H.; Mathiesen, B.V.; Leahy, M. A Review of Computer Tools for Analysing the Integration of Renewable Energy into Various Energy Systems. *Appl. Energy* **2010**, *87*, 1059–1082. [CrossRef]
85. Bajpai, P.; Dash, V. Hybrid Renewable Energy Systems for Power Generation in Stand-Alone Applications: A Review. *Renew. Sustain. Energy Rev.* **2012**, *16*, 2926–2939. [CrossRef]
86. Cui, W.; Li, X.; Li, X.; Si, T.; Lu, L.; Ma, T.; Wang, Q. Thermal Performance of Modified Melamine Foam/Graphene/Paraffin Wax Composite Phase Change Materials for Solar-Thermal Energy Conversion and Storage. *J. Clean. Prod.* **2022**, *367*, 133031. [CrossRef]
87. Ani, V.A. Feasibility and Optimal Design of a Stand-Alone Photovoltaic Energy System for the Orphanage. *J. Renew. Energy* **2014**, *2014*, 379729. [CrossRef]
88. Li, H.; Hou, K.; Xu, X.; Jia, H.; Zhu, L.; Mu, Y. Probabilistic Energy Flow Calculation for Regional Integrated Energy System Considering Cross-System Failures. *Appl. Energy* **2022**, *308*, 118326. [CrossRef]
89. Schelly, C.; Louie, E.P.; Pearce, J.M. Examining Interconnection and Net Metering Policy for Distributed Generation in the United States. *Renew. Energy Focus* **2017**, *22–23*, 10–19. [CrossRef]
90. Revesz, R.L.; Unel, B. The Future of Distributed Generation: Moving Past Net Metering. *Envtl. L. Rep. News Anal.* **2018**, *48*, 10719–10725.
91. Bruno, R.; Bevilacqua, P.; Carpino, C.; Arcuri, N. The Cost-Optimal Analysis of a Multistory Building in the Mediterranean Area: Financial and Macroeconomic Projections. *Energies* **2020**, *13*, 1243. [CrossRef]
92. Angenendt, G.; Zurmühlen, S.; Rücker, F.; Axelsen, H.; Sauer, D.U. Optimization and Operation of Integrated Homes with Photovoltaic Battery Energy Storage Systems and Power-to-Heat Coupling. *Energy Convers. Manag. X* **2019**, *1*, 100005. [CrossRef]
93. Beck, T.; Kondziella, H.; Huard, G.; Bruckner, T. Optimal Operation, Configuration and Sizing of Generation and Storage Technologies for Residential Heat Pump Systems in the Spotlight of Self-Consumption of Photovoltaic Electricity. *Appl. Energy* **2017**, *188*, 604–619. [CrossRef]
94. Lindberg, K.B.; Doorman, G.; Fischer, D.; Korpås, M.; Ånestad, A.; Sartori, I. Methodology for Optimal Energy System Design of Zero Energy Buildings Using Mixed-Integer Linear Programming. *Energy Build.* **2016**, *127*, 194–205. [CrossRef]
95. Lyden, A.; Tuohy, P.G. Planning Level Sizing of Heat Pumps and Hot Water Tanks Incorporating Model Predictive Control and Future Electricity Tariffs. *Energy* **2022**, *238*, 121731. [CrossRef]
96. Dongellini, M.; Naldi, C.; Morini, G.L. Influence of Sizing Strategy and Control Rules on the Energy Saving Potential of Heat Pump Hybrid Systems in a Residential Building. *Energy Convers. Manag.* **2021**, *235*, 114022. [CrossRef]
97. Bruno, R.; Bevilacqua, P.; Arcuri, N. Assessing Cooling Energy Demands with the EN ISO 52016-1 Quasi-Steady Approach in the Mediterranean Area. *J. Build. Eng.* **2019**, *24*, 100740. [CrossRef]
98. NSRDB. Available online: https://nsrdb.nrel.gov/ (accessed on 6 November 2023).
99. McQuiston, F.C.; Parker, J.D.; Spitler, J.D.; Taherian, H. *Heating, Ventilating, and Air Conditioning: Analysis and Design*; John Wiley & Sons: Hoboken, NJ, USA, 2023; ISBN 978-1-119-89416-2.
100. Rana, S.; Jamil, U.; Asgari, N.; Hayibo, K.S.; Groza, J.; Pearce, J.M. Residential Sizing of Solar Photovoltaic Systems and Heat Pumps to Provide Net Zero Sustainable Electrical and Thermal Building Energy. *Open Sci. Framew.* 2023. Available online: https://osf.io/msrgk, (accessed on 19 July 2023).
101. Knapstein, K. Below-Grade Insulation—Part 2: Preventing Heat Transfer. Available online: https://framebuildingnews.com/below-grade-insulation-part-2-preventing-heat-transfer/ (accessed on 12 February 2024).

102. Horan, P.; Luther, M.B. Using the Psychrometric Chart in Building Measurements. In Proceedings of the 44th Annual Conference of the Architectural Science Association, Auckland, New Zealand, 24 November 2010; pp. 1–8.
103. Heat Pump | GSZ16 | up to 16 SEER | 9.0 HSPF | Goodman. Available online: https://www.goodmanmfg.com/products/heat-pumps/16-seer-gsz16 (accessed on 8 January 2023).
104. Li, S.; Gong, G.; Peng, J. Dynamic Coupling Method between Air-Source Heat Pumps and Buildings in China's Hot-Summer/Cold-Winter Zone. *Appl. Energy* **2019**, *254*, 113664. [CrossRef]
105. Hayibo, K.S.; Pearce, J.M. Vertical Free-Swinging Photovoltaic Racking Energy Modeling: A Novel Approach to Agrivoltaics. *Renew. Energy* **2023**, *218*, 119343. [CrossRef]
106. Hayibo, K.S.; Pearce, J.M. Vertical Free-Swinging Photovoltaic Racking Energy Modelling—Data and Performance Code. *Open Sci. Framew.* 2023. Available online: https://osf.io/jhx4b/ (accessed on 27 July 2023).
107. Vandewetering, N.; Hayibo, K.S.; Pearce, J.M. Impacts of Location on Designs and Economics of DIY Low-Cost Fixed-Tilt Open Source Wood Solar Photovoltaic Racking. *Designs* **2022**, *6*, 41. [CrossRef]
108. Ciocia, A.; Amato, A.; Di Leo, P.; Fichera, S.; Malgaroli, G.; Spertino, F.; Tzanova, S. Self-Consumption and Self-Sufficiency in Photovoltaic Systems: Effect of Grid Limitation and Storage Installation. *Energies* **2021**, *14*, 1591. [CrossRef]
109. Zheng, Z.; Zhuang, Z.; Lian, Z.; Yu, Y. Study on Building Energy Load Prediction Based on Monitoring Data. *Procedia Eng.* **2017**, *205*, 716–723. [CrossRef]
110. An, J.; Yan, D.; Hong, T. Clustering and Statistical Analyses of Air-Conditioning Intensity and Use Patterns in Residential Buildings. *Energy Build.* **2018**, *174*, 214–227. [CrossRef]
111. SunPower M Series SPR-M430-H-AC | EnergySage. Available online: https://www.energysage.com/solar-panels/sunpower/2730/SPR-M430-H-AC/ (accessed on 28 May 2024).
112. Abbes, D.; Martinez, A.; Champenois, G. Life Cycle Cost, Embodied Energy and Loss of Power Supply Probability for the Optimal Design of Hybrid Power Systems. *Math. Comput. Simul.* **2014**, *98*, 46–62. [CrossRef]
113. Coppitters, D.; De Paepe, W.; Contino, F. Robust Design Optimization of a Photovoltaic-Battery-Heat Pump System with Thermal Storage under Aleatory and Epistemic Uncertainty. *Energy* **2021**, *229*, 120692. [CrossRef]
114. Wolisz, H.; Schütz, T.; Blanke, T.; Hagenkamp, M.; Kohrn, M.; Wesseling, M.; Müller, D. Cost Optimal Sizing of Smart Buildings' Energy System Components Considering Changing End-Consumer Electricity Markets. *Energy* **2017**, *137*, 715–728. [CrossRef]
115. Liu, X.; Zhang, P.; Pimm, A.; Feng, D.; Zheng, M. Optimal Design and Operation of PV-Battery Systems Considering the Interdependency of Heat Pumps. *J. Energy Storage* **2019**, *23*, 526–536. [CrossRef]
116. Duman, A.C.; Erden, H.S.; Gönül, Ö.; Güler, Ö. Optimal Sizing of PV-BESS Units for Home Energy Management System-Equipped Households Considering Day-Ahead Load Scheduling for Demand Response and Self-Consumption. *Energy Build.* **2022**, *267*, 112164. [CrossRef]
117. Fioriti, D.; Pellegrino, L.; Lutzemberger, G.; Micolano, E.; Poli, D. Optimal Sizing of Residential Battery Systems with Multi-Year Dynamics and a Novel Rainflow-Based Model of Storage Degradation: An Extensive Italian Case Study. *Electr. Power Syst. Res.* **2022**, *203*, 107675. [CrossRef]
118. Cruz-Peragón, F.; Gómez-de La Cruz, F.J.; Palomar-Carnicero, J.M.; López-García, R. Optimal Design of a Hybrid Ground Source Heat Pump for an Official Building with Thermal Load Imbalance and Limited Space for the Ground Heat Exchanger. *Renew. Energy* **2022**, *195*, 381–394. [CrossRef]
119. Government of Canada, Canada Energy Regulator. CER—Provincial and Territorial Energy Profiles—Ontario. Available online: https://www.cer-rec.gc.ca/en/data-analysis/energy-markets/provincial-territorial-energy-profiles/provincial-territorial-energy-profiles-ontario.html (accessed on 28 November 2023).
120. Household Energy Use and Greenhouse Gas Emissions. Available online: https://caroliniancanada.ca/article/household-energy-use-and-greenhouse-gas-emissions-20201125 (accessed on 28 November 2023).
121. Melo, F.C.; Carrilho da Graça, G.; Oliveira Panão, M.J.N. A Review of Annual, Monthly, and Hourly Electricity Use in Buildings. *Energy Build.* **2023**, *293*, 113201. [CrossRef]
122. Ermel, C.; Bianchi, M.V.A.; Cardoso, A.P.; Schneider, P.S. Thermal Storage Integrated into Air-Source Heat Pumps to Leverage Building Electrification: A Systematic Literature Review. *Appl. Therm. Eng.* **2022**, *215*, 118975. [CrossRef]
123. Li, Y.; Rosengarten, G.; Stanley, C.; Mojiri, A. Electrification of Residential Heating, Cooling and Hot Water: Load Smoothing Using Onsite Photovoltaics, Heat Pump and Thermal Batteries. *J. Energy Storage* **2022**, *56*, 105873. [CrossRef]
124. Aneli, S.; Arena, R.; Marco Tina, G.; Gagliano, A. Improvement of Energy Self-Sufficiency in Residential Buildings by Using Solar-Assisted Heat Pumps and Thermal and Electrical Storage. *Sustain. Energy Technol. Assess.* **2023**, *60*, 103446. [CrossRef]

MDPI AG
Grosspeteranlage 5
4052 Basel
Switzerland
Tel.: +41 61 683 77 34

Computation Editorial Office
E-mail: computation@mdpi.com
www.mdpi.com/journal/computation

Academic Open
Access Publishing

mdpi.com

ISBN 978-3-7258-3463-1